

Kamal K. Kar
Jitendra K. Pandey
Sravendra Rana *Editors*

Handbook of Polymer Nanocomposites. Processing, Performance and Application

Volume B: Carbon Nanotube Based
Polymer Composites

INCLUDED IN
SPRINGERMATERIALS.COM

 Springer

Handbook of Polymer Nanocomposites. Processing, Performance and Application

Volume B: Carbon Nanotube Based
Polymer Composites

Kamal K. Kar • Jitendra K. Pandey
Sravendra Rana
Editors

Handbook of Polymer Nanocomposites. Processing, Performance and Application

Volume B: Carbon Nanotube Based
Polymer Composites

With 265 Figures and 64 Tables

 Springer

Editors

Kamal K. Kar
Department of Mechanical Engineering
and Materials Science Programme
Indian Institute of Technology Kanpur
Kanpur, India

Jitendra K. Pandey
University of Petroleum and Energy
Studies (UPES)
Bidholi Campus Office Energy Acres
Dehradun, India

and

Advanced Nanoengineering Materials
Laboratory
Department of Mechanical Engineering
Indian Institute of Technology Kanpur
Kanpur, India

Pravendra Rana
School of Materials Science and Engineering
Nanyang Technological University
Singapore

ISBN 978-3-642-45228-4

ISBN 978-3-642-45229-1 (eBook)

DOI 10.1007/978-3-642-45229-1

Springer Heidelberg New York Dordrecht London

Library of Congress Control Number: 2013955726

© Springer-Verlag Berlin Heidelberg 2015

This work is subject to copyright. All rights are reserved by the Publisher, whether the whole or part of the material is concerned, specifically the rights of translation, reprinting, reuse of illustrations, recitation, broadcasting, reproduction on microfilms or in any other physical way, and transmission or information storage and retrieval, electronic adaptation, computer software, or by similar or dissimilar methodology now known or hereafter developed. Exempted from this legal reservation are brief excerpts in connection with reviews or scholarly analysis or material supplied specifically for the purpose of being entered and executed on a computer system, for exclusive use by the purchaser of the work. Duplication of this publication or parts thereof is permitted only under the provisions of the Copyright Law of the Publisher's location, in its current version, and permission for use must always be obtained from Springer. Permissions for use may be obtained through RightsLink at the Copyright Clearance Center. Violations are liable to prosecution under the respective Copyright Law.

The use of general descriptive names, registered names, trademarks, service marks, etc. in this publication does not imply, even in the absence of a specific statement, that such names are exempt from the relevant protective laws and regulations and therefore free for general use.

While the advice and information in this book are believed to be true and accurate at the date of publication, neither the authors nor the editors nor the publisher can accept any legal responsibility for any errors or omissions that may be made. The publisher makes no warranty, express or implied, with respect to the material contained herein.

Printed on acid-free paper

Springer is part of Springer Science+Business Media (www.springer.com)

Contents

1 The High Energy Ion Irradiation Impact on Carbon Nanotubes	1
Pankaj Koinkar, Amit Kumar, Dinesh Kumar Avasthi, Mahendra More, and Ri-ichi Murakami	
2 Surface Modification of Carbon Nanotubes for High-Performance Polymer Composites	13
Soo-Jin Park, Seul-Yi Lee, and Fan-Long Jin	
3 Mechanical Properties of Boron-Added Carbon Nanotube Yarns	61
Yoshinori Sato, Mei Zhang, and Kazuyuki Tohji	
4 Synthesis and Characterization of Poly(Phenylene Sulfide)-Grafted Carbon Nanotube Nanocomposites	75
Ana M. Díez-Pascual and Mohammed Naffakh	
5 Functionalization of Carbon Nanotubes and Their Polyurethane Nanocomposites	103
Sravendra Rana, Raghavan Prasanth, and Lay Poh Tan	
6 Electrical Conductivity and Morphology of Polyamide6/Acrylonitrile-Butadiene-Styrene Copolymer Blends with Multiwall Carbon Nanotubes: A Case Study	123
Suryasarathi Bose, Arup R. Bhattacharyya, Rupesh A. Khare, and Ajit R. Kulkarni	
7 Mechanical Behavior of Starch–Carbon Nanotubes Composites	141
Lucía M. Famá, Silvia Goyanes, Valeria Pettarin, and Celina R. Bernal	
8 PCL–CNT Nanocomposites	173
Feng Luo, Lanlan Pan, Xibo Pei, Rui He, Jian Wang, and Qianbing Wan	

9 Fabrication and Characterization of Carbon Nanotube/Cellulose Composite Paper	195
Eiichi Sano, Tomo Tanaka, and Masanori Imai	
10 Polystyrene Carbon Nanotube Nanocomposites	213
Ehsan Zeimaran, Abozar Akbarivakilabadi, and Mainak Majumder	
11 Preparation, Properties, and Processibility of Nanocomposites Based on Poly(ethylene-Co-Methyl Acrylate) and Multiwalled Carbon Nanotubes	245
Utpal Basuli, Sudipta Panja, Tapan Kumar Chaki, and Santanu Chattopadhyay	
12 Poly(lactic Acid (PLA) Carbon Nanotube Nanocomposites	283
Abozar Akbari, Mainak Majumder, and A. Tehrani	
13 Carbon Nanotube-Based Poly(ethylene oxide) Nanocomposites	299
Ramanan Krishnamoorti and Tirtha Chatterjee	
14 Advances in Carbon Nanotube Technology for Corrosion Applications	335
Alina Pruna	
15 Polymer Electrolyte Membrane Fuel Cells: Role of Carbon Nanotubes/Graphene in Cathode Catalysis	361
Raghunandan Sharma, Jayesh Cherusseri, and Kamal K. Kar	
16 Application of Carbon Nanotubes in Dye-Sensitized Solar Cells	391
Lina Ma and Haijun Niu	
17 Application of Carbon Nanotubes for Resolving Issues and Challenges on Electrochemical Capacitors	415
Raghavan Prasanth, Ravi Shankar, Nutan Gupta, Sravendra Rana, and Jou-Hyeon Ahn	
18 Advances in Lithium-Ion Battery Technology Based on Functionalized Carbon Nanotubes for Electrochemical Energy Storage	447
Raghavan Prasanth, Ravi Shankar, Nutan Gupta, and Jou-Hyeon Ahn	
19 Nanotechnology Advancements on Carbon Nanotube/Polypyrrole Composite Electrodes for Supercapacitors	479
Jayesh Cherusseri, Raghunandan Sharma, and Kamal K. Kar	
20 Carbon Nanotube for Bone Repair	511
Jayachandran Venkatesan and Se Kwon Kim	

21	The Role of CNT and CNT/Composites for the Development of Clean Energy	527
	Samantha Wijewardane	
22	CNT-Based Inherent Sensing and Interfacial Properties of Glass Fiber-Reinforced Polymer Composites	543
	Zuo-Jia Wang, Dong-Jun Kwon, Ga-Young Gu, and Joung-Man Park	
23	Polymer/Carbon Composites for Sensing	577
	Peter Lobotka and Pavol Kunzo	

Contributors

Jou-Hyeon Ahn Department of Chemical and Biological Engineering and Research Institute for Green Energy Convergence Technology, Gyeongsang National University, Jinju, Republic of Korea

Abozar Akbari Nanoscale Science and Engineering Laboratory (NSEL), Department of Mechanical and Aerospace Engineering, Monash University, Clayton, VIC, Australia

Abozar Akbarivakilabadi Nanoscale Science and Engineering Laboratory (NSEL), Department of Mechanical and Aerospace Engineering, Monash University, Clayton, VIC, Australia

Dinesh Kumar Avasthi Materials Science Group, Inter University Accelerator Centre, New Delhi, India

Utpal Basuli Rubber Technology Centre, Indian Institute of Technology, Kharagpur, India

Celina R. Bernal Grupo de Materiales Avanzados, INTECIN (UBA-CONICET), Departamento de Ingeniería Mecánica, Facultad de Ingeniería, Universidad de Buenos Aires, Ciudad Autónoma de Buenos Aires, Argentina

Arup R. Bhattacharyya Department of Metallurgical Engineering and Materials Science, Indian Institute of Technology Bombay, Powai, Mumbai, India

Suryasarathi Bose Department of Metallurgical Engineering and Materials Science, Indian Institute of Technology Bombay, Powai, Mumbai, India

Department of Materials Engineering, Indian Institute of Science, Bangalore, India

Tapan Kumar Chaki Rubber Technology Centre, Indian Institute of Technology, Kharagpur, India

Tirtha Chatterjee Analytical Sciences, The Dow Chemical Company, Midland, MI, USA

Santanu Chattopadhyay Rubber Technology Centre, Indian Institute of Technology, Kharagpur, India

Jayesh Cherusseri Advanced Nanoengineering Materials Laboratory, Materials Science Programme, Indian Institute of Technology Kanpur, Kanpur, India

Ana M. Díez-Pascual Instituto de Ciencia y Tecnología de Polímeros, ICTP-CSIC, Madrid, Spain

Lucía M. Famá Grupo de Materiales Avanzados, INTECIN (UBA–CONICET), Departamento de Ingeniería Mecánica, Facultad de Ingeniería, Universidad de Buenos Aires, Ciudad Autónoma de Buenos Aires, Argentina

LP&MC, Departamento de Física, Facultad de Ciencias Exactas y Naturales, IFIBA – CONICET, Universidad de Buenos Aires, Ciudad Autónoma de Buenos Aires, Argentina

Silvia Goyanes LP&MC, Departamento de Física, Facultad de Ciencias Exactas y Naturales, IFIBA – CONICET, Universidad de Buenos Aires, Ciudad Autónoma de Buenos Aires, Argentina

Ga-Young Gu School of Materials Science and Engineering, Engineering Research Institute Gyeongsang National University, Jinju, South Korea

Nutan Gupta School of Materials Science and Engineering, and Energy Research Institute @ NTU, Nanyang Technological University, Singapore

Rui He West China School of Stomatology, Sichuan University, Chengdu, Sichuan, China

Masanori Imai Fundamental Laboratory, Technical Research Div, Tokushu Tokai Paper, Nagaizumi, Shizuoka, Japan

Fan-Long Jin Department of Chemistry, Inha University, Nam-gu, Incheon, South Korea

Kamal K. Kar Advanced Nanoengineering Materials Laboratory, Materials Science Programme, Indian Institute of Technology Kanpur, Kanpur, India

Advanced Nanoengineering Materials Laboratory, Department of Mechanical Engineering, Indian Institute of Technology Kanpur, Kanpur, India

Rupesh A. Khare Department of Metallurgical Engineering and Materials Science, Indian Institute of Technology Bombay, Powai, Mumbai, India

Reliance Technology Centre, Reliance Industries Limited, Patalganga, Mumbai, India

Se Kwon Kim Department of Chemistry, Marine Bioprocess Research Center, Pukyong National University, Busan, Republic of Korea

Pankaj Koinkar Center for International Cooperation in Engineering Education (CICEE), University of Tokushima, Tokushima, Japan

Ramanan Krishnamoorti Department of Chemical and Biomolecular Engineering, University of Houston, Houston, TX, USA

Ajit R. Kulkarni Department of Metallurgical Engineering and Materials Science, Indian Institute of Technology Bombay, Powai, Mumbai, India

Amit Kumar School of Materials Science and Technology, Indian Institute of Technology (BHU), Varanasi, India

Pavol Kunzo Institute of Electrical Engineering, Slovak Academy of Sciences, Bratislava, Slovak Republic

Dong-Jun Kwon School of Materials Science and Engineering, Engineering Research Institute Gyeongsang National University, Jinju, South Korea

Seul-Yi Lee Korea CCS R&D Center, Korea Institute of Energy Research, Yuseoung-gu, Daejeon, South Korea

Department of Chemistry, Inha University, Nam-gu, Incheon, South Korea

Peter Lobotka Institute of Electrical Engineering, Slovak Academy of Sciences, Bratislava, Slovak Republic

Feng Luo West China School of Stomatology, Sichuan University, Chengdu, Sichuan, China

Lina Ma Key Laboratory of Functional Inorganic Material Chemistry, Ministry of Education, Department of Macromolecular Science and Engineering, Heilongjiang University, Harbin, China

Mainak Majumder Nanoscale Science and Engineering Laboratory (NSEL), Department of Mechanical and Aerospace Engineering, Monash University, Clayton, VIC, Australia

Mahendra More Department of Physics, University of Pune, Pune, India

Ri-ichi Murakami Department of Mechanical Engineering, University of Tokushima, Tokushima, Japan

Mohammed Naffakh Departamento de Ingeniería y Ciencia de Los Materiales, Escuela Técnica Superior de Ingenieros Industriales, Universidad Politécnica de Madrid, Madrid, Spain

Haijun Niu Key Laboratory of Functional Inorganic Material Chemistry, Ministry of Education, Department of Macromolecular Science and Engineering, Heilongjiang University, Harbin, China

Lanlan Pan Department of Periodontics, The Affiliated Stomatology Hospital of Chongqing Medical University, Chongqing, China

Sudipta Panja Rubber Technology Centre, Indian Institute of Technology, Kharagpur, India

Joung-Man Park School of Materials Science and Engineering, Engineering Research Institute Gyeongsang National University, Jinju, South Korea

Department of Mechanical Engineering, The University of Utah, Salt Lake City, UT, USA

Soo-Jin Park Korea CCS R&D Center, Korea Institute of Energy Research, Yuseoung-gu, Daejeon, South Korea

Department of Chemistry, Inha University, Nam-gu, Incheon, South Korea

Xibo Pei West China School of Stomatology, Sichuan University, Chengdu, Sichuan, China

Valeria Pettarin Grupo de Ciencia e Ingeniería de Polímeros, INTEMA (UNMdP-CONICET). Departamento de Ingeniería en Materiales, Universidad Nacional de Mar del Plata, Mar del Plata, Argentina

Raghavan Prasanth Department of Materials Science and Nanoengineering, Rice University, Houston, TX, USA

School of Materials Science and Engineering, and Energy Research Institute @ NTU, Nanyang Technological University, Singapore, Singapore

Department of Chemical and Biological Engineering and Research Institute for Green Energy Convergence Technology, Gyeongsang National University, Jinju, Republic of Korea

Alina Pruna University Bucharest, Bucharest – Magurele, Romania

Institute of Materials Technology, University Politecnica de Valencia, Valencia, Spain

Sravendra Rana School of Materials Science and Engineering, and Energy Research Institute @ NTU, Nanyang Technological University, Singapore

Institute of Chemistry, Martin-Luther University Halle-Wittenberg, Halle (Saale), Germany

Eiichi Sano Research Center for Integrated Quantum Electronics, Hokkaido University, Sapporo, Hokkaido, Japan

Yoshinori Sato Graduate School of Environmental Studies, Tohoku University, Sendai, Japan

PRESTO, Japan Science and Technology Agency, Saitama, Japan

Ravi Shankar Nanoscience and Engineering Program, South Dakota School of Mines and Technology, Rapid City, SD, USA

Raghuandan Sharma Advanced Nanoengineering Materials Laboratory, Materials Science Programme, Indian Institute of Technology Kanpur, Kanpur, India

Lay Poh Tan School of Materials Science, Nanyang Technological University, Singapore

Tomo Tanaka Research Center for Integrated Quantum Electronics, Hokkaido University, Sapporo, Hokkaido, Japan

A. Tehrani School of Industrial Technology, Universiti Sains Malaysia, USM, Penang, Malaysia

Kazuyuki Tohji Graduate School of Environmental Studies, Tohoku University, Sendai, Japan

Jayachandran Venkatesan Department of Chemistry, Marine Bioprocess Research Center, Pukyong National University, Busan, Republic of Korea

Qianbing Wan Department of Prosthodontics, West China School of Stomatology, Sichuan University, Chengdu, Sichuan, China

Jian Wang Department of Prosthodontics, West China School of Stomatology, Sichuan University, Chengdu, Sichuan, China

Zuo-Jia Wang School of Materials Science and Engineering, Engineering Research Institute Gyeongsang National University, Jinju, South Korea

Samantha Wijewardane Clean Energy Research Center, College of Engineering, University of South Florida, Tampa, FL, USA

Ehsan Zeimaran Department of Polymer Engineering, Faculty of Chemical Engineering, Universiti Teknologi Malaysia, Johor Bahru, Malaysia

Mei Zhang High-Performance Materials Institute, Florida State University, Tallahassee, FL, USA

Department of Industrial and Manufacturing Engineering, FAMU-FSU College of Engineering, Tallahassee, FL, USA

The High Energy Ion Irradiation Impact on Carbon Nanotubes

1

Pankaj Koinkar, Amit Kumar, Dinesh Kumar Avasthi,
Mahendra More, and Ri-ichi Murakami

Contents

1	Introduction	2
2	Synthesis, Ion Irradiation, and Field Emission Measurement	3
2.1	Synthesis of MWCNT	3
2.2	Synthesis of DWCNT	4
2.3	Ion irradiation	4
2.4	Field Emission Measurement of MWCNTs and DWCNTs	4
3	Field Emission Properties from Carbon Nanotubes	5
4	Impact of High-Energy Ion Irradiation	10
	References	10

Abstract

High-energy ion irradiation can create defects, defects annealing depending on various parameters such as ion fluence and the energy loss of ions in the materials. The present report is concerned with the field emission properties of

P. Koinkar (✉)

Center for International Cooperation in Engineering Education (CICEE), University of Tokushima, Tokushima, Japan

e-mail: koinkar@tokushima-u.ac.jp

A. Kumar

School of Materials Science and Technology, Indian Institute of Technology (BHU), Varanasi, India

D.K. Avasthi

Materials Science Group, Inter University Accelerator Centre, New Delhi, India

M. More

Department of Physics, University of Pune, Pune, India

R. Murakami

Department of Mechanical Engineering, University of Tokushima, Tokushima, Japan

ion-irradiated multiwalled carbon nanotubes (MWCNTs) and double-walled carbon nanotubes (DWCNTs). The carbon nanotubes synthesized by a chemical vapor deposition method were irradiated by high-energy (90 MeV) Au ions with different ion fluence from 4×10^{11} to 1×10^{13} ions/cm². After ion irradiation, the field emission properties of MWCNTs and DWCNTs were greatly influenced. The change in the emission characteristics is due to structural defects caused by the high-energy ion irradiation. The emission characteristic of MWCNTs was improved and turn-on field decreased from 5.43 to 3.10 V/μm by ion irradiation. Noticeable improvement in emission characteristics of MWCNTs was observed at a fluence of 1×10^{13} ions/cm². The emission characteristics of DWCNTs deteriorated and the turn-on field was increased from 2.44 to 7.76 V/μm. This results show the distinctly different behavior of ion-irradiated MWCNTs and DWCNTs.

Keywords

Carbon nanotube • Field emission • Irradiation

1 Introduction

The carbon nanotubes (CNTs) have attracted much attention because of their high aspect ratio, excellent electrical conductivity, chemical stability, and mechanical robustness [1–4]. Among the various applications due to their unique and excellent properties, field emission displays (FEDs) and other vacuum microelectronics devices are being considered for the realistic applications area because of their high aspect ratio leading to high electric field enhancement and low operating voltage [5–7].

There have been great advances in fundamental properties and applications of the field emission from CNTs. Especially, enormous efforts in controlling and modifying their unique structure and remarkable properties induced many kinds of field emission applications. It is well known that surface modification of CNTs is preferable to obtain the high-performance field emitters. According to previous works, the improvement in the emission characteristics of CNT could be achieved by various surface treatments such as plasma treatment, laser irradiation, focused ion beam, and ion irradiation [8–12].

The effect of ion irradiation on the solid surface has been extensively studied due to its scientific and technological importance. Ion irradiation can change the physical and chemical properties as well as modify the morphology of solid surface because of lattice damage, ion sputtering, ion-induced diffusion, and chemical reaction which either change sp² content of G phase or decrease sp³ content of D phase. The ion irradiation creates local amorphous region and re crystallizes the lattice. The possible surface modification depends on the type of ion-irradiated material.

Despite the technical importance and its unique features, there have been very few reports about ion irradiation effects on CNTs, especially surface changes and structure destruction. Several studies have been carried out to change the

morphology and the properties of CNTs using ion irradiation. Wei et al. performed the 50 keV Ga⁺ ion irradiation on MWCNTs and showed the formation of highly ordered pillbox-like nanocompartment [13]. The nanotubes defects could be formed by introducing the irradiation with highly charged particles. It has been shown that both electron and heavy ion irradiation could modify the structure and the dimension of the CNTs [14, 15]. Zhu et al. have shown that energetic Ar⁺ ion irradiation generates dangling bonds (vacancies) on the surface of CNTs [16]. Some research groups reported that ion irradiation is an effective tool to modify the surface and dimension of CNTs [17, 18].

Recently, studies on effects of laser and energetic ion irradiation and its field emission studies of fullerene and MWCNTs have been extensively studied [19, 20]. A. Kumar et al. has illustrated that the ordering of carbon nanostructure under high energetic ion irradiation at low fluence ($<5 \times 10^{11}$ ions/cm²) [19]. This report confirms that the improvement of vibration strength in low-fluence irradiated carbon nanostructured films. The effect of intense laser and energetic ion irradiation on Raman modes of MWCNTs shows that the decrease of disordered parameter (I_D/I_G) in case of laser-irradiated MWCNTs indicates the purification of carbon nanotubes' at low fluence while a damage in carbon nanotube's high-fluence irradiation [20].

Moreover, the influence of high-energy electron irradiation on field emission properties of MWCNT films deposited on silicon studied by S. Patil et al. [21]. The result shows that the field emission properties observed to improve after high electron irradiation. The high electron irradiation causes the separation and improvement in the structural quality of nanotubes due to removal of carbon particles/clusters adhered to the wall nanotubes.

Interestingly, it has been reported that low-energy ion irradiation can improve the field emission characteristics of CNTs. Kim et al. successfully demonstrated that the CNTs with Ar ion irradiation exhibited better field emission characteristics due to the straightening of CNTs and the increase in the number of defects [11, 22]. However, in most cases, low Z ion mainly has been used with low energy of about 30 keV to few MeV. We considered that, in case of ion irradiation, the structural modification is generated as a function of energy and mass of incident ion. Thus, we use high Z ion with high energy to get more concrete effects of ion irradiation. In this report, the effect of high-energy ion irradiation on the field emission characteristics of MWCNTs and DWCNTs has been investigated. Our purpose is to modify the morphology and structure of CNTs and to evaluate the emission characteristics of CNTs with ion irradiation treatment.

2 Synthesis, Ion Irradiation, and Field Emission Measurement

2.1 Synthesis of MWCNT

The synthesis of as-grown MWCNTs was carried out using chemical vapor deposition (CVD). The n-Si substrate, on which Fe catalyst with thickness of 10 nm was

sputtered, is used to grow the MWCNTs. The acetylene (C_2H_2) and ammonia (NH_3) were used as source gases with a flow rate of 30 sccm and 300 sccm for 10 min at $750\text{ }^\circ\text{C}$, respectively. The NH_3 pretreatment was employed prior to the growth of MWCNTs.

2.2 Synthesis of DWCNT

As-grown DWCNTs were synthesized by CVD using Fe–Mo/MgO catalysts. The synthesis was carried out in a quartz tube reactor (70 mm i.d., and 700 mm long) mounted in a tube furnace. Fe–Mo catalyst ($\sim 200\text{ mg}$) was put into a quartz boat at the center of the reactor tube and then quartz tube was heated up to $900\text{ }^\circ\text{C}$ in an Ar atmosphere. The DWCNTs were grown with gas flow of CH_4 (300 sccm) and a mixture of Ar (500 sccm) and H_2 (100 sccm) for 20 min at $900\text{ }^\circ\text{C}$.

2.3 Ion irradiation

The ion irradiation was carried out using 90 MeV Au ion at room temperature from 15 UD pelletron accelerator. The ion current was about 1 pA (particle nanoampere) which is equivalent to $\sim 6.25 \times 10^9$ ions/s. The samples were mounted inside the irradiation chamber which was evacuated at $\sim 1 \times 10^{-6}$ mbar. The samples were irradiated with different ion fluence of 4×10^{11} , 4×10^{12} , and 1×10^{13} ions/cm².

2.4 Field Emission Measurement of MWCNTs and DWCNTs

For the field emission measurement from MWCNTs and DWCNTs, we have fabricated the field emitters as follows. In case of MWCNTs, as-grown MWCNTs on n-Si/Fe(10 nm) are used as cathode. For DWCNTs, field emitters were fabricated by depositing DWCNTs on Ag paste-coated n-Si substrate using a sieving method with brush. The substrate was dried in air for 1 h, followed by baking at $80\text{ }^\circ\text{C}$ for 1 h for keeping good adhesion and ohmic contact property between DWCNTs and substrates.

The field emission studies of as-grown and Au^+ ion-irradiated CNTs were carried out in a vacuum chamber with a base pressure $\sim 2 \times 10^{-7}$ torr. The CNT films were used as cathode and stainless steel plate ($\Phi = 5\text{ mm}$) was used as anode. The distance between anode and cathode was $300\text{ }\mu\text{m}$ and the measured emission area was 0.19625 cm^2 . Emission current was measured with a Keithley 6517 A, and DC power was supplied with a constant voltage and current controller (HCN140–3500 of Hochspannungs-Netzgerät: 0–3.5 kV, 0–40 mA). The macroscopic field was defined as the values of applied voltages divided by the gap between the anode and cathode.

3 Field Emission Properties from Carbon Nanotubes

The MWCNTs, used in present work, were prepared by CVD method and are about 30 nm diameter and 4.5 μm in length. The typical results of emission current density (J) and electric field (E) for as-grown and ion-irradiated MWCNTs are presented in Fig. 1.1a. In this work, the MWCNTs were irradiated with by Au^+ ion with 90 MeV at different ion fluence of 4×10^{11} , 4×10^{12} , and 1×10^{13} ions/ cm^2 . The J - E characteristic shows very different results in ion-irradiated MWCNTs and DWCNTs. Here the turn-on field and threshold field are defined as the electric field at which emission current reaches to $3 \mu\text{A}/\text{cm}^2$, and $1 \text{mA}/\text{cm}^2$ respectively. It can be seen that the turn-on field and threshold field of as-grown MWCNTs are found to be 3.52 and 5.41 $\text{V}/\mu\text{m}$, respectively. The emission of electrons comes from the CNT tips only. The field emission properties are relatively steady after voltage cycling.

After the irradiation, at ion fluence of 4×10^{11} ions/ cm^2 , the turn-on field and threshold field are measured to be 3.66 and 5.31 $\text{V}/\mu\text{m}$, respectively. These values

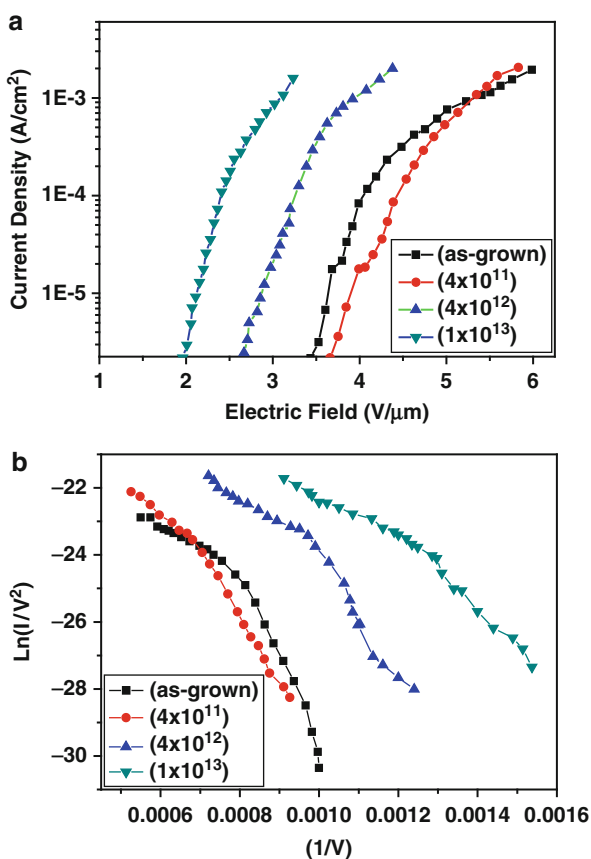


Fig. 1.1 (a) J - E characteristics of as-grown and irradiated MWCNTs. (b) Corresponding F - N plots of as-grown and irradiated MWCNTs

are almost comparable with as-grown MWCNTs sample. But, the careful observation of J - E characteristics of MWCNT at ion fluence 4×10^{11} ions/cm² reveals that the emission current density increases slightly above the threshold field because of irradiation as compared to as-grown MWCNTs. In general, electrons transport along the NTs and could emit from the CNT tips. However, if the defects are created on the walls of NTs due to irradiation, then electron could emit from there as well. The energetic ions strike the CNTs tips and protruding CNT tips are destroyed gradually. Subsequently, the non-protruding CNT tips start to emit because the number of sites was increased after the irradiation at ion dose of 4×10^{11} ions/cm². As a result of this, the improvement in the emission current above the threshold field was observed as compared to as-grown MWCNTs.

The turn-on field and threshold field are decreased further from 2.69 to 2.01 V/ μ m and 3.92 to 3.10 V/ μ m respectively for an increase in ion fluence of 4×10^{12} , and 1×10^{13} ions/cm². The noticeable improvement in the emission characteristics of MWCNTs was observed for ion fluence of 1×10^{13} ions/cm². The highest emission current density of 1 mA/cm² at electric field as low as 3.10 V/ μ m has been seen for ion fluence of 1×10^{13} ions/cm². Hence the ion irradiation of MWCNTs with different ion fluence exhibits the enhancement in the emission current density and reduction in the threshold field. The reduction in the electric field may be attributed to the surface modification in NTs. The incident ion creates the defects into the outer NT wall of the surface. These defects on the outer wall could be responsible for increase in the emission sites favorable for field emission. Although the electrons emit from CNT tips before ion irradiation, majority of electrons come from the defects-induced walls of CNTs after the ion irradiation. As the ion fluence increases, more protruding features could be generated by the impact of highly energetic ion. Each ion may produce a protrusion since incident ion pass through surface which causes damage protrusion. Thus the increase in the number of defects and surface modification due to ion irradiation plays a vital role in exhibiting better field emission characteristics.

According to the Fowler–Nordheim (F–N) equation, the field emission current density (J) is given by

$$J = A(\beta^2 V^2 / \phi d^2) \exp\left(-B\phi^{3/2} d / \beta V\right)$$

where $A (= 1.54 \times 10^{-6} \text{ (AV}^{-2} \text{ eV)})$ and $B (= 6.83 \times 10^9 \text{ (VeV}^{-3/2} \text{ Vm}^{-1}))$ are the proportionality constants, β is the field enhancement factor, ϕ is the work function, $E = (V/d)$, d is the distance between anode and cathode, and V is the applied voltage [23, 24]. β can be calculated as $\beta = -6.83 \times 10^9 \times \Phi^{3/2} / m$, where m is the slope obtained from the F–N plot. Figure 1.1b shows F–N plots of as-grown and ion-irradiated MWCNTs. The field enhancement factor β is found to be increased from 833 to 2,071. The increase in the field enhancement factor can be explained as follows. After ion irradiation, most of the CNTs have sharp tips and these sharpened tips may act as sharp field emitters. Moreover, the CNTs may be well separated on the surface which reduces the screening effect between two neighboring tips.

The MWCNT films irradiated with different ion fluence have lower threshold field as compared to as-grown film. This is attributed to the defects generation on the wall of CNTs. The better emission may be due to existence of the defects, and these defects also contribute to the electron field emission as the tips of CNTs. A detailed explanation is given below. It is believed that the ion irradiation effects in CNTs are different from those occur in common crystals. During the ion irradiation treatment, ion preferentially attacks the protruding CNTs tips and wall of the CNTs and generates planer defects on the walls of CNTs. When an energetic ion strikes on the CNTs, it transfers energy to one to three atoms in the uppermost shell by creating many primary carbon recoils and a single-/multiple-atoms vacancy. It is shown that, for MWCNTs, ion-irradiation produced vacancies in graphene networks and causes removal of many carbon atoms from sp^2 -bonded carbon nets of NTs and intershell links due to the saturation of dangling bonds at carbon interstitials and atoms nearby the vacancies [13, 25–29]. The number of defects in CNTs can be created if the incident ion energetic is enough to displace the carbon atom. Upon ion irradiation, the number of structural defects and amorphous carbon increases the degree of disorder produced, due to the mechanical impact of high energetic ion. Pomoell et al. performed the simulation about high-energy ion irradiation on MWCNTs [30]. They explained that the damage created in the NTs quickly increases with irradiation fluence. But, at higher ion fluence, the number of defects saturates, because at certain irradiation fluence, the system has reaches the degree of disorder so large that incoming ion will not result in any further significant change on the wall of CNTs. Recently, there are few reports on the ion irradiation of MWCNTs which explain that the irradiation-induced defects appear hillock-like protrusions on the CNT wall [27, 31–34] and number of defects with formation of nanocompartment with bamboo-like structure inside the tube after ion irradiation [35].

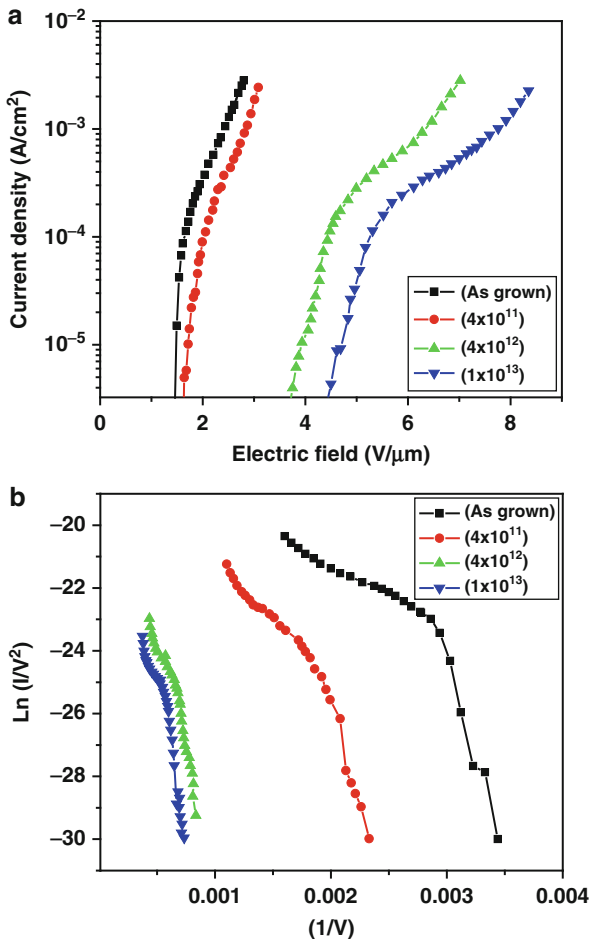
However, the effect of plasma ion irradiation for the improvement of field emission properties has been studied by several researchers [8, 9, 36–45]. It is proved that the improvement in the field emission characteristics occurs for MWCNTs irradiated with Ga^+ ion with energy 30 keV at low ion fluence. The enhancement in field emission characteristics is due to ion irradiation, which creates more the emission site and, presumably, lowers the work function, by dangling bonds [9]. Moreover, the Ar^+ plasma treated MWCNT gives rise to better field emission properties. After Ar ion plasma treatment, Ar ion penetrates the layer of CNTs which leads to formation of dangling bonds. The dangling bonds on the top of the surface works as emission site to enhance the field emission [8]. The oxygen plasma treatment has been employed to improve the field emission characteristics of MWCNT. The density of CNTs decreases as results of CNTs destruction after plasma treatment. The graphitic structure of the outer wall of the NTs was destroyed and the tips of the CNTs were sharpened by plasma treatment. The structural defects serve as emission sites. Thus the defects and sharpened tip are the main reasons for enhanced field emission properties after O_2 plasma treatment [36].

According to some research group, the enhancement in the field emission characteristics after plasma treatment is due the change in surface morphology,

formation of nanoparticle, and structural defects [37–39]. Similar studies have been carried to improve the field emission properties of CNTs with Ar, O₂, and H₂ plasma treatments. After the plasma treatment, the amorphorism of CNT structure was produced with few defects such as dangling bonds, interlayer cross-linking, sp³ defects, and the structural changes in surface due to high energetic ion bombardment from the plasma. Thus the improvement in field emission performance of CNTs was attributed to the surface reconstruction, many defects, and sharpening of emitter [40, 41]. Recently similar reports appeared on the enhancement in the field emission properties of aligned MWCNTs after laser irradiation and plasma ion (like CF₄ and O₂ and Ar) irradiation [42–45]. According to these reports, the possible factors for increase in field emission properties of CNTs after ion bombardment by plasma treatment are structure modification, reduction in surface density, generation of large defects, formation of sharp CNT tips, and reduction of work function of CNT film. The above all results are based on the plasma and laser ion irradiation with low energy about few keV. However, present study shows the field emission improvement after high-energy (90 MeV) ion irradiation. We suggest that the enhancement in the current density and decrease in the threshold field probably come from the generation number of defects into the outer NT wall of the surface. The presence of the defects on the surface of CNTs greatly influences the structural transformation in the CNT structure under high-energy ion irradiation. The increase in the structural defects is the origin of generating more emitting site which easily emits the electrons and also contributes for better field emission characteristics of MWCNT films. Thus, the change in electronic structure (like defects on the wall of the NTs) caused by ion irradiation is an effective way to enhance the field emission properties of CNTs.

The emission current density (J) and electric field (E) characteristics for as-grown and ion-irradiated DWCNTs are presented in Fig. 1.2a. In this work, the DWCNTs were irradiated by 90 MeV Au ion different ion fluence of 4×10^{11} , 4×10^{12} , and 1×10^{13} ions/cm². The J–E characteristic shows very different results as compared to irradiated MWCNTs with increase in ion fluence. The turn-on field and threshold field of as-grown DWCNTs are found to be 1.46 and 2.44 V/μm, respectively. After irradiation at ion dose of 4×10^{11} ions/cm², the turn-on field and threshold field are increased to be 1.63 and 2.85 V/μm, respectively. Also, the current density has been decreased with increase in ion irradiation. These results are in contrary to those reported above for MWCNT. In case of MWCNTs, the change in ion fluence leads to the significant improvement in emission current density and the enhancement in field emission characteristics and this is because of defects generated by irradiation. But, in case of DWCNTs, we observed the degradation of emission current which may be attributed to severe structural damages created during ion irradiation. At ion fluence of 4×10^{12} ions/cm² and 1×10^{13} ions/cm², the turn-on fields are increased from 3.70 to 4.44 V/μm, while threshold fields are also increased from 6.35 to 7.76 V/μm. Figure 1.2b shows F–N plots of as-grown and ion-irradiated MWCNTs. The field enhancement factor β is found to be decreased from 1,386 to 920. This clearly shows the reduction in emission current density of DWCNTs with ion irradiation treatment. Hence, the ion irradiation of DWCNTs with different ion fluence exhibits the

Fig. 1.2 (a) J–E characteristics of as-grown and irradiated DWCNTs. (b) Corresponding F–N plots of as-grown and irradiated DWCNTs



degradation in the emission current density and increase in the threshold field, which deteriorate the emission characteristics.

The reason for degradation in the emission characteristics and increase in the electric field of DWCNTs is quite different from those of MWCNTs. After ion irradiation with high ion fluence, the DWCNTs quickly undergo structural modification as compared to MWCNTs. During the high energetic ion bombardment, the DWCNTs are subjected to structural change because of continuous collisions of Au ions with the carbon atoms in DWCNTs. At the end of the ion irradiation, the structural rearrangement into graphene layers of DWCNTs took place. The Au ion passes through the uppermost graphitic layer of the DWCNTs and ion can penetrate the second graphitic layer as well. Hence, ion irradiation leads to deterioration and finally amorphization of the CNT wall resulting in a noticeable loss of mechanical strength to the bundles of DWCNTs. Thus, the mechanical damage results in the severe destruction of DWCNTs. Since DWCNTs exhibit less mechanical

strength than MWCNTs, the mechanical damage caused by the high ion irradiation may not be resisted by DWCNTs which leads to amorphization. Therefore, the graphite structure of the wall of DWCNTs may be destroyed. The possible justification is that, since the DWCNTs have only two graphene layers, ion irradiation causes more damage on the walls of NTs. This will generate defects and original graphitic structure may be destroyed. The mechanical damage quickly increases with increase in ion fluence. As ion fluence increases, there will be more and more destruction of DWCNTs caused by mechanical impact of accelerated high-energy ion irradiation. Hence, more structural damage of DWCNTs results in degradation of field emission characteristics.

4 Impact of High-Energy Ion Irradiation

The field emission characteristics of MWCNTs and DWCNTs are significantly influenced by high-energy Au⁺ ion irradiation. The noticeable improvement has been observed in the emission current from MWCNTs and degradation in emission current from DWCNTs after high-energy Au ion irradiation treatment. The enhancement in emission characteristics of MWCNTs is due to defects created on the wall of CNTs caused by Au⁺ ion irradiation. On the other hand, in case of DWCNTs, the degradation in emission current density is due to more destruction of DWCNTs caused by higher excessive defect generated by high-energy ion. This clearly suggests that MWCNTs have more radiation resistance than DWCNTs. This study gives a contrasting behavior of DWCNTs and MWCNTs under high-energy ion irradiation.

References

1. Iijima S (1991) Helical microtubules of graphitic carbon. *Nature* 354:56
2. Smith BW, Monthieux M, Luzzi DE (1998) Encapsulated C60 in carbon nanotubes. *Nature* 396:323
3. Meyer RR, Sloan J, Dunin-Borkowski RE, Kirkland AI, Novotny MC, Bailey SR, Hutchison JL, Green MLH (2001) Discrete atom imaging of one dimensional crystals formed within single walled carbon nanotubes. *Science* 289:1324
4. Dresselhaus MS, Dresselhaus G, Avouris P (2001) Carbon nanotubes; synthesis, structure, properties, and application. Springer, Heidelberg
5. de Heer WA, Chatelain A, Ugarte D (1995) Nanotubes and the pursuit of applications. *Science* 270:1179
6. Tans SJ, Devoret MH, Dai H, Thess A, Smalley RE, Geerli LJ, Dekker C (1997) Individual single-wall carbon nanotubes as quantum wires. *Nature (London)* 386:474
7. Wang H, Corrigan TD, Dai JY, Chang RPH, Krauss AR (1997) Field emission from nanotube bundle emitters at low fields. *Appl Phys Lett* 70:3308
8. Kanazawa Y, Oyama T, Murakami K, Takai M (2004) Improvement in electron emission from carbon nanotube cathodes after Ar plasma treatment. *J Vac Sci Technol B* 22:1342
9. Sawada A, Iriguchi M, Zhao WJ, Ochiai C, Takai M (2002) Emission site control in carbon nanotube field emitters by focused ion and laser irradiation. *J Vac Sci Technol B* 21:362

10. Chai G, Lee C, Zhou D, Byahut SR (2005) Focused-ion-beam assisted fabrication of individual multiwall carbon nanotube field emitter. *Carbon* 43:2083
11. Kim DH, Kim CD, Lee HR (2004) Effects of the ion irradiation of screen-printed carbon nanotubes for use in field emission display applications. *Carbon* 42:1807
12. Hwang JD, Chen KF, Chan LH, Chang YY (2006) Using infrared laser to enhance field emission of carbon nanotube. *Appl Phys Lett* 89:033103
13. Wei BQ, D'Arcy-Gall J, Ajayan PM, Ramanath G (2003) Tailoring structure and electrical properties of carbon nanotubes using kilo-electron-volt ions. *Appl Phys Lett* 83:3581
14. Ajayan PM, Ravikumar V, Charlier JC (1998) Surface Reconstructions and Dimensional Changes in Single-Walled Carbon Nanotubes. *Phys Rev Lett* 81:1437
15. Raghuvveer MS, Ganeshan PG, D'Arcy-Gall JDJ, Ramanath G (2004) Nanomachining carbon nanotubes with ion beams. *Appl Phys Lett* 84:4484
16. Zhu Y, Yi T, Zheng B, Cao L (1999) The interaction of C60 fullerene and carbon nanotube with Ar ion beam. *Appl Surf Sci* 137:83
17. Krashinnov A, Nordlund K (2004) Irradiation effects in carbon nanotubes. *Nucl Instrum Methods B* 216:355
18. Hashimoto A, Suenaga K, Glotter A, Urita K, Ijima S (2004) Direct evidence for atomic defects in graphene layers. *Nature* 430:870
19. Kumar A, Avasthi DK, Pivin JC, Koinkar PM (2008) Ordering of fullerene and carbon nanotube thin films under energetic ion impact. *Appl Phys Lett* 92:221904
20. Kumar A, Singh F, Koinkar PM, Avasthi DK, Pivin JC, More MA (2009) Effect of intense laser and energetic ion irradiation on Raman modes of Multiwalled Carbon Nanotubes. *Thin Solid Films* 517:4322–4324
21. Patil SS, Koinkar PM, Dhole SD, More MA, Murakami R (2011) Influence of high-energy electron irradiation on field emission properties of multi-walled carbon nanotubes (MWCNTs) films. *Physica B* 406:1809–1813
22. Kim DH, Jang SH, Kim CD, Cho DS, Kang HD, Lee HR (2003) Enhancement of the field emission of carbon nanotubes straightened by application of argon ion irradiation. *Chem Phys Lett* 378:232
23. Lee CJ, Lee TJ, Lyu SC, Zhang Y, Ruh H, Lee HJ (2001) Field emission from well-aligned zinc oxide nanowires grown at low temperature. *Appl Phys Lett* 81(19):3648
24. Araki H, Katayama T, Yoshino K (2001) Field emission from aligned carbon nanotubes prepared by thermal chemical vapor deposition of Fe-phthalocyanine. *Appl Phys Lett* 79(16):2636
25. Krashennnikov AV, Nordlund K, Sirviö M, Salonen E, Keinonen J (2000) Formation of ion-irradiation-induced atomic-scale defects on walls of carbon nanotubes. *Phys Rev B* 63:245405
26. Krashennnikov AV, Nordlund K, Keinonen J (2002) Production of defects in supported carbon nanotubes under ion irradiation. *Phys Rev B* 65:165423
27. Osvath Z, Vertesy G, Tapasztó L, Weber F, Horvath ZE, Gyulai J, Biro LP (2005) Atomically resolved STM images of carbon nanotube defects produced by Ar⁺ irradiation. *Phys Rev B* 72:045429
28. Jeong GH, Hatakeyama R, Hirata T, Tohji K, Motomiya K, Sato N, Kawazoe Y (2001) Structural deformation of single-walled carbon nanotubes and fullerene encapsulation due to magnetized-plasma ion irradiation. *Appl Phys Lett* 79:4213
29. Suzuki M, Ishibashi K, Toratani K, Tsuya D, Aoyagi Y (2002) Tunnel barrier formation using argon-ion irradiation and single quantum dots in multiwall carbon nanotubes. *Appl Phys Lett* 81:2273
30. Pomoell JAV, Krashinnov AV, Nordlund K, Keinonen J (2004) Ion ranges and irradiation-induced defects in multiwalled carbon nanotubes. *J Appl Phys* 96(5):2864
31. Jung YJ, Homma Y, Vajtai R, Kobayashi Y, Ogino T, Ajaya PM (2004) Straightening suspended single walled carbon nanotubes by ion irradiation. *Nano Lett* 4(6):1109

32. Jeong GH, Farajin AA, Hirata T, Hatakeyama R, Tohji K, Briere TM, Mizuseki H, Kawazoe Y (2003) Encapsulation of cesium inside single-walled carbon nanotubes by plasma-ion irradiation method. *Thin Solid Films* 435:307
33. Lim H, Jung HJ, Joo SK (2003) Control of carbon nanotube's shape by ion bombardment. *Microelectro Eng* 69:81
34. Osvath Z, Vertesy G, Tapasztó L, Weber F, Horvath ZE, Gyulai J, Biro LP (2006) Scanning tunneling microscopy investigation of atomic-scale carbon nanotube defects produced by Ar⁺ ion irradiation. *Mat Sci Eng C* 26:1194
35. Kim KM, Kim HS, Park SK, Joo J, Lee TJ, Lee CJ (2005) Morphological change of multiwalled carbon nanotubes through high-energy (MeV) ion irradiation. *J Appl Phys* 97:026103
36. Juan CP, Tsai CC, Chen KH, Chen LC, Cheng HC (2005) Effects of High-Density Oxygen Plasma Posttreatment on Field Emission Properties of Carbon Nanotube Field-Emission Displays. *J Jpn Appl Phys* 11(44):8231
37. Zhang J, Feng T, Yu W, Liu X, Wang X, Li Q (2004) Enhancement of field emission from hydrogen plasma processed carbon nanotubes. *Diam Rel Mater* 13:54
38. Yu K, Zhu Z, Xu M, Li Q, Lu W, Chen Q (2004) Soluble carbon nanotube films treated using a hydrogen plasma for uniform electron field emission. *Surf Coat Technol* 179:63
39. Yan B, Qian K, Zhang Y, Xu D (2005) Effects of argon plasma treating on surface morphology and gas ionization property of carbon nanotubes. *Physica E* 28:88
40. Liu Y, Liu L, Liu P, Sheng L, Fan S (2004) Plasma etching carbon nanotube arrays and the field emission properties. *Diam Rel Mater* 13:1609
41. Yu K, Zhu Z, Zhang Y, Li Q, Wang W, Luo L, Yu X, Ma H, Li Z, Feng T (2004) Change of surface morphology and field emission property of carbon nanotube films treated using a hydrogen plasma. *Appl Sur Sci* 225:380
42. Chen Z, den Engelsen D, Bachmann PK, van Elsbergen V, Koehler I, Merikhi J, Wiechert DU (2005) High emission current density microwave-plasma-grown carbon nanotube arrays by postdepositional radio-frequency oxygen plasma treatment. *Appl Phys Lett* 87:243104
43. Lee JA, Lee JW, Yoon DS, Park KK, Lee YH, Ju BK (2006) Improvement of Field-Emission Properties of Screen Printed Carbon Nanotube Films via Argon Plasma Treatment. *J Electrochem Soc* 6:H111
44. Chen KF, Chen KC, Jiang YC, Jiang LY, Chang YY, Hsiao MC, Chan LH (2006) Field emission image uniformity improvement by laser treating carbon nanotube powders. *Appl Phys Lett* 88:193127
45. Zhu YW, Cheong FC, Yu T, Xu XJ, Lim CT, Thong JTL, Shen ZX, Ong CK, Liu YJ, Wee ATS, Sow CH (2005) Effects of CF₄ plasma on the field emission properties of aligned multi-wall carbon nanotube films. *Carbon* 43:395

Surface Modification of Carbon Nanotubes for High-Performance Polymer Composites

2

Soo-Jin Park, Seul-Yi Lee, and Fan-Long Jin

Contents

1	Part 1. Preparation and Properties of Carbon Nanotube-Reinforced Polymer Composites	14
1.1	Introduction	14
1.2	Polymer/CNT Composites	15
1.3	Conclusions	31
2	Part 2. Recent Advances in Carbon Nanotube-Based Epoxy Composites	32
2.1	Introduction	32
2.2	Surface Modification of CNTs	32
2.3	Oxidation of CNTs (O-CNTs)	33
2.4	Chemical Treatment of CNTs	36
2.5	Preparation Methods for Epoxy/CNT Composites	41
2.6	Direct Mixing Processing	41
2.7	Mechanical and Electrical Properties	44
2.8	Conclusions	52
	References	53

Abstract

Carbon nanotubes (CNTs) are increasingly attracting scientific and industrial interest because of their outstanding characteristics, such as high Young's modulus and tensile strength, low density, and excellent electrical and thermal properties, which make them ideal fillers for polymer composites. The incorporation of CNTs into polymer matrices greatly improves the electrical, thermal,

S.-J. Park (✉) • S.-Y. Lee

Korea CCS R&D Center, Korea Institute of Energy Research, Yuseoung-gu, Daejeon, South Korea

Department of Chemistry, Inha University, Nam-gu, Incheon, South Korea

e-mail: sjpark@inha.ac.kr

F.-L. Jin

Department of Chemistry, Inha University, Nam-gu, Incheon, South Korea

and mechanical properties of the materials. Surface modification of CNTs can be carried out in order to improve their processibility and dispersion within the composites. Homogeneous dispersion of CNTs in a polymer matrix plays a crucial role in the preparation of polymer composites based on interfacial interactions between CNTs and the polymer matrix. This chapter aims to review the surface modification of CNTs, the processing technology, and improvement of properties of CNT-reinforced polymer composites.

Keywords

Carbon nanotubes • Surface modification • Electrical properties • Thermal properties • Mechanical properties • Polymer composites

1 Part 1. Preparation and Properties of Carbon Nanotube-Reinforced Polymer Composites

1.1 Introduction

Carbon nanotubes (CNTs) have attracted extensive attention from researchers after their unique structure was identified in the early 1990s. Structures of CNTs are graphene sheets that are cylindrically curled. CNTs have been constructed with high length-to-diameter ratio, significantly larger than that of any other material, giving them outstanding electronic, mechanical, and thermal properties [1, 2]. With these strengths, CNTs have tremendous potential for applications in many scientific and technological fields, especially for use as composite fillers in polymers to improve the mechanical, thermal, and electrical properties of resulting composites [3, 4].

CNTs are categorized as single-walled CNTs (SWCNTs), double-walled CNTs (DWCNTs), triple-walled CNTs, and multi-walled CNTs (MWCNTs). The electronic properties significantly vary depending on the chirality and the number of graphene walls [5].

However, the insolubility and weak dispersibility of CNTs in common solvents and matrices have limited their applications. An effective method to improve dispersion of nanotubes is the modification of CNTs by polymers. The modification of CNTs may be divided into two categories on the basis of either non-covalent or covalent bonding between the CNTs and the polymer. Non-covalent modification of CNTs is the physical adsorption and/or wrapping of polymers to the surface of the CNTs. Covalent modification of CNTs is the covalent chemical bonding (grafting) of polymer chains to CNTs, a process that dramatically improves the interfacial interactions between nanotubes and the polymer matrix. Interfacial interaction is one of the most critical issues in polymer/CNT composites [6–9].

Polymer/CNT composites can be prepared by solution processing (thermosetting and thermoplastic matrices), bulk mixing (thermoplastic matrices), melt mixing (thermosetting and thermoplastic matrices), and in situ polymerization (thermosetting and thermoplastic matrices) [6, 7]. Polymer matrices have epoxy resins, polyamide-6 (PA-6), polyacrylonitrile (PAN), polycarbonate (PC),

polyethylene (PE), ultrahigh molecular weight polyethylene (UHMWPE), polyimide (PI), poly(methyl methacrylate) (PMMA), polypropylene (PP), polystyrene (PS), polyurethane (PU), poly(vinyl alcohol) (PVA), and others.

In this part 1, we review the processing methods and properties, such as mechanical, thermal, and electrical properties, of CNT-reinforced polymer composites.

1.2 Polymer/CNT Composites

1.2.1 Epoxy/CNT Composites

Epoxy/CNT composites have been extensively investigated due to their industrial and technological applications. Epoxy/CNT composites were fabricated using melt-mixing or solution-mixing methods. A typical procedure for the preparation of a composite by melt-mixing method is as follows: CNTs are directly added to epoxy resin and then sonicated using an ultrasonic machine at an elevated temperature. Curing agent is added into the mixture and the mixture is degassed in a vacuum oven. Finally, mixture is injected into sample molds and is cured in an oven [10].

A typical procedure for preparation of the composites by solution-mixing method is as follows: CNTs are dispersed in solution by sonication. Epoxy resin and curing agent are dissolved in acetone and mixed with the CNT suspension. This mixture is mechanically stirred and sonicated in a water bath. Acetone is removed by rotation evaporation and the mixture is cured in an oven [11].

Liu et al. [11] reported MWCNT-reinforced epoxy composites using polyethylenimine as a dispersant. Figure 2.1 shows the electrical conductivity and modulus of the MWCNT-polyethylenimine/epoxy composites. The covalently modified composites are 10,000 times more resistive than their non-covalent counterparts. Storage modulus of the composites containing covalently functionalized nanotubes is increased, relative to the non-covalent composites, due to the stronger

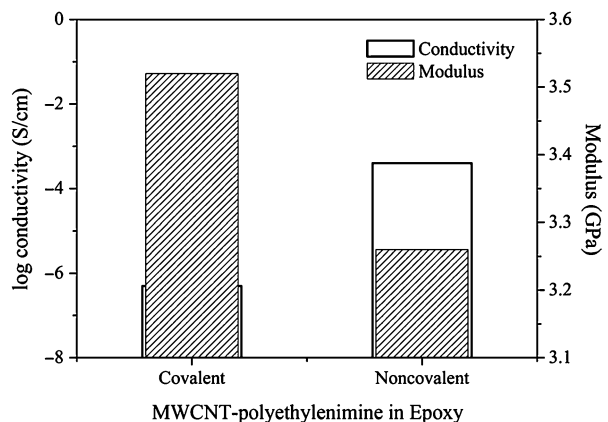


Fig. 2.1 Electrical conductivity and modulus of epoxy/MWNT-PEI composites [11]. MWCNT multi-walled nanotube

Fig. 2.2 Evolution of conductivity of epoxy/MWCNT composite samples as a function of nanotube concentrations for three treatments [13]. MWCNT multi-walled carbon nanotube

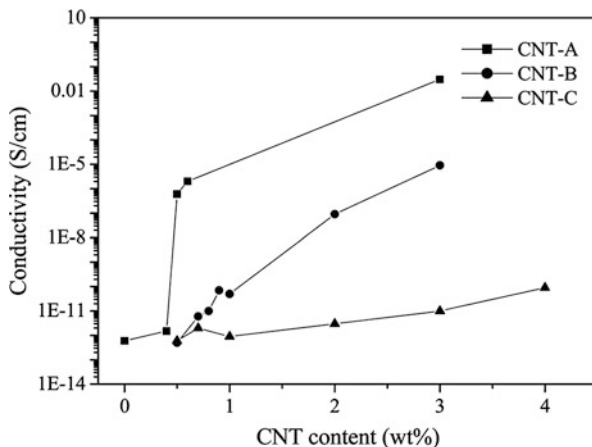
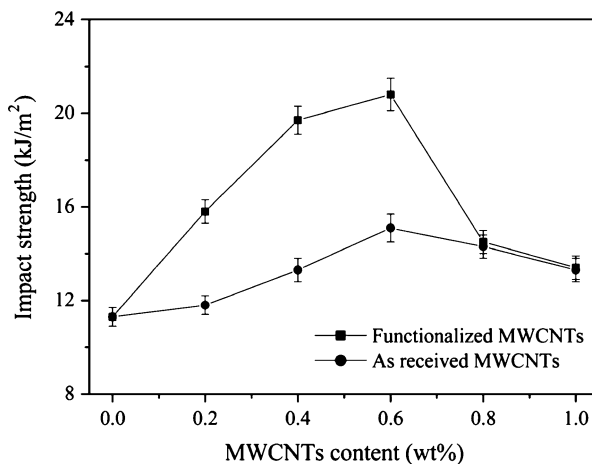


Fig. 2.3 Effect of MWCNT content on impact strength of epoxy/MWCNT composites [14]. MWCNT multi-walled carbon nanotube



polymer/nanotube interaction. Similar results were observed by Spitalsky et al. [12] for $\text{H}_2\text{O}_2/\text{NH}_4\text{OH}$ mixture-treated MWCNT/epoxy composites.

Bai and Allaoui [13] studied the effect of MWCNT length and aggregate size on the mechanical and electrical properties of epoxy/MWCNT composites. The insulator-to-conductor transition was found to occur at 0.5 wt% of the as-prepared MWCNTs (Fig. 2.2).

Yang et al. [14] prepared amide-functionalized MWCNT/bisphenol A epoxy resin/2-ethyl-4-methylimidazole composites. Transmission electron microscopy (TEM) showed that there was an organic thin layer on the MWCNT surface, which contributed to the homogeneous dispersion of the MWCNTs in the epoxy matrix and to the improvement of the MWCNT-epoxy interfacial interaction. Thus the impact strength, bending strength, and thermal conductivity of the composites were enhanced, as shown in Fig. 2.3. Similar results were observed

Fig. 2.4 Effects of MWCNT content on tensile strength of epoxy/MWCNT composites [10]. MWCNT multi-walled carbon nanotube

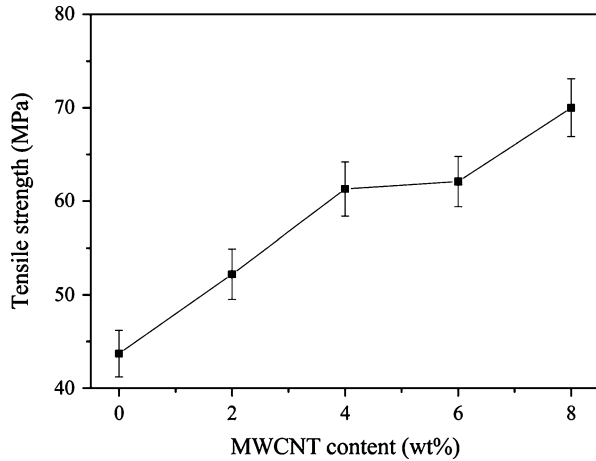


Table 2.1 Storage moduli and glass transition temperatures of epoxy/CNT composites [16]

Samples	G' (GPa)			T_g ($^{\circ}\text{C}$)	G''
	-60°C	-20°C	20°C	$\tan \delta$	
Epoxy	1.9	1.65	1.43	63	50
Epoxy + C_{12}EO_8	1.53	1.38	1.2	62	47
Epoxy + 1% CNT	2.12	1.9	1.6	72	53
Epoxy + C_{12}EO_8 + 1% CNT	2.54	2.18	1.8	88	64

CNT carbon nanotube

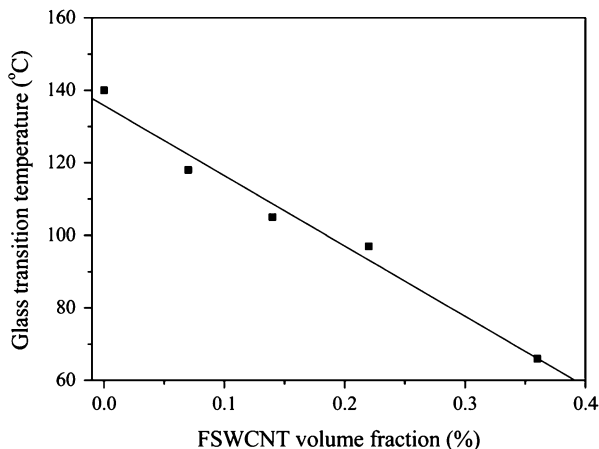
by Gojny et al. [15] for different types of nanofillers-reinforced epoxy nanocomposites. Guo et al. [10] fabricated epoxy/MWCNT nanocomposites using an ultrasonication and cast molding method. As shown in Fig. 2.4, the tensile strength improved with the increase of MWCNT addition. In addition, the fracture strain was also distinctly enhanced, implying that MWCNT loading not only elevated the tensile strength of the epoxy matrix but also increased the fracture toughness.

Gong et al. [16] investigated the effect of a nonionic surfactant on the thermomechanical properties of epoxy/CNT composites. With the surfactant (C_{12}EO_8) as the processing aid, the addition of only 1 wt% CNTs in the composite increases the glass transition temperature (T_g) from 63°C to 88°C , as shown in Table 2.1.

Miyagawa and Drzal [17] reported on the thermophysical properties and impact strength of diglycidyl ether of bisphenol F epoxy nanocomposites reinforced with fluorinated SWCNTs (FSWCNTs). As shown in Fig. 2.5, the T_g decreased approximately 30°C with the addition of 0.2 wt% FSWCNTs.

Kim and Park [18] studied the effect of aminized MWCNTs (NH-MWCNTs) on the mechanical interfacial properties of epoxy nanocomposites. The mechanical interfacial properties of the nanocomposites were remarkably improved with

Fig. 2.5 Glass transition temperature of anhydride-cured epoxy nanocomposites versus FSWCNT volume content [17]. *FSWCNT* fluorinated single-walled carbon nanotube



increase of the NH-MWCNT content. Similar results were observed by Jung et al. [19] for amine-epoxy adducts/thin MWCNT composite particles.

Lee et al. [20] investigated the surface treatment effect of reinforcement filler on the dynamic mechanical properties of epoxy/MWCNT composites. The storage modulus of the epoxy/MWCNT composite was enhanced about 1.27 times through oxyfluorination of MWCNTs at 25 °C.

1.2.2 PA-6/CNT Composites

PA-6/CNT composites were prepared via a melt-compounding method or by polymerization of caprolactam. A typical procedure for preparation of the composites via the melt-compounding method is as follows: PA-6 is extruded with CNTs using a corotating twin-screw extruder at a barrel temperature of 260 °C and a throughput of 5 kg/h. The dried pellets are injection-molded into test specimens. The molding temperature is 250–260 °C and the mold temperature is 70 °C [21].

A typical procedure for preparation of the composites by polymerization is as follows [22]: CNTs and caprolactam are loaded into a flask, and the mixtures are sonicated at 80 °C for 2 h; 6-aminocaproic acid is added to the suspension. The suspension is heated to 250 °C with mechanical stirring under an argon atmosphere. After 6 h, the product mixture is poured into water, and a very hard polymer precipitates. The precipitate is chopped into small pieces and washed with hot water.

Meincke et al. [21] prepared PA-6/CNT composites using a corotating twin-screw extruder. Table 2.2 shows the mechanical and electrical properties of the composites. The CNT-filled PA-6 shows an onset of electrical conductivity at low filler loadings. Tensile tests of the composites show a significant increase of 27 % in Young's modulus. Similar results were observed by Xia et al. [23] for PA-6/CNT composites.

Gao et al. [22, 24] reported a chemical processing technology that allows the continuous spinning of PA-6/SWCNT fibers by in situ polymerization of caprolactam in the presence of amide-functionalized SWCNTs. The number of grafted PA-6

Table 2.2 Mechanical and electrical properties of PA-6/CNT composites [21]

Nanotubes (wt%)	Young's modulus (MPa)	Elongation at break (%)	Izod impact strength (kJ/m ²)	Resistivity (Ω cm)
0	1,970	105 \pm 15	71	$>10^{10}$
0.9	2,100	70 \pm 12	60	$>10^{10}$
2.2	2,160	60 \pm 15	56	2×10^8
2.7	2,200	54 \pm 9	53	1.5×10^5
4.5	2,330	49 \pm 13	n/a	6×10^3
7.2	2,510	44 \pm 11	28	1.7×10^2

PA-6 polyamide-6, CNT carbon nanotube

Table 2.3 Mechanical properties of PA-6/SWCNT composite fibers [24]

SWCNT content (wt%)	0	0.1	0.2	0.5	1	1.5
Tensile strength (MPa)	40.9	86	92.7	83.4	83	75.1
Young's modulus (MPa)	440	540	657	840	1,115	1,200

PA-6 polyamide-6, SWCNT single-walled carbon nanotube

chains that are attached to the SWCNTs can be adjusted by controlling the concentration of the initiator. As shown in Table 2.3, Young's modulus, tensile strength, and thermal stability of the composite fibers produced by this process are significantly improved. Similar results were observed by Zhao et al. [25] and Shao et al. [26] for polymer-encapsulated and cut MWCNT-reinforced PA-6 composites.

Liu et al. [27] prepared PA-6/MWCNT nanocomposites with different MWCNT loadings by a simple melt-compounding approach. Compared with the values for neat PA-6, the elastic modulus and yield strength of the composite are greatly improved by about 214 % and 162 %, respectively, with the incorporation of only 2 wt% MWCNTs. Similar results were observed by Zhang et al. [28] for PA-6/MWCNT nanocomposites.

1.2.3 PAN/CNT Composites

A typical procedure for preparation of PAN/CNT composites is as follows [29]: PAN is dissolved in the stable suspension of CNTs in solvent. The PAN/CNT solutions are spun at room temperature by spinning system.

Chae et al. [29] spun PAN/CNT composite fibers from monomer solutions and MWCNTs. Table 2.4 shows the properties of the fibers. The maximum increase in modulus and reduction in thermal shrinkage were observed in the SWCNT-containing composites, and the maximum improvement in tensile strength, strain to failure, and work of rupture was observed in the multi-walled nanotubes (MWNTs)-containing composites.

Hou et al. [30] prepared well-aligned PAN/MWCNT composite nanofiber sheets by electrospinning an MWCNT-suspended solution of PAN. TEM observation

Table 2.4 Properties of control PAN and PAN/SWCNT composite fibers [29]

Sample	Control PAN	PAN/SWCNTs	PAN/DWCNTs	PAN/MWCNTs
Modulus (GPa)	7.8 ± 0.3	13.6 ± 0.5	9.7 ± 0.5	10.8 ± 0.4
Strength at break (MPa)	244 ± 12	335 ± 9	316 ± 15	412 ± 23
Strain to failure (%)	5.5 ± 0.5	9.4 ± 0.3	9.1 ± 0.7	11.4 ± 1.2
Toughness (MPa)	8.5 ± 1.3	20.4 ± 0.8	17.8 ± 1.7	28.3 ± 3.3
Shrinkage at 160 °C (%)	113.5	6.5	11.5	8
T _g (°C)	100	109	105	103
Crystallinity (%)	58	54	57	55

PAN polyacrylonitrile, SWCNTs single-walled carbon nanotubes, DWCNTs double-walled CNTs, MWCNTs multi-walled CNTs

Table 2.5 Mechanical properties of PAN/MWCNT composite nanofiber sheets [30]

CNT content (%)	Elongation at break (%)	Tensile module (GPa)	Tensile strength (MPa)
0	10.7	1.8	45.7
2	9.8	2	62.9
5	2.5	3.1	80
10	1.3	3.7	48.6
20	0.9	4.4	37.1

PAN polyacrylonitrile, MWCNT multi-walled carbon nanotube

showed that the MWCNTs were parallel and oriented along the axes of the nanofibers. The mechanical properties of the composite nanofibers were significantly increased with the increase of MWCNT content, as shown in Table 2.5. Similar results were observed by Chae et al. [31] for PAN/SWCNT fibers.

1.2.4 PC/CNT Composites

PC/CNT composites with different loadings of CNTs were prepared by solution blending. A typical procedure is as follows [32]: A dispersion of CNTs in solvent is sonicated for 1 h. The dispersed solution is then added to a PC solution. The mixture is sonicated for an additional 10 min and precipitated in excess methanol. The precipitate is dried under vacuum. PC/CNT films are prepared by solution casting.

Fornes et al. [32] prepared PC fibers based on SWCNTs and MWCNTs by first dispersing the nanotubes via solvent blending and/or melt extrusion followed by melt spinning. TEM results reveal that MWCNTs more readily disperse within the PC matrix and have higher aspect ratios than do SWCNT. As shown in Table 2.6, MWCNTs provide greater stiffness and strength than do SWCNTs. Similar results were observed by Singh et al. [33] for PC/SWCNT composites.

Kim and Jo [34] synthesized poly(3-hexylthiophene)-*g*-polycaprolactones (P3HT-*g*-PCLs) with different degrees of polymerization and used the resulting material as a compatibilizer for PC/MWCNT composites. As shown in Table 2.7, the electrical properties of PC/MWCNT composites are dramatically improved when a small amount of P3HT-*g*-PCL is added to PC/MWCNT composites.

Table 2.6 Tensile and electrical properties of PC nanocomposite fibers based on MWCNTs and SWCNTs [32]

CNTs (wt%)	Modulus (GPa)	Yield strength (MPa)	Elongation at break (%)
Pure PC	1.82 ± 0.11	43.0 ± 2.5	>140
1 wt% MWCNT	2.20 ± 0.21	52.8 ± 1.4	>140
3 wt% MWCNT	2.54 ± 0.50	60.1 ± 2.1	80 ± 23
5 wt% MWCNT	3.12 ± 0.20	63.9 ± 3.4	47 ± 8
1 wt% SWCNT	2.20 ± 0.11	54.3 ± 2.0	>140
3 wt% SWCNT	2.41 ± 0.15	53.4 ± 2.2	139 ± 8
5 wt% SWCNT	2.77 ± 0.12	56.4 ± 1.6	96 ± 8

PC polycarbonate, MWCNTs multi-walled carbon nanotubes, SWCNTs single-walled CNTs

Table 2.7 Electrical conductivity of PC, PC/MWCNT, and PC/P3HT-*g*-PCL/MWCNT composite films [34]

Sample	MWCNT content (wt%)	Conductivity (S/cm)
Neat PC	–	10 ⁻¹⁵
PC/MWCNT	1	10 ⁻¹⁵
PC/MWCNT/C30	1	5.8 × 10 ⁻²
PC/MWCNT/C30	5	6.4 × 10 ⁻¹
PC/MWCNT/C50	1	8.8 × 10 ⁻⁴
PC/MWCNT/C50	5	3.5 × 10 ⁻¹

Mn of C30 and C50 is 3,100 and 48,000, respectively

PC polycarbonate, MWCNTs multi-walled carbon nanotubes, P3HT-*g*-PCL poly (3-hexylthiophene)-*g*-polycaprolactone

1.2.5 PE/CNT Composites

A typical procedure for the preparation of PE/CNT composites using screw extrusion and injection technique is as follows [35]: CNTs are added to a solvent and sonicated for 1 h. The CNTs are dried in a vacuum oven and then broken into small pieces and mixed with PE. The mixture obtained is extruded with a corotating twin-screw compounding extruder. Finally, the composite is dried in an oven.

Zou et al. [35] fabricated high-density PE (HDPE)/MWCNT composites using screw extrusion and injection technique. Figure 2.6 shows the Izod impact strength of the composites. At a critical MWCNT concentration of around 1 wt%, the HDPE/MWCNT composites show much improved mechanical properties.

Kanagaraj et al. [36] reported HDPE reinforced with CNTs using injection molding. As shown in Table 2.8, a considerable improvement in the mechanical properties of the composites can be observed when the volume fraction of CNTs is increased. The composite reinforcement shows a good load transfer effect and interface link between CNTs and HDPE. Similar results were observed by Tang et al. [37] for HDPE/MWCNT composite films.

Xiao et al. [38] investigated the mechanical and rheological properties of low-density PE (LDPE) composites reinforced by MWCNTs. Young's modulus

Fig. 2.6 Change of Izod impact strength of HDPE/MWCNT composites [35]. *HDPE* high-density polyethylene, *MWCNT* multi-walled carbon nanotube

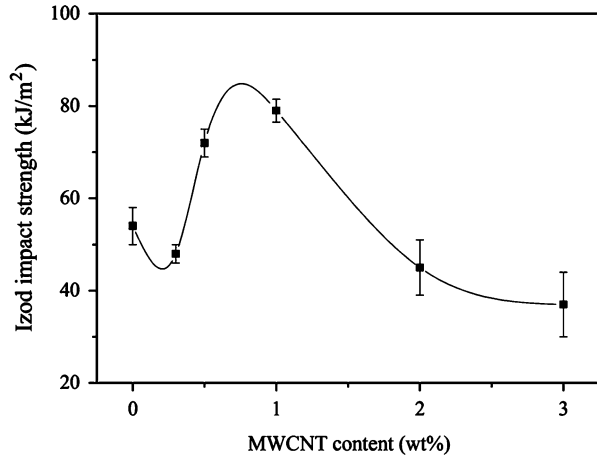


Table 2.8 Mechanical properties of HDPE/CNT nanocomposites [36]

CNT content (vol%)	Young's modulus (GPa)	Strain at fracture (%)	Toughness (J)
0	1.095	863.4	634.53
0.11	1.169	948.5	743.35
0.22	1.228	978.5	756.24
0.33	1.287	1,020.4	776.27
0.44	1.338	1,069	842.47

CNT carbon nanotube, *HDPE* high-density polyethylene

and tensile strength of the composites can increase by 89 % and 56 %, respectively, when the nanotube loading reaches 10 wt%.

Tong et al. [39] reported PE-modified SWCNTs by in situ Ziegler-Natta polymerization. The yield strength, tensile strength and modulus, strain at break, and fracture energy of the PE/modified-SWCNT composites were improved by 25 %, 15 %, 25 %, 21 %, and 38 % in comparison with those values for PE/raw-SWCNT composites.

Gorrasi et al. [40] prepared PE/CNT composites using high energy ball milling. The thermal degradation was already significantly delayed with 1–2 wt% CNTs. The resulting mechanical properties were greatly improved for low filler content. The electrical measurements showed a percolation threshold in the range 1–3 wt% CNTs, as shown in Fig. 2.7.

1.2.6 UHMWPE/CNT Composites

A typical procedure for the preparation of UHMWPE/CNT composite films is as follows [41]: CNTs are dispersed in xylene by magnetic stirring and ultrasonic vibration. The mixture is poured into the UHMWPE-xylene solution and refluxed for 1 h. The UHMWPE/CNT films are prepared by solution casting.

Fig. 2.7 Electrical conductivity of LLDPE/CNT composites as function of MWCNT content [40]. *LLDPE* linear low-density polyethylene, *MWCNT* multi-walled carbon nanotube

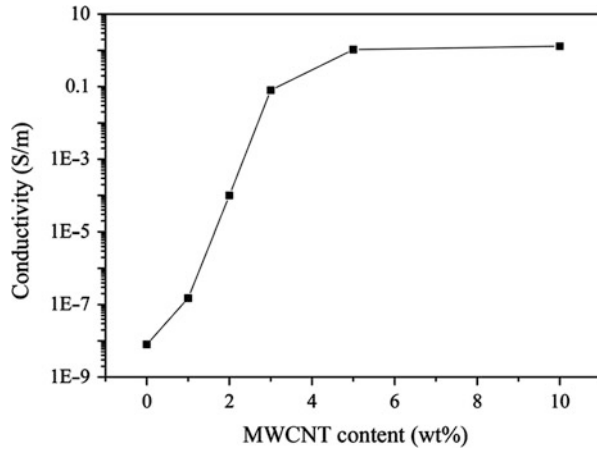


Table 2.9 Mechanical properties of UHMWPE fiber and UHMWPE/MWNT composite fibers [42]

MWNTs content (wt%)	Tensile strength (cN/dtex)	Elongation at break (%)	Yang's modulus (cN/dtex)
0	27.36	4.48	847.32
0.25	28.44	4.55	897.23
1	29.79	4.42	966.96
2	29.64	4.24	959.51
3	29.18	4.19	894.48

UHMWPE ultrahigh molecular weight polyethylene, *MWCNT* multi-walled nanotube

A typical procedure for preparation of UHMWPE/CNT composite fibers is as follows [42]: The mixture of olefin and CNTs is ultrasonicated until the CNTs are uniformly dispersed. Then, the UHMWPE powder is added to the mixture. The mixture is then heated until a homogeneous UHMWPE solution is obtained. The solution is subsequently spun into gel fibers by gel spinning.

Wang et al. [42] prepared UHMWPE/CNT composite fibers by gel spinning. The results showed that a good interaction between functionalized CNTs and UHMWPE matrix was established. Table 2.9 shows the mechanical properties of the fibers. The mechanical and thermal properties of the UHMWPE/CNT fibers were improved compared with those properties for pure UHMWPE fiber. Similar results were observed by Ruan et al. [43, 44] for UHMWPE/MWCNT films.

Bin et al. [41] prepared UHMWPE/MWCNT composites by gelation/crystallization from solution. As shown in Fig. 2.8, the electric conductivity was 10^{-3} S/cm, which qualifies these materials as conductive; Young's modulus reached 58 GPa at room temperature.

Fig. 2.8 Electric conductivity of UHMWPE-based composites as a function of MWCNT content [41]. *UHMWPE* ultrahigh molecular weight polyethylene, *MWCNT* multi-walled carbon nanotube

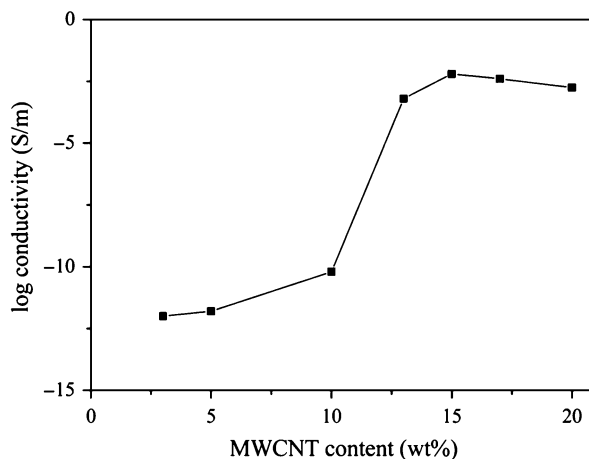


Table 2.10 Properties of PI/MWCNT composites [46]

CNT (wt%)	T_g ($^{\circ}\text{C}$)	Elastic modulus (GPa)	Yield strength (MPa)
0	335	2.84	69.8
3.3	339	3.07	80.5
7.7	350	3.28	84.6
14.3	357	3.9	92.6

PI polyimide, *MWCNT* multi-walled carbon nanotube

1.2.7 PI/CNT Composites

PI/CNT composites were prepared by melt blending, in situ polymerization, and thermal imidization. A typical procedure for preparation of the composites by melt blending is as follows [45]: PI and CNTs are melted-mixed at 325°C for 1 h using a Brabender. After melt mixing, the resulting material is ground through a 1 mm mesh screen and extruded with a single-screw extruder. Extrudates from the first pass are ground and re-extruded two more times to obtain the fibers.

A typical procedure for the preparation of composites by in situ polymerization and thermal imidization is as follows [46]: CNTs/imide oligomer mixtures containing CNTs are prepared using a mechanical blender for several minutes. The CNT/imide oligomer mixture is melted at 320°C for 10 min on a steel plate in a hot press and then cured at 370°C for 1 h.

Ogasawara et al. [46] prepared PI/MWCNT composites by in situ polymerization and thermal imidization. Table 2.10 shows the properties of the composites. The T_g , elastic modulus, and the yield strength were increased with the incorporation of MWCNTs. Similar results were observed by Yu et al. [47] for individual and small bundle CNT-reinforced PI composites.

Siochi et al. [45] prepared PI/SWCNT nanocomposite fibers by melt processing. SWCNT alignment in the fiber direction was induced by the shear forces present during the melt extrusion and fiber drawing processes. This alignment resulted in

Table 2.11 Tensile properties of PI/SWCNT nanocomposite fibers [45]

SWCNT content (wt%)	Tensile modulus (GPa)	Elongation (%)	Toughness (mJ/mm ³)	Yield stress (MPa)
0	2.2	175	123	74
0.1	2.6	125	100	86
0.3	2.8	110	92	94
1	3.2	20	6	100

PI polyimide, SWCNT single-walled carbon nanotube

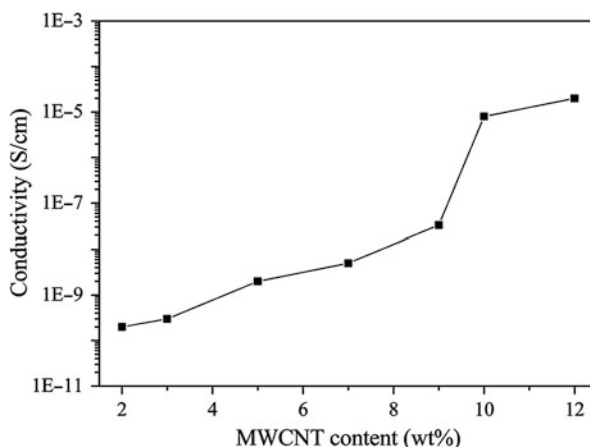


Fig. 2.9 Variation of electrical conductivity of PI/MWNTs nanocomposites with MWCNT content (10 kHz) [49]. PI polyimide, MWNT multi-walled carbon nanotube, MWCNT multi-walled carbon nanotube

significantly higher tensile moduli and yielded stress in the PI/SWCNT nanocomposite fibers relative to those values for unoriented nanocomposite films having the same SWCNT concentration, as shown in Table 2.11.

Liu et al. [48] prepared polyetherimide (PEI)/MWCNT nanocomposite films by casting and imidization. With the addition of 1 wt% MWCNTs, the T_g of PEI increases by about 10 °C and the elastic moduli of the nanocomposites significantly improved by about 250 %, comparable to that of the matrix.

Zhu et al. [49] prepared PI/MWCNT nanocomposite films by casting and thermal imidization. As shown in Fig. 2.9, the electrical properties of the nanocomposite films were greatly improved with the incorporation of MWCNTs due to the strong interfacial interaction between the modified MWCNTs and the PI matrix. Similar results were observed by So et al. [50] and Yuen et al. [51] for PI/MWCNT nanocomposites.

1.2.8 PMMA/CNT Composites

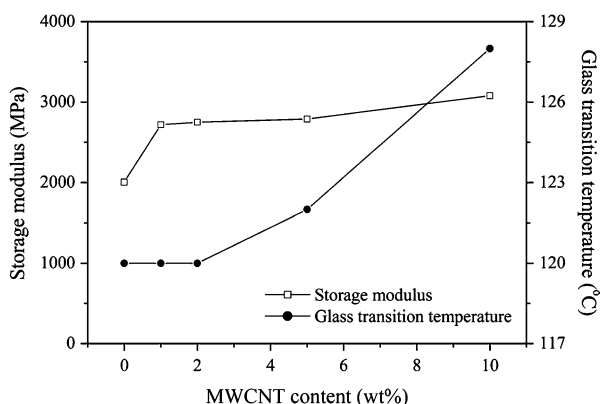
PMMA/CNT composites were prepared using melt blending and in situ polymerization. A typical procedure for preparation of the composites by melt blending method is as follows [52]: CNTs and PMMA are blended in a Mixing Molder. The resulting materials are then pressed in a hydraulic press under atmospheric pressure.

Table 2.12 Properties of PMMA/CNT composites [53]

Treated CNT (wt%)	Tensile strength (MPa)	Toughness (kJ/m ²)	Hardness HB (kg/m ²)	Heat deflection temperature (K)
0	54.9	1.34	19.21	386–388
1	58.7	1.45	26.7	406–408
3	66.8	1.47	26.9	418–420
5	71.66	1.49	27.3	425–427
7	71.65	1.49	28.5	427–429
10	47.15	0.86	28.2	–

PMMA poly(methyl methacrylate), CNT carbon nanotube, HB Brinell hardness number

Fig. 2.10 Storage moduli at 40 °C and T_g values of PMMA/MWCNT composites [58]. PMMA poly(methyl methacrylate), MWCNT multi-walled carbon nanotube



A typical procedure for preparation of composites by in situ polymerization method is as follows [53]: CNTs are dispersed in a liquid state of methyl methacrylate (MMA) monomer. An ultrasound is then applied to the CNT dispersion. Polymerizations of MMA/CNTs are conducted using an initiator.

Jia et al. [53] prepared PMMA/CNT composites by in situ process. Table 2.12 shows the properties of the composites. The mechanical properties and the heat deflection temperatures of the composites rise with the increase of CNTs. The dispersion ratio of CNTs in the PMMA matrix is proportional to the reaction time of the polymerizing MMA before CNTs are added into the PMMA mixture. Similar results were observed by other researchers for PMMA/CNT composites [54–57].

Wang et al. [58] studied the dynamic mechanical behavior of PMMA/acidified MWCNT composites compatibilized with amine-terminated poly(ethylene oxide) (PEO). The miscibility between PEO and PMMA improves the interfacial adhesion between the polymer matrix and the MWCNTs, leading to an increase in the storage modulus values of the composites, as shown in Fig. 2.10. Similar results were observed by Velasco-Santos et al. [59] for PMMA/MWCNT composites.

Seo et al. [52] prepared PMMA/MWCNT composites via in situ polymerization. The results indicate that the radical initiator 2,2'-azobis-isobutyronitrile (AIBN) and MWCNT increase the polymerization rate and the MWCNT diameter.

Induced radicals on the MWCNT due to AIBN were found to trigger the grafting of PMMA. Moreover, the solvent cast film showed a better nanoscopic dispersion of MWNTs, which could lead to the possibility of CNT composites in engineering applications.

Park et al. [60] prepared a PMMA/MWCNT nanocomposite by in situ polymerization of MMA dispersed with MWCNTs. The acid-treated MWNTs were well dispersed in MMA with fairly good dispersion stability, while flocculation and sedimentation were observed from raw MWCNTs in MMA.

1.2.9 PP/CNT Composites

A typical procedure for the preparation of PP/CNT composites by solvent-mixing method is as follows [61]: PP is added to a solvent and dissolved by mechanical stirring. The obtained gel-like solution is poured onto aluminum foil and placed in a vacuum oven. After drying, the material is left to cool to ambient and is then broken into small pieces. The fibers are spun using an Instron capillary rheometer.

A typical procedure for preparation of the composites by melt-mixing method is as follows [62]: Composites are prepared in an internal mixer, equipped with a pair of high-shear roller-type rotors. The temperature of the mixing chamber is set at 190 °C and the blending time is 15 min. Once the polymer is molten, the appropriate percentage of CNTs is added. The obtained compounds are subject to compression at 200 °C for 15 min in a colling press.

Manchado et al. [61] investigated the dispersion of SWCNTs in isotactic PP (iPP) by shear mixing. The results indicate that the addition of low SWNT amounts led to an increase in the rate of polymer crystallization with no substantial changes in the crystalline structure. As shown in Fig. 2.11, Young's modulus and tensile strength considerably increase in the presence of nanotubes. Various results were observed by other researchers for PP/CNT composites [52, 63–65].

Kearns and Shambaugh [62] reported that the strength properties of PP fibers were enhanced with SWCNTs. For a 1 wt% loading of nanotubes, the tensile

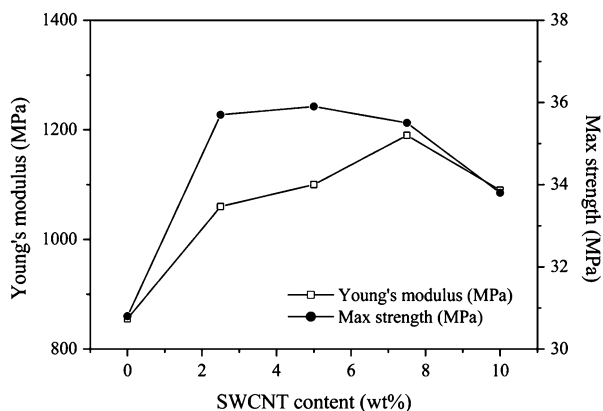


Fig. 2.11 Variation of Young's modulus and yield strength as a function of SWCNT content in PP/SWCNT composites [61]. PP polypropylene, SWCNT single-walled carbon nanotube

Table 2.13 Mechanical properties of PP/SWCNT composite fibers as a function of nanotube loading [62]

CNT content (%)	Tensile strength (MPa)	Modulus (GPa)	Tenacity (g/den)
0	709	6.3	9
0.5	838	9.3	10.6
1	1032	9.8	13.1

PP polypropylene, SWCNT single-walled carbon nanotube

Table 2.14 Properties of PS/MWCNT composite films [69]

MWCNT content (vol%)	Elastic modulus (MPa)	Tensile strength (MPa)
0	1,530 ± 110	19.5 ± 3.0
0.487	2,100 ± 180	24.5 ± 3
0.98	2,730 ± 220	25.7 ± 1.2
2.49	3,400 ± 190	30.6 ± 2.7

PS polystyrene, MWCNT multi-walled carbon nanotube

strength of the fibers increased 40 % and the modulus increased 55 %, as can be seen in Table 2.13.

Grady et al. [66] reported on the nonisothermal and isothermal crystallization of PP/CNT systems. Nanotubes promoted growth of the less-preferred beta form of crystalline PP at the expense of the alpha form. The rate of crystallization was substantially higher in the CNT-filled systems. The results clearly show that CNTs nucleate crystallinity in PP.

Shim and Park [67] studied the effect of glycidyl methacrylate-grafted MWCNTs (GMA-MWCNTs) on the viscoelastic behaviors of PP-based nanocomposites. The PP/GMA-MWCNT nanocomposites showed higher storage modulus, loss modulus, and shear viscosity compared to those values for pure PP.

Karevan et al. [68] investigated the effect of filler content, presence of interphase, and agglomerates on the effective Young's modulus of PP-based nanocomposites reinforced with CNTs. It was found that the interphase has an average width of ~30 nm and modulus in the range of 5–12 GPa.

1.2.10 PS/CNT Composites

A typical procedure for the preparation of a PS/CNT composite is as follows [69]: CNTs are dispersed in toluene using an ultrasonic wand dismembrator. The CNT suspensions are then admixed with toluene solutions of PS to yield PS/CNT solutions. These mixtures are further homogenized in an ultrasonic bath. Thin composite films are then produced from these solutions using two different techniques, film casting and spin casting.

A typical procedure for film casting is as follows: Solution is poured into a flat-bottomed glass culture dish, and the toluene is allowed to evaporate. Thin uniform films are obtained and dried in a vacuum oven.

A typical procedure for spin casting is as follows: PS/CNT solutions are deposited at the center of a rotating disk and spun on a Spin Coater. Thin films are formed, and the films are subsequently dried in a vacuum oven.

Safadi et al. [69] reported on the basic relationships between processing conditions and the mechanical and electrical properties of MWCNT-reinforced PS composites. Table 2.14 shows the properties of the composites. The presence of 2.5 vol% MWCNTs approximately doubles the tensile modulus and transforms the film from insulating to conductive.

Andrews et al. [70] investigated the dispersion of nanotubes in polymer matrices to derive new and advanced engineering materials. The nanotube concentration at which conductivity was initiated varied with the host polymer. In PP, this concentration was as low as 0.05 vol%, while higher concentrations were required for PS and particularly for ABS.

Xie et al. [71] prepared SWCNTs with high covalent bonding density of polymer layers by a “grafting to” approach. Only 0.06 wt% of SWCNTs resulted in 82 % and 78 % increases in tensile strength and elastic modulus of polymer composites, respectively, indicating an efficient interfacial stress transfer between SWCNTs and polymer.

1.2.11 PU/CNT Composites

PU/CNT membranes were prepared by electrospinning/electrospraying technique and sol–gel process. PU/CNT films were made using a convenient solution process. A typical procedure for preparation of the composites by in situ polymerization is as follows [72]: CNTs are dispersed in dried polyoxytetramethylene glycol via an ultrasonicator for 1 h at room temperature to form a suspension. Then, toluene diisocyanate is added to the suspension and reacted with the modified CNTs at 40 °C for 1 h. Subsequently, the system is moved immediately to an oil bath and reacted for at 80 °C 1.5 h.

A typical procedure for preparation of composite films is as follows [73]: PU is dissolved in THF and the CNTs are added to the PU solution, with continuous stirring. The solution is then sonicated for 2 h in a sonic bath, followed by subsequent casting and controlled solvent evaporation. Free-standing PU/SWNT composite films are obtained by peeling them from the Teflon disk.

Koerner et al. [73] reported the addition of small amounts of MWCNT to thermoplastic elastomer produced polymer nanocomposites with high electrical conductivity, low electrical percolation, and enhancement of mechanical properties including increased modulus and yield stress, as shown in Fig. 2.12.

Xu et al. [74] prepared a series of novel self-cross-linkable PU/MWCNT composites using the sol–gel process. As shown in Table 2.15, a small amount of amide-functionalized MWCNT in the samples may increase Young’s modulus and tensile strength significantly, with no loss of elongation. Various results were observed by Eceiza et al. [75] and Chen and Tao [76] for PU/CNT composites.

Xiong et al. [72] synthesized a PU/amide-functionalized MWCNT elastomer composite. As shown in Fig. 2.13, the T_g of the composite was increased by about 10 °C, and its thermal stability was obviously improved, in comparison with those properties for pure PU.

Fig. 2.12 DC bulk conductivity of PU/CNT composites as a function of CNT content [73]. *PU* polyurethane, *CNT* carbon nanotube

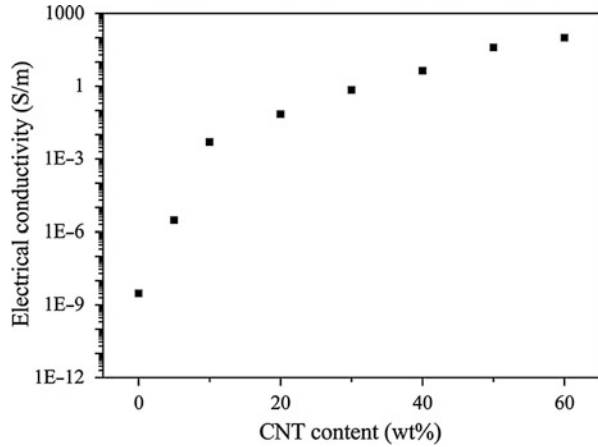
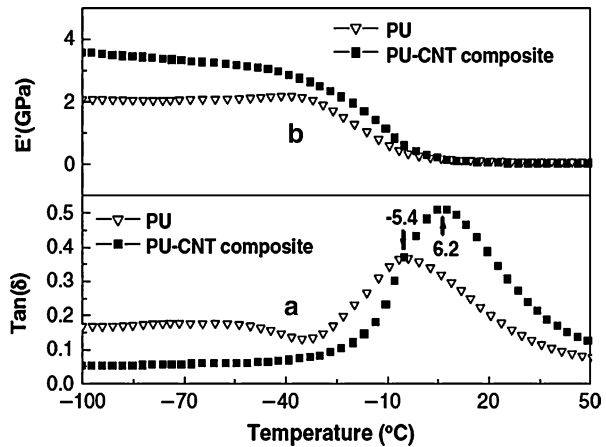


Table 2.15 Tensile properties of PU/MWNT composites [74]

MWNT content (wt%)	Strain (%)	Tensile (MPa)	Modulus (MPa)
0	249 ± 20	22.1 ± 2.5	9.7 ± 0.08
0.1	296 ± 22	24.4 ± 3.1	10.2 ± 0.11
0.3	252 ± 10	26.1 ± 1.6	20.2 ± 0.17
0.5	222 ± 6	35.2 ± 2.2	36.4 ± 0.34

PU polyurethane, *MWNT* multi-walled nanotube

Fig. 2.13 Dynamic mechanical thermal analysis curves of PU/CNT composites with 2 wt% CNT: (a) loss factors ($\tan\delta$) and (b) storage modulus (E') [72]. *PU* polyurethane, *CNT* carbon nanotube



Kim et al. [77] investigated the DC conductivity of PU/MWCNT composites with a variety of oxidation conditions, surfactants, and surfactant contents. It was found that in order to enhance DC conductivity of the composites containing oxidized MWCNT (oxidized multi-walled carbon nanotube), a better dispersion of MWCNT

Table 2.16 Tensile properties of PVA/CNT composite films [78]

Sample	Young's modulus (GPa)	Yield stress (MPa)
PVA	4.0 ± 0.1	83 ± 1
PVA + 2.5 wt% functionalized SWCNT	5.6 ± 0.4	97 ± 15
PVA + 5 wt% functionalized SWCNT	6.2 ± 0.1	128 ± 2
PVA + 2.5 wt% pure SWCNT	5.4 ± 0.4	79 ± 1

PVA poly(vinyl alcohol), SWCNT single-walled carbon nanotube

should be obtained by effective functionalities and surfactant adsorption while preserving the intrinsic geometry of the pristine MWCNT.

1.2.12 PVA/CNT Composites

A typical procedure for preparation of PVA/CNT composite films is as follows [78]: A PVA polymer sample is dissolved in water to obtain a PVA solution. CNTs solution is added to the PVA solution, and the solution is stirred. The resulting solution is cast onto a glass slide and the film is dried at room temperature.

Paiva et al. [78] prepared PVA/water-soluble PVA-functionalized CNT composites via a wet-casting method. Table 2.16 shows the tensile properties of the composites. The mechanical properties of the nanocomposite films were significantly improved compared to those of neat polymer film. Functionalization allowed good distribution of the nanotubes in the matrix, leading to higher film strength.

Ryan et al. [79] reported a 4.5-fold increase in Young's modulus of PVA with the addition of CNTs. It is suggested that in PVA/CNT systems, with non-covalent bonding between the filler and the matrix, the formation of nanotube-induced crystalline polymer domains is the dominant reinforcement mechanism and not stress transfer to the nanotube; the role of the nanotube lies in nucleating crystallization. Similar results were observed by other researchers for PVA/MWCNT composites [80–83].

1.3 Conclusions

In this part 1, we reviewed the preparation and properties of CNT-reinforced polymer composites. For a certain polymer matrix, different treatments of CNTs and processing methods were used. Homogeneous dispersion of CNTs in the polymer matrix is very important to improve the properties of the polymer composites. The electrical, thermal, and mechanical properties of the composites were significantly increased with the addition of a small amount of CNTs. CNT-reinforced polymer composites as multifunctional high-performance materials are currently of great interest for use in an extensive range of electronic, aerospace, and military applications.

2 Part 2. Recent Advances in Carbon Nanotube-Based Epoxy Composites

2.1 Introduction

Epoxy resins are widely used in practical applications such as coatings, electronics, adhesives, and as matrices for composites because of their excellent mechanical properties, high adhesiveness to many substrates, and good heat and chemical resistances. However, the materials are inherently brittle as a result of the high cross-linking density, which puts a constraint on many engineering applications. Many attempts have been made to improve their physical properties using liquid elastomers, thermoplastics, and inorganic particles [1, 84–87].

Recently, epoxy composites containing carbon nanotubes (CNTs) have received a tremendous amount of attention. CNTs can be constructed with length-to-diameter ratios that are significantly higher than those of any other materials, providing them with extraordinary mechanical, electronic, and thermal properties [2, 4]. Thus, CNTs have tremendous potential in many scientific and technological applications. In particular, they would be useful as a filler in epoxy composites for improving the performance of the resulting composites [3, 6, 88].

However, the low solubility and weak dispersibility of CNTs in common solvents and epoxy matrices have limited their application in this area. Methods that have proven effective for improving the dispersion of CNTs can be divided into the categories of mechanical, physical, and chemical. Ultrasonic dispersing and high-shear mixing are examples of commonly used mechanical methods. Physical methods involve the adsorption and/or wrapping of polymers or surfactants to the surface of the CNTs, and chemical methods consist of covalent chemical bonding (grafting) of polymer chains to the CNT surfaces, dramatically improving interfacial interactions between them and the epoxy matrix [7–9, 19, 20, 89].

In this paper, the surface modification of CNTs and methods used to process them are reviewed in detail. In addition, the mechanical and electrical properties of CNT-based epoxy composites are discussed.

2.2 Surface Modification of CNTs

Pristine CNTs (P-CNTs) are difficult to disperse in a polar epoxy matrix because of their large surface area and strong intrinsic van der Waals forces, which cause them to aggregate. The dispersion of CNTs in epoxy resins is one of the most important challenges that need to be overcome in order to fully realize their potential in epoxy-based CNT composites. Therefore, development of processing techniques that effectively reduce the aggregation of nanotubes within an epoxy resin is vital [90, 91].

Many different chemical modification techniques have been studied for enhancing interfacial adhesion between CNTs and an epoxy matrix. Both covalent and non-covalent methods have been investigated for functionalizing the CNT surfaces.

Covalent surface modification involves the formation of a chemical linkage between the polymer chains of the epoxy resins and functional groups on the surface of the CNTs. Non-covalent functionalization methods, which include solution mixing, melt mixing, and in situ polymerization, enable the conjugated structure of CNT sidewalls to be retained. However, the interfacial interaction between the nanotubes and the epoxy matrix is generally poor. For both of these approaches, it is necessary that the sidewalls are modified without significantly altering the desirable properties of the CNTs [92–95].

Acid oxidation is a well-known method for introducing reactive oxygen-containing moieties, such as carboxyl, carbonyl, and hydroxyl groups, onto CNT surfaces. This method uses strong acids, such as HNO_3 and H_2SO_4 . Oxidized CNTs (O-CNTs) have demonstrated improved dispersion and interfacial behavior within various polymer matrices [95, 96].

Sidewall functionalization of CNTs with organic chains or functional groups is another effective way to improve the dispersion and reinforce the combination of CNTs with the epoxy matrix. Reactive oxygen-containing moieties produced by acid oxidation can be further transformed into other functional groups using acryl chloridization, amination, esterification, and a variety of other methods [97, 98].

Attachment of functional groups and polymer chains to CNTs can not only improve dispersion of CNTs in the epoxy matrix but also enhance the binding strength at the polymer-CNT interface. Coupling between CNTs and the polymer matrix is also extremely important for efficient transfer of external stress to the nanotube structures [99, 100].

2.3 Oxidation of CNTs (O-CNTs)

2.3.1 Oxidation by a Mixture of $\text{H}_2\text{SO}_4/\text{HNO}_3$

A general procedure for the oxidation of P-CNTs using a mixture of $\text{H}_2\text{SO}_4/\text{HNO}_3$ is as follows: P-CNTs were placed in an oven at $100\text{ }^\circ\text{C}$ for 2 h. The oxidation of CNTs was carried out in a three-necked round-bottomed flask, equipped with a reflux condenser, mechanical stirrer, and thermometer. P-CNTs (0.2 g) were immersed in a mixture of concentrated $\text{H}_2\text{SO}_4/\text{HNO}_3$ (3:1 v/v) in order to remove impurities from the nanotubes surface. The mixture was then sonicated in a water bath at $40\text{ }^\circ\text{C}$ for 1–3 h and filtered, and the remaining solid was washed by repeated rinsing with deionized water until the pH reached 6–7. Finally, the acid-treated CNTs were dried at $100\text{ }^\circ\text{C}$ for 24 h in a vacuum oven. This procedure resulted in the formation of carboxyl groups on the surface of the CNTs (abbreviated to O-CNTs) [90, 101].

Jin et al. [90] demonstrated the oxidation of P-CNTs with a 3:1 mixture of concentrated H_2SO_4 and HNO_3 by stirring at $40\text{ }^\circ\text{C}$ for 4 h. Table 2.17 shows the elemental composition of CNTs before and after acid treatment. The O/C ratios of P-CNTs and O-CNTs samples were 1.6 % and 5.5 %, respectively, confirming the effectiveness of the acid treatment process in generating carboxyl groups on the CNT surfaces. Raman spectroscopy was employed to probe the structural

Table 2.17 Elemental composition of CNTs before and after acid treatment [90]

Element (atomic %)	C	O	N	O/C (%)
P-CNTs	94.8	1.5	0	1.6
O-CNTs	92.0	5.1	0	5.5

P-CNTs pristine carbon nanotubes, *O-CNTs* oxidized carbon nanotubes

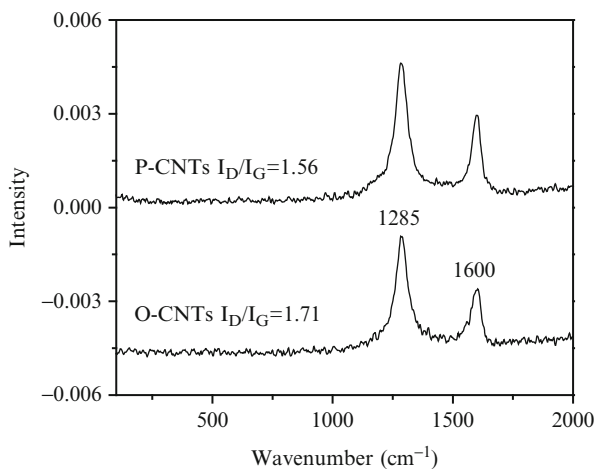


Fig. 2.14 Raman spectra of CNTs before and after acid oxidation [90]. *P-CNTs* pristine carbon nanotubes, *O-CNTs* oxidized carbon nanotubes

alterations of the CNTs, and the results are shown in Fig. 2.14. The intensity ratio of the D and G bands (I_D/I_G) of the CNTs increased from 1.56 to 1.71 on acid treatment, as a result of the formation of sp^3 -hybridized carbon defect sites that result from the creation of functional groups. Similar results were observed by Hsu [89] and Hadjiev et al. [101] using multi-walled CNTs (MWCNTs).

2.3.2 Oxidation by a Mixture of H_2SO_4/H_2O_2

A general procedure for the oxidation of P-CNTs using a mixture of H_2SO_4/H_2O_2 is as follows: P-CNTs were oxidized by a mixture of H_2SO_4/H_2O_2 (3:1 v/v) in a round-bottomed flask at 40 °C for 4 h. The resulting dispersion was diluted in deionized water to remove the residual acid and then filtered. O-CNTs were then obtained after drying under vacuum at 60 °C for 12 h [102].

Luo et al. studied the oxidation of P-MWCNTs using a mixture of H_2SO_4/H_2O_2 . The results of Raman spectroscopy indicated that the I_D/I_G of O-MWCNTs (1.543) was higher than that of P-MWCNTs (1.244), which was the result of some of the sp^2 carbon atoms being converted to sp^3 carbon atoms on the surface of the MWCNTs as carboxyl groups were formed by the acid treatment [102].

2.3.3 Oxidation by HNO_3

A general procedure for the oxidation of P-CNTs using HNO_3 is as follows: Dried P-CNTs were stirred into a HNO_3 solution (1:3 w/w) and the mixture was boiled at

Table 2.18 Raman spectroscopy of untreated and treated MWCNTs [103]

Treatment method	Raman shift (cm ⁻¹)		I _D /I _G intensity ratio
	D	G	
Untreated	1,340	1,581	1.42
5 M HNO ₃ treated	1,344	1,578	1.50
16 M HNO ₃ treated	1,340	1,578	1.54
(3 M HNO ₃ + 4 M HCl) treated	1,344	1,582	1.52
(16 M HNO ₃ + 18 M H ₂ SO ₄) treated	1,348	1,583	1.55

MWCNTs multi-walled carbon nanotubes

Table 2.19 Chemical composition of the functional groups on surface of P-MWCNTs, O-MWCNTs, and H₂O-A-MWCNTs [104]

Sample	O/C	C = C%	C-O%	C = O%	O = C-O%	π-π*%
		(284.6 eV)	(285.6 eV)	(287 eV)	(289.5 eV)	(291 eV)
p-MWCNTs	0.01	65	8	12	–	15
O-MWCNTs	0.07	55	16	14	15	–
H ₂ O-O-MWCNTs	0.14	45	15	16	24	–

P-MWCNTs pristine multi-walled carbon nanotubes, *O-MWCNTs* oxidized multi-walled carbon nanotubes, *H₂O-O-MWCNTs* H₂O–O₃-treated multi-walled carbon nanotubes

100 °C for 1–2 h with stirring at 300 rpm. To eliminate the HNO₃, the mixture was washed repeatedly with deionized water until the pH approached 6–7, then the modified CNTs were dried in an oven at 100 °C [103].

Kim et al. demonstrated the oxidation of MWCNTs using HNO₃. The Raman shift values and the I_D/I_G intensity ratios are presented in Table 2.18. The I_D/I_G values of the O-MWCNTs clearly exceeded those of the P-MWCNTs, because of the presence of carbon defect sites on the MWCNT walls [103].

2.3.4 UV/O₃-Treated CNTs (UV/O₃-CNTs)

A general procedure for the oxidation of P-CNTs using O₃ is as follows: P-CNTs (1 g) were placed in a homemade vertical reactor. O₃ (5 wt% in O₂) was continuously passed through the reaction chamber at room temperature during the oxidation process. The gas flow rate and humidity inside the reactor were kept at 150 L/h and 2 %, respectively, and the reaction time varied from 0.5 to 6 h. For H₂O-assisted ozonolysis, H₂O and O₃ were introduced into the reaction chamber simultaneously. The humidity in the chamber and the flow rate of the mixture were kept at approximately 60 % and 150 L/h, respectively [104].

Peng et al. described a method for CNT oxidation at room temperature using O₃ with added H₂O vapor. The resulting CNTs were characterized using Fourier-transform infrared (FT-IR) spectroscopy, X-ray photoelectron spectroscopy (XPS), scanning electron microscope (SEM) spectroscopy, and transmission electron microscopy (TEM). As shown in Table 2.19, the O/C atom ratio obtained from the XPS was seen to increase from 0.01 (P-MWCNTs) to 0.07 for O-MWCNTs and

0.14 for H₂O-O-MWCNTs. In the presence of H₂O vapor, the O₃ oxidant might partially decompose to generate hydroxyl radicals. TEM imaging revealed damaged graphite sheets as well as formed amorphous carbon entities, implying that the ozonization was initiated at the outer layer and subsequently progressed to the inner layer of the MWCNTs [104].

2.4 Chemical Treatment of CNTs

Enhancement of the interaction of CNTs with an epoxy matrix can be achieved by covalent attachment of functional groups to the nanotube walls that can react directly with the epoxy chains. The key issue in obtaining a successful covalent functionalization is the selection of the correct organic molecule that provides both efficient grafting to the CNT surface and reactivity towards the epoxy matrix. The construction of a CNT-epoxy matrix covalent bond constitutes the strongest type of interfacial interaction and is superior to physical interactions such as van der Waals forces [90, 95, 102, 105].

2.4.1 Amine Functionalization of CNTs Amine Functionalized Carbon Nanotubes (Amino-CNTs)

Amino-CNTs have been developed in recent years for improving the dispersion and interfacial adhesion of CNTs within epoxy resins. The amino-CNTs were obtained by direct coupling between an organic amine and carboxylic acid groups previously formed on the CNT surface. In a typical procedure, 50 mg of O-CNTs were dispersed in 50 mL of toluene, using ultrasonication in a water bath for 60 min. Subsequently, 5 mL of a 10 wt% solution of ethylenediamine in toluene, 800 mg of dicyclohexylcarbodiimide, and 100 mg of dimethylaminopyridine were sequentially added, and the mixture was stirred magnetically at 60 °C for 2 h. After the reaction, 50 mL of ethanol were added in order to dilute the unreacted ethylenediamine and the catalytic molecules. Amino-CNTs were obtained by filtration and washing with ethanol and water, three times each. The product was dried under vacuum at 60 °C for 4 h [95].

Ma et al. studied the amino-functionalization of UV/O₃-treated CNTs. Surface functionalization was confirmed by FT-IR and XPS. The results of static contact angle measurements indicated that the amino-CNTs contained both amine and amide groups on the surface, resulting in enhanced hydrophilicity, and therefore adhesivity, to the epoxy resin, as shown in Table 2.20 [95].

Table 2.20 Contact angles of various droplets on CNT substrate [95]

CNTs	Water (°)	Ethylene glycol (°)	DGEBA (°)
P-CNTs	72.0±3.1	31.8±2.4	74.1±2.6
Amino-CNTs	43.0±2.1	21.8±3.7	61.5±3.2

P-CNTs pristine carbon nanotubes, *amino-CNTs* amine-functionalized carbon nanotubes, *DGEBA* diglycidyl ether of bisphenol A

Fig. 2.15 TGA thermograms of CNT samples [90]. *P-CNTs* pristine carbon nanotube, *O-CNTs* oxidized carbon nanotube, *amino-CNTs* dodecylamine-functionalized carbon nanotube

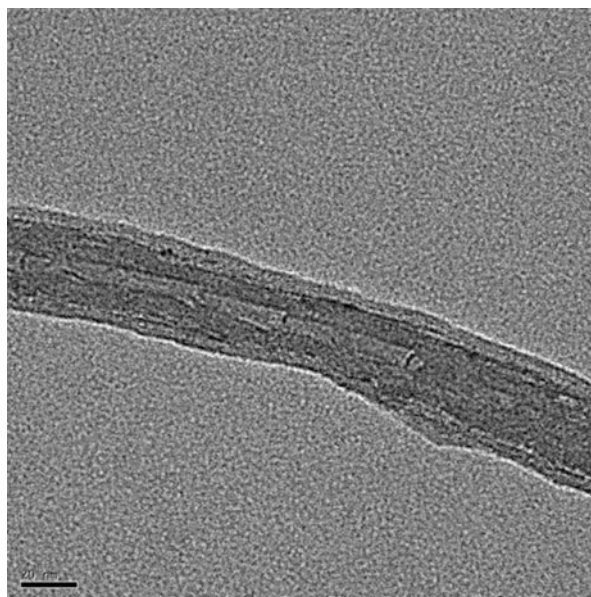
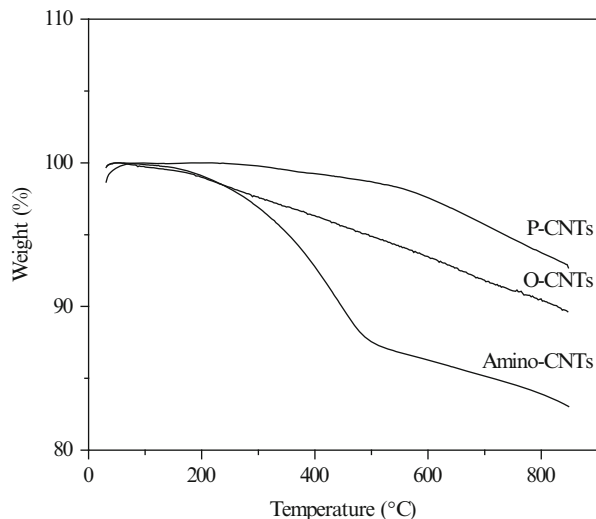


Fig. 2.16 TEM image of amino-CNT [90]. *Amino-CNTs* dodecylamine-functionalized carbon nanotubes

Jin et al. prepared dodecylamine-functionalized CNTs (amino-CNTs). As shown in Fig. 2.15 in thermogravimetric analysis (TGA), the temperature of 5% weight loss of P-CNTs was 735 °C. The weight loss of the amino-CNT sample at this temperature was significantly higher, at 15.2%, which was mainly attributed to the decomposition of dodecyl groups. TEM images demonstrated that the outer shell of the amino-CNTs was covered with a thin layer of amorphous material, as shown in Fig. 2.16 [90].

Table 2.21 Dispersive surface energies (γ_S^D) and specific free energies (ΔG_{sp}) of different MWCNTs [102]

Sample	γ_S^D (mJ/m ²)	ΔG_{sp} in acetone (kJ/mol)	ΔG_{sp} in ethanol (kJ/mol)
P-MWCNTs	122.95	10.74	9.41
Dicyanodiamide-functionalized MWCNTs	18.65	1.14	0.53
Phenylbiguanide-functionalized MWCNTs	25.69	2.84	3.96

P-MWCNTs pristine multi-walled carbon nanotubes

Zheng et al. studied the effect of functionalization on epoxy/CNT nanocomposites. TEM results showed that amino-CNTs were efficiently dispersed into nanometric-class microfibers in the epoxy matrix. The diameter of the amino-CNTs ranged from 20 to 30 nm, and the length reached several hundred microns. The amino-CNTs were evenly distributed in the epoxy resin, ensuring a greater interfacial strength, which is beneficial for improving the properties of the epoxy resin [105].

Luo et al. investigated the effect of amino-functionalization on the interfacial adhesion of epoxy/CNT nanocomposites. As shown in Table 2.21, the grafting of amino-organics onto the surface of MWCNTs resulted in a reduction in dispersive surface energy, γ_S^D . The specific free energies, ΔG_{sp} , of functionalized MWCNTs were significantly decreased, reflecting the reduced interaction between functionalized MWCNTs and polar probe molecules [102].

Armstrong et al. investigated improved performance of epoxy nanocomposites containing amine-functionalized CNTs. SEM images showed wormlike structures, and the nanotubes were thicker and appeared inflated. The images also showed a Y-junction where two CNTs were connected together. The junctions, as well as the inflation of the amino-CNTs, would be expected to affect the properties of the final epoxy/CNT composites [106].

Yang et al. studied the effects of grafting triethylenetetramine to CNTs on the dispersion, filler-matrix interfacial interactions, and thermal properties of epoxy nanocomposites. TEM images demonstrated the appearance of an extra phase on the MWCNT wall after chemical modification, indicating that the grafting reactions had successfully occurred. SEM images showed that the triethylenetetramine grafting could break up large agglomerations and produce individual MWCNTs [107].

2.4.2 Silane Modification of CNTs

The silanization of CNTs is another method that has been used to enhance the interfacial adhesion between nanotubes and the matrix. The silane coupling agents most commonly used are organosilanes, which readily react with hydroxyl groups produced on the CNT surface using oxidation and/or reduction processes.

A general procedure for silane modification of CNTs is as follows: O-CNTs were dispersed in a silane solution via ultrasonication for 30 min, which was then

Table 2.22 Element composition of MWCNTs by EDS analysis [103]

Sample	Element (atom %)					
	C	O	Al	Fe	Si	Si/C
P-MWCNTs	94.53	4.68	0.42	0.38	-	-
S1-MWCNTs	92.85	6.44	0.21	0.15	0.35	0.0038
S2-MWCNTs	95.0	4.06	0.23	0.20	0.51	0.0054
S3-MWCNTs	87.31	9.62	0.20	0.15	2.71	0.0310
S4-MWCNTs	82.76	14.23	-	0.20	2.81	0.0340

P-MWCNTs pristine multi-walled carbon nanotubes, *S1-MWCNTs* silanized multi-walled carbon nanotubes (oxidized with 5 M HNO₃), *S2-MWCNTs* silanized multi-walled carbon nanotubes (oxidized with 16 M HNO₃), *S3-MWCNTs* silanized multi-walled carbon nanotubes (oxidized with 3 M HNO₃), *S4-MWCNTs* silanized multi-walled carbon nanotubes (oxidized with H₂SO₄/HNO₃ (3:1 by volume) solution)

added to a mixture of ethanol/water (95:5 v/v). The reaction was conducted with stirring at 65 °C for 4 h. The resulting silanized CNTs were separated by filtration, washed with distilled water and acetone, and dried under vacuum at 80 °C for 20 h [103].

Lee et al. studied silane modification of O-CNTs using 3-aminopropyltriethoxysilane (APTES). The surface modification and subsequent interactions with epoxy resin were characterized by FT-IR spectroscopy and SEM, respectively. The SEM results showed that the dispersion and impregnation of silanized CNTs in the epoxy resin were improved compared to the O-CNTs [99].

Kim et al. showed the silanization of O-MWCNTs, again using APTES. From the results of energy-dispersive X-ray spectroscopy (EDS) analysis, the attachment of the silane molecules to the surface of the O-MWCNTs was confirmed, as shown in Table 2.22 [103].

Kuan et al. used a free radical reaction to silane-functionalized CNTs. FT-IR was used to monitor the reaction between the coupling agent and the CNTs. Solid-state ²⁹Si NMR spectroscopy revealed that the reactant components underwent a sol-gel reaction to form covalent bonds between the organic and inorganic phases [108].

2.4.3 Fluorination of CNTs

A general procedure for fluorinating CNTs is as follows: O-MWCNTs (1 g), 15 mL of 2-methoxyethyl ether, and 3.1 mL of 4-fluoroaniline were added to a flame-dried three-necked round-bottomed flask fitted with a condenser. While maintaining a N₂ atm, 4 mL of amyl nitrate were added slowly. The mixture was stirred at room temperature for 1 h and then the temperature was raised to 70 °C, followed by mixing for 3 h. The product was cooled, diluted with diethyl ether, filtered, and then washed with copious amounts of distilled water. The wet product was dried under vacuum at 60 °C for 24 h [109].

Abdalla et al. studied the link between the nature of the CNT surface modification and the quality of dispersion in an epoxy resin. Acid-treated and fluorinated

MWCNTs were characterized by FT-IR and Raman spectroscopy and SEM. The SEM images showed very good dispersion of the fluorinated CNTs in the epoxy matrix [109].

2.4.4 Epoxy Functionalization of CNTs

A general procedure for epoxy functionalization of CNTs is as follows: O-CNTs (2.00 g) and 3.00 g of 4,4'-bis(2,3-epoxypropoxy)biphenyl (BP) epoxy resin were dispersed in 200 mL of tetrahydrofuran (THF) and then ultrasonicated in a 100 W bath sonicator at room temperature for 1 h. KOH (8.96 g) were added to the solution as a catalyst, and the solution was refluxed at 70 °C for 6 h. The epoxy-functionalized CNTs were collected by filtration and then dried, resulting in a black powder [89].

Hsu et al. functionalized CNTs using a liquid crystalline (LC) BP epoxy resin. The FT-IR spectra contained an epoxide ring peak, implying that not all of the rings opened and reacted during the functionalization process. TEM images of O-CNTs showed a rough and damaged surface, whereas those of epoxy-functionalized CNTs showed a smoother surface [89].

2.4.5 Poly(glycidyl Methacrylate) (PGMA)-Grafted CNTs

A general procedure for the production of PGMA-grafted CNTs is as follows: CNTs, glycidyl methacrylate (GMA), and 2,2'-azobis-isobutyronitrile (AIBN) were mixed in a 6.2:1:1 M ratio. The mixture was dispersed in *N*-methylpyrrolidone and sonicated at 65 °C in a N₂ atm for 2 h and then stirred for 24 h. After the reaction, the PGMA-grafted CNT slurry was washed several times with acetone to remove all non-grafted GMA, filtered, and then dried under vacuum for 24 h [110].

Teng et al. studied the thermal conductivity of epoxy composites containing both functionalized CNTs and aluminum nitride. XPS and SEM were used to investigate P-MWCNTs and GMA-grafted MWCNTs. SEM images indicated that an interconnected macro-nano binary network structure was constructed between the aluminum nitride and MWCNT fillers [110].

2.4.6 Esterification of CNTs

A general procedure for the esterification of CNTs is as follows. O-CNTs (1 g), phenyl glycidyl ether (PGE) (molar ratio PGE/COOH = 3), and triphenylphosphine (TPP) (molar ratio TPP/PGE = 0.2) were dispersed in 200 ml of THF. The esterification reaction was conducted with a refluxing solvent for 96 h. After centrifugation and extensive washing with THF to remove unreacted PGE and TPP, the esterified nanotubes were dried under a vacuum at 90 °C for 24 h [111].

Auad et al. studied the esterification of both single-walled CNTs (SWCNTs) and MWCNTs. TGA thermograms indicated that the organic mass attached to the carbon surface increased after the oxidation process because of the generation of carboxyl groups and increased further after esterification with PGE. Raman spectra demonstrated that the quality of the dispersion decreased in the following order: O-SWCNTs > P-SWCNTs > PGE-functionalized SWCNTs [111].

2.5 Preparation Methods for Epoxy/CNT Composites

The surface area of CNTs is several times greater than that of conventional fillers used in epoxy composites. This makes it difficult to homogeneously disperse CNTs within the epoxy matrix and improve the interfacial bonding between the two components. Therefore, a key requirement for improved processing techniques for epoxy/CNT composites is the prevention of nanotube aggregation. Various investigations focusing on methods of mixing CNTs into the polymer matrix have been reported in the literature [112–121].

As previously mentioned, the principal methods for achieving dispersion of CNTs can be categorized as mechanical, physical, and chemical. Section 2.3 of this article dealt with chemical approaches to improving CNT dispersion. This section will focus on the mechanical methods currently under investigation, including ultrasonication and high-shear and high-impact mixing. It should be noted that mechanical methods do not permanently stabilize the dispersion [113].

Sonication is a commonly used technique for distributing CNTs in an epoxy matrix and involves the application of ultrasound energy to agitate particles in a solution. In the laboratory, it is usually achieved using an ultrasonic bath or an ultrasonic probe/horn. However, this technique is not easily scalable to industrial-level production, where other technologies, such as three-roll or ball mills, can assure a comparable high quality of mixing together with the possibility of treating a large amount of material [112, 114].

Recently, several methods have been developed for the preparation of epoxy/CNT composites with high nanotube contents, including the hot-press molding process, the mechanical densification method, and the layer-by-layer (LBL) method. In hot-press molding, a filtration system was employed to impregnate the epoxy resin into CNT buckypaper. In mechanical densification, vertically aligned CNT forests were densified followed by capillarity-induced wetting with epoxy resin. In the LBL method, the composites were formed on solid substrates by the sequential deposition of layers of oppositely charged polymers and CNTs [115].

The preparation methods for epoxy/CNT composites are discussed with respect to direct mixing processing and solution processing in the following Sections.

2.6 Direct Mixing Processing

A general procedure for the direct mixing process is as follows: CNTs were added to epoxy resin and dispersed at an elevated temperature by application of intense shear forces (such as sonication or magnetic stirring). A curing agent was added to the epoxy/CNT mixture and agitated using magnetic stirring. To remove entrapped air and voids, the mixture was degassed under vacuum. Finally, the mixture was transferred to silicone rubber molds and cured using the usual temperature profile.

Rahatekar et al. studied the dispersion of CNTs in bisphenol A epoxy resin using high-shear mixing at 200 rpm for 2 h. Samples were cured at 60 °C for 2 h and

post-cured at 90 °C for 15 h. The optical microstructure showed a weak aggregation of CNTs, as a result of unfavorable interactions with the epoxy matrix [116].

Gkikas et al. used an ultrasonic mixer to disperse CNTs in epoxy resin. In order to avoid overheating and induction of defects on the CNT surfaces, the temperature of the mixture was kept low by submerging the container in an ice bath. Initial experiments were carried out for four different sonication time periods to thoroughly investigate the effect of the sonication conditions. The results showed that the duration and amplitude of the sonication process was of key importance for the dispersion of the CNTs in the epoxy resin [113].

Loos et al. prepared suspensions of CNTs in epoxy resin with different amounts of block copolymers using a tip sonicator. SEM images showed that the dispersion of CNTs treated by block copolymers in the composites was enhanced [117].

Saw et al. made transparent, electrically conductive, and flexible films by addition of CNTs to the epoxy resin followed by sonication using a probe sonicator at room temperature. Optical micrographs showed that the short CNTs were well dispersed within the epoxy resin [118].

Gojny et al. used a mini-calendar and high-shear mixing to enhance the dispersibility of CNTs in epoxy resin. TEM images showed that the amino groups seemed to stabilize the CNT dispersion by forming stronger interactions with the epoxy matrix [119].

Schulz et al. produced CNT suspensions using two common dispersion methods, sonication using a horn ultrasonicator and milling by means of a three-roll mill. Sonication is often used to produce small batches, whereas milling is more favorable for achieving good dispersion for larger amounts of material. Light microscopy images showed that milling was able to produce a fine and uniform dispersion of CNTs, but short sonication times were not able to break up the initial nanotube agglomerates [112].

Jin et al. prepared epoxy/amino-CNT composites using a sonicator. As shown in Fig. 2.17, SEM images demonstrated that the amino-CNTs were well dispersed in the epoxy matrix. TEM micrographs also showed that the functionalized CNTs were separated and dispersed uniformly in the epoxy matrix, as shown in Fig. 2.18 [90].

2.6.1 Solution Processing

A general procedure for solution processing of CNTs is as follows: CNTs were dispersed in a solvent using sonication, and the resulting solution was added to epoxy resin and dispersed by the application of intense shear forces. The curing agent was then added to the epoxy/CNT mixture and magnetic stirring was used for further agitation. The resulting mixture was degassed at elevated temperature to eliminate the remaining solvent and trapped air. The composite resin was then molded in a steel mold and cured using the traditional temperature profile.

Feng et al. dispersed CNTs in *N,N*-dimethylformamide (DMF) using sonication. Epoxy composite films with different CNT loadings, 80–110 μm thick, were obtained using the mixed-curing-agent-assisted LBL method. SEM images showed that the high-loading CNTs were uniformly dispersed in the epoxy matrix [115].

Fig. 2.17 SEM images of the fracture surface in DGEBA/ amino-CNT/DDM composites [90]. *Amino-CNTs* dodecylamine-functionalized carbon nanotubes

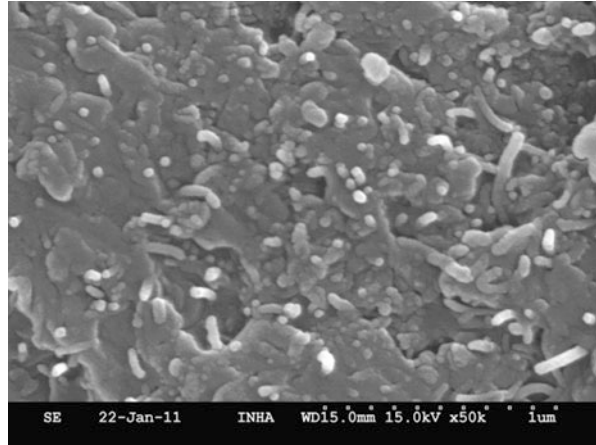
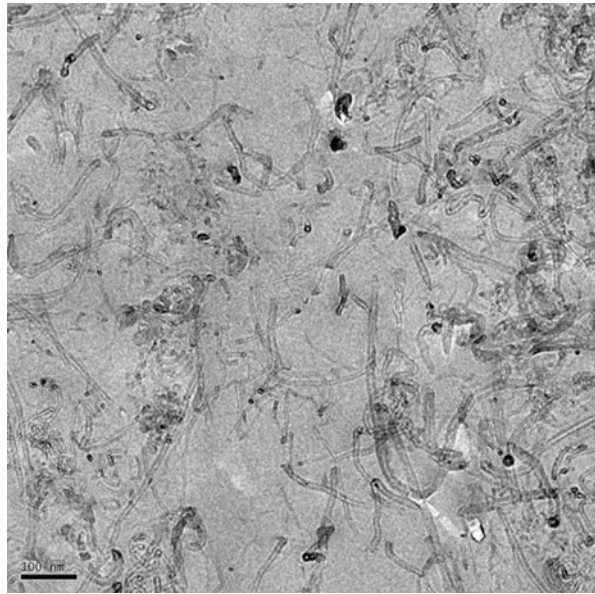


Fig. 2.18 TEM photographs of DGEBA/amino-CNT/DDM composites [90]. *Amino-CNT* dodecylamine-functionalized carbon nanotube



Prolongo et al. reported dispersion of CNTs in chloroform using magnetic stirring at 45 °C. Composites with different amino-CNT contents were prepared with and without the pre-curing treatment. Field emission gun SEM (FEG-SEM) micrographs showed that the degree of dispersion achieved for the pre-cured samples was better than that for the untreated samples [120].

Cividanes et al. studied the dispersion of CNTs in acetone using an ultrasonic bath and then mixing with epoxy resin. SEM micrographs showed that amine-functionalized CNTs had more disorganized microstructures, which led to greater dispersion of CNTs [121].

2.7 Mechanical and Electrical Properties

2.7.1 Mechanical Properties

It is known that the mechanical performance of epoxy/CNT composites strongly depends on the uniformity of nanotube dispersion within the polymer matrix and the strong interfacial interactions between the two components [95, 96, 120]. It has been shown that functionalized CNTs are more readily dispersed in an epoxy matrix and have better interfacial interactions, which is beneficial for improving the properties of the composites [105].

Many researchers have reported that the formation of covalent bonding between functionalized CNTs and an epoxy matrix leads to more effective stress transfer and a denser cross-linked structure. This could limit the mobility of the matrix backbone and therefore improve the mechanical properties of epoxy composites [90].

Fracture toughness has been demonstrated to be improved by surface functionalization of CNTs, which was attributed to the improved interfacial bonding strength between the nanotubes and the epoxy matrix. This would lead to a suppression of debonding at the interface and crack propagation [122].

Many studies have shown that CNTs are able to elastically deform under relatively large stresses, both in tension and compression, leading to highly energy-absorbing processes. It has also been shown that the unique flexibility and geometric features of the CNTs contribute to continuous absorption of energy, resulting in increased elongation in the epoxy component [91, 123].

Jin et al. [90] studied the mechanical interfacial properties of diglycidyl ether of bisphenol A (DGEBA) epoxy resin reinforced with amino-CNTs using critical stress intensity factor (K_{IC}) measurements. As shown in Fig. 2.19, the K_{IC} value of neat DGEBA was $0.71 \text{ MPa m}^{1/2}$. In contrast, the attained K_{IC} values of DGEBA/O-CNT and DGEBA/amino-CNT composites were 22 % higher, at $0.87 \text{ MPa m}^{1/2}$, and 38 % higher, at $0.98 \text{ MPa m}^{1/2}$, respectively. These results were attributed to the

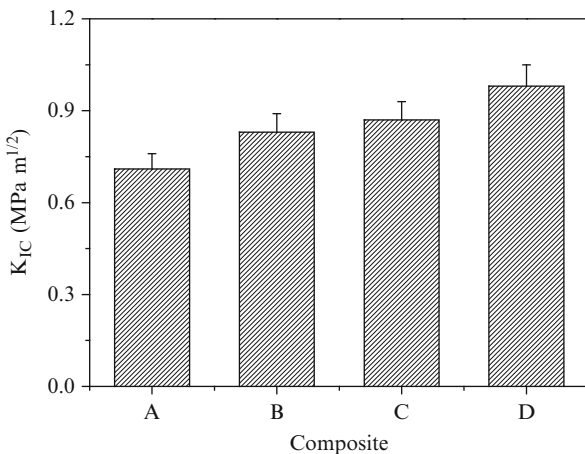


Fig. 2.19 K_{IC} values of DGEBA/CNT composites; A DGEBA/DDM, B DGEBA/P-CNT/DDM, C DGEBA/O-CNT/DDM, D DGEBA/amino-CNT/DDM [90]. P-CNT pristine carbon nanotube, O-CNT acid-treated carbon nanotube, amino-CNT dodecylamine-functionalized carbon nanotube

Fig. 2.20 Modulus of epoxy/CNT nanocomposites [124]. *A* neat epoxy, *B* 0.5 wt%-purified single-walled carbon nanotubes/epoxy, *C* 0.5 wt%-biofunctionalized single-walled carbon nanotubes/epoxy, *D* 1 wt%-purified single-walled carbon nanotubes/epoxy, *E* 1 wt%-biofunctionalized single-walled carbon nanotubes/epoxy

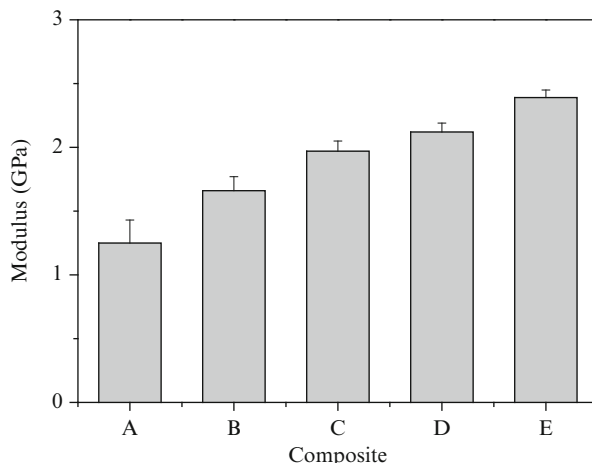


Table 2.23 Hardness of ef-CNT/epoxy/DDS composites [89]

ef-CNT content (wt%)	0.0	0.5	1.0	2.0	4.0	10.0
Hardness	16.62±0.48	20.99±0.5	24.52±0.8	27.14±1.22	27.86±2.2	28.02±1.8

ef-CNT epoxy-functionalized carbon nanotube

improved dispersion of CNTs in the epoxy matrix and better interfacial interactions between the functional groups on the CNT surfaces and the polymer matrix.

Farahani et al. [124] investigated the use of biotin-streptavidin interactions to reinforce epoxy nanocomposites containing functionalized CNTs. The improvement of the tensile modulus for epoxy/CNT composites with 1 wt% biofunctionalized CNT loading was found to be 93 % compared to that of the neat epoxy resin, as shown in Fig. 2.20. The increased stiffness could be attributed to the proper dispersion, as well as beneficial orientation, of the nanotubes that may occur during the extrusion of the composite through the micronozzle.

Hsu et al. [89] assessed the mechanical properties of biphenyl liquid crystalline epoxy/CNT composites. As shown in Table 2.23, the Vickers hardness of the neat epoxy resin was only 16.62 Hv, whereas that of the composite with 2.00 wt% epoxy-functionalized CNT (ef-CNT) was 63 % higher, at 27.14 Hv. This was the result of homogeneously dispersion of the CNTs and improved rigidity and hardness via improved interfacial interaction with the epoxy matrix.

Luan et al. [92] studied the effect of pyrene-modified MWCNTs on the properties of epoxy composites. Figure 2.21 shows the effect of MWCNT content on the impact toughness of the composites. Compared with the neat resin, the impact toughness values of P-CNT composite and poly(styrene-*b*-pyrene) (PS-*b*-PAH)-modified CNT composite were improved by 33.09 % and 127.94 %, respectively, when the CNT content was increased to 0.6 wt%. SEM images of the

Fig. 2.21 Effect of CNT content on impact toughness of epoxy/CNT composites [92]. *PS-b-PAH-CNTs* poly (styrene-*b*-pyrene) (*PS-b-PAH*)-modified carbon nanotubes

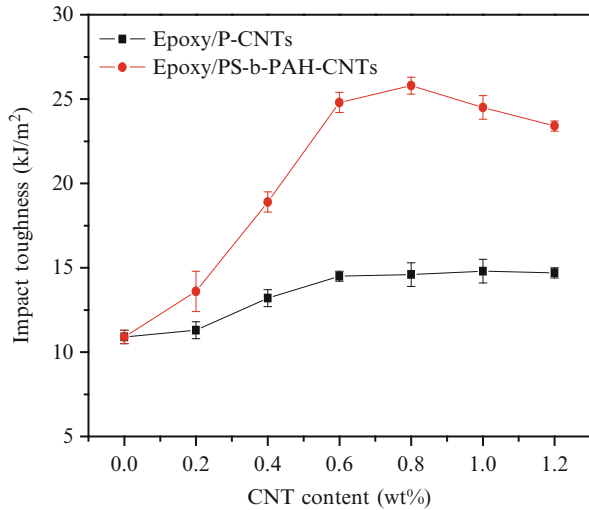
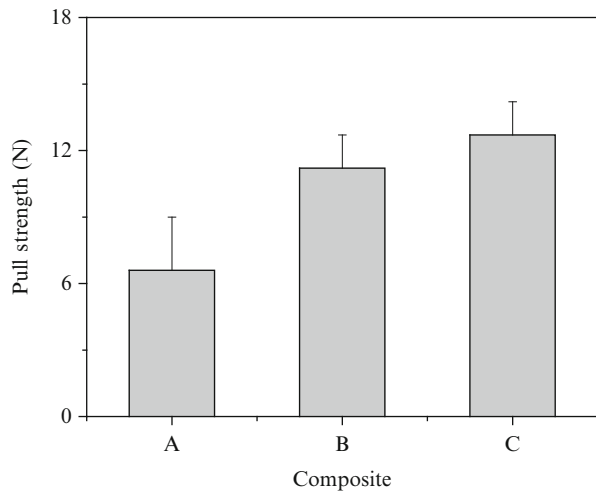


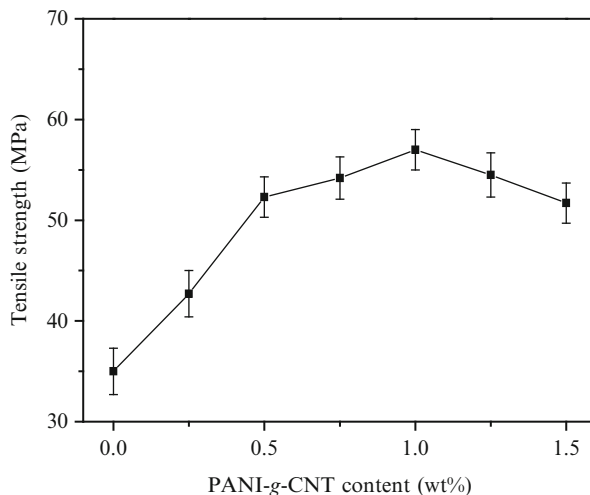
Fig. 2.22 Pull strengths of the QFP leads [125]. *A* epoxy/P-CNTs, *B* epoxy/A-CNTs, *C* epoxy/Amine-CNTs. *P-CNT* pristine carbon nanotube, *A-CNT* acid-treated carbon nanotube, *D-CNT* dodecylamine-functionalized carbon nanotube



epoxy/*PS-b-PAH*-modified CNT composite indicated that the block copolymer modifier acted as a dispersant of the MWCNTs within the matrix.

Kwon et al. [125] studied the dispersion, hybrid interconnection, and heat dissipation properties of functionalized CNTs in epoxy composites. The mechanical characteristics of the composites were confirmed by measuring the mechanical strengths of completely interconnected quad flat packages (QFPs). Figure 2.22 shows the pull strength data for the QFP solder joints for all epoxy/CNT composites. In the case of DGEBA, the pull strengths of P-CNT, O-CNT, and amino-CNT composites were 6.6, 11.2, and 12.6 N, respectively. The pull strength of the DGEBA/amino-CNT composite was twice as high as the

Fig. 2.23 Tensile strength of epoxy composites as a function of PANI-g-MWCNT content [126]. *PAni-g-MWCNTs* polyaniline-grafted multi-walled carbon nanotubes



composite containing P-CNTs. This can be attributed to the strong covalent bonds formed between the amino groups on the CNT surfaces and the epoxy matrix, which resulted in improved mechanical properties.

Xu et al. [126] studied the tensile strength of conducting epoxy/polyaniline-grafted CNT (PAni-g-CNT) composites. As shown in Fig. 2.23, the tensile strength increased by 61 % from 35.26 (neat epoxy) to 56.93 MPa, when the PANI-g-CNT content was raised from 0 to 1 wt%. This was attributed to the reaction of amino groups on the CNT surfaces with the epoxy matrix during curing, providing interfacial adhesion for load transfer between the polymer and the nanotubes.

Xu et al. [96] reported the reinforcement of epoxy nanocomposites with poly-(2-hydroxyethyl methacrylate) (PHEMA)-grafted CNTs (PHEMA-g-CNTs). Figure 2.24 shows the flexural moduli of the epoxy/PHEMA-g-CNT nanocomposites as a function of CNT content. The results revealed that the flexural modulus increased steadily with the amount of CNTs incorporated, as a result of stronger interfacial interactions between the PHEMA-g-MWCNTs and the epoxy matrix, which enabled a more effective transfer of stress from the polymer to the CNTs.

Prolongo et al. [120] studied the flexural properties of epoxy/amino-CNT composites prepared using a pre-curing treatment. As shown in Fig. 2.25, the epoxy resin reinforced with 0.40 % CNTs exhibited an increase of 45 % in flexural strength. However, at lower CNT contents, the composite with 0.25 % CNTs, which was subjected to pre-curing thermal treatment, showed improved mechanical properties, with a 58 % increase in strength over the pristine epoxy resin. This indicated that the pre-curing treatment induced interfacial bonding, enabling effective stress transfer between the epoxy matrix and the amino-functionalized CNTs.

Fig. 2.24 Flexural modulus of epoxy/CNT nanocomposites [96]. *PHEMA-g-CNTs*: poly (2-hydroxyethyl methacrylate)-grafted multi-walled carbon nanotubes

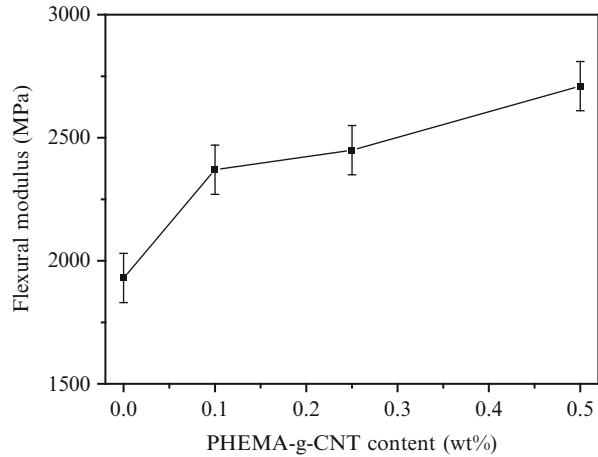
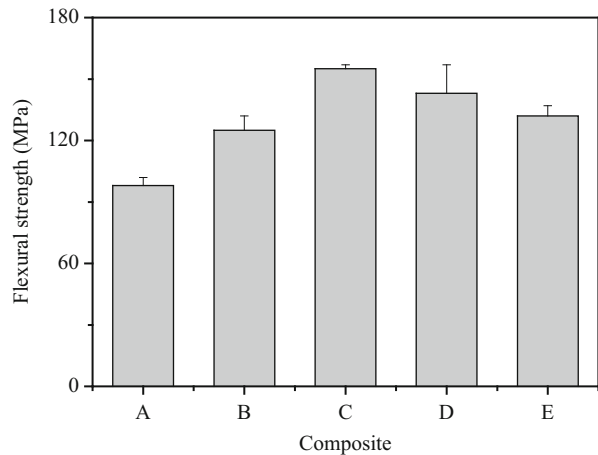


Fig. 2.25 Ultimate flexural strength neat epoxy resin, untreated and thermal pre-cured CNT/epoxy composites [120]. *A* DGEBA/DDS, *B* DGEBA/CNT/DDS (0.25 wt% CNTs), *C* DGEBA/CNT/DDS (0.25 wt% CNTs, pre-cured), *D* DGEBA/CNT/DDS (0.4 wt% CNTs), *E* DGEBA/CNT/DDS (0.4 wt% CNTs, pre-cured)



Guo et al. [10] investigated the effects of MWCNT addition and surface modification on the mechanical performance of epoxy/MWCNT composites. As shown in Fig. 2.26, the tensile strength of the composites improved with increasing MWCNT addition. In addition, the fracture strain was also distinctly enhanced, implying that MWCNT loading not only elevated the tensile strength of the epoxy matrix but also increased the fracture toughness.

Kim et al. [18] studied the effect of amine functionalized multi-walled carbon nanotubes (amino-MWCNTs) on the mechanical interfacial properties of epoxy nanocomposites. The impact strengths of epoxy/amino-MWCNT composites with different nanotube content are shown in Fig. 2.27. The impact strengths of the nanocomposites were remarkably improved with increasing amino-MWCNT content up to 0.6 wt%.

Fig. 2.26 Effects of MWCNT content on tensile strength of epoxy/MWCNT composites [10]. MWCNT multi-walled carbon nanotube

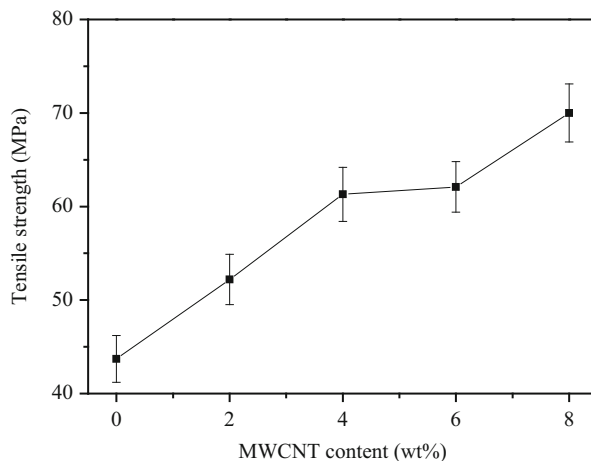
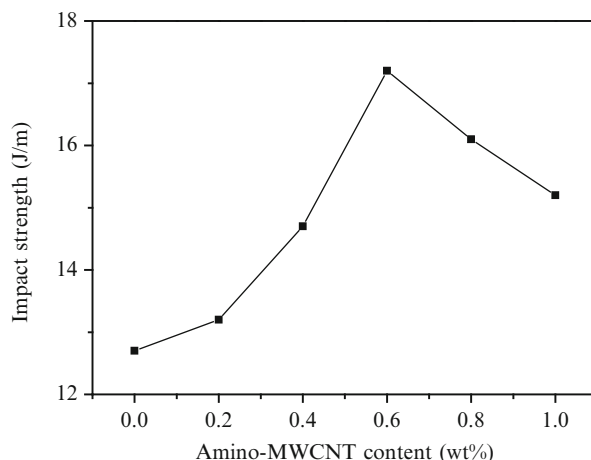


Fig. 2.27 Impact strength of epoxy/MWCNT nanocomposites with different amino-MWCNT content [18]. Amino-MWCNT amine-functionalized multi-walled carbon nanotubes



2.7.2 Electrical Properties

CNTs exhibit excellent electrical properties (of the order of 10^3 – 10^4 S/cm). Their high conductivity makes them excellent candidates for the production of conductive polymer composites. The formation of an electrically conductive nanotube pathway in a polymer composite is characterized by the percolation threshold, which is the minimum concentration of conductive filler required to form a three-dimensional network [125, 127]. It is well known that the percolation thresholds of polymer/CNT composites in general depend on the aspect ratio of the conducting fillers and degree of dispersion of CNTs. The higher the aspect ratio is, the lower the percolation threshold. Experimental results have shown that homogeneous dispersion and alignment of CNTs in the matrix increases the electrical conductivity of CNT-filled composites. Moreover, the conductivity

Table 2.24 Electrical conductivity of various PANi-CNTs/EP composites [93]

Type of composites	PAni content (wt%)	Electrical conductivity (s/cm)
P-CNTs/EP	0	0.39
PAni/EP	100	0
PAni-O-CNTs/EP	6.1	0.08
PAni-K-CNTs/EP	1.2	0.34
PAni-K-O-CNTs/EP	8.9	0.06
PAni-S-CNTs/EP	0.6	0.39
PAni-S-O-CNTs/EP	5.6	0.07

P-CNTs pristine carbon nanotubes, *PAni* polyaniline, *PAni-O-CNTs* PANi-coated oxidized carbon nanotubes, *PAni-K-CNTs* PANi-coated KPS-treated carbon nanotubes, *PAni-K-O-CNTs* PANi-coated KPS-treated oxidized carbon nanotubes, *PAni-S-CNTs* PANi-coated SDS-treated carbon nanotubes, *PAni-S-O-CNTs* PANi-coated SDS-treated oxidized carbon nanotubes

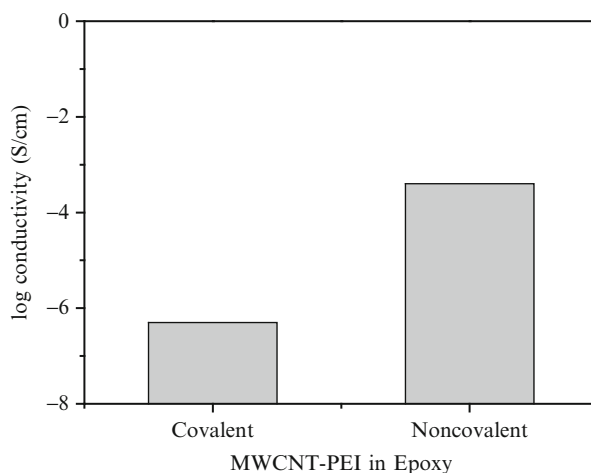


Fig. 2.28 Electrical conductivity and modulus of epoxy/CNT-PEI composites [11]. *CNT-PEI* polyethylenimine-grafted multi-walled carbon nanotubes

continues to increase with increasing CNT content, even after the percolation threshold has been reached [115, 118].

Park et al. [93] studied the effects on the electrical properties of epoxy/CNT composites of coating the CNTs with polyaniline (PANi-CNTs). As shown in Table 2.24, epoxy/P-CNT composite exhibited the highest conductivity among those tested, with the conductivity decreased with increasing PANi coating thickness. The epoxy/PAni-coated, potassium persulfate-treated O-CNTs (PAni-K-O-CNTs) composite showed the lowest electrical conductivity among the composites as a result of the presence of a thicker electrically insulating layer.

Liu et al. [11] reported MWCNT-reinforced epoxy composites with polyethylenimine as a dispersant. Figure 2.28 shows the electrical conductivities of the epoxy/MWCNT-polyethylenimine composites. The covalently modified composites were 10,000 times more resistive than their non-covalent counterparts. The storage moduli of the composites containing covalently functionalized nanotubes

Fig. 2.29 Evolution of conductivity of epoxy/CNT composites as a function of CNT content for three treatments [128]. *CNT* carbon nanotube

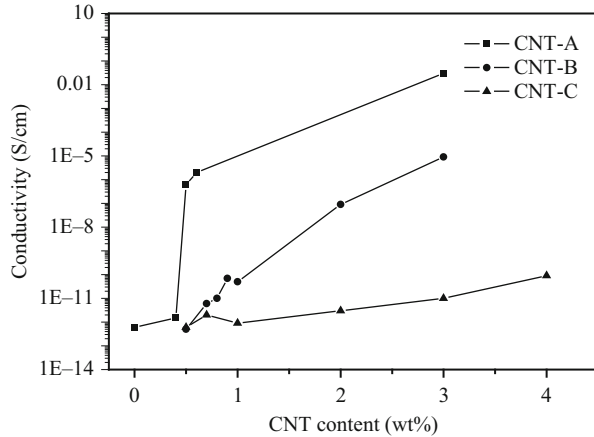
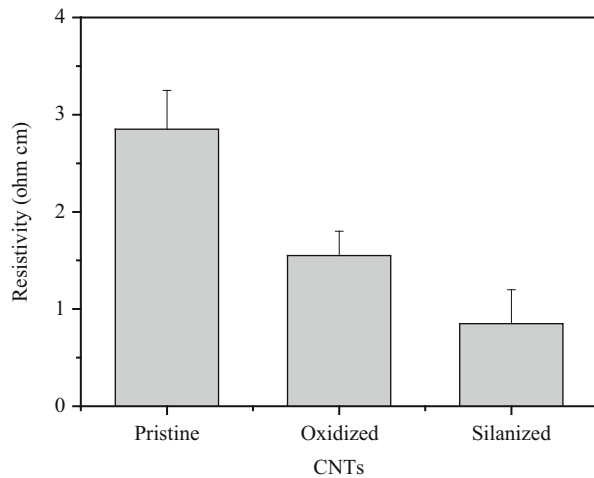


Fig. 2.30 Volume resistivities of epoxy/carbon/unmodified, oxidized, and silanized CNT composites [99]. *CNT* carbon nanotube

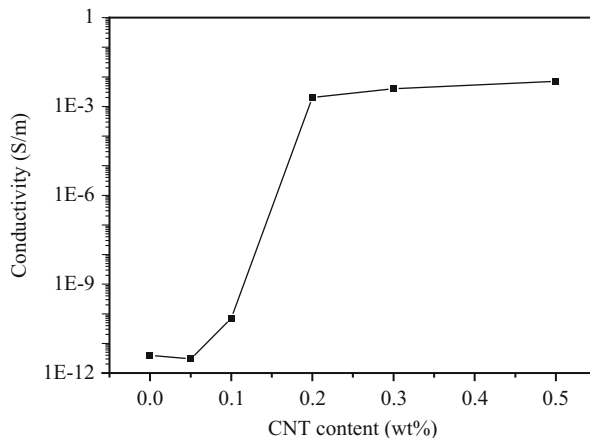


were increased relative to the non-covalent, as a result of the stronger polymer-nanotube interactions.

Bai et al. [128] studied the effect of CNT length and aggregate size on the electrical properties of epoxy/CNT composites. The insulator-to-conductor transition was found to occur at 0.5 wt% P-MWCNTs, as shown in Fig. 2.29.

Lee et al. [99] studied the effects of silane modification of CNTs on the electrical properties of epoxy/carbon/CNT three-phase composites. Figure 2.30 shows the volume resistivities of the epoxy/carbon/unmodified, oxidized, and silanized CNT composites, which were measured to be 2.8, 1.5, and 0.6 Ω cm, respectively. The lower volume resistivity of the silanized composites may be a result of the formation of a continuous network structure caused by homogeneous dispersibility of CNTs between the carbon fibers.

Fig. 2.31 Conductivity of CNT/epoxy composites prepared by sonication-aided dispersion at 120 °C versus CNT content [114]. *CNT* carbon nanotube



Xu et al. [126] studied the electrical properties of conducting epoxy/PANI-g-MWCNT composites. The electrical conductivity for neat epoxy is 2.848×10^{-13} S/cm. Incorporation of 1.0 wt% PANI-g-MWCNTs increased this by seven order of magnitude to 1.975×10^{-6} S/cm. This increase in electrical conductivity implies that the percolation threshold for the composites was between 0.25 and 1.0 wt% of PANI-g-MWCNT content. Because of the encapsulation by the swelling PANI coatings, PANI-g-MWCNTs could not aggregate and were homogeneously dispersed in the epoxy resin, resulting in the formation of electrical networks.

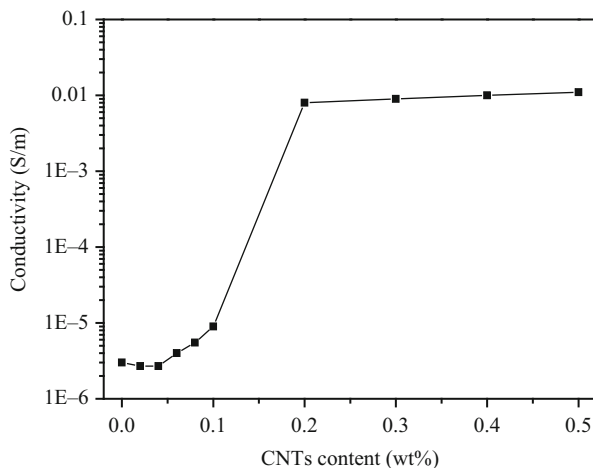
Martone et al. [114] studied the electrical conductivity of epoxy/MWCNT nanocomposites. Figure 2.31 shows the electrical conductivities of the nanocomposites as a function of MWCNT content. A percolative transition between the insulating and conducting behavior occurred above 0.1 wt% MWCNTs.

Saw et al. [118] prepared transparent, electrically conductive, and flexible films from epoxy/MWCNT composites. Figure 2.32 shows the electrical conductivities of the composite films plotted as a function of CNT content for two different types of CNT. The conductivity increased with increasing CNT content, and there was a jump in conductivity by almost four orders of magnitude when the CNT content reached 1 wt%. After the percolation threshold was reached, the electrical conductivity showed a further gradual increase.

2.8 Conclusions

In this part, we have reviewed the surface modification of CNTs, processing methods, and mechanical and electrical properties of epoxy/CNT composites. The surfaces of CNTs were treated using oxidation and chemical treatment methods to improve the dispersion stability of CNTs and interactions between them and epoxy resins. The electrical and mechanical properties of the composites were

Fig. 2.32 Electrical conductivity of epoxy/MWCNT composites as a function of MWCNT content [118]. MWCNT multi-walled carbon nanotube



significantly improved by the addition of CNTs. CNT-based epoxy composites are of great interest as multifunctional high-performance materials for use in aircraft and electronic products.

Acknowledgements This work was supported by the Korea CCS R&D Center (KCRC) grant funded by the Korean government (Ministry of Education, Science and Technology) (0031985) and published as a review article in the Carbon Letters (2012, 2013).

References

1. Iijima S (1991) Helical microtubules of graphitic carbon. *Nature* 354:56
2. Ajayan PM, Stephan O, Colliex C, Trauth D (1994) Aligned carbon nanotube arrays formed by cutting a polymer resin–nanotube composite. *Science* 265:1212
3. Hong J, Park DW, Shim SE (2010) A review on thermal conductivity of polymer composites using carbon-based fillers: carbon nanotubes and carbon fibers. *Carbon Lett* 11:347
4. Zhang J, Zou H, Qing Q, Yang Y, Li Q, Liu Z, Guo X, Du Z (2003) Effect of chemical oxidation on the structure of single-walled carbon nanotubes. *J Phys Chem B* 107:3712
5. Kim KS, Rhee KY, Lee KH, Byun JH, Park SJ (2010) Rheological behaviors and mechanical properties of graphite nanoplate/carbon nanotube-filled epoxy nanocomposites. *J Ind Eng Chem* 16:572
6. Zhang X, Zhang J, Wang R, Liu Z (2004) Cationic surfactant directed polyaniline/CNT nanocables: synthesis, characterization, and enhanced electrical properties. *Carbon* 42:1455
7. Sahoo NG, Rana S, Cho JW, Li L, Chan SH (2010) Polymer nanocomposites based on functionalized carbon nanotubes. *Prog Polym Sci* 35:837
8. Spitalsky Z, Tasis D, Papagelis K, Galiotis C (2010) Carbon nanotube-polymer composites: chemistry, processing, mechanical and electrical properties. *Prog Polym Sci* 35:357
9. Kim KS, Park SJ (2010) Influence of enhanced dispersivity of chemically treated MWNTs on physical properties of MWNTs/PVDF films. *Macromol Res* 18:981
10. Guo P, Chen X, Gao X, Song H, Shen H (2007) Fabrication and mechanical properties of well-dispersed multiwalled carbon nanotubes/epoxy composites. *Compos Sci Technol* 67:3331

11. Liu L, Etika KC, Liao KS, Hess LA, Bergbreiter DE, Grunlan JC (2009) Comparison of covalently and noncovalently functionalized carbon nanotubes in epoxy. *Macromol Rapid Commun* 30:627
12. Spitalsky Z, Krontiras CA, Geoga SN, Galiotis C (2009) Effect of oxidation treatment of multiwalled carbon nanotubes on the mechanical and electrical properties of their epoxy composites. *Compos Part A: Appl Sci Manuf* 40:778
13. Bai JB, Allaoui A (2003) Effect of the length and the aggregate size of MWNTs on the improvement efficiency of the mechanical and electrical properties of nanocomposites-experimental investigation. *Compos Part A: Appl Sci Manuf* 34:689
14. Yang M, Gao Y, Li H, Adronov A (2007) Functionalization of multiwalled carbon nanotubes with polyamide 6 by anionic ring-opening polymerization. *Carbon* 45:2327
15. Gojny FH, Wichmann MHG, Fiedler B, Schulte K (2005) Influence of different carbon nanotubes on the mechanical properties of epoxy matrix composites—a comparative study. *Compos Sci Technol* 65:2300
16. Gong X, Liu J, Baskaran S, Voise RD, Young JS (2000) Surfactant-assisted processing of carbon nanotube/polymer composites. *Chem Mater* 12:1049
17. Miyagawa H, Drzal LT (2004) Thermo-physical and impact properties of epoxy nanocomposites reinforced by single-wall carbon nanotubes. *Polymer* 45:5163
18. Kim KS, Park SJ (2010) Influence of surface treatment of multi-walled carbon nanotubes on interfacial interaction of nanocomposites. *Carbon Lett* 11:102
19. Jung HT, Cho Y, Kim T, Kim TA, Park M (2010) Preparation of amine-epoxy adducts (AEA)/thin multiwalled carbon nanotubes (TWCNTs) composite particles using dry processes. *Carbon Lett* 11:107
20. Lee YS, Im JS, Yun SM, Nho YC, Kang PH, Jin H (2009) X-ray photoelectron spectroscopic analysis of modified MWCNT and dynamic mechanical properties of e-beam cured epoxy resins with the MWCNT. *Carbon Lett* 10:314
21. Meincke O, Kaempfer D, Weickmann H, Friedrich C, Vathauer M, Warth H (2004) Mechanical properties and electrical conductivity of carbon-nanotube filled polyamide-6 and its blends with acrylonitrile/butadiene/styrene. *Polymer* 45:739
22. Gao J, Zhao B, Itkis ME, Bekyarova E, Hu H, Kranak V, Yu A, Haddon RC (2006) Chemical engineering of the single-walled carbon nanotube–nylon 6 interface. *J Am Chem Soc* 128:7492
23. Xia H, Wang Q, Qiu G (2003) Polymer-encapsulated carbon nanotubes prepared through ultrasonically initiated in situ emulsion polymerization. *Chem Mater* 15:3879
24. Gao J, Itkis ME, Yu A, Bekyarova E, Zhao B, Haddon RC (2005) Continuous spinning of a single-walled carbon nanotube–nylon composite fiber. *J Am Chem Soc* 127:3847
25. Zhao C, Hu G, Justice R, Schaefer DW, Zhang S, Yang M, Han CC (2005) Synthesis and characterization of multi-walled carbon nanotubes reinforced polyamide 6 via in situ polymerization. *Polymer* 46:5125
26. Shao W, Wang Q, Wang F, Chen Y (2006) The cutting of multi-walled carbon nanotubes and their strong interfacial interaction with polyamide 6 in the solid state. *Carbon* 44:2708
27. Liu T, Phang IY, Shen L, Chow SY, Zhang WD (2004) Morphology and mechanical properties of multiwalled carbon nanotubes reinforced nylon-6 composites. *Macromolecules* 37:7214
28. Zhang WD, Shen L, Phang IY, Liu T (2003) Carbon nanotubes reinforced nylon-6 composite prepared by simple melt-compounding. *Macromolecules* 37:256
29. Chae HG, Sreekumar TV, Uchida T, Kumar S (2005) A comparison of reinforcement efficiency of various types of carbon nanotubes in polyacrylonitrile fiber. *Polymer* 46:10925
30. Hou H, Ge JJ, Zeng J, Li Q, Reneker DH, Greiner A, Cheng SZD (2005) Electrospun polyacrylonitrile nanofibers containing a high concentration of well-aligned multiwall carbon nanotubes. *Chem Mater* 17:967
31. Chae HG, Minus ML, Kumar S (2006) Oriented and exfoliated single wall carbon nanotubes in polyacrylonitrile. *Polymer* 47:3494

32. Fornes TD, Baur JW, Sabba Y, Thomas EL (2006) Morphology and properties of melt-spun polycarbonate fibers containing single-and multi-wall carbon nanotubes. *Polymer* 47:1704
33. Singh S, Pei Y, Miller R, Sundararajan PR (2003) Long-range, entangled carbon nanotube networks in polycarbonate. *Adv Funct Mater* 13:868
34. Kim KH, Jo WH (2009) A strategy for enhancement of mechanical and electrical properties of polycarbonate/multi-walled carbon nanotube composites. *Carbon* 47:1126
35. Zou Y, Feng Y, Wang L, Liu X (2004) Processing and properties of MWNT/HDPE composites. *Carbon* 42:271
36. Kanagaraj S, Varanda FR, Zhil'tsova TV, Oliveira MSA, Simoes JAO (2007) Mechanical properties of high density polyethylene/carbon nanotube composites. *Compos Sci Technol* 67:3071
37. Tang W, Santare MH, Advani SG (2003) Melt processing and mechanical property characterization of multi-walled carbon nanotube/high density polyethylene (MWNT/HDPE) composite films. *Carbon* 41:2779
38. Xiao KQ, Zhang LC, Zarudi I (2007) Mechanical and rheological properties of carbon nanotube-reinforced polyethylene composites. *Compos Sci Technol* 67:177
39. Tong X, Liu C, Cheng HM, Zhao H, Yang F, Zhang X (2004) Surface modification of single-walled carbon nanotubes with polyethylene via in situ Ziegler–Natta polymerization. *J Appl Polym Sci* 92:3697
40. Gorrasi G, Sarno M, Di Bartolomeo A, Sannino D, Ciambelli P, Vittoria V (2007) Incorporation of carbon nanotubes into polyethylene by high energy ball milling: Morphology and physical properties. *J Polym Sci Part B: Polym Phys* 45:597
41. Bin Y, Kitanaka M, Zhu D, Matsuo M (2003) Development of highly oriented polyethylene filled with aligned carbon nanotubes by gelation/crystallization from solutions. *Macromolecules* 36:6213
42. Wang Y, Cheng R, Liang L, Wang Y (2005) Study on the preparation and characterization of ultra-high molecular weight polyethylene-carbon nanotubes composite fiber. *Compos Sci Technol* 65:793
43. Ruan SL, Gao P, Yang XG, Yu TX (2003) Toughening high performance ultrahigh molecular weight polyethylene using multiwalled carbon nanotubes. *Polymer* 44:5643
44. Ruan S, Gao P, Yu TX (2006) Ultra-strong gel-spun UHMWPE fibers reinforced using multiwalled carbon nanotubes. *Polymer* 47:1604
45. Siochi EJ, Working DC, Park C, Lillehei PT, Rouse JH, Topping CC, Bhattacharyya AR, Kumar S (2004) Melt processing of SWCNT-polyimide nanocomposite fibers. *Compos Part B Eng* 35:439
46. Ogasawara T, Ishida Y, Ishikawa T, Yokota R (2004) Characterization of multi-walled carbon nanotube/phenylethynyl terminated polyimide composites. *Compos Part A Appl Sci Manuf* 35:67
47. Yu A, Hu H, Bekyarova E, Itkis ME, Gao J, Zhao B, Haddon RC (2006) Incorporation of highly dispersed single-walled carbon nanotubes in a polyimide matrix. *Compos Sci Technol* 66:1190
48. Liu T, Tong Y, Zhang WD (2007) Preparation and characterization of carbon nanotube/polyetherimide nanocomposite films. *Compos Sci Technol* 67:406
49. Zhu BK, Xie SH, Xu ZK, Xu YY (2006) Preparation and properties of the polyimide/multi-walled carbon nanotubes (MWNTs) nanocomposites. *Compos Sci Technol* 66:548
50. So HH, Cho JW, Sahoo NG (2007) Effect of carbon nanotubes on mechanical and electrical properties of polyimide/carbon nanotubes nanocomposites. *Eur Polym J* 43:3750
51. Yuen SM, Ma CCM, Lin YY, Kuan HC (2007) Preparation, morphology and properties of acid and amine modified multiwalled carbon nanotube/polyimide composite. *Compos Sci Technol* 67:2564
52. Seo DW, Yoon WJ, Park SJ, Jo MC, Kim JS (2006) The preparation of multi-walled CNT-PMMA nanocomposite. *Carbon Lett* 7:266

53. Jia Z, Wang Z, Xu C, Liang J, Wei B, Wu D, Zhu S (1999) Study on poly(methyl methacrylate)/carbon nanotube composites. *Mater Sci Eng A* 271:395
54. Cooper CA, Ravich D, Lips D, Mayer J, Wagner HD (2002) Distribution and alignment of carbon nanotubes and nanofibrils in a polymer matrix. *Compos Sci Technol* 62:1105
55. Kim KH, Jo WH (2008) Improvement of tensile properties of poly(methyl methacrylate) by dispersing multi-walled carbon nanotubes functionalized with poly(3-hexylthiophene)-graft-poly(methyl methacrylate). *Compos Sci Technol* 68:2120
56. Sabba Y, Thomas EL (2004) High-concentration dispersion of single-wall carbon nanotubes. *Macromolecules* 37:4815
57. Bae DY, Lee HS (2010) Enhanced compatibility of PC/PMMA alloys by adding multiwall carbon nanotubes. *Carbon Lett* 11:83
58. Wang M, Pramoda KP, Goh SH (2006) Enhancement of interfacial adhesion and dynamic mechanical properties of poly(methyl methacrylate)/multiwalled carbon nanotube composites with amine-terminated poly(ethylene oxide). *Carbon* 44:613
59. Velasco-Santos C, Martínez-Hernandez AL, Fisher FT, Ruoff R, Castano VM (2003) Improvement of thermal and mechanical properties of carbon nanotube composites through chemical functionalization. *Chem Mater* 15:4470
60. Park SJ, Cho MS, Lim ST, Choi HJ, Jhon MS (2003) Synthesis and dispersion characteristics of multi-walled carbon nanotube composites with poly(methyl methacrylate) prepared by in-situ bulk polymerization. *Macromol Rapid Commun* 24:1070
61. Machado MAL, Valentini L, Biagiotti J, Kenny JM (2005) Thermal and mechanical properties of single-walled carbon nanotubes-polypropylene composites prepared by melt processing. *Carbon* 43:1499
62. Kearns JC, Shambaugh RL (2002) Polypropylene fibers reinforced with carbon nanotubes. *J Appl Polym Sci* 86:2079
63. Shen J, Champagne MF, Yang Z, Yu Q, Gendron R, Guo S (2012) The development of a conductive carbon nanotube (CNT) network in CNT/polypropylene composite films during biaxial stretching. *Comp Part A: Appl Sci Manuf* 43:1448
64. Daugaard AE, Jankova K, Marín JMR, Bøgelund J, Hvilsted S (2012) Poly(ethylene-co-butylene) functionalized multi walled carbon nanotubes applied in polypropylene nanocomposites. *Eur Polym J* 48:743
65. Zhao P, Wang K, Yang H, Zhang Q, Du R, Fu Q (2007) Excellent tensile ductility in highly oriented injection-molded bars of polypropylene/carbon nanotubes composites. *Polymer* 48:5688
66. Grady BP, Pompeo F, Shambaugh RL, Resasco DE (2002) Nucleation of polypropylene crystallization by single-walled carbon nanotubes. *J Phys Chem B* 106:5852
67. Shim YS, Park SJ (2010) Influence of glycidyl methacrylate grafted multi-walled carbon nanotubes on viscoelastic behaviors of polypropylene nanocomposites. *Carbon Lett* 11:311
68. Karevan M, Pucha RV, Bhuiyan MA, Kalaitzidou K (2010) Effect of interphase modulus and nanofiller agglomeration on the tensile modulus of graphite nanoplatelets and carbon nanotube reinforced polypropylene nanocomposites. *Carbon Lett* 11:325
69. Safadi B, Andrews R, Grulke EA (2002) Multiwalled carbon nanotube polymer composites: synthesis and characterization of thin films. *J Appl Polym Sci* 84:2660
70. Andrews R, Jacques D, Minot M, Rantell T (2002) Fabrication of carbon multiwall nanotube/polymer composites by shear mixing. *Macromol Mater Eng* 287:395
71. Xie L, Xu F, Qiu F, Lu H, Yang Y (2007) Single-walled carbon nanotubes functionalized with high bonding density of polymer layers and enhanced mechanical properties of composites. *Macromolecules* 40:3296
72. Xiong J, Zheng Z, Qin X, Li M, Li H, Wang X (2006) The thermal and mechanical properties of a polyurethane/multi-walled carbon nanotube composite. *Carbon* 44:2701
73. Koerner H, Liu W, Alexander M, Mirau P, Dowty H, Vaia RA (2005) Deformation-morphology correlations in electrically conductive carbon nanotube-thermoplastic polyurethane nanocomposites. *Polymer* 46:4405

74. Xu M, Zhang T, Gu B, Wu J, Chen Q (2006) Synthesis and properties of novel polyurethane-urea/multiwalled carbon nanotube composites. *Macromolecules* 39:3540
75. Fernández-d' Arlas B, Khan U, Rueda L, Martín L, Ramos JA, Coleman JN, González ML, Valea A, Mondragon I, Corcuera MA, Eceiza A (2012) Study of the mechanical, electrical and morphological properties of PU/MWCNT composites obtained by two different processing routes. *Comp Sci Technol* 72:235
76. Chen W, Tao X (2005) Self-organizing alignment of carbon nanotubes in thermoplastic polyurethane. *Macromol Rapid Commun* 26:1763
77. Kim YJ, Jang YK, Kim WN, Park M, Kim JK, Yoon HG (2010) Electrical enhancement of polyurethane composites filled with multiwalled carbon nanotubes by controlling their dispersion and damage. *Carbon Lett* 11:96
78. Paiva MC, Zhou B, Fernando KAS, Lin Y, Kennedy JM, Sun YP (2004) Mechanical and morphological characterization of polymer-carbon nanocomposites from functionalized carbon nanotubes. *Carbon* 42:2849
79. Ryan KP, Cadek M, Nicolosi V, Blond D, Ruether M, Armstrong G, Swan H, Fonseca A, Nagy JB, Maser WK, Blau WJ, Coleman JN (2007) Carbon nanotubes for reinforcement of plastics? A case study with poly(vinyl alcohol). *Compos Sci Technol* 67:1640
80. Zhang X, Liu T, Sreekumar TV, Kumar S, Moore VC, Hauge RH, Smalley RE (2003) Poly(vinyl alcohol)/SWNT composite film. *Nano Lett* 3:1285
81. Kim YY, Yun J, Lee YS, Kim HI (2010) Electro-responsive transdermal drug release of MWCNT/PVA nanocomposite hydrogels. *Carbon Lett* 11:211
82. Liu W, Zhao H, Inoue Y, Wang X, Bradford PD, Kim H, Qiu Y, Zhu Y (2012) Poly(vinyl alcohol) reinforced with large-diameter carbon nanotubes via spray winding. *Comp Part A: Appl Sci Manuf* 43:587
83. Castell P, Cano M, Maser WK, Benito AM (2013) Combination of two dispersants as a valuable strategy to prepare improved poly(vinyl alcohol)/carbon nanotube composites. *Compos Sci Tech* 80:101
84. Bauer RS (1979) Epoxy resin chemistry, vol 114, Advanced in chemistry series. American Chemical Society, Washington, DC, p 1
85. Serrano E, Tercjak A, Kortaberria G, Pomposo JA, Mecerreyes D, Zafeiropoulos NE, Stamm M, Mondragon I (2006) Nanostructured thermosetting systems by modification with epoxidized styrene-butadiene star block copolymers. Effect of epoxidation degree. *Macromolecules* 39(2254)
86. Chen JL, Jin FL, Park SJ (2010) Thermal stability and impact and flexural properties of epoxy resins/epoxidized castor oil/nano-CaCO₃ ternary systems. *Macromol Res* 18:862
87. Jin FL, Park SJ (2009) Thermal stability of trifunctional epoxy resins modified with nanosized calcium carbonate. *Bull Korean Chem Soc* 30:334
88. Jin FL, Park SJ (2011) A review of the preparation and properties of carbon nanotubes-reinforced polymer composites. *Carbon Lett* 12:57
89. Hsu SH, Wu MC, Chen S, Chuang CM, Lin SH, Su WF (2012) Synthesis, morphology and physical properties of multi-walled carbon nanotube/biphenyl liquid crystalline epoxy composites. *Carbon* 50:896
90. Jin FL, Ma CJ, Park SJ (2011) Thermal and mechanical interfacial properties of epoxy composites based on functionalized carbon nanotubes. *Mater Sci Eng A* 528:8517
91. Liu L, Wagner HD (2005) Rubbery and glassy epoxy resins reinforced with carbon nanotubes. *Compos Sci Technol* 65:1861
92. Luan J, Zhang A, Zheng Y, Sun L (2012) Effect of pyrene-modified multiwalled carbon nanotubes on the properties of epoxy composites. *Compos Part A Appl Sci Manuf* 43:1032
93. Park OK, Kim NH, Yoo GH, Rhee KY, Lee JH (2010) Effects of the surface treatment on the properties of polyaniline coated carbon nanotubes/epoxy composites. *Compos Part B Eng* 41:2

94. Barghamadi M, Behmadi H (2012) Influence of the epoxy functionalization of multiwall carbon nanotubes on the nonisothermal cure kinetics and thermal properties of epoxy/multiwall carbon nanotube nanocomposites. *Polym Compos* 33:1085
95. Ma PC, Mo SY, Tang BZ, Kim JK (2010) Dispersion, interfacial interaction and re-agglomeration of functionalized carbon nanotubes in epoxy composites. *Carbon* 48:1824
96. Xu L, Fang Z, Song P, Peng M (2010) Functionalization of carbon nanotubes by corona-discharge induced graft polymerization for the reinforcement of epoxy nanocomposites. *Plasma Process Polym* 7:785
97. Yang SY, Ma CCM, Teng CC, Huang YW, Liao SH, Huang YL, Tien HW, Lee TM, Chiou KC (2010) Effect of functionalized carbon nanotubes on the thermal conductivity of epoxy composites. *Carbon* 48:592
98. Wang J, Fang Z, Gu A, Xu L, Liu F (2006) Effect of amino-functionalization of multi-walled carbon nanotubes on the dispersion with epoxy resin matrix. *J Appl Polym Sci* 100:97
99. Lee JH, Rhee KY, Park SJ (2011) Silane modification of carbon nanotubes and its effects on the material properties of carbon/CNT/epoxy three-phase composites. *Compos Part A Appl Sci Manuf* 42:478
100. Špitalský Z, Matějka L, Šlouf M, Konyushenko EN, Kovářova J, Zemek J, Kotek J (2009) Modification of carbon nanotubes and its effect on properties of carbon nanotube/epoxy nanocomposites. *Polym Compos* 30:1378
101. Hadjiev VG, Warren GL, Luyi S, Davis DC, Lagoudas DC, Sue HJ (2010) Raman microscopy of residual strains in carbon nanotube/epoxy composites. *Carbon* 48:1750
102. Luo Y, Zhao Y, Cai J, Duan Y, Du S (2012) Effect of amino-functionalization on the interfacial adhesion of multi-walled carbon nanotubes/epoxy nanocomposites. *Mater Design* 33:405
103. Kim HC, Kim SK, Kim JT, Rhee KY, Kathi J (2010) The effect of different treatment methods of multiwalled carbon nanotubes on thermal and flexural properties of their epoxy nanocomposites. *J Polym Sci Part B Polym Phys* 48:1175
104. Peng K, Liu LQ, Li H, Meyer H, Zhang Z (2011) Room temperature functionalization of carbon nanotubes using an ozone/water vapor mixture. *Carbon* 49:70
105. Zheng Y, Zhang A, Chen Q, Zhang J, Ning R (2006) Functionalized effect on carbon nanotube/epoxy nano-composites. *Mater Sci Eng A* 435–436:145
106. Armstrong G, Ruether M, Blighe F, Blau W (2009) Functionalized multi-walled carbon nanotubes for epoxy nanocomposites with improved performance. *Polym Int* 58:1002
107. Yang K, Gu M (2009) The effects of triethylenetetramine grafting of multi-walled carbon nanotubes on its dispersion, filler-matrix interfacial interaction and the thermal properties of epoxy nanocomposites. *Polym Eng Sci* 49:2158
108. Kuan CF, Chen WJ, Li YL, Chen CH, Kuan HC, Chiang CL (2010) Flame retardance and thermal stability of carbon nanotube epoxy composite prepared from sol–gel method. *J Phys Chem Solids* 71:539
109. Abdalla M, Dean D, Adibempe D, Nyairo E, Robinson P, Thompson G (2007) The effect of interfacial chemistry on molecular mobility and morphology of multiwalled carbon nanotubes epoxy nanocomposite. *Polymer* 48:5662
110. Teng CC, Ma CCM, Chiou KC, Lee TM (2012) Synergetic effect of thermal conductive properties of epoxy composites containing functionalized multi-walled carbon nanotubes and aluminum nitride. *Compos Part B* 43:265
111. Auad ML, Mosiewicki MA, Uzunpinar C, Williams RJJ (2010) Functionalization of carbon nanotubes and carbon nanofibers used in epoxy/amine matrices that avoid partitioning of the monomers at the fiber interface. *Polym Eng Sci* 50:183
112. Schulz SC, Faiella G, Buschhorn ST, Prado LASA, Giordano M, Schulte K (2011) Combined electrical and rheological properties of shear induced multiwall carbon nanotube agglomerates in epoxy suspensions. *Eur Polym J* 47:2069

113. Gkikas G, Barkoula NM, Paipetis AS (2012) Effect of dispersion conditions on the thermo-mechanical and toughness properties of multi walled carbon nanotubes-reinforced epoxy. *Compos Part B Eng* 43:2697
114. Martone A, Formicola C, Giordano M, Zarrelli M (2010) Reinforcement efficiency of multi-walled carbon nanotube/epoxy nano composites. *Compos Sci Technol* 70:1154
115. Feng QP, Yang JP, Fu SY, Mai YW (2010) Synthesis of carbon nanotube/epoxy composite films with a high nanotube loading by a mixed-curing-agent assisted layer-by-layer method and their electrical conductivity. *Carbon* 48:2057
116. Rahatekar SS, Zammarano M, Matko S, Koziol KK, Windle AH, Nyden M, Kashiwagi T, Gilman JW (2010) Effect of carbon nanotubes and montmorillonite on the flammability of epoxy nanocomposites. *Polym Degrad Stabil* 95:870
117. Loos MR, Yang J, Feke DL, Manas-Zloczower I (2012) Effect of block-copolymer dispersants on properties of carbon nanotube/epoxy systems. *Compos Sci Technol* 72:482
118. Saw LN, Mariatti M, Azura AR, Azizan A, Kim JK (2012) Transparent, electrically conductive, and flexible films made from multiwalled carbon nanotube/epoxy composites. *Compos Part B* 43:2973
119. Gojny FH, Wichmann MHG, Fiedler B, Schulte K (2005) Influence of different carbon nanotubes on the mechanical properties of epoxy matrix composites. A comparative study. *Compos Sci Technol* 65(2300)
120. Prolongo SG, Gude MR (2011) Ureña A. Improving the flexural and thermomechanical properties of amino-functionalized carbon nanotube/epoxy composites by using a pre-curing treatment. *Compos Sci Technol* 71:765
121. Cividanés LS, Brunelli DD, Antunes EF, Corat EJ, Sakane KK, Thim GP (2012) Cure study of epoxy resin reinforced with multiwalled carbon nanotubes by Raman and Luminescence spectroscopy. *J Appl Polym Sci* 127:544
122. Kim MT, Rhee KY, Park SJ, Hiu D (2012) Effects of silane-modified carbon nanotubes on flexural and fracture behaviors of carbon nanotube-modified epoxy/basalt composites. *Compos Part B* 43:2298
123. Qu Z, Wang G (2012) A comparative study on the properties of the different amino-functionalized multiwall carbon nanotubes reinforced epoxy resin composites. *J Appl Polym Sci* 124:403
124. Farahani RD, Dalir H, Borgne VL, Gautier LA, Khakani MAE, Lévesque M, Therriault D (2012) Reinforcing epoxy nanocomposites with functionalized carbon nanotubes via biotin-streptavidin interactions. *Compos Sci Technol* 72:1387
125. Kwon Y, Yim B, Kim J, Kim J (2011) Dispersion, hybrid interconnection and heat dissipation properties of functionalized carbon nanotubes in epoxy composites for electrically conductive adhesives (ECAs). *Microelectron Reliab* 51:812
126. Xu J, Yao P, Jiang Z, Liu H, Li X, Liu L, Li M, Zheng Y (2012) Preparation, morphology, and properties of conducting polyaniline-grafted multiwalled carbon nanotubes/epoxy composites. *J Appl Polym Sci* 125:E334–E341
127. Martin CA, Sandler JKW, Shaffer MSP, Schwarz MK, Bauhofer W, Schulte K, Windle AH (2004) Formation of percolating networks in multi-wall carbon-nanotube–epoxy composites. *Compos Sci Technol* 64:2309
128. Bai JB, Allaoui A (2003) Effect of the length and the aggregate size of MWNTs on the improvement efficiency of the mechanical and electrical properties of nanocomposites-experimental investigation. *Compos Part A* 34:689

Mechanical Properties of Boron-Added Carbon Nanotube Yarns

3

Yoshinori Sato, Mei Zhang, and Kazuyuki Tohji

Contents

1	Carbon Nanotube Yarns	62
1.1	Electrical Properties of CNT Yarns	62
1.2	Mechanical Properties of CNT Yarns	63
1.3	Application of CNT Yarns	65
2	Strong Boron-Added MWCNT Yarns	67
2.1	Synthesis of a Vertically Aligned MWCNT Forest	67
2.2	Preparation and Characterization of Boron-Added MWCNT Yarns	68
2.3	Mechanical Properties of Boron-Added MWCNT Yarns	69
3	Conclusions	72
	References	73

Abstract

Carbon nanotube (CNT)-containing materials with a binder are expected to be used for the fabrication of structural materials, electrodes, and biomaterials. These structures could then take advantage of the outstanding characteristics of individual CNTs, which could possess a large specific surface area and

Y. Sato (✉)

Graduate School of Environmental Studies, Tohoku University, Sendai, Japan

PRESTO, Japan Science and Technology Agency, Saitama, Japan

e-mail: hige@ncsimd.kankyo.tohoku.ac.jp

M. Zhang

High-Performance Materials Institute, Florida State University, Tallahassee, FL, USA

Department of Industrial and Manufacturing Engineering, FAMU-FSU College of Engineering, Tallahassee, FL, USA

e-mail: mzhang@eng.fsu.edu

K. Tohji

Graduate School of Environmental Studies, Tohoku University, Sendai, Japan

e-mail: tohjik@mail.kankyo.tohoku.ac.jp

intriguing electronic and tremendous mechanical properties. Additionally, covalent 2D and 3D network-carbon structures from 1D building nanomaterials are gaining importance due to their fascinating mechanical properties. In this chapter, we introduce binder-free CNT yarns and report on the mechanical properties of boron-added MWCNT yarns.

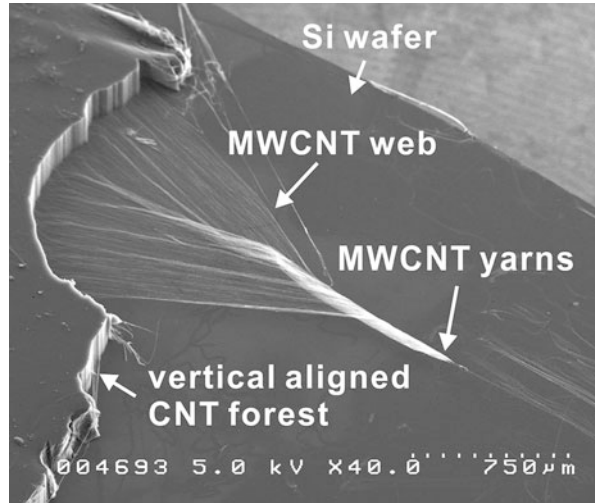
1 Carbon Nanotube Yarns

Composites including carbon nanotube (CNT) show promise for application as multifunctional structural materials, electrodes, and biomedical materials. In an effort to develop these CNT composites, the outstanding features of individual CNTs, which include a large specific surface area, anomalous electron density of states, and remarkable mechanical strength, have to be present all over the composites. However, CNT composites have shown no drastic features because CNTs have not dispersed well in a matrix. Recently, CNT fibers consisting only of CNTs in the absence of a matrix were fabricated by two different breakthroughs. One involves spinning from aerosol CNTs synthesized by the floating catalyst method. Li et al. have shown that it is possible to wind up a continuous fiber without an apparent limit to the length by mechanically drawing the CNTs directly from the gaseous reaction zone [1]. The key points for continuous spinning are the rapid production of high-purity nanotubes to form an aerogel in the furnace hot zone and the forcible removal of the product from reaction by continuous windup. They selected ethanol as the carbon source, in which 0.23–2.3 wt% ferrocene and 1.0–4.0 wt% thiophene were dissolved. The solution was then injected at 0.08–0.25 ml/min from the top of the furnace into a hydrogen carrier gas that flowed at 400–800 ml/min, with the furnace hot zone in the range 1,050–1,200 °C. The other breakthrough involves spinning from a vertically aligned CNT forest synthesized on a substrate. Zhang et al. synthesized a vertically aligned CNT forest on silicon wafers bearing a native oxide or thermal oxide layer and iron catalyst coating of 5 nm using a furnace equipped with a quartz tube (45 mm in diameter) by atmospheric pressure chemical vapor deposition of acetylene (5 %) in helium at 680 °C, at a total flow rate of 580 sccm for 10 min [2]. During CNT yarn production, the forest was attached to a spindle that rotated at a high speed while the CNTs were drawn from the CNT forest in the form of a continuous web. The scanning electron microscope (SEM) photograph in Fig. 3.1 shows the drawing of a CNT web from a CNT forest in our system. In this chapter, we focus on the latter CNT yarns.

1.1 Electrical Properties of CNT Yarns

A single-walled carbon nanotube (SWCNT) becomes either metallic or semiconducting depending on how the graphene is wrapped into a cylinder. Multi-walled carbon nanotube (MWCNT) consists of a series of coaxial graphene cylinders.

Fig. 3.1 SEM micrograph of the drawing of a CNT web from a CNT forest in our system



The electrical resistivity through the same graphite cylinder in an MWCNT is much lower than that between the shells [3]. In conventional graphite, the electrical resistivity is in the order of $2.5 \times 10^{-4} \sim 5.0 \times 10^{-4} \Omega\text{cm}$ in the direction perpendicular to the basal plane and approximately $3.0 \times 10^{-1} \Omega\text{cm}$ in the direction parallel to the basal plane [4]. The resistivity of individual MWCNTs produced by the arc discharge method has been reported to be in the range $5.8 \sim 5.1 \times 10^{-6} \Omega\text{cm}$ [5]. Using the needle of a scanning tunneling microscope as an electric contact, Dai et al. found that the resistivity of individual MWCNTs produced by the catalytic process was in the range $1.2 \times 10^{-2} \sim 7.8 \times 10^{-4} \Omega\text{cm}$ [6]. Meanwhile, un-densified MWCNT yarns with a diameter of 2–10 μm had an electrical conductivity of $2.4 \times 10^{-3} \sim 3.3 \times 10^{-3} \Omega\text{cm}$ at room temperature [2, 7]. The electrical resistivity of acetone-densified MWCNT yarns decreases with a reduction of yarn diameter [8]. At diameters below 20 μm , the resistivity remains almost constant at $1.1 \times 10^{-3} \Omega\text{cm}$. The reason why the electrical resistivity of MWCNT yarns is higher than that of individual SWCNT or MWCNT is thought to be due to interface resistance between the nanotubes in the yarn.

1.2 Mechanical Properties of CNT Yarns

Table 3.1 shows the mechanical properties of typical CNT fibers or yarns and features of the CNT component [1, 2, 7, 9]. The specific stress of as-prepared MWCNT fibers spun from aerosol MWCNTs is stronger than that spun from a vertically aligned MWCNT forest. The intertwining of floating CNTs with each other in a random manner is considered as a key factor. The MWCNT yarn spun from the vertically aligned MWCNT forest results from transverse forces that bind

Table 3.1 Mechanical properties of typical CNT fibers or yarns and features of the CNT component

Characteristics of the CNT component		Characteristics and mechanical properties of CNT yarns								
Materials	Inner diameter [nm]	Outer diameter [nm]	Length [μm]	Spinning type	Densification	Specific stiffness [$\text{GPa}/\text{g}/\text{cm}^3$]	Specific stress [$\text{GPa}/\text{g}/\text{cm}^3$]	Toughness [J/g]	References	Remarks
MWCNT yarns	8	15	300	Spinning from vertically aligned MWCNT forest	No	6	0.2	14	M. Zhang et al., Science, 306, 1358 (2004)	Mechanical test: gauge length is 10 mm
MWCNT yarns	~ 6	10 ~ 11	300, 500, 650	Spinning from vertically aligned MWCNT forest	No	110 ~ 412	0.4 ~ 2.4	2 ~ 111	X. Zhang et al., Small, 3, 244 (2007)	Mechanical test: gauge length is 10 mm
MWCNT yarns	4	10	350	Spinning from vertically aligned MWCNT forest	No	14	0.7	unknown	M. Miao et al., Carbon, 48, 2802 (2010)	Mechanical test: gauge length is 10 mm
MWCNT fibers	Mainly DWCNTs (4 to 10 nm)		1000	Spinning from aerosol MWCNTs	Acetone densification	87	1.5	13	K. Koziol et al., Science, 318, 1892 (2007)	Mechanical test: gauge length is 20 mm

the MWCNT assembly together. In general, the tensile strength of a twisted yarn can be described by the following equation:

$$\sigma_y/\sigma_{\text{CNT}} \approx \cos \alpha [1 - (k \operatorname{cosec} \alpha)]$$

where σ_y and σ_{CNT} are the tensile strength of the twisted yarn and the MWCNT, respectively. α is the twist angle, and $k = (dQ/\mu)^{1/2}/3L$. Here, d is the MWCNT diameter, L is the MWCNT length, μ is the friction coefficient between MWCNTs, and Q is the MWCNT migration length. According to the equation, the mechanical strength of MWCNT yarn depends on these parameters [2]. Some experimental researches indicate that MWCNT yarn strength increases with increasing MWCNT length [7, 10]. The effect of surface twist angle on the specific stress of MWCNT yarn was also investigated [9, 10] and indicated that the surface twist angle for the maximum tensile strength is $10 \sim 20^\circ$ [9] or $15 \sim 20^\circ$ [10]. Furthermore, the tensile strength of MWCNT yarns is improved by densifying each MWCNT component using acetone and ethanol [8].

1.3 Application of CNT Yarns

Some studies have investigated the use of CNT yarns. Zakhidov et al. showed a field emission with high current density at low operating voltage for MWCNT yarn [11]. The lowest threshold field of about $0.7 \text{ V}/\mu\text{m}$ was obtained after a few cycles of applied field increase. In this report, prototypes involving cathodoluminescent lamps and alphanumeric indicators based on MWNT twist-yarn cold cathodes were demonstrated. Xiao et al. reported that barium-functionalized multi-walled carbon nanotube yarns were fabricated by drawing and twisting MWCNT forests through a solution containing barium nitrate [12]. The cathodes exhibited good thermionic properties, with a work function as low as $1.73 \sim 2.06 \text{ eV}$ and a thermionic current density that exceeded $185 \text{ mA}/\text{cm}^2$ in a field of $850 \text{ V}/\mu\text{m}$ at $1,044^\circ\text{C}$. The barium-functionalized yarns had a high tensile strength of up to 420 MPa and a retained strength of $\sim 250 \text{ MPa}$ after a 2 h activation process. Since Ba-MWCNT yarns of a micrometer diameter exhibit good thermionic and mechanical properties, they can be used as miniature thermionic electron sources in devices such as vacuum fluorescent displays, x-ray tubes, and electron guns. Additionally, the research group studied the reaction of MWCNT yarns with a hafnium coating by self-electrical heating [13]. The HfC nanocrystals were fabricated by heating them to $1,327^\circ\text{C}$. The work function of the HfC-decorated MWCNT yarns was determined to be 3.9 eV by the thermionic emission method, 0.7 eV lower than that of pure CNT yarns. HfC-MWCNT yarn emitters were obtained by further heating to $1,863^\circ\text{C}$ and breakdown. These emitters consist of HfC nanorods. They can provide a current density of $800 \text{ A}/\text{cm}^2$ and can operate under a rough vacuum of 10^{-2} Pa without obvious degradation. Researchers have noted that these excellent field-emission properties make them promising for use as large-current and durable cold cathodes, which could be used in many potential applications such as microwave devices, x-ray tubes, vacuum gauges, and display devices.

Mirfakhrai et al. investigated actuation in high tensile strength yarns of twist-spun MWCNTs [14]. Actuation in response to voltage ramps and potentiostatic pulses was studied to quantify the dependence of actuation strain on the applied voltage. Strains of up to 0.5 % were obtained in response to applied potentials of 2.5 V. The dependence of strain on applied voltage and charge was found to be quadratic. The specific capacitance reached 26 F/g. The modulus of the yarns was independent of applied load and voltage within the experimental uncertainty.

CNT yarn is a promising candidate for lightweight cables. Xu et al. demonstrated a continuous process that combined yarn spinning, MWCNT anodization, and metal deposition, to fabricate lightweight and strong Cu-MWCNT yarn with metal-like conductivities [15]. The composite yarn with anodized MWCNTs exhibited a conductivity of $4.08 \times 10^4 \sim 1.84 \times 10^5$ S/cm and a mass density of $1.87 \sim 3.08$ g/cm³, as the Cu thickness changes from 1.0 to 3.0 μ m. The yarn can have a strength of 600 \sim 811 MPa, which is as strong as the un-anodized pure MWCNT yarn (656 MPa).

In the meantime, CNT yarns have been studied in the field of biomedical applications. Galvan-Garcia et al. demonstrated that highly oriented 50 nm-thick semitransparent MWCNT sheets and yarns, produced with a minimal residual content of catalytic transition materials, support the long-term growth of a variety of cell types ranging from skin fibroblasts and Schwann cells to postnatal cortical and cerebellar neurons [16]. They showed that MWCNT sheets stimulate fibroblast cell migration compared to plastic and glass culture substrates. These findings have positive implications for the use of MWCNTs in applications such as tissue engineering, wound healing, neural interfaces, and biosensors.

CNT yarns have also attracted attention as a sensing material. Ammonia gas-sensing characteristics for gold-decorated MWCNT yarns at room temperature were reported by Randeniya et al. [17]. The MWCNT yarns were first treated either with a strong acid or in a pulsed direct-current plasma containing Ar and either oxygen or hydrogen. A self-fuelled electrodeposition method was used and was shown to be a useful method for incorporating nanocrystalline Au particles onto the surfaces of MWCNT yarns. The plasma treatments lead to surface modifications that result in dense and uniformly distributed Au particles smaller than 3 nm along the lengths of MWCNT yarns. Nanocrystalline Au particle distributions in cases of untreated and acid-treated MWCNT yarns were sparse, and the particle sizes were larger (10 \sim 20 nm). In all cases, the introduction of Au to the yarns increased the sensitivity (measured as a change in resistance in a chemiresistor arrangement) to NH₃ by about a factor of 10 in comparison to yarns with no Au. The lowest concentration of NH₃ detectable using this method was close to 500 ppb. Plasma-treated and Au-decorated samples showed a stable, reproducible response and recovery. Furthermore, the research group demonstrated that robust and flexible chemiresistors fabricated from MWCNT yarns decorated with nanocrystalline Pd (Pd-MWCNT yarns) could detect hydrogen at a concentration of at least 20 (ppm) in nitrogen at room temperature [18]. Additionally, the lower limit of detection was found to extend down to 5 ppm, with the chemiresistors fabricated by introducing a layer of Pt on Pd which was decorated on the surface of MWCNT yarns (Pt-Pd-MWCNT yarns).

2 Strong Boron-Added MWCNT Yarns

The mechanical properties of CNT composites are strongly dependent on the mechanical strength of an individual CNT, the bonding strength (or strength of interfacial interaction) between the CNT and matrix, and the dispersion of CNTs in the matrix. One of the problems for production of strong CNT composites is that CNTs cannot transfer the load to a matrix because of the slipping between the CNT and matrix. Highly graphitized MWCNTs are chemically stable and hard to bond or fuse among themselves. Sato et al. succeed in producing large-size binder-free MWCNT solids from fluorinated MWCNTs using a thermal heating and compression method in vacuum as one of the methods to obtain bonds between CNTs [19, 20]. This technique resulted in the formation of covalent MWCNT networks generated by the introduction of sp^3 -hybridized carbon atoms that cross-link between nanotubes upon defluorination. In contrast to this method, Endo et al. have studied the effect of boron on the structure of double-walled carbon nanotubes (DWCNTs) at high temperature under atmospheric pressure using argon gas [21]. They discovered various nanotube complexes by incorporation of boron, such as covalent nanotube “Y” junctions, DWCNT coalescence, and the formation of flat MWCNTs. Based on this phenomenon, Sato et al. prepared boron-mixed MWCNT solids by heating and pressing the powder of purified MWCNTs mixed with 1, 5, and 10 wt% boron in the temperature range 1,400–1,800 °C every 200 °C under a constant pressure of 20 MPa in vacuo and investigated the influence of boron addition on nanotube structure and the mechanical and electrical properties of the resulting boron-mixed MWCNT solids. It is notable that part of the nanotubes in the boron-mixed MWCNT solids solidified at 1,800 °C and dramatically changed into rod-like graphitic carbons [22].

In the case of CNT yarns, if each building block, CNT, is ideally bonded or coarsened between contacting nanotubes by a method to joint CNTs [23], the CNT yarns can possess a flexible and remarkable mechanical strength due to individual CNTs. For example, if each graphene of the CNT component in CNT yarn bonds or coalesces by addition of a boron element, which is lighter than carbon, lightweight, soft, and strong CNT yarns can be produced. In this section, we report on the effect of boron addition on the mechanical properties of MWCNT yarns.

2.1 Synthesis of a Vertically Aligned MWCNT Forest

The substrate used was a p-type silicon wafer bearing thermal oxide. The catalyst was 3 nm of an iron film deposited by electron beam (e-beam) evaporation. The wafer is scored on the back and snapped into rectangles of 30 × 30 mm. The cut wafers were placed on a quartz plate (0.5 × 25 × 120 mm) which was slid into the reactor from the outlet end to the center position. After loading and closure of the reactor, it was evacuated and flowed with He (99.9999 %). A helium flow rate of 496 sccm was used as the temperature was ramped for 20 min to the reaction temperature of 678 °C and then held for 10 min. Following this procedure, aligned

MWCNT forests were synthesized using an atmospheric pressure of 3 mol% acetylene (99.9999 %) in helium at 678 °C using a total flow rate of 512 sccm for 15 min.

2.2 Preparation and Characterization of Boron-Added MWCNT Yarns

As shown in Fig. 3.2, a custom-made system to spin MWCNT yarns from a vertically aligned MWCNT forest was used. The vertically aligned MWCNT forest was on the left side. The MWCNT strip was passed into a boron-containing solution in a Teflon boat (Fig. 3.2b) in order to add the boron element and to form yarn densification, and the MWCNT strip was twisted at the pulley and drawn in by a spinning motor. MWCNT yarns were spun under the following conditions: MWCNT width of 2 mm, motor rotation of 1,360 rpm, drawing velocity of

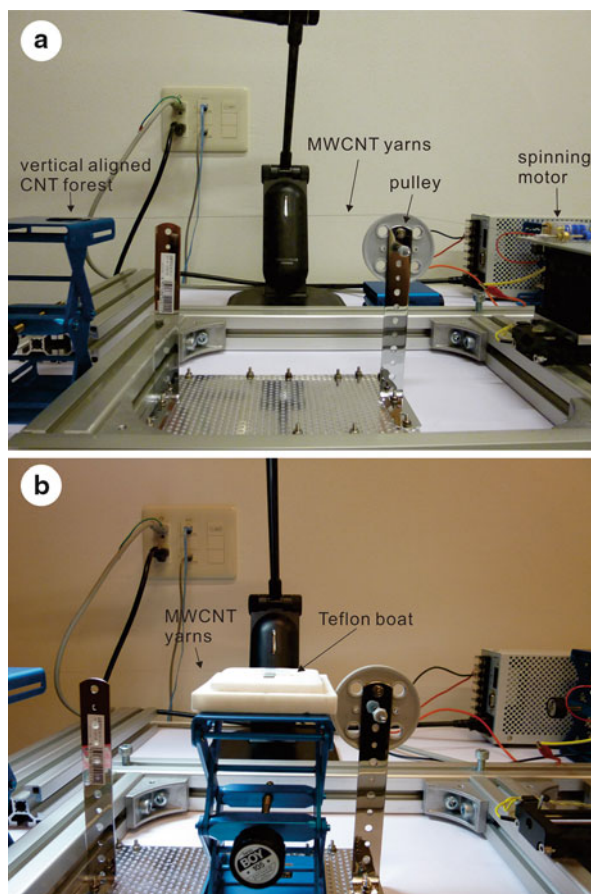


Fig. 3.2 (a) Picture of the custom-made system to spin CNT yarns from a vertically aligned CNT forest. (b) Picture of the setup that adds a boron-containing solution (or suspension) to CNT yarns

5 cm/min, and drawing distance of 12 cm. In order to give high orientation to the yarn, a pulley is set at the center of the spinning system. An amorphous boron dispersion of 0.001 mol/L in ethanol and a phenylboronic acid solution of 0.001 mol/L in toluene were prepared as the boron-containing solution. The boron-added MWCNT yarn was heated at 2,000 °C for 5 h, with an applying load of 136 μ N.

The sample morphologies were determined by scanning electron microscopy (SEM) equipped with a field emission gun, which was operated at 5 kV. The high-resolution transmission electron microscopy equipped with a field emission gun was operated at 200 kV. In addition, energy loss near-edge structure (ELNES) spectra of cross-sectioned boron-added MWCNT yarns using a parallel electron energy loss spectroscopy (EELS) detector equipped with HF-2000 were measured in an effort to gather information concerning boron and carbon atoms in the yarns. Raman scattering spectroscopy studies were used to analyze the vibrational modes of the graphitic materials. The measurement was carried out at room temperature using an Ar ion laser with an excitation wavelength of 488.0 nm. The MWCNT yarn was fixed across a 10-mm square hole in the center of a 15 mm-wide paper frame. After this paper frame containing the MWCNT yarn was mounted in a tensile test apparatus, the opposite sides of the paper frame were cut to free the MWCNT yarn. The MWCNT yarn gauge length was 10 mm, and the tensile tests were conducted at a constant rate of extension of 1 % per minute. The diameter of the MWCNT yarn was measured using a scanning electron microscope before measuring the mechanical test in order to convert the applied force to the engineering stress.

2.3 Mechanical Properties of Boron-Added MWCNT Yarns

HRTEM revealed that aligned CNTs comprised 300 μ m-length MWCNTs with an average inner diameter of 5.0 ~ 6.5 nm and outer diameter of 10 ~ 13 nm, which showed that MWCNT consisted of 9 ~ 12 layers of MWCNTs (Fig. 3.3). As-prepared MWCNT yarns had an average diameter of 8.2 μ m, a surface twist angle of 17.5°, and a linear density of 0.62 μ g/cm (Fig. 3.4). As shown in Fig. 3.5, the specific stress of the *heated a-boron-added* MWCNT yarns (a-boron-added MWCNT yarns heated at 2,000 °C) and *heated PBA-added* MWCNT yarns (PBA-added MWCNT yarns heated at 2,000 °C) were stronger than that of the *heated toluene-densified* MWCNT yarns. Table 3.2 shows the mechanical properties of each yarn and includes details for as-prepared MWCNT yarns, MWCNT yarns densified by ethanol (*EtOH-densified* MWCNT yarns), *EtOH-densified* MWCNT yarns heated at 2,000 °C (*heated EtOH-densified* MWCNT yarns), toluene-densified MWCNT yarns heated at 2,000 °C (*heated toluene-densified* MWCNT yarns), and carbon fibers (Torayca T300B; Toray). The specific stress and stiffness of *heated a-boron-added* MWCNT yarns were 0.87 ~ 0.90 and 28 ~ 77 GPa/g/cm³, respectively, and were larger than those of *heated EtOH-densified* MWCNT yarns. As shown in Fig. 3.6, CNT aggregation was partly observed on the surface of *heated a-boron-added* MWCNT yarns. As this

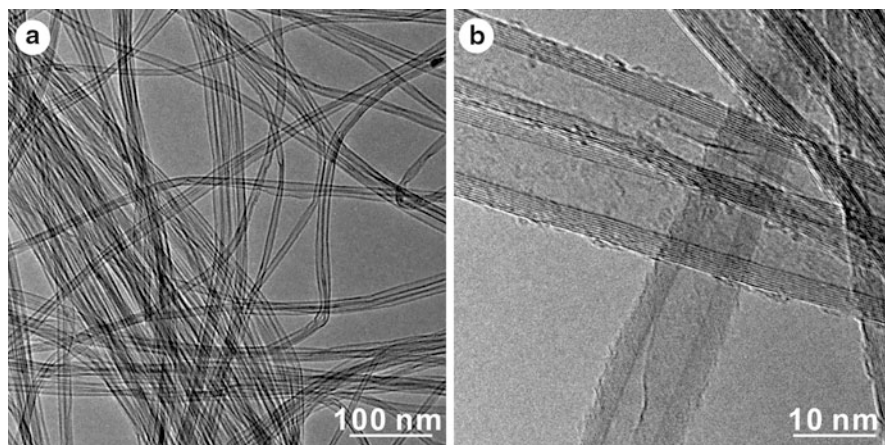


Fig. 3.3 (a) Low and (b) high magnification HRTEM images of MWCNTs

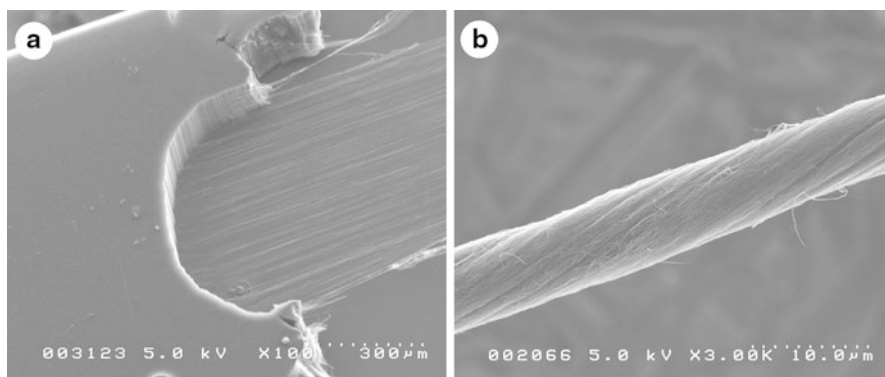


Fig. 3.4 SEM micrographs of (a) the drawing of an MWCNT web from an MWCNT forest and (b) as-prepared MWCNT yarns

aggregation was not observed on the surface of *EtOH-densified* MWCNT yarns heated at 2,000 °C, CNTs in the yarn were changed by adding the amorphous boron. From these experiments, the dispersion of atom-scale boron onto a yarn can contribute to bonding between nanotubes and improvement in the mechanical strength of CNT yarns. Furthermore, the specific stress, specific stiffness, and toughness of *heated PBA-added* MWCNT yarns were 0.95 ~ 1.40 GPa/g/cm³, 28 ~ 82 GPa/g/cm³, and 14 ~ 28 J/g, respectively, which were respectively 2.0, 2.2, and 1.8 times those of *heated toluene-densified* MWCNT yarns and 1.4, 0.6, and 2.5 times those of the measured carbon fibers. The increased strength is thought to be derived from a homogeneous dispersion of phenylboronic acid to the yarns, suggesting that the addition of boron affects the bonding or structure of CNT component in the yarn. Recently, gamma irradiation of MWCNT yarns in air has

Fig. 3.5 Plots of the specific stress against strain of boron-added MWCNT yarns.

Heated PBA-added MWCNT yarns (top), heated a-boron-added MWCNT yarns (middle), and heated toluene-densified MWCNT yarns (bottom)

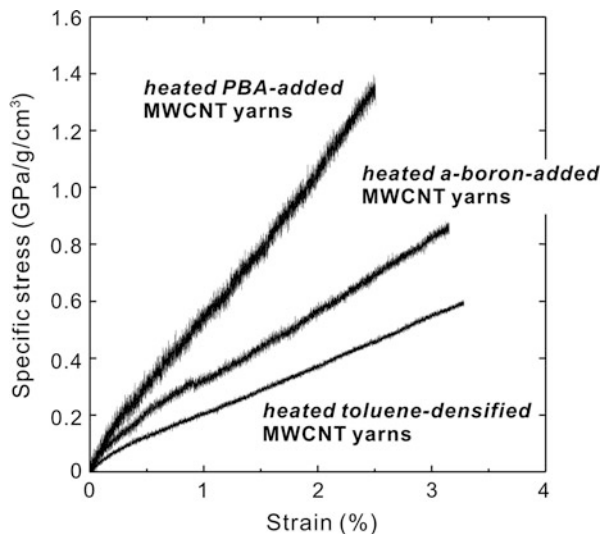


Table 3.2 Mechanical properties of boron-added MWCNT yarns

Materials	Specific stress [GPa/g/cm ³]	Specific stiffness [GPa/g/cm ³]	Toughness [J/g]
As-prepared MWCNT yarns	0.65 ~ 0.68	32.5 ~ 37.4	11 ~ 15
<i>EtOH</i> -densified MWCNT yarns	0.59 ~ 0.65	10 ~ 27	15 ~ 22
<i>Heated EtOH</i> -densified MWCNT yarns	0.61 ~ 0.69	21 ~ 37	7 ~ 14
<i>Heated a-boron-added</i> MWCNT yarns	0.87 ~ 0.90	28 ~ 77	14 ~ 19
<i>Heated toluene-densified</i> MWCNT yarns	0.58 ~ 0.72	23 ~ 30	7 ~ 10
<i>Heated PBA-added</i> MWCNT yarns	0.95 ~ 1.40	28 ~ 82	14 ~ 28
Carbon fibers (Torayca T300B; Toray)	1.07	127	6.2

significantly improved the tensile strength and modulus of the yarns. Maio and colleagues irradiated MWCNT fiber in air to a total dose of 250 kGy at a dose rate of 4.2 kGy/h. They found that the grand average specific stress of all the irradiated MWCNT yarns was 27 % higher than that of unirradiated MWCNT yarns [24]. They suggested that oxygen atoms and carboxyl groups appeared in the MWCNT component after being gamma-irradiated in air, which could result in cross-linking between nanotubes through atoms or groups added to the MWCNT surfaces during irradiation. In the case of our experiment, the specific stress of all the *heated PBA-added* MWCNT yarns was 81 % higher than that of the *heated toluene-densified* MWCNT yarns. At the present stage, the boron in *heated PBA-added* MWCNT yarns was not detected by TEM-EELS, which may reflect an analytical limit. From Raman scattering spectroscopy, the *R*-value (the ration of D-band to G-band) of *heated PBA-added* MWCNT yarns was 0.25 larger than that of *heated*

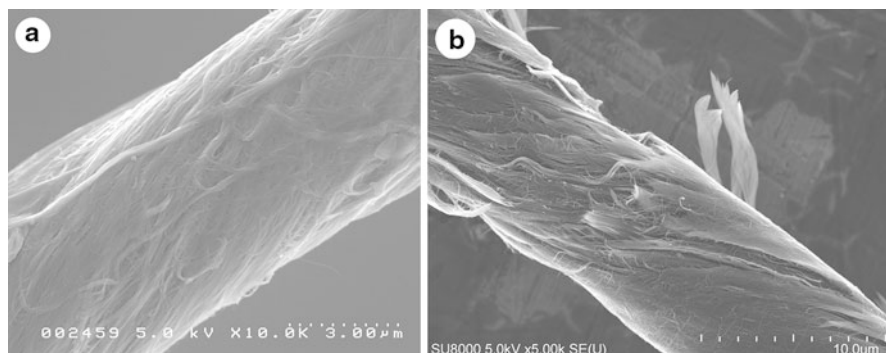


Fig. 3.6 (a) SEM micrograph of the surface of *heated a-boron-added* MWCNT yarns. (b) SEM micrograph of the fracture surface of *heated a-boron-added* MWCNT yarns after the tensile test

toluene-densified MWCNT yarns (R -value; 0.20). This phenomenon generally occurs when boron atoms are substituted into the network frame of carbon [25–27], indicating that boron interacted with the nanotube in the *heated PBA-added* MWCNT yarns.

3 Conclusions

In this chapter, we focused on the production procedure, properties, and application of CNT yarns. Additionally, we reviewed the effect of boron addition on the mechanical properties of CNT yarns in an effort to make lightweight and strong CNT yarns. The specific stress, specific stiffness, and toughness of the *heated phenylboronic acid-added* MWCNT yarns were $0.95 \sim 1.40$ GPa/g/cm³, $28 \sim 82$ GPa/g/cm³, and $14 \sim 28$ J/g, respectively, which were respectively 2.0, 2.2, and 1.8 times those of *toluene-densified* MWCNT yarns, showing the production of highly flexible and strong MWCNT yarns following addition of boron.

If flexible and strong CNT yarns or fibers are exchanged instead of traditional carbon fibers, CNT fiber-consisting mobile systems utilized in airplanes, the super express, cars, and ships will improve fuel efficiency and lower costs, as well as decrease carbon dioxide emission. Meanwhile in the field of electronics, the wires and cables of electric devices are essential, and opportunities exist to develop new materials with reduced resistance, mass, and/or susceptibility to fatigue. The lightweight and strong CNTs offer opportunities for integration into wires and cables for both power and data transmission due to their unique physical and electronic properties [28]. Macroscopic CNT wires and ribbons are presently viable replacements for metallic conductors in lab-scale demonstrations of coaxial, USB, and Ethernet cables [29]. In certain applications, CNT fibers may be positioned to displace the traditional carbon fibers and metal wires to achieve substantial benefits.

Acknowledgment This work was supported by PRESTO-JST from the Ministry of Education, Science, Culture and Sport of Japan.

References

1. Li Y-L, Kinloch IA, Windle AH (2004) *Science* 304:276
2. Zhang M, Atkinson KR, Baughman RH (2004) *Science* 306:1358
3. Hone J, Llaguno MC, Nemes NM, Johnson AT, Fischer JE, Walters DA, Casavant MJ, Schmidt J, Smalley RE (2000) *Appl Phys Lett* 77:666
4. Pierson HO (1993) *Handbook of carbon, graphite, diamond and fullerenes: properties, processing, and applications*. Noyes Publications, New Jersey, p 61
5. Ebbesen TW, Lezec HJ, Hiura H, Bennett JW, Ghaemi HF, Thio T (1996) *Nature* 382:54
6. Dai HJ, Wong EW, Lieber CM (1996) *Science* 272:523
7. Zhang X, Li Q, Tu Y, Li Y, Coulter JY, Zheng L, Zhao Y, Jia Q, Peterson DE, Zhu Y (2007) *Small* 3:244
8. Liu K, Sun Y, Zhou R, Zhu H, Wang J, Liu L, Fan S, Jiang K (2010) *Nanotechnology* 21:045708
9. Miao M, McDonnell J, Vuckovic L, Hawkins SC (2010) *Carbon* 48:2802
10. Fang S, Zhang M, Zakhidov AA, Baughman RH (2010) *J Phys Condens Matter* 22:334221
11. Zakhidov ALA, Nanjundaswamy R, Obratsov AN, Zhang M, Fang S, Klesch VI, Baugman RH, Zakhidov AA (2007) *Appl Phys* A88:593
12. Xiao L, Liu P, Jiang K, Feng X, Wei Y, Qian L, Fan S, Zhang T (2008) *Appl Phys Lett* 92:153108
13. Yang Y, Liu L, Wei Y, Liu P, Jiang K, Li Q, Fan S (2010) *Carbon* 48:531
14. Mirfakhrai T, Oh JY, Kozlov M, Fok ECW, Zhang M, Fang SL, Baughman RH, Madden JDW (2007) *Smart Mater Struct* 16:S243
15. Xu G, Zhao J, Li S, Zhang X, Yong Z, Li Q (2011) *Nanoscale* 3:4215
16. Galvan-Garcia P, Keefer EW, Yang F, Zhang M, Fang S, Zakhidov AA, Baughman RH, Romero MI (2007) *J Biomater Sci Polym Ed* 18:1245
17. Randeniya LK, Martin PJ, Bendavid A, McDonnell J (2011) *Carbon* 49:5265
18. Randeniya LK, Martin PJ, Bendavid A (2012) *Carbon* 50:1786
19. Sato Y, Ootsubo M, Yamamoto G, Van Lier G, Terrones M, Hashiguchi S, Kimura H, Okubo A, Motomiya K, Jeyadevan B, Hashida T, Tohji K (2008) *ACS Nano* 2:348
20. Sato Y, Nishizaka H, Sawano S, Yoshinaka A, Hirano K, Hashiguchi S, Arie T, Akita S, Yamamoto G, Hashida T, Kimura H, Motomiya K, Tohji K (2012) *Carbon* 50:34
21. Endo M, Muramatsu H, Hayashi T, Kim YA, Van Lier G, Charlier JC, Terrones H, Terrones M, Dresselhaus MS (2005) *Nano Lett* 5:1099
22. Sato Y, Nishizaka H, Motomiya K, Yamamoto G, Okubo A, Kimura H, Ishikuro M, Wagatsuma K, Hashida T, Tohji K (2011) *ACS Appl Mater Interfaces* 3:2431
23. Roberts GS, Singjai P (2011) *Nanoscale* 3:4503
24. Miao MH, Hawkins SC, Cai JY, Gengenbach TR, Knott R, Huynh CP (2011) *Carbon* 49:4940
25. Wang Y, Alsmeyer DC, McCreery RL (1990) *Chem Mater* 2:557
26. Hishiyama Y, Irumano H, Kaburagi Y (2001) *Phys Rev B* 63:245406
27. Lyu SC, Han JH, Shin KW, Sok JH (2011) *Carbon* 49:1532
28. Bradford PD, Bogdanovich AE (2008) *J Compos Mater* 42:1533
29. Jarosz P, Schauerma C, Alvarenga J, Moses B, Mastrangelo T, Raffaele R, Ridgley R, Landi B (2011) *Nanoscale* 3:4542

Synthesis and Characterization of Poly (Phenylene Sulfide)-Grafted Carbon Nanotube Nanocomposites

4

Ana M. Díez-Pascual and Mohammed Naffakh

Contents

1	Introduction	76
2	Poly(phenylene sulfide): Structure and Properties	78
3	Preparation and Characterization of the Polymer Derivatives	78
4	Synthesis of Functionalized Carbon Nanotubes	84
5	Grafting Approaches to Prepare the Nanocomposites	86
6	Characterization of the Nanocomposites	86
6.1	IR and NMR	86
6.2	Morphology	89
6.3	Thermal Stability	90
6.4	Crystallization and Melting Behaviour	93
6.5	Crystalline Structure	94
6.6	Mechanical Properties	95
6.7	Electrical Conductivity	98
7	Future Potential Applications	98
8	Concluding Remarks	99
	References	100

Abstract

Poly(phenylene sulfide) (PPS) is a semicrystalline engineering thermoplastic with outstanding mechanical and thermal properties, good chemical and flame resistance, as well as easy processability, widely used in the electronics, automotive, aeronautic, and chemical industries. To further extend its structural applications, different types of fillers such as carbon nanotubes (CNTs) have been incorporated

A.M. Díez-Pascual (✉)

Instituto de Ciencia y Tecnología de Polímeros, ICTP-CSIC, Madrid, Spain

e-mail: adiez@ictp.csic.es

M. Naffakh

Departamento de Ingeniería y Ciencia de Los Materiales, Escuela Técnica Superior de Ingenieros Industriales, Universidad Politécnica de Madrid, Madrid, Spain

e-mail: mohammed.naffakh@upm.es

in this polymer. However, the direct integration of CNTs leads to nanocomposites with poor mechanical performance. An alternative approach is the chemical modification of PPS via nitration and amination reactions. The modified polymers maintain the exceptional properties of the parent PPS and simultaneously display higher hydrophilicity and a number of reactive groups capable of interacting with functionalized CNTs. Thus, an aminated derivative (PPS-NH₂) has been covalently anchored onto the surface of epoxy and acid-functionalized CNTs in a one-pot process. The resulting PPS-NH₂-grafted-CNT nanocomposites have been extensively characterized through different techniques to obtain information about the extent of the grafting reactions, their morphology, thermal stability, crystallization behavior, and mechanical and electrical properties, and the results are compared with those attained in nanocomposites prepared by direct reinforcement. The formation of covalent linkages at the polymer-nanotube interface enables improved CNT dispersion, facilitating the stress transfer and enhancing the thermal stability and electrical conductivity of the composites. The results herein offer useful insights into the development of proper functionalization routes and grafting approaches for enhancing the properties of thermoplastic/CNT nanocomposites.

Keywords

Thermoplastics • Nanocomposite materials • Morphology • Thermal properties • Mechanical properties

1 Introduction

Composites of carbon nanotubes (CNTs) within a polymer matrix have received considerable attention in both research and industrial fields due to their high stiffness, strength, and thermal stability at relatively low nanofiller content [1, 2]. The key issues in the preparation of CNT-reinforced nanocomposites are to attain a homogenous filler dispersion and good interfacial adhesion with the host matrix. However, processing is hindered by the poor solubility of the CNTs and the intermolecular van der Waals interactions between them, thus resulting in the formation of aggregates [3]. The anchoring of functional groups onto the CNT surface has been proven to be an effective approach to develop polymer composites. It consists in the chemical modification of CNTs followed by blending with polymers through “grafting to” or “grafting from” strategies [2]. The most common functionalization processes are based on the oxidation of the CNTs with strong acids [4] such as nitric or sulfuric to produce surface groups such as hydroxyl, carbonyl, and carboxyl that can subsequently react with functional groups of the polymer leading to an ester [5, 6] or amide bond [7, 8]. Nevertheless, this approach can bring significant damage such as sidewall opening or tube breakage [9], introducing defects in the tubular framework that can adversely impact their mechanical properties and/or disrupt the electronic continuum, reducing their surface electrical and thermal conductivities. Therefore, other functionalization

methods that maintain the integrity of the CNTs to be further covalently grafted to polymers or their derivatives are required.

CNTs belong to the fullerene family, and in terms of reactivity, both types of carbon-based materials are very similar. A new efficient route to synthesize functionalized CNTs is the anchoring of epoxy groups onto their surface under mild conditions following an organometallic approach [10]. The strategy involves two reactive steps: firstly, the nucleophilic addition of an organolithium reactant to double bonds of the hexagonal rings of the CNTs and, secondly, the nucleophilic substitution with halogen or hydroxyl oxacyclopropanes such as epichlorohydrin. The epoxy group may then be converted into different kinds of functionalities through a ring-opening process, enabling cross-linking reactions with amines, carboxylic acids, anhydrides and hydroxyl-containing polymers [11]. Thus, epoxy-functionalized CNTs provide opportunities for various applications such as fillers in composite materials for electronic devices and high-performance membranes [12].

Poly(phenylene sulfide) (PPS) is a widely used engineering thermoplastic that possesses excellent mechanical, chemical, and thermal properties. Most PPS products are reinforced with carbon or glass fibers for high-performance applications in the aerospace sector [13], such as in “J-Nose” wing substructures of the Airbus A340-500/600, replacing the aluminum parts of the old “D-Nose,” which leads to a 20 % reduction in weight. Recently, it has also been used in the electronics industry for the fabrication of connectors, chip carriers, printed-wiring-board substrates, etc. [14]. However, certain applications of this polymer are somewhat limited due to its brittleness and relatively low strength as well as electrically insulating character. In addition, it is insoluble in common organic solvents [15], which represents the main obstacle for its functionalization, hence the ability to interact with other substances. To overcome the aforementioned drawbacks, different nanoscale fillers such as multiwalled carbon nanotubes (MWCNTs) have been incorporated in this polymer matrix [16–20]. However, the improvements in thermal and mechanical properties attained lie far below the theoretical predictions.

Chemical modifications of PPS have emerged as an interesting strategy for the development of materials with improved properties for new potential applications. In this regard, it is interesting to prepare PPS derivatives that incorporate reactive functional groups while maintaining the excellent properties of the parent polymer. The presence of the aromatic rings in the polymer backbone is crucial for its functionalization, since they can act as an electron source for electrophilic substitution reactions. In the literature, studies related to the preparation of PPS derivatives are very scarce. Barique et al. [21] synthesized sulfonated PPS membranes by immersion in chlorosulfonic acid solution. Jeon et al. [22] functionalized MWCNTs with 4-chlorobenzoic acid by Friedel-Crafts acylation in polyphosphoric acid (PPA) and subsequently carried out the in situ electrophilic grafting of linear PPS (LPPS) or hyperbranched PPS (HPPS) onto functionalized MWCNTs. This method is difficult to scale up, since specific monomers must be employed to obtain high-molecular-weight polymers. The resulting composites exhibited good electrical conductivity albeit lower thermal stability than the neat polymers.

This chapter provides an example on the preparation of multifunctional PPS-grafted single-walled carbon nanotube (SWCNT) nanocomposites with enhanced performance through a simple and economic process, suitable to scale-up. The nanocomposites have been extensively characterized through different techniques to obtain information about the extent of the grafting reactions, their morphology, thermal stability, crystallization behavior, and mechanical and electrical properties, and the results are compared with those attained by direct integration of unfunctionalized SWCNTs. The influence of the synthesis route and SWCNT type on the final properties of the resulting nanocomposite materials is discussed.

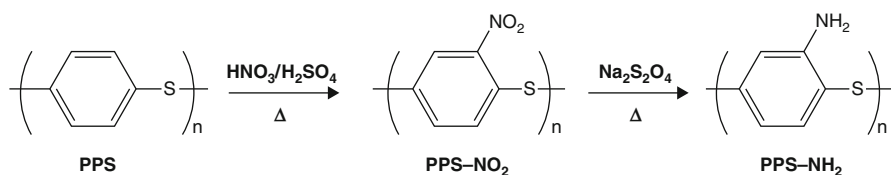
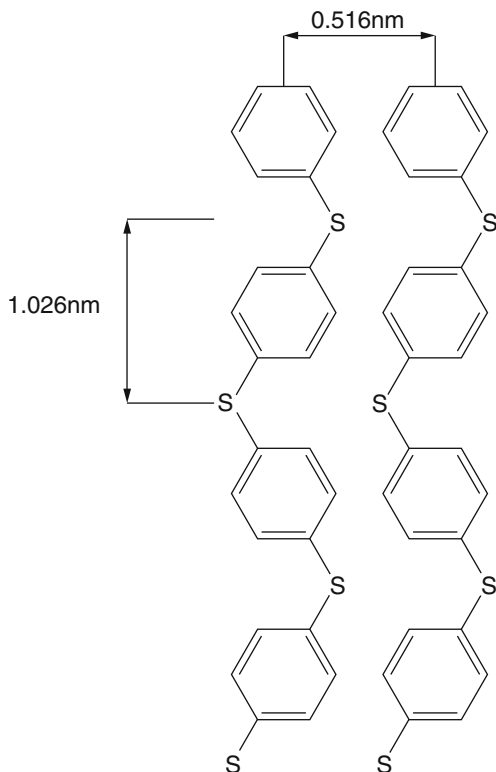
2 Poly(phenylene sulfide): Structure and Properties

PPS was discovered as a by-product of the Friedel-Crafts reaction in 1888 and first commercialized by Phillips Petroleum in 1973 under the trade name of Ryton. It is a semicrystalline engineering thermoplastic with a symmetrical rigid backbone chain composed of recurring para-substituted aromatic rings and sulfur atoms that exhibits outstanding physical and chemical properties such as high thermal stability, high deflection temperature, excellent mechanical and friction properties, flame retardancy, resistance to common organic solvents below 200 °C, electrical insulation, antiaging, and precision moldability [23]. The molecular weight of PPS is generally quite low ($\leq 30,000$); it possesses low glass transition temperature ($T_g \sim 90$ °C) compared to its high melting temperature ($T_m \sim 280$ °C) and density of 1.35 g/cm³. Low-molecular-weight PPS tends to crystallize rapidly during cooling from a molten state, leading to a high degree of crystallinity (typically ≥ 50 %) that limits its impact strength [14]. Heat treatment of PPS leads to two complex reactions, chain elongation and cross-linking caused by the formation of thioether bonds, which are practical ways to increase molecular weight and improve impact properties. The crystalline structure of PPS is orthorhombic and belongs to the spatial group $P_{bcn} - D_{2h}^{14}$, with two parallel chains per unit cell. The sulfur atoms of each chain lie on the same plane in a zigzag-like arrangement, and the phenylene rings alternately form an angle of $\pm 45^\circ$ to this plane as shown in Fig. 4.1. The angle between the C-S bonds is about 110°. The unit cell dimensions (nm) are $a = 0.867$, $b = 0.561$, and $c = 1.026$ [24].

3 Preparation and Characterization of the Polymer Derivatives

PPS derivatives can be prepared in two reaction steps, as shown in Scheme 4.1. Firstly, the nitrated polymers (PPS-NO₂) with different degrees of nitration can be synthesized by addition of a nitric/sulfuric acid mixture (4:1 v/v) under different reaction conditions (Table 4.1) [25]. The suspensions are then filtered at room temperature under vacuum; washed with water, ethanol, and acetone; and dried in

Fig. 4.1 Crystal structure of PPS



Scheme 4.1 Synthesis procedure of nitrated and aminated PPS derivatives (Taken from reference [25], with permission from Elsevier, copyright 2012)

an oven at 80 °C for 24 h. Secondly, the corresponding aminated derivatives (PPS-NH₂) can be obtained by reduction of the nitro group to its respective amine using sodium dithionite as reduction agent in *N,N*-dimethylformamide (DMF) medium. The solutions are then heated to reflux under a nitrogen atmosphere, filtered hot, precipitated in a mixture of methanol and 1 N nitric acid solution, washed, and finally oven dried at 80 °C.

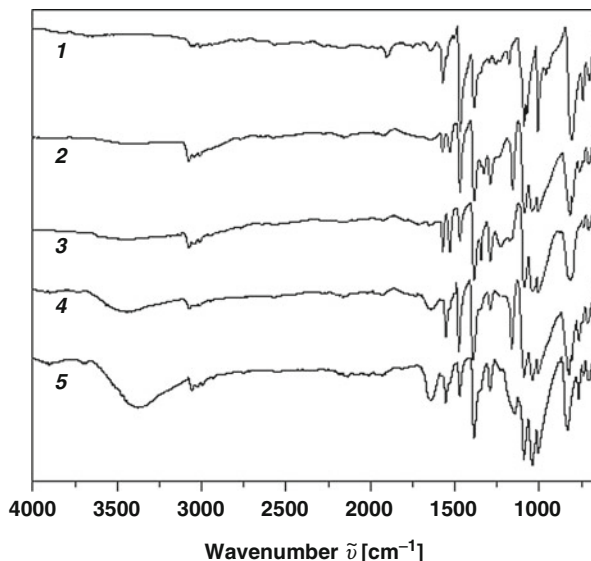
The functionalization degree (FD) of the derivatives (defined as number of nitro or amino groups per polymer repeat unit) can be calculated from elemental analysis [25], and the results are summarized in Table 4.1. The nitration degree rises upon

Table 4.1 Conditions of the nitration/amination reactions, characteristic degradation temperatures obtained from TGA under a nitrogen atmosphere, and DSC thermal parameters for the PPS derivatives. All the experiments correspond to a rate of 10 °C/min. The nitrated and aminated polymer derivatives are designated as PPS-NO₂ (x) and PPS-NH₂ (x), where x indicates the degree of functionalization (Data taken from [25])

Material Designation	Reaction conditions T [°C]	t [min]	$T_{i,1}$ [°C]	$T_{max,1}$ [°C]	$T_{i,2}$ [°C]	$T_{max,2}$ [°C]	X_c [%]	T_g [°C]	T_m [°C]	T_c [°C]
PPS	–	–	–	–	458	540	52	91	–257	252
PPS-NO ₂ (19)	60	30	385	436	446	572	42	99	257	248
PPS-NO ₂ (31)	65	60	344	415	435	568	30	110	252	235
PPS-NO ₂ (54)	100	90	304	385	422	551	11	116	248	226
PPS-NO ₂ (83)	100	180	281	362	417	549	–	130	–	–
PPS-NH ₂ (19)	120	360	–	–	377	556	46	104	–253	245
PPS-NH ₂ (54)	120	480	–	–	296	505	16	122	–242	222

T_i : initial degradation temperature, T_{max} : temperature of maximum rate of degradation. The subscripts 1 and 2 refer to the first and second degradation stage, respectively. T_c : crystallization temperature, T_m : melting temperature, X_c : degree of crystallinity determined from the relation between the melting enthalpy of the functionalized PPS and that of a 100 % crystalline PPS [23], T_g : glass transition temperature determined as the midpoint of the baseline shift

Fig. 4.2 IR spectra of PPS (1), PPS-NO₂ with 19 % FD (2), PPS-NO₂ with 54 % FD (3), PPS-NH₂ with 19 % FD (4), and PPS-NH₂ with 54 % FD (5) (Adapted from reference [25], with permission from Elsevier, copyright 2012)



increasing temperature and reaction time following a logarithmic growth; FD increases sharply up to 31 % for a reaction time of 1 h at 65 °C, whereas it only reaches 86 % after a reaction time of 3 h at 100 °C. The slow rate of nitration is probably related with the low solubility of PPS, since part of the precursor polymer remains insoluble even after several hours of reaction. In contrast, the amination reaction proceeds more easily, and all the nitro groups are reduced to amino.

At room temperature, the pure PPS is soluble only in strong acids. The solubility of PPS-NO₂ derivatives increases with the extent of modification, and for FD \geq 54 % they become soluble in nucleophilic polar aprotic solvents such as DMF, dimethylacetamide (DMAc), dimethylsulfoxide (DMSO) or *N*-methylpyrrolidone (NMP), due to the electronic interactions with the electrophilic nitrated phenylene moieties of the PPS-NO₂. The nitration process modifies the chemical nature and chain regularity of PPS, reducing its strong intercrystalline forces and increasing its polarity, hence resulting in enhanced solubility. Nevertheless, all the nitrated derivatives remain completely insoluble in common polar (i.e., methanol, water) or nonpolar (i.e., benzene, toluene) solvents. Regarding the aminated derivatives, all are soluble in DMF, DMAc, DMSO, and NMP; the amino group in the aromatic ring provides a highly basic nature, increasing the polymer solubility.

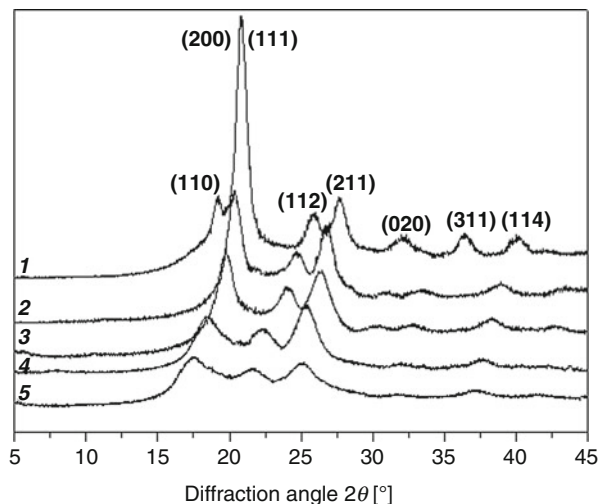
IR spectroscopy is a useful tool to obtain information about the changes in the chemical structure of PPS induced by the nitration and amination processes (Fig. 4.2). The spectrum of neat PPS shows characteristic peaks at 1,570 and 1,010 cm⁻¹, attributed to the symmetric stretching of the para-disubstituted ring and the in-plane C-H bending vibration [26], respectively; the C = C stretching of the aromatic ring appears at 1,470 cm⁻¹ and the out-of-plane deformation vibration of = C-H in 1,4 place of benzene at 818 cm⁻¹. Moreover, phenylene-sulfur

stretching modes occur in the range 1,120–1,030 cm^{-1} . In the spectra of the PPS- NO_2 derivatives, new absorption peaks appear at 1,517 and 1,340 cm^{-1} , arising from the asymmetrical and symmetrical stretching of the nitro group, respectively [49]. The band at 1,280 cm^{-1} corresponds to the C-N stretching and the shoulder at 1,230 cm^{-1} to the angular deformation of the C-H bond of the three-substituted ring [27]. The comparison of the spectra for derivatives with nitration degrees of 19 and 54 % reveals a broadening and an increase in the intensity of the bands related to the NO_2 group with increasing FD. The spectra of the aminated derivatives show the disappearance of the bands related to the NO_2 and the appearance of peaks at 3,420, 1,630, and 800 cm^{-1} ascribed to the stretching, in-plane deformation, and out-of-plane bending of the N-H, respectively. The N-H stretching band becomes more intense and shifts to lower wave numbers as the extent of modification rises, caused by the increase in the intermolecular interactions through hydrogen bonding. The total disappearance of the characteristic peaks of the NO_2 corroborates that all the nitro groups have been reduced to amino.

The characteristic degradation temperatures under inert conditions for PPS and the functionalized polymers are collected in Table 4.1. Neat PPS has a single degradation stage that starts (T_i) at ~ 458 °C and exhibits the maximum rate of weight loss (T_{max}) at ~ 540 °C. In contrast, the nitrated derivatives exhibit two degradation stages [25], the first corresponds to the elimination of the nitro groups and the second to the decomposition of the main chain. With increasing FD, T_i and T_{max} of the first step decrease while the mass loss rises. Thus, for PPS- NO_2 with nitration degree of 19 %, T_i and T_{max} occur at 385 °C and 436 °C, respectively, while for the derivative with the highest nitration degree, they take place at about 281 °C and 362 °C. The second degradation stage also initiates at temperatures below that of the parent polymer, and the loss in thermal stability rises with increasing FD. Thus, for the aforementioned derivatives, T_i of the second step is around 12 °C and 40 °C lower than that of PPS, respectively. These drops can be induced by changes in the polarity of the polymer chains as a result of the inductive and resonance effects exerted by the substituent groups and are also related to changes in the spatial organization of the molecules caused by the nitration process, since it has been reported [28] that the efficiency of chain packing falls strongly by the incorporation of randomly distributed end groups along the polymer backbone. The aminated derivatives also exhibit lower thermal stability than neat PPS, and it deteriorates with increasing FD; thus, for PPS- NH_2 with amination degrees of 19 % and 54 %, the degradation of the backbone initiates at ~ 70 °C and 126 °C below that of the nitrated precursor polymer, respectively. Similar trends are found for T_{max} , albeit the decreases are considerably smaller (~ 16 °C and 46 °C, respectively). The highly basic nature of the aminated derivatives makes them less stable than the nitrated polymers, as reported for other nitrated and aminated thermoplastics [27].

The thermal parameters obtained from the crystallization and melting thermograms of the different derivatives are tabulated in Table 4.1. The crystallization temperature T_c is ~ 252 °C for PPS and diminishes gradually with increasing extent

Fig. 4.3 X-ray diffraction patterns of PPS (1), PPS-NH₂ with 19 % FD (2), PPS-NO₂ with 19 % FD (3), PPS-NO₂ with 54 % FD (4), and PPS-NH₂ with 54 % FD (5) (Adapted from reference [25], with permission from Elsevier, copyright 2012)



of modification, by 26 °C and 30 °C for PPS-NO₂ and PPS-NH₂ with an FD of 54 %, respectively. Analogously, the melting peak T_m of these derivatives drops by ~ 9 °C and 15 °C in comparison with that of the parent PPS (~ 257 °C). The inclusion of the substituent groups hinders the mobility of the polymer chains, slowing down the overall crystallization process, and inhibits the molecular packing, leading to the formation of smaller and more imperfect crystallites that present lower T_m . The aminated derivatives possess lower T_c than the corresponding nitrated polymers due to the formation of strong intermolecular hydrogen bonds that impose intense restrictions on the diffusion of the polymeric segments. The level of crystallinity shows a strong reduction by ~ 78 % and 69 % for the aforementioned nitrated and aminated derivatives, respectively, and PPS-NO₂ with an FD of 83 % is amorphous. The glass transition temperature T_g rises as FD increases, the increment being nearly 40 °C for this amorphous derivative in comparison with the T_g of PPS (~ 91 °C). The raise in T_g is caused by the increase in the intermolecular interactions between adjacent chains due to the presence of the polar functional groups and the hindering of chain rotation due to steric effects. Comparing the same FD, the aminated derivatives show slightly higher T_g than the nitrated polymers, due to the formation of hydrogen bonds (confirmed by the IR spectra) that increase considerably the chain resistance to rotation. With increasing FD, the number of hydrogen bonds rises, leading to a progressive immobilization of the polymer chains.

X-ray diffractograms (Fig. 4.3) provide information about the morphology of the polymer derivatives in terms of structure, overall crystallinity, crystallite size, etc. The diffraction pattern of neat PPS shows the most intense reflection at $2\theta \approx 20.8^\circ$, corresponding to the overlap of the [111] and [200] diffractions; other peaks are found at 19.2°, 25.8°, and 27.6°, arising from the [110], [112], and [211]

crystalline planes, respectively [29]. In the case of the derivatives, the reflection corresponding to the [110] plane disappears, and the rest of the diffractions shift to lower 2θ values. As FD increases, peaks become wider and less intense, caused by a decrease in the degree of crystallinity (estimated from the relation between the integrated intensities of the crystalline and amorphous phases) and in the crystallite size (D_{hkl}), which can be roughly estimated according to the Scherrer equation:

$$D_{\text{hkl}} = K\lambda/\beta\cos\theta \quad (4.1)$$

where λ is the X-ray wavelength, θ is the Bragg angle of the (hkl) reflection, β is the full width at half maximum (in rad) of the crystalline reflection, and K the Scherrer constant (0.9 [30]). The reduction in crystallinity and crystallite size is more drastic for the nitrated derivatives (which exhibit broader diffractions) compared to the aminated polymers. The steric hindrance of the bulky nitro groups disrupts the molecular packing, resulting in the formation of smaller and less perfect crystals. Nevertheless, all the derivatives retain the orthorhombic structure of the parent polymer. The unit cell dimensions can be estimated from the interplanar distance (d_{hkl}) between crystallographic planes, which can be calculated from the diffraction patterns as

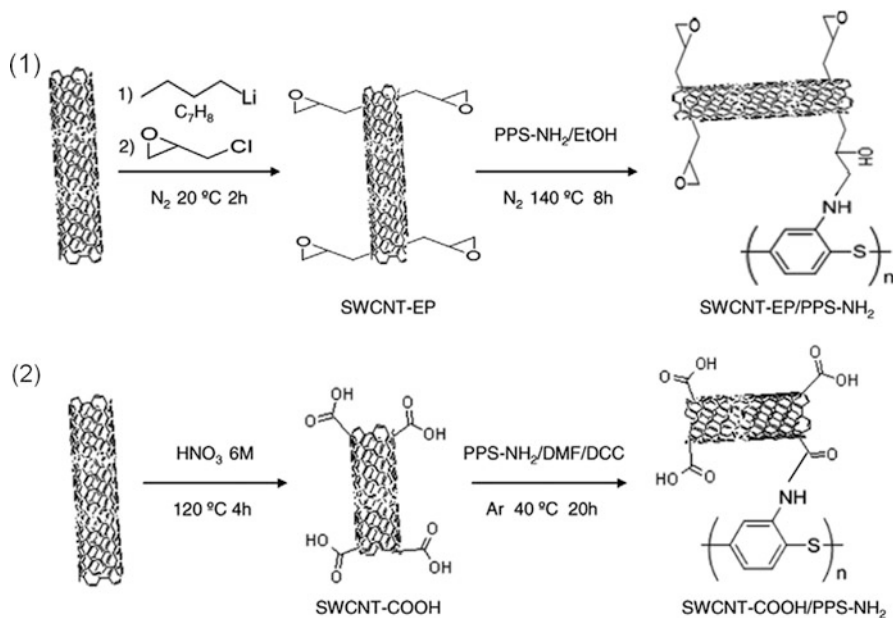
$$d_{\text{hkl}} = \lambda/2 \sin\theta \quad (4.2)$$

With increasing nitration degree, both a and b lattice parameters rise almost linearly, whereas the c parameter corresponding to the direction of the polymer backbone remains merely unchanged. The presence of the NO_2 groups inhibits a dense chain packing, causing an expansion of the unit cell in perpendicular direction to the backbone plane. The aminated derivatives show a smaller unit cell in comparison to the nitrated polymers, since the smaller size of the NH_2 group enables a closer packing.

Overall, the different characterizations confirm that the nitration and amination reactions lead to a reduction in the level of crystallinity, thermal stability, crystallization, and melting temperatures of PPS combined with an increase in solubility that result in easier processability and blending with other materials (i.e., thermoplastics, CNTs, CNFs) that incorporate suitable functional groups. The functionalization methods described are cost-effective and clean processes, feasible to scale-up; each type of derivative can be easily prepared in a one-pot reaction in suspension.

4 Synthesis of Functionalized Carbon Nanotubes

As mentioned in the introduction, the most common functionalization route is the oxidation of the CNTs with strong acids. In a typical procedure, as-grown SWCNTs are refluxed in HNO_3 for several hours under constant stirring, sonicated in water at room temperature, centrifuged, vacuum filtered, and dried in an oven to yield acid-functionalized carbon nanotubes (SWCNT-COOH, Scheme 4.2.1). This process



Scheme 4.2 Synthetic routes used for the preparation of PPS-NH₂/SWCNT-COOH (1) and PPS-NH₂/SWCNT-EP (2) nanocomposites (Adapted from reference [33], with permission from Elsevier, copyright 2012)

can impart some structural damage to the CNTs, even in slightly acidic conditions, leading to a shortening of the tubes. Recently, other less destructive chemical modifications of CNTs have been reported. A few papers [31, 32] have investigated the nucleophilic addition of Grignard and alkyllithium reagents onto SWCNTs; the organolithium can attack the more reactive sidewall defects, tips, and other non-hexagonal regions without disrupting the original structure of the tubes. These non-hexagonal structures can act as electrophiles due to their higher density of states. The process involves binding alkyl groups to the SWCNT surface with the formation of nanotube carbanions, e.g., $(SWCNT^{n-}) Li^+_n$. The subsequent nucleophilic attack of these carbanions to halogen or hydroxyl oxacyclopropanes, e.g., epichlorohydrin, via elimination of lithium halides leads to the anchoring of epoxy groups onto the CNT surface. A detailed description of this functionalization procedure is given in [33]: firstly, SWCNTs are suspended in toluene and sonicated for 4 h under a nitrogen atmosphere. Subsequently, a solution of n-butyllithium in toluene is added and the mixture is sonicated for 1 h. Then, epichlorohydrin is added and the mixture is stirred for 1 h at RT, followed by several centrifugation cycles. Finally, the product (SWCNT-EP, Scheme 4.2.2) is vacuum dried in an oven for a few hours.

The functionalization of CNTs under mild conditions can also be carried out via electrophilic substitution reaction in PPA/P₂O₅ medium [22]. In a typical process, MWCNTs, 4-chlorobenzoic acid, PPA, and P₂O₅ are placed in a flask under nitrogen inlet and stirred at 80 °C for 2 h, followed by heating to 130 °C for 72 h.

The mixture is then precipitated in water, washed with methanol, and finally freeze-dried to yield CB-MWCNTs. Subsequent reaction of these MWCNTs with 4-methylbenzenethiol and sodium carbonate in NMP/toluene medium at 160 °C for 10 h leads to 4-(4-methylbenzenethiol)benzoyl-functionalized MWCNTs (MB-MWCNTs). The benzoyl moieties covalently bonded to the surface of the nanotubes are useful sites for the introduction of various functionalities via nucleophilic substitution reaction.

5 Grafting Approaches to Prepare the Nanocomposites

PPS-NH₂ derivative can be covalently anchored to the surface of acid and epoxy-functionalized SWCNTs following two different routes [33], as shown in Scheme 4.2. In the first approach, both SWCNT-COOH and PPS-NH₂ are sonicated in DMF. Subsequently, a solution of *N,N*-dicyclohexylcarbodiimide (DCC) in DMF is added, and the reaction proceeds for 20 h at 40 °C under argon flow and mechanical stirring. The reaction mixture is coagulated in methanol, and the resulting product (PPS-NH₂-g-SWCNT-COOH, Scheme 4.2.1) is filtered, washed with methanol, and dried under vacuum at ~50 °C for 24 h. In the second procedure, both reactants are sonicated in ethanol, and the mixture is refluxed at 140 °C for 8 h under constant stirring in a nitrogen atmosphere. The resulting nanocomposite (PPS-NH₂-g-SWCNT-EP, Scheme 4.2.2) is finally filtered, washed until neutral, and dried under vacuum at ~50 °C for 24 h.

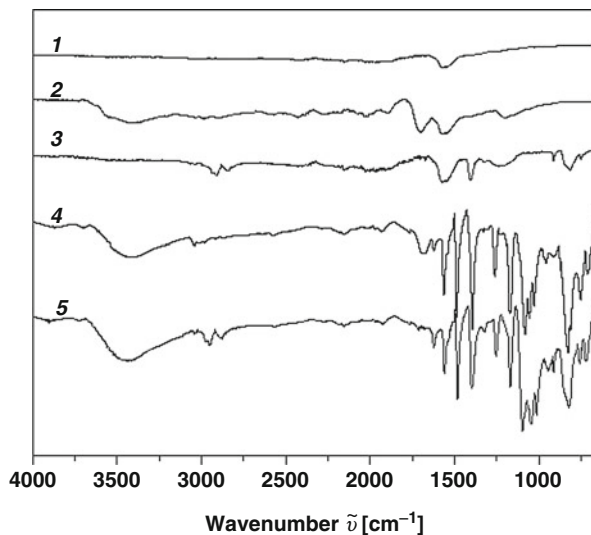
Jeon et al. [22] carried out the nucleophilic substitution reaction between the sites activated by carbonyl groups of CB-MWCNTs and 4-chlorobenzenethiol as an AB monomer or 3,5-dichlorobenzenethiol as an AB₂ monomer to graft LPPS or HPPS, respectively, onto CB-MWCNTs in NMP/toluene medium in the presence of sodium carbonate at 160 °C. The resulting nanocomposites (LPPS-g-MWCNT and HPPS-g-MWCNT) show improved dispersibility and melt processability and can be easily compression molded. LPPS can be synthesized by reaction between 1, 4-dichlorobenzene and sodium sulfide [34] and is soluble in strong acids such as sulfuric, methanesulfonic, and trifluoroacetic, as well as in polar aprotic solvents such as DMF, DMAc, DMSO, and NMP. HPPS is soluble in THF and in common chlorinated solvents such as dichloromethane, chloroform, chlorobenzene, etc., albeit remains merely insoluble in polar aprotic solvents. LPPS-g-MWCNT and HPPS-g-MWCNT are only partially soluble in all the abovementioned solvents.

6 Characterization of the Nanocomposites

6.1 IR and NMR

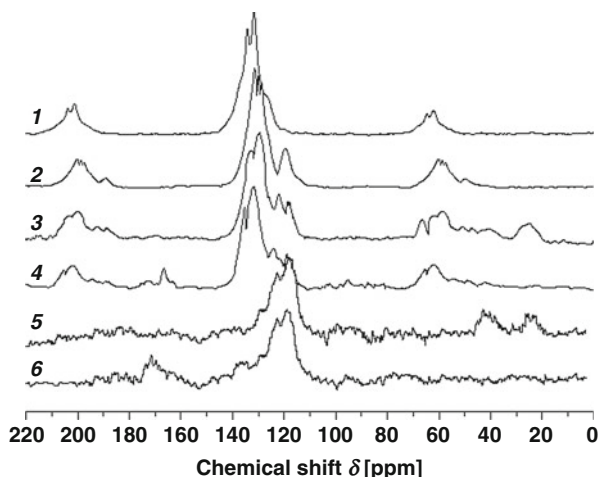
The grafting processes can be monitored through IR spectroscopy by comparing the spectra of the functionalized SWCNTs, the polymer derivative, and the resulting

Fig. 4.4 IR spectra of pristine SWCNT (1), SWCNT-COOH (2), SWCNT-EP (3), PPS-NH₂-g-SWCNT-COOH (4), and PPS-NH₂-g-SWCNT-EP (5) (Adapted from reference [33], with permission from Elsevier, copyright 2012)



nanocomposites (Fig. 4.4) [33]. The spectrum of as-grown SWCNTs only shows a band at $1,560\text{ cm}^{-1}$ attributed to the C = C stretching of the nanotube structure. Additionally, SWCNT-COOH exhibits bands at $3,400$, $1,710$, and $1,152\text{ cm}^{-1}$ assigned to the O-H, C = O and C-O stretching vibrations of the carboxylic groups, respectively [35]. SWCNT-EP presents three characteristic peaks related to vibrations of the epoxy ring: the bands at $1,250$ and 830 cm^{-1} correspond to symmetric and asymmetric stretching vibrations of C-O-C group in monosubstituted epoxy rings [36], respectively, and the band at 914 cm^{-1} is ascribed to the stretching of the CH₂ groups [37]. Besides, the peaks centered at $2,920$ and $2,850\text{ cm}^{-1}$ are attributed to sp³ C-H stretching vibrations [35], and the C-H bending of methylene groups appears at $1,405\text{ cm}^{-1}$. The spectrum of PPS-NH₂-g-SWCNT-COOH shows similar bands to those of PPS-NH₂ (Fig. 4.2). The broad absorption in the range of $3,600\text{--}3,100\text{ cm}^{-1}$ corresponds to the overlapping of the O-H stretching of unreacted COOH groups of the SWCNTs and the N-H stretching of amine and amide groups; the existence of free NH₂ is also evidenced through the N-H deformation band at $1,620\text{ cm}^{-1}$ that shows less intensity in relation to that of the polymer derivative. Moreover, the C = O stretching corresponding to the acid-functionalized SWCNTs and the bands ascribed to the C-N stretching and the N-H out-of-plane deformation downshift to $1,680$, $1,250$, and 748 cm^{-1} , respectively, due to the formation of amide bonds. The spectrum of PPS-NH₂-g-SWCNT-EP is also similar to that of PPS-NH₂. The most notable difference is the appearance of peaks at $2,915$ and $2,848\text{ cm}^{-1}$ assigned to C-H stretching vibrations, which are more intense in comparison to those of SWCNT-EP as a result of the methylene groups formed by the ring opening. The peak at 914 cm^{-1} related to the stretching of CH₂ groups of the epoxy appears less intense than that of SWCNT-EP, due to the reaction with amine groups of PPS-NH₂. A broad band is found at $3,430\text{ cm}^{-1}$,

Fig. 4.5 Solid-state ^{13}C MAS-NMR spectra of PPS (1), PPS-NH₂ (2), PPS-NH₂-g-SWCNT-EP (3), PPS-NH₂-g-SWCNT-COOH (4), SWCNT-EP (5) and SWCNT-COOH (6) (Taken from reference [33], with permission from Elsevier, copyright 2012)



arising from the overlapping of the O-H stretching of the hydroxyl group generated through the ring opening and the N-H stretching. The presence of unreacted NH₂ groups is confirmed through the band at 1,620 cm⁻¹, which is more intense than that of PPS-NH₂-g-SWCNT-COOH, indicating lower extent of grafting reaction. The features of the IR spectra evidence that part of the PPS-NH₂ chains are attached onto the surface of epoxy or acid-functionalized SWCNTs.

The covalent anchoring of LPPS and HPPS onto CB-MWCNTs can be also confirmed through IR spectroscopy [22]. The starting monomers show the S-H stretching in the range of 2,570–2,575 cm⁻¹ and the C-S stretching at about 800 cm⁻¹. Both LPPS-g-MWCNT and HPPS-g-MWCNT display peaks at around 800 cm⁻¹, albeit the S-H peak disappears, indicative of the grafting reaction. The amount of unreacted polymer can be estimated by extracting the nanocomposites with THF for 24 h. Their weight losses after extraction are very low ($\leq 3\%$), which implies a grafting extent close to 100 %, indicating that CB-MWCNTs are completely wrapped by the polymer.

Solid-state magic-angle-spinning (MAS) nuclear magnetic resonance (NMR) spectroscopy can also be used to obtain information about the grafting processes. The ^{13}C MAS-NMR spectrum of neat PPS (Fig. 4.5) shows a doublet at 120–140 ppm ascribed to the carbons of the aromatic rings and their related spinning sidebands (± 70 ppm) caused by the anisotropic effect of the carbon nuclei and the homonuclear dipole couplings in solid-state samples. The aromatic carbon signal appears upfield in the spectrum of PPS-NH₂, due to the electron donating effect of the amino group. Moreover, the signal splits into two separated peaks, one at ~ 120 ppm, attributed to the carbon joined to the NH₂, and the other appearing as a triplet at ~ 130 ppm. The spectrum of SWCNT-COOH exhibits a strong signal at ~ 120 ppm corresponding to the sp² carbon resonance in the CNT structure [38], and the peak at 173 ppm is assigned to the carbon of the COOH group. SWCNT-EP also presents the broad signal at ~ 120 ppm; the peak at ~ 42 ppm corresponds to the

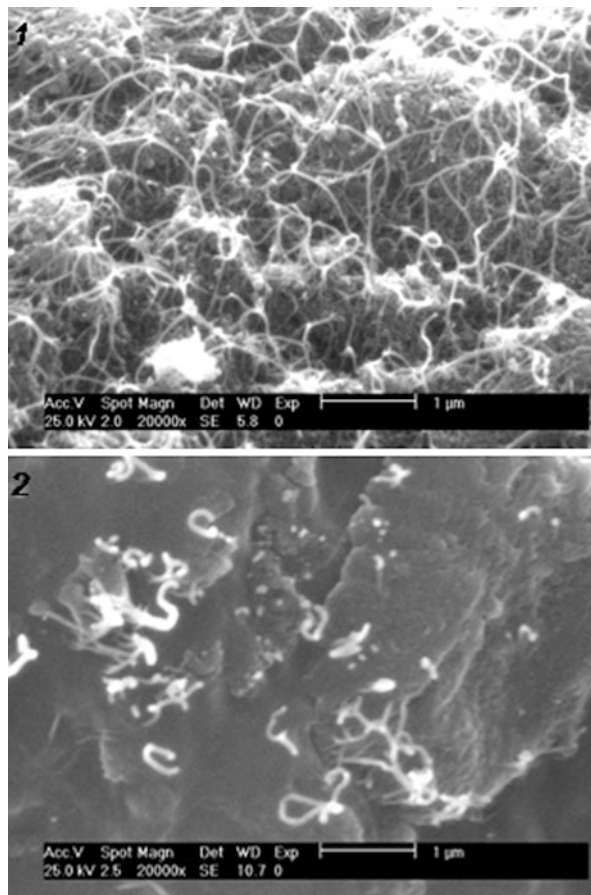
carbons of the monosubstituted epoxy ring, and the signal in the range of 20–28 ppm is related to sp^3 C atoms. The spectrum of PPS-NH₂-g-SWCNT-COOH is similar to that of PPS-NH₂, with new peaks at ~166 ppm, referring to the carbon of the amide group [39], and at 120 ppm, related to the sp^2 C atoms of the SWCNTs. The signal at 173 ppm shows less intensity, indicative of the reaction of some COOH with NH₂ groups; moreover, the peak referring to the aromatic carbon linked to the substituent group shifts to higher frequencies, due to the weaker donating effect of the amide group in comparison to the amine. PPS-NH₂-g-SWCNT-EP exhibits a signal at ~65 ppm related to the carbon linked to the new hydroxyl group [39]. Moreover, the band corresponding to the carbons of the epoxy ring is less intense than that of SWCNT-EP, and the peak referring to sp^3 C atoms appears stronger, thereby confirming the ring-opening reaction. Therefore, RMN spectra indirectly mean that the polymers have been grafted onto the functionalized SWCNTs.

6.2 Morphology

The surface morphology of the functionalized SWCNTs and the nanocomposites can be characterized by scanning and transmission electron microscopies (SEM and TEM). Figure 4.6 shows typical SEM micrographs of the acid-functionalized SWCNTs and the corresponding grafted nanocomposite, illustrating the size and distribution of the nanotubes. The image of SWCNT-COOH (Fig. 4.6.1) reveals a high degree of agglomeration and a homogeneous size distribution, with an average bundle diameter of 26 nm. Neither amorphous carbon particles nor metal catalyst impurities are detected, since they were completely removed after the oxidation process. The image of PPS-NH₂-g-SWCNT-COOH (Fig. 4.6.2) shows an average SWCNT bundle diameter about double that of acid-treated SWCNTs, indicating that the nanotube surfaces are wrapped by the polymer chains. An analogous behavior of increase in the tube diameter was drawn from images of the nanocomposite incorporating SWCNT-EP, pointing out that the morphology is not affected by the synthesis procedure. The SWCNTs are randomly and well dispersed through the polymer, without forming agglomerates, which corroborates that the covalent attachment is an effective method to prepare PPS/CNT nanocomposites with improved nanofiller dispersion at high loadings. Jeon et al. [22] also investigated the morphology of LPPS-g-MWCNT and HPPS-g-MWCNT nanocomposites by SEM analysis. The average diameter of pristine and CB-MWCNTs was about 20 and 40 nm, respectively, and increased up to 100 nm after the grafting reactions, indicative that the polymers are densely covering the nanotube side walls.

Typical TEM images of SWCNT-COOH and PPS-NH₂-g-SWCNT-COOH are displayed in Fig. 4.7.1 and 4.7.2, respectively [33]. The functionalized SWCNTs consist in small nanotube bundles, each composed of 8–10 individual tubes that appear as fine stripes; they exhibit a smooth surface, and no extra phase or stain is adhered to the sidewalls. In contrast, the grafted nanocomposite presents a rougher surface, and the SWCNT bundles are coated

Fig. 4.6 SEM images of SWCNT-COOH (1) and PPS-NH₂-g-SWCNT-COOH (2) nanocomposite

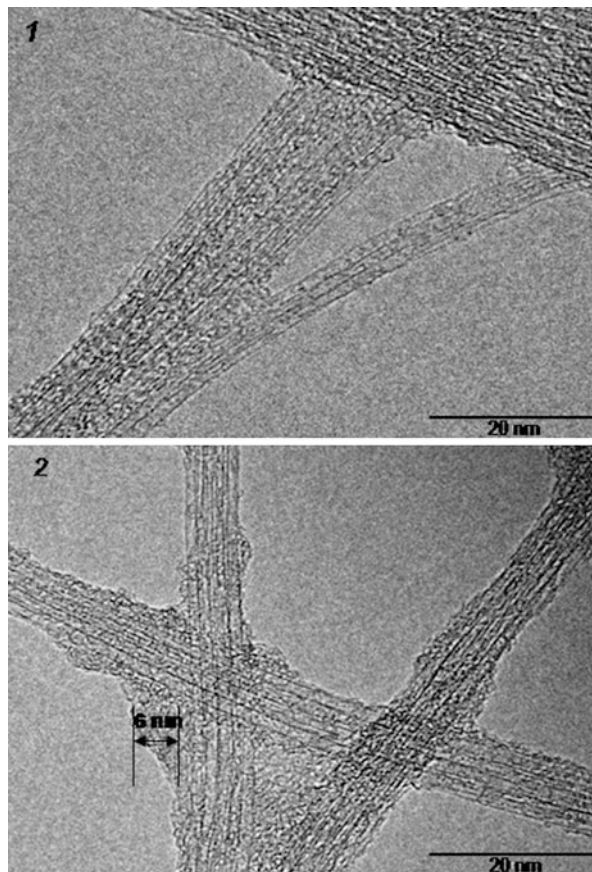


by a 4–6 nm thick polymer layer. Furthermore, the clear wall-to-wall stripes of the CNT framework suggest the structural stability of the SWCNTs under the functionalization and grafting reaction conditions and that they maintained their structural integrity throughout the whole synthesis procedure. No defects (i.e., voids or discontinuities) are detected between the CNTs and the polymer; PPS-NH₂ wraps around the bundles forming a tight interfacial layer, leading to a strong SWCNT-matrix interfacial adhesion, a prerequisite to obtain enhanced mechanical properties.

6.3 Thermal Stability

Figure 4.8 presents the degradation curves obtained from thermogravimetric analysis (TGA) under a nitrogen atmosphere for the polymer derivative, the

Fig. 4.7 Typical TEM images of SWCNT-COOH (1) and PPS-NH₂-g-SWCNT-COOH (2) nanocomposite (Taken from reference [33], with permission from Elsevier, copyright 2012)



functionalized SWCNTs, and the grafted nanocomposites, and their characteristic degradation temperatures are compared to those of nanocomposites prepared by direct integration of CNTs into PPS in Table 4.2. SWCNT-COOH starts to degrade about 20 °C lower than SWCNT-EP, albeit exhibits higher T_{max} . Nevertheless, both types of functionalized nanotubes are thermally less stable than pristine SWCNTs that only experience a very small weight loss (~ 3 wt%) before 800 °C caused by the decomposition of amorphous carbon. The functionalized SWCNTs present a weight loss in the range of 150–450 °C arising from the decomposition of chemical groups covalently attached to the tube sidewalls. Their FD, defined as moles of covalent functional groups per mole of carbon atoms, can be estimated from the TGA curves according to the equation [33]

$$FD = 12 L/R M_w \quad (4.3)$$

where L is the percentage of weight loss between 150 °C and 450 °C, R is the residual mass at 450 °C, and M_w is the molecular weight (in $\text{g}\cdot\text{mol}^{-1}$) of the

Fig. 4.8 TGA curves under a nitrogen atmosphere at a heating rate of 10 °C/min of pristine SWCNT (1), SWCNT-EP (2), SWCNT-COOH (3), PPS-NH₂-g-SWCNT-EP (4), PPS-NH₂-g-SWCNT-COOH (5), PPS-NH₂ (6), and neat PPS (7). The inset is a magnification of the temperature range 50–550 °C (Adapted from reference [33], with permission from Elsevier, copyright 2012)

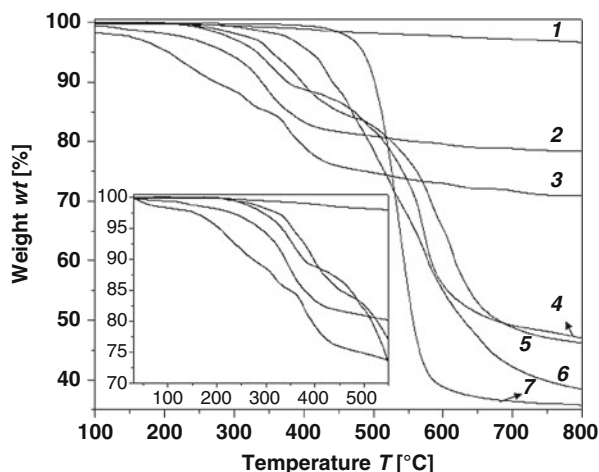


Table 4.2 Thermal properties for functionalized CNTs, polymer derivatives, and grafted nanocomposites obtained from TGA under a nitrogen atmosphere and DSC experiments. For comparison, data of nanocomposites prepared by direct blending of CNTs with PPS are also included

Material (wt% CNT)	T_i [°C]	T_{10} [°C]	T_{max} [°C]	X_c [%]	T_g [°C]	T_m [°C]	T_c [°C]	Reference
PPS-NH ₂	377	441	556	46.3	104	275	239	[33]
SWCNT-EP	207	348	344	–	–	–	–	[33]
SWCNT-COOH	186	290	377	–	–	–	–	[33]
PPS-NH ₂ -g-SWCNT-COOH (8.3)	303	402	608	24.6	131	269	226	[33]
PPS-NH ₂ -g-SWCNT-EP (8.3)	284	380	576	30.3	124	271	229	[33]
LPPS	371	450	530	33.7	–	248	219	[22]
HPPS	451	500	505	–	75	–	–	[22]
CB-MWCNT	750	–	–	–	–	–	–	[22]
LPPS-g-MWCNT (10.0)	376	460	540	26.3	–	242	228	[22]
HPPS-g-MWCNT (10.0)	420	510	550	–	80	306	–	[22]
PPS/SWCNT (0.1)	462	505	544	–	94	–	249	[40]
PPS/SWCNT (0.5)	470	509	553	–	100	–	248	[40]
PPS/SWCNT (1.0)	472	511	556	–	99	–	245	[40]
PPS/SWCNT (2.0)	479	517	565	–	104	–	246	[40]
PPS/MWCNT (0.5)	468	490	524	78.0	–	279	236	[16]
PPS/MWCNT (1.0)	470	493	527	78.9	–	279	236	[16]
PPS/MWCNT (2.0)	473	495	531	79.7	–	280	236	[16]
PPS/MWCNT (5.0)	476	498	535	77.5	–	279	231	[16]
PPS/MWCNT (7.0)	480	500	538	78.1	–	279	232	[16]

T_i initial degradation temperature, T_{10} temperature corresponding to 10 % weight loss, T_{max} temperature of maximum rate of degradation, T_c crystallization temperature, T_m , melting temperature, X_c degree of crystallinity, T_g glass transition temperature

desorbed moieties. This equation is an approximation since it considers that SWCNTs are entirely composed of carbon. FD of SWCNT-COOH is $\sim 7.1\%$, considerably larger than that of SWCNT-EP of around 3.9% , ascribed to the higher yield of the oxidation treatment in nitric acid compared to the reaction between epichlorohydrin and butyllithium-functionalized SWCNTs. PPS-NH₂ shows a single step degradation process that initiates around $377\text{ }^\circ\text{C}$, whereas the nanocomposites exhibit two different stages, the first associated with the decomposition of non-reacted chemical groups from the SWCNT surface and the second to the degradation of the polymer backbone that takes place at higher temperatures compared to the aminated derivative ($\sim 20\text{ }^\circ\text{C}$ and $50\text{ }^\circ\text{C}$ increase in T_{max} for PPS-NH₂-g-SWCNT-EP and PPS-NH₂-g-SWCNT-COOH, respectively). This rise is ascribed to the presence of the SWCNTs covalently anchored to the polymer chains that effectively hinder the diffusion of volatiles from the bulk of the matrix to the gas phase. The amount of amine groups chemically bounded to the SWCNTs can be estimated as difference between the weight loss of the first step of the functionalized SWCNTs and that of the grafted nanocomposites. The extent of the grafting process is about 25.3% and 38.7% for the abovementioned nanocomposites; PPS-NH₂-g-SWCNT-EP has a smaller number of grafted moieties due to the lower functionalization degree of these SWCNTs, hence less potential anchorage points for the polymer chains. Therefore, the higher thermal stability of the nanocomposite incorporating acid-functionalized SWCNTs compared to that reinforced with epoxy-functionalized SWCNTs is attributed to its larger number of covalent bonds. It is worth noting that T_{max} of PPS-NH₂-g-SWCNT-COOH (with $\sim 8.3\text{ wt}\%$ nanotube content) is more than $40\text{ }^\circ\text{C}$ higher than that of a non-grafted composite incorporating $2.0\text{ wt}\%$ SWCNT loading [40] (Table 4.2). This is of a great interest since it is difficult to homogeneously disperse high SWCNT contents within the PPS matrix by direct mixing due to the strong agglomerating tendency of these nanotubes and the elevated viscosity of the polymer melt.

Regarding LPPS-g-MWCNT and HPPS-g-MWCNT nanocomposites (with $\sim 10\text{ wt}\%$ MWCNT content), significant raises in the degradation temperatures are encountered compared to their respective polymers [22]. Thus, T_{max} increases by about $10\text{ }^\circ\text{C}$ and $45\text{ }^\circ\text{C}$, respectively, which is another indirect proof of the polymer grafting onto the surface of CB-MWCNTs, since the thermal interfacial resistance CNT-polymer decreases with the formation of chemical bonds, leading to an increase in thermal conductivity that facilitates heat dissipation within the nanocomposite. Nevertheless, similar thermal stability enhancements have been reported by Yu et al. [16] for a non-grafted composite filled with $7.0\text{ wt}\%$ MWCNTs, which shows a T_{max} comparable to that of LPPS-g-MWCNT and only $\sim 12\text{ }^\circ\text{C}$ lower than that of HPPS-g-MWCNT (Table 4.2).

6.4 Crystallization and Melting Behaviour

The crystallization and melting behavior of the grafted nanocomposites can be investigated by differential scanning calorimetry (DSC), and the calorimetric

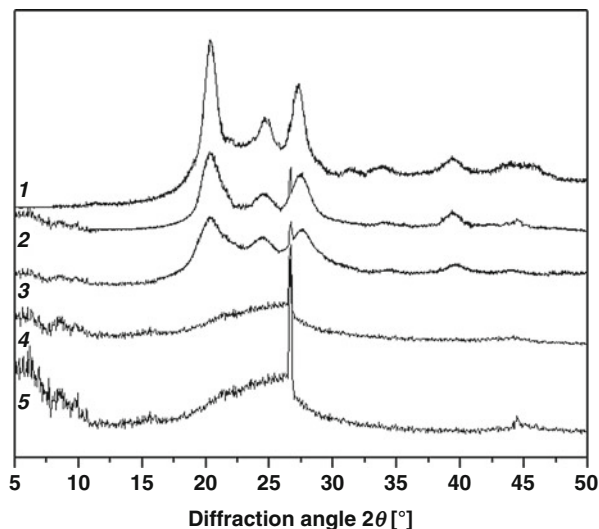
parameters derived from non-isothermal scans are listed in Table 4.2, along with those of composites prepared by direct reinforcement for comparison. The covalent attachment to the functionalized SWCNTs leads to a noticeable fall in the T_c of PPS-NH₂ (by about 10 °C and 13 °C for PPS-NH₂-g-SWCNT-EP and PPS-NH₂-g-SWCNT-COOH, respectively). The stronger decrease found for the second nanocomposite is related to its higher degree of covalent grafting, as revealed by TGA. Moreover, the degree of crystallinity also decreases considerably, from ~46 % for PPS-NH₂ to ~30 % and 25 % for the abovementioned nanocomposites, while only a slight drop is found in T_m , by ~4 °C and 6 °C, respectively. Clearly, neither SWCNT-COOH nor SWCNT-EP exerts a nucleating effect on the polymer crystallization; the covalent anchoring of the polymer chains to the functionalized SWCNTs combined with the intermolecular interactions between the free NH₂ groups of the aminated derivative and the unreacted carboxylic acids of the SWCNTs strongly hampers the diffusion and arrangement of the long polymer chains and thereby postpones the overall crystallization process (i.e., nucleation and crystal growth), leading to the formation of smaller and less perfect crystals, thus resulting in lower crystallinity, crystallization, and melting temperatures for the nanocomposites. This behavior differs from that reported for LPPS-g-MWCNT [22], where the MWCNTs act as nucleating agents for polymer crystallization. The different synthetic routes used for the synthesis of the nanocomposites combined with the lower degree of entanglement of the MWCNTs, which are easier to disperse than the SWCNTs, explain the mentioned discrepancy. On the other hand, no significant change in T_c or in the degree of crystallinity was found in nanocomposites prepared by direct integration of SWCNT [40] or MWCNT [16] loadings <2.0 wt%, while higher concentrations resulted in a slight decrease in T_c due to an impeding and confinement effect of the CNT network on polymer chain diffusion. At 2.0 wt% MWCNT loading, a rheological network is formed [17] resulting in decreased mobility of the PPS chains. Similar results have been reported for poly(ϵ -caprolactone)/MWCNT nanocomposites [41].

With regard to the T_g , nanocomposites incorporating SWCNT-EP and SWCNT-COOH exhibit increases of 20 °C and 27 °C, respectively, in comparison to that of PPS-NH₂ (Table 4.2); this is consistent with the intense intermolecular interactions between the polymer chains, the restrictions on mobility imposed by the rigid SWCNTs and the decrease in crystallinity of these nanocomposites. These T_g enhancements are significantly larger than those reported for PPS/SWCNT [42] and HPPS-g-MWCNT [22] nanocomposites, yet another indication of the efficiency of the grafting routes is described in this chapter to covalently anchor polymer derivatives onto epoxy and acid-functionalized SWCNTs.

6.5 Crystalline Structure

The X-ray diffractograms of the functionalized SWCNTs and the grafted nanocomposites are displayed in Fig. 4.9. SWCNT-COOH shows small peaks in the range of 5–10° corresponding to nanotube bundles [3]; the intense signal

Fig. 4.9 X-ray diffractograms of PPS-NH₂ (1), PPS-NH₂-g-SWCNT-EP (2), PPS-NH₂-g-SWCNT-COOH (3), SWCNT-COOH (4), and SWCNT-EP (5) (Adapted from reference [33], with permission from Elsevier, copyright 2012)

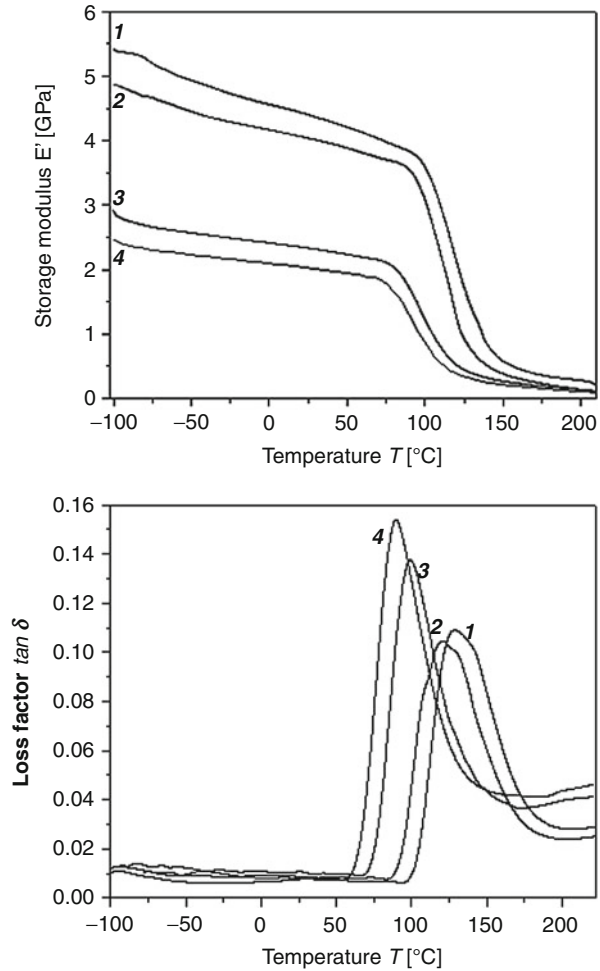


at $2\theta = 26.6^\circ$ is ascribed to the [002] diffraction plane of the impurity graphite [43]. The diffractogram does not exhibit any reflection related to metal catalyst impurities, indicative that they were effectively removed during the oxidation treatment in nitric acid. The diffraction pattern of SWCNT-EP is almost identical to that of the acid-functionalized SWCNTs, although with more intense bundle peaks, suggesting a lower degree of debundling; moreover, a small peak appears at 44.4° ascribed to α -Fe [110] and/or Ni [111] diffractions [44]. PPS-NH₂-g-SWCNT-EP presents low intense reflections at 26.6° and 44.4° , referring to the abovementioned impurities of the SWCNTs; PPS-NH₂-g-SWCNT-COOH also exhibits the diffraction corresponding to graphite. However, the SWCNT bundle peaks are hardly visible in their diffractograms, indicating that the grafting processes induced CNT disentanglement and debundling within the polymer matrix, as revealed by SEM images. Both nanocomposites have qualitatively similar diffraction pattern to that of PPS-NH₂ (described in Sect. 3), with wider and less intense peaks caused by a diminution in the spatial order. An analogous behavior of decrease in the local order of the polymer after a grafting reaction has been reported for SWCNTs [43] and MWCNTs [45] covalently attached to poly(ether ketone)s. D_{111} estimated using Eq. 4.1 drops by $\sim 31\%$ and 42% for nanocomposites with epoxy and acid-functionalized SWCNTs, respectively, in comparison to PPS-NH₂. The lower crystal size of PPS-NH₂-g-SWCNT-COOH is related to its higher extent of grafting, lower degree of crystallinity as well as lower crystallization and melting temperatures, as revealed by DSC.

6.6 Mechanical Properties

The mechanical behavior of polymers and composites can be investigated by dynamic mechanical analysis (DMA), technique that monitors changes in the

Fig. 4.10 Evolution of the storage modulus E' and loss angle $\tan \delta$ at a frequency of 1 Hz for PPS (1), PPS-NH₂ (2), PPS-NH₂-g-SWCNT-EP (3), and PPS-NH₂-g-SWCNT-COOH (4) (Adapted from reference [33], with permission from Elsevier, copyright 2012)



stiffness of the material as a function of temperature. DMA tests are sensitive to the transitions and relaxation processes of the matrix in the composite, and provide information about filler-matrix interactions. Figure 4.10 shows the temperature dependence of the storage modulus (E') and loss factor ($\tan \delta$) for neat PPS, PPS-NH₂ and the grafted nanocomposites at the frequency of 1 Hz. E' is indicative of the elastic energy stored in the material and is highly affected by its composition and morphology. E' of PPS-NH₂ at 25 °C is ~ 2.3 GPa, about 11 % higher than that of neat PPS; this enhancement is related with the increment in the number of intermolecular interactions between the polymer chains and the formation of small imperfect crystals that are known to increase the rigidity of semicrystalline PPS [14]. At temperatures below T_g , E' of PPS-NH₂-g-SWCNT-COOH and PPS-NH₂-g-SWCNT-EP are on average 91 % and 76 % higher than that of PPS-NH₂, respectively. Table 4.3 compares their room temperature modulus with

Table 4.3 Mechanical and electrical properties for PPS-grafted nanocomposites at room temperature. For comparison, data of nanocomposites prepared by direct integration of CNTs within the polymer are also included

Material (wt% CNT)	E' [GPa]	S [MPa]	σ [$S \cdot \text{cm}^{-1}$]	Reference
PPS-NH ₂ -g-SWCNT-COOH (8.3)	4.45	–	0.22	[33]
PPS-NH ₂ -g-SWCNT-EP (8.3)	4.10	–	0.87	[33]
LPPS-g-MWCNT (10.0)	–	–	11.76	[22]
HPPS-g-MWCNT (10.0)	–	–	3.56	[22]
PPS/SWCNT (0.1)	2.23	66.5	–	[42]
PPS/SWCNT (0.5)	2.56	76.3	$9.1 \cdot 10^{-7}$	[42]
PPS/SWCNT (1.0)	2.84	89.3	$2.3 \cdot 10^{-4}$	[42]
PPS/SWCNT (2.0)	3.27	114.7	$1.2 \cdot 10^{-3}$	[42]
PPS/MWCNT (1.0)	1.85	20.5	$3.0 \cdot 10^{-16}$	[16]
PPS/MWCNT (2.0)	2.18	36.0	$9.5 \cdot 10^{-6}$	[16]
PPS/MWCNT (5.0)	2.38	54.5	$2.0 \cdot 10^{-2}$	[16]
PPS/MWCNT (7.0)	2.41	62.5	$5.0 \cdot 10^{-2}$	[16]

E' storage modulus, S tensile strength, σ electrical conductivity

that of nanocomposites prepared by direct integration of SWCNTs [42] or MWCNTs [16]. The improvements attained in the grafted nanocomposites are noticeably higher than that reported by the addition of 2.0 wt% SWCNTs or 7.0 wt% MWCNTs to PPS (around 50 % and 25 %, respectively). The exceptional enhancements achieved by the grafting processes are attributed to a very effective load transfer from the polymer to the SWCNTs due to the strong interfacial adhesion attained through the covalent bonding, which also leads to higher degree of cross-linking, combined with an improved dispersion. The larger increment in modulus for the nanocomposite incorporating acid-functionalized SWCNTs in comparison with that reinforced with epoxy-modified SWCNTs is related to its higher degree of grafting.

The loss factor ($\tan \delta$) is a measure of the damping characteristics of the material and correlates with its impact resistance. The maximum of $\tan \delta$ curve corresponds to the T_g . The grafted nanocomposites show a significant increase in this parameter compared with that of PPS-NH₂, consistent with DSC results (Sect. 6.4), due to the strong restrictions on chain mobility imposed by the attachment to the SWCNTs and the intermolecular interactions between polar groups, mainly hydrogen bonds. Moreover, a broadening and diminution of the height of the $\tan \delta$ peak is found (Fig. 4.10). The broadening is attributed to the effect of confinement of the PPS chains within the SWCNT network, as well as to the heterogeneous nature of the nanocomposites, since only part of the polymer chains are anchored to the SWCNT surfaces. An analogous behavior of widening of $\tan \delta$ maximum has been reported for PPS/MWCNT nanocomposites [17]. The decrease in height is indicative of the strong SWCNT-polymer interactions due to the formation of covalent and hydrogen bonds. In summary, the grafting approach is an effective method to improve the mechanical properties of PPS-based CNT nanocomposites.

6.7 Electrical Conductivity

Certain potential application areas of neat PPS such as self-health monitoring, electro-actuation, etc., are limited due to its insulating character ($\sigma \sim 10^{-16} \text{ S} \cdot \text{cm}^{-1}$) [16]. The incorporation of CNTs as conductive nanofillers is known to improve the electrical performance of this polymer [16, 17]. On one hand, the grafting approach is expected to be effective for enhancing the nanocomposite conductivity since it improves CNT dispersion. On the other hand, the covalent attachment of the polymer onto the surface of functionalized CNTs can disrupt the electronic continuum medium and reduce their electrical conductivity [1]. Moreover, the oxidation treatment used for the synthesis of SWCNT-COOH may introduce defects on the nanotube sidewalls that adversely impact the nanocomposite conductivity. Table 4.3 compares σ values of PPS-NH₂-g-SWCNT-EP and PPS-NH₂-g-SWCNT-COOH with those of nanocomposites prepared by direct reinforcement; both grafted nanocomposites exhibit semiconducting behavior, with conductivities of ~ 0.87 and $0.22 \text{ S} \cdot \text{cm}^{-1}$, respectively, about fifteen orders of magnitude higher than that of PPS-NH₂ [33] and more than two orders of magnitude higher than that of PPS/SWCNT (2.0 wt%) [42]. Jeon et al. [22] also found an increase of around sixteen orders of magnitude for HPPS-g-MWCNT and LPPS-g-MWCNT nanocomposites compared to their respective polymers, values considerably higher than those reported for PPS/graphite [46] and PPS/MWCNT [16] nanocomposites prepared by melt blending, which possess conductivities in the range of 10^{-2} – $10^{-3} \text{ S} \cdot \text{cm}^{-1}$ for 10.0 and 7.0 wt% loading, respectively. The high electrical conductivity of these grafted systems implies that the basic structure of the SWCNTs has been slightly damaged (if any) during the functionalization processes. Comparing the grafted nanocomposites, HPPS-g-MWCNT presents the highest conductivity (Table 4.3), due to the *para*-conjugated structure of HPPS. Between the two nanocomposites with SWCNTs, PPS-NH₂-g-SWCNT-EP exhibits higher σ value, most likely because the incorporation of epoxy groups hardly induces structural damage to the SWCNTs. The minimization of conductivity loss upon CNT functionalization is an important objective towards the development of multifunctional CNT-reinforced nanocomposites.

7 Future Potential Applications

PPS based nanocomposites have emerged as ideal engineering materials for industrial applications such as aerospace and defense, automotive, oil and gas as well as electronics and applications that require a relatively high level of electrical conductivity. The reduction in the melting temperature and level of crystallinity of the nanocomposites attained by the grafting processes leads to an improvement in their melt processability, thus enabling the fabrication of cost-effective high-performance materials for both structural and nonstructural applications [13, 47], particularly in wind turbine blades, pressure vessels, bridges, aircraft elements (i.e., J-Nose wing substructures, fuel tank manhole covers, seating parts, landing gear hubcaps, pylon fairings), and automobile parts (i.e., air intake systems, seals, fuel rails, valve covers).

PPS composites outperform metals and other traditional materials due to their lightweight, durability, high strength, and resistance to fatigue, abrasion, hydrolysis, and aggressive chemicals, even at elevated temperatures. This exceptional combination of properties is suitable for developing improved equipments for oil and gas retrieval and energy production. It has been demonstrated that the addition of CNTs or CNFs to this polymer matrix improves its mechanical and tribological performances [42, 48]: hence these nanocomposites are ideal candidates to be employed in oil and gas tubes and pipes. They can also be used for electromagnetic shielding [18], particularly in aerospace devices, and are suitable as flame retardant materials due to their excellent thermal stability and low flammability.

Further research is required to extend the potential use of these nanocomposites. Thus, in-depth studies on structure–property relationships of these new materials, as well as their manufacturing and characterization at a large scale, will allow new and specific technological applications. However, an efficient and large-scale fabrication of this type of nanocomposites is still a challenge. The practical and wide-scale use of these nanocomposites depends on how efficiently can be overcome these challenges.

8 Concluding Remarks

PPS derivatives can be covalently attached onto the surface of functionalized CNTs, and the grafting processes can be monitored through IR and/or NMR spectra due to the appearance of signals related to the covalent moieties. The extent of the grafting reactions can be estimated from TGA curves; nanocomposites incorporating acid-functionalized SWCNTs exhibit larger number of interactions through covalent and hydrogen bonds than those reinforced with epoxy-functionalized SWCNTs. Significant improvements in the storage modulus, glass transition temperature, and electrical conductivity of the polymer have been attained after the grafting processes, ascribed to a homogeneous nanofiller dispersion and a strong CNT-polymer interfacial adhesion. The grafting leads to a drop in the melting temperature as well as in the level of crystallinity of the polymer due to the inactive nucleating role of the CNTs and the intense restrictions on chain mobility caused by the CNT-polymer interactions. PPS-based nanocomposites synthesized through grafting approaches show improved thermal, mechanical, and electrical properties in comparison to those prepared by direct reinforcement. They are suitable for potential use in a wide variety of applications in fields ranging from the electronics to the aerospace, automobile, as well as oil, gas, and chemical industries. The proper CNT functionalization route and grafting process should be selected based on the specific polymer properties to be enhanced.

Acknowledgments AD acknowledges the Consejo Superior de Investigaciones Científicas (CSIC) for a JAE Postdoctoral Fellowship and MN the Ministerio de Economía y Competitividad (MINECO) for a “Ramón y Cajal” Research Fellowship.

References

1. Moniruzzaman M, Winey KI (2006) Polymer nanocomposites containing carbon nanotubes. *Macromolecules* 39:5194
2. Spitalskya Z, Tasis D, Papagelis K, Galiotis C (2010) Carbon nanotube–polymer composites: chemistry, processing, mechanical and electrical properties. *Prog Polym Sci* 35:357
3. Thess A, Lee R, Nikolaev P, Dai H, Petit P, Robert J (1996) Crystalline ropes of metallic carbon nanotubes. *Science* 273:483
4. Monthioux M, Smith BW, Bureaux B, Claye A, Fischer JE, Luzzi DE (2001) Sensitivity of single-wall carbon nanotubes to chemical processing: an electron microscopy investigation. *Carbon* 39:1251
5. Wang W, Lin Y, Sun YP (2005) Poly(*N*-vinyl carbazole)functionalized single walled carbon nanotubes: synthesis, characterization, and nanocomposite thin films. *Polymer* 46:8634
6. Zhao B, Hu H, Yu A, Perea D, Haddon RC (2005) Synthesis and characterization of a water soluble single-walled carbon nanotube graft copolymer. *J Am Chem Soc* 127:8197
7. Lin Y, Rao AM, Sadanadan B, Kenik EA, Sun YP (2002) Functionalizing multiple-walled carbon nanotubes with aminopolymers. *J Phys Chem B* 106:1294
8. Qu L, Lin Y, Hill DE, Zhou B, Wang W, Sun X (2004) Polyimide functionalized carbon nanotubes: synthesis and dispersion in nanocomposite films. *Macromolecules* 37:6055
9. Huang W, Lin Y, Taylor S, Gaillard J, Rao AM, Sun YP (2002) Sonication-assisted functionalization and solubilization of carbon nanotubes. *Nano Lett* 2:231
10. Baudot C, Volpe MV, Kong JC, Tan CM (2009) Epoxy functionalized carbon nanotubes and methods of forming the same. US Patent 299082
11. Wade JLG (1999) Organic chemistry, 4th edn. Prentice Hall, Englewood Cliffs
12. Mao Y, Gleason KK (2004) Positive-tone nanopatterning of chemical vapor deposited polyacrylic thin films. *Langmuir* 20:2484
13. Mitschang P, Blinzler M, Woginger A (2003) Processing technologies for continuous fibre reinforced thermoplastics with novel polymer blends. *Compos Sci Technol* 63:2099
14. Lu D, Mai Y-W, Li RKY, Ye L (2003) Impact strength and crystallization behavior of nano-SiO₂/poly(phenylene sulfide) (PPS) composites with heat treated PPS. *Macromol Mater Eng* 288:693
15. Beck HN (1992) Solubility characteristics of poly (etheretherketone) and poly (phenylene sulfide). *Appl Polym Sci* 45:1361
16. Yu S, Wong WM, Hu S, Juay YK (2009) The characteristics of carbon nanotube-reinforced poly(phenylene sulfide) nanocomposites. *J Appl Poly Sci* 113:3477
17. Yang J, Xu T, Lu A, Zhang Q, Tan H, Fu Q (2009) Preparation and properties of poly (*p*-phenylene sulfide)/multiwall carbon nanotube composites obtained by melt compounding. *Compos Sci Technol* 69:147
18. Han MS, Lee YK, Lee HS, Yun CH, Kim WN (2009) Electrical, morphological and rheological properties of carbon nanotube composites with polyethylene and poly(phenylene sulfide) by melt mixing. *Chem Eng Sci* 64:4649
19. Wu D, Wu L, Zhou W, Yang T, Zhang M (2009) Study on physical properties of multiwalled carbon nanotube/poly(phenylene sulfide) composites. *Polym Eng Sci* 49:1727
20. Jiang Z, Hornsby P, McCool R, Murphy A (2012) Mechanical and thermal properties of polyphenylene sulfide/multiwalled carbon nanotube composites. *J Appl Polym Sci* 123:2676
21. Barique MA, Seesukphronorarak SS, Wu L, Ohira A (2011) A comparison between highly crystalline and Low crystalline poly(phenylene sulfide) as polymer electrolyte membranes for fuel cells. *J Phys Chem B* 115:27
22. Jeon I-Y, Lee H-J, Choi YS, Tan L-S, Baek J-B (2008) Semimetallic transport in nanocomposites derived from grafting of linear and hyperbranched poly(phenylene sulfide)s onto the surface of functionalized multi-walled carbon nanotubes. *Macromolecules* 41:7423
23. Brady DG (1981) Poly(phenylene sulfide)-how, when, why, where, and where now. *J Appl Polym Sci Appl Polym Symp* 36:231

24. Tabor BJ, Magre EP, Boon J (1971) The crystal structure of poly-*p*-phenylene sulphide. *Eur Polym J* 7:1127
25. Diez-Pascual AM, Naffakh M (2012) Synthesis and characterization of nitrated and aminated poly(phenylene sulfide) derivatives. *Mater Chem Phys* 131:605
26. Piaggio C, Cuniberti G, Dellepiane E, Cmapani G, Goiri G, Masetti M, Novi G, Petrillo G (1989) Vibrational spectra and assignment of poly-(*p*-phenylene sulfide) and its oligomers. *Spectrochim Acta Part A* 45:347
27. Conceicao TF, Barra GMO, Joussef AC, Bertolino JR, Mireski S, Pires ATN (2008) Preparation and characterization of poly(ether ether ketone) derivatives. *J Braz Chem Soc* 19:111
28. Chung T-S (2001) Thermotropic liquid crystal polymers: thin-film polymerization, characterization, blends and application. CRC Press, New York, p 14
29. Chung JS, Bodziuch J, Cebe PJ (1992) Effects of thermal history on crystal structure of poly(phenylene sulphide). *Mater Sci* 27:5609
30. Patterson AL (1939) The Scherrer formula for X-ray particle size determination. *Phys Rev* 56:978
31. Viswanathan G, Chakrapani N, Yang H, Wei B, Chung H, Cho K, Ryu CY, Ajayan PM (2003) Single-step in situ synthesis of polymer-grafted single-wall nanotube composites. *J Am Chem Soc* 125:925
32. Blake R, Gun'ko YK, Coleman J, Cadek M, Fonseca A, Nagy JB, Blau WJ (2004) A generic organometallic approach toward ultra-strong carbon nanotube polymer composites. *J Am Chem Soc* 126:10226
33. Diez-Pascual AM, Naffakh M (2012) Grafting of an aminated poly(phenylene sulfide) derivative to functionalized single-walled carbon nanotubes. *Carbon* 50:857
34. Baek J-B, Tan L-S (2003) Improved syntheses of poly(oxy-1,3-phenylenecarbonyl-1,4-phenylene) and related poly(ether-ketones) using polyphosphoric acid/P₂O₅ as polymerization medium. *Polymer* 44:4135
35. Colthup NB, Day LH, Wiberley SE (1990) Introduction to infrared and Raman spectroscopy, 3rd edn. Academic, San Diego, p 225
36. Shreve OD, Heether MR, Knight HB, Swern D (1951) Infrared absorption spectra of some epoxy compounds. *Anal Chem* 23:277
37. Chen S, Hsu S-H, Wu M-C, Su WF (2011) Kinetics studies on the accelerated curing of liquid crystalline epoxy resin/multi-walled carbon nanotube nanocomposites. *J Polym Sci B Polym Phys* 49:301
38. Tang XP, Kleinhammes A, Shimoda H, Fleming L, Bennoune KY, Shinha S (2000) Electronic structures of single-walled carbon nanotubes determined by NMR. *Science* 288:492
39. Ernst M, Meier BH (1998) Studies in physical and theoretical chemistry. In: Ando I (ed) Solid state NMR of polymers, vol 84. Elsevier, Amsterdam, p 713
40. Naffakh M, Diez-Pascual AM, Marco C, Ellis G (2012) Morphology and thermal properties of novel poly(phenylene sulfide) hybrid nanocomposites based on single-walled carbon nanotubes and inorganic fullerene-like WS₂ nanoparticles. *J Mater Chem* 22:1418
41. Mitchell CA, Krishnamoorti R (2007) Dispersion of single-walled carbon nanotubes in poly(*ε*-caprolactone). *Macromolecules* 40:1538
42. Diez-Pascual AM, Naffakh M, Marco C, Ellis G (2012) Mechanical and electrical properties of carbon nanotube/poly(phenylene sulphide) composites incorporating polyetherimide and inorganic fullerene-like nanoparticles. *Compos Part A* 43:603
43. Diez-Pascual AM, Martinez G, Gonzalez-Dominguez JM, Anson A, Martinez MT, Gomez MA (2010) Grafting of a hydroxylated poly(ether ether ketone) to the surface of single-walled carbon nanotubes. *J Mater Chem* 38:8285
44. Perez-Cabero M, Rodríguez-Ramos I, Guerrero-Ruiz A (2003) Characterization of carbon nanotubes and carbon nanofibers prepared by catalytic decomposition of acetylene in a fluidized bed reactor. *J Catal* 215:305

45. Jeon I-Y, Tan L-S, Baek J-B (2008) Nanocomposites derived from in situ grafting of linear and hyperbranched poly(ether-ketone)s containing flexible oxyethylene spacers onto the surface of multi-walled carbon nanotubes. *J Polym Sci A Polym Chem* 46:3471
46. Zhao YF, Xiao M, Wang SJ, Ge XC, Meng YZ (2007) Preparation and properties of electrically conductive PPS/expanded graphite nanocomposites. *Compos Sci Technol* 67:2528
47. Parlevliet PP, van der Werf WAW, Bersee HEN, Beukers A (2008) Thermal effects on microstructural matrix variations in thick-walled composites. *Compos Sci Technol* 68:896
48. Cho MH, Bahadur S (2007) A study of the thermal, dynamic mechanical, and tribological properties of polyphenylene sulfide composites reinforced with carbon nanofibers. *Tribol Lett* 25:237
49. Kuwae AK, Machida S (1979) Vibrational spectra of nitrobenzene-d₀, -p-d and -d₅ and normal vibrations of nitrobenzene. *Spectrochim Acta* 35:27

Functionalization of Carbon Nanotubes and Their Polyurethane Nanocomposites

5

Sravendra Rana, Raghavan Prasanth, and Lay Poh Tan

Contents

1	Introduction	104
2	Functionalization of CNTs	104
2.1	Noncovalent Functionalization	105
2.2	Covalent Functionalization	106
2.3	CNT Functionalization via Click Chemistry	108
2.4	CNT Functionalization via Dendritic Polymers	111
3	Polyurethane/CNT Composites	113
4	Conclusions	116
	References	117

Abstract

Carbon nanotubes (CNTs) exhibit a unique combination of electrical, mechanical, and magnetic properties as well as nanometer-scale diameter and high aspect ratio, which make them an ideal reinforcing agent for high-strength

S. Rana

School of Materials Science and Engineering, and Energy Research Institute @ NTU, Nanyang Technological University, Singapore

Institute of Chemistry, Martin-Luther University Halle-Wittenberg, Halle (Saale), Germany

e-mail: RanaSravendra@ntu.edu.sg

R. Prasanth

Department of Materials Science and Nanoengineering, Rice University, Houston, TX, USA

School of Materials Science and Engineering, and Energy Research Institute @ NTU, Nanyang Technological University, Singapore, Singapore

Department of Chemical and Biological Engineering and Research Institute for Green Energy

Convergence Technology, Gyeongsang National University, Jinju, Republic of Korea

e-mail: praghavan@ntu.edu.sg

L.P. Tan (✉)

School of Materials Science, Nanyang Technological University, Singapore

e-mail: lptan@ntu.edu.sg

polymer composites. However, there is still challenge to achieve the simple and economical method for improving the dispersion and solubilization of CNTs. To improve the dispersion of CNTs, several approaches have been applied by using covalent and noncovalent functionalization methods. Herein, in particular, we focused on CNT functionalization using dendritic polymer and click chemistry approach. The impact of CNT dispersion on the property improvement of composite materials is discussed. In particular, the polyurethane block copolymer-CNT composites are discussed in details.

Keywords

Carbon nanotubes • Click chemistry • Dendritic polymers • Composites

1 Introduction

Carbon nanotubes exhibit excellent and unique mechanical and physical properties, and immediately after their discovery, those are regarded as new materials for future technologies [1]. Depending on their preparation conditions and diameter, CNTs may be identified as multiwalled, single walled, and double walled [2–4]. Their outstanding properties, shape, and small scale pose a unique combination for using small molecules as assembly molecules in the area of electronics and sensing as well as in biodevices [5, 6]. Due to their excellent properties, CNTs have already been used as ultimate reinforcing agents for high-performance polymer composites [7]. The presence of CNT nanofiller is very useful to improve the properties of polymer composites including toughness, tensile modulus, tensile strength, glass transition temperature, thermal and electrical conductivity, optical properties, etc. [8–13]. As CNTs usually aggregate due to van der Waals force, it is enormously difficult to disperse them in the polymer matrix. A significant confront in developing the polymer/CNTs nanocomposites is to introduce the individual CNTs in a polymer matrix to achieve better dispersion and alignment, and strong interfacial interactions, to improve the load transfer across the CNT-polymer matrix interface. The functionalization of CNTs is an efficient way to prevent nanotube agglomeration, which helps to achieve better dispersion and stabilization of CNTs in a polymer matrix.

2 Functionalization of CNTs

The functionalization of CNT is an effective way to prevent nanotube agglomeration, which helps to better disperse the CNTs within a polymer matrix. There are several approaches for the functionalization of CNTs including covalent and noncovalent functionalization [14]. These functionalization methods are summarized here.

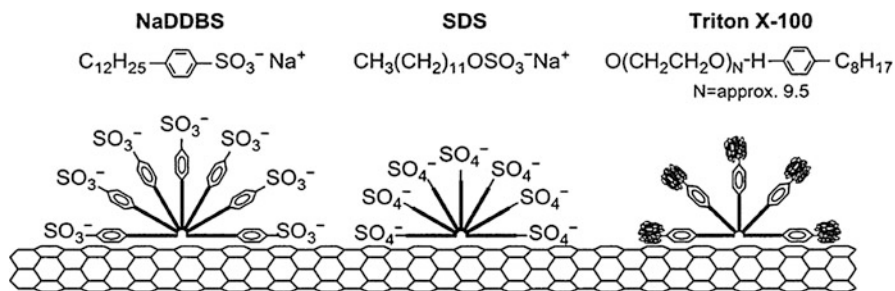


Fig. 5.1 Schematic representation of how surfactant may adsorb onto the nanotube surface (Reprinted with permission from Ref. [16])

2.1 Noncovalent Functionalization

For preparing the large-scale composites without compromising the physical properties of CNTs with advance solubility and processability, noncovalent functionalization of nanotubes is of particular interest. This type of functionalization mainly involves wrapping with polymers, biomacromolecules, and surfactants. CNTs can be well dispersed in water using nonionic, anionic, and cationic surfactants [15–18]. Anionic surfactants such as sodium dodecyl sulfate (SDS) [19, 20] and sodium dodecylbenzene sulfonate (NaDDBS) [21] are commonly used to reduce CNT agglomeration in water. The interaction between the surfactants and the CNTs depends on the nature of the surfactants, such as its alkyl chain length, headgroup size, and charge. SDS has a weaker interaction with the nanotube surface compared to that of NaDDBS and Triton X-100 because it does not have a benzene ring. Indeed π -stacking interaction of the benzene rings on the surface of graphite increases the binding and surface coverage of surfactant molecules to graphite significantly. NaDDBS disperses better than TritonX-100 because of its headgroup and slightly longer alkyl chain. Figure 5.1 represents the adsorption of different surfactants onto the nanotube surfaces.

Immobilization of proteins onto SWNTs has been developed via noncovalent functionalization [22]. Protein immobilization onto nanotubes involves the nucleophilic substitution of *N*-hydroxysuccinimide by an amine group on the protein. The noncovalent functionalization is accomplished by the interaction of delocalized π bonds on the CNTs wall due to sp^2 hybridization with π bonds of polymer molecules of the matrix [22, 23]. The physical association of polymers with CNT results in the dispersion of CNT in both organic solvents [24] and water [25]. A supramolecular complex could be formed via the polymer wrapping around CNTs [26, 27]. In these cases, π -stacking interactions between the polymer and the nanotube surface are responsible for the close association of the structures. Polymer-wrapped nanotube hybrids were prepared by suspending SWNTs in organic solvents poly(*p*-phenylenevinylene-co-2,5-dioctyloxy-*m*-phenylenevinylene). Compared to individual components, higher electrical properties were observed for these hybrid materials.

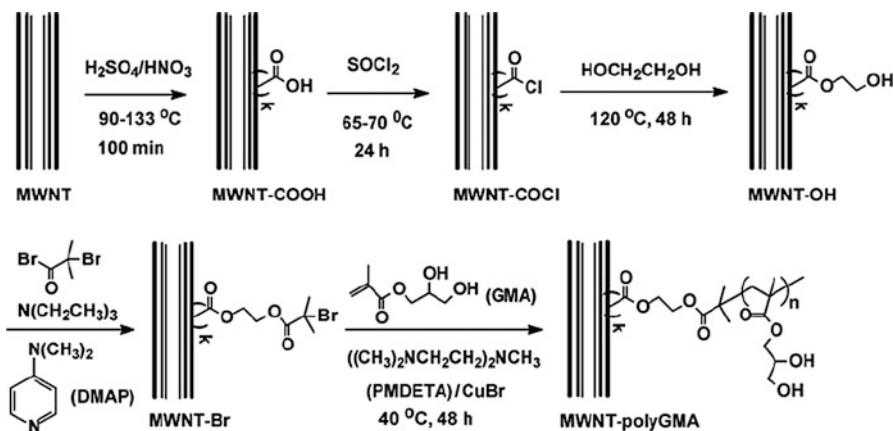
A noncovalent method has been used to modify SWNTs by encapsulating SWNTs within cross-linked and amphiphilic poly(styrene)-block-poly(acrylic acid) copolymer micelles [28]. The encapsulation enhanced the dispersion of CNTs in polar and nonpolar solvents and polymer matrices. The dispersion and solubility of CNT in different media were also achieved via nonwrapping approaches [29]. In such cases, copolymers of a variety of structures and compositions act efficiently as stabilizers. Nativ-Roth et al. [30] suggested that the block copolymers adsorbed to the nanotubes by a nonwrapping mechanism and the solvophilic blocks act as a steric barrier that leads to the formation of stable dispersions of individual CNTs above a threshold concentration of the polymer. The strong π - π interaction between polymer backbone and nanotube surface leads to soluble CNTs. The main potential disadvantage of noncovalent attachment is that the forces between the wrapping molecule and the nanotube might be weak; thus, as a filler in a composite, the efficiency of the load transfer might be low.

2.2 Covalent Functionalization

In the case of covalent functionalization, the translational regularity of CNTs is disrupted by changing sp^2 carbon atoms to sp^3 carbon atoms and the electronic and transport properties of CNT get influenced [31]. The functionalization of CNT via covalent functionalization is more dominant for improving solubility as well as dispersion in solvents and polymers. Covalent functionalization can be accomplished either by modification of surface-bound carboxylic acid groups on the nanotubes or by direct reagents to the sidewalls of nanotubes. Generally, functional groups such as $-\text{COOH}$ or $-\text{OH}$ are created on the CNTs during the oxidation by oxygen, air, concentrated sulfuric acid, nitric acid, aqueous hydrogen peroxide, and acid mixture. The number of $-\text{COOH}$ groups on the surface of CNT depends on acid treatment temperature and time, increasing with increasing temperature [32]. The extent of the induced $-\text{COOH}$ and $-\text{OH}$ functionality also depends on the oxidation procedures and oxidizing agents [33].

The $-\text{COOH}$ or $-\text{OH}$ groups onto the nanotube surface are very helpful for the attachment of organic [34] or inorganic materials, which is important for achieving good dispersion of nanotubes. CNTs can be functionalized at end caps or at the sidewall to enhance their dispersion as well as solubilization in solvents and in polymer matrices [35]. Fluorinated SWNTs were prepared by passing elemental fluorine at different temperatures [36], and such fluorinated SWNTs exhibited improved solubility in different organic solvents [37]. Fluorinated SWNTs may be converted to sidewall-alkylated SWNTs by reaction with Grignard reagent or alkyllithium compounds that are soluble in chloroform [38]. Nitrenes [39] and carbenes [40], functional groups containing SWNTs, were also prepared.

The “grafting to” and “grafting from” approaches have been reported for the covalent functionalization of CNTs with polymer molecules [41]. The “grafting to” approach is based on the attachment of as-prepared or commercially available polymer molecules onto the CNT surface by chemical reactions, such as radical



Scheme 5.1 Functionalization of MWNTs with polyGMA by ATRP (Reprinted with permission from Ref. [54])

coupling, amidation, esterification, etc. The polymer must have suitable reactive functional groups for the preparation of composites in this approach. Fu et al. [42] refluxed acid functional group-decorated CNTs with thionyl chloride to convert acid groups to acyl chlorides, which were used in the esterification reactions with the hydroxyl groups of dendritic poly(polyethylene glycol) polymer. Polymer-grafted CNTs have been formed by covalently attaching nanotubes to highly soluble linear polymers, such as poly(propionylethylenimine-co-ethylenimine) (PPEI-EI) via amide linkages or poly(vinyl acetate-co-vinyl alcohol) (PVA-VA) via ester linkages [43, 44]. The synthesized PVA-CNT nanocomposite films showed very high optical quality without any observable phase separation.

A novel route to polymer reinforcement via preparation of polymer-functionalized nanotubes using organometallic approach has been reported [45]. In the work, CNTs were first functionalized by organometallic *n*-butyllithium and then covalently attached to a chlorinated polypropylene via a coupling reaction. The main limitation of the “grafting to” method is that the grafted polymer content is quite low due to the relatively small fraction of active sites on the CNT and the depressing effects of steric hindrance in the reactivity of polymer [46].

In the “grafting from” approach, the polymer is bound to the CNT surface via in situ polymerization of monomers in the presence of reactive CNT or CNT-supported initiators. The main advantage of this approach is that the polymer/CNT composites can be prepared with high grafting density. This approach has been used successfully to graft many polymers such as polyamide 6 [47], PMMA [48], PS [49], poly(acrylic acid) (PAA) [50], poly(*N*-isopropylacrylamide) (PNIPAM) [51], poly(4-vinylpyridine) [52], and poly(*N*-vinylcarbazole) [53] on CNT via radical, cationic, anionic, ring-opening, and condensation polymerizations. Glycerol monomethacrylate (GMA)-functionalized MWNT composites were prepared by the “grafting from” approach (Scheme 5.1) [54].

In this effort, the oxidized MWNTs were treated with thionyl chloride, glycol, and 2-bromo-2-methylpropionyl bromide to produce MWNT-Br macroinitiators for the ATRP of GMA. The grafted polymer content can be controlled by the feed ratio of monomer to macroinitiators. The hydroxyl groups of the polyGMA chains grafted on the MWNTs are highly active and can be further converted to carboxylic acid groups. CNT-graft-poly(L-lactide) by using surface-initiated ring-opening polymerization has been reported [55].

2.3 CNT Functionalization via Click Chemistry

Click chemistry may provide an ideal modular methodology for the introduction of a wide variety of molecules onto the CNT surface. Click reaction, a set of atom economic reactions, which can be done successfully under the easiest reaction conditions, being the most popular reactions for chemists, since reestablished by Sharpless and coworkers [56]. The Cu(I)-catalyzed Huisgen [3 + 2] cycloaddition reaction between azide and alkyne moieties is the most successful variant forming a 1,4-substituted 1,2,3-triazole. Due to its high regioselectivity, yield, easy reaction condition, reliability, and a wide range of functional group tolerance, click reactions have emerged as a strategy for creating the rapid and efficient assembly of molecules on industrial and academic viewpoints [57, 58].

The first report on CNT functionalization using click chemistry was disclosed by Adronov and coworkers in 2005 [59]. The authors discussed the functionalization of SWNTs with polystyrene using Huisgen [3+2] cycloaddition reaction. To achieve a high degree of functionalization, the alkyne moiety was introduced on the SWNTs surface using the Pschorr-type arylation [60]. Polystyrene was synthesized via ATRP and further modified with azide-terminated polystyrene. The formation of Cu(I)-catalyzed 1,2,3-triazoles by the coupling of azide-terminated polymer and alkyne-functionalized SWNTs was found to occur in an efficient manner under a variety of favorable conditions. This reaction was extremely efficient at low reaction temperature and short reaction time to produce the organo-soluble polymer-nanotube conjugates with a high graft density and controlled polymer molecular weight. The authors further achieved the water-soluble SWNTs via sulfonation of grafted polystyrene chains [61]. However, after polystyrene sulfonation, the sample was completely insoluble in organic medium.

The functionalization of CNTs with biological molecules opened up a new vista for biochemists, using nanotechnology in bio-applications especially for drug delivery. Guo and coworkers [62] reported β -cyclodextrin-modified SWNT nanohybrid through “click” coupling. β -Cyclodextrin, an oligosaccharide, is well known to encapsulate the biological molecules in their hydrophobic cavities in aqueous solution, which enhance their importance as drug carriers and enzyme mimics. β -Cyclodextrin was treated with *p*-toluenesulfonyl chloride to produce mono-6-*O*-(*p*-toluenesulfonyl)- β -cyclodextrin, which was further treated with sodium azide, to convert to azide-functionalized cyclodextrin and further coupled with alkynated SWNTs via Huisgen [3 + 2] cycloaddition. The β -cyclodextrin-functionalized SWNTs show good solubility in water,

which enhances its biological importance for drug delivery applications. Kumar and coworkers [63] focused on the functionalization of SWNTs with bioactive molecules based on amino acids. The solvent-free diazotization procedure was applied between *p*-amino propargyl ether and SWNTs to get the alkyne-functionalized SWNTs. A series of well-defined chiral azides from corresponding amino acids were prepared by converting their acid part to alcohol and further converting into azido derivatives. The azides derived from different amino acids were coupled with alkyne-functionalized SWNTs through 1,2,3-triazole ring using Cu(I)-catalyzed Huisgen [3 + 2] cycloaddition click chemistry between alkyne and excess of azides.

The click chemistry has been applied for the preparation of the nanostructured materials composed of SWNTs and multiblock copolymer polyurethane (PU) [64]. Alkyne-decorated SWNTs were prepared firstly using the same method as discussed earlier by Li and coworkers [59] and then reacted with azide moiety containing poly(ϵ -caprolactone)-based polyurethane by using Cu(I)-catalyzed Huisgen [3 + 2] cycloaddition. The diol used for the synthesis of PU block copolymer was composed of two blocks of poly(ϵ -caprolactone) with and without the azide moiety, synthesized by the copolymerization of α -chloro- ϵ -caprolactone with ϵ -caprolactone using ring-opening polymerization. The azide block in synthesized diol was associated with alkynated SWNTs, and the block without azide moiety was responsible for crystallization of poly(ϵ -caprolactone) (PCL). The polyurethane-grafted SWNTs showed excellent dispersion of SWNTs in polymer matrix and good solubility in organic solvents. The PCL crystallization in this polymer is an important factor for using PU as a smart material, whereas due to the stored elastic strain energy behavior of SWNTs [65], the PU-*g*-SWNTs show the excellent shape recovery properties.

Li and coworkers [66] prepared the covalent-functionalized MWNTs with thermoresponsive diblock copolymer micelles using the Cu(I)-catalyzed Huisgen [3 + 2] cycloaddition. The alkyne moiety-functionalized MWNTs were prepared by the reaction of isocyanate-functionalized MWNTs with propargyl alcohol. The thermoresponsive diblock copolymer was composed of *N,N*-dimethylacrylamide (DMA) and *N*-isopropylacrylamide (PNIPAM). The copolymer containing hydrophilic DMA, as well as a smart NIPAM block, is capable of forming micelles with response to changes in the aqueous solution temperature. On the basis of PNIPAM block length, the micelle size and transition temperature can be controlled. Due to the higher azide concentration on their periphery, micelles favored the improved grafting efficiency and solubility of nanotubes, compared to coil in solution. Amphiphilic polymer brushes-decorated CNT were prepared by using clickable macro initiator groups onto CNTs surface [67]. The bromo and azido groups functionalized CNTs were prepared by the reaction of poly(3-azido-2-(2-bromo-2-methylpropanoyloxy)propyl methacrylate with alkynated CNTs. One pot click chemistry and ATRP could be achieved using bromo and azido moieties as initiators for polystyrene and polyethylene glycol grafting (Fig. 5.2).

The hybrid materials based on CNTs and metal nanoparticles have emerged as a new area of research [68]. Due to the synergetic properties of carbon nanotubes and metal particles, the resulting hybrid nanomaterials would be useful for several

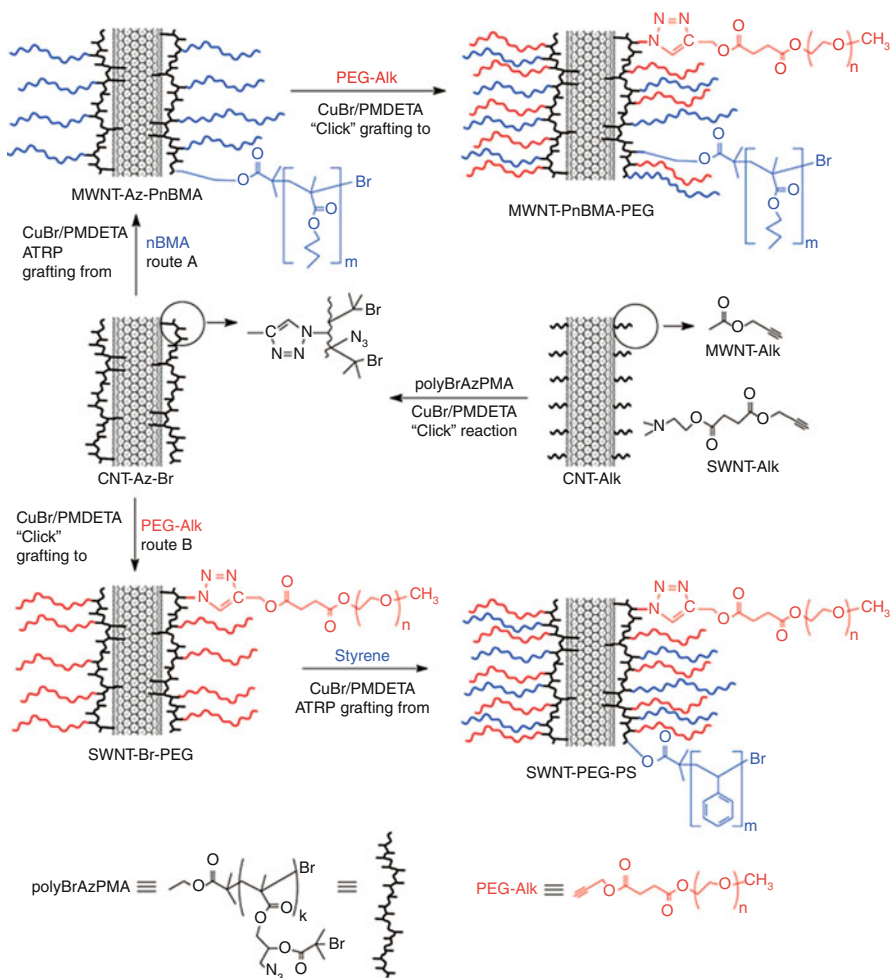


Fig. 5.2 Synthesis of amphiphilic polymer brushes-grafted multiwalled and single-walled carbon nanotubes by a combination of click chemistry and ATRP (Reprinted with permission from Ref. [67])

application areas including electronic, optical, catalytic, and magnetic applications. Voggu and coworkers [69] have synthesized a novel material by functionalization of SWNTs with gold nanocrystals by using the same approach. The authors functionalized SWNTs with amido butane containing the terminal azido group and further treated with Au nanocrystals capped with the hex-5-yne-1-thiol. This reaction yielded SWNT-Au nanomaterial, where the gold nanocrystals decorate the SWNTs. A further study was done by Rana and coworkers [70], wherein the authors achieved the functionalization of SWNTs by gold nanoparticles through click chemistry.

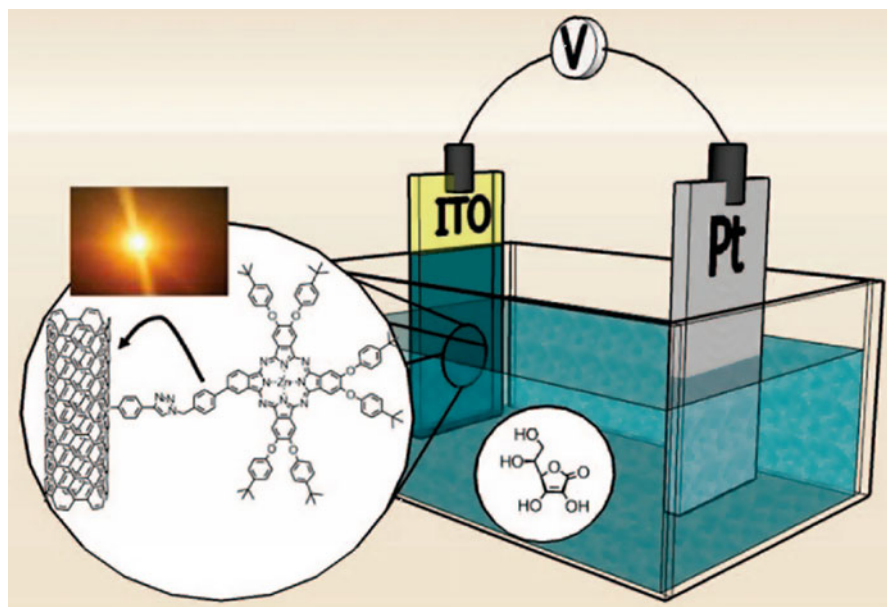


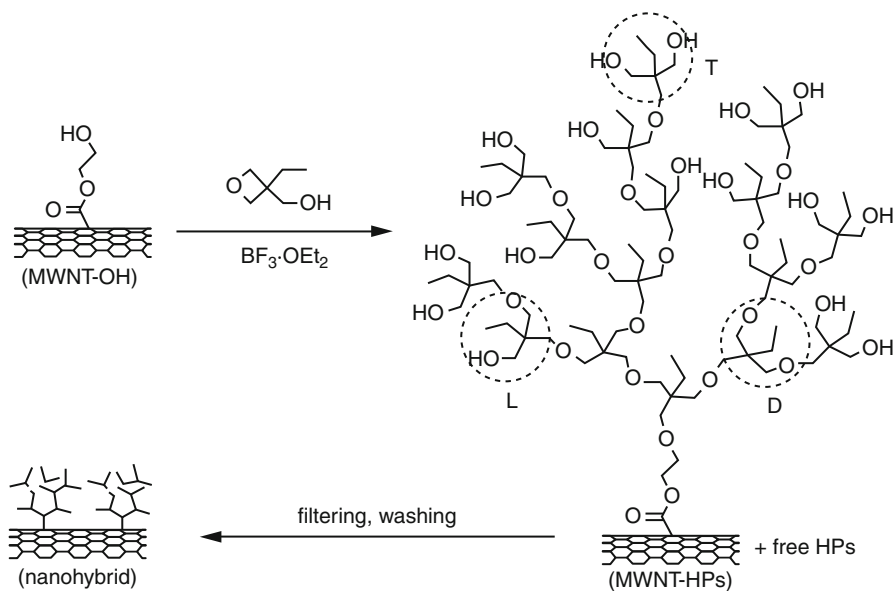
Fig. 5.3 Schematic representation of the photoelectrochemical cell used for the measurement (Reprinted with permission from Ref. [72])

Gold nanoparticles containing octanethiol moieties were prepared by the reduction of tetrachloroauric acid using sodium borohydride in the presence of alkanethiol [71]. The alkyl thiol-protected gold nanoparticles were further treated with azidoundecane-thiol to get the azide moiety containing gold nanoparticles. As a strategy for the attachment of metal nanoparticles, 1,2,3-triazole ring was utilized as a linker between the azide-decorated nanoparticles and alkyne-functionalized SWNTs. Campidelli and coworkers [72] used Huisgen 1,3-dipolar cycloaddition reaction to synthesize the phthalocyanines-functionalized SWNTs (Fig. 5.3).

The alkylation of SWNTs, which is an essential functionality for click coupling, was accomplished using purified SWNTs with 4-(2-trimethylsilyl)ethynylaniline in the presence of isoamyl nitrite, which were further treated with azide moiety containing zinc-phthalocyanine (ZnPc) in the presence of CuSO_4 and sodium ascorbate to give the nanotube-phthalocyanine assembly. The authors studied the photovoltaic properties of synthesized materials and observed that the photocurrent of SWNT-ZnPc was about 30 % higher than pristine SWNTs under short-circuit conditions.

2.4 CNT Functionalization via Dendritic Polymers

Dendritic polymers such as dendrimeric and hyperbranched polymers have generated great excitement in polymer research, due to their spherical and



Scheme 5.2 Synthetic process for the MWNT-hyperbranched polyether nano hybrids (Reprinted with permission from Ref. [80])

three-dimensional globular structural architectures [73]. Due to their highly functionalized three-dimensional globular, and non-entangled structures, dendritic polymers have been used to enhance the dispersion of CNTs in polymer matrices [74]. They exhibit higher solubility, lower melt, and solution viscosity compared to linear polymers of the same molar mass. There are two approaches to form the dendritic polymer/CNT nanocomposites via covalent and noncovalent functionalization of CNTs. Herein, we are focused on the covalent functionalization of CNTs with dendritic polymers.

Grafting of dendritic polymers onto CNTs is a novel approach for fabricating the nanomaterials and nanodevices [75]. CdS quantum dot assemblies were prepared by using the dendronized SWNT-based template [76]. First [(Den)_n-SWNT] were prepared by the reaction of acyl chloride-functionalized MWNTs with amino-polyester dendron. The ester groups were further cleavage into carboxylic groups using the formic acid and reacted with $\text{Cd}(\text{NO}_3)_2$ to generate the encapsulated CdS quantum dots tethered onto the SWNT surface. Campidelli et al. [77] synthesized the polyamidoamine dendrimer-functionalized SWNTs. The dendrimer-functionalized SWNTs were further decorated with porphyrin moieties, and the photophysical properties of nanoconjugates were studied. In the presence of visible light irradiation, porphyrin-SWNT nanoconjugate gives rise to fast charge separation. Tao et al. [78] synthesized poly(amidoamine) (PAMAM)dendrimer-functionalized MWNTs and further used them as a template for the deposition of silver nanoparticles on the MWNT surface. The antimicrobial effects of silver

nanoparticle-functionalized PAMAM-MWNTs nanohybrids were also studied [79]. The Ag nanoparticles containing dendritic MWNT showed stronger antimicrobial effect than dendritic MWNTs without Ag particles. Xu et al. [80] prepared hyperbranched polymer on the surface of MWNTs (Scheme 5.2). In situ ring-opening polymerization was employed for growing multihydroxyl dendritic macromolecules on the surface of MWNTs.

Treelike multihydroxy hyperbranched polyether was covalently grafted on the MWNT using MWNTs-OH as an initiator. The amount of polymer grafted is controllable using this approach. The molecular weight of the grafted hyperbranched polymer increases with increasing feed ratios of the monomer. Biocompatible hyperbranched glycopolymer-functionalized MWNTs were prepared by ATRP [81]. The authors prepared 3-*O*-methacryloyl-1,2:5,6-di-*O*-isopropylidene-D-glucofuranose (MAIG)-functionalized MWNTs and self-condensing vinyl copolymerization (SCVCP) of MAIG and AB* inimer, 2-(2-bromoisobutyryloxy)ethyl methacrylate. Such a biocompatible polymer-functionalized CNTs would be very useful for bionanotechnology applications.

Hyperbranched poly(urea-urethane) (HPU) and MWNT-based core-shell nanostructures were prepared, where MWNTs were used as the core and hyperbranched poly(urea-urethane) (HPU) as the shell component [82]. The authors have synthesized HPU-functionalized MWNTs by polycondensation approach. A large number of proton-donor and proton-acceptor groups were located in the HPU-functionalized MWNT; intra- and intermolecular H bonds were easily formed by their interactions. At low temperature, shearing forces induce the conversion from intra- to intermolecular H bonds. The rheological behaviors of the HPU-functionalized MWNT solutions showed a strong dependence on concentration, temperature, and thermal and shearing prehistory. Due to molecular architecture of hyperbranched polymers, mushroom-like clusters on MWNT stalks were observed from hyperbranched poly(ether ketone) (PEK)-grafted nanotubes. These conditions were found very useful for the functionalization of CNTs without any damage but found strong enough to promote the covalent attachment of PEK on the surface of electron-deficient MWNTs [83]. The hyperbranched polyester-functionalized MWNTs were synthesized and further treated with difunctional molecules synthesized from toluene 2,4-diisocyanate (TDI) and hydroxyethyl acrylate to get UV-curable hyperbranched polymer. The modified MWNTs containing a large amount of UV curable acrylate group were dispersed with UV curable aliphatic urethane acrylate resins. In the presence of UV irradiation, cross-linking reaction happened between MWNTs and acrylate resins leading to the covalent bonding of MWNTs to the matrix, which is more stable than simply physical bonding.

3 Polyurethane/CNT Composites

Due to their good biocompatibility and a high resistance to chemicals as well as excellent processability, polyurethane (PU) block copolymers have been widely

used in regular life as adhesives, coatings, elastomers, and biomedical materials [84, 85]. For enhancing the applications of PU, researchers have improved its thermal, mechanical, and electrical properties by adding fillers to the polymer matrix [86]. However, there is an inverse relationship between modulus enhancement and recoverable strain ratio. Mostly, recoverable strain decreases in the presence of filler. Many of these issues can be alleviated by reducing filler loading, e.g., by the incorporation of a small fraction of nanoscopic fillers or by designing the fillers in an appropriate manner for the polymer system.

Ohki et al. [87] observed a 50 % increase in elastic modulus of PU in the presence of 10 wt% chopped glass fibers, but recovery ratio decreased from 60 % to 25 %. Li et al. [88] prepared PCL-based PU with carbon black filler. The authors observed a significant increment in electrical conductivity and storage modulus at about 20 wt% loading of carbon black. Cho et al. [89] prepared the silica-filled PU nanocomposites, where the author found that filler did not affect recoverable strain and only a small increase in modulus was observed. After adding the silica percentage beyond 10 wt%, the modulus, ultimate stress, and ultimate strain decreased. And also nanocomposites of PU with carbon nanotubes (CNTs) showed promising improvement in both strain and stress recovery [90]. However, it is still a challenge to find an efficient and general way to construct an extensive practical material that simultaneously possesses all these desirable features rather than an approach that improves only one feature at the expense of another.

The influence of SWNTs on the thermal, mechanical, and electrical behavior of shape-memory polyurethane (SMPU) has been studied [91]. The SMPU displays high elasticity (~ 700 %) and strain-induced crystallization. High concentrations of SWNTs were uniformly dispersed in SMPU matrix. The authors observed that only 5 wt% of SWNT was enough to increase the rubbery modulus by a factor of 5 at room temperature. Furthermore, the SWNTs provide a conductivity of 1 S cm^{-1} at 0.9 vol.% percolation threshold. Shape and stress recovery characteristics of the SMPU/SWNT nanocomposites (1 wt%) are qualitatively depicted. The shape-memory effect of these nanocomposites was actuated thermally, optically, and electrically. Exposed to near-infrared radiation (NIR), the nanocomposite deformed to 300 % exerting ~ 19 J to lift a 60 g weight more than 3 cm. The resistivity of the nanocomposites was directly related to the concentration of CNT, its aspect ratio, and orientation distribution. The shape fixity rate and recovery constraint stress of a nanocomposite with 5 vol.% (2.9 wt%) SWNT increased from approximately 0.56 to 0.70 and from 0.6 to 1.4 MPa compared with pure SMPU, respectively. Cho et al. [92] synthesized the electro-active shape-memory nanocomposites using PU and MWNTs. MWNTs of 10-20 nm diameter and 20 μm length were used after their surface treatment in mixed solvents of nitric acid and sulfuric acid (3:1 molar ratio) at 140 °C for 10 min. Surface modification of MWNTs improved the mechanical properties of the nanocomposites. The modulus and stress at 100 % elongation increased with increasing surface-modified MWNTs content, while elongation at break decreased. MWNT surface modification also resulted in a decrease in the electrical conductivity of the nanocomposites. However, as the surface-modified MWNT concentration increased, the conductivity also increased.

A homogenous distribution of MWNT in PU could be reached by mixing the MWNT with the prepolymer mixture prior to the addition of chain extender (BD). The in situ polymerization process normally provided a good opportunity of interaction between the polymer chains and nanofillers. Highly conductive PU actuators prepared by in situ polymerization of PU in the presence of surface-modified MWNT were reported [93]. Different concentrations of MWNTs up to 10 wt% were mixed with the prepolymer solutions. The PU/MWNTs nanocomposites were also synthesized with different hard-segment contents (25–40 wt%) to tailor the overall physical and mechanical properties as well as shape-memory properties. The nanocomposites were elongated by 100 % at 32 °C and the temporary shape fixed by cooling to 10 °C. The permanent shape was recovered by the application of different voltages. This nanocomposite actuator was explored for controlling the surface of a micro aerial vehicle. When the electrical power was supplied, the actuator shrunk increasingly, and accordingly, the control surface was deflected gradually.

Fibers from SMPU/MWNT nanocomposites were prepared using a melt-spinning technique to improve the mechanical, thermal, morphological, and viscoelastic properties as well as the shape-memory properties of the polymer matrix [94]. The efficiency to produce fibers with smooth surfaces decreased with increasing concentration of MWNTs in the nanocomposite. The fiber surface of the nanocomposite became rough with increasing MWNT content particularly when the MWNTs concentration increased from 3 wt% to 7 wt%. Homogenous distribution of MWNTs with very high tendency to align parallel to the drawing direction could be achieved with concentrations less than 7 wt%. [94]. MWNTs were mixed initially with MDI in DMF prior to adding PCL-diol, and it was expected that the MWNTs were strongly linked to the hard segments. This interaction could contribute greatly to increase the mechanical stability of the fibers particularly at program temperature. Therefore, the maximum stress at 100 % deformation increases with increasing the MWNT content, indicating that the SMPU/MWNT fibers were able to withstand higher stress. At the same time, the MWNTs having good interactions with the SMPU chains, particularly with the hard-segment regions, helped to store the internal stress during stretching and shape fixation. As a result, recovery ratio (R_r) value increased. At high concentrations, the MWNTs were not homogeneously distributed in the polymer matrix, and aggregated MWNTs lead to the incompatibility of the two components and weakening of the interfacial adhesion; consequently R_r decreased [94].

Kuan et al. [95] incorporated amino-functionalized MWNTs into waterborne PU. They found an increase in modulus from 77 MPa for the polymer to 131 MPa for a 4 phr composite (an increase of 70 %) and a tensile strength increase from 5.1 MPa to 18.9 MPa (an increase of 270 %) at the same loading level. Covalent bond formation between amino-functionalized MWNTs and PU promoted increased interfacial strength and tensile strength. MWNT is more effective to the improvement of modulus, while SWNT is better for elongation and tensile strength. The different reinforcing effects of MWNT and SWNT on PU were correlated to the shear thinning exponent and the shape factor of CNTs in polyol dispersion.

Polymer grafting is very effective in increasing dispersion and the mechanical properties of composites due to its strong chemical bonding between

polymer and CNTs. Xia et al. [96] studied polycaprolactone-based PU-grafted SWNTs (SWNT-g-PU) and poly(propylene glycol)-grafted MWNTs into PU by in situ polymerization. Mechanical property improvements were observed in both cases. The incorporation of 0.7 wt% SWNT-g-PU into PU improved the Young's modulus by $\sim 278\%$ and $\sim 188\%$ compared to the pure PU and ungrafted pristine SWNT/PU composites, respectively. This is due to the better dispersion of SWNT-g-PU and MWNT-g-PU and stronger interfacial interactions between the CNTs and PU. Wang et al. [97] also found that adding 1–10 wt% PU-functionalized MWNT to PU increased the tensile strength by 63–210%. The storage modulus and soft segment T_g (from $\tan\delta$) increased with increasing PU-functionalized MWNT in the PU. The T_g of the soft segments of the nanocomposite films shifted from $-20\text{ }^\circ\text{C}$ to $-5\text{ }^\circ\text{C}$, suggesting that PU-functionalized MWNTs are compatible with the amorphous regions of the soft segments in the PU matrix. Recently, McClory et al. [98] reported thermosetting PU/MWNT nanocomposites by an addition polymerization reaction. The Young's modulus increased by 97% and 561% on the addition of 0.1 wt% and 1 wt% MWNTs in the PU, respectively, whereas ultimate tensile strength increased by 397% when either 0.1 or 1 wt% MWNTs added to PU. In this composite, the percentage of elongation at break increased from 83% to 302% on the addition of 0.1 wt% CNT compared to pure PU resin. So, these enhancements in mechanical properties can be attributed to the high dispersion of CNTs through the polymer matrix and good interfacial interaction between CNT and PU.

4 Conclusions

In summary, the key challenges for the development of high-performance CNT-polymer composites are the dispersion of CNTs and interfacial adhesion between CNTs and a polymer matrix. Despite various methods, such as melt processing, solution processing, in situ polymerization, and chemical functionalization, there are still opportunities and challenges to be found in order to improve dispersion and modify interfacial properties. A specific functionalization of CNTs is required for strong interfacial adhesion between CNTs and a given polymer matrix, which may also simultaneously improve the dispersion of CNTs in the polymer matrix. The mechanical properties of CNT-polymer nanocomposites may be compromised between carbon-carbon bond damage and increased CNT-polymer interaction due to CNT functionalization. Similarly, electrical conductivity of a CNT-polymer nanocomposite is determined by the negative effect of carbon-carbon bond damage and the positive effect of improved CNT dispersion due to CNT functionalization. In either case, the choice and control of tailored functionalization sites for chemical modification of CNTs are necessary. As an example, selective CNT functionalization can be achieved via click chemistry by preparing azide-functionalized polymers. The employment of hyperbranched polymers for improving CNT dispersion may be also useful because it can result in enhanced electrical conductivity as well as mechanical properties of nanocomposites, without modification of CNT.

References

1. Ajayan PM, Stephan O, Colliex C, Trauth D (1994) Aligned carbon nanotube arrays formed by cutting a polymer resin-nanotube composite. *Science* 265:1212
2. Iijima S (1991) Helical microtubules of graphitic carbon. *Nature* 354:56
3. Iijima S, Ichihashi T (1993) Single-shell carbon nanotubes of 1-nm diameter. *Nature* 363:603
4. Sugai T, Yoshida H, Shimada T, Okazaki T, Shinohara H (2003) New synthesis of high-quality double-walled carbon nanotubes by high temperature pulsed arc discharge. *Nano Lett* 3:769
5. Grunes J, Zhu A, Samorjai GA (2003) Catalysis and nanoscience. *Chem Commun* 18:2257
6. Akthakul A, Hochbaum AI, Stellacci F, Mayes AM (2005) Size fractionation of metal nanoparticles by membrane filtration. *Adv Mater* 17:532
7. Moniruzzaman M, Winey KI (2006) Polymer nanocomposites containing carbon nanotubes. *Macromolecules* 39:5194
8. Gong XY, Liu J, Baskaran S, Voise RD (2000) Surfactant-assisted processing of carbon nanotube/polymer composites. *Chem Mater* 12:1049
9. Ichida M, Mizuno S, Kataura H, Achiba Y, Nakamura A (2004) Anisotropic optical properties of mechanically aligned single-walled carbon nanotubes in polymer. *Appl Phys A* 78:1117
10. Sergei S, Xue L, Rahmi O, Pawel K, David GC (2004) Role of thermal boundary resistance on the heat flow in carbon-nanotube composites. *J Appl Phys* 95:8136
11. Kim JY, Han SI, Kim SH (2007) Crystallization behaviors and mechanical properties of poly(ethylene 2,6-naphthalate)/multiwall carbon nanotube nanocomposites. *Polym Eng Sci* 47:1715
12. Sankapal BR, Setyowati K, Chen J, Liu H (2007) Electrical properties of airstable, iodine-doped carbon-nanotube-polymer composites. *Appl Phys Lett* 91:173103
13. Wang Z, Ciselli P, Peijs T (2007) The extraordinary reinforcing efficiency of single-walled carbon nanotubes in oriented poly(vinyl alcohol) tapes. *Nanotechnology* 18:455709
14. Hirsch A (2002) Functionalization of single-walled carbon nanotubes. *Angew Chem Int Ed* 41:1853
15. Duesberg GS, Muster J, Krstic V, Burghard M, Roth S (1998) Chromatographic size separation of single-wall carbon nanotubes. *Appl Phys A* 67:117
16. Islam MF, Rojas E, Bergey DM, Johnson AT, Yodh AG (2003) High weight fraction surfactant solubilization of single-wall carbon nanotubes in water. *Nano Lett* 3:269
17. Moore VC, Strano MS, Haroz EH, Hauge RH, Smalley RE, Schmidt J, Talmon Y (2003) Individually suspended single-walled carbon nanotubes in various surfactants. *Nano Lett* 3:1379
18. Paredes JI, Burghard M (2004) Dispersions of individual single-walled carbon nanotubes of high length. *Langmuir* 20:5149
19. Polulin P, Vigolo B, Launois P (2002) Films and fibers of oriented single wall Nanotubes. *Carbon* 40:1741
20. Yurekli K, Mitchell CA, Krishnamoorti R (2004) Small angle neutron scattering from surfactant assisted aqueous dispersion of carbon nanotubes. *J Am Chem Soc* 126:9902
21. Tan Y, Resasco DE (2005) Dispersion of single-walled carbon nanotubes of narrow diameter distribution. *J Phys Chem B* 109:14454
22. Chen RJ, Zhang Y, Wang D, Dai H (2001) Noncovalent sidewall functionalization of single-walled carbon nanotubes for protein immobilization. *J Am Chem Soc* 123:3838
23. Lordi V, Yao N (2000) Molecular mechanics of binding in carbon nanotube-polymer composites. *J Mater Res* 15:2770
24. Wu HX, Qiu XQ, Cao WM, Lin YH, Cai RF, Qian SX (2007) Polymer-wrapped multiwalled carbon nanotubes synthesized via microwave assisted in situ emulsion polymerization and their optical limiting properties. *Carbon* 45:2866
25. Bandyopadhyaya R, Nativ-Roth E, Regev O, Yerushalmi-Rozen R (2002) Stabilization of individual carbon nanotubes in aqueous solutions. *Nano Lett* 2:25

26. Ogoshi T, Yamagishi TA, Nakamoto Y (2007) Supramolecular single walled carbon nanotubes (SWCNTs) network polymer made by hybrids of SWCNTs and water-soluble calix[8]arenes. *Chem Commun* 45:4776
27. Cheng F, Imin P, Maunders C, Botton G, Adronov A (2008) Soluble, discrete supramolecular complexes of single-walled carbon nanotubes with fluorene-based conjugated polymers. *Macromolecules* 41:2304
28. Kang Y, Taton TA (2003) Micelle-encapsulated carbon nanotubes: a route to nanotube composites. *J Am Chem Soc* 125:5650
29. Shvartzman-Cohen R, Kalisman YL, Navi-Roth E, Yerushalmi-Rozen R (2004) Generic approach for dispersing single-walled carbon nanotubes: the strength of a weak interaction. *Langmuir* 20:6085
30. Nativ-Roth E, Shvartzman-Cohen R, Bounioux C, Florent M, Zhang D, Szleifer I (2007) Physical adsorption of block copolymers to SWNT and MWNT: a non-wrapping mechanism. *Macromolecules* 40:3676
31. Zhang X, Sreekumar TV, Liu T, Kumar S (2004) Properties and structure of nitric acid oxidized single wall carbon nanotube films. *J Phys Chem B* 108:16435
32. Georgakilas V, Kordatos K, Prato M, Guldi DM, Holzinger M, Hirsch A (2002) Organic functionalization of carbon nanotubes. *J Am Chem Soc* 124:760
33. Park H, Zhao J, Lu JP (2006) Effects of sidewall functionalization on conducting properties of single wall carbon nanotubes. *Nano Lett* 6:916
34. Hemon MA, Chen J, Hu H, Chen Y, Itkis ME, Rao AM (1999) Dissolution of single-walled carbon nanotubes. *Adv Mater* 11:834
35. Niyogi S, Hamon MA, Hu H, Zhao B, Bhowmik P, Sen R (2002) Chemistry of single-walled carbon nanotubes. *Acc Chem Res* 35:1105
36. Mickelson ET, Huffman CB, Rinzler AG, Smalley RE, Hauge RH, Margrave JL (1998) Fluorination of single-wall carbon nanotubes. *Chem Phys Lett* 296:188
37. Kelly KF, Chiang IW, Mickelson ET, Hauge RH, Margrave JL, Wang X (1999) Insight into the mechanism of sidewall functionalization of single-walled nanotubes: an STM study. *Chem Phys Lett* 313:445
38. Boul PJ, Liu J, Mickelson ET, Huffman CB, Ericson LM, Chiang IW (1999) Reversible sidewall functionalization of bucky tubes. *Chem Phys Lett* 310:367
39. Bahr JL, Mickelson ET, Bronikowsky MJ, Smalley RE, Tour JM (2001) Dissolution of small diameter single-wall carbon nanotubes in organic solvents. *Chem Commun* 2:193
40. Holzinger M, Vostrowsky O, Hirsch A, Hennrich F, Kappes M, Weiss R (2001) Sidewall functionalization of carbon nanotubes. *Angew Chem Int Ed* 40:4002
41. Baek JB, Lyons CB, Tan LS (2004) Grafting of vapor-grown carbon nanofibers via in situ polycondensation of 3-phenoxybenzoic acid in poly(phosphoric acid). *Macromolecules* 37:8278
42. Fu K, Huang W, Lin Y, Riddle LA, Carroll DL, Sun YP (2001) Defunctionalization of functionalized carbon nanotubes. *Nano Lett* 1:439
43. Riggs JE, Guo Z, Carroll DL, Sun YP (2000) Strong luminescence of solubilised carbon nanotubes. *J Am Chem Soc* 122:5879
44. Lin Y, Zhou B, Fernando KAS, Liu P, Allard LF, Sun YP (2003) Polymeric carbon nanocomposites from carbon nanotubes functionalized with matrix polymer. *Macromolecules* 36:7199
45. Blake R, Gunko YK, Coleman J, Cadek M, Fonseca A, Nagy JB (2004) A generic organo-metallic approach toward ultra-strong carbon nanotube polymer composites. *J Am Chem Soc* 126:10226
46. Cao L, Yang W, Yang J, Wang C, Fu S (2004) Hyperbranched poly(amidoamine)-modified multi-walled carbon nanotubes via grafting-from method. *Chem Lett* 33:490
47. Qu L, Veca LM, Lin Y, Kitaygorodskiy A, Chen B, McCall AM (2005) Soluble nylon-functionalized carbon nanotubes from anionic ring opening polymerization from nanotube surface. *Macromolecules* 38:10328

48. Park SJ, Cho MS, Lim ST, Cho HJ, Jhon MS (2003) Synthesis and dispersion characteristics of multi-walled carbon nanotube composites with poly(methyl methacrylate) prepared by in-situ bulk polymerization. *Macromol Rapid Commun* 24:1070
49. Baskaran D, Mays JW, Bratcher MS (2004) Polymer-grafted multiwalled carbon nanotubes through surface-initiated polymerization. *Angew Chem Int Ed* 43:2138
50. Kong H, Luo P, Gao C, Yan D (2005) Polyelectrolyte-functionalized multiwalled carbon nanotubes: preparation, characterization and layer-by-layer self-assembly. *Polymer* 46:2472
51. Kong H, Li W, Gao C, Yan D, Jin Y, Walton DRM (2004) Poly(N-isopropylacrylamide)-coated carbon nanotubes: temperature sensitive molecular nanohybrids in water. *Macromolecules* 37:6683
52. Qin S, Qin D, Ford WT, Herrera JE, Resasco DE (2004) Grafting of poly(4-vinylpyridine) to single-walled carbon nanotubes and assembly of multilayer films. *Macromolecules* 37:9963
53. Wu W, Zhang S, Li Y, Li J, Liu L, Qin Y (2003) PVK-modified single walled carbon nanotubes with effective photo induced electron transfer. *Macromolecules* 36:6286
54. Gao C, Vo CD, Jin YZ, Li W, Armes SP (2005) Multihydroxy polymer functionalized carbon nanotubes: synthesis, derivation, and metal loading. *Macromolecules* 38:8634
55. Chen GX, Kim HS, Park BH, Yoon JS (2007) Synthesis of poly(L-lactide)-functionalized multiwalled carbon nanotubes by ring-opening polymerization. *Macromol Chem Phys* 208:389
56. Kolb HC, Finn MG, Sharpless KB (2001) Click chemistry: diverse chemical function from a few good reactions. *Angew Chem Int Ed* 40:2004
57. Antoni P, Nystrom D, Hawker CJ, Hult A, Malkoch M (2007) A chemoselective approach for the accelerated synthesis of well-defined dendritic architectures. *Chem Commun* 22:2249
58. Service RF (2008) Click chemistry clicks along. *Science* 320:868
59. Li H, Cheng F, Duft AM, Adronov A (2005) Functionalization of singlewalled carbon nanotubes with well-defined polystyrene by click coupling. *J Am Chem Soc* 127:14518
60. Dyke CA, Tour JM (2003) Solvent-Free functionalization of carbon nanotubes. *J Am Chem Soc* 125:1156
61. Li H, Adronov A (2007) Water soluble SWCNTs from sulfonation of nanotube-bound polystyrene. *Carbon* 45:984
62. Guo Z, Liang L, Liang JJ, Ma YF, Yang XY, Ren DM, Chen YS, Zheng JY (2008) Covalently β -cyclodextrin modified single-walled carbon nanotubes: a novel artificial receptor synthesized by click chemistry. *J Nanopart Res* 10:1077
63. Kumar I, Rana S, Rode CV, Cho JW (2008) Functionalization of single walled carbon nanotubes with azides derives from amino acids using click chemistry. *J Nanosci Nanotechnol* 8:3351
64. Rana S, Cho JW, Kumar I (2010) Synthesis and characterization of polyurethane-grafted single-walled carbon nanotubes via click chemistry. *J Nanosci Nanotechnol* 10:5700
65. Ni QQ, Zhang CS, Fu Y, Dai G, Kimura T (2007) Shape memory effect and mechanical properties of carbon nanotube/shape memory polymer nanocomposites. *Compos Struct* 81:176
66. Liu J, Nie Z, Gao Y, Adronov A, Li H (2008) Click coupling between alkyne-decorated multiwalled carbon nanotubes and reactive PDMA-PNIPAM micelles. *J Polym Sci Part B Polym Chem* 46:7187
67. Zhang Y, He H, Gao C (2008) Clickable macro initiator strategy to build amphiphilic polymer brushes on carbon nanotubes. *Macromolecules* 41:9581
68. Georgakilas V, Gourmis D, Tzitzios V, Pasquato L, Guldi DM, Prato M (2007) Decorating carbon nanotubes with metal or semiconductor nanoparticles. *J Mater Chem* 17:2679
69. Voggu R, Suguna P, Chandrasekaran S, Rao CNR (2007) Assembling covalently linked nanocrystals and nanotubes through click chemistry. *Chem Phys Lett* 443:118
70. Rana S, Kumar I, Yoo HJ, Cho JW (2009) Assembly of gold nanoparticles on single-walled carbon nanotubes by using click chemistry. *J Nanosci Nanotech* 9:3261
71. Brust M, Walker M, Bethell D, Schiffrin DJ, Whyman R (1994) Synthesis of thiol-derivatised gold nanoparticles in a two-phase Liquid-Liquid system. *J Chem Soc Chem Commun* 7:801

72. Campidelli S, Ballesteros B, Filoramo A, Diaz DD, Torre G, Torres T, Rahman GMA, Ehli C, Kiessling D, Werner F, Sgobba V, Guldi DM, Cioffi C, Prato M, Bourgoin JP (2008) Facile decoration of functionalized single-wall carbon nanotubes with phthalocyanines via click chemistry. *J Am Chem Soc* 130:11503
73. Tomalia DA, Baker H, Dewald J, Hall M, Kallos G, Martin S (1986) Dendritic macromolecules: synthesis of starburst dendrimers. *Macromolecules* 19:2466
74. Rana S, Karak N, Cho JW, Kim YH (2008) Enhanced dispersion of carbon nanotubes in hyperbranched polyurethane and properties of nanocomposites. *Nanotechnology* 19:495707
75. Davis JJ, Coleman KS, Azamian BR, Bagshaw CB, Green MLH (2003) Chemical and biochemical sensing with modified single walled carbon nanotubes. *Chem Eur J* 9:3732
76. Hwang SH, Moorefield CN, Wang P, Jeong KU, Cheng SZD, Kotta KK (2006) Dendron-tethered and templated CdS quantum dots on single-walled carbon nanotubes. *J Am Chem Soc* 128:7505
77. Campidelli S, Soombar C, Lozano DE, Ehli C, Guldi DM, Prato M (2006) Dendrimer-functionalized single-wall carbon nanotubes: synthesis, characterization, and photo induced electron transfer. *J Am Chem Soc* 128:12544
78. Tao L, Chen G, Mantovani G, York S, Haddleton DM (2006) Modification of multi-wall carbon nanotube surfaces with poly(amidoamine) dendrons: synthesis and metal templating. *Chem Commun* 47:4949
79. Yuan W, Jiang G, Che J, Qi X, Xu R, Chang MW (2008) Deposition of silver nanoparticles on multiwalled carbon nanotubes grafted with hyperbranched poly(amidoamine) and their antimicrobial effects. *J Phys Chem C* 112:18754
80. Xu Y, Gao C, Kong H, Yan D, Jin YZ, Watts PCP (2004) Growing multihydroxyl hyperbranched polymers on the surfaces of carbon nanotubes by in situ ring-opening polymerization. *Macromolecules* 37:8846
81. Gao C, Muthukrishnan S, Li W, Yuan J, Xu Y, Mueller AHE (2007) Linear and hyperbranched glycopolymer-functionalized carbon nanotubes: synthesis, kinetics, and characterization. *Macromolecules* 40:1803
82. Yang Y, Xie X, Wu J, Yang Z, Wang X, Mai YW (2006) Multiwalled carbon nanotubes functionalized by hyperbranched poly(ureaurethane)s by a one-pot polycondensation. *Macromol Rapid Commun* 27:1695
83. Jeon IY, Tan LS, Baek JB (2008) Nanocomposites derived from in situ grafting of linear and hyperbranched poly(ether-ketone)s containing flexible oxyethylene spacers onto the surface of multiwalled carbon nanotubes. *J Polym Sci Polym Chem* 46:3471
84. John WC, Bogart V, Gibson E, Copper SL (1983) Structure-property relationships in polycaprolactone-polyurethanes. *J Polym Sci Polym Phys Ed* 21:65
85. Hepburn C (1993) *Polymer elastomer*. Elsevier Applied Science, London/New York
86. Wang Z, Pinnavia TJ (1998) Nanolayer reinforcement of elastomeric polyurethane. *Chem Mater* 10:3769
87. Ohki T, Ni QQ, Ohsako N, Iwamoto M (2004) Mechanical and shape memory behavior of composites with shape memory polymer. *Compos Part A Appl Sci Manufac* 35:1065
88. Li F, Qi L, Yang J, Xu M, Luo X, Ma D (2000) Polyurethane/conducting carbon black composites: Structure, electric conductivity, strain recovery behavior, and their relationships. *J Appl Polym Sci* 75:68
89. Cho JW, Lee SH (2004) Influence of silica on shape memory effect and mechanical properties of polyurethane-silica hybrids. *Eur Polym J* 40:1343
90. Mondal S, Hu JL (2006) Shape memory studies of functionalized MWNT-reinforced polyurethane Copolymers. *Iran Polym J* 15:135
91. Koerner H, Price G, Nathan A, Alexander M, Vaia RA (2004) Remotely actuated polymer nanocomposites-stress-recovery of carbon nanotube-filled thermoplastic elastomers. *Nat Mater* 3:115

92. Cho JW, Kim JW, Jung YC, Goo NS (2005) Electroactive shape-memory polyurethane composites incorporating carbon nanotubes. *Macro Rapid Commun* 26:412
93. Paik IH, Goo NS, Jung YC, Cho JW (2006) Development and application of conducting shape memory polyurethane actuators. *Smart Mater Struct* 15:1476
94. Meng Q, Hu J, Zhu Y (2007) Shape-memory polyurethane/multiwalled carbon nanotube fibers. *J Appl Polym Sci* 106:837
95. Kuan HC, Ma CCM, Chang WP, Yuen SM, Wu HH, Lee TM (2005) Synthesis, thermal, mechanical and rheological properties of multiwall carbon nanotube/waterborne polyurethane nanocomposite. *Compos Sci Technol* 65:1703
96. Xia H, Song M, Jin J, Chen L (2006) Poly(propylene glycol)-grafted multiwalled carbon nanotube polyurethane. *Macromol Chem Phys* 207:1945
97. Wang TL, Tseng CG (2007) Polymeric carbon nanocomposites from multiwalled carbon nanotubes functionalized with segmented polyurethane. *J Appl Polym Sci* 105:1642
98. McClory C, McNally T, Brennan GP, Erskine J (2007) Thermosetting polyurethane multiwalled carbon nanotube composites. *J Appl Polym Sci* 105:1003

Electrical Conductivity and Morphology of Polyamide6/Acrylonitrile-Butadiene-Styrene Copolymer Blends with Multiwall Carbon Nanotubes: A Case Study

Suryasarathi Bose, Arup R. Bhattacharyya, Rupesh A. Khare, and Ajit R. Kulkarni

Contents

1	Introduction	124
2	Experimental Section	125
2.1	Materials and Sample Preparation	125
2.2	Characterization	126
3	Results and Discussion	127
3.1	Variation in Mixing Time and Screw Speed: Effect on Bulk Electrical Conductivity	127
3.2	Matrix-Dependent Electrical Percolation Threshold	128
3.3	Electrical Conductivity and Phase Morphology of PA6/ABS Blends with MWNTs	130
3.4	Electrical Conductivity and Phase Morphology of PA6/ABS Blends with MWNTs: Influence of Specific Interaction	134
4	Conclusions	139
	References	140

S. Bose (✉)

Department of Metallurgical Engineering and Materials Science, Indian Institute of Technology Bombay, Powai, Mumbai, India

Department of Materials Engineering, Indian Institute of Science, Bangalore, India

e-mail: sbose@materials.iisc.ernet.in; bose154@gmail.com

A.R. Bhattacharyya (✉) • A.R. Kulkarni

Department of Metallurgical Engineering and Materials Science, Indian Institute of Technology Bombay, Powai, Mumbai, India

e-mail: arupranjan@iitb.ac.in; ajit.kulkarni@iitb.ac.in

R.A. Khare

Department of Metallurgical Engineering and Materials Science, Indian Institute of Technology Bombay, Powai, Mumbai, India

Reliance Technology Centre, Reliance Industries Limited, Patalganga, Mumbai, India

e-mail: Rupesh.Khare@ril.com

Abstract

The effect of multiwall carbon nanotubes (MWNTs) on the bulk electrical conductivity and phase morphology of melt-mixed blends of polyamide 6 (PA6)/acrylonitrile-butadiene-styrene copolymer (ABS) has been investigated in this work. The bulk electrical conductivity of the blends with MWNTs was strongly dependent on the selective localization of MWNTs in the PA6 phase of the blends. Further, the selective localization of MWNTs in the PA6 phase led to a significant change in the phase morphology. The dual phase continuity was broader over a much larger composition range in the presence of MWNTs. In order to facilitate 3D “network-like” structure of MWNTs in the blends, a unique reactive modifier has been utilized. Significant changes in both bulk electrical conductivity and phase morphology have been found in the presence of modified MWNTs in the blends. An attempt has been made to understand the varying electrical conductivity in these blends through the alteration of phase morphology along with “aggregated” versus “uniform” dispersion of MWNTs in unmodified and modified MWNTs-based blends.

Keywords

PA6/ABS blends • MWNTs • Phase morphology • Electrical conductivity

1 Introduction

In order to replace the conventional filler like carbon black, carbon nanotubes (CNTs) have been exploited in the recent years in the scientific as well as in the industrial community to develop CNTs-based conducting polymer composites. In this context, a majority of the research work is focused towards understanding the 3D “network-like” structure involving CNTs in a polymer matrix leading to electrical percolation. Even if homogeneous dispersion and subsequent “network-like” structure formation of CNTs preferably at low CNTs content depends primarily on overcoming high inter-tube van der Waals forces of interactions, it also depends on the type of polymer matrix. This is associated with the surface free energy differences between CNTs and the respective polymer matrix, and if favorable, one can even observe the wetting of polymer matrix on CNT’s surface, which can otherwise impede the geometrical contacts between the CNTs. Polymer blends with conducting filler have been recently realized as a prospective candidate for numerous potential applications like antistatic devices, EMI shielding materials, bipolar plates for PEM fuel cell and sensors, etc. [1–4]. The morphology of the blends developed during melt-blending is a key parameter behind designing conductive polymer blends with a very low level of conducting filler. Confining the conducting filler in any one of the phases or at the interface of a co-continuous polymer blends can reduce the electrical percolation threshold to a significant extent [5]. However, the localization of the conducting filler in a specific phase or at the interface of immiscible polymer blends typically depends on the melt-viscosity of the constituent phases, surface free energy differences between the

filler and the individual components, processing parameters adopted during mixing, extent of crystallinity of the phases, etc. [6, 7]. It is further envisaged that CNTs lead to stabilization of phase morphology and act as compatibilizers in binary immiscible polymer blends either manifesting in a drastic reduction in the domain size of the minor phase or exhibiting finer ligament size in the co-continuous morphology in the blends [8]. Further, the dual phase continuity has been observed to be extended over a much larger composition range in the presence of the filler in binary immiscible blends [7]. These observations have been related to either changes in the interfacial tension of the blends or change in the melt-viscosity ratio in the presence of the filler. Earlier, we have noticed the effect of various multiwall carbon nanotubes (MWNTs; $\sim\text{NH}_2$ functionalized MWNTs, purified MWNTs) on the electrical percolation threshold in 50/50 (wt/wt) polyamide 6/acrylonitrile-butadiene-styrene copolymer (PA6/ABS) blends [9–11]. In order to facilitate debundling and subsequent formation of the 3D “network-like” structure of MWNTs, a unique reactive modifier (sodium salt of 6-amino hexanoic acid, Na-AHA) has been developed in our laboratory [12]. Further, the influence of Na-AHA-modified MWNTs on the bulk electrical conductivity of the 50/50 (wt/wt) PA6/ABS blends has been investigated in detail [10].

The objective of this work is to systematically study various parameters (viz., screw speed and mixing time) that affect the final state of dispersion of MWNTs during melt-mixing on the bulk electrical conductivity of PA6/ABS blends. Further, the influence of MWNTs on the dual phase continuity has been investigated. The observed changes in the phase morphology of the blends on varying the ABS content from 20 to 80 wt% were correlated with the bulk electrical conductivity in the blends. The influence of Na-AHA-modified MWNTs on the phase morphology and the electrical conductivity of the blends have also been investigated and have been compared with the phase morphology of the blends in the presence of unmodified MWNTs.

2 Experimental Section

2.1 Materials and Sample Preparation

CCVD synthesized thin purified MWNTs were obtained from Nanocyl SA Belgium (NC 3100, L/D 100–1000, purity >95 %). Acrylonitrile-butadiene-styrene copolymer (ABS) (Absolac-120, with typical composition consisting of acrylonitrile (24 wt%), rubber (16.5 wt%), and styrene (59.5 wt%)) was procured from Bayer India Ltd. Polyamide 6 (PA6) with a zero shear viscosity of 180 Pa.s at 260 °C was obtained from GSFC, Gujarat, India (Gujlon M28RC, relative viscosity 2.8, M_v is 38642 in 85 % formic acid). Neat blends of PA6/ABS and blends with MWNTs were melt-mixed in a conical twin-screw microcompounder (Micro 5, DSM Research, Netherlands) at 260 °C with a rotational speed of 150 rpm for 15 min. All the experiments were performed under nitrogen atmosphere in order to prevent oxidative degradation. 6-aminohexanoic acid (AHA) (Sigma Aldrich, $M_w = 132.18$; purity, 98 %) was neutralized using sodium hydroxide to obtain sodium

Table 6.1 Sample codes with their composition of 50/50 PA6/ABS blends with MWNTs and 50/50 PA6/ABS blends with Na-AHA-modified MWNT

Sample	Codes
Polyamide 6	PA6
Acrylonitrile-butadiene-styrene	ABS
Thin purified MWNT	T
50/50 blends of PA6 and ABS	N50A50
[PA6 + T (5 wt%)] followed by ABS	N50T5A50
x/y blends of PA6 and ABS + 3 wt% Na-AHA-modified MWNTs (modified in the wt. ratio of 1:1, Na-AHA:MWNTs)	(1:1), 3 wt%
x/y blends of PA6 and ABS + 0.5 wt% Na-AHA-modified MWNTs (modified in the wt. ratio of 1:15, Na-AHA:MWNTs)	(1:15), 0.5 wt%

salt of AHA (Na-AHA). The detailed procedure to obtain Na-AHA and the solid mixtures of MWNT and Na-AHA is described elsewhere [12]. The blend compositions with their sample codes are listed in Table 6.1. Injection-molded samples (according to ASTM D 638, Type V, thickness, 3 mm; gauge length, 6.2 mm; width, 10 mm) were prepared using a mini injection-molding machine.

2.2 Characterization

The AC electrical conductivity measurements were performed on the injection-molded samples (across the thickness ~ 3 mm) in the frequency range between 10^{-2} and 10^7 Hz using alpha high-resolution analyzer coupled with Novocontrol interface (broadband dielectric converter). The DC electrical conductivity of the samples was determined from the AC conductivity plots in the region of low-frequency plateau by fitting the power law equation ($\sigma_{AC} = \sigma_{DC} + A\omega^n$, $0 < n < 1$), which is in consistent with Jonscher's "universal power law" for solids [13]. The state of dispersion and preferential localization of MWNTs was evaluated through the scanning electron microscopic analysis (SEM). The extruded strands were cryofractured using liquid nitrogen and etched with formic acid for 24 h at room temperature to remove PA6 phase of the blends. Cryofractured strands were also etched with boiling tetrahydrofuran (THF) to remove the ABS phase. The etched samples were observed under SEM using Hitachi S3400N. The continuity of the ABS phase (% continuity) in PA6/ABS blends was determined by a selective extraction technique. For the blend system used, ABS can be extracted using THF, which does not dissolve, swell, or penetrate the PA6 phase. Extruded strands of 2 cm length were kept in THF at room temperature for 4 days, to remove the ABS phase from the blends. Samples were washed with fresh solvent after 24 h and were kept in the fresh solvent. At the end of the 4th day, samples were removed and dried in the vacuum oven. The continuity of the ABS phase (% continuity) was calculated by taking the ratio of weight difference before and after the selective extraction process and the initial weight of the ABS portion in the blends.

3 Results and Discussion

3.1 Variation in Mixing Time and Screw Speed: Effect on Bulk Electrical Conductivity

The state of dispersion of MWNTs in the polymer matrix processed by melt-mixing technique is reported to be dependent on the mixing energy input during melt-mixing in a microcompounder [14]. The later factor is dependent on the screw speed, mixing time, etc., employed during processing. Hence, it is necessary to optimize the processing conditions and quantify, which again varies with the type of polymer and the type of internal mixers employed. Additional complexity arises in binary blends where mixing protocols (sequential or two-step mixing) influence the final state of dispersion of the filler in the composites. In a typical two-step mixing, the filler is initially mixed with polymer A for a specified time (step 1) followed by the addition of polymer B (step 2) without interrupting the mixing process in an internal mixer (like the one employed here). In a two-step mixing in an internal mixer, the torque recorded during mixing varies with time and depends on the amount of material fed in and varies substantially for both the steps of mixing. To address these issues, the processing parameters (viz., the screw speed and mixing time) during melt-mixing have been varied to get insight into the factors that affect the final state of dispersion of MWNTs in the PA6/ABS blends. In the present context, the two-step mixing protocol has been adopted to disperse MWNTs in PA6/ABS blends for a specific set of blends with 5 wt% of MWNTs. In a typical mixing protocol, MWNTs (5 wt%) were initially mixed with PA6 (step 1) followed by the addition of ABS phase (step 2). Further, the screw speed has been varied (from 50 to 200 rpm) for a fixed mixing time (15 min), and later, the mixing time has been varied (10–20 min) for a fixed screw speed (150 rpm) for this particular set of batch. It is necessary to note that the melt-mixing temperature was kept fixed at 260 °C for all these sets of blends. It has been reported that higher melt-mixing temperature favors the state of dispersion of MWNTs due to the infiltration of polymer chains in the MWNT aggregates [15]. In order to assess the state of dispersion of MWNTs in the blends and to optimize the processing conditions, AC electrical conductivity measurements have been carried out. The main objective of this work is to develop conducting composites involving a PA6/ABS/MWNTs multicomponent system, and hence, the optimization has been carried out in that direction.

Figure 6.1a shows the variation in AC electrical conductivity as a function of frequency for 50/50 (wt/wt) PA6/ABS blends with MWNTs (5 wt%) prepared with varying the screw speed from 50 to 200 rpm at a fixed mixing time (15 min). It is evident from Fig. 6.1a that a certain mixing energy input (in terms of screw speed) is required to disentangle the primary agglomerates and subsequently disperse them in the polymer. This is manifested in a higher electrical conductivity (\sim five orders of magnitude higher) in blends with either 150 or 200 rpm as compared to blends prepared employing a lower screw speed (50 rpm). It is further observed that blends prepared by using a screw speed of 100 rpm exhibited a DC electrical conductivity of $\sim 1\text{E-}7$ S/cm, which is one order less as compared to blends prepared by using either 150 or 200 rpm.

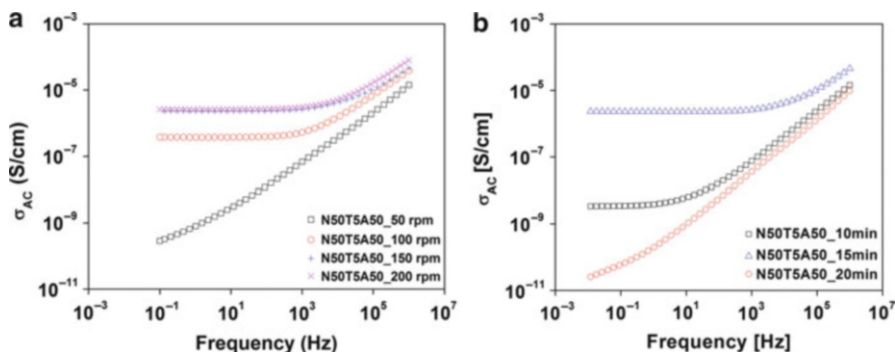


Fig. 6.1 Effect of (a) screw speed; (b) mixing time on the bulk electrical conductivity of PA6/ABS blends with MWNTs

Figure 6.1b shows the variation of AC electrical conductivity for the blends (PA6/ABS blends with 5 wt% MWNTs), which have been prepared by varying mixing time (10, 15, and 20 min) at a fixed screw speed of 150 rpm. Interestingly, the DC electrical conductivity of the blends with MWNTs with 15 min of mixing shows four orders of magnitude higher than the blends mixed for 10 min and five orders of magnitude higher than the blends mixed for 20 min. It is clear that in the case of blends with MWNTs mixed at a screw speed of 150 rpm, the mixing time plays an important role in the final state of dispersion of MWNTs. This is manifested in the AC electrical conductivity measurements of these sets of blends, where the blends show nearly insulating behavior when mixed for 20 min at a fixed screw speed of 150 rpm or mixed for 15 min at a screw speed of 200 rpm indicating the possibility of MWNTs breakage as the mixing energy is dependent both on the screw speed and the time of mixing. It is well reported in the literature that high shear rates in an internal mixer damage the nanotubes (lower the aspect ratio) but at the same time result in better dispersion. From the above discussion, an optimum screw speed of 150 rpm and a mixing time of 15 min have been fixed for further composites studied in this work.

Next to the processing parameters employed during melt-mixing, the percolation threshold of MWNTs depends strongly on the nature of the polymer matrix. To address these issues, we have checked the percolation threshold of MWNTs in the individual components, i.e., PA6 and ABS, keeping the same processing conditions as optimized earlier, which are discussed in the subsequent section.

3.2 Matrix-Dependent Electrical Percolation Threshold

Figure 6.2a–b shows the variation in AC electrical conductivity as a function of frequency for ABS/MWNTs and PA6/MWNTs composites, respectively. The bulk electrical conductivity of pure PA6 increases with an increase in frequency, as expected for an insulating material, with a value about $\sim 1\text{E-}13 \text{ S cm}^{-1}$ at 0.01 Hz.

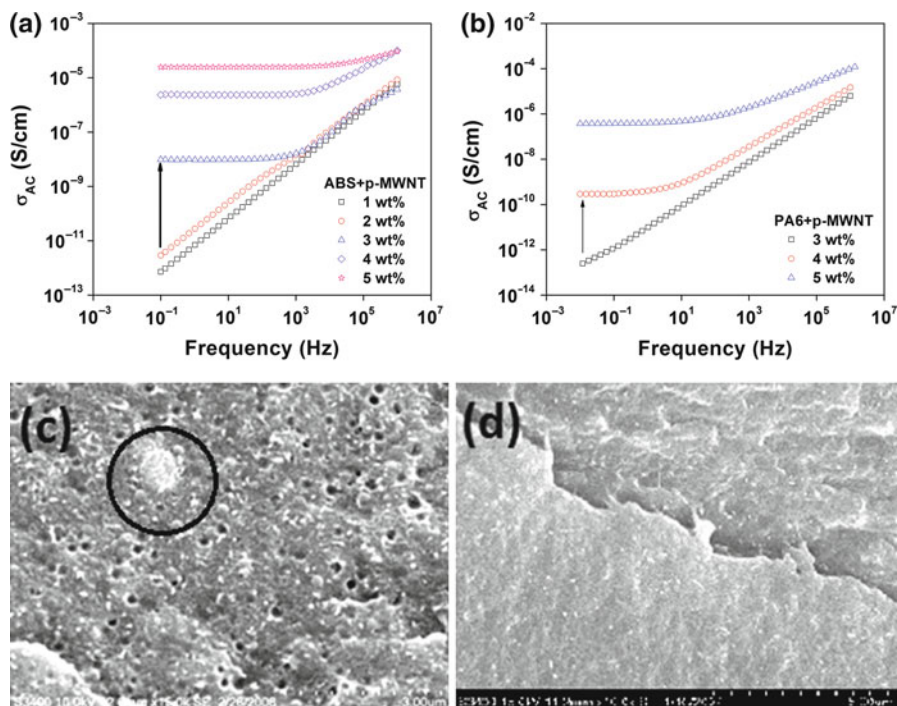


Fig. 6.2 Percolation threshold of MWNTs in (a) ABS; (b) PA6; SEM of (c) ABS + 3 wt% MWNTs; (d) PA6 + 3 wt% MWNTs

It is to be noted that the extent of percolation threshold is strongly dependent on the surface tension of the individual blend components, polarity, crystallinity, melt-viscosity of the constituent components, surface affinity, specific interaction, etc., which further manifests in a varying extent of percolation threshold in the composites. It has been found that the percolation threshold of MWNTs on the account of the various factors mentioned above led to a different degree of percolation threshold in both PA6/MWNTs ($\sim 3\text{--}4$ wt%) and ABS/MWNTs ($\sim 2\text{--}3$ wt%) composites.

The geometrical connectivity of the filler (i.e., filler-filler interaction) is a prerequisite factor in obtaining conducting composites at a desired concentration of the filler. However, good matrix-filler interaction impedes the geometrical contacts between the filler and results in higher percolation threshold in the system. It has been reported earlier that MWNTs have different affinities towards the SAN and polybutadiene (PB) phases in ABS copolymer. In the present context, MWNTs establish a different degree of interactions with either SAN or PB phase resulting in the segregation of MWNTs in the vicinity of that specific phase. This is well evident from the SEM micrographs, where one can find smaller aggregated domains of MWNTs existing in the matrix (see Fig. 6.2c). MWNTs are also found to be distributed in other parts of the matrix. This observation can be well correlated

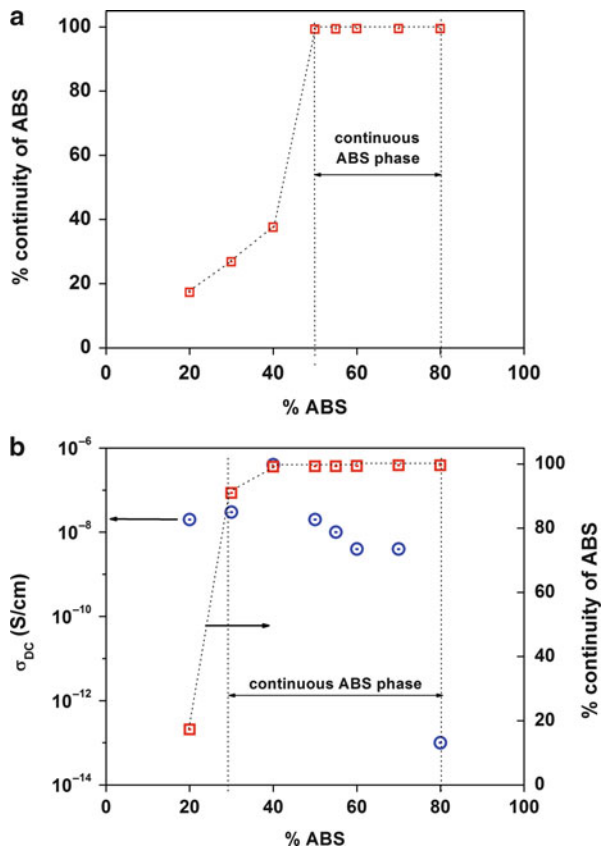
with the observed changes in the electrical conductivity in ABS where higher percolation threshold is found as compared to theoretically predicted values. On the other hand, PA6 phase wets MWNTs well, which is in consistent with the thermodynamic consideration. This would result in an improved matrix-filler interaction manifesting in the higher electrical percolation threshold in PA6 matrix. This observation is supported by the state of dispersion of MWNTs observed from the SEM micrographs, where the MWNTs are found to be relatively well dispersed in the PA6 matrix (see Fig. 6.2d).

3.3 Electrical Conductivity and Phase Morphology of PA6/ABS Blends with MWNTs

In order to investigate the influence of MWNTs on the morphology and electrical conductivity in PA6/ABS blends, a range of blend compositions (varying the ABS content from 20 to 80 wt%) at a fixed MWNTs content (4 wt%) have been prepared. The concentration of MWNTs chosen here is just above the percolation threshold. This concentration of MWNTs has been chosen based on our previous studies, which deal in detail with the bulk electrical conductivity in 50/50 (wt/wt) PA6/ABS blends with MWNTs [11]. The percolation threshold of MWNTs in the 50/50 (wt/wt) PA6/ABS blends has been found to be $\sim 3\text{--}4$ wt% of MWNTs.

The morphology of the PA6/ABS blends has been investigated by SEM, and the % continuity of ABS phase in the blends has been analyzed by the selective extraction technique. The continuity of ABS phase has been calculated by taking the ratio of the ABS phase before and after selective extraction in THF from the respective blend composition and is shown in Fig. 6.3. The continuity values of the ABS phase (%) further indicate that PA6/ABS blends exhibit a matrix-dispersed droplet type morphology up to 40 wt% ABS above which the blends exhibit a continuous ABS phase. Figure 6.4 shows the SEM micrographs of the blends studied here. PA6/ABS blends up to 40 wt% ABS show a matrix-dispersed droplet type of morphology wherein etched out ABS domains are observed in the continuous PA6 matrix (Fig. 6.4). 50/50 (wt/wt) and 40/60 (wt/wt) PA6/ABS blends show co-continuous and sea-island type of morphology respectively whereas, other compositions represent PA6 domains in a continuous ABS matrix (see Fig. 6.4). Interestingly, significant changes in the blends morphology have been observed in the presence of MWNTs. For example, a significant reduction in the droplet size of the ABS phase has been observed in 80/20 (wt/wt) PA6/ABS blends in the presence of MWNTs. This observation is consistent with increasing MWNTs content in 80/20 (wt/wt) PA6/ABS blends (figures not shown here). Such a reduction in droplet size of the dispersed phase has also been earlier observed in the presence of MWNTs in PP/ABS blends and was explained on the basis of a kinetic barrier provided by MWNTs, which further led to suppression of coalescence [8]. Further, the composition range, in which the dual phase continuity is observed, is shifted towards lower ABS percentages (i.e., in the range of 30–80 wt% ABS) in the presence of MWNTs. The selective localization of 4 wt% MWNTs in the PA6

Fig. 6.3 (a) % continuity of ABS in neat PA6/ABS blends; (b) comparing the DC electrical conductivity and % continuity of ABS as a function of ABS content in the blend with MWNTs



phase is responsible for the extension of the dual phase morphology over a remarkably broader composition range. This is well supported by the SEM micrographs of the blends with MWNTs (see Fig. 6.4). PA6/ABS blends above 30 wt% ABS (and up to 70 wt%) show a co-continuous morphology in the presence of MWNTs. Such changes in phase morphology manifest the fact that MWNTs act as a suitable compatibilizer for PA6/ABS blends. This observation has been found to be consistent with increasing content of MWNTs in 50/50 (wt/wt) PA6/ABS blends where significant refinement in the microstructure has been observed earlier [9]. Further, higher magnification SEM micrographs of the blends show that MWNTs are selectively localized in the PA6 phase (see Fig. 6.5). It is worth mentioning at this point that the selective localization of MWNTs in the PA6 phase is favored both thermodynamically (considering the surface free energy difference between PA6 and MWNTs) and also considering the melt-viscosity factor. Therefore, selective localization of MWNTs is more likely to increase the melt-viscosity of the PA6 phase and perturbs the kinetics of phase coalescence. This may presumably have resulted in broader dual phase continuity in the blends. The observed changes in phase morphology of the blends in the presence of

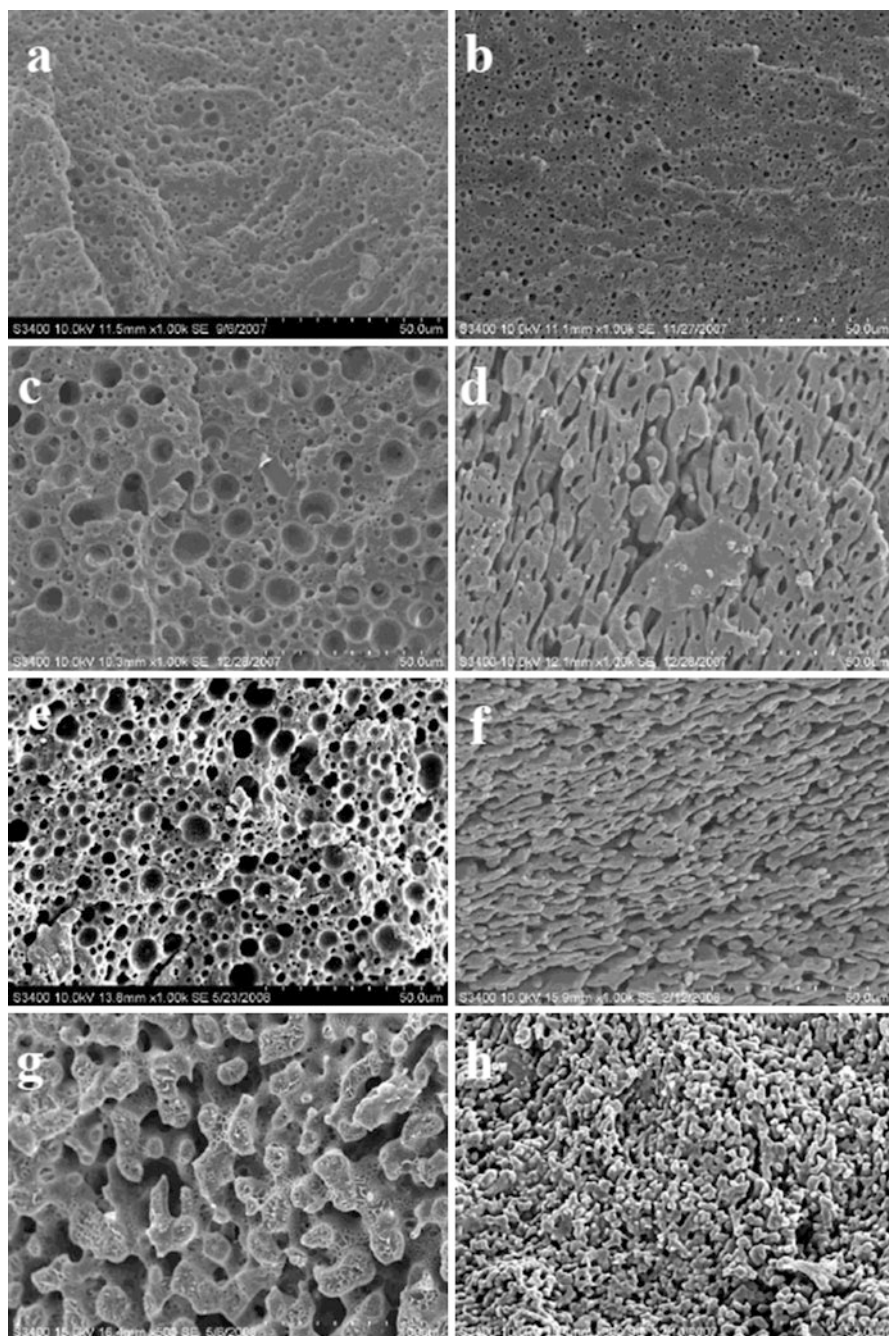


Fig. 6.4 (continued)

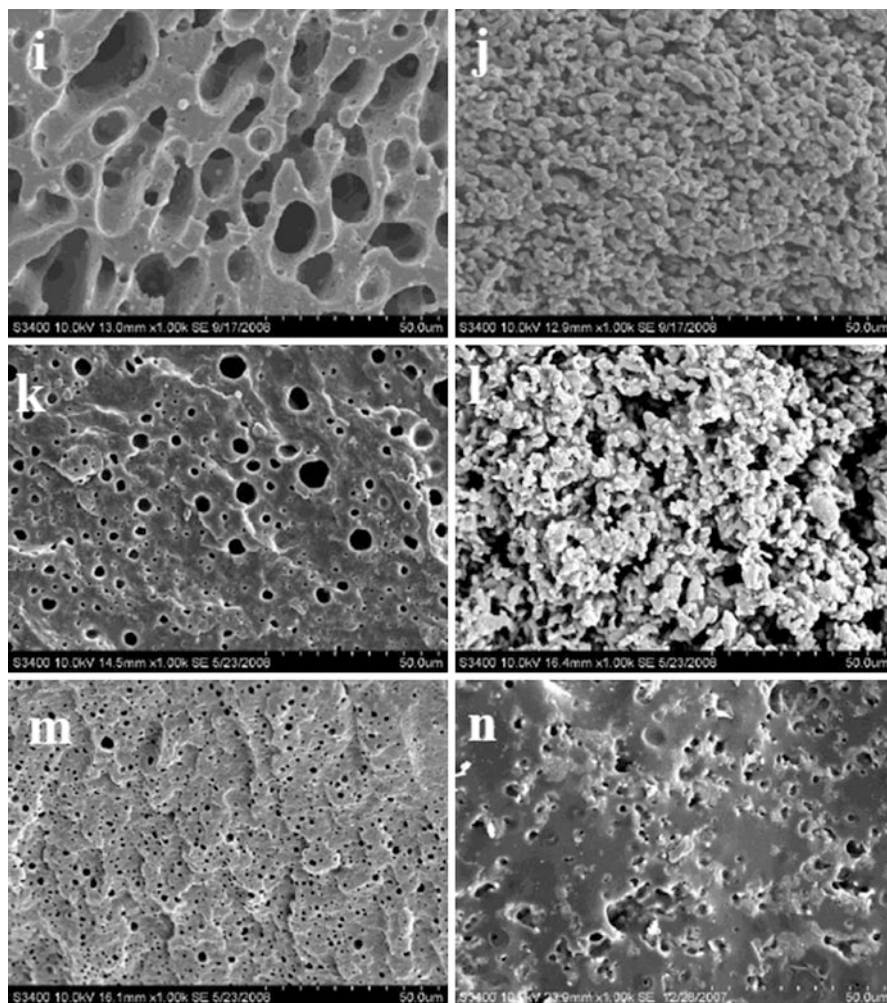


Fig. 6.4 SEM micrographs of PA6/ABS blends (a) 80/20; (b) 80/20 with 4 wt% MWNTs; (c) 70/30; (d) 70/30 with 4 wt% MWNTs; (e) 60/40; (f) 60/40 with 4 wt% MWNTs; (g) 50/50; (h) 50/50 with 4 wt% MWNTs; (i) 40/60; (j) 40/60 with 4 wt% MWNTs; (k) 30/70; (l) 30/70 with 4 wt% MWNTs; (m) 20/80; (n) 20/80 with 4 wt% MWNTs

MWNTs can be well correlated with the observation in AC electrical conductivity measurements, where the conductivity values almost remain comparable (within one order of magnitude) in the continuous ABS range except for 20/80 (wt/wt) PA6/ABS blends (see Fig. 6.4n). The 20/80 (wt/wt) PA6/ABS blend shows insulating behavior, which is mainly related to non-interconnectivity of MWNTs as the MWNTs are dispersed and localized in the PA6 domains. This observation is further supported by the SEM micrograph where one could observe entangled MWNTs mass in the etched PA6 droplets (see Fig. 6.5).

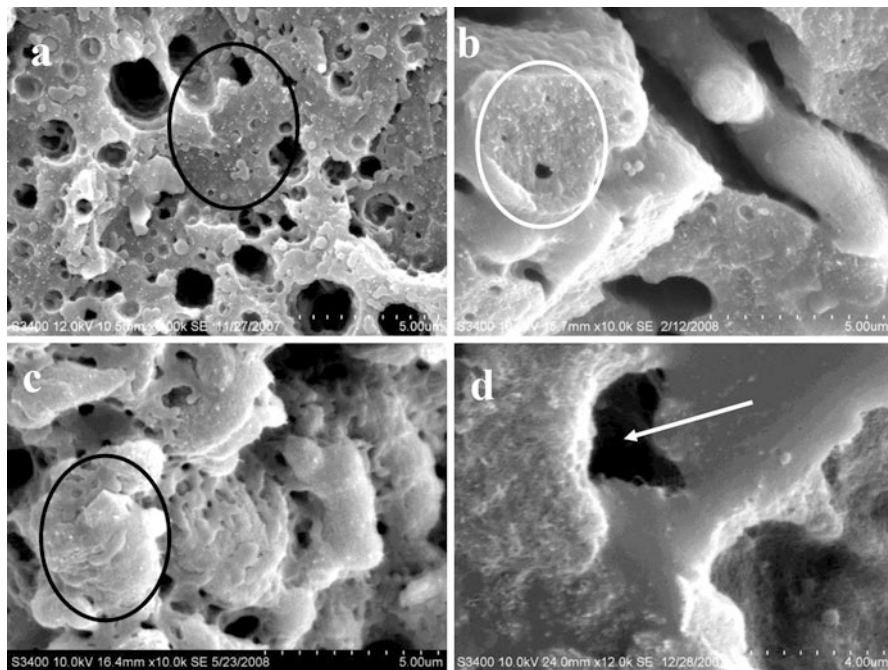
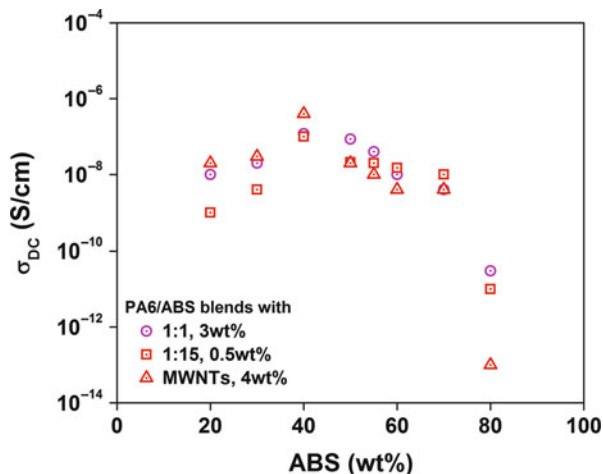


Fig. 6.5 Higher magnification SEM micrographs of PA6/ABS blends with MWNTs (a) 80/20; (b) 60/40; (c) 40/60; (d) 20/80

3.4 Electrical Conductivity and Phase Morphology of PA6/ABS Blends with MWNTs: Influence of Specific Interaction

It is well reported in the literature that overcoming the primary agglomerates of MWNTs is a challenge due to inter-tube van der Waals forces of interactions and entanglements between nanotubes. A generic approach utilizing specific interactions along with melt-interfacial reactions has been adopted to overcome the strong inter-tube van der Waals forces and facilitate uniform dispersion of MWNTs in the blends. Moreover, this strategy retains the “network-like” structure of MWNTs in the final composites. This has been achieved by utilizing a reactive modifier, viz., sodium salt of 6-amino hexanoic acid (Na-AHA), which has been developed in our laboratory. In a typical recipe, solid mixtures of Na-AHA and MWNTs (of different ratio) were prepared and have been added to PA6/ABS blends using the same protocol of mixing as described earlier. In an earlier study, we have observed a significant improvement in the bulk electrical conductivity in 50/50 (wt/wt) PA6/ABS blends in the presence of Na-AHA-modified MWNTs [11]. Further, a significant refinement in the “network-like” structure of MWNTs has been observed on varying the ratio of Na-AHA to MWNTs, and the percolation threshold has been observed to be ~ 0.25 wt% MWNTs, where the ratio of MWNTs to

Fig. 6.6 Comparing the DC conductivity as a function of ABS content in the blends with Na-AHA-modified MWNTs



Na-AHA was 1:15. In this work we have extended this strategy to further investigate the role of Na-AHA-modified MWNTs on the morphology and bulk electrical conductivity of PA6/ABS blends in the entire composition range (20–80 wt% ABS). Further, the observed changes in morphology and the bulk electrical conductivity of PA6/ABS blends in the presence of Na-AHA-modified MWNTs have been compared with blends with purified MWNTs. For comparison purpose, two sets of blends have been compared for each composition to investigate the changes in phase morphology on the incorporation of Na-AHA-modified MWNTs. It is worth pointing out at this stage that the concentrations of Na-AHA-modified MWNTs have been so chosen that it is just above the percolation threshold. In these sets of blends, the ratio of Na-AHA to MWNTs has been fixed at 1:1 and 1:15 for a fixed concentration of MWNTs, i.e., 3 and 0.5 wt%, respectively.

Figure 6.6 shows the variation in DC electrical conductivity in the entire range of compositions of PA6/ABS blends in the presence of Na-AHA-modified MWNTs. The DC electrical conductivity in PA6/ABS blends with purified MWNTs has also been plotted in the same graph for comparison purpose. It is evident that the DC electrical conductivity values of blends with either 1:1, 3 wt% MWNTs, or 1:15, 0.5 wt% MWNTs, are comparable with the DC conductivity values of blends with 4 wt% MWNTs, manifesting the fact that Na-AHA has led to significant refinement in the “network-like” structure of MWNTs. This has resulted in substantial changes in the percolation threshold of MWNTs in the blends in the presence of Na-AHA. Interestingly, the variations in DC electrical conductivity are similar to that of blends with purified MWNTs with a maximum for 60/40 (wt/wt) PA6/ABS blends. In addition, the DC electrical conductivity of blends with Na-AHA-modified MWNTs is almost similar in the co-continuous region. In view of the selective localization of MWNTs in the dispersed domain of PA6, the 20/80 (wt/wt) blend shows insulating behavior as the interconnectivity of MWNTs is lost. Similar observations were found in blends with purified MWNTs.

The phase morphology of these sets of blends will provide more insight into the state of dispersion of MWNTs in the PA6/ABS blends. Figure 6.7 shows the SEM micrographs of the blends with Na-AHA-modified MWNTs in the entire composition range (20–80 wt% ABS). Interestingly, we have observed coalescence in 80/20 (wt/wt) PA6/ABS blends in the presence of Na-AHA-modified MWNTs. It should be pointed out at this stage that we have also observed a significant reduction in the droplet size in 80/20 (wt/wt) PA6/ABS blends in the presence of purified MWNTs. In this context, suppression of coalescence in the presence of solid fillers can be explained on the basis of either change in the free energy of mixing or change in the viscosity ratio. Lipatov [16] correlated such phenomenon in immiscible polymer blends with a decrease in the free energy of mixing in the presence of solid inorganic filler. In the presence of the filler (S), the free energy of mixing of blend components (A and B) is given by

$$\Delta G_m = \Delta G_{AS} + \Delta G_{BS} - \Delta G_{AB} \quad (6.1)$$

where the negative value of ΔG_m indicates a thermodynamically stable system. The addition of “ S ” thus stabilizes the morphology by adsorption of polymers on their surface. Such adsorption will be favored by fillers with a large surface area per unit weight, viz., nanoclay, CNTs, etc. [17]. Further, it is reported that such an adsorption of polymers on the filler surface will be plausible when the surface free energies of polymer and fillers are comparable. It can be commented that MWNTs are presumably acting as a kinetic barrier between the adjacent droplets suppressing the coalescence process. Invariably, such changes in the morphology of blends have direct impact on the interfacial tension through the correlation [18]:

$$F(\eta_d/\eta_m) = \eta_m G d / \gamma \quad (6.2)$$

where η_d and η_m are the melt viscosities of dispersed and matrix phase, respectively, G is the shear rate, and γ is the interfacial tension. Thus, when all other parameters are the same, the matrix phase viscosity (η_m) will be inversely proportional to the droplet size (d). The observed coalescence can be explained by this relation. It is worth pointing out at this stage that we have observed a significant drop in melt-viscosity in the composites with increasing concentration of Na-AHA in 50/50 (wt/wt) PA6/ABS blends [11]. This observation has been further supported by decreased torque values recorded during the melt-mixing of these composites. Such phenomenon has also been observed in PA6/Na-AHA composites. The reduction in matrix phase viscosity has led to the coalescence of droplets in the blends in the presence of Na-AHA and is consistent with increasing concentration of Na-AHA. Such coalescence phenomenon has been observed in other compositions as well.

The higher magnification SEM images of the blends with Na-AHA-modified MWNTs can be found from Fig. 6.8. One can find relatively well dispersed MWNTs in the PA6 phase of the blends. The level of exfoliation of MWNTs rendered by Na-AHA has led to a significant improvement in the bulk electrical

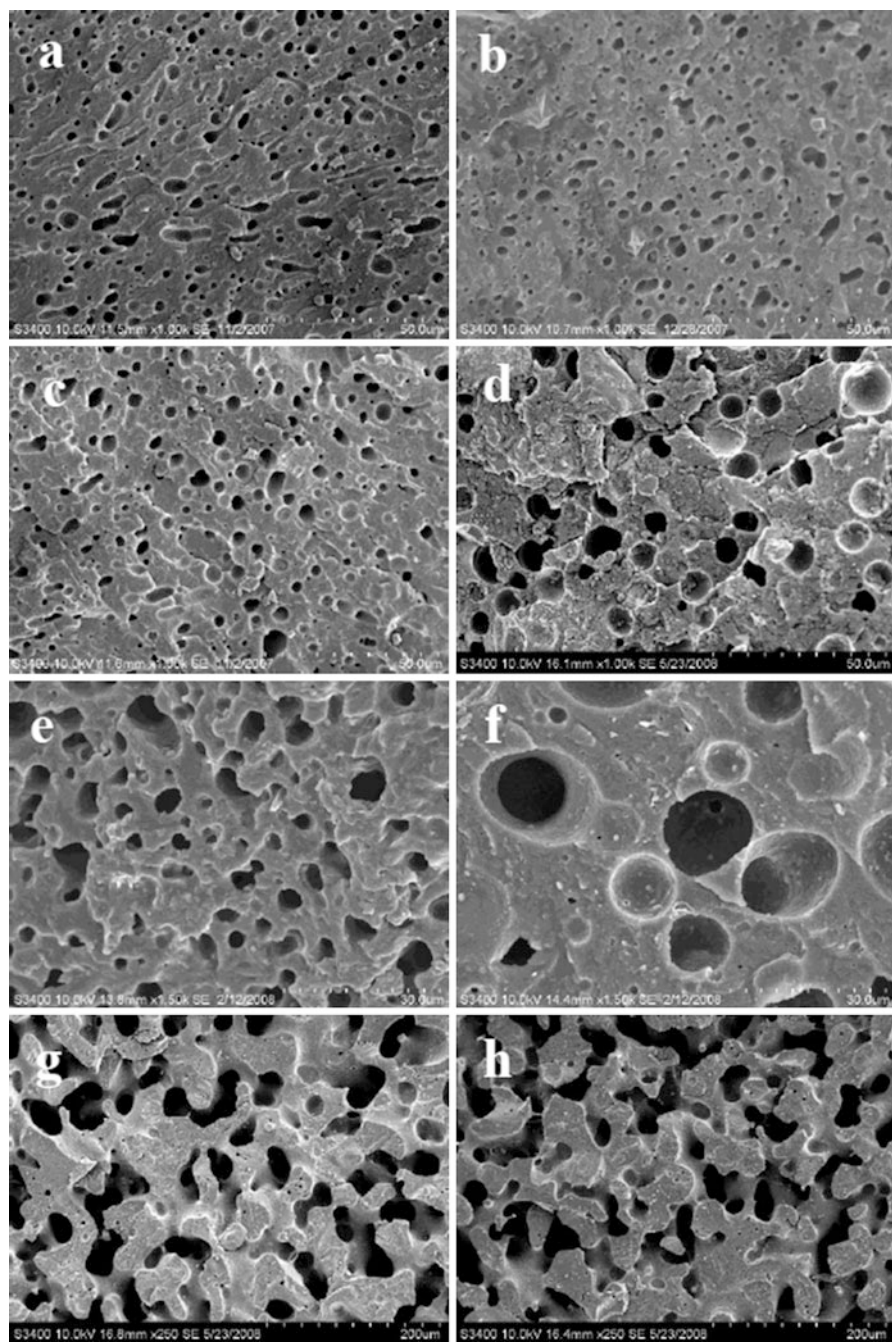


Fig. 6.7 (continued)

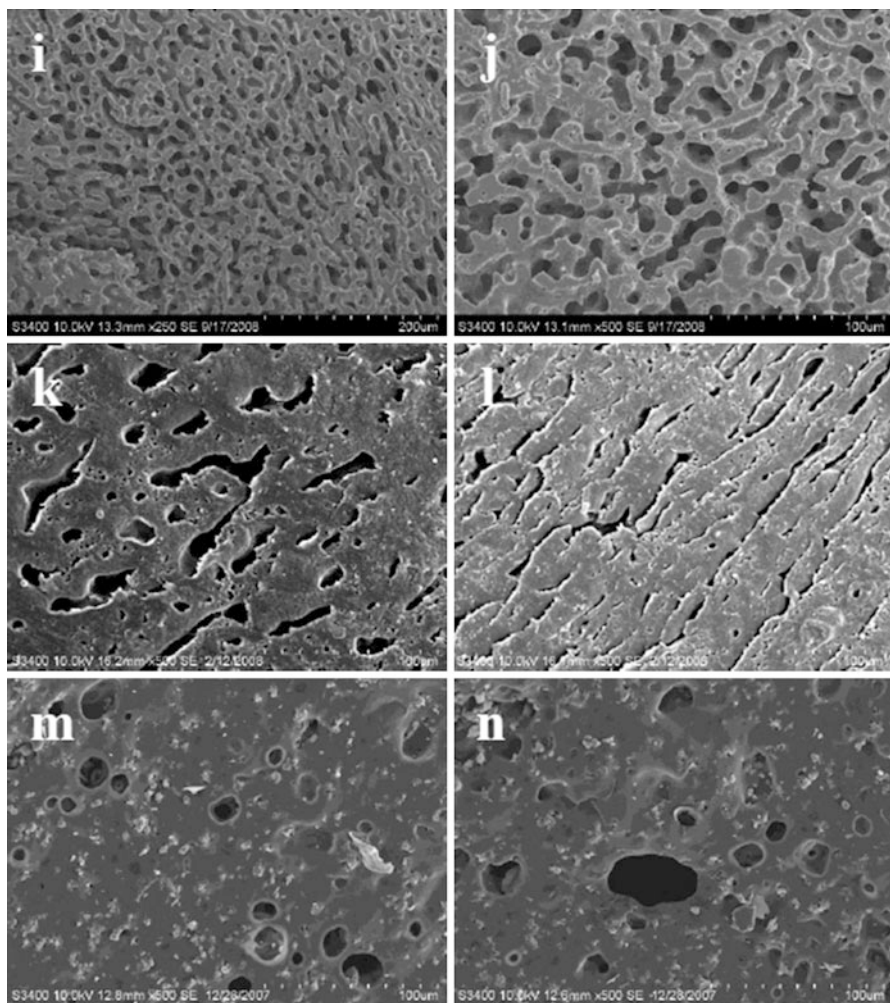


Fig. 6.7 SEM micrographs of PA6/ABS blends with Na-AHA-modified MWNTs (a) 80/20 (1:1, 3 wt%); (b) 80/20 (1:15, 0.5 wt%); (c) 70/30 (1:1, 3 wt%); (d) 70/30 (1:15, 0.5 wt%); (e) 60/40 (1:1, 3 wt%); (f) 60/40 (1:15, 0.5 wt%); (g) 50/50 (1:1, 3 wt%); (h) 50/50 (1:15, 0.5 wt%); (i) 40/60 (1:1, 3 wt%); (j) 40/60 (1:15, 0.5 wt%); (k) 30/70 (1:1, 3 wt%); (l) 30/70 (1:15, 0.5 wt%); (m) 20/80 (1:1, 3 wt%); (n) 20/80 (1:15, 0.5 wt%)

conductivity of the system. Moreover, the drop in the melt-viscosity of the PA6 phase has rendered fluidity and subsequent enhanced dispersion of MWNTs in the blends in the presence of Na-AHA [19]. This has led to an improvement in the bulk electrical conductivity in the blends in the presence of Na-AHA-modified MWNTs as compared to blends with purified MWNTs. Further, the drop in the melt-viscosity of the PA6 phase has led to significant changes in the phase morphology of the blends.

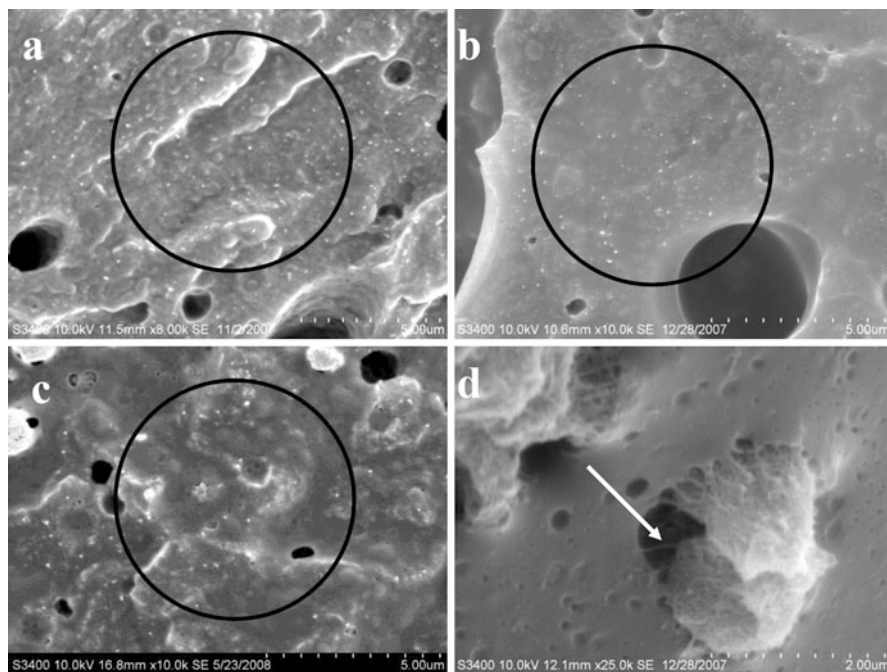


Fig. 6.8 Higher magnification SEM micrographs of PA6/ABS blends with Na-AHA-modified MWNTs (a) 80/20; (b) 40/60; (c) 60/40; (d) 20/80

4 Conclusions

The effect of multiwall carbon nanotubes (MWNTs) on the bulk electrical conductivity and phase morphology of melt-mixed blends of polyamide 6 (PA6)/acrylonitrile-butadiene-styrene copolymer (ABS) has been investigated. During melt-mixing, the processing parameters (viz., mixing time and rotational speed of the screw) were optimized on the basis of electrical conductivity values for PA6/ABS blends with MWNTs. The bulk electrical conductivity of the blends with MWNTs has been observed to be dependent on the selective localization of MWNTs in the PA6 phase of the blends. Moreover, the selective localization of MWNTs in the PA6 phase leads to a significant change in the phase morphology of the blends. The dual phase continuity has been found to be broader over a much larger composition range in the presence of MWNTs. In order to facilitate the 3D “network-like” structure of MWNTs in the blends, a unique reactive modifier has been utilized. Significant changes in both bulk electrical conductivity and phase morphology have been found in the presence of modified MWNTs in the blends.

Acknowledgments The authors duly acknowledge the financial support from the Department of Science & Technology (DST), India (Project No. 08DST016). The authors would also like to acknowledge “Microcompounder Central Facility” and SAIF IIT Bombay.

References

1. Colaneri NF, Shacklette LW (1992) *IEEE Trans Instrum Meas* 41:291
2. Narkis M, Lidor G, Vaxman A, Zuri L (2000) *IEEE Trans Electr Pack Manuf* 23:239
3. Srivastava S, Tchoudakov R, Narkis M (2000) *Polym Eng Sci* 40:1522
4. Wu M, Shaw LL (2005) *Int J Hydrog Energy* 30:373
5. Sumita M, Sakata K, Hayakawa Y, Asai S, Miyasaka K, Tanemura M (1992) *Colloid Polym Sci* 270:134
6. Sumita M, Sakata K, Asai S, Miyasaka K, Nakagawa H (1991) *Polym Bull* 25:265
7. Gubbels F, Blacher S, Vanlathem E, Jerome R, Deltour JR, Brouers OF, Teyssibt P (1996) *Macromolecules* 28:1559
8. Khare R, Bhattacharyya AR, Kulkarni AR, Saroop M, Biswas A (2008) *J Polym Sci B: Phys* 46:2286
9. Bose S, Bhattacharyya AR, Bondre A, Kulkarni AR, Pötschke P (2008) *J Polym Sci Phys* 46:1619
10. Bose S, Bhattacharyya AR, Kodgire PV, Kulkarni AR, Misra A (2008) *J Nanosci Nanotech* 8:1867
11. Bose S, Bhattacharyya AR, Kulkarni AR, Pötschke P (2008) *Compos Sci Technol* 69:365
12. Kodgire PV, Bhattacharyya AR, Bose S, Gupta N, Kulkarni AR, Misra A (2006) *Chem Phys Lett* 432:480
13. Jonscher AK (1977) *Nature* 267:673
14. Krause B, Pötschke P, Häußler L (2009) *Compos Sci Tech* 69:1505
15. Tambe PB, Bhattacharyya AR (2013) *J Appl Polym Sci* 127:1017
16. Liptov YS (2002) *Prog Polym Sci* 27:1721
17. Ray SS, Pouliot S, Bousmina M, Utracki LA (2004) *Polymer* 45:8403
18. Majumadar B, Keskkula H, Paul DR (1994) *Polymer* 35:1386
19. Gubbels F, Jérôme R, Vanlathem E, Deltour R, Blacher S, Brouers F (1998) *Chem Mater* 10:1227

Mechanical Behavior of Starch–Carbon Nanotubes Composites

7

Lucía M. Famá, Silvia Goyanes, Valeria Pettarin, and
Celina R. Bernal

Contents

1	Introduction	142
2	Starch	143
2.1	Gelatinization of Starch	146
2.2	Retrogradation of Starch	147
3	Mechanical Behavior of Starch	148
3.1	Quasi-Static Tensile Behavior	149
3.2	Dynamic Mechanical Properties	153
4	Carbon Nanotubes	155
5	Performance of Starch–Carbon Nanotubes Nanocomposites	157
5.1	Quasi-Static Tensile Behavior	158

L.M. Famá

Grupo de Materiales Avanzados, INTECIN (UBA–CONICET), Departamento de Ingeniería Mecánica, Facultad de Ingeniería, Universidad de Buenos Aires, Ciudad Autónoma de Buenos Aires, Argentina

LP&MC, Departamento de Física, Facultad de Ciencias Exactas y Naturales, IFIBA – CONICET, Universidad de Buenos Aires, Ciudad Autónoma de Buenos Aires, Argentina

e-mail: lfama@df.uba.ar

S. Goyanes

LP&MC, Departamento de Física, Facultad de Ciencias Exactas y Naturales, IFIBA – CONICET, Universidad de Buenos Aires, Ciudad Autónoma de Buenos Aires, Argentina

e-mail: goyanes@df.uba.ar

V. Pettarin

Grupo de Ciencia e Ingeniería de Polímeros, INTEMA (UNMdP-CONICET). Departamento de Ingeniería en Materiales, Universidad Nacional de Mar del Plata, Mar del Plata, Argentina

e-mail: vpettarin@hotmail.com

C.R. Bernal (✉)

Grupo de Materiales Avanzados, INTECIN (UBA–CONICET), Departamento de Ingeniería Mecánica, Facultad de Ingeniería, Universidad de Buenos Aires, Ciudad Autónoma de Buenos Aires, Argentina

e-mail: cbernal@fi.uba.ar

5.2 Dynamic Mechanical Behavior	160
5.3 Biaxial Impact Behavior	161
6 Concluding Remarks and Future Trends	164
References	165

Abstract

This chapter is focused on the mechanical behavior of plasticized starch-based nanocomposites reinforced with carbon nanotubes. It starts with a general introduction about the most important materials that involve those nanocomposites, such as starch and multiwalled carbon nanotubes. Then, a presentation of the most relevant published results on the mechanical properties of starch matrix and starch–carbon nanotubes composites is reported. Factors affecting these properties such as crystallinity, water content and plasticizers are discussed. The mechanical behavior of these composites is discussed in separate sections regarding tensile properties, impact behavior, and viscoelastic behavior as well as the most important influencing factors on these properties. Finally, concluding remarks and future trends on the improvement of the mechanical response of starch–carbon nanotubes composites are presented.

Keywords

Biaxial impact behavior • Dynamic mechanical properties • Quasi-static tensile behavior

1 Introduction

Over the recent years significant effort has been devoted to the use of environmentally friendly materials as a replacement of their conventional synthetic counterparts. An important reason to replace synthetic thermoplastic by biodegradable polymers-based materials is the possible environmental pollution they can provoke. Moreover, cost reduction is also a current point of interest. Among potential biodegradable polymers, starch is viewed by different companies as a good alternative in biodegradable formulations, in particular for packaging and medical applications [1–6].

Starch has advantages over other biodegradable polymers such as low cost, wide availability, and total compostability without toxic residues. In addition, it is odorless, tasteless, colorless, nontoxic, and biologically absorbable [7]. In the presence of low contents of plasticizers such as water or glycerol, starch materials can be processed into a variety of products such as sheets/films, foams, and other specific shapes by extrusion, injection molding, compression molding, and others [8]. The processing conditions are dependent on the techniques used and/or the final products [9].

Although starch has many advantages over synthetic thermoplastic materials as stated above, its use is still strongly limited because of its poor mechanical properties and high permeation compared to other nonnatural polymers [10].

The incorporation of micro- and nanosized fillers into starch has been the topic of many studies in order to overcome these disadvantages [1, 5, 6, 11–15]. It has been well established that the filler size greatly influences mechanical properties of the final composite. In general, smaller-size fillers improve several mechanical properties, such as Young's modulus, but with a detrimental effect on ductility [16, 17].

The use of attractive fillers such as carbon nanotubes due to their high aspect ratio, Young's modulus, tensile strength, and electrical conductivity is currently investigated. These properties make them very promising to reinforce different types of polymers [18–23].

The use of attractive fillers such as carbon nanotubes (CNTs) is currently investigated. They consist in thin sheets of benzene ring carbons rolled up into the shape of a seamless tubular structure that belongs to the family of fullerenes. Due to their unique physical and chemical properties, such as high aspect ratio, ultralight weight, high mechanical strength, high electrical conductivity, and high thermal conductivity, etc., they seem to be very promising to reinforce different types of polymers [18–23]. The high aspect ratio ($k = L/d$) and large surface area per unit volume of carbon nanotubes results in very good transfer of their properties to the matrix polymers more effectively [24–26].

In particular, some research found that composites with CNTs with large aspect ratio impart much higher storage modulus, viscosity [27, 28], electrical percolation, and dielectric behavior [29] to the composites compared with those containing filler with low aspect ratio.

There are many others factors that also affect mechanical properties of the final composite: size, shape, and interfacial adhesion between the polymer and the filler [5, 6]. In general, smaller-size fillers lead to materials with several improved mechanical properties, such as higher Young's modulus, but with a detrimental effect in ductility [16, 17].

In this chapter, the mechanical behavior of starch-based nanocomposites reinforced with multiwalled carbon nanotubes is presented. The most important influencing factors and future trends on the improvement of this behavior are also discussed.

2 Starch

Starch is a semicrystalline polysaccharide that can be found in various vegetable kingdom sources, such as cereal grains (corn, wheat, rice), seeds, legumes (lentils), and tubers (potato and cassava), and represents one of the most important raw materials for industrial use. It is present in the form of granules that vary in shape, size, and structure. Its functional properties depend on their origin (different botanical sources) and the treatment starch has received. Different kinds of starch are available in the market, including corn, cassava, wheat, and rice. Others, as yam starch, are not commercially available. Worldwide corn represents the major commercial source of starch, while cassava is an important starch source in some parts of the world, like Brazil, which is the largest cassava-producing country. In particular, cassava starch is appreciated for its paste clarity, low gelatinization

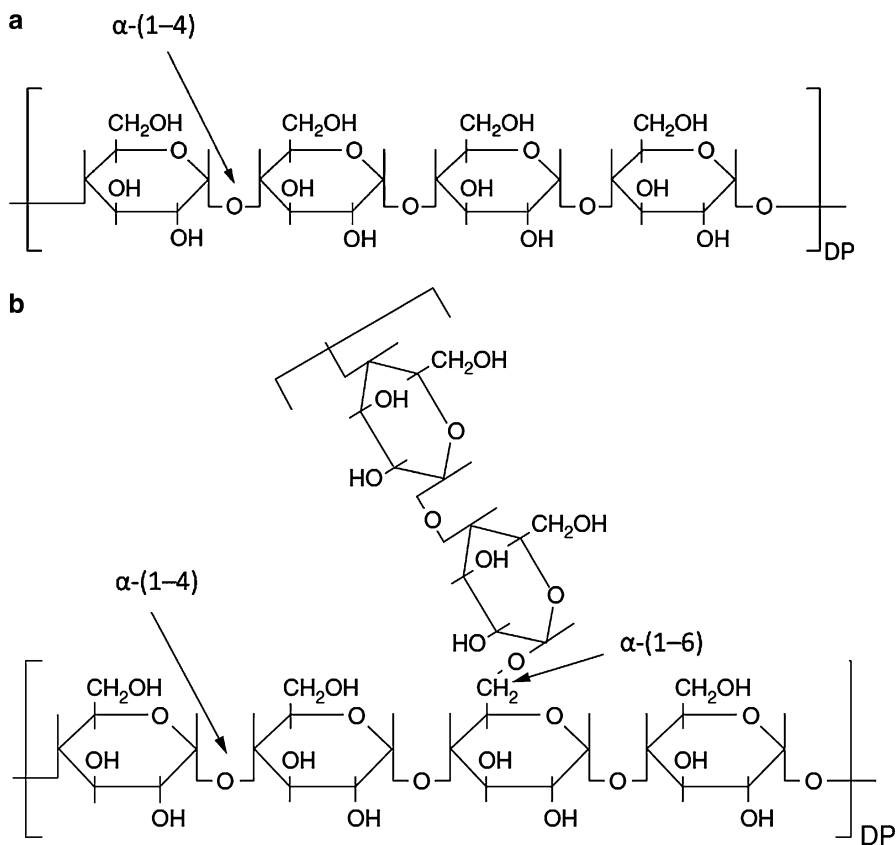


Fig. 7.1 Structure of amylose (a) and amylopectin (b)

temperature, and well stability. Native yam starch contains about 30 % of amylose, which makes it very attractive for film production [30].

Starch is a polymeric carbohydrate consisting of anhydroglucose units linked together primarily through α -(1 \rightarrow 4) glucosidic bonds. Usually it is mostly composed by a mixture of two biopolymers (glucans): amylose (straight chain) and amylopectin (branched chain). The structure of the starch granule depends on the way in which amylose and amylopectin are associated and distributed [31]. The ratio between amylose and amylopectin varies depending on the starch source. In regular starches, amylose constitutes about 15–30 % of total starch [32].

Amylose is essentially a linear structure of α -1,4-linked glucose units (Fig. 7.1a). It has a large number of hydroxyl groups, giving as a result hydrophilic properties to the polymer and resulting in a high affinity for moisture. Because of its linear nature, mobility, and the presence of many hydroxyl groups along the polymer chains, amylose molecules tend to orient themselves parallel to each other and approach each other near enough to allow formation of hydrogen bonds between adjacent chains. It is widely accepted that the most favorable three-dimensional

Table 7.1 Amylose and amylopectin content of starch from different sources [36]

Type of starch	Amylose [%]	Amylopectin [%]
Amylomaize	77	23
Banana	17	83
Corn	25	75
Chickpeas	40	60
Potato	23	77
Rice	15–35	65–85
Sorghum	25	75
Tapioca (cassava)	20	80
Waxy maize ^a	0	100
Wheat	20	80

^aObtained by genetic modifications

conformation for amylose is a double helix, which is able to pack into regular arrays [30].

Amylopectin is a highly branched structure of short α -1,4 chains linked by α -1,6 bonds containing 10–60 glucose units and side chains with 15–45 glucose units with an average of 5 % of links α -(1–6) in branching points (Fig. 7.1b) [33]. The molecular weight of amylopectin is about 1,000 times the molecular weight of amylose and ranges from 1×10^7 to 5×10^8 g/mol [34]. Amylopectin chains are arranged radially within the granule with their nonreducing terminal ends oriented toward the surface, and these are arranged with alternating crystalline areas (as a double helix) and amorphous areas (with regions of branching points) [31].

The linear structure of amylose makes its behavior more closely resemble that of conventional synthetic polymers. Depending on its source and the processing conditions employed during extraction, the molecular weight of amylose is about 1×10^6 , which is 10 times higher than that of conventional synthetic polymers. The high molecular weight and branched structure of amylopectin reduce the mobility of the polymer chains and interfere with any tendency for them to become oriented closely enough to allow significant levels of hydrogen bonding.

Starch granules present crystalline and amorphous regions. The crystalline regions are composed by branched chains of amylopectin molecules and are alternated with amorphous layers [8]. The semicrystalline structure of starch granules is composed of linear and branched macromolecules arranged in the radial direction; the macromolecules form hydrogen bonds because they are associated in parallel, which results in the appearance of crystalline regions [35]. Most native starches are semicrystalline, having a crystallinity of about 20–45 %, which depends largely on the content of amylose and amylopectin. They have three crystalline polymorphs A, B, or C type. A-type polymorph appears in cereal starches, B-type polymorph mostly in potato and other tuber starches, and C-type polymorph in the pea starch.

Table 7.1 shows the content of amylose and amylopectin of starch from different sources [36].

2.1 Gelatinization of Starch

Starch granules are insoluble in cold water. Their insolubility is due to strong hydrogen bonds which hold the starch chains together. When starch is heated in excess water above a characteristic temperature – which depends on the starch source – the crystalline structure is disrupted due to the relaxation of hydrogen bonds, and the water molecules interact with the hydroxyl groups of amylose and amylopectin, causing an increase in granule size and partial solubilization of starch [31, 32, 37, 38]. This behavior provokes an irreversible transition called gelatinization. The above phase transition is associated with the diffusion of water into the granule, water uptake by the amorphous background region, hydration and radial swelling of the starch granules, loss of birefringence, uptake of heat, loss of crystalline order, uncoiling and dissociation of double helices, and amylose leaching [32, 39–42].

Previous investigations on starch/water suspensions showed that amylose and amylopectin are partly separated during gelatinization [43, 44], because they are incompatible [43, 45]. Low water content in a thermoplastic starch system may hinder this separation. On the other hand, shear stress during extrusion may enhance separation, whereby amylose may be partly leached out of the amylopectin. Gelatinized amylopectin initially is in an amorphous state, even though there is still a small amount of ungelatinized amylopectin. Although the double-helical crystalline structure formed by the short-branched chains in amylopectin is torn apart during gelatinization, the chains remain in a regular pattern and keep a certain “memory” [46].

In addition, V-type single-helix crystals have been found to form directly after extrusion, which initially results in higher modulus and yield stress for amylose-rich materials. The crystallinity of the V-type crystals increases with the gelatinization process time, which depends mainly on water content and temperature conditions. During the initial stage of thermal processing as the temperature is increased from room temperature to 60 °C, water is thought to be reversibly complexed with starch molecules, thus decreasing its mobility [47]. At this time, the starch granular structure remains stable, with the constituent molecules hold together in spherules by van der Waals forces or hydrogen bonds, and the granules still exhibit a typical birefringence under polarized light due to their large intact crystalline components. The temperature at this stage is usually referred to as the “initial gelatinization temperature.” When an aqueous starch suspension is heated beyond its gelatinization temperature, hydrogen bonding is disrupted and water molecules become attached to the hydroxyl groups in the starch molecules, resulting in greater swelling and the dissolution of crystallites [48]. During this time, all amylopectin double helices become dissociated, although the swollen granular structure will be retained until a higher temperature is applied to disrupt it [8, 49].

Table 7.2 shows the temperature and enthalpy of gelatinization of starch from different sources.

It is important to note that there are other factors that affect the gelatinization temperature of the starch such as starch granule size, salts and sugars content, and pH [50]. Few studies are found in the literature about the influence of the addition of

Table 7.2 Temperatures and enthalpy of gelatinization for starch obtained from different sources

Origin	T ₀ [°C]	T _p [°C]	T _f [°C]	ΔH [j/g]	Reference
Amaranth	67.7	72.6	78.1	13.4	[137]
Creole banana	71.4	75.0	80.4	14.8	[137]
Banana male	69.6	74.5	81.6	13.0	[137]
Barley	46.7	56.5	73.7	10.5	[138]
Yuca	62.4	69.3	84.1	4.8	[138]
Cocoyam	74.0	78	87.0	3.98	[138]
High-amylose maize	67.6	74.6	105.7	8.18	[139]
Corn	65.5	71.1	76.4	13.2	[139]
Potato	60.0	69	80.0	4.64	[138]
Sago	61.6	64.8	74.5	1.8	[140]
Waxy maize	64.9	71.7	77.8	16.8	[139]
Wild rice	63.0	67.0	73.0	–	[141]

T₀, T_p, and T_f: initial, middle, and final temperature of gelatinization. H: enthalpy of gelatinization

carbon nanotubes in the process of starch gelatinization. In her PhD thesis Fama [51] reported that the addition of nano- and microparticles retards the gelatinization of that polymer.

2.2 Retrogradation of Starch

As explained before, when starch granules are heated in excess water, they undergo an order–disorder phase transition called gelatinization. On cooling, the starch chains (amylose and amylopectin) in the gelatinized paste interact, leading to the formation of a more ordered structure, passing from an initially amorphous state to a more ordered or crystalline state.

These molecular interactions are collectively termed retrogradation [8]. This phenomenon does occur not only after further heating but also during storage and depends on factors such as the source of starch, amylose and amylopectin ratio, molecular weight, and the particular structure of the starch molecules [52]. Retrogradation is accompanied not only by increases in the degree of crystallinity and gel firmness but also by exudation of water (syneresis), and “B”-type X-ray pattern appears [53]. Short-term development of gel structure and crystallinity in starch gels during retrogradation is dominated by irreversible (T < 100 °C) gelation and crystallization (within gelatinized granules) involving amylopectin. The process is accompanied by the loss of water from the gel and is called syneresis [31].

Despite the number of existing methods for measuring high retrogradation, it is normal to determine it by measuring the amount of water exuded (syneresis) when a frozen gelatinized starch gel is thawed at room temperature [31].

Some researches investigate the effect of the incorporation of nanofillers in the starch retrogradation and found that the addition of nanoparticles diminishes the retrogradation of the polymer [55, 74, 69, 125]. The fillers interrupt the structural

regularity of the starch and thereby restrict retrogradation and crystallization. Generally, the retrogradation of PS is greatly dependent on the hydrogen bond forming abilities of the additives with starch molecules. The stronger the hydrogen bond between starch and the additives, the more difficult for starch to recrystallize. In particular, Cao et al. [55] demonstrated that the MWNTs can form relative strong hydrogen bonding with PS suppressing starch retrogradation.

From the above discussion, it is clear that many factors significantly affect the condition of starch and also final properties of the materials containing starch. Some properties of different materials containing starch are presented below.

3 Mechanical Behavior of Starch

Several studies have been reported on the mechanical properties of starch-based films [56–62]. Many reviews can be found in the literature about the effect of the structure of starch [57, 63–65], crystallinity, and water content on the mechanical properties of biodegradable plasticized starch films [12, 50, 65–68], among other characteristics [58, 64, 69, 70]. Two very important variables, which will be discussed in this chapter, are the crystallinity and humidity of the different biofilms.

In starch film formation, a process of amylose crystallization is involved. The amount of crystallized amylose is proportional to the amylose content. For example, in waxy starch materials which contain little or no amylose, no single-helix-type crystallinity is observed.

In starch films, the typical C-type crystallinity pattern with peaks at $2\theta = 5.6^\circ$ (characteristic of B-type polymorphs), 15.0° (characteristic of A-type polymorphs), 17.2° (characteristic of both A- and B-type polymorphs), and 20.1° and 22.5° (characteristic of B-type polymorphs) has been clearly observed in X-ray diffraction patterns. The crystalline structure which results from spontaneous recrystallization or retrogradation of starch molecules after melting or gelatinization has often been detected in thermoplastic materials [71].

Crystallinity in native starch has been shown to correlate with amylose content [72]. The amylose and amylopectin ratio in the starch may affect the properties of starch-based products. A high amylose content of starch may increase crystallinity of starch-based films [73].

In addition, the relative amounts of the various amylose single-helical structures are influenced by the temperature and humidity. At higher humidity, the materials present a further increase in the amount of B-type crystallinity [66].

Furthermore, the use of plasticizers modifies the moisture content of the films [58, 63, 74]. The concentration and the type of plasticizer used are factors that significantly alter starch film properties.

In the following section, we describe the most relevant published results on the mechanical response of starch-based films. Quasi-static uniaxial tensile, dynamic mechanical, and biaxial impact behaviors as well as the main factors affecting them are discussed.

3.1 Quasi-Static Tensile Behavior

It is well established in the literature that the mechanical properties of plasticized starch materials (PS) show a strong dependency on both plasticizer content and starch source. Typical stress–strain curves obtained under quasi-static uniaxial tensile loading conditions for plasticized starch with different amylose/amylopectin ratio [75] and plasticizer content [74] are shown in Fig. 7.2a, b, respectively.

As it is clearly observed in Fig. 7.2, features of stress–strain curves of starch from different source or with different plasticizer concentration exhibit a first linear part followed by a nonlinear behavior until maximum stress σ_b (tensile strength at break) is reached. It is observed that all conditioned materials showed relatively high ε_b and low σ_b values in comparison with synthetic plastics [76].

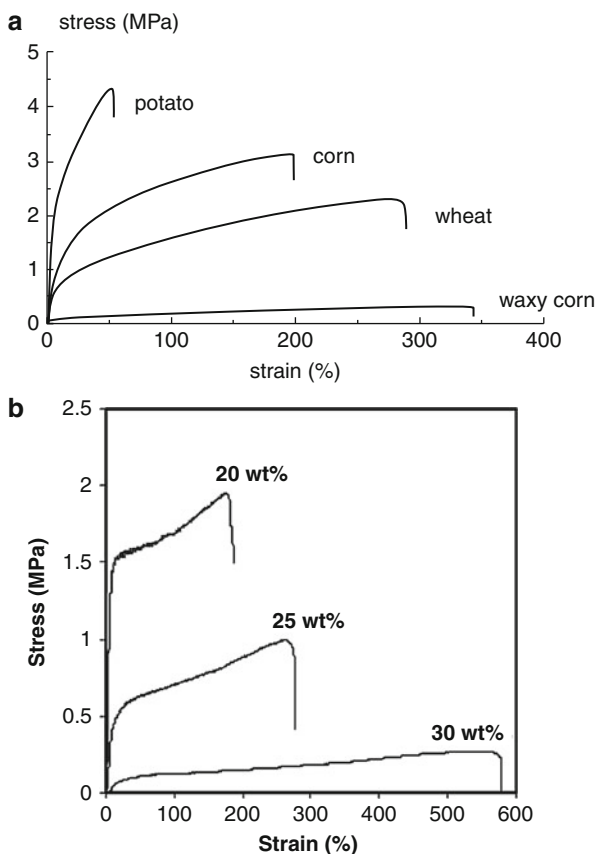
As it can be seen in Fig. 7.2a, Hulleman et al. well showed that the highest percentage of amylopectin leads to the highest strain at break and the lowest break stress and modulus. These authors explained this behavior taking into account the crystallinity and water content of the materials generated by different amylose/amylopectin ratio in the starch films [75]. They reported that corn and wheat starch presented a small amount of V_H -type crystallinity caused by crystallization of amylose [77], and potato, corn, and wheat starch films had low amounts of presumably B-type crystallinity which was related to the recrystallization of amylose or the outer chains of amylopectin or both into the B-type lattice [78]. Waxy corn starch film was amorphous after conditioning (room temperature and 20 % of water content) probably due to the absence of amylose and the relatively short outer chains of amylopectin which led to a lower recrystallization rate [79]. However, the authors concluded that differences were not significant, and they finally attributed the variations of mechanical properties to changes in water content. With increasing water content, polysaccharides increase the leaching out of the granules. The materials become more deformable without losing coherence [75].

In contrast, Lourdin et al. [57] reported that the mechanical properties of plasticized starch films were dependent on amylose/amylopectin ratio because the linear amylose and the branched amylopectin exhibit different behavior with regard to gelation, development of crystallinity, and film-forming ability. Linear chains of amylose in solution present a strong tendency to interact by hydrogen bonds, and consequently, amylose gels and films are stiffer and stronger than amylopectin ones [20, 63].

Table 7.3 shows tensile parameter values for biodegradable PS obtained with starch from different sources and containing different kinds and concentration of polyols. As it can be seen, values of stiffness are in the order of $1\text{--}10^3$ MPa, strength at break (σ_b) around $1\text{--}10$ MPa, and deformations up to 550 %. When the amylose content is higher, E and σ_b increase, while ε_b decreases practically one order of magnitude.

Rindlav-Westling et al. [63] observed that amylose films were stiffer and stronger than amylopectin films. The increase in relative crystallinity of amylopectin films with increased relative air humidity during film formation has also a clear impact on the mechanical properties of solid films. They observed that amylose

Fig. 7.2 Stress–strain curves obtained under quasi-static uniaxial tensile for PS films: (a) from different starch sources and (b) for different contents of glycerol



films with corresponding plasticization were stronger than amylopectin films, with higher σ_b and E , but lower ε_b [57]. Amylose films had an almost constant degree of crystallinity, irrespectively of the relative air humidity during film formation. On the other hand, the microstructure probably changed with different relative air humidity during film formation [63].

As expected, pure starch films from both the LA (low-amylose) and HA (high-amylose) starches were found to be quite strong. The LA and HA films without plasticizer displayed high stress at break and elastic modulus. The high values exhibited by these films were attributed to the extensive intramolecular hydrogen bonds between amylose, amylopectin, and amylose/amylopectin molecules in the absence of a plasticizer. Muscat et al. [83] also showed that for all plasticizer concentrations, irrespectively of the type of plasticizer used, the films derived from high-amylose starch showed higher tensile strength and modulus and lower elongation properties than materials derived from low-amylose starch. They explained this observation in terms of the higher gelatinization and glass transition temperatures of the amylose fraction of starch.

Table 7.3 Tensile parameter values for different plasticized starch films

Starch	Plasticizer	Plasticizer [%]	Young's modulus E [MPa]	Tensile strength σ [MPa]	Strain at break ε [%]	Reference	
Amylose amylopectin	Glycerol	20	–	23	10	57	
			–	5	25		
Cassava	Glycerol	33	2.5	1.1	80	70	
Corn	Glycerol	20	180	4.8	50	69	
Corn	Glycerol sorbitol	30	–	4.6	50.7	55	
			–	9.1	69.2		
HA corn	Glycerol	20	1080	30.7	4.6	83	
			30	323	12.2		21.8
			40	80	5.1		23.1
	Xylitol	20	1178	337.1	4		
			30	547	18.3		11.1
			40	384	14		15.1
LA corn	Glycerol	15	1341	46.1	3.4		
			20	805	27.6		13.2
			30	64	5.1		70.7
	Xylitol	15	1344	45	2.8		
			20	887	32.2		3.7
			30	533	183		24.5
Corn	Glycerol	0	1188	37	3	80	
			20	550	17		9
			40	162	9		28
Cassava			0	737	26	6	
			20	409	10	33	
			40	9	4	46	
Yam			0	1003	49	3	
			20	546	30	13	
			40	159	10	25	
Pea	Glycerol	20	110	4.6	36.1	81	
Potato	Glycerol	40	117	4.5	56	82	
			164	10	49		
Waxy	Glycerol	20	49	2.4	182	54	
			25	11	1		297
			30	0.46	0.26		551

Thunwall et al. [84] studied tensile properties of normal potato and high-amylose starch and also observed that starch with higher amylose content performed better from a mechanical point of view, increasing the tensile modulus and the strength at break, whereas the ultimum elongation decreases.

Myllärinen et al. [64] investigated amylose and amylopectin films. They observed that the tensile response had a more brittle character in the case of the film prepared with amylopectin.

Figure 7.2b shows that the increase in plasticizer content (in this case glycerol) leads to a more ductile behavior: strain at break increases, whereas stress at break decreases. Similar results have been also reported for potato starch [85], amylose isolate from potato [64], and for other polyols such as sorbitol [86].

Many works (Table 7.3) have also investigated the addition of plasticizers to pure starch-based materials. Mali et al. [20] reported that tensile strength, strain at break, and Young's modulus of starch films were affected by glycerol content. σ_b and E decreased and ε_b increased with the increase in glycerol content in all starch films. When a plasticizer such as glycerol was incorporated in a starch network, direct interactions and the proximity between starch chains were reduced; thus, under tensile loading, movements of starch chains were favored improving starch's flexibility.

Among different films, those from cassava starch were weaker and more flexible for all glycerol contents, and with increasing the glycerol content, a higher decrease in σ_b and E and a higher increase in ε_b were observed, probably because cassava starch presented the lowest amylose content [61].

Similar behavior has also been reported for amylose and amylopectin films [64], cassava starch materials [87], tapioca [88], and waxy starch [74], all plasticized with different glycerol content. The latter study explained the effect of the plasticizer considering that glycerol plays the role of an internal lubricant, enhancing the softening and mobility of the chains at room temperature.

Elastic and flexible potato starch-based films plasticized with different polyols have been studied successfully by Talja et al. [4]. These authors observed that Young's modulus and tensile strength of the films decreased and elongation at break increased with increasing plasticization.

Tensile parameters of high- and low-amylose composites prepared with different plasticizers were recently studied by Muscat et al. [83]. They showed that samples containing higher concentrations of glycerol to 20 % exhibited greater flexibility than those of films plasticized with xylitol. Thus, with increasing concentration of plasticizer, σ_b and E' decrease accompanied with an increment in deformation at break.

Qiao et al. [89] have also observed in composites containing 40 % or more of plasticizer that in comparison with the starch composite plasticized by glycerol, starch composites plasticized by polyol mixtures show higher mechanical strength due to the existence of a high molecular weight plasticizer and the formation of a uniform morphology without the defect of starch granules. The small-molecule plasticizer is helpful for the reduction of the molecular interaction of starch along with the increase of the free volume and the improvement of the processability and toughness due to its higher mobility; but more plasticizer molecules will cause negative effect for the mechanical strength.

In general, when a material is affected in its crystallinity, concentration of plasticizer, and water content, the impact on the mechanical properties is noticeable. A semicrystalline polymer generally has greater mechanical strength than the same material with amorphous structure. The greater resistance or higher modulus is due to the large number and regular spacing of the intermolecular spaces in the

crystal structures. In amorphous polymers, the number of these interactions and their spacing is less erratic, so that when subjected to efforts, many sections of polymer freely expand or deform. The addition of plasticizers to pure starch-based materials overcomes film brittleness caused by high intermolecular forces. Plasticizers increase film flexibility due to their ability to reduce internal hydrogen bonding between polymer chains while increasing molecular volume [20].

3.2 Dynamic Mechanical Properties

Glass transition temperature (T_g) is one of the most important parameters in determining the mechanical properties of semicrystalline polymers and also in studying the kinetics of crystallization of amorphous materials [90–93]. The glass transition of a material is a characteristic temperature in which the amorphous phase turns from the glassy to the rubbery state gradually during heating. Depending on the physical state of the material, either glassy or rubbery state, its properties may be significantly different [15, 94, 95].

As it has been reviewed in the previous section, water content of starch films is one of the key variables in terms of finding the transitions of any starch material. Orford et al. [92] estimated the T_g of dry amylose and amylopectin to be around 227 °C, which shifts to ~ 56 °C in the presence of water (13 %), and Bizot et al. [96] observed that the T_g of dry starch was at 332 °C. When other authors analyzed $\tan \delta$ curves of starch with 22 % [97] and 21 % [64] of water content, both detected the glass transition at around room temperature.

The glass transition of starch biofilms is also influenced by the addition of a plasticizer. It changes as a result of the type and concentration of the polyol used. For example, glycerol has their transition around -86 °C, xylitol at ~ -26 °C, and sorbitol at ~ -9 °C [131].

When glycerol-plasticized starch films with concentrations higher than 30 % of glycerol were studied, two peaks in $\tan \delta$ curves was found [50, 87, 98, 99] and only one glass transition temperature for xylitol- and sorbitol-plasticized materials [68, 98]. It has been established in the literature that starch–glycerol films are partially miscible systems giving rise to starch-rich phases, glycerol-rich phases, or both, depending on the plasticizer content [98, 100, 101]. Those phases are reflected in the dynamic mechanical response of the materials by one or two relaxation peaks. The low-temperature peak is related to the main relaxation that presents either transitions of the plasticizer-rich phase, and the high-temperature relaxation peak is attributed to the glass transition temperature of the corresponding thermoplastic starch [102, 103].

Figure 7.3 shows $\tan \delta$ values as a function of temperature for the glycerol-plasticized waxy maize and cassava starch films developed by García et al [65]. The low-temperature peak located around -60 °C is associated to the relaxation of the glycerol-rich phase, and it appears at a higher temperature for the cassava starch film compared to the waxy maize starch film. Considering this and the fact that the glass transition temperature, T_g , of pure glycerol is located between -90 °C and -75 °C [104], it is suggested that glycerol interacts more strongly

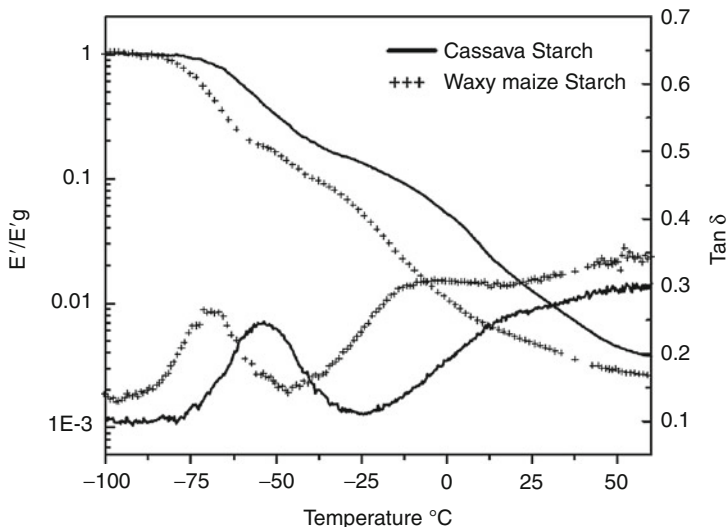


Fig. 7.3 Loss tangent as a function of temperature for glycerol-plasticized waxy maize and cassava starch films

with cassava starch. The higher interaction of glycerol with cassava starch compared to waxy maize can be explained by the formation of hydrogen bonding between glycerol and amylose.

The peak observed between $-30\text{ }^{\circ}\text{C}$ and $5\text{ }^{\circ}\text{C}$ in $\tan \delta$ curves (Fig. 7.3) is more pronounced in the waxy maize starch, which retained more moisture [65]. According to Mathew et al. [98], this very broad and low-intensity relaxation may be associated to the rearrangement of amorphous amylopectin chains in the presence of moisture. This process should appear more intensely in the case of waxy maize starch because it contains around 99 wt% amylopectin.

Table 7.4 shows glass transition temperatures for different PS films. It can be observed that increasing plasticizer content shifts the glass transition toward lower temperatures. During the plasticizing process, intermolecular and intramolecular hydrogen bonds of the native starch are substituted by the hydrogen bonds between starch and plasticizer; as a result, T_g of the starch decreases [99].

Talja et al. [4] studied potato starch films plasticized with sorbitol. They observed that these films had a glass transition temperature at higher temperatures than xylitol-plasticized materials, and the peak shifted to lower temperatures when the concentration of the polyols increased.

Angellier et al. [74] analyzed the influence of glycerol in waxy starch films, observing that a small increase in the plasticizer content (from 20 % to 30 %) did not change the relaxation of plasticizer-rich domains. Similar results were reported by Fishman et al. [106] and Bonacucina et al. [54] for starch acetate–glycerol films. However, an increase in the plasticizer content shifted the peak near $0\text{ }^{\circ}\text{C}$ to lower temperatures for the films investigated by Angellier et al. [74].

Table 7.4 Glass transition temperature (T_g) for different PS films

Starch	Plasticizer	Plasticizer [%]	T_g [°C]	Reference
Barley	Glycerol	14	–67	105
		20	–69	
		29	–71	
		39	–82	
Corn	Glycerol	17	35	80
		20	3	59
		30	–55.9, 38.3	55
Cassava	Glycerol	30	–55.7, 62.2	22
		45	–58.8, 42.1	
Cassava	Glycerol	33	–62, –30/5	17
Potato	Sorbitol	30	–32.2	4
		50	–48.4	
	Xylitol	30	–56.7	
		50	–47.9	
Waxy maize	Glycerol	33	–48, 27	98
	Xylitol		–40	
	Sorbitol		–7	
Waxy maize	Glycerol	20	–61.2, 10	54
		25	–62.2, 3	
		30	–62.2, –12.4	

Similar behavior in the highest peak was observed by Bergo et al. [87] for cassava starch films, when glycerol content was increased from 30 % to 45 %. In contrast, they showed a significant shift in the lower transition as the plasticizer content increased. These results are in agreement with those reported by Forsell et al. [105] for barley starch–glycerol materials and by Mali et al. [61] for yam starch-based films.

In semicrystalline polymers, the fact that the amorphous and crystalline phases are intimately connected to each other has a significant effect on the relaxation at the glass temperature, resulting usually on broadening of the transition region. As the relaxation broadens, the loss peak shifts to higher temperatures.

T_g values of polymers are seriously affected by the presence of even small amount of absorbed moisture. The moisture acts as a diluent or plasticizer and lowers the glass transition temperature.

4 Carbon Nanotubes

Carbon nanotubes (CNTs) are an allotrope of carbon. Their diameter is on the order of a few nanometers and can be up to several micrometers in length. The nanotubes come from the fullerene structural family and are composed of sp^2 bonds, similar to those observed in graphite, and they naturally align themselves into ropes held

Table 7.5 Mechanical properties of different engineering materials

Materials	Specific density	E [TPa]	Strength [GPa]	Strain at break [%]
Carbon nanotube	1.3–2	1	10–60	10
HS steel	7.8	0.2	4.1	<10
Carbon fiber – PAN	1.7–2	0.2–0.6	1.7–5	0.3–2.4
Carbon fiber – Pitch	2–2.2	0.4–0.96	2.2–3.3	0.27–0.6
E/S – glass	2.5	0.07–0.08	2.4/4.5	4.8
Kevlar ^a 49	1.4	0.13	3.6–4.1	2.8

^aKevlar is a registered trademark of DuPont

together by van der Waals forces. Carbon nanotubes (CNTs) are cylindrical carbon molecules with novel properties which make them potentially useful in a wide variety of applications [107–109].

Taking into account their mechanical properties, carbon nanotubes show a unique combination of stiffness, strength, and toughness compared to other fiber materials which usually lack from one or more of these properties (Table 7.5) [110].

As it can be observed in Table 7.5, carbon nanotubes reach values of strength more than one order of magnitude higher than other materials. They also present plastic deformation, achieving strains of approximately 5 %.

Thermal and electrical conductivity are also very high and comparable to other conductive materials (100 times stronger than steel and in the order of that of diamond).

There are two types of CNT: single-walled carbon nanotubes (SWNTs) and multiwalled nanotubes (MWNTs). SWNTs were discovered in 1993 and most of these have a diameter close to 1 nm, with a tube length that may be many thousands of times larger and up to orders of centimeters. Its structure can be conceptualized by wrapping a one-atom-thick layer of graphite (or graphene) into a seamless cylinder. This type of carbon exhibits more important electric properties than MWNTs. They are excellent conductors. Multiwalled nanotubes are similar to a collection of concentric SWNTs. The length and diameter of these structures differ a lot from those of SWNTs and, of course, their properties are also very different. MWNTs consist of an array of such cylinders formed concentrically and separated by 0.35 nm, similar to the basal plane separation in graphite. MWNTs can have diameters from 2 to 100 nm and lengths of tens of microns [111]. In a recent work Nuriel et al. studied the characteristic of MWNT with only 15–30 nm of diameter obtaining a surface tension of $\sim 40\text{--}45 \text{ mJ/m}^2$ [112].

The small size of these nanofillers is comparable to the size of polymer molecular chains and results in a considerably higher interaction surface area between the filler and the matrix than conventional micro-sized fillers. Improvements in the mechanical properties of polymers are achieved with little increase in the material weight.

The important properties of carbon nanotubes make them potentially useful in a wide variety of applications [113, 114]. In recent years wide attention has been dedicated to analyze the eventual interactions of carbon nanotubes with living entities and any biomedical application, where suitably modified CNTs can serve as vaccine delivery systems [115] or protein transporters [134]. There have been

several investigations concerning the use of carbon nanotubes for biological purposes and their introduction in biological systems taking advantage of the fact that all living entities are carbon based and nanotubes are solely made of carbon with a similar scale size of DNA.

Bianco et al. [114] report a study of the most recent achievements of CNTs in drug delivery. Nanopenetration was also recently suggested by Cai et al. [116], who proposed an efficient *in vitro* delivery technique called nanotube spearing. In other hand, Cherukuri et al. [117] showed that macrophage cells could ingest significant amounts of nanotubes without apparent toxic effects. It has been shown that carbon nanotubes excrete *in vivo* and so could be cleared from the body once they are no longer needed [07Har]. For their size, these charges can be filtered by the spleen and kidney, becoming a great alternative to the therapeutic area.

In addition, the capability of creating nanosized sensors may provide key information regarding tissue microenvironments thus yielding new insight into the cell–matrix interface. Demonstrations of drug and DNA intercellular delivery using carbon nanotubes show promise for carbon nanotubes to be used as alternatives to viruses for transfection [07Har].

CNTs could be also ideal in designing new tissue-engineered products in biological applications, and promising possibilities can be expected by introducing them to reinforce scaffolds for tissue engineering.

5 Performance of Starch–Carbon Nanotubes Nanocomposites

There are many studies reporting possible formulations of biodegradable composites that propose to incorporate carbon nanotubes to reinforce a starch matrix. However, a good dispersion of this filler in such polymer matrix is very difficult without an appropriate functionalization of the nanotubes and/or some modification of starch [14, 15, 55, 69, 81, 123, 125, 133, 136].

Plasticized starch films are generally prepared by heating starch and plasticizer in excess of water until the starch gelatinization occurs [14, 15, 98, 120, 121]. After gelatinization, the solution is poured onto glassy, plastic, or Teflon plates, and finally, water is evaporated from the film at various conditions (room temperature or controlled vacuum conditions) [20, 64, 98, 104, 121].

In the case of nanocomposites, they can be differently formed: (i) from a solution or dispersion-forming agent, followed by some method of separation of the fluid agent “carrier” (solvent), or (ii) directly by solidification of the solvent.

The process of film forming comprises a stage that involves heating, alteration of the pH, and addition of solvents or alteration of the charge on the polymer involved and another stage in which the solidification of the material is produced through cooling. The speed and temperature at which these steps are performed have much influence on the physicochemical properties of the resulting film [98].

Processing of starch, however, is much more complicated and difficult to control than that of traditional petroleum-based plastics and conventional polymers, due to

the unsatisfactory processing properties resulting from its unique phase transitions, high viscosity, water evaporation, fast retrogradation, etc. However, with proper formulation development and suitable processing conditions, many of these challenges can be overcome.

Extrusion [66], injection molding, spray [122], and film casting [123] are some of the common processing techniques applied to obtain this kind of materials [68]. In particular, extrusion is the most widely used technique for processing starch-based polymers. Its advantage includes the ability to handle high-viscosity polymers in the absence of solvents and the large operational flexibility and control of the degree of mixing.

The effective utilization of composite materials strongly depends on the homogeneous dispersion of the filler throughout the polymer matrix and the adequate interfacial adhesion between phases [21]. A few years ago, Star et al. showed an effective technique to disperse carbon nanotubes by wrapping the surface of the fillers in an aqueous system of a starch–iodine complex. Those authors reported that the technique was ideal for introducing fillers in a starch-based matrix. They ensured a good dispersion of the wrapped filler in starch matrix and excellent interfacial adhesion because the same material was used as the matrix and in the system that wrapped the nanotubes [124].

The structure of carbon nanotubes, along with their low density, high aspect ratio, and extraordinary mechanical properties described in Sect. 4 makes them particularly attractive for reinforcement of composite materials [19, 21, 22, 23, 80, 135]. Some works on starch–carbon nanotube composites in which different methods were used to disperse the filler into the matrix have been published [28, 31, 69, 125]. Very recently, Famá et al. [14, 15] observed important improvements in the mechanical properties of cassava starch-based nanocomposites with very small amounts of carbon nanotubes previously wrapped with a starch–iodine complex.

In the following sections, we describe in detail these studies of Famá et al. [14, 15] as well as the results reported in the literature for similar materials. In particular, quasi-static uniaxial tensile, dynamic mechanical and biaxial impact behaviors, as well as the main factors affecting them are presented.

5.1 Quasi-Static Tensile Behavior

Figure 7.4 shows typical nominal stress–strain curves obtained under quasi-static uniaxial tensile loading conditions for cassava starch-based films plasticized by glycerol reinforced with different concentration of carbon nanotubes. It is seen that the stress–strain behavior of PS materials did not qualitatively change with the addition of carbon nanotubes. All materials exhibited nonlinear behavior until failure which occurs with a precipitous drop of the load at the maximum stress with no necking before fracture. Young's modulus (E), ultimate strength (σ_u), strain at break (ε_b), and tensile toughness values reported by the authors are shown in Table 7.6. They were originally reported in Reference [14].

A significant improvement in Young's modulus and an enhancement in tensile strength values have been found by Famá et al [14] from the incorporation of very

Fig. 7.4 Stress–strain curves for cassava starch–glycerol–MWNTs nanocomposites [14]

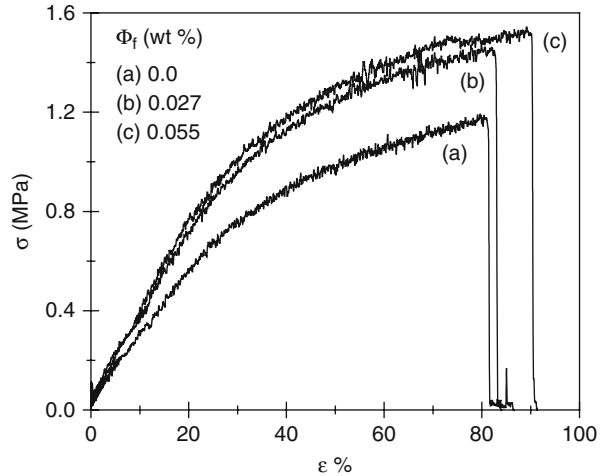


Table 7.6 Tensile parameters for the different materials investigated by Famá et al [14]. Young's modulus (E), ultimate strength (σ_u), strain at break (ε_b), and tensile toughness

	ϕ_f [wt%]		
	0	0.027	0.055
E [MPa]	2.5 ± 0.2	3.6 ± 0.4	4.2 ± 0.5
σ_u [MPa] (± 0.1)	1.1	1.4	1.5
ε_b [%]	80 ± 1	82 ± 2	90 ± 2
Toughness $\times 10^{-5}$ [J/m ³]	6.4 ± 0.5	8.4 ± 0.8	9.9 ± 0.9

small amounts of MWNT to a cassava starch matrix, keeping deformations higher than 80 %. They observed that stiffness increased almost 70 % and ultimate tensile strength ~ 35 % with only 0.055 wt% of multiwalled carbon nanotubes. They reported that all tensile parameters increased when the wrapped filler was added. As a result, they observed that toughness also increased with filler loading.

The above behavior is not very frequently found in the literature, especially with so small fractions of filler, and can be attributed to the good dispersion of the MWNTs in the starch matrix and also to the strong interfacial adhesion achieved. Thus, efficient load transfer from the matrix to the filler was attained and the high tensile strength and strain at break of the nanotubes was transferred to the composites. The good interfacial adhesion inhibited the formation of holes keeping the high deformations.

To the authors' knowledge, in all previous works reported in the literature about this kind of materials, concentrations used are higher than 0.1 wt%, and/or covalent functionalization was applied to the filler.

In particular, Liu et al. [81] used a mix of water and glycerol to disperse multiwalled carbon nanotubes into a corn starch matrix. MWNTs loading levels from 0.5 to 3 wt% were used. They observed that the addition of the filler improved

the tensile strength of the matrix, increasing with the increase in CNT concentration till filler loading of 1.5 wt% (from 4.5 to 7.7 MPa). Then, from 1.5 to 3 wt% of MWNT, some decrease in σ_u was found. They explained this result as follows: acid-treatment process incorporated polar groups with MWNT, improving the hydrophilicity of the filler and reducing agglomerations [82]. Therefore, it enhanced the hydrogen-bonding interactions as well as the dispersion of the filler in the matrix, resulting in an improvement of the mechanical performance of the PS–MWNT nanocomposites. At high filler content, MWNT deteriorated the plasticization and destructed the continuity of starch matrix, and then, it could deteriorate the mechanical properties of the composites [81]. In contrast to Famá et al. [15], Liu et al. reported that the deformation at break decreased with the increase in filler content for all concentrations of nanotubes [81].

Similar behavior than Liu et al. was reported by Ma et al. in corn starch–glycerol–MWNT functionalized by aid of SDS [69]. They observed that tensile strength and Young's modulus increased as the content of filler was increased up to 4.75 wt% (from 4.8 to 7.5 MPa and from ~ 180 to ~ 250 MPa), and both elongation at break and energy at break decreased. The authors explained that behavior in terms of the improvement in the interactions between the MWNTs when filler content increased; then, crack propagation was inhibited, which resulted in strength and stiffness improvements. On the other hand, having interfacial adhesion between MWNT and corn starch–glycerol might induce premature composite failure because the reinforcing nanotubes were simply pulled out of the matrix without contributing to the strength or stiffness of the material. The toughness of these nanocomposites was reduced and addition of the nanofiller yielded increasingly brittle samples [80].

Cao et al. [55] investigated the mechanical properties of pea starch–glycerol–MWNT nanocomposites with smaller filler concentration (from 0.1 to 3 wt%) dispersed in deionized water. They observed important improvements in tensile properties, even at the presence of a small filler amount. Tensile strength and Young's modulus increased significantly from ~ 2.9 to ~ 4.7 MPa and from ~ 20.7 to ~ 39.2 MPa, respectively. In contrast to the previously described results, they showed that the increase in strength did not come at the expense of the elongation at break as in conventional filled polymer systems: values of elongation at break can increase [14] or decrease [8] with an increase of MWNT content in the range of 0–1.0 wt%. The results show a maximum value of elongation at break: 34 % for pure matrix, maximum value at ~ 50 % for the sample with 1.0 wt% of filler, and a decrease for all the values when the MWNT content was higher than 1.0 wt%.

5.2 Dynamic Mechanical Behavior

Figure 7.5 presents the dependence of $\tan \delta$ with temperature for the different glycerol-plasticized composites investigated by Famá et al. [15].

It can be observed that $\tan \delta$ curves reveal two thermal transitions corresponding to the two phases of the PS: the glycerol-rich phase at around -60 °C and the starch-rich phase between -5 °C and 30 °C, as previously explained. The lower-temperature

peak seems to remain unchanged with the addition of carbon nanotubes. This suggests that the filler used did not modify the distribution of the glycerol in the matrix. However, the width of this peak decreases with the incorporation of a small amount of MWNT, indicating that some restriction in the number of relaxation mechanisms exists in the nanocomposites investigated by Famá et al. [15].

The “upper” transition peak broadened is shifted to higher temperatures and diminished in intensity with the increase in MWNT content. Then, the wrapped filler would have been interacting with the starch but not with glycerol. The authors attributed the observed behavior to the higher surface area promoted by the incorporation of the nanotubes and the very good adhesion between the matrix and the wrapped filler. During the glass transition temperature, the long-range polymer chain acquires mobility and therefore dissipates a great amount of energy through viscous movement.

The depression in loss tangent values would indicate the reduction of the number of mobile chains of starch in contact with the carbon nanotubes surface during the glass transition [69, 125].

At the time of writing, no other reports have been found in the literature about the effect of carbon nanotubes as reinforcement of starch-plasticized thermoplastic films on dynamic mechanical properties and, in particular, on their relaxations.

5.3 Biaxial Impact Behavior

In recent times, the demand for tests simulating accurately the final terms of use has considerably increased. Among them, impact tests have become particularly important within the polymer industry for several reasons: in principle, they are useful to compare the dynamic response of different materials, also they are used for purposes of research and development in different applications, and they are considered a quality control parameter of a given manufacturing process. Furthermore, impact tests are conducted to simulate conditions of final use of a material or product, so that it is manufactured to survive impact associated with lifetime [126].

Very few authors have studied the biaxial impact behavior of nanocomposite materials. Mohagheghian et al. investigated the quasi-static puncture tests on linear low-density polyethylene (LLDPE) and two nanocomposites consisting of LLDPE filled with 1 % carbon black and 0.5 % nanoclay fillers. They observed in force–displacement curves that in each case the load increased to a maximum, at which point a tensile neck appears. The neck then propagated, accompanied by a load drop before final rupture. The results of the reinforced materials, with both carbon black and nanoclay absorbed less energy at rupture than the unfilled polymer [118].

Famá et al. [14] reported a study of the biaxial impact behavior of MWNT-reinforced PS–MWNT nanocomposites. Thickness-related force versus displacement traces obtained under biaxial impact conditions for cassava starch-based films plasticized by glycerol and reinforced by different concentration of carbon nanotubes are shown in Fig. 7.6, and a typical macrophotograph of the impacted area of a nanocomposite sample is presented in Fig. 7.7.

Fig. 7.5 Tangent of the loss angle as a function of temperature for cassava starch–glycerol–MWNTs nanocomposites [15]

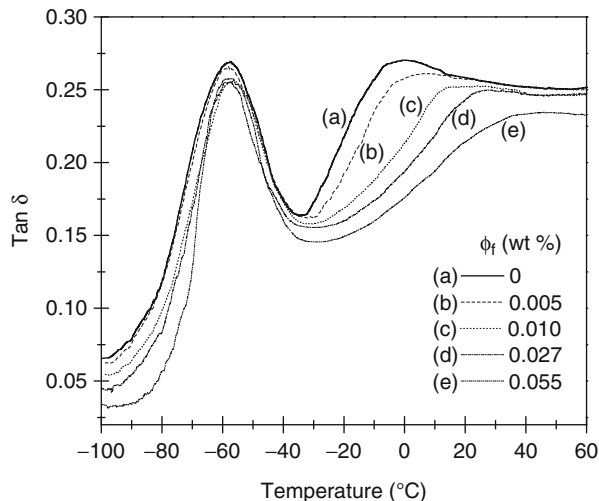
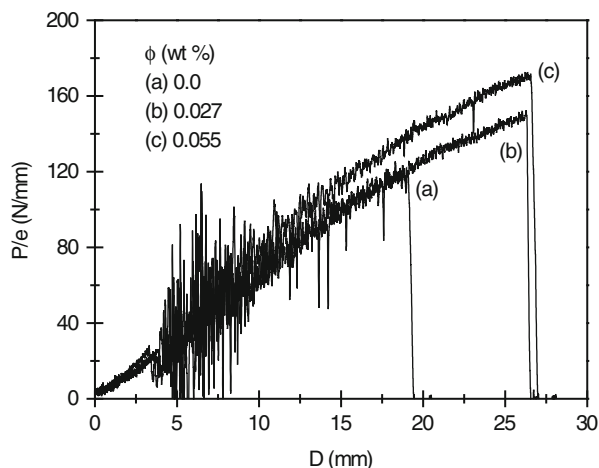


Fig. 7.6 Force versus displacement curves obtained in biaxial impact tests for cassava starch–glycerol–MWNTs nanocomposites [14]



In agreement with the results obtained under quasi-static loading conditions, features of impact load–displacement curves of PS films did not change with the addition of MWNTs. As it can be seen in Fig. 7.6, all samples exhibited semi-brittle fracture behavior which can be deduced from the nonlinear force–displacement curve which dropped to zero immediately upon reaching maximum load.

In addition, typical radial cracks were observed around the hole area of impacted samples, which were responsible for final failure of specimens. These cracks and the small deformed area around the hole also confirmed the semi-brittle fracture behavior reflected by load–displacement records.

The values of biaxial impact parameters reported by Famá et al. are presented in Table 7.7 along with their deviations [14]. Thickness-related perforation energy,

Fig. 7.7 Macrophotograph of the impacted area of cassava starch–glycerol–MWNTs composites [14]

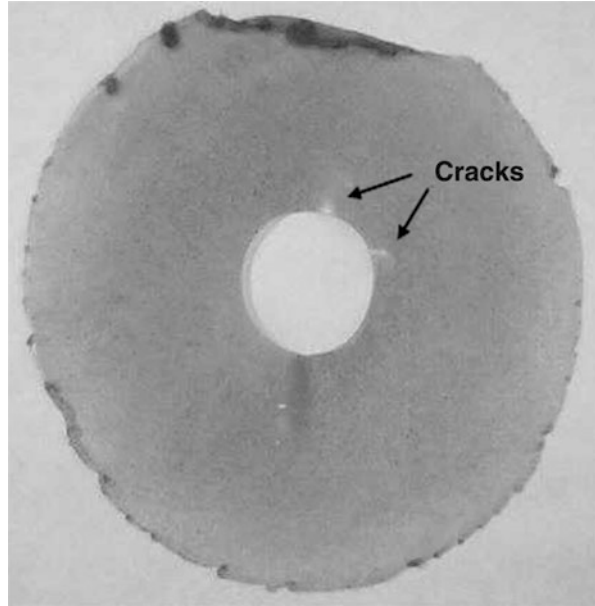


Table 7.7 Parameters obtained under biaxial impact conditions: thickness-related energy (U/e), disc strength (σ_d), and maximum displacement (d_d) [14]

	ϕ_f [wt%]		
	0	0.027	0.055
U/e [N]	1212 ± 2	2174 ± 3	2578 ± 4
σ_d [N/mm^2]	3225 ± 25	6040 ± 33	6324 ± 67
d_d [mm]	19.0 ± 0.5	26 ± 1	27 ± 1

disc maximum strength, and maximum displacement (d_d) values significantly increased with filler content, reaching to improvements of up to $\sim 100\%$ in both U/e and σ_d . These results demonstrate that the addition of even a very small fraction of carbon nanotubes to a starch matrix is also an efficient way to improve the material impact fracture behavior. The authors explained that in agreement with tensile results, the improvements observed in impact properties were also the result of an efficient load transfer from the matrix to the filler, which is determined by the following concomitant effects:

1. Carbon nanotubes have an extremely high area-to-volume ratio. This is about 1,000 times that of spheres with similar radius [111].
2. The aspect ratio of CNT is high.
3. The surface-modified nanotubes developed by Famá et al. [14] were highly compatible with the starch matrix, as they were wrapped with a starch–iodine complex composed by the same starch of the matrix, and thus, excellent adhesion between phases and good dispersion of the filler in the matrix was achieved.

In summary, they concluded that the excellent filler–matrix adhesion of these composites induced a cohesive fracture of the matrix and the good dispersion of nanotubes gave place to a tortuous crack path, resulting in an increase of toughness with nanotubes content.

6 Concluding Remarks and Future Trends

In this chapter a review of the most important recent results on the mechanical behavior of starch-based nanocomposites reinforced with carbon nanotubes is presented.

Many factors significantly affect the condition of starch and consequently the final properties of the materials containing starch such as its nanocomposites.

Many reviews can be found in the literature about the effect of the structure of starch, crystallinity, water content, and starch source, among others, on the mechanical properties of biodegradable plasticized starch-based films. However, the relation among those factors makes the interpretation of results very difficult and sometimes they appear contradictory.

It is well known that effective utilization of composite materials strongly depends on the homogeneous dispersion of the filler throughout the polymer matrix and the adequate interfacial adhesion between phases.

There are many studies reporting possible formulations of biodegradable composites from the addition of carbon nanotubes to reinforce a starch matrix. However, a good dispersion of this filler in such polymer matrix is very difficult without an appropriate functionalization of the nanotubes and/or some modification of starch.

Recently, Famá et al. [14, 15] reported significant improvements in the mechanical performance of nanocomposites based on starch reinforced with MWNTs previously wrapped with a starch–iodine complex following the method of Star et al. [124]. The strategy used by the authors was highly effective to obtain very well-dispersed nanotubes in a starch matrix and strong adhesion between the phases. Stress transfer was maximized and important improvements in the mechanical properties (uniaxial tensile, dynamic mechanical and impact properties) were obtained with very small amounts of carbon nanotubes. This result is not very frequently found in the literature, especially with extremely small fractions of filler.

Based on the results reported in the literature for MWNTs–starch nanocomposites, it can be concluded that it is possible to develop novel nanocomposites from biodegradable, renewable, and low-cost source, reinforced with very small quantities of MWNTs to replace synthetic materials in many applications.

Since the early 1970s, biopolymers have been studied as potential replacements for synthetic polymers to reduce pollution. Nowadays there are few companies that use starch-based polymer materials in the packaging industry and food products. For example, Mater-Bi (Novamont) and Bioplast (Biotec) manufacture disposable products like plates, cutlery, glasses, plates, etc., thermoformed trays, film, and bags for agriculture. In this context, the nanocomposite of starch and carbon nanotubes is

a new formulation that is incorporated in the biopolymers, and with different results its use is advancing in the global industry to replace synthetic polymers. That material could be used to improve existing biodegradable products enriching in their properties, without prejudice. That nanocomposite, characterized by its biodegradability, has great economic potential in the area of packaging due to its similarity with synthetic materials, especially in mechanical properties, barrier, and light transparency.

Furthermore, the important properties of conductivity of CNTs enable possible use of active and intelligent packaging systems.

In the area of biomedicine, it has highlighted the important uses of CNTs due their nanometric size. When they are incorporated in the starch matrix, these nanocomposites could be used as prosthetic implants, sutures, etc. Though it is still too early to establish nanocomposite reinforced by CNTs for clinical use, these novel carriers are undoubtedly interesting and deserve further investigation.

The composites developed presents novel behavior in the world, placing into the new trends for the conservation and protection of health and environment, which are increasingly important in the eyes of consumers.

Although the above results are very promising, much more effort should be done to bridge the gap between laboratory-scale and industrial applications through the development of large-scale processing technologies.

Acknowledgments The authors want to thank the National Research Council of Argentina (CONICET) (Project 11220090100699) and the UniversDonovanity of Buenos Aires (UBACyT) (Projects: 20020090300055 and 20020100100350) for financial support.

References

1. Katz HS, Milewsky JV (1978) Handbook of fillers and reinforcements for plastics. Van Nostrand Reinhold/Springer, London, p 652
2. Shogren RL, Lawton JW, Doane WM, Tiefenbacher KF (1998) Structure and morphology of baked starch foams. *Polymer* 39:6649
3. Sorrentino A, Gorrasi G, Vittoria V (2007) Potential perspectives of bio-nanocomposites for food packaging applications. *Trends Food Sci Technol* 18:84
4. Talja RA, Helén H, Roos YH, Jouppila K (2007) Effect of various polyols and polyol contents on physical and mechanical properties of potato starch-based films. *Carbohydr Polym* 67:288
5. Fu S-Y, Feng X-Q, Lauke B, Mai Y-W (2008) Effects of particle size, particle/matrix interface adhesion and particle loading on mechanical properties of particulate-polymer composites. *Compos Part B Eng* 39:933
6. Siqueira G, Bras J, Dufresne A (2009) Walled carbon nanotubes. *Biomacromolecules* 10:425
7. Wong M, Paramsothy M, Xu XJ, Ren Y, Li S, Liao K (2003) Physical interactions at carbon nanotube–polymer interface. *Polymer* 44:7757
8. Liu H, Xie F, Yu L, Chen L, Li L (2009) Thermal processing of starch-based polymers. *Prog Polym Sci* 34:1348
9. Schwach E, Avérous L (2004) Tarch-based biodegradable blends: Morphology and interface properties. *Polym Int* 53:2115
10. Hansen NML, Plackett D (2008) Sustainable films and coatings from hemicelluloses: A review. *Biomacromolecules* 9:1494

11. Alvarez V, Vazquez A (2006) Influence of fibre chemical modification procedure on the mechanical properties and water absorption of MaterBi-Y/sisal fibre composites. *Compos Part A* 37:1672
12. Alemdar A, Sain M (2008) Biocomposites from wheat straw nanofibers: morphology, thermal and mechanical properties. *Compos Sci Technol* 68:557
13. Famá L, Gerschenson L, Goyanes S (2009) Starch-vegetable fibre composites to protect food products. *Carbohydr Polym* 75:230
14. Famá LM, Pettarin V, Goyanes SN, Bernal CR (2011) Starch/multi-walled carbon nanotubes composites with improved mechanical properties. *Carbohydr Polym* 83:1226
15. Famá L, Gañán Rojo PG, Bernal C, Goyanes S (2012) Biodegradable starch based nanocomposites with low water vapor permeability and high storage modulus. *Carbohydr Polym* 87:1989
16. Wisse E, Govaert LE, Meijer HEH, Meijer EW (2006) Unusual tuning of mechanical properties of thermoplastic elastomers using supramolecular fillers. *Macromolecules* 39:7425
17. So HH, Cho JW, Sahoo NG (2007) Effect of carbon nanotubes on mechanical and electrical properties of polyimide/carbon nanotubes nanocomposites. *Eur Polym J* 43:3750
18. Jia Z, Wang Z, Xu C, Liang J, Wei B, Wu D, Zhu S (1999) Study on poly(methyl methacrylate) carbon nanotube composites. *Mater Sci Eng A* 271:395
19. Ruan SL, Gao P, Yang XG, Yu TX (2003) Toughening high performance ultrahigh molecular weight polyethylene using multiwalled carbon nanotubes. *Polymer* 44:5643
20. Mali S, Grossmann E, García MA, Martino MN, Zaritzky NE (2006) Effects of controlled storage on thermal, mechanical and barrier properties of plasticized films from different starch sources. *Glass* 75:453
21. Zilli D, Goyanes S, Escobar MM, Chilotte C, Bekeris V, Cukierman AL, Rubiolo GH (2007) Comparative analysis of electric, magnetic, and mechanical properties of epoxy matrix composites with different contents of multiple walled carbon nanotubes. *Polym Compos* 28:612
22. De Falco A, Marzocca AJ, Corcuera MA, Ecesiza A, Mondragon I, Rubiolo GH, Goyanes S (2009) Accelerator adsorption onto carbon nanotubes surface affects the vulcanization process of styrene-butadiene rubber composites. *J Appl Polym Sci* 113:2851
23. De Falco A, Fascio M, Lamanna M, Corcuera M, Mondragon I, Rubiolo G, D'Accorso N, Goyanes S (2009) Thermal treatment of the carbon nanotubes and their functionalization with styrene. *Physi B Condens Matter* 404:2780
24. Jin L, Bower C, Zhou O (1998) Alignment of carbon nanotubes in a polymer matrix by mechanical stretching. *Appl Phys Lett* 73:1197
25. Qian D, Dickey EC, Andrews R, Rantell T (2000) Load transfer and deformation mechanism in carbon nanotube-polystyrene composites. *Appl Phys Lett* 76:2868
26. Wang Y, Wu J, Wei F (2003) A treatment method to give separated multi-walled carbon nanotubes with high purity, high crystallization and a large aspect ratio. *Carbon* 41:2939
27. Potschke P, Fornes TD, Paul DR (2002) Rheological behavior of multiwalled carbon nanotube/polycarbonate composites. *Polymer* 43:3247
28. Cipriano BH, Kashiwagi T, Raghavan SR, Yang Y, Grulke EA, Yamamoto K, Shields JR, Douglas JF (2007) Effects of aspect ratio of MWNT on the flammability properties of polymer nanocomposites. *Polymer* 48:6086
29. Huang XY, Jiang PK, Kim C, Liu F, Yin Y (2009) Morphological, electrical, electromagnetic interference (EMI) shielding, and tribological properties of functionalized multi-walled carbon nanotube/poly-methyl methacrylate (PMMA) composites. *Eur Polym J* 45:377
30. Zobel HF (1994) In: Alexander RJ, Zobel HF (eds) *Starch granule structure*. The American Association of cereal chemists. Springer, St Saint Paul, p 1
31. Zavareze E, Guerra Días A (2011) Impact of heat-moisture treatment and annealing in starches: A review. *Carbohydr Polym* 83:317
32. Hoover R, Hughes T, Chung HJ, Liu Q (2010) Composition, molecular structure, properties, and modification of pulse starches: A review. *Food Res Int* 43:399

33. Van der Maarel MJEC, Van der Veen B, Uitdehaag JCM, Leemhuis H, Dijkhuizen L (2002) Properties and applications of starch-converting enzymes of the α -amylase family. *J Biotechnol* 94:137
34. You S, Stevenson SG, Izydorczyk MS, Preston KR (2002) Separation and characterization of barley starch polymers by a flow field-flow fractionation technique in combination with multiangle light scattering and differential refractive index detection. *Cereal Chem* 79:624
35. Gallant DJ, Bouchet B, Baldwin PM (1997) Microscopy of starch: Evidence of a new level of granule organization. *Carbohydr Polym* 32:177
36. Cuq JL, Aymard C, Cheftel C (1977) Effects of hypochlorite treatments on a methionyl peptide. *Food Chem* 2:309
37. Lelievre J (1974) Starch gelatinization. *J Appl Polym Sci* 18:293
38. Atwell WA, Hood LF, Lineback DR, Varriano-Marston E, Zobel HF (1988) The terminology and methodology associated with basic starch phenomena. *Cereal Food World* 33:306
39. Donovan JW (1979) Phase transitions of the starch-water system. *Biopolymers* 18:263
40. Hoover R, Hadziyev D (1981) Characterization of potato starch and its monoglyceride complexes. *Starch* 33:290
41. Jenkins PJ, Donald AM (1998) Gelatinization of starch: a combined SAXS/WAXS/DSC and SANS study. *Carbohydr Res* 308:133
42. Waigh TA, Gidley MJ, Komanshek BU, Donald AM (2000) The phase transformations in starch during gelatinisation: a liquid crystalline approach. *Carbohydr Res* 328:165
43. Kalichevsky MT, Ring SG (1987) Incompatibility of amylose and amylopectin in aqueous solution. *Carbohydr Res* 162:323
44. Keetels CJAM, Van Vliet T, Walstra P (1996) Elongation and retrogradation of concentrated starch system: 2. Retrogradation. *Food Hydrocoll* 10:355
45. Doublier JL, Llamas GA (1993) In: Dickinson E, Walstra P (eds) A rheological description of amylose-amylopectin mixtures. Food colloids and polymers: stability and mechanical properties. Royal Society of Chemistry, Cambridge, p 138
46. Xie F, Yu L, Su B, Liu P, Wang J, Liu H, Chen L (2009) Rheological properties of starches with different amylose/amylopectin ratios. *J Cereal Sci* 49:371
47. Olkku J, Rha C (1978) Gelatinization of starch and wheat flour starch—a review. *Food Chem* 32:293
48. Lim MH, Wu HB, Reid DS (2000) The effect of starch gelatinization and solute concentrations on T_g of starch model system. *J Sci Food Agric* 80:1757
49. Tester RF, Debon SJJ (2000) Annealing of starch – a review. *Int J Biol Macromol* 27:1
50. Famá L, Goyanes S, Gerschenson L (2007) Influence of storage time at room temperature on the physicochemical properties of cassava starch films. *Carbohydr Polym* 70:265
51. Famá L (2008) Estudio de las propiedades físico-químicas de recubrimientos compuestos comestibles y biodegradables. Tesis de Doctorado en Ciencias Exactas y Naturales. Área Física. FCEyN. UBA
52. Chang P, Chea PB, Seow CC (2000) Plasticizing-anti-plasticizing effects of water on physical properties of tapioca starch films in the glassy state. *J Food Sci* 65:445
53. Lan H, Hoover R, Jayakody L, Liu Q, Donner E, Baga M, Asare EK, Hucl P, Chibbar RN (2008) Impact of annealing on the molecular structure and physicochemical properties of normal, waxy and high amylose bread wheat starches. *Food Chem* 111:663
54. Bonacucina G, Martino PD, Piombetti M, Colombo A, Roversi F, Palmieri GF (2006) Effect of plasticizers on properties of pregelatinised starch acetate (Amprac 01) free films, *International Journal of Pharmaceutics*. *J Pharm* 313:72
55. Cao X, Chen Y, Chang PR, Huneault MA (2007) Preparation and properties of plasticized starch/multiwalled carbon nanotubes composites. *J Appl Polym Sci* 106:1431
56. Lawton JW, Fanta GF (1994) Glycerol-plasticized films prepared from starch- poly(vinyl alcohol) mixtures: effect of poly(ethylene-co-acrylic acid). *Carbohydr Polym* 23:261
57. Lourdin D, Della Valle G, Colonna P (1995) Influence of amylose content on starch films and foams. *Carbohydr Polym* 27:275

58. Lawton JW (1996) Effect of starch type on the properties of starch containing film. *Carbohydr Polym* 29:203
59. Arvanitoyannis I, Billiaderis CG, Ogawa H, Kawasaki N (1998) Biodegradable films made from low-density polyethylene (ldpe), rice starch and potato starch for food packaging applications. Part 1. *Carbohydr Polym* 36:89
60. García MA, Martino MN, Zaritzky NE (2001) Composite starch-based coatings applied to strawberries (*Fragaria ananassa*). *Nahrung/Food* 45:267
61. Mali S, Grossmann MV, García MA, Martino MN, Zaritzky NE (2002) Microstructural characterization of yam starch films. *Carbohydr Polym* 50:379
62. Vicentini NM, Dupuy N, Leitzelman M, Cereda MP, Sobral PJA (2005) Prediction of cassava starch edible film properties by chemometric analysis of infrared spectra. *Spectrosc Lett* 38:749
63. Rindlav-westling A, Stadingb M, Gatenholma P (1998) Structure, barrier and mechanical properties of amylose and amylopectin films. *Carbohydr Polym* 36:217
64. Myllärinen P, Partanen R, Seppälä J, Forssell P (2002) Effect of glycerol on behaviour of amylose and amylopectin films. *Carbohydr Polym* 50:355
65. García NL, Famá L, Dufresne A, Aranguren M, Goyanes S (2009) A comparison between the physico-chemical properties of tuber and cereal starches. *Food Res Int* 42:976
66. Van Soest JJ, Vliegthart JF (1997) Crystallinity in starch plastics: consequences for material properties. *Trends Biotechnol* 15:208
67. Famá L, Rojas AM, Goyanes S, Gerschenson L (2005) Mechanical properties of tapioca-starch edible films containing sorbates. *LWT* 38:631
68. Talja RA, Hele H, Roos H, Jouppila K (2008) Effect of type and content of binary polyol mixtures on physical and mechanical properties of starch-based edible films. *Carbohydr Polym* 71:269
69. Ma X, Yu J, Wang N (2008) Glycerol plasticized-starch/multiwall carbon nanotube composites for electroactive polymers. *Compos Sci Technol* 68:268
70. Li R, Liu C, Ma J (2011) Studies on the properties of graphene oxide-reinforced starch biocomposites. *Carbohydr Polym* 84:631
71. Souza Rosa RCR, Andrade CT (2004) Effect of chitin addition on injection-molded thermoplastic corn starch. *J Appl Polym Sci* 92:2706
72. Cheetham NWH, Tao L (1998) Solid state NMR studies on the structural and conformational properties of natural maize starches. *Carbohydr Polym* 36:277
73. Biliaderis CG (1992) Structures and phase transitions of starch in food systems. *Food Technol* 46:98
74. Angellier H, Molina-Boisseau S, Dole P, Dufresne A (2006) Thermoplastic starch-waxy maize starch nanocrystals nanocomposites. *Biomacromolecules* 7:531
75. Hulleman SHD, Janssen FHP, Feil H (1998) The role of water during plasticization of native starches. *Science* 39:2043
76. Chaudhry H (1987) *Applied hydraulic transients*, 2nd edn. van Nostrand Reinhold, New York
77. Shogren RL, Jasberg BK (1994) Aging properties of extruded high-amylose starch. *J Environ Polym Degrad* 2:99
78. Godet MC, Buleon A, Tran B, Colonna P (1993) Structural features of fatty acids-amylose complexes. *Carbohydr Polym* 21:91
79. Kalichevski M, Orford PD, Ring SG (1990) The retrogradation and gelation of amylopectins from various botanical sources. *Carbohydr Polym* 198:49
80. Moniruzzaman M, Winey K (2006) Polymer nanocomposites containing carbon nanotubes. *Macromolecules* 39:5194
81. Liu Z, Zhao L, Chen M, Yu J (2011) Effect of carboxylate multiwalled carbon nanotubes on the performance of thermoplastic starch nanocomposites. *Carbohydr Polym* 83:447
82. Wang GJ, Qu ZH, Guo JL, Li Y, Liu L (2006) Study of Multiple-Wall Carbon Nanotubes Functionalized by the Poly(styrene-co-maleic Anhydride). *Acta Chim Sin* 64:2505

83. Muscat D, Adhikari B, Adhikari R, Chaudhary DS (2012) *J Food Eng* 109:189
84. Thunwall M, Boldizar A, Rigdahl M (2006) Compression molding and tensile properties of thermoplastic potato starch materials. *Biomacromolecules* 7:981
85. Lourdin D, Bizot H, Colonna PJ (1997) Antiplasticization in starch–glycerol films. *Appl Polym Sci* 63:1047
86. Gaudin S, Lourdin D, Le Botlan D, Ilari JL, Colonna PJ (1999) Plasticisation and mobility in starch-sorbitol films. *Cereal Sci* 29:273
87. Bergo PVA, Sobral PJA, Prison JM (2009) Physical Properties of Cassava Starch Films Containing Glycerol. Food Engineering Department, FZEA, University of São Paulo, Brazil
88. Chen C-H, Lai L-S (2008) Mechanical and water vapor barrier properties of tapioca starch/ decolorized hsian-tsao leaf gum films in the presence of plasticizer. *Food Hydrocoll* 22:1584
89. Qiao X, Tang Z, Sun K (2011) Plasticization of corn starch by polyol mixtures. *Carbohydr Polym* 83:659
90. Biliaderis CG, Page CM, Maurice TJ, Juliano BO (1986) Thermal characterisation of rice starches: A polymeric approach to phase transitions of granular starch. *J Agric Food Chem* 34:6
91. Levine H, Slade L (1986) A polymer physico-chemical approach to the study of commercial starch hydrolysis products (SHPs). *Carbohydr Polym* 6:213
92. Orford PD, Prker R, Ring SG, Smith AC (1989) Effect of water as a diluent on the glass-transition behavior of malto-oligosaccharides, amylose and amylopectin. *Int J Biol Macromol* 11:91
93. Schenz TW (1995) Glass transition and product stability—An overview. *Food Hydrocoll* 9:307
94. Roos YH (1987) Effect of Moisture on the Thermal Behavior of Strawberries Studied Using Differential Scanning Calorimetry. *J Food Sci* 52:146
95. Roos Y, Karel M (1991) Plasticizing effect of water on thermal behavior and crystallization of amorphous food models. *J Food Sci* 56:38
96. Bizot H, Le Bail B, Lroux J, Davy P, Parker P, Buleon A (1997) Alorimetric evaluation of the glass transition in hydrated, linear and branched polyanhydro glucose compounds. *Carbohydr Polym* 32:33
97. Zeleznak KJ, Hosene RC (1987) The glass transition in starch. *Cereal Chem* 64:121
98. Mathew AP, Dufresne A (2002) Plasticized wazy maize starch: Effect of polyols and relative humidity on material properties. *Biomacromolecules* 3:1101
99. Yang J, Yu J, Ma X (2006) Study on the properties of ethylenebisformamide and sorbitol plasticized corn starch (ESPTPS). *Carbohydr Polym* 66:110
100. Curvelo AAS, Carvalho AJF, Agnelli JAM (2001) Thermoplastic starch–cellulosic fibers composites: Preliminary results. *Carbohydr Polym* 45:183
101. Da Roz AL, Carvalho AJF, Gandini A, Curvelo AAS (2006) The effects of plasticizers on the thermoplastic starch compositions obtained by melt processing. *Carbohydr Polym* 63:417–424
102. Ogale AA, Cunningham P, Dawson PL, Acton JC (2000) Viscoelastic, thermal, and microstructural characterization of soy protein isolate film. *J Food Sci* 65:672
103. Wilhelm HM, Sierakowski MR, Souza GP, Wypych F (2003) Starch films reinforced with mineral clay. *Carbohydr Polym* 52:101
104. Standing M, Rindlav-Westling A, Gatenholm P (2001) Humidity-induced structural transitions in amylose and amylopectin film. *Carbohydr Polym* 45:209
105. Forsell P, Mikkilä J, Moates G, Parker R (1997) Phase and glass transitions behaviour of concentrated barley starch–glycerol mixtures, a model for thermoplastic starch. *Carbohydr Polym* 34:275
106. Fishman ML, Coffin DR, Konstance RP, Onwulata CI (2000) Extrusion of pectin/starch blends plasticized with glycerol. *Carbohydr Polym* 41:317
107. Baughman RH, Cui CX, Zakhidov AA, Iqbal Z, Barisci JN, Spinks GM, Wallace GG, Mazzoldi A, De Rossi D, Rinzler AG, Jaschinski O, Roth S, Kertesz M (1999) Carbon nanotubes actuors. *Sci* 284:1340
108. Dresselhaus MS, Dresselhaus G, Eklund PC (1999) Science of fullerenes and carbon nanotubes. Academic, San Diego

109. Harris PJF (1999) Carbon nanotube and related structures. New materials for the 21st century. Cambridge University Press, Cambridge, UK
110. Nanocyl (2009) <http://www.nanocyl.com/CNT-Expertise-Centre/Carbon-Nanotubes>
111. Coleman J, Khan U, Blau W, Gunko Y (2006) Small but strong: a review of the mechanical properties of carbon nanotube-polymer composites. *Carbon* 44:1624
112. Nuriel S, Liu L, Barber AH, Wagner HD (2005) Direct measurement of multiwall nanotube surface tension. *Chem Phys Lett* 404:263
113. Baughman RH, Zakhidov AA, de Heer WA (2002) Carbon nanotubes—the route toward applications. *Science* 297:787
114. Bianco A, Kostarelos K, Prato M (2005) Applications of carbon nanotubes in drug delivery. *Curr Opin Chem Biol* 9:674
115. Bianco A, Prato M (2003) Can carbon nanotubes be considered useful tools for biological applications? *Adv Mater* 15:1765
116. Cai D, Mataraza JM, Qin ZH, Huang Z, Huang J, Chiles TC, Carnahan D, Kempa K, Ren Z (2005) Highly efficient molecular delivery into mammalian cells using carbon nanotube spearing. *Nat Methods* 2:449
117. Cherukuri P, Bachilo SM, Litovsky SH, Weisman RB (2004) Near-infrared fluorescence microscopy of single-walled carbon nanotubes in phagocytic cells. *J Am Chem Soc* 126:15638
118. Mohagheghian I, McShane GJ, Stronge WJ (2011) Impact response of polyethylene nanocomposites. *Proc Eng* 10:704
119. Fattahpour V, Moosavi M, Mehranpour M (2012) An experimental investigation on the effect of rock strength and perforation size on sand production. *J Petrol Sci Eng.* 86–87:172
120. Krogars K, Antikainen O, Heinämäki J, Laitinen N, Yliruusi J (2002) Tablet film-coating with amylose-rich maize starch. *Eur J Pharm Sci* 17:23
121. Mehvar GF, Han JH (2004) Physical and mechanical properties of high amylose rice and pea starch films as affected by relative humidity. *J Food Sci* 69:449
122. Krogars K, Heinämäki J, Antikainen O, Karjalainen M, Yliruusi J (2003) A novel of amylose corn starch dispersion as an aqueous film coating for tablets. *Pharm Develop Technol* 8:211
123. Yan L, Chang PR, Zheng P (2011) Preparation and characterization of starch-grafted multiwall carbon nanotube composites. *Carbohydr Polym* 84:1378
124. Star A, Stoddart JF (2002) Dispersion and solubilization of single-walled carbon nanotubes with a hyperbranched polymer. *Macromolecules* 35:7516
125. Ma X, Chang PR, Yu J, Lu P (2008) Characterization of glycerol plasticized-starch (GPS)/carbon black (CB) membranes prepared by melt extrusion and microwave radiation. *Carbohydr Polym* 74:895
126. Macking TJ (1992) A comparison of instrumented impact testing and Gardner impact testing. Santa Barbara, CA: Dynatup Products Division General Research Corp
131. Talja RA, Roos YH (2001) Phase and state transition effects on dielectric, mechanical, and thermal properties of polyols. *Thermochim Acta* 380:109
133. Casey A, Farrell GF, McNamara M, Byrne HJ, Chambers G (2005) Interaction of carbon nanotubes with sugar complexes. *Synth Metals* 153:357
134. Shi Kam NW, Dai H (2005) Carbon nanotubes as intracellular protein transporters: generality and biological functionality. *J Am Chem Soc* 127:6021
135. Jiang W, Qiao W, Sun K (2006) Mechanical and thermal properties of thermoplastic acetylated starch/poly(ethylene-co-vinyl alcohol) blends. *Carbohydr Polym* 65:139
136. Chang PR, Zheng P, Liu B, Anderson DP, Yu J, Ma X (2011) Characterization of magnetic soluble starch-functionalized carbon nanotubes and its application for the adsorption of the dyes. *J Hazard Mater* 186:2144
137. Bello-Pérez LA, Roger P, Colonna P, Paredes-López (1998) Macromolecular features of amaranth starch. *Cereal Chem* 75:395

138. Pérez E, Breene W and Bahanasey Y (1998) Gelatinizations profiles of Peruvian carrot, cocoyam and potato starches a measured with Brabender Viscoamylograph, Rapid Viscoanalyzer and Differential Scanning Calorimeter. *Starch/Stärke* 50:14
139. Yuan RC, Thompson DB, Boyer CD (1993) Fine structure of amylopectin in relation to gelatinization and retrogradation behavior of maize starches from three wax-containing genotypes in two inbred lines. *Cereal Chemistry* 70:81
140. Maauf AG, Che Man YB, Asbi BA, Junainah AH, Kennedy JF (2001) Gelatinization of sago starch in the presence of sucrose and sodium chloride in assessed by differential scanning calorimetry. *Carbohydrate Polymers* 45:335
141. Hizukuri S, Takeda Y, Manuta N, Juliano BO (1989) Molecular structures of rice starches. *Carbohydr Res* 147:227

Feng Luo, Lanlan Pan, Xibo Pei, Rui He, Jian Wang, and
Qianbing Wan

Contents

1	CNTs	174
2	PCL	176
3	Tissue Engineering	177
4	Composite Processing	181
4.1	Solution Processing of CNTs and Polymer	181
4.2	Bulk Mixing	181
4.3	Melt Mixing	182
4.4	In Situ Polymerization	182
4.5	CNT-Based Fibers and Films	182
5	Applications	183
5.1	CNTs as Scaffolds for Bone Regeneration	183
5.2	CNTs for Neural Applications	184
6	PCL–CNTs Nanocomposites	185
	References	190

Abstract

Many biomaterial applications have been realized by using polymeric scaffolds among which the biodegradable polymers, such as polycaprolactone (PCL), have drawn extensive attention with regard to tissue regeneration. However,

F. Luo (✉) • X. Pei • R. He

West China School of Stomatology, Sichuan University, Chengdu, Sichuan, China

e-mail: luofeng0122@sina.com; pxb1024@163.com; heruiminli@sina.com

L. Pan

Department of Periodontics, The Affiliated Stomatology Hospital of Chongqing Medical University, Chongqing, China

e-mail: shellypan09@163.com

J. Wang • Q. Wan

Department of Prosthodontics, West China School of Stomatology, Sichuan University, Chengdu, Sichuan, China

e-mail: ferowang@hotmail.com; champion@scu.edu.cn

J.K. Pandey et al. (eds.), *Handbook of Polymer Nanocomposites. Processing, Performance and Application – Volume B: Carbon Nanotube Based Polymer Composites*,
DOI 10.1007/978-3-642-45229-1_41, © Springer-Verlag Berlin Heidelberg 2015

PCL does not have the mechanical properties to be applied in high load bearing situation, which has limited its use in bone tissue engineering. One of the most effective methods of increasing the mechanical properties (elastic modulus and tensile strength) of a polymer is by reinforcing with a second-phase material. Hence, researchers have used different types of second-phase materials for mechanical strengthening of PLA, PCL, and their copolymers (PLC). Among all of these, carbon nanotubes (CNT) seem to be the reinforcement with most potential, due to their very high mechanical properties (Young's modulus 0.2–1 TPa, tensile strength 11–63 GPa) and fiber-like structure. Furthermore, the addition of carbon nanotubes to PCL can enhance the conductivity, thermal, mechanical and gas barrier properties of PCL. All these findings have caused carbon nanotubes to be the suitable second-phase reinforcement for biodegradable polymers in orthopedic scaffold applications.

Keywords

Polycaprolactone • Carbon nanotubes • Tissue engineering • Nanocomposites

1 CNTs

The properties and applications of carbon nanotubes (CNTs) and related materials have been very active research fields over the last decade [1, 2]. CNTs possess high flexibility, low mass density, and large aspect ratio (typically >1,000), whereas predicted and some experimental data indicate extremely high tensile modulus and strengths for these materials. The excellent properties of CNTs are attributed to its unique structural features, which are well-ordered, hollow nanostructures consisting of carbon atoms bonded to each other via sp^2 bonds that are stronger than sp and sp^3 bonds. Individual single-walled carbon nanotubes (SWCNTs) can be metallic or semiconducting. The latter can transport electrons over long lengths without significant interruption which makes them more conductive than copper [3, 4]. It is indeed the combination of mechanical and electrical properties of individual nanotubes that makes them the ideal reinforcing agents in a number of applications. The first ever polymer nanocomposites using CNTs as fillers were reported in 1994 by Ajayan et al. [5]. Since then, there have been many papers dedicated to study the mechanical and electrical properties of polymer–CNTs nanocomposites. However, as-grown CNTs are normally mixtures of various chiralities, diameters, and lengths, not to mention the presence of impurities and other defects. Furthermore, CNT aggregation has been found to dramatically hamper the mechanical properties of fabricated nanocomposites. Finally, due to their small size, CNTs are normally curled and twisted, and therefore, individual CNTs embedded in a polymer only exhibit a fraction of their potential. Thus, the superb properties of CNTs cannot as yet be fully translated into finished products with high strength and stiffness.

Lots of researchers hold that functionalized CNTs (carboxylated or hydroxylated CNTs) are water soluble and could eventually be cleared from systemic blood

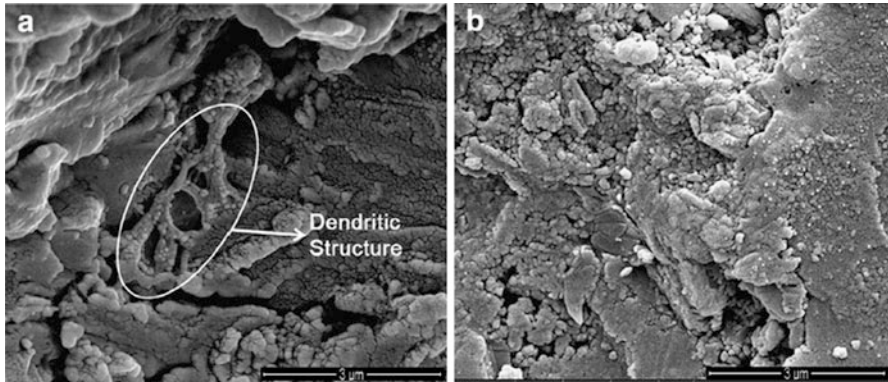


Fig. 8.1 Surface morphologies of the functionally graded composite coating (a) and pure HA coating (b). The CNTs were entangled with each other to form a dendritic structure, which was almost fully covered by nano-sized nodular HA particles [10]

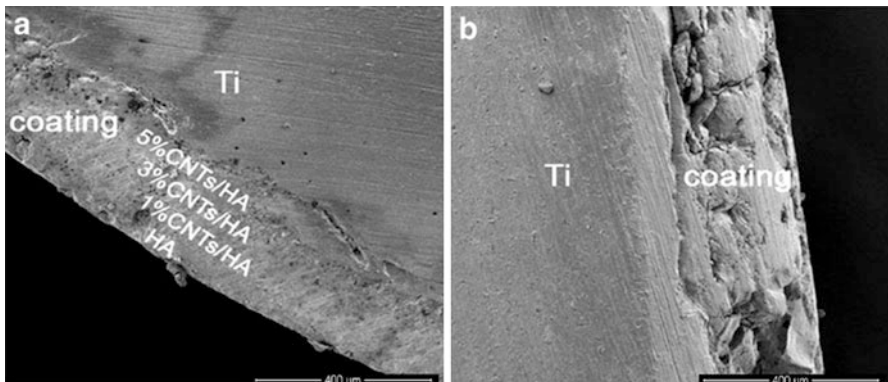


Fig. 8.2 The typical cross-sectional appearance of (a) functionally graded CNTs/HA composite coating (the bottom layer with 5 % CNTs/HA composite powders, the intermediate layers with 3 % CNTs/HA and 1 % CNTs/HA composite powders, and the top layer with pure HA) and (b) pure HA coating; all the thickness of the coatings ranged from 180 to 220 μm [10]

circulation through the renal excretion route [6], which means that functionalized CNTs are safe in biomedical application such as scaffold [7]. In addition, some reports also pointed out that the mechanical properties of some biodegradable materials were improved with the incorporation of carbon nanotubes [8, 9]. One of our investigations (Figs. 8.1, 8.2, and 8.3) shows that functionally graded carbon nanotubes/hydroxyapatite (CNTs/HA) composite coatings have been fabricated by laser cladding technique using CNTs/HA composite powders and deposited on the Ti substrate by laser deposition successfully. The CNTs were dispersed homogeneously in the coatings to form an interconnected web and the cylinder graphic structure of CNTs was not changed after laser irradiation. The bonding strength of

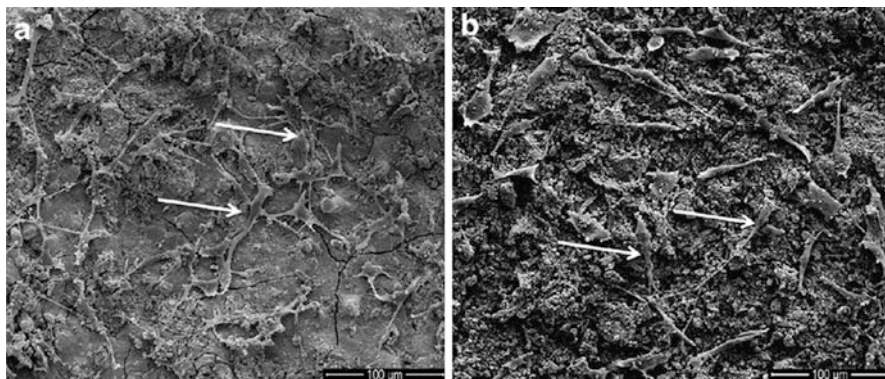


Fig. 8.3 SEM micrographs of MC3T3-E1 cells on the pure HA coating (a) and functionally graded CNTs/HA composite coating (b) after culturing for 7 days. As marked by the arrows, cells exhibit normal morphologies, with spreading and process formation indicative of well attachment and growth [10]

the functionally graded coating was nearly twice higher than that of pure HA coating, and the *in vitro* cellular biocompatibility tests also reveal that the functionally graded composite coating has comparable *in vitro* bioactivity with pure HA coating. Furthermore, the addition of CNTs enhances the mechanical performance of the coating without deteriorating the properties of HA [10]. What's more, plenty of researches have confirmed that CNTs could be used as excellent substrates for cellular growth [11, 12]. For example, substrates made from MWNT as well as SWNT have been used as the biocompatible platforms for neuronal growth and differentiation [13]. Furthermore, MWNTs were also proved to be an osteoproliferative material (i.e., a material that can elicit both intracellular and extracellular cell responses at the material surface) [14].

2 PCL

Polycaprolactone (PCL) was one of the earliest polymers synthesized by the Carothers group in the early 1930s [15]. It became commercially available following efforts to identify synthetic polymers that could be degraded by microorganisms [16]. PCL can be prepared either by ring-opening polymerization of ϵ -caprolactone using a variety of anionic, cationic, and coordination catalysts or via free radical ring-opening polymerization of 2-methylene-1-3-dioxepane [17]. PCL is a hydrophobic, semicrystalline polymer; its crystallinity tends to decrease with increasing molecular weight. The good solubility of PCL, its low melting point (59–64 °C), and exceptional blend-compatibility have stimulated extensive research into its potential application in the biomedical field [18, 19].

Consequently, during the resorbable-polymer-boom of the 1970s and 1980s, PCL and its copolymers were used in a number of drug delivery devices. Attention

was drawn to these biopolymers owing to their numerous advantages over other biopolymers in use at that time. These included tailorable degradation kinetics and mechanical properties, ease of shaping and manufacture enabling appropriate pore sizes conducive to tissue ingrowth, and the controlled delivery of drugs contained within their matrix. Functional groups could also be added to make the polymer more hydrophilic, adhesive, or biocompatible which enabled favorable cell responses. Due to the fact that PCL degrades at a slower rate than polyglycolide (PGA), poly(d,l-lactide) (PDLA) and its copolymers were originally used in drug delivery devices and slowly degrading suture materials (MaxonTM).

PCL is a thermoplastic biodegradable polyester synthesized by chemical conversion of crude oil. PCL has good water, oil, solvent, and chlorine resistance, low melting point, and low viscosity and is easily processed using conventional melt blending technologies [20]. PCL is being investigated for use in biomedical utensils, in pharmaceutical controlled release systems, and in biodegradable packaging [21]. PCL is suitable for controlled drug delivery due to a high permeability to many drugs, excellent biocompatibility, and the ability to be fully excreted from the body. PCL is applied in medical devices, such as sutures, wound dressings, contraceptive devices, fixation device, and dentistry. PCL can also be used as scaffold material for tissue engineering, such as cartilage engineering, tendon and ligament engineering, blood vessel engineering, skin engineering, and nerve engineering.

3 Tissue Engineering

Tissue engineering can be defined as “an interdisciplinary field that applies the principles of engineering and life sciences toward the development of biological substitutes that restore, maintain, or improve tissue function or a whole organ” [22]. Tissue engineering was once categorized as a subfield of “biomaterials,” but having grown in scope and importance, it can now be considered as a field in its own right. It is the use of a combination of cells, engineering and materials methods, and suitable biochemical and physiochemical factors to improve or replace biological functions. Tissue engineering is closely associated with applications that repair or replace portions of whole tissues (e.g., bone, cartilage, blood vessels, and bladder). Usually, the tissues involved require certain mechanical and structural properties for proper functioning.

Powerful developments in tissue engineering have yielded a novel set of tissue replacement parts and implementation strategies. Scientific advances in biomaterials, stem cells, growth and differentiation factors, and biomimetic environments have created unique opportunities to fabricate tissues in the laboratory from combinations of engineered extracellular matrices (“scaffolds”), cells, and biologically active molecules. A schematic showing this type of approach is depicted in Fig. 8.4, which shows the combination of cells and biomolecules with a scaffold. The scaffold must be capable of supporting cell attachment, proliferation, and differentiation *in vitro* and may then be transplanted *in vivo*. Among the major challenges now facing tissue engineering

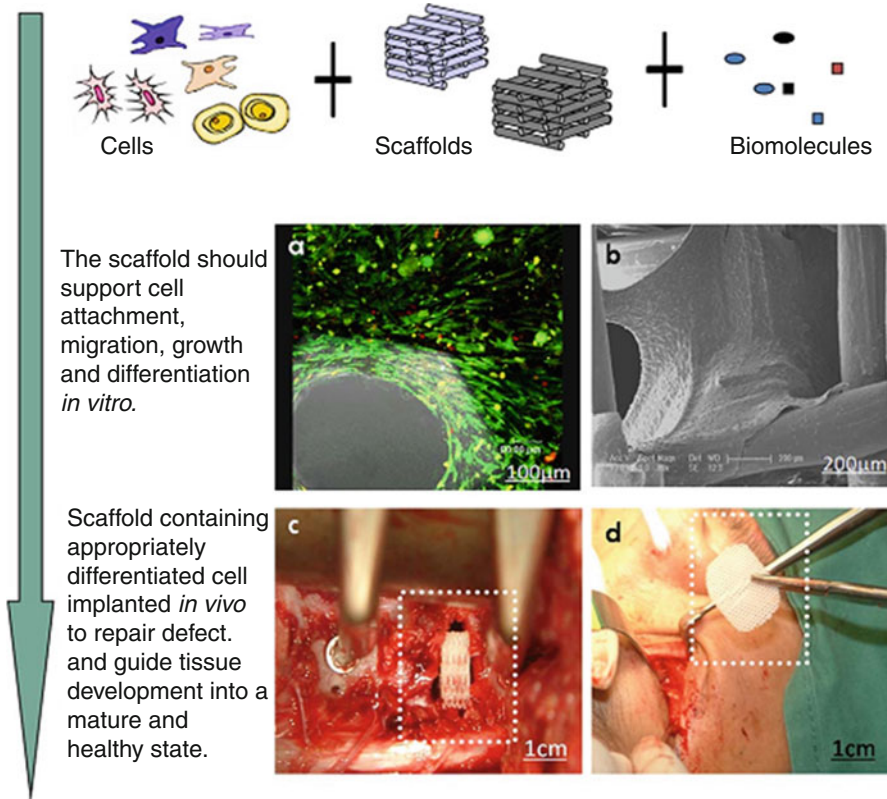


Fig. 8.4 Scaffold-based tissue engineering aims to promote the repair and/or regeneration of tissues through the incorporation of cells and/or biomolecules within a 3D scaffold system which can be maintained *in vitro* culture conditions until implantation (Reproduced with permission from (2008) CRC Press [24])

is the need for more complex functionality, as well as both functional and biomechanical stabilities in laboratory-grown tissues destined for transplantation. The continued success of tissue engineering, and the eventual development of true human replacement parts, will grow from the convergence of engineering and basic research advances in tissue, matrix, growth factor, stem cell, and developmental biology, as well as materials science and bioinformatics.

There are a vast array of manufacturing techniques to create scaffolds for tissue engineering, but one must pay special attention to the scaffold specifications and understand the interplay of factors affecting the material composition and design criteria. The desirable feature of any implantable polymeric scaffold material would be synchronization of polymer degradation with the replacement by natural tissue produced from cells. Figure 8.5 gives a graphical illustration of this complex interplay showing the molecular weight loss of a resorbable scaffold, and how this relates to its mass loss and also to the growth of tissue *in vitro* prior to implantation.

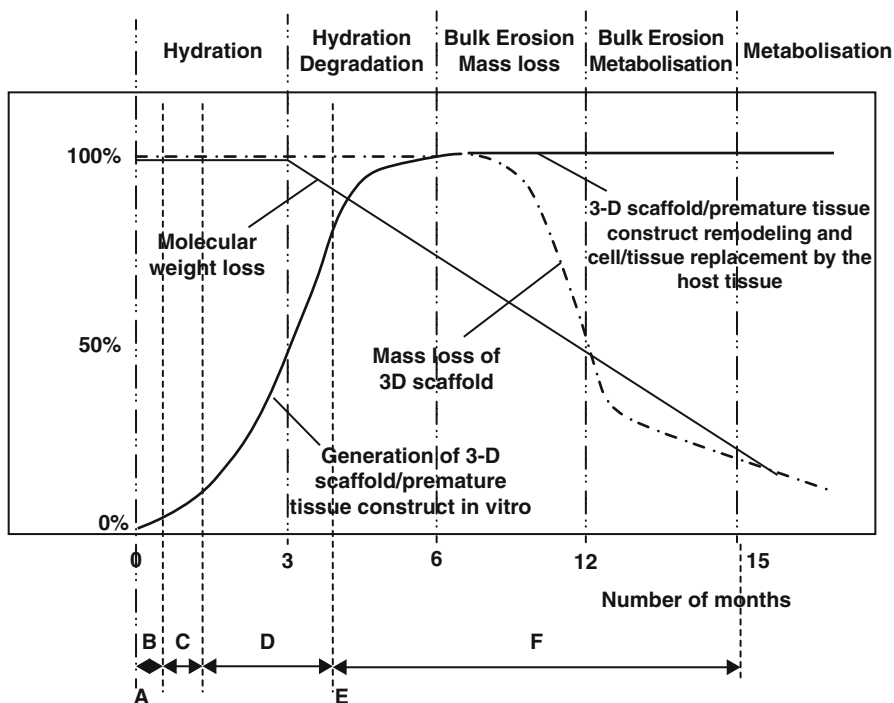


Fig. 8.5 Graphical illustration of the complex interdependence of molecular weight loss and mass loss of a 3D scaffold plotted against the time frame for tissue engineering of a bone transplant. Fabrication of a bioresorbable scaffold (A). Seeding of the osteoblast population into the scaffold in static culture (Petri dish) (B). Growth of premature tissue in a dynamic environment (spinner flask) (C). Growth of mature tissue in a physiological environment (bioreactor) (D). Surgical transplantation (E). Tissue-engineered transplant assimilation/remodeling (F) (Reproduced with permission from (2000) Elsevier [23])

The degradation and resorption kinetics of the scaffold are designed to allow the seeded cells to proliferate and secrete their own extracellular matrix in the static and dynamic cell-seeding phase (weeks 1–12), as concomitantly the scaffold gradually resorbs, leaving sufficient space for cell proliferation and new tissue growth.

The physical support by the 3D scaffold is maintained until the engineered tissue has sufficient mechanical integrity to support itself. The following characteristics are desirable for scaffold candidates: (i) three-dimensional and highly porous structures with an interconnected pore network, for cell growth and flow transport of nutrients and metabolic waste; (ii) biocompatible and bioresorbable with a controllable degradation and resorption rate to match cell/tissue growth in vitro and/or in vivo; (iii) suitable surface chemistry for cell attachment, proliferation, and differentiation; and (iv) mechanical properties to match those of the tissues at the site of implantation [23]. In addition, the demanding requirements dictated by


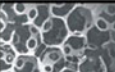

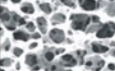

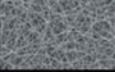
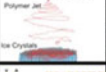
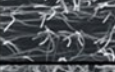
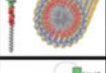

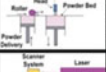
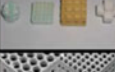
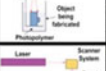


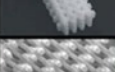
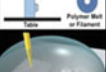



	Scaffold Name	Porosity & Size	Schematic	Advantage & Disadvantages	Image
Conventional Scaffolds	a Particulate Leaching	Porosity < 90% Pore Size 5-100 μ m		Adv: Simple and user friendly method, suitable with a range of biomaterials and no special equipment is needed. Disadv: Density differences result in non uniform pore size distribution. Difficult to achieve full interconnectivity and large pore interconnections. Skinning effect on outside surfaces of scaffolds. Organic solvents typically required.	
	b Thermally Induced Phase Separation (TIPS)	Porosity < 70% Pore Size 5-100 μ m		Adv: Simple method, suitable with a range of biomaterials and no special equipment is needed fully interconnecting pores and large pore interconnections can be fabricated if spinodal decomposition is achieved. Disadv: Skinning effect on outside surfaces of scaffolds. Organic solvents typically required.	
Nano-scale Scaffolds	c Electrospinning	Porosity < 90% Pore Size < 1-10 μ m		Adv: Inexpensive method to produce nano/micro fibers from a wide range of polymers. Excellent cell and tissue compatibility for mesenchymal cells. By using ice crystals as a collector, scaffolds with large pores and significant volume may be fabricated.	
	d Electrospinning onto ice crystals	Porosity 95% Pore Size 20-200 μ m		Disadv: Organic solvents often required, scaffolds with volume, and large pore size or thickness are difficult to manufacture except by using ice crystal technique which has the disadvantage that sublimation required that increases complexity of manufacture. Mechanical properties of electrospun fibers is generally poor.	
	e Self-assembling Nanofibers	Porosity > 95% Pore Size 200-800 nm		Adv: Self assembling system, typically in water and can be formed in the presence of cells, with bioactive functionality. Disadv: Relatively expensive to manufacture in significant quantities. Weak mechanical properties probably restrict this type of scaffold to soft tissues.	
Solid Freeform Fabrication (SFF) Scaffolds	f 3 Dimensional Printing (3DP)	Porosity < 45-60% Pore Size 45-1600 μ m		Adv: SFF techniques have accurate control over pore size and interconnectivity over conventional/nanoscale approaches. The layer-by-layer process allows fabrication of complex and anatomically-shaped structures. Disadv: Expensive machinery required, resolution limitations at lower pore sizes. Biomaterials need to come in powder form with controlled particle size.	
	g Stereolithography	Porosity < 90% Pore Size 175+ μ m		Adv: Accurate control over pore size and interconnectivity. Layer-by-layer process allows fabrication of complex and anatomically-shaped structures. Disadv: Expensive machinery required. Polymers compatible with UV curing is required.	
	h Selective Laser Sintering (SLS)	Porosity < 25% Pore Size 30-2500 μ m		Adv: Accurate control over pore size and interconnectivity. Layer-by-layer process allows fabrication of complex pore architectures and anatomically-shaped structures. Disadv: Expensive machinery required, resolution limitations at lower pore sizes. Biomaterials need to come in powder form with light controlled particle size, mainly applicable to ceramic materials.	
	i Fused Deposition Modelling/3D Plotting	Porosity < 90% Pore Size 100-2000 μ m		Adv: Accurate control over pore size and interconnectivity. Layer-by-layer process allows fabrication of complex pore architectures and anatomically-shaped structures with good resolution. Disadv: Since the technique uses polymer melts, it is limited to thermoplastics. Low pore sizes difficult to achieve while maintaining high porosity.	
	j Direct Writing	Porosity < 90% Pore Size: 5-100 μ m		Adv: Accurate control over pore size and interconnectivity. Layer-by-layer process allows fabrication of complex architectures with excellent resolution. Disadv: Expensive machinery required. Biomaterials used need to be able to form polyelectrolyte inks. Significant times are required to manufacture scaffolds with suitable thickness.	

Fig. 8.6 Snapshot: polymer scaffolds for tissue engineering. Fabrication routes for PCL scaffolds (Reproduced with permission from (2009) Elsevier [69])

orthopedic scenarios require a certain degree of initial mechanical support, and as such, polymeric devices alone are insufficient and must be combined with additional components such as cells, growth factors, and appropriate environments [24]. The degradation properties of a scaffold are therefore of crucial importance for biomaterial selection and design but also the long-term success of a tissue-engineered construct.

Scaffolds for tissue engineering have become a large focus of research attention and can be fabricated in a wide variety of ways, and a biomaterial which lends itself very well to scaffold fabrication is PCL. PCL is an incredibly versatile bioresorbable polymer, and by way of its superior rheological properties, it can be used by almost any polymer processing technology to produce an enormous array of scaffolds. The major scaffold fabrication technologies in which PCL has been used extensively are summarized in Fig. 8.6.

4 Composite Processing

To maximize the advantage of CNTs as effective reinforcement for high-strength polymer composites, the CNTs should not form aggregates and must be well dispersed to enhance the interfacial interaction with the matrix. Several processing methods available for fabricating CNT/polymer composites based on either thermoplastic or thermosetting matrices have been described in past review articles [25–27]. They mainly include solution mixing, in situ polymerization, melt blending, and chemical modification processes. Although inherently different processing routes have been attempted, they all address important issues that affect composite properties, such as exfoliation of CNT bundles and ropes, homogeneous dispersion of the individual tubes into the matrix, alignment, and interfacial bonding.

The effective utilization of CNT material in composite applications depends strongly on their ability to be dispersed individually and homogeneously within a matrix. An optimized interfacial interaction between the CNT side walls and the matrix should result in an efficient load transfer to the “hard” component of the composite. All processing methods known thus far for CNT-based composites are described below. Due to the huge volume of related literature, only the seminal works will be discussed for each processing method.

4.1 Solution Processing of CNTs and Polymer

The most common method for preparing CNT–polymer composites has been to mix both components into a certain solvent and evaporate the latter to form a composite film. The general protocol for all solution processing methods includes the dispersion of CNT powder in a liquid medium by vigorous stirring and/or sonication, mixing the CNT dispersion with a polymer solution and controlled evaporation of the solvent with or without vacuum conditions. In general, the most efficient dispersion of tubes during the first step is achieved by bath or tip sonication.

4.2 Bulk Mixing

Milling is a mechanical process that leads to local generation of high pressure as a result of collisions throughout the grinding media. Concerning applications in CNT nanotechnology, this method has been used to shorten the lengths of carbon nanostructures [28]. A solid-state mechanochemical pulverization process, namely, pan milling, was used to prepare a CNT/polypropylene composite powder [29]. This powder was subsequently melt mixed with a twin-roll masticator to obtain a homogeneous composite. The length of the CNTs was reduced from a few micrometers to 500 nm.

4.3 Melt Mixing

Due to the fact that thermoplastic semicrystalline polymers soften when heated above their melting point, melt processing has been a very valuable technique for the fabrication of CNT-based composites. In addition, the method is suitable for polymers that cannot be processed with solution techniques due to their insolubility in common solvents.

In general, melt processing involves the blending of polymer melt with CNT material by application of intense shear forces. Depending on the final morphology/shape of the composites, the bulk samples can then be processed by several techniques, such as extrusion.

4.4 In Situ Polymerization

Since 1999, in situ polymerization of vinyl monomers in the presence of CNT material has been extensively studied for the preparation of functional composites. The main advantage of this method is that it produces polymer-grafted tubes, mixed with free polymer chains. Moreover, due to the small size of monomeric molecules, the homogeneity of the resulting composite adducts is much higher than mixing CNTs and polymer chains in solution. In this sense, the method allows the preparation of composites with high CNT weight fraction.

4.5 CNT-Based Fibers and Films

4.5.1 Composite Fibers

For many applications, fibrous materials are more suitable than bulk materials. In addition, fiber production techniques tend to be suited for the alignment of nanotubes within the polymer matrix. A number of studies have focused on the production of composite fibers by melt processing.

Electrospinning is a simple, relatively efficient technique to fabricate polymer fibers with diameters ranging from several nanometers to several micrometers [30]. The electrospun fibers are expected to have wide applications, such as electronic devices, filters, sensors, protective clothes, and biomaterials (e.g., wound dressing, scaffolds in tissue engineering, drug delivery system, etc.) because of their high surface area-to-volume ratio and porosity [31, 32]. Recently, carbon nanotubes (CNTs) have been compounded to impart more functions in polymeric materials, such as thermal, electrical, magnetic, optical, and increased mechanical properties [33].

Saeed et al. [34] attempted to prepare electrospun PCL/MWNT nanocomposite fibers and found that the PCL/*p*-amino benzoic acid-functionalized MWNT nanocomposite fibers had better thermal stability than PCL and PCL/pristine MWNT nanocomposite fibers. The functionalized nanocomposite fibers also showed a relatively broader diameter than the pure PCL nanofibers and formed fewer

beads than the PCL/pristine MWNT nanocomposite fibers. When the content of functionalized MWNTs exceeded 2 wt%, the nanocomposites could not be electrospun.

4.5.2 Composite Films

In 2002, Kotov and co-workers [35] developed a sophisticated method for the preparation of CNT-based composites, the layer-by-layer (LBL) assembly process. This involves building up a layered composite film by alternating adsorption of monolayers of CNTs and polyelectrolyte chains (PEI), attracted to each other by electrostatic and van der Waals interactions. Actually, the composite film could be formed by dipping a glass substrate into dispersions of CNTs and polymer solutions. In this way as many as 40 layers could be assembled. In order to further enhance the structural integrity of the film, cross-linking was induced. After every fifth deposition cycle, a layer of CNTs was replaced with a layer of poly(acrylic acid) (PAA) to introduce carboxyl functionalities for amide cross-linking between polyelectrolytes. The film was then heated to 120 °C, resulting in amide bonds between PAA and PEI. In addition, covalent bonds were also formed between PEI and CNTs at these temperatures, and finally, the film was cross-linked by a glutaraldehyde solution. This method has significant advantages since very high CNT weight fractions can be obtained (~50 %) which brings about an improvement of the mechanical properties of the composite films.

5 Applications

5.1 CNTs as Scaffolds for Bone Regeneration

The bone is a hard tissue that provides mechanical support to our bodies, protects other internal organs, and produces and stores blood cells in bone marrow. Hence, a prerequisite is that the materials used as bone scaffold must possess superior mechanical properties. Considering the excellent mechanical strength of CNTs, for example, CNTs are the strongest known material with Young's (elastic) modulus higher than 1 T Pa [36, 37] (comparable to that of diamond) and a tensile strength up to 63 GPa [38]. Naturally, there are kinds of studies focusing on using these carbon nanostructures as reinforcing agents in composite materials [39, 40] and especially in bone scaffolds [41, 42]. Furthermore, compared to other metallic or ceramic-based bone scaffolds used in orthopedics (such as titanium, stainless steel, alumina, etc.), SWNTs are less dense and therefore will make lighter scaffolds with very high strength. Also, CNTs can be functionalized with different side groups which can improve the biocompatibility properties [43, 44] and/or mechanical strength [45] of the tube/fiber-based scaffolds. Such as (i) mixed purified SWCNTs and aniline are together [46], (ii) through oxidation and carboxyl-based couplings, CNTs can be conjugated with various functional groups such as bioactive agents (e.g., peptides [47], proteins [12], and nucleic acids [48]) and therapeutic agents (such as anticancer drugs [49]). Importantly, by bonding with suitable groups,

CNTs can become soluble in aqueous [50] or organic solvents [70]. In addition, MWCNTs can be considered to be an osteopductive material (i.e., a material that can elicit both intracellular and extracellular cell responses at the material surface) [73, 14]. Compared to osteoconductive materials (which only elicit an extracellular response at their interfaces), osteopductive materials are more desirable in orthopedic implants since they promote faster integration of bone to the implant surface.

5.2 CNTs for Neural Applications

With the increasing age and population of the world, a greater number of patients will need various neural implants. However, traditional neural implantation and surgery (such as using autografts, allografts, xenografts, and silicon probes for the continuous diagnosis and treatment of neural tissue and other biomaterial nerve graft devices) have a variety of problems and cannot satisfy the high performance demands necessary for today's patient. Specifically, for autografts in which implant donor nerves from other parts of the body are used (such as the sensory nerves in the upper extremity [51]), it is difficult to obtain enough donor nerves, and this lack of available nerves may result in functional impairment [52, 53]. In addition, allografts and xenografts have the risk of transmitting diseases and the foreign body response, which frequently lead to high implant failure rates [54, 55]. Unfortunately, due to the complexity of the nervous system anatomy and function, repairing damaged nerves as well as recovering full function of injured nerves have been challenging when compared to other tissue repairs (such as bone repair). As an emerging interdisciplinary field, neural tissue engineering has evoked increasing interest from scientists wishing to develop novel and improved biological scaffolds that restore, maintain, or improve neural tissue functions.

In addition to the nanostructured features, similar to the characteristics of natural neural tissues (such as nanostructured extracellular matrices that neural cells interact with), CNTs also have exceptional electrical, mechanical, and biocompatible properties, which make CNTs excellent candidates for neural tissue repair. Specifically, with the rapid development of CNT production technologies, a variety of CNTs with nanometer to millimeter lengths and widths have been synthesized and widely investigated for various neural applications [56, 57]. For example, as described, Mattson et al. provided the first evidence that MWCNTs can be used to support neuronal cell attachment and growth [58]. Furthermore, studies have shown that CNTs chemically functionalized with various bioactive molecules can improve neural regeneration activity including neurite branching, outgrowth, and attachment of growth cones [13]. Matsumoto et al. demonstrated that MWCNTs can regulate and promote neurite outgrowth when covalently bonded with neurotrophin [59]. Hu et al. reported that a 18–19 wt% SWCNT with polyethyleneimine (PEI) copolymer has been synthesized to effectively lengthen neurites and increase neurite branches approximately comparable to those on polyethyleneimine [13]. In addition, the high electrical conductivity of CNTs can enhance neuronal

circuit network activities. Lovat et al. reported that the electrical signal transfer on neuronal networks can potentially be improved by using purified MWCNTs [60]. Besides, various patterned CNT islands, matrices, and films have been fabricated in order to improve neural applications [61]. Moreover, in order to overcome the mechanical failure of polymer/CNT composites mainly originating from weak CNT connectivity in composites, Mamedov et al. prepared freestanding SWCNT/polyelectrolyte membranes via a layer-by-layer assembly [35]. Freestanding SWCNT/polyelectrolyte membranes have exceptional tensile strength even approaching those of hard ceramics. CNTs may also potentially serve as substrates to impregnate progenitor cells (such as stem cells) and selectively differentiate them into favorable neuronal cells at injury sites. Jan and Kotov [62] reported that the layer-by-layer assembled SWCNT/polyelectrolyte composites improved the differentiation of mouse embryonic neural stem cells into neurons as well as astrocytes and helped neurite outgrowth, for instance.

6 PCL–CNTs Nanocomposites

As previously detailed, both carbon nanotubes (CNTs) and polycaprolactone (PCL) possess advanced properties; in order to combine the advantages of these two materials, as well as overcome the disadvantages, researchers have done a lot of work, which opens up the field of biomedical/biomechanical applications of these hybrids. Lots of studies have tried kinds of techniques, “grafting to” technique, “grafting from” method, melt mixing method, etc., to get PCL–CNTs nanocomposites. Currently, most researches only focused on the performance of a particular aspect of this nanocomposite material. In addition, some papers have been published utilizing these characteristics for engineering applications such as bone tissue engineering, nanosensors, and so on.

Trujillo et al. [63] studied the nucleation and crystallization behavior of melt-mixed PCL–CNT nanocomposites. In their work, the mixtures of PCL and pristine MWNTs were prepared by extrusion with different nanofiller contents: 0.3 %, 0.5 %, 0.7 %, 1 %, and 3 %. They reported that the nucleation effect saturates at only 0.5 % (a value much lower than those previously reported in the literature for similar nanocomposites), indicating that the dispersions obtained were excellent, which was corroborated both by TEM observations and by the determination of a very low dielectric percolation threshold (i.e., 0.3 %). Furthermore, supernucleation effects were obtained up to a maximum of approximately 200 % efficiency in their self-nucleation experiments, which was attributed to the excellent dispersion achieved. Isothermal crystallization experiments performed by differential scanning calorimeter (DSC) showed an increase in the crystallization kinetics of PCL with increases in MWNT content as a consequence of the supernucleation effect.

Kim et al. [72] demonstrated that poly(ethylene 2,6-naphthalate) (PEN) nanocomposites reinforced with a very small quantity of carbon nanotube (CNT) were prepared by melt compounding using a twin-screw extruder. Morphological observations revealed that the modified CNT was uniformly dispersed in the PEN

matrix and increased interfacial adhesion between the nanotubes and the polymer matrix, as compared to the untreated CNT. Furthermore, a very small quantity of the modified CNT could improve the mechanical and thermal properties of the PEN nanocomposites. This study also demonstrated that the non-isothermal crystallization behaviors of the PEN nanocomposites were strongly dependent on the presence of the modified CNT and cooling rate.

Monica Mattioli-Belmonte et al. [64] reported the mechanical, thermal, and biological characterizations of a solid free form microfabricated carbon nanotube–polycaprolactone composite, in which both the quantity of nanotubes in the matrix and the scaffold design varied in order to tune the mechanical properties of the material. The creep and stress relaxation behavior of the composite materials were also analyzed to identify an optimal composition for bone tissue engineering. Moreover, the morphology and viability of osteoblast-like cells (MG63) on composite scaffolds were analyzed using scanning electron microscopy and MTT assays. The data showed that by changing the ratio of CNT to PCL, the elastic modulus of the nanocomposite could be varied between 10 and 75 MPa. In this range, the geometry of the scaffold can be used to finely tune its stiffness. The PCL–CNT nanocomposites were able to sustain osteoblast proliferation and modulate cell morphology, which showed the potential of custom-designed CNT nanocomposites for bone tissue engineering.

The authors' group [65] carried out some research concerning incorporating low-concentration MWNTs into PCL using a solution evaporation technique (Figs. 8.7, 8.8, and 8.9). Results showed that mechanical properties of the composite scaffolds were improved with the addition of MWNTs (0.2–2 wt%), which was consistent with the results of the previous, and rat bone marrow-derived stroma cells (BMSCs) on the composite scaffolds differentiated down the osteogenic lineage and expressed high levels of bone marker ALP. Accordingly, we concluded that MWNTs/PCL composite scaffolds have the potential for bone tissue engineering and the relatively low concentration of MWNTs (0.5 wt%) is preferred.

Castro et al. [66] studied the influence of carbon nanotube (CNT) grafted with poly(ϵ -caprolactone) (PCL) on vapor sensing properties, which had been investigated for a series of Conductive Polymer Composite (CPC) transducers developed by layer-by-layer spray from PCL–CNT solutions. Grafting of ϵ -caprolactone on the CNT surface through in situ ring-opening polymerization was demonstrated by nuclear magnetic resonance after solvent extraction of ungrafted chains. Atomic force microscopy observations allowed an evaluation of CNT coating and dispersion level. Chemo-electrical properties of CPC sensors exposed to different vapors: water, methanol, toluene, tetrahydrofuran, and chloroform have been analyzed in terms of signal sensitivity, selectivity, reproducibility, and stability. An increase of sensor response amplitude was observed when using PCL-grafted CNT (PCL-g-CNT) composites in formulations.

In another report [66], the conductive polymer nanocomposite (CPC) of multiwall carbon nanotubes (MWNT) filled polycaprolactone (PCL) was formulated by melt mixing method. PCL-based conductive phase served as disperse phase blended with polypropylene (PP) and polyamide 12 (PA12), respectively.

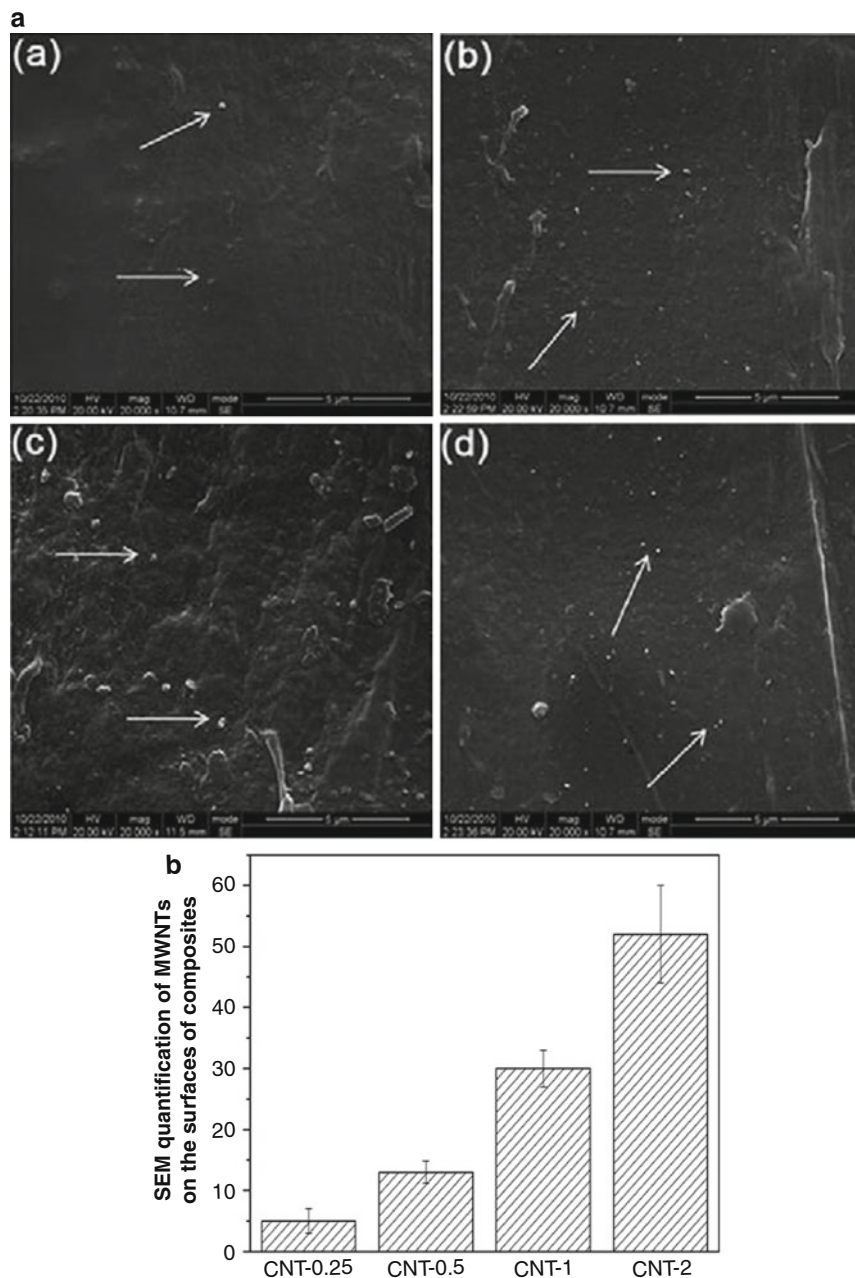


Fig. 8.7 (a) Scanning electron micrographs of composite scaffolds with carbon nanotubes (a) CNT-0.25, (b) CNT-0.5, (c) CNT-1, (d) CNT-2 (scale marker is 5 μm). MWNTs can be seen homogeneously distributed in the polymer matrix. (b) The MWNTs distribution has been quantified using image analysis. Data represents mean \pm standard deviation for $n = 10$ [65]

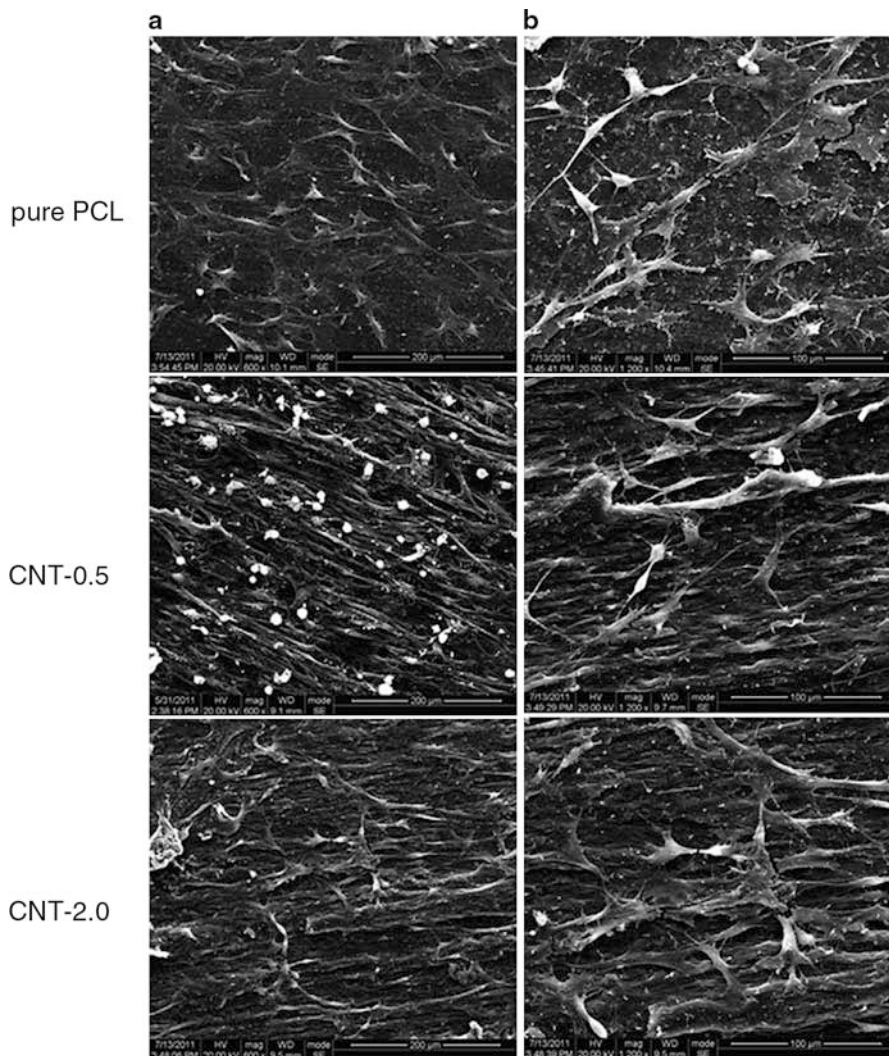


Fig. 8.8 SEM images of the BMSCs cultured on composite scaffolds (CNT-0.5 and CNT-2) and pure PCL scaffold under the same culture condition. Magnification: (a) 600 \times , (b) 1200 \times [65]

The thermo- and chemo-electrical properties of mono- and bicomponent CPC have been investigated independently. The experiment indicated that PP/PCL–CNT CPC was a good temperature sensor, whereas no significant response was observed while exposing to toluene vapor. In contrast, PA12/PCL–CNT exhibits good vapor sensing capability instead of temperature sensor. It was assumed that PP phase prevented the diffusion of vapor molecules within PCL conductive phase. The vapor sensing results indicated that PP external matrix provides the CPC with higher barrier effects than PA12.

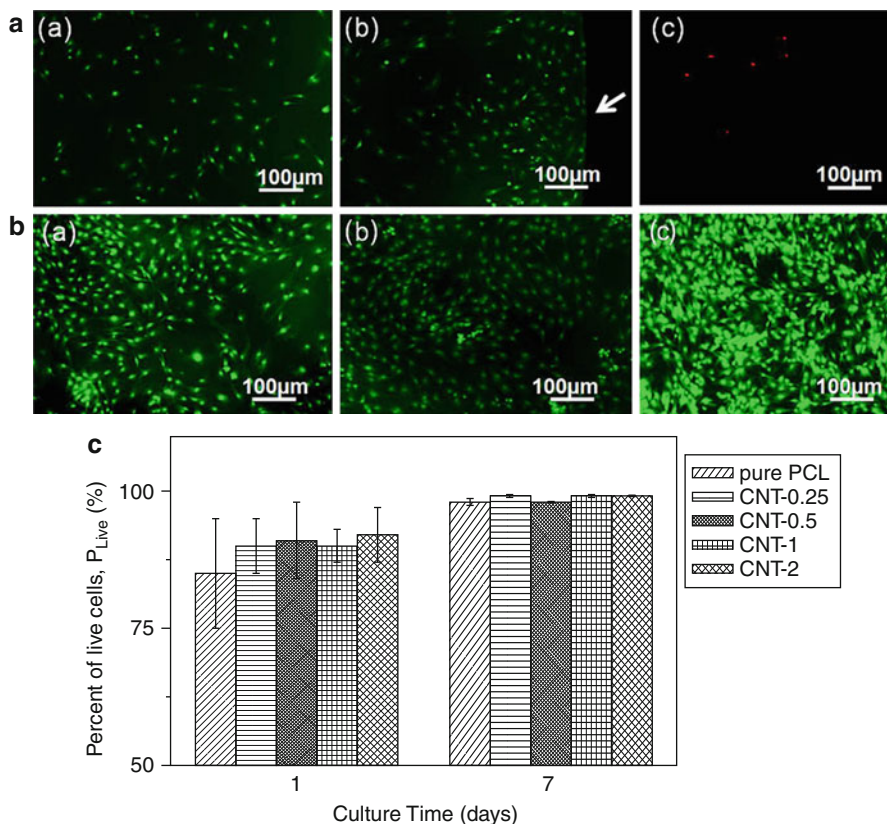


Fig. 8.9 (a) Live/dead staining of BMSCs cultured for 1 day. (a) Live cells on pure PCL. (b) Live cells on MWNTs/PCL composite (CNT-0.25). (c) Dead cells on MWNTs/PCL composite. The live BMSCs were stained green and appeared to have adhered and attained a normal polygonal morphology on all materials. Dead cells were stained red and were very few on all materials. (b). BMSCs proliferation on pure PCL and MWNTs/PCL composite scaffolds. (a) Cells on pure PCL and (b) cells on MWNTs/PCL composite (CNT-0.25); (c) confluent monolayer of BMSCs on MWNTs/PCL composite (CNT-0.5). (c). Percentage of live BMSCs, P_{Live} . Each value is mean \pm deviation, $n = 5$ (For interpretation of the references to color in this figure legend, the reader is referred to the web version of the article) [65]

Many papers have been published utilizing CNTs as the sensing material in pressure, flow, thermal, gas, optical, mass, strain, stress, chemical, and biological sensors. Sumanasekera et al. have created a thermoelectrical chemical sensor to measure reversibly thermoelectrical power changes of carbon nanotubes in contact with He, N₂, and H₂ [67]. Kang et al. from the University of Cincinnati have worked on polymethyl methacrylate (PMMA)-based CNT/PMMA strain sensors for structural health monitoring [71]. Among many of their superior electromechanical properties, the piezoresistive effect in CNTs is attractive for designing strain sensors. When CNTs are subjected to a mechanical strain, a change in their chirality leads to

modulation of the conductance. According to a article included in the book named *Nanotechnological Basis for Advanced Sensors* published in 2011 [68], the resulted crystalline structure clearly indicates that the PCL/MWCNT polycaprolactone (PCL)-based nanocomposites (PCL/MWCNT) could be used in sensor devices. In this chapter, the nanocomposites were prepared by mixing the MWCNTs and PCL in a tetrahydrofuran solution for 24 h. Characterization of the PCL/MWCNTs nanocomposite film was performed by differential scanning calorimetry (DSC), thermogravimetric analysis (TGA), Fourier transform infrared (FTIR), and scanning electron microscopy (SEM), as well as by mechanical and electrical measurements. The results indicate that introducing MWCNT into PCL significantly changes the properties of the obtained nanocomposites. The crystallization temperature for the PCL/MWCNT nanocomposites decreased with increasing cooling rate for a given MWCNT content. The incorporation of MWCNT accelerates the mechanism of nucleation and crystal growth of PCL.

A clear upward trend in this hybrid usage in research signifies the recognition of these PCL–CNTs nanocomposites with both the properties of CNTs' electronic mechanical properties and PCL's rheological and viscoelastic properties. Data analyzed and discussed in this chapter allow us to conclude that PCL–CNTs nanocomposites provide a promising platform for the production of bone tissue engineering and nanosensors. As an emerging field, however, most studies still focus on the performance of this material, and there are still lots of difficulties prior to its tissue engineering, such as the long-term degradation and biocompatibility and the toxicity effects of these materials. The use of PCL–CNTs nanocomposites and the excellent researches which are already well underway translating material science into the clinic holds great promise for future medical applications.

References

1. Guldi DM, Rahman GMA, Zerbetto F, Prato M (2005) Carbon nanotubes in electron donor–acceptor nanocomposites. *Acc Chem Res* 38:871–878
2. Bandaru PR (2007) Electrical properties and applications of carbon nanotube structures. *J Nanosci Nanotechnol* 7:1239–1267
3. Wei BQ, Vajtai R, Ajayan PM (2001) Reliability and current carrying capacity of carbon nanotubes. *Appl Phys Lett* 79:1172–1174
4. Durkop T, Kim BM, Fuhrer AMS (2004) Properties and applications of high-mobility semiconducting nanotubes. *J Phys Condens Matter* 16:R553–R580
5. Ajayan PM, Stephan O, Colliex C, Trauth D (1994) Aligned carbon nanotube arrays formed by cutting a polymer resin–nanotube composite. *Science* 265:1212–1214
6. Singh R, Pantarotto D, Lacerda L, Pastorin G, Klumpp C, Prato M, Bianco A, Kostarelos K (2006) Tissue biodistribution and blood clearance rates of intravenously administered carbon nanotube radiotracers. *Proc Natl Acad Sci USA* 103:3357
7. Abarrategi A, Gutiérrez MC, Moreno-Vicente C, Hortigüela MJ, Ramos V, López-Lacomba JL, Ferrer ML, Monte FD (2008) Multiwall carbon nanotube scaffolds for tissue engineering purposes. *Biomaterials* 29:94–102
8. Chrissafis K, Antoniadis G, Paraskevopoulos KM, Vassiliou A, Bikiaris DN (2007) Comparative study of the effect of different nanoparticles on the mechanical properties and thermal

- degradation mechanism of in situ prepared poly ([epsilon]-caprolactone) nanocomposites. *Compos Sci Technol* 67:2165–2174
9. Saeed K, Park SY (2007) Preparation and properties of multiwalled carbon nanotube/polycaprolactone nanocomposites. *J Appl Polym Sci* 104:1957–1963
 10. Pei XB, Wang J, Wan QB, Kang LJ, Xiao ML, Bao H (2011) Functionally graded carbon nanotubes/hydroxyapatite composite coating by laser cladding. *Surf Coat Technol* 205:4380–4387
 11. Abrams GA, Goodman SL, Nealey PF, Franco M, Murphy CJ (2000) Nanoscale topography of the basement membrane underlying the corneal epithelium of the rhesus macaque. *Cell Tissue Res* 299:39–46
 12. Kam NWS, Jessop TC, Wender PA, Dai H (2004) Nanotube molecular transporters: internalization of carbon nanotube-protein conjugates into mammalian cells. *J Am Chem Soc* 126:6850–6851
 13. Hu H, Ni Y, Mandal SK, Montana V, Zhao B, Haddon RC, Parpura V (2005) Polyethyleneimine functionalized single-walled carbon nanotubes as a substrate for neuronal growth. *J Phys Chem B* 109:4285–4289
 14. Tran PA, Sarin L, Hurt RH, Webster TJ (2009) Opportunities for nanotechnology-enabled bioactive bone implants. *J Mater Chem* 19:2653–2659
 15. Van NFJ, Hill JW, Carruthers WH (1934) Polymerization and ring formation, ϵ -caprolactone and its polymers. *J Am Chem Soc* 56:455–459
 16. Huang S (1985) Biodegradable polymers. In: Mark F, Bikales N, Overberger C, Menges G, Kroshwitz J (eds) *Encyclopedia of polymer science and engineering*. Wiley, New York, pp 220–243
 17. Pitt CG (1990) Poly- ϵ -caprolactone and its copolymers. In: Chasin M, Langer R (eds) *Biodegradable polymers as drug delivery systems*. Marcel Dekker, New York, pp 71–120
 18. Chandra R, Rustgi R (1998) Biodegradable polymers. *Progr Polym Sci* 23:1273–1335
 19. Nair LS, Laurencin CT (2007) Biodegradable polymers as biomaterials. *Progr Polym Sci* 32:762–798
 20. Gross RA, Kalra B (2002) Biodegradable polymers for the environment. *Science* 297:803–807
 21. PigŁowski J, Kiersnowski A (2006) Preparation, structure and useful properties of poly (ϵ -caprolactone)/layered silicates nanocomposites. *Polymers* 51(10):704–715
 22. Langer R, Vacanti JP (1993) *Tissue engineering*. *Science* 260:920–926
 23. Hutmacher DW (2000) Scaffolds in tissue engineering bone and cartilage. *Biomaterials* 21:2529–2543
 24. Hutmacher DW, Woodruff MA (2008) Fabrication and characterisation of scaffolds via solid free form fabrication techniques. In: Chu PK, Liu X (eds) *Handbook of fabrication and processing of biomaterials*. CRC Press/Taylor and Francis Group, Boca Raton, pp 45–68
 25. Breuer O, Sundararaj U (2004) Big returns from small fibers: a review of polymer/carbon nanotube composites. *Polym Compos* 25:630–645
 26. Coleman JN, Khan U, Blau WJ, Gun'ko YK (2006) Small but strong: a review of the mechanical properties of carbon nanotube polymer composites. *Carbon* 44:1624–1652
 27. Moniruzzaman M, Winey KI (2006) Polymer nanocomposites containing carbon nanotubes. *Macromolecules* 39:5194–5205
 28. Pierard N, Fonseca A, Konya Z, Willems I, Van TG, Nagy JB (2001) Production of short carbon nanotubes with open tips by ball milling. *Chem Phys Lett* 335:1–8
 29. Xia H, Wang Q, Li K, Hu GH (2004) Preparation of CNT/polypropylene composite powder with a solid state mechanochemical pulverization process. *J Appl Polym Sci* 93:378–386
 30. Doshi J, Reneker DH (1995) Electrospinning process and applications of electrospun fibers. *J Electrostat* 35:151–160
 31. Huang MH, Li SM, Vert M (2004) Synthesis and characterization of block copolymers of ϵ -caprolactone and DL-lactide initiated by ethylene glycol or poly(ethylene glycol). *Polymer* 45:8675–8681

32. Baji A, Mai Y-W, Wong SC, Abtahi M, Chen P (2010) Electrospinning of polymer nanofibers: effects on oriented morphology, structures and tensile properties. *Compos Sci Technol* 70:703–718
33. Xie XL, Mai Y-W, Zhou XP (2005) Dispersion and alignment of carbon nanotubes in polymer matrix: a review. *Mater Sci Eng R* 49:89–112
34. Saeed K, Park SY, Lee HJ, Baek JB, Huh WS (2006) Preparation of electrospun nanofibers of carbon nanotube/polycaprolactone nanocomposite. *Polymer* 47:8019–8025
35. Mamedov AA, Kotov NA, Prato M, Guldi DM, Wickstedt JP, Hirsch A (2002) Molecular design of strong single-wall carbon nanotube/polyelectrolyte multilayer composites. *Nat Mater* 1:190–194
36. Treacy MMJ, Ebbesen TW, Gibson JM (1996) Exceptionally high Young's modulus observed for individual carbon nanotubes. *Nature* 381:678–680
37. Wong EW, Sheehan PE, Lieber CM (1997) Nanobeam mechanics: elasticity, strength, and toughness of nanorods and nanotubes. *Science* 277:1971–1975
38. Yu MF, Lourie O, Dyer MJ, Moloni K, Kelly TF, Ruoff RS (2000) Strength and breaking mechanism of multiwalled carbon nanotubes under tensile load. *Science* 287:637–640
39. Qian D, Dickey EC, Andrews R, Rantell T (2000) Load transfer and deformation mechanisms in carbon nanotube–polystyrene composites. *Appl Phys Lett* 76:2868–2870
40. Erik TT, Tsu WC (2002) Aligned multi-walled carbon nanotube-reinforced composites: processing and mechanical characterization. *J Phys D Appl Phys* 35:L77
41. Shi X, Hudson JL, Spicer PP, Tour JM (2005) Rheological behaviour and mechanical characterization of injectable poly (propylene fumarate)/single-walled carbon nanotube composites for bone tissue engineering. *Nanotechnology* 16:S531–S538
42. Balani K, Anderson R, Laha T, Andara M, Tercero J, Crumpler E, Agarwal A (2007) Plasma-sprayed carbon nanotube reinforced hydroxyapatite coatings and their interaction with human osteoblasts in vitro. *Biomaterials* 28:618–624
43. Zhao B, Hu H, Mandal SK, Haddon RC (2005) A bone mimic based on the self-assembly of hydroxyapatite on chemically functionalized single-walled carbon nanotubes. *Chem Mater* 17:3235–3241
44. Zanello LP, Zhao B, Hu H, Haddon RC (2006) Bone cell proliferation on carbon nanotubes. *Nano Lett* 6:562–567
45. Shi X, Hudson JL, Spicer PP, Tour JM, Krishnamoorti R, Mikos AG (2006) Injectable nanocomposites of single-walled carbon nanotubes and biodegradable polymers for bone tissue engineering. *Biomacromolecules* 7:2237–2242
46. Dyke CA, Tour JM (2004) Overcoming the insolubility of carbon nanotubes through high degrees of sidewall functionalization. *Chem Eur J* 10:812–817
47. Pantarotto D, Briand J-P, Prato M, Bianco A (2004) Translocation of bioactive peptides across cell membranes by carbon nanotubes. *Chem Commun* 1:16–17
48. Lacerda L, Bianco A, Prato M, Kostarelos K (2008) Carbon nanotube cell translocation and delivery of nucleic acids in vitro and in vivo. *J Mater Chem* 18:17–22
49. Liu Z, Chen K, Davis C, Sherlock S, Cao Q, Chen X, Dai H (2008) Drug delivery with carbon nanotubes for in vivo cancer treatment. *Cancer Res* 68:6652–6660
50. Fernando KA, Lin Y, Sun YP (2004) High aqueous solubility of functionalized single-walled carbon nanotubes. *Langmuir* 20:4777–4778
51. Gregory RDE (2001) Peripheral nerve injury: a review and approach to tissue engineered constructs. *Anat Rec* 263:396–404
52. Millesi H (1991) Indications and techniques of nerve grafting. In: Gelbertman RH (ed) *Operative nerve repair and reconstruction*. Lippincott J.B, Philadelphia, pp 525–544
53. Terzis JK, Sun DD, Thanos PK (1997) Historical and basic science review: past, present, and future of nerve repair. *J Reconstr Microsurg* 13:215–225
54. Zalewski AA, Gulati AK (1981) Rejection of nerve allografts after cessation of immunosuppression with cyclosporin A. *Transplantation* 31:88–89

55. James RB (2000) Peripheral nerve and neuromuscular allotransplantation: current status. *Microsurgery* 20:384–388
56. Seidllits SK, Lee JY, Schmidt CE (2008) Nanostructured scaffolds for neural applications. *Nanomedicine* 3:183–199
57. Zhang L, Webster TJ (2009) Nanotechnology and nanomaterials: promises for improved tissue regeneration. *Nano Today* 4:66–80
58. Mattson M, Haddon R, Rao A (2000) Molecular functionalization of carbon nanotubes and use as substrates for neuronal growth. *J Mol Neurosci* 14:175–182
59. Matsumoto K, Sato C, Naka Y, Kitazawa A, Whitby RL, Shimizu N (2007) Neurite outgrowths of neurons with neurotrophin-coated carbon nanotubes. *J Biosci Bioeng* 103:216–220
60. Lovat V, Pantarotto D, Lagostena L, Cacciari B, Grandolfo M, Righi M, Spalluto G, Prato M, Ballerini L (2005) Carbon nanotube substrates boost neuronal electrical signaling. *Nano Lett* 5:1107–1110
61. Gabay T, Jakobs E, Ben-Jacob E, Hanein Y (2005) Engineered self-organization of neural networks using carbon nanotube clusters. *Phys A Stat Mech Appl* 350:611–621
62. Jan E, Kotov NA (2007) Successful differentiation of mouse neural stem cells on layer-by-layer assembled single-walled carbon nanotube composite. *Nano Lett* 7:1123–1128
63. Trujillo M, Arnal ML, Müller AJ, Mujica MA (2011) Supernucleation and crystallization regime change provoked by MWNT addition to poly(ϵ -caprolactone). *Polymer* 53:832–841
64. Mattioli-Belmonte M, Vozzi G, Whulanza Y (2011) Tuning polycaprolactone–carbon nanotube composites for bone tissue engineering scaffolds. *Mater Sci Eng C* 32:152–159
65. Pan LL, Pei XB, He R, Wan QB, Wang J (2012) Multiwall carbon nanotubes/polycaprolactone composites for bone tissue engineering application. *Colloids Surf B Biointerfaces* 93:226–234
66. Castro M, Lu J, Bruzaud S, Kumar B, Feller JF (2009) Carbon nanotubes/poly(ϵ -caprolactone) composite vapour sensors. *Carbon* 47:1930–1942
67. Sumanasekera GU, Pradhan BK, Romero HE, Adu CKW, Foley HC, Eklund PC (2002) Thermoelectric chemical sensor based on single wall carbon nanotubes. *Mol Cryst Liq Cryst* 387:31
68. Reithmaier JP, Paunovic P, Kulisch W, Popov C (2011) Nanotechnological basis for advanced sensors. Springer, Dordrecht, pp 149–154
69. Dalton PD, Woodfield T, Huttmacher DW (2009) Publisher’s note: Erratum to: “SnapShot: polymer scaffolds for tissue engineering” [30/4 (2009) 701–702]. *Biomaterials* 30:2420
70. Chen J, Rao AM, Lyuksyutov S, Itkis ME, Hamon MA, Hu H, Cohn RW, Eklund PC, Colbert DT, Smalley RE, Haddon RC (2001) Dissolution of full-length single-walled carbon nanotubes. *J Phys Chem B* 105:2525–2528
71. Wong YM, Kang WP, Davidson JL, Wisitsora-at A, Soh KL (2003) A novel microelectronic gas sensor utilizing carbon nanotubes for hydrogen gas detection. *Sens Actuators B* 93:327–332
72. Kim JY, Han SI, Kim DK, Kim SH (2009) Mechanical reinforcement and crystallization behavior of poly(ethylene 2,6-naphthalate) nanocomposites induced by modified carbon nanotube. *Compos Appl Sci Manuf* 40:45–53
73. Li XM, Gao H, Uo M, Sato Y, Akasaka T, Feng Q, Cui F, Liu X, Watari F (2009) Effect of carbon nanotubes on cellular functions in vitro. *J Biomed Mater A* 91:132–139
74. Lu J, Castro M, Kumar B (2009) Thermo- and chemo-electrical behavior of carbon nanotube filled co-continuous conductive polymer nanocomposites (CPC) to develop amperometric sensors. *Mater Res Soc* 1143:1143–KK05–14

Fabrication and Characterization of Carbon Nanotube/Cellulose Composite Paper

9

Eiichi Sano, Tomo Tanaka, and Masanori Imai

Contents

1	Introduction	196
2	Fabrication	197
3	Property Analysis	199
3.1	Mechanical Strength and Electrical Conductivity at Room Temperature	199
3.2	Temperature Dependence of Electrical Conductivity	201
3.3	Permittivity	204
4	EMI Shielding Effectiveness	206
5	Conclusion and Future Direction	208
	References	209

Abstract

Carbon nanotube (CNT)/cellulose composite materials were fabricated in a papermaking process optimized to form a CNT network on cellulose fibers. The measured electrical conductivity ranged from 0.05 to 671 S/m for a CNT content of 0.5–16.7 wt%, which was higher than that for other polymer composites. The measured temperature dependences of electrical conductivity were described with the fluctuation-induced tunneling model. The real permittivities were the highest in the microwave region. The unique CNT network structure is thought to be the reason for the high conductivity and permittivity values. Our CNT/cellulose composite material exhibited improved parameters without any decrease in mechanical strength, compared to other carbon materials.

E. Sano (✉) • T. Tanaka

Research Center for Integrated Quantum Electronics, Hokkaido University, Sapporo, Hokkaido, Japan

e-mail: esano@rciqe.hokudai.ac.jp; tomotanaka@rciqe.hokudai.ac.jp

M. Imai

Fundamental Laboratory, Technical Research Div, Tokushu Tokai Paper, Nagaizumi, Shizuoka, Japan

e-mail: mimai@m.tt-paper.co.jp

The near-field electromagnetic shielding effectiveness (EMI SE) measured using a microstrip line method depended on the sheet conductivity and qualitatively matched the results of electromagnetic field simulations using a finite-difference time-domain simulator. A high near-field EMI SE of 50 dB was achieved in the 5–10-GHz frequency region with 4.8-wt% composite paper. The far-field EMI SE was measured using a free-space method. Fairly good agreement was obtained between the measured and calculated results. Approximately 10-wt% CNT is required to achieve composite paper with 20-dB far-field EMI SE.

Keywords

Multi-walled carbon nanotube • Cellulose paper • Electromagnet shielding

1 Introduction

Carbon-nanotubes (CNTs) are considered to be a new class of material with reduced dimensionality. They have unique properties such as high mechanical strength as well as high thermal and electrical conductivity. Much work has been done on CNT composites as well as on CNT sheets to fully utilize these properties for many kinds of applications [1–3]. Technical improvements in the electronics field in recent years have led to diversified and advanced electromagnetic wave applications. An example is the rapidly increasing use of wireless telecommunications systems such as cellular phones and RFID tags. In particular, technology intended to achieve a higher frequency and wider bandwidth for establishing high-speed communication system continues to advance. Against this background, however, concerns about deterioration of the radio wave environment have arisen. A deteriorated radio wave environment has adverse effects on electronic equipment, such as false operation due to unnecessary electromagnetic waves and leakage of information in wireless telecommunications. Due to these circumstances, electromagnetic wave absorption materials have attracted attention as technological countermeasures from the viewpoint of electromagnetic compatibility. Usage of these materials is expected to increase in the future. CNTs are candidate materials for this application.

Several studies describe the preparation and characterization of CNT reinforced composite materials as electromagnetic interference (EMI) shielding materials. For example, Zanfeng et al. prepared single-walled (SW) CNT/epoxy composites and measured the EMI shielding effectiveness (SE) of these materials [4]. Grimes et al. fabricated CNT/polyethylmethacrylate composite thick films and determined the permittivity spectra of these composites [5]. The common characteristic of those composite materials is their higher electrical conductivity compared with conventional carbon black/polymer composites due to the high aspect ratio of CNT.

To control their electrical conductivity, the electrical conduction mechanism of CNT composites needs to be elucidated, and to do this, the dependence of electrical conductivity on temperature for CNT composites is very useful [6, 7]. There are two major mechanisms of electrical conduction for composite materials: variable range hopping (VRH) [8] and fluctuation-induced tunneling (FIT) [9]. The VRH model

matches the electrical conductivities of single-walled (SW) CNT mats [10] and networks [11, 12], while the FIT model matches those of SWCNT mats [13, 14], SWCNT bundles [15], and SWCNT/polymer composites [10]. In contrast, the FIT model matches the electrical conductivities of multi-walled (MW) CNT composites [16–22]. The electrical conduction through the CNT-CNT junctions dominates the conductivity of the CNT network in the FIT model. The tunnel width w and barrier height V_0 can be estimated from two specific temperatures T_0 and T_1 obtained by fitting the FIT law to the measured temperature dependence of the conductivity. However, only a few papers have reported w and V_0 . Kim et al. estimated a w of 3.5 nm and a V_0 of 0.1 eV for a SWCNT network [13], while Mdarhri et al. estimated a w of 5 nm and a V_0 of 15 meV for MWCNT composites [21]. These heights and widths seem to be too low and wide to be clearly explained. Salvato et al. reported the dependence of the barrier height on current and temperature in SWCNT bundles [15]. The physical reason for this phenomenon is still unclear.

CNT/cellulose composite papers have also been reported [23–26]. Fugetsu et al. fabricated electrically uniform MWCNT/cellulose composite papers using a CNT water dispersion and indicated the possibility of applying the papers as EMI shielding material [23]. Jung et al. described MWCNT/bacterial cellulose composite paper with silk fibroin coating [24]. Oya et al. [25] and Anderson et al. [26] fabricated and characterized SWCNT/cellulose composite papers.

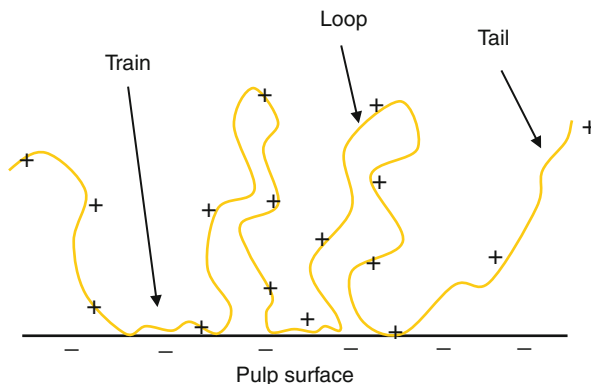
This chapter reviews the mechanical and electrical properties of CNT/cellulose composite materials prepared using a papermaking process. The temperature dependence of the electrical conductivity of the fabricated composite papers and the possible conduction mechanism are discussed based on the FIT model. The measured EMI SE characteristics of the composite papers are compared to theoretical characteristics using an electromagnetic field simulator. The feasibility of applying the composite paper to the EMI problem is discussed.

2 Fabrication

To optimize the papermaking process for CNT/cellulose composites as well as the quality of the resulting paper, it is important to improve the interaction between the pulp fibers and paper chemicals used in the process. These include starches, sizing agents (bleeding inhibitor of ink), fillers, and pigments [27]. The main interaction between these chemicals is ion binding; whether or not these chemicals bond with the pulp fibers depends on the charge of the pulp suspension. Pulp fibers have a negative charge because they generate carboxyl groups during papermaking processes such as cooking or bleaching [28]. When anionic surfactant is used to disperse CNTs, the CNT surfaces also have a negative charge. Therefore, a cationic fixer can be applied to fix the CNTs to the pulp.

CNTs are known to make strong aggregates due to Van der Waals' force. Therefore, it is important to prevent dispersed CNTs from self-agglomerating before bonding them to cellulose fibers. For this purpose, a cationic fixer is mixed with the cellulose fibers so that it adsorbs on the cellulose surfaces before the CNT

Fig. 9.1 Adsorb states of polymers on solid surfaces in water dispersions [30]



water dispersion is added. Polymers have three adsorption states on the cellulose surfaces: train, tail, and loop (Fig. 9.1) [29]. The train segments are the parts that contact the surface, and the loop and tail segments diffuse in solvents. When a CNT anionic dispersant is added to the cellulose-fixer mixture, the loops and tails of the fixer adsorb on the CNT surfaces and create a cross-linkage between the cellulose fibers and CNTs; this facilitates the bonding of CNTs to cellulose fibers. If the fixer is added after the CNT dispersant is mixed with the cellulose, many CNTs will agglomerate form in the mixture, resulting in nonuniform paper (data not shown).

Jung et al. used a cationic surfactant, cetyltrimethylammonium bromide, to disperse MWCNTs, which resulted in efficient adsorption of the MWCNTs onto a bacterial cellulose hydrogel [24]. Anderson et al. reported that SWCNT suspensions were stabilized by carboxymethyl cellulose (CMC) and a positively charged additive, alum, acted as a bridge between two anionic surfaces (cellulose fiber-fiber, fiber-CMC, CMC-CMC) [26]. These methods also are effective for adsorbing CNTs on cellulose surfaces.

Bleached hardwood Kraft pulp (50 wt%) and bleached softwood Kraft pulp (50 wt%) were dispersed in water and beaten using a Tappi standard Niagara beater until freeness of 500 ml was obtained. The freeness of the pulp was measured using a Schopper-Riegler freeness tester in accordance with JIS P 8121. Then, a fixer of 2 % cationized starch (Neotack L-1, from Nihon Shokuhin Kako Co., Ltd.) water solution was added to the pulp and mixed with the CNT dispersion. Handmade CNT/cellulose composite material was prepared using 25 × 25 cm wire cloth. The added amount of CNT was varied, and six kinds of paper were prepared. The CNT content of a composite is usually measured using thermogravimetric analysis (TGA) [23]. However, this method could not be applied to our composite paper because the TG curves of the CNTs and cellulose could not be distinguished with high enough accuracy when the components were mixed. Thus, CNT content was calculated by dividing the added amount of CNTs by the sum of the weight of the CNTs and cellulose.

Carbon black (Mitsui Chemicals #41) and carbon fiber (Kureha C-103 T) were used as control materials instead of CNT to produce composite papers. Plain paper was also prepared in the same way.

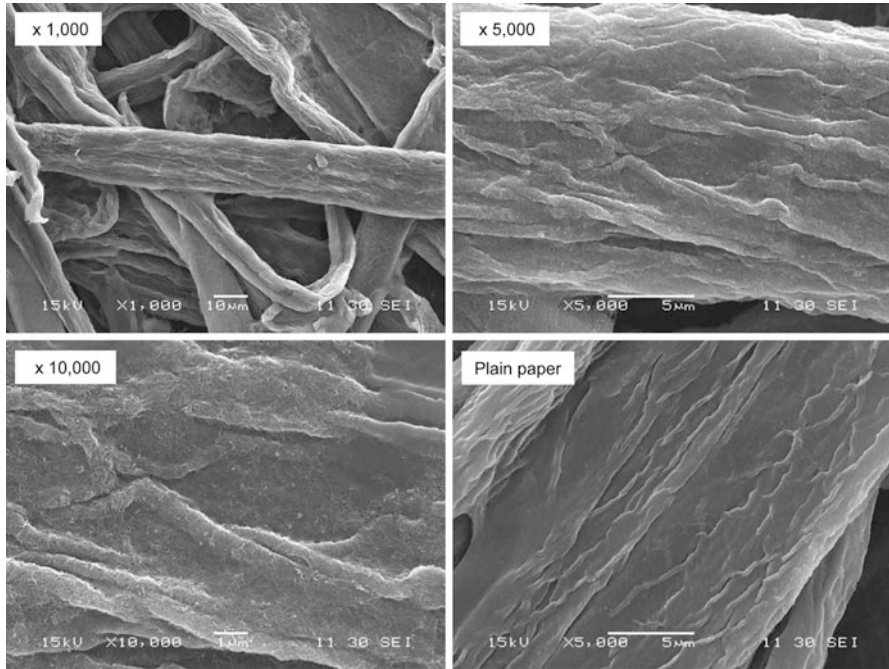


Fig. 9.2 SEM images of CNT/cellulose composite materials and plain paper [30]

The CNT/cellulose composite material was coated in gold and observed with a JEOL JSM-6360LA scanning electron microscope (SEM). SEM images of the material are shown in Fig. 9.2 [30]. As shown, CNT networks can be observed on the cellulose fibers.

3 Property Analysis

3.1 Mechanical Strength and Electrical Conductivity at Room Temperature

The CNT/cellulose composite papers were kept for 24 h at 23 °C, 50 % RT in order to control the humidity of the paper. The tension strength of the papers was measured in accordance with JIS P 8113 using a tensile tester (Kumagaya Riki Kogyo Co., Ltd.). After the humidity control, the electrical conductivity was determined using a four-point contact method with a resistivity meter (Mitsubishi Chemistry Loresta MCP-T600) in accordance with JIS K7194.

The properties of each composite material are listed in Table 9.1 [30]. The CNT/cellulose composites showed electrical conductivity even when the CNT content was much lower than the carbon material content in the other composites. This is attributed to the high aspect ratio of CNTs, which form a network as many conduction

Table 9.1 Properties of composite materials [30]

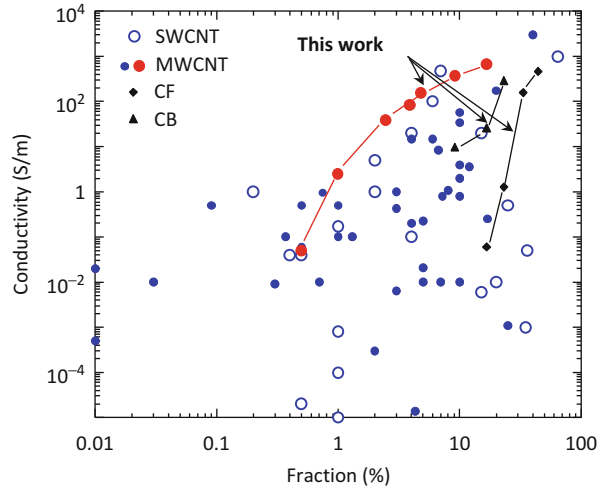
Material	Content [wt%]	Basis weight [g/m ²]	Thickness [mm]	Surface resistivity [Ω/sq.]	Volume resistivity [Ω cm]	Tensile strength [N/m]
CNT	0.5	110	0.166	3.39×10^5	2.00×10^3	6.21
	1.0	116	0.186	4.51×10^2	7.25	6.33
	2.4	118	0.192	5.81×10	1.11	6.50
	4.8	122	0.191	2.89×10	5.21×10^{-1}	6.40
	9.1	117	0.195	1.29×10	2.66×10^{-1}	4.60
	16.7	126	0.166	9.12	1.49×10^{-1}	4.36
Carbon black	9.1	115	0.212	7.51×10^3	1.01×10	4.37
	16.7	122	0.224	7.74×10^2	3.83	2.96
	23.0	134	0.268	4.21×10^2	4.37×10^{-1}	2.03
Carbon fiber	10.0	116	0.222	3.39×10^{11}	6.81×10^{11}	6.29
	30.0	106	0.265	4.61×10^2	4.73×10	3.20
	80.0	102	0.529	1.61×10	2.14×10^{-1}	1.77
Plain paper	–	104	0.169	–	–	6.33

paths are effectively created. The fabrication method needs to be optimized for different CNT dispersions. Various methods have been proposed for fabricating CNT/cellulose composite paper, e.g., adjusting the pH of the suspension solution [23] or mixing a CNT dispersion with cellulose without using a fixer [25]. However, when these methods were applied to this CNT anionic dispersion, the CNT yield was low compared to that when a cationic fixer was used. When 2.5-wt% CNT was added during the fabrication process, the surface resistivity of the CNT/cellulose composite paper using a cationic fixer was 58 Ω/sq., but it was 17,800 Ω/sq when the adjusting-pH method was used. The resistance obtained using the method without a fixer was too high to measure with the four-point contact method. Also, adjusting the pH becomes more difficult when the scale of the papermaking process is larger. The use of a fixer is thought to be an easier method when using manufacturing machinery.

The tensile strengths of the composites are also given in Table 9.1. When the CNT content was under 5 %, the tensile strength of the CNT/cellulose composite was almost the same as that of plain paper. The interfiber bonding of cellulose is hydrogen bonding, and the addition of a lot of carbon or fibers without hydroxyl groups to the pulp inhibits the interaction between cellulose fibers. As indicated in Table 9.1, the tensile strength decreased when the added amount of carbon material was increased. However, as described above, CNTs can improve the electrical conductivity even when added in small amounts because they form a network structure in the material. Because of this, they interfere with the hydrogen bonding of the cellulose fibers less than other carbon materials do, resulting in very strong material.

Figure 9.3 plots the measured dependence of conductivity on the CNT content for CNT/cellulose composite papers along with that for the carbon black (CB)/cellulose and carbon fiber (CF)/cellulose composite papers fabricated for

Fig. 9.3 Measured conductivity dependence on CNT content for CNT/cellulose, CB/cellulose, and CF/cellulose composite papers and CNT composites with insulating matrices reported in the literature [30]



comparison. The effectiveness of the cellulose fiber network as a matrix for increasing the electrical conductivity is compared with CNT composites whose matrices are homogeneous. The figure contains the measured conductivities for CNT composites with insulating matrices reported in the literature [5, 10, 16–18, 31–79]. Our CNT/cellulose composite papers have the highest conductivity reported to date for CNT content of 1–5-wt%. The high conductivity of our composite paper is due to the unique network topology in the paper. A large number of conductive CNT networks are efficiently formed with the help of the cellulose network. This results in high conductivity with very low CNT content. The advantage of CNT over CB and CF is also clearly demonstrated in the figure.

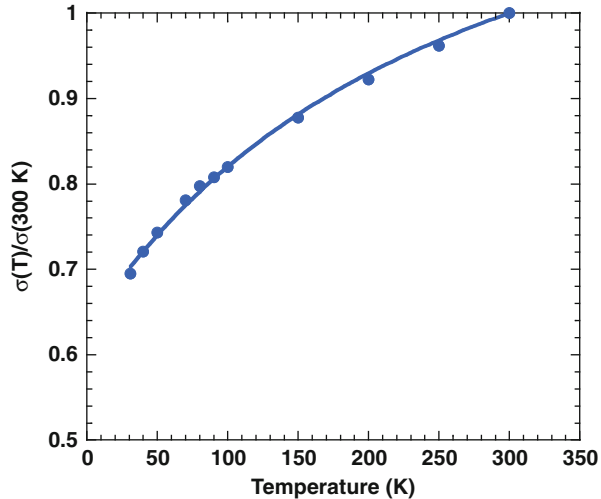
Other methods can be used to increase the electrical conductivity of CNT-based materials. One interesting method involves the use of CNT buckypapers [80]. An extremely large conductance of more than 10^5 S/m was reported for SWCNT buckypaper [81]. Aligning CNTs is particularly effective for increasing the conductivity [82, 83]. Although CNT buckypapers are useful for electrode applications, they are unsuitable for EMI shielding. They are metallic and are expected to be less effective for near-field EMI shielding as described by Fugetsu et al. [23].

3.2 Temperature Dependence of Electrical Conductivity

The dependence of electrical conductivity on temperature was measured using a four-probe method with a source meter (Keithley 2636A). Small pieces of indium were bonded to the samples to ensure that there was proper contact with the probe. The current was increased from 0 to 0.1 mA to check the linearity of current-voltage characteristics. The temperature was increased from 10 to 300 K.

The temperature dependence of electrical conductivity normalized with the conductivity at 300 K for the composite paper with a CNT content of 9.1 wt% is

Fig. 9.4 Measured temperature dependence of electrical conductivity normalized with conductivity at 300 K for composite paper with CNT content of 9.1 wt%. *Solid circles*: measured conductivity. *Curve*: fitted with fluctuation-induced tunneling model



shown in Fig. 9.4. Based on Sheng's model of fluctuation-induced tunneling (FIT) [9], the conductivity is expressed as

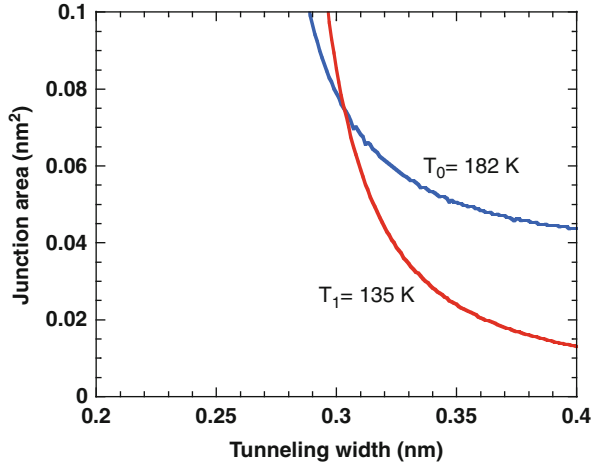
$$\sigma = \sigma_0 \exp\left(-\frac{T_1}{T + T_0}\right), \quad (9.1)$$

where T_0 and T_1 are the specific temperatures. The measured dependence of electrical conductivity on temperature can be fitted to the FIT model with $T_0 = 182$ K and $T_1 = 135$ K as shown by the line in Fig. 9.4. The same procedure revealed that $T_0 = 401$ K and $T_1 = 443$ K for 1.0-wt%, $T_0 = 602$ K and $T_1 = 543$ K for 2.4-wt%, and $T_0 = 105$ K and $T_1 = 192$ K for 4.8-wt% composite papers [84].

The probability for tunneling at the Fermi energy through a junction between two CNTs is proportional to $\exp(-T_1/T_0)$. Our T_1/T_0 values were close to those for SWCNT composites [10] and MWCNT composites [16, 18, 22]. As mentioned before, the tunnel width w and barrier height V_0 can be estimated from T_0 and T_1 . Kim et al. [13] and Mdarhri et al. [21] used approximate expressions for T_0 and T_1 . Because there are three unknown parameters (w , V_0 , and the junction area A) in the two equations, we cannot determine unique values. Applying the equations to our values of T_0 and T_1 leads to $wV_0^{1/2} = 1.37 \times 10^{-10}$. When V_0 is assumed to be 4.4 eV (the work function of MWCNT [85]), w becomes 0.065 nm. This is an unrealistic value because it is smaller than the distance between two carbon atoms in the hexagonal cell.

Since almost all the surfactant was removed in the papermaking process, two CNTs are thought to form a junction with no inclusion. Therefore, we estimate w and A by assuming V_0 to be 4.4 eV. According to the FIT model [9], the specific temperatures are:

Fig. 9.5 Calculated T_0 and T_1 in tunneling width – junction area plane for composite paper with a CNT content of 9.1 wt%



$$T_1 = a\varepsilon_0^2 / k, \tag{9.2}$$

$$T_0 = T_1 / 2xw\xi(0), \tag{9.3}$$

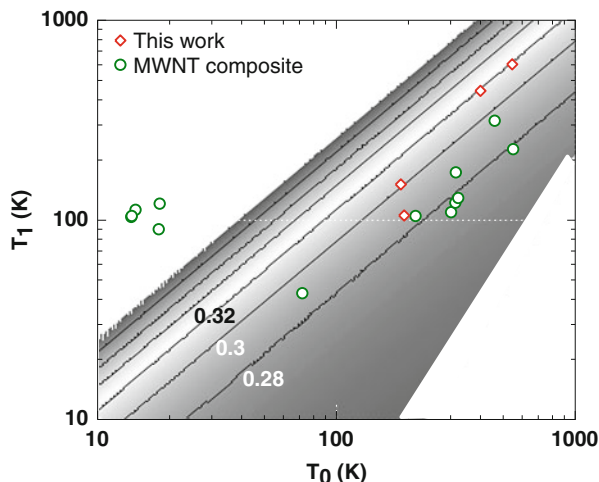
where $a \equiv wA/8\pi$ is the junction volume, w is the tunnel width, A is the junction area, k is the Boltzmann constant, and $x = (2mV_0/\hbar^2)^{1/2}$ is the tunneling constant. Here, $\xi(0)$ is defined as follows:

$$\xi(0) = \int_{u_3}^{u_4} \left(1 - \frac{\lambda}{u(1-u)}\right)^{1/2} du, \tag{9.4}$$

where $u_3, u_4 (>u_3)$ denotes the two zeros of potential $V(u, \varepsilon)$ and $\lambda = 0.795e^2/4wKV_0$ with K being the dielectric constant of the barrier region. In Eq. 9.2, ε_0 is the electrical field at which the potential maximum equals 0. More details can be found in Sheng’s paper [9].

The calculated T_0 and T_1 in the w - A plane for the composite paper with a CNT content of 9.1 wt% are plotted in Fig. 9.5. The intersection of the two contours for T_0 and T_1 gives a set of solution for w and A . The contour for T_0 did not cross the contour for T_1 in the region shown in Fig. 9.5 when assuming that $\xi(0) = 1$. The calculation suggests that w was around 0.3 nm smaller than the interlayer distance of graphite. Crossed MWCNTs might be deformed at the junction as calculated by the first principles method [86, 87]. A map of the tunneling width w in the T_0 - T_1 plane is shown in Fig. 9.6, where the junction area A was varied. The T_0 and T_1 reported in the literature [15, 17, 18, 22] are also plotted in Fig. 9.6. It is noted that the exact area and width of the junction should be calculated with the first principles method and the accuracy of the map should be improved in a future study. However, the present map of tunneling width w may be useful for qualitatively elucidating the properties of CNT networks.

Fig. 9.6 Map of tunneling width w in T_0 - T_1 plane. Circles: reported in the literature. diamonds: our data



3.3 Permittivity

The scattering (S) parameters for the CNT/cellulose composite papers were measured using a vector network analyzer (VNA) with a bandwidth of 67 GHz (Agilent E8361C) and a K-band (18–26.5 GHz) waveguide. A sample piece of paper was inserted in the waveguide. The permittivity and permeability of the composite papers were extracted from the measured S parameters using material measurement software (Agilent 85071E).

The Cole-Cole plot of permittivity extracted from S parameters measured for CNT/cellulose composite papers is shown in Fig. 9.7. Both the real and imaginary parts of permittivity (ϵ_r' and ϵ_r'' , respectively) increase as the CNT content increases. Scattered data for higher content are caused by the fluctuating frequency dependence of ϵ_r' and ϵ_r'' as shown in the inset of Fig. 9.7. The imaginary part ϵ_r'' for all samples was about half of the value calculated by $\sigma/(\omega\epsilon_0)$, where σ is the measured conductivity, ω is the angular frequency, and ϵ_0 is the vacuum permittivity. We were not able to conclusively determine the reason for this difference. One possible reason might be due to the accuracy of the software we used to extract the permittivity of materials with high conductivity. In fact, the extracted real parts of permeability μ_r' for the papers ranged from 0.7 to 1.5. Figure 9.8 summarizes ϵ_r' as a function of frequency for our composites along with those reported in the literature [45, 46, 55, 61, 65, 70, 88–98]. Our composite papers are among the highest in the microwave region. The reason for this high ϵ_r' is the same as that for the high conductivity. The unique CNT network forms a large number of nanometer-sized capacitors, which results in large polarization and thus large ϵ_r' . The effective permittivities of composites have been evaluated with effective medium theories (EMTs), such as the Maxwell-Garnett formula. Grimes et al. [88] successfully reproduced their experimental permittivity of MWCNT/polystyrene composites with an EMT modified by Lagarkov and

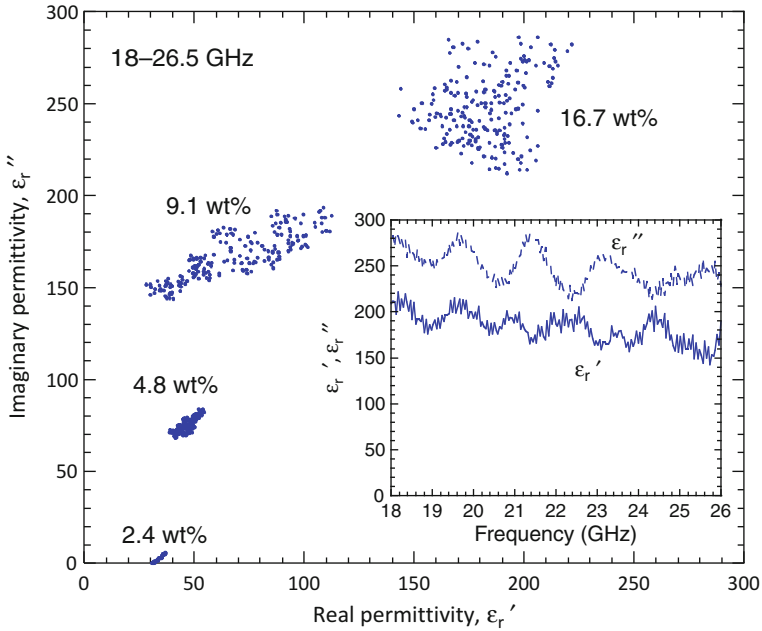


Fig. 9.7 Cole-Cole plot of permittivity extracted from measured S parameters for CNT/cellulose composite papers. Inset: frequency dependence of permittivity [30]

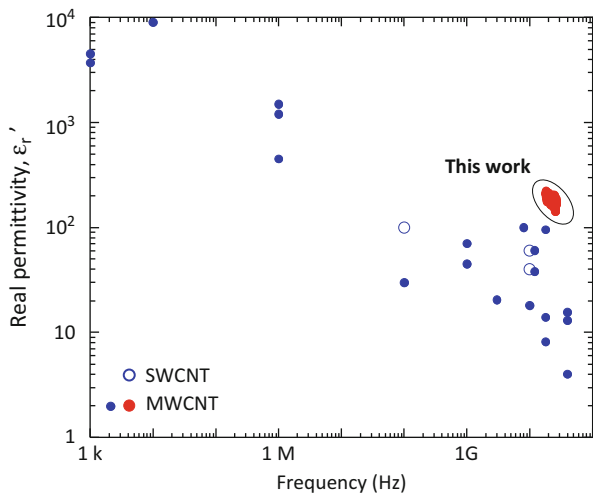


Fig. 9.8 ϵ_r' of CNT/cellulose composite papers as function of frequency, and those reported in the literature [30]

Sarychev [99]. We tried to reproduce the measured data by using the Lagarkov-Sarychev, Maxwell-Garnett, and Bruggeman formulae but unfortunately did not succeed. A novel formula will be required to describe the permittivity of our composites due to their unique CNT networks.

4 EMI Shielding Effectiveness

The EMI shielding effectiveness (SE) for the near and far fields was measured using a microstrip line (MSL) and free-space methods, as illustrated in Fig. 9.9a, b, respectively. The VNA was used for both methods. An MSL with a characteristic impedance of $50\ \Omega$ was fabricated with an FR4 board. The measured frequency range was determined to range from 50 MHz to 25.05 GHz due to the bandwidth of the MSL. The EMI SE was defined by the ratio of transmission when the MSL was not shielded by the sample paper to the transmission when the MSL was shielded by a thin insulating sheet and the sample paper. For the free-space method, a pair of horn antennas with a bandwidth of 15–40 GHz was used and the measurement system including the antennas was calibrated using gated reflection line method.

An example of near-field EMI SE for CNT/cellulose composite papers sized 21×21 cm measured with an MSL method is shown in Fig. 9.10. The fluctuations observed for CNT/cellulose composite papers with 4.8-wt% CNT might be due to impedance mismatch between the $50\text{-}\Omega$ measurement system and the MSL shielded by the composite paper. A high near-field EMI SE of 50 dB was achieved in the 5–10-GHz frequency region with the 4.8-wt% CNT composite paper. We fabricated CNT/cellulose composite papers with several levels of CNT content and found that the near-field EMI SE had a notable dependence on the sheet resistance of the papers. The near-field EMI SEs at 5 GHz as a function of sheet resistance are shown in Fig. 9.11. As can be seen, a sheet resistance of around $40\ \Omega/\text{sq.}$ was optimum for achieving the maximum EMI SE at 5 GHz. Note that the optimum sheet resistance depends on the target frequency. To theoretically confirm this dependence, we performed electromagnetic field simulations using a commercially available finite-difference time-domain simulator. The measured ϵ_r' and conductivity were used in the simulations. The simulation results, shown as a curve in Fig. 9.11, qualitatively

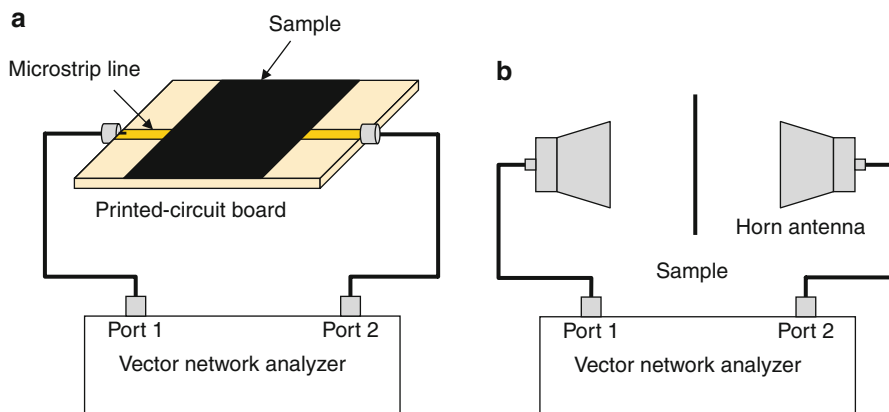


Fig. 9.9 Measurement setups of (a) MSL method and (b) free space method [30]

Fig. 9.10 Example of near-field EMI SE for CNT/cellulose composite papers measured with MSL method [30]

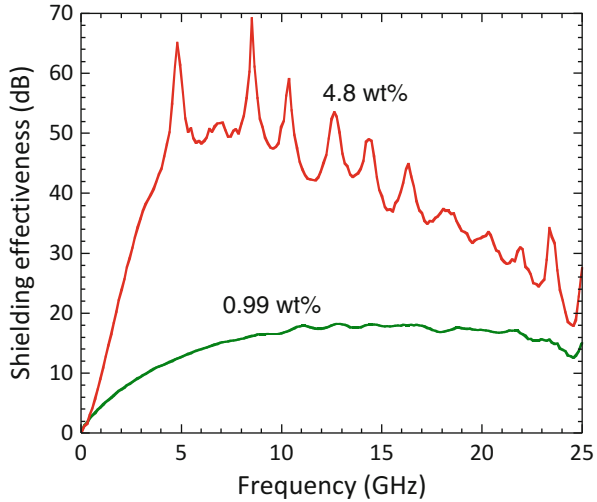
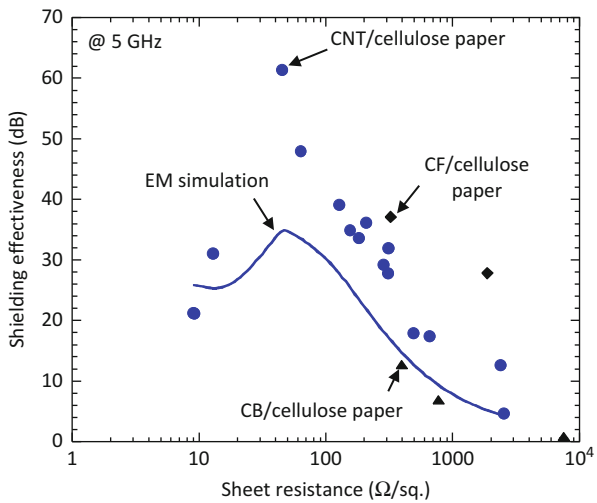


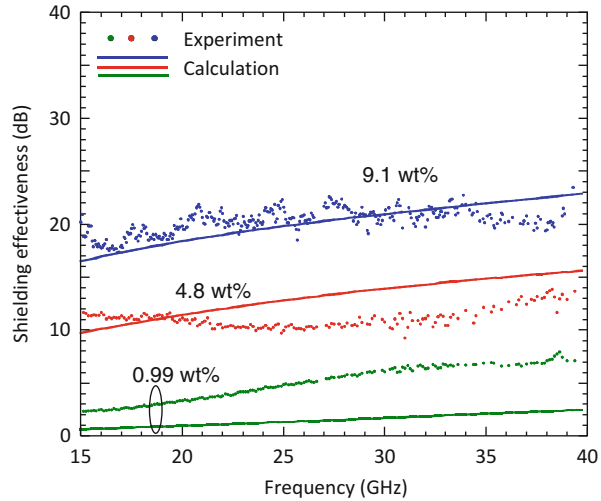
Fig. 9.11 Near-field EMI SEs at 5 GHz as function of sheet resistance [30]



matched the measured data. More than 30-wt% CF was required to achieve an EMI SE of 30 dB for CF/cellulose composite papers, and the EMI SE for CB/cellulose composite paper with 30-wt% CB was 13 dB. This also demonstrates the advantage of CNT over CB and CF. Metal shielding is less effective for near-field EMI shielding because the metal resistance is too low, as can be seen from Fig. 9.11.

The far-field EMI SEs measured with the free-space method along with theoretical curves are shown in Fig. 9.12. The theoretical far-field EMI SE was calculated by

Fig. 9.12 Far-field EMI SEs measured with free-space method and their theoretical curves [30]



$$SE = -10 \log_{10} |t|^2$$

$$t = \frac{(1 - r_i^2) \exp(-\gamma d)}{1 - r_i^2 \exp(-2\gamma d)}, \quad (9.5)$$

where r_i is the reflection at the air and paper interface, γ is the propagation constant in the paper, and d is the paper thickness. The measured ϵ_r' and conductivity were used in the calculations. Fairly good agreement was obtained between the measured and calculated EMI SEs. About 10-wt% CNT was required to achieve 20-dB far-field EMI SE. A metal plate reflects incident waves almost perfectly, but perfect reflection is undesirable for shielding applications such as those with electronic components.

5 Conclusion and Future Direction

The properties of CNT/cellulose composite material were reviewed, and paper-making process was given a special focus. Higher electrical conductivity and permittivity values compared to those for polymer-based composite materials were achieved without decreasing the paper strength.

Measured temperature dependences of electrical conductivity for CNT/cellulose composite paper were described with Sheng's FIT model. The tunneling widths and junction areas were estimated from the specific temperatures T_0 and T_1 deduced through rigorous calculations. The estimated widths were close to the interlayer distance of graphite. This suggested that the electrical conduction in CNT/cellulose composite paper was dominated by the fluctuation-induced tunneling between the CNT-CNT junctions and there was no inclusion.

The EMI SE characteristics measured using the MSL method and the free-space method were qualitatively matched to the theoretical characteristics obtained through the simulations. Our CNT/cellulose composite, with its improved near-field EMI SE characteristics, can be used to reduce electromagnetic wave interference, control undesired reflection, prevent cross talk, and suppress noise in printed circuit boards (PCBs). The design and fabrication of PCBs incorporating CNT/cellulose composite is expected to be a promising application in the future.

Although the far-field EMI SE of 20 dB can be achieved with CNT/cellulose composite paper, the absorption ratio was about 50 %. The design and control of the permittivity is necessary in order to increase the absorption ratio. Another effective means for absorbing EM waves involves the use of multilayered composite structures with metal backplanes, although the operating frequency is limited to a specific range and the thickness is larger than with a single sheet. The CNT/cellulose composite paper with high permittivity reduces the thickness of the absorbing structures. In addition, CNT/cellulose composite paper with high conductivity may replace metal films as backplanes. The detailed design and fabrication of EM absorbers will also be necessary in the future.

References

1. Zhang M, Fang S, Zakhidov AA, Lee SB, Aliev AE, Williams CD, Atkinson KR, Baughman RH (2005) *Science* 309:1215
2. Gruner G (2006) *J Mater Chem* 16:3533
3. Cao Q, Rogers JA (2009) *Adv Mater* 21:29
4. Zanfeng L, Gang B, Yi H, Yanfeng M, Feng D, Feifei L, Tianying G, Yangsheng C (2007) *Carbon* 45:821
5. Grimes CA, Mungle C, Kouzoudis D, Fang S, Eklund PC (2000) *Chem Phys Lett* 319:460
6. Kaiser AB (2001) *Adv Mater* 13:927
7. Aleshin AN (2006) *Adv Mater* 18:17
8. Mott NF, Davis GA (1979) *Electronic properties in noncrystalline materials*, 2nd edn. Clarendon, Oxford
9. Sheng P (1980) *Phys Rev B* 21:2180
10. Kymakis E, Amaratunga GAJ (2006) *J Appl Phys* 99:084302
11. Skakalova V, Kaiser AB, Woo YS, Roth S (2006) *Phys Rev B* 74:085403
12. Jaiswal M, Wang W, Shiral Fernando KA, Sun YP, Menon R (2007) *J Phys Condens Matter* 19:446006
13. Kim GT, Jhang SH, Park JG, Park YW, Roth S (2001) *Synth Met* 117:123
14. Shiraishi M, Ata M (2002) *Synth Met* 128:235
15. Salvato M, Cirillo M, Lucci M, Orlanducci S, Ottaviani I, Terranova ML, Toschi F (2008) *Phys Rev Lett* 101:246804
16. Kim HM, Kim K, Lee CY, Joo J, Cho SJ, Yoon HS, Pejakovic DA, Yoo JW, Epstein AJ (2004) *Appl Phys Lett* 84:589
17. Kim HM, Choi MS, Joo J, Cho SJ, Yoon HS (2006) *Phys Rev B* 74:054202
18. Shi SL, Liang J (2007) *J Appl Phys* 101:023708
19. Simsek Y, Ozyuzer L, Seyhan AT, Tanoglu M, Schulte K (2007) *J Mater Sci* 42:9689
20. Zhang R, Baxendale M, Peijs T (2007) *Phys Rev B* 76:195433
21. Mdarhri A, Carmona F, Brosseau C, Delhaes P (2008) *J Appl Phys* 103:054303
22. Ahmad K, Pan W (2009) *Compos Sci Technol* 69:1016

23. Fugetsu B, Sano E, Sunada M, Sambongi Y, Shibuya T, Wang X, Hiraki T (2008) *Carbon* 46:1256
24. Jung R, Kim HS, Kim Y, Kwon SM, Lee HS, Jin HJ (2008) *J Polym Sci Part B Polym Phys* 48:1235
25. Oya T, Ogino T (2008) *Carbon* 46:169
26. Anderson RE, Guan J, Ricard M, Dubey G, Su J, Lopinski G, Dorris G, Bourne O, Simard B (2010) *J Mater Chem* 20:2400
27. Swanson JW (1961) *Tappi* 44:142
28. Kato M, Isogai A, Onobe F (1998) *J Wood Sci* 44:361
29. Scheutjens JM, Fleer GJ (1980) *J Phys Chem* 84:178
30. Imai M, Akiyama K, Tanaka T, Sano E (2010) *Compos Sci Technol* 70:1564
31. Sandler J, Shaffer MSP, Prasse T, Bauhofer W, Schulte K, Windle AH (1999) *Polymer* 40:5967
32. Allaoui A, Bai S, Cheng HM, Bai JB (2002) *Compos Sci Technol* 62:1993
33. Kilbride BE, Coleman JN, Fraysse J, Fournet P, Cadek M, Drury A, Hutzler S, Roth S, Blau WJ (2002) *J Appl Phys* 92:4024
34. Kymakis E, Alexandou I, Amaratunga GAJ (2002) *Synth Met* 127:59
35. Park C, Ounaies Z, Watson KA, Crooks RE, Smith J Jr, Lowther SE, Connell JW, Siochi EJ, Harrison JS, St Clair TL (2002) *Chem Phys Lett* 364:303
36. Ounaies Z, Park C, Wise KE, Siochi EJ, Harrison JS (2003) *Compos Sci Technol* 63:1637
37. Ramasubramaniam R, Chen J, Liu H (2003) *Appl Phys Lett* 83:2928
38. Sandler JKW, Kirk JE, Kinloch IA, Shaffer MSP, Windle AH (2003) *Polymer* 44:5893
39. Grunlan JC, Mehrabi AR, Bannon MV, Barh JL (2004) *Adv Mater* 16:150
40. Martin CA, Sandler JKW, Shaffer MSP, Schwarz MK, Bauhofer W, Schulte K, Windle AH (2004) *Compos Sci Technol* 64:2309
41. Meincke O, Kaempfer D, Weickmann H, Friedrich C, Vathauer M, Warth H (2004) *Polymer* 45:739
42. Aarab H, Baitoul M, Wery J, Almairac R, Lefrant S, Faulques E, Duvail JL, Hamedoun M (2005) *Synth Met* 155:63
43. McNally T, Potschke P, Halley P, Murphy M, Martin D, Bell SEJ, Brennan GP, Bein D, Lemoine P, Quinn JP (2005) *Polymer* 46:8222
44. Wang L, Dang ZM (2005) *Appl Phys Lett* 87:042903
45. Ahmad K, Pan W, Shi SL (2006) *Appl Phys Lett* 89:133122
46. Chang TE, Kisliuk A, Rhodes SM, Brittain WJ, Sokolov AP (2006) *Polymer* 47:7740
47. Dalmas F, Dendievel R, Chazeau L, Cavaille JY, Gauthier C (2006) *Acta Mater* 54:2923
48. Hu G, Zhao C, Zhang S, Yang M, Wang Z (2006) *Polymer* 47:480
49. Moiala A, Li Q, Kinloch IA, Windle AH (2006) *Compos Sci Technol* 66:1285
50. Thostenson ET, Chou TW (2006) *Carbon* 44:3022
51. Bonnet P, Sireude D, Garnier B, Chauvet O (2007) *Appl Phys Lett* 91:201910
52. Broza G, Piszczek K, Schulte K, Sterzynski T (2007) *Compos Sci Technol* 67:890
53. Dai J, Wang Q, Li W, Wei Z, Xu G (2007) *Mater Lett* 61:27
54. Francis LF, Grunlan JC, Sun J, Gerberich WW (2007) *Colloids Surf A Physicochem Eng Aspects* 311:48
55. Huang Y, Li N, Ma Y, Du F, Li F, He X, Lin X, Gao H, Chen Y (2007) *Carbon* 45:1614
56. Jeon K, Lumata L, Tokumoto T, Steven E, Brooks J, Alamo RG (2007) *Polymer* 48:4751
57. Jiang MJ, Dang ZM, Xu HP (2007) *Appl Phys Lett* 90:042914
58. Jiang MJ, Dang ZM, Xu HP (2007) *Eur Polym J* 43:4924
59. Kovacs JZ, Velagala BS, Schulte K, Bauhofer W (2007) *Compos Sci Technol* 67:922
60. Lisunova MO, Mamunya YP, Lebovka NI, Melezhyk AV (2007) *Eur Polym J* 43:949
61. Liu L, Matitsine S, Gan YB, Chen LF, Kong LB, Rozanov KN (2007) *J Appl Phys* 101:094106
62. Ma PC, Kim JK, Tang BZ (2007) *Compos Sci Technol* 67:2965
63. Musumeci AW, Silva GG, Liu JW, Martens WN, Waclawik ER (2007) *Polymer* 48:1667
64. So HH, Cho JW, Sahoo NG (2007) *Eur Polym J* 43:3750
65. Xiang C, Pan Y, Guo J (2007) *Ceram Int* 33:1293
66. Zhang CS, Ni QQ, Fu SY, Kurashiki K (2007) *Compos Sci Technol* 67:2973

67. Chou WJ, Wang CC, Chen CY (2008) *Compos Sci Technol* 68:2208
68. Grossiord N, Kivitt PJJ, Loos J, Meuldijk J, Kyrylyuk AV, van der Schoot P, Koning CE (2008) *Polymer* 49:2866
69. Kim DO, Lee MH, Lee JH, Lee TW, Kim KJ, Lee YK, Kim T, Choi HR, Koo JC, Nam JD (2008) *Org Electron* 9:1
70. Li Q, Xue Q, Hao L, Gao X, Zheng Q (2008) *Compos Sci Technol* 68:2290
71. Li Y, Chen C, Zhang S, Ni Y, Huang J (2008) *Appl Surf Sci* 254:5766
72. Mamunya Y, Boudenne A, Lebovka N, Ibos L, Candau Y, Lisunova M (2008) *Compos Sci Technol* 68:1981
73. Mu M, Walker AM, Torkelson JM, Winey KI (2008) *Polymer* 49:1332
74. Murthy DVB, Subramanian V, Sundaray B, Natarajan TS (2008) *Appl Phys Lett* 92:222111
75. Show Y, Itabashi H (2008) *Diam Relat Mater* 17:602
76. Valentino O, Sarno M, Rainone NG, Nobile MR, Ciambelli P, Neitzert HC, Simon GP (2008) *Phys E* 40:2440
77. Wang Q, Dai J, Li W, Wei Z, Jiang J (2008) *Compos Sci Technol* 68:1644
78. Wu TM, Chen EC (2008) *Compos Sci Technol* 68:2254
79. Rosca ID, Hoa SV (2009) *Carbon* 47:1958
80. Liu J, Rinzler AG, Dai H, Hafner JH, Bradley RK, Boul PJ, Lu A, Iverson T, Shelimov K, Huffman CB, Rodriguez-Macias F, Shon YS, Lee TR, Colbert DT, Smalley RE (1998) *Science* 280:1253
81. Wu Z, Chen Z, Du X, Logan JM, Sippel J, Nikolou M, Kamaras K, Reynolds JR, Tanner DB, Hebard AF, Rinzler AG (2004) *Science* 305:1273
82. Park JG, Li S, Liang R, Fan X, Zhang C, Wang B (2008) *Nanotechnology* 19:185710
83. Wang D, Song P, Liu C, Wu W, Fan S (2008) *Nanotechnology* 19:075609
84. Tanaka T, Sano E, Imai M, Akiyama K (2010) *J Appl Phys* 107:054307
85. Ago H, Kugler T, Cacialli F, Salaneck WR, Shaffer MSP, Windle AH, Friend RH (1999) *J Phys Chem B* 99:103
86. Hertel T, Walkup RE, Avouris P (1998) *Phys Rev B* 58:13870
87. Fuhrer MS, Nygard J, Shih L, Forero M, Yoon YG, Mazzoni MSC, Choi HJ, Ihm J, Louie SG, Zettl A, McEuen PL (2000) *Science* 288:494
88. Grimes CA, Dickey EC, Mungle C, Ong KG, Qian D (2001) *J Appl Phys* 90:4134
89. Watts PCP, Ponnampalam DR, Hsu WK, Barnes A, Chambers B (2003) *Chem Phys Lett* 378:609
90. Wu J, Kong L (2004) *Appl Phys Lett* 84:4956
91. Xiang C, Pan Y, Liu X, Sun X, Shi X, Guo J (2005) *Appl Phys Lett* 87:123103
92. Saib A, Bednarz L, Daussin R, Bailly C, Lou X, Thomassin JM, Pagnoulle C, Detrembleur C, Jérôme R, Huynen I (2006) *IEEE Trans Microw Theory Tech* 54:2745
93. Zhu H, Lin H, Guo H, Yu L (2007) *Mater Sci Eng B* 138:101
94. Konyushenko EN, Kazantseva NE, Stejskal J, Trchova M, Kovarova J, Sapurina I, Tomishko MM, Demicheva OV, Prokes J (2008) *J Mag Mag Mater* 320:231
95. Liu L, Kong LB, Matitsine S (2008) *Appl Phys Lett* 93:113106
96. Shi SL, Liang J (2008) *Nanotechnology* 19:255707
97. Thomassin JM, Pagnoulle C, Bednarz L, Huynen I, Jerome R, Detrembleur C (2008) *J Mater Chem* 18:792
98. Zhao X, Koos AA, Chu BTT, Johnston C, Grobert N, Grant PS (2009) *Carbon* 47:561
99. Lagarkov AN, Sarychev AK (1996) *Phys Rev B* 53:6318

Ehsan Zeimaran, Abozar Akbarivakilabadi, and Mainak Majumder

Contents

1	Introduction	214
2	Literature Review	215
2.1	Functionalization with Matrix	215
2.2	Acid and Ultrasonic Treatment	220
2.3	Preparation Methods	236
3	Conclusion	242
	References	243

Abstract

Carbon nanotubes (CNTs) exhibit excellent mechanical, electrical, and magnetic properties as well as nanometer-scale diameter and high aspect ratio, which give them a great deal of attention and have been the focus of extensive research efforts as model systems in nanotechnology. Since CNTs usually agglomerate due to van der Waals forces, it is extremely difficult to disperse and align them in a polymer matrix, which consequently leading to many defect sites in the composites and limiting the efficiency of CNTs on polymer matrices. In this chapter, we focus on recent development in preparation and characterization and also review effective parameters on CNT dispersion in polystyrene carbon nanotube nanocomposites.

E. Zeimaran

Department of Polymer Engineering, Faculty of Chemical Engineering, Universiti Teknologi Malaysia, Johor Bahru, Malaysia

e-mail: ehsan_zeimaran@yahoo.com

A. Akbarivakilabadi (✉) • M. Majumder

Nanoscale Science and Engineering Laboratory (NSEL), Department of Mechanical and Aerospace Engineering, Monash University, Clayton, VIC, Australia

e-mail: Abozar.Akbarivakilabadi@monash.edu; Mainak.Majumder@monash.edu

J.K. Pandey et al. (eds.), *Handbook of Polymer Nanocomposites. Processing, Performance and Application – Volume B: Carbon Nanotube Based Polymer Composites*,

DOI 10.1007/978-3-642-45229-1_44, © Springer-Verlag Berlin Heidelberg 2015

Keywords

Polystyrene • Carbon nanotube • Nanocomposite • Functionalization • Ultrasonication

1 Introduction

Polystyrene (PS) is one of the most widespread polymers due to low price and significant mechanical properties and electrical insulation characteristic. PS synthesizes via some techniques such as emulsion polymerization, precipitation polymerization, solution polymerization, suspension polymerization, dispersion polymerization, and seeded polymerization with a great monodispersability, useful for biomedical, electrical, architecture, automotive, and packaging application. Owing to some characteristics such as modest synthesis procedure, versatility, clarity, and solubility in common solvent, researchers have encouraged applying it as matrix in polymer composite. It is worth mentioning that clarity of PS leads to easy observation of fillers (i.e., CNTs) embedded in that. Although PS has many desirable properties, its disadvantages are low impact strength and poor chemical resistance at room temperature, especially to ketones and ethers. Thus, addition of latter material is required to optimize the inappropriate properties. Copolymerization, blending, and filling techniques have been used to overcome the PS drawbacks, but since carbon nanotube can yield the required properties, scientists were more interested to use it as filler in polymer composite.

Today one of the most applied modern technologies is the use of polymer/carbon nanotube nanocomposites (P/CNTs), since they have the capacity to generate new polymer properties. Incorporation of just few percentages of nanotubes has been found to greatly increase a polymer's properties such as conductivity, tensile strength, impact strength, and storage modulus. Even though, final properties of P/CNTs depend on several factors such as type, orientation, and treatment of fillers. Carbon nanotubes are a class of nanofillers with normally nanometer size in diameter and micrometer size in length that have attracted attention since discovery by Ijima in 1991 [11]. In the last two decades, CNTs have achieved more interest rather than other additives such as carbon black and nanoclay due to superb mechanical, thermal, and electrical properties as well as good chemical stability. They are one of the strongest fillers, since tensile strength of the tubes goes over 1 TPa and Young's modulus is 1,000 GPa, and prove much more stiffness compared to steel [1, 3, 16]. Besides mechanical properties, high thermal conductivity of CNTs, approximately 6,000 W/mK and 3,000 W/mK for SWCNTs and MWCNTs, respectively, made them a good candidate to increase thermal stability (twice as high as diamond) of composites via small loading (0.1–5 wt%). In addition, high electrical conductivity of CNTs (around 10^4 S/cm²) which is owing to high aspect ratio, render composites considerable conductivity with a low percolation threshold roughly 1–3 wt% [14]. CNTs are tubed hollow graphene sheet (mostly one dimensional) which have carbon bonded to only three other carbon atoms. Three kinds of nanotube have been produced: single-walled carbon nanotube (SWNT), multi-walled carbon nanotube (MWNT), and double-walled carbon nanotube (DWNT) in which single-walled nanotube has made of

one-wrapped graphene sheet and consequently multi-walled nanotube consists of a few concentric cylindrical graphene sheets. Among these DWNTs can be highly purified compared to MWNTs that contain some percentage of SWNT [25]. The as-produced CNTs usually have a length of 1 μm , and they can be shortened in smaller size via few techniques such as sonication in solution and mechanical milling and also high shear dispersion. Excellent structural properties of CNTs yielded them many potential applications in aerospace, electronics, sport goods, and nanocomposites.

To achieve good properties from carbon nanotube's composites, some factors should be optimized: (1) dispersion of CNTs in matrix, (2) alignment, and (3) loading percentage. It is worth noting that fiber can enhance the strength and stiffness of composite as same as highest strength polymer fibers if they are embedded with good dispersion and orientation. Since carbon nanotube has a tendency to agglomerate owing to the intermolecular van der Waals interaction, dispersibility is a problem in CNT nanocomposite. A number of approaches have been employed in order to increase dispersion of CNTs in the aqueous media and inorganic solvent such as functionalization with strong acid (i.e., sulfuric acid or nitric acid) or polymer, ultrasonic treatment, and mixing of acid and ultrasonic treatment (Woo and Lee 2010).

In the present chapter, we report on the various features of nanocomposite composed of polystyrene and carbon nanotubes particularly conductivity and mechanical properties. To optimize the nanocomposite features, several researches were carried out in which different methods of polymerization were employed, and some attempts have been done to modify the nanotubes via functionalization and ultrasonication with the intention of increasing interaction with polymer. Hence, the chapter is divided according to the effect of polymer functionalization, acid and ultrasonic treatments, and various methods on the final properties of PS/CNT nanocomposite.

2 Literature Review

Carbon nanotubes tend to aggregate due to van der Waals forces, and with normal synthesis, feasibility of agglomeration will increase. Agglomeration will affect mainly on the mechanical and conductive properties of composite since they are sites of stress accumulation. To improve dispersibility and overcome the mentioned difficulty, scientists employed different approaches such as functionalization with matrix, acid, and ultrasonic treatment and studied the influence of method of preparation.

2.1 Functionalization with Matrix

As previously mentioned, carbon nanotubes have a tendency to bundle due to van der Waals attraction between them, and to overcome this limitation, one suitable method is the functionalization with the polymer. In this regard, recent paper by Hu and co-workers [9] reported on the modification of MWCNTs with grafted PS

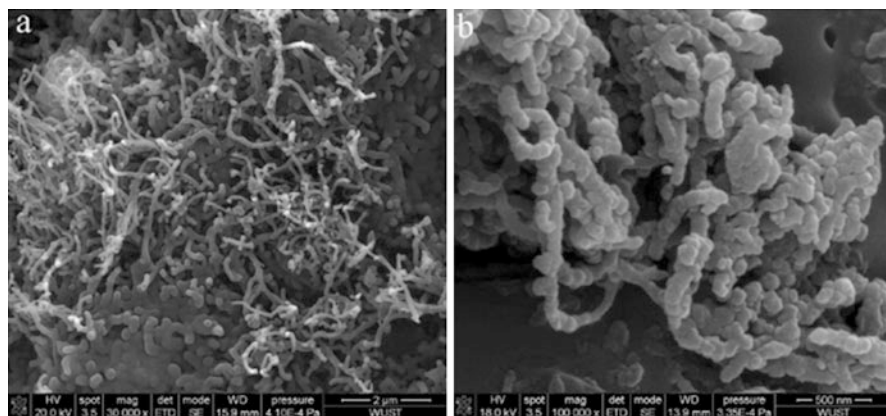


Fig. 10.1 SEM images of (a) purified MWNTs and (b) MWNT/PS

particle onto their wall. They synthesized the PS microspheres and PS/MWCNT composite via emulsion polymerization under sonication. TEM revealed that washing with chloroform cannot remove the PS-decorated MWCNTs as a result of covalent bond between PS and sidewall of tubes. The SEM images (Fig. 10.1) confirmed the grafting of PS on the sidewalls of CNTs. These images clearly show improvement in dispersibility and wettability which finally led to better performance. Moreover, FTIR and Raman spectrums illustrate the presence of the PS band after washing which verify the PS-grafted CNTs. This result proved changing of sp^2 - to sp^3 -hybridized carbon. Thermal investigation showed an 11 °C increase in T_g for composite. The nanocomposite was tested under electric field in which thin and dense chains formed in the direction of electric current and when turned off, returned to original shape. This property makes them suitable for electrorheological (ER) fluids.

In another study, Yuan and co-workers [28] coated MWCNTs with the polymerized styrene using microwave irradiation and incorporated them into the PS matrix via melt-mixing method. Morphological features demonstrated the higher dispersibility of modified nanotubes (m-MWCNT) compared to purified nanotubes (p-MWCNT). This phenomenon was due to the effective interfacial adhesion between PS layer-coated CNTs and matrix. They observed that coated CNTs have better interaction and would break instead of pulling out as a result of cryofracture as approved by Fragneaud et al. [6] and Safadi et al. [19]. The SEM images (Fig. 10.2) evidently represented the white dots (related to broken CNTs) and black points (due to cavities) were attributed to pulling the tubes out. They considered two reasons for altering in impact strength through izod impact test: (1) orientation and (2) interfacial adhesion. Both reasons proved the higher impact strength for PS-m-MWCNT composite, whereas purified MWCNT was lack of sufficient orientation and interfacial adhesion. Furthermore, it was evident that PS-m-MWCNT possesses higher tensile strength and ascends by increasing

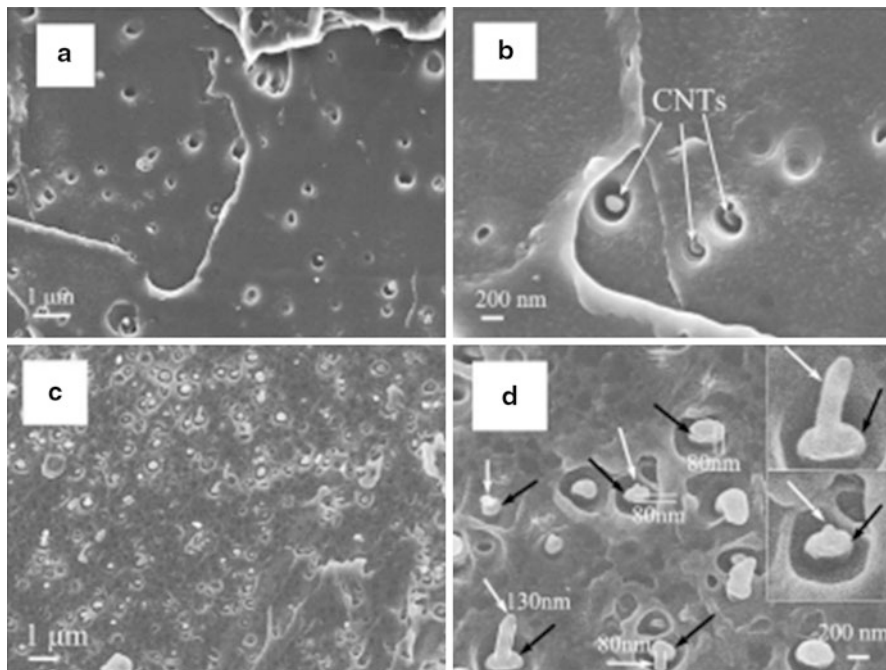


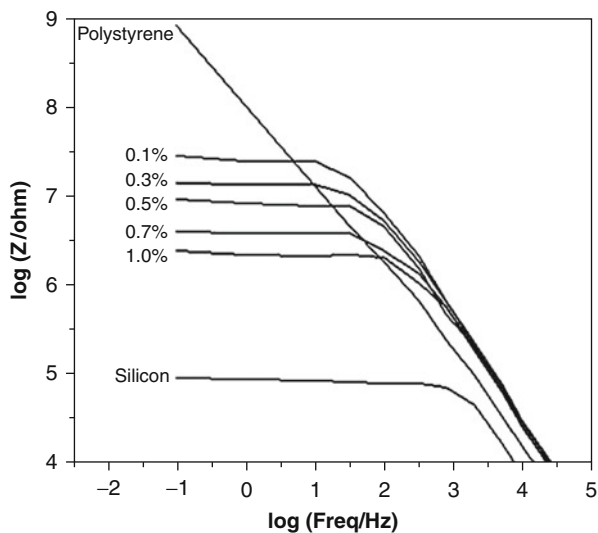
Fig. 10.2 SEM images of the cryofracture faces of PS-p-MWCNT (a, b) and PS-m-MWCNT (c, d) composites with 0.32 wt% nanotube content; Image of the broken nanotube tip on the cryofracture face of PS-m-MWCNT

nanotube content in contrast with PS-p-MWCNT composite which slightly decreases with addition of nanotubes.

Fragneau and co-workers [6] studied the effect of PS-grafted N-doped MWCNT (PS-g-CN_x) in the composite. Grafting was carried out with atom transfer radical polymerization, and the result was compared with the untreated MWCNT/PS (CN_x-a-PS) composite. They observed improved dispersion for PS-g-CN_x when very small aggregation appeared. The improvement in dispersion caused better load transferring and accordingly higher Young's modulus. Beside good dispersion, the better adhesion of tubes to matrix was observed as the tubes were cut inside CN_x-g-PS composite instead of pulling out. This phenomenon can explain higher yield stress in PS-g-CN_x composite. In addition, significant decrease in T_g of composite containing 2.5 vol% CN_x-g-PS was due to plasticizing features of the nanotubes in matrix. This indicates smaller distance between CNTs than the interphase thickness which confirms the effective dispersion. On the other hand, increasing a-CN_x prevents the flowing of composite in experimental temperature whereas the PS-g-CN_x, flow behavior was somewhat the same as PS instead of 2.5 vol%.

The effect of SWCNTs on the electrical conductivity of PS composites was sought in the last decade. Some researchers such as Wang et al. [23] identified the

Fig. 10.3 Bode diagram of SWNT–PS composites as a function of loading of SWNTs



raising of electrical conductivity via addition of very low percentage of carbon nanotube (1 wt%). They distinguished that all the nanocomposites are semiconductors in which enhancing the CNT can modify the composite to a clear ohmic material. Further, measuring of DC and AC impedance of PS/SWCNT displayed the very small resistivity value in 1 wt% loading, ten times lower than the neat PS. Figure 10.3 clearly shows the frequency dependence of composite compared to pristine dielectric PS and semiconductive silicon. At low frequency, the increase of SWCNTs brings about the falling resistivity down, and at high frequency, capacitance in the direction of resistivity led to high reduction of resistivity. To increase the rate of dispersion, they coated the nanotubes with PS and incorporated them into the matrix using suspension polymerization technique. SEM image (Fig. 10.4) exhibited even though coated CNTs are well dispersed and fabricated a continuous network; there are small clusters which are distributed all over the matrix. There were small clusters which distributed all over the matrix.

Hill et al. [8] functionalized SWCNT and MWCNT with copolymer of poly(styrene-co-p-(4-(4'-vinylphenyl)-3-oxabutanol)) (PSV), and it led to esterification of carboxylic acid-bonded nanotubes. The attached PSV gave the polymer solubility in general organic solvent and ability to embed in polystyrene. Further, nanocomposites of PS/CNTs were prepared via wet-casting method. TEM images (Fig. 10.5) clearly show the distribution of modified nanotubes in solvent. It also reveals the presence of PSV-coated nanotubes. The broader signal of functionalized CNTs in NMR was relative to interaction of nanotubes with polymer. The comparison of functionalized PSV before and after hydrolysis was observed by UV-visible and confirmed the removal of some nanotubes from solution due to defunctionalization. It was demonstrated that composite is transparent and possesses high optical quality as well.

Fig. 10.4 SEM micrographs showing SWNTs with an adsorbed polystyrene layer in a 1 % weight SWNT–PS composite

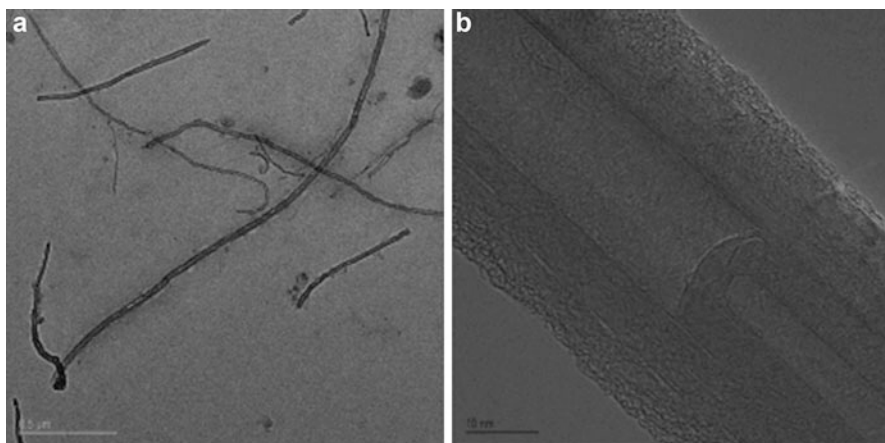
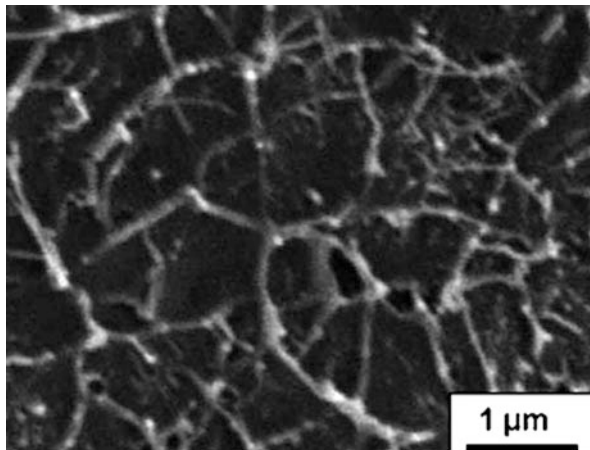
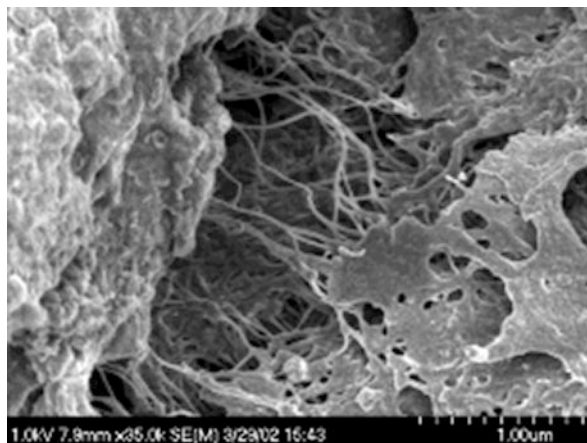


Fig. 10.5 TEM images of PSV-functionalized MWNTs: ((a, left) scale bar) 500 nm and ((b, right) scale bar) 10 nm

SEM micrograph (Fig. 10.6) shows the covalent bond between PSV and nanotubes obtained by esteric linkage. It also proved the presence of large amount of SWCNTs in composite. The thermal investigation showed that amounts of SWCNTs and MWCNTs in functionalized nanotubes are roughly 12 % and 18 %.

In general, functionalization with polystyrene improves the compatibility between matrix and CNTs and has attracted attention of researchers since it enhances the homogenous dispersion for achieving the better properties.

Fig. 10.6 An SEM image of the solid precipitate obtained from the chemical defunctionalization of PSV-functionalized SWNTs. The sample was coated with platinum via sputtering for 30 s



2.2 Acid and Ultrasonic Treatment

Acid treatment and ultrasonic treatment were also used to improve dispersion of nanotubes in PS matrix. Acid treatment was carried out with strong acids to attach the functional groups (carboxyl groups) on the CNTs wall and improve the interaction with matrix whereas ultrasonic treatment can separate the bundle CNTs as an effect of ultrasonic cavitations. Nevertheless, both methods enhance dispersion of nanotubes in PS; they can damage the tubes and make them shorter. In general treatment with acid can have some drawback related to CNTs while it may bend the tubes or open the ends of tubes or sp^3 hybridizing or possibly physical damages to tube chirality. In addition, functionalization generally carries out with toxic acid through multistep reaction. Besides that, sonication sacrifices nanotube properties while it leads to shorter and thinner tubes over time and a combination of methods also may break the nanotubes (Woo and Lee 2010).

Amr and co-workers [3] studied the effect of treated and untreated MWCNTs on the morphological, mechanical, rheological, and thermal properties of PS. The MWCNT/PS composites were synthesized with thermal bulk polymerization and without using initiator. Morphological test demonstrated that CNTs are hollow and tubular with uniform diameter distribution and without distortion. It also indicated that a great distribution can be gained for the lower loading of treated CNTs due to less interaction of fillers. FTIR spectra revealed the presence of extra peaks of carbonyl on the treated tubes. Notably, more dispersion brings about more stress transferring and consequently higher Young's modulus. However, Young's modulus for composite with 1 and 2 wt% loading untreated CNT was lower than neat PS which attributed to reduction of molecular weight of polymer. The lower molecular weight led to reduction in T_g . As predicted the elongation at break increased with increasing both types of CNTs. The rheological studies showed an increment in storage and loss modulus with frequency for all percentage of CNT loading and above 1 wt% treated CNT loading. Moreover, investigation of complex viscosity

showed the increase of viscoelasticity for all the samples instead of 0.5 and 1 wt% treated CNT because CNTs act as plasticizer. TGA analysis revealed the improvement in thermal stability with CNT addition.

Very recently Al-Shabanat [2] investigated the electrical properties of PS/MWCNT composite that was prepared via solution evaporation polymerization. XRD results (Fig. 10.7) pointed out that most of CNTs were well distributed in the PS and the characteristic peaks of individual components are shown. The morphology investigation by TEM revealed that nanotubes dispersed homogeneously with random orientation since ultrasonication was driven. Notably the CNT diameters in composite were larger than neat nanotubes as they are covered by PS during process. The conductivity of pure PS was modified from 7.2×10^{-16} to $3.49 \times 10^{-8} \Omega/\text{cm}^{-1}$ for 1 wt% MWCNT addition. They deduced that by increasing MWCNTs, the dielectric constant and dielectric loss will be enhanced evidently. Dielectric properties were reliant on the temperature and frequency and decrease with rising frequency. Since the temperature goes up to T_g , there is an increase in dielectric properties which is attributed to the arrangement of the dipoles in low viscous system. Further, the peaks related to T_g point strengthen via raising the MWCNTs amount in matrix owing to higher cross-linking density.

The AC conductivity is interpreted by universal power law as below:

$$\sigma_{ac} = \sigma_{dc} + A\omega^S$$

where σ_{ac} and σ_{dc} are ac and dc conductivity, respectively, and $\omega = 2\pi f$ and S is frequency exponent.

The observation of AC conductivity indicated that for 1 wt% sample, it increases linearly; thus, $\sigma_{ac} = A\omega^S$. However, there is a critical frequency for 2.5 and 5 wt% samples that separate the two regions of frequency-dependent $\sigma_{ac} = \sigma_{dc} + A\omega^S$ and frequency-independent $\sigma_{ac} = \sigma_{dc}$.

In another study, Kim and co-workers (2007) introduced MWCNTs into PS via in situ bulk polymerization. Ultrasonic energy was applied to open the π -bonds of nanotubes and improve the dispersion rate [12]. FTIR confirmed the covalent bond between CNTs and PS. This was supported by polydispersity index since it was increased with enhancing nanotubes. Furthermore, TGA graph (Fig. 10.8) discloses the presence of 37 % polystyrene grafted to MWCNTs which is an evidence for covalent bonding. It is noteworthy that addition of CNTs raised the thermal stability of nanocomposite. The morphological investigation by SEM and TEM presented wettability of MWCNTs with polymer and well distribution of nanotubes as well as smoother images of MWCNTs contrasted to grafted one. Two methods of synthesizing were compared via photographic and optical microscopy. In the first experiment, nanocomposite was prepared via in situ polymerization and gained good dispersion. In the second method, solutions mixing, regardless of simple procedure, some aggregation were observed. Therefore, in situ polymerization was preferred for manufacturing the MWCNT/PS nanocomposite. The sharp increase in conductivity was the result of formation of

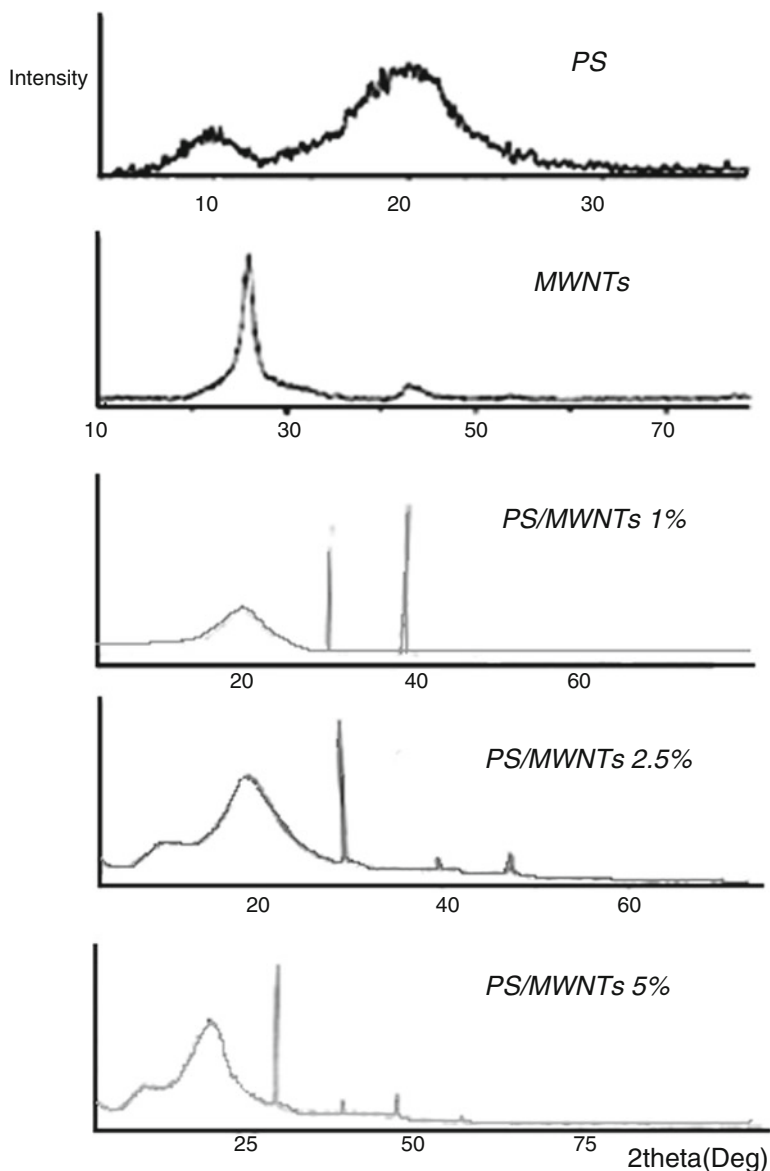
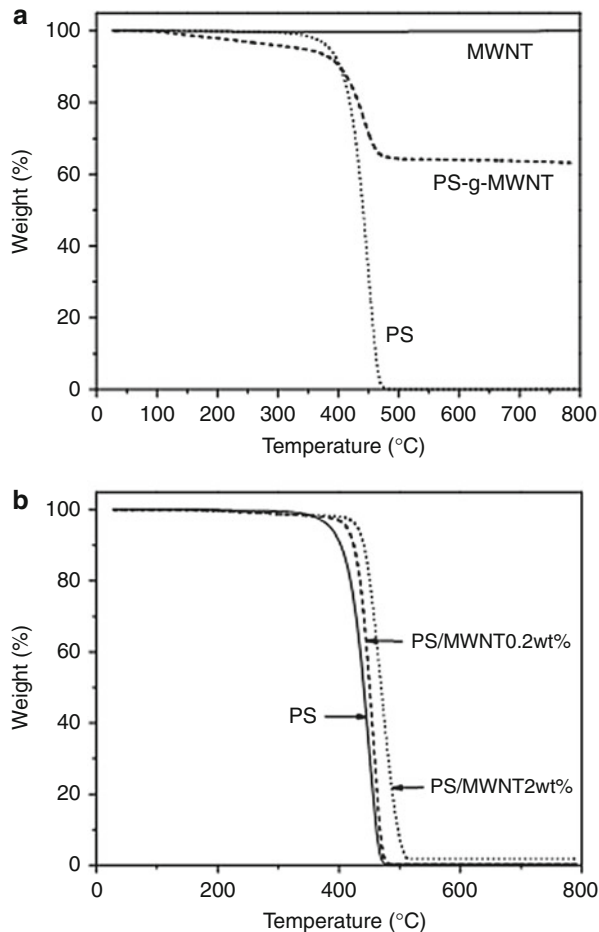


Fig. 10.7 XRD patterns of PS, MWNTs, and PS nanocomposites

continuous network for MWCNT loading more than 5 wt%. Depending on percolation theory, 1 wt% is the optimized amount in using MWCNTs.

Bermúdez and co-workers [4] reported studies of nanocomposite of SWCNT and polystyrene and compared to the embedded modified SWCNT (NTMs) with the room temperature ionic liquid (IL) 1-octyl, 3-methylimidazolium

Fig. 10.8 TGA curves of (a) PS, pristine MWNT, and PS-g-MWNT and (b) PS, PS/MWNT (0.2 wt%), and PS/MWNT (2 wt%) (20 °C /min under N₂)



tetrafluoroborate ([OMIM]BF₄). Melt-mixing methods such as compression and injection moldings have been used for processing the nanocomposites. The effect of nanotube and orientation of them was investigated under several scratching. They observed that more damage goes through compression-molded PS after multiple scratching owing to crack propagation and debris formation. They found that addition of nanotubes can give rise to strain hardening and decrease surface damage, residual depth, and friction coefficient and viscoelastic recovery. The modified nanotubes had a crucial effect on the reduction of the above factors. They attributed this reduction to improved dispersion of nanotubes in PS. However, the influence of sliding in injection-molded specimens was dependent upon the direction of scratches to orientation of nanotubes. The lowest friction coefficient and residual depth and the highest scratch resistance and viscoelastic recovery were attained for parallel direction opposed to perpendicular direction. In addition, compression-molded specimen with random orientation of nanotubes

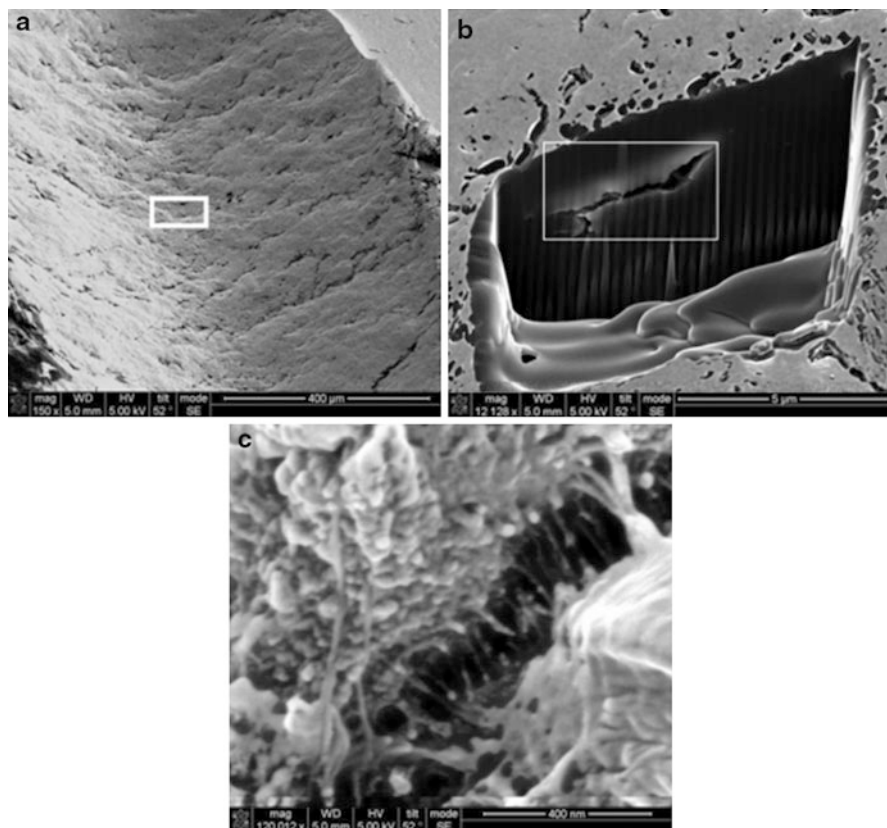
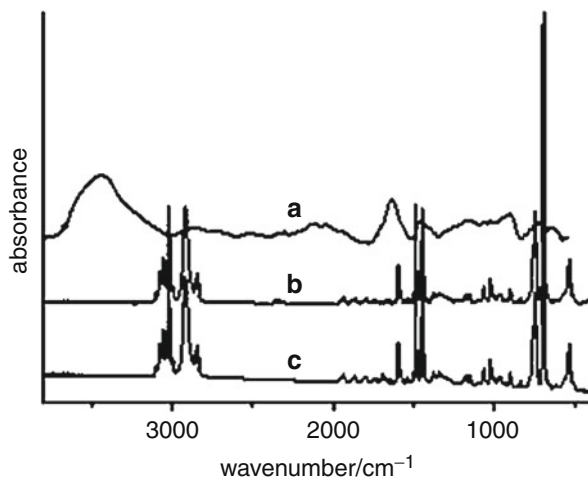


Fig. 10.9 (a) FESEM micrograph of the scar on PS + NTm-L after 15 scratches (25 N; 10 mm/min); (b) FIB-FESEM micrograph of the region selected in (a) showing subsurface crack; (c) magnification of (b) showing carbon nanotube bundles across the crack

possesses intermediate properties between injection-molded specimen in longitudinal and transverse direction. FIB-FESEM (Fig. 10.9) indicated the presence of some bundles of NTMs all over the matrix and emerged the holding of cracks by nanotubes bundles. Therefore, the abrasive wear can be controlled via processing condition, the sliding direction, and the additives.

Yuan and co-workers [27] intensively investigated the effect of draw ratio on the orientation of PS/MWCNT nanocomposite prepared via solution dispersion under ultrasonic energy. The spectroscopic results demonstrated that the orientation degree of MWCNTs enhanced with increasing draw ratio and preferred orientation assessed by I_{0°/I_{90° . The parallel orientation in the stretching direction was also approved by large amount of orientation function (f). It was evident that addition of nanotubes reduced the orientation. However, the characteristic bands of CNTs did not identify with FTIR (Fig. 10.10) due to utilizing low percentage of nanotubes. In addition, they investigated the differences in dichroic ratio (R) as a function of draw

Fig. 10.10 FTIR spectra of (a) MWCNT powder, (b) pure sPS film and (c) sPS/MWCNT nanocomposite film at MWCNT content of 3.0 wt%



ratio for nanocomposite. It was deduced the parallel orientations of characteristic bands of $-\text{CH}_2-$ and benzene rings with rising stretch. Moreover, MWCNTs were hindrances for the suitable orientations of side groups and main chains of PS due to effective interactions. Further, they found that enhancing draw ratio has lower influence on proper orientation of nanocomposite rather than pristine PS.

Recently Huang and Wang [10] introduced MWCNTs into syndiotactic polystyrene (sPS) via coagulation method. Ultrasonic treatment was used to improve dispersibility of nanotubes. They have reported that during melt crystallization, orthorhombic crystallization (β -form) is favored regardless of condition either isothermal or nonisothermal. However, to gain β -form crystallization, the melt-holding temperature should be adjusted; otherwise, hexagonal (α) will be remained. FTIR (Fig. 10.11) and WAX (Fig. 10.12) data indicated that CNTs enhance the β -form during melt crystallization of composite regardless of crystallization condition, while on the contrary, cold crystallization was not affected with CNTs. The crystals of β -form appeared at 858 and 911 cm^{-1} as shown in FTIR graph. Overall, sPS crystallization will rise by increasing the CNT loading and will be unchanged at high loading. DSC thermal analysis (Fig. 10.13) clearly revealed the constant T_g and melting temperature of cold-crystallized composite at 96 and 290 $^\circ\text{C}$ that was ascribed to lack interaction between sPS and CNTs. In addition, based on the DSC analysis, CNT loading led to decrease in chain mobility and peak of cold-crystallized temperature ($T_{p,cc}$) had a reduction of 20 $^\circ\text{C}$ at 1 wt% loading nanotubes in contrary to melt crystallization with 14 $^\circ\text{C}$ growth in 5 wt% CNTs. Moreover, crystallization increases due to nucleation site produced by CNT, giving rise to formation of transcrystalline layer (TCL) on the nanotube surface. They used Avrami equation to explain the percolation threshold and deduced that percolation threshold appeared at 1 wt% CNTs.

Woo and Lee (2010) have reported the fabrication of a nanocomposite from latex-blended polystyrene and MWCNT. Three methods of modification such as

Fig. 10.11 FTIR spectra of as-prepared sPS/CNT samples held at $T_{\max} = 275^\circ\text{C}$ for 10 min and cooled to room temperature at a rate of $10^\circ\text{C}/\text{min}$. The characteristic absorbance peaks for β -form sPS are 858 and 911 cm^{-1} (arrows), and those for α -form are 852 and 902 cm^{-1} . The inset shows the content of α -form crystallites (P_α) developed in the samples after being held at different T_{\max}

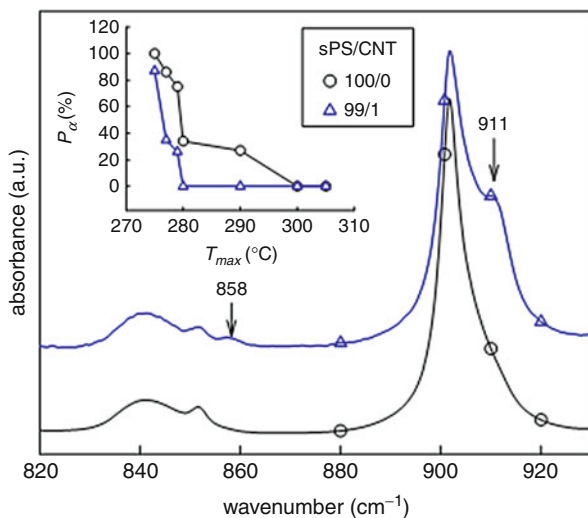
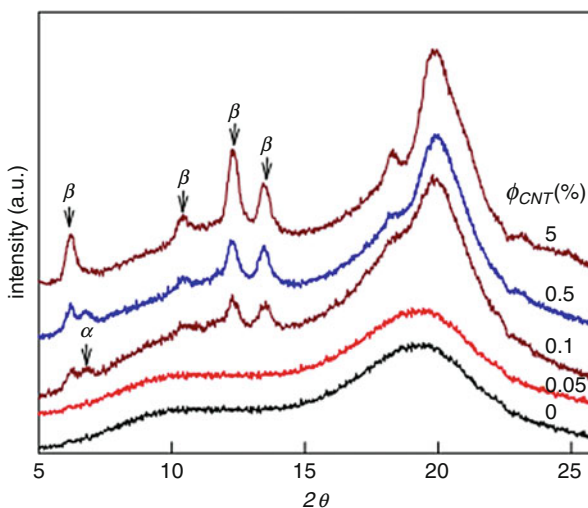


Fig. 10.12 WAXD intensity profiles of melt-quenched sPS/CNT composites. The composites are held at 300°C for 10 min, followed by quenching into liquid nitrogen



acid treatment via sulfuric and nitric acid, ultrasonic treatment, and combination of acid and ultrasonic treatment were used to improve rheological and morphological properties accompanied with better dispersion of nanotubes. However, combined method has a disadvantage as it cut the nanotubes length. They synthesized the monodispersed polystyrene with 500 nm particle size in which addition of ethanol reduced the particle size. This phenomenon took place due to decrease in polarity of solution in order to enhance the solubility of styrene in water. The FESEM images (Fig. 10.14) indicate the composite of pristine (PS/P-CNT), acid treatment (PS/A-CNT), ultrasonic treatment (PS/U-CNT), and combination of

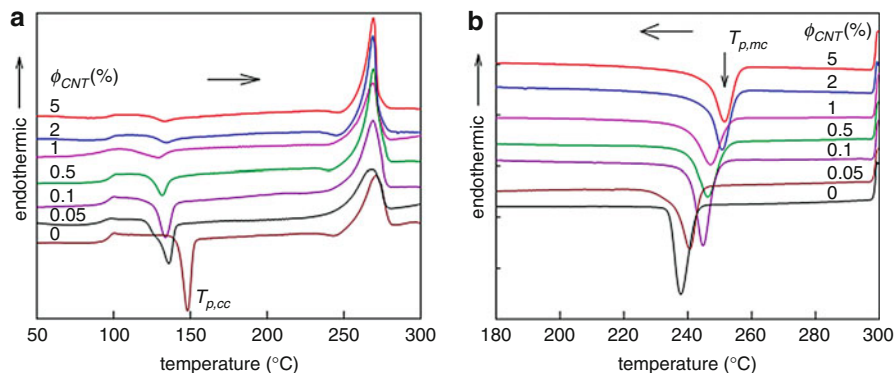


Fig. 10.13 (a) DSC heating traces of neat sPS and CNT-filled composites for cold crystallization studies. The melt-quenched samples are heated at $10^{\circ}\text{C}/\text{min}$ to 300°C . (b) DSC cooling curves for composites for melt crystallization studies. After holding 300°C for 10 min, the samples are cooled at a rate of $10^{\circ}\text{C}/\text{min}$

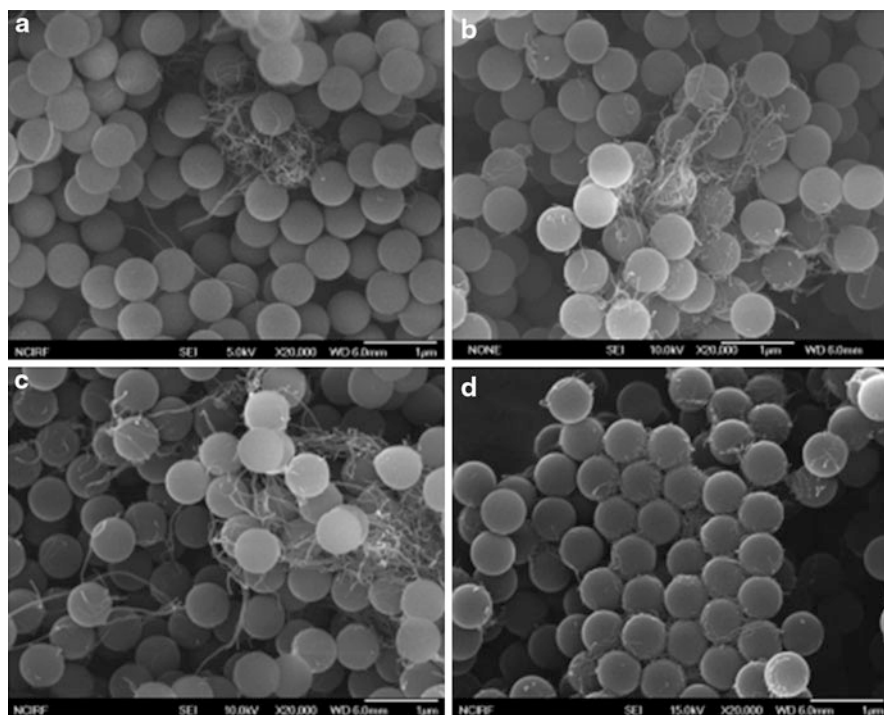


Fig. 10.14 FFE-SEM micrographs showing the dispersion state of MWCNTs in freeze-dried PS/MWCNT nanocomposites: (a) PS/P-CNT, (b) PS/A-CNT, (c) PS/U-CNT and (d) PS/AU-CNT

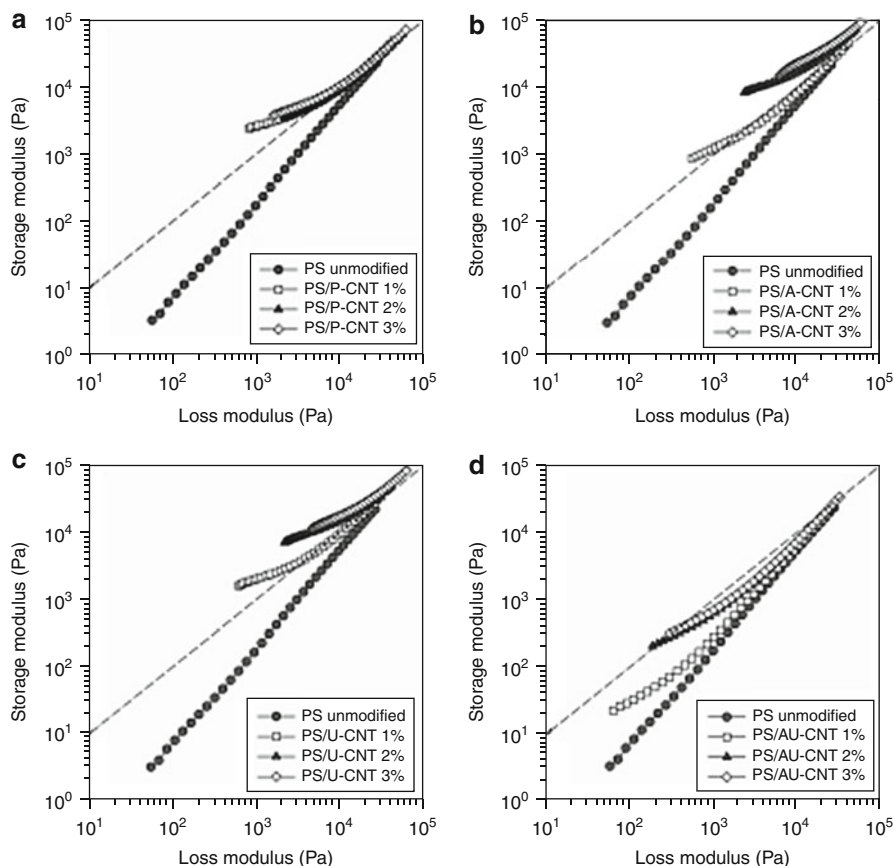
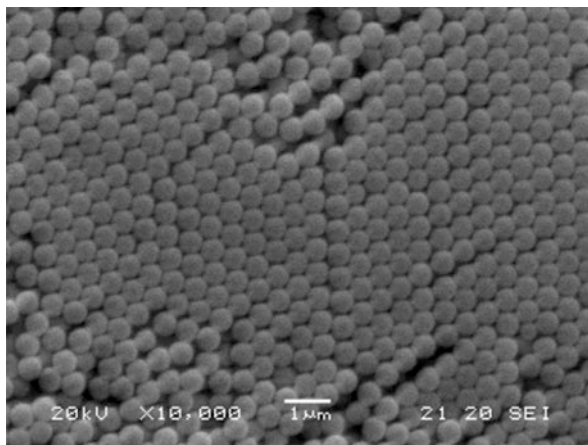


Fig. 10.15 Effect of MWCNT content on storage modulus versus loss modulus of PS/MWCNT nanocomposites prepared by latex technology: (a) PS/P-CNT, (b) PS/A-CNT, (c) PS/U-CNT and (d) PS/AU-CNT

methods (PS/AU-CNT). The best dispersion acquired for PS/AU-CNT and the worse one was for PS/P-CNT due to highly entangled and aggregated nanotubes. The rheological investigation revealed the improved storage modulus and complex viscosity for acid-treated and ultrasonic-treated samples with increasing nanotube concentration. This was caused by good dispersion as a result of using treatment. The plot of storage modulus versus loss modulus is illustrated in Fig. 10.15. Storage modulus was laid above loss modulus for 2 wt% CNT loading for both PS/A-CNT and PS/U-CNT compared to 3 wt% for PS/P-CNT. Moreover, PS/AU-CNT composite showed the lower storage laid down of loss modulus even in 3 wt% CNT content. According to these explanations, acid treatment and ultrasonic treatment can gain better result related to PS/MWCNT nanocomposite compared with pristine and combined method.

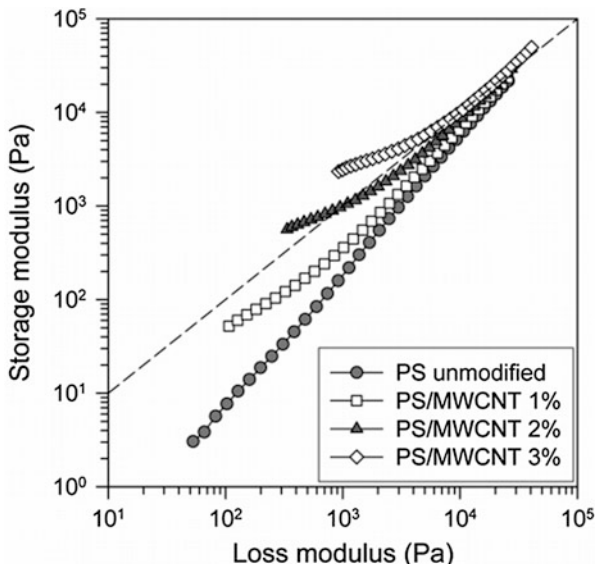
Fig. 10.16 SEM micrograph of PS particles prepared by emulsifier-free emulsion polymerization in the presence of ethanol



Woo et al. (2009) used latex technology to prepare PS/MWCNT nanocomposite with purified nanotubes in the presence of ultrasonicator. They synthesized styrene monomer by emulsion polymerization and without using emulsifier in which two peaks 10–100 K and 100 K were observed for molecular weight distribution. Furthermore, the addition of ethanol assisted to solubility and led to preferred homogenous nucleation. SEM microscopy (Fig. 10.16) indicated the uniform hexagonal spherical styrene particles which were monodispersed. The FESEM result obviously showed the presence of some CNT bundles even after sonication. They also explored the trend in increasing the complex viscosity and modulus with adding more nanotubes. They attributed the growth of complex viscosity to shear thinning at low frequency. Conspicuously enhancement in storage modulus was more pronounced than loss modulus. The higher rising of storage modulus in low frequency associated with formation of network via nanotubes. The network was formed at the 3 wt% CNT content since storage modulus lays above loss modulus in all frequencies shown in Fig. 10.17.

A study on composite of SWCNTs/PS prepared with precipitation method was carried out via [7]. They drove sonication to improve dispersion and subsequently reduce the amount of nanotubes to reach percolation threshold. The result of electrical conductivity revealed that the good dispersion of CNTs and percolation threshold occurred for less than 0.5 wt%. Moreover, they found that CNTs possess low quality which is deduced from low plateau conductivity. Glass-transition temperature of nanocomposite was enhanced at low CNT content about 6–7 °C rather than neat PS for both heating and cooling and then reached a plateau for loading more than 1 % CNTs. The increase of T_g was attributed to reduction of mobility by addition of nanotubes since polymer is in close proximity of CNTs. The heat capacity changed at T_g and decreased with increasing nanotube concentration, except at very high SWCNT contents (>10 wt%), where the heat capacity change began to increase. In addition, relaxation rate followed a same qualitative behavior at T_g and dropped with reduction of mobility. The activation energy was enhanced

Fig. 10.17 Effect of MWCNT content on storage modulus versus loss modulus of PS/MWCNT composites prepared by latex technology



at low CNT loading and diminished at high CNT loading. Besides, an increase in activation energy is consistent with an increase in the cooperative motion associated with the T_g . Notably activation energy had the highest value at percolation threshold.

Peters and co-workers [18] processed a nanocomposite of PS/SWCNT through solution mixing to improve thermal conductivity. They used sonication for better dispersion of nanotubes amid latex of styrene. DSC demonstrated the reduction of T_g with increasing nanotubes as a result of lower heat capacity related to CNTs. They observed that thermal conductivity (Fig. 10.18) enhances 4.5 orders of magnitude with nanotube content of 10%. However, more than 10% loading have a slight influence in T_g due to appearance of agglomeration. On the other hand, temperature increased the conductivity until T_g which was surprising. In addition, they measured the thermal conductivity by using modulated DSC. According to this model, molten polymers have less conductivity than glassy one, and heating the polymers leads to declining stiffness and increasing Kapitza resistance.

Tchoul and co-workers [22] published composite of PS with various types of SWCNTs like HiPco, CoMoCat, and pulsed laser vaporization (PLV). Two different methods were applied to prepare the composites: (i) solution evaporation and (ii) coagulation method. They have also reported the use of two kinds of functionalization with poly [(m-phenylenevinylene)-co-(2,5-dioctoxy-p-phenylenevinylene)] (PmPV) and oxidized nitric acid to investigate the influence of functionalities on the electrical features and dispersion of tubes in PS. They observed that percolation threshold was 0.13–0.17% and 0.4–0.5% for functionalized nanotubes with PmPv

Fig. 10.18 Thermal conductivities as measured using modulating temperature cycle around a single temperature. For polystyrene, data at 25, 80, and 150 °C represents method 1 while method 2 data are presented for 0 and 50 °C. Lines are drawn to guide the eye

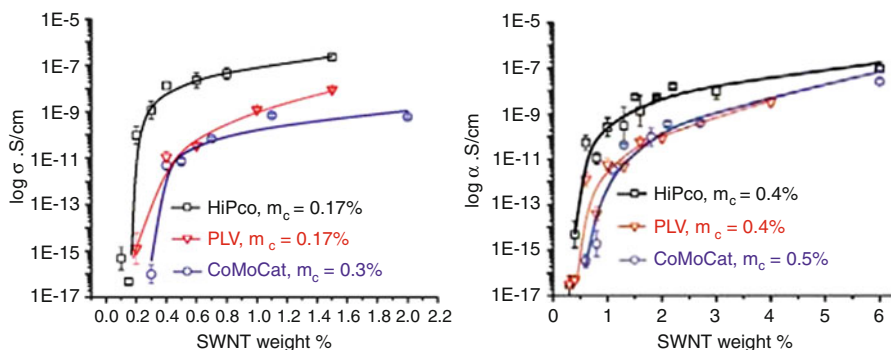
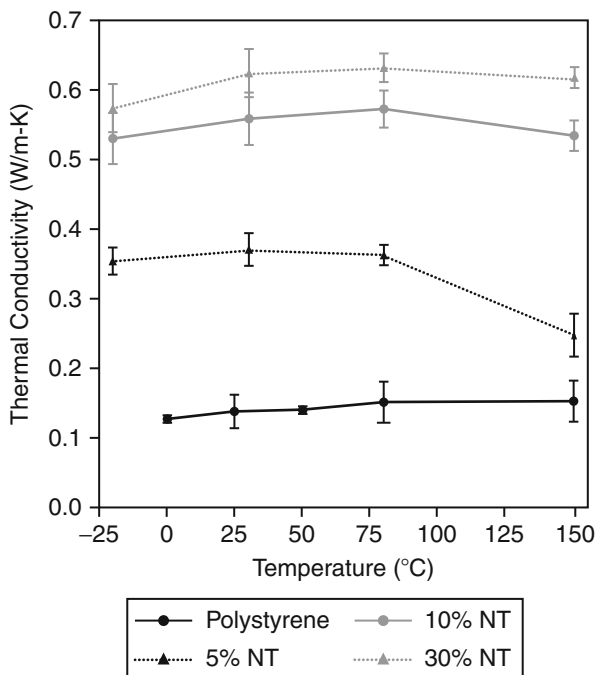


Fig. 10.19 Electrical conductivity of the composites of SWNT dispersed by PmPV in polystyrene (*left*) and oxidized SWNT in polystyrene (*right*). Error bars are two standard deviations

and oxidized nitric acid, respectively. This discrepancy comes from the higher aspect ratio of PmPv tubes which resulted in lower loading ratio. Consequently, CoMoCat with smaller L/D ratio has higher percolation threshold. The plateau conductivity is the highest for HiPco at 1 wt% CNT loading as can be seen in Fig. 10.19. They also found three points to distinguish the carbon nanotubes: (1) the resistance at bundle to

bundle, (2) the density of nanotube bundle, and (3) the quantity of nanotubes. AFM images (Fig. 10.20) revealed the presence of globular particles in both pure and PmPV-functionalized nanotubes which SEM clearly showed these particles as winding nanotubes. The nanocomposite modified with PmPV indicated some black particles that were recognized as agglomeration of nanotubes as confirmed with SEM (Fig. 10.21). The better dispersion of nanotubes was approved by optical absorption and attributed to less agglomeration of nanotubes during evaporation of chloroform and coagulation of the dispersion in water.

Yu et al. [26] used latex technology to prepare conductive composite with incorporation of MWCNTs in PS. Applying sonication significantly ascended dispersion rate of CNTs in sodium dodecyl sulfate (SDS). Percolation threshold reached at 1.5 wt%, while a good dispersion composed network in composite. Conductivity of composite went up to 1 S m^{-1} for loading of 5.5 wt% since pristine polystyrene conductivity was $10^{-10} \text{ S m}^{-1}$. The related graph is shown in Fig. 10.22 in logarithmic scale. The morphology investigation of composites clearly showed that minimum ratio of 1.5:1 wt% for SDS and MWCNT, respectively, required achieving highest dispersion. Morphology tests were conducted by SEM, TEM, and electron tomography and inducted that nanotubes were well dispersed, and hardly agglomeration observed.

Yang and co-workers [25] employed in situ polymerization to fabricate nanocomposite from carbon nanotubes and polystyrene with the aid of ultrasonicator. TEM confirmed the hollow structure of nanotubes. They found that microhardness, friction coefficient, and wear rate had the most improvement in addition of 1.5 wt% CNTs. After 1.5 wt% loading, deterioration in the properties was observed due to agglomeration of CNTs. A noticeable reduction in wear rate from 1.3×10^{-4} to 8.0×10^{-6} was observed for nanocomposite containing 1.5 wt% CNTs. Moreover, they used SEM for further investigation of worn surface and distinguished the more uniform and smooth surface for composite with 1.5 wt% CNTs. Hence, they inferred carbon nanotubes can improve the wear resistance of PS and prevent the composite from scuffing and adhesion of the matrix in sliding against steel counter face.

Loos et al. [15] visualized the morphological features of SWCNT/PS composite by using microscopy tests. AFM micrographs (Fig. 10.23) display both types of height and phase contrast images in which straight and bended nanotubes appeared, and the dark valley in the center shows that nanotubes pull out. Although AFM and TEM were capable to identify the individual and bundled SWCNT, they are unable to demonstrate distribution of nanotubes and construct network properly. Thus, another approach like SEM should be used to complete the research about morphology of nanotubes in matrices. In this regard, low and high acceleration voltage (Fig. 10.24) applied to the samples and indicated that low acceleration voltage can only emerge the nanotubes on surface opposed to deeper penetration of high voltage charging. Additionally, in raising the voltage, more nanotubes will be identified due to contrast between SWCNT and PS. In contrast to AFM and TEM the obtained diameter by SEM was one order of magnitude higher, approximately 30 nm. They also used high acceleration voltage SEM in order to detect the quasi-three-dimensional network in

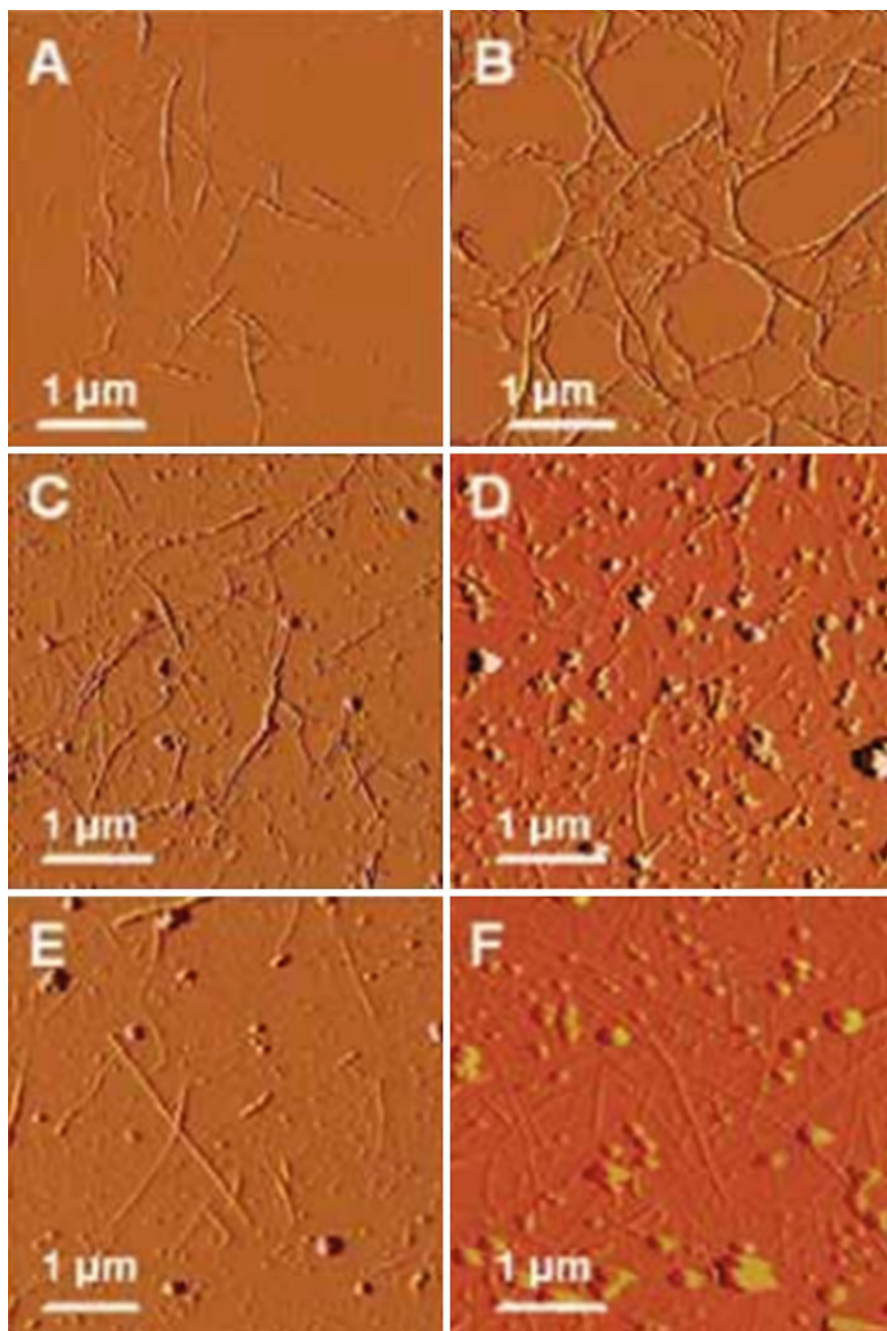


Fig. 10.20 AFM of the pristine and PmPV-functionalized SWNT deposited on mica. (a, c, e) Pristine (a) HiPco, (c) CoMoCat, and (e) PLV. (b, d, f) PmPV-functionalized (b) HiPco, (d) CoMoCat, and (f) PLV

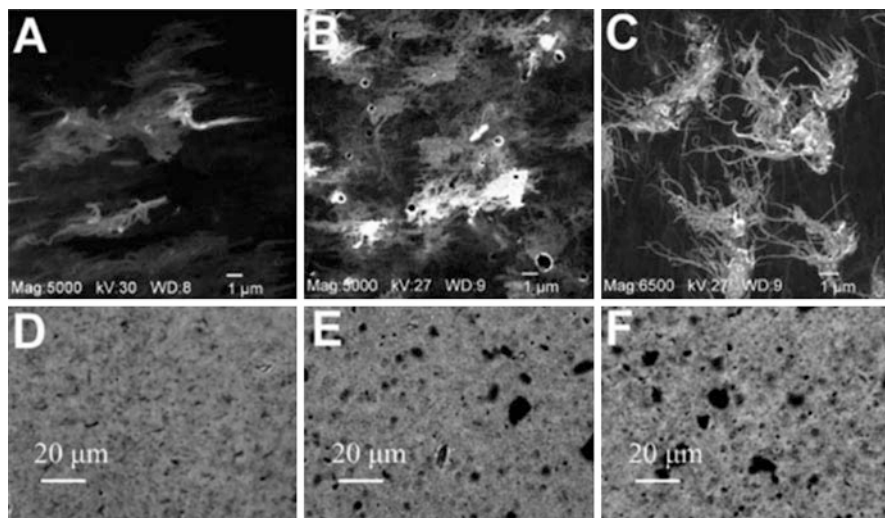
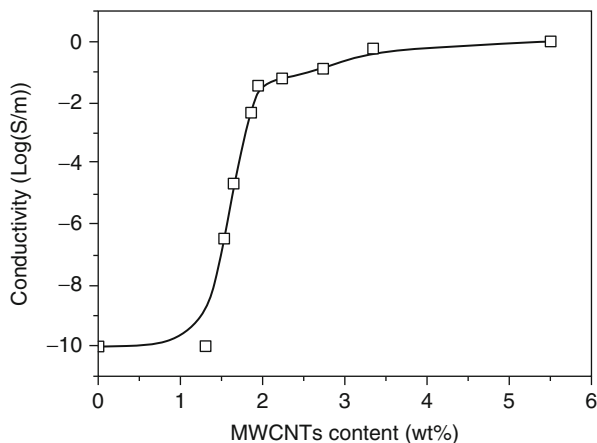


Fig. 10.21 (a–c) Scanning electron microscopy and (d–f) optical microscopy images of pressed films of SWNT-PmPV-PS composites made from (a, d) HiPco, (b, e) CoMoCat, and (c, f) PLV nanotubes

Fig. 10.22 Volume conductivity of MWCNT/PS composites as a function of MWCNT concentration. Values represent an average of 10 measurements; standard variation is below 10 %



the samples and observed in samples with SWCNT less than percolation threshold details could not be seen owing to strong charging.

Safadi et al. [19] fabricated MWCNT/PS composite using solution casting, particularly spin and film casting. Ultrasonic energy was applied to disperse the nanotubes in the solution instead of chemical modification to preserve the intrinsic physical properties. They observed that increasing the CNTs content give rise to descend in surface resistivity and the percolation threshold reached at 2.5 Vol%. The same electrical conductivity was measured for both spun and cast films.

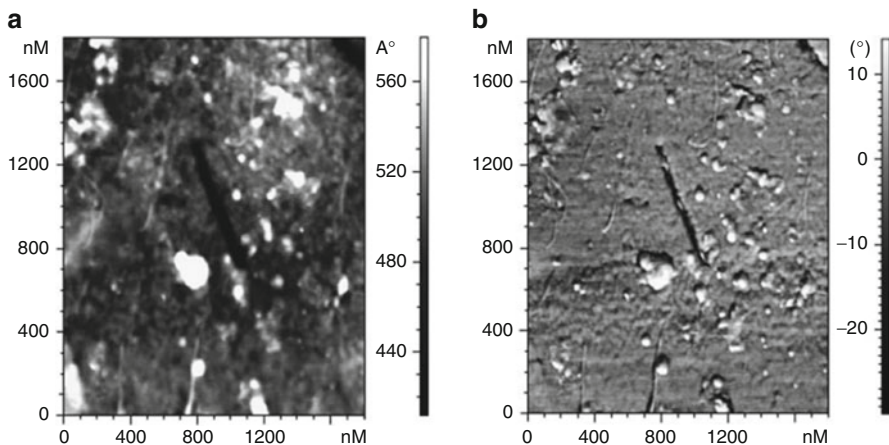


Fig. 10.23 Atomic force microscope (AFM) images of the surface of a SWNT/PS nanocomposite having a SWNT concentration of 1.6 wt%; (a) height contrast, and (b) phase contrast

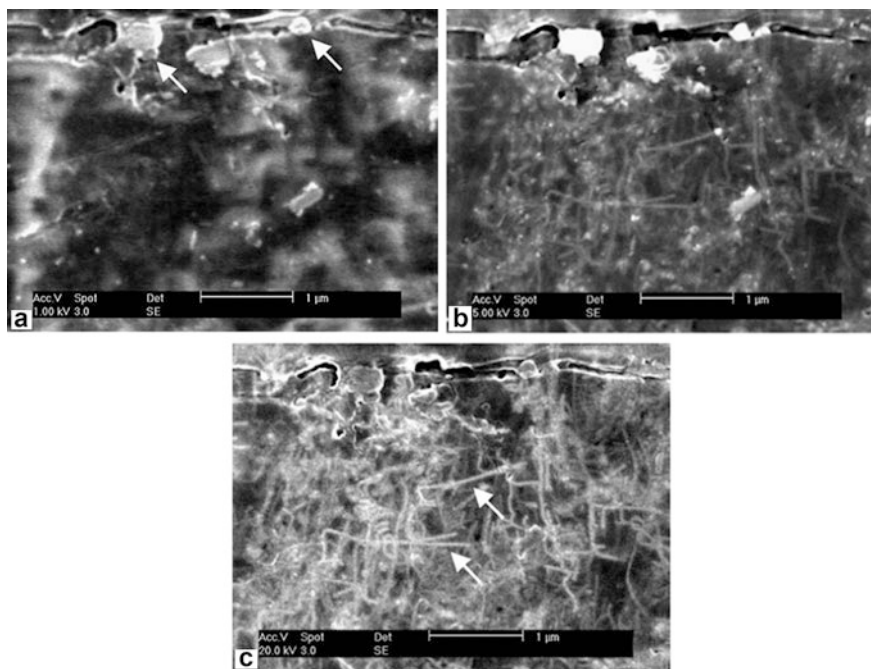


Fig. 10.24 Series of high-resolution SEM images of the same region of a SWNT/PS nanocomposite having a SWNT concentration of 1.6 wt%, using an acceleration voltage of (a) 1, (b) 5, and (c) 20 kV. The *arrows* in (a) indicate reference particles, the *arrows* in (c) indicate SWNTs also visible in Fig. 10.3b

They found that thickness of films was depending on the spinning time and long fiber lies flat and perpendicular to radial direction as confirmed with SEM data. Observation verified the oriented nanotubes in spin casting; however, alignment of nanotubes was not effective on mechanical properties, and tensile strength and elongation at break increased with rising CNT content approximately two orders of magnitude for 2.5 vol% loading of MWCNTs. SEM results of fractured surface clearly showed the two mechanisms of defect: (1) breaking CNTs and (2) pulling out from matrix. Nanotubes were pulling out from matrix because of low interfacial adhesion.

2.3 Preparation Methods

Method of preparation of PS/CNT nanocomposites is another most effective parameter to enhance dispersibility. Many scientists investigated the different methods of preparation of nanocomposites such as melt mixing (i.e., high-speed vibration milling, extruder, injection molding, and compression molding), atom transfer radical polymerization, in situ polymerization (i.e., emulsion, suspension, microemulsion, and bulk polymerization), coagulation method, solution evaporation, solution casting (i.e., film and spin), and latex technology to decrease the agglomeration of CNTs and improve the homogenous dispersion and interfacial adhesion of tubes in PS. They have tried to design simple method of preparation by descending the steps and using less material to decrease the cost. It was found that dispersion of carbon nanotubes can be modified with various methods of preparation.

Currently Al-Ghamdi and Ali [1] investigated the influence of MWCNTs on the rheological and thermal properties of high-impact polystyrene (HIPS). They used melt-mixing method to achieve more dispersion accompanied by simplicity of usage in industry. The viscosity of HIPS had a sharp increase with addition of CNTs to 7.5 wt% and astonishingly decreased at 10 wt% loading. However viscosity did not have any impact on improvement or spoiling the performance of materials since it modified with processing condition. According to Fig. 10.25, complex viscosity and storage modulus were growing with addition of nanotubes in all levels. Besides, DSC result was very unique while it did not display the even association of CNTs content in T_g , and it was changed slightly for the entire nanocomposites. The results are shown in Table 10.1.

Among the researchers, Patole et al. [17] fabricated a novel hybrid composite from polystyrene, graphene, and MWCNT by using in situ microemulsion polymerization in aqueous media. They investigated the morphological properties by using SEM (Fig. 10.26) and observed MWCNT bridges formed between exfoliated graphene. Generally, the composite looked like a sandwich in which graphene and CNTs linked with PS particles, indicative of a uniform network. TEM results were also in agreement with SEM one and proved the PS-grafted agglomerated MWCNT at the folding edges of graphene. Raman spectrum (Fig. 10.27) revealed the presence of high amount of PS on the surface of graphene and nanotubes. On the other hand,

Fig. 10.25 Variation in (a) complex viscosity (η^*), (b) Storage modulus (G').

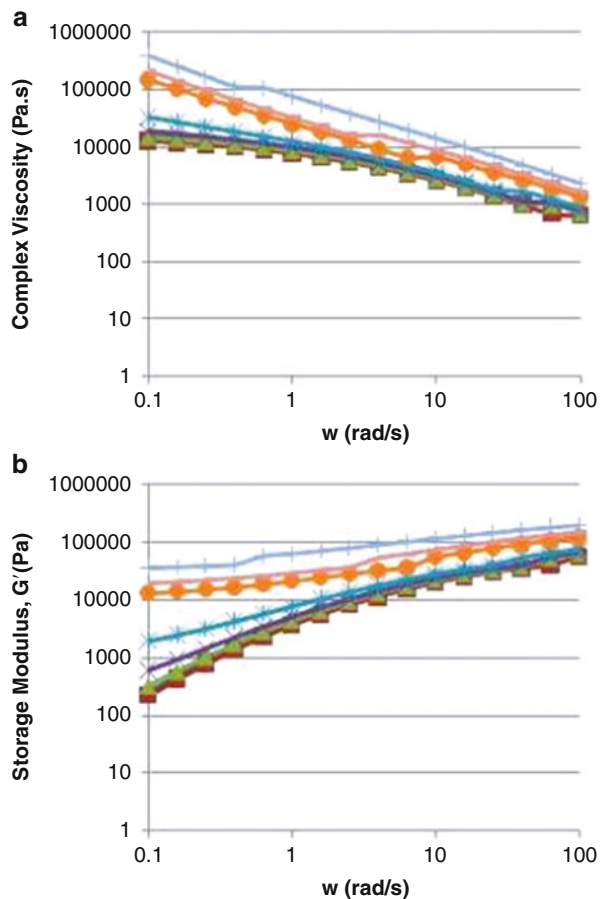


Table 10.1 Changes in glass-transition temperature (T_g) of HIPS/MWCNTs

MWCNTs (%)	Increase/decrease (%)
0.10	-0.14
0.50	-0.75
1.00	-1.65
2.50	-0.81
5.00	0.43
7.50	0.93
10.0	1.37

FTIR spectra (Fig. 10.27) confirmed that the PS peak appeared as a new peak at $1,632\text{ cm}^{-1}$ which printed out the linkage between graphene, MWCNT, and PS. The enhancement in molecular weight and polydispersity index emerged that by GPC analysis was relative to consumption of Azobisisobutyronitrile (AIBN) as a result of

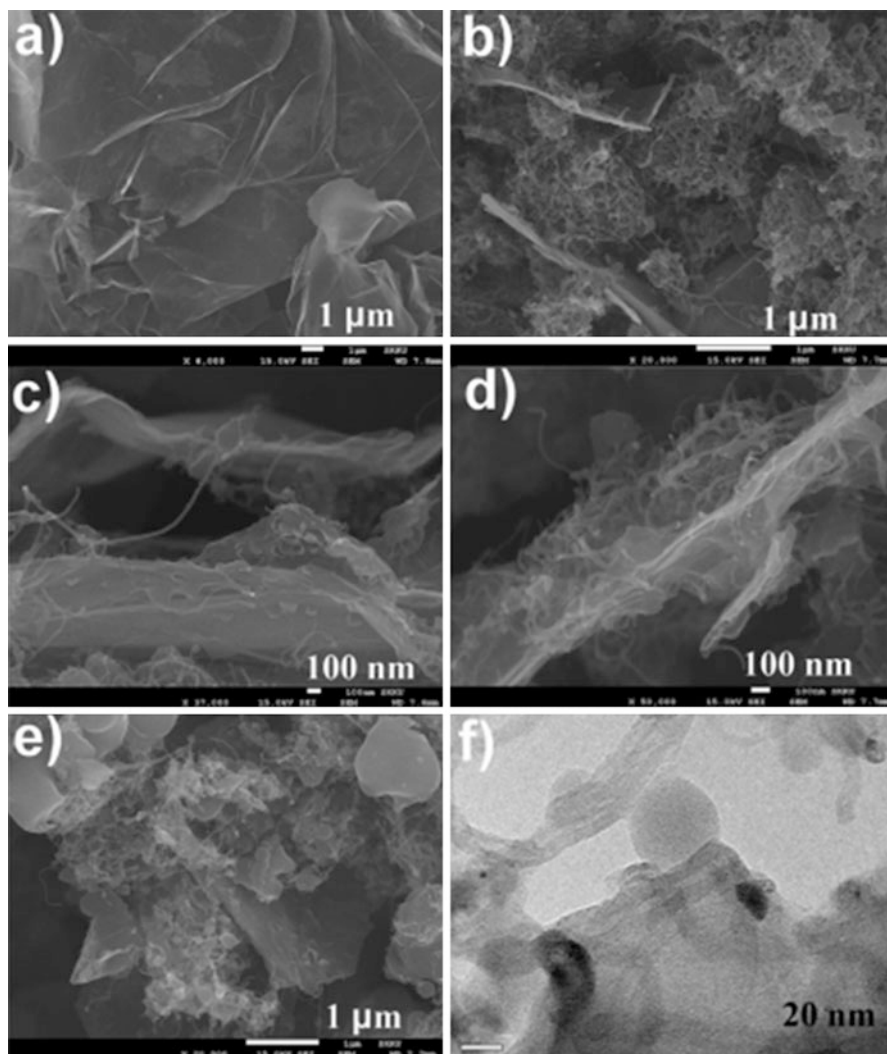


Fig. 10.26 (a) SEM image of exfoliated graphene from expandable graphite, (b–d) self assembled graphene/MWCNT/PS nanocomposite, (e) crumbled graphene in the composites and (f) TEM image of the graphene/MWCNT/PS nanocomposite

participation of graphene and CNT in the reaction. DSC result (Fig. 10.28) disclosed 70 °C increases in T_g of nanocomposite due to heat absorption via graphene and nanotubes. Besides, TGA thermogram illustrated single peaks for both PS and nanocomposite and the lower intensity of nanocomposite peaks show the higher thermal stability. The comparison of pristine PS and nanocomposite demonstrated a higher storage modulus and loss modulus for nanocomposite due to reduction of mobility with graphene and nanotubes. Moreover, they found that sheet resistivity

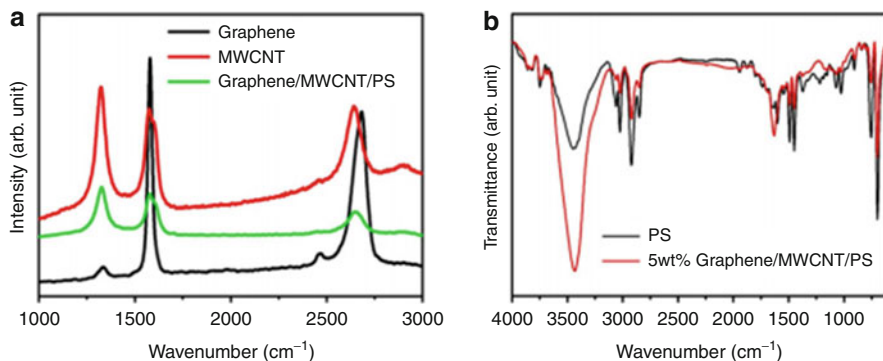


Fig. 10.27 (a) Comparative Raman spectrum of graphene, MWCNT and graphene/MWCNT/PS nanocomposite. (b) Comparative FT-IR spectrum of PS and graphene/MWCNT/PS nanocomposite

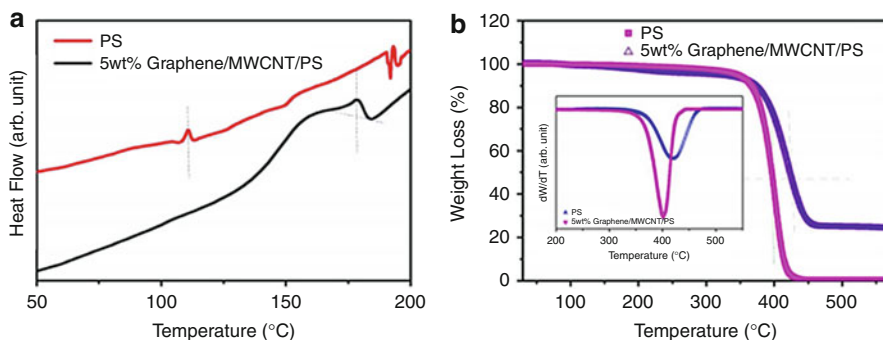


Fig. 10.28 The comparative thermal properties of PS and graphene/MWCNT/PS nanocomposite (a) DSC, (b) TGA and (Inset b) DTA

reduced with increasing nano-filler in PS and eventually more electrical conductivity gained as a construction of a continuous network.

Shrivastava and Khatua [21] synthesized the styrene monomer via bulk polymerization in the presence of MWCNTs and PS beads. They found that PS beads bring about the better distribution of CNTs in matrix and increase conductivity. A very low percolation threshold (0.08 wt%) was attained due to formation of continuous network. As it is shown in Fig. 10.29, by enhancing the PS beads to 70 wt%, an increase in electrical conductivity was observed with constant percentage of MWCNTs. Furthermore, they elucidated that more than 70 wt% PS beads will decrease the conductivity as the blockage of conducting way with insulating PS beads. They also applied two other methods such as solution mixing and melt mixing to preparation of PS/MWCNT composite. A comparable DC conductivity (1.3×10^{-3}) was observed at 3 wt% loading

Fig. 10.29 Conductivity of MWCNT/PS composites with the wt.% of PS bead in PS matrix

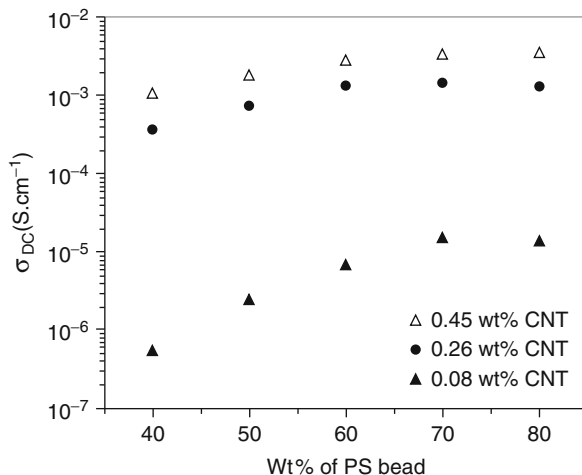
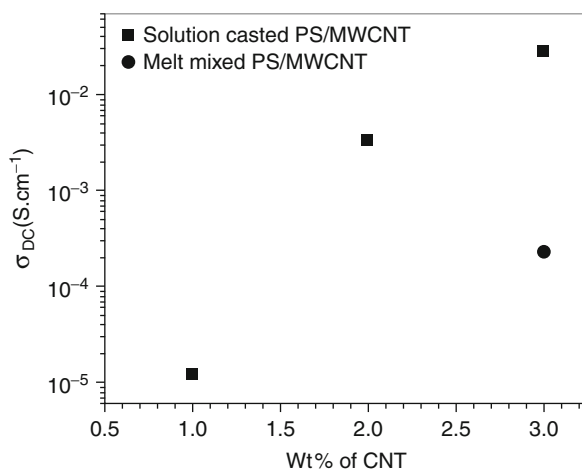
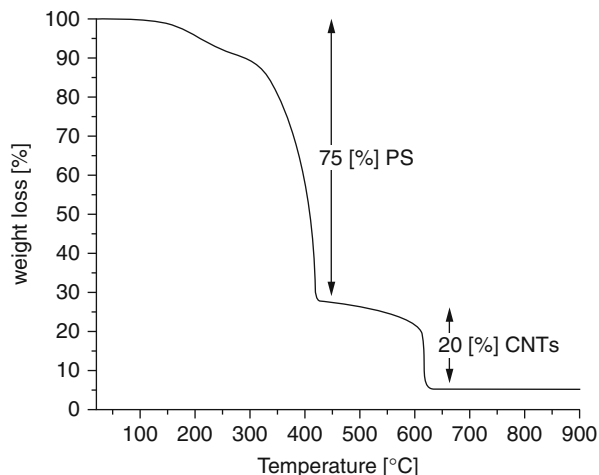


Fig. 10.30 DC conductivity for the solution casted and melt-mixed MWCNT/PS composites



of MWCNTs in solution mixing versus 0.26 wt% of bulk polymerization. Surprisingly, melt mixing shows noticeably lower conductivity (2.3×10^{-4}) at 3 wt% loading of MWCNTs as illustrated in Fig. 10.30. Meanwhile the dielectric constant decreased dramatically at low frequencies with increasing both PS beads and CNTs to above percolation threshold which was attributed to polarization in all types and enhancing the capacitance between CNTs and dead ends. Morphological data obviously showed the existence of individual CNTs all over the matrix. PS beads can bring about the selectivity of dispersion and obtaining the well-associated networks in low CNT quantity.

Fig. 10.31 TGA analysis of in situ polymerized CNT/PSs composite containing five layers



A composite with aligned CNTs embedded in PS showed an increase in electrical conductivity regardless of the number of stacked layers in composite (Kaziol et al. [13]). This phenomenon shows the perfect connection between the layers. In addition increment of conductivity occurs for both direction of parallel and perpendicular; however, perpendicular direction had lower conductivity ($0.04 \pm 0.01 \text{ S cm}^{-1}$) compared to parallel one. SEM results exhibited CNTs entirely wrapped with PS and stacked layers are lack of voids. The study of thermal properties by DSC showed the lower T_g for the composite compared to melt-infiltrated PS and in situ polymerized PS owing to decline in molecular weight. TGA data (Fig. 10.31) revealed three regions, decomposition of styrene, rapid oxidation of PS, and oxidation of CNT, and determine the percentage of PS against CNTs (75 to 20 wt%) in the nanocomposite. The anisotropic character of the aligned nanocomposite was confirmed with the elevated thermal conductivity of parallel form to perpendicular.

Shin and Geckeler (2009) investigated the properties of SWCNT/PS nanocomposite in powder and solution form. The nanocomposite was prepared with high-speed vibration milling technique in the form of solid through ultrasonication and centrifugation [20]. Although this method is very simple and fast, the nanotubes did not wrap entirely with PS and damage can go through CNTs due to harsh condition. UV-visible revealed that the dispersion of nanotubes in matrix takes 20–25 min. The entire morphological tests confirmed that the PS-wrapped SWNTs showed a much higher dispersibility in organic media compared to that of the pristine SWNTs.

Wu and co-workers [24] reported the fabrication of PS/MWCNTs nanocomposite with latex technology when driven by ultrasonic energy to disperse the nanotubes in solution. FESEM and HRTEM proved that the uniform size of monodispersed styrene is 230 nm with deviation less than 2 %. Besides that, HRTEM evidently demonstrated well-distributed nanotubes among spherical styrene. However, Raman spectroscopy represented a peak at $1,355 \text{ cm}^{-1}$ which may have resulted from the imperfection in

graphene sheets or tube end. The result of electrical conductivity shows a growing in the conductivity up to four orders of magnitude with 1.5 wt% MWCNTs. The conductivity increased by addition of MWCNTs and reached to 4.9×10^{-4} S/cm for 6.5 wt% loading. They found that in situ polymerization can give a better result relative to covalent bonding between PS and carbon. Thermal study of nanocomposite similar to others' research displayed an increase in T_g and thermal stability with addition of CNTs. Moreover, they elucidated the improved storage modulus with better interaction between CNTs and matrix. Although storage modulus enhances with adding more nanotubes, it shows a considerable reduction with raising temperature.

Choi and co-workers [5] published a nanocomposite from polystyrene and MWCNT via melt-mixing method using corotating twin-screw extruder. FESEM micrograph indicated the random orientation of nanotubes within PS as well as bended MWCNTs as a result of interlocking of nanotubes. TEM evidently showed that incorporated nanotubes were uniformly dispersed and no aggregation is visible. It was also in agreement with SEM and showed the random alignment of nanotubes owing to high aspect ratio, high matrix viscosity, and curved shape of primary nanotubes. They also observed that storage and loss modulus of nanocomposite with 5 wt% loading level was more than neat PS at low frequency because of higher dispersion originates from larger surface area. Moreover, the thermal investigation conducted with DSC and TGA, respectively, revealed the enhancement in T_g and stability of nanocomposite with adding nanotubes.

3 Conclusion

In summary, the best method to obtain high electrical conductivity with the lowest percolation threshold is in situ polymerization. Furthermore, highest conductivity was achieved when the dispersion of CNTs was homogeneously all over the matrix. It was the result of the formation of continuous network which can transfer the electricity from one tube to another. Besides that, well dispersion was gained with modification of nanotubes through functionalization and ultrasonication. Since Woo and Lee (2012) have reported modification with these methods can improve the mechanical, thermal, and rheological properties; however, it can bring about damage to nanotube surface which deteriorates the intrinsic properties of nanotubes. The studies by most researchers indicate that percolation threshold will reach for CNT loading between 0.5 and 3 wt%. However, Shrivastava and Khatua embedded a much lower quantity, 0.08 wt% CNTs for percolation threshold. Furthermore, the results of most researches show an improvement of thermal stability and bulk T_g of composite owing to excellent thermal properties of CNTs. On the other hand, some researchers proved the effect of CNTs as plasticizer on the composite which decreases T_g of composite less than pristine PS at high CNT concentration. The mechanical properties of PS/CNT nanocomposites were intensively investigated by scientist and mostly showed enhancement in tensile strength and reduction of elongation at break. The investigation of storage and loss modulus also indicated a trend to growth.

References

1. AL-Ghamdi AS, Ali MY (2012) Rheological and thermal behaviour of high impact polystyrene nanocomposite. *Adv Mater Res* 383–390:3849–3853. doi:10.4028/www.scientific.net/AMR.383-390.3849
2. Al-Shabanat M (2012) Electrical studies of nanocomposites consisting of MWNTs and polystyrene. *J Polym Res* 19(2):1–8. doi:10.1007/s10965-011-9795-z
3. Amr IT, Al-Amer APST, Al-Harhi M, Girei SA, Sougrat R, Atieh MA (2011) Effect of acid treated carbon nanotubes on mechanical, rheological and thermal properties of polystyrene nanocomposites. *Compos Part B: Eng* 42(6):1554–1561. doi:10.1016/j.compositesb.2011.04.013
4. Bermúdez MD, Carrión FJ, Espejo C, Martínez-López E, Sanes J (2011) Abrasive wear under multiscratching of polystyrene + single-walled carbon nanotube nanocomposites. Effect of sliding direction and modification by ionic liquid. *Appl Surf Sci* 257(21):9073–9081. doi:10.1016/j.apsusc.2011.05.103
5. Choi Y-J, Hwang S-H, Hong YS, Kim J-Y, Ok C-Y, Huh W, Lee S-W (2005) Preparation and characterization of PS/multi-walled carbon nanotube nanocomposites. *Polym Bull* 53(5–6):393–400. doi:10.1007/s00289-005-0348-7
6. Fragneaud B, Masenelli-Varlot K, Gonzalez-Montiel A, Terrones M, Cavaillé JY (2008) Mechanical behavior of polystyrene grafted carbon nanotubes/polystyrene nanocomposites. *Compos Sci Technol* 68(15–16):3265–3271. doi:10.1016/j.compscitech.2008.08.013
7. Grady BP, Paul A, Peters JE, Ford WT (2009) Glass transition behavior of single-walled carbon nanotube – polystyrene composites. *Macromolecules* 42(16):6152–6158. doi:10.1021/ma900375g
8. Hill DE, Lin Y, Rao AM, Allard LF, Sun Y-P (2002) Functionalization of carbon nanotubes with polystyrene. *Macromolecules* 35(25):9466–9471. doi:10.1021/ma020855r
9. Hu H, Hui KN, Hui KS, Lee SK, Zhou W (2012) Facile and green method for polystyrene grafted multi-walled carbon nanotubes and their electroresponse. *Colloids Surf A Physicochem Eng Asp* 396:177–181. doi:10.1016/j.colsurfa.2011.12.066
10. Huang C-L, Wang C (2011) Polymorphism and transcrystallization of syndiotactic polystyrene composites filled with carbon nanotubes. *Eur Polym J* 47(11):2087–2096. doi:10.1016/j.eurpolymj.2011.08.006
11. Iijima S (1991) Helical microtubules of graphitic carbon. *Nature* 354:56–58. doi:10.1038/354056a0
12. Kim ST, Choi HJ, Hong SM (2006) Bulk polymerized polystyrene in the presence of multiwalled carbon nanotubes. *Colloid Polym Sci* 285(5):593–598. doi:10.1007/s00396-006-1599-z
13. Koziol KKK, Boncel S, Shaffer MSP, Windle AH (2011) Aligned carbon nanotube-polystyrene composites prepared by in situ polymerisation of stacked layers. *Compos Sci Technol* 71(13):1606–1611. doi:10.1016/j.compscitech.2011.07.007
14. Lahelin M, Annala M, Nykänen A, Ruokolainen J, Seppälä J (2011) In situ polymerized nanocomposites: polystyrene/CNT and Poly(methyl methacrylate)/CNT composites. *Compos Sci Technol* 71(6):900–907. doi:10.1016/j.compscitech.2011.02.005
15. Loos J, Alexeev A, Grossiord N, Koning CE, Regev O (2005) Visualization of single-wall carbon nanotube (SWNT) networks in conductive polystyrene nanocomposites by charge contrast imaging. *Ultramicroscopy* 104(2):160–167. doi:10.1016/j.ultramic.2005.03.007
16. Mazov IN, Kuznetsov VL, Krasnikov DV, Rudina NA, Romanenko AI, Anikeeva OB, Suslyayev VI et al (2011) Structure and properties of multiwall carbon nanotubes/polystyrene composites prepared via coagulation precipitation technique. *J Nanotechnol* 2011:1–7. doi:10.1155/2011/648324
17. Patole AS, Patole SP, Jung S-Y, Yoo J-B, An J-H, Kim T-H (2012) Self assembled graphene/carbon nanotube/polystyrene hybrid nanocomposite by in situ microemulsion polymerization. *Eur Polym J* 48(2):252–259. doi:10.1016/j.eurpolymj.2011.11.005

18. Peters JE, Papavassiliou DV, Grady BP (2008) Unique thermal conductivity behavior of single-walled carbon nanotube–polystyrene composites. *Macromolecules* 41(20):7274–7277
19. Safadi B, Andrews R, Grulke EA (2002) Multiwalled carbon nanotube polymer composites: synthesis and characterization of thin films. *J Appl Polym Sci* 84(14):2660–2669. doi:10.1002/app.10436
20. Shin J, Kim C, Geckeler KE (2009) Single-walled carbon nanotube-polystyrene nanocomposites: dispersing nanotubes in organic media. *Polym Int* 58(5):579–583. doi:10.1002/pi.2550
21. Shrivastava NK, Khatua BB (2011) Development of electrical conductivity with minimum possible percolation threshold in multi-wall carbon nanotube/polystyrene composites. *Carbon* 49(13):4571–4579. doi:10.1016/j.carbon.2011.06.070
22. Tchoul MN, Ford WT, Ha MLP, Chavez-Sumarriva I, Grady BP, Lolli G, Resasco DE et al (2008) Composites of single-walled carbon nanotubes and polystyrene: preparation and electrical conductivity. *Chem Mater* 20(9):3120–3126. doi:10.1021/cm703625w
23. Wang Z, Lu M, Li H-L, Guo X-Y (2006) SWNTs–polystyrene composites preparations and electrical properties research. *Mater Chem Phys* 100(1):77–81. doi:10.1016/j.matchemphys.2005.12.008
24. Wu T, Chen E (2008) Preparation and characterization of conductive carbon nanotube–polystyrene nanocomposites using latex technology. *Compos Sci Technol* 68(10–11):2254–2259. doi:10.1016/j.compscitech.2008.04.010
25. Yang Z, Dong B, Huang Y, Liu L, Yan F-Y, Li H-L (2005) Enhanced wear resistance and micro-hardness of polystyrene nanocomposites by carbon nanotubes. *Mater Chem Phys* 94(1):109–113. doi:10.1016/j.matchemphys.2005.04.029
26. Yu J, Lu K, Sourty E, Grossiord N, Koning CE, Loos J (2007) Characterization of conductive multiwall carbon nanotube/polystyrene composites prepared by latex technology. *Carbon* 45(15):2897–2903. doi:10.1016/j.carbon.2007.10.005
27. Yuan C, Wang J, Chen G, Zhang J, Yang J (2011) Orientation studies of uniaxial drawn syndiotactic polystyrene/carbon nanotube nanocomposite films. *Soft Matter* 7(8):4039. doi:10.1039/c0sm01475c
28. Yuan J-M, Fan Z-F, Chen X-H, Chen X-H, Wu Z-J, He L-P (2009) Preparation of polystyrene–multiwalled carbon nanotube composites with individual-dispersed nanotubes and strong interfacial adhesion. *Polymer* 50(14):3285–3291. doi:10.1016/j.polymer.2009.04.065

Preparation, Properties, and Processibility of Nanocomposites Based on Poly(ethylene-Co-Methyl Acrylate) and Multiwalled Carbon Nanotubes

11

Utpal Basuli, Sudipta Panja, Tapan Kumar Chaki, and Santanu Chattopadhyay

Contents

1	Introduction	246
1.1	Poly(ethylene-Co-Methyl Acrylate) (EMA) Copolymers	247
1.2	Nanocomposites Based on CNTs with EMA and Related Polymers	248
2	Preparation of EMA/MWNT Nanocomposites	249
3	Structure and Properties of EMA/MWNT Nanocomposites	250
3.1	Structure and Morphology	250
3.2	Mechanical Properties	253
3.3	Thermal Properties	255
4	Kinetics of Thermal Decomposition	259
4.1	TGA Mass Spectroscopy	262
4.2	Isothermal Decomposition	265
4.3	Melt Viscosity (Capillary Flow)	267
4.4	Activation Energy of Flow	268
4.5	Morphology of Extrudate Surfaces	269
5	Electrical Properties	270
5.1	Effect of Conductivity and Dielectric Constant	270
5.2	Effect of MWNT Loading on DC Resistivity	272
6	EMI Shielding Effectiveness (EMI SE)	274
7	Summary	278
	References	278

Abstract

In this chapter, the preparation, characterization, processibility, and properties of nanocomposites based on multiwall carbon nanotubes (MWNTs) and different commercial grades of poly(ethylene-co-methyl acrylate) (EMA) having a variable methyl acrylate (MA) content are covered. The results showed that melt blending

U. Basuli • S. Panja • T.K. Chaki • S. Chattopadhyay (✉)
Rubber Technology Centre, Indian Institute of Technology, Kharagpur, India
e-mail: ubasuli@gmail.com; sudiptapanjachem@gmail.com; tapan@rtc.iitkgp.ernet.in;
santanu@rtc.iitkgp.ernet.in

after solution mixing offers a simple and effective means to fabricate EMA/MWNT nanocomposites. The mechanical electrical properties and thermal degradation characteristics of the nanocomposites improve with increase in wt% of MWNT loading. The states of dispersions of the unmodified MWNTs are found to be inferior with increasing MA content in the EMA matrix. Better dispersions of MWNTs in EMA matrix lead to increased crystallite size and increased temperature of crystallization. The capillary rheological parameters can be correlated with the developed morphology under steady shear conditions. The effects of MWNTs and MA content in EMA on thermal stability and degradation kinetics are also presented. The kinetic parameters of degradation can be correlated with the degree of conversion. A promising mechanism is proposed over a different range of temperatures of degradation. The significant improvements in the mechanical and electrical properties of the polymeric matrix are observed by the addition of commercially available functionalized (hydroxyl and carboxyl) MWNTs. However, the states of dispersion of the functionalized MWNTs are found to be inferior in EMA matrix having lower MA contents. The morphology and properties of EMA-/modified MWNT-based nanocomposites are also investigated by using the plasma exposed, γ -ray irradiated, and chemically modified MWNTs. The improvement of technical properties of the matrix has been found to be higher with the plasma-modified MWNTs among all. It is also found that the electrical conductivity and EMI shielding effectiveness depend heavily on the type of functional groups present on the surface of MWNTs and also on MA content in EMA. These EMA/MWNT nanocomposites have potential applications especially, as a semiconductive layer in nuclear power plant cables, as an EMI shielding materials or as reinforced functional materials.

1 Introduction

Composites are the materials made by the synergistic assembly of two or more constituting materials in such a way that they form a single component and yet can be distinguished on a macroscopic level. Composites are classified into several broad categories depending upon the type of matrix and reinforcements used. In the polymer industry, there is a continuous search towards new materials with improved properties. In the area of nanotechnology, polymer matrix-based nanocomposites have generated a significant amount of attention in the recent literature. Polymer nanocomposites are composites with a polymer matrix and filler with at least one dimension less than 100 nm. These composites have exhibited extraordinary performance properties. Nature has created many nanocomposite materials, such as diatoms, radiolarian, and bone [5, 41], from which scientists can learn and discover new material. Over the last few years, different nanoscaled particles such as layered silicates, nanosilica, carbon nanotubes (CNTs), expandable graphite, inorganic nanoparticles, metal oxides, layered titanate, inorganic nanotubes, cellulose nano-whiskers, polyhedral oligomeric silsesquioxanes (POSS), etc., have been used by academic and industrial researchers to prepare

organic/inorganic hybrid systems. CNTs and many others are among the popular choices of nanofillers used today. CNTs exhibit excellent thermal, mechanical, electrical, and optoelectrical properties and possess nanometer scale diameter and high aspect ratio, which make them an ideal reinforcing agent for high-strength and high-performance nanostructure composites. Interests from the scientific community have been first focused on their outstanding electronic properties which are attractive for diverse potential applications ranging from nano-electronics to biomedical devices [1, 18, 34].

CNT-polymer nanocomposites are potential alternative materials for various applications, including flexible electrodes in displays, electronic papers, antistatic coatings, bulletproof vests, protective clothing, and high-performance composites for aircraft and automotive industries [2, 3, 15, 16, 19, 36, 37, 39, 42].

CNTs can dramatically improve following the properties of polymeric matrix:

Mechanical properties including strength, modulus, and dimensional stability	Photoconductivity and photovoltaic effect
Electrical conductivity	Piezoresistivity
Decreased gas, water, and hydrocarbon permeability	Flame retardancy
Photoelectric effect	Capacitance
Gas and vapor sensitivity	Thermal stability
Electroluminescence and light emission	Chemical resistance
Magnetic storage	Surface appearance
	Optical clarity

These make the polymer matrix more efficient for various applications.

In this chapter, aspects of nanoscale morphology/dispersion and mechanical, thermal, rheological, and electrical properties of poly(ethylene-co-methyl acrylate) (EMA) nanocomposites containing carbon nanotubes are discussed at lengths.

1.1 Poly(ethylene-Co-Methyl Acrylate) (EMA) Copolymers

Ethylene-acrylate copolymers were introduced by DuPont in 1975 under the trade name of Elvaloy[®]. Elvaloy[®] dipolymer is a poly(ethylene-co-methyl acrylate) (EMA) copolymer. This material is mainly used for the electrical insulation for low to medium voltage cables. The general characteristics of EMA include excellent ageing and weather resistance, resistant to hydrocarbon oil with very good low-temperature flexibility, and a wide range of temperature of applications. It exhibits enhanced flame resistance when compounded with flame retarding agents like aluminum hydroxide, antimony trioxide, etc. Moreover, EMA can easily be cross-linked either by electron beam irradiation or by using peroxides to further enhance their technical properties making it suitable for high-temperature applications [29–31]. EMA copolymers are comparable with ethylene vinyl acetate (EVA) copolymers due to their common backbone structure (polyethylene type)

Fig. 11.1 Chemical structure of poly(ethylene-co-methyl acrylate) (EMA)

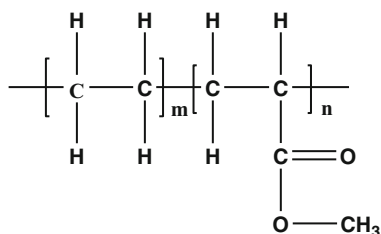


Table 11.1 Properties of various EMA polymers used

Grades of EMA	Melt flow index (MFI) ^a	Density (g/cc)	DSC melting point (°C)	Crystallinity (%)	% of methyl acrylate
Elvaloy [®] 1209	2.0	0.927	101	30.3	9
Elvaloy [®] 1224	2.0	0.944	91	13.8	24
Elvaloy [®] 1125	0.5	0.944	90	11.1	25
Elvaloy [®] 1330	3.0	0.950	85	7.2	25

^aAccording to ASTM D1238 and ISO 1133, g/10 min

having similar polarity. The EMA copolymer has a higher thermal, aging, and degradation resistance than EVA [21].

The generalized structural representation of the base EMA is shown in Fig. 11.1. The common characteristics of commercially available Elvaloy[®] grades (DuPont, USA) of EMA are displayed in Table 11.1.

1.2 Nanocomposites Based on CNTs with EMA and Related Polymers

Ethylene vinyl acetate (EVA) is widely used as an insulating and sheathing material for low to medium voltage cables and also in the footwear and toy industries due to its high flexibility and chemical inertness. The nanocomposites of EVA with MWNTs are of special interest because incorporation of suitable amount of MWNT in EVA matrix leads to significant enhancement of its thermal and mechanical properties. The effect of the vinyl acetate (VA) content in elastomeric grade of EVA copolymers on the state of dispersion of three different carbon nanofillers, e.g., expanded graphite (EG), MWNTs, and carbon nanofibers (CNFs), on the morphological, mechanical, dynamic mechanical, and thermal properties of the resulting nanocomposites has been reported by George and Bhowmick [20]. The effect of VA content in EVA on the mechanical properties of the resulting MWNT-based nanocomposites has also been studied by Peeterbroeck et al. [32]. The effect of MWNT on the fire retardancy and electromagnetic interference shielding properties of EVA has been investigated

by different researchers [17, 33]. Lee and Kim [27] have reported that CNTs can improve physical characteristics of EVAs, particularly radiation resistance and thermal properties significantly.

EMA is advantageous over EVA as a matrix for CNT nanocomposites because of its superior thermal stability and higher temperature ranges of applications. Shaffer and Windle et al. [38] have reported the process of fabrication of CNT/poly(vinyl alcohol) (PVA) nanocomposites by solution mixing. To prevent agglomeration, the nanotubes have been chemically treated to produce an electrostatically stabilized dispersion in with aqueous PVA solution. Poly(methyl methacrylate) (PMMA) is a commonly used thermoplastic matrix for carbon nanofiber (CNF). Composites of oxidized CNFs and PMMA and thermoplastic polyurethane (TPU) have been studied, and their electrical and mechanical properties are compared with those prepared with untreated CNFs by Jimenez and Jana [44]. There have been several studies on CNT/PMMA nanocomposites prepared by in situ polymerization [24, 40], by solution mixing [26], or by melt blending technique [25]. The component material of a semiconductive layer in nuclear power plant cables has been prepared by adding MWNT to ethylene ethyl acrylate (EEA) resin using the melt blending method by Lee et al. [28].

2 Preparation of EMA/MWNT Nanocomposites

Very recently, the EEA/MWNT nanocomposite has been produced by solution mixing for the high-voltage underground power usage [23]. The EEA/MWNT nanocomposite showed the best combination of tensile strength, elongation at break, and Young's modulus. The presence of vinyl acetate and methyl acrylate comonomers appears to reduce the total heat released during combustion of the composites [35]. Yang et al. [43] modified MWNTs via amidation reaction of octadecylamine with purified MWNTs. The modified MWNTs have been found to be easily dispersible into copolymers of methyl and ethyl methacrylate (poly (MMA-co-EMA)). Barrau et al. [4] found that amphiphilic palmitic acid facilitates an efficient dispersion of CNTs into the epoxy matrix. The hydrophobic part of palmitic acid is absorbed onto the nanotube surface, whereas the hydrophilic head group induces electrostatic repulsions between nanotubes, preventing their tendency of aggregation. The presence of a cosolvent was also found to affect the degree of the dispersion of nanotubes into polymer matrix.

Recently, Basuli et al. [6, 7, 14] have used toluene as a solvent for the dispersion of MWNTs into EMA through a solution mixing process. Scanning electron microscopy (SEM) and transmission electron microscopy (TEM) studies revealed that the improved dispersion of CNTs into polymer matrixes can be obtained by solution melt process. Many other polymer composites can also be fabricated following this method. For example, Hagenmuller et al. [22] and Basuli et al. [6, 7, 14] applied a method combining solvent casting and melt processing together to produce films of poly(methyl methacrylate) (PMMA) and EMA containing single-walled carbon nanotubes (SWCNTs) and MWNTs, respectively.

The films obtained by this processing technique exhibited a more uniform nanotube distribution of nanotubes into polymer than the simple cast film and led to much better mechanical properties. In the next sections the nanocomposites based on MWNTs and EMA will be discussed.

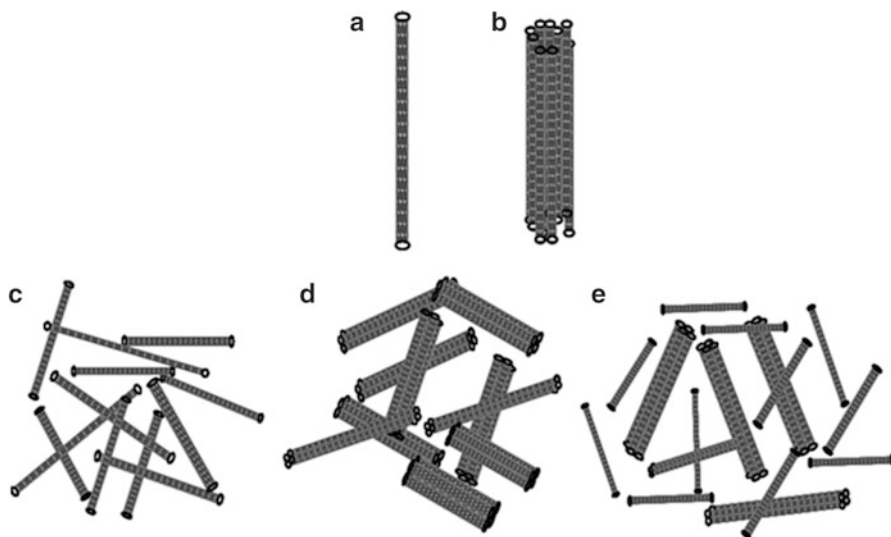
3 Structure and Properties of EMA/MWNT Nanocomposites

3.1 Structure and Morphology

An important issue is to relate the performance of nanocomposites to their morphology or structure; evaluation of performance is certainly easier than the characterization of their morphology. Wide-angle X-ray scattering, WAXS, is frequently used to evaluate the performance of polymer/clay nanocomposites because such analyses are relatively simple to conduct. The qualitative and quantitative characterizations of dispersion of CNTs are comparatively difficult tasks. This is because CNTs do not possess characteristic layer-to-layer registry that could be observed by XRD. The morphology of nanocomposites was examined to evaluate states of dispersion and distribution of nanotube in the matrices. In this context, the dispersion refers to how well the nanotubes are separated in the form of single tubes at the nanoscale. On the other hand, the nanotubes are well distributed if single nanotubes or sets of nanotubes like bundles are uniformly placed within the whole matrix, even though in such case nanotube aggregates might be observed. Different types of morphology have been proposed for CNT-polymer composites [8]. Scheme 11.1 shows schematics of a single tube (Scheme 11.1a), a nanotube bundle (Scheme 11.1b), and aggregates (Scheme 11.1c–e). A nanotube bundle consists of many single tubes sticking together. The bundle can be viewed as an equivalent tube with a larger diameter having a smaller effective aspect ratio. It is worthwhile to mention that both single tubes and tube bundles can participate in the formation of a network or aggregates. Aggregates could be formed by single tubes (Scheme 11.1c), tube bundles (Scheme 11.1d), or inclusive of both (Scheme 11.1e).

Recently, a simple procedure of preparing EMA-based nanocomposite using toluene as a solvent has been reported (Basuli et al. 2010). The nanocomposites were prepared by using pristine as well as chemically functionalized (–COOH and –OH) MWNTs. The final products displayed a significant enhancement of mechanical properties at low MWNT loading: a 100 % improvement of tensile strength and a nearly 63 % increase of modulus were achieved at a MWNT loading of only 2.0 wt%. The value of the elongation at break was not affected much for the composite with the same loading, which was attributed to a large aspect ratio and the interaction between MWNTs and the matrix, which restricts the movement of the polymer chains. Usually, to achieve good dispersions of MWNTs in a polar polymeric matrix, functionalization of MWNTs is necessary.

Lately, EMA24/MWNT nanocomposites have been prepared ([8] Ph.D. Thesis) by solution mixing followed by melt blending technique using plasma- and piranha-modified MWNTs.



Scheme 11.1 Schematic representation of nanotube morphology: (a) single tube (b) nanotube bundle (c) aggregate of single tubes (d) aggregate of nanotube bundles (e) aggregate of single tube and nanotube bundles

Figure 11.2(a, b, c, d, e and f) represent the HRTEM photomicrograph of the EMA09-, EMA24-, and EMA30-based nanocomposites with 1 and 2.5 wt% MWNT loadings, respectively. The figures show that the nanotubes are randomly oriented in the polymer matrix. From Fig. 11.2(a and b), it can be found that the distribution of MWNTs is more homogeneous and less entangled in the EMA09 matrix. Individual MWNTs can be seen clearly. The tendency of aggregations is not observed even at 2.5 wt% concentration of MWNTs. Figure 11.2(c and d) shows inferior dispersion, with a few areas in which one can observe aggregation of nanotubes (for EMA24), while in EMA30 matrix (highest MA content), MWNTs are found acutely entangled, forming agglomeration or clusters in matrix (Fig. 11.2 (e and f)). This indicates overall dispersion of MWNTs is significantly poor in EMA30. Limited degrees of breakdown of MWNTs are noticed especially for EMA09. In all cases, the hollow portions of the nanotubes are visible. The dispersion of the MWNTs is significantly superior in EMA09 and EMA24 compared to EMA30. The highest degree of dispersion of MWNTs in EMA09 possibly stems from its favorable interaction with the MWNTs.

Figure 11.3(a–e) represents the HRTEM photomicrograph of the composites with 1.0–10.0 wt% MWNT loadings, respectively, in EMA09 matrix. The figures show that the nanotubes are randomly oriented in the polymer matrix. From Fig. 11.3a, b, it can be found that the distribution of MWNTs is more homogeneous and less entangled in the EMA matrix particularly at lower MWNT contents. Individual MWNTs can be distinguished clearly. The tendency of aggregations is not seen by and large even if the concentration of MWNTs

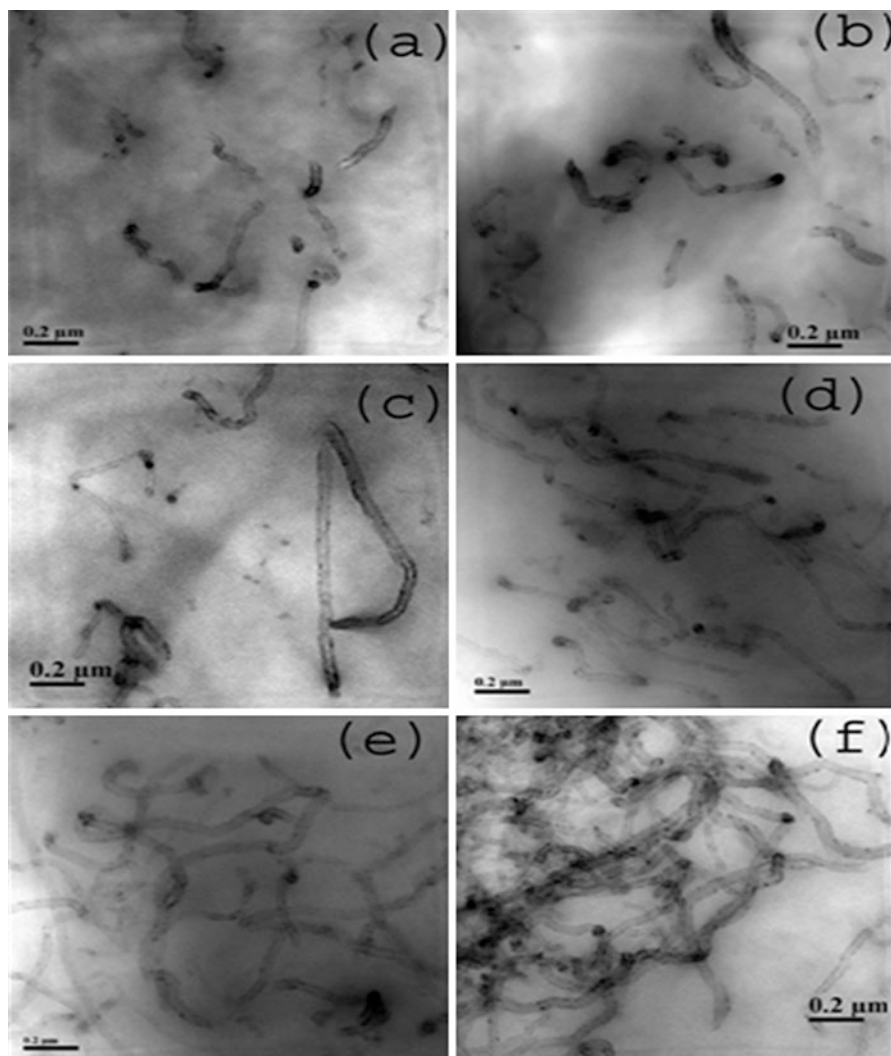


Fig. 11.2 HRTEM photomicrograph (at 12 kX magnification) of MWNT/EMA nanocomposites: (a) E09N1.0 (b) E09N2.5 (c) E24N1.0 (d) E24N2.5 (e) E30N1.0 and (f) E30N2.5

increased up to 3.5 % (Fig. 11.3c). Figure 11.3d (E09N5.0) displays inferior quality of dispersion, with a few areas in which one can observe massive aggregation of nanotubes, where MWNTs are acutely entangled, forming agglomeration or clusters in matrix. However, at a higher loading of 10.0 wt%, the agglomerations start prevailing, as evident from Fig. 11.4e. The highest degree of dispersion of MWNTs in EMA possibly stems from its favorable interaction with the MWNTs. It is also confirmed that the size of MWNTs in the composites is about 40–60 nm in diameter and several microns in length.

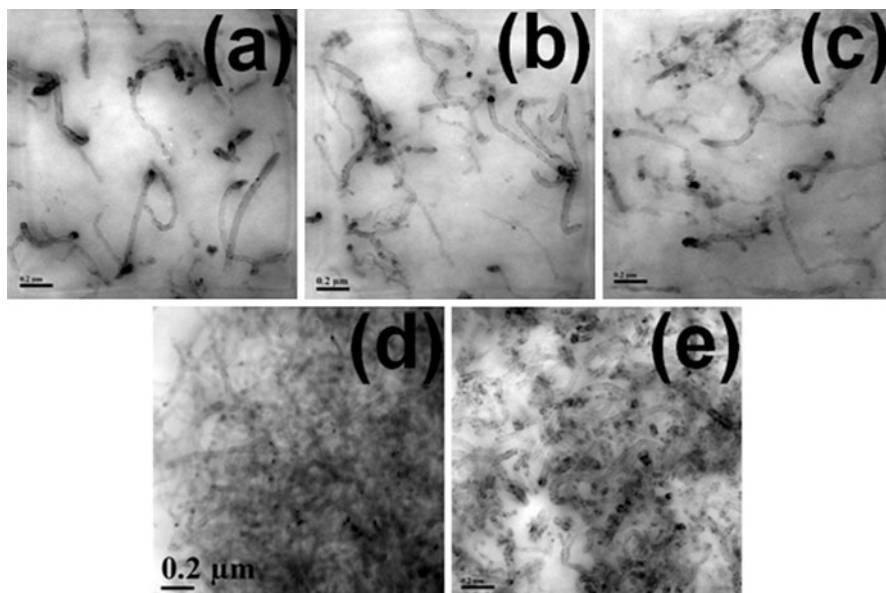


Fig. 11.3 HRTEM photomicrograph (at 10 kX magnification) of EMA/MWNT nanocomposites: (a) E09N1.0 (b) E09N2.5 (c) E09N3.5 (d) E09N5.0 (e) E09N10.0

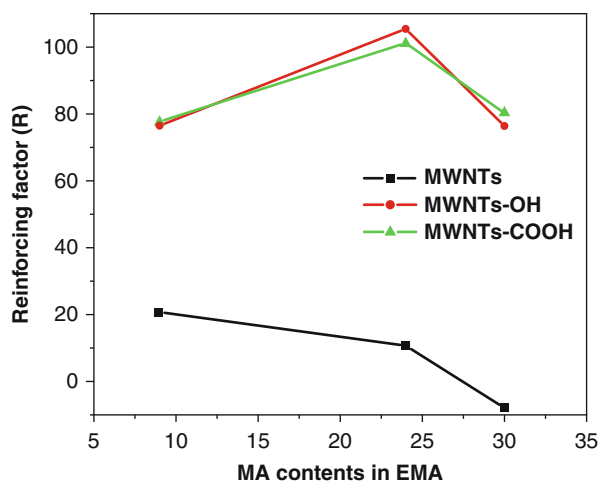


Fig. 11.4 The reinforcing factors of various EMA nanocomposites against the MA contents

3.2 Mechanical Properties

The incorporation of functionalized MWNTs (f-MWNTs) into EMAs considerably increases the tensile strength and tensile modulus as compared to that with pristine MWNTs (Table 11.2). The tensile moduli of the nanocomposites increased on an average of 10 % as compared with the pristine polymer for EMA09 and EMA24,

Table 11.2 Mechanical properties of the different nanocomposites^a

Sample no	Tensile strength (MPa)	Reinforcing factor (R)	Elongation at break (%)	Modulus (MPa)		
				100 %	200 %	300 %
E09N0	11.1	–	625	6.3	6.9	8.8
E09N2	13.2 (18.9) ^b	20.6	593 (–5.1)	7.1 (12.7)	7.5 (8.7)	8.7 (0)
E09N2f-OH	18.9 (70.3)	76.5	558 (–10.7)	7.95 (26.2)	8.6 (24.5)	9.5 (8.5)
E09N2f-COOH	19.0 (71.2)	77.5	542 (–13.3)	8.0 (26.9)	8.6 (24.6)	9.9 (13.0)
E24N0	7.3	–	752	2.75	3.5	3.8
E24N2.0	8.0 (9.6)	10.2	710 (–5.6)	3.2 (16.4)	3.7 (5.7)	4.3 (13.2)
E24N2f-OH	14.5 (98.6)	105.5	765 (1.7)	4.5 (63.6)	5.1 (45.7)	5.9 (55.3)
E24N2f-COOH	14.2 (94.5)	101.1	760 (1.0)	4.5 (63.6)	5.2 (48.6)	5.9 (55.3)
E30N0	5.3	–	1,230	1.9	2.3	2.6
E30N2	4.9 (–7.5)	–8.02	891 (–38.0)	2.2 (15.7)	2.4 (4.3)	2.8 (7.7)
E30N2f-OH	9.1 (71.7)	76.2	1,300 (5.7)	2.2 (15.8)	2.6 (13.0)	3.0 (15.4)
E30N2f-COOH	9.3 (75.5)	80.2	1,310 (6.5)	2.2 (15.8)	2.6 (13.0)	3.0 (15.4)

^aAverage variations in tensile strength, elongation at break, and tensile modulus were within $\pm 2\%$, $\pm 4\%$, and $\pm 0.5\%$, respectively

^bValues given in the parenthesis represent the % increase/decrease with respect to controlled sample

when pristine MWNTs are used. The addition of pristine MWNTs almost has no reinforcing effect on EMA30 and it mainly enhances the modulus. The tensile strength decreases, and modulus value remains almost unaltered for E30N2 composites, suggesting relatively more inter-nanotube interaction than the nanotube-polymer interaction. However, the elongation at break of EMA decreases due to the addition of the pristine MWNTs. The aggregation plays the role of “micro” defect in the nanocomposites. Such defect results in low tensile strength and low elongation at break of nanocomposites. On the other hand, all the EMA grades show an increase in tensile strength and modulus with the incorporation of f-MWNTs (Table 11.2). This may be due to the enhancement in the interfacial interaction, which ultimately promotes a better stress transfer between MWNTs and the polymer matrix. It is now well known and commonly admitted that the mechanical properties of polymer nanocomposites, especially the tensile modulus, depend to a great extent on the filler loading, state of filler dispersion, and interfacial interaction. In EMA09, dispersion of f-MWNTs seems to be poor, although the mechanical properties are improved significantly. This may be due to the increased crystallite size of matrix polymer in the presence of nanotubes. In the presence of

f-MWNTs, the maximum improvement in tensile strength and modulus is exhibited by EMA24 and EMA30, when MA content is higher. On the contrary, the addition of f-MWNTs results in least increment in tensile strength and modulus for EMA09. The increased tensile modulus is due to the improvement of the dispersion of MWNTs in EMA matrix together with superior polymer-MWNTs interaction in the presence of functional group attached to the nanotube. The addition of 2 wt% of MWNTs-COOH and MWNTs-OH enhances the tensile strength of EMA24 by 94.5 and 98.6 %, respectively, whereas pristine MWNT increases it by only 9.6 %.

The tensile strength of various nanocomposites can be correlated to the volume fraction of a nanofiller by the following equation (Eq. 11.1):

$$\frac{\sigma_c}{\sigma_m} = 1 + R(\phi_f) \quad (11.1)$$

where σ_c and σ_m are the tensile strength of the composite and the virgin matrix, respectively. R and ϕ_f are the reinforcing factor and the volume fraction of filler, respectively. The relative tensile strength, $\frac{\sigma_c}{\sigma_m}$, is plotted against volume fraction of filler ϕ_f for all the three fillers with the same EMA matrix. The reinforcing factor of each MWNTs in EMA matrix (shown in Table 11.2) has been calculated using Eq. 11.1. The reinforcing factors of various EMA nanocomposites are also plotted against the MA contents of EMAs in Fig. 11.4. From the plots, it is clear that the reinforcing factor of MWNTs-COOH and MWNTs-OH increases drastically with the MA content in EMA. The reinforcing effect of pristine MWNTs seems to be lower.

3.3 Thermal Properties

3.3.1 Differential Scanning Calorimetry (DSC)

Figures 11.5(a–c) display the DSC thermogram of the nanocomposites. T_m and T_g of the matrix are not affected much by the contents of MWNTs. A multi-peak crystalline melting (T_{m1a}) around 48–50 °C and a higher temperature crystalline melting (T_{m1b}) of around 84–102 °C are observed (Table 11.3). The T_{m1a} may result due to short-range orders or quasi-crystals and later is possibly due to the melting of more perfect crystals (oriented in more ordered fashion). The crystallization exotherms of neat EMA and EMA/MWNT nanocomposites at cooling rates of 10 °C/min are shown in Fig. 11.5b. It is apparent that the DSC exotherms exhibit only one crystallization peak (second cycle) and the peaks of the EMA/MWNT nanocomposite become wider compared to those for the neat EMA. This is more pronouncing in E09N2.5. The crystallization temperature (T_c) of EMA09 and EMA24 in MWNT/EMA nanocomposites noticeably increases with MWNT loading, whereas in EMA30, T_c decreases with MWNT loading as shown in Table 11.3. The crystallinity of the EMA copolymer originates from the polyethylene sequence of the backbone. The MWNTs being more interactive to hydrocarbon part of the polymer reduce the quasi-crystalline order during crystallization. MWNTs act as a nucleating agent to increase the crystallization and melting temperatures of EMA09/MWNT and EMA24/MWNT nanocomposites [45–47]. However, the

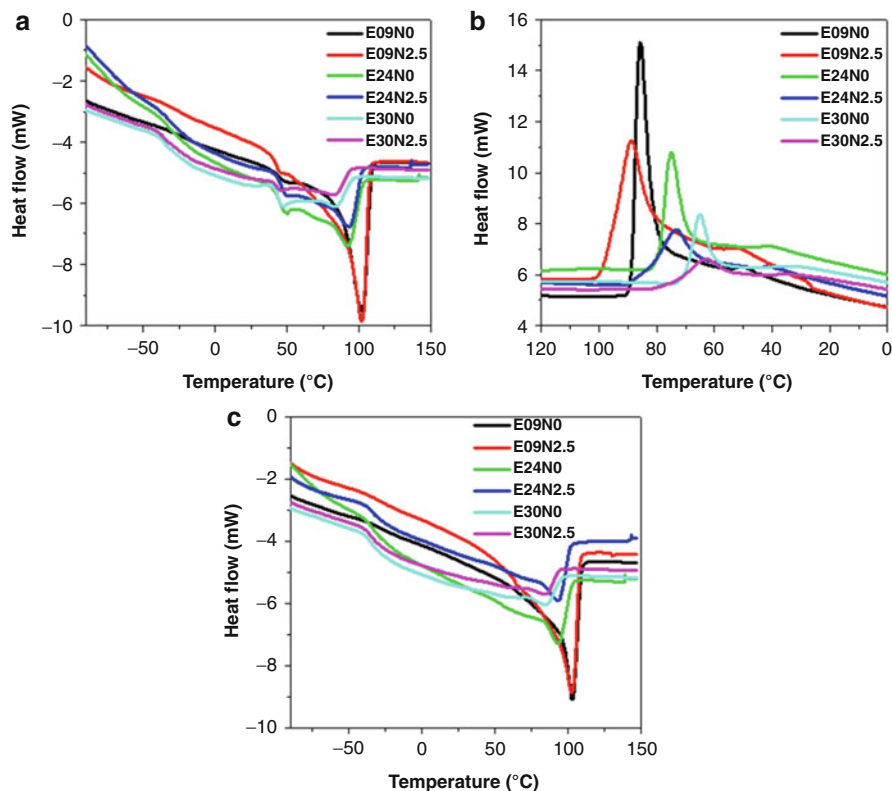


Fig. 11.5 DSC thermograms for pure EMA and various nanocomposites at a heating/cooling rate of 10 °C/min: (a) DSC heating first cycle (b) Second cycle cooling (c) DSC heating third cycle

increased thermal conductivity of nanocomposites (due to the presence of nanotubes) may also physically shift the crystallization temperature. The DSC thermograms (third heating cycle) of EMA/MWNT nanocomposite are shown in Fig. 11.5c where pure EMA has a single glass transition temperature (T_{g2}). The glass transition temperatures of the nanocomposites are not affected much with the addition of MWNTs as observed in the first and third heating cycles of DSC thermograms. Table 11.5 shows the variation of crystallization enthalpy (ΔH , J/g) as a function of composition, which is more significant for E09N2.5, showing that the ΔH of the nanocomposite is decreased by 16.6 J/g after addition of nanotubes. Apparently, the enthalpy of crystallization decreases gradually for all nanocomposites with an increase in content of MWNTs. The trend is slightly different or inconsistent with EMA30-based nanocomposites. It decreases initially (up to 1 wt%), and then increases (at 2.5 wt%) for EMA30. The MWNTs being more interactive to the hydrocarbon part of the polymer reduce the quasi-crystalline order during crystallization and reduces the enthalpy of crystallization.

Table 11.3 Parameters obtained from XRD^a and DSC^b thermograms of EMA/MWNT nanocomposites

Sample no	XRD % crystallinity	Crystallite size (Å)	T_{g1} (°C)	T_c (°C)	T_{m1a} (°C)	T_{m1b} (°C)	T_{m2} (°C)	T_{g2} (°C)	ΔH (J/g)
E09N0	30.3	166.9	–	86	50	102	103	–	56.6
E09N1.0	28.9	171.3	–	89	50	102	103	–	42.3
E09N2.5	24.2	177.2	–	89	50	102	103	–	40.0
E24N0	13.8	141.7	–35	70	48	93	93	–34	24.4
E24N1.0	11.5	159.6	–35	74	48	92	93	–34	20.1
E24N2.5	11.2	151.1	–34	74	49	94	93	–33	18.6
E30N0	7.2	125.7	–34	65	48	84	85	–34	12.9
E30N1.0	7.5	127.9	–35	64	48	84	85	–35	7.1
E30N2.5	7.2	133.2	–35	62	48	85	85	–35	9.0

T_g (DSC) glass transition temperature obtained from DSC temperature sweep experiments, ΔH crystallization enthalpy

^a% error in measurement is ± 0.2 %

^b% error in measurement is ± 0.2 %

3.3.2 Thermogravimetric Analysis (TGA)

Thermal stability and degradation kinetics might be another issue in many applications. The mechanism of degradation was studied by examining the evolved gaseous products during the course of degradation using TGA mass spectrometry. TGA thermograms for mass loss rate curves for pure EMAs and corresponding nanocomposites are shown in Fig. 11.6. In order to differentiate the overlapping degradation steps, DTG curves were further analyzed by carrying out peak deconvolution using the multi-Gaussian deconvolution technique. The TGA curves of EMA and their nanocomposites exhibit apparently single-step degradation, but if the curves are fitted using the multi-Gaussian deconvolution, it results in two overlapping Gaussian curves. Thus, it is actually a two-step degradation process. Each curve has two maxima, one corresponding to the lower temperature representing the degradation of methyl acrylate part (mainly) and the other corresponding to the higher temperature representing disintegration of polyethylene moieties. The random scission of EMA (around 420–480 °C) is possibly initiated by homolytic scission of a methoxycarbonyl side group followed by β scission rather than by main chain scission [48, 49]. The methoxycarbonyl side group makes the β C–C scission easier due to its electronic and steric effects in EMA moieties [50]. The loss of a methoxycarbonyl side group is believed to be the initial degradation step. Scission in ethylene chains is the major degradation process.

In the case of 1.0 wt% MWNT-loaded EMA/MWNT nanocomposites, the onset of degradation occurs at a higher temperature, i.e., 432, 419, and 413 °C, respectively, for EMA09, EMA24, and EMA30. These are 12.7, 3.5, and 3.4 °C higher than those for corresponding various grades of pristine EMA, respectively. The DTG maxima shifts towards higher temperature as the MWNT content in the EMA matrix is increased from 1.0 to 2.5 wt% expected for E30N2.5. The maximum value

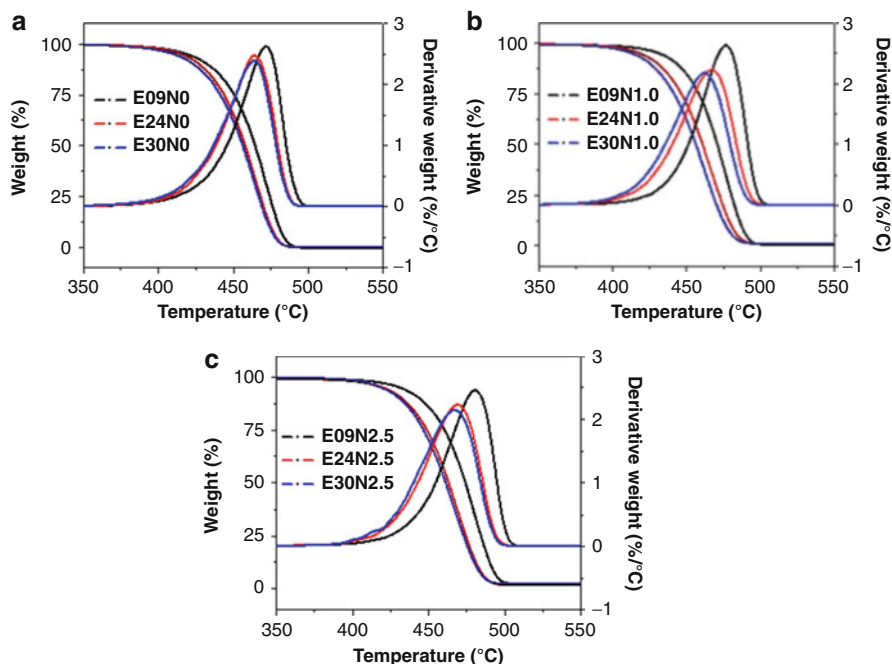


Fig. 11.6 TGA thermograms of EMA and its various nanocomposites: (a) Pure EMA (b) Nanocomposites containing 1 wt% MWNTs and (c) Nanocomposites containing 2.5 wt% MWNTs

Table 11.4 Results obtained from TGA^a thermogram analysis

Sample no	T_{onset} (°C)	T 10 % loss (°C)	T 20 % loss (°C)	T 30 % loss (°C)	T 50 % loss (°C)	T 70 % loss (°C)	T_{max} (°C)
E09N0	419.2	433.1	446.3	454.4	464.7	472.5	471.9
E09N1.0	431.9	443.7	454.9	461.7	471.1	478.7	477.0
E09N2.5	431.2	443.9	456.6	464.2	474.4	482.7	480.9
E24N0	415.5	427.5	439.9	447.7	458.2	466.3	464.4
E24N1.0	419.0	430.7	442.7	450.4	461.2	470.2	467.5
E24N2.5	420.3	432.5	444.8	452.6	463.6	472.4	469.5
E30N0	410.4	423.8	437.0	445.5	456.7	465.0	464.0
E30N1.0	413.8	425.6	437.6	445.4	456.6	465.9	463.0
E30N2.5	419.0	430.5	442.8	450.6	461.5	470.9	453.6

^a% of error in measurement is ± 0.5 %

of dW/dT also reduces with the increase in the contents of MWNT contents. In addition, it can be noted that the temperatures corresponding to different %wt. loss shift towards lower temperatures with the increase in MA content irrespective of the amount of MWNTs present inside the matrix polymers (Table 11.4). All the above observations suggest that the thermal stability of the matrix polymers is enhanced in the presence of MWNTs and the thermal stability is decreased with an

increase in MA content. From Table 11.4, it is found that the improvements in thermal stability are always higher for EMA09/MWNT nanocomposites. This is again a reflection of a better dispersion of nanotubes in EMA09 due to the greater polymer-filler interaction. However, in terms of stabilization, MWNTs do not offer any preference either to the degradation of MA or ethylenic moieties. A gross stabilization effect is observed as explained earlier. A closer look into the thermogram reveals that the maximum weight loss for pure EMA30 occurs at 471.9 °C, whereas for E09N2.5 it occurs at 480.9 °C. The residual weights of the nanocomposites remain fairly constant at the temperature beyond 500 °C, indicating that the EMA matrix has degraded completely and the residue contains mainly the MWNTs. The following are the degradation behaviors as observed: (i) a relatively lower-temperature region where the initial mass loss occurs and (ii) an intermediate-temperature zone where major degradation occurs (corresponding roughly to the maximum rate of mass loss). Additionally, at higher temperature region the shoulders in DTG mass loss rate curves appeared.

4 Kinetics of Thermal Decomposition

The study of degradation and stabilization of polymers is an extremely important area from the scientific, industrial, environmental, and safety point of views. TGA is an excellent tool for studying the kinetics of thermal degradation of polymeric samples. The knowledge of thermal stability and thermal degradation kinetics is significant for the production and application. Detailed non-isothermal and isothermal kinetic analyses of the nanocomposites and neat system have been performed to realize their degradation behavior at different heating rates under inert atmosphere (using different kinetic methods). An attempt has been made to understand the influence of MA content on the overall fragmentation process of these composites.

Typical Kissinger plots for various nanocomposites are shown in Fig. 11.7(a–c). The E_a has been estimated from the slope of a straight line obtained from the plot of $\ln(\beta/T_{\max}^2)$ versus $1,000/T_{\max}$ (plots are not shown). A very good correlation coefficient of fitment (R^2 value >0.95) has been obtained. The slope obtained from the above plot is used to calculate the E_a . All figures show that the linearly fitted straight lines are nearly parallel and thus confirm the applicability of these methods within the conversion range studied. Similar plots have also been obtained with more than 93–95 % confidence for the other nanocomposites (not shown here).

The characteristic temperatures and the mean E_a for thermal degradation of EMAs and their respective nanocomposites as calculated by the Kissinger technique are summarized in Table 11.5. The E_a of the pristine EMAs are lower than those of the filled composites in general. However, E_{as} of EMA30-based nanocomposites are surprisingly lower than those of the other nanocomposites. A similar trend has been observed with the 1.0 wt% MWNT-loaded composites. This implies that the thermal stability of E09N2.5 is more than both of the E24N2.5 and E30N2.5.

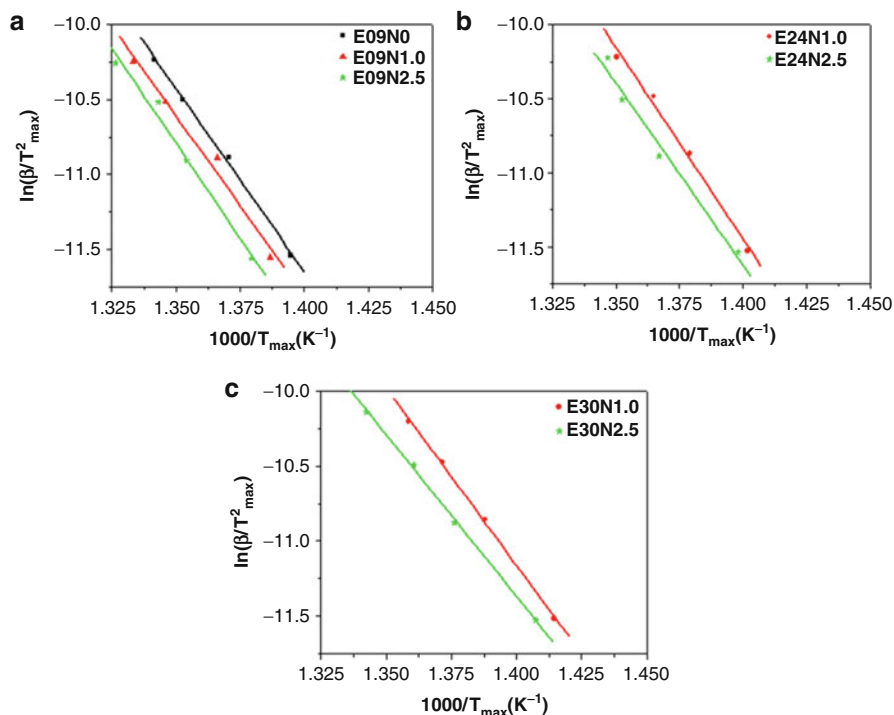


Fig. 11.7 (a-c) Typical Kissinger plot from the experimental data at different heating rates

The kinetic parameters, such as the E_a and pre-exponential factor (A) which characterize the thermal decomposition process, were calculated. The results obtained using Flynn-Wall-Ozawa methods are presented in Figs. 11.8 and 11.9. The lower degree of conversion (α) range of 0.1–1.0 was taken into account. The increase in E_a and $\log A$ with the increase of α is indicative of complex reactions during decomposition (involving several mechanisms) [52]. This variation of E_a , especially at higher α , is a sign of the complexity of the process. For pure EMA30, in particular, the trend of variation of kinetic parameters with conversion can possibly be explained on the basis of increased complication of thermal degradation mechanism at higher temperatures.

However, from the application point of view, for polymeric materials, the onset of degradation is the most important factor. The mean E_a obtained using the Flynn-Wall-Ozawa method is also listed in Table 11.5, and typical Flynn-Wall-Ozawa plots for E09N2.5, E24N2.5, and E30N2.5 are shown in Fig. 11.10 (a), (b), and (c), respectively. Figures show that the best fit straight lines are nearly parallel and thus confirm the applicability of this method within the conversion range studied. The E_a values computed using Flynn-Wall-Ozawa method also show that the thermal stability of the samples decreases in the following way: E09N2.5 > E24N2.5 > E30N2.5.

Table 11.5 Kinetic parameters for the thermal degradation of various EMA/MWNT composites

Sample	Parameter	Heating rate (°C/min)				Mean activation energy, E_a (kJ/mol)	
		5	10	15	20	Kissinger	Flynn-Wall-Ozawa
E09N0	T_{onset}	390.0	405.5	417.1	419.2	200	167
	T_{max}	445.1	456.6	466.2	471.9		
E09N1.0	T_{onset}	401.0	407.5	423.7	431.9	213	175
	T_{max}	450.2	459.0	470	477.0		
E09N2.5	T_{onset}	408.0	422.7	429.4	431.2	236	203
	T_{max}	455.0	465.5	471.5	480.9		
E24N0	T_{onset}	383.0	383.7	408.7	415.5	190	162
	T_{max}	436.7	445.5	458.4	464.4		
E24N1.0	T_{onset}	391.5	404.2	411.2	419.0	211	186
	T_{max}	440.3	452.0	459.7	467.5		
E24N2.5	T_{onset}	394.5	409.0	418.2	420.3	205	185
	T_{max}	442.3	458.5	466.4	469.5		
E30N0	T_{onset}	380.5	381.8	388.0	410.4	183	117
	T_{max}	439.0	445.0	448.0	464.0		
E30N1.0	T_{onset}	385.0	399.4	408.8	413.8	195	169
	T_{max}	434.0	447.5	456.0	463.0		
E30N2.5	T_{onset}	391.5	403.4	415.1	419.0	180	174
	T_{max}	437.5	453.6	461.9	453.6		

T_{onset} was determined from the respective TG curve with 5 wt% loss, T_{max} was determined from the respective DTG curve peaks

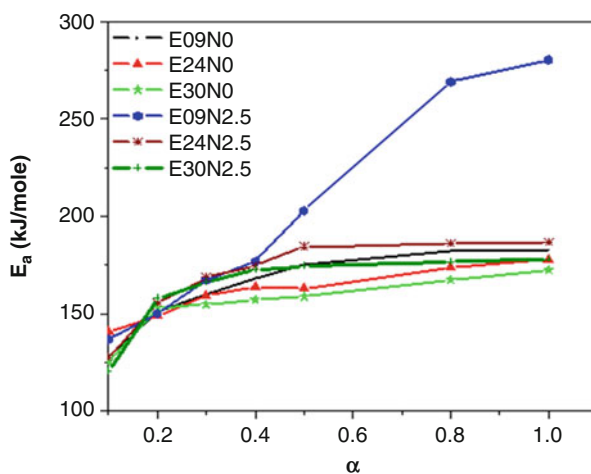


Fig. 11.8 Activation energies values with conversion degree for pristine EMA and their respective nanocomposites

A similar trend in the thermal stability of the samples is reflected from both the Kissinger and Flynn-Wall-Ozawa methods, corresponding to E_a of the samples. However, both methods have some difficulties in calculating kinetic parameters such as reaction order, pre-exponential factor, etc.

Fig. 11.9 Variation of pre-exponential factor (A) values with conversion degree for pristine EMA and their respective nanocomposites

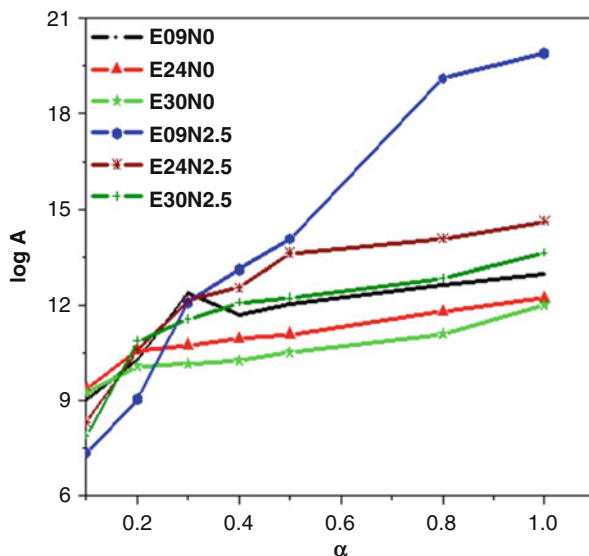


Table 11.6 Activation energy (E_a) of melt flow at three different shear rates calculated from an MPT study

Sample code	Activation energy, E_a (kJ/mole)		
	Shear rate 61.30 (s^{-1})	Shear rate 122.60 (s^{-1})	Shear rate 306.50 (s^{-1})
E09N0	22.4	23.5	23.5
E09N1.0	23.9	24.6	23.5
E09N2.5	25.0	24.7	23.5
E24N0	17.4	16.0	14.7
E24N1.0	18.5	17.0	15.2
E24N2.5	17.3	15.7	13.8
E30N0	20.7	18.1	17.0
E30N1.0	19.4	18.8	16.0
E30N2.5	20.2	19.2	16.2

4.1 TGA Mass Spectroscopy

Decomposition products of polymers have been determined by many investigators, but the results are often conflicting because of difficulties in analyzing a large number of products. A comprehensive analysis of the thermal decomposition products of EMA has been made with the help of TGA mass spectroscopy techniques. The structures for most of the compounds as obtained from above scans were determined. The evidence supporting the proposed mechanism is based on smaller fragments. The initiation of thermal degradation involves the loss of a hydrogen atom from the polymer chain as a result of energy input in the form of heat. This creates a highly reactive and unstable polymer “free radical” and

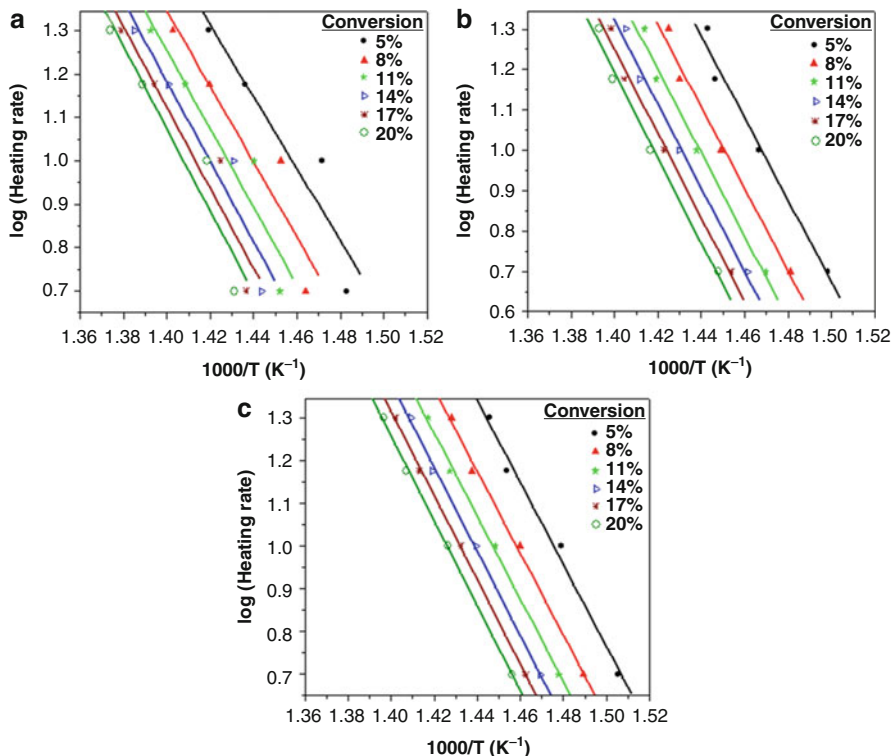
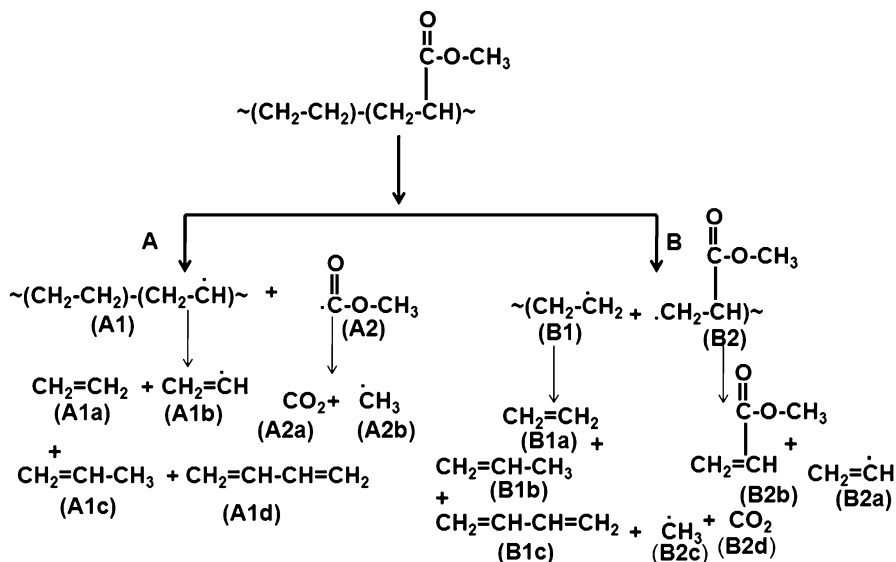


Fig. 11.10 Typical Flynn-Wall-Ozawa plots for (a) E09N2.5 and (b) E24N2.5 (c) E30N2.5

a hydrogen atom with an unpaired electron. Groups that are attached to the side of the backbone are held by bonds which are weaker than the bonds connecting the chain. When the polymer is being heated, the side groups are stripped off from the chain before it is broken into smaller pieces.

The backbone can break down randomly, and it could occur at any position of the backbone. The molecular weight decreases rapidly, evolving a combination of lower molecular weight fragments along with the monomers. This is because it forms new free radicals which have a high activity leading to intermolecular chain transfer and disproportion termination with the $>CH_2$ group. The mechanisms of thermal decomposition have been proposed and summarized in Scheme 11.2. It has been proposed that initial degradation occurs by side-group elimination (path A), leading to the formation of unsaturated products. At the same time, the scission of the main chain (path B) starts. The random scission of EMA is initiated by a homolytic scission of a methoxycarbonyl side group followed by β scission. Side-group elimination is a more dominant process than main chain scission at least in the lower-temperature regions.

At high temperatures, the components of the long chain backbone of the polymer can begin to separate (molecular scission) and react with one another. Under



Scheme 11.2 The proposed degradation mechanism of EMA and EMA/MWNTs nanocomposites

thermal effect, the end of polymer chain departs, giving rise to a lower yield of free radicals. Then, following the chain reaction mechanism, the polymer loses the monomer one by one. However, the molecular chain is supplied not to change a lot within a short span of time.

The average mass fraction of nanocomposites (with respect to the total mass) decreased from 90 to 80 % as the temperature was increased from 300 °C to 450 °C. The evolution of the large number of volatile gaseous species released between 350 °C and 450 °C confirms the complexity of thermal degradation process. The generation of monomer was accompanied by the formation of a number of low molecular weight stable species (H_2 , CO , CO_2 , CH_4 , C_2H_4 , C_2H_6 , HCOOCH_3) in trace amounts.

Scheme 11.2 lists the structures of the possible degradation products formed from the EMA. The degradation of neat EMA and its nanocomposites yields CO_2 (m/z 44), CH_4 (m/z 16), $\text{CH}_2=\text{CH}_2$ (m/z 28), HCOOCH_3 (m/z 60), and other MA monomers (m/z 86). The TGA mass spectroscopy showing an intense peak at m/z 18 is possibly due to the Ar gas used in as a carrier gas. Peak corresponding $m/z = 28$ is due to the formation of $\text{CH}_2=\text{CH}_2$ from the thermal decomposition of EMA main chain. The spectrum also displays two intense peaks at high a temperature corresponding to $m/z = 42$ and $m/z = 54$ possibly due to the formation of $\text{CH}_2=\text{CH-CH}_3$ and $\text{CH}_2=\text{CH-CH}=\text{CH}_2$, respectively. These are formed due to the thermal decomposition of polyethylene backbone or EMA main chain. The peak corresponding to m/z 60 refers to the possible formation of HCOOCH_3 from a macro-radical formed after the rupture of a C-COOCH_3 bond at the end unit containing an unsaturated bond: the rupture energy of a C-COOCH_3 is

approximately $10 \text{ kcal mole}^{-1}$ less than that of a C–C bond in the main chain [51]. The formation CO_2 and CH_4 is due to the degradation of $-\text{COOCH}_3$ side chain. CO is produced mainly from the incomplete combustion of macromolecular chain. The TGA mass spectrum of neat EMA shows a peak at m/z 86 probably due to the molecular ion of the MA monomer derived from a macro-radical formed after the scission of the main backbone.

The m/z values corresponding to the degradations in 400°C and 500°C were also calculated. The amount of MA produced is clearly dependent on the temperature or degradation time. At 420°C , more intense peak corresponding to scission of MA was observed than that obtained at 500°C or above. This shows that there is a decreasing involvement of side-group elimination with increasing temperature. It should be noted that even at moderate conversions, the actual degree of decomposition is likely to be different from the initial degradation. Accordingly, at high temperatures, the peak corresponding to the ion at m/z 86 and 60 has not been observed. Most importantly, in terms of stabilization, MWNTs do not offer any preference either to the degradation of side groups or main chain of EMA. However, a gross stabilization effect is observed in general.

4.2 Isothermal Decomposition

Isothermal TGA studies at 375°C , 400°C , 425°C , and 450°C for EMA09-, EMA24-, and EMA30-based nanocomposites are also reported. Nanocomposites exhibit a slow and steady decomposition at 375°C , and it becomes relatively more rapid with increasing temperature as shown in Fig. 11.11(a–d). The single-step weight loss and drastic degradation of EMA have been observed during the first 20 min of isothermal decomposition. The decomposition of EMA30 and its nanocomposites becomes relatively more rapid under isothermal heating at higher temperatures, viz., $400\text{--}450^\circ\text{C}$. This relates well with the non-isothermal decomposition in nitrogen as depicted earlier. At a higher temperature (450°C and above), all nanocomposites rapidly degrade similar to the respective neat EMAs. This indicates that the thermal stability of the nanocomposites contributed from the incorporation of MWNTs is not pronounced at higher temperatures. The thermal stabilities of the E09N2.5 nanocomposites are much higher compared to those of the pure EMA containing 9 wt% MA. Distributed MWNTs in E09N2.5 possibly prevent small gaseous molecules permeating out from the nanocomposites during initial stages of thermal decomposition, and consequently, the nanocomposites exhibit higher thermal stability.

The isothermal decomposition data of the neat polymer and their nanocomposites, viz., the time at maximum weight loss (t_{max}) and rate of weight loss $(d\alpha/dt)_{\text{max}}$, are calculated. The t_{max} of the nanocomposites are slightly higher than neat EMA counterparts, whereas $(d\alpha/dt)_{\text{max}}$ values are much higher especially in EMA30-based nanocomposites indicating the rapid weight loss. The amount of residue for the neat EMAs and their nanocomposites is decreased progressively with raising isothermal set temperatures. Mass loss and mass loss rates have been

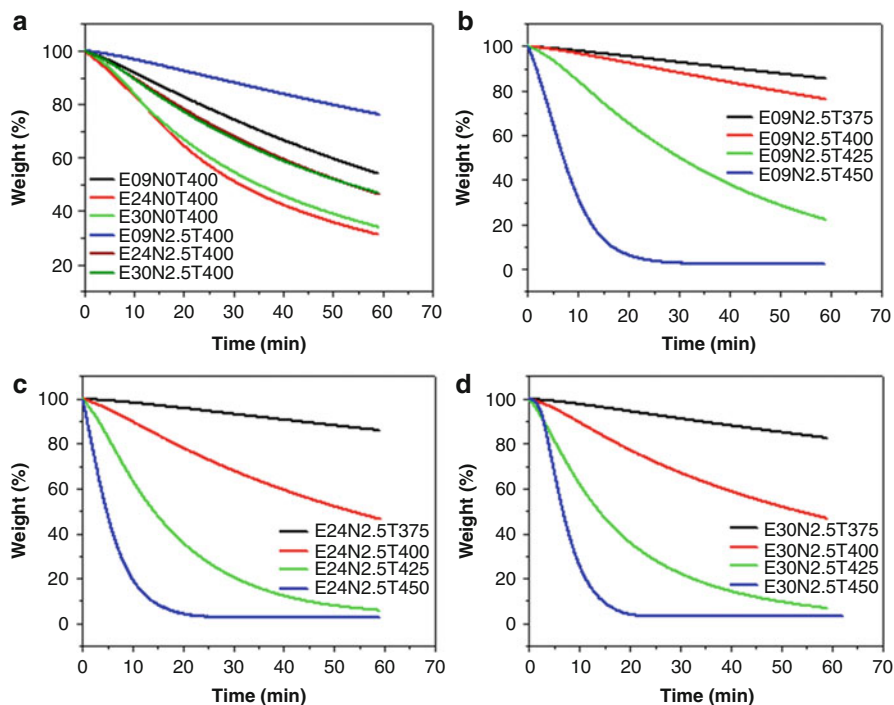


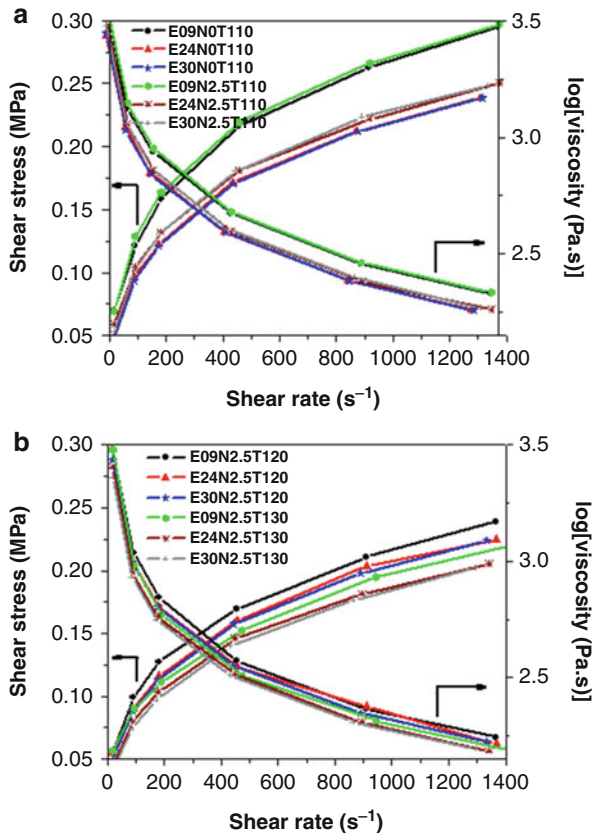
Fig. 11.11 (a-d) Isothermal TGA curves of pure EMA and its nanocomposites at different temperatures for 60 min in nitrogen atmosphere

strongly affected by isothermal set temperature. In addition, it can be noted that the rapid degree of weight loss occurs with the increase in MA content of the matrix. The remaining weights of the nanocomposites after 60 min of decomposition is higher for E09N2.5. The high residual weight of the nanocomposites indicates that the EMA matrix has not completely degraded within this stipulated time.

Based on the isothermal degradation results (time vs. conversion), fitments have been done considering various orders of reactions (0, 0.5, 1.0, 1.5, 2.0, 2.5, 3.0, etc.) with their rate equations. Plot of time versus conversion at a particular temperature for various nanocomposites has been carried out. A very good correlation coefficient (R^2 value >0.98) is observed, indicating a good fit of data (plots are not shown).

The decomposition of EMA and its nanocomposites follows pseudo-order reaction. As the set temperatures are increased, the minor change in “ n ” is observed. The initial reaction order of the samples ranged from 0 to 5 min (first 5 min) does not show good fitment with respect to a particular reaction order. The data corresponding to decomposition of initial 5–10 min can be closely fitted with the order of 1.0 and 1.5. The final parts of data (from 10 to 60 min) fit well with second-order decomposition kinetics. Results show that the overall order of thermal decomposition reaction has been of pseudo first and second, for initial and final phase of decomposition, respectively.

Fig. 11.12 (a–b) Variation of shear stress and viscosity of various nanocomposites with increasing shear rate in MPT study



4.3 Melt Viscosity (Capillary Flow)

From processing and application points of view, the rheological results at wider ranges of shear rates ($\dot{\gamma}$) of a material are very important. Keeping this in mind, steady shear viscosity measurements were performed. Figure 11.12(a–b) shows the plot of shear stress (τ) versus $\dot{\gamma}$ and $\log(\eta)$ versus $\dot{\gamma}$, respectively, for pristine EMAs and their various nanocomposites at three different temperatures. At lower shear rate regions, the shear viscosity does not exhibit a Newtonian plateau. τ of the nanocomposites increases with increasing $\dot{\gamma}$, and η decreases with increasing $\dot{\gamma}$ indicating the pseudoplastic behavior of the nanocomposites. The same trend is also observed for all EMA/MWNT nanocomposites at the other two temperatures (viz., 120 °C and 130 °C). However, η decreases with increasing temperature. It is also observed that τ and η increase with decreasing MA content and with the addition of MWNTs into matrix polymer.

EMA09 displays the highest shear stress values while EMA24 and EMA30 register lower values at all shear rates. However, the difference of shear stresses between EMA24 and EMA30 at low to high shear rates is much less, as compared

to EMA09. In the EMA09 matrix, MWNTs are more dispersed; thus, η is higher. The shear viscosities are higher at a lower shear rate region and exhibit a large dependency on the shear rate. At a higher shear rate, the viscosity is drastically reduced possibly due to the disruption of structural networks. Lower viscosity at high shear rates is due to a shear thinning effect of the nanocomposites. As MWNT loading is increased, both τ and η are increased, indicating the improvements in the melt strength. The sample shows the predominance of viscous and elastic behavior at low and high shear rate regions, respectively. The power law equation is applied to quantify the rheological behavior of this system at moderate shear rates. The flow behavior index, “ n ,” and the consistency index, “ k ,” are calculated using a linear regression analysis. The pseudoplasticity index varies from 0.32 to 0.40.

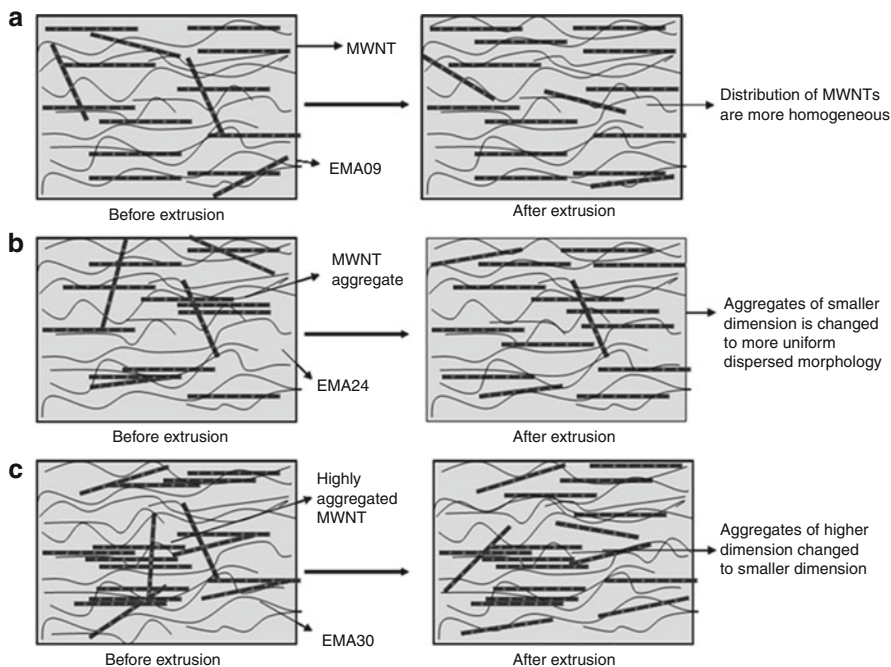
4.4 Activation Energy of Flow

The activation energy (E_a) of melt flow can be calculated from the plot of $\log\eta$ versus $1/T$ by using the Arrhenius type of Eq. 11.2 [53, 54]:

$$\eta = A e^{E_a/RT} \quad (11.2)$$

where η is the melt viscosity; A , the pre-exponential factor; E_a , the activation energy; T , the absolute temperature; and R , the universal gas constant. The E_a has been estimated from the slope of a straight line plot of the log (melt viscosity) against the reciprocal of the absolute temperature (plots are not shown).

A very good correlation coefficient (R^2 value >0.95) is observed, indicating a good fitment of data. The slope obtained from the above plot is used to calculate the E_a of melt flow. Table 11.6 displays the dependence of E_a on the shear rate of filled and unfilled systems. The variation of E_a may be attributable to the change in phase morphology of the system under shear deformation. The E_a for EMA09-based nanocomposites is increased initially with the increase in the shear rate, and then it decreases or changes marginally with the increase in the shear rate. For other systems, a slight decrease in E_a is observed with the increase in the shear rate. The E_a values increase with increasing nanotube content up to 2.5 wt% for EMA09-based nanocomposites. Whereas for EMA24-based nanocomposites, the activation energy values increase with increasing nanotube content up to 1 wt%, and then it decreases at 2.5 wt% MWNT loading. In addition, it can be noted that the E_a corresponding to different %wt. of MWNTs decreases with the increase in MA content irrespective of the amount of MWNTs present inside the matrix polymers. The reduction in E_a of filled system may be due to the aggregation effect of MWNTs in the polymer matrix with increasing MA content. The E_a of flow is the minimum energy requirement for the molecules to just flow which is equivalent to the energy necessary to overcome the intermolecular forces of attraction (and resistance owing to the entanglements). A scheme has been used (Scheme 11.3a–c) to explain the above observations at an experimental condition.



Scheme 11.3 (a-c) Schematic depiction of role of morphology during extrusion (steady shear flow)

4.5 Morphology of Extrudate Surfaces

Since the surface topography depends on the flow behavior and hence on the processing conditions (temperature, shear rate), the extrudate surface morphology is investigated using SEM for different systems. The morphology of the extrudate and phenomenon of the melt fracture were studied at a constant temperature (120 °C) over different shear rates. Figures 11.13, 11.14, and 11.15 represent the SEM photomicrograph of the EMA09-, EMA24-, and EMA30-based nanocomposites with 0, 1, and 2.5 wt% MWNT loadings, respectively, at the shear rates of 12.26, 306.5, and 919.5 s⁻¹. From these, it is clear that the surface finishes for pure EMA09 and its nanocomposites are better at a lower shear rate as compared to those obtained at a higher shear rate (Figs. 11.13, 11.14, and 11.15). Eventually, the shear stress or rate reaches a critical value and melt fracture occurs.

The extrudates are smooth at shear rates of 12.26 s⁻¹, and weak shark skin appears at a shear rate of 306.5 s⁻¹ and grows gradually with increasing shear rate and reaches elastic failure at 919.5 s⁻¹. The fractures could result because the stress exceeds the melt strength as a result of slower time of relaxation relative to the deformation rate. In general, 1 wt% MWNT-loaded nanocomposites display better surface finishes than that of the neat EMAs and their nanocomposites. On the contrary, if EMA24- and EMA30-based nanocomposites are subjected to the above mentioned conditions, they do not show melt fracture and shark skin effect.

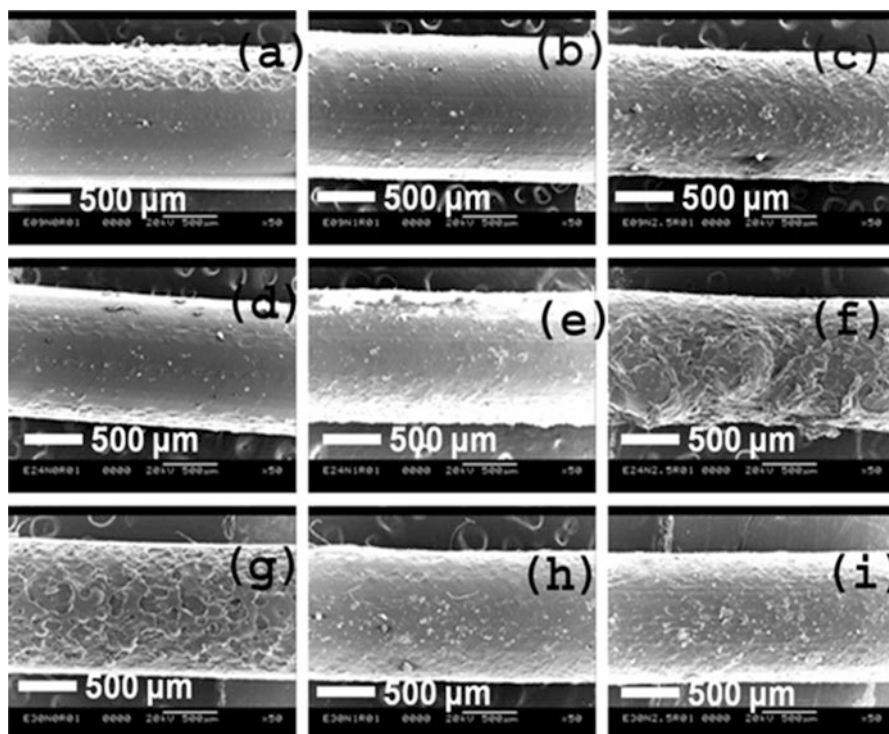


Fig. 11.13 SEM photomicrographs for the extrudates at a temperature of 120 °C and shear rate of 12.26 s^{-1} : (a) E09N0 (b) E09N1.0 (c) E09N2.5 (d) E24N0 (e) E24N1.0 (f) E24N2.5 (g) E30N0 (h) E30N1.0 (i) E30N2.5

Other than E24N2.5, all EMA24-based nanocomposites exhibit smooth surface finish over the experimental range of shear rates. This is possibly due to a uniform distribution of stresses because of the amorphous phase morphology of the systems. From extrudates, surface finish is very easy to understand which molding technique is suitable for these composites. Table 11.7 represents the process shear rate used for different molding techniques.

5 Electrical Properties

5.1 Effect of Conductivity and Dielectric Constant

The variation of AC conductivity (σ) with frequency for different MWNT content of nanocomposites is shown in Fig. 11.16. With increasing MWNT contents, the electrical conductivity of the nanocomposites increases with increasing frequency, and then it decreases slightly with further increment of frequency. At lower filler loading, specimens show a typical insulating behavior for a frequency-dependent conductivity. When the MWNT content reaches 7 wt%, there is a transition of level of conductivity

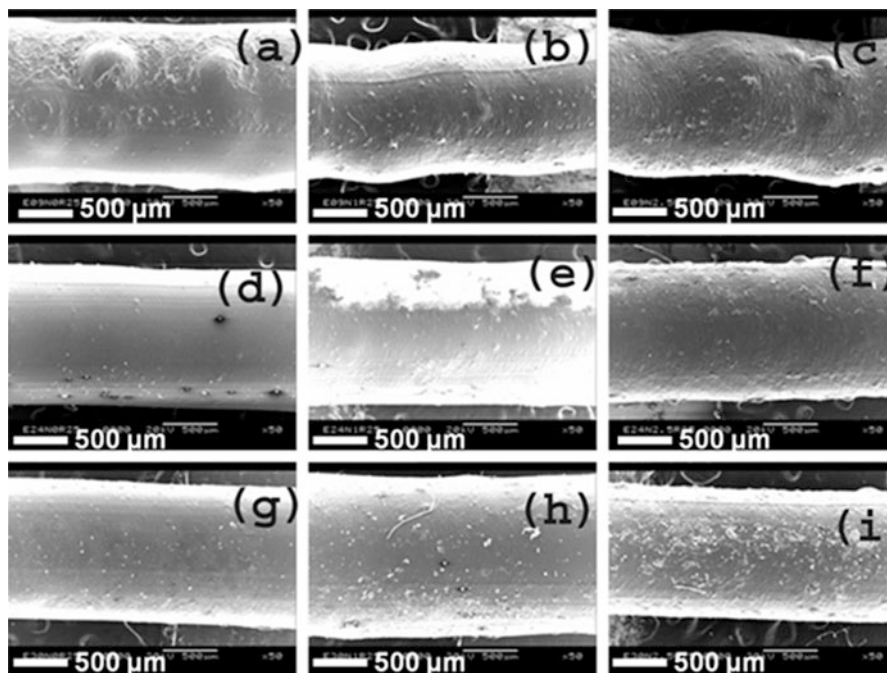


Fig. 11.14 SEM photomicrographs for the extrudates at a temperature of 120 °C and shear rate of 306.5 s^{-1} : (a) E09N0 (b) E09N1.0 (c) E09N2.5 (d) E24N0 (e) E24N1.0 (f) E24N2.5 (g) E30N0 (h) E30N1.0 (i) E30N2.5

from an insulator to a semiconductor. The electrical conductivity of pure MWNTs is approximately $1.85 \times 10^3 \text{ S/cm}$. The conductivity of the nanocomposites reduced remarkably particularly at a high frequency for all nanocomposites other than E09N7.0 and E09N10.0, and gradually, the nanocomposites show a typical semiconducting to conducting behavior. The dielectric constants of all nanocomposites always increased with an increase in MWNT contents, but it has less effect dependency on frequency. Due to the presence of more percentage amount of MWNT in EMA matrix, the value of the dielectric constant is high, and MWNTs improve the dielectric constant and decrease the loss of the nanocomposite.

The effect of surface and volume resistivity of MWNT-reinforced EMA nanocomposites at a fixed (2.0 wt%) loading (Fig. 11.17) indicates resistivity of the nanocomposites depends strongly on the type of functional group present onto the surface of MWNT surface and also on MA content of EMA. Among the two types ($-\text{OH}$, $-\text{COOH}$) of f-MWNTs, the nanocomposite containing 30 wt% MA displays the lowest DC surface and volume resistivity. However, the difference in resistivity between the two nanocomposites (containing EMA of 24 % and 30 % MA content) is not very significant, with MWNTs-COOH and MWNTs-OH. At a particular MWNT content, a transition of order of resistivity from an insulator to a semiconductor is observed.

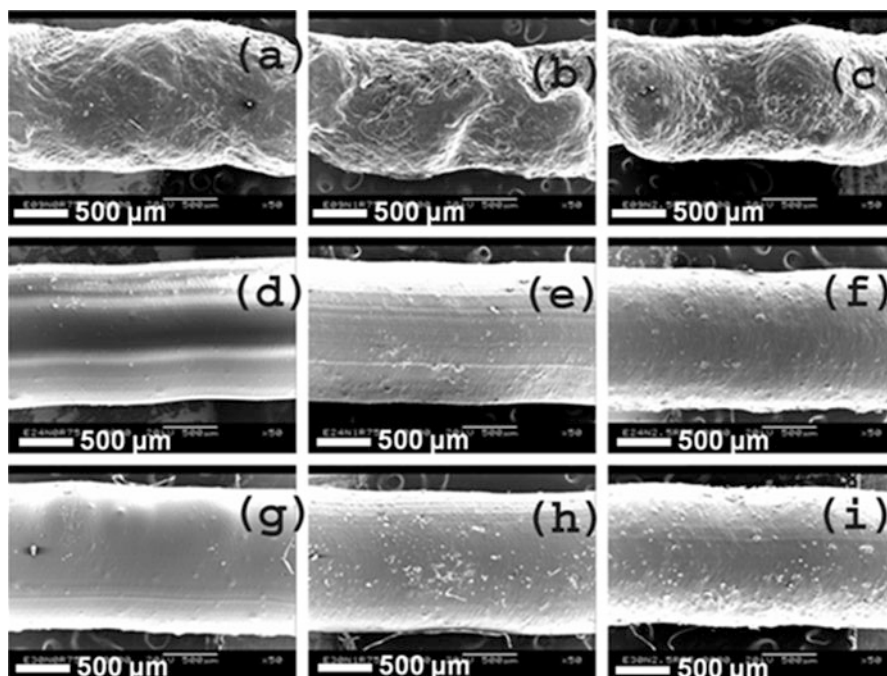


Fig. 11.15 SEM photomicrographs for the extrudates at a temperature of 120 °C and shear rate of 919.5 s⁻¹: (a) E09N0 (b) E09N1.0 (c) E09N2.5 (d) E24N0 (e) E24N1.0 (f) E24N2.5 (g) E30N0 (h) E30N1.0 (i) E30N2.5

Table 11.7 Process shear rate ranges for molding technique

Process	Typical process shear rate (s ⁻¹)
Injection molding	1,000–10,000
Extrusion	100–1,000
Transfer molding	1–100
Rotational molding/lining	<100
Compression molding	<1
Blow molding	–

The O₂ plasma treatment applied to the nanotubes brings about a significant improvement of the AC conductivity. Combined improvement of both tensile modulus and AC conductivity can only be achieved by mild oxidative treatments such as that provided by the O₂ plasma treatment on MWNTs.

5.2 Effect of MWNT Loading on DC Resistivity

Figure 11.18 shows the effect of MWNT content on surface and volume resistivity of MWNT-reinforced EMA nanocomposites. For all nanocomposite, the resistivity

Fig. 11.16 Frequency dependence of conductivity at room temperatures

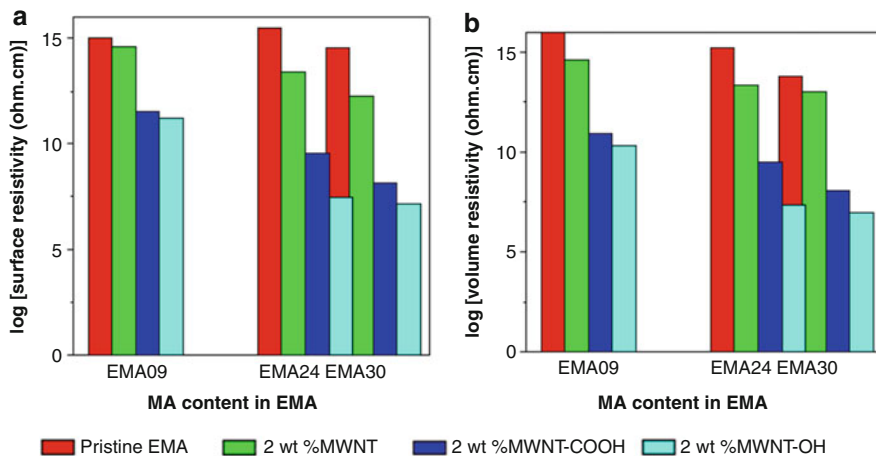
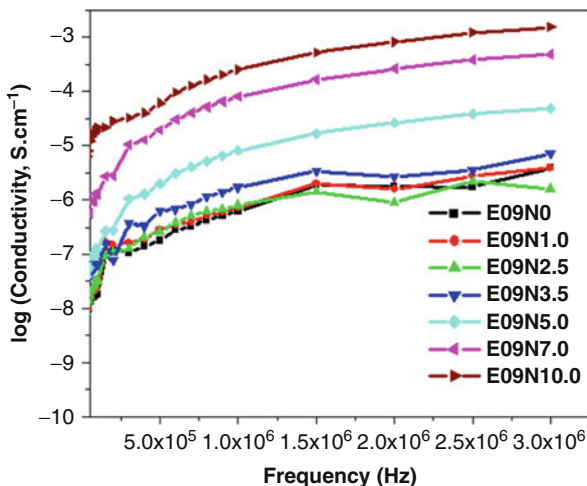
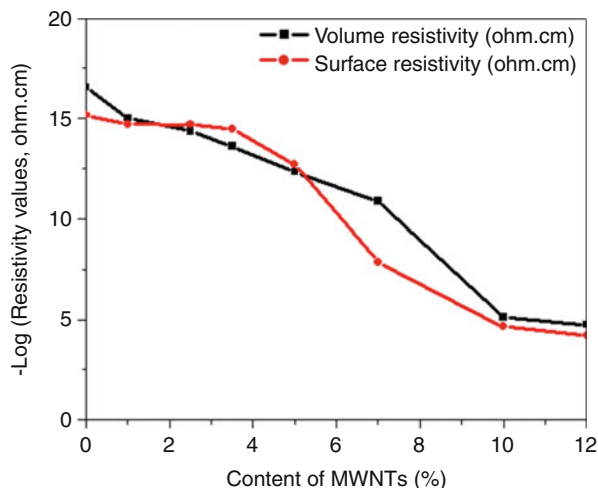


Fig. 11.17 (a–b) Effect of MA content on the surface and volume resistivity of EMA/MWNTs nanocomposites

decreases with the increase in MWNT loading. The nature of variation of resistivity with nanotube concentration depends on MWNT loading and their state of dispersion. The resistivity gradually decreases with increasing nanotube content. However, at 7 wt% MWNT loading, a definite reduction in resistivity is observed. But with further addition of MWNTs beyond 10 wt% loading, changes in the resistivity become marginal. This stepwise change in resistivity is a result of the formation of an interconnected structure of MWNTs. The progressive addition of conductive particles into an insulating polymer matrix leads to the formation of discrete conductive aggregates network which finally grows into a continuous conductive network chain at some critical concentration known as percolation threshold.

Fig. 11.18 Surface and volume resistivity of EMA/MWNTs nanocomposites as a function of the MWNTs mass concentrations



At loading beyond percolation, only the number of such conductive chain increases; consequently the decrease in resistivity becomes marginal. It is observed that the resistivity has some dependence on the composition of matrix polymer. This dependency can be attributed to viscosity of matrix during mixing. If the viscosity of nanocomposites is less, then the shear stress exerted on nanotube aggregates during mixing will be less; as a result, the breakdown of the aggregate (structure) will be less. But if the viscosity of matrix polymer during mixing is high (at high MWNT loading), then there will be an extensive breakdown of the nanotube structure, and chain-like particle aggregates will disintegrate and will be more isolated in the matrix polymer.

The morphology and electrical properties of EMA-/modified MWNT-based nanocomposites have also been investigated by using plasma, γ -ray irradiation, and chemically modified MWNTs, respectively. The improvement of technical properties of the matrix has been found to be highest with the plasma-modified MWNTs among others. The resistivity of the nanocomposites depends strongly on the type of modification and functional group present on MWNT surface. Among modified MWNTs studied here, the nanocomposite containing O₂ plasma-modified MWNTs displays the lowest DC surface and volume resistivity (Fig. 11.19). However, the difference in resistivity between the nanocomposites containing N₂ plasma-, O₂ plasma-, and piranha-treated MWNTs is not very significant.

6 EMI Shielding Effectiveness (EMI SE)

The electromagnetic wave consists of a magnetic field and electric field that change periodically, while the two components induct each other and propagate at right angles to the plane containing two components perpendicular each other. To check the effect of MWNT concentration on EMI SE, the measurement at any particular

Fig. 11.19 Effect of modified MWNTs on the surface and volume resistivity of EMA24/MWNTs nanocomposites

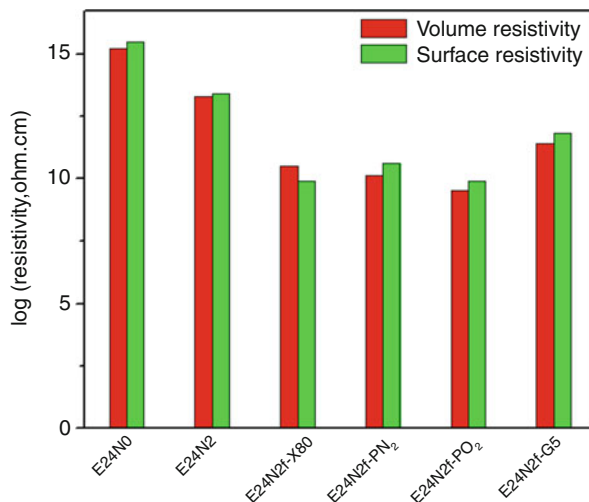
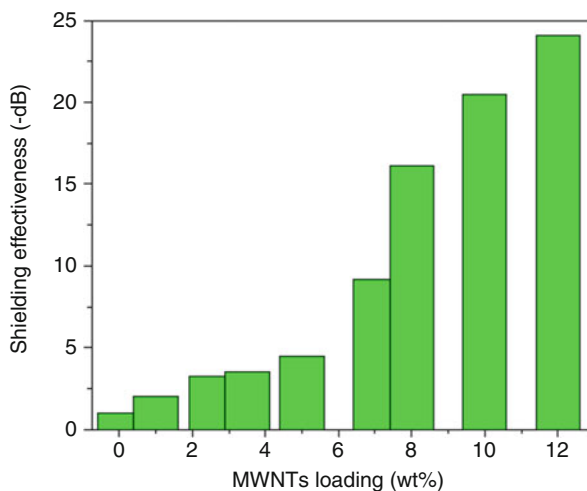


Fig. 11.20 MWNTs loading versus EMI SE of EMA/MWNTs nanocomposites at 10 GHz



reference frequency may be taken into consideration. The shielding effectiveness at the measurement frequency of 10 GHz for composites having different filler amount of loadings has been depicted in Fig. 11.20.

It can be seen clearly from the figure that the EMI SE increases with MWNT loading, and that is mainly because, with the increase in nanotube loading, the resistivity decreases which in turn increases the EMI SE. The rate of increase of EMI SE against MWNT loading is initially slow up to 5.0 wt% loading of MWNTs, but beyond that, a sharp increase is observed. EMI SE increases progressively with filler loading. As such, insulating polymer matrix is transparent to incident radiation; the conductive networks formed due to the addition of conductive particles interact with incident ray and account for shielding effectiveness. In fact, in

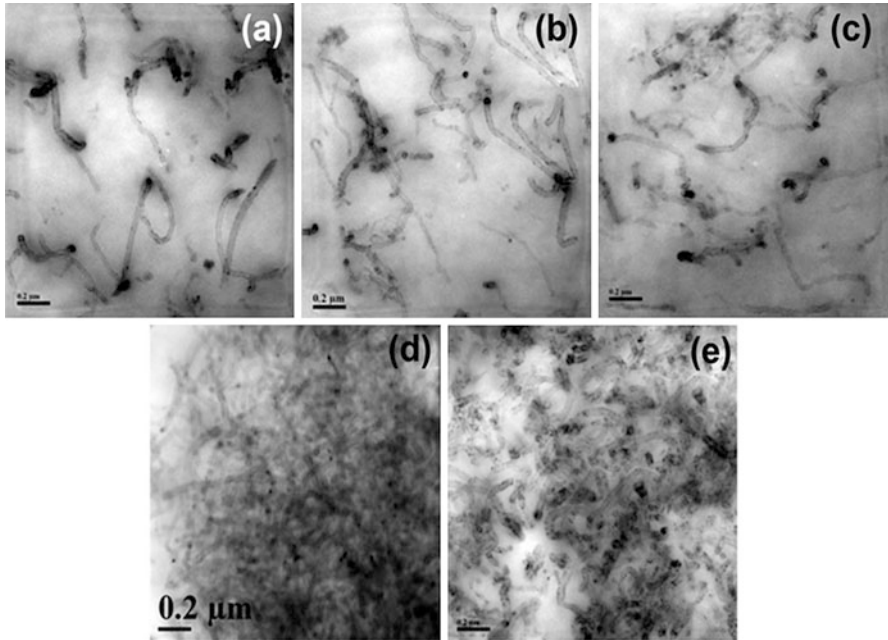


Fig. 11.21 HRTEM photomicrograph (at 10 kX magnification) of MWNT/EMA nanocomposites: (a) E09N1.0, (b) E09N2.5, (c) E09N3.5, (d) E09N5.0, and (e) E09N10.0

a composite with high filler loading (at and beyond percolation), there is a formation of mesh of conductive networks. With the increase in filler loading, the network size decreases which means conductive meshes become finer and finer with increased MWNT loading. Thus, their ability to absorb electromagnetic radiation increases, and consequently, the EMI SE increases. The EMI SE of metals is due to reflection whereas EMI SE of conductive composites is mainly due to absorption. The highest EMI SE value obtained for composites is around -22 dB at the highest loading, studied here.

The formation of a conductive network through aggregation of MWNT particles in the insulating polymer matrix is the key reason for EMI SE and conductivity. The closer the conductive network formed, the better will be the EMI SE. HRTEM photomicrographs (Fig. 11.21) show that the MWNTs are well dispersed in EMA matrix. In addition to this, they have high conductivity and tend to form special network-like morphology. The effect of nanocomposite thickness on EMI SE has been studied at the reference frequency of 10.0 GHz for all nanocomposites. The plot of EMI SE versus nanocomposite thickness is presented in Figure 11.22. It shows that EMI SE increases almost linearly with the increase in thickness. The formation of conductive mesh in the matrix intercepts electromagnetic radiation. This situation can be visualized as follows: with the increase in nanocomposite thickness, the number of conductive mesh increases and they are randomly placed in the system one after another in a thick sample. Thus, with continuous increase in

Fig. 11.22 EMI SE versus sample thickness at a frequency of 10.0 GHz for different nanocomposites

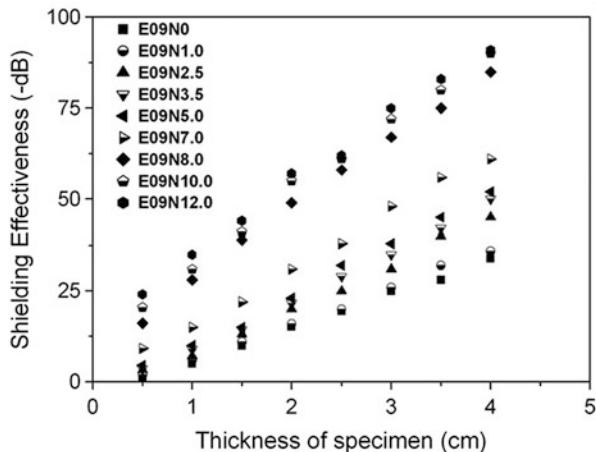
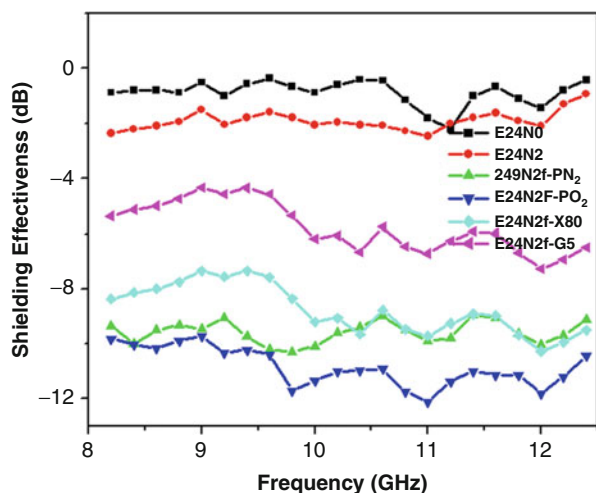


Fig. 11.23 Effect of modified MWNTs on the EMI shielding effectiveness of various EMA24/MWNT nanocomposites (N.B. This modified MWNTs based nanocomposites are designated as E24N2f-PN₂, E24N2f-PO₂, E24N2f-X80 and E24N2f-G5 for N₂ plasma, O₂ plasma, Piranha treated (at 80 °C) and 50 kGy γ -ray irradiated MWNT based EMA24/MWNT nanocomposites, respectively)



thickness, the number of mesh increases and mesh size decreases, and as a result, EMI SE progressively increases. This variation of resistivity versus EMI SE further corroborates our idea about the conductive network formation through MWNT particle aggregation in the matrix polymer. In the present system, the slope which indicates the rate of increase of EMI SE with thickness is found to be the highest for E09N12 in the system which has 12 wt% MWNTs followed by E09N10, the system containing 10 wt% MWNTs, and so on.

The EMI SE of the EMA/MWNT nanocomposites depends not only on the type of functional group present on MWNTs but also on the polarity of the matrix polymer. Figure 11.23 illustrates the EMI SE of the nanocomposites increased when plasma-modified MWNTs are used. For example, the effectiveness of nanocomposites is -1 dB for pure EMA24 and -9 to -11 dB at 2 wt% N₂ and O₂ plasma-modified MWNTs, respectively. The SE of EMA24/MWNTs-OH

nanocomposite is significantly higher than rest of the nanocomposites at all frequencies studied here. This result once again substantiates our observations with electrical and dielectric properties as discussed earlier. The highest SE (~ 15 dB) of these nanocomposites (EMA24 and EMA30 based) is considerably good for an engineering application in the X-band region.

7 Summary

Based on the experimental results, it is concluded that the volume resistivity strongly depends on the degree of crystallinity of the polymer used and the change of morphology of nanotubes in the nanocomposites. Applied strain also affects the volume resistance and morphology of MWNT. At relatively small extensions below 20 %, the volume resistance decreases due to the compression effect, providing an opportunity of closer contacts among MWNTs. The EEA/MWNT nanocomposite can be the potential material as an EMI shield material especially in the X-band region. Details of the kinetic studies of thermal degradation of various EMA/MWNT nanocomposites have been studied, and a promising mechanism has been proposed over different ranges of temperatures of degradation. The mechanism of thermal degradation has reflected degradation of side chain and chain scission processes, following pseudo first-order and second-order reactions. The major volatile gases evolved upon thermal decomposition of EMA are water, carbon dioxide, methane, carbon monoxide, and MA, respectively. Overall, it has been observed that the MWNT (both functionalized and pristine) plays an important role in affecting the morphology, mechanical properties, crystallization behavior, thermal degradation, processibility, electrical conductivity, and EMI SE of the resulting nanocomposites. The MWNTs treated by the O₂ plasma provide EMA nanocomposites with a low electrical resistivity than those produced by chemical oxidation and γ -ray irradiation. Therefore, the surface functionalizations or modifications of MWNTs along with perceptible dispersion of nanotubes in the matrix are the key issues in developing EMA/MWNT nanocomposites.

References

1. Ajayan PM (1999) Nanotubes from carbon. *Chem Rev* 99:1787–1799
2. Ando Y, Zhao X, Shimoyama H, Sakai G, Kaneto K (1999) Physical properties of multiwalled carbon nanotubes. *Int J Inorg Mater* 1:77–82
3. Avouris P (2002) Molecular electronics with carbon nanotubes. *Acc Chem Res* 35:1026–1034
4. Barrau S, Demont P, Perez E, Peigney A, Laurent C, Lacabanne C (2003) Effect of palmitic acid on the electrical conductivity of carbon nanotubes-epoxy resin composites. *Macromolecules* 36:9678–9680
5. Barthelat F, Rabiei R (2011) Toughness amplification in natural composites. *J Mech Phys Solids* 59:829–840
6. Basuli U, Chaki TK, Chattopadhyay S, Sabarwal S (2010) Thermal and mechanical properties of polymer-nanocomposites based on ethylene methyl acrylate and multiwalled carbon nanotube. *Polym Compos* 31:1168–1178

7. Basuli U, Chaki TK, Chattopadhyay S (2010) Influence of acrylate content on the properties of ethylene methyl acrylate-multi walled carbon nanotube composites. *Adv Sci Lett* 3:10–19
8. Basuli U, Nah C (2012) Functionalizing multi-wall carbon nanotubes by plasma modification for the preparation of high performance ethylene methyl acrylate (EMA) nanocomposites. In: International conference and workshop on nanostructured ceramics and other nanomaterials (ICWNCN), 13–16 Mar 2012, New Delhi
9. Basuli U, Chaki TK, Setua DK, Chattopadhyay S (2011) A comprehensive examination on the thermal degradation of multi-walled carbon nanotubes-reinforced EMA nanocomposites. *J Therm Anal Calorim* 108:1223–1234
10. Basuli U, Chaki TK, Chattopadhyay S (2012) Rheological signatures of ethylene methyl acrylate-ed carbon nanotube nanocomposites. *Polym Adv Technol* 23:65–76
11. Basuli U, Chaki TK, Nah C, Chattopadhyay S (2012) Rheological behaviors and electrical properties of nanocomposites based on poly(ethylene-co-methyl acrylate) and multi-walled carbon nanotubes. *Adv Sci Lett* 5:1–13
12. Basuli U, Chaki TK, Chattopadhyay S (2012) Mechanical, thermal and rheological behavior of ethylene methyl acrylate-MWNT nanocomposites. *Polym Eng Sci* 52:277–288
13. Basuli U, Chattopadhyay S, Nah C, Chaki TK (2012) Electrical properties and electromagnetic interference shielding effectiveness of multi-walled carbon nanotubes-reinforced EMA nanocomposites. *Polym Compos* 33:897–903
14. Basuli U, Chaki TK, Nah C, Chattopadhyay S (2012) Rheological behaviors and electrical properties of nanocomposites based on poly(ethylene-co-methyl acrylate) and multi-walled carbon nanotubes. *Adv Sci Lett* 17:27–39
15. Baughman RH, Zakhidov AA, de Heer WA (2002) Carbon nanotubes-the route toward applications. *Science* 297:787–792
16. Cheng Y, Zhou O (2003) Electron field emission from carbon nanotubes. *C R Phys* 4:1021–1033
17. Das NC, Maiti S (2008) Electromagnetic interference shielding of carbon nanotube/ethylene vinyl acetate composites. *J Mater Sci* 43:1920–1925
18. Dresselhaus MS, Dresselhaus G, Eklund PC (1996) *Science of fullerenes and carbon nanotubes*. Academic, New York/San Diego
19. Dresselhaus MS, Dresselhaus G, Avouris P (2001) *Carbon nanotubes: synthesis, structure, properties, and applications*. Springer, Berlin/Heidelberg
20. George JJ, Bhowmick AK (2009) Influence of matrix polarity on the properties of ethylene vinyl acetate-carbon nanofiller nanocomposites. *Nanoscale Res Lett* 4:655–664
21. Gururajan G, Froude V, Riutta S, Thomas A, Gao I, Samuels SL, Massouda DF, Weinberg M, Ogale AA (2008) Effect of poly (ethylene methyl acrylate) copolymer on thermal, morphological, and mechanical properties of polypropylene copolymer blown films. *J Appl Polym Sci* 107:2500–2508
22. Haggemueller R, Gommans HH, Rinzler AG, Fischer JE, Winey KI (2000) Aligned single-wall carbon nanotubes in composites by melt processing methods. *Chem Phys Lett* 330:219–225
23. Jeong KU, Lim JY, Lee JY, Kang SL, Nah C (2010) Polymer nanocomposites reinforced with multi-walled carbon nanotubes for semiconducting layers of high-voltage power cables. *Polym Int* 59:100–106
24. Jia ZJ, Wang Z, Xu C, Liang J, Wei B, Wu D, Zhu S (1999) Structural materials: properties, microstructure and processing. *Mater Sci Eng A* 271:395–400
25. Jin ZX, Pramoda KP, Xu GQ, Goh SH (2001) Dynamic mechanical behavior of melt-processed multi-walled carbon nanotube/poly(methyl methacrylate) composites. *Chem Phys Lett* 337:43–47
26. Lamy de la Chapelle M, Stéphan C, Nguyen TP, Lefrant S, Journet C, Bernier P, Munoz E, Benito A, Maser WK, Martinez MT, de la Fuente GF, Guillard T, Flamant G, Alvarez L, Laplaze D (1999) Raman characterization of singlewalled carbon nanotubes and PMMA-nanotubes composites. *Synth Met* 103:2510–2512

27. Lee KY, Kim KY (2008) ^{60}Co γ -ray irradiation effect and degradation behaviors of a carbon nanotube and poly(ethylene-co-vinyl acetate) nanocomposites. *Polym Degrad Stab* 93:1290–1299
28. Lee KY, Kim KY, Han WY, Park DH (2008) Thermal, electrical characteristics and morphology of poly(ethylene-co-ethyl acrylate)/CNT nanocomposites. *IEEE Trans Dielectr Electr Insul* 15:205–213
29. Moly KA, Oommen Z, Bhagawan SS, Groeninckx G, Thomas S (2002) Melt rheology and morphology of LLDPE/EVA blends: effect of blend ratio, compatibilization, and dynamic crosslinking. *J Appl Polym Sci* 86:3210–3225
30. Mongal N, Chakraborty D, Bhattacharyya R, Chaki TK, Bhattacharya P (2010) Characterization of electron beam irradiated ethylene methyl acrylate copolymer. *Ind Eng Chem Res* 49:7113–7120
31. Mongal N, Chakraborty D, Bhattacharyya R, Chaki TK, Bhattacharya P (2010) Engineering properties of electron beam-crosslinked ethylene methyl acrylate copolymer. *J Appl Polym Sci* 117:75–83
32. Peeterbroeck S, Breugelmans L, Alexandre M, Nagy JB, Viville P, Lazzaroni R, Dubois P (2007) The influence of the matrix polarity on the morphology and properties of ethylene vinyl acetate copolymers-carbon nanotube nanocomposites. *Compos Sci Technol* 67:1659–1665
33. Peeterbroeck S, Laoutid F, Swoboda B, Lopez-Cuesta JM, Moreau N, Nagy JB, Alexandre M, Dubois P (2007) How carbon nanotube crushing can improve flame retardant behaviour in polymer nanocomposites. *Macromol Rapid Commun* 28:260–264
34. Poncharal P, Wang ZL, Ugarte D, de Heer WA (1999) Electrostatic deflections and electro-mechanical resonances of carbon nanotubes. *Science* 283:1513–1516
35. Preston CML, Amarasinghe G, Hopewell JL, Shanks RA, Mathys Z (2004) Evaluation of polar ethylene copolymers as fire retardant nanocomposite matrices. *Polym Degrad Stab* 84:533–544
36. Robertson J (2004) Realistic applications of CNTs. *Mater Today* 7:46–52
37. Saito Y, Uemura S (2000) Field emission from carbon nanotubes and its application to electron sources. *Carbon* 38:169–182
38. Shaffer MSP, Windel AH (1999) Fabrication and characterization of carbon nanotube/poly(vinyl alcohol) composites. *Adv Mater* 11:937–941
39. Tang ZK, Zhang L, Wang N, Zhang XX, Wen GH, Li GD, Wang JN, Chan CT, Sheng P (2001) Superconductivity in 4 angstrom single-walled carbon nanotubes. *Science* 201(292):2462–2465
40. Velasco-Santos C, Martinez-Hernandez AL, Fisher FT, Ruoff R, Castano VM (2003) Improvement of thermal and mechanical properties of carbon nanotube composites through chemical functionalization. *Chem Mater* 15:4470–4475
41. Volkmer D (1999) Von Biomaterialien zu biomimetischen Materialien: Der weg ist das Zie. *Chemie in unserer Zeit* 33:6–19
42. Wei D, Liu Y (2008) The intramolecular junctions of carbon nanotubes. *Adv Mater* 20:2815–2841
43. Yang J, Hu J, Wang C, Qin Y, Guo Z (2004) Fabrication and characterization of soluble multi-walled carbon nanotubes reinforced P(MMA-co-EMA) composites. *Macromol Mater Eng* 289:828–832
44. Jimenez GA, Jana SC (2007) Oxidized carbon nanofiber/polymer composites prepared by chaotic mixing. *Carbon* 44:2079–2091
45. Assouline E, Lustiger A, Barber AH, Cooper CA, Klein E, Wachtel E, Wagner HD (2003) Nucleation ability of multiwall carbon nanotubes in polypropylene Composites. *J Polym Sci Polym Phys* 41:520–527
46. Hagenmueller R, Zhou W, Fischer JE, Winey KI (2003) Production and characterization of polymer nanocomposites with highly aligned single-walled carbon nanotubes. *J Nanosci Nanotechnol* 3:105–110
47. Li SN, Li ZM, Yang MB, Hu ZQ, Xu XB, Huang R (2004) Carbon nanotubes induced nonisothermal crystallization of ethylene-vinyl acetate copolymer. *Mater Lett* 58:3967–3970

48. Jäger KM, Dammert RC, Sultan BÅ (2002) Thermal degradation studies of different polar polyethylene copolymers. *J Appl Polym Sci* 84:1465–1473
49. Poomalai P, Ramaraj B, Siddaramaiah (2007) Thermal and mechanical properties of poly (methyl methacrylate) and ethylene vinyl acetate copolymer blends. *J Appl Polym Sci* 106:684–691
50. Gao Z, Kanekob T, Houc D, Nakadab M (2004) Kinetics of thermal degradation of poly (methyl methacrylate) studied with the assistance of the fractional conversion at the maximum reaction rate. *Polym Degrad Stab* 84:399–403
51. Shibaev LA, Antonova TA, Vinogradova LV, Ginzburg BM, Ginzburg VG, Zgonnik VN, Melenevskaya EY (1997) Mass-spectrometric investigation of the thermal stability of polymethyl methacrylate in the presence of C60 fullerene. *Tech Phys Lett* 23:730–731
52. Rosu D, Cascaval CN, Ciobanu C, Rosu L (2004) An investigation of the thermal degradation of epoxy maleate of bisphenol A. *J Anal Appl Pyrol* 72:191–196
53. Wang M, Wang W, Liu T, Zhang WD (2008) Melt rheological properties of nylon 6/multi-walled carbon nanotube composites. *Compos Sci Technol* 68:2498–2502
54. Wagener R, Reisinger TJG (2003) A rheological method to compare the degree of exfoliation of nanocomposites. *Polymer* 44:7513–7518

Abozar Akbari, Mainak Majumder, and A. Tehrani

Contents

1	Introduction	284
2	PLA/CNT (SWCNT) Nanocomposites	287
3	PLA/MWCNT	289
4	Future Direction	294
	References	295

Abstract

In recent years, much attention has been paid to biodegradable polymers due to their wide range of applications in biomedical, packaging, agriculture fields and also economic and environmental consideration. Meanwhile, poly(lactic acid (PLA) is a more considerable biopolymer in comparison with other biopolymers. One of the most applicable methods to improve PLA performance is the combination of PLA with different materials. Today's carbon nanotubes (CNTs) are a more interesting additive because of excellent mechanical, electrical, and magnetic properties as well as nanometer scale diameter and high aspect ratio. This chapter aims to highlight on the recent development in preparation and characterization of PLA/CNT nanocomposites and also reviews effective parameters on CNT dispersion in PLA matrix.

A. Akbari (✉) • M. Majumder

Nanoscale Science and Engineering Laboratory (NSEL), Department of Mechanical and Aerospace Engineering, Monash University, Clayton, VIC, Australia
e-mail: abozar.akbarivakilabadi@monash.edu

A. Tehrani

School of Industrial Technology, Universiti Sains Malaysia, USM, Penang, Malaysia

Keywords

Poly(lactic acid (PLA) • Carbon nanotube (CNT) • Single-walled nanotubes (SWNTs) • Multiwalled nanotubes (MWNTs) • Nanocomposite

1 Introduction

In recent years, the uses of the renewable resources as chemical feedstock for the synthetic polymeric materials have attracted considerable attention. The reason for such activity is due to the finite nature of traditional petrochemical derived composites, in addition to economic and environmental considerations. Among wide range of the biopolymers available, polylactic acid (PLA) is one of the most widely used biodegradable polymers in medical and packaging industries due to its superior mechanical properties, low cost, good biocompatibility, and processability. PLA is obtained from ring-opening polymerization of lactide, a dimer of lactic acid which is obtained from fermentation of cornstarch. Due to the existence of a chiral carbon in lactic acid, the repeating unit of PLA can have two different configurations (D-(dextro) or L-(levo)), and the relative amount and distribution of these stereoisomers influences various properties of the resulting PLA. In general, PLA built with L-stereoisomer monomer is referred to as poly(L-lactic acid) (PLLA), whereas PLA which contains both D- and L-stereoisomer monomers is referred to as PDLLA. The life cycle of PLA is shown in Fig. 12.1. It is known that agricultural raw materials such as sugarcane or corn can be used as basic materials in PLA production. It is proven that PLA is superior to conventional petroleum products in respect to the total energy consumption and CO₂ emission in the life cycle assessment [1, 2].

Recent researches in life cycle assessments (LCA) have also focused to enable PLA to find its place among traditional commodity polymers for many applications in the agricultural sector as well as in the packaging field (the food and nonfood sector). It was found that PLA can be processed like all other thermoplastic polymers with extrusion, injection molding, blow molding, thermoforming, or fiber spinning processes into various products.

PLA is a stiff and brittle polymer owing to its high glass transition of 55 °C and a melting temperature around 170 °C. However, as it has aforementioned, stereoisomeric nature of lactic acid and type of monomers used in polymerization are effective in these temperatures. The typical values of mechanical properties of such a PLA polymer are displayed in Table 12.1.

Some properties of PLA such as good stiffness and strength have enabled it to contest with other exciting general-purpose plastics. Previous study on the mechanical properties of neat PLA by Jacobsen et al. [3] showed that PLA has great potential to be a substitute polymer for petroleum-based plastic. The respective values of mechanical properties of PLA in comparison with other petroleum-based plastics, e.g., polypropylene (PP) [4], polystyrene (PS) [5], high-density polyethylene (HDPE) [6], and polyamide (PA6) [7], are shown in Fig. 12.2.

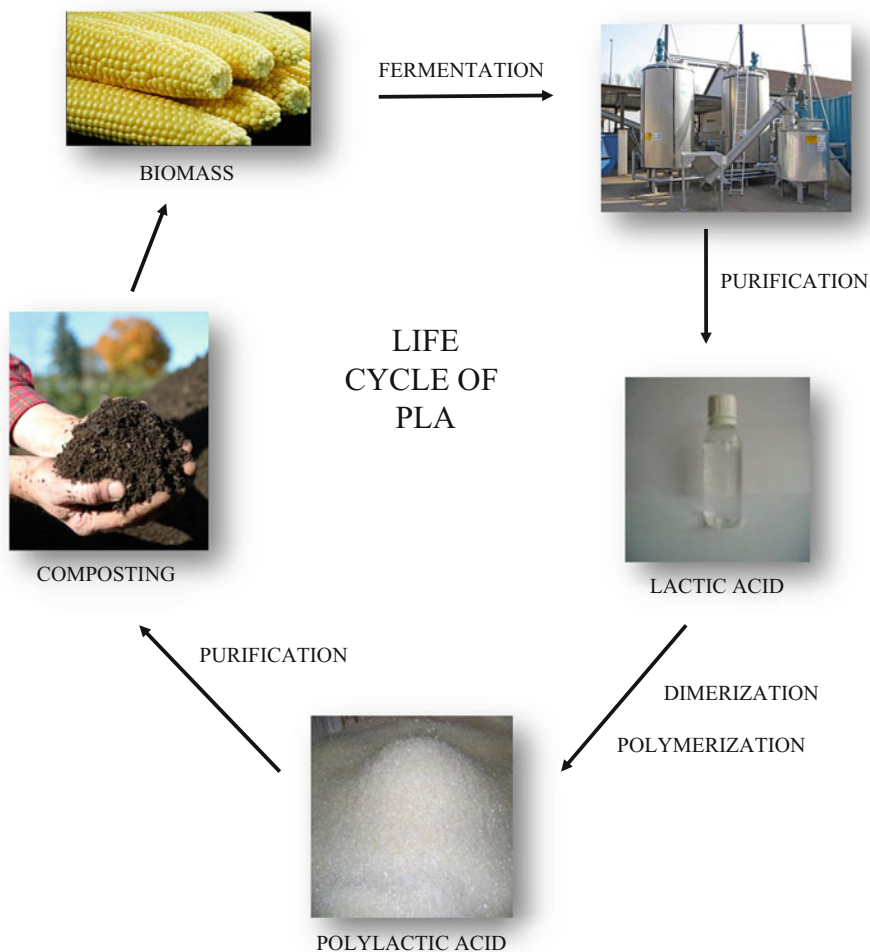


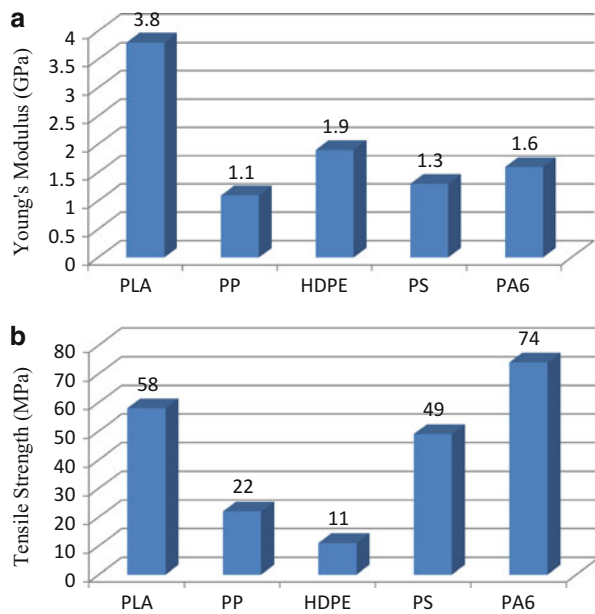
Fig. 12.1 Life cycle of PLA

Although some properties of PLA such as stiffness and strength caused it to be considered as a suitable substitute for polymer-based petroleum, some properties such as high cost, low elongation at break, and brittleness had restricted its use in a wide range of application. Therefore, modification of these biopolymers through innovative technology is a formidable task for materials scientists. Copolymerization and blending and filling techniques have been used to overcome the PLA drawbacks, but one of the most interesting methods to reach the desired properties of PLA is the addition of carbon nanotubes.

Since carbon nanotubes' discovery in 1991 by Iijima [8], they have been the subject of considerable attention because of their exceptional physical and mechanical properties. No previous material has displayed the combination of enhanced

Table 12.1 Mechanical properties of PLA

Properties	Values
Young's modulus (MPa)	3,600
Tensile strength (MPa)	70
Elongation at break (%)	2.4
Flexural strength (N/mm ²)	98
Impact strength (kJ/m ²)	16.5
Notched impact strength (kJ/m ²)	3.3
MFI (g/10 min)	3–6
Density (g/cm ³)	1.25
Moisture absorption (%)	0.3

**Fig. 12.2** Mechanical properties of PLA and other commodity plastics: (a) Young's Modulus (b) Tensile strength

mechanical, thermal, and electronic properties attributed to them [9]. Carbon nanotubes also possess high flexibility, low mass density, and large aspect ratio (typically ca. 300–1,000). These properties observed at the nanoscale have motivated researchers to utilize carbon nanotubes as reinforcement in composite materials. CNTs have a unique combination of mechanical, electrical, and thermal properties that make nanotubes excellent candidates to substitute or complement the conventional nanofillers in the fabrication of multifunctional polymer nanocomposites. Some nanotubes are stronger than steel, lighter than aluminum, and more conductive than copper [10]. In particular, this combination of properties makes them ideal candidates as advanced filler materials in nanocomposites. The first polymer nanocomposites using carbon nanotubes as reinforcing filler were

reported in 1994 by Ajayan et al. [11]. Nanotubes are categorized as single-walled nanotubes (SWNTs) and multiwalled nanotubes (MWNTs). Although SWNTs and MWNTs have some similarities, they also have striking differences. MWNTs are like a series of single-walled tubes nested within one another. In MWNTs only the outer wall generally contributes significantly to the electrical and mechanical properties when used in composites. In comparison to MWNTs, single-walled nanotubes are the more remarkable. They can be highly electrically conducting or semiconducting and have outstanding strength and very large surface area per unit mass, and also they have unique optical properties. These unique properties of CNTs made them an interesting area of research and have opened the doors to advances in performance in a wide range of materials and devices. On the other hand, CNTs have some drawbacks which limit their applications as additives in polymer matrixes. CNTs are grown as entangled bundles that are difficult to disperse in polymer matrices, or even in solvents. A number of methods have been used for the efficient dispersion of CNT in polymer matrices, ranging from the CNT chemical modification to the use of different mixing techniques. It has been found from previous studies that the filler dispersion is strongly dependent on the characteristics of the melt mixing equipment or other processing devices and also the dispersion level of nanofillers affects the final nanocomposite properties [12–14]. Over the past decade, scientists have done many investigations on the effects of carbon nanotube in final properties of PLA.

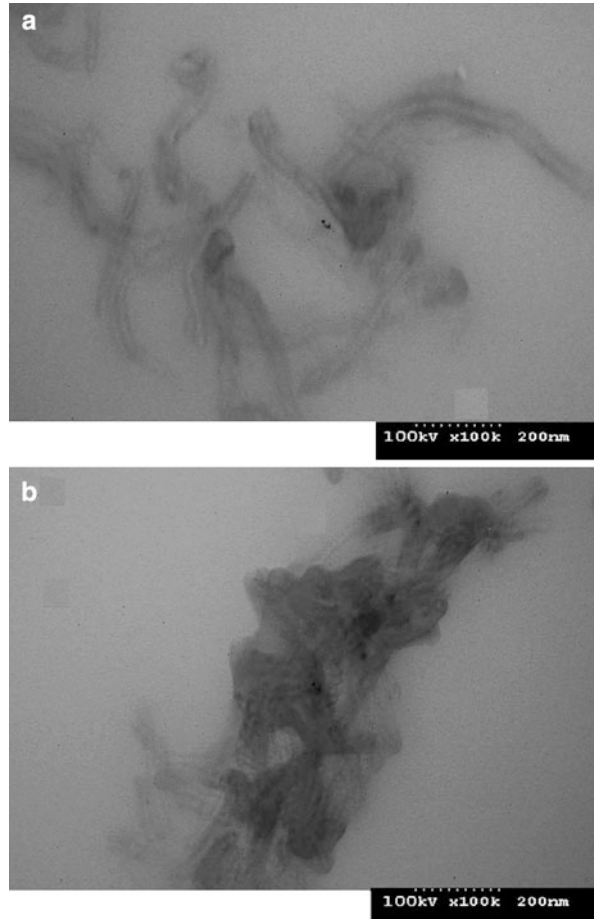
2 PLA/CNT (SWCNT) Nanocomposites

The development of PLA/carbon nanotube (CNT) nanocomposites is favored due to CNT's unique structure and properties. Recent studies have focused on the functionalization of CNT, and then, the modified CNTs are used to incorporate in PLA. Nevertheless, the addition of CNT as reinforcing nanofillers into PLA has been less quantitatively understood, especially with respect to its effect on the thermal and mechanical behaviors.

The effect of aspect ratio on the network structure of CNTs and final properties of the composites were investigated by Wu et al. [15]. The composites with high aspect ratio CNTs (HAR CNTs) revealed higher modulus than those with low aspect ratio fillers (LAR CNTs) owing to the great dependence of the CNTs mesoscopic dispersion structure on the aspect ratio. The huge difference in the mesoscopic structure of the CNTs, especially at small loading levels, was contributed to their different structural characteristics at the experimental processing conditions, e.g., the HAR CNTs are much more flexible in the PLA matrix than the LAR CNTs [16].

In another study, Moon et al. [17] investigated electrical conductivity and mechanical and thermal properties of the PLLA/CNT composite. They revealed a reduction in tensile strength and ultimate elongation by loading of CNT into the PLA matrix, while Young's modulus was partially enhanced. Moreover, the thermal stability and the electrical surface resistivity of the derived composites were

Fig. 12.3 (a) PLA/1 wt% MWCNT and (b) PLA/3 wt% MWCNT nanocomposites [27]



increased and decreased, respectively. An improvement in electromagnetic wave shielding effectiveness and electrical conductivity was also obvious for the resultant composites [17].

Chiu et al. [18] developed non-purified and purified CNT-reinforced PLA via fabrication process. The purified CNTs showed a sufficient dispersion in the free volume of PLA matrix leading to improved mechanical properties (elastic modulus and hardness) and thermal stability of the resultant composite. The polar functional groups on the CNTs surface after purification which makes them easy to disperse in polar solvents compared to non-purified CNTs to avoid agglomeration of a large quantity of nanotubes, formation of wider conduction distribution, and decrease of the surface resistance of the composite were found [18].

Song et al. [19] successfully prepared PLA/CNT nanocomposites through one step based on in situ polycondensation of the commercially available lactic acid monomer in the presence of purified CNTs [19]. The TEM image (Fig. 12.3) of

core/shell nanostructures clearly revealed that the coating of grafted polymer was uniform on both the CNT's sidewall and tip. It was suggested that the incorporation of CNT into PLA will improve its solubility and biocompatibility as it may promise a good future in biomedical systems and the development of bio-nanomaterials. The researchers also suggested that the current method of PLA/CNT nanocomposite preparation should be favored in industrialization as it takes less steps and cheaper.

PLA/CNT nanocomposite was prepared by solution and melt mixing and analyzed in terms of non-isothermal and isothermal crystallization behavior by Barrau et al. [20]. The nucleating effect of the homogenous nanofillers was verified by Raman spectroscopy. The presence of CNTs significantly increased the crystallization kinetics of the PLA matrix. In other words, according to the optical microscopy results, nanofillers increase the number of nucleation sites and thus decrease the average crystallite size.

In an attempt by Yang et al. [21], PLA/CNT composite was prepared via electrospinning process [21]. The morphologies and structure of electrospun products were strongly dependent on the solution concentration and solvents, as well as CNT loading levels. The low CNT content can be well embedded in the PLA matrix, oriented along the fiber axis and forming nanowire structure, while at the high loadings, CNTs will be dispersed as entangled bundles along the fiber axis resulted in composites with tortuous or misshaped structures. However, the overall morphologies of the composites are relatively degraded due to the presence of some small CNT aggregates in the solutions which lead to the formation of beaded structure.

3 PLA/MWCNT

High aspect ratio, large surface area, and extremely high strength to weight ratio of multiwalled carbon nanotubes (MWCNTs) offer the potential to improve the stiffness of the polymer matrix. MWCNTs are electrically conductive and have potential to reach the percolation threshold with small volume fraction loading.

Variation of MWNT loading, temperature profile, screw profile, and rotation speed dispersion during the twin-screw extrusion process were investigated by Villmow and coworkers [22]. Among the above factors, the highest impact was determined for the rotation speed, for which an increase from 100 rpm to 500 rpm led to considerably better MWNT dispersions with a lower number of agglomerates within the PLA matrix. This effect can be related to the increase in applied shear stress with rotation speed, and the level of shear stress effect on the primary agglomerates is a significant issue regarding the individualization of MWNT during melt mixing. Moreover, the amount of incorporated nanotubes as well as the state of nanotube dispersion is reflected in the degree of crystallinity.

Incorporation of MWCNT into the PLA via electrospinning by using a combination of solvent system (chloroform and dimethyl formamide) was carried

out by McCullen et al. [23]. Filler loading led to the 70 % reduction in fiber diameter to form fibers with a mean diameter of 700 nm which is attributed to the improvement of surface charge density for the MWCNT/polymer solution. It was also signified that an increase in the tensile modulus and conductance of the produced scaffold form the composite at an optimal loading level of 0.25 wt% MWCNT.

In another study, Kobashi et al. investigated the electrical resistance of melt-processed PLA/MWCNT nanocomposites [24]. They found good responses; reversibility and reproducibility of the resistance in 0.5–2.0 wt% MWCNT filled PLA/MWCNT nanocomposites depending on the kind of solvent as well as immersion and drying time. The MWCNT loading had a significant influence on the resistance change as larger changes were registered at lower MWCNT loadings with higher signal noises. It was also reported that PLA/MWCNT nanocomposites can sense poor solvents for PLA like ethanol, *n*-hexane, and water as well as good solvents like toluene, chloroform, tetrahydrofuran, and dichloromethane.

In the similar work by Pötschke et al., the relative resistance change of the fibers caused by contact with different solvents (water, *n*-hexane, ethanol, methanol) and solvent concentrations was used as liquid sensing response, while the time-dependent resistance was recorded during immersion and drying cycles [25]. It was obvious that enhanced orientation of MWCNT along the fiber axis with take-up velocity resulted in decreased sensitivity during solvent contact. Furthermore, sensitivity decreased as the weight content of MWCNT increased and was additionally dependent on the characteristics of used solvents.

MWCNT was used as reinforcement for both low-crystalline (LC-PLA) and high-crystalline (HC-PLA) structures by using a corotating-type twin-screw extruder. It was proved that the degree of PLA crystallinity obviously affects the electrical property of MWCNT/PLA composites; at the same time, high electrical conductivity can be obtained at a low carbon nanotube loading. Additionally, an improvement in filler dispersion was exhibited after creating covalent or hydrogen bonding between modified MWCNT (MA-g-MWCNT) and PLA. It was concluded from this study that carbon nanotubes as reinforcement were more favored for LC-PLA than HC-PLA in terms of electrical conductivity and mechanical properties improvement [13]. Incorporation of 0.5 parts per hundred parts of resin (phr)-modified MWCNT to LC-PLA decreased the surface resistance of the composite by 10–13 orders due to the improved MWCNT dispersion by covalent or hydrogen bonding between the filler and matrix. Moreover, the degree of crystallinity of PLA could rather affect the electrical property of MWCNT/PLA composites [13, 26].

Wu and Liao successfully prepared biodegradable PLA/multiwalled carbon nanotube (PLA/MWCNT) hybrids by means of a melt blending and acrylic acid-grafted polylactide (PLA-g-AA), and the multihydroxyl-functionalized MWCNTs (MWCNT-OH) were developed for a comparative purpose to investigate the compatibility between PLA and MWCNTs [27]. The researchers found that the formation of ester bonds through dehydration of carboxylic acid groups in the PLA-g-AA matrix with grafted hydroxyl groups in the MWCNT-OH resulted in better adhesion of MWCNT-OH in PLA-g-AA compared to the adhesion

of MWCNTs in PLA. The TEM examination also proves that the formation of agglomerates of carbon nanotubes can be observed for hybrids with higher (>1 wt%) MWCNT-OH content. As the result of DSC analysis, it can be also found that the gap between T_g and T_m of the PLA-g-AA/MWCNT-OH hybrid is smaller than that of the PLA/MWCNT hybrid implying that the compatibility between PLA and MWCNTs has been enhanced. TGA tests showed that the PLA-g-AA/MWCNT-OH hybrid with 1 wt% MWCNT-OH gives an increment of 77 °C for the initial decomposition temperature. The effect of MWCNT-OH content on tensile strength at break of PLA-g-AA/MWCNT-OH hybrids was also similar. Maximum values of tensile strength of hybrid occurred at about 1 wt% of MWCNT-OH, and excess MWCNT-OH reduced the compatibility of hybrid due to the inevitable aggregation of carbon nanotubes.

Wu et al. focused on the development of the PLA nanocomposites with various functionalized MWCNTs prepared by melt mixing for morphological, rheological, and thermal measurements [28]. The surface functionalization influences the dispersion state of MWCNTs in the PLA matrix strongly as the carboxylic-functionalized MWCNTs show relatively better dispersion than that of hydroxy and purified MWCNTs, which is due to the nice affinity between carboxylic group and PLA. For all composites, no remarkable improvement in thermal stability is seen at the initial stage of degradation, while with increase of decomposition level, the presence of carboxylic and purified MWCNTs retards the thermal depolymerization of PLA due to their barrier and thermal conductive effects, respectively.

In another research in 2010 by Chrissafis, nanocomposites of PLA with oxidized MWCNT (2.5 wt% MWCNTs-COOH) were produced by solved evaporation method [12]. It was found from thermogravimetric analysis that PLA/MWCNTs-COOH nanocomposites demonstrate a relatively better thermostability than PLA. Moreover, variation of the activation energy (E) with increasing degree of mass conversion revealed complexity of reaction mechanism for all of the samples.

Different functionalized MWCNTs were melt compounded in PLA to prepare nanocomposites by Wu et al. [28]. Among the three different CNTs, carboxylic MWCNTs show better dispersion in PLA matrix than the hydroxyl and purified MWCNTs because of the good attraction between carboxylic group and PLA and also the lowest rheological percolation threshold of resultant composite. Any considerable improvement in thermal stability of all composites at the early stages of degradation was not found; however, the carboxylic and purified MWCNTs further will hinder thermal depolymerization of PLA due to their barrier properties and thermal conductivity, respectively.

In similar research of Wu and Liao, melt blending method was used for preparation of PLA/MWCNT hybrids [27]. They applied the acrylic acid-grafted polylactide (PLA-g-AA) and the multihydroxyl-functionalized MWCNTs (MWCNT-OH) instead of PLA and MWCNT in order to improve the compatibility between the filler and matrix. MWCNT-OH could be incorporated into the PLA-g-AA copolymer through the formation of strong covalent bonds that resulted to the reaction between carboxylic acid groups of PLA-g-AA and hydroxyl groups of MWCNT-OH.

Therefore, MWCNT-OH played a reinforcement role in the PLA-g-AA polymer matrix leading to great improvement in thermal and mechanical properties of PLA. On the other hand, the optimal amount of MWCNT-OH was only 1 wt%, and the excess amount of MWCNT-OH caused a separation in organic and inorganic phases and a reduction in their compatibility.

In another investigation, Chen et al. functionalized MWCNTs with hydroxyl groups via surface-initiated ring-opening polymerization in order to use as co-initiators to polymerize L-lactide [29]. The amount of PLLA grafted was increased with the reaction time, and its dispersion was dependent on either the reaction time or the type of the solvent as the reaction medium. Incorporation of MWCNT-g-PLLA in PLA matrix enhanced the tensile modulus and strength to a great extent without a significant loss of the elongation at break.

In similar interesting study by Kim et al., PLLA was melt compounded with MWCNTs in order to enhance the degree of dispersion of the MWCNTs in the composites made from grafting PLLA onto the MWCNTs (PLLA-g-MWCNTs). The experimental results indicated the mechanical properties of the PLLA/PLLA-g-MWCNT composite were higher than those of the PLLA/MWCNT composite. Moreover, the activation energy of PLLA/PLLA-g-MWCNT was higher than that of PLLA/MWCNT, which revealed that the composite made from the PLLA-g-MWCNTs solid fillers was more thermally stable than the composite made with the MWCNTs. However, the former composite exhibited lower electrical conductivity than the latter since the grafted PLLA molecules decreased the electrical conductivity of the PLLA by hindering the direct contact between the conducting fillers [30]. The Raman spectroscopic analysis promoted that the interaction between PLLA and MWCNT occurred mainly through the hydrophobic C-CH₃ functional groups. Additionally, the DC conductivity of the composite increased as the MWCNT loading is increased. The reason is the effect of plasticizing and inducing crystallization by MWCNTs in the polymer matrix [31].

In another research, a series of MWCNTs grafted with PLA chains of various lengths (MWCNT-g-PLAs) were also produced by ring-opening polymerization of L-lactide with carboxylic acid-functionalized MWCNT (MWCNT-COOH) followed by mixing with commercial PLA to obtain PLA/MWCNT-g-PLA nanocomposites. Morphological studies proved that nanocomposites containing MWCNT-g-PLA with longer grafted PLA chains displayed better dispersion of MWCNTs in the PLA matrix. Furthermore, tensile strength, initial modulus, and electrical resistivity of PLA/MWCNT-g-PLA nanocomposites improved with the increase in molecular weight of grafted PLA chains of MWCNT-g-PLA due to the improved interfacial reinforcement of PLA chains grafted on MWCNT in the PLA matrix. However, the electrical resistivity increased up to ~200 g/mol and remained constant. It takes place when MWCNT-g-PLAs prevent the formation of electrical conduction paths of MWCNTs in the PLA matrix [32].

Moreover, the glass transition temperatures of PLA/MWCNT-g-PLA nanocomposites were found to be higher than that of neat PLA as well as PLA/MWCNT and PLA/MWCNT-COOH nanocomposites. The overall

crystallization rates of the nanocomposites, especially for PLA/MWCNT-g-PLA, were faster than that of the neat PLA homopolymer due to the contribution of MWCNT as a nucleating agent [33].

Wu et al. also revealed that the existence of nanotubes had nucleating effect on melt crystallization and the cold crystallization of PLA, although the nanotubes also play the role of physical barrier, that is, hindering the overall kinetics of the cold crystallization [34]. The biodegradation rate of PLA was reduced due to the inhibiting effects of CNTs, and the amorphous samples represented the highest degradation levels. Additionally, a lower degradation level could be found both on the surface and inside the samples with melt crystallization history in contradiction of the ones with cold crystallization history. Thus, it was confirmed that the biodegradation behavior is strongly dependent on the crystallization histories.

The MWNTs bonded with the polycaprolactone chains demonstrated outstanding homogeneous dispersion in PLA solution by comparing with the acid-functionalized MWCNTs and amino-functionalized MWCNTs. It was concluded from various test methods such as field emission scanning electron microscopy (FESEM), Raman spectroscopy, and transmission electron microscopy (TEM) that the MWCNTs-PCL were embedded within the fibers and well oriented along the fiber axis during electrospinning process. The dispersion and alignment of MWCNTs embedded in PLA matrix was also improved during the electrospinning process elsewhere [35, 36].

Kuan et al. also successfully prepared PLA/MWCNT nanocomposites through melt blending, performed with corotating extruder [37]. The researchers used water-cross-linking reaction in their effort to perform silane grafting to improve interfacial adhesion of MWCNT with PLA. Mechanical analysis showed that the addition of 1 phr of MWCNT would improve the tensile strength of PLA/MWCNT nanocomposites by 13 %, while the degradation temperature of PLA improved with increasing MWCNT content. The researchers also found that the heat deflection temperature (HDT) of PLA (62 °C) improved to 106 °C with the addition of 1 phr MWCNT in PLA/MWCNT nanocomposites after 7 h of cross-linking reaction. This finding is useful in the application of biodegradable container. However, further addition of MWCNT can reduce the degree of water cross-linking; thus, the tensile strength of PLA/MWCNT nanocomposites has no significant improvement after long water-cross-linking reaction time and at higher loadings of MWCNT.

Three different modifiers, maleic anhydride, methyl methacrylate, and vinyltrimethoxysilane, were also applied to modify MWCNT in a research study by Peng et al. [38]. MWCNT dispersion was improved by covalent or hydrogen bonding between modified MWCNT and biodegradable blend of PLA/Ecoflex (80:20 by weight). The enhanced electrical conductivity and tensile strength were reported at 1 wt% and 4 wt% of MWCNT loading, respectively.

In another study, two types of multiwalled carbon nanotubes, Fe₃O₄/MWCNTs and MWCNTs, were prepared by solution casting and incorporated into the PLLA matrix [39]. The crystallization rate of PLLA was increased by addition of MWCNTs, while it decreased as Fe₃O₄/MWCNTs were loaded. Furthermore,

mechanical properties such as the tensile strength, Young's modulus, and elongation at break of $\text{Fe}_3\text{O}_4/\text{MWCNT}/\text{PLLA}$ composite were improved compared to the neat PLLA and MWCNT/PLLA composite due to the excellent dispersion of $\text{Fe}_3\text{O}_4/\text{MWCNTs}$ through the PLLA matrix.

Chen et al. converted the oxidized MWCNT (MWCNT-COOH) to the acylchloride-functionalized MWCNT (MWCNT-COCl) by treatment with thionyl chloride (SOCl_2) and then reacting with PLLA to prepare the MWCNT-g-PLLA [40]. It was apparently demonstrated from the experimental results that the amount of grafted PLLA and its squid leglike morphology depended strongly on the molecular weight of the PLLA.

In a research study by Kim et al., thermal degradation behavior of PLLA/MWCNT composites was investigated by determination of the molecular weight, mechanical properties, and weight loss during non-isothermal and isothermal degradation [41]. A significant improvement in the mechanical properties and thermal stability of the PLLA matrix was evident after incorporation of MWCNTs.

Elsewhere, MWCNT-reinforced PLA nanocomposite prepared by melt extrusion presented improved inherent properties of PLA such as glass transition temperature, dynamic mechanical properties, strength, elongation at break, and crystallization kinetic due to the strong interfacial interaction between the nanotubes' outer surface and the PLA chains [42].

Reaction to fire of PLA/MWCNT nanocomposites indicated a slight improvement of the flame retardancy in Bourbigot et al.'s study, and the nanodispersion could be improved to obtain the best flame retardancy [43]. In another work, the synergic effect of MWCNT and sepiolite nanoclay (Sep) utilization in PLA nanocomposite demonstrated improved flame retardancy as well [44].

4 Future Direction

In spite of many attempts by scientists to improve commercial potential of PLA to create a sustainable environment and also deal with finite nature of chemical feedstock, there are a number of challenging issues. PLAs have to enable to compete with petroleum-based plastics, economically. One future challenge should be looking for new cheap methods of obtaining lactic acid and then polymerization process to produce PLA. Another challenge is related to the technical point; the limited toughness (i.e., impact strength) has urged researchers to develop a biodegradable impact modifier in the recent decade.

Generally, hybrid materials based on carbon nanotubes (CNTs) and polymers have shown improved properties and potential applications in many fields. However, CNTs usually agglomerate due to van der Waals force; they are extremely difficult to disperse and align in a polymer matrix, leading to many defect sites in the composites and limiting the efficiency of CNTs on polymer matrices. Although many methods have been investigated to improve performance of nanotube in polymer matrixes,

they have been along with some defects and are not well succeeded. Thus, another significant challenge in developing high-performance PLA/CNT nanocomposites is how to enhance dispersion and alignment of CNTs in the PLA matrix.

References

1. Garlotta D (2000) A literature review of poly(lactic acid). *J Polym Environ* 9(2):63–84
2. Ruksakulpiwat Y, Tonimit P, Kluengsamrong J (2010) Mechanical properties of PLA-Jute composites by using natural rubber and epoxidized natural rubber as impact modifiers: effect of molding technique. Chapter 6: green chemistry, buildings, and constructions, In: *Clean technology 2010*, pp. 310–313, Edited by: NSTI, Published by: CRC Press Inc., Texas, USA, 21 June 2010
3. Jacobsen S, Fritz HG (1999) Plasticizing polylactide – the effect of different plasticizers on the mechanical properties. *Polym Eng Sci* 39:1303–1310
4. Lim JW, Hassan A, Rahmat AR, Wahit MU (2006) Morphology, thermal and mechanical behavior of polypropylene nanocomposites toughened with poly (ethylene-co-octene). *Polym Int* 55:204–215
5. Hasegawa N, Okamoto H, Kawasumi M, Usuki A (1999) Preparation and mechanical properties of polystyrene-clay hybrids. *J Appl Polym Sci* 74:3359–3364
6. Gupta K, Rana SK, Deopura B (1992) Mechanical properties and morphology of high-density polyethylene/liner low-density polyethylene blend. *J Appl Polym Sci* 46:99–108
7. Wahit MU (2006) Rubber toughened polyamide 6/polypropylene nanocomposites: mechanical, thermal and morphological properties. Ph.D Thesis. University Technology Malaysia, Skudai
8. Iijima S (1991) Helical microtubules of graphitic carbon. *Nature* 354:56–58
9. Coleman JN, Khan U, Blau WJ, Gunko YK (2006) Small but strong: a review of the mechanical properties of carbon nanotube–polymer composites. *Carbon* 44:1624–1652
10. Moniruzzaman M, Winey KI (2006) Polymer nanocomposites containing carbon nanotubes. *Macromolecules* 39:5194–5205
11. Ajayan PM, Stephan O, Colliex C, Trauth D (1994) Aligned carbon nanotube arrays formed by cutting a polymer resin – nanotube composite. *Science* 265:1212–1214
12. Chrissafis K (2010) Detail kinetic analysis of the thermal decomposition of PLA with oxidized multi-walled carbon nanotubes. *Thermochim Acta* 511:163–167
13. Kuan CF, Kuan HC, Ma CCM, Chen CH (2008) Mechanical and electrical properties of multi-wall carbon nanotube/poly(lactic acid) composites. *J Phys Chem Solid* 69:1395–1398
14. Novais RM, Paiva MC, Covas JA (2011) Dispersion of carbon nanotubes in poly(lactic acid). VI international materials symposium materiais, Guimarães, Portugal
15. Wu CS (2009) Renewable resource-based composites of recycled natural fibers and maleated polylactide bioplastic: characterization and biodegradability. *Polym Degrad Stab* 94:1076–1084
16. Wu D, Wu L, Zhou W, Sun Y, Zhang M (2010) Relations between the aspect ratio of carbon nanotubes and the formation of percolation networks in biodegradable polylactide/carbon nanotube composites. *J Polym Sci B* 48:479–489
17. Moon S, Jin F, Lee C, Tsutsumi S, Hyon S (2005) Novel carbon nanotube/poly(L-lactic acid) nanocomposites; their modulus, thermal stability, and electrical conductivity. *Macromol Symp* 224:278–295
18. Chiu W, Chang Y, Kuo H, Lin M, Wen H (2008) A study of carbon nanotubes/biodegradable plastic polylactic acid composites. *J Appl Polym Sci* 108:3024–3030
19. Song W, Zheng Z, Tang W, Wang X (2007) A facile approach to covalently functionalized carbon nanotubes with biocompatible polymer. *Polymer* 48:3658–3663
20. Barrau S, Vanmansart C, Moreau M, Addad A, Stoclet G, Lefebvre JM, Seguela A (2011) Crystallization behavior of carbon nanotube polylactide nanocomposites. *Macromolecules* 44:6496–6502

21. Yang T, Wu D, Lu L, Zhou W, Zhang M (2011) Electrospinning of polylactide and its composites with carbon nanotubes. *Polym Compos* 32:1280–1288
22. Villmow T, Potschke P, Pegel S, Haussler L, Kretzschmar B (2008) Influence of twin-screw extrusion conditions on the dispersion of multi-walled carbon nanotubes in a poly(lactic acid) matrix. *Polymer* 49:3500–3509
23. McCullen SD, Stano KL, Stevens DR, Roberts WA, Monteiro-Riviere NA, Clarke LI, Gorga RE (2007) Development, optimization, and characterization of electrospun poly(lactic acid) nanofibers containing multi-walled carbon nanotubes. *J Appl Polym Sci* 105:1668–1678
24. Kobashi K, Villmow T, Andres T, Pötschke P (2008) Liquid sensing of melt-processed poly(lactic acid)/multi-walled carbon nanotube composite films. *Sens Actuators B* 134:787–795
25. Pötschke P, Andres T, Villmow T, Pegel S, Brünig H, Kobashi K, Fischer D, Häussler L (2010) Liquid sensing properties of fibres prepared by melt spinning from poly(lactic acid) containing multi-walled carbon nanotubes. *Compos Sci Technol* 70:343–349
26. Avella M, Buzarovska A, Errico ME, Gentile G, Grozdanov A (2009) Eco-challenges of bio-based polymer composites. *Materials* 2:911–925
27. Wu CS, Liao HT (2007) Study on the preparation and characterization of biodegradable polylactide/multi-walled carbon nanotubes nanocomposites. *Polymer* 48:4449–4458
28. Wu D, Wu L, Zhang M, Zhao Y (2008) Viscoelasticity and thermal stability of polylactide composites with various functionalized carbon nanotubes. *Polym Degrad Stab* 93:1577–1584
29. Chen GX, Kim HS, Park BH, Yoon JS (2007) Synthesis of poly(L-lactide)-functionalized multiwalled carbon nanotubes by ring-opening polymerization. *Macromol Chem Phys* 208:389–398
30. Kim HS, Park BH, Yoon JS, Jin HJ (2007) Thermal and electrical properties of poly(L-lactide)-graft-multiwalled carbon nanotube composites. *Eur Polym J* 43:1729–1735
31. Zhang D, Kandadai MA, Cech J, Roth S, Curran SA (2006) Poly(L-lactide) (PLLA)/Multiwalled Carbon Nanotube (MWCNT) composite: characterization and biocompatibility evaluation. *J Phys Chem* 110:12910–12915
32. Yoon JT, Lee SC, Jeong YG (2010) Effects of grafted chain length on mechanical and electrical properties of nanocomposites containing polylactide-grafted carbon nanotubes. *Compos Sci Technol* 70:776–782
33. Yoon JT, Jeong YG, Lee SC, Min BG (2009) Influences of poly(lactic acid)-grafted carbon nanotube on thermal, mechanical, and electrical properties of poly(lactic acid). *Polym Adv Technol* 20:631–638
34. Wu D, Wu L, Zhou W, Zhang M, Yang T (2010) Crystallization and biodegradation of polylactide/carbon nanotube composites. *Polym Eng Sci* 50:1721–1733
35. Kong Y, Yuan J, Qiu J (2012) Preparation and characterization of aligned carbon nanotubes/poly(lactic acid) composite fibers. *Physica B* 407:2451–2457
36. Shao S, Zhou S, Li L, Li J, Luo C, Wang J, Li X, Weng J (2011) Osteoblast function on electrically conductive electrospun PLA/MWCNTs nanofibers. *Biomaterials* 32:2821–2833
37. Kuan CF, Chen CH, Kuan HC, Lin KC, Chiang CL, Peng HC (2008) Multi-walled carbon nanotube reinforced poly(L-lactic acid) nanocomposites enhanced by water-crosslinking reaction. *J Phys Chem Solid* 69:1399–1402
38. Peng HC, Kuan CF, Chen CH, Lin KC, Kuan HC (2011) Study on the preparation and properties of multiwall carbon nanotube reinforced biodegradable polymer blend. *Adv Mater Res* 239–242:145–149
39. Feng J, Sui J, Cai W, Wan J, Chakoli AN, Gao Z (2008) Preparation and characterization of magnetic multi-walled carbon nanotubes–poly(L-lactide) composite. *Mater Sci Eng B* 150:208–212
40. Chen GX, Kim HS, Park BH, Yoon SN (2005) Controlled functionalization of multiwalled carbon nanotubes with various molecular-weight poly(L-lactic acid). *J Phys Chem B* 109:22237–22243

41. Kim HS, Chae YS, Kwon HI, Yoon JS (2009) Thermal degradation behaviour of multi-walled carbon nanotube-reinforced poly(L-lactide) nanocomposites. *Polym Int* 58:826–831
42. Ramontja J, Ray SS, Pillai SK, Luyt AS (2009) High performance carbon nanotube-reinforced bioplastic. *Macromol Mater Eng* 294:839–846
43. Bourbigot S, Fontaine GI, Gallos A, Bellayer SV (2011) Reactive extrusion of PLA and of PLA/carbon nanotubes nanocomposite: processing, characterization and flame retardancy. *Polym Adv Technol* 22:30–37
44. Hapuarachchi TD, Peijs T (2010) Multiwalled carbon nanotubes and sepiolite nanoclays as flame retardants for polylactide and its natural fibre reinforced composites. *Compos: Part A* 41:954–963

Ramanan Krishnamoorti and Tirtha Chatterjee

Contents

1	Introduction	300
2	Dispersion Strategies	302
2.1	Dispersion Techniques	303
2.2	Characterization of Dispersion	303
3	Nanocomposite Structure	307
4	Flow Properties	310
4.1	Linear Viscoelastic Properties	310
4.2	Nonlinear Viscoelastic Properties	313
4.3	Effect of Steady Shear	315
5	Crystallization of PEO in the Presence of Carbon Nanotubes	318
6	Nanocomposite Applications	324
6.1	Electronic Materials	324
6.2	Electrospinning	325
6.3	Biological Applications	326
7	Concluding Remarks	327
	References	328

Abstract

Carbon nanotubes (CNTs) with their remarkable set of intrinsic properties are outstanding materials to incorporate in and augment the properties of polymer matrices. Poly(ethylene oxide) (PEO) is a water-soluble, biocompatible polymer that has found various technological applications including as solid electrolytes in lithium-ion batteries and in various biomedical and tissue engineering applications.

R. Krishnamoorti (✉)

Department of Chemical and Biomolecular Engineering, University of Houston, Houston, TX, USA

e-mail: RKrishna@Central.UH.EDU

T. Chatterjee

Analytical Sciences, The Dow Chemical Company, Midland, MI, USA

Homogeneous dispersion of anisotropic nanoparticles, especially carbon nanotubes, in a matrix polymer is hindered by strong inter-tube attraction and a weak entropic driving force for the disruption of nematic order of such rodlike nanoparticles. In this chapter, we discuss different pathways to disperse carbon nanotubes in PEO matrix and techniques to quantitatively characterize the state of dispersion. Beyond the geometrical percolation threshold, in their quiescent state, dispersed nanotubes show hierarchical fractal network consisting of aggregated flocs. Internal to the flocs, individual or small bundles of nanotubes overlap each other to form a dense mesh. The inter-floc interaction dominates the linear viscoelasticity. The nonlinear viscoelastic behavior is independent of network size and dominated by cluster dynamics. Interestingly, significant changes in the melting and crystallization behavior of PEO along with a decrease in fractional crystallinity in the presence of carbon nanotubes have been observed. The observed changes significantly exceed those observed for an equivalent Li^+ ion concentration mixture. This finding is particularly interesting considering amorphous segment of PEO chains are responsible for ion transport in solid polymer electrolytes. Besides this other technological applications of the carbon nanotube-based PEO nanocomposites will also be discussed.

Keywords

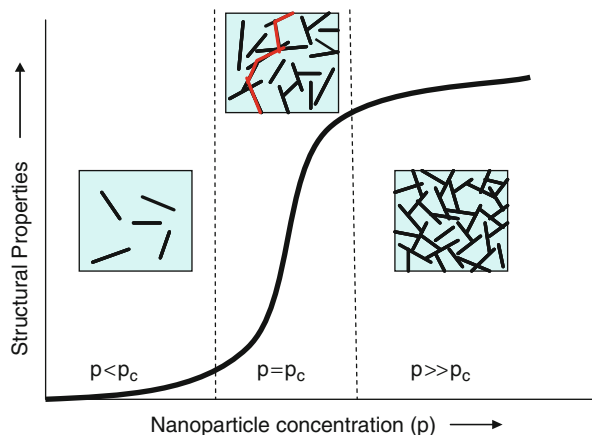
Battery • Biocompatible • Carbon nanotube • Nanocomposites • PEO • Polymer

1 Introduction

The reinforcement of polymers with disperse nanoscale inorganic materials has generated much scientific and commercial interest over the last two decades [1–3]. Collectively, these materials are classified as polymer nanocomposites, where the nanoparticles which possess *at least* one dimension of ~ 1 –100 nm are incorporated in the polymer matrix. These materials are truly inorganic–organic hybrids at the molecular level with unique physical properties, often multifunctional, and targeting advanced material applications. Modest nanoparticle loading (< 2 –5 wt%)-based nanocomposites that maintain the manufacturing and processing flexibility of the parent polymer are considered as a potential solution for the next generation of materials with controlled and tailored combinations of mechanical, thermal, electrical, optical, and physical properties.

Nanoparticles are available in a variety of sizes and shapes. Some, such as alumina or silica spheres, are isotropic, while others are highly anisotropic such as the dislike nanoclays or rodlike nanotubes. Among different nanoparticles, the major characteristics are the leading dimension of the smallest dispersible unit and aspect ratio (α , defined as ratio of the long axis to the short axis irrespective of shape). As the smallest dispersible length decreases, the overall polymer–nanoparticle interfacial area increases (at a fixed total particle volume). Depending on the strength of polymer–nanoparticle interaction, polymer chains close to the nanoparticle surface can undergo significant changes in their structure and

Fig. 13.1 The classical *sigmoidal curve* shown by the enhancement of polymer nanocomposite structural properties as a function of the nanoparticle loading. The critical path at the onset of percolation is denoted by *red line*



dynamics compared to their bulk counterpart. Clearly, the higher the interfacial surface area, a larger fraction of polymer chains is affected. Additionally, at low loading and a true dispersed state, these nanoparticles act as mechanical reinforcers. With increasing loading, the amount of nanoparticles in polymer increases, and at a particular concentration, these nanoparticles create a critical path which spans the whole matrix. This critical path formation is referred to as the percolation process, and the nanoparticle concentration associated with this phenomenon is termed the percolation threshold. Beyond the percolation threshold, nanoparticles network in polymer matrix grows with multiple connectivities/branching. A schematic of this process is presented in Fig. 13.1. Mechanically, in soft polymer matrices, percolation is a process by which liquid is transformed into a solid-like material (at geometrical percolation threshold, p_c , for mechanical reinforcement) and is similar to an insulator to conductor transition (at electrical percolation threshold, φ_c , for conducting nanoparticles in a nonconducting matrix) with almost a steplike jump in the properties of the nanocomposites. Finally, a higher aspect ratio yields a lower percolation threshold. Therefore, carbon nanotubes (CNTs), with their nanometer length scale (diameter) and high aspect ratio ($\alpha = L/d$ where L and d are CNT length and diameter, respectively), are an excellent choice as nanoparticles to prepare polymer nanocomposites with low percolation thresholds.

Besides their nanoscale dimension and high aspect ratio, the extraordinary mechanical, electrical, and thermal properties of CNTs make them outstanding nanoparticles to blend with polymers to prepare potentially multifunctional nanocomposites [4–7]. Poly(ethylene oxide) (PEO) is a water-soluble, biocompatible polymer that has found applications in a variety of technologies including as solid electrolytes in lithium-ion batteries [8–12] and as scaffold in tissue engineering [13, 14]. CNT-based PEO nanocomposites are interesting materials considering CNT's multifunctionality and wide technological uses of PEO. However, the development of polymer nanocomposites with dispersed carbon

nanotubes, with some notable exceptions [15–18], has been largely stymied by the lack of dispersion of the nanotubes perhaps due to the strong inter-tube interactions. In this book chapter, we will briefly discuss about the problems related to dispersion and different dispersion routes focusing CNT-based PEO nanocomposites. We will further discuss polymer nanocomposite structure with particular emphasis on CNT loading beyond the percolation threshold. The flow properties (both linear and nonlinear) of the nanocomposites will be discussed followed by the effect of carbon nanotubes' presence on the PEO crystallization. Finally, different technological applications of carbon nanotubes–PEO nanocomposites will be presented.

2 Dispersion Strategies

Nanotubes are members of the fullerene family where a graphene sheet rolled over to yield a seamless hollow cylinder with diameter ~ 1 nm. A single cylindrical tube is referred to as single-walled carbon nanotubes (SWNTs), whereas multiple rolled layers of graphene which produces concentric cylinders are referred to as multiwalled carbon nanotubes (MWNTs). Depending on the atomic configuration (governed by the tube diameter and chirality), carbon nanotubes can be metallic, semiconducting, or insulating which further expands their application spectrum. One of the major challenges for successful dispersion arises from the π – π interactions between CNTs leading to strong aggregation. For the nano-sized particles, interparticle forces, such as van der Waals attraction, become significant [19], and carbon nanotubes show high affinity for each other. Strong inter-tube cohesive force leads to the formation of SWNT rope or bundles. Here, ropes refer to collection of SWNTs that are sufficiently uniform in diameter to form a triangular lattice as opposed to bundles which are noncrystalline collection of nanotubes [20]. To exfoliate a nanotube from the rope structure, one needs to overcome an attractive energy barrier ~ 500 eV/ μm [21]. Moreover, in their pristine form, the insolubility of nanotubes in aqueous and other organic solvents makes dispersion of tubes even more challenging [22]. Ausman and coworkers demonstrated that solvents with high electron-pair density and low hydrogen bond parameter are suitable for SWNTs dispersion [23].

The dispersion of nanoparticles in polymer matrices is largely controlled by the enthalpy of mixing and seldom driven by entropic driving forces alone. The enthalpy of mixing depends on nanoparticles' chemical nature, size, shape, fictionalization, etc. For CNTs van der Waals attraction is dominant and is directly proportional to the size of the particles and inversely related to the interparticle distance [24]. Further, being highly anisotropic, in the absence of polymer–nanotube attractive interaction, isotropic to nematic transition occurs at nanotubes concentration $\sim 1/\alpha$ (where $\alpha = \text{aspect ratio} = L/d$). Therefore, in addition to inter-CNT attractions, overcoming entropic effect is also a substantial challenge to disperse modest concentration of nanotubes in polymer matrix.

2.1 Dispersion Techniques

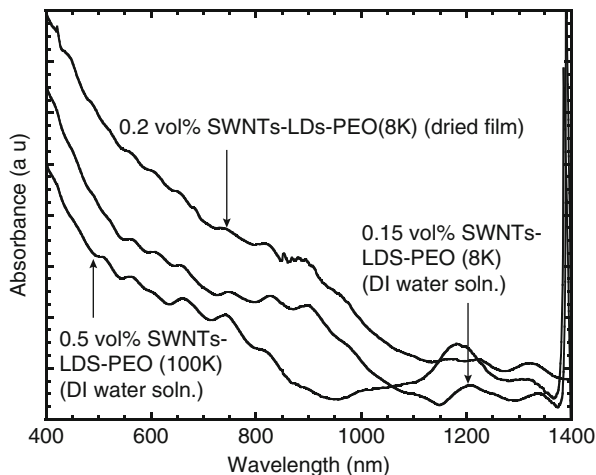
Several methods are used to obtain successful dispersion of nanotubes in polymer matrices. Among them chemical modification or functionalization (exploiting the strained aromatic structure or the defects in nanotube carbon atoms) of the CNT sidewalls [25–29], in situ polymerization with pristine or functionalized CNTs [30–32], and noncovalent surface modification or surfactant-assisted dispersion [17, 33–35] are notable and widely applied techniques. For surfactant-assisted dispersion, surfactant molecules get randomly adsorbed on the nanotube surface and act as bridges between the nanotubes and polymer chains [35]. Recently, Clark and Krishnamoorti [36] demonstrated that surfactant-assisted SWNTs' dispersion trend is unreliable to predict MWNTs' dispersibility, where the lower curvature presumably results in ordered adsorption of the surfactants similar to that observed on graphite/graphene surfaces.

Among the wide array of surfactants, Li^+ - and Na^+ -based anionic surfactants are strategic choices for dispersion of carbon nanotubes in PEO matrices. Billups and coworkers [37] demonstrated that reductive alkylation of SWNTs using lithium metal and alkyl halide in liquid ammonia yields sidewall-functionalized nanotubes which are soluble in organic solvent. On the other hand, Li^+ and Na^+ ions are known for their crown-ether complexation with PEO molecules [38, 39]. Inspired by this, Krishnamoorti and coworkers [33] used a lithium-based anionic surfactant (lithium dodecyl sulfate, LDS) to compatibilize SWNTs and PEO. The surfactant molecules de-rope the nanotube bundles and PEO chains complex around lithium ions to develop well-homogenized nanocomposites. Following the same route [33], Park and coworkers dispersed MWNTs in PEO using a cost-effective evaporation (using DI water, a good solvent for PEO chains) casting technique which is suitable for large-scale applications [40]. Besides simplicity, this dispersion pathway is technologically important as lithium salts, for their low lattice energy, high coordination number, and crown-ether formation capability, are often used in solid electrolytes which make the PEO chains amorphous and improve room temperature ionic conductivity [12, 41]. Finally, amphiphilic block copolymers are also effective in dispersing CNTs [42–44] and have been utilized to obtain successful dispersion of MWNTs in PEO matrix [45].

2.2 Characterization of Dispersion

Characterization of the dispersion state of nanoparticles in polymer is challenged by the (a) hierarchy of structure present in the system, (b) absence of any single method/measurement/instrument that can evaluate the dispersion state over a wide length scale, and, finally, (c) requirement of rapid screening and in-line monitoring for commercial productions [19]. Typically, electron microscopy and scattering (light, X-ray, and/or neutron), chemical, electric, dielectric, as well as mechanical spectroscopies are used to address the wide length-scale variability of

Fig. 13.2 Solution-phase UV–Vis–NIR spectra for SWNTs dispersed in PEO by help of an anionic surfactant, LDS. Presence of peaks between 400 and 1,000 nm (associated with van Hove singularities) establishes a well-dispersed system. Sharper peaks for solution compared to bulk phase indicate reaggregation of some tubes during drying (Reprinted with permission from Ref. [33])



dispersion characterization. In solutions, dispersion can easily be characterized by absorption and/or fluorescence spectral features exclusively arising from single or small bundle of SWNTs [46]. Krishnamoorti and coworkers systematically investigated the CNT dispersion state by using UV–Vis–NIR spectroscopy as local probe of dispersion and melt-state rheological measurements as meso-scale probe of dispersion [17, 29, 33]. Sharp absorption peaks, termed as van Hove singularities, are observed for polymer SWNT solution as well as for bulk nanocomposites and are good qualitative indicators of reasonably well-dispersed blends of SWNTs and PEO [33]. However, during the solvent evaporation process, a fraction of nanotubes reaggregates (broadening of van Hove singularities), and the final dispersion state in solid polymer nanocomposites decreases as shown in Fig. 13.2. Alternatively, Strano and coworkers have demonstrated the use of fluorescence measurements to establish the nanotube dispersion state [47]. Fagan and coworkers reported that use of near-infrared fluorescence was more effective to characterize dispersion compared to optical absorption spectroscopy and resonance Raman scattering [48]. Vaisman and coworkers developed a MWNTs dispersion state quantification in PEO using particle size analysis (based on dynamic light scattering (DLS)), while visual characterization was based on optical and electron microscopy [49]. Park and coworkers used field emission scanning electron microscopy (FE-SEM) as well as ex situ small-angle X-ray scattering to characterize MWNTs dispersion state in PEO matrix [40].

It is essential to characterize the dispersion state of nanotubes in polymer matrix quantitatively. In globally isotropic systems for systems with better dispersion of nanoparticles, we anticipate a higher anisotropy (α) of the primary dispersible unit and consequently lower percolation threshold (p_c or φ_c for geometrical and electrical percolation, respectively). The critical nature of the percolation process can be utilized to develop nanotubes loading (p , volume %, and $\varphi = p/100$) dependent expression for structural properties (X) or electrical conductivity (σ_{dc}) and can be expressed as

$$X = 1 + 0.62(xp) + 1.62(xp)^2 + m(p - p_c)^t \quad (13.1)$$

$$\sigma_{dc} = m(\varphi - \varphi_c)^t \quad (13.2)$$

At low nanotube loadings ($p < p_c$), the CNTs act as isolated objects and the structural properties (e.g., viscosity or modulus) dominated by the matrix contribution can be modeled along the lines adopted by Guth [50]. Beyond their geometrical percolation, the CNTs form a network superstructure that dominates the mechanical response and follows typical power-law-like behavior associated with systems near the percolation threshold [51]. At high concentrations, on the other hand, the addition of nanotubes results in some aggregation of the tubes and weaker enhancement to the reinforcement with concentration of CNTs. Similarly, as individual nanotubes or as isolated small-cluster phase, the polymer nanocomposites act as insulator, and beyond the electrical percolation threshold (φ_c), a continuous conducting path spanning the matrix is developed and the nanocomposites behave as a conductor. Note that for mathematical similarity, the power-law prefactor (m) and exponent (t) are kept identical in Eqs. 13.1 and 13.2, but these values are not the same and depends on the system as well as selection of the property one intends to model (X or σ_{dc}). The aspect ratio (x) is related to the geometrical percolation threshold (for instance, using or extrapolating the calculation of percolating ellipsoids in the absence of excluded volume by Garboczi et al. [52]) and requires an iterative solution of Eq. 13.1.

Use of Eqs. 13.1 and 13.2 to obtain the geometric and electrical percolation threshold for SWNTs in PEO matrix is well documented in literature. Using reduced viscosity as a structural parameter for Eq. 13.1, ($X = \frac{\eta^*}{\eta_0^*}$), with η_0^* being the zero shear viscosity of the pure polymer (PEO) and η^* collected at a fixed frequency (in this case 10 rad/s), Krishnamoorti and coworkers reported $p_c = 0.09$ vol% with scaling exponent (t) 1.55 and effective aspect ratio $\alpha = 650$ (Fig. 13.3a) [33]. For electrical conductivity, they reported $\varphi_c = 0.0003$ (or, 0.03 vol%) and $t = 2.4$ (Fig. 13.3b) [33]. For amphiphilic block copolymer (PE-*b*-PEO)-wrapped MWNTs, dispersed in PEO matrix, Semaan and coworkers reported two geometrical percolation thresholds based on nanotube concentration-dependent reduced viscosity data [45]. The earlier percolation occurs at $p_c = 0.085$ wt% with $t = 0.2$ and the second percolation occurs at $p_c = 2.0$ wt% with $t = 1.9$ [45]. Interestingly, the second geometrical percolation coincides with electrical percolation for which the threshold is 2.25 wt% and $t = 2.4$ [45]. Note that universal scaling exponent (t) values reported for MWNT and SWNT dispersion in PEO matrix are similar [33, 45]. This indicates that beyond the percolation threshold, cluster effect is more pronounced than the individual nanoparticles' dispersion state. Park et al. observed a percolation threshold between 1.0 and 2.0 vol% for MWNTs in PEO and summarized the percolation threshold for carbon nanotubes-PEO nanocomposites reported by different research groups [40]. Finally, while many of the previous studies have shown that electrical and geometrical percolations are coincident [53, 54] or that the value for the electrical percolation threshold is somewhat greater than the corresponding geometrical

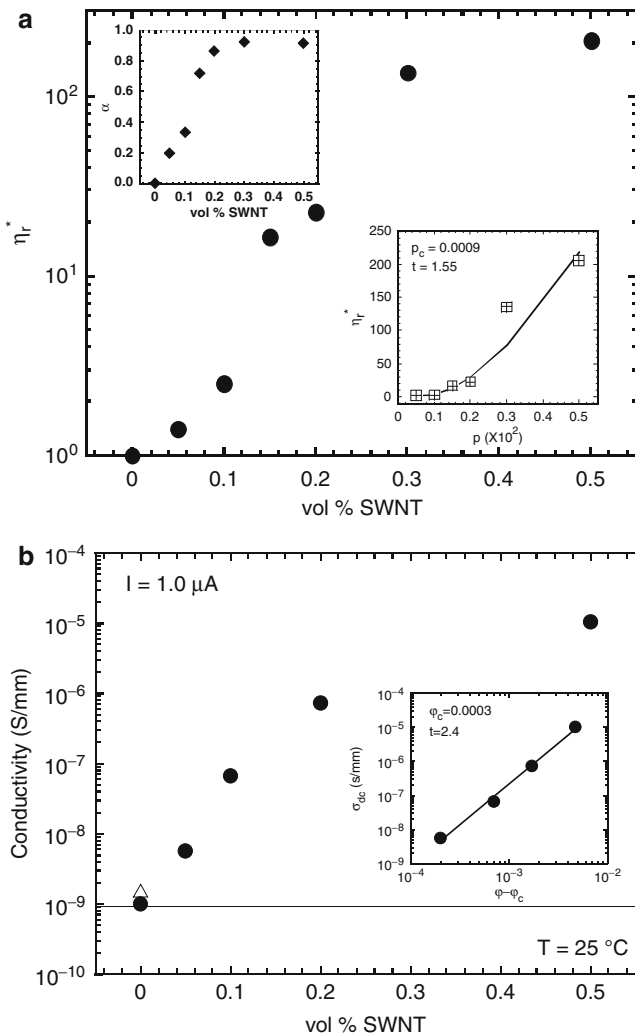


Fig. 13.3 (a) Reduced viscosity plot against different vol% SWNTs loading for SWNT-LDS-PEO ($M_w = 8,000$ Da) samples. The classical sigmoidal nature of the curve indicates the presence of a geometrical percolation. [Top Inset: low-frequency dependence of η_r^* ($\eta_r^* \sim \omega^{-\alpha}$), Bottom Inset: hydrodynamic percolation threshold volume fraction ($p_c/100$) is obtained from plot of η_r^* vs. $(p-p_c)$. Model fit (Eq. 13.1) yields a threshold volume fraction ($p_c/100$) = 0.0009 with a scaling exponent (t) = 1.55] (b) The composition dependence dc conductivity (σ_{dc}) for different samples obtained using a four-point probe. Pure polymer and sample LDS-PEO (no SWNTs) (Δ) are either insulating or below the lower measurement limit of the instrument. Electrical percolation threshold (φ_c) is calculated from a best fit (using Eq. 13.2) plot of σ_{dc} vs. $(\varphi-\varphi_c)$ [inset]. The best fit gives φ_c value 0.0003 (=0.03 vol%) with a scaling exponent 2.4 (Reprinted with permission from Ref. [33])

percolation [55, 56], it is anticipated [57] and observed for multiwalled carbon nanotube–polymer composites that the connectivity (i.e., electrical) percolation precedes the rigidity (i.e., geometrical) percolation [58]. Undoubtedly, low electrical and geometrical percolation threshold and a corresponding high value of anisotropy indicate well-dispersed nanoparticles in PEO matrix.

3 Nanocomposite Structure

Unlike the dispersion characterization of low concentration CNT-based polymer nanocomposites, the structural characterization of the nanotube network structure above the percolation threshold is relatively less explored. Scheafer and coworkers investigated nanotube network morphology in different matrices using combined real-space (microscopy) and reciprocal-space (scattering) techniques [59–61]. Even in solution state (aqueous medium), both single- and multiwalled carbon nanotubes are found to develop mass fractal network (fractal dimension lies between 2 and 3) with hierarchical morphology. As discussed before, for well-dispersed CNTs, the entropic barrier to dispersion offers a limited concentration window between the percolation threshold and isotropic to nematic transition. For SWNT–PEO nanocomposites with the nanotube concentration window ($2 \leq p/p_c \leq 10$), the network structure was systematically investigated using small- and ultrasmall-angle neutron-scattering methods [62]. These systems thus represent a semi-dilute dispersion of nanoparticles, a range of significant practical importance for technological applications. A three-dimensional network of anisotropic nanoparticles is expected to show multiple length scales, and small- and ultrasmall-angle neutron scattering (SANS and USANS, respectively [63, 64]) are ideal techniques to probe the hierarchical structure [62, 65] of such a network. The scattering vector q ($=4\pi/\lambda \sin(\theta/2)$, with λ and θ as the wavelength and scattering angle, respectively) dependence of the scattered intensity, $I(q)$, is found to be roughly independent of nanotube loading over the entire q range ($3 \times 10^{-5} < q < 0.1 \text{ \AA}^{-1}$) studied. The scattered intensity, when scaled by the composition of the mixtures, $p \times (1 - p)$ (expected for disordered systems), forms a mastercurve [62]. This superposition which indicates that the structure of the network is over a length-scale ($=2\pi/q$) range of 6 nm to 20 μm for a broad range of semi-dilute compositions (p/p_c) is **self-similar**.

A schematic of the nanotube network is shown in Fig. 13.4a. At the top, a matrix spanning network is formed which consists of a number of aggregated clusters or flocs that are in dynamic equilibrium [68]. The associated scattering length scale is the average density correlation length between two clusters which can also be conceived as the average cluster/floc size (R). Inside the floc, individual or small bundles of nanotubes (depending on the dispersion state) overlap each other, and the average distance between two adjacent contacts is the network mesh size (ζ). At even smaller length scale, individual CNTs should display rigid rod scattering ($I(q) \sim q^{-1}$) which was not found for SWNT–PEO system (Fig. 13.4b). This absence may stem from the presence of highly flexible tubes or small tube bundles

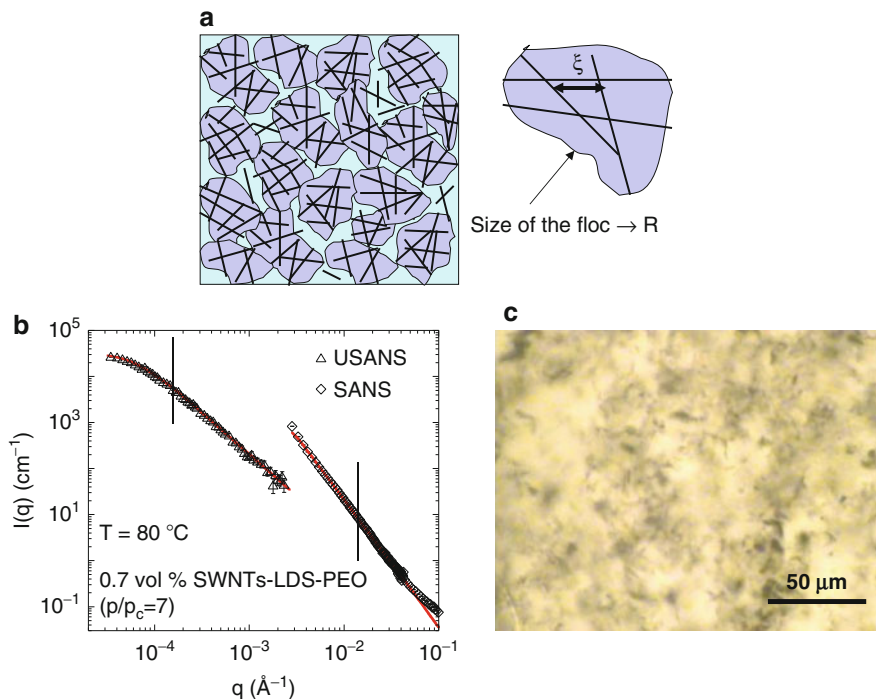


Fig. 13.4 (a) A schematic of the hierarchical network structure showing different length scales. (b) A representative fit [66] of the smeared unified model [67] (solid red line) to the smeared scattering data. The solid vertical lines represent q values associated with different network length scales. The intensity mismatch is due to instrument smearing. (c) Optical microscopic image of a representative SWNTs network ($p/p_c = 4.0$, in PEO) verifies the presence of micron-sized flocs as obtained from scattering data fitting (Reprinted with permission from Ref. [62])

even at the highest q value probed. Such absence of single rigid rodlike particle scattering from nanotube network has also been reported previously [59, 61].

Scattering from hierarchical fractal structures can be described by a unified equation [67] with multiple structural levels where the scattering from each structural level is expressed as the combination of the q -independent Guinier scattering and structurally limited power-law scattering. The model fit (Fig. 13.4b) of the SANS and USANS scattering to the unified equation provides a fractal dimension (d_f) of $\sim 2.3 \pm 0.2$, indicating a mass fractal network of SWNTs in PEO matrix. The fractal dimension is inversely related to the dispersion state; poor dispersion is characterized by a fractal dimension d_f approaching 3. For the case of PEO–SWNT (as well as nanocomposites of bisphenol-A and SWNT as well as bisphenol-F and SWNT) semi-dilute nanocomposites, the average floc size is found to be ~ 4 μm and roughly independent of the particle concentration and the dispersing medium. The presence of such micron-sized flocs is also confirmed by optical microscopy (Fig. 13.4c). The other prominent length scale of the network extracted from the fitting is the mesh size (ζ) and varies significantly with nanotube loading.

With increasing amounts of SWNT, ζ decreases and follows a power law ($\zeta \sim p^{-\nu}$) similar to previously reported results [69]. However, the concentration dependence is much weaker than that predicted based on a fractal scaling argument [70] ($\nu = 1/(3-d_f)$) or derived from the random contact model [71] for uncorrelated rods ($\nu = 1$). Rather it shows closeness to the diffusion limited concentration dependence ($\nu = 0.5$) calculated for the semiflexible rods in semi-dilute concentration regime [72]. On the other hand, the number of flocs present in the system shows an almost linear relation with concentration ($\sim p^{1.2 \pm 0.1}$). This demonstrates that beyond percolation threshold, with increasing SWNTs loading in a PEO matrix, the mesh size decreases, the floc size remains unchanged, and the network primarily grows through the formation of new flocs [62].

Finally, one important aspect worth discussion is the nature of individual CNTs inside the network. Duggal and Pasquali reported the dynamics of individual SWNTs which resembles the diffusion of rigid Brownian rods [73]. Yodh and coworkers explored the viscoelastic properties considering rigid rod network where nanotubes form a rigidity percolation at a low volume fraction and the elasticity of the network arises from the freely jointed bonds of interaction energy $\sim 40 k_B T$ [69]. However, at the smallest length scale, scattering from CNTs is more like from semiflexible rods [59, 61, 62], and still considerable debate exists whether nanotubes inside the network behave as semiflexible or rigid rods.

Besides quiescent state network structure, there has been a significant interest in preparing aligned or self-assembled SWNT or MWNT structure in PEO matrix. Such aligned nanocomposites are essential for microelectronics device fabrications [74]. Excellent review papers on carbon nanotubes alignment in different polymer matrices are available elsewhere, and many of the details are not reproduced here [75, 76]. Sano and coworkers [77] synthesized PEO-grafted-SWNTs in DMF–water medium. Further, dispersing the reaction solution in chloroform collapses PEO chains in globular aggregates. A Langmuir-Blodgett film made from this solution afforded a surface-micelle structure in which collapsed SWNT cores are surrounded by extended PEO patches. By adding DMF to chloroform, conformational change takes place though the structural change which is not completely reversible. Inspired by these findings, Nativ-Roth and coworkers [78] developed a “nanowrapping” mechanism to disperse nanotubes using solvophobic–solvophilic block copolymer. This approach is especially applicable for Pluronic[®] system where PEO is one of the major blocks. Using experimental observations, computer simulations, and theory, they have shown that solvophobic block adsorbs on the carbon nanotubes (both SWNTs and MWNTs) surface and the solvophilic block provides a steric barrier that leads to stable dispersion. Recently, using cryo-transmission electron microscopy (cryo-TEM) and SANS, Cohen and coworkers [79] revealed CNT/Pluronic[®] (with hydrophobic polypropylene oxide, PPO, as mid-block) hybrid structure in aqueous medium. A small bundle of carbon nanotubes (~ 3 – 4 nanotubes together) and a dense PPO layer adsorbed on CNT surfaces form a concentric core-shell cylindrical structure. Further this concentric cylinder is surrounded by the hydrophilic PEO chains. Dubois and coworkers [80]

utilized the block copolymer self-assembly concept to develop hierarchical nanocomposites where LiCl molecules acted as structure-directing agent. By this methodology, they made *one-pot synthesis* of poly(ethylene oxide)-*b*-poly(L-lactide)-based nanocomposites (PEO-*b*-PLLA)/LiCl/CNT, a biocompatible system which is soluble in organic media. Known crown-ether complexation or cation-ethylene oxide interaction drives the nanocomposite structure where nanotubes preferentially surrounded by LiCl and ethylene oxide moieties and L-lactide molecules act as the solubilizing group.

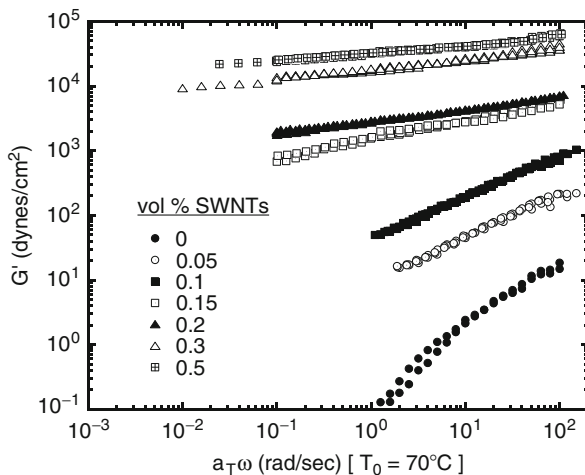
4 Flow Properties

The flow properties (both linear and nonlinear) of CNT-based polymer nanocomposites show resemblance to the broad class of soft-glassy materials [81, 82]. For polymer-based nanocomposites, the melt-state rheological properties are dictated by a combination of the mesoscale structure and the strength of the interaction between the polymer and the nanoparticles [83, 84]. The mesoscale structure is crucially dependent not only on the strength of the polymer–nanoparticle interaction but also on the inherent viscoelastic properties of the matrix in which the nanoparticles are dispersed. Detailed discussions of polymer nanocomposites rheology are documented elsewhere [85, 86]. In this section, we discuss the linear and nonlinear viscoelastic behavior of the CNT-based PEO nanocomposites.

4.1 Linear Viscoelastic Properties

Melt-state linear viscoelastic measurements capture the liquid-like to solid-like transition with increasing nanoparticle loading in polymer matrix. In linear dynamic oscillatory measurements, a small amplitude oscillatory strain, $\gamma(t)$ of the form $\gamma(t) = \gamma_0 \sin(\omega t)$, where γ_0 is the strain amplitude, is applied. Values of γ_0 are kept as low as possible to apply a minimal deformation as well as not to change the quiescent state microstructure of the nanocomposites. The resulting time-dependent linear shear stress, $\sigma(t)$, is recorded and interpreted as $\sigma(t) = \gamma_0[G' \sin(\omega t) + G'' \cos(\omega t)]$, where G' and G'' are the storage and loss modulus, respectively. Other rheological properties derived include the complex modulus ($G^* = \sqrt{(G')^2 + (G'')^2}$) and the complex viscosity ($\eta^* = G^*/\omega$). For pure polymers, at measurement times much longer than the longest relaxation time, a liquid-like response is observed where $G' \sim \omega^2$ and $G'' \sim \omega$. Well above the percolation of nanoparticles, beyond the terminal relaxation time, polymer nanocomposites behave as a solid where at long time G' and $G'' \sim \omega^0$. Similarly, for liquid-like polymer, the viscosity of the system is independent of the frequency (or time), whereas, for solid-like polymer nanocomposites, at long time viscosity overshoots ($\eta^* \sim \omega^{-1}$).

Fig. 13.5 Reduced frequency ($a_T\omega$) dependence of the dynamic storage modulus (G') compared for different vol% SWNTs loading in PEO ($M_w = 8,000$ Da). Above the percolation threshold a nonterminal frequency-independent behavior of G' is observed (Reprinted with permission from Ref. [33])



For SWNT–PEO nanocomposites, in Fig. 13.5, frequency dependence of the storage modulus (G') is plotted as a function of nanotube loading [33]. The pure polymer behaves like a Newtonian liquid with characteristic low-frequency terminal behavior (complex viscosity $\eta^* \propto \omega^0$; $G' \propto \omega^\beta$, $\beta = 2.0$). The incorporation of SWNTs results in an increase in G' at all frequencies and a decreased low-frequency power-law scaling of G' . In fact, the low-frequency moduli become independent of frequency for the higher volume fraction SWNT nanocomposites and consistent with solid-like behavior. This progression from liquid-like to solid-like behavior is attributed to the presence of a network superstructure of the nanotubes. This transition is better visualized through the viscosity (Fig. 13.3a) and can be used to determine the geometrical percolation threshold and effective aspect ratio of the dispersed SWNTs as discussed in the *Dispersion Characterization* section. Similar transitions in linear viscoelastic behavior with changing CNT loading in PEO matrix are also reported by others [45, 87, 88]. Using short fiber theory, Zhou and coworkers [87] calculated an elastic modulus 0.1 TPa for functionalized SWNTs indicating effective load transfer from the PEO matrix to nanotubes. However, the mechanical reinforcement due to presence of CNTs cannot be explained using the traditional Fukuda–Kawata model (isolated long fiber theory) [89] or the Halpin–Tsai model [90] (multi-fiber interaction) or the Mori–Tanaka model [91] (treating the fiber as an ellipsoid of revolution) or the Schaefer and Justice model [92]. The failure of the most of these traditional fiber theories stems from treating CNTs a fiber of finite length and (for well-dispersed system) excellent stress transfer from polymer to tube under deformation.

The selection of compatibilizer (e.g., surfactant or amphiphilic block copolymer) plays a crucial role in CNT dispersion state which in turn controls rheological properties (above the percolation threshold). The rheological behavior of SWNT–PEO nanocomposites, compatibilized using different surfactants (LDS, SDS, and DTAB, all have 12 member alkyl chain as tail but different head groups,

Table 13.1 Rheological parameters for nanocomposites compatibilized with different surfactants. All concentrations are in vol % (Reprinted with permission from Ref. [33])

Sample	β ($G' \sim \omega^\beta$)	α ($\eta \sim \omega^{-\alpha}$)	$G' _{\omega = 10 \text{ rad/s}}$ (dynes/cm ²)	$G^* _{\eta^* \rightarrow \infty}$ (dynes/cm ²)
PEO (8 K)	1.8	0.0	2	–
0.2 SWNT–LDS–PEO	0.14	0.86	2,500	2,000
0.2 SWNT–SDS–PEO	0.06	0.94	4,000	3,000
0.2 SWNT–DTAB–PEO	0.50	0.63	300	100

Li⁺, Na⁺, and Br[−], respectively) at the same surfactant and nanotube loadings, is presented in Table 13.1 [33]. The low-frequency power-law scaling of G' and η^* for all the nanocomposites indicates the formation of a SWNT superstructure at 0.2 vol% loading. Nevertheless, the two measures of the extent of network superstructure reinforcement of the polymer, G' at a fixed ω (10 rad/s) and the value of $G^* |_{\eta^* \rightarrow \infty}$, indicate that the nanocomposites prepared with anionic surfactants (LDS and SDS) are significantly better dispersed than the cationic analog. While it has been previously demonstrated that anionic, cationic, and non-ionic surfactants produce well-dispersed SWNTs in water [46], presumably the better dispersion of the SWNTs in the LDS- and SDS-compatibilized system emerges from the strong interactions between PEO and those cations. PEO in the presence of alkali metal ions is capable of forming crown ethers that are a ring-like structure of carbon and oxygen molecules with a positive charge spread over the peripheral area and a strong negative charge developed at the center of the cavity [39]. On the other hand, for the case of alkylammonium-based cationic surfactants, a positive head group is attached to a long alkyl tail, and the imposed steric constraints render it impossible for such crown ether formation.

The linear rheological behavior of SWNT–PEO nanocomposites, beyond the percolation threshold, p_c , is dominated by the nanotubes network. In this regime, beyond the typical time–temperature superposition, the SWNT–PEO nanocomposites demonstrate *time–temperature–composition* superposition which is a characteristic of the weakly attracting systems such as dispersed carbon black fillers in water [93]. Chatterjee and Krishnamoorti [94] observed validity of empirical two-point collocation, developed by Ferry and coworkers [95, 96], where linear dynamic oscillatory shear measurements are comparable with the linear stress relaxation. Noting the similarity of the time-dependent stress relaxation profile for SWNT–PEO nanocomposite samples with varying nanotube concentration, a *time–temperature–composition* mastercurve can be successfully created for the nanotube loading $3 \leq p/p_c \leq 10$ [94]. For nanocomposites just above the percolation ($1 \leq p/p_c \leq 3$), superpositioning fails because of a combination of the competing magnitudes of the viscoelastic response from the polymer and that of the fractal network as well as the changing nature of the nanotube network superstructure at concentrations close to the percolation threshold. On the other hand, at high concentrations, the dispersed anisotropic nanotubes exhibit a tendency to form nematically ordered structures and do not allow for a comparison with

the nanocomposites with fractal networks. Further, for high nanotube loading samples, alignment of the nanotubes in response to the handling becomes a significant experimental issue, and disorientation in such nanocomposites is shown to be extremely slow [97].

The linear viscoelastic data, for PEO-based nanocomposites with SWNTs concentration well in excess of the percolation threshold (i.e., $p \gg p_c$), are representative of a solid-like material and indicate that the superstructure of the nanotube dominates the viscoelastic response, as has been observed in general for the class of materials known as soft-glassy materials [81, 98]. Further, the superpositioning of the linear viscoelastic response with composition indicates that the superstructure responsible for the dominant viscoelastic behavior in these nanocomposites is self-similar. This self-similar nature of the carbon nanotube network is verified using ultrasmall-angle neutron scattering where a fractal dimension (d_f) = 2.3 ± 0.2 is observed. This fractal dimension is consistent with previous observations of Hobbie and Fry [99] for MWNT networks in polyisobutylene (PIB) and the simulation study reported by Ganesan and coworkers [83] for polymer-bridged gels. Finally, the elastic strength (G_p) of this self-similar network superstructure measured as the vertical shift factor in time–temperature–composition superpositioning scales as $(p)^{4.3 \pm 0.7}$. The large value of the exponent is consistent with previous experiments observing elastic percolation in three dimensions [70, 93, 100], although somewhat lower than the values obtained for MWNT dispersions [99], and indicative of the significant increase in the network elasticity with added connections or bonds to the percolative network.

4.2 Nonlinear Viscoelastic Properties

4.2.1 Strain-Dependent Nonlinear Behavior

For semi-dilute SWNTs in PEO, the stress relaxation behavior as a function of applied strain amplitude can be briefly summarized as follows: (a) there is a linear regime that occurs at relatively low strain amplitude values where the relaxation modulus, $G(t)$, is independent of the strain amplitude; (b) increasing the strain beyond the linear region ($\gamma_{\text{critical}} = 0.003$ for $p/p_c = 7.0$) leads to a strain-softening behavior with conservation of the relaxation spectrum and suggesting the possibility of applying time-strain separability for these data (i.e., $G(t, \gamma) = G(t) \otimes h(\gamma)$, where $G(t)$ is the linear relaxation modulus and $h(\gamma)$ is the damping function); and (c) application of higher strain amplitude ($\gamma \geq 0.08 \pm 0.02$ for $p/p_c = 7.0$), the relaxation spectrum is no longer conserved and time-strain superposability is no longer valid [94].

Interestingly, the value of critical strain (strain amplitude at which transition from linear to nonlinear deformation takes place) decreases with increasing CNT loading (Fig. 13.6a), suggesting that structural transformations occur at progressively smaller deformation. Further, γ_{critical} scales as $p^{-2.3 \pm 0.2}$ indicating inter-nanotube interaction and multiple connectivities between percolating

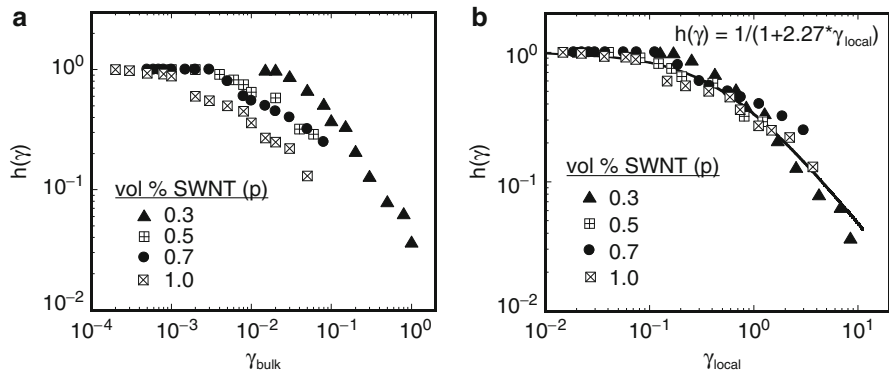


Fig. 13.6 (a) Damping function $h(\gamma)$ required for the time-strain superposition for different nanocomposites is plotted against the applied or bulk strain (γ_{bulk}). (b) The local strain (Eq. 13.3) dependence of $h(\gamma)$. The onset of the shear thinning is observed at $\gamma_{\text{local}} \sim 0.1$ and is similar to other nanocomposite systems with short-range interactions (Reprinted with permission from Ref. [63])

networks dominate the onset of shear thinning behavior. This scaling of γ_{critical} and the previously demonstrated strong composition scaling of the elastic modulus is typical of fractal networks such as those of colloidal gels [70], layered silicate [97], flocculated silica spheres [101], and multiwalled carbon nanotube [99] dispersions which with increasing nanoparticle loading becomes stiffer and more fragile. Similar scaling is anticipated from theoretical efforts [102, 103] examining the three-dimensional percolation of random percolating elements and from computer simulations [104, 105] considering individual bonds resist both bending and stretching (i.e., enthalpic networks [83]). Specifically, using the scaling argument developed by Shih and coworkers [70] for fractal networks well above the percolation threshold ($p \gg p_c$) where the interactions between flocs dominate over those within a floc (the strong link regime), one can evaluate the nature of the fractal network in these nanocomposites. It is anticipated that the scaling for the elasticity (G_p) and critical strain (γ_{critical}) follow p^μ and $p^{-\kappa}$, respectively, with $\mu = (D + d_b)/(D - d_f)$ and $\kappa = (1 + d_b)/(D - d_f)$, where d_b and d_f are the backbone and fractal dimensions of the network, respectively, and D is the Euclidian dimension. From the observed values of $\mu = 4.3 \pm 0.6$ and $\kappa = 2.3 \pm 0.2$ for the SWNT-PEO systems, the backbone and fractal dimensions of the network are calculated to be $d_b = 1.1 \pm 0.2$ and $d_f = 2.1 \pm 0.3$, respectively. The value for the backbone dimension is within the theoretically predicted [106] range of $1 \leq d_b \leq \min(d_f, 5/3)$ and suggests that the nanotubes are close to rodlike objects, at least at a local length scale, in these nanocomposites. On the other hand, the fractal dimension of the nanotube network deduced from the rheological measurements is in good agreement with those obtained from the neutron-scattering measurements [62, 94]. This internally consistent scaling of G_p and γ_{critical} with nanotube concentrations indicates that, in fact, the weak and relatively short-range interactions between nanotubes and multiple pathways between percolating paths dominate the network properties.

For the strain amplitude range over which time-strain separability is applicable, the self-similarity of fractal network controls the deformation. Due to the presence of the network, the strain experienced by individual nanotube inside the network is a function of the network size and different from the applied strain (γ_{bulk}). To accommodate network size effect, a local strain is calculated where bulk strain is modified for dispersed filler effect along the lines adopted by Watanabe et al. [107]

$$\gamma_{\text{local}} = \left[1 + 0.67(\alpha p/100) + 1.62(\alpha p/100)^2 \right] * \gamma_{\text{bulk}} \quad (13.3)$$

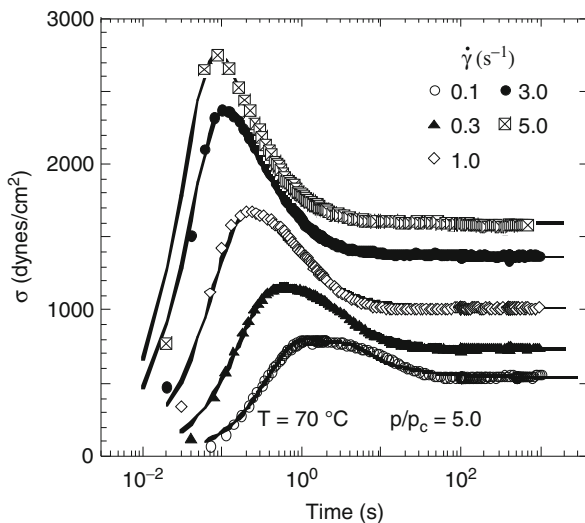
with α being the effective anisotropy of the SWNTs and for these nanocomposites $\alpha = 650$. The local strain used here is reflective of the local stress on the network objects. Under these conditions, the stresses that arise from the collective network (i.e., stress contributions from the percolated structures) are neglected in order to calculate the local strain as demonstrated in Eq. 13.3. Plotting $h(\gamma)$ as a function of local strain (Fig. 13.6b) shows good superpositioning of the data. Finally, the development of *time–temperature–composition–local strain* viscoelastic mastercurves with a universal damping function suggests that the linear and nonlinear viscoelasticity is dominated by the quiescent state network structure and the local strain experienced by the network elements. Clearly, the addition of nanotubes leads to additional pathways for the interconnection of already formed percolative backbone structures and is directly responsible for the strong concentration scaling of G_p and the large value of the modulus. The onset of shear thinning is accompanied by the removal of one of these additional pathways of connecting the backbone of the network and not by the breakdown of the backbone of the network itself. On the other hand, the onset of the failure of the time-strain superposability is perhaps related to the irreversible deformation of the backbone of the fractal network.

Finally, examination of similar viscoelastic data for organoclay-based nanocomposites with a disordered polystyrene–polyisoprene diblock [97], a system dominated by weak short-range interactions, indicates a similar superpositioning of the damping function with local strain and the onset of shear thinning at a similar value of the local strain ($\gamma_{\text{local}} \sim 0.1$). On the other hand, for the cases of strongly interacting systems such as those observed for a brominated paramethylstyrene–isobutylene polymer with dispersed carbon black [108], aqueous solutions of unmodified clays dispersed in PEO [109], and silica nanoparticles dispersed in PEO [110], such a simple superpositioning fails and is perhaps reflective of the long-range interactions (due to ionic, H-bonding, and bridging interactions caused by long-chain polymers bridging between nanoparticles) that dominate those systems.

4.3 Effect of Steady Shear

The application of large deformations in stress relaxation measurements of SWNT–PEO nanocomposites described above demonstrates the vestiges of the nanotube network as even at long times after the application of the deformation

Fig. 13.7 Representative transient shear stress response obtained during start-up of steady shear measurements for SWNT–PEO dispersion ($p/p_c = 5.0$). For all shear rates, the stress data exhibit an initial overshoot arising from the shear-induced cluster aggregation, and in the long time, the network breaks to reach a steady state. *Solid lines* are model fits to the experimental data as described in Eq. 13.4 (Reprinted with permission from Ref. [113])



($t \sim 10,000$ s), such nanocomposites exhibit residual stress [94]. Start-up of steady shear measurements is performed to investigate the evolution of the network structure under continuous shear [111]. Under constant rate steady shear, these nanocomposites demonstrate non-Newtonian behavior similar to a range of complex fluids such as emulsions, pastes, and slurries [112]. In particular, the shear stress (σ) response to the constant shear rate ($\dot{\gamma}$) shows the presence of a yield stress (σ_y), and the system flows like power-law fluids beyond that point. However, the presence of structure with multiple hierarchical length and time scales significantly impacts the flow properties of the nanocomposite. Under continuous shear, the temporal development of the shear stress shows an initial stress overshoot that equilibrates to a well-defined steady-state value (σ_∞) without any oscillations as seen in representative data in Fig. 13.7 for the SWNT–PEO system with $p/p_c = 5$ [113]. The stress overshoot behavior is attributed to the competing processes that affect the nanotube network superstructure as the parent polymer molecular weight is too low ($M_w/M_e \approx 3.6\text{--}5.0$; where, M_e , the entanglement molecular weight of PEO is 1,600–2,200) [95] to result in a chain entanglement-caused stress overshoot. This stress overshoot feature is also absent in the steady shear response of the nanocomposites with nanotube loading below the percolation threshold. The steady shear viscosity ($\eta = \sigma_\infty/\dot{\gamma}$) demonstrates a shear thinning behavior with power-law exponent -0.7 ± 0.03 . Application of increasing shear rate results in the network becoming weaker. Assuming a three-dimensional isotropic network, roughly 1/3rd of the network elements and junctions will be in flow direction, and from the scaling exponent value, it can be inferred that the network elements that resist deformation in flow direction are eliminated.

The steady shear response of CNT in PEO matrix can be modeled using two time scales. At short times after start-up, the material, behaving like a solid, generates

a stress that is roughly proportional to the total strain. On the other hand, the strain also induces structural rearrangement of the nanoparticle network, akin to a shear melting process, and these structural rearrangements and altered network structure would act to dissipate the stress generated or stored in the system. Whittle and Dickinson using Brownian dynamics have observed stress overshoot in model particle-based gels and suggested a semiempirical model to describe the time evolution of the stress as [114]

$$\sigma(t) = \sigma_0 \frac{t/\tau_a}{1 + (t/\tau_a)^{1+\delta}} + \sigma_\infty \left\{ 1 - \exp\left(-\frac{t}{\tau_r}\right) \right\} \quad (13.4)$$

where τ_a and τ_r are the characteristic aggregation and relaxation times, respectively, and δ is a phenomenological parameter. The parameter σ_0 is related to the shear rate-dependent elastic modulus of the material and σ_∞ is the steady-state shear stress at the shear rate. This model fits to the experimental data quite well (solid lines in Fig. 13.7) with exception of short times. This discrepancy which is a consequence of the prediction by the model for the elastic response at short times (for $t/\tau_a \ll 1.0$, the evolved stress is given by $\sigma(t) = \sigma_0 t/\tau_a$) does not represent the reality of the simultaneous processes of mutually opposing aggregation and shear rejuvenation phenomena. As noted by Whittle and Dickinson, for measurement times that are in the intermediate zone, i.e., $t > \tau_a$, the first term reduces to a power-law decay process whose rate depends on the numerical value of δ . For the nanocomposites considered here, δ is found to gradually increase with increasing shear rate from a value of 0.5 to a value of 1.4. This implies that with increasing shear rate, the decay process becomes increasingly more important compared to the elastic response. The second term (exponential term), in the expression (Eq. 13.4) above, is related to the relaxation process which leads to the steady flow with an equilibrium stress value (σ_∞) at long time.

Detailed observation of the model returned time scales revealed that [113]:

- (a) Aggregation time was consistently smaller than the relaxation time. This clearly shows that the aggregation occurs before the relaxation process.
- (b) The characteristic time scales for aggregation and relaxation are independent of the nanocomposite loading. This suggests that the steady shear behavior of the nanocomposites system is primarily dominated by the applied shear rate.
- (c) Both the aggregation and relaxation times scale with the shear rate (power-law scaling), while the relaxation time shows much stronger dependence on the applied shear rate.

The steady shear response can be explained through shear rate-dependent cluster dynamics. Under quiescent conditions, the nanotube network is made of flocs or clusters of roughly same size. The initial shear thickening behavior is an outcome of the cluster structure adjustment without any breaking or flow under shear. For $p/p_c \gg 1$, since the underlying cluster size remains independent of the nanotube loading, the rearrangement of structure follows the same and displays only shear rate-controlled behavior. This feature gets reflected in nanotube concentration-independent aggregation time scales observed for the system.

Considering the high viscosity of the system, the imposed shear is expected to set the time scale for cluster–cluster collisions. The collision frequency factor (k_{ij}) for fractal systems is given by [115] $k_{ij} = \frac{2k_B T (R_i^{1/d_f} + R_j^{1/d_f})}{3\eta (R_i^{1/d_f} R_j^{1/d_f})}$ where R_i and R_j are the cluster sizes and d_f is the overall mass fractal dimension of the system. For concentration-invariant cluster sizes, the aggregation time scale ($= 1/k_{ij}$) should show the same shear rate dependence as shown by the viscosity (η). Hence, for comparable viscosities of the fully grown network system ($p/p_c \gg 1$), saturation regime of the structural properties, the aggregation time follows network-independent behavior and depends on the applied shear only.

On the other hand, for highly non-Brownian systems, the shear melting and rejuvenation process is largely controlled by the applied shear rate. As a consequence irrespective of the network size or the nanotube loading, the relaxation time (τ_r) of the nanocomposite systems shows a strong and similar shear rate dependence. The breakup process is expected to vary linearly with concentration of CNTs as the Smoluchowski rate coefficient for breakup process, g_n , scales with both shear rate and concentration: $g_n = \frac{4\dot{\gamma}\phi}{\pi}$, where ϕ ($= p/100$) is the volume fraction of particles [114, 116]. According to this expression for a particular nanotube concentration (fixed ϕ), the structural relaxation time should show an inverse relation with the applied shear which in fact holds for the shear rates examined here ($\tau_r \sim (\dot{\gamma})^{-0.9 \pm 0.05}$). However, the underlying phenomenon of a size invariant relaxation time for such nanocomposites is not presently clear and needs further effort. Nonetheless, the above discussion indicates that the overall macroscopic steady shear response in SWNT–PEO system can be viewed in terms of the cluster dynamics to quantitatively understand the underlying basis for the observed macroscopic behavior.

5 Crystallization of PEO in the Presence of Carbon Nanotubes

One of the most significant influences of nanoparticle incorporation in polymer matrices results from the convergence of relevant length scales that control the underlying physics of the structure and dynamics of such systems [2, 3]. In semicrystalline polymers, the average inter-nanoparticle distance is comparable or significantly smaller than the crystalline lamellae length scale, even at modest loadings of nanoparticles. As a consequence, the nanoparticles act as impenetrable objects and result in substantial changes in the polymer crystallization behavior. In this context, investigation of polymer crystallization in the presence of well-dispersed nanoparticles is an interesting and fundamental problem.

Carbon nanotubes are found to act as nucleating system for many families of semicrystalline polymers (such as poly(ϵ -caprolactone), poly(vinyl alcohol), poly(ethylene), poly(propylene), etc.) [17, 18, 117–120]. However, especially for poly(ethylene oxide), SWNTs are known to disturb the crystal formation and

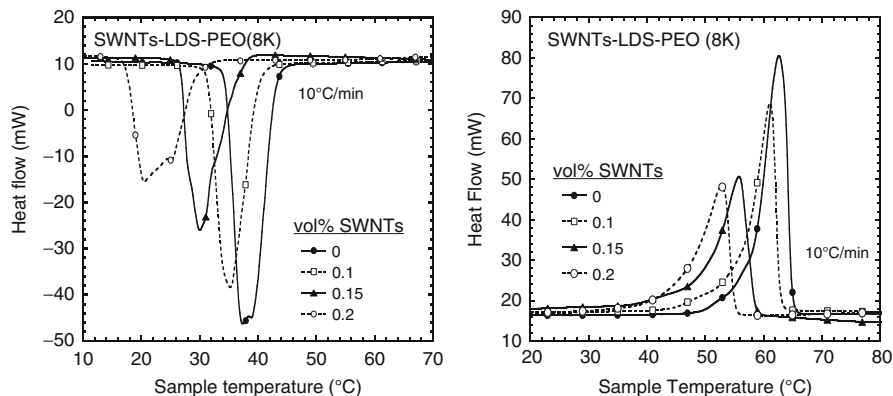


Fig. 13.8 Melting (*left*) and crystallization (*right*) behavior for PEO and different nanocomposites for a constant heating (cooling) rate of 10 °C/min (Reprinted with permission from Ref. [33])

decrease the overall crystallinity of the system [33, 87, 121, 122]. Zhou and coworkers [87] first reported a decrease in PEO peak melting temperature from 72.0 °C to 65.0 °C in the presence of 10 wt% functionalized SWNTs for non-isothermal crystallization process. Below 6 wt% F-SWNTs loading, the nanocomposites behave homogeneously (a single PEO melting peak in non-isothermal DSC thermogram), but at higher loading phase, separation takes place which results in a low peak melting temperature (65 °C) for PEO chains in vicinity to the CNTs and a high peak melting temperature (72.3 °C) for the bulk PEO. Krishnamoorti and coworkers [33] reported DSC-based thermograms for non-isothermal heating and cooling with a decrease in area (i.e., decrease in fractional crystallinity) and a depression in the peak melting ($T_{m,p}$) and peak crystallization ($T_{c,p}$) temperature at low (0.05–0.5 vol%) SWNT loading (Fig. 13.8). Interestingly, wide-angle X-ray measurements (Fig. 13.9a) revealed that the PEO unit cell structures in these nanocomposites are preserved with little broadening of major reflection peaks indicating more disorder.

Lithium-based salts are known to destabilize the crystals of PEO through the formation of crown-ether complexes. In that case, lowering of both the $T_{m,p}$ and $T_{c,p}$ in this nanocomposites may be an outcome of the destabilization of the crystalline state and the local perturbation of the crystalline order due presence of a Li^+ -based surfactants. However, for the control sample (with the same amount of compatibilizer LDS loading but no SWNTs), while a small decrease is observed in the fractional crystallinity and the values of $T_{m,p}$ and $T_{c,p}$, the effects are significantly larger in the case of the SWNTs nanocomposites. Additionally, the dispersions of the SWNTs in PEO with SDS and DTAB while being good, the melting and crystallization character of the PEO in these nanocomposites do not change significantly. The result for the crystallization and melting behavior of the SDS-compatibilized nanocomposites is somewhat

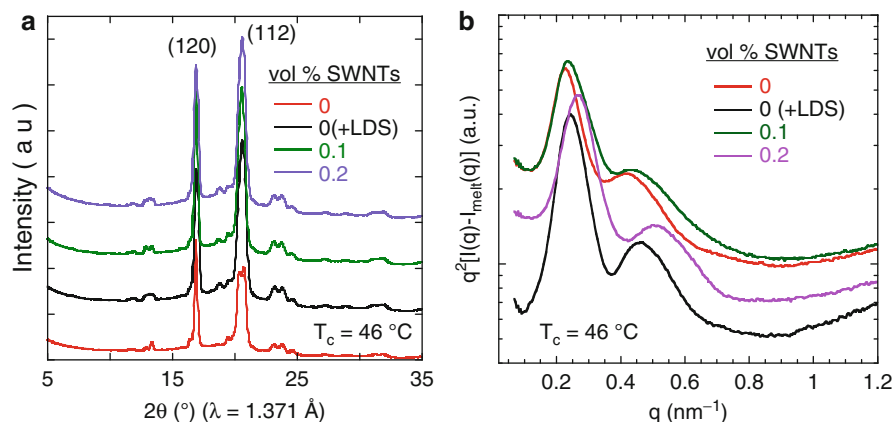


Fig. 13.9 (a) (left) Wide-angle X-ray scattering (WAXS) profile and (b) (right) Lorentz-corrected small-angle X-ray scattering (SAXS) data ($q^2[I(q) - I_{\text{meit}}(q)]$) vs. q for the PEO ($M_w = 100 \text{ K}$) and different SWNT–LDS–PEO nanocomposites. All data were collected after the completion of the isothermal crystallization at $T_c = 46 \text{ }^\circ\text{C}$. The prominent WAXS peaks originating from the PEO unit cell correspond to the (120) and (112) planes and occur at d -spacing values of 0.463 and 0.386 nm corresponding to 2θ values of 17.2° and 20.9° , respectively, for $\lambda = 1.371 \text{ \AA}$. The peak positions are unchanged in the PEO nanocomposites, indicating that incorporation of the SWNTs did not alter the unit cell structure of the PEO. However, for the nanocomposites, some broadening of the crystallographic peaks is observed and may loosely be related to the disorder of the crystal structure (i.e., crystal defects). In contrast, compared to the pure polymer, small-angle scattering peaks in polymer nanocomposites are shifted to higher q values demonstrating reduction in the long spacing (Reprinted with permission from Ref. [41])

surprising, as it is anticipated that the Na^+ should also be able to form crown ethers with PEO. However, it is possible that Na^+ -based surfactant is less compatible with the SWNTs (in the presence of the PEO) and results in less synergy between the SWNTs and the anionic surfactant. Hence, in SWNT–LDS–PEO nanocomposites, the depression of PEO melting temperature and overall crystallinity is observed at extremely low ratios of Li^+ to PEO units ($\sim 1:1,000$) as well as at very low filler loading ($\sim 0.2 \text{ vol\% SWNTs}$). These possibly indicate some synergism between the effect of the nanotubes and the lithium-based surfactants which is responsible for change in crystallization character of the PEO.

It is fundamentally essential to understand whether the SWNTs and LDS hinder the nucleation of PEO crystals or slow down the growth process or both. Additionally it is pertinent to investigate the PEO lamellar morphology in these nanocomposites. Overall crystallization rate can be expressed as $1/\tau_{50\%}(T_c)$ where $\tau_{50\%}$ is the crystallization half time during isothermal crystallization at a crystallization temperature T_c [41, 123]. Overall crystallization rates are often treated as the growth rate and are modeled using Lauritzen–Hoffman theory [124–127]. The most important parameter extracted from the model fit is K_g^τ which is equivalent to the energy barrier for crystallization. The parameter K_g^τ has the following expression:

Table 13.2 Values obtained by fitting the Lauritzen–Hoffman model to DSC isothermal experimental data and $\sigma\sigma_e$ values calculated using Eq. 13.5. All concentrations are in vol% (Reprinted with permission from Ref. [41])

Samples	$K_g^\tau (\times 10^4 \text{ K}^2)^a$	$\sigma \cdot \sigma_e (\text{erg}^2 \cdot \text{cm}^{-4})^a$
PEO	9.29 ± 0.15	1,016 ± 2
PEO–LDS	14.02 ± 0.45	1,532 ± 3
0.05 SWNT–LDS–PEO	11.73 ± 0.64	1,248 ± 3
0.10 SWNT–LDS–PEO	13.15 ± 0.53	1,440 ± 2
0.15 SWNT–LDS–PEO	19.24 ± 0.79	2,099 ± 4
0.20 SWNT–LDS–PEO	23.31 ± 0.73	2,542 ± 3
0.20 SWNT–SDS–PEO	12.60 ± 0.44	1,380 ± 5
0.20 SWNT–DTAB–PEO	12.74 ± 0.39	1,395 ± 3

^aConstants employed: $a_0 = 4.5 \text{ \AA}$, $b_0 = 4.65 \text{ \AA}$, $\rho_c = 1.239 \text{ g/cc}$, $\rho_a = 1.124 \text{ g/cc}$, $\Delta H_m^\circ = 203 \text{ J/g}$, $T_m^\circ = 69 \text{ }^\circ\text{C}$, $T_g = -55 \text{ }^\circ\text{C}$

$$K_g^\tau = \frac{j b_0 \sigma \sigma_e T_m^\circ}{k \Delta h_f} \quad (13.5)$$

where k is the Boltzmann's constant. The parameter $j = 2$ for regime II (where growth and nucleation rates are comparable) and $j = 4$ for regime I (nucleation is slower than growth) and III (nucleation is faster than growth), respectively. σ is the lateral surface free energy, σ_e is the fold surface free energy, and Δh_f is the heat of fusion of a perfect crystal. The product of surface free energies $\sigma\sigma_e$ can be calculated directly from K_g^τ and the following expression for lateral surface free energy $\sigma = 0.1 \Delta h_f \sqrt{a_0 b_0}$; where a_0 and b_0 correspond to the projected chain length and chain width, respectively, within the crystal, the σ_e value can further be calculated. Also, $\sigma_e = W/2a_0 b_0$ where $-W$ is the work done by the chain during the folding process.

Using isothermal crystallization data as a function of $T - T_c$, for a series of SWNT-based PEO nanocomposites, Krishnamoorti and coworkers [41] extracted and compared the K_g^τ and $\sigma\sigma_e$ parameters as a function of (a) nanotube loading and (b) different surfactant as compatibilizing agent (Table 13.2). The $\sigma\sigma_e$ values increase as the SWNTs loading increases within the PEO nanocomposites. The variations in $\sigma\sigma_e$ arise from the change in fold surface free energy since the lateral surface free energy, σ , is a constant (WAXS, Fig. 13.9a, data show conservation of monoclinic unit cell structure and lattice parameters) [33, 41]. In the presence of LDS only, the $\sigma\sigma_e$ value becomes ~ 1.5 times larger than that of the pure PEO. Incorporation of LDS-stabilized nanotubes provides a higher energy barrier, and the $\sigma\sigma_e$ value for 0.2 vol% SWNT–LDS–PEO (the highest SWNTs loading studied) is ~ 2.5 times that of the pure PEO. Previously, Huang and Goh also observed 1.7 times increase in fold surface free energy (σ_e), when one end of PEO is capped with C_{60} molecules but at a much higher nanoparticle concentration (23 % by weight of C_{60}) [128]. The ~ 2.5 increase in the energy barrier (or fold surface free energy) is based on the assumption that the segmental transports of the PEO chains are unperturbed in the presence of nanotubes.

Rheological studies [33, 94, 113] did not reveal any difference in segmental transport between nanotube-based nanocomposites and pure PEO. Further, there is also no change in the glass transition temperature between pure PEO- and SWNT-based PEO nanocomposites [33].

PEO forms crystals with a monoclinic unit cell with four helical molecules passing through the *c*-axis of the unit cell. The helix has a 7/2 conformation which corresponds closely to *gauche*–*trans*–*trans* sequence of bond rotation, whereas *gauche* conformation exists between two CH₂ groups [129, 130]. Such helical conformation requires chain flexibility, and increased chain stiffness is detrimental to crystal formation. As a result, substantial reduction in the crystal growth rate is observed in the LDS–PEO system. Further incorporation of LDS-stabilized CNTs acts as confining surfaces for the polymer chains which not only make them more restrained but also provide additional diffusion barrier to chain transport. These coupled effects lead to dramatic slowing down in PEO growth kinetics and creates a highly amorphous PEO matrix. Similar to the trends observed in the non-isothermal crystallization behavior described previously for the case of SDS- and DTAB-compatibilized SWNT–PEO nanocomposites, no significant change in K_g^τ values compared to that of pure PEO were observed. This indicates that the PEO chain mobility has not been constrained in the presence of SDS or DTAB molecules. This further leads credence to the hypothesis that the nanotubes help better exposure of PEO chains to the Li⁺ ions in the case of LDS-stabilized SWNT-based PEO dispersions and are critical in controlling the overall crystallization behavior of PEO in such nanocomposites.

Interestingly, small-angle X-ray scattering (SAXS) measurements (Fig. 13.9b) show a clear shift in the Lorentz-corrected SAXS intensity peak position for the nanocomposites. The first scattering peak which corresponds to the long spacing ($\ell_b = 2\pi/q_1^*$) yields a value of ℓ_b of ~ 30 nm for the pure PEO ($M_w = 100$ K). However, in the nanocomposite samples, the peak positions are substantially shifted to higher q values, corresponding to a decrease in the long spacing of the PEO crystal. For example, the 0.2 vol% SWNT–LDS–PEO nanocomposite shows a value of ℓ_b of ~ 23 nm. Closer inspection of the SAXS peak also reveals broadening of the peaks in the nanocomposites which is associated with disorder or less perfect lamellar structure. The smaller long spacing is also evident in correlation function calculated from SAXS data [41]. Using two-phase theory, proposed by Strobl and coworkers [131], the long spacing can be deconvoluted into lamellar thickness and interlamellar spacing. For SWNT-based PEO nanocomposites, the changes in the long spacing (ℓ_b) solely arise from the lamellar thickness (ℓ_c) variation, whereas the interlamellar spacing (ℓ_a) remains constant. The LDS–PEO sample (without any SWNTs) displays the formation of thinner lamellae, but with the introduction of nanotubes, the PEO lamellae get further thinner. The PEO chains in the vicinity of the highly coordinated Li⁺ ions which adopt the solvated structures associated with crown ethers are usually amorphous [38, 39]. Due to significant interactions between Li⁺ ions and CNTs, the volume surrounding the SWNTs is preferentially occupied by the amorphous segments of PEO chains [33]. This structural organization is illustrated in a schematic presented

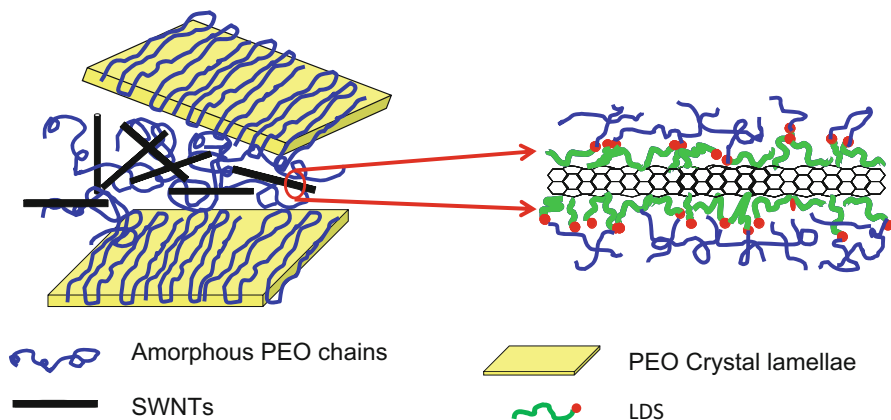


Fig. 13.10 Structural organization in SWNT–LDS–PEO nanocomposite system. Li-based surfactants compatibilize the nanocomposite by acting as bridges between SWNTs and PEO. Due to Li^+ –EO complexation and the barrier offered by SWNTs to chain diffusion to the growing lamellae, PEO crystals are formed away from nanotubes. The nanotubes are, thus, preferentially surrounded by amorphous PEO chains (Reprinted with permission from Ref. [41])

in Fig. 13.10. Consequently, the nucleation events for PEO crystallization only occur at points distant from the nanotube surface. During the growth process, the developing crystal phase requires a continuous supply of polymer which is hindered because of the diffusional barrier from the topological restrictions imposed by the well-dispersed nanotubes. Finally, a similar behavior has also been observed experimentally for PEO/ Na^+ MMT nanocomposites and predicted for PEO/ Li^+ MMT nanocomposites through computer simulations [132, 133].

There are several opposing observations reported in literature on PEO crystallization in the presence of MWNTs. Park et al. found that MWNTs hinder PEO crystallization, and above 10 % nanotube loading the SAXS pattern does not show any lamellar reflection from PEO crystals [40]. Similarly, Abraham and coworkers reported ~ 10 % decrease in PEO % crystallinity at ~ 3 – 4 % MWNTs loading [122]. Song and coworkers, using DSC and optical microscopy, reported a decrease in number of nucleation site (which results in larger spherulites) and restricted PEO crystal growth in the presence of both MWNTs and chemically modified MWNTs [121]. For double- C_{60} -end-capped PEO (FPEOF), reinforced with acid-treated MWNTs, there is not any substantial change in the PEO crystallization and melting temperatures [123]. On the other hand, for PEO chain grafted on functionalized MWNTs (2-hydroxyethyl benzocyclobutane functionalization followed by ring opening catalyzed anionic polymerization) [134] or MWNTs in PMMA-*b*-PEO matrix where PMMA chains are grafted on MWNTs [135], the overall PEO crystallization kinetics accelerates significantly. Presumably, due to lattice mismatch between helical PEO chains and CNT surface, the nanotubes do not act as nucleating agent for PEO crystallization. Additionally they act as transport barrier to chain transport. However, when the CNT surface is modified (either by

polymer chain grafted or grafted from the sidewall), nanotubes do not take active part in PEO crystallization. In that case, the polymer chain-surrounded MWNTs probably act as nucleating agent which promotes increase in PEO % crystallinity and overall crystallization kinetics.

6 Nanocomposite Applications

6.1 Electronic Materials

Solvent-free PEO–alkali metal salt complex is widely used as solid electrolytes in Li-ion batteries [12, 136, 137]. The amorphous phase of PEO has been identified as the ion-transporting medium, and a high degree of PEO crystallinity at ambient temperature leads to low ionic conductivity [138, 139]. To overcome this effect, the alkali metal salts (especially lithium-based salts) are used which favorably interact with the PEO to make it more amorphous at the ambient temperature. Unfortunately, at ambient temperature, the solubility of the Li salts in the PEO is low, and additionally, the degree of salt dissociation decreases with increasing salt concentration in the matrix. For most of the PEO–LiX systems, an optimum molar ratio $[Li^+]/[O^-] \sim 0.04$ has been found to demonstrate the highest ambient temperature ionic conductivity [12]. But at these high Li^+ ion concentrations, PEO degrades rapidly and in turn reduces the battery lifetime. One of the approaches to address these issues is the use of liquid plasticizers which cost the electrolyte's mechanical properties and increases its reactivity towards lithium anode [136, 140]. Scrosati and coworkers introduced solid plasticizers (ceramic powder with average particle size 6–13 nm) in the PEO– $LiClO_4$ matrix which showed substantial room temperature conductivity enhancement [136].

A potential advantage of CNT-based PEO nanocomposite use is it suppresses the formation of crystalline domains at an extremely low Li^+ concentration ($O^-: Li^+ = 1,000:1$ as well as low nanoparticle loading ~ 0.2 vol% SWNTs) and without compromising the mechanical properties of the solid electrolytes [33]. Previously Edman and coworkers [11] reported that inclusion of small amount of C_{60} in the complex of PEO and $LiCF_3SO_3$ salts ($O^-: Li^+: C_{60} = 300:20:1$) reduces the degree of PEO crystallinity at ambient temperature. They have shown that C_{60} does not only act as an effective structure-breaking agent, but also helps to stabilize PEO/Li salt complex at high temperature. Undoubtedly the interfacial area between the polymer and nanoparticles is a governing factor behind the structure-breaking roles of the nanoparticles. The state of nanotube dispersion is also crucial since the bundling of the nanotubes will decrease the polymer–nanoparticle interfacial area. However, a three-dimensional network of electron-conducting CNT in PEO cannot be used as electrolyte materials since it will result in the transport of electrons. To overcome this challenge, some of the possible solutions are to (a) use insulating (nonmetallic) CNTs for PEO-based electrolyte preparation, (b) functionalize the CNT surface using a nonconducting group (e.g., alkyl chains), or (c) align the tube in conducting plane to break the electron pathway. Recently, Ouyang and

coworkers [141] have demonstrated \sim three times enhancement of PEO/LiClO₄ ionic conductivity (at 20 °C) within the presence of \sim 2.5 wt% pristine MWNTs. In this case, the carboxylic group-functionalized MWNTs, in addition to suppressing PEO crystallinity, assisted in dissociating LiClO₄ through Lewis acid–Lewis base interaction. Interestingly, high loading of MWNTs does not further improve ionic conductivity probably due to poor dispersion.

Another use of CNT and PEO/Li salt mixture is in CNT-based field-effect transistors (FET). Liu and coworkers fabricated single-walled carbon nanotube-based field-effect transistors using solid electrolyte (PEO and LiClO₄) as gating materials [142]. The SWNT–FETs demonstrated strong gate–channel coupling with improved device characteristics compared with back-gated devices. A single SWNT when placed between two metal electrodes exhibits p-type behavior. It is generally considered to be a result of atmospheric oxygen adsorption on the tube sidewall. After application of PEO/LiClO₄ mixture on the top of the device, it gets converted to n-type FET. The p-type to n-type FET transition stems from either donation of an electron to SWNTs from lone pair electron in oxygen atom of PEO or the atmospheric oxygen, adsorbed by tube gets dissolved in bulk PEO matrix and no longer contribute in SWNT doping. The use of a strong electron acceptor, such as DDQ (2,3-dichloro-5,6-dicyanobenzoquinone) to PEO/LiClO₄ mixture, again turns the FET to a p-type device [142]. It shows that the transport type of the devices can be easily controlled through doping [142, 143]. High gate efficiencies, low voltage of operation, and absence of hysteresis make PEO/LiClO₄-based gates as an effective candidate to analyze transport process and to prepare SWNT-based FET [144]. These devices, while cost-effective, are mostly suitable for applications without demanding speed requirements. Finally, an excellent review on this topic is available elsewhere [145].

6.2 Electrospinning

Electrospinning is widely used to prepare ultrathin polymer nanofiber with consistent diameter ranging from \sim 3 nm to 1 μ m. The process generates a three-dimensional porous network or random mat of polymer nanofiber with high aspect ratio and specific surface area which find many applications including as nanosensor, filter membrane, and tissue engineering scaffolding [146]. Electrospinning of polyethylene oxide from different solvents such as DI water, chloroform, isopropanol–water mixture, etc., are reported in the literature [147–151]. Electrospun PEO fibers are used for microelectronic wiring interconnects [152], collagen–PEO composites are widely used for tissue engineering scaffolding [13] and wound healing [153, 154], and polyaniline–PEO blends are used as conducting fibers [149, 155].

Utilizing biocompatibility of PEO and multifunctionality of CNTs, nanotube-based PEO electrospun nanocomposites are suitable candidates for sensor and biomedical applications. The presence of CNT renders the device to be electrically conducting (PEO is a non-electron-conducting polymer) as well as mechanically robust. Cohen and coworkers attempted to create both SWNTs and MWNTs

embedded oriented PEO nanofiber by electrospinning [156, 157]. Due to sink-like flow in a wedge, initially randomly oriented CNTs in polymer solution (solvent is a mixture of DI water and ethanol) gradually orient along the streamline and retain the directionality in the polymer-embedded nanofiber. As a result, in final product, CNTs display excellent orientation along the fiber direction. For MWNTs [156], the nanotubes are embedded in nanofiber mostly as individual elements. However, there are cases where MWNTs appear twisted, bent, and other irregularities which probably get carried over from the dispersion state in solution itself. Interestingly, the axial orientation of the PEO reduces significantly in these nanotube-embedded nanofibers. Small-angle X-ray scattering (SAXS) study shows that electrospun PEO crystals, in the absence of any CNT, get oriented with chain direction along the fiber axis. This is evident from strong equatorial reflection of (120) plane (in PEO unit cell, c -axis is the chain axis). For MWNTs embedded PEO system, isotropic (120) plane reflection is observed indicating random orientation. In the same study, when performed in the presence of SWNTs [157], well-dispersed and separated nanotubes get embedded and aligned. The only difference, for SWNTs, is that PEO chains maintain their high order of axial orientation.

Gorga and coworkers [158, 159] performed detailed mechanical and electrical characterization of electrospun MWNT–PEO nanofibers. A conducting random mat (diameter ~ 100 – 200 nm) is formed which exhibits conductivity above the percolation threshold ~ 0.35 wt% of the MWNTs. The conductance increased by a factor of 10^{12} and reached a plateau at the saturation loading zone (~ 1.0 wt%) [158]. Further, using core–sheath fabrication technology, coaxial nanofiber having pure PEO as the core and PEO doped with MWNTs in the sheath are also produced [159]. The advantage of core–sheath structure is that you obtain the same electrical conductivity at ~ 10 times less MWNT loading compared to the random mat. Also due to superior dispersion state in the core–sheath structure, significant improvement in mechanical properties is also observed [159]. For MWNTs and polyaniline (PANI)/PEO blend-based random mats, a surprising transition in conductivity is observed in I–V measurements [150]. At low voltage, a linear I–V characteristic is observed which turns unstable at voltage ~ 7.0 V. This transition is closely related to the self-heating of MWNTs which alters the localization length in the composite nanofiber. This type of conducting nanofibers can be used in chemical and biosensors which require a high sensitivity.

6.3 Biological Applications

For the past few years, considerable efforts have been directed to explore CNT applications in biological and biomedical applications, both in vivo and in vitro [160]. Surface-modified nanotubes are used for ultrasensitive detection of biological species. Other potential application areas are resistance to nonspecific binding of biomolecules, biological detection (electrical nanosensor), or as contrast agent for bioimaging. In most of the biological applications, SWNTs are modified by either (a) noncovalently using phospholipid (PL)-PEG or (b) covalently by

PEGylation of $-COOH$ groups on oxidized nanotubes generated by refluxing in nitric acid. In both cases, the SWNTs are water soluble, and serum-stable nanotubes are nontoxic and biocompatible. Noncovalent adsorption of phospholipid (PL) molecules with PEG chains renders nanotubes water soluble. Two alkyl chains in the PL bind with SWNTs' sidewall due to strong van der Waals and hydrophobic interactions, and dangling PEG chains make this hybrid water soluble. A cleavable disulfide linkage with PEG chains ensures the whole system as an excellent biological cargo for a wide range of molecules including nucleic acids and proteins [161].

These functionalized nanotubes can adsorb a wide variety of aromatic molecules including drugs like doxorubicin or daunorubicin forming "forest-scrub"-like assembly [162]. These complexes are stable in physiological buffers but exhibit a fast release in acidic environment which make them ideal candidate for in vivo drug release. It is also found that the drug adsorption and release depends on nanotube diameter and the release kinetics is inversely related to the tube diameter [162]. A similar strategy has been exploited to develop SWNT-PEO-based hybrid biomaterial with ultralong blood circulation ($t_{1/2} = 22.1$ h) [163]. PEG-grafted branched polymer such as poly(γ -glutamic acid) or poly(maleic anhydride-*alt*-1-octadecene) can be noncovalently attached to the SWNTs' sidewall. Noncovalent addition enables SNWTs to retain their intrinsic physical properties including fluorescence and Raman scattering which later can be exploited for bioimaging. These materials show excellent stability in aqueous solution over a wide pH and temperature range and have potential use in drug delivery (slow kinetics) and imaging.

Finally, in spite of several lab-scale biological and biomedical applications of CNT-based PEO nanocomposites, considerable debate exists on nanotube toxicity and potential side effects [164]. Nevertheless, the molecular level modification of carbon nanotubes using biocompatible polymers or other biological molecules opens up an entirely new and exciting research direction in biomedical and biotechnology applications, finally aiming to target and to alter the cellular behavior.

7 Concluding Remarks

In this book chapter, we discussed about different aspects of CNT-based PEO nanocomposites. Some of the discussions, for example, the dispersion strategy, characterization of the dispersion state, CNT network structure above the percolation threshold, or network structure-dominated linear and nonlinear viscoelastic properties, are quite universal and applicable for other polymer-CNT systems which demonstrate a weak attraction force between polymer and matrix. However, some of these effects, for example, nanotube dispersion route exploiting Li^+ ions, which exfoliates nanotube as well as create complexion with PEO, is only unique for this system. As a result, while for most of the polymeric system, CNTs act as a secondary nucleation site and accelerates the kinetics, for PEO it actually hinders

the crystallization process. In this case, nanotubes preferentially remain surrounded by amorphous part of the chain. Distant nucleation sites and transport barrier yield thinner PEO lamellae even when the overall crystallization kinetics is slow. A notable advantage of sluggish crystallization and reduced crystallinity of PEO chains is higher ionic conductivity at room temperature which is beneficial for their use as solid electrolytes in Li-ion batteries applications.

References

1. Balazs AC, Emrick T, Russell TP (2006) Nanoparticle polymer composites: where two small worlds meet. *Science* 314(5802):1107–1110
2. Krishnamoorti R, Vaia RA (2007) Polymer nanocomposites. *J Polym Sci B* 45:3252–3256
3. Winey KI, Vaia RA (2007) Polymer nanocomposites. *MRS Bull* 32(4):314–319
4. Iijima S (1991) Helical microtubules of graphitic carbon. *Nature* 354(6348):56–58
5. Tasis D et al (2006) Chemistry of carbon nanotubes. *Chem Rev* 106(3):1105–1136
6. Ajayan PM (1999) Nanotubes from carbon. *Chem Rev* 99(7):1787–1799
7. Saito R, Dresselhaus G, Dresselhaus MS (1998) Physical properties of carbon nanotubes. Imperial College Press, London
8. Edman L (2000) Ion association and ion solvation effects at the crystalline-amorphous phase transition in PEO-LiTFSI. *J Phys Chem B* 104(31):7254–7258
9. Edman L et al (2000) Transport properties of the solid polymer electrolyte system P(EO)(n) LiTFSI. *J Phys Chem B* 104(15):3476–3480
10. Edman L, Ferry A, Doeff MM (2000) Slow recrystallization in the polymer electrolyte system poly(ethylene oxide)(n)-LiN(CF₃SO₂)(2). *J Mater Res* 15(9):1950–1954
11. Edman L, Ferry A, Jacobsson P (1999) Effect of C-60 as a filler on the morphology of polymer-salt complexes based on poly(ethylene oxide) and LiCF₃SO₃. *Macromolecules* 32(12):4130–4133
12. Meyer WH (1998) Polymer electrolytes for lithium-ion batteries. *Adv Mater* 10(6):439–448
13. Ojha SS et al (2008) Fabrication and characterization of electrospun chitosan nanofibers formed via templating with polyethylene oxide. *Biomacromolecules* 9(9):2523–2529
14. Shi XF et al (2006) Injectable nanocomposites of single-walled carbon nanotubes and biodegradable polymers for bone tissue engineering. *Biomacromolecules* 7(7):2237–2242
15. Barraza HJ et al (2002) SWNT-filled thermoplastic and elastomeric composites prepared by miniemulsion polymerization. *Nano Lett* 2(8):797–802
16. Du FM, Fischer JE, Winey KI (2003) Coagulation method for preparing single-walled carbon nanotube/poly(methyl methacrylate) composites and their modulus, electrical conductivity, and thermal stability. *J Polym Sci B Polym Phys* 41(24):3333–3338
17. Mitchell CA, Krishnamoorti R (2007) Dispersion of single-walled carbon nanotubes in poly(epsilon-caprolactone). *Macromolecules* 40(5):1538–1545
18. Probst O et al (2004) Nucleation of polyvinyl alcohol crystallization by single-walled carbon nanotubes. *Polymer* 45(13):4437–4443
19. Krishnamoorti R (2007) Strategies for dispersing nanoparticles in polymers. *MRS Bull* 32(4):341–347
20. Moniruzzaman M, Winey KI (2006) Polymer nanocomposites containing carbon nanotubes. *Macromolecules* 39(16):5194–5205
21. Girifalco LA, Hodak M, Lee RS (2000) Carbon nanotubes, buckyballs, ropes, and a universal graphitic potential. *Phys Rev B* 62(19):13104–13110
22. Bahr JL et al (2001) Dissolution of small diameter single-wall carbon nanotubes in organic solvents? *Chem Commun* 2:193–194

23. Ausman KD et al (2000) Organic solvent dispersions of single-walled carbon nanotubes: toward solutions of pristine nanotubes. *J Phys Chem B* 104(38):8911–8915
24. Israelachvili J (1992) Intermolecular and surface forces, 2nd edn. Elsevier, New York
25. Dyke CA, Tour JM (2004) Covalent functionalization of single-walled carbon nanotubes for materials applications. *J Phys Chem A* 108(51):11151–11159
26. Dyke CA, Tour JM (2003) Solvent-free functionalization of carbon nanotubes. *J Am Chem Soc* 125(5):1156–1157
27. Banerjee S, Hemraj-Benny T, Wong SS (2005) Covalent surface chemistry of single-walled carbon nanotubes. *Adv Mater* 17(1):17–29
28. Bahr JL, Tour JM (2002) Covalent chemistry of single-wall carbon nanotubes. *J Mater Chem* 12(7):1952–1958
29. Mitchell CA et al (2002) Dispersion of functionalized carbon nanotubes in polystyrene. *Macromolecules* 35(23):8825–8830
30. Park C et al (2002) Dispersion of single wall carbon nanotubes by in situ polymerization under sonication. *Chem Phys Lett* 364(3–4):303–308
31. Putz KW et al (2004) Elastic modulus of single-walled carbon nanotube/poly(methyl methacrylate) nanocomposites. *J Polym Sci B Polym Phys* 42(12):2286–2293
32. Zhang XF et al (2003) Poly(vinyl alcohol)/SWNT composite film. *Nano Lett* 3(9):1285–1288
33. Chatterjee T et al (2005) Single-walled carbon nanotube dispersions in poly(ethylene oxide). *Adv Funct Mater* 15(11):1832–1838
34. Hough LA et al (2006) Structure of semidilute single-wall carbon nanotube suspensions and gels. *Nano Lett* 6(2):313–317
35. Yurekli K, Mitchell CA, Krishnamoorti R (2004) Small-angle neutron scattering from surfactant-assisted aqueous dispersions of carbon nanotubes. *J Am Chem Soc* 126(32):9902–9903
36. Clark MD, Subramanian S, Krishnamoorti R (2011) Understanding surfactant aided aqueous dispersion of multi-walled carbon nanotubes. *J Colloid Interface Sci* 354(1):144–151
37. Liang F et al (2004) A convenient route to functionalized carbon nanotubes. *Nano Lett* 4(7):1257–1260
38. Pedersen CJ (1967) Cyclic polyethers and their complexes with metal salts. *J Am Chem Soc* 89:7017–7036
39. Pedersen CJ (1988) The discovery of crown ethers. *Science* 241(4865):536–540
40. Park M et al (2011) Excellent dispersion of MWCNTs in PEO polymer achieved through a simple and potentially cost-effective evaporation casting. *Nanotechnology* 22(41):415703
41. Chatterjee T, Lorenzo AT, Krishnamoorti R (2011) Poly(ethylene oxide) crystallization in single walled carbon nanotube based nanocomposites: kinetics and structural consequences. *Polymer* 52(21):4938–4946
42. Shvartzman-Cohen R et al (2004) Selective dispersion of single-walled carbon nanotubes in the presence of polymers: the role of molecular and colloidal length scales. *J Am Chem Soc* 126(45):14850–14857
43. Szeleifer I, Yerushalmi-Rozen R (2005) Polymers and carbon nanotubes – dimensionality, interactions and nanotechnology. *Polymer* 46(19):7803–7818
44. Yerushalmi-Rozen R, Szeleifer I (2006) Utilizing polymers for shaping the interfacial behavior of carbon nanotubes. *Soft Matter* 2(1):24–28
45. Semaan C, Schappacher M, Soum A (2012) Dispersion of carbon nanotubes through amphiphilic block copolymers: rheological and dielectrical characterizations of poly(ethylene oxide) composites. *Polym Compos* 33(1):1–9
46. Moore VC et al (2003) Individually suspended single-walled carbon nanotubes in various surfactants. *Nano Lett* 3(10):1379–1382
47. Graff RA et al (2005) Achieving individual-nanotube dispersion at high loading in single-walled carbon nanotube composites. *Adv Mater* 17(8):980–984
48. Fagan JA et al (2006) Comparative measures of single-wall carbon nanotube dispersion. *J Phys Chem B* 110(47):23801–23805

49. Vaisman L, Marom G, Wagner HD (2006) Dispersions of surface-modified carbon nanotubes in water-soluble and water-insoluble polymers. *Adv Funct Mater* 16(3):357–363
50. Guth EJ (1945) Theory of filler reinforcement. *J Appl Phys* 16:20–25
51. Schaefer DW, Chen CY (2002) Structure optimization in colloidal reinforcing fillers: precipitated silica. *Rubber Chem Technol* 75(5):773–793
52. Garboczi EJ et al (1995) Geometrical percolation threshold of overlapping ellipsoids. *Phys Rev E* 52:519–528
53. Meincke O et al (2004) Mechanical properties and electrical conductivity of carbon-nanotube filled polyamide-6 and its blends with acrylonitrile/butadiene/styrene. *Polymer* 45(3):739–748
54. Potschke P, Fornes TD, Paul DR (2002) Rheological behavior of multiwalled carbon nanotube/polycarbonate composites. *Polymer* 43:3247–3255
55. Du FM et al (2004) Nanotube networks in polymer nanocomposites: rheology and electrical conductivity. *Macromolecules* 37(24):9048–9055
56. Potschke P et al (2004) Rheological and dielectrical characterization of melt mixed polycarbonate-multiwalled carbon nanotube composites. *Polymer* 45:8863–8870
57. Head DA et al (2003) Distinct regimes of elastic response and deformation modes of cross-linked cytoskeletal and semiflexible polymer networks. *Phys Rev E* 68:061907
58. Kharchenko SB et al (2004) Flow-induced properties of nanotube-filled polymer materials. *Nat Mater* 3(8):564–568
59. Brown JM et al (2005) Hierarchical morphology of carbon single-walled nanotubes during sonication in an aliphatic diamine. *Polymer* 46(24):10854–10865
60. Schaefer D et al (2003) Structure and dispersion of carbon nanotubes. *J Appl Crystallogr* 36:553–557
61. Schaefer DW et al (2003) Morphology of dispersed carbon single-walled nanotubes. *Chem Phys Lett* 375(3–4):369–375
62. Chatterjee T, Jackson A, Krishnamoorti R (2008) Hierarchical structure of carbon nanotube networks. *J Am Chem Soc* 130(22):6934–6935
63. Barker JG et al (2005) Design and performance of a thermal-neutron double-crystal diffractometer for USANS at NIST. *J Appl Crystallogr* 38:1004–1011
64. Glinka CJ et al (1998) The 30 m small-angle neutron scattering instruments at the National Institute of Standards and Technology. *J Appl Crystallogr* 31:430–445
65. Ortony JH et al (2011) Self-assembly of an optically active conjugated oligoelectrolyte. *J Am Chem Soc* 133(21):8380–8387
66. Kline SR (2006) Reduction and analysis of SANS and USANS data using IGOR Pro. *J Appl Crystallogr* 39:895–900
67. Beaucage G (1996) Small-angle scattering from polymeric mass fractals of arbitrary mass-fractal dimension. *J Appl Crystallogr* 29:134–146
68. Bauer BJ, Hobbie EK, Becker ML (2006) Small-angle neutron scattering from labeled single-wall carbon nanotubes. *Macromolecules* 39(7):2637–2642
69. Hough LA et al (2004) Viscoelasticity of single wall carbon nanotube suspensions. *Phys Rev Lett* 93(16):168102
70. Shih WH et al (1990) Scaling behavior of the elastic properties of colloidal gels. *Phys Rev A* 42(8):4772–4779
71. Philipse AP (1996) The random contact equation and its implications for (colloidal) rods in packings, suspensions, and anisotropic powders. *Langmuir* 12(5):1127–1133
72. Schmidt CF et al (1989) Chain dynamics, mesh size, and diffusive transport in networks of polymerized actin – a quasielastic light-scattering and microfluorescence study. *Macromolecules* 22(9):3638–3649
73. Duggal R, Pasquali M (2006) Dynamics of individual single-walled carbon nanotubes in water by real-time visualization. *Phys Rev Lett* 96(24):246104–246107
74. Li XL et al (2007) Langmuir-Blodgett assembly of densely aligned single-walled carbon nanotubes from bulk materials. *J Am Chem Soc* 129(16):4890–4891

75. Xie XL, Mai YW, Zhou XP (2005) Dispersion and alignment of carbon nanotubes in polymer matrix: a review. *Mater Sci Eng R-Rep* 49(4):89–112
76. Hussain F et al (2006) Review article: polymer-matrix nanocomposites, processing, manufacturing, and application: an overview. *J Compos Mater* 40(17):1511–1575
77. Sano M et al (2001) Self-organization of PEO-graft-single-walled carbon nanotubes in solutions and Langmuir-Blodgett films. *Langmuir* 17(17):5125–5128
78. Nativ-Roth E et al (2007) Physical adsorption of block copolymers to SWNT and MWNT: a nonwrapping mechanism. *Macromolecules* 40(10):3676–3685
79. Granite M et al (2011) Interactions between block copolymers and single-walled carbon nanotubes in aqueous solutions: a small-angle neutron scattering study. *Langmuir* 27(2):751–759
80. Meyer F et al (2011) Poly(ethylene oxide)-b-poly(L-lactide) diblock copolymer/carbon nanotube-based nanocomposites: LiCl as supramolecular structure-directing agent. *Biomacromolecules* 12(11):4086–4094
81. Sollich P (1998) Rheological constitutive equation for a model of soft glassy materials. *Phys Rev E* 58(1):738–759
82. Sollich P et al (1997) Rheology of soft glassy materials. *Phys Rev Lett* 78(10):2020–2023
83. Surve M, Pryamitsyn V, Ganesan V (2006) Universality in structure and elasticity of polymer-nanoparticle gels. *Phys Rev Lett* 96(17):177805–177808
84. Salaniwal S, Kumar SK, Douglas JF (2002) Amorphous solidification in polymer-platelet nanocomposites. *Phys Rev Lett* 89(25):258301
85. Hobbie EK (2010) Shear rheology of carbon nanotube suspensions. *Rheologica Acta* 49(4):323–334
86. Krishnamoorti R, Chatterjee T (2012) Rheology and processing of polymer nanocomposites. In: Kontopoulou M (ed) *Applied polymer rheology: polymeric fluids with industrial applications*. Wiley, Toronto, pp 153–178
87. Geng HZ et al (2002) Fabrication and properties of composites of poly(ethylene oxide) and functionalized carbon nanotubes. *Adv Mater* 14(19):1387–1390
88. Song YS (2006) Rheological characterization of carbon nanotubes/poly(ethylene oxide) composites. *Rheologica Acta* 46(2):231–238
89. Fukuda H, Kawata K (1974) On young's modulus of short fibre composites. *Fiber Sci Technol* 7:207–222
90. Halpin JC (1992) *Primer on composite materials analysis*. Technomic Publishing Company, Lancaster
91. Mori T, Tanaka K (1973) Average stress in matrix and average elastic energy of materials with misfitting inclusions. *Acta Metall* 21(5):571–574
92. Schaefer DW, Justice RS (2007) How nano are nanocomposites? *Macromolecules* 40(24):8501–8517
93. Trappe V, Weitz DA (2000) Scaling of the viscoelasticity of weakly attractive particles. *Phys Rev Lett* 85(2):449–452
94. Chatterjee T, Krishnamoorti R (2007) Dynamic consequences of the fractal network of nanotube-poly(ethylene oxide) nanocomposites. *Phys Rev E* 75(5):050403
95. Ferry JD (1980) *Viscoelastic properties of polymer*. Wiley, New York
96. Ninomiya K, Ferry JD (1959) Some approximate equations useful in the phenomenological treatment of linear viscoelastic data. *J Colloid Sci* 14:36
97. Ren JX, Krishnamoorti R (2003) Nonlinear viscoelastic properties of layered-silicate-based intercalated nanocomposites. *Macromolecules* 36(12):4443–4451
98. Berthier L (2003) Yield stress, heterogeneities and activated processes in soft glassy materials. *J Phys-Condens Matter* 15(11):S933–S943
99. Hobbie EK, Fry DJ (2006) Nonequilibrium phase diagram of sticky nanotube suspensions. *Phys Rev Lett* 97(3):036101–036104
100. Prasad V et al (2003) Universal features of the fluid to solid transition for attractive colloidal particles. *Faraday Discuss* 123:1–12

101. Chen M, Russel WB (1991) Characteristic of flocculated silica dispersions. *J Colloid Interface Sci* 141(2):564–577
102. Feng S et al (1984) Percolation on two-dimensional elastic networks with rotationally invariant bond-bending forces. *Phys Rev B* 30(9):5386–5389
103. Kantor Y, Webman I (1984) Elastic properties of random percolating systems. *Phys Rev Lett* 52(21):1891–1894
104. Arbabi S, Sahimi M (1993) Mechanics Of Disordered Solids. 1. Percolation On Elastic Networks With Central Forces. *Phys Rev B* 47(2):695–702
105. Sahimi M, Arbabi S (1993) Mechanics of disordered solids. 2. Percolation on elastic networks with bond-bending forces. *Phys Rev B* 47(2):703–712
106. Derooij R et al (1994) Elasticity of weakly aggregating polystyrene latex dispersions. *Phys Rev E* 49(4):3038–3049
107. Aoki Y et al (2001) Nonlinear stress relaxation of ABS polymers in the molten state. *Macromolecules* 34(9):3100–3107
108. Yurekli K et al (2001) Structure and dynamics of carbon black-filled elastomers. *J Polym Sci B Polym Phys* 39(2):256–275
109. Schmidt G, Nakatani AI, Han CC (2002) Rheology and flow-birefringence from viscoelastic polymer-clay solutions. *Rheologica Acta* 41(1–2):45–54
110. Zhang Q, Archer LA (2002) Poly(ethylene oxide)/silica nanocomposites: structure and rheology. *Langmuir* 18(26):10435–10442
111. Goel V et al (2006) Viscoelastic properties of silica-grafted poly(styrene-acrylonitrile) nanocomposites. *J Polym Sci B Polym Phys* 44(14):2014–2023
112. Larson RG (1999) The structure and rheology of complex fluids, 1st edn. Oxford University Press, New York
113. Chatterjee T, Krishnamoorti R (2008) Steady shear response of carbon nanotube networks dispersed in poly(ethylene oxide). *Macromolecules* 41(14):5333–5338
114. Whittle M, Dickinson E (1997) Stress overshoot in a model particle gel. *J Chem Phys* 107(23):10191–10200
115. Axford SDT (1996) Theoretical calculations on Smoluchowski kinetics: perikinetic reactions in highly aggregated systems. *Proc R Soc Lond A Math Phys Eng Sci* 452(1953):2355–2368
116. Axford SDT (1996) Non-preserving cluster size distributions in the initial stages of orthokinetic aggregation. *J Chem Soc-Faraday Trans* 92(13):1007–1015
117. Bhattacharyya AR et al (2003) Crystallization and orientation studies in polypropylene/single wall carbon nanotube composite. *Polymer* 44(8):2373–2377
118. Haggemueller R, Fischer JE, Winey KI (2006) Single wall carbon nanotube/polyethylene nanocomposites: nucleating and templating polyethylene crystallites. *Macromolecules* 39:2964–2971
119. Mitchell CA, Krishnamoorti R (2005) Non-isothermal crystallization of in situ polymerized poly(epsilon-caprolactone) functionalized-SWNT nanocomposites. *Polymer* 46(20):8796–8804
120. Chatterjee T et al (2007) Hierarchical polymer-nanotube composites. *Adv Mater* 19(22):3850–3853
121. Jin J, Song M, Pan F (2007) A DSC study of effect of carbon nanotubes on crystallisation behaviour of poly(ethylene oxide). *Thermochimica Acta* 456(1):25–31
122. Abraham TN et al (2008) Rheological and thermal properties of poly(ethylene oxide)/multiwall carbon nanotube composites. *J Appl Polym Sci* 110(4):2094–2101
123. Goh HW et al (2003) Crystallization and dynamic mechanical behavior of double-C-60-end-capped poly(ethylene oxide)/multi-walled carbon nanotube composites. *Chem Phys Lett* 379(3–4):236–241
124. Hoffman JD (1982) Role of reputation in the rate of crystallization of polyethylene fractions from the melt. *Polymer* 23(5):656–670

125. Hoffman JD (1983) Regime-iii crystallization in melt-crystallized polymers – the variable cluster model of chain folding. *Polymer* 24(1):3–26
126. Hoffman JD (1986) Onset of chain folding in low-molecular-weight poly(ethylene oxide) fractions crystallized from the melt. *Macromolecules* 19(4):1124–1128
127. Hoffman JD, Miller RL (1988) Test of the reptation concept – crystal-growth rate as a function of molecular-weight in polyethylene crystallized from the melt. *Macromolecules* 21(10):3038–3051
128. Huang XD, Goh SH (2001) Crystallization of C-60-end-capped poly(ethylene oxide)s. *Macromolecules* 34(10):3302–3307
129. Takahashi Y, Tadokoro H (1973) Structural studies of polyethers, $-(\text{CH}_2)_m\text{-O})_n\text{X}$. Crystal Structure of Poly(ethylene oxide). *Macromolecules* 6:672–675
130. Zhu L et al (2000) Crystallization temperature-dependent crystal orientations within nano-scale confined lamellae of a self-assembled crystalline-amorphous diblock copolymer. *J Am Chem Soc* 122(25):5957–5967
131. Strobl GR, Schneider M (1980) Direct evaluation of the electron-density correlation-function of partially crystalline polymers. *J Polym Sci B Polym Phys* 18(6):1343–1359
132. Kuppa V, Manias E (2002) Computer simulation of PEO/layered-silicate nanocomposites: 2. Lithium dynamics in PEO/Li⁺ montmorillonite intercalates. *Chem Mater* 14(5):2171–2175
133. Strawhecker KE, Manias E (2003) Crystallization behavior of poly(ethylene oxide) in the presence of Na plus montmorillonite fillers. *Chem Mater* 15(4):844–849
134. Priftis D et al (2009) Surface modification of multiwalled carbon nanotubes with biocompatible polymers via ring opening and living anionic surface initiated polymerization. Kinetics and crystallization behavior. *J Polym Sci A Polym Chem* 47(17):4379–4390
135. Shieh YT et al (2005) Crystallization, melting and morphology of PEO in PEO/MWNT-g-PMMA blends. *Polymer* 46(24):10945–10951
136. Croce F et al (1998) Nanocomposite polymer electrolytes for lithium batteries. *Nature* 394(6692):456–458
137. Song JY, Wang YY, Wan CC (1999) Review of gel-type polymer electrolytes for lithium-ion batteries. *J Power Sources* 77(2):183–197
138. Berthier C et al (1983) Microscopic investigation of ionic-conductivity in Alkali-metal salts poly(ethylene oxide) adducts. *Solid State Ion* 11(1):91–95
139. Fullerton-Shirey SK, Maranas JK (2009) Effect of LiClO₄ on the structure and mobility of PEO-based solid polymer electrolytes. *Macromolecules* 42(6):2142–2156
140. Yue R et al (2009) Suppression of crystallization in a plastic crystal electrolyte (SN/LiClO₄) by a polymeric additive (polyethylene oxide) for battery applications. *Polymer* 50(5):1288–1296
141. Zhou D, Mei XG, Ouyang JY (2011) Ionic conductivity enhancement of polyethylene oxide-LiClO₄ electrolyte by adding functionalized multi-walled carbon nanotubes. *J Phys Chem C* 115(33):16688–16694
142. Lu CG et al (2004) Polymer electrolyte-gated carbon nanotube field-effect transistor. *Nano Lett* 4(4):623–627
143. Siddons GP et al (2004) Highly efficient gating and doping of carbon nanotubes with polymer electrolytes. *Nano Lett* 4(5):927–931
144. Ozel T et al (2005) Polymer electrolyte gating of carbon nanotube network transistors. *Nano Lett* 5(5):905–911
145. Koh J et al (2008) Nanotube-based chemical and biomolecular sensors. *J Mater Sci Technol* 24(4):578–588
146. Huang ZM et al (2003) A review on polymer nanofibers by electrospinning and their applications in nanocomposites. *Compos Sci Technol* 63(15):2223–2253
147. Deitzel JM et al (2001) The effect of processing variables on the morphology of electrospun nanofibers and textiles. *Polymer* 42(1):261–272

148. Deitzel JM et al (2001) Controlled deposition of electrospun poly(ethylene oxide) fibers. *Polymer* 42(19):8163–8170
149. MacDiarmid AG et al (2001) Electrostatically-generated nanofibers of electronic polymers. *Synth Met* 119(1–3):27–30
150. Shin MK et al (2008) Enhanced conductivity of aligned PANi/PEO/MWNT nanofibers by electrospinning. *Sens Actuators B-Chem* 134(1):122–126
151. Shin YM et al (2001) Experimental characterization of electrospinning: the electrically forced jet and instabilities. *Polymer* 42(25):9955–9967
152. Theron A, Zussman E, Yarin AL (2001) Electrostatic field-assisted alignment of electrospun nanofibres. *Nanotechnology* 12(3):384–390
153. Huang L, Apkarian RP, Chaikof EL (2001) High-resolution analysis of engineered type I collagen nanofibers by electron microscopy. *Scanning* 23(6):372–375
154. Huang L et al (2001) Engineered collagen-PEO nanofibers and fabrics. *J Biomater Sci Polym Ed* 12(9):979–993
155. Norris ID et al (2000) Electrostatic fabrication of ultrafine conducting fibers: polyaniline/polyethylene oxide blends. *Synth Met* 114(2):109–114
156. Dror Y et al (2003) Carbon nanotubes embedded in oriented polymer nanofibers by electrospinning. *Langmuir* 19(17):7012–7020
157. Salalha W et al (2004) Single-walled carbon nanotubes embedded in oriented polymeric nanofibers by electrospinning. *Langmuir* 20(22):9852–9855
158. McCullen SD et al (2007) Morphological, electrical, and mechanical characterization of electrospun nanofiber mats containing multiwalled carbon nanotubes. *Macromolecules* 40(4):997–1003
159. Ojha SS et al (2008) Characterization of electrical and mechanical properties for coaxial nanofibers with poly(ethylene oxide) (PEO) core and multiwalled carbon nanotube/PEO sheath. *Macromolecules* 41(7):2509–2513
160. Liu Z et al (2009) Carbon nanotubes in biology and medicine: in vitro and in vivo detection, imaging and drug delivery. *Nano Res* 2(2):85–120
161. Kam NWS, Liu Z, Dai HJ (2005) Functionalization of carbon nanotubes via cleavable disulfide bonds for efficient intracellular delivery of siRNA and potent gene silencing. *J Am Chem Soc* 127(36):12492–12493
162. Liu Z et al (2007) Supramolecular chemistry on water-soluble carbon nanotubes for drug loading and delivery. *Acs Nano* 1(1):50–56
163. Prencipe G et al (2009) PEG branched polymer for functionalization of nanomaterials with ultralong blood circulation. *J Am Chem Soc* 131(13):4783–4787
164. Lam CW et al (2006) A review of carbon nanotube toxicity and assessment of potential occupational and environmental health risks. *Crit Rev Toxicol* 36(3):189–217

Alina Pruna

Contents

1	Introduction	336
2	Corrosion Protection	338
3	CNT-Based Composites for Corrosion Applications	340
3.1	Introduction	340
3.2	Metal–CNT Composites	341
3.3	Conductive Polymer–CNT Composites	349
4	Conclusions	355
	References	356

Abstract

Corrosion is known as one of the most significant reasons of degradation in industrial parts and therefore the methods of reducing corrosion and wear costs are being greatly investigated. Under this aspect, the focus is now shifting from synthesis to manufacture of advanced coatings having improved properties. Thanks to their exceptional morphological, electrical, thermal, and mechanical characteristics, carbon nanotubes (CNTs) represent an extremely attractive alternative for corrosion applications. Therefore, addition of CNTs to composites has been indicated to improve corrosion resistance based on the chemically inert nature of CNTs, their filling up of the voids in the coatings or by changing the protection mechanism to cation transport as in the case of conducting polymers. This chapter reviews on exploitation of CNTs as an alternative to enhance the efficiency of anticorrosion coatings with emphasis in the development of metal–CNT and conducting polymer–CNT composite coatings.

A. Pruna

University Bucharest, Bucharest – Magurele, Romania

Institute of Materials Technology, University Politecnica of Valencia, Valencia, Spain

e-mail: apruna@itm.upv.es; ai.pruna@gmail.com

Keywords

Carbon nanotubes • Composite • Corrosion • Polarization • Impedance spectroscopy • Molecular modeling

1 Introduction

Even if mankind had taken advantage of nanosized structures since very long time, the “nanotechnology” term was first introduced by N. Taniguchi in 1974 [1]. Nanostructured materials are known to exhibit outstanding mechanical and physical properties, thanks to their extremely fine grain size and high grain boundary volume fraction. Among these materials, carbon nanotubes (CNTs) are exceptional ones having unique mechanical, electric, electronic, thermal, and magnetic properties that made them the subject of many investigations. Their synthesis has been triggered by the discovery of buckminsterfullerene – a closed cage of 60 carbon atoms often referred to as bucky ball – just a few years later. First to be reported were the almost concentric multiwall carbon nanotubes (c-MWCNTs) synthesized via the electric-arc technique in 1991 [2], and 2 years later, the single-wall carbon nanotubes (SWCNTs) were simultaneously reported by Iijima and Ichihashi [3] and Bethune et al. [4].

Single-walled nanotubes (SWCNTs) are nano-objects consisting of a graphene sheet rolled up into a cylindrical tube, while multiwalled ones refer to an array of nanotubes with various arrangements within filamentary morphology: they can be disposed concentrically (c-MWCNTs), or the wrapped graphenes can form an angle with the nanotube axis (h-MWCNTs). A particular feature of both c-MWCNTs and h-MWCNTs is the so-called bamboo texture (perpendicularly oriented graphenes to the nanotube axis) resulting in bc-MWCNTs or bh-MWCNTs.

The terms of tube chirality or helicity are employed to describe the atomic structure of nanotubes, e.g., the chiral angle, θ , determines the amount of “twist” in the tube (Fig. 14.1). The CNTs chirality has a significant impact on their properties. In particular, tube chirality is known to have a strong effect on the electronic properties of CNTs: they can be either metallic or semiconducting, depending on this parameter [5, 6]. The reason for the high resistance of CNTs to deformations is given by their symmetric structure that results into a strong bonding between the carbons of the graphene sheet. Various theoretical and experimental results in the literature have reported tensile strength of SWCNTs 20 times higher than that of steel [7], extremely high tensile modulus: MWCNTs showed 1 TPa [8] and SWCNTs – 1.3 TPa [9], while the elastic modulus of diamond is 1.2 TPa. Yakobson et al. showed that CNTs are remarkably resilient, sustaining extreme strain with no signs of brittleness or plasticity [10]. In addition to the exceptional mechanical properties associated with CNTs, they also exhibit superior thermal and electric properties: thermal stability up to 1,500–1,800 °C in inert atmosphere [11], thermal conductivity about twice as high as diamond, and electric-current-carrying capacity 1,000 times higher than copper wires [12].

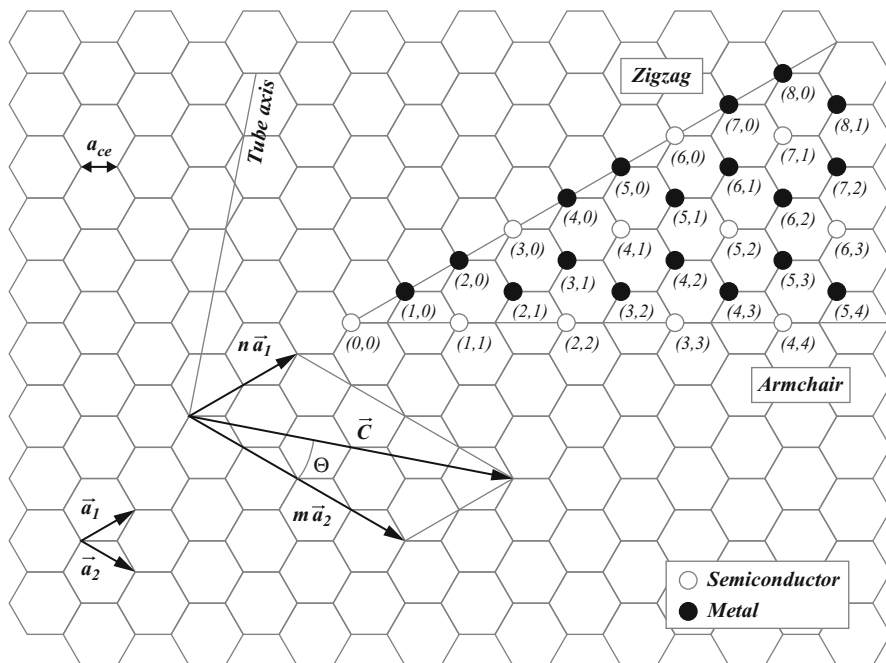


Fig. 14.1 Chiral vector and chiral angle (θ) definition for a (2, 4) nanotube on graphene sheet. The chiral angle θ is defined as the angle between chiral vector and the zigzag axis [5]

Depending on the synthesis methods, defects can be introduced in the CNTs structure. This will lead to the formation of localized double bonds between the carbon atoms involved in the defect (instead of these electrons participating in the delocalized electron cloud above the graphene as usual) and therefore to enhanced chemical reactivity of CNTs [13]. In comparison with SWCNTs, the reactivity of h-MWCNTs is intrinsically higher, due to the occurrence of accessible graphene edges at the nanotube surface. As a function of their reactivity, functionalization of CNTs can be achieved by chemical oxidation (by which carboxylic, carbonyl, and/or hydroxyl functions are introduced) and further functionalization reactions or by direct addition to the graphene-like surface of the nanotubes.

Since carbon nanotubes were discovered, there have been a variety of production techniques: arc discharge [2], laser ablation [14], gas-phase catalytic growth from carbon monoxide [15], and chemical vapor deposition (CVD) from hydrocarbons [16]. Provided the production cost is sufficiently low, a large number of applications are available for CNTs. Specific applications for which CNTs are required to have preferred properties necessitate further understanding and improved control of the physical and chemical nature of the processing conditions. For the composite application of CNTs, large quantities of nanotubes are

required, but the scale-up limitations of the arc discharge and laser ablation techniques make the cost of nanotube-based composites prohibitive. Moreover, purification steps are required to separate the CNTs from the impurities produced as catalyst particles, amorphous carbon, and non-tubular fullerenes. These limitations have motivated the development of gas-phase techniques, such as chemical vapor deposition (CVD), by which CNTs are formed by the decomposition of a carbon-containing gas.

Although the applications of CNTs have had a limited success on the market till recently, the fabrication of these nanoscale materials has known significant progress in various aspects of synthesis. For example, the large-scale manufacturing of MWCNTs by CVD registered reasonable success, while for the SWCNTs, the amounts are still restricted to gram quantities. Anyhow, as the focus is now shifting from synthesis to manufacture of useful structures and coatings having greater wear and corrosion resistance, CNTs represent an extremely attractive option for corrosion applications, thanks to their exceptional morphological, electrical, thermal, and mechanical characteristics.

This chapter is not intended to be comprehensive, as the focus is on exploiting the exceptional properties of carbon nanotubes towards the development of anticorrosion coatings.

2 Corrosion Protection

When metal surfaces are subjected to corrosive environments – atmospheric, underground/soil waste, acid, alkaline, and combination of these – irreversible disintegration is generally produced in the form of oxides, hydroxides, and salts. Beside the loss of aesthetic finishing, ion dissolution could have harmful effects on the environment. Moreover, the degradation of structural strength induced by corrosion results in increasing fatigue crack growth rate. In addition to these effects, corrosion also causes lost production, inefficient operation, wastage of valuable resources, product contamination, high maintenance, cost of corrosion control chemicals, serious damages, and even plant shutdowns. One of most important aspects related to corrosion is the high cost of detecting and repairing/replacing the corroded components.

The protection methods commonly used till present include alloying with inhibiting elements, protective coatings, anodic and cathodic protection, and corrosion inhibitors. Alloying by addition of inhibiting components, nonmetallic (e.g., P, N or Si) or metallic (e.g., Cr or Mo), results in the blocking of the active areas of the alloy surface by the formation of adsorbed intermediate products and therefore leading to the decrease of corrosion rate.

Addition of small amounts of corrosion inhibitors (inorganic, organic, and surfactant inhibitors and mixed material inhibitors) to a medium proved to be favorable for the control, reducing, or prevention of the reactions between a metal and its surroundings. The mechanism for corrosion inhibition is complex and depends on the formation of mono- or multidimensional protective layers

on the metal surface for which either physisorption or chemisorption of the inhibitor on the metal surface may be involved. The efficiency of an inhibitor depends on the ability to transfer water from the metal surface, to interact with anodic or cathodic reaction sites in order to retard the oxidation and reduction corrosion reaction, and also to prevent transportation of water and corrosion-active species on the metal surface. Therefore, the selection of an appropriate inhibitor is complicated due to the specificity of inhibitors and great variety of corrosion related applications.

With the aim of replacing the corrosion inhibitors based on chromates which are prone to produce environmental pollution and health hazard, intensive research was devoted to designing of new coatings with passivating nature. A satisfactory barrier between the metal and its environment can be provided by metallic, inorganic, organic, or composite-based anticorrosion coatings. Cathodic metallic coatings are based on corrosion-resistant metals (e.g., Ni, Cu, noble metals such as Au, Pt, Ag) which are more noble than underlying metal surface in corrosive medium (are cathodic with respect to the protected metal). On the other hand, anodic coatings can be composed from Zn, Cd, or Al which show more negative stationary potential in corrosive medium.

There is great number of research works devoted to protective coatings such as noble metals and conducting polymers. However, depending on the application, the cost of noble metal coatings appears too high. The alternative of ceramic coatings shows good thermal and electrical properties and higher resistance to oxidation, corrosion, erosion, and wear than metals in high-temperature environments. In automotive industry, the incorporation of suitable ceramic nanoparticles in paints resulted in effective scratch protection against normal wear and tear, beside maintaining the glossy aspect of the paint. The hydrophobic coatings based on ceramic nanoparticles such as nano-titania exhibit excellent corrosion resistance in wet environments as underlined by Shen et al. [17].

Thanks to their interesting mechanical, optical, and thermal properties, the organic–inorganic hybrid coatings attracted high interest being considered the most promising candidates for corrosion inhibition especially for their inert and nontoxic nature. Depending on the type and proportion of the constituting phases, the resulting material exhibits unique properties by combining those of the components. Sarmiento et al. showed that the inorganic phase plays an important role in promoting the adhesion between the film and metal substrate, while the organic one seals the film structure [18].

Conducting polymers attracted much interest in this field, as well, due to their electrochemical properties and mixed ionic/electronic conductivity properties [19]. Improved properties such as increased electroactivity have already been reported for conducting polymers doped with nanosized particles [20]. Therefore, by combining the remarkable properties of conducting polymers with the thermal, chemical, and mechanical stability of CNTs, a very attractive alternative should result in developing advanced composite coatings.

Generally, the assessment of corrosion can be done by visual inspection and chemical and electrochemical techniques. The chemical method refers to

the immersion of the given material in the test solution and the gravimetric measurement of the metal loss in the corrosive medium, by the equation:

$$\Delta W = W_1 - W_2 \quad (1)$$

where W_1 and W_2 represent the weight of metal before and after exposure to the corrosive solution, respectively. Further, the inhibition efficiency (% *IE*) can be calculated from the following equation:

$$\% IE = [1 - (\Delta W_{\text{inh}}/\Delta W_{\text{free}})] \times 100 \quad (2)$$

where ΔW_{inh} and ΔW_{free} represent the weight losses of metal per unit area in absence and presence of inhibitor.

Electrochemical techniques such as potentiostatic and potentiodynamic polarization studies or cyclic voltammetry can be performed for the determination of corrosion current density, i_{corr} , which is a measure of corrosion rate [21]. The potentiodynamic methods measure the passivation behavior of a metal in an electrochemical system. Cyclic polarization can quantitatively measure pitting of the metal, and galvanic corrosion techniques can be employed to examine quantitatively corrosion reactions between two dissimilar metals that are in a corrosive environment.

Stern–Geary method, for example, is performed by extrapolation of anodic and cathodic Tafel lines of charge transfer controlled corrosion reactions to a point which gives i_{corr} and the corresponding corrosion potential (E_{corr}) [22]. Taking into account these parameters, corrosion rate is obtained. Further, inhibition efficiency is calculated by equation:

$$\% IE = [1 - (i_{\text{corr (inh)}}/i_{\text{corr (free)}})] \times 100 \quad (3)$$

Another electrochemical monitoring process is called electrochemical impedance spectroscopy (EIS) [23]. These measurements can provide information regarding the kinetics of an electrochemical corrosion system.

3 CNT-Based Composites for Corrosion Applications

3.1 Introduction

Increased interest for CNTs application in corrosion field has been showed in recent years. For example, Tan and colleagues [24] used MWCNTs and Nafion to fabricate a corrosion sensor by using traditional solution-casting technique. Their impedance measurements indicated high sensitivity of the electrical resistance to the corrosion reaction. Baghalha et al. studied the effect of a CNT/surfactant-based nanofluid on the corrosion rate of copper [25]. They observed that copper corrosion rate increased with employed surfactant concentration while in the presence of CNTs of up to 1 %, the copper corrosion current density sharply dropped, being

explained by the high mass transport resistance of the CNT film formed on the copper surface.

The high thermal and mechanical stability, lightweight, and strength of CNTs together with their chemical inert nature triggered many researchers to use them as reinforcement for a variety of materials, including polymers, metals/alloys, and ceramics in order to endow the advanced composite materials with one or more of their exceptional features. Nevertheless, the complexity of composite applications of CNTs is very high as these require control of many parameters such as nanotubes dispersion, the control of the nanotube/matrix bonding, the densification of bulk composites, nanotubes alignment, surface reactivity, and aspect ratio of the reinforcement. For example, mechanical strengthening of the composites is enhanced when isolated SWCNTs are employed while MWCNTs are beneficial for tailoring of the nanotube/matrix interface with respect to the matrix. Various mechanical and chemical means were reported for improving dispersion of CNTs in polymers. As-produced CNTs are held together in bundles formed by individual CNTs, but due to evidences of diminished mechanical and electrical properties of the composites, another approach is studied according to which the aligned CNTs are to be coated with polymer rather than randomly entangled in the matrix.

Although the field of CNT-based hybrid materials presents great potential, it is still not much exploited due to the mentioned issues. Statistically speaking, the majority of papers from the existing works till now deal with CNT reinforcement of polymers, even if metal–CNT composites attracted increased interest starting 2003. Even if the existing references only give some partial and simple researches on CNT-based composites, the applicability of CNTs in corrosion field has been demonstrated [26, 27]. The following sections will overview the current works on metal–CNT and conducting polymer–CNT composites applied in corrosion field.

3.2 Metal–CNT Composites

Till now, the reports on metal–CNT composites dealt with Al, Cu, Mg, Ni, Ni–P, Ti, WC–Co, and Zr metal matrices. The materials were prepared by various techniques such as standard powder metallurgy [28–30], electrodeposition [26, 31–33] and electroless deposition [34–37], plasma spray forming [38–40], spark plasma sintering [41–43], nanoscale-dispersion method [44], the rapid solidification technique [45], or CVD [46, 47].

The main challenges in the synthesis processes of CNT-based composites are the homogeneity of CNTs dispersion in the metal matrix, the interfacial bond strength between CNTs and the matrix, and the chemical and structural stability of CNTs. It is well known that the elastic modulus, strength, and thermal properties of a composite are related to the volume fraction of the reinforcement added. Therefore, homogeneous dispersion of the reinforcement results beneficial to the composite properties. Since blending of large volume fractions of CNTs proved to be detrimental for the mechanical properties of the composites [48–50], other methods have been proposed to uniformly distribute CNTs such as ball milling [51]

combined with hot extrusion to achieve CNT alignment [52], molecular-level mixing method [42], or spray drying [53]. The quality of CNT reinforcement is also an important issue, and various studies on the statistical distribution of horizontal and vertical separation distances between the peripheries of the nanotubes and spatial distribution based on transmission electron microscopy or binary scanning electron microscopy images were proposed for the calculation of clustering parameter [54, 55]. As obvious, a good quality of CNTs dispersion in the matrix would be given by a large dispersion parameter and small clustering one. Various studies showed that the presence of CNT clusters hinders the electron transfer through the metal–CNT composite [49], increases the coefficient of thermal expansion [56], and reduces thermal conductivity of composites as their density decreases due to the increase in pore volume [29]. Addition of CNTs to metal composites has been indicated to improve also the corrosion resistance based on the chemically inert nature of CNTs and their filling up of the voids in the coatings impeding the initiation of localized corrosion. In the following section, some examples of corrosion application of CNT–metal composites are presented.

Zn–CNT Composites. For long time, zinc metal has been used for plating steel articles, thanks to its high corrosion resistance [57, 58]. Anyhow, there is a drawback in the appearance of the white rust on the surface of the articles exposed to corrosive environments. The need to control the white zinc formation required post-plating treatments such as chromating, but this is environmentally dangerous, and therefore various methods have been studied in order to avoid its usage. One of the methods employs electro-active compounds with N- or S-containing functional groups [59, 60] as they can form protecting complexes at zinc surface. Another method is coating the articles with composites of zinc with ceramic, metal oxides, or polymers. Recently, Praveen et al. found the use of CNTs attractive for achieving performant composite coatings [27]. He studied the corrosion behavior of a composite obtained by co-electrodeposition method from a bath containing 1 g L^{-1} of MWCNTs and zinc precursor. Acid treatment of nanotubes, together with the usage of cetyl trimethyl ammonium bromide as cationic surfactant and mechanical stirring, was employed for achieving high dispersion of MWCNTs in the composite material. The addition of MWCNTs resulted in a less porous coating and proved to be beneficial to reducing the corrosion rate of the coating (see Fig. 14.2), which was in agreement with weight loss measurements and electrochemical tests. As an indication of corrosion resistance, salt spray test was performed and revealed a delay of 42 h in the appearance of white rust at the surface of the coating containing MWCNTs with respect to the pure zinc one of 20 h. A physical barrier afforded by the MWCNTs to the corrosion process by filling in pores in the composite was accounted for the increase in corrosion resistance.

Although the literature is poor regarding these coatings, there is evidence of higher performance of CNT–Zn composite coatings, given the production at large scale by the Tesla Nano Coatings company.

Ni–CNT Composites. The interesting properties such as high wear resistance, good ductility, and ferromagnetism exhibited by Ni made it an attractive material for use in composite coatings together with CNTs for applications in

Fig. 14.2 Variation of the corrosion rate with immersion time for Zn-coated and CNTs–Zn-coated samples in 3.5 % NaCl solution [27]

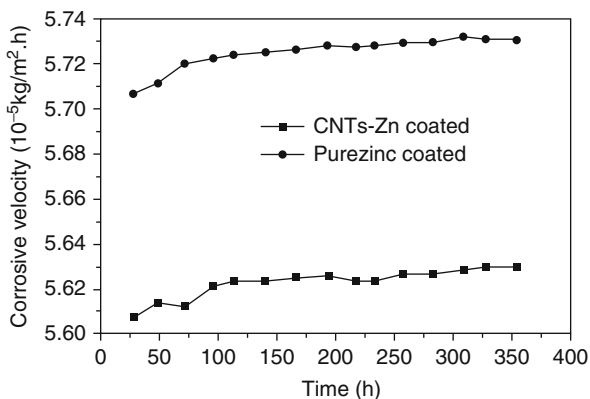
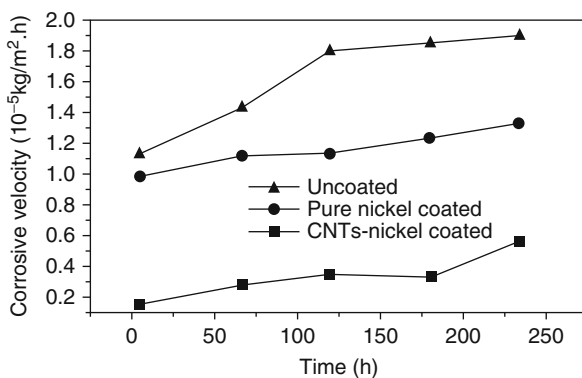


Fig. 14.3 Variation of the corrosion rate (mass loss) with immersion time for uncoated, Ni-coated, and CNTs–nickel-coated samples in 3.5 % NaCl solution [26]



wear-resistance materials, microelectromechanical systems, or corrosion-resistance coatings [31, 35, 61]. The studies on Ni–CNT composites generally deal with electrodeposited or electrolessly deposited materials. Improvement of mechanical properties such as increase of hardness of electrolessly deposited composite with 44 % upon addition of 2 vol.% CNTs [62] or tensile strength increment values of 320 % and 270 % following the addition of SWCNTs and MWCNTs, respectively, was reported [33]. Although the improvement of mechanical properties was generally evidenced, the influence of CNTs addition to the composite coatings on corrosion behavior has been reported with different results in different groups. For example, Chen and colleagues reported in 2001 on high wear resistance of electrodeposited Ni–CNTs composite [31]. In a later study, his group employed acid-treated MWCNTs obtained by catalytic decomposition of acetylene over Ni–Mg–O catalysts and cetyl trimethyl ammonium bromide (CTAB) as cationic surfactant in order to achieve high dispersion degree of CNTs [26]. According to their mass loss results, a higher corrosion resistance was obtained for Ni–CNTs composite (see Fig. 14.3). Resistance to pitting corrosion was also reported upon CNTs addition to the composites. Chen and his group explained their findings on

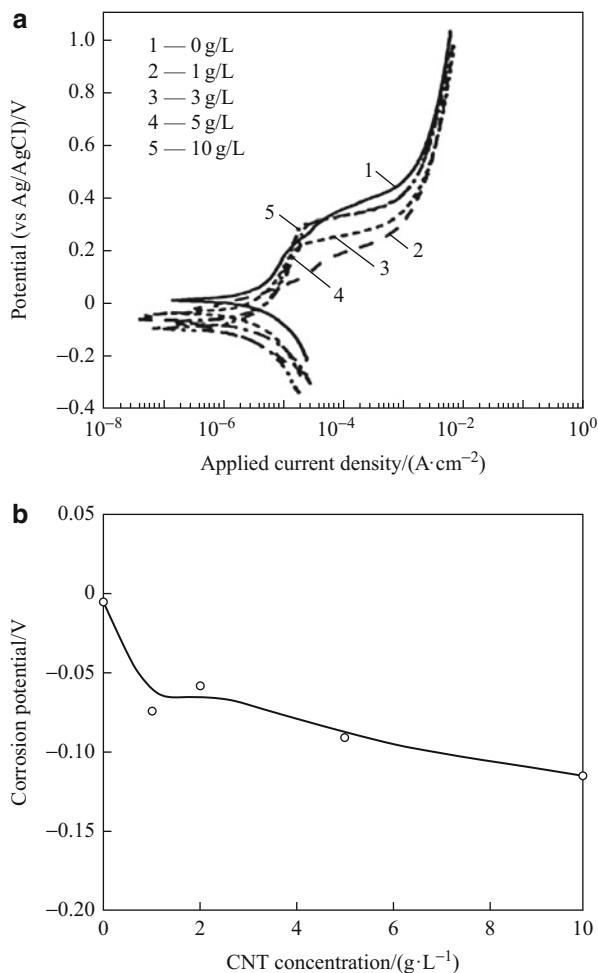
the basis of a homogeneous distribution of the deeply embedded CNTs in the matrix that resulted in the formation of microgalvanic cells thereby inhibiting localized corrosion. For further insight, Guo et al. investigated the effect of 0.6 g L^{-1} addition of sodium dodecyl sulfate (SDS) or CTAB on the co-electrodeposition of Ni with $0.1\text{--}0.3 \text{ g L}^{-1}$ MWCNTs (that were obtained by catalytic decomposition of acetylene over Fe–Mo/ Al_2O_3) [63]. Although surfactants are usually employed to improve dispersion of nanoparticles, they also affect the polarization of CNTs and subsequently the coatings properties [64, 65]. Therefore, according to Guo's results, SDS addition to the deposition bath slightly decreased the CNT content in the composite while CTAB increased it. As CNT concentration in the bath increased, the deposited composites were more homogeneous, and the (220) growth plane was changed to (200) and (111) planes, respectively, when SDS or CTAB were used. Regarding the corrosion resistance of the composite coatings, CTAB proved to be detrimental while SDS slightly improved it.

Recently, Kim et al. presented a study on the effect of CVD-produced CNTs concentration of up to 10 g L^{-1} on the hardness and corrosion characteristics of the Ni composites obtained by electrodeposition method [66]. They showed that increasing CNT concentration in the deposition bath resulted in increased amount of CNTs in the composite of increased porosity. Hardness characteristic of the coatings was found to be independent of the CNT concentration or the electrodeposition current used. Although the previous studies on corrosion resistance of Ni–CNT composite reported beneficial effect of CNTs addition [27, 57], Kim's results showed that corrosion resistance decreases with CNT concentration (see Fig. 14.4 depicting the effect of CNTs concentration on corrosion potential). It was suggested that the poor adhesion of CNTs to Ni matrix caused the increased porosity and therefore higher area was exposed to corrosive environment resulting in poor resistance.

Ni–P–CNT Composites. Ternary Ni–P alloys received a growing interest due to the higher quality and longer lifetime they can provide to the articles used in various industries [67]. Addition of CNTs to Ni–P composites proved to be advantageous for better corrosion performance [68–71], and according to Chen and his colleagues, it increases the wear resistance and lowers the friction coefficient [72]. For example, the weight loss and polarization results obtained by Zhao et al. on electrolessly deposited Ni–P–CNT composites indicated that the previously oxidized, purified, and ball-milled CNTs are beneficial to enhancing the corrosion resistance of the composite coating [73]. Also Alishahi et al. reported in a recent study the effect of ball-milled CVD-grown MWCNTs on the corrosion behavior of the electrolessly deposited Ni–P–CNT composites [74]. According to their results, the higher corrosion resistance observed for Ni–P–MWCNT deposited onto Ni–P-coated substrate could be explained on the basis of an enhanced chemical passivation in the presence of MWCNTs that results in a thick protecting phosphorous-rich film or on the accounts of a physical barrier afforded by the formation of a MWCNT layer at the coating/electrolyte interface.

Heat treatment is an important parameter known to affect the mechanical and electrochemical properties of electroless Ni–P composites [75–78]. For example,

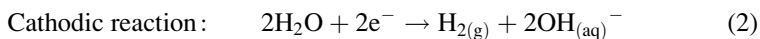
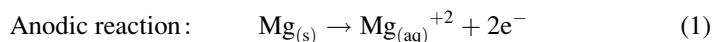
Fig. 14.4 Polarization curves (a) and corrosion potentials (b) of Ni–CNT composite coatings electrodeposited in solutions with different CNT concentrations [66]



Rabizadeh et al. reported improved corrosion resistance for heat-treated nanocrystalline Ni–P coating due to decreased grain boundaries [78]. Coating density and structure improvement upon proper heat treatment justified the enhanced corrosion resistance obtained by Huang and colleagues for Ni–P–PTFE–SiC composite coatings [79]. Therefore, the concern on heat-treatment effects on the properties of Ni–P–CNT composites has been raised as well [80, 81]. Chen et al. reported on higher wear resistance of Ni–P–CNT coatings after a heat treatment at 400 °C for 2 h on the accounts of Ni₃P hard phases formed in Ni matrix [80]. The electrochemical measurements presented by Zarebidaki et al. in a recent work indicate a better corrosion protective ability of heat-treated Ni–P–CNT coatings explained as follows [81]: when heat treatment is performed at 200 °C for 2 h, the better corrosion resistance exhibited by the composites is related to the reduced grain

boundaries that result in a denser and less porous coating. With increasing the temperature to 400 °C, for 1 h, formation of Ni₃P second phases starts, but grain growth takes over it and corrosion resistance of the coatings increases. After further increase of the temperature to 600 °C, for 15 min, the formation of second phases of Ni₃P continues and become dominant, therefore the coating shows poorer corrosion resistance with respect to the one treated at 400 °C.

Mg–CNT Composites. Automotive industry, electronics, or biodegradable implants are some of the fields where lightweight materials based on magnesium alloys have been applied [82]. Anyhow, due to the very low standard electrode potential of magnesium, the Mg-based alloys are prone to galvanic corrosion, and therefore, special coating techniques are necessary. The following equations present the reaction of Mg in aqueous solutions [83]:



According to these equations, the corrosion product is constituted of Mg(OH)₂.

Relatively few studies reported on the incorporation of MWCNTs as a filler material in the Mg alloy matrix as an alternative to improving their corrosion resistance [84, 85]. Beside the improvement of the elastic modulus and tensile strength of Mg alloy composites with 25 and 11 %, respectively, following the addition of short, linear, and well-ordered MWCNTs [86] by powder blending, Endo et al. [84] showed that also water repellence characteristic of the Mg AZ91D alloy surface increased with MWCNTs concentration in the composite due to the fact that most of the nanotube content was mainly localized at the surface. The group claimed that no trace of corrosion was indicated for an addition of 5 wt% of MWCNTs as a result of reinforcement of the oxide layer with MWCNTs.

Regardless of this first study, corrosion of Mg alloy was reported to deteriorate upon addition of CNTs [87–90]. Aung et al. fabricated alloys with 0.3 and 1.3 wt% CVD-grown MWCNTs using the disintegrated melt deposition technique [87]. He showed that increased content of MWCNTs resulted into higher corrosion rate and higher hydrogen evolution rate. Turhan and his group studied the corrosion behavior of Mg alloy reinforced with 0.1 wt% MWCNTs [91] with and without a pre-dispersion treatment. His polarization results confirmed Aung's ones that presence of MWCNTs enhanced hydrogen evolution reaction, but it had little effect on the anodic dissolution kinetics.

Further, their measurements showed the corrosion behavior of the alloy is strongly dependent on the MWCNTs dispersion: the electrochemical impedance results showed that presence of highly dispersed MWCNTs increased significantly the dissolution rate of the alloys [89] due to the creation of a larger number of local galvanic couples on the surface which would result into an increase of the electrochemically active surface area (see Fig. 14.5 presenting electrochemical impedance

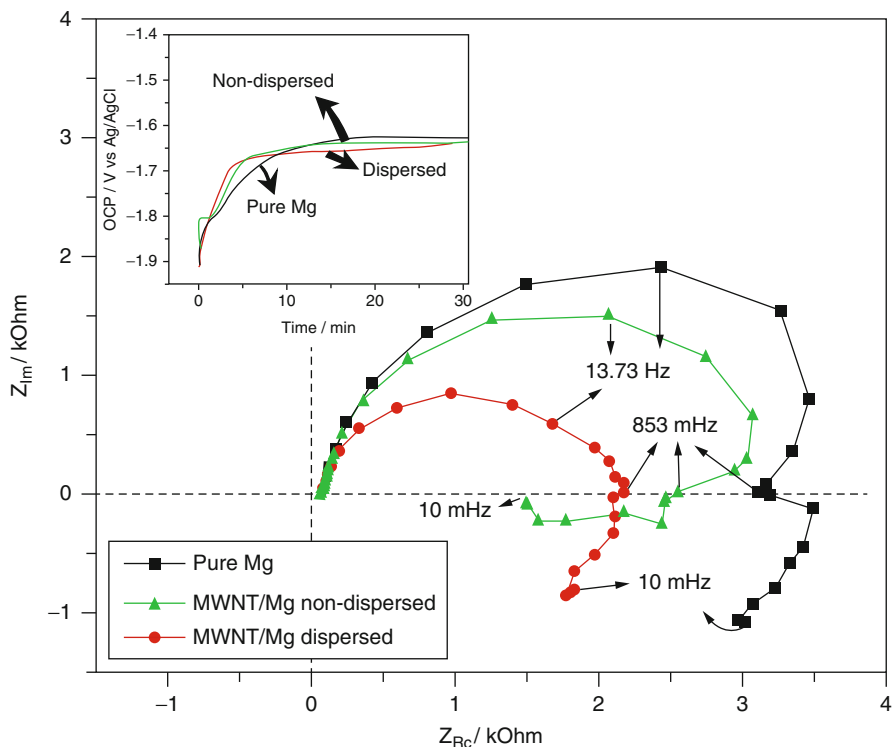


Fig. 14.5 Nyquist plots of pure Mg and Mg–MWCNTs composites in 3.5 % NaCl after 30 min at open circuit potential. Inset: open circuit potential versus time curves of pure Mg and Mg–MWCNTs composites in 3.5 % NaCl [91]

spectra corresponding to Mg and Mg–MWCNTs composite). Focused Ion Beam cut images were taken to observe the corrosion product layers formed during 90 min of exposure in 3.5 % NaCl. The dispersed MWCNTs–Mg alloys presented the thinnest corrosion product layer, due to the higher corresponding hydrogen evolution reaction rate. The morphology of the corrosion products was influenced by the dispersion level of CNTs as well: higher dispersion resulted in smoother film (see Fig. 14.6). For a better exemplification, Fig. 14.6d presents a schematic illustration of dependence of the anodic and cathodic reactions on the CNTs dispersion suggested by Turhan [91].

Other Metals–CNT Composites. Research into incorporation of CNTs has been pursued in other metal composites, as well, such as Pb–Sn or Zn–Ni ones [92, 93], having possible applications as antifriction layers in sliding bearings or protection coatings in marine environment. Hu et al. used 2 g L^{-1} of purified acid-treated MWCNTs for the electrodeposition of Pb–Sn–CNT composites [93]. His measurements indicate higher corrosion resistance for the composite obtained in presence of MWCNTs, and this was explained by the creation of more nucleation sites which in turn results in composite coatings with smaller grain size and therefore more

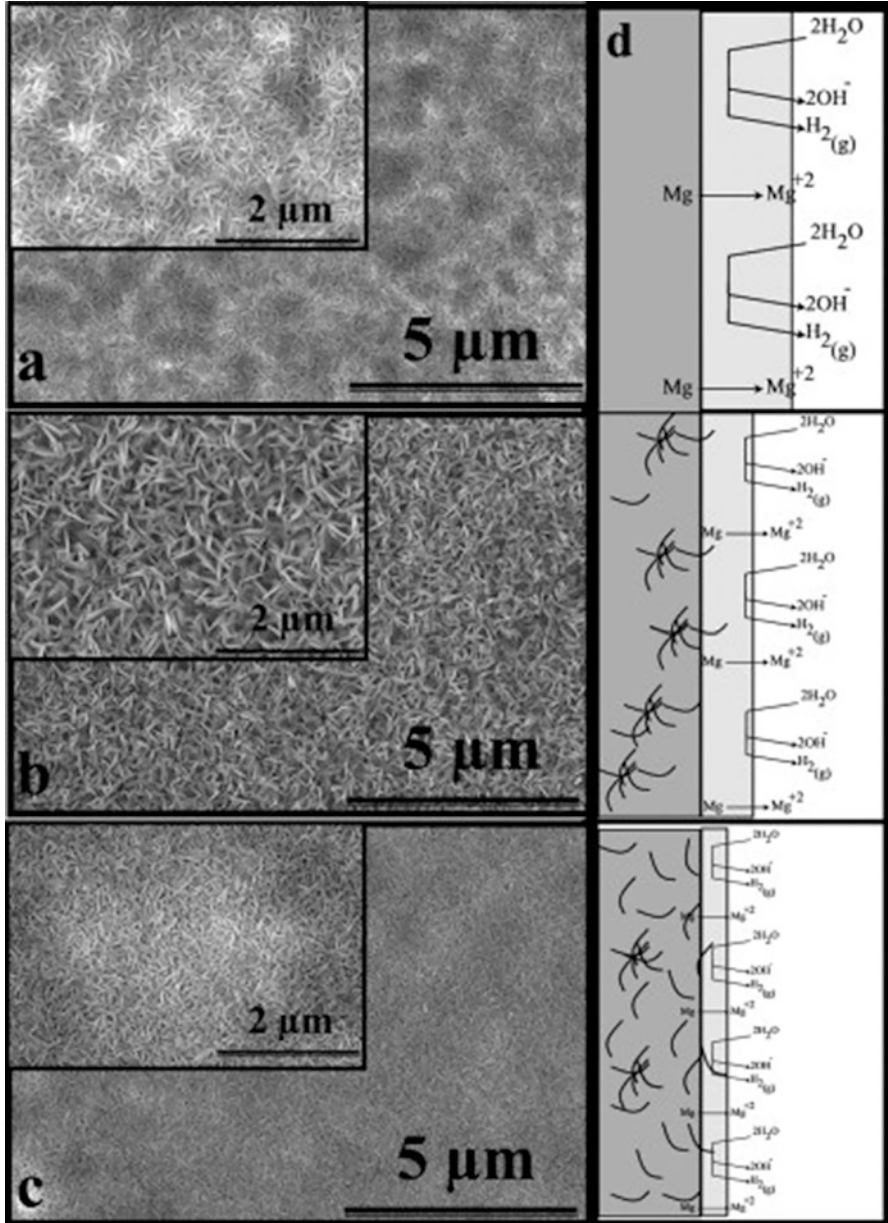


Fig. 14.6 SEM images of (a) pure Mg, (b) non-dispersed MWCNTs-Mg, and (c) dispersed MWCNTs-Mg after exposed in NaCl for 90 min. (d) Model showing the relationship between a, b, and c [91]

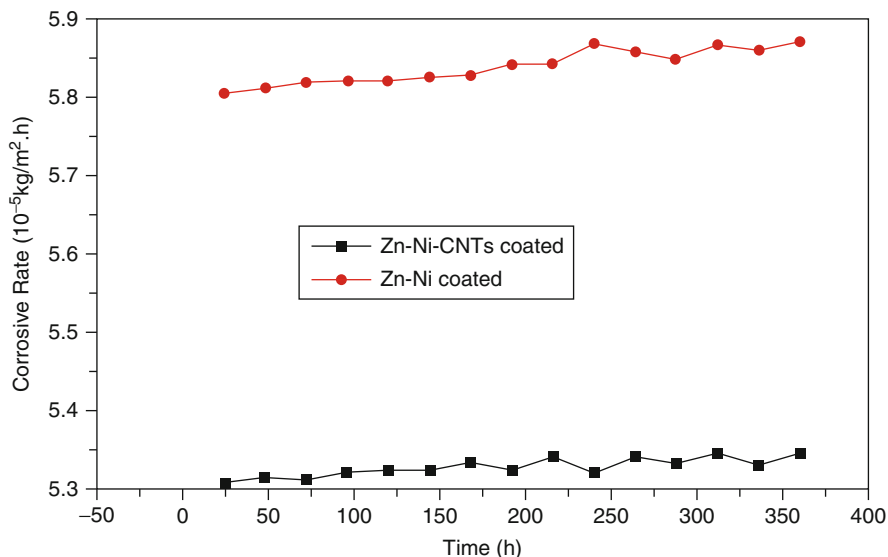


Fig. 14.7 Variation of the corrosion rate with immersion time for Zn–Ni- and Zn–Ni–CNT-coated samples in 3.5 wt% NaCl solution [92]

compact and able to inhibit localized corrosion. Praveen and his group reported on the corrosion behavior of Zn–Ni composite electrodeposited in the presence of 0.1–1 g L⁻¹ MWCNTs and 2 g L⁻¹ CTAB [92]. The presence of CNTs decreases corrosion rate of the composite with 9 % after exposure for 360 h in 3.5 % NaCl (see Fig. 14.7), and the white rust formation was delayed with 45 h, while in absence of CNTs, it appeared after 30 h.

3.3 Conductive Polymer–CNT Composites

Owing to their remarkable properties such as electrical conductivity, low cost, stability, nontoxicity, ease in synthesis, and doping primacy, conducting polymers gained particular interest in corrosion protection. The polymer groups of polypyrrole (PPy), polyaniline (PANI), polythiophene (PTh), and their derivatives are the mainly ones considered for corrosion protection of metals such as mild steel, zinc, or copper [94, 95].

The mechanisms commonly used to explain corrosion protection afforded by these materials are related to electronic barrier protection, corrosion inhibitor, and anodic or cathodic protection, e.g., the polymer film either isolates the metal surface from the environment by impeding the electron transfer from the metal through the passive layer, it forms a monomolecular layer at the surface of the metal able to

slow down corrosion rate, or it can result in the formation and stabilization of a passive oxide layer [96]. The electronic conductivity of these polymer films plays an important role not only in the galvanic coupling between the metal and the polymer but also for providing an interface at which the cathodic reaction can take place, thus maintaining the polymer in an oxidized state.

Electrodeposition (– by cyclic voltammetry, galvanostatic or potentiostatic techniques), paint blending, or casting techniques – are usually employed in order to achieve a conducting polymer film at the surface of a structure [94, 95, 97–99]. Oxidizable metals are more difficult to be electro-coated with polymers, as they are thermodynamically unstable and will dissolve before the electrodeposition of the polymer takes place. Thus, suitable electrochemical conditions have to be met in order to achieve electropolymerization at the electrode.

Besides specific deposition technique, the choice of the electrolyte and incorporation of dopants are required in order to improve the corrosion resistance, adhesion, wear resistance, and hardness properties of conducting polymer coatings. It is known that incorporation of nanoparticles in sol–gel systems not only increases their corrosion protection properties but it can also result in self-repairing pretreatment based on controlled release [100, 101]. In this context, Fe₃O₄ nanoparticle-doped PPy was reported to show better corrosion protection than un-doped polymer by Garcia et al. [102].

It was already reported that addition of CNTs to a polymer matrix may improve the electrical conductivity and mechanical properties of the composite [103]. Although many research works were devoted to CNT-doped polymers for achieving high-strength, lightweight, and high-performance composites, there are only few studies showing their advantages for corrosion protection. One of the main causes for limited studies is associated with entangled CNTs and poor interfacial interaction between CNTs and the polymer matrix. In order to facilitate the dispersion of CNTs, chemical or physical functionalization methods are usually performed, improving also the interfacial interactions between the CNTs and polymer matrix. The random orientation and alignment of CNTs has been reported to strongly affect various properties of composites [104]. Regarding the potential of CNTs for application in polymer nanocomposites, one must fully understand not only the mechanical properties but also the interactions at the nanotube/matrix interface. For example, a strong nanotube/polymer interface has been reported through selectively functionalizing CNT ends and midsection, followed by chemically binding to the polymer [105].

Although little research work has been performed on the corrosion application of polymer–CNT composites, there is evidence of protection afforded by CNTs while more work has to be performed in order to understand the corrosion protection mechanism. Recently, Lee et al. conducted potentiodynamic measurements to study the corrosion resistance of CNTs-covered 304 stainless steel cores as PEM fuel cell bipolar plates [106]. Their results showed that the use of CNTs obtained by direct growth by catalytic decomposition of C₂H₂ resulted in a good corrosion resistance of the sandwiched structure under PEM fuel cell operating conditions.

In order to understand the electronic barrier protection of CNTs, Streevatsa and colleagues considered a multilayered layout in their study [107]. The acid-treated

CNTs were functionalized with polyethyleneimine (PEI) and polyvinylpyrrolidone (PVP) to obtain n-type and p-type CNTs, respectively. Drop casting was employed to coat the AISI 4340 steel substrate with CNT-based coatings in a controlled order. Their results showed that the coating order in the structures affects the corrosion protection properties. The authors suggested that the corrosion protection observed for the substrate/p/n configuration was obtained on the basis of on the electronic barrier across the p–n junction that prohibited the hydroxyl ions from reaching the substrate. Better corrosion protection was achieved when PEI- and PVP-functionalized CNTs were embedded in polymethyl methacrylate and polyurethane, respectively. The electrochemical tests, on the other hand, gave contradictory results: the double-layer capacitance of substrate/p/n structure was larger than for substrate/n/p one.

Polyaniline is a typical phenylene-based polymer having a chemical flexible–NH group in the polymer chain which was accounted for its protonation/deprotonation properties. Due to its environment stability, ease of synthesis, and redox cyclability, PANI has been widely employed in various applications. Modified CNT reinforcement of PANI exhibiting promising protection against corrosion of stainless steel was reported by Hermas et al. [123]. Later, Ionita et al. reported electrochemical results for PANI composites with SWCNTs and poly(m-aminobenzenesulfonic acid) (PABS)-functionalized SWCNTs [108]. Multistep coating structures obtained by water-dispersed SWCNTs drop casting onto the surface of OL 48–50 steel (previously electrodeposited with PANI layer) were investigated in 3.5 % NaCl environment. Recently, it was demonstrated that the ability to design coating components from the molecular level upward offers great potential for creating advanced coatings [109, 110]. Ionita and colleagues coupled molecular simulation approaches with electrochemical tests to enhance the understanding in agreement of mechanical properties and CNTs dispersion with corrosion protection properties. Therefore, following equilibration of 30 Å bulk models, virtual traction tests and dissipative particle dynamics (DPD) simulations were run to investigate the mechanical properties and dispersion of SWCNTs in the composites. The computational results showed an increase of elastic moduli of 50 % and 80 % upon the addition of SWCNTs and PABS–SWCNTs, respectively. The polarization measurements revealed a higher corrosion protection ability upon addition of PABS-functionalized SWCNTs to conductive PANI matrix than for nonfunctionalized SWCNTs. It can be said that the enhanced protection ability is related to the presence of functionalities on CNTs. Moreover, several works in the literature have reported on selective interaction of the CNTs with the quinoid ring of PANI [111] and on the enhanced chemical interaction of both the monomer and the polymer during its generation due to the presence of functional groups on CNTs [112]. Regarding the composites morphology, Ionita et al. reported that similar, uniform distribution of both types of SWCNTs was achieved according to the computed equilibrium structures obtained after a DPD simulation of 100,000 steps, in agreement with microscopy results of real samples. These results could be limited due to the fact that the microholes and inhomogeneities in the composite are not counted for in the computed models since these are very small, making necessary the implementation of larger models.

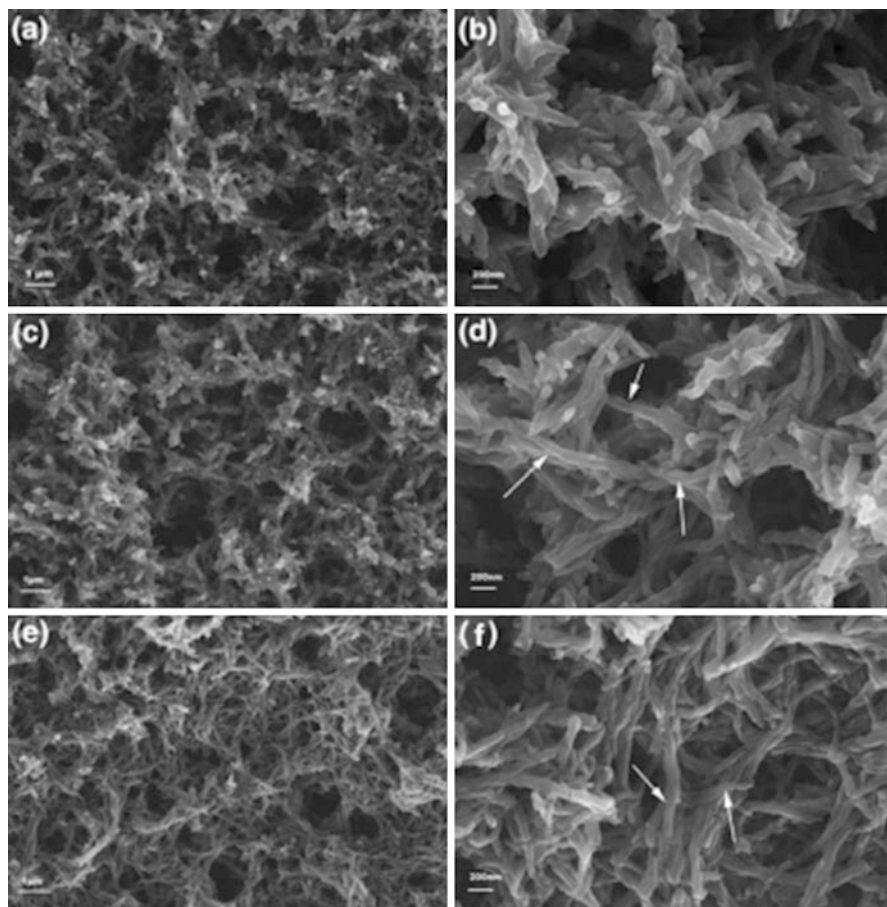


Fig. 14.8 SEM images of the surface of PANI and CNTs–PANI composite films: PANI (a, b), 0.3 % v/v CNT_c/PANI (c, d), and 0.3 % v/v CNT_{nm}/PANI (e, f) [113]

Martina et al. also reported on corrosion ability of co-electrodeposited PANI–CNT composite [113]. Two kinds of CNTs were employed: ones with diameter of 110–170 nm and length 5–9 μm , denoted CNT_c, and others with diameter of 30 nm and length 5–20 μm , denoted with CNT_{nm}. Triton-X 100 was used as surfactant to enhance CNTs dispersion in the deposition bath. The results obtained by the group showed that addition of CNTs to the deposition bath favors the monomer oxidation, a stronger catalytic effect being observed in the case of CNT_{nm} [114]. The authors suggested that CNTs and aniline strongly interact leading to charge stabilization, promoting the protonation of PANI, or that CNTs act as condensation nuclei promoting the polymer aggregation. In fact, the scanning microscopy results presented in Fig. 14.8 show that PANI was electrogenerated at the surface of CNTs, by wrapping them and confirming other

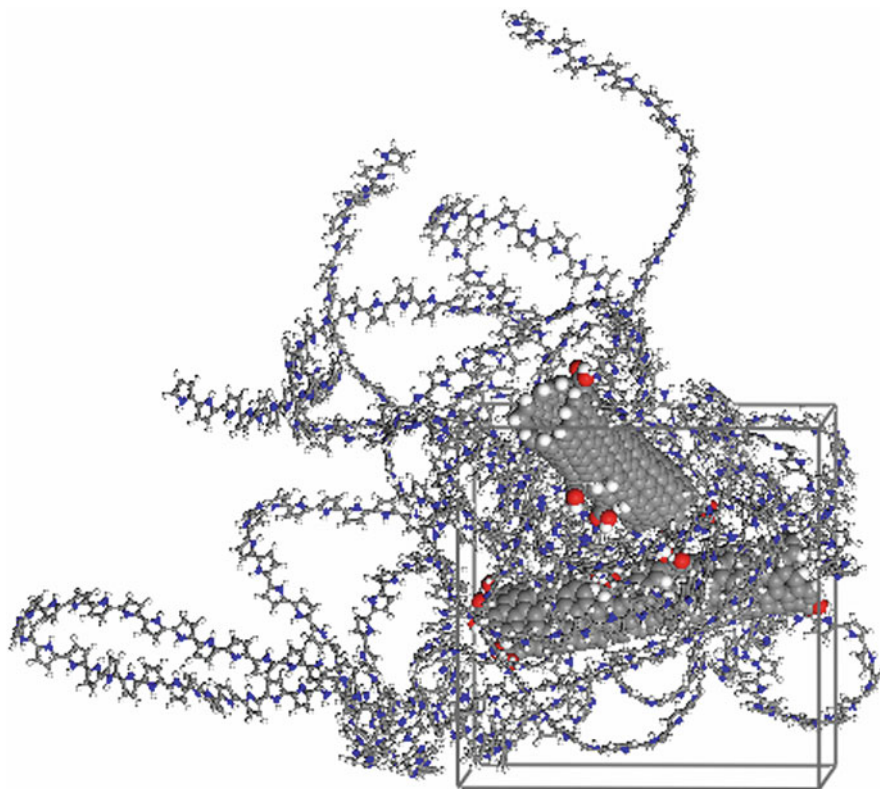


Fig. 14.9 PPy/CNT-CA bulk model after refinement stage [118]

reported results [112, 115]. From the electrochemical and subtractively normalized interfacial FT-IR results, it can be concluded that the addition of CNTs to PANI composites generally enhances the corrosion protection ability for AISI 304 while CNT_c proved better performance in impeding the diffusion of corrosion products to the substrate.

Among the conducting polymers, polypyrrole (PPy) is one of the most studied for corrosion inhibition of iron and steel [116, 117]. Ionita et al. reported on corrosion ability of PPy-CNTs composites obtained by galvanostatic co-electrodeposition of PPy in the presence of PABS-functionalized SWCNTs and carboxylic acid (CA)-functionalized SWCNTs in varying concentration in the range 0–10 mg L⁻¹ [118]. Atomistic molecular modeling technique was coupled to electrochemical and microscopy techniques in order to assess the correspondence between the mechanical properties, CNTs dispersion, and protection ability. Computational bulk models of about 40 Å in dimension containing about 5,000 atoms were designed by constructing a covalent bond between the CNT (5, 6) and PABS and CA groups, respectively. The molecular dynamics simulation resulted in random distribution of PPy chains and CNTs (see Fig. 14.9), while the

assessment of mechanical properties showed that increasing CNT concentration results in enhanced material stiffness. A concentration of about 5 % CNTs added to the composite resulted optimal for mechanical properties of the coatings and predicted Young's moduli values of 2.67 GPa for PPy and for PPy/CNT-CA, and PPy/CNT-PABS of 3.35–3.96 GPa and 4.15–4.61 GPa, respectively, showed better reinforcement obtained upon addition of PABS-functionalized SWCNTs. The reinforcing efficiency was suggested to rely on the differences in interaction energy between the differently functionalized SWCNTs and PPy. The experimental results showed that increasing CNT concentration leads to decreasing polymerization potential for the different systems. Regarding the corrosion protection, PPy-CNTs composites were reported to have higher ability due to the barrier property of PPy that is enhanced by the addition of CNTs, and therefore the electron transport through the coating gets hindered. The addition of PABS-functionalized SWCNTs resulted in better protection efficiency than CA-functionalized ones were into agreement with computational results.

In a recent work, Gergely et al. reported on the corrosion protection properties of alkyd paint coatings based on nanosized alumina, PPy, and MWCNTs (different types: pristine, poly(4-ammonium styrenesulfonic acid) (PSS) – modified and sulfonated ones) [119]. According to their results, improvement of corrosion protection ability has been observed upon addition of MWCNTs, and close interaction between PPy and MWCNTs and high dispersity are requisites for a good performance of the composites. Even if moderate barrier nature was observed, the enhanced redox activity and increased conductivity of doped PPy facilitated protection effectiveness of the composite coatings.

Another composite, namely, poly(*o*-phenylenediamine) (PoPD)-CNT composite, was also reported to have protection ability by Salam and colleagues [120]. Purified acid-treated CNTs were used in a 50 g L^{-1} concentration for the synthesis of PoPD-CNT composites by cyclic voltammetry technique. The results show that CNT addition increased the polymer deposition probably due to an increase of reaction sites number [112], since carboxylic and phenolic groups located at their surface lead to an increase of adsorption capacity for organic compounds. This polymer deposition enhancement was more significant in the case of SWCNTs than for MWCNTs. The composite coating proved efficiency in maintaining the steel substrate in passive state during immersion in acidic solution. The protection was assigned not only to barrier property of the coating but also to the electronic interaction.

The outstanding properties of aluminum made it an excellent choice for many applications, but in case of lithium ion batteries, the oxide layer formed at its surface suffers from localized corrosion thereby reduces the battery performance. By incorporation of negatively charged dopant, such as COOH-functionalized CNTs, in a polymer matrix, the ion transport mechanism is changed to cation-specific property, and together with the electrostatic repulsion against the electrolyte ions, a promising candidate for corrosion protection could be developed. A recent study reported on the use of MWCNTs coated with poly(ethylenedioxythiophene) (PEDOT) nanospheres for the protection of aluminum in LiPF_6 in

order to obtain high-performance lithium ion batteries [121]. Nanospheres of PEDOT were synthesized on COOH-functionalized MWCNTs using Cu₂O-assisted microemulsion polymerization. The MWCNTs–PEDOT ratio was found to greatly affect the size of formed PEDOT nanospheres. The MWCNTs coated with PEDOT nanospheres were showed to almost completely suppress aluminum corrosion. The enhanced efficiency was explained on the basis of a synergy of cation exchange PEDOT and the anion-repulsive pristine MWCNT surface resulting into cooperative electrostatic repulsion, thanks to which transport of PF₆[−] anions towards aluminum surface is slowed down and leads to negligible corrosion reaction within the potential range under examination (1.0–5.0 V vs. Li/Li⁺).

4 Conclusions

With great advancement of modern coatings, corrosion protection is still of great interest in research and development. According to this literature survey, the application of the CNT-based nanocomposite layers for the protection of metals is still in its infancy. Although careful handling is required and health risks associated with CNT exposure are to be taken into account [122], the few existing studies on corrosion protection afforded by CNTs showed some positive results, but still more work has to be performed in order to understand the corrosion protection mechanism. In order to realize the potential of CNT composite materials for application in corrosion protection, it is necessary to underline the most important issues:

- The excellent properties of CNTs must be balanced with reasonable costs.
- The quality of CNTs requires reliable characterization methods which are still under development.
- Dispersion and orientation of the CNTs should be better controlled in order to incorporate individual CNTs or at least relatively thin CNT bundles in the matrix.
- Simulations are recommended to determine whether the significant surface area of CNTs promotes interactions sufficient for load transfer between the phases of the composite.
- Better understanding on how interaction between the CNTs and matrix can enhance protection abilities against corrosion.

Despite of the problems encountered in the production of CNTs, PolyOne/Unidym, a leading global supplier of polymer materials, joined Tesla NanoCoatings Limited, Ohio, and US Army Engineer Research and Development Center, Construction Engineering Research Laboratory and started the fabrication of CNT-based Teslan coatings with the aim of creating innovative anticorrosion coatings for steel. This coating is an epoxy polyamide product having a reduced zinc content and added CNTs that allow zinc particles to remain in electric contact. The anticorrosion property is explained by the “cathodic protection mechanism in which the CNTs transfer electrons between the sacrificial metal and the protected metal.

Compared to zinc-rich systems, CNT-based coatings offer easier application and better corrosion protection. They are more environmentally tolerant than inherently conductive polymer (ICP) systems” (<http://www.unidym.com>).

In other words, nanotechnology gained an important role in the corrosion protection of metal, as nanoscale materials improve the corrosion protection ability with respect to the bulk materials. Taking into account the extensive research undergoing in the nanocoating field towards the incorporation of CNTs in anticorrosion coatings with enhanced properties, considerable improvement is expected for the overall performance of anticorrosion CNT-based coatings with positive effects in different industries such as marine or defense.

Acknowledgments Romanian Authority for Scientific Research – UEFISCDI (project no. PN-II-RU-PD-2012-3-0124) is gratefully acknowledged for financial support.

References

1. Taniguchi N (1974) On the basic concept of nanotechnology. In: Proceeding of the ICPE, Tokyo, Part II, pp 18–23
2. Iijima S (1991) *Nature* 354:56
3. Iijima S, Ichihashi T (1993) *Nature* 363:603
4. Bethune DS, Kiang CH, de Vries MS, Gorman G, Savoy R, Vazquez J, Beyers R (1993) *Nature* 363:605
5. Belin T, Epron F (2005) *Mater Sci Eng B* 119:105
6. Dresselhaus MS, Dresselhaus G, Eklund PC (1996) *Science of fullerenes and carbon nanotubes*. Academic Press, San Diego
7. Yu M-F, Lourie O, Dyer MJ, Moloni K, Kelley TF, Ruoff RS (2000) *Science* 287:637
8. Treacy MMJ, Ebbesen TW, Gibson JM (1996) *Nature* 381:678
9. Yao N, Lordie V (1998) *J Appl Phys* 84:1939
10. Yakobson BI, Samsonidze G (2000) *Carbon* 38:1675
11. Méténier K, Bonnamy S, Béguin F, Jourmet C, Bernier P, de la Chapelle LM, Chauvet O, Lefrant S (2002) *Carbon* 40:1765
12. Collins PG, Avouris P (2000) *Sci Am* 283:62
13. Monthieux M (2002) *Carbon* 40:1809
14. Rinzler AG, Liu J, Dai H, Nikolaev P, Huffman CB, Rodriguez-Macias FJ, Boul PJ, Lu AH, Heymann D, Colbert DT, Lee RS, Fischer JE, Rao AM, Eklund PC, Smalley RE (1998) *Appl Phys A* 67:29
15. Nikolaev P, Bronikowski MJ, Bradley RK, Fohmund F, Colbert DT, Smith KA, Smalley K (1999) *Chem Phys Lett* 313:91
16. Ren ZF, Huang ZP, Xu JW, Wang JH, Bush P, Siegal MP, Provencio PN (1998) *Science* 282:1105
17. Shen GX, Chen YC, Lin L, Lin CJ, Scantlebury D (2005) *Electrochim Acta* 50:5083
18. Sarmiento VHV, Schiavetto MG, Hammer P, Benedetti AV, Fugivara CS, Suegama PH, Pulcinelli SH, Santilli CV (2010) *Surf Coat Technol* 204:2689
19. Rout TK, Jha G, Singh AK, Bandyopadhyay N, Mohanty ON (2003) *Surf Coat Technol* 167:16
20. Maeda S, Armes SP (1994) *J Mater Chem* 4:935
21. Lu W-K, Basak S, Elsenbaumer RL (1998) Corrosion inhibition of metals by conductive polymers. In: Skotheim TA, Elsenbaumer RL, Reynolds JR (eds) *Handbook of conducting polymers*, 2nd edn. Marcel Dekker, New York, pp 881–920

22. Stern M, Geary AIJ (1957) *J Electrochem Soc* 104:56
23. Mansfeld F (1995) *ACH-Model Chem* 132:619
24. Tan A, Yong C, Joo J, Kang I (2011) Proceedings of the thermal and materials nanoscience and nanotechnology for structural health monitoring. Begell House, Antalya
25. Baghalha M, Kamal-Ahmadi M (2011) *Corr Sci* 53:4241
26. Chen XH, Chen CS, Xiao HN, Cheng FQ, Zhang G, Yi GJ (2005) *Surf Coat Technol* 191:351
27. Praveen BM, Venkatesha TV, Arthoba Naik Y, Prashantha K (2007) *Surf Coat Technol* 201:5836
28. Yang J, Schaller R (2004) *Mater Sci Eng A* A370:512
29. Shi XL, Yang H, Shao GQ, Duan XL, Yan L, Xiong Z, Sun P (2006) *Mater Sci Eng A* A457:18
30. He C, Zhao N, Shi C, Du X, Li J, Li H, Cui Q (2007) *Adv Mater* 19:1128
31. Chen XH, Peng JC, Li XQ, Deng FM, Wang JX, Li WZ (2001) *J Mater Sci Lett* 20:2057
32. Xu Q, Zhang L, Zhu J (2003) *J Phys Chem B* 107B:8294
33. Sun Y, Sun J, Liu M, Chen Q (2007) *Nanotechnology* 18:505
34. Chen WX, Tu JP, Wang LY, Gan HY, Xu ZD, Zhang XB (2003) *Carbon* 41:215
35. Chen X, Zhang G, Chen C, Zhou L, Li S, Li X (2003) *Adv Eng Mater* 5:514
36. Yang Z, Xu H, Shi Y-L, Li M-K, Huang Y, Li H-L (2005) *Mater Res Bull* 40:1001
37. Liu Y-M, Sung Y, Chen Y-C, Lin C-T, Chou Y-H, Ger M-D (2007) *Electrochem Solid-State Lett* 10:101
38. Laha T, Agarwal A, McKechnie T, Seal S (2004) *Mater Sci Eng A* 381:249
39. Balani K, Anderson R, Laha T, Andara M, Tercero J, Crumpler E, Agarwal A (2007) *Biomaterials* 28:618
40. Balani K, Zhang T, Karakoti A, Li WZ, Seal S, Agarwal A (2008) *Acta Mater* 56:571
41. Kim KT, Lee KH, Cha SI, Mo C-B, Hong SH (2004) *Mater Res Soc Symp Proc* 821:111
42. Cha SI, Kim KT, Arshad SN, Mo CB, Hong SH (2005) *Adv Mater* 17:1377
43. Kwon H, Estili M, Takagi K, Miyazaki T, Kawasaki A (2009) *Carbon* 47:570
44. Noguchi T, Magario A, Fukazawa S, Shimizu S, Beppu J, Seki M (2004) *Mater Trans* 45:602
45. Li YB, Ya Q, Wei BQ, Liang J, Wu DH (1998) *J Mater Sci Lett* 17:607
46. Goyal A, Wiegand DA, Owens FJ, Iqbal Z (2006) *J Mater Res* 21:522
47. Kim T, Mo YH, Nahm KS, Oha SM (2006) *J Power Sources* 162:1275
48. Tu JP, Yang YZ, Wang LY, Ma XC, Zhang XB (2001) *Tribol Lett* 10:225
49. Feng Y, Yuan HL, Zhang M (2005) *Mater Charact* 55:211
50. Nai SML, Wie J, Gupta M (2006) *Mater Sci Eng A* A423:166
51. Esawi A, Morsi K (2007) *Compos A* 38A:646
52. Choi HJ, Kwon GB, Lee GY, Bae DH (2008) *Scr Mater* 59:360
53. Bakshi SR, Singh V, Seal S, Agarwal A (2009) *Surf Coat Technol* 203:1544
54. Luo ZP, Koo JH (2005) *J Microsc* 225:118
55. Pegel S, Potschke P, Villmow T, Stoyan D, Heinrich G (2009) *Polymer* 50:2123
56. Tang Y, Cong H, Zhong R, Cheng H-M (2004) *Carbon* 42:3260
57. Lin KL, Yang CF, Lee JT (1991) *Corrosion* 47:9
58. Hosny AY, El-Rofei ME, Ramadan TA, El-Gafari BA (1995) *Met Finish* 93:55
59. El-Rehim SSA, Ibrahim MAM, Khaled KF (1999) *J Appl Electrochem* 29:593
60. TamilSelvi S, Raman V, Rajendran N (2003) *J Appl Electrochem* 33:1175
61. Chen XH, Cheng FQ, Li SL, Zhou LP, Li DY (2002) *Surf Coat Technol* 155:274
62. Zhao G, Deng F (2005) *Key Eng Mater* 280–283:1445
63. Guo C, Zuo Y, Zhao X, Zhao J, Xiong J (2008) *Surf Coat Technol* 202:3385
64. Gomez E, Pane S, Alcobe X (2006) *Electrochim Acta* 51:5703
65. Lin YC, Duh JG (2007) *J Alloys Compd* 439:74
66. Kim SK, Oh TS (2011) *Trans Nonferrous Met Soc China* 21:s68
67. Mallory GO, Hajdu JB (2002) *Electroless plating-fundamentals and applications*, reprint edn. AESF, New York
68. Shi YL, Yang Z, Xu H, Li MK, Li HL (2004) *J Mater Sci* 39:5809

69. Yang Z, Xu H, Li M-K, Shi Y-L, Huang Y, Li H-L (2004) *Thin Solid Films* 466:86
70. Li ZH, Wang XQ, Wang M, Wang FF, Ge HL (2006) *Tri Int* 39:953
71. Zarebidaki A, Allahkaram S-R (2010) *J Alloys Compd* 509:1836
72. Chen CS, Chen XH, Yang Z, Li WH, Xu LS, Yi B (2006) *Diam Relat Mater* 15:151
73. Zhao G, Zhang H, Wang Z, Zhang YC (2007) *Key Eng Mat* 336–338:2142
74. Alishahi M, Monirvaghefi SM, Saatchi A, Hosseini SM (2012) *Appl Surf Sci* 258:2439
75. Stacia MH, Puchi ES, Castroa G, Ramirez FO, Lewis DB (1999) *Thin Solid Films* 355–356:472
76. Huang YS, Zeng XT, Hub XF, Liu FM (2004) *Electrochim Acta* 49:4313
77. Balaraju JN, Kalavati Rajam KS (2006) *Surf Coat Technol* 200:3933
78. Rabizadeh T, Allahkaram SR, Zarebidaki A (2010) *Mater Des* 31:3174
79. Huang YS, Zeng XT, Hub XF, Liu FM (2005) *Surf Coat Technol* 198:173
80. Chen WX, Tu JP, Xu ZD, Chen WL, Zhang XB, Cheng DH (2003) *Mater Lett* 57:1256
81. Zarebidaki A, Allahkaram SR (2012) *Micro Nano Lett* 7:90. <http://www.unidym.com>
82. Staiger MP, Pietak AM, Huadmai J, Dias G (2006) *Biomaterials* 27:1728
83. Turhan MC, Lynch R, Killian MS, Virtanen S (2009) *Electrochim Acta* 55:250
84. Endo M, Hayashi T, Itoh I, Kim YA, Shimamoto D, Muramatsu H, Shimizu Y, Morimoto S, Terrones M, Iino S, Koide S (2008) *Appl Phys Lett* 92:063105
85. Li Q, Viereckl A, Rottmair CA, Singer RF (2009) *Comp Sci Technol* 69:1193
86. Shimizu Y, Miki S, Soga T, Itoh I, Todoroki H, Sakaki K, Hosono T, Kim YA, Hayashi T, Endo M (2008) *Scr Mater* 58:267
87. Aung NN, Zhou W, Goh CS, Mui S, Nai L, Wei J (2010) *Corros Sci* 52:1551
88. Fukuda H, Szpunar JA, Kondoh K, Chromik R (2010) *Corros Sci* 52:3917
89. Li Q, Turhan MC, Rottmair CA, Singer RF, Virtanen S (2011) *Mater Corros* 62:9999
90. Li Q, Turhan MC, Rottmair CA, Singer RF, Virtanen S (2012) *Mater Corros* 63:384
91. Turhan MC, Li Q, Jha H, Singer RF, Virtanen S (2011) *Electrochim Acta* 56:7141
92. Praveen BH, Venkatesha TV (2009) *J Alloys Compd* 482:53
93. Hu Z, Jie X, Lu G (2010) *J Coat Technol Res* 7:809
94. Bernard M, Hugot-Le Goff A, Joiret S, Phong P (2001) *Synth Met* 119:283
95. Ding K, Jia Z, Ma W, Tong R, Wang X (2002) *Mat Chem Phys* 76:137
96. Spinks G, Dominis A, Wallace G, Tallman D (2002) *J Solid State Electrochem* 6:85
97. Sazou S (2001) *Synth Met* 118:133
98. Shinde V, Sainkar S, Gangal S, Patil P (2006) *J Mater Sci* 41:2851
99. Pruna A, Pilan L (2012) *Compos Part B* 43:3251
100. Zheludkevich ML, Miranda Salvado IM, Ferreira MGS (2005) *J Mater Chem* 15:5099
101. Zheludkevich ML, Serra R, Montemor MF, Miranda Salvado IM, Ferreira MGS (2006) *Surf Coat Technol* 200:3084
102. Garcia B, Lamzoudi A, Pillier F, Le HNT, Deslouis C (2002) *J Electrochem Soc* 149:52
103. Qian D, Dickey EC, Andrews R, Rantell T (2000) *Appl Phys Lett* 76:2868
104. Kim JK, Mai YW (1998) *Engineered interfaces in fiber reinforced composites*. Elsevier, Oxford
105. Barrera EV (2000) *J Minerals Metals Mater Soc* 52:38
106. Lee Y-B, Lee C-H, Lim D-S (2009) *Intl J Hydrogen Energy* 34:9781
107. Sreevatsa S, Grebel H (2009) *ECS Trans* 19:91
108. Ionita M, Branzoi IV, Pilan L (2010) *Surf Interface Anal* 42:987
109. Balbyshev VN, Anderson KL, Sinsawat A, Farmer BL, Donley M (2003) *Prog Org Coat* 47:337
110. Maiti A, Wescott J, Kung P (2005) *Mol Sim* 31:143
111. Zengin H, Zhou W, Jin JY, Czerw R, Smith DW, Echevoya L, Carroll DL, Foulger SH, Battato J (2002) *Adv Mater* 14:1480
112. Peng C, Jin J, Chen GZ (2007) *Electrochim Acta* 53:525
113. Martina V, De Riccardis MF, Carbone D, Rotolo P, Bozzini B, Mele C (2011) *J Nanopart Res* 13:6035

114. Wu G, Li L, Li JH, Xu BQ (2006) *J Power Sources* 155:118
115. Cochet M, Masser WK, Benito AM, Callejas MA, Martinez MT, Benoit JM, Schreiber J, Chauvet O (2001) *Chem Commun* 16:1450
116. Hien NTL, Garcia B, Pailleret A, Deslouis C (2005) *Electrochim Acta* 50:1747
117. Bazzaoui M, Martins JI, Costa SC, Bazzaoui EA, Reis TC, Martins L (2006) *Electrochim Acta* 51:4516
118. Ionita M, Pruna A (2011) *Prog Org Coat* 72:647
119. Gergely A, Pászti Z, Hakkell O, Drotár E, Mihály J, Kálmán E (2012) *Mater Sci Eng B* 177:1571–1582
120. Salam MA, Al-Juaid SS, Qusti AH, Hermas AA (2011) *Synth Met* 161:153
121. Prabakar RSJ, Pyo M (2012) *Cor Sci* 57:42
122. Maruyama B, Alam K (2002) *SAMPE J* 38:59
123. Hermas AEA, Salam MA, Al-Juaid SS, Al-Thabaiti SA (2009) *Int J of Nanomanufacturing* 4:166–174

Polymer Electrolyte Membrane Fuel Cells: Role of Carbon Nanotubes/Graphene in Cathode Catalysis

15

Raghunandan Sharma, Jayesh Cherusseri, and Kamal K. Kar

Contents

1	Introduction	362
1.1	Fuel Cells	363
1.2	Evolution of Fuel Cells	363
1.3	Polymer Electrolyte Membrane Fuel Cells	366
1.4	Working Principle and Components	366
2	PEM Fuel Cell Catalysis	370
2.1	ORR Mechanism in PEMFCs	371
2.2	Issues with PEMFC Catalysis	372
2.3	CNT as Catalyst Support	374
2.4	Pt/Non-Precious Metals Alloys for ORR Catalysts	378
2.5	Platinum-Free Catalysts	379
3	Conclusions	385
	References	385

Abstract

Fuel cells are power generation devices converting chemical energy into electric energy by electrochemical reactions. Among various types of fuel cells, hydrogen-oxygen (H₂-O₂) based proton exchange membrane (PEM) fuel cells have attracted special attention due to their high efficiency, low temperature

R. Sharma • J. Cherusseri

Advanced Nanoengineering Materials Laboratory, Materials Science Programme, Indian Institute of Technology Kanpur, Kanpur, India

e-mail: raghumsp@iitk.ac.in; jayesh@iitk.ac.in

K.K. Kar (✉)

Advanced Nanoengineering Materials Laboratory, Materials Science Programme, Indian Institute of Technology Kanpur, Kanpur, India

Advanced Nanoengineering Materials Laboratory, Department of Mechanical Engineering, Indian Institute of Technology Kanpur, Kanpur, India

e-mail: kamalkk@iitk.ac.in

operation, and suitability for low to medium power generation. However, the requirement of high cost catalysts (platinum and its alloys) for both cathodic and anodic reactions makes them unsuitable for commercial applications. Development of efficient catalysts with reduced cost has drawn considerable scientific attention. This chapter reviews the PEM fuel cell cathode catalysis in terms of challenges and progress in the field with an emphasis on the application of carbon nanomaterials such as carbon nanotubes and graphene. Owing to their promising properties such as high electronic conductivity, corrosion resistance, and large surface area, carbon nanomaterials are suitable for catalyst support materials. Apart from this, doped carbon nanomaterials show potential toward the development of metal-free catalysts.

Keywords

Fuel cells • PEM fuel cell • Electrochemical reactions • Oxygen reduction reaction • ORR catalyst • CNT • Nitrogen-doped CNT • Nitrogen-doped graphene • Platinum-free catalyst

1 Introduction

In view of the increasing world energy requirements and depleting fossil fuel resources, it is crucial to use the available energy resources efficiently and to explore the renewable energy sources. Presently, fossil fuels, i.e., petroleum oil, coal, and natural gas, contribute nearly 80 % of our energy requirements [1]. Heat engines are mostly used to generate power from these fuels. For example, the electric power is generated by steam and gas turbines, whereas internal combustion engines (ICEs) are used for mechanical work as well as electric power generation. In these heat engines, the combustion of fuel takes place, which converts the stored chemical energy into thermal energy. Finally, the thermal energy is used to perform mechanical work or to generate power. There are two major drawbacks of the combustion-based power generation, i.e., the low power conversion efficiency (η) and the emission of pollutants hazardous to the environment. The η of the thermal engines cannot exceed the Carnot limit given by $\eta = (1 - T_2/T_1)$, where T_1 and T_2 are the absolute temperatures of source and sink, respectively [2]. For practical thermal engines, the efficiencies are well below the theoretical limit. Diesel and petrol engines, for example, have efficiencies $\sim 40\%$ and $\sim 30\%$, respectively. Furthermore, the combustion of fossil fuels produces various pollutants and greenhouse gases, causing serious environmental concerns such as global warming, climate change, and health problems. In view of this, the development of efficient and environmentally friendly power generation technologies is of prime interest to the scientific community. Among others, hydrogen is being explored as a renewable energy source to reduce the greenhouse emissions and other pollutants. In a sustainable and emission-free energy cycle, hydrogen can be produced from electrochemical or photocatalytic hydrolysis of water.

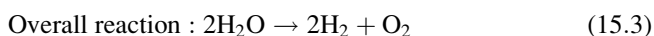
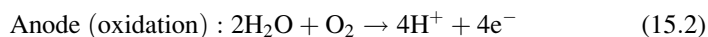
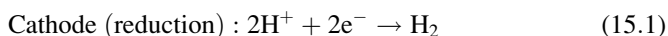
Although, the power generation from hydrogen is possible by using heat engines, but in the last decade, more efficient electrochemical energy conversion devices are being explored.

1.1 Fuel Cells

As an alternative of heat engines, power generation through the electrochemical conversion has attained significant interest. Galvanic cells are being used commercially for the small-scale power requirements since long back. Similar concept can be employed for the large-scale power generation. Fuel cells (FCs) are a class of such devices converting chemical energy to electric energy through electrochemical route. They differ from the dry cells in terms of fuel supply and by-product removal. Dissimilar to dry cells, where the cell becomes useless once all the reactants are consumed, FCs use a continuous feeding of reactants and removal of by-products. The basic advantage of FCs over the heat engines is the absence of the combustion step and hence, their efficiency is not limited by the Carnot limit (Fig. 15.1). This makes it possible to generate the power at very high efficiencies. Thermodynamically, the η for FCs is given by: $\eta = (\Delta G_f / \Delta H_f)$, where ΔG_f and ΔH_f represent the Gibbs free energy and the enthalpy of formation, respectively [2]. For a H₂-O₂ fuel cell (FC), the thermodynamical η can be as high as 91 %.

1.2 Evolution of Fuel Cells

History of FCs goes back to 1800 when Nicholson and Carlisle, using a silver-zinc voltaic pile, have observed bubbles of gases formed on both the silver as well as the zinc side of the piles, essentially splitting water to its components by electricity [3]. Later studies have proved the gases to be hydrogen and oxygen produced by the electrolysis of water, according to the following electrochemical reactions.



The inverse process – formation of water by combining hydrogen and oxygen – has been demonstrated by Grove in 1839 [4, 5]. Using a setup shown in Fig. 15.2, with lower ends of each platinum (Pt) electrodes immersed in sulfuric acid (H₂SO₄) electrolyte and upper ends covered with glass tubes containing oxygen and hydrogen, Grove has observed a constant current flow between the electrodes with a consumption of both gases.

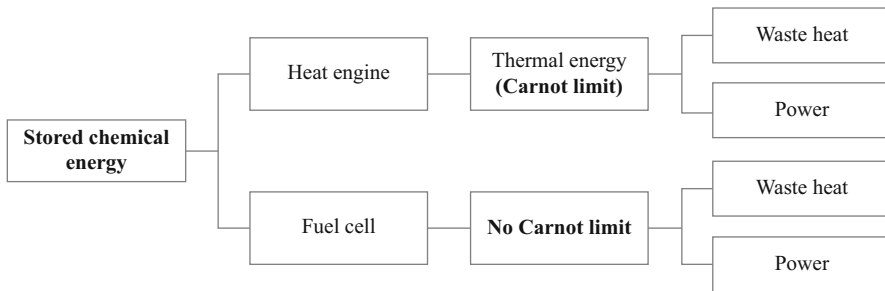


Fig. 15.1 Principal difference between FCs and heat engines

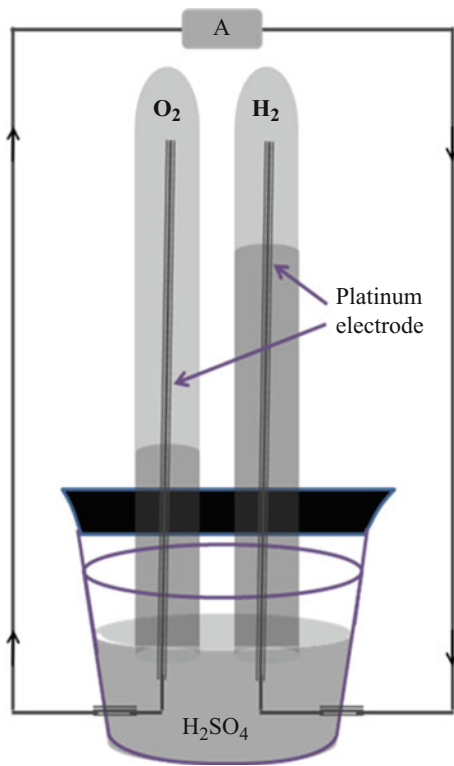
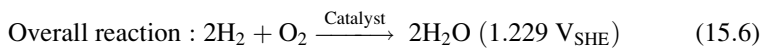
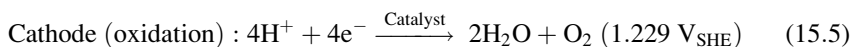


Fig. 15.2 Schematic of gas voltaic battery

The electrochemical reactions occurring in an H₂-O₂ FC are:



In a further development in 1889, Mond and Langer have developed a FC based on hydrogen/coal gas and achieved a power conversion efficiency of $\sim 50\%$ at a close circuit voltage of 0.73 [6]. Their system can be considered as the first real FC system since the design allowed supplying oxidant and fuel continuously with a provision to simultaneous removal of by-products. In another significant advancement in 1893, Ostwald has studied the thermodynamical aspects of the FCs. He has suggested the possibility of a combustion-free energy conversion device, which is not subjected to the limitations of second law of thermodynamics, leading to higher efficiencies compared to that of heat engines [7]. The first practical H_2 - O_2 FC, having a power capacity of up to 5 kW, has been fabricated by Bacon [8]. Starting experiments on alkaline FCs (AFCs) in 1932, he has built a cell with nickel gauze electrodes in 1939. His successful work on nickel electrodes to replace costly Pt catalyst is considered another milestone in FC history as it highlights the need to develop Pt-free catalysts with other abundant materials [9]. Nevertheless the FCs research has received a real thrust when National Aeronautics and Space Administration (NASA) decided to use FCs as an auxiliary power source in their space missions. The Gemini earth-orbiting mission (1962–1965) has used FCs based on solid polymer electrolytes made of sulfonated polystyrene resin. This is an example of the first polymer electrolyte membrane (PEM) FC (PEMFC) used for space applications. Later, highly efficient AFCs ($\eta \sim 70\%$) based on Bacon's technology have been used in Apollo mission [8, 9].

The obvious advantages of FCs have led intense research and development of various types of FCs covering a vast range of power outputs (few mW to MW). Based on the types of the fuels and/or the electrolytes, FCs have a range of operating temperatures, power outputs, and applications. Table 15.1 summarizes some of the important types of the FCs with their operating parameters. Selection of a suitable type of the FCs for a particular application depends on their power output, ease of operation, cost, and related safety issues. High temperature FCs such as solid oxide FCs (SOFCs), phosphoric acid FCs (PAFCs), and molten carbonate FCs (MCFCs) are suitable for stationary power generation plants with a few MW capacity. Hydrogen-based PEMFCs are more suitable for the medium power

Table 15.1 Types of fuel cells

FC type	Mobile ion	Electrolyte	Operating temp. ($^{\circ}C$)	Efficiency (%)	Power density (kW/m^2)	Application
AFCs	OH^-	KOH 30 %	50–200	60–70	2	Space vehicles
PEMFCs	H^+	Nafion	30–100	40–60	3	Lower power systems
DMFCs	H^+	Porous polyethylene	60–130	30–40		Portable applications
PAFCs	H^+	H_3PO_4	220	55	1.3	Large systems
SOFCs	O^{2-}	ZrO_2/Y_2O_3	500–1000	60–65	6	Multi kW systems
MCFCs	CO_3^{2-}	Li_2CO_3 Na_2CO_3	650	65	1.4	Up to MW capacity

outputs such as transport vehicles, whereas direct methanol FCs (DMFCs), another type of PEM-based FCs, suit to portable devices and household applications (laptops, mobiles, etc.).

1.3 Polymer Electrolyte Membrane Fuel Cells

PEMFCs are low operating temperature FCs consisting of a polymer membrane as electrolyte [10]. As the polymer membranes conduct H^+ ions, PEMFCs are also termed as “proton exchange membrane FCs.” They use hydrogen or low molecular weight hydrocarbons as the fuel at anode and oxygen/air as the oxidizer at cathode. Among others, hydrogen, being one of the potential futuristic energy sources, is the key fuel for PEMFCs. Grubb and Niedrach have developed the first PEMFC in the early 1960s. They have used sulfonated polystyrene membrane as electrolyte and Pt-deposited membrane as the catalyst for oxygen reduction and hydrogen oxidation reactions [11]. Apart from H_2 -based PEMFCs, methanol-based PEMFCs, namely, DMFCs, have been studied thoroughly due to their feasibility for small-scale portable applications. In principle, both of these fuel cells have similar structures. This report is focused on the H_2 -based PEMFCs due to their better performance in terms of futuristic power devices.

1.4 Working Principle and Components

In a PEMFC, hydrogen is oxidized at anode to produce H^+ ions, which migrate through the PEM to the cathode. Reduction of oxygen takes place at cathode to form O^{2-} ions, which combine with the H^+ ions to form H_2O (Eqs. 15.4 and 15.5). This develops a net cell potential (Eq. 15.6) that equals the difference between electrochemical potentials of hydrogen oxidation reaction (HOR) and oxygen reduction reaction (ORR). When connected to an external load, a constant current can be drawn if the reactant gases are supplied and the reaction product (H_2O) is removed continuously to maintain the system in steady state.

Figure 15.3a shows the schematic of H_2 - O_2 PEMFC with various components such as bipolar plates (BPs) with flow channels, gas diffusion layer (GDL), and membrane electrode assembly (MEA). The MEA is the part of FC consisting of the cathode and anode catalyst layers (CLs), and the PEM itself. Each of these components uses different materials based on their particular functions [12]. Additionally, a practical FC consists of a few auxiliary components for continuous power generation. As shown in Fig. 15.3b, it has to perform a number of tasks such as (i) supply and transport of fuel and oxidant to the appropriate electrodes, (ii) removal of by-products, (iii) electron transfer to the external load, (iv) H^+ ion transport through the membrane, (v) proper humidification of membrane, and (vi) maintaining the temperature at an optimum level. For high power generation, FC units are stacked in a series by using BPs. In a FC stack, other auxiliary components such as the humidifier, heat exchanger, compressor, heating system, etc. may be required occasionally [13].

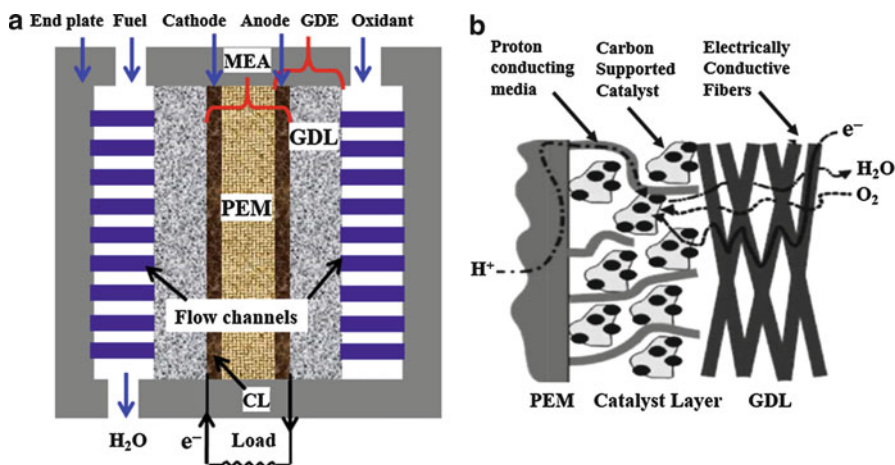


Fig. 15.3 (a) Schematic of a PEMFC and (b) transport of reactants and products in the PEMFC electrodes (part (b) has been reprinted with permission from [12])

1.4.1 Bipolar Plates

BPs, being an important component of PEMFC, contribute a significant weight (80 %) [14] and cost (25 %) of the FC stack [15]. As shown in Fig. 15.3a, in a single FC, two plates are placed on either side (cathode and anode) of the gas diffusion electrodes (GDE) containing gas flow channels. In a FC stack, each of such plate separates the GDE of two adjacent cells such that the one side works as anode plate, whereas the other side serves as cathode plate, signifying the name “bipolar plate” (BP). Gas flow channels formed on either side of the BP work as H₂ flow channel for the anode side and O₂/air flow channel for the cathode side. BPs perform a number of functions such as supply and uniform distribution of the reactants (fuel and oxidizer) to the GDL, facilitation of water and heat management, separation of individual cells, and transportation of electrons from cell to external load [16]. Also, BPs provide strength to the mechanically weak MEA [17]. For uniform distribution of gases, the flow channels of BPs have to be designed properly. Again, the materials should possess certain properties such as high electronic conductivity (>100 S/cm), high tensile and flexural strengths (>41 MPa and > 59 MPa, respectively), low corrosion rate (<1 μA/cm²), low hydrogen permeability (<2 × 10⁻⁶ cm³/(cm²s)), low contact resistance (<20 MΩ cm²), low density (<5 g/cm³), and high thermal conductivity (>10 W/mk) [15]. Based on these criteria, a number of materials have been investigated for BPs, which can be classified as metals, non-metals, and composites. Metallic BPs have good mechanical strength and electronic conductivity compared to the graphite and composite materials. In addition, they are easy to machine and are cost effective as well. However, the lower chemical resistance of metals makes them corrosion prone in the harsh FC environment [15, 18]. In addition to this, metallic BPs increase the weight of the stack, which is undesired for portable applications. Improving corrosion resistance of the metals has been another active area of FC research. The corrosion resistance of metallic BPs is

improved by coating corrosion resistive materials on the metal surfaces. The frequently used coating materials include carbon-based materials such as graphite, diamond-like carbon; noble metals such as gold and Pt; metal carbides such as WC; metal nitrides (TiN, CrN, NbN, ZrN) [19, 20]; conductive polymers and organic self-assembled monopolymers [16]. However, the high specific density of metals remains an issue.

Graphite is considered a standard material for BPs due to its low resistivity and excellent corrosion resistance. However, due to the brittle nature and lack of mechanical strength, graphite BPs are not suitable for transport applications, where vibrations may lead to their failure. Again, it becomes difficult to fabricate gas flow channels through machining and the process is not cost effective as well [16]. To overcome these issues, graphite-reinforced polymer composites have been proposed as the alternatives to graphite BPs. The polymer matrix provides mechanical stability to the plates by reducing their brittle nature. Moreover, the polymers exhibit high corrosion resistance and a cost-effective fabrication is possible. The main drawback of these composite materials is the reduced electronic and thermal conductivities, which affects the cell performance adversely. Other reinforcing materials, such as carbon black (CB), carbon nanotubes (CNTs), and graphene, have been used to improve the mechanical strength and electronic as well as thermal conductivities of polymer composite BPs [21–23]. CNT-reinforced polymer composites exhibit large improvements in the properties [24].

1.4.2 Gas Diffusion Layer

GDL is a multifunctional component of a PEMFC. It is a thin layer (thickness ranging between 100 and 300 μm) of porous conducting material sandwiched between the BP and the CL [12]. GDL facilitates the diffusion of reactant gases to the CL and controls the humidity level of the cell. In addition, it provides a conducting path for the electrons from CL to BP and supports CL physically. Apart from this, GDL also plays a key role in transporting the heat generated at the electrodes to the gas flow channels [25, 26]. To perform these functions, a combination of suitable materials and proper designing the GDL is required. Material parameters affecting the GDL performance include hydrophobicity, porosity, pore-size distribution, pore connectivity, contact resistance, thermal and electronic conductivity, and corrosion resistance. Carbon-based materials, namely, carbon fiber (CF), carbon paper (CP), carbon cloth (CC), CNTs, CB, and graphite, are most widely used for GDL. These materials exhibit good corrosion resistance, pore connectivity, and electronic conductivity, which are appropriate for the GDL [27]. Proper functioning of GDL with improved performance can be obtained by modifying its porosity and pore-size distribution, hydrophobicity, morphology, and electronic conductivity [28]. The commonly used GDLs are having both single and double layered structures. Single layered GDL generally consists of a 150–400- μm thick macroporous layer of CF/CP [29]. Double layered GDL includes a woven or unwoven CF layer and a second microporous layer (MPL) comprising of CB and PTFE. Here, the first layer works as the GDL while the second microporous layer functions as water management layer [30]. Moreover, the MPL also provides

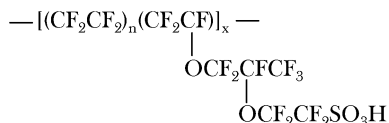
a better contact with the CL [31]. Structure of GDL plays a crucial role in FC water management. Effective water management through GDL has found significant scientific interest in PEMFC research. Carefully designed GDL may eliminate the need of humidifier in PEMFC [32]. Efforts toward the improved water management include the use of novel GDL materials such as CNTs, graphene, etc., altering the contact angle by surface modifications such as polymer coatings, and changing the pore-structure and morphology. In single layered GDL, coating of polytetrafluoroethylene (PTFE) on CF is applied to increase the hydrophobicity. A balanced combination of hydrophobic and hydrophilic pores is required. Lin et al. have found that under flooding conditions, coating of PTFE enhances the gas and water transport [33]. Excessive loading of PTFE reduces the hydrophilic pores responsible for water transport and leads to more electrode flooding. Park et al. have found an optimum PTFE loading of 20 wt% to balance the water saturation in GDL and CL giving best cell performance. Porosity measurements have revealed that the PTFE loading decreases porosity and increases the hydrophobic pore-volume [34]. Moreover, the loading of PTFE increases the contact resistance of the GDL due to its insulating nature. The through-plane (along the thickness) conductivity of the layer decreases significantly. The in-plane (parallel to the GDL plane) electronic conductivity, however, is not affected significantly as the charge is conducted by the carbon fibers (CFs) [30].

1.4.3 Electrolyte Membrane

Electrolytes with good ionic conductivity are one of the essential parts of devices such as batteries and FCs. In H_2 - O_2 PEMFCs, transport of H^+ ions from anode to cathode is performed through a polymer-based membrane. Polymer electrolyte membranes (PEMs) are solid state electrolytes developed initially by GE for the Gemini space missions. The basic material requirements of an electrolyte for PEMFCs include high H^+ ion conductivity and no electronic conductivity. In order to form a robust structure and to provide enough support to the CL, the membrane should have adequate mechanical strength. To sustain the corrosive FC environment, high corrosion resistance and chemical inertness are also needed. In addition, the membrane should be impermeable to the fuel/oxygen to prevent the crossover. The methodologies opted for the synthesis of electrolyte membranes seek their large-scale production with low costs [35].

Initially, polystyrene sulfonic acid membranes were used in PEMFCs, which suffered a drawback of being less durable. This issue was addressed well by perfluorinated sulfonic acid membranes (trade name Nafion[®]) developed by DuPont in 1960 [36]. Nafion[®] consists of a PTFE backbone with perfluorinated vinyl polyether side-chains, bonded by the oxygen atoms. The chemical structure of the Nafion[®] monomer unit is shown in Fig. 15.4. The sulfonic acid groups at the end of the side-chains provide free H^+ ions for conduction in the hydrated conditions. The conductivity depends on the degree of hydration of the membrane. Membrane thickness is another important parameter affecting the cell performance. Smaller thickness is preferred due to the reduced membrane resistance, ease of hydration, and lower cost. However, the risk of fuel crossover increases with decreasing the

Fig. 15.4 Chemical structure of perfluorinated polymer (Nafion[®]) from DuPont



thickness. The thickness has to be optimized to best performance without the fuel crossover.

Cost reduction, improved durability and cell performance, and proper water management are the major issues related to the electrolyte membrane. Various PEM materials being studied for FC membrane are [35, 37]:

- (i) Perfluorinated ionomers: Sulfonic group attached perfluorinated polymers such as Nafion[®] are use most frequently for PEMs.
- (ii) Partially fluorinated polymers: These polymers have fluorocarbon backbones and hydrocarbon or aromatic side-chains. The ionic conductivity is lower than that of the perfluorinated ones.
- (iii) Non-fluorinated polymers: These polymers have hydrocarbon or aromatic backbones. The side-chains are modified with polar or sulfonic acid groups. These membranes show good mechanical properties but have poor conductivity.
- (iv) Acid–base blends: These membranes consist of an alkaline backbone modified by incorporation of an acid component. The acid component imparts the ionic conductivity comparable to that of Nafion[®] membrane.

1.4.4 Catalyst Layer

The anode and cathode CLs are coated on either sides of an electrolyte membrane. Properties such as high catalytic activity, high surface area, high corrosion resistance, good chemical inertness, excellent electronic conductivity, etc. are mandatory for the CLs. Conventionally, high surface area Pt particles coated on CB are being used as catalysts for both ORR and HOR in a PEMFC. CB, being electrically conductive and corrosion resistant, is used as support material for the nanosized Pt. However, Pt is not a suitable catalyst material for large-scale applications due to its high cost and scarce nature. For commercial applications, the exploration of alternate catalysts is indispensable as the high efficiency of FCs is of less importance without their cost effective fabrication [38]. Significant efforts have been made toward the synthesis of low Pt or Pt-free catalysts during the last few decades.

2 PEM Fuel Cell Catalysis

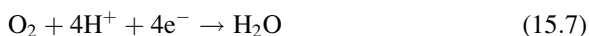
Electrochemical reactions on both the electrodes of a PEMFC have an activation energy barrier. Thermal energy at normal working temperatures of a PEMFC (80 °C) is not significant to cross this barrier. Catalysts, in general, alter the activation energy by changing the reaction path. In PEMFCs, heterogeneous catalysis is used to attain a practically significant reaction rate. Both the electrochemical

half-cell reactions, namely, HOR at the anode and ORR at the cathode, require catalysts. Among the cathode and anode reactions, the sluggish nature of the former reaction makes its catalysis more challenging. Large Pt-loading as compared to anode is required at the cathode.

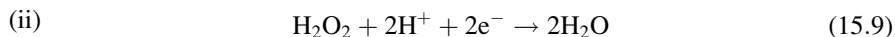
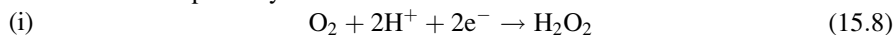
2.1 ORR Mechanism in PEMFCs

The ORR has been studied extensively, and a number of possible pathways are proposed. Its mechanism depends on the nature of the media as well as the catalyst sites. The two pathways – four-electron and two-electron pathways – are possible in both acidic and alkaline media [39]. While the four-electron pathway is a single step process, the two-electron process involves two steps with H_2O_2 as an intermediate. In PEMFCs (acidic media), the ORR pathways are represented as

Four-electron pathway:



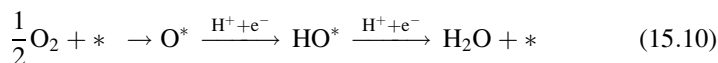
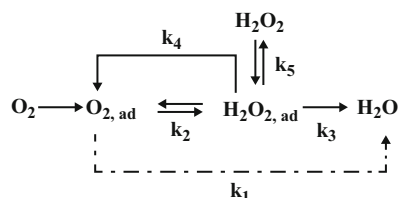
Two-electron pathway:



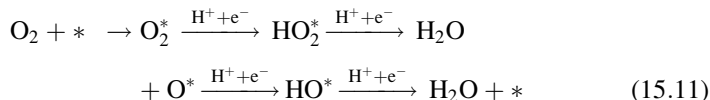
The reactions need high activation energies, which necessitates the presence of a catalyst to attain practically significant reaction rates. Since the catalyst systems should have practically significant stability under the acidic media, Pt/Pt-alloy-based catalysts remain the most suitable ORR catalysts for PEMFCs. In the presence of the heterogeneous catalyst, molecular oxygen (O_2) is adsorbed on the catalyst surface to form O_2^* , which either can be desorbed or reduced. The most accepted possible reduction pathways for Pt surface, proposed by Wroblowa et al., are shown in Fig. 15.5 [40, 41]. The ORR can proceed either by a single step four-electron process (Eq. 15.7) or by a couple of two-electron reactions (Eqs. 15.8 and 15.9). The former process, where the O_2^* is directly reduced to H_2O , is shown in Fig. 15.5 with a rate constant of k_1 . The latter two-electron process proceeds via an intermediate step forming adsorbed hydrogen peroxide (H_2O_2^*) as an intermediate with a rate constant of k_2 . The H_2O_2^* either can be reduced to form H_2O with a rate constant k_3 or desorbed with a rate constant k_5 . In addition to this, the H_2O_2^* can decompose chemically with a rate constant of k_4 . In PEMFC, the direct pathway (k_1) is the most preferred pathway as the production of H_2O_2 lowers the system performance.

The above reactions involve several sub-steps. Norskov et al. have proposed dissociative and associative pathways for ORR on Pt surface [42]. In the dissociative pathway, the O-O bond is broken to form adsorbed O (O^*), which, on reacting with an H^+ , forms adsorbed HO (HO^*). Finally, HO^* forms H_2O by combining with another H^+ [42, 43]. The dissociative mechanism is given in the equation below, where the catalytic site is represented by (*) [44].

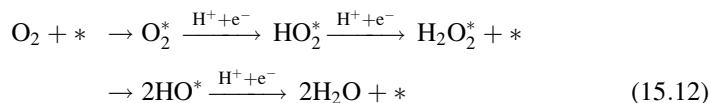
Fig. 15.5 ORR pathways proposed by Wroblowa et al. [40]



The dissociative process reduces the oxygen directly without the formation of H_2O_2 intermediate, and hence, it is a four-electron process with rate constant k_1 (Fig. 15.5). In this process, the step involving the hydrogenation of OH is the rate-determining step due to its high activation energy. While the O-O bond breaks in the dissociative mechanism, the associative mechanism involves the adsorption of O_2 without breaking the O-O bond. The reduction of adsorbed O_2 (O_2^*) takes place according to the following chain of reactions:



Similar to the dissociative mechanism, this process does not produce H_2O_2 . However, the presence of molecular O_2 (O-O bond) may result in H_2O_2 formation with the following reaction:



The catalytic activity of any catalyst is a wise interplay between the adsorption energies of various intermediate species. A good catalyst adsorbs the reactants in such a way that the binding energy of most stable species (O and OH) remains minimum to obtain a lower overpotential (potential required to overcome the activation barrier).

2.2 Issues with PEMFC Catalysis

Owing to their high stability and catalytic activity, Pt-based systems are the mostly used catalysts for PEMFC cathode and anode CLs. Apart from high cost, the catalysts suffer from other issues such as low durability, carbon monoxide (CO) poisoning, and other contaminations. The CO poisoning occurs mostly at the anode side due to the

presence of CO impurity in the steam-reformed H₂. For cathode CL, requirement of high Pt-loading and low durability are the major concerns.

2.2.1 High Cost and Scarcity of Platinum

Among other issues with FC catalysts, the high cost and scarcity of Pt is of utmost concern. For large-scale application of FCs, such as public transport, it is estimated that the Pt amount as large as one fourth of the total estimated Pt deposits would be required to produce one billion cars [45]. The available amount of Pt is insufficient to meet its possible demand by the FC industry. In addition, the scarcity of Pt combined with its high demand makes it one of the most valuable metals having high cost (last 15 years average price: ~1,000 \$/Oz). In case of the adoption of FC-based power sources, owing to increased demand, the Pt cost would further increase significantly. This would increase the fractional cost of CL in a FC stack, which is estimated to be ~35 % of the stack cost based on present market prices. Therefore, search for novel Pt-free or low-level Pt catalysts is inevitable.

2.2.2 Durability

During PEMFC operation, the performance of the CL decreases with time due to the reduction in the effective surface area of the catalyst. This causes a serious concern to PEMFC catalysis. The performance change is due to the irreversible changes happening in the CL. Numerous studies exploring the durability have revealed several mechanisms responsible for the catalyst degradation. Studies show that the important mechanisms responsible for catalytic activity decay in PEMFC are: (i) dissolution of Pt during the cyclic or steady-state operation, (ii) detachment of catalyst particles by corrosion of carbon support, (iii) reduction in the effective surface area due to the particle size growth, and (iv) poisoning/contamination of catalyst particles. The PEMFC catalyst degradation becomes more prominent under variable loads, which is a serious concern toward their application in vehicles.

The dissolution of Pt takes place primarily during the potential cycling at high potentials and is more prominent at the cathode. With increasing temperature, the dissolution rate also increases. Dissolved Pt-ionomers are either redeposited on the larger sized particles or diffused through the membrane. The previous case, where larger particles grow at the cost of smaller ones, is termed as Ostwald ripening [46]. Parthasarathy et al. have studied the coarsening of graphite-supported Pt-nanoparticles in a solution containing Pt ions (0.1 M PtCl₄ in dimethyl sulfoxide) [47, 48]. TEM images of Pt samples reveal a significant coarsening effect (Fig. 15.6). The average particle size increases by a factor of ~5 by the deposition of Pt from the solution. In another stability test of Pt/C catalyst, Zhai et al. have observed a roughly 100 % increment in the Pt particle size after 300 h of testing [49]. The electrochemical surface area is reduced from 17.2 to 7.8 m²/g_{Pt}. XRD analysis of FC electrodes shows smaller FWHM for samples tested for 300 h. Moreover, the rate of change of the particle size decreases with increasing testing time as there is no significant change in FWHM for higher durations. The increased particle size effectively reduces the surface area, which in turn leads to the lower electrocatalytic activity [50]. On the other hand, when ionomers are diffused in the membrane, they either

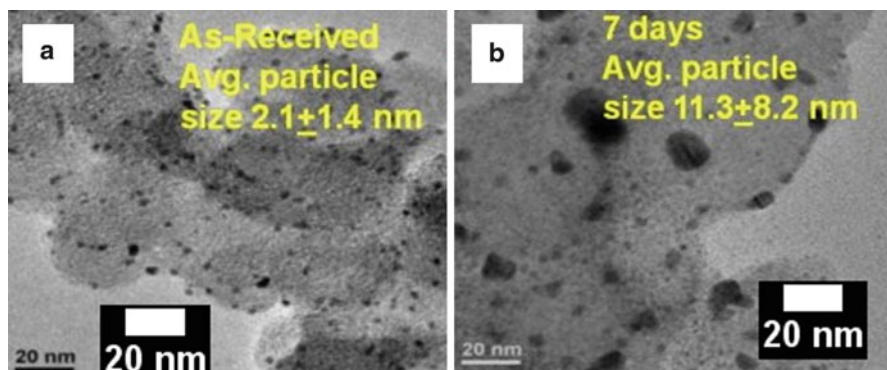


Fig. 15.6 TEM images of graphite-supported Pt (a) before and after the electrochemical test (Reprinted with permission from [48])

react with the crossed over hydrogen to form Pt deposits inaccessible for the catalysis or replace H^+ ions of the membrane [51]. As a result, the H^+ ion concentration in the membrane is reduced, which in turn reduces the ionic conductivity of the PEM. Secondly, at nanometer scale, small particles can form agglomerates by random cluster–cluster collisions to form larger clusters. In a third mechanism, nanoparticles may grow at atomic level to minimize their Gibb's free energy.

The corrosion of carbon support material is another important process responsible for the loss of the catalyst surface area [52]. In acidic media, carbon support corrodes slowly due to the electrochemical oxidation in the presence of Pt [53]. This leads to unsupported catalyst nanoparticles, which remain either unconnected electrically to the outer circuit or covered by the carbon particles to become inaccessible to the reactants. The oxidation behavior of highly oriented pyrolytic graphite (HOPG) under potential cycling in an acidic media has been studied by Choo et al. [54]. The study reveals that the HOPG surface corrodes severely for a potential cycling while remaining almost unaffected when kept at a constant potential. Scanning electron microscope (SEM) images of HOPG reveal that the samples remain unaffected when kept at a constant potential of 1.0 V, whereas severe corrosion is observed for a potential cycling between 0.8 and 1.0 V at a sweep rate of 90 mV/s (Fig. 15.7). Moreover, the corrosion becomes more prominent under high sweep rate of potential cycling. The atomic force microscope (AFM) images of the HOPG surfaces before and after a potential cycling between 0.8 and 1.0 V at a sweep rate of 10 mV/s are shown in Fig. 15.8a, b, respectively. Formation of pits by surface oxidation due to the potential cycling is clearly visible.

2.3 CNT as Catalyst Support

The cost issue of the FC is mainly due to the expensive Pt-based catalyst. Hence, in order to reduce the cost, loading of catalyst must be minimized. One of the

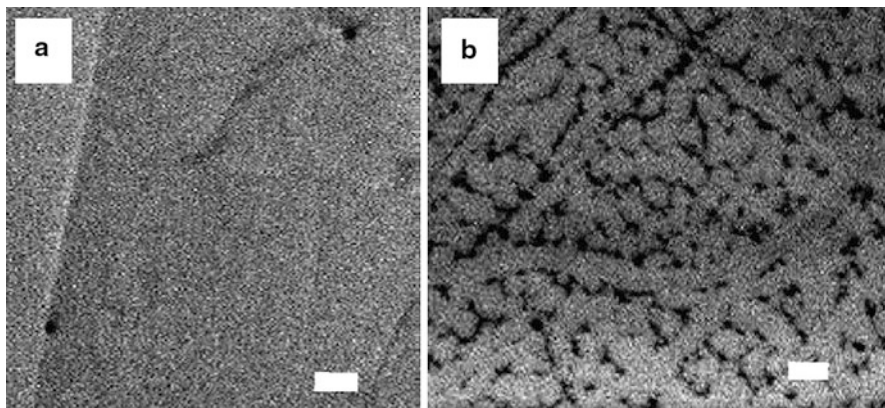


Fig. 15.7 SEM image of HOPG after (a) holding at 1.0 V and (b) potential cycling for 22.2 h (scale bar: 1 μm) (Reprinted with permission from [54])

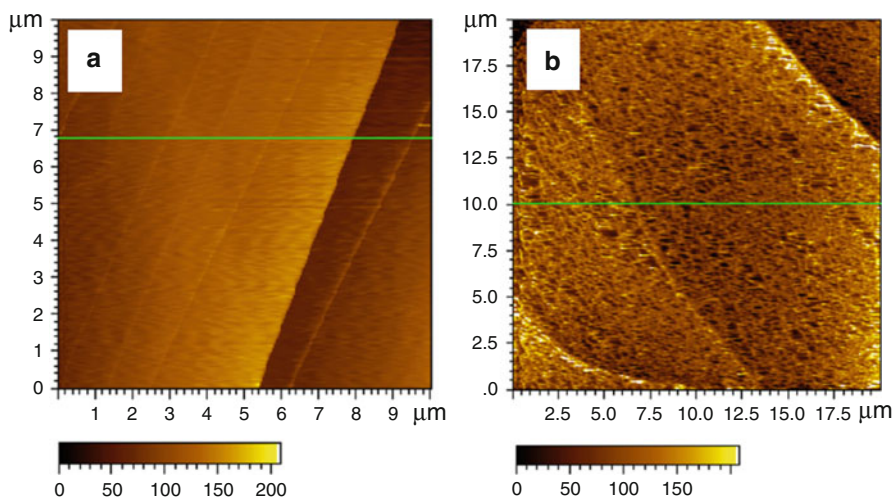


Fig. 15.8 AFM images of HOPG surface (a) before and (b) after electrochemical corrosion (Reprinted with permission from [54])

important challenges towards reducing the Pt-loading in FCs is the low durability of catalysts due to the catalyst support corrosion [55]. In case of catalyst support corrosion, high Pt-loading is required to obtain a reasonable durability. Owing to their high corrosion resistance, CNTs-based thin CLs can be used with less Pt-loading [56]. In addition, when compared to CC/CP-based CL, more uniform dispersion of Pt nanoparticles without agglomeration is possible to achieve. Hence, in the case of CNT-supported CL, the size distribution of Pt nanoparticles is found

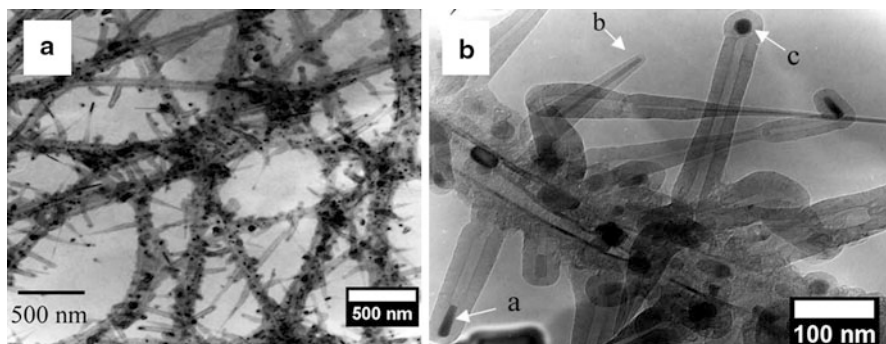


Fig. 15.9 TEM images of two stage MWCNTs network grown on the fibers of a CP at different magnifications (Reprinted with permission from [63])

to be narrower [57]. This improves the Pt catalyst surface area and activity to reduce the total catalyst amount to be loaded. Use of CNTs shows promising improvement in terms of the size miniaturization, chemical and electrochemical stability, improved durability, and cost reduction of FCs.

CNTs, owing to their high specific surface area ($\sim 1,000\text{--}1,500\text{ m}^2/\text{g}$) [58–60] combined with conductive nature, are utilized in the CL of the PEMFCs. Effective surface area of the CL can be increased significantly by using CNTs as catalyst support. The increased effective area of the CL results in an improved FC performance [61]. The catalyst particles are coated on CNTs by various physical and chemical techniques such as deposition by chemical or electrochemical reduction of catalyst precursors, sputtering, thermal CVD, etc. [62]. Uniformity of coating, particle size distribution, CNTs–catalyst particle interaction, and electric connectivity of CNTs with GDL are the key parameters governing the catalyst performance. Sun et al. have synthesized a 3D network of electrically connected multiwalled CNTs (MWCNTs) on CP by a two-step CVD process (Fig. 15.9). A good electrical connectivity of such a network in PEMFC catalyst support provides effective electron transport [63]. Catalyst metal particles can be deposited on the CNTs coated CP/CC by various physical and chemical techniques [62]. In order to utilize the large, surface area of CNTs, a uniform loading of catalyst particles is mandatory. A comparatively high loading of Pt nanoparticles (2–4 nm) have been obtained by Saha et al. using glacial acetic acid to reduce Pt acetylacetonate [64]. Figure 15.10 shows the transmission electron microscope (TEM) images of the Pt-nanoparticle-loaded CNTs with uniform particle distribution without a sign of agglomeration. Moreover, the density of Pt-nanoparticles can be controlled by monitoring the Pt-precursor concentration during deposition. Table 15.2 summarizes a few research works using CNTs as catalyst support for reduced Pt-loading. For similar Pt-loading, the Pt/CNTs catalysts show up to 50 % enhanced (in terms of maximum power output) performance as compared to CB based catalysts.

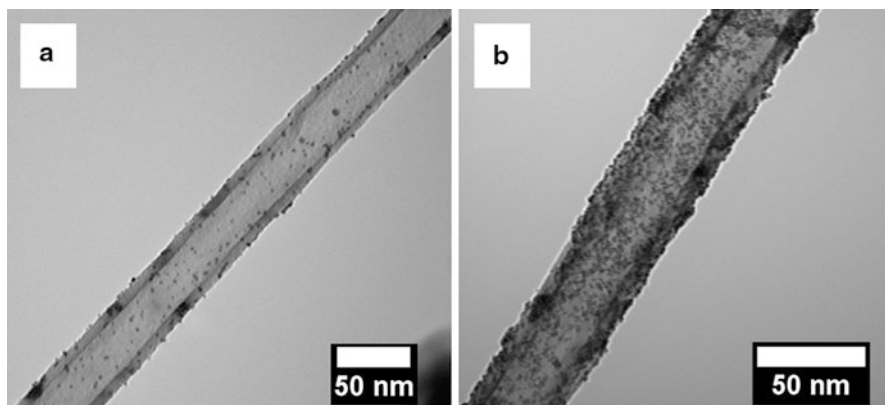


Fig. 15.10 TEM images showing CNTs coated with Pt nanoparticles for varying Pt-precursor concentration (a) 1 mM and (b) 4 mM (Reprinted with permission from [64])

Table 15.2 CNT-coated CC/CP-based catalyst support layer for PEMFCs

Catalyst (coated on CC/CP)	Improvements (compared to conventional catalyst supports)	References
N ₂ doped CNT (CN _x)/Pt	Good dispersion of Pt, high surface area compared to CNT	[65]
Pt-Ru/CNTs	Max. Power density: 145 %	[66]
Pt/Porous CP/CNTs	Max. Power density: 124 %	[61]
Pt/CNTs with 2-nm Pt size	Improved dispersion of Pt with high density	[64]
Pt/CNTs thin film	Flexible thin electrode with low Pt-loading	[67]
Pt/CNTs, Pt/CNTs/CB	Max. Power density: 136 %	[68]
Pt/CNTs	High catalyst utilization, In situ deposition of Pt on CVD grown CNTs	[69]
Pt-Ru(20/10 wt%)/CNTs,	Max. Power density: 150 %	[70]
CNT/CC for microbial FC	Max. Power density 65mWm ⁻²	[71]
Pt-Ru(40/20 wt%)/CNTs	Thin CL with better performance	[72]
Pt/Single-walled CNTs	Max. Power density:120 %, Low corrosion	[73]

CL may be applied either to the electrolyte membrane or to the GDL. Improvement in cell performance has been observed by using CNTs in both the cases. Lebert et al. have obtained improved cell performance by combining Pt/CNTs-based CL with Nafion membrane [67]. Similarly, Tang and coworkers have obtained improved polarization curve by using Pt/CNTs layer and Pt/CNTs-CB (Pt coated on CNT-CB blend), which works as both CL and GDL [68, 69]. Similar improvements have been observed in DMFCs using CNT-supported Pt/Ru as anode catalyst [70].

Table 15.3 CNT-based catalyst support layers for high durability

Catalyst (coated on CC/CP)	Improvements (compared to conventional catalyst supports ^a)	References
SiO ₂ coated Pt/CNTs	No growth in particle size, high durability	[46]
Pt/CNTs (20 wt% metal)	Surface area reduction 52 %	[74]
Pt/MWCNTs	Less corrosion (70 % of Pt/CP)	[75]
SiO ₂ coated Pt/CNTs	High activity and durability. Optimum thickness of SiO ₂ = 6 nm	[76]
Pt/MWCNTs	Well dispersed Pt with 1–3 nm size, high durability, and performance	[56]
Pt/CNTs/CNF Bucky paper	Carbon corrosion ~26 %, Surface area reduction: 53 % (of Pt/C)	[77]
Pt/CNTs/CNF Bucky paper	Carbon corrosion ~26 %, Surface area reduction ~53 % (of Pt/C)	[77]
Multifunctionalized Pt/Single-walled CNTs	Thin GDL/Electrode without using CP/CC	[78]
Graphitized Pt/CNTs	Very high durability and corrosion resistance	[79]
Pt/MWCNTs	Pt/CNTs: stable performance after first 8 h, Pt/CP: continuous oxidation	[57]
Pt/MWCNTs	High stability, small change in particle size	[80]

^aConventional catalyst supports are not the same for all the cases. The variation is shown in comparison to the supports used in the individual studies

To resolve the durability issues, novel materials for catalyst support as well as catalyst are being explored. Carbon nanomaterials such as CNTs are one of the well-studied and promising catalyst support materials for improved durability. These have been investigated with higher thermal stability and durability for CLs [74, 75]. Table 15.3 summarizes a few of such studies. The long-term chemical stability of the CNT-coated CF-based electrodes has been found to improve significantly [81]. This is attributed to the improved thermal stability and higher oxidation resistance of support layer, and less agglomeration of catalyst particles. The migration of catalyst particles can be minimized by increasing their adhesion to the supporting CNT/CP layer. This can be obtained by using functionalized CNTs having active groups [65]. CNT-supported catalyst particles covered with silica layer have been found to be highly active with increased durability under potential cycling [46, 76].

2.4 Pt/Non-Precious Metals Alloys for ORR Catalysts

Transition metals such as Sc, Cr, Fe, Co, Ni, Cu, W, Sn. etc. are termed as non-precious metals (NPMs). Pt/NPM-alloys have been explored for ORR catalysts with low Pt-loading. The Pt/NPM-alloys exhibit improved activities in terms of the power density per unit Pt-loading. An enhancement by a factor of 3–5 has been observed. However, the enhancement factor varies widely, which depends on particle size, shape, composition, and crystallographic orientation. To compare

the catalytic activity of Pt vs. Pt-alloy a simple normalization over mass or surface area is insufficient. Furthermore, the effect of surface electronic structure on the reactivity is still unknown.

The specific activity of Pt alloy catalysts exhibits a strong correlation with the Pt-Pt nearest neighbor (n-n) distance. As revealed by Min et al., smaller n-n distance helps the oxygen adsorption, leading to high specific activity. Among the studied Pt-alloy catalysts, with its smallest n-n distance, Pt₃Ni exhibits the highest activity [82].

Li et al. have studied a tri-metallic alloy (Pt-Fe-Ni) ORR catalyst synthesized by electrodeposition. Power output of ~ 0.5 W/cm² at 0.5V with an ultra-low Pt loading of 0.05 mg Pt cm⁻² has been reported [83]. Similar to Pt, carbon nanomaterials have been used as catalyst supports for Pt/NPMs-alloy catalysts as well [84]. While the alloying can help reducing the required Pt amount, the leaching of base metals from the Pt-alloy catalyst is of major concern. In PEMFC operating potentials, the Pt-alloys are thermodynamically unstable. Incomplete alloying, presence of excess amounts of base metal, are the other factors leading to the leaching of base metals. The leached metal ions may replace the conducting H⁺ ions in the electrolyte membrane, effectively reducing its conductivity significantly. Furthermore, this also leads to the CL depletion and low durability [85].

2.5 Platinum-Free Catalysts

The replacement of Pt-based catalysts with Pt-free catalysts has been appreciated since the discovery of PEMFCs. The requirement of larger Pt-loading at cathode has fascinated special attention toward the development of Pt-free ORR catalysts. Intensive efforts toward the Pt-free ORR catalysis have offered a number of such material systems. The key problem toward the replacement of Pt is the acidic environment of PEMFCs, which discards the use of NPMs as ORR catalysts. While NPMs have low corrosion resistance, their compounds and complexes with the non-metals such as nitrogen (N), boron (B) and chalcogens exhibit the opposite nature, which makes them stable in the PEMFC environment. The development of Pt-free catalysts for ORR dates back to the study by Jasinski, showing the ORR catalytic activity of transition metal porphyrins and phthalocyanines [86]. Since then, transition metal-/N-containing carbon-based materials have been studied significantly as a substitute of Pt for ORR catalysis. The reported Pt-free catalysts are either the NPMs-based or the metal-free materials. Among others, the transition metal-based complexes exhibit promising results. A review on the developments in the NPM-based catalysts for PEMFC cathode by Othman et al. suggests that NPM-based ORR catalysts can be classified as NPM-based macrocycles, chalcogenides, electroconductive polymers, nitrides, and carbons [87]. The metal-free catalysts include carbon nanomaterials (porous carbon, CNTs, graphene, etc.) doped with various impurities such as N- and B-atoms. A classification of various Pt-free ORR catalysts is shown in Fig. 15.11.

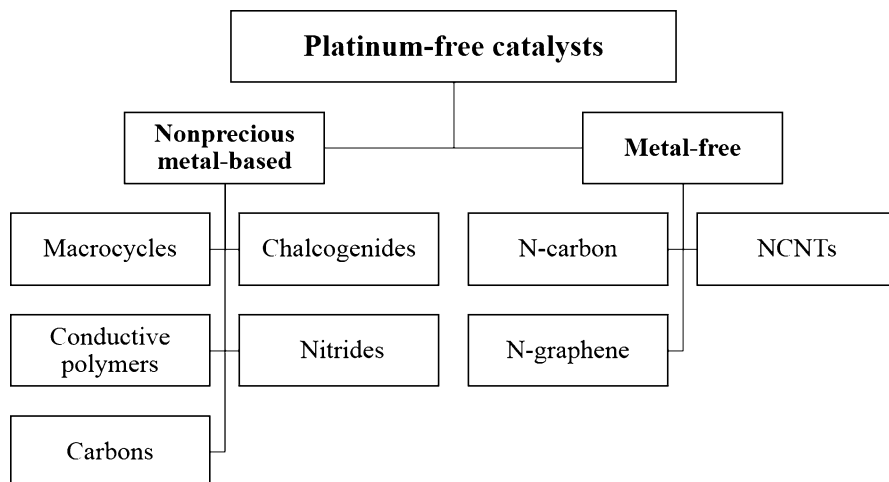


Fig. 15.11 Classification of Pt-free ORR catalysts

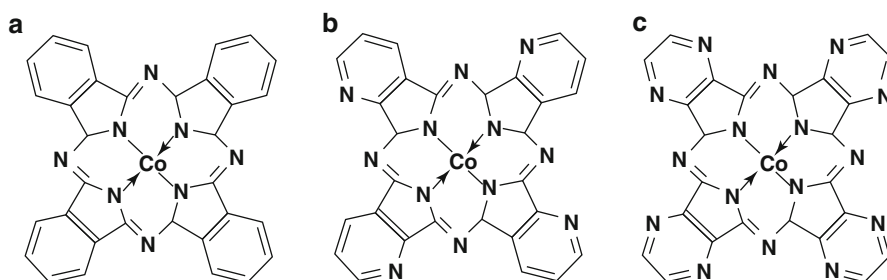


Fig. 15.12 Structures of (a) cobalt phthalocyanine (CoPc), (b) cobalt tetrapyridinoporphyrazine (CoTAP), and (c) cobalt tetrapyrazinoporphyrazine (CoPTpz) (Reprinted with permission from [88])

2.5.1 NPMs-Based Pt-Free Catalysts

In 1964, Jasinski has reported the use of metal porphyrins and phthalocyanines as NPM catalysts for ORR for the first time [86]. This has led to a new class of NPM catalysts for ORR named metal-N₄-macrocycles (planer molecules), having a central metal ion surrounded by four N-atoms symmetrically. Figure 15.12 shows a few cobalt-N₄-macrocycle molecules explored for ORR activity.

Among other macrocycles, transition metal (Fe, Co, Ni and Cu)-N₄-macrocyclic molecules have been explored more frequently as PEMFC cathode catalysts [89, 90]. Numerous studies during the last few decades have revealed that Fe- and Co-macrocylic complexes possess high electrocatalytic activity. The metal-N₄ macrocycles show both two-step and one-step pathways for reduction of oxygen. Xu et al. have studied the ORR activity of MWCNT supported cobalt phthalocyanine (CoPc), cobalt tetrapyridinoporphyrazine (CoTAP), and cobalt

tetrapyrazinoporphyrazine (CoTPtz) and suggested a two-step pathway for CoPc while a one-step pathway for CoTAP- and CoTPtz-based catalysts [88]. The reaction mechanism and active site structures in metal-N₄ macrocycles are, however, debatable due to their complex structures. The metal-N bonds participate in the process. Different types of active sites are proposed. More than one type of active sites may exist simultaneously in a catalyst material. The ORR activity depends strongly on the oxidation state of the metal ions and atomic arrangements [43].

Recently, transition metal complexes of heterocyclic electroconductive polymers such as polyaniline (PANI), polypyrrole (PPY), polythiophenes (PThs), poly(3-methylthiophene), etc. have been reported to have high ORR activity and durability. Bashyam et al. have used Co-PPY composite as an ORR catalyst for PEMFC [91]. The composite is prepared by entrapping cobalt precursor such as CoNO₃·6H₂O in the polymer matrix followed by the reduction with NaBH₄. The catalytic activity is attributed to the interaction of Co atoms with polypyrrole, forming the CoN_x active sites. Millan et al. have found that among various catalyst systems based on cobalt-modified electroconductive polymer supported on CB, PPY-based catalysts show superior ORR properties [92]. The Co-PPY composites having ORR activity and stability comparable to that of the commercial Pt/C catalysts (30 wt% Pt supported on Vulcan XC-72, a commercially available high surface area carbon) have been reported for direct borohydride fuel cells (DBFCs) [93]. The superior properties are attributed to the specific structure of the composites having N-Co-N bonds, as shown in Fig. 15.13.

Pyrolysis of N-containing organic compounds in the presence of the transition metals such as Fe, Co, Ni, etc. produces metal/N-C composites having ORR activity. Studies by Wu et al. have revealed such ORR catalysts synthesized by pyrolysis of PANI in the presence of Fe/Co precursors [94–97]. The catalysts show high ORR activity with high selectivity for four-electron pathway.

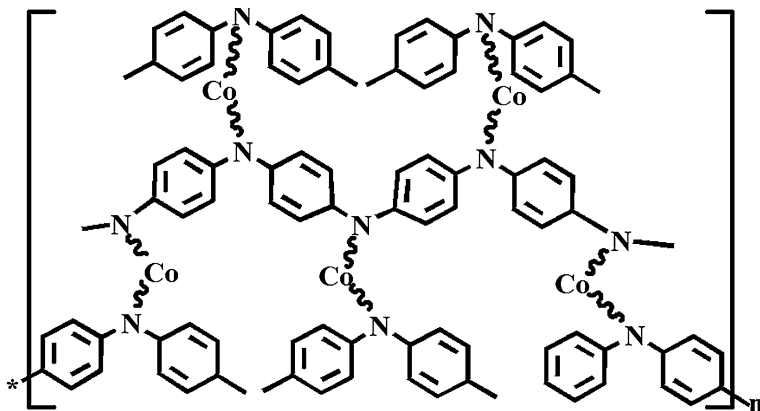
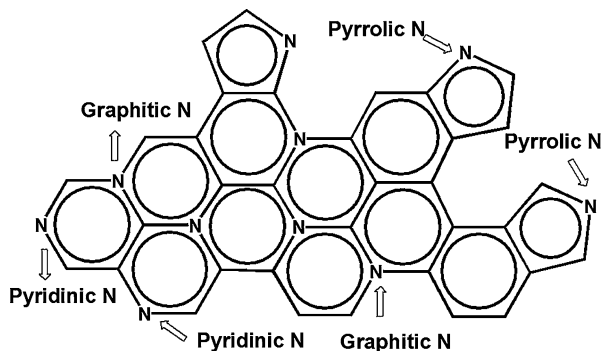


Fig. 15.13 Proposed structure of Co-PPY composites [92]

Fig. 15.14 Possible N-sites in N-doped graphitic carbon



2.5.2 Metal-Free ORR Catalysts

Metal-free ORR catalysts are principally the graphitic carbons with impurity (N, B, etc.) doping in the regular graphitic structure. N-containing carbon materials exhibit catalytic properties toward the ORR. As shown in Fig. 15.14, three different types of N-C sites, graphitic-N, pyridinic-N and pyrrolic-N, are possible. The graphitic-N is formed when the N-atom replaces a C-atom of the regular hexagonal network. Here, three C-atoms form bonds with the N-atom. On the other hand, the pyridinic-N site consists of C-N bonds located at the edge of the graphitic network. The N-atom, bonded by two C-atoms, becomes a part of the six-membered ring. Finally, the pyrrolic-N is formed by incorporation of the N-atom in a five-membered ring, as shown in Fig. 15.14.

Mutter et al., by studying various N- and metal-containing carbons, have determined that the pyridinic-N sites exhibit highest catalytic activity. Since the pyridinic-N sites are located at the edges of graphitic planes, the number of these sites is governed by the extent of edge plane exposure [98, 99].

Recently, N-doped CNTs (NCNTs) have been reported to have high catalytic activity toward ORR [100]. Vertically aligned NCNTs produced by pyrolysis of iron (II) phthalocyanine are employed as metal-free electrodes for ORR in AFCs. The NCNTs electrodes exhibit superior electrocatalytic activity with 4.1 mA/cm^2 at -0.22 V compared to 1.1 mA/cm^2 at -0.22 V for the standard Pt/C electrode in 0.1 M KOH saturated with air. Again, dissimilar to Pt/C, NCNTs catalysts exhibit immunity to CO poisoning. The electrocatalytic properties of NCNTs are attributed to the modified charge distribution in the presence of the electron-accepting N-atoms. The doping modifies the energy band structure, spin density, and charge density in the proximity of the dopant, forming high charge/spin density sites [101]. These sites are responsible for the enhanced ORR activity. For example, incorporation of N-atoms in a regular hexagonal carbon network of CNTs has been found to induce positive charges on the adjacent C-atoms. Density functional theory (DFT) calculations by Gong et al. have revealed the presence of the small positive charges on the C-atoms adjacent to the N-atom in NCNTs [100]. This positive charge facilitates the oxygen adsorption and weakens the O-O bond [102]. Apart from this, NCNT contain pyridinic-N, which acts as the ORR active site [103–105].

The number of these sites depends on the extent of N-doping. The catalytic activity exhibits increasing trend with increasing the N-doping [106, 107]. Rao et al. have studied the effect of N-content in vertically aligned NCNTs with a varying dopant concentration (0, 4.3, 5.6, 8.4, and 10.7 at.%) and obtained highest ORR activity for 8.4 at.% N-doping. Here, the catalytic activity is attributed to the presence of pyridinic-N sites, which adsorb O₂ and weaken the O-O bond. However, the activity of NCNTs remains inferior to that of Pt/C [105]. The number of active sites, and hence the catalytic activity of NCNTs, is affected by the synthesis parameters such as precursor and temperature. Kundu et al. have reported the ORR activity of NCNT synthesized by pyrolysis of acetonitrile at 550 °C to be 10 % of that of a commercial Pt/C (20 wt% Pt). At higher processing temperature (750 °C), the activity decreases due to the reduced number of pyridinic-N sites [103].

Similar to NCNTs, N-doped graphene (NG) is another potential ORR catalyst material. Despite being comparatively emerging material, the ORR activity of NG has attained considerable scientific interest. NG is generally synthesized by pyrolyzing graphene oxide (GO) with an N-containing precursor [108]. Recently, the NG-based catalysts having ORR activity comparable or higher than that of Pt-based catalysts have been reported [109–111]. The ORR activity of NCNTs/NG can also be exploited by using it as a catalyst support material for both noble as well as non-noble metal-based catalysts. High ORR activity with nearly four-electron transfer mechanism has been observed for iron-incorporated NG [112]. Byon et al., for example, have used NG, prepared by reducing graphite oxide (GO), to form an NPM-based catalysts [113]. Fe-N-C moieties containing 40 % pyridinic-N and an average N/Fe coordination of three (FeN₃) are used as ORR catalysts. For comparison, various support materials such as CB, oxidized CB, and NG are used. The ORR activity is measured by rotating disk electrode (RDE) in O₂-saturated 0.05 M H₂SO₄ electrolyte. Compared to the carbon black (CB), the NG-supported catalyst (Fe-NG) exhibits ~13 times enhanced ORR activity (Fig. 15.15).

Apart from N-doping, co-doping of B, sulfur (S), halogens, etc. with nitrogen improves the ORR activity further [114, 115]. Wang et al. have reported an NG-based ORR catalyst having superior catalytic activity when compared with a commercial Pt/C (20 wt% Pt) by co-doping of graphene with B and N. The catalysts are prepared by heating GO in the presence of boric acid (H₃BO₃) and ammonia (NH₃). Similar co-doping of B and N is obtained by Xue et al. using melamine diborate as a precursor for CVD synthesis of graphene foams (GFs) [115]. Separate samples of the N-/B-doped GFs are prepared by using ammonia and triethyl borate as the N-/B- precursors, respectively. Cyclic voltammetry (CV) measurements show much higher ORR activity for the doped GFs as compared to the undoped ones. Moreover, the co-doped GFs show highest catalytic activity when compared with the single N- or B-doped samples. Figure 15.16a, b show the SEM image and cyclic voltammograms (N₂- and O₂-saturated 0.1 M KOH) of BN-doped GFs. A large reduction peak in presence of oxygen exhibits the high ORR activity. The BN-doped GFs show high CO tolerance when compared to the Pt-based catalysts.

Fig. 15.15 ORR mass activity of graphene-supported catalyst vs. carbon black-supported catalysts (Reprinted with permission from [113])

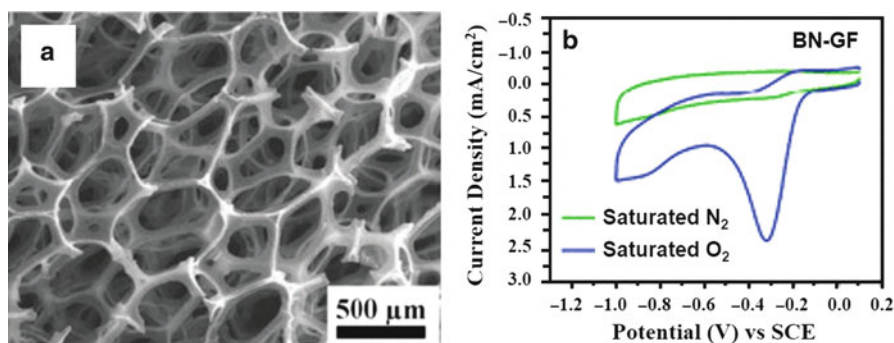
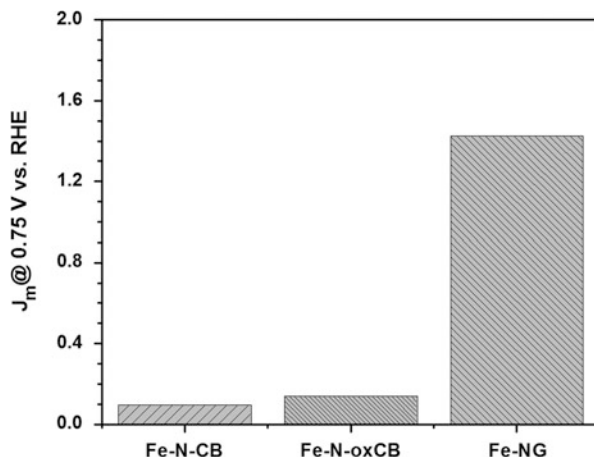


Fig. 15.16 (a) SEM image and (b) cyclic voltammograms of BN-doped GFs (Reprinted with permission from [115])

Similar to pyridinic-N catalytic active sites, ORR active edge-halogenated graphene has been reported recently by Jeon et al. [116]. The halogenated graphenes having halogen atoms (Cl/Br/I) at the graphene edges have been synthesized by ball-milling the pristine graphene in the presence of the respective halogens (Cl₂/Br₂/I₂). The catalysts show high stability and low CO poisoning along with promising ORR activity. Similar to NG, the halogens help in the O₂ adsorption and weaken the O-O bonds.

Materials with a combination of CNTs and NG may possess unique properties. In a study, Li et al. have synthesized NG nanosheets attached with CNTs by a heat treatment in NH₃ [117]. The outer layers of CNTs are partially unzipped to form NG nanosheets, which remain attached to the parent CNT. The exfoliated outer walls contain small amounts of catalysts (Fe) and N impurities acting as catalytic sites, whereas the intact inner CNT facilitates the charge transport. The other forms of carbon nanomaterials such as carbon nanocups, and carbon nano-onions, when doped with N also exhibit catalytic activities similar to

that of NCNTs. Tang et al. have studied the catalytic activity of N-doped carbon nanocups (NCNCs) for H_2O_2 oxidation, a reverse process to the ORR [118]. With an activity comparable to that of Pt/CNT (11.5 wt% Pt), NCNCs show potential to replace Pt-based catalysts. The high activity of NCNCs over NCNTs originates from the inhomogeneous N distribution within the cups. N-atoms are concentrated on the rims of the nanocups, which work as ORR active sites [119].

3 Conclusions

Owing to their high efficiency, PEMFCs are promising prospective power generation devices. However, the dependence on noble metal-based catalysts hinders their large-scale applicability. For successful commercialization of PEMFC, replacement of Pt-based CL with other low-cost and abundant catalysts is inevitable. Considerable efforts are being made toward the development of low-cost and stable catalysts for PEMFCs. Numerous low Pt/Pt-free ORR catalysts are widely investigated. ORR catalysts based on the transition metals demonstrate promising properties. Recently, carbon nanomaterials have shown considerable potential for ORR catalysis. The CNT-supported CLs show improved ORR activity and high durability due to their large surface area, high electronic conductivity, and high corrosion resistance. In addition, the ORR activity and stability of NCNTs and NG is promising toward complete replacement of Pt-based catalysts. However, large-scale production of CNTs/graphene-based catalysts for commercial applications remains challenging. The knowledge regarding the nature of the active sites and their dependence on experimental parameters is not well established. More efforts toward the development and performance evolution of FC stacks based on these catalysts are required.

Acknowledgements The authors acknowledge the financial support provided by Department of Science and Technology Nano Mission, India, for carrying out this work.

References

1. Key World Energy Statistics (2011) International Energy Agency, Paris, p 6
2. Larminie J, Dicks A, Knovel (2003) Fuel cell systems explained. Wiley, Chichester, p 406
3. Macinnis P (2009) 100 discoveries: the greatest breakthroughs in history. Pier 9, Millers Point, p 287
4. Grove WR (1843) On the gas voltaic battery. Experiments made with a view of ascertaining the rationale of Its action and its application to eudiometry. Philos Trans R Soc Lond 133:91
5. Grove WR, Esq MA (1839) XXIV. On voltaic series and the combination of gases by platinum. Philos Mag 14:127
6. Mond L, Langer C (1889) A new form of gas battery. Philos Trans R Soc Lond 46:296
7. Bagotsky VS (2009) Fuel cells: problems and solutions. Wiley, Hoboken, p 320
8. Warshay M, Prokopius PR (1989) The fuel cell in space: yesterday, today and tomorrow. In: Grove anniversary (1839–1989) fuel cell symposium, London

9. Bacon FT, Fry TM (1973) Review lecture: the development and practical application of fuel cells. *Philos Trans R Soc Lond A* 334:427
10. Barbir F (2005) Chapter 1 – introduction. In: *PEM fuel cells*. Academic, Burlington, pp 1–16
11. Andujar JM, Segura F (2009) Fuel cells: history and updating. A walk along two centuries. *Renew Sustain Energy Rev* 13:2309
12. Litster S, McLean G (2004) PEM fuel cell electrodes. *J Power Sources* 130:61
13. Li H, Tang Y, Wang Z, Shi Z, Wu S, Song D, Zhang J, Fatih K, Zhang J, Wang H (2008) A review of water flooding issues in the proton exchange membrane fuel cell. *J Power Sources* 178:103
14. Tsuchiya H, Kobayashi O (2004) Mass production cost of PEM fuel cell by learning curve. *Int J Hydrogen Energy* 29:985
15. Antunes RA, Oliveira MCL, Ett G, Ett V (2010) Corrosion of metal bipolar plates for PEM fuel cells: a review. *Int J Hydrogen Energy* 35:3632
16. Hermann A, Chaudhuri T, Spagnol P (2005) Bipolar plates for PEM fuel cells: a review. *Int J Hydrogen Energy* 30:1297
17. Li X, Sabir I (2005) Review of bipolar plates in PEM fuel cells: flow-field designs. *Int J Hydrogen Energy* 30:359
18. Tawfik H, Hung Y, Mahajan D (2007) Metal bipolar plates for PEM fuel cell – a review. *J Power Sources* 163:755
19. Cha B-C, You Y-Z, Hong S-T, Kim J-H, Kim D-W, Lee B-S, Kim S-K (2011) Nitride films as protective layers for metallic bipolar plates of polymer electrolyte membrane fuel cell stacks. *Int J Hydrogen Energy* 36:4565
20. Dur E, Cora M, Koç M (2011) Experimental investigations on the corrosion resistance characteristics of coated metallic bipolar plates for PEMFC. *Int J Hydrogen Energy* 36:7162
21. Ramasubramaniam R, Chen J, Liu H (2003) Homogeneous carbon nanotube/polymer composites for electrical applications. *Appl Phys Lett* 83:2928
22. Lee JH, Jang YK, Hong CE, Kim NH, Li P, Lee HK (2009) Effect of carbon fillers on properties of polymer composite bipolar plates of fuel cells. *J Power Sources* 193:523
23. Antunes RA, de Oliveira MCL, Ett G, Ett V (2011) Carbon materials in composite bipolar plates for polymer electrolyte membrane fuel cells: a review of the main challenges to improve electrical performance. *J Power Sources* 196:2945
24. Wu M, Shaw LL (2005) A novel concept of carbon-filled polymer blends for applications in PEM fuel cell bipolar plates. *Int J Hydrogen Energy* 30:373
25. Cindrella L, Kannan AM, Lin JF, Saminathan K, Ho Y, Lin CW, Wertz J (2009) Gas diffusion layer for proton exchange membrane fuel cells – a review. *J Power Sources* 194:146
26. Park S, Lee J-W, Popov BN (2012) A review of gas diffusion layer in PEM fuel cells: materials and designs. *Int J Hydrogen Energy* 37:5850
27. Lysenko V (2008) Current trends in the design of gas-diffusion layers for fuel cells. *Fibre Chem* 40:226
28. Jordan LR, Shukla AK, Behrsing T, Avery NR, Muddle BC, Forsyth M (2000) Diffusion layer parameters influencing optimal fuel cell performance. *J Power Sources* 86:250
29. Pozio A, Cemmi A, Carewska M, Paoletti C, Zaza F (2010) Characterization of gas diffusion electrodes for polymer electrolyte fuel cells. *J Fuel Cell Sci Technol* 7:041003
30. Ismail MS, Damjanovic T, Ingham DB, Pourkashanian M, Westwood A (2010) Effect of polytetrafluoroethylene-treatment and microporous layer-coating on the electrical conductivity of gas diffusion layers used in proton exchange membrane fuel cells. *J Power Sources* 195:2700
31. Zhan Z, Xiao J, Li D, Pan M, Yuan R (2006) Effects of porosity distribution variation on the liquid water flux through gas diffusion layers of PEM fuel cells. *J Power Sources* 160:1041
32. Chen J, Matsuura T, Hori M (2004) Novel gas diffusion layer with water management function for PEMFC. *J Power Sources* 131:155
33. Lin G, Van Nguyen T (2005) Effect of thickness and hydrophobic polymer content of the gas diffusion layer on electrode flooding level in a PEMFC. *J Electrochem Soc* 152:A1942

34. Park S, Lee J-W, Popov BN (2008) Effect of PTFE content in microporous layer on water management in PEM fuel cells. *J Power Sources* 177:457
35. Smitha B, Sridhar S, Khan AA (2005) Solid polymer electrolyte membranes for fuel cell applications - a review. *J Membr Sci* 259:10
36. Hoogers G (2003) Fuel cell technology handbook. CRC Press, Boca Raton, Florida
37. Neburchilov V, Martin J, Wang H, Zhang J (2007) A review of polymer electrolyte membranes for direct methanol fuel cells. *J Power Sources* 169:221
38. Mench MM (2008) Fuel cell engines. Wiley, Hoboken, New Jersey, pp 1–26
39. Song C, Zhang J (2008) Electrocatalytic oxygen reduction reaction. In: Zhang J PEM fuel cell electrocatalysts and catalyst layers. Springer, London, pp 89–134
40. Wroblowa HS, Yen Chi P, Razumney G (1976) Electroreduction of oxygen: a new mechanistic criterion. *J Electroanal Chem Interfacial Electrochem* 69:195
41. Marković NM, Schmidt TJ, Stamenković V, Ross PN (2001) Oxygen reduction reaction on Pt and Pt bimetallic surfaces: A selective review. *Fuel Cells* 1:105
42. Norskov JK, Rossmeisl J, Logadottir A, Lindqvist L, Kitchin JR, Bligaard T, Jonsson H (2004) Origin of the overpotential for oxygen reduction at a fuel-cell cathode. *J Phys Chem B* 108:17886
43. Shi Z, Liu H, Lee K, Dy E, Chlistunoff J, Blair M, Zelenay P, Zhang J, Liu Z-S (2011) Theoretical study of possible active site structures in cobalt- polypyrrole catalysts for oxygen reduction reaction. *J Phys Chem C* 115:16672
44. Nilekar AU, Mavrikakis M (2008) Improved oxygen reduction reactivity of platinum monolayers on transition metal surfaces. *Surf Sci* 602:L89
45. Jaouen F, Proietti E, Lefevre M, Chenitz R, Dodelet J-P, Wu G, Chung HT, Johnston CM, Zelenay P (2011) Recent advances in non-precious metal catalysis for oxygen-reduction reaction in polymer electrolyte fuel cells. *Energy Environ Sci* 4:114
46. Takenaka S, Matsumori H, Matsune H, Tanabe E, Kishida M (2008) High durability of carbon nanotube-supported Pt electrocatalysts covered with silica layers for the cathode in a PEMFC. *J Electrochem Soc* 155:B929
47. Parthasarathy P, Virkar AV (2013) A study of electrochemical Ostwald ripening in Pt and Ag catalysts supported on carbon. *ECS Trans* 50:1547
48. Parthasarathy P, Virkar AV (2013) Electrochemical Ostwald ripening of Pt and Ag catalysts supported on carbon. *J Power Sources* 234:82
49. Zhai Y, Zhang H, Xing D, Shao Z-G (2007) The stability of Pt/C catalyst in H₃PO₄/PBI PEMFC during high temperature life test. *J Power Sources* 164:126
50. Akita T, Taniguchi A, Maekawa J, Siroma Z, Tanaka K, Kohyama M, Yasuda K (2006) Analytical TEM study of Pt particle deposition in the proton-exchange membrane of a membrane-electrode-assembly. *J Power Sources* 159:461
51. Borup RL, Davey JR, Garzon FH, Wood DL, Inbody MA (2006) PEM fuel cell electrocatalyst durability measurements. *J Power Sources* 163:76
52. Wilson MS, Garzon FH, Sickafus KE, Gottesfeld S (1993) Surface area loss of supported platinum in polymer electrolyte fuel cells. *J Electrochem Soc* 140:2872
53. Stevens DA, Dahn JR (2005) Thermal degradation of the support in carbon-supported platinum electrocatalysts for PEM fuel cells. *Carbon* 43:179
54. Choo H-S, Kinumoto T, Nose M, Miyazaki K, Abe T, Ogumi Z (2008) Electrochemical oxidation of highly oriented pyrolytic graphite during potential cycling in sulfuric acid solution. *J Power Sources* 185:740
55. Borup R, Meyers J, Pivovar B, Kim YS, Mukundan R, Garland N, Myers D, Wilson M, Garzon F, Wood D, Zelenay P, More K, Stroh K, Zawodzinski T, Boncella J, McGrath JE, Inaba M, Miyatake K, Hori M, Ota K, Ogumi Z, Miyata S, Nishikata A, Siroma Z, Uchimoto Y, Yasuda K, Kimijima KI, Iwashita N (2007) Scientific aspects of polymer electrolyte fuel cell durability and degradation. *Chem Rev* 107:3904
56. Lin JF, Kamavaram V, Kannan AM (2010) Synthesis and characterization of carbon nanotubes supported platinum nanocatalyst for proton exchange membrane fuel cells. *J Power Sources* 195:466

57. Li L, Xing Y (2006) Electrochemical durability of carbon nanotubes in noncatalyzed and catalyzed oxidations. *J Electrochem Soc* 153:A1823
58. Yin YF, Mays T, McEnaney B (1999) Adsorption of nitrogen in carbon nanotube arrays. *Langmuir* 15:8714
59. Peigney A, Laurent C, Flahaut E, Bacsá RR, Rousset A (2001) Specific surface area of carbon nanotubes and bundles of carbon nanotubes. *Carbon* 39:507
60. Pinero R, Amoro's C, Linares Solano A, Delpoux S, Frackowiak E, Szostak K, Beguin F (2002) High surface area carbon nanotubes prepared by chemical activation. *Carbon* 40:1614
61. Maheshwari PH, Mathur RB (2009) Improved performance of PEM fuel cell using carbon paper electrode prepared with CNT coated carbon fibers. *Electrochim Acta* 54:7476
62. Lee K, Zhang J, Wang H, Wilkinson DP (2006) Progress in the synthesis of carbon nanotube- and nanofiber-supported Pt electrocatalysts for PEM fuel cell catalysis. *J Appl Electrochem* 36:507
63. Sun X, Li R, Stansfield B, Dodelet JP, Désilets S (2004) 3D carbon nanotube network based on a hierarchical structure grown on carbon paper backing. *Chem Phys Lett* 394:266
64. Saha MS, Li R, Sun X (2008) High loading and monodispersed Pt nanoparticles on multiwalled carbon nanotubes for high performance proton exchange membrane fuel cells. *J Power Sources* 177:314
65. Saha MS, Li R, Sun X, Ye S (2009) 3-D composite electrodes for high performance PEM fuel cells composed of Pt supported on nitrogen-doped carbon nanotubes grown on carbon paper. *Electrochem Commun* 11:438
66. Wang CH, Du HY, Tsai YT, Chen CP, Huang CJ, Chen LC, Chen KH, Shih HC (2007) High performance of low electrocatalysts loading on CNT directly grown on carbon cloth for DMFC. *J Power Sources* 171:55
67. Lebert M, Kaempgen M, Soehn M, Wirth T, Roth S, Nicoloso N (2009) Fuel cell electrodes using carbon nanostructures. *Catal Today* 143:64
68. Tang Z, Poh CK, Lee KK, Tian Z, Chua DHC, Lin J (2010) Enhanced catalytic properties from platinum nanodots covered carbon nanotubes for proton-exchange membrane fuel cells. *J Power Sources* 195:155
69. Tang Z, Ng HY, Lin J, Wee ATS, Chua DHC (2010) Pt/CNT-based electrodes with high electrochemical activity and stability for proton exchange membrane fuel cells. *J Electrochem Soc* 157:B245
70. Jeng KT, Chien CC, Hsu NY, Yen SC, Chiou SD, Lin SH, Huang WM (2006) Performance of direct methanol fuel cell using carbon nanotube-supported Pt-Ru anode catalyst with controlled composition. *J Power Sources* 160:97
71. Tsai HY, Wu CC, Lee CY, Shih EP (2009) Microbial fuel cell performance of multiwall carbon nanotubes on carbon cloth as electrodes. *J Power Sources* 194:199
72. Jeng KT, Chien CC, Hsu NY, Huang WM, Chiou SD, Lin SH (2007) Fabrication and impedance studies of DMFC anode incorporated with CNT-supported high-metal-content electrocatalyst. *J Power Sources* 164:33
73. Girishkumar G, Rettker M, Underhile R, Binz D, Vinodgopal K, McGinn P, Kamat P (2005) Single-wall carbon nanotube-based proton exchange membrane assembly for hydrogen fuel cells. *Langmuir* 21:8487
74. Shao Y, Yin G, Gao Y, Shi P (2006) Durability study of Pt/C and Pt/CNTs catalysts under simulated PEM fuel cell conditions. *J Electrochem Soc* 153:A1093
75. Wang X, Li W, Chen Z, Waje M, Yan Y (2006) Durability investigation of carbon nanotube as catalyst support for proton exchange membrane fuel cell. *J Power Sources* 158:154
76. Matsumori H, Takenaka S, Matsune H, Kishida M (2010) Preparation of carbon nanotube-supported Pt catalysts covered with silica layers; application to cathode catalysts for PEFC. *Appl Catal Gen* 373:176
77. Zhu W, Zheng JP, Liang R, Wang B, Zhang C, Au G, Plichta EJ (2009) Durability study on SWNT/nanofiber buckypaper catalyst support for PEMFCs. *J Electrochem Soc* 156:B1099

78. Kaempgen M, Lebert M, Roth S, Soehn M, Nicoloso N (2008) Fuel cells based on multifunctional carbon nanotube networks. *J Power Sources* 180:755
79. Wang J, Yin G, Shao Y, Wang Z, Gao Y (2008) Investigation of further improvement of platinum catalyst durability with highly graphitized carbon nanotubes support. *J Phys Chem C* 112:5784
80. Li L, Xing Y (2008) Electrochemical durability of at 80 °C. *J Power Sources* 178:75
81. Chen J, Wang JZ, Minett AI, Liu Y, Lynam C, Liu H, Wallace GG (2009) Carbon nanotube network modified carbon fibre paper for Li-ion batteries. *Energy Environ Sci* 2:393
82. Min M-k, Cho J, Cho K, Kim H (2000) Particle size and alloying effects of Pt-based alloy catalysts for fuel cell applications. *Electrochim Acta* 45:4211
83. Li B, Chan SH (2013) PtFeNi tri-metallic alloy nanoparticles as electrocatalyst for oxygen reduction reaction in proton exchange membrane fuel cells with ultra-low Pt loading. *Int J Hydrogen Energy* 38:3338
84. Vinayan BP, Jafri RI, Nagar R, Rajalakshmi N, Sethupathi K, Ramaprabhu S (2012) Catalytic activity of platinum/cobalt alloy nanoparticles decorated functionalized multiwalled carbon nanotubes for oxygen reduction reaction in PEMFC. *Int J Hydrogen Energy* 37:412
85. Gasteiger HA, Kocha SS, Sompalli B, Wagner FT (2005) Activity benchmarks and requirements for Pt, Pt-alloy, and non-Pt oxygen reduction catalysts for PEMFCs. *Appl Catal, B* 56:9
86. Jasinski R (1964) A new fuel cell cathode catalyst. *Nature* 201:1212
87. Othman R, Dicks AL, Zhu Z (2012) Non precious metal catalysts for the PEM fuel cell cathode. *Int J Hydrogen Energy* 37:357
88. Xu Z, Li H, Cao G, Zhang Q, Li K, Zhao X (2011) Electrochemical performance of carbon nanotube-supported cobalt phthalocyanine and its nitrogen-rich derivatives for oxygen reduction. *J Mol Catal A Chem* 335:89
89. Wiesener K, Ohms D, Neumann V, Franke R (1989) N₄ macrocycles as electrocatalysts for the cathodic reduction of oxygen. *Mater Chem Phys* 22:457
90. Bezerra CWB, Zhang L, Lee K, Liu H, Marques ALB, Marques EP, Wang H, Zhang J (2008) A review of Fe-N/C and Co-N/C catalysts for the oxygen reduction reaction. *Electrochim Acta* 53:4937
91. Bashyam R, Zelenay P (2006) A class of non-precious metal composite catalysts for fuel cells. *Nature* 443:63
92. Martinez Millan W, Toledano Thompson T, Arriaga LG, Smit MA (2009) Characterization of composite materials of electroconductive polymer and cobalt as electrocatalysts for the oxygen reduction reaction. *Int J Hydrogen Energy* 34:694
93. Qin HY, Liu ZX, Yin WX, Zhu JK, Li ZP (2008) A cobalt polypyrrole composite catalyzed cathode for the direct borohydride fuel cell. *J Power Sources* 185:909
94. Wu G, More KL, Johnston CM, Zelenay P (2011) High-performance electrocatalysts for oxygen reduction derived from polyaniline, iron, and cobalt. *Science* 332:443
95. Wu G, Artyushkova K, Ferrandon M, Kropf AJ, Myers D, Zelenay P (2009) Performance durability of polyaniline-derived non-precious cathode catalysts. *ECS Trans* 25:1299
96. Wu G, Chen Z, Artyushkova K, Garzon FH, Zelenay P (2008) Polyaniline-derived non-precious catalyst for the polymer electrolyte fuel cell cathode. *ECS Trans* 16:159
97. Wu G, Johnston CM, Mack NH, Artyushkova K, Ferrandon M, Nelson M, Lezama-Pacheco JS, Conradson SD, More KL, Myers DJ, Zelenay P (2011) Synthesis-structure-performance correlation for polyaniline-Me-C non-precious metal cathode catalysts for oxygen reduction in fuel cells. *J Mater Chem* 21:11392
98. Matter PH, Wang E, Arias M, Biddinger EJ, Ozkan US (2007) Oxygen reduction reaction activity and surface properties of nanostructured nitrogen-containing carbon. *J Mol Catal A Chem* 264:73
99. Matter PH, Zhang L, Ozkan US (2006) The role of nanostructure in nitrogen-containing carbon catalysts for the oxygen reduction reaction. *J Catal* 239:83
100. Gong K, Du F, Xia Z, Durstock M, Dai L (2009) Nitrogen-doped carbon nanotube arrays with high electrocatalytic activity for oxygen reduction. *Science* 323:760

101. Wang S, Zhang L, Xia Z, Roy A, Chang DW, Baek J-B, Dai L (2012) BCN graphene as efficient metal-free electrocatalyst for the oxygen reduction reaction. *Angew Chem Int Ed* 51:4209
102. Zheng Y, Jiao Y, Jaroniec M, Jin Y, Qiao SZ (2012) Nanostructured metal-free electrochemical catalysts for highly efficient oxygen reduction. *Small* 8:3550
103. Kundu S, Nagaiah TC, Xia W, Wang Y, Dommele SV, Bitter JH, Santa M, Grundmeier G, Bron M, Schuhmann W, Muhler M (2009) Electrocatalytic activity and stability of nitrogen-containing carbon nanotubes in the oxygen reduction reaction. *J Phys Chem C* 113:14302
104. Subramanian NP, Li X, Nallathambi V, Kumaraguru SP, Colon-Mercado H, Wu G, Lee J-W, Popov BN (2009) Nitrogen-modified carbon-based catalysts for oxygen reduction reaction in polymer electrolyte membrane fuel cells. *J Power Sources* 188:38
105. Rao CV, Cabrera CR, Ishikawa Y (2010) In search of the active site in nitrogen-doped carbon nanotube electrodes for the oxygen reduction reaction. *J Phys Chem Lett* 1:2622
106. Chen Z, Higgins D, Tao H, Hsu RS, Chen Z (2009) Highly active nitrogen-doped carbon nanotubes for oxygen reduction reaction in fuel cell applications. *J Phys Chem C* 113:21008
107. Chen Z, Higgins D, Chen Z (2010) Nitrogen doped carbon nanotubes and their impact on the oxygen reduction reaction in fuel cells. *Carbon* 48:3057
108. Lin Z, Song M-k, Ding Y, Liu Y, Liu M, Wong C-p (2012) Facile preparation of nitrogen-doped graphene as a metal-free catalyst for oxygen reduction reaction. *Phys Chem Chem Phys* 14:3381
109. Ci S, Wu Y, Zou J, Tang L, Luo S, Li J, Wen Z (2012) Nitrogen-doped graphene nanosheets as high efficient catalysts for oxygen reduction reaction. *Chin Sci Bull* 57:3065
110. Lin Z, Waller GH, Liu Y, Liu M, Wong C-p (2012) Simple preparation of nanoporous few-layer nitrogen-doped graphene for use as an efficient electrocatalyst for oxygen reduction and oxygen evolution reactions. *Carbon* 53:130
111. Zheng B, Wang J, Wang F-B, Xia X-H (2013) Synthesis of nitrogen doped graphene with high electrocatalytic activity toward oxygen reduction reaction. *Electrochem Commun* 28:24
112. Parvez K, Yang S, Hernandez Y, Winter A, Turchanin A, Feng X, Müllen K (2012) Nitrogen-doped graphene and its iron-based composite as efficient electrocatalysts for oxygen reduction reaction. *ACS Nano* 6:9541
113. Byon HR, Suntivich J, Shao-Horn Y (2011) Graphene-based non-noble-metal catalysts for oxygen reduction reaction in acid. *Chem Mater* 23:3421
114. Su Y, Zhang Y, Zhuang X, Li S, Wu D, Zhang F, Feng X (2013) Low-temperature synthesis of nitrogen/sulfur co-doped three-dimensional graphene frameworks as efficient metal-free electrocatalyst for oxygen reduction reaction. *Carbon* 62:296
115. Xue Y, Yu D, Dai L, Wang R, Li D, Roy A, Lu F, Chen H, Liu Y, Qu J (2013) Three-dimensional B, N-doped graphene foam as a metal-free catalyst for oxygen reduction reaction. *Phys Chem Chem Phys* 15:12220
116. Jeon I-Y, Choi H-J, Choi M, Seo J-M, Jung S-M, Kim M-J, Zhang S, Zhang L, Xia Z, Dai L, Park N, Baek J-B (2013) Facile, scalable synthesis of edge-halogenated graphene nanoplatelets as efficient metal-free electrocatalysts for oxygen reduction reaction. *Sci Rep* 3:1
117. Li Y, Zhou W, Wang H, Xie L, Liang Y, Wei F, Idrobo J-C, Pennycook SJ, Dai H (2012) An oxygen reduction electrocatalyst based on carbon nanotube-graphene complexes. *Nat Nano* 7:394
118. Tang Y, Allen BL, Kauffman DR, Star A (2009) Electrocatalytic activity of nitrogen-doped carbon nanotube cups. *J Am Chem Soc* 131:13200
119. Allen BL, Kichambare PD, Star A (2008) Synthesis, characterization, and manipulation of nitrogen-doped carbon nanotube cups. *ACS Nano* 2:1914

Lina Ma and Haijun Niu

Contents

1	Introduction	392
2	Application in Counter Electrodes	392
2.1	Poly(3,4-ethylenedioxythiophene): Multi-Walled Carbon Nanotubes	393
2.2	Carbon Nanotubes/Platinum	396
2.3	CoS/Multi-Walled Carbon Nanotubes	400
2.4	Carbon Nanotubes/Polypyrrole	401
2.5	Carbon Nanotubes/Polyaniline	403
2.6	Multi-Walled Carbon Nanotubes/Graphenes	403
3	Application in Anodes	404
4	Application in Electrolyte	407
5	Conclusions	410
	References	411

Abstract

In recent years, carbon nanotubes(CNTs) have attracted more and more attention due to their special electric structure, large specific surface area, hollow and layered structures, extraordinary mechanical and chemical stability properties and their widely potential applications. Especially, CNTs not only have a large electrons-storage capacity, but also show electronic conductivity similar to that of metals. Taking account of their 1D nano-structures and good electrical conductivity, it is reasonable to conclude that CNTs are beneficial to transport the electrons and enhance photoelectric conversion efficiencies of dye-sensitized

L. Ma • H. Niu (✉)

Key Laboratory of Functional Inorganic Material Chemistry, Ministry of Education, Department of Macromolecular Science and Engineering, Heilongjiang University, Harbin, China
e-mail: malinabrave@126.com; haijunniu@hotmail.com

solar cells (DSSCs). This review surveys the literature and highlights recent progress in the three possible applications (as counter electrode, anode, and electrolyte) of CNTs in DSSCs, and the mechanism of increasing electron transport and conversion efficiency is analyzed.

Keywords

Carbon Nanotubes • Dye-sensitized solar cells • Composites

1 Introduction

Since Grätzel and O'Regan first reported on DSSCs in 1991, DSSCs have attracted increasing interest. A DSSC is composed of dye molecules, nanocrystalline titanium dioxide, and electrolytes containing a redox couple and counter electrode. Among solar cell materials, CNTs have attracted popular attention, attributable to their extraordinary specific surface area and rapid electron transfer rate. CNTs have three possible applications in DSSCs:

1. CNTs are promising candidates for counter electrode materials in DSSCs because of properties such as inexpensiveness and catalytic activity for I_3^- reduction.
2. CNTs added to TiO_2 films help to establish a good interconnection among TiO_2 particles, improve electron diffusion coefficients and electron lifetimes, and enhance the solar energy conversion.
3. CNTs have been added to electrolyte for increasing conversion efficiency.

In this chapter, the three primary applications of CNTs in DSSCs are described, as counter electrode, anode, and electrolyte, and the mechanism of increasing electron transport and conversion efficiency is analyzed.

2 Application in Counter Electrodes

The counter electrode (CE), a key component in a DSSC, has the essential function of conversion of tri-iodide (I_3^-) into iodide (I^-) in the electrolyte of the cell, thereby completing the cycle of operation of the cell. Because of its extraordinary catalytic ability and rapid electron transfer nature, a noble metals such as platinum (Pt) is usually employed as the catalytic film on the conducting substrate of a CE. However, because of the low abundance and high cost of Pt, it is necessary to improve the stability of the cell and lower the production cost by using a more stable and inexpensive noble metal catalyst. Previous reports have described Pt-free CEs for DSSCs, which include graphite, carbon black, carbon nanotubes, cobalt sulfide (CoS), and conducting polymers. Of these CEs, carbon nanotubes and conducting polymers are the most promising candidates for CE materials and are used in DSSCs because of their low cost, high conductivity, and excellent catalytic activity for I_3^- reduction.

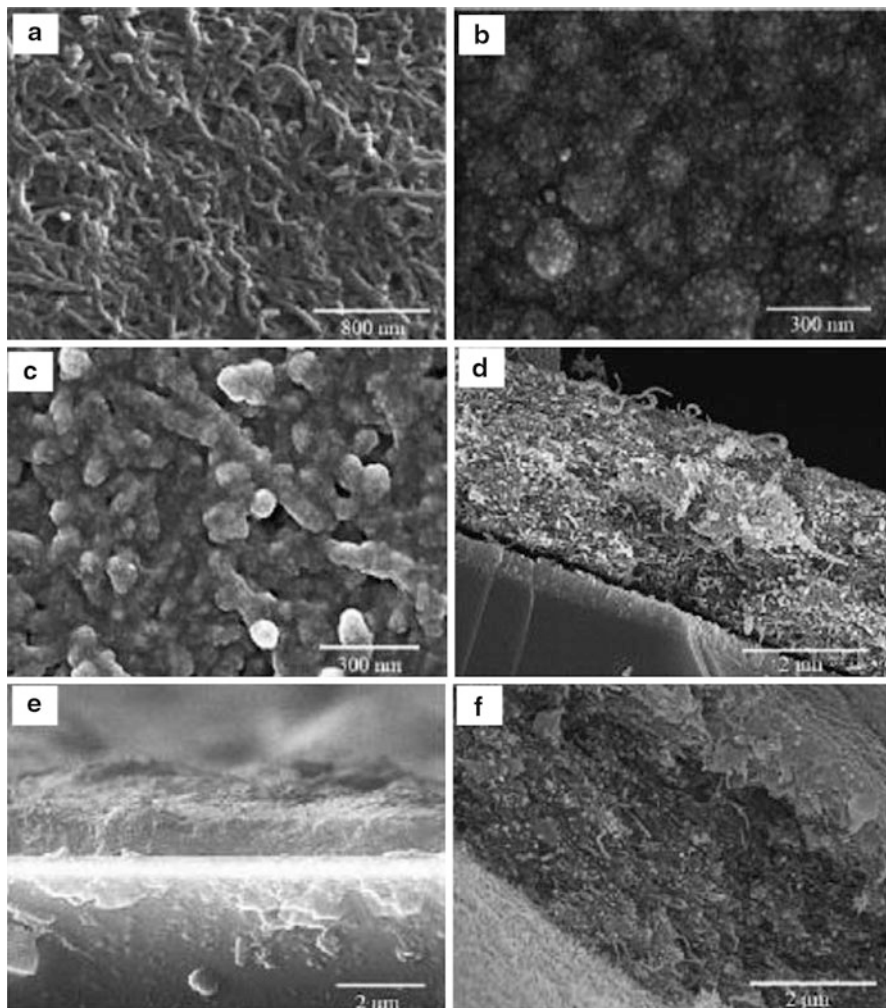


Fig. 16.1 SEM images of films MWCNT (a, d), PTh (b, c), and MWCNT/PTh (c, f); (d, e, and f are cross-sections) (Reprinted from Luo et al. [3], Enhancement of the efficiency of dye-sensitized solar cell with multi-wall carbon nanotubes/polythiophene composite counter electrodes prepared by electrodeposition, Pages No.5, Copyright (2012) with permission from Elsevier)

2.1 Poly(3,4-ethylenedioxythiophene): Multi-Walled Carbon Nanotubes

Polythiophene (PTh) and poly(3,4-ethylenedioxythiophene) (PEDOT) have been presented as candidates for counter electrode (CE) in the DSSCs. Yanagida et al. used chemically polymerized PEDOT on fluorine-doped tin oxide (FTO)

glass as the CE and obtained a conversion efficiency (η) of 3.6 % under 100 mW cm^{-2} [1]. Furthermore, the incorporation of multi-walled carbon nanotubes (MWCNTs) in the PEDOT film that was coated on various substrates was investigated. The DSSC containing the PEDOT films with 0.6 wt. % of MWCNTs on stainless steel as CE had the best cell performance of ($\eta =$) 8.08 %, with short-circuit current density (J_{sc}), open-circuit voltage (V_{oc}), and fill factor (FF) of 17.00 mA cm^{-2} , 720 mV, and 0.66, respectively [2].

In order to increase the energy conversion efficiency of DSSCs, our group fabricated MWCNT/PTh composite film counter electrode by electrophoresis and cyclic voltammetry (CV) in sequence [3]. The morphology and chemical structure were characterized by transmission electron microscopy (TEM), scanning electron microscope (SEM), and Raman spectroscopy, respectively (shown in Fig. 16.1). The PTh electrodeposited on MWCNT was spherical and porous, which not only improved the roughness and specific surface area of MWCNT but also the electronic transmission capacity of PTh [4]. The overall energy conversion efficiency (η) of the DSSC employing the MWCNT/PTh composite film reached 4.72 %, which is close to that of the DSSC with a platinum (Pt) counter electrode (5.68 %). Compared with a standard DSSC with MWCNT counter electrode, with efficiency of 2.68 %, the η was increased by 76.12 % for the DSSC with MWCNT/PTh counter electrode. These results indicated that the composite film with high conductivity, high active surface area, and good catalytic properties for I_3^- reduction can potentially be used as the counter electrode in a high-performance DSSC.

Composite films of PEDOT and functionalized MWCNT (called PEDOT–MWCNT) were fabricated by a simple oxidative electropolymerization method [5]. These films were formed on fluorine-doped, tin oxide, glass substrates as counter CEs of Pt-free DSSCs. The surface morphology, formation mechanism, and electrochemical nature of PEDOT–MWCNT films were investigated using SEM, atomic force microscopy (AFM), CV, and alternating current (AC) impedance spectroscopy. The SEM and AFM images showed that PEDOT–MWCNT films were more porous than PEDOT films (shown in Fig. 16.2). Here, the J_{sc} , FF, and η of the PEDOT–MWCNT CE were higher than those of the Pt and PEDOT CEs formed with the same deposition charge density (list in Table 16.1). CV and AC impedance spectroscopy revealed that the PEDOT–MWCNT electrode had higher electrocatalytic activity for the I_3^-/I^- redox reaction and a smaller charge transfer resistance than the PEDOT electrodes. The η of the DSSC with a PEDOT–MWCNT CE was 13.0 % higher than with a PEDOT CE using the same conditions with a ruthenium sensitizer.

Lee et al. also used chemically polymerized PEDOT and incorporated MWCNTs in the PEDOT film as CEs, which were coated on stainless steel to achieve better conversion efficiencies [2]. Unfortunately, the chemically prepared PEDOT CEs required complicated fabrication processes. However, the electropolymerization method has been successfully employed to prepare composite films of polythiophene derivatives and polyanilines with MWCNTs [6–10]. These homogeneous and well-adhesive polymer films were obtained on FTO glass (Fig. 16.3).

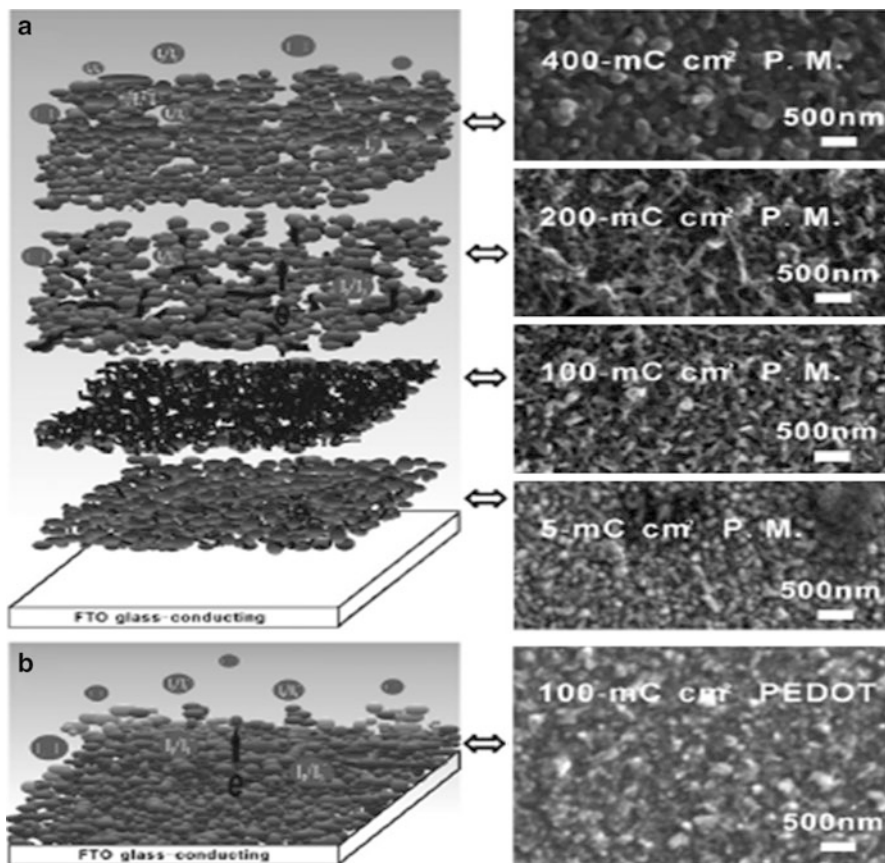


Fig. 16.2 Schematic representation of the geometric structures and their corresponding SEM images (on the right) for the (a) PEDOT-MWCNT (P.M.) and (b) PEDOT films growing on FTO glass (Reprinted from Zhang et al. [5], Electropolymerization of a poly (3,4-ethylenedioxythiophene) and functionalized, multi-walled, carbon nanotubes counter electrode for dye-sensitized solar cells and characterization of its performance, Pages No. 6, Copyright (2011) with permission from Elsevier)

CNT/PEDOT nanostructures composed of CNT cores and PEDOT shells were synthesized by chemical oxidative polymerization of 3,4-ethylenedioxythiophene (EDOT) using FeCl_3 and dodecylbenzene sulfonic acid (DBSA) as the oxidant and surfactant, respectively [11]. The resulting CNT/PEDOT nanostructures had a PEDOT layer thickness of 2–5 nm that exhibited not only higher polymerization yield but also enhanced thermal stability and electrical conductivity relative to pure PEDOT. N-Methyl-2-pyrrolidone (NMP)-based CNT/PEDOT paste containing polyvinylidene fluoride (PVDF) as a binder was painted directly onto FTO glass for use as a CE material in DSSCs. While DSSCs made of pure CNT and PEDOT CE exhibited η_s of $\sim 3.88\%$ and 4.32% under standard air mass (AM) 1.5 sunlight

Table 16.1 Photovoltaic parameters of the DSSCs base on the CEs of the Pt, 100 mC cm⁻² PEDOT, and 100 mC cm⁻² PEDOT–MWCNT films (Reprinted from Zhang et al. [5], Electropolymerization of a poly(3,4-ethylenedioxythiophene) and functionalized, multi-walled, carbon nanotubes counter electrode for dye-sensitized solar cells and characterization of its performance, Pages No. 6, Copyright (2011) with permission from Elsevier)

Counter electrode	J_{sc} (mA cm ⁻²)	V_{oc} (V)	FF	η (%)
Pt	11.3	0.759	0.631	5.43
PEDOT–MWCNT	11.5	0.742	0.641	5.47
PEDOT	10.3	0.744	0.632	4.84

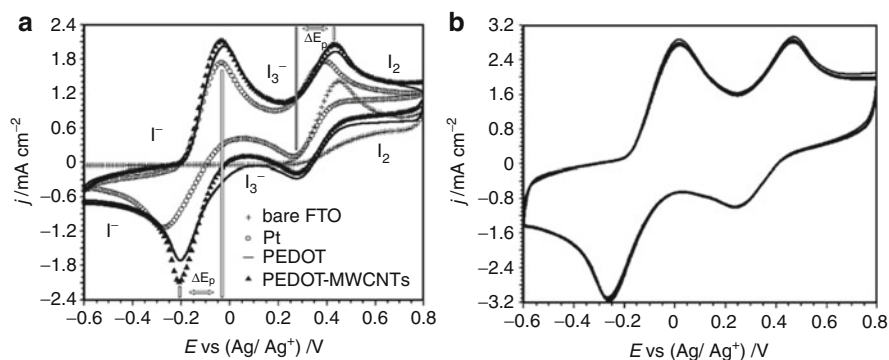


Fig. 16.3 (a) Cyclic voltammograms of the Pt, 100 mC cm⁻² PEDOT, and 100 mC cm⁻² PEDOT–MWCNT electrodes on FTO glass in 0.01 M LiI, 0.001 M I₂, and 0.1 M LiClO₄ acetonitrile solutions; init E = -0.5 V, high E = 0.8 V, low E = -0.5 V, and scan rate = 50 mVs⁻¹; (b) 30 consecutive cyclic voltammograms of the I₂/I⁻ system for the 100 mC cm⁻² PEDOT–MWCNT electrode in 0.01 M LiI, 0.001 M I₂ and 0.1 M LiClO₄ acetonitrile solutions, with a scan rate = 110 mVs⁻¹ (Reprinted from Zhang et al. [5], Electropolymerization of a poly(3,4-ethylenedioxythiophene) and functionalized, multi-walled, carbon nanotubes counter electrode for dye-sensitized solar cells and characterization of its performance, Pages No. 6, Copyright (2011) with permission from Elsevier)

illumination, respectively, the cell efficiency was enhanced to about 4.62 % with the CNT/PEDOT CE. This enhancement was due to the improved FF of the CNT/PEDOT-based DSSC realized by the increased electrical conductivity of the CNT/PEDOT composite.

2.2 Carbon Nanotubes/Platinum

Recently, carbon materials have been investigated in DSSCs in order to produce low-cost solar cells with reasonable performance [12–22]. Pt has been the preferred material for counter electrodes because of its high conductivity [23]. However, the cost of Pt prohibits use the materials for large-scale applications in solar cells. The η is expected to become higher by using electrodes of carbon nanomaterials because

contact between the electrode and electrolyte is even, and this is expected to enhance the electrochemical activity of electrode. Cells with CNT counter electrodes show better performance, especially compared with cells with other carbon counter electrodes [15]. Use of CNTs as counter electrodes to replace Pt is expected to afford the following advantages: (i) nanoscale conducting channels, (ii) large surface area, (iii) lightweight, (iv) high flexibility, and (v) low cost. In addition to enhancing conversion efficiency, the incorporation of CNTs can potentially improve mechanical and environmental stability [23].

A Pt/single-wall carbon nanotube (Pt/SWCNT) film was sprayed onto a flexible ITO-coated polyethylene naphthalate (ITO/PEN) substrate to form a CE for use in a flexible DSSC using a vacuum thermal decomposition method at low temperature (120 °C) [24]. The obtained Pt/SWCNT electrode showed good chemical stability and light transmittance and had lower charge transfer resistance and higher electrocatalytic activity for the I_3^-/I^- redox reaction compared with the flexible Pt electrode or a commercial Pt/Ti electrode. The light-to-electric η of the flexible DSSC based on the Pt/SWCNT/ITO/PEN CE and the TiO_2/Ti photoanode reached 5.96 % under irradiation with a simulated solar light intensity of 100 $mW\ cm^{-2}$. The η was increased by 25.74 % compared with the flexible DSSC with an unmodified Pt CE.

Hong and coworkers used two different powders containing SWCNT and MWCNT. CNTs were added to $PtCl_4^-$ treated electrode (called CNT-CE), and four kinds of DSSCs with SWCNT-CE and MWCNT-CE were then fabricated. The η of CNT-CE DSSC was improved to 4.03 % (SWCNT) and 4.36 % (MWCNT), respectively [25]. Compared with a standard DSSC without CNTs whose η was 3.22 %, the η was increased up to about 26 % for the MWCNT-CE DSSC.

Lee et al. investigated a complex composed of a CNT and Pt as a CE in a DSSC. The mechanism for the improved DSSC was studied by electron transfer time and electron lifetime [26]. The results demonstrated that the electron transfer time decreased and that the electron lifetime increased in CEs. The high η of the CNT–Pt complex CE was obtained because of the electrical properties of CNTs and the catalytic activity of Pt. The CNT–Pt CE showed the high η of 88 % with highly reduced Pt amount compared with pure Pt electrode.

Mohan Rao et al. have employed MWCNT, decorated with Pt as catalytic layer, for the reduction of tri-iodide ions in DSSC [27]. MWCNTs have been prepared by a simple one-step pyrolysis method using ferrocene as the catalyst and xylene as the carbon source. Pt-decorated MWCNTs have been prepared by chemical reduction method.

Figure 16.4 reveals the formation of nanotubes having a diameter of 50–70 nm and length of several micrometers. Pt nanoparticles having size of 3–5 nm were properly dispersed on the surface of MWCNTs. The corresponding HRTEM image clearly showed the crystalline nature of both MWCNTs and Pt nanoparticles. They also revealed proper adhesion of Pt on the surface of MWCNTs. Figure 16.4e confirmed the presence of Pt on the surface of MWCNTs.

The catalytic performance of Pt/MWCNT electrode was further evaluated by measuring the charge-transfer resistance (R_{ct}) in a thin-layer symmetric cell

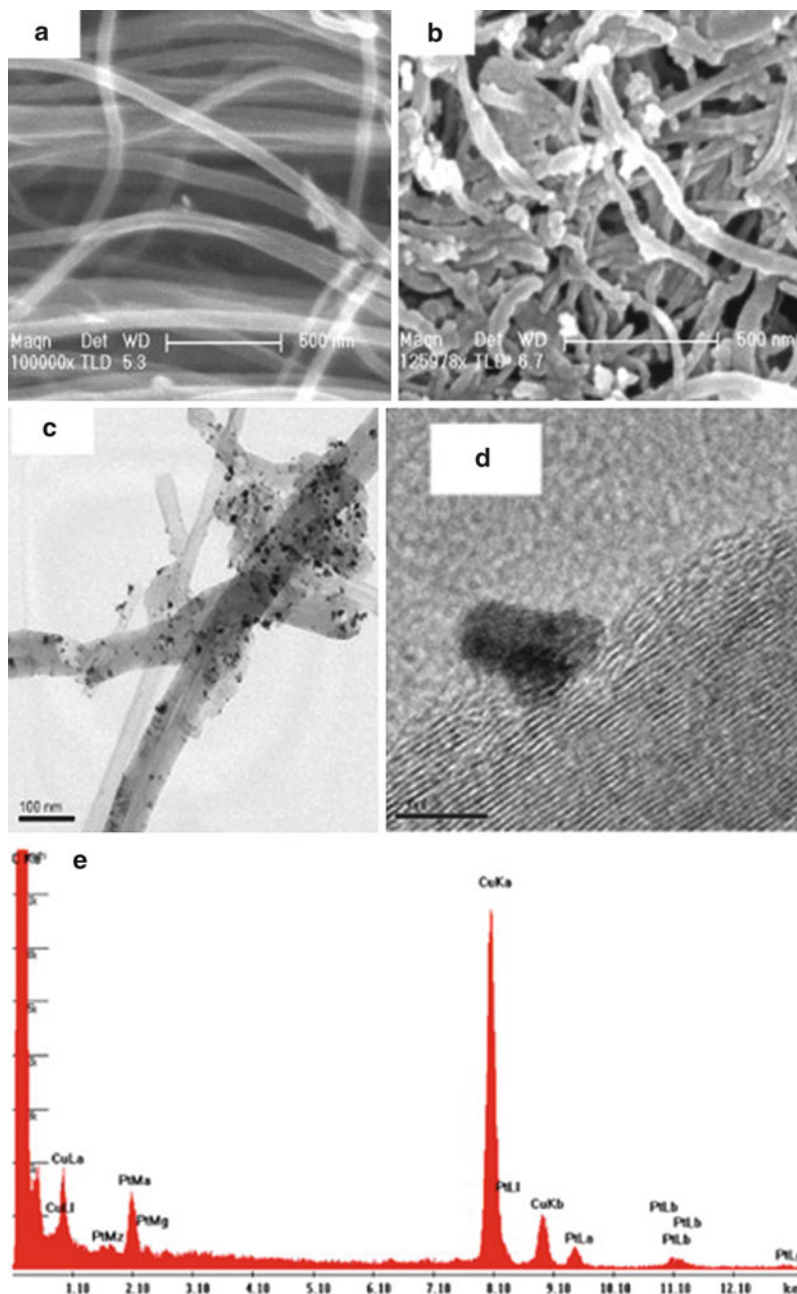


Fig. 16.4 (a) SEM images of MWCNT; (b), (c), (d), and (e) are SEM, TEM, and HRTEM images, and EDAX of Pt/MWCNT, respectively (Reprinted from Mathew et al. [27], Dye sensitized solar cell based on platinum decorated multiwall carbon nanotubes as catalytic layer on the counter electrode, Pages No. 5, Copyright (2011) with permission from Elsevier)

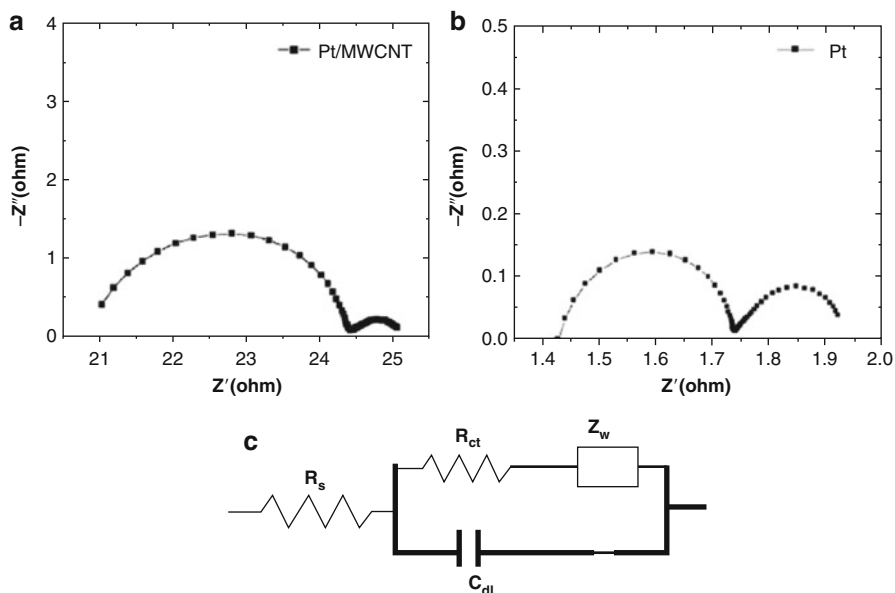


Fig. 16.5 (a) and (b) Nyquist plot for Pt/MWCNT and Pt electrodes towards I_3^-/I^- ions. (c) Equivalent circuit used for analyzing EIS spectra (Reprinted from Mathew et al. [27], Dye sensitized solar cell based on platinum decorated multiwall carbon nanotubes as catalytic layer on the counter electrode, Pages No. 5, Copyright (2011) with permission from Elsevier)

configuration. The electrolyte used was the same as that used in DSSC. Figure 16.5a, b shows the Nyquist plots of Pt/MWCNT and Pt counter electrodes towards the I_3^-/I^- electrolyte. The equivalent circuit used for analyzing the symmetric cell is shown in Fig. 16.5c. Here, R_s is the series resistance, R_{ct} is the charge transfer resistance, C_{dl} is the double layer capacitance, and Z_w is the Nernst diffusion impedance of the electrolyte.

The R_{ct} value of Pt/MWCNT was found to be 1.1 Vcm^2 and that of Pt as 0.20 Vcm^2 . Ideally, the charge transfer resistance R_{ct} at 0 V (in CE–CE cells) should be below $4\text{--}6 \text{ Vcm}^2$, which corresponds to $2\text{--}3 \text{ Vcm}^2$ for each electrode. It suggests a similar catalytic activity of these electrodes toward I_3^-/I^- electrolyte. The Nernst diffusion impedance of the electrolyte Z_w with Pt/MWCNT (0.24 Vcm^2) CE is very close to that of Pt (0.22 Vcm^2). This is due to the impedance offered to the I^-/I_3^- ions by the catalytic material present in the CE diffusing into it. Although the catalytic material has changed from Pt to Pt/MWCNT composite, there is no change in the diffusion impedance of the electrolyte, confirming the possibility of using Pt/MWCNT composite as an alternative catalyst.

The prepared MWCNTs and Pt/MWCNTs have been characterized by X-ray diffraction (XRD), SEM, and TEM. In combination with a dye-adsorbed TiO_2 photoanode and an organic liquid electrolyte, Pt/MWCNT composite CE showed an enhanced I_{sc} of 16.12 mA/cm^2 , leading to a cell η of 6.50 %, which is comparable to that of Pt.

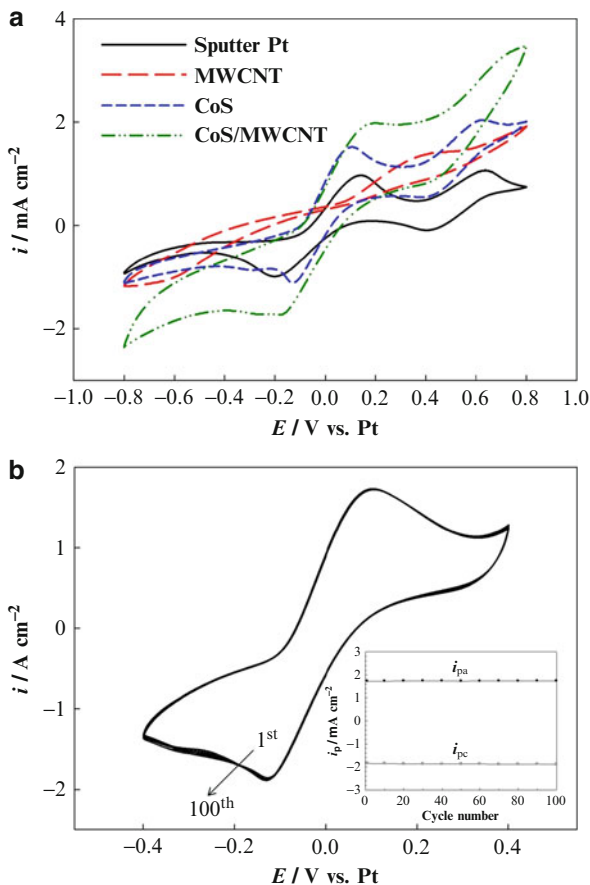
A composite film is coated on the FTO using a solution containing a synthesized dispersant, poly(oxyethylene)-segmented imide (POEM), H_2PtCl_6 , and MWCNT; the coated FTO is used as the CE for a DSSC [28]. The annealing temperature of the composite film, in the range of 110–580 °C, is found to be crucial for optimizing its catalytic ability to obtain the best possible performance for the DSSC. About 47 % loss in mass for the POEM/ H_2PtCl_6 /MWCNT composite is observed from 110 °C to 390 °C, due to not only the progressive formation of PtNPs from H_2PtCl_6 but the decomposition of POEM. Therefore, the η of DSSCs applying these CEs is enhanced from 1.28 ± 0.08 % (110 °C) to 8.47 ± 0.21 % (390 °C). The mass of the composite is lost dramatically under heating above 390 °C, due to the decomposition of MWCNTs. The η decreases to 7.77 ± 0.15 % at 450 °C because of the decrease in surface roughness of film. PtNPs grow in sizes from 450 °C to 580 °C, resulting in the further decrease in catalytic ability of film and the observed η from 7.77 ± 0.15 % to 7.19 ± 0.21 %.

MWCNTs were grown using thermal CVD at a low temperature of 530 °C to be fabricated as a CE of DSSCs [29]. Ammonia gas and acetylene gas were introduced as reactive gas sources with 90 sccm and 108 sccm, respectively. DSSCs using CNT and Pt counter electrodes were fabricated using the conventional method to compare their efficiencies. As a result, comparable electrical and optical properties were obtained for both electrodes. UV transmittance for the fabricated CNTs was higher than that for Pt electrode. Moreover, the cell η of each DSSC was measured to be 0.99 % and 0.85 % using CNT and Pt counter electrodes, respectively. Therefore, the cell η using the CNT CE was comparable to that using the Pt CE. Overall, it was found that directly grown MWNTs at low temperature are a highly promising material to be used as a CE for DSSC.

2.3 CoS/Multi-Walled Carbon Nanotubes

CoS-coated MWCNT CE was first incorporated into Pt-free DSSC [30]. This composite film was fabricated using an electrophoresis of MWCNTs onto a FTO substrate and then subjected to CoS electrodeposition. The cyclic voltammetric tests recorded an enhanced electrocatalytic activity (Fig. 16.6a) when the CoS was deposited onto the surface of the MWCNTs. Additionally, consecutive cyclic voltammetric tests demonstrated that the CE possessed excellent electrochemical stability (Fig. 16.6b). Thus, the DSSC assembled with CoS/MWCNT CE showed an enhanced η of 6.96 % (compared with 2.91 % for DSSCs with MWCNT CE or 5.86 % for CoS CE alone) under full sunlight illumination (100 mW cm^{-2} , AM 1.5G) due to the superior electrocatalytic activity of the out-shell CoS material and highly specific surface of the MWCNTs. Although, the study of this kind of CoS/MWCNT film is still very much in the primary stages, in view of its superior electrocatalytic performance and excellent electrochemical stability, the CoS/MWCNT composite can be viewed as a promising CE alternative for use in low-cost DSSCs.

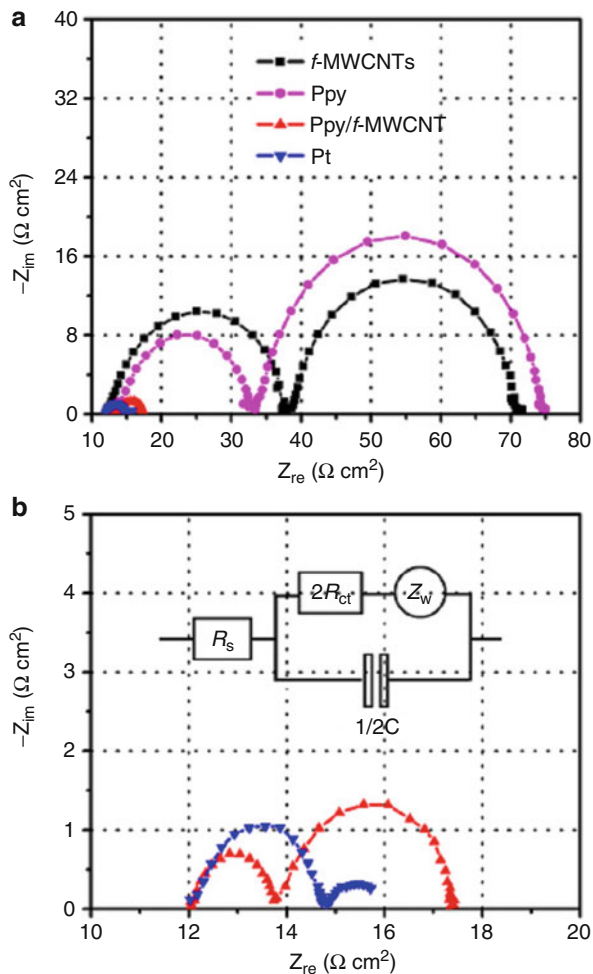
Fig. 16.6 (a) CVs of sputtered-Pt, MWCNTs, CoS, and CoS/MWCNT CE at a scan rate of 10 mV s^{-1} . (b) Consecutive 100 CVs of I_3^-/I^- for CoS/MWCNT CE. The inset in (b) shows the relationship between cycle times and the redox peak currents (Reprinted from Lin et al. [30], A composite counter electrode of CoS/MWCNT with highly electrocatalytic activity for dye-sensitized solar cells, Pages No 4, Copyright (2011) with permission from Elsevier)



2.4 Carbon Nanotubes/Polypyrrole

Peng et al. report facile fabrication of polypyrrole (PPy)/functionalized MWCNT (f-MWCNT) nanocomposite films on rigid FTO and flexible ITO-coated polyethylene naphthalate (PEN) substrates by a drop-casting method, and their application as CEs in DSSCs [31]. The electrochemical impedance spectroscopy (EIS) and CV measurements of this solution-processed PPy/f-MWCNT nanocomposite film display good catalytic performance for I_3^-/I^- solution. The photoelectric conversion efficiency of the DSSCs with the PPy/f-MWCNT CEs on FTO and PEN substrates reaches 7.02 % and 4.04 %, respectively, under AM1.5 illumination of 100 mW cm^{-2} , comparable to that of DSSCs based on sputtered-Pt electrodes. The fabrication method for such counter electrodes is simple under room temperature and can be applicable in large-scale production. It is believed that the results may expand the scope of low-cost, high-efficiency, flexible DSSCs for practical applications.

Fig. 16.7 Nyquist plots for the counter electrodes (f-MWCNTs, PPy, PPy/f-MWCNT, and Pt), respectively (a), and the magnified view for the PPy/f-MWCNT and Pt counter electrode (b). Z_w Nernst diffusion impedance, R_{ct} charge-transfer resistance of electrode/electrolyte interface, CPE constant phase element of electrical double layer, R_s serial resistance. The inset shows the equivalent circuit for the impedance spectra (Reprinted from Peng et al. [31], Facile fabrication of polypyrrole/functionalized multiwalled carbon nanotubes composite as counter electrodes in low-cost dye-sensitized solar cells, Pages No. 6, Copyright (2011) with permission from Elsevier)



In the Nyquist plot (Fig. 16.7), which is similar to that in Fig. 16.3c, the semicircle at the high-frequency range corresponds to the charge-transfer resistance (R_{ct}) of the counter electrode, which describes catalytic activity for reducing triiodide ions, whereas the semicircle at the low-frequency side represents diffusion impedance (Z_w) of the I_3^-/I^- redox couple in the electrolyte. The R_{ct} can be deduced for f-MWCNTs, PPy, PPy/f-MWCNT, and Pt films, respectively. The obtained R_{ct} value of PPy/f-MWCNT electrode is found to be much lower than those of PPy and f-MWCNTs electrodes, and even lower than that in the case of Pt film, indicating a higher catalytic performance characteristic of PPy/f-MWCNT, which is due to the high electrical conductivity and superior electrocatalytic activity of PPy/f-MWCNT electrodes.

In our group, for the purpose of replacing the precious Pt counter electrode in DSSCs with higher η , we also fabricated MWCNT/PPy double-layer film CE by

electrophoresis and CV layer-by-layer (the results have not been published yet). AFM demonstrated the morphology of the composite and Raman spectroscopy verified the PPy had come into being. The overall η of the DSSC employing the MWCNT/PPy CE reached 3.78 %. Compared with a reference DSSC using single MWCNT film CE with efficiency of 2.68 %, the η was increased by 41.04 %. The result of impedance showed that the charge transfer resistance, R_{ct} , of the MWCNT/PPy CE had the lowest value compared with MWCNT or PPy electrode. These results indicated that the composite film with high conductivity, high active surface area, and good catalytic properties for I_3^- reduction can potentially be used as the CE in a high-performance DSSC.

2.5 Carbon Nanotubes/Polyaniline

As a type of functional conductive polymer, polyaniline (PANI) has been used for decades owing to its easy fabrication, high electric conductivity, and fast doping/dedoping nature. Electrodes fabricated by casting PANI onto FTO glass from its suspension have shown good catalytic activity for I_3^- reduction [32]. However, complex processes and high-temperature treatments are required in the method mentioned above.

Meng fabricated a new kind of flexible composite electrode by in situ polymerizing a thin layer of conductive PANI on a flexible graphite (FG) substrate. The electrochemical characterizations have confirmed that the composite electrode shows a good catalytic activity for I_3^- reduction and a reduced sheet resistance, which lead to high J_{sc} , FF, and final η for the fabricated DSSCs. Further investigation reveals the relationship between the performance of the PANI/FG electrode and its synthesis conditions, such as reaction time, monomer concentrations, and doping acids. A thin layer (ca. 50 nm) of emeraldine PANI deposited on FG can promote the cell efficiency greatly, suggesting the excellent electrochemical activity comes from the nature of the emeraldine PANI. The type of doping acid (sulfuric acid or perchloride acid) has almost no influence on the photoelectron conversion performance in DSSCs. An optimizing overall η of 7.36 %, which is comparable to 7.45 % of that with Pt electrode under the same test condition, has been obtained by using the composite CE with PANI film thickness of 330 nm. The facile chemical polymerization procedure, flexibility, low cost, and good photovoltaic properties allow the PANI/FG composite electrode to be a promising alternative CE used in future large-scale fabrication of DSSCs [33].

2.6 Multi-Walled Carbon Nanotubes/Graphenes

Ma and coworkers have reported using the bulk molding compound (BMC) process to prepare the polymer composite conductive plates [34, 35]. Several nanomaterials, including graphite, clay, and CNTs, have been used to improve the mechanical properties and electrical conductivity of the composite plates.

Among these nanomaterials, CNTs form the most efficient electronic conductive network, effectively increasing the electrical conductivity [35]. However, with higher CNT loading, the electrical properties of the composite plates level off due to CNTs' aggregation. Hence, cost-effective and high-performance composite conductive plates have been developed for use in DSSCs [36]. Composite plates with various graphite contents at a constant CNT loading were prepared by the BMC process. Results showed that the bulk electrical resistance of the composite plate gradually decreases from 6.7 to 1.7 m Ω cm as the graphite content increases, which is due to the formation of efficient electronic conducting networks. For DSSCs, the composite plates may be suitable substitutes for the conductive glass plates in the CE substrates of DSSCs. Results reveal that composite plates at the optimum level (80 wt% graphite loading) provide lower cell resistance, lower preparation cost, and higher cell performance than common conductive glass plates. Therefore, in order to decrease the cost of the cells and to maintain good cell performance, this graphite-like composite plate prepared by the BMC process is a promising substitute component for DSSCs.

Choi and colleagues recently reported MWCNTs/graphenes composite electrode for DSSCs [37]. In their composite electrode, MWCNT layers were prepared on top of the graphene layers using chemical vapor deposition. The MWCNTs/graphenes composite CE in DSSCs showed efficient electrocatalytic properties and η of 3.0 %, which is higher than those of MWNTs and grapheme CE. However, their method has disadvantages such as relatively high production cost and complications of the synthesis process. Therefore, it should be necessary that a facile method is developed to prepare the MWNTs/graphene composite on electrode substrates.

The group of Soo-Hyoung Lee adopted a facile method to prepare the MWCNTs/graphenes composite on electrode substrates using a simple doctor blade method and composite paste [38]. They found that the photovoltaic performance was strongly influenced by the concentration of graphene nano-sheets (GNS) in composite electrode. The composite electrode with 60 % MWCNTs and 40 % GNS-based DSSCs showed the maximum η of 4.0 %, while sputter-deposited Pt electrode-based DSSCs showed a η of 5.0 %.

3 Application in Anodes

Semiconductor photocatalysis has important applications such as achieving sustainable energy generation and treating environmental pollution. TiO₂ has been the most widely researched photocatalyst, but it suffers from low efficiency and narrow light response range. Combining TiO₂ with carbonaceous nanomaterials is being increasingly investigated as a means to increase photocatalytic activity, and demonstrations of enhancement are plentiful [39].

Carbon nanotubes have attracted more and more attention due to their special electric structure, large specific surface area, hollow and layered structures, extraordinary mechanical and chemical stability properties, and their wide number of

potential applications [40]. Carbon nanotubes especially not only have a large electron-storage capacity but also show electronic conductivity similar to that of metals [41]. Taking into account their 1D nano-structures and good electrical conductivity, it is reasonable to conclude that CNT/TiO₂ composites are beneficial to transport the electrons within TiO₂ films and enhance their photocatalytic and photoelectric conversion efficiencies [42]. Many experimental results have confirmed this point. For example, Yu et al. reported that CNT/TiO₂ composites obtained by ultrasonic irradiation showed the enhanced photocatalytic activity toward decomposing gas acetone in air as well as azo dyes in water [43]. Muduli et al. demonstrated the enhanced η in DSSCs based on the hydrothermally synthesized TiO₂-MWCNT nanocomposites [44]. Lee et al. reported DSSCs based on nanocomposites of preprocessed MWCNT with carboxylic acid groups and TiO₂ nanoparticles (NPs) synthesized via a sol-gel process, showing a η of 4.97 % [45]. Yen et al. synthesized MWCNT-TiO₂ nanocomposites by a modified acid-catalyzed sol-gel method and examined their application in DSSCs; they emphasized the importance of optimum MWCNT loading to realize an efficiency of 4.62 % [46]. Kim et al. further obtained a DSSC efficiency of 5.02 % using MWCNT-TiO₂ nanocomposites, which exhibit enhancement by ~ 50 % over the case without MWCNT [47]. More recently, Sawatsuk et al. have shown the improvement in the η of DSSC by almost 60 % by a simple mixing process [48].

DSSCs based on anatase TiO₂ hollow spheres (HS)/MWCNT nanocomposite films are fabricated by a direct mechanical mixing and doctor blade method [49]. The CNT loading clearly influences the textural properties (including crystallite size, specific surface areas, porosity, and pore volume) and η of the TiO₂ HS/CNT nanocomposite film electrodes. As a result, TiO₂ HS/CNT nanocomposite films with low loadings (<0.1 wt%) show enhanced η , as compared with pristine TiO₂ counterparts. On the other hand, high CNT loadings (>0.1 wt%) result in a decrease in efficiency. Under optimal conditions, the η of the CT-0.1 solar cell is 4.71 %, which is higher than that (3.94 %) of pure TiO₂ cells. The improvement is due to the fact that CNTs reduce the electrolyte/electrode interfacial resistance and the recombination rate of excited electrons and holes, and they enhance the transport of electrons from the films to FTO substrates. The decrease of the conversion efficiency at high CNT loadings (>0.1 wt%) is to the result of light harvesting competition between CNT and dye molecules, which influences the light adsorption of the dye-sensitizer, and consequently reduces the efficiency. The performances of TiO₂ HS/CNT cells are also compared with P25/CNT composite cells at the same film thickness, and their optimal η s under the experimental conditions are 4.71 % and 4.52 %, respectively. The enhanced performance of TiO₂ HS/CNT cells is due to their higher surface area and hierarchically nanoporous structures. This study will provide new insight into fabrication and structural design of highly efficient DSSCs.

Li et al. have demonstrated the successful fabrication of DSSCs based on the architecture of vertically aligned carbon nanofiber (VACNF) nanobrushes coated with a nanoneedle-textured anatase TiO₂ film by a metal organic chemical vapor deposition (MOCVD) strategy [50] (shown in Fig. 16.8). The VACNF array was

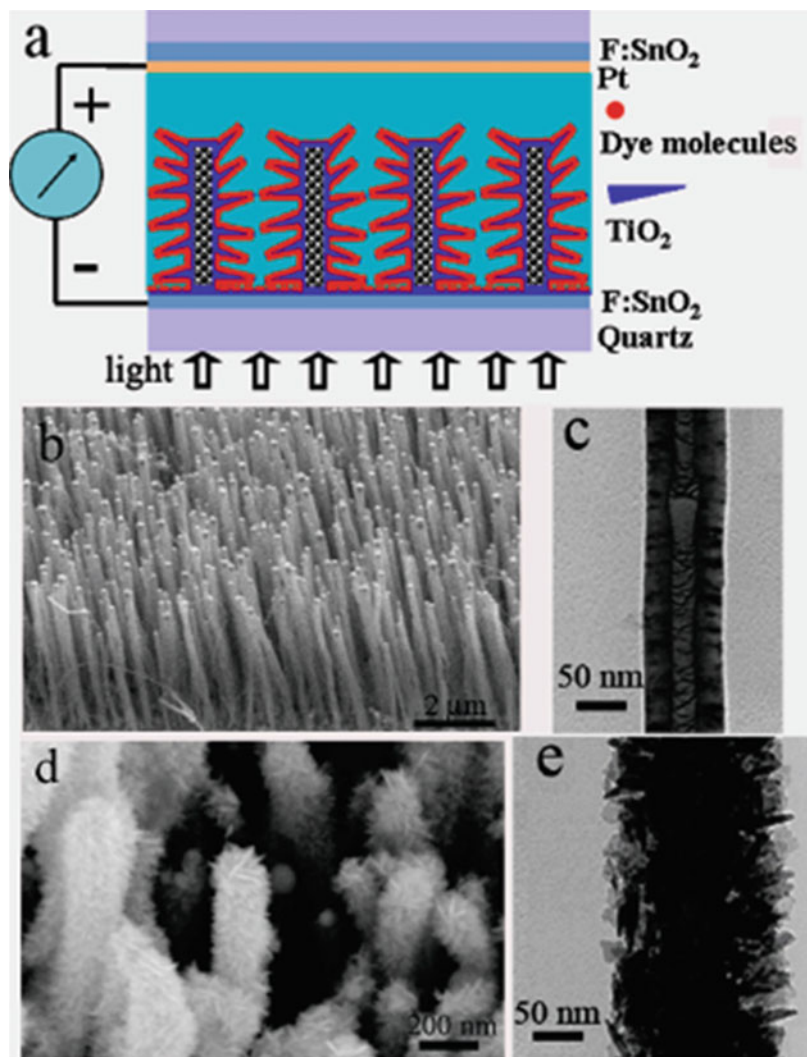


Fig. 16.8 (a) Schematic of VACNF arrays coated with anatase TiO₂ nanoneedles for DSSCs. (b) SEM image at a 45° perspective view of an as-grown VACNF array. (c) TEM image of an as-grown CNF. (d) SEM image at a 45° perspective view of the VACNF array after being coated with anatase TiO₂ nanoneedles. (e) TEM image of a CNT after being coated with anatase TiO₂ needles (Reprinted from Liu et al. [50], Novel Dye-Sensitized Solar Cell Architecture Using TiO₂-Coated Vertically Aligned Carbon Nanofiber Arrays, 1645–1649, Copyright (2009) with permission from American Chemical Society)

grown on a transparent electrode consisting of a FTO film on quartz. Optical spectra indicate that VACNF has much less light absorption because of the vertically aligned structure. This ensures that the light can reach a much larger volume of active photovoltaic materials. TiO₂ coating and dye derivatization further enhance

the utilization of photons at the TiO₂ shell surface and reduce the loss of photons by CNF absorption. The enhanced optical depth allows the use of a 5- μ m-long VACNF array for DSSCs. The *I-V* characterization under 100 mW/cm² sunlight gives an encouraging η of 1.09 % and a rather high V_{oc} of 0.64 V, comparable to those of DSSCs made with ZnO or TiO₂ NWs/NTs. This new core-shell vertical architecture presents a large open spacing, allowing homogeneous dye derivatization, quantum dots attachment, and mediator/electrolyte access. The ability to separate multiple roles in a DSSC by integrating various materials on the VACNF template provides new routes to investigate the mechanisms in solar energy capture and conversion. Optimization is in process to reach the intrinsic performance that this architecture may offer.

Ming-Yu Yen employed a solution-based method to prepare a three-dimensional (3-D) hybrid material comprising graphene and acid-treated MWCNTs [51]. The adsorption of MWCNTs on graphene reduces the $\pi-\pi$ interaction between graphene sheets resulting from steric hindrance, providing a subsequent reduction in aggregation. Optimal proportions of MWCNTs to graphene (2:1) enabled the even distribution of individual MWCNTs deposited on the surface of the graphene. The hybrid 3-D material was incorporated within a TiO₂ matrix and used as a working electrode in DSSCs. The hybrid material provides a number of advantages over electrodes formed of either MWCNTs or graphene alone, including a greater degree of dye adsorption and lower levels of charge recombination. In this study, DSSCs incorporating 3-D structured hybrid materials demonstrated a η of 6.11 %, which is 31 % higher than that of conventional TiO₂-based devices.

DSSCs were fabricated based on MWCNT–TiO₂ photo-anodes, which were prepared by the procedures of cutting MWCNTs and subsequent immobilization TiO₂ on MWCNTs. Through a detailed study, it was found that cut-MWCNTs with proper ultrasonication time (2 h) and proper content (0.075 %) resulted in 58 % and 40 % increases in short-circuit photocurrent and η , respectively, compared with that of a DSSC using only TiO₂ photo-anode [52]. The enhancement of cut-MWCNTs for DSSC was attributed to the introduction of percolative conductive paths, which facilitate the rapid electron transfer.

Yu-Chen Tsai demonstrated the fabrication of MWCNT–TiO₂ nanocomposite for use as a secondary layer in DSSCs to improve the η [53]. A noncovalent method to disperse MWCNTs and TiO₂ in aqueous solution with chitosan was used. In the secondary layer, TiO₂ clusters formed in the presence of MWCNT and MWCNT acted as an efficient conduit for electron transfer that can enhance the η of the DSSC. The parameters that could affect the photovoltaic performance of the DSSCs were evaluated and the photoelectrochemical characteristics were described and discussed.

4 Application in Electrolyte

For the purpose of increasing the energy conversion efficiency of DSSCs, CNTs were added to electrolyte. Hong and coworkers used two different powders

containing SWCNT and MWCNT to fabricate two kinds of DSSCs with SWCNT-electrolyte and MWCNT-electrolyte [25]. MWCNT-electrolyte DSSC showed higher η (4.2 %) than SWCNT-electrolyte DSSC (3.62 %). Compared with a standard DSSC without CNTs whose η was 3.22 %, the η increased up to about 26 % and 24 % for the MWCNT-electrode DSSC and the MWCNT-electrolyte DSSC, respectively. This indicates that MWCNT has higher purity for carbon content than SWCNT, and this result is similar to that obtained in the study by Usui et al. [54]. Also, it was difficult to uniformly disperse SWCNTs in the electrolyte. However, MWCNTs were well dispersed into the electrolyte, so they effectively supported the electrons' transfer from the counter electrode to the dye.

The liquid electrolyte usually employed in DSSC is still faced major drawbacks for long-term practical operation due to potential evaporation and leaking. To solve these problems, solid and quasi-solid electrolytes have been advances as alternative candidates to replace the liquid electrolytes.

Quasi-solid-state ionic liquid (IL) gel electrolytes for DSSCs are prepared via dispersion of MWCNTs in room temperature ILs. Addition of MWCNTs significantly increases the viscosity as well as the conductivity of MWCNT-based IL gels. Compared with raw MWCNTs, acid-oxidized MWCNTs improve the miscibility with ILs, which results in an enhanced gel-forming ability of MWCNT/IL gels [55]. The solar cells based on acid-oxidized MWCNT/IL gel electrolytes yield the power conversion efficiency of 5.74 % under the simulated AM1.5 solar spectrum illumination at 100 mW cm^{-2} . The superior long-term stability of fabricated DSSCs indicates that the cells based on acid-oxidized MWCNT/IL gel electrolyte could overcome the drawbacks of volatile liquid electrolytes.

Recently, CNT-polymer composite electrolytes have shown the ability to promote electron-transfer reactions in many electrochemical systems such as fuel cells, solar cells, and lithium batteries [56–58]. Thus, the highly flexible nature of CNTs may improve the interaction and cross-linking with polymer molecules as a nanofiller, which may significantly enhance the morphological and electrical properties of composite electrolytes [59]. In their previous work, the CNT-polyethylene oxide (PEO) composite electrolyte has been used for the fabrication of solid-state DSSCs in which the introduction of CNTs into PEO matrix significantly improved the electrolyte properties of DSSC such as roughness, amorphicity, and ionic conductivity [57]. A new CNT-polyacrylonitrile (PAN) composite electrolyte was prepared by the thermal polymerization of acrylonitrile (AN) with CNTs for solid-state DSSCs. It was found that the uniform CNT-PAN composite was formed due to the thermal polymerization of AN on CNTs. The strong bonding between CNTs and PAN could be confirmed by the characterization of XPS and Raman spectroscopy, resulting in the lowering of crystallinity and an increase in ionic conductivity of composite electrolytes. In comparison with bare CNTs and the other composite electrolytes, the formation of triiodide (I_3^-) ions in CNT-PAN composite electrolytes was drastically increased, which was expected from the high ionic conductivity of electrolyte via I_3^-/I^- redox couple. DSSCs fabricated with CNT-PAN composite electrolytes achieved relatively high η of 3.9 % with V_{OC} of 0.57 V, J_{SC} of 10.9 mA/cm^2 , and FF of

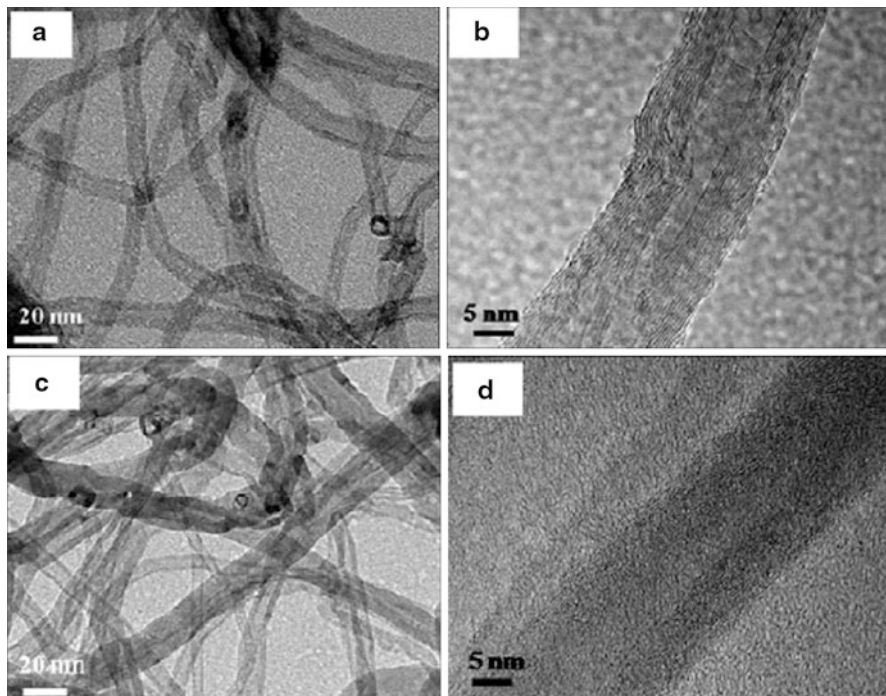


Fig. 16.9 TEM and HR-TEM images of (a, b) bare CNTs and (c, d) CNT-PAN composite, respectively (Reprinted from Akhtar et al. [59], A new carbon nanotubes (CNTs)-poly acrylonitrile (PAN) composite electrolyte for solid state dye sensitized solar cells, Pages No. 7, Copyright (2011) with permission from Elsevier)

63.6 %, which was attributed to supply the higher extent of I_3^- ions from CNT-PAN composite electrolyte during the charge transport process.

Figure 16.9 shows the TEM and high-resolution (HR)-TEM images of CNT-PAN composite electrolytes. Bare CNTs exhibit the typical crystalline tubes with the diameter of about ~ 6 nm (ID) \times ~ 12 nm (OD). Bare CNTs showed quite clear fringes, with 0.30 nm distance of two adjacent fringes, which have undamaged inside walls with some defect on the outer walls. The fringes of CNT-PAN composites are not clear, with highly damaged outer walls and quite distorted inner-tube walls. The distance between two adjacent fringes in the CNT-PAN composite is slightly increased to ca. 0.40–0.45 nm. After polymerization of PAN, a distortion takes place because of the coating of polymer on the crystalline portion of CNTs, which increases the distance of two adjacent fringes. This HR-TEM result clearly indicates that PAN moieties were embedded in the CNTs. It has been reported that the appearance of shades and spots in the polymer composite materials are ascribed to the presence of polymer molecules on the surface of composite materials of polymer and nanomaterials.

Lin Xin reported the fabrication of solid-state DSSC using in situ electrochemically polymerized poly(o-phenylenediamine) (PoPD)/MWNT composite film as

a hole transport phase [60]. The in situ electrochemical polymerization of PoPD/MWNTS in the mesoporous electrodes could make a good contact between the dye molecules and hole transport material. The electrochemical behaviors of PoPD/MWNTs indicated that the electron exchange efficiency improves obviously after the addition of carbon nanotubes in PoPD. The PoPD/MWNT composite film was deposited on the dye-anchored porous TiO_2 electrode, and I–V characterization was performed under simulated AM1.5 illumination.

Fabricated devices for the PoPD/MWNT composites prepared in 0.1 g/L MWNTs showed a photoresponse with V_{OC} of 479 mV and I_{SC} of 0.572 mA/cm² with the overall conversion efficiency of 0.13 %, higher than those of the cell with only PoPD (i.e., $I_{\text{SC}} = 0.275$ mA/cm², $V_{\text{OC}} = 462$ mV, FF = 0.35, $\eta = 0.04$ %). It is obvious that the introduction of MWNTs to PoPD composites could improve the cell performance.

5 Conclusions

CNTs have been widely used in DSSCs because of their inexpensiveness, extraordinary specific surface area, and rapid electron transfer nature, and they significantly improve electron lifetime, catalytic activity for I_3^- reduction, and cell conversion efficiency.

In this chapter, the prospect of using CNTs as the electron transport materials in DSSCs through three main ways, CE, anode, and electrolyte, are reviewed. The CNTs could be metallic or semiconducting, depending on their chirality (spiral conformation) and diameter, making them ideal reinforcing fillers in composite materials and enhancing the performance of pure conducting polymer electrodes or electrolytes such as V_{OC} , I_{SC} , and η .

The composite electrodes composed of CNT and conducting polymers that possess similar catalytic activity toward I_3^-/I^- electrolyte compared with Pt could be promising alternatives to Pt noble CE. CNTs could also improve the interaction and cross-linking with polymer molecules as a nanofiller, which may significantly enhance the morphological and electrical properties of composite electrolytes.

CNTs combined semiconductors such as TiO_2 or SnO are beneficial to transport the electrons within TiO_2 films and enhance their photocatalytic and photoelectric conversion efficiencies.

Overall, CNTs are promising candidates and perfect electrode transport materials for application in DSSCs, and this potential has led to a surge in interest. However, while the potential is undoubted, greater mechanistic understanding is required. This ongoing challenge is likely to be taken up by increasing numbers of academic and commercial institutions. As carbon levels on the bulk scale (in the form of fossil fuels, CO_2 , and other greenhouse gases, etc.) lie at the heart of many global environmental concerns, carbon on the nanoscale, for application in DSSCs, may be expected to lie at the center of efforts toward development of sustainable solutions.

Acknowledgment The authors are grateful for the support of the National Science Foundation of China (Grant No.21074031), Foundation of Heilongjiang Education Bureau.

References

1. Saito Y, Kubo W, Kitamura T, Wada Y, Yanagida S (2004) I_3^- redox reaction behavior on poly(3,4-ethylenedioxythiophene) counter electrode in dye-sensitized solar cells. *J Photochem Photobiol A Chem* 164:153
2. Lee KM, Chiu WH, Wei HY, Hu CW, Suryanarayanan V, Hsieh WF, Ho KC (2010) Effects of mesoscopic poly(3,4-ethylenedioxythiophene) films as counter electrodes for dye-sensitized solar cells. *Thin Solid Films* 518:1716
3. Luo J, Niu HJ, Wu WJ, Wang C, Bai XD, Wang W (2012) Enhancement of the efficiency of dye-sensitized solar cell with multi-wall carbon nanotubes/polythiophene composite counter electrodes prepared by electrodeposition. *Solid State Sci* 14:145
4. Yu JG, Ma TT, Liu SW (2011) Enhanced photocatalytic activity of mesoporous TiO_2 aggregates by embedding carbon nanotubes as electron-transfer channel. *Phys Chem Chem Phys* 13:3491
5. Zhang J, Li XX, Guo W, Hreid T, Hou JF, Su HQ, Yuan ZB (2011) Electropolymerization of a poly(3,4-ethylenedioxythiophene) and functionalized, multi-walled, carbon nanotubes counter electrode for dye-sensitized solar cells and characterization of its performance. *Electrochim Acta* 56:3147
6. Lee SU, Choi WS, Hong BY (2010) A comparative study of dye-sensitized solar cells added carbon nanotubes to electrolyte and counter electrodes. *Energy Mater Sol Cells* 94:680
7. Bhandari S, Deepa M, Srivastava AK, Lal C, Kant R (2008) Poly(3,4-ethylenedioxythiophene) (PEDOT)-Coated MWCNTs Tethered to Conducting Substrates: Facile Electrochemistry and Enhanced Coloring Efficiency *Macromol Rapid Commun* 29:1959
8. Byrne M, Gun'ko Y (2010) Recent Advances in Research on Carbon Nanotube-Polymer Composites. *Adv Mater* 22:1672
9. Bhandari S, Deepa M, Srivastava AK, Joshi AG, Kant R (2009) Poly(3,4-ethylenedioxythiophene)-Multiwalled Carbon Nanotube Composite Films: Structure-Directed Amplified Electrochromic Response and Improved Redox Activity. *J Phys Chem B* 113:9416
10. Abidian MR, Corey JM, Kipke DR, Martin DC (2010) Conducting polymer nanotubes improve electrical properties, mechanical adhesion, neural attachment, and neurite outgrowth of neural electrodes. *Small* 6:421
11. Shin HJ, Jeon SS, Im SS (2011) CNT/PEDOT core/shell nanostructures as a counter electrode for dye-sensitized solar cells. *Synth Met* 161:1284
12. Kay A, Gratzel M (1996) Low cost photovoltaic modules based on dye sensitized nanocrystalline titanium dioxide and carbon powder. *Sol Energy Mater Sol Cells* 44:99
13. Suzuki K, Yamaguchi M, Kumagai M, Yanagida S (2003) Application of carbon nanotubes to counter electrodes of dye-sensitized solar cells. *Chem Lett* 32:28
14. Lee WJ, Ramasamy E, Lee DY, Song JS (2008) Spray coated multi-wall carbon nanotube counter electrode for tri-iodide (I_3^-) reduction in dye-sensitized solar cells. *Sol Energy Mater Sol Cells* 92:814
15. Ramasamy E, Lee WJ, Lee DY, Song JS (2008) Performance variation of carbon counter electrode based dye-sensitized solar cells. *Electrochem Commun* 10:1087
16. Zhu HW, Zeng HF, Subramanian V, Masarapu C, Hung KH, Wei BQ (2008) Anthocyanin-sensitized solar cell using carbon nanotube films as counter electrodes. *Nanotechnology* 19:465204-1
17. Cherepy NJ, Smestad GP, Gratzel M, Zhang JZ (1997) Ultrafast electron injection: Implications for a photoelectrochemical cell utilizing an anthocyanin dye-sensitized TiO_2 nanocrystalline electrode. *J Phys Chem B* 101:9342

18. Wongcharee K, Meeyoo V, Chavadej S (2007) Dye-sensitized solar cell using natural dyes extracted from rosella and blue pea flowers. *Sol Energy Mater Sol Cells* 91:566
19. Hao SC, Wu JH, Huang YF, Lin JM (2006) Natural dyes as photosensitizers for dye-sensitized solar cell. *Sol Energy* 80:209
20. Huang Z, Liu XH, Li KX, Li DM, Luo YH, Li H, Song WB, Chen LQ, Meng QB (2007) Application of carbon materials as counter electrodes of dye-sensitized solar cells. *Electrochem Commun* 9:596
21. Lai WH, Su YH, Teoh LG, Hon MH (2008) Commercial and natural dyes as photosensitizers for a water-based dye-sensitized solar cell loaded with gold nanoparticles. *J Photochem Photobiol* 195:307
22. Robertson N (2006) Optimizing dyes for dye-sensitized solar cells. *Angew Chem Int Ed* 45:2338
23. Zhu HW, Wei JQ, Wang KL, Wu DH (2009) Applications of carbon materials in photovoltaic solar cells. *Sol Energy Mater Sol Cells* 93:1461
24. Xiao YM, Wu JH, Yue GT, Lin JM, Huang ML, Lan Z (2011) Low temperature preparation of a high performance Pt/SWCNT counter electrode for flexible dye-sensitized solar cells. *Electrochim Acta* 56:8545
25. Lee SU, Choi WS, Hong BY (2010) A comparative study of dye-sensitized solar cells added carbon nanotubes to electrolyte and counter electrodes. *Sol Energy Mater Sol Cells* 94:680
26. Im JS, Lee SK, Yun J, Lee YS (2012) CNT-Pt counter electrode prepared using a polyol process to achieve high performance in dye-sensitized solar cells. *J Ind Eng Chem* 25:581
27. Mathew A, Rao GM, Munichandraiah N (2011) Dye sensitized solar cell based on platinum decorated multiwall carbon nanotubes as catalytic layer on the counter electrode. *Mater Res Bull* 46:2045
28. Huang KC, Wang YC, Chen PY, Lai YH, Huang JH, Chen YH, Dong RX, Chuc CW, Lin JJ, Ho KC (2012) High performance dye-sensitized solar cells based on platinum nanoparticle/multi-wall carbon nanotube counter electrodes: The role of annealing. *J Power Sources* 203:274
29. Roh JY, Kim YH (2011) Synthesis of MWNTs using thermal chemical vapor deposition for the application of a counter electrode for DSSCs. *Curr Appl Phys* 11(S70):S69
30. Lin JY, Liao JH, Hung TY (2011) A composite counter electrode of CoS/MWCNT with highly electrocatalytic activity for dye-sensitized solar cells. *Electrochem Commun* 13:977
31. Peng SJ, Wu YZ, Zhu PN, Thavasi V, Mhaisalkar SG, Ramakrishna S (2011) Facile fabrication of polypyrrole/functionalized multiwalled carbon nanotubes composite as counter electrodes in low-cost dye-sensitized solar cells. *J Photochem Photobiol A Chem* 223:97
32. Li QH, Wu JH, Tang QW, Lan Z, Li PJ, Lin JM, Fan LQ (2008) Application of microporous polyaniline counter electrode for dye-sensitized solar cells. *Electrochem Commun* 10:101299
33. Sun HC, Luo YH, Zhang YD, Li DM, Yu ZX, Li KX, Meng QB (2010) In Situ Preparation of a Flexible Polyaniline/Carbon Composite Counter Electrode and Its Application in Dye-Sensitized Solar Cells. *J Phys Chem C* 114:11673
34. Kuan HC, Ma CCM, Chen KH, Chen SM (2004) Preparation, electrical, mechanical and thermal properties of composite bipolar plate for a fuel cell. *J Power Sources* 134:7
35. Liao SH, Hung CH, Ma CCM, Yen CY, Lin YF, Weng CC (2008) Preparation and properties of carbon nanotube-reinforced vinyl ester/nanocomposite bipolar plates for polymer electrolyte membrane fuel cells. *J Power Sources* 176:175
36. Yen MY, Yen CY, Liao SH, Hsiao MC, Weng CC, Lin YF, Ma CCM, Tsai MC, Sud A, Ho KK, Liu PL (2009) A novel carbon-based nanocomposite plate as a counter electrode for dye-sensitized solar cells. *Compos Sci Technol* 69:2193
37. Choi H, Kim H, Hwang S, Choi W, Jeon M (2011) Dye-sensitized solar cells using graphene-based carbon nano composite as counter electrode. *Sol Energy Mater Sol Cells* 95:323
38. Battumur T, Mujawar SH, Truong QT, Ambade SB, Lee DS, Lee WJ, Han SH, Lee SH (2012) Graphene/carbon nanotubes composites as a counter electrode for dye-sensitized solar cells. *Curr Appl Phys*. 12:49
39. Leary R, Westwood A (2011) Carbonaceous nanomaterials for the enhancement of TiO₂ photocatalysis. *Carbon* 49:741

40. Iijima S (1991) Helical microtubules of graphitic carbon. *Nature* 354:56
41. Kongkanand A, Kamat PV (2007) Electron Storage in Single Wall Carbon Nanotubes. Fermi Level Equilibration in Semiconductor-SWCNT Suspensions. *ACS Nano* 1:13
42. Yu HT, Quan X, Chen S, Zhao HM (2007) TiO₂-Multiwalled Carbon Nanotube Heterojunction Arrays and Their Charge Separation Capability. *J Phys Chem C* 111:12987
43. Yu Y, Yu CJ, Yu JG, Kwok YC, Che YK, Zhao JC, Ding L, Ge WK, Wong PK (2005) Enhancement of photocatalytic activity of mesoporous TiO₂ by using carbon nanotubes. *Appl Catal A* 289:186
44. Muduli S, Lee W, Dhas V, Mujawar S, Dubey M, Vijayamohan K, Han SH, Ogale S (2009) Enhanced Conversion Efficiency in Dye-Sensitized Solar Cells Based on Hydrothermally Synthesized TiO₂-MWCNT Nanocomposites. *ACS Appl Mater Interface* 1:2030
45. Lee TY, Alegaonkar PS, Yoo JB (2007) Fabrication of dye sensitized solar cell using TiO₂ coated carbon nanotubes. *Thin Solid Films* 515:5131
46. Yen CY, Lin YF, Liao SH, Weng CC, Huang CC, Hsiao YH, Ma CCM, Chang MC, Shao H, Tsai MC, Hsieh CK, Tsai CH, Weng FB (2008) Preparation and properties of a carbon nanotube-based nanocomposite photoanode for dye-sensitized solar cells. *Nanotechnology* 19:375305/1
47. Kim SL, Jang SR, Vittal R, Lee J, Kim KJ (2006) Rutile TiO₂-modified multi-wall carbon nanotubes in TiO₂ film electrodes for dye-sensitized solar cells. *J Appl Electrochem* 36:1433
48. Sawatsuk T, Chindaduang A, Sae-kung C, Pratontep S, Tumcharern G (2009) Dye-sensitized solar cells based on TiO₂-MWCNTs composite electrodes: Performance improvement and their mechanisms. *Diamond Relat Mater* 18:524
49. Yu JG, Fan JJ, Cheng B (2011) Dye-sensitized solar cells based on anatase TiO₂ hollow spheres/carbon nanotube composite films. *J Power Sources* 196:7891
50. Liu JW, Kuo YT, Klabunde KJ, Rochford C, Wu J, Li J (2009) Novel Dye-Sensitized Solar Cell Architecture Using TiO₂-Coated Vertically Aligned Carbon Nanofiber Arrays. *ACS Appl Mater Interface* 1:1645
51. Yen MY, Hsiao MC, Liao SH, Liu PI, Tsai HM, Ma CCM, Pu NW, Ger MD (2011) Preparation of graphene/multi-walled carbon nanotube hybrid and its use as photoanodes of dye-sensitized solar cells. *Carbon* 49:3597
52. Sun SG, Gao L, Liu YQ (2011) Optimization of the cutting process of multi-wall carbon nanotubes for enhanced dye-sensitized solar cells. *Thin Solid Films* 519:2273
53. Lin WJ, Hsu CT, Tsai YC (2011) Dye-sensitized solar cells based on multiwalled carbon nanotube-titania/titania bilayer structure photoelectrode. *J Colloid Interface Sci* 358:562
54. Usui H, Matsui H, Tanabe N, Yanagida S (2004) Improved dye-sensitized solar cells using ionic nanocomposite gel electrolytes. *J Photochem Photobiol A* 164:97
55. Zhang YG, Zhao J, Sun BQ, Chen XJ, Li Q, Qiu LH, Feng YN (2012) Performance enhancement for quasi-solid-state dye-sensitized solar cells by using acid-oxidized carbon nanotube-based gel electrolytes. *Electrochim Acta* 61:185
56. Emery KA, Osterwald CR, Aharoni H (1987) Spectral mismatch correction for GaAs solar cells with varying junction depths. *Solid State Electron* 30:213
57. Akhtar MS, Park JG, Lee HC, Lee SK, Yang OB (2010) Carbon nanotubes-polyethylene oxide composite electrolyte for solid-state dye-sensitized solar cells *Electrochim Acta* 55:2418
58. Novák P, Müller K, Santhanam KSV, Haas O (1997) Electrochemically Active Polymers for Rechargeable Batteries. *Chem Rev* 97:207
59. Akhtar MS, Li ZY, Park DM, Oh DW, Kwak DH, Yang OB (2011) A new carbon nanotubes (CNTs)-poly acrylonitrile (PAN) composite electrolyte for solid state dye sensitized solar cells. *Electrochim Acta* 56:9973
60. Zhang XH, Wang SM, Xu ZX, Wu J, Xin L (2008) Poly(o-phenylenediamine)/MWNTs composite film as a hole conductor in solid-state dye-sensitized solar cells. *J Photochem Photobiol A Chem* 198:288

Application of Carbon Nanotubes for Resolving Issues and Challenges on Electrochemical Capacitors

17

Raghavan Prasanth, Ravi Shankar, Nutan Gupta, Sravendra Rana, and Jou-Hyeon Ahn

Contents

1	Introduction	416
1.1	Types of Supercapacitors	417
1.2	Characteristics of Electrode	418
2	Use of Carbon Nanotubes as Electrode Material	419
2.1	Metal Oxides/CNT Composite	420
3	Conducting Polymer/CNT Composite	426
3.1	Conducting Polymer-CNT Composite by Chemical Polymerization	427
3.2	Electrochemical Deposition of Conducting Polymers on CNT Electrodes	431
4	Self-Supported and Functionalized CNTs	434

R. Prasanth (✉)

Department of Materials Science and Nanoengineering, Rice University, Houston, TX, USA

School of Materials Science and Engineering, and Energy Research Institute @ NTU, Nanyang Technological University, Singapore, Singapore

Department of Chemical and Biological Engineering and Research Institute for Green Energy Convergence Technology, Gyeongsang National University, Jinju, Republic of Korea
e-mail: prasanth.praghavan@rice.edu

R. Shankar

Nanoscience and Engineering Program, South Dakota School of Mines and Technology, Rapid City, SD, USA

N. Gupta

School of Materials Science and Engineering, and Energy Research Institute @ NTU, Nanyang Technological University, Singapore

S. Rana

School of Materials Science and Engineering, and Energy Research Institute @ NTU, Nanyang Technological University, Singapore

Institute of Chemistry, Martin-Luther University Halle-Wittenberg, Halle (Saale), Germany

J.-H. Ahn

Department of Chemical and Biological Engineering and Research Institute for Green Energy Convergence Technology, Gyeongsang National University, Jinju, Republic of Korea

5	Graphene-CNT Composite	436
6	Carbon-CNT Composite	438
7	Conclusion	440
	References	440

Abstract

In electrochemical capacitors electrode is the key factor to determine the energy density and power density; hence the selection of electrode materials is the most crucial part. The specific energy of commercial supercapacitors is limited to 5–6 Wh kg⁻¹, whereas for batteries the lower limit is 35–40 Wh kg⁻¹. In this chapter, the type of electrochemical capacitors, the storage principles, and the characteristics of composite electrode based on carbon nanotubes and carbon-based materials, transition metal oxides, and conducting polymers are briefly discussed. The composites combine the large pseudocapacitance with the fast charging/discharging double-layer capacitance and excellent mechanical properties of the carbon nanotubes. Most of the commercially available devices use carbon electrodes and organic electrolytes, and research efforts have been done to increase the specific capacitance of supercapacitor electrodes based on carbon nanotubes. Composite electrodes based on carbon nanotubes exhibit excellent electronic conductivity, electrochemical charge-storage properties, fast charge/discharge switching, and specific power making them promising electrode materials for high-power supercapacitors due to their unique properties of carbon nanotubes.

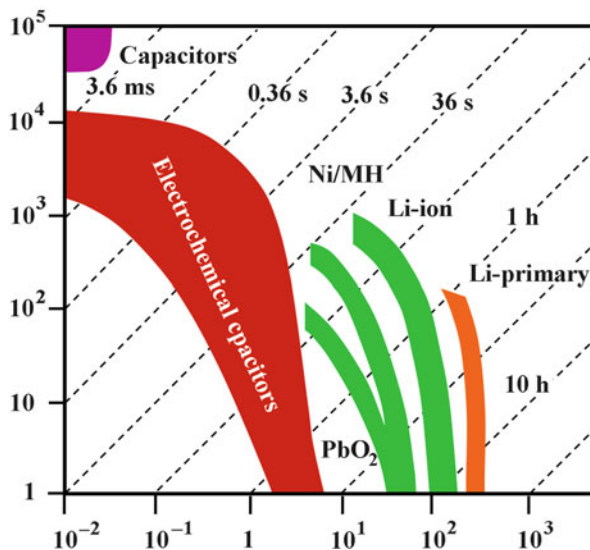
Keywords

Supercapacitor • Carbon nanotubes • Cathode • Anode • Electrochemical properties

1 Introduction

Supercapacitors are a class of electrochemical energy storage devices which can rapidly store electrical energy through double-layer charging, faradic process, or a combination of both and release energy instantaneously. They are also known as ultracapacitors and electrochemical double-layer capacitors. Supercapacitors can store hundreds or thousands of times more charge than the conventional capacitors. According to the intrinsic principles of charge storage and discharge in supercapacitors, there are two kinds of capacitance: double-layer and pseudocapacitance. The latter involves a faradic process, while the former is nonfaradic. They can provide fast charge/discharge process (in seconds) and high specific power (10KW kg⁻¹) while maintaining a longer cycle life (>10⁵) [1–6]. The role of supercapacitors becomes important because their parameters complement the deficiencies of other electrochemical power sources such as batteries and fuel cells. Ragone plot as shown in Fig. 17.1 illustrates that batteries suffer from slower power delivery when compared to supercapacitors. This indicates that supercapacitors can be used when fast storage coupled with high power is required from the energy storage systems [7–9].

Fig. 17.1 Ragone plot showing the specific power against specific energy for various electrochemical systems



1.1 Types of Supercapacitors

Based on their mode of energy storage, supercapacitors are divided into two main areas: (i) redox supercapacitor and (ii) electrochemical double-layer capacitor (EDLCs). Redox supercapacitors are also called as pseudocapacitors as the capacitance in this case is associated with a fast and reversible oxidation/reduction or faradic charge-transfer reactions of electroactive species on the electrode surface [10–16]. This type of supercapacitor somewhat behaves like a battery as the charge-storage process is based on redox reaction. Commonly used electrode materials for this class of supercapacitor are transition metal oxides and conducting polymers. For such supercapacitors, the capacitance is related to the electrode potential, as $C = dQ/dv$, where C represents the capacitance of pseudocapacitor, Q is the quantity of charge, and V is the electrode potential.

The EDLCs are also like a battery where there are two electrodes immersed in an electrolyte. During the charging process the positive electrode attracts anions from the electrolyte and similarly negative electrode attracts cations. However, unlike the batteries the electrolyte ions do not react with the electrode material as shown in Fig. 17.2 [17–20]. For such supercapacitors, the double-layer capacitance at each electrode surface can be related to the effective surface area of the electrode and to the effective thickness of the double layer and can be given by $C = \epsilon A/d$, where ϵ is the dielectric constant of the double layer and A is the surface area of the electrode. Here, d represents the effective thickness of the double layer. Because of this kind of surface dependent for charge storage, optimization of pore size and structure, surface properties, and conductivity of electrode materials become very important.

Fig. 17.2 Representation of an electrochemical double layer capacitor (charged state)

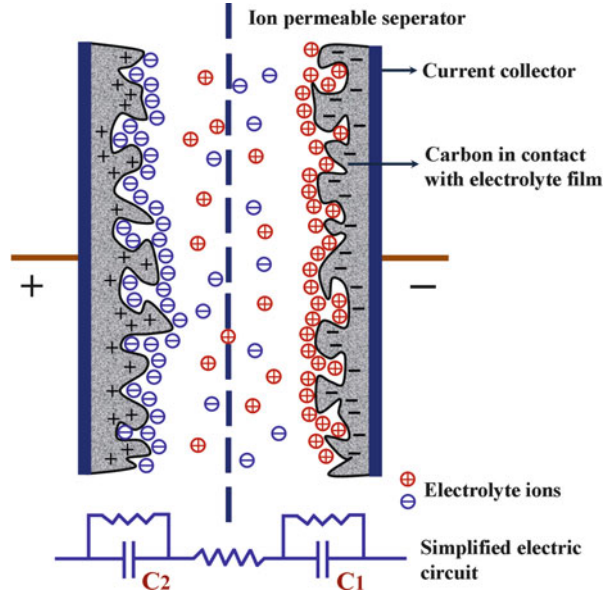
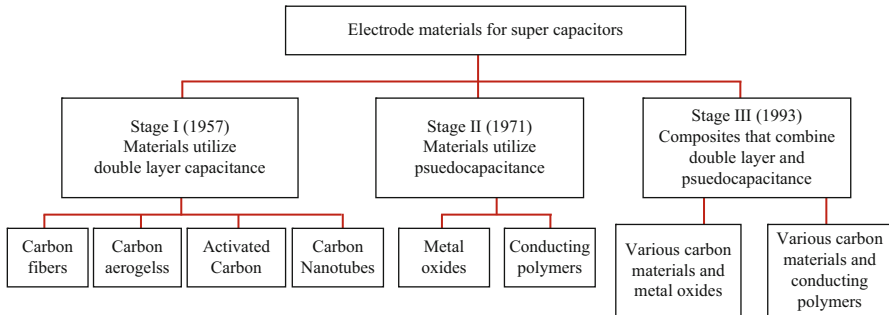


Table 17.1 Classification of electrode materials for supercapacitor applications



1.2 Characteristics of Electrode

Supercapacitors can be made from a variety of materials whose selection depends largely on the type of capacitance to be utilized, as shown in Table 17.1 [21]. Carbon in its dispersed and conducting form is the most widely used commercial material for supercapacitors. The first report of the use of carbon as an electrode for electrochemical capacitor was published by Becker in 1957 [22]. Carbon has been a popular choice since then because of its unique combination of physical and chemical properties, which can be listed as follows: (i) high surface area (dependent on allotrope in range of $\sim 1\text{--}2,000\text{ m}^2\text{ g}^{-1}$), (ii) good conductivity, (iii) good corrosion resistance, (iv) ability to control the pore structure, (v) high-temperature stability,

Table 17.2 Typical values for electrochemical double-layer capacitance of carbonaceous materials

Carbonaceous material	Electrolyte	Double-layer capacitance [$\mu\text{F cm}^{-2}$] ^a	Remarks
Activated carbon	10 % NaCl	19	S. area ^b 1,200 $\text{m}^2 \text{g}^{-1}$
Carbon black	1 M H_2SO_4	8	S. area 80–230 $\text{m}^2 \text{g}^{-1}$
	31 wt% KOH	10	
Carbon fiber cloth	0.5 M Et_4NBF_4 in PC	6.9	S. area 1,630 $\text{m}^2 \text{g}^{-1}$
Graphite			Highly oriented pyrolytic graphite
Basel plane	0.9 N NaF	3	
Edge plane	0.9 N NaF	50–70	
Graphite powder	10 % NaCl	35	S. area 4 $\text{m}^2 \text{g}^{-1}$
Graphite cloth	0.168 N NaCl	10.7	S area 630 $\text{m}^2 \text{g}^{-1}$
Glassy carbon	0.9 N NaF	~13	Solid
Carbon aerogel	4 M KOH	23	S. area 650 $\text{m}^2 \text{g}^{-1}$

^aValues based on estimates^bSurface area. For a comprehensive discussion see Ref. [33]

(vi) ease in processing, and (vii) low cost. Carbon materials such as carbon black, activated carbon, vitreous carbon, carbon aerogel, and graphite have been reported to produce porous carbon material with high surface areas up to 3,000 $\text{m}^2 \text{g}^{-1}$ [23–26]. The double-layer capacitance of carbon materials is proportional to their specific area. The specific capacitance of different carbon materials may vary, e.g. 4.5–10 $\mu\text{F cm}^{-2}$ for carbon black [27, 28], 10–15 $\mu\text{F cm}^{-2}$ for activated carbons [29], and approximately 20–35 $\mu\text{F cm}^{-2}$ for graphite powders [1]. Most carbon materials have surface oxygen groups, such as carboxyl, carboxylic, phenolic, ether groups, etc., which can enhance the hydrophilicity in aqueous solutions and introduce redox processes, and also contribute pseudocapacitance to the overall capacitance [30, 31]. The presence of oxygen enhances the stability of the activated carbon when it is used for anode, but decreases when used for the cathode [32]. However, recent research in carbon materials reveals the ability to further increase the porosity and surface area by introducing nanoscale structures. Recently, due to the ultrahigh mechanical strength, good electrical properties, high specific area, and high dimensional ratios, carbon nanotubes (CNTs) are widely studied as electrode material singly or as a composite with carbon, graphene, metal oxides, polymers, and conducting polymers in super capacitors. Table 17.2 shows a list of the specific double-layer capacitance measurement for different carbon materials [33].

2 Use of Carbon Nanotubes as Electrode Material

The unique tubular morphology of CNTs offers a combination of high conductivity and high porosity which makes them very attractive to be used as an electrode material for supercapacitors. Studies have been reported for the use of SWNTs and

MWNTs as the electrode material in aqueous and nonaqueous electrolyte media [34–37]. The electronic transport in both SWNTs and MWNTs has been reported as ballistic transport means over long-tube range without any scattering. This kind of transport phenomena allows CNTs to carry high current densities without any energy dissipation [38]. Also, the internal mesopores of CNTs formed during the entanglement of CNTs allow fast solvated ionic diffusion during the charge and discharge process. The specific capacitance in the range of 15–80 F g⁻¹ has been reported corresponding to the surface areas that range from 120 m² g⁻¹ to 400 m² g⁻¹ [39, 40]. The following sections discuss on the application of CNTs and its composite with different materials as electrodes in supercapacitors.

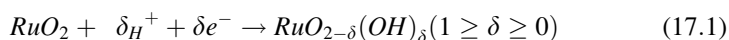
2.1 Metal Oxides/CNT Composite

Metal oxides have been studied as electrode materials for pseudocapacitor applications because of high energy density and possess many oxidation numbers which can contribute fast, reversible redox reactions at or near their solid electrode surfaces [41]. In addition, high specific capacitance of metal oxides coupled with very low resistance resulting in a high specific power, which makes them very appealing in commercial applications. Transition metal oxides such as RuO₂ [42], NiO_x [43], MnO_x [44], IrO₂ [45], and many others are recognized as excellent electrode materials for supercapacitors; however, the cycle life and rate capability of electrodes based on these transition metals are poor. Among the different efforts employed to enhance the electrochemical properties of metal oxides, composite electrodes with CNTs are reported to be the good candidate, which shown much higher specific capacity and good cycling properties compared to the use of these materials individually [30, 46–49].

2.1.1 RuO₂/CNT Composite

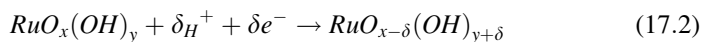
Among the metal oxides RuO₂ is a unique candidate due to its high capacitance (>700 F g⁻¹), long cycle life, high conductivity, and rate capability. Unfortunately the lack of abundance and cost of the precious metal (Ru) are limits to the commercial production of RuO₂ [50–53]. The specific capacity, cycle life, and rate capability of RuO₂ are enhanced using its composite with CNTs [54, 55]. Supercapacitive properties of RuO₂/MWNT composite prepared by catalytically grown RuO₂/MWNTs [55], electrochemical deposition of RuO₂ (12 % by mass) onto a thin MWNT [54], impregnation of RuO₂ into MWNTs (nitric acid treated), heat treatment [56], RuO₂/purified and acid functionalized nanotube (p-MWNT and a-MWNT) composites by the spontaneous reduction of Ru (VI) and Ru(VII) [57], and polyol process [58] have been reported. The highest specific capacity of 1,170 F g⁻¹ is obtained with 12 % RuO₂ (by mass) [54] and 800–900 F g⁻¹ for 2–13 % RuO₂ component [56]. The RuO₂/p-MWNT composite was shown to be stable over 20,000 charge/discharge cycles [57]. The enhanced charge storage and transfer capabilities of these composites attributed to the high surface area, conductivity, and electrolyte accessibility of the nanoporous structure.

Yan et al. reported RuO₂/MWNT nanocomposites prepared by microemulsion method and coated on carbon paste electrode (CPE). The specific capacitance of composite electrode is increased with increasing RuO₂ content in the voltage range of 0–1.0 V at various potential scan rates using 1 M H₂SO₄ as an electrolyte. The specific capacitance follows the order: CPE/MWNTs/40 % Ru > CPE/MWNTs/20 % Ru > CPE/MWNTs > CPE [59]. Nanocrystalline RuO₂ decorated CNTs [42] and RuO₂ nanoparticles were directly synthesized and attached onto MWNTs [60] are reported. Cyclic voltammetry results demonstrated that RuO₂/MWNTs had significantly greater specific capacitance of 168 F g⁻¹ (15 % RuO₂) [42] and 232.5 F g⁻¹ [60] which is much higher than the specific capacitance of MWNTs. The pronounced enhancement in the capacitance of the modified CNT composite electrode arises from a pseudocapacitance of RuO₂, available for the oxidation and reverse reduction through the following electrochemical protonation as shown in Eq. 17.1 [42]:



Kim et al. improved the specific capacity and rate capability of composite electrodes by co-deposition of Ru-Co (Ru:Co is 13.13:2.89 wt%) on the surface of CNTs. The composite electrode exhibited specific capacitance of ~ 620 F g⁻¹ at low potential scan rates of 10 mV s⁻¹ and 570 F g⁻¹ at higher scan rates of 500 mV s⁻¹, when compared to the RuO₂ electrode (475 F g⁻¹) prepared by electrochemical deposition. This increase in capacitance at high scan rates is attributed to the role of the Co in providing enhanced electronic conduction [61].

An amorphous phase of RuO₂.xH₂O, a mixed electronic-protonic conductor [62, 63] shows a specific capacitance as high as 720 F g⁻¹ in an acidic electrolyte which is higher than RuO₂ [50]. The higher capacity is due to the ability of RuO₂.xH₂O to store charges by reversibly accepting and donating protons from an aqueous electrolyte governed by the potential-dependent equilibrium as shown in Eq. 17.2. The electrochemical properties depend on the amount of water incorporated in its structure and the change of oxidation state (Ru⁴⁺/Ru³⁺) of ruthenium:



The specific capacitance of RuO₂.xH₂O/CNT composite electrode with 20 wt% RuO₂.xH₂O filled in CNTs [64], pseudocapacitive behavior of MWNTs functionalized with RuO₂.H₂O [65], and tertiary composite of RuO₂.xH₂O/MWNT/Ti in 1 M H₂SO₄ [66] are reported to have significantly higher capacity. CNT/Ru composites were grown directly on graphite substrate by typical chemical vapor deposition (CVD) using electrodeposited Ni-Ru catalysts. RuO₂.xH₂O/CNT electrode was then obtained by electrooxidation of CNT/Ru composites. The electrochemical properties of RuO₂.xH₂O/CNT electrodes have been investigated in 0.5 M H₂SO₄ solutions and showed improved electrochemical properties and long-term cycle stability [67]. The specific capacity reached up to 1,652 F g⁻¹ at a scan rate of 10 mV s⁻¹, which is larger than RuO₂.xH₂O/Ti, MWNT/Ti, and

MWCNT [66]. The entangled network of nanotubes which forms open mesopores and their chemical stability with a basal geometry and oxidative treatment to generate oxygenated functional groups on the tube ends and along the sidewalls enables facile derivatization by $\text{RuO}_2 \cdot \text{H}_2\text{O}$ to enhance the inherent capacitance. As commercial use of RuO_2 is limited by its high cost, therefore, there has been considerable effort on the search for alternative electrode materials, such as manganese oxide (MnO_2), cobalt oxide (CoO_2), and nickel oxide (NiO), which are inexpensive and show similar pseudocapacitive behavior to $\text{RuO}_2 \cdot x\text{H}_2\text{O}$.

2.1.2 MnO_2/CNT Composite

MnO_2 is the most promising pseudocapacitor electrode materials due to its large specific capacitance ($1,100 \text{ F g}^{-1}$), environmentally benign nature, and cost-effectiveness [68–72]. The electrochemical performances of MnO_2 electrodes are reported to significantly improve by preparing composite with CNTs [73–78] which make well-controlled microstructures with MnO_2 for supercapacitor applications, such as MnO_2 nanowires on CNT paper [79], coaxial MnO_2/CNT arrays [80], and MnO_2 nanoflowers on vertically aligned CNT arrays [81]. Various methods are employed to effectively synthesize MnO_2/CNT nanocomposites, which can be classified into physical/mechanical mixing [82, 83] and chemical/electrochemical deposition [73, 75, 77, 78, 84–86]. Hybrid MnO_2/CNT films with 0.05 wt% MWNTs prepared by sol–gel process showed specific capacitance of 340 F g^{-1} which is 295 % higher than pristine MnO_x electrode. After 1,000 CV cycles the hybrid electrode exhibited 82 % of initial capacity, while the pristine MnO_x retains only 57 % of its capacity [87]. MnO_2 deposited by potentiostatic and galvanostatic methods on vertically aligned CNTs in a single sequential process of sputtering, annealing, and plasma-enhanced chemical vapor deposition [88], cathodic electro-deposition of MnO_2 grown by chemical vapor deposition on CNTs [89], MnO_2 nanowires electrodeposited onto CNT paper, and MnO_2 deposited on MWNT by solution reduction process [90]. The composite electrode prepared by galvanostatic deposition showed a specific capacitance of 642 F g^{-1} at a scan rate of 10 mV s^{-1} [88], 356 F g^{-1} at a scan rate of 2 mV s^{-1} [89] in Na_2SO_4 electrolyte solution, and 309 F g^{-1} [90] and 167.5 F g^{-1} at a current density of 77 mA g^{-1} [79] with good stability during 800 [88] or 3,000 cycles (88 % of initial capacitance) [79]. A hybrid of MnO_2 nanowires/MWNTs [91], and a three-dimensional (3D) MnO_2/CNT nanocomposites are prepared by a simple one-pot hydrothermal method and are reported to have specific capacitance of 292 F g^{-1} at a scanning rate of 5 mV s^{-1} [92] and energy density of 17.8 Wh kg^{-1} at 400 W kg^{-1} , which is maintained almost constant even at $3,340 \text{ W kg}^{-1}$ with excellent rate capability [91]. The higher specific capacitance of the hybrid electrodes owing to its highly porous, interwoven, and homogeneous nanostructure [92]. Subramanian et al. reported MnO_2/CNTs (20 wt%) composites with excellent cycling capability, even at the high current of 2 A g^{-1} , showing the best combination of coulombic efficiency of 75 % and specific capacitance of 110 F g^{-1} after 750 cycles. However, the composite with 5 wt% CNTs showed the highest specific capacitance during initial cycles [69].

MnO₂ was synthesized and dispersed on CNT (grown directly on graphite disk) [84] and binder-free, robust, with preformed electrical pathways and excellent electrode structures MnO₂/CNT hybrid films [93] synthesized by chemical vapor deposition technique (CVD). MnO₂/CNT composites in 1 M Na₂SO₄ aqueous solutions showed specific capacitance of 568 F g⁻¹ at current density of 1 mA cm⁻² [84] or 150 F g⁻¹, energy density of 70 Wh kg⁻¹, and power density of 79 kW kg⁻¹ in 1M tetraethylammonium tetrafluoroborate (TEABF₄)/propylene carbonate (PC) organic electrolyte [93]. Both composites exhibited excellent charge/discharge cycle stability (88 % retention after 2,500 cycles) [84] or 98.5 % retention at current densities of 50 A g⁻¹ and 2 A g⁻¹, after 15,000 and 1,000 cycles, respectively [93].

MnO₂/CNT composite with 15 % double-walled CNTs [94] and 85 % MWNTs [95] is synthesized by microwave irradiation method. The electrode exhibited high specific capacitance of 240 F g⁻¹ (2 mV s⁻¹) [94] and 944 (85 % of the theoretical capacitance) and 522 F g⁻¹ at 1 and 500 mV s⁻¹, respectively [95], and good cycling stability (6.8 % capacity loss after 2,000 cycles) [94]. Flexible MnO₂/CNT composite electrode prepared by [96] and microwave heating deposition of MnO₂/CNTs followed by electrophoretic deposition of the MnO₂-coated CNTs on a flexible graphite sheet (FGS) [97] showed good capacitance of 540 F g⁻¹ [96] or 442.9 F g⁻¹ at 2 mV s⁻¹ and exhibited excellent cycling stability (<1.1 % capacitance loss after 1,000 cycles at 50 mV s⁻¹) [97]. A ternary composite of CNT/polypyrrole (PPy)/MnO₂ (CPM) [98] and MnO₂/polyaniline (PANI)/MWNTs (MPM) [99] prepared by chemical method suggested that appropriate thickness of conducting polymer layers is important for building coaxial structures without the agglomeration of MnO₂ nanoflakes. The specific capacitances of the ternary composite, CNT/MnO₂, and PPy/MnO₂ binary composites in 1 M Na₂SO₄ electrolyte are 281, 150, and 35 F g⁻¹ at 20 mV s⁻¹ and 209, 75, and 7 F g⁻¹ at 200 mV s⁻¹, respectively. The electrochemical stability of ternary composite electrode is investigated by switching the electrode back and forth for 10,000 times between 0.1 V and 0.9 V versus Ag/AgCl at 100 mVs⁻¹. The electrode exhibits good cycling stability, retaining up to 88 % of its initial charge at 10,000th cycle. A full cell assembled with CPM electrodes shows a specific capacitance of 149 F g⁻¹ at a current loading of 1 mA cm⁻² during initial cycling, which decreased drastically to 35 F g⁻¹ at 2000th cycle [98]. The ternary composite provides large interaction area between the MnO₂ nanoflakes and electrolyte, conducting polymer layer on CNT improved electronic conductivity which leads to efficient electrochemical utilization [99].

MnO₂/MWNTs nanocomposites synthesized by a facile redox reaction [100] and oxidation of manganese acetate with poly(4-styrenesulfonic acid) (PSS) dispersed MWCNTs [101]. The composite showed specific capacitance of 162.2 F g⁻¹ at the current density of 0.2 A g⁻¹ and excellent cycling property with 90 % of its specific capacitance kept after 2,000 cycles at the current density of 5 A g⁻¹ [100]. MnO₂/activated CNT (chemically activated by KOH) [102] and core-shell structured material consisting of MnO₂ nanoflake-MWNTs [103] are prepared by the coprecipitation method. A specific capacitance of 250 F g⁻¹ at scan

rates of 10 mVs^{-1} compared to 215 F g^{-1} for the MnO_2/CNT [102] and 380 F g^{-1} at the current density of 5 A g^{-1} , which is retain its 83 % of initial capacity after 3,500 cycles [103] in Na_2SO_4 electrolyte. Sandwiched film of MnO_2 nanosheet (MONS) and MWNT was assembled by using the layer-by-layer method, based on electrostatic interaction of positively charged poly(diallyldimethylammonium chloride) and negatively charged MONS and MWNT. The multilayer film electrode presents excellent electrochemical capacitance properties, which were observed to be highly dependent upon the deposition sequence and the order of structural components in sandwiched film [104]. Asymmetric hybrid capacitor using LiMn_2O_4 and MnO_2/CNT nanocomposite as the positive and negative electrode materials, respectively, in 1 M LiClO_4 in PC as the electrolyte delivered specific energy as high as 56 Wh kg^{-1} at a specific power of 300 W kg^{-1} , based on the total weight of LiMn_2O_4 and MnO_2/CNT nanocomposite in both electrodes [105]. MnO_2/CNT -embedded carbon nanofiber (CNF) nanocomposites prepared using electrospinning and in situ redox deposition technique showed higher specific capacitance (374 F g^{-1}) and better rate capability (53.4 %). Excellent capacitance retention of 94 % of the initial capacitance after 1,000 cycles was achieved on the freestanding MnO_2/CNT -CNF nanocomposites electrode. The specific capacitance was found to increase significantly with the increase in the electrolyte temperature [106].

2.1.3 NiO/CNTs Composites

Nickel oxide (NiO) is another potential electrode material for supercapacitor applications, which can be prepared by a variety of synthetic routes, such as the thermal treatment of an electrodeposited or sol-gel-prepared nickel hydroxide [107, 108], liquid crystal templating electrodeposition [109], simple liquid-phase process [110], and the replication of a mesoporous silica template [111]. The specific capacitance of NiO electrode materials ranges from 50 F g^{-1} to 350 F g^{-1} depending on the method of synthesis, which is still far from the theoretical value of $2,584 \text{ F g}^{-1}$. The electrochemical performance of NiO electrodes is significantly improved with CNTs. 3D nanoporous network structure with an extremely thin NiO_x layer on the CNT film substrate (electrochemical deposition) [112] and NiO nanostructures were synthesized on random CNTs growing on a carbon cloth substrate processed using vacuum annealing, and oxygen plasma treatment [113] improved the specific capacitance to 162.4 [113] or $1,701 \text{ F g}^{-1}$ with excellent high rate capability [112] than that observed for $36.6 \text{ wt\% NiO}_x/\text{CNT}$ electrode [112] or 53.75 F g^{-1} for the CNTs/carbon cloth electrode [113] in a 1 M KOH solution. The pseudocapacitance of the NiO_x/CNT electrodes originates from redox reactions of $\text{NiO}_x/\text{NiO}_x\text{OH}$ and $\text{Ni}(\text{OH})_2/\text{NiOOH}$ [112]. Lee et al. reported NiO/CNTs nanocomposite formed by a simple chemical precipitation method. The presence of CNT network in the NiO significantly improved the electrical conductivity of the host NiO by the formation of conducting network of CNTs and the active sites for the redox reaction of the metal oxide by increasing its specific surface area. The specific capacitances of the bare NiO and NiO/CNT (10 %) nanocomposite are 122 and 160 F g^{-1} , respectively, at a discharge current density of 10 mA g^{-1} [114]. NiO- MnO_2/MWNT composite formed by a simple chemical

precipitation method pretreated by ultrasonication, followed by thermal annealing at 300 °C tested in 6 M KOH aqueous solution, demonstrated that the maximum specific capacitance of 193.50 F g⁻¹, which is significantly higher than MWNT electrode [115]. Nickel oxide hydroxide (NiOOH)/MWNTs (50 wt%) composites formed by a chemical precipitation method showed specific surface area of 274.32 m² g⁻¹ and specific capacitance of 2,436 F g⁻¹ at a scan rate of 10 mV s⁻¹. The nanocomposites delivered energy density and power density of 82.8 Wh kg⁻¹ and 8.5 kW kg⁻¹, respectively. The enhanced electrochemical properties are attributed to the higher surface area, formation of conducting network, and fibrous morphology with MWNT network [116].

2.1.4 Other Metal Oxides

ZnO/CNT

Zinc oxide (ZnO) nanodots deposited onto CNT films by ultrasonic spray pyrolysis from 2 min to 30 min were employed as the electrode and tested in gel poly(vinyl alcohol)-phosphomolybdic acid electrolyte. The results of electrochemical measurements showed that the electrode with ZnO deposited in 5 min had the optimal capacitive properties among the experimental series, with a lowest interfacial electron transfer resistance, a very high capacitance of 323.9 F g⁻¹ much better than pure CNT electrode, and a good reversibility in the repetitive charge/discharge cycling test. However, excess ZnO in CNT/ZnO nanocomposite deteriorates the capacitive performance by destroying the network structure of the CNT matrix and lowering the conductivity of the electrode [117, 118].

CuO-CNT Composite

Kim et al. prepared activated MWNTs (ACNTs) by chemical activation using KOH. Copper oxide (CuO) nanoparticle was deposited on by chemical deposition method of ACNTs to get composite electrode and evaluated as supercapacitor electrodes. The results showed that CuO/ACNT electrodes had typical pseudocapacitive behavior and greater specific capacitance (60 F g⁻¹) than CuO-CNT electrodes (43 F g⁻¹) at 0.5A g⁻¹ in 6 M KOH electrolyte due to synergistic effect of large surface area of ACNTs and high pseudocapacitive reaction by the presence of CuO [119].

SnO₂/CNT Composite

Core-shell nanowires of SnO₂ and SWNTs were synthesized by electrodeposited technique [120], and nanoscaled SnO₂-V₂O₅ prepared by hydrothermal process is mechanically mixed with CNT to form composite [121]. The electrochemical performance of the core-shell structures as electrode materials of supercapacitor showed typical capacitive behavior with higher specific capacitance of 320 F g⁻¹, at a scan rate of 6 mV s⁻¹ and excellent cycling capability in 1 M Na₂SO₄ electrolyte [120]. In mixed oxides, the presence of SnO₂ increases the electronic and redox properties of V₂O₅ and improves the capacitive behavior. SnO₂-V₂O₅/CNT electrode provides the best performance, viz., 121.4 F g⁻¹ at a scan rate of 100 mV s⁻¹ in 0.1 M KCl solution in contrast with their individual components or mutual combinations [121].

Co₃O₄/MWNT Composite

Cobalt oxide/MWNT composites are synthesized by a facile chemical coprecipitation method followed by a simple thermal treatment process. The value of the specific capacitance for pure MWNT, Co₃O₄, Co₃O₄/MWNT (3 %), Co₃O₄/MWNT(5 %), Co₃O₄/MWNT (7 %), and Co₃O₄/MWNT (15 %) electrodes was calculated to be 95, 263, 287, 418, 315, and 285 F g⁻¹, respectively, at a current density of 0.625 A g⁻¹ in 2 M KOH electrolyte. The Co₃O₄/MWNT (5 %) composite exhibits the highest specific surface area of 137 m² g⁻¹ with narrow distribution of pore size from 2 nm to 10 nm and thus the largest specific capacitance of 418 F g⁻¹. The well-dispersed MWCNTs acted as loose 3D template for growing Co₃O₄ crystallites as a result of improved connectivity between Co₃O₄ particles, electronic conductivity, and electrochemical utilization of the Co₃O₄ [122]. The capacitance of electrochemical capacitors based on Co₃O₄ is further enhanced by incorporating MWCNTs and graphene nanosheets (GNS) to Co₃O₄ paste. The composite film based on Co₃O₄/MWCNT/GNS (95:4:1 wt%) exhibited a capacitance of 294 F/g, while the capacitance of Co₃O₄/MWCNT (95:5 wt%) and pure Co₃O₄ film is 205 and 163 F/g, respectively. The enhanced capacitance of Co₃O₄/MWCNT/GNS composite film was attributed to the electrochemical contributions of the Co₃O₄ nanoparticle attached to the GNS as well as their significantly increased specific surface areas by MWCNTs [123].

MoO₃/CNT Nanocomposites

Nanocomposites of intertwined MWNTs and MoO₃ nanowires were synthesized using a hydrothermal method and showed specific capacitance of 210 F g⁻¹ in safe aqueous electrolyte of Na₂SO₄. The measured specific capacitances at the lowest scan rate of 5 mV s⁻¹ (at E_v = 0) were 23, 80, and 210 F g⁻¹ for nanowires, MWNT, and MoO₃/MWNT composite electrodes, respectively. The energy density was greatly improved to 71.6 Wh kg⁻¹ with a power density of 600 W kg⁻¹ compared to those of pristine MWNTs and MoO₃ nanowires. The composite electrodes exhibited an excellent charge/discharge rate and long-term cyclic stability in terms of capacitance with an efficiency of more than 95 % after 2,000 cycles [124].

3 Conducting Polymer/CNT Composite

With the discovery of the intrinsically conducting polymer in 1963 [125], an extensive research on the conducting polymers was initiated by MacDiarmid in 1976 for their possible applications in sensors [126], energy storage, and actuators [1]. Conducting polymers are the class of materials explored for supercapacitors due to their good electronic conductivity [127–129], large pseudocapacitance [130–132], and economic viability. Polyaniline (PANI), polypyrrole (PPy), and poly(3,4-ethylenedioxythiophene) (PEDOT) are the most widely studied conducting polymers for supercapacitors which have high specific capacitance that is close to ruthenium oxides. The specific capacity of PANI is 775 [132],

PPy is 480 [133], and PEDOT is 210 F g⁻¹ [134]. Aside from the advantages of conducting polymers, they suffer poor mechanical stability due to repeated intercalation and deintercalation of ions during cycling, relatively poor charge/discharge kinetics, and very poor cycling stability [135]. Recently, to overcome these disabilities, composite of conducting polymers with CNTs which combine two relatively cheap materials to attain large pseudocapacitance of conducting polymers and the conductivity and mechanical strength of CNTs are widely reported. Composites of conducting polymers and CNT have exhibited great promise as supercapacitor electrodes due to their good electronic conductivity, high surface area, and the ability to store energy via two charge-storage mechanisms.

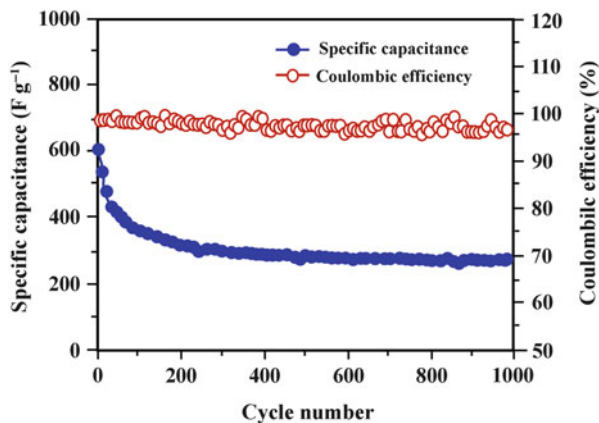
3.1 Conducting Polymer-CNT Composite by Chemical Polymerization

Chemical polymerization is a cheap and efficient route for the mass production of conducting polymers, and the resulting polymer exhibits high conductivity, good stability, and negligible solubility in aqueous solutions [136, 137]. In chemical synthesis, conducting polymers are simply prepared by oxidation of corresponding monomers (aniline, pyrrole, and thiophene/its derivatives) using an oxidizing agent which is capable of withdrawing a proton molecule without forming a strong coordination bond (either with the substrate/intermediate or with the final product) [138]. Aniline can be chemically oxidized into polymer in an aqueous solution by a variety of oxidants such as (NH₄)S₂O₈, K₂Cr₂O₇, KIO₃, FeCl₃, KMnO₄, KBrO₃, and KClO₃ [138]. Similarly, pyrrole could be oxidized by a variety of transition metal ions from metallic salts, such as FeCl₃, Fe(NO₃)₃, Fe₂(SO₄)₃, K₃Fe(CN)₆, and CuCl₂, all of which are common oxidizing agents for the synthesis of highly conducting PPy [139]. Due to the good solubility of aniline and pyrrole monomers in water, chemical synthesis of PANI and PPy is more cost-effective and environmentally friendly, while thiophene derivatives can be polymerized in organic solvents. However, the conducting polymers prepared by chemical polymerization show inferior homogeneity and integrity compared to the electrochemical polymerization in which an integrated electrode film can be easily obtained. Lots of efforts have been carried out to enhance the specific capacity, cyclability, and rate capability of chemically synthesized conducting polymers by preparing composite with CNTs.

3.1.1 PANI/CNT Composites

Among the intrinsically conducting polymers, PANI is considered as the most promising electrode material for supercapacitors due to its excellent capacity for energy storage, easy synthesis, high conductivity, good environmental stability, low price of aniline monomers, ease of manipulation, and color change corresponding to diverse redox states [6, 21, 140]. Because of the better accessibility of the ions to the electrochemically active surface, which is responsible for higher values of capacitance, nanometer-sized and well-ordered mesoporous structures should be

Fig. 17.3 Cycling performance of PANI/CNT composite-based cell, which is cycled in the voltage range of 0–0.4 V at a current loading of 1.0 Ag^{-1} (Adapted from Ref. [143] with permission from Elsevier, copyright 2012)



suitable for further increasing the capacitive performance of conducting polymers. Over the past several years, there are many reports on optimizing the composite properties by altering the synthetic conditions for their preparation, yielding differences in nanotube content of composites and polymer morphology. Among these studies, Frackowiak et al. prepared conducting polymer/MWNT (PANI/MWNT, PPy/MWNT, and PEDOT/MWNT) composites, and the capacitance values ranging from 100 F g^{-1} to 330 F g^{-1} were obtained for different asymmetric configurations. The combination of PANI/CNT (80:20 wt%) as the positive electrode and activated carbon as the negative electrode was reported to be the best among all the couplings, with a specific capacitance of 330 F g^{-1} at a potential window of 1 V [141]. Deng et al. also prepared PANI/MWNT electrode material and reported specific capacitance of 183 F g^{-1} being achieved [142]. Further experiments showed that specific capacitance of the composites with a core-shell structure was higher than blended composites. Sivakkumar et al. synthesized a composite of PANI covered on MWNTs by in situ chemical polymerization, and a high initial specific capacitance of 606 F g^{-1} is reported. However, it showed (Fig. 17.3) poor capacity retention of 63.7 % (based on initial capacity) after 1,000 cycles [143]. Influence of the thickness of the PANI layer covering MWNTs surfaces on the specific capacitance is studied by Zhou et al. The strong interaction in such conjugated systems greatly improves the charge-transfer reaction between PANI and CNT. The highest specific capacitance of 560 F g^{-1} at a scan rate of 1 mV s^{-1} was achieved by using a composite with 66 wt% PANI. The reduction in the specific capacitance was only 29.1 % after 700 cycles, and then remained stable [144].

Meng et al. improved the specific capacity and cycling properties of PANI/MWNT by preparing paperlike composites by using CNT network as the template. Compared with the conventional brittle PANI/CNT composites, these paperlike composites were much thin and flexible. These thin film electrodes (buckypaper) showed much superior electrochemical performance such as higher specific capacitance, lower internal resistivity, and more stability under different current loads. From 100 mA g^{-1} to 1.7 A g^{-1} , the specific capacitance of buckypaper varied from

424 F g⁻¹ to 347 F g⁻¹. The relative decrease in specific capacity was 18 %, in contrast with 27 and 40 % for PANI/MWNT composite powder and the pristine PANI, respectively [145]. All of these results demonstrated that the combination of PANI and MWCNT to form composites is a simple, cheap, and effective method to increase the specific capacitance of electrodes, because the storage of energy in supercapacitors combines the pure electrostatic attraction of ions in the electrical double layer with the pseudocapacitance faradic reactions.

3.1.2 Popyrrole/CNT Composites

Use of PPy/CNT composite electrodes in supercapacitors, PPy provides not only additional capacitance as an active material but also enhances the adhesion between the CNTs. Furthermore, PPy acts as a conducting binder for connecting every individual CNT to increase the capacitance. Lee et al. fabricated PPy/CNT composite electrodes on ceramic fabrics and studied its electrochemical properties. The CNTs are grown on the ceramic fabrics by the CVD method and PPy is subsequently coated on them by chemical polymerization. The specific capacitances of the CNTs and PPy on the ceramic fabrics activated with 1 M LiClO₄ in PC were 6.44 and 101.46 F g⁻¹, while that of PPy/CNT on the ceramic fabrics was 152.78 F g⁻¹, and its stability was well retained after 5,000 redox cycles at current density of 1 mA cm⁻². The large surface area and high conductivity of CNTs on the porous ceramic fabrics enhance their energy storage capacity [146]. Mi et al. prepared thornlike, organometallic-functionalized (methyl orange-FeCl₃ complex) CNTs via a novel microwave hydrothermal route, and PPy/CNT composite with controllable morphology was obtained by oriented polymerization of pyrrole on the modified CNTs with the aid of MO-FeCl₃ complex without the assistance of other oxidants. A specific capacitance of 304 F g⁻¹ was obtained at a current density of 1 mA cm⁻² within the potential range of -0.5 to 0.5 V in 1 M KCl solution. The enhanced specific capacity may be due to the good dispersion of the as-prepared PPy nanoparticles based on the oriented thorns on the CNTs, which could help to provide a largely electrolyte-accessible surface area to improve the utilization of PPy for redox reaction [147]. The MWNT-embedded activated carbon nanofibers (ACNF/MWNT) and ACNF were prepared by stabilizing and activating the nonwoven web of polyacrylonitrile (PAN) or PAN/CNT prepared by electrospinning. Both ACNF and ACNF/MWN were partially aligned along the winding direction of the fibers on collection drum. The average diameter of ACNF was 330 nm, while that of ACNF/MWNT was lowered to 230 nm with rough surface due to the increasing electrical conductivity of the spinning solution. The specific surface area and electrical conductivity of ACNF were 984 m² g⁻¹ and 0.42 S cm⁻¹, while those of ACNF/MWNT were 1,170 m² g⁻¹ and 0.98 S cm⁻¹, respectively. PPy was coated on the electrospun ACNF/MWNT (PPy/ACNF/MWNT) by in situ chemical polymerization in order to improve the electrochemical performance. The capacitances of the ACNF and PPy/ACNF electrodes were 141 and 261 F g⁻¹ at 1 mA cm⁻², respectively, whereas that of PPy/ACNF/MWNT was 333 F g⁻¹. At 10 mA cm⁻², ACNF, PPy/ACNF, and PPy/ACNF/MWNT electrode showed ~80 % of its specific capacity obtained at a current density of

1 mA cm⁻², while ACNF/MWNT showed ~90 % (163 F g⁻¹) of its specific capacity at a current density of 1 mA cm⁻². The improvement in capacitance was attributed to the following: (i) the aligned nano-sized ACNF/MWNT with lower fiber diameter and high surface area, (ii) a refined three-dimensional network due to the highly porous structure, (iii) the presence of CNT, (iv) the increase in electrical conductivity due to the PPy coating, and (iv) the formation of a good charge-transfer complex by the PPy coating on the surface of the aligned nano-sized ACNF/MWNT [148]. The flexible electrodes based on thin films with PPy/CNT composite homogeneously distributed between graphene (GN) sheets are reported. The unique flexible films with PPy/CNT is prepared by flow assembly of the mixture dispersion of GN and PPy/CNT, which is prepared by in situ chemical polymerization of pyrrole on CNTs (24 wt% of CNT in PPy/CNT composite). In such layered structure, the coaxial PPy/CNT nanocables cannot only enlarge the space between GN sheets but also provide pseudocapacitance to enhance the total capacitance of electrodes. Galvanostatic charge/discharge analysis showed superior mass and volume specific capacitances of GN-PPy/CNT and excellent cycling stability (5 % capacity loss after 5,000 cycles) due to the flexible GN layer and the rigid CNT core synergistically releasing the intrinsic differential strain of PPy chains during long-term charge/discharge cycles. The gravimetric and volumetric specific capacitances of GN-PPy/CNT (52 wt% PPy/CNT) are 211 F g⁻¹ and 122 F cm⁻³ at a current density of 0.2 A g⁻¹, higher than those of the GN film (73 F g⁻¹ and 79 F cm⁻³) and PPy/CNT (164 F g⁻¹ and 67 F cm⁻³) [149]. In another recent study, PPy/MnO₂ is grown on MWNT wrapped with poly(4-styrenesulfonic acid) (PSS). During polymerization the negatively charged PSS layer on MWNTs attracted pyrrole and metal ions and served as templates for subsequent nanostructure formation. Synergetic interaction between PPy and MnO₂ significantly improves the electrical properties and the mechanical stability of the electrode that yields high rate capability. The (-SO₃-) surface functionalities on MWNT-PSS facilitate an ordered growth, and the molecular level dispersion of MnO₂ in PPy matrix enhances the electrode performance. As an electrochemical electrode the MWNT-PSS/PPy:MnO₂ nanocomposite exhibits ~268 F g⁻¹ specific capacitance at 5 mV s⁻¹. The excellent rate capability and stability of the electrode is demonstrated by only 7 % fade in the specific capacity at 100 mV s⁻¹ (compared to the specific capacity at 5 mV s⁻¹) and 10 % fade in the same after 5,000 CV cycles [150].

3.1.3 PEDOT/CNT Composite

PEDOT is one of the conducting polymers widely studied as electrode materials in supercapacitors due to its unique properties such as optical transparency in its conducting state, high stability among other conducting polymers, moderate band gap, and wide redox potential window [151]. There were lots of studies focused on enhancing the specific capacitance of PEDOT-based supercapacitors by preparing composite with MWNTs. A high specific capacitance of about 120 F g⁻¹ was achieved with PEDOT/MWNTs due to the synergistic effect of the two components, with an efficient energy extraction from PEDOT by simple mechanical

mixing of MWNTs and chemically polymerized PEDOT. The composite which contained 15 wt% of PEDOT showed a good capacitance value of 95 F g^{-1} in a three-electrode system, compared with the capacitance of pure CNTs ($10\text{--}15 \text{ F g}^{-1}$) and the capacitance of pure PEDOT ($80\text{--}100 \text{ F g}^{-1}$). The effect of electrolyte during the electrochemical characterization has been studied. It was found that for the PEDOT/MWNT composite, acidic medium ($1 \text{ M H}_2\text{SO}_4$) was the preferable electrolyte resulting in the capacitance of 120 F g^{-1} in a two-electrode system, whereas the alkaline (6.0 M KOH) and organic solution (1 M TEABF_4 in acetonitrile) produced only 80 and 60 F g^{-1} , respectively [131]. PEDOT/MWNT composite with different loading of PEDOT was studied for their performance as electrode materials in supercapacitors with $1 \text{ M H}_2\text{SO}_4$ as electrolyte. The composite electrode that showed specific capacitance of 100 and 120 F g^{-1} , respectively, for the composite contains 80 and 70 wt% PEDOT and excellent stability during cycling. Because of a limited solubility of the EDOT monomer in aqueous medium, the polymerization was performed in aprotic medium such as acetonitrile (AN) with Fe(III) playing the role of oxidant. The prepared PEDOT/CNT composite claimed to have a possibility of operating in acidic, alkaline, and organic electrolytic solutions [141]. As discussed, the composites of PANI, PPy, and PEDOT with CNT have been proven to be a powerful candidate for application in supercapacitor as electrodes.

3.2 Electrochemical Deposition of Conducting Polymers on CNT Electrodes

The first attempt to electrochemically deposit conducting polymers on CNTs was made in 1999 [152], where MWNT electrodes were used for the deposition of PANI films, and higher current density and more effective polymerization were found compared with those deposited on platinum (Pt) electrode. Later the method was elaborated to prepare conducting polymer/CNT composite electrodes for supercapacitors. Chen et al. coated a thin and uniform PPy film, on the surface of well-aligned CNT arrays via potentiodynamic polymerization in aqueous solution. The speed of coating and faradic current for PPy deposition on CNTs is much higher than titanium (Ti) or Pt substrate. The ion diffusion and migration pathways are short due to the unique structure of the electrode material. PPy-coated CNT array electrodes show significantly improved redox performance compared with PPy coated on Ti or Pt substrates [153].

Frackowiak et al. deposited PPy on CNTs through galvanostatic oxidation of monomers in sulfuric acid in order to find an alternative and relatively cheap method to enhance the capacitance of CNTs. The PPy-modified electrodes had an elevated specific capacitance of 180 F g^{-1} compared with 50 F g^{-1} for the unmodified CNT electrode. The charge loss of the PPy-modified CNT electrode was less than 20 % after 2,000 galvanostatic charge/discharge cycling [40]. Xiangqin et al. reported remarkably high specific capacity and cycle performance of PPy/MWNT composite electrodes, which is synthesized by a facile method

involving one-step electrochemical deposition from a thin layer of ionic liquid solution attached on a glassy carbon electrode. The PPy/MWCNT composites have a porous 3D nanostructure, with high specific capacitance and cycling stability. The composite electrode exhibits 890 F g^{-1} specific capacitance at 2 mV s^{-1} in 1 M KCl solution and retains 91% capacitance after 1,000 cycles [154]. Self-supported supercapacitor electrodes with high specific capacitance have been developed by coating PPy on MWNT membranes. A thin film of PPy is wrapped around the individual MWNTs in a uniform manner throughout the MWCNT membrane via a pulsed electrochemical deposition method. This approach optimizes the pseudocapacitance of the membrane. The composite membranes can be directly used as supercapacitor electrodes without backing metal films or binders. Good specific capacitance of 427 F g^{-1} has been achieved using 5-s electrodeposition pulses [155]. Very recently, Hu et al. reported the use of superlong CNT arrays as a platform for convenient fabrication of electrodes. The study demonstrated that electrochemical cyclic voltammetric (CV) scanning can be applied to effectively tailor the surface chemistry of CNTs and introduce physical defects into the CNT walls, which has drastically enhance the electrochemical capacitance performance of CNTs and their composites with PPy. The induced active sites along CNTs allow the coating of PPy on both the outer and inner walls of the defective CNTs. As a consequence, the highest capacitance of 587 F g^{-1} is achieved at a current density of 3 A g^{-1} in the potential range of $0\text{--}0.5 \text{ V}$, in an organic medium of 0.1 M NaClO_4 , which is ten times higher than that of defect-free counterparts. The relatively low capacitance of untreated CNTs and PPy/CNTs is mainly attributed to their hydrophobic character and poor accessibility to the aqueous electrolyte as mentioned above. The related drawback has been greatly overcome by CV pretreatment, and thus the PPy/d-CNT electrode presents the longest discharge duration and the largest specific capacitance (587 F g^{-1}) among all the tested samples [156].

PANI/SWNT composites were prepared by in situ potentiostatic deposition of PANI onto SWCNTs at the potential of 0.75 V versus saturated calomel electrode, with the aim to investigate the influence of microstructure on the specific capacitance of PANI/SWNT composites. It was found that the specific capacitance of the PANI/SWNT composites is strongly influenced by their microstructure, which is correlated to the wt% of the PANI deposited onto the SWCNTs. The optimum condition, corresponding to the highest specific capacitance, 463 F g^{-1} (at 10 mA cm^{-2} , $1 \text{ M H}_2\text{SO}_4$), was obtained for $73 \text{ wt}\%$ PANI deposited onto SWNTs. The specific capacitance of the PANI/SWNT composite electrode was highly stable, with a capacitive decrease of 5% during the first 500 cycles and just 1% fade during the next 1,000 cycles, indicative of the excellent cyclic stability of the composite for supercapacitor applications [157]. In another study Gupta et al. prepared PANI/SWNT composites by electrochemical polymerization of PANI onto SWNTs, and their capacitive performance was compared with its counterparts bare PANI and SWNT electrode in $1 \text{ M H}_2\text{SO}_4$ electrolyte. The PANI/SWNT composite single electrode showed much higher specific

capacitance (485 F g^{-1}), specific energy (228 Wh kg^{-1}), and specific power ($2,250 \text{ W kg}^{-2}$) with stable cycle performance ($\sim 6\%$ capacity fade observed after 1,500 cycles) for 73 wt% PANI deposited onto SWCNTs [158]. Zhang et al. prepared a combination of vertically aligned CNT (CNTA) array framework and tube-covering-tube nanostructured PANI/CNTA composite electrode by electrodeposition technique. The thickness of PANI nanolayer was controlled to 7 nm. The composite electrode exhibited hierarchical porous structure, large surface area, superior conductivity and specific capacitance ($1,030 \text{ F g}^{-1}$ at a current density of 5.9 A g^{-1} in $1 \text{ M H}_2\text{SO}_4$), superior rate capability (95 % capacity retention at 118 A g^{-1}), and high stability (5.5 % capacity loss after 5,000 cycles) [159]. Zhang et al. also prepared electrochemical polymerization of a composite of PANI covered on MWCNTs, and the highest specific capacitance value of 500 F g^{-1} was obtained with poor retention upon cycling, retaining 68 % of the maximum capacity after 1,000 cycles [160].

In summary these studies have been done to investigate the properties and applications of conducting polymers/CNT composite electrodes. Among the reports, PPy [40, 153, 161] and PANI [152, 157, 158, 162–164] have been the most successful in forming a coating on nanotubes via electrochemical polymerization. Composite of conducting polymers with both MWNTs [40, 152–154, 164] and SWNTs [157, 158, 161, 163] was studied as electrodes. The preparation varies in terms of both substrate and electrochemical methods: well-aligned CNT arrays [153], pellets pressed with binder [40, 157, 158], CNT buckypaper [161, 163], and CNT films by solvent casting [164] have been used as a substrate for electrodeposition of conducting polymers. PANI or PPy was coated on CNT by potentiodynamic [152, 153, 162, 163], galvanostatic [40, 161, 164], or potentiostatic [152, 157, 158] electropolymerization [155]. Electrochemically grown conducting polymers decreased the contact resistance between CNTs [161], producing composites with improved electrical conductivity. As electrode materials for supercapacitors, the composites exhibited high specific capacitance, specific energy, and power than CNT or intrinsically conducting polymers alone [157, 158]. The enhanced electrochemical properties of conducting polymer/CNT composite electrode are attributed to the following: (i) very high real surface area of the electrode due to the nanometer size of CNTs; (ii) surface of electrode is more active than flat metal substrates, and lower nucleation energy is required at the beginning of PPy/PANI polymerization; (iii) the pretreatment of carbon nanotubes in nitric acid solution introduced chemical functional groups such as carboxylic acids on the surface of the nanotubes [165–167] which led to the ionized (anionic) CNTs to act as the dopant [168] and improve the polymerization of PPy/PANI; and (iv) good interaction between the CNTs and conducting polymer. Raman [160, 162] and FTIR [162] spectroscopy showed evidence of possible interaction between CNTs and polymers. Electrochemical data and Raman spectra indicate that high specific capacitance is not only due to more uniform PPy coating but also higher redox activity that is likely associated with a more ordered PPy packing [155].

4 Self-Supported and Functionalized CNTs

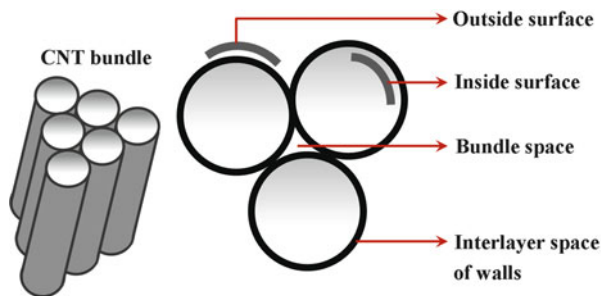
The unique tubular morphology of CNTs offers a combination of high conductivity and high porosity which makes them very attractive to be used as an electrode material for supercapacitors. CNTs are commonly divided into two types, i.e., single-walled (SWNT) and multiple-walled (MWNT) nanotubes. Studies have been reported for the use of SWNTs and MWNTs as the electrode material in aqueous and nonaqueous electrolyte media [34–37]. The electronic transport in both SWNTs and MWNTs has been reported as ballistic transport means over long-tube range without any scattering. This kind of transport phenomena allows CNTs to carry high current densities without any energy dissipation [38]. Also, the internal mesopores of CNTs formed during the entanglement of CNTs allow fast solvated ionic diffusion during the charge and discharge process. The specific capacitance in the range of 15–80 F g⁻¹ has been reported corresponding to the surface areas that range from 120 m² g⁻¹ to 400 m² g⁻¹ [39, 40]. Supercapacitor electrodes built with MWNTs have reported to show specific capacitances in a range of 4–135 F g⁻¹ [169], whereas for SWNTs maximum reported specific capacity is 180 F g⁻¹ in KOH electrolyte media [170].

Surface oxidation of CNTs usually shows improved capacitances. Increased specific capacitance (~130 F g⁻¹) has been reported by the CNT surface modification with oxidative treatment and/or by introduction of additional surface functionality [18, 169]. Li et al. have used a mixture of H₂SO₄ and HNO₃ to activate the CNTs. These activated CNTs exhibited specific capacitance 2.5 times higher than that of the initial CNTs. These activated CNTs exhibited specific capacitance 2.5 times higher than that of the initial CNTs [171]. Figure 17.4 shows the schematic illustration of the space in carbon nanotube bundle for the storage of electrolyte ions.

MWNTs with diameter of 8 nm when treated with nitric acid and formed into electrodes have shown increased surface area of 430 m² g⁻¹ [172]. The specific capacitance of such electrodes in acid media was reported to be 102 F g⁻¹. The electrodes consist of freestanding mats of entangled CNTs which may contain micropores, slit-shaped pores, or dead-end pores, but these might be difficult to access, but the porosity of these electrodes is mainly due to the interstitial spaces created by entangled CNT network.

Another surface treatment to improve the capacitance of CNTs is the use of bases like potassium hydroxide (KOH). Usually this kind of surface treatments increases the surface area 2–3 times without losing its unique nanotubular morphology [173]. Jiang and Lin have reported the use of a vertically grown CNT forest as electrode material for supercapacitor. These CNT forests compared to disoriented CNT network could have high porosity up to 99.6 % and small density as 0.01–0.02 g m⁻³. A two-step process of mechanical bending and liquid densification of these CNT forests grown on silicon surface produce densified CNT electrode. This results in increased specific capacitance as well as enhances the energy density of the supercapacitor up to 10 times. The volumetric specific capacitance was increased from 1.07 F cm⁻³ to 10.7 F cm⁻³ for this densified CNT electrode [174].

Fig. 17.4 Schematic illustration of the space in carbon nanotube bundle for the storage of electrolyte ions (Adapted from Ref. [171] with permission from Elsevier, copyright 2012)



The functionalization and solubilization of SWNTs and MWNTs is important and has been studied extensively. Investors have used strong acids/bases to remove the impurities like metals and amorphous carbon from the CNTs by oxidizing them and at the same time generate functional groups like $-\text{COOH}$ (carboxylic acid group) to incorporate reactive sites at the end and side walls of the CNTs [175–178]. Masarapu et al. have studied the effect of temperature on the kinetics and diffusion mechanism of ions in supercapacitor using a SWNT film electrode and organic electrolyte. At room temperature, they observed an improved performance due to the combined effects of an increase in CNT conductivity and surface modifications by repeatedly heating and cooling the device between the temperatures of 25 and 100 °C [179].

CNTs are usually used in the formation of electrodes using mainly binder-enriched or binderless fabrication methods. However, both methods cause high contact resistance between the current collector and the active CNT material. An approach of developing the CNT electrode directly onto a conductive substrate minimizes the contact resistance between the collector material and the active material. Moore et al. have reported SWNT-coated electrodes which were prepared from the SWNT aqueous suspensions using various methods in order to create uniform nanoporous networks of SWNTs on stainless steel current collectors. These electrodes consisted of nanopore diameters in the range of 0.9–1.2 nm with specific surface areas of approximately $197\text{--}394\text{ m}^2\text{ g}^{-1}$ [180]. Emmenegger et al. have reported electrode fabrication with well-aligned MWNT film grown on aluminum support. The MWNTs were with lengths in the range of 1–10 μm and had a diameter in the range of 5–100 nm. A volumetric capacitance of $\sim 120\text{ F cm}^{-3}$ with high power density was reported using this electrode [181].

Wang et al. have successfully synthesized the partially exfoliated MWNTs and studied the capacitive performance of these Ex-CNT-coated electrodes. They reported a maximum specific capacitance of 165 F g^{-1} and a coulombic efficiency of $\sim 98\%$. This capacitance value is significantly higher than untreated MWNTs and graphene. They attributed the enhanced capacities to the increase surface area and defect density in the partially exfoliated tubular structure [182].

Though in CNTs a conducting and well-accessible carbon network provides a moderate surface area ($100\text{--}400\text{ m}^2\text{ g}^{-1}$), the supercapacitor performance is highly dependent on available mesopores for ion transportation, and pure CNTs

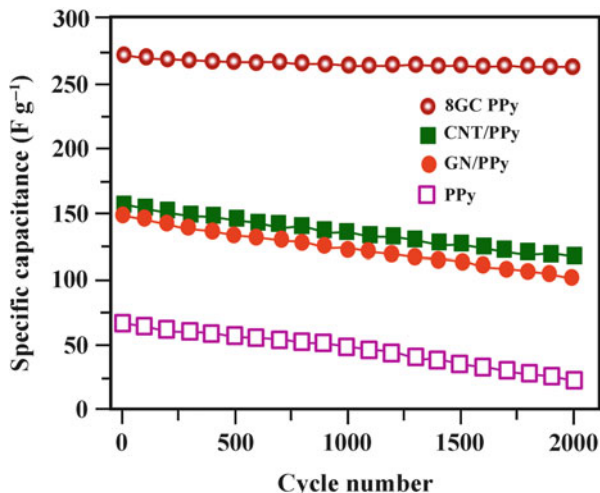
provide only moderate number of these mesopores. Therefore, pure CNTs as an electrode material only supply very moderate specific capacitance values depending on their microtexture. So efforts are being done to develop new composite materials which combine the advantages of CNTs with the other material that can provide properties like increased surface area or flexibility.

5 Graphene-CNT Composite

The research on the use of graphene as an electrode material for energy storage has begun very recently due to its superior properties such as low weight, chemical inertness, and the possibility of availability at low price. Graphene is a monolayer sheet of carbon bonded with sp^2 -hybridization which is conductive and can be easily functionalized with other molecules [183]. The high surface area, i.e., $2,630 \text{ m}^2 \text{ g}^{-1}$, together with their conductivity is highly desired for their application in supercapacitors [184]. Ruoff et al. were the first to explore the use of chemically modified graphene in supercapacitors. They reported capacities of 135 and 99 F g^{-1} for aqueous and organic electrolyte media, respectively [185]. However, the direct use of graphene showed difficulty in capacitive measurements and exhibited different values because the exfoliated chemically reduced graphene sheets tend to restack and thus create graphitic structures. This tendency reduces the available surface area and thus reduces the effective capacity of graphene for energy storage [20, 185]. One suggested approach was to insert nanostructures as spacers to improve the capacitance, and one of the candidates is the carbon nanotubes. Various reports have been published which discuss that the graphene and CNT composite results in increased capacitance [44, 45, 186–189]. The most common process for the preparation of graphene involves the use of graphite. A single layer of graphite oxide is prepared from graphite from oxidation and consequent exfoliation (e.g., by sonication or thermal exfoliation). This method can be modified to obtain nanoarchitected design of graphene-CNT composite as reported by Buglione and Pumera [184]. They studied the composite graphene-CNT electrodes prepared using three different kinds of CNTs: (a) single-walled nanotubes, SWNTs; (b) double-walled nanotubes, DWNTs; and (c) multiwalled nanotubes, MWNTs. They found that resulting capacitance improvement is close to the average of capacitances of the two components used in the graphene-CNT composite contrary to some previous reports referring a synergic effect between graphene and CNTs for capacitance increase.

Rakhi and Alshareef have reported the use of a graphene-CNT composite electrode where MWNTs were loaded with transition metal oxide. SnO_2 was of particular interest due to its good chemical stability, easy availability, high conductivity, low cost, and environmentally benign nature. They reported specific capacitance of 224 F g^{-1} with high power and energy density (17.6 kW g^{-1} and 31 Wh kg^{-1} , respectively). Also, excellent life cycle was reported where $\sim 81 \%$ of initial specific capacitance was retained after 6,000 cycles [190].

Fig. 17.5 Specific capacity of CNT/PPy, GN/PPy and 8GCPPy as a function of cycle number at a current density of 6 A g^{-1} (Adapted from Ref. [191] with permission from Elsevier, copyright 2012)



Polymers such as polypyrrole (PPy), polyacrylonitrile (PAN), and polyaniline have been extensively studied as electrode materials for supercapacitors. Advantages of using these polymers include their low cost, environmental friendliness, high capacitive capability, and ease of processing. The combination of polymers with graphene-CNTs has attracted a great deal of attraction as the graphene-CNTs bring excellent conductivity and provide high surface area to deposit the polymers which add up good elasticity to accommodate the strain of volume change. Lu et al. prepared the ternary nanocomposite of graphene, CNTs, and PPy via in situ chemical polymerization. These ternary composites when used as an electrode material bring good electrical conductivity and a tailored structure. The combined properties of each component of the composite material exhibit synergistic properties where graphene-polypyrrole-CNT shows both the fast and reversible faradic capacitance and indefinitely reversible double-layer capacitance at the electrode-electrolyte interfaces. Such superior cyclability is more advantageous for supercapacitors as compared to ordinary batteries. Scheme shows the microstructure of this ternary composite. Figure 17.5 shows the cyclability tests combined with the specific capacitance values recorded for individual, i.e., graphene, PPy, and CNT electrodes as well as their composite electrodes [191]. Similarly, Yan et al. reported the graphene-CNT/polyaniline composite electrode for supercapacitors which exhibits the specific capacitance of $1,035 \text{ F g}^{-1}$. Also, using this ternary electrode even after 1,000 cycles, only 6 % of decrease in capacitance was observed which shows improved performance compared to many other composite electrodes [192]. However, it has also been reported that these conducting polymers lack long-term stability which can affect the supercapacitor performance [6].

Due to increased attention toward the flexibility of energy storage devices, some studies have also been reported for flexible freestanding, binder-free electrodes made of graphene papers with few micrometers of thickness. Such freestanding

graphene films have shown capacitances ranging from 100 F g^{-1} to 300 F g^{-1} [193, 194]. It has been reported that energy and power densities of these graphene films decrease steadily with increased film thickness [186]. Also, the paper processing parameters especially the reduction step affect the electrode performance of these films. Huang et al. have reported the flexible CNT coated graphene paper electrode in the supercapacitor device. They measured the parameters such as interlayer spacing, degree of functionalization, sheet resistance, and contact angles to establish the correlation between the material characteristics and the supercapacitive performance of the resulting binder-free graphene paper electrodes [195]. Lu et al. have reported the electrochemical data for the graphene/MWNT film electrode which shows a specific capacitance of 265 F g^{-1} at 0.1 A g^{-1} and a specific capacitance of 130 F g^{-1} even at 50 A g^{-1} . The electrode shows a capacitive degradation of only 3 % after 2,000 cycles [196].

6 Carbon-CNT Composite

Various carbon materials such as carbon black, carbon aerogels, carbon fibers, glassy carbons, etc., have been extensively studied and used as electrode materials due to their low cost, abundance, and chemical stability [197, 198]. The surface area for these materials typically ranges from $86 \text{ m}^2 \text{ g}^{-1}$ to $3,000 \text{ m}^2 \text{ g}^{-1}$ which highly depends on the porosity [19]. The energy density of a supercapacitor can be enhanced significantly by increasing the surface area accessible to the electrolyte, whereas the power density of the supercapacitor can be improved by increasing the conductivity of the electrode as well as by improving the diffusion kinetics of electrolyte in the electrode. Various kinds of porous carbon electrodes with reduced particle size and aligned pore channel, i.e., with macro-, meso-, and micropores, were developed to improve the electrolyte transport in the electrode [199–203]. Zheng et al. have developed an in situ method to integrate CNTs into activated carbon (AC) matrix to improve the performance as supercapacitor electrode. This modified electrode combined both advantages of CNT and AC, where one has high electrical conductivity and the other has very high surface area, respectively. This improves the performance as well as exhibits high cycling stability. Specific area of pristine CNT was $250 \text{ m}^2 \text{ g}^{-1}$ which increases to $1,626 \text{ m}^2 \text{ g}^{-1}$ in the CNT-AC composite [204]. Addition of large number of micropores of 1–2 nm caused this significant increase which is very appropriate for holding electrolyte ions in large amounts to create the sufficient electrolyte-electrode interface for charge accumulation [205]. With increased surface area, added high conductivity of CNTs improved the ability for quick charge propagation in the electrolyte of the electrode. The modified electrode exhibited capacitance of 378 F g^{-1} in aqueous KOH electrolyte and showed only $\sim 5 \%$ drop in capacitance after 2,000 cycles [204]. Similarly, Li et al. reported the fabrication of modified supercapacitor electrode using a CNT composite with activated mesocarbon microbeads (AMCMBs) and reported a specific capacitance of 243 F g^{-1} [206].

Lei et al. have described a template approach to fabricate electrode consisting of mesoporous carbon interconnected by CNTs using pyridine as a carbon precursor on mesoporous silica (SBA-15) template. The performance of the electrode was found dependent on the doping level of nitrogen, CNT content, and other structural parameters of this composite. This mesoporous composite offers appropriate pore size and high surface area together with reduced resistance between carbon particles which leads to a high rate performance. They reported a maximum specific capacitance of 208 F g^{-1} with good cyclability showing no capacitance loss up to 1,000 cycles [207]. Similarly, Yi et al. have reported the fabrication of a composite electrode using CNT-implanted mesoporous carbon spheres using gelatin as a soft template. The reported surface area for this composite was $284 \text{ m}^2 \text{ g}^{-1}$ with average pore size of $\sim 4 \text{ nm}$. A maximum specific capacitance of 189 F g^{-1} with power density of 8.7 kW kg^{-1} and energy density of 6.6 Wh kg^{-1} was reported for this CNT-carbon electrode [208].

Another carbon-CNT composite developed by Bordjiba et al. shows the use of a highly attractive nanostructured sample derived from a microfibrinous carbon paper (MFCP) decorated with MWNTs. Oxidation of these nanostructures significantly increases their specific surface area from $71 \text{ m}^2 \text{ g}^{-1}$ to $208 \text{ m}^2 \text{ g}^{-1}$. The oxidation process also changes the electrode wettability behavior and enhances their electrochemical activity. It has been noticed that CNT synthesis is rather difficult on metallic conducting substrates compared to that of insulating glass or silicon substrates. Also, the use of additional binders or adhesives can occlude the CNT surface. Citing these reasons they have described carbon paper substrate as an ideal conductive substrate/electrode for supercapacitor application. Also, it is a thin, lightweight matrix with pore size in micrometer scale which can also be rolled into any shape. The maximum specific capacitance reported for these composite electrodes is 165 F g^{-1} [209].

Kim et al. demonstrated the synthesis of vertically aligned CNTs directly on conductive carbon papers and used them as electrode materials. In this nanoarchitectured structure the CNT forest showed microscale patterns which were defined by the structure of underlying carbon papers. They tested the adhesion of CNTs with paper using mild sonication and found that it adheres well. This direct integration leads to a naturally patterned structure which shows good alignment of CNTs and results in excellent performance as an electrode material for supercapacitors. The maximum specific capacitance measured for this binder-free CNT composite electrode was 200 F g^{-1} [210]. Portet et al. compared the electrochemical performances of MWNTs, nanodiamonds, carbon black, and carbon onions for supercapacitor application [211]. The pore size and defects vary in all these carbon structures. It was believed that a pore size of two or three times larger than the solvated electrolyte size is optimal for high capacity performances [197, 212]. However, they reported that not only pore size but defects in the carbon structure can also affect the electrolyte ion transport by electrode [211–214].

7 Conclusion

Applications of self-supported and functionalized CNTs and its composite with various electrode materials in supercapacitors are discussed by referring a wide range of materials including metal oxides, conducting polymers, carbon, and graphenes. The superior electrochemical performance indicates that exploitation of unique properties of CNTs is an effective strategy for developing multifunctional nanocomposite electrodes for effective electrochemical energy storage devices. The architecture and high electronic conductivity of CNTs enables excellent capacitance and cycling performance of the supercapacitors. It has been shown that addition of metallic oxides or conductive polymers resulted in CNT composite, and use of such material in supercapacitor as electrodes provides significant higher capacitance than CNT alone. Supercapacitors based on nanocomposite freestanding electrode outperform and exhibited high rate capability due to the improved electrical conductivity, strong structural integrity, and synergetic effect of the component materials in the composites. The three-dimensional porous electrode also facilitates large mass loading of active materials which leads to high specific capacity. The effect of type (SWNTs and MWNTs), structure (aligned or nonaligned), and functionalization of the nanotubes embedded in the nanocomposite electrodes was also highlighted. The mesoporous structure and size effect of CNTs significantly contribute to specific surface area that results in higher electrode conductivity and consequently higher specific power. Composites of conducting polymers and CNTs show improved mechanical, electrical, and electrochemical properties compared with conducting polymers alone. Conducting polymer/CNT composites combined the large pseudocapitance of the polymers and the mechanical and structural properties of the nanotubes and thus highly promising in novel supercapacitors with ultrahigh capacitance and power density. The good rate capability and long-term cycling stability of the CNT-based nanocomposite electrodes endow the important suggestions for designing high-performance electrodes for supercapacitors. However, CNT is an expensive material and for this reason is not used in commercial supercapacitors.

References

1. Conway BE (1999) *Electrochemical supercapacitors: scientific fundamentals and technological applications*. Kluwer Academic/Plenum Publisher, New York
2. Burke A (2000) *J Power Sources* 91:37
3. Winter M, Brodd RJ (2004) *Chem Rev* 104:4245
4. Miller JR, Simon P (2008) *Science* 321:651
5. Simon P, Gogotsi Y (2008) *Nat Mater* 7:845
6. Zhang Y, Feng H, Wu XB, Wang LZ, Zhang AQ, Xia TC, Dong HC, Li XF, Zhang LS (2009) *Int J Hydrogen Energy* 34:4889
7. Zheng JP (2005) *J Electrochem Soc* 152:A1864
8. Miller JR (2006) *Electrochim Acta* 52:1703
9. Yuan CZ, Gao B, Zhang XG (2007) *J Power Sources* 173:606

10. Fan Z, Chen JH, Cui KZ, Sun F, Xu Y, Kuang YF (2007) *Electrochim Acta* 52:2959
11. Kim IH, Kim KB (2006) *J Electrochem Soc* 153:A383
12. Lao ZJ, Konstantinov K, Tournaire Y, Ng SH, Wang GX, Liu HK (2006) *J Power Sources* 162:1451
13. Toupin M, Brousse T, Belanger D (2002) *Chem Mater* 14:3946
14. Wu MS, Huang YA, Yang CH, Jow HH (2007) *Int J Hydrogen Energy* 32:4153
15. Wu NL (2002) *Mater Chem Phys* 75:6
16. Yang XH, Wang YG, Xiong HM, Xia YY (2007) *Electrochim Acta* 53:752
17. Kotz R, Carlen M (2000) *Electrochim Acta* 45:2483
18. Frackowiak E, Beguin F (2001) *Carbon* 39:937
19. Pandolfo AG, Hollenkamp AF (2006) *J Power Sources* 157:11
20. Zhang LL, Zhao XS (2009) *Chem Soc Rev* 38:2520
21. Peng C, Zhang S, Jewell D, Chen GZ (2008) *Prog Nat Sci* 18:777
22. Becker HL (1957) US Patent 2,800,616
23. Pierson HO (1993) *Handbook of carbon, graphite, diamond and fullerenes*. Noyes Publications, Park Ridge
24. Fitzer E, Köchling KH, Boehm HP, Marsh H (1995) *Pure Appl Chem* 67:473
25. McEnaney B (1999) *Structure and bonding in carbon materials*. In: Burchell TD (ed) *Carbon materials for advanced technologies*. Pergamon/Elsevier, Amsterdam, p 1
26. Inagaki M, Radovic LR (2002) *Carbon* 40:2263
27. Bockris JO'M, Kita H (1961) *J Electrochem Soc* 108:676
28. Engelsman K, Lorenz WJ, Schmidt E (1980) *J Electroanal Chem* 114:1
29. Rudge A, Raistrick I, Gottesfeld S, Ferraris JP (1994) *Electrochim Acta* 39:273
30. Andreas HA, Conway BE (2006) *Electrochim Acta* 28:6510
31. Li HF, Xi H, Zhu SM, Wen ZY, Wang RD (2006) *Micropor Mesopor Mater* 96:357
32. Nakamura M, Nakanishi M, Yamamoto K (1996) *J Power Sources* 60:225
33. Kinoshita K (1988) *Carbon: electrochemical and physicochemical properties*. Wiley-Interscience, New York
34. An KH, Kim WS, Park YS, Moon JM, Bae DJ, Lim SC, Lee YS, Lee YH (2001) *Adv Funct Mater* 11:387
35. An KH, Jeon KK, Heo JK, Lim SC, Bae DJ, Lee YH (2002) *J Electrochem Soc* 149:A1058
36. Lee YH, An KH, Lim SC, Kim WS, Jeong HJ, Doh CH, Moon SI (2002) *New Diam Front Carbon Technol* 12:209
37. McEnaney B (2002) *Energy storage in carbon materials*, IV International Conference Catalysis and Adsorption in Fuel Processing and Environmental Protection, Kudowa Zdrój, Poland, *Prace Naukowe Instytutu Chemii i Technologii Nafty i Węgla. Politechniki Wrocławskiej, Konferencje* 10(57):s.11
38. Baughman RH, Zakhidov AA, de Heer WA (2002) *Science* 297:787
39. Frackowiak E, Delpeux S, Jurewicz K, Szostak K, Cazorla-Amoros D, B'eguín F (2002) *Chem Phys Lett* 361:35
40. Frackowiak E, Jurewicz K, Szostak K, Delpeux S, B'eguín F (2002) *Fuel Process Tech* 77/78:213
41. Brezesinski T, Wang J, Tolbert SH, Dunn BJ (2011) *Sol-gel Sci Technol* 57:330
42. Sun Z, Liu Z, Han B, Miao S, Du J, Miao Z (2006) *Carbon* 44:888
43. Tao B, Zhang J, Miao F, Hui S, Wan L (2010) *Electrochim Acta* 55:5258
44. Byon HR, Lee SW, Chen S, Hammond PT, Yang SH (2011) *Carbon* 49:457
45. Chen YM, Cai JH, Huang YS, Lee KY, Tsai DS (2011) *Nanotechnology* 22:115706
46. Lee JY, An KH, Heo JK, Lee YH (2003) *J Phys Chem B* 107:8812 C
47. Zhou CF, Kumar S, Doyle CD, Tour JM (2005) *Chem Mater* 17:1997
48. Vidotti M, Salvador RP, Ponzio EA, De-Torresi SIC (2007) *J Nanosci Nanotech* 7:3221
49. Vidottia M, Silva MR, Salvador RP, De-Torresi SIC, Dall'Antonia LH (2008) *Electrochim Acta* 53:4030
50. Zheng JP, Cygan PJ, Jow TR (1995) *J Electrochem Soc* 142:2699

51. Zheng JP, Jow TR (1996) *J Power Sources* 62:155
52. Lee BJ, Sivakkumar SR, Ko JM, Kim JH, Kim DY (2006) *J Power Sources* 168:546
53. Wen J, Zhou Z (2006) *Mater Chem Phys* 98:442
54. Kim IH, Kim JH, Lee YH, Kim KB (2005) *J Electrochem Soc* 152:A2170
55. Lee JK, Pathan HM, Jung KD, Joo OS (2006) *J Power Sources* 159:1527
56. Park JH, Ko JM, Park OO (2003) *J Electrochem Soc* 150:A864
57. Liu X, Huber TA, Kopac MC, Pickup PG (2009) *Electrochim Acta* 54:7141
58. Seo MK, Saouab A, Park SJ (2010) *Mater Sci Eng B* 167:65
59. Yan S, Qu P, Wang H, Tian T, Xiao Z (2008) *Mater Res Bull* 43:2818
60. Yan S, Wang H, Qu P, Zhang Y, Xiao Z (2009) *Synth Met* 159:158
61. Kim BC, Wallace GG, Yoon YI, Ko JM, Too CO (2009) *Synth Met* 159:1389
62. McKeown DA, Hagans PL, Carette LPL, Russell AE, Swider KE, Rolison DR (1999) *J Phys Chem B* 103:4825
63. Dmowski W, Egami T, Swider-Lyons KE, Love CT, Rolison DR (2002) *J Phys Chem B* 106:12677
64. Qin X, Durbach S, Wu GT (2004) *Carbon* 42:451
65. Arabale G, Wagh D, Kulkarni M, Mulla IS, Vernerkar SP, Vijayamohan K, Rao AM (2003) *Chem Phys Lett* 376:207
66. Hsieh TF, Chuang CC, Chen WJ, Huang JH, Chen WT, Shu CM (2012) *Carbon* 50:1740
67. Deng GH, Xiao X, Chen JH, Zeng XB, He DL, Kuang YF (2005) *Carbon* 43:1557
68. Chen Y, Liu C, Li F, Cheng HM (2005) *J Alloys Compd* 397:282 [79]
69. Subramanian V, Zhu HW, Wei BQ (2006) *Electrochem Commun* 8:827
70. Taguchi A, Inoue S, Akamaru S, Hara M, Watanabe K, Abe T (2006) *J Alloys Compd* 414:137
71. Wang HE, Lu Z, Qian D, Fang S, Zhang J (2008) *J Alloys Compd* 466:250
72. Adelkhani H, Ghaemi M (2010) *J Alloys Compd* 493:175
73. Gong K, Yu P, Su L, Xiong S, Mao L (2007) *J Phys Chem C* 111:1882
74. Fan Z, Chen J, Zhang B, Sun F, Liu B, Kuang Y (2008) *Mater Res Bull* 43:2085
75. Li J, Yang Q, Zhitomirsky I (2008) *J Power Sources* 185:1569
76. Ma SB, Nam KW, Yoon WS, Yang XQ, Ahn KY, Ohd KH, Kim KB (2008) *J Power Sources* 178:483
77. Yue H, Huang X, Yang Y (2008) *Mater Lett* 62:3388
78. Bordjiba T, Bélanger D (2009) *J Electrochem Soc* 156:A378
79. Chou SL, Wang JZ, Chew SY, Liu HK, Dou SX (2008) *Electrochem Commun* 10:1724
80. Reddy ALM, Shaijumon MM, Gowda SR, Ajayan PM (2009) *Nano Lett* 9:1002
81. Zhang H, Cao G, Wang Z, Yang Y, Shi Z, Gu Z (2008) *Nano Lett* 9:2664
82. Zhou Y, He B, Zhang F, Li H (2004) *J Solid State Electrochem* 8:482
83. Raymond-Pinero E, Khomenko V, Frackowiak E, Beguin F (2005) *J Electrochem Soc* 152:A229
84. Fan Z, Chen J, Wang M, Cui K, Zhou H, Kuang Y (2006) *Diam Relat Mater* 15:1478
85. Li J, Zhitomirsky I (2009) *J Mater Process Tech* 209:3452
86. Nam KW, Lee CW, Yang XQ, Cho BW, Yoon WS, Kim KB (2009) *J Power Sources* 188:323
87. Lin CK, Wu CH, Tsai CY, Chen CY, Wang SC (2010) *Surf Coat Tech* 205:1595
88. Amade R, Jover E, Caglar B, Mutlu T, Bertran E (2011) *J Power Sources* 196:5779
89. Wang Y, Liu H, Sun X, Zhitomirsky I (2009) *Scr Mater* 61:1079
90. Lin YP, Tsai CB, Ho WH, Wu NL (2011) *Mater Chem Phys* 130:367
91. Tang W, Hou YY, Wang XJ, Bai Y, Zhu YS, Sun H, Yue YB, Wu YP, Zhu K, Holze R (2012) *J Power Sources* 197:330
92. Teng F, Santhanagopalan S, Wang Y, Meng DD (2010) *J Alloys Compd* 499:259
93. Li X, Wei B (2012) *Nano Energy* 1:479
94. Fan Z, Xie M, Jin X, Yan J, Wei T (2011) *J Electroanal Chem* 659:191
95. Yan J, Fan Z, Wei T, Cheng J, Shao B, Wang K, Song L, Zhang M (2009) *J Power Sources* 194:1202

96. Kang YJ, Kim B, Chung H, Kim W (2010) *Synth Met* 160:2510
97. Zhang J, Wang Y, Zang J, Xin G, Yuan Y, Qu X (2012) *Carbon* 50:5196
98. Sivakkumar SR, Ko JM, Kim DY, Kim BC, Wallace GG (2007) *Electrochim Acta* 52:7377
99. Li Q, Liu J, Zou J, Chunder A, Chen Y, Zhai L (2011) *J Power Sources* 196:565
100. Wang H, Peng C, Peng F, Yu H, Yang J (2011) *Mater Sci Eng B* 176:1073
101. Li Q, Anderson JM, Chen Y, Zhai L (2012) *Electrochim Acta* 59:548
102. Ko JM, Kim KM (2009) *Mater Chem Phys* 114:837
103. Zheng H, Wang J, Jia Y, Ma C (2012) *J Power Sources* 216:508
104. Zheng H, Tang F, Jia Y, Wang L, Chen Y, Lim M, Zhang L, Lu GM (2009) *Carbon* 47:1534
105. Ma SB, Nam KW, Yoon WS, Yang XQ, Ahn KY, Oh KH, Kim KB (2007) *Electrochem Commun* 9:2807
106. Wang JG, Yang Y, Huang ZH, Kang F (2012) *Electrochim Acta* 75:213
107. Nam KW, Kim KB (2002) *J Electrochem Soc* 149:A346
108. Cheng J, Gao GP, Yang YS (2006) *J Power Sources* 159:734
109. Nelson PA, Owen JR (2003) *J Electrochem Soc* 150:A1313
110. Zhang FB, Zhou YK, Li HL (2004) *Mater Chem Phys* 83:260
111. Wang YG, Xia YY (2006) *Electrochim Acta* 51:3223
112. Nam KW, Kim KH, Lee ES, Yoon WS, Yang XQ, Kim KB (2008) *J Power Sources* 182:642
113. Chang HY, Chang HC, Lee KY (2013) *Vacuum* 87:164
114. Lee JY, Liang K, An KH, Lee YH (2005) *Synth Met* 150:153
115. Hwang SG, Ryu SH, Yun SR, Ko JM, Kim KM, Ryu KS (2011) *Mater Chem Phys* 130:507
116. Kim SJ, Park GJ, Kim BC, Chung JK, Wallace GG, Park SY (2012) *Synth Met* 161:2641
117. Zhang Y, Sun X, Pan L, Li H, Sun Z, Sun C, Tay BK (2009) *J Alloys Compd* 480:L17
118. Zhang Y, Sun X, Pan L, Li H, Sun Z, Sun C, Tay BK (2009) *Solid State Ion* 180:1525
119. Kim DW, Rhee KY, Park SJ (2012) *J Alloys Compd* 530:6
120. Li ZJ, Chang TX, Yun GQ, Jia Y (2012) *Powder Technol* 224:306
121. Jayalakshmi M, Rao MM, Venugopal N, Kim KB (2007) *J Power Sources* 166:578
122. Lang J, Yan X, Xue Q (2011) *J Power Sources* 196:7841
123. Battumur T, Ambade SB, Ambade RB, Pokharel P, Lee DS, Han SH, Lee W, Lee SH (2013) *Curr Appl Phys* 13:196–204
124. Shakir I, Shahid M, Cherevko S, Chung CH, Kang DJ (2011) *Electrochim Acta* 58:76
125. Bolto BA, McNeill R, Weiss DE (1963) *Aust J Chem* 16:1090
126. Chiang CK, Fincher CR, Park YW, Heeger AJ, Shirakawa H, Louis EJ, Gau SC, McDiarmid AG (1977) *Phys Rev Lett* 39:1098
127. Boara G, Sparpaglione M (1995) *Synth Met* 72:135
128. Morvant MC, Reynolds JR (1998) *Synth Met* 92:57
129. Hung S, Wen T, Gopalan A (2002) *Mater Lett* 55:165
130. Noh KA, Kim DW, Jin CS, Shin KH, Kim JH, Ko JM (2003) *J Power Sources* 124:593
131. Lota K, Khomenko V, Frackowiak E (2004) *J Phys Chem Solids* 65:295
132. Gupta V, Miura N (2006) *Mater Lett* 60:1466
133. Fan LZ, Maier J (2006) *Electrochem Commun* 8:937
134. Xu Y, Wang J, Sun W, Wang S (2006) *J Power Sources* 159:370
135. Chen WC, Wen TC, Teng HS (2003) *Electrochim Acta* 48:641
136. Laforgue A, Simon P, Fauvarque JF, Sarrau JF, Lailler P (2001) *J Electrochem Soc* 148:A1130
137. Laforgue A, Simon P, Fauvarque JF, Mastragostino M, Sovai F, Sarrau JF, Lailler P, Conte M, Rossi E, Saguatti S (2003) *J Electrochem Soc* 150:A645
138. Feast WJ (1986) *Synthesis of conducting polymers*. In: Skotheim TA (ed) *Handbook of conducting polymers*, vol 1. Marcel Dekker Inc, New York, pp 1–43, 981
139. Nalawa HS, Dalton LR, Schmidt WF, Rabe JG (1985) *Polym Commun* 27:240
140. Burke A (2007) *Electrochim Acta* 53:1083
141. Frackowiak E, Khomenko V, Jurewicz K, Lota K, Beguin F (2006) *J Power Sources* 153:413
142. Deng MG, Yang BC, Hu YD (2005) *J Mater Sci* 40:5021

143. Sivakkumar SR, Kim WJ, Choi JA, MacFarlane DR, Forsyth M, Kim DW (2007) *J Power Sources* 171:1062
144. Zhou Y, Qin ZY, Li L, Zhang Y, Wei YL, Wang LF, Zhu MF (2010) *Electrochim Acta* 55:3904
145. Meng C, Liu C, Fan S (2009) *Electrochem Commun* 11:186
146. Lee H, Kim H, Cho MS, Choi J, Lee Y (2011) *Electrochim Acta* 56:7460
147. Mi H, Zhang X, Xu Y, Xiao F (2010) *Appl Surf Sci* 256:2284
148. Ju YW, Choi GR, Jung HR, Lee WJ (2008) *Electrochim Acta* 53:5796
149. Lu X, Dou H, Yuan C, Yang S, Hao L, Zhang F, Shen L, Zhang L, Zhang X (2012) *J Power Sources* 197:319
150. Sharma RK, Karakoti A, Seal S, Zhai L (2010) *J Power Sources* 195:1256
151. Liu R, Cho S, Lee SB (2008) *Nanotechnology* 19:215710
152. Downes C, Nugent J, Ajayan PM, Duquette C, Santhanam KSV (1999) *Adv Mater* 11:1028
153. Chen JH, Huang ZP, Wang DZ, Yang SX, Li WZ, Wen JG, Ren ZF (2001) *Synth Met* 125:289
154. Lin X, Xu Y (2008) *Electrochim Acta* 53:4990
155. Fanga Y, Liua J, Yuda DJ, Wickstedt JP, Kalkane K, Topale CO, Flandersb BN, Wuc J, Li J (2010) *J Power Sources* 195:674
156. Hu Y, Zhao Y, Li Y, Li H, Shao H, Qu L (2012) *Electrochim Acta* 66:279
157. Gupta V, Miura N (2006) *J Power Sources* 157:616
158. Gupta V, Miura N (2006) *Electrochim Acta* 52:1721
159. Zhang H, Cao G, Wang Z, Yang Y, Shi Z, Gu Z (2008) *Electrochem Commun* 10:1056
160. Zhang J, Kong LB, Wang B, Luo YC, Kang L (2009) *Synth Met* 159:260
161. Nuria FA, Martti K, Viera S, Ursula DW, Siegmars R (2004) *Diam Relat Mater* 13:256
162. Gao M, Huang S, Dai L, Wallace G, Gao R, Wang Z (2000) *Angew Chem* 39:3664
163. Baibarac M, Baltog I, Godon C, Lefrant S, Chauvet O (2004) *Carbon* 42:3143
164. Guo M, Chen J, Li J, Tao B, Yao S (2005) *Anal Chim Acta* 532:71
165. Shaffer MSP, Fan X, Windle AH (1998) *Carbon* 36:1603
166. Sandler J, Shaffer M, Prasse T, Bauhofer W, Schulte K, Windle AH (1999) *Polymer* 40:5967
167. Shaffer MSP, Windle AH (1999) *Adv Mater* 11:937
168. Chen GZ, Shaffer MSP, Coleby D, Dixon G, Zhou W, Fray DJ, Windle AH (2000) *Adv Mater* 12:522
169. Frackowiak F, Metenier K, Bertagna V, B'eguine F (2000) *Appl Phys Lett* 77:2421
170. An KH, Jeon KK, Kim WS, Park YS, Lim SC, Bae DJ, Lee YH (2001) *J Korean Phys Soc* 39:S511
171. Inagaki M, Konno H, Tanaike O (2010) *J Power Sources* 195:7880
172. Niu C, Sichel EK, Hoch R, Moy D, Tennent H (1997) *Appl Phys Lett* 70:1480
173. Jiang Q, Qu MZ, Zhou GM, Zhang BL, Yu ZL (2002) *Mater Lett* 57:988
174. Jiang Y, Lin L (2012) *Sens Actuatur A Phys* doi:10.1016/j.sna.2012.04.012
175. Frehill F, Vos JG, Benrezzak S, Koos AA, Konya Z, Ruther MG, Blau WJ, Fonseca A, Nagy JB, Biro LP, Minett AI, Panhuis M (2002) *J Am Chem Soc* 124:13694
176. Georgakilas V, Kordatos K, Prato M, Guldi DM, Holzinger M, Hirsch A (2002) *J Am Chem Soc* 124:760
177. Fu K, Li HP, Zhou B, Kitaygorodskiy A, Allard LF, Sun YP (2004) *J Am Chem Soc* 126:4669
178. Paiva MC, Zhou B, Fernando KAS, Lin Y, Kennedy JM, Sun YP (2004) *Carbon* 42:2849
179. Masarapu C, Zeng HF, Hung KH, Wei B (2009) *ACS Nano* 3:2199
180. Moore JJ, Kang JH, Wen JZ (2012) *Mater Chem Phys* 134:68
181. Emmenegger C, Mauron P, Züttel A, Nützenadel C, Schneuwly A, Gally R, Schlapbach L (2000) *Appl Surf Sci* 162/163:452
182. Wang G, Ling Y, Qian F, Yang X, Liu XX, Li Y (2011) *J Power Sources* 196:5209
183. Pumera M (2011) *Energy Environ Sci* 4:668
184. Buglione L, Pumera M (2012) *Electrochem Commun* 17:45
185. Stoller MD, Park S, Zhu Y, An J, Ruoff RS (2008) *Nano Lett* 8:3498
186. Qiu L, Yang X, Gou X, Yang W, Ma ZF, Wallace GG, Li D (2010) *Chem Eur J* 16:10653

187. Kim KS, Park SJ (2011) *Electrochim Acta* 56:1629
188. Lu T, Pan L, Li H, Nie C, Zhu M, Sun Z (2011) *J Electroanal Chem* 661:270
189. Yang SY, Chang KH, Tien HW, Lee YF, Li SM, Wang YS, Wang JY, Ma CCM, Hu CC (2011) *J Mater Chem* 21:2374
190. Rakhi RB, Alshareef HN (2011) *J Power Sources* 196:8858
191. Lu X, Zhang F, Dou H, Yuan C, Yang S, Hao L, Shen L, Zhang L, Zhang X (2012) *Electrochim Acta* 69:160
192. Yan J, Wei T, Fan Z, Qian W, Zhang M, Shen X, Wei F (2010) *J Power Sources* 195:3041
193. Yu AP, Roes I, Davies A, Chen ZW (2010) *Appl Phys Lett* 96:253105
194. Yang XW, Zhu JW, Qiu L, Li D (2011) *Adv Mater* 23:2833
195. Huang ZD, Zhang B, Liang R, Zheng QB, Oh SW, Lin XY, Yousefi N, Kim JK (2012) *Carbon* 50:4239
196. Lu X, Dou H, Gao B, Yuan C, Yang S, Hao L, Shen L, Zhang X (2011) *Electrochim Acta* 56:5115
197. Endo M, Maeda T, Takeda T, Kim YJ, Koshiba K, Hara H et al (2001) *J Electrochem Soc* 148:A910
198. Endo M, Kim YJ, Maeda T, Koshiba K, Katayama K, Dresselhaus MS (2001) *J Mater Res* 16:3402
199. Wang DW, Li F, Liu M, Lu GQ, Cheng HM (2008) *Angew Chem Int Ed* 47:373
200. Korenblit Y, Rose M, Kockrick E, Borchardt L, Kvit A, Kaskel S, Yushin G (2010) *Am Chem Soc Nano* 4:1337
201. Miller JR, Outlaw RA, Holloway BC (2010) *Science* 329:1637
202. Pech D, Brunet M, Durou H, Huang P, Mochalin V, Gogotsi Y, Taberna PL, Simon P (2010) *Nat Nano* 5:651
203. Lei ZB, Christov N, Zhang LL, Zhao XS (2011) *J Mater Chem* 21:2274
204. Zheng C, Qian W, Wei F (2012) *Mater Sci Eng B* 177:1138
205. Chmiola J, Yushin G, Gogotsi Y, Portet C, Simon P, Taberna PL (2006) *Science* 313:1760
206. Li QY, Li ZS, Lin L, Wang XY, Wang YF, Zhang CH, Wang HQ (2010) *Chem Eng J* 156:500
207. Lei Z, Bai D, Zhao XS (2012) *Microporous Mesoporous Mater* 147:86
208. Yi B, Chen X, Guo K, Xu L, Chen C, Yan H, Chen J (2011) *Mater Res Bull* 46:2168
209. Bordjiba T, Mohamedi M, Dao LH, Aissa B, El Khakani MA (2007) *Chem Phys Lett* 441:88
210. Kim B, Chung H, Kim W (2010) *J Phys Chem C* 114:15223
211. Portet C, Yushin G, Gogotsi Y (2007) *Carbon* 45:2511
212. Salitra G, Soffer A, Eliad L, Cohen Y, Aurbach D (2000) *J Electrochem Soc* 147:2486
213. Chang KH, Hu CC (2006) *Appl Phys Lett* 88:193102
214. Cheng Q, Tang J, Ma J, Zhang H, Shinya N, Qinc LC (2011) *Phys Chem Chem Phys* 13:17615

Advances in Lithium-Ion Battery Technology Based on Functionalized Carbon Nanotubes for Electrochemical Energy Storage

18

Raghavan Prasanth, Ravi Shankar, Nutan Gupta, and
Jou-Hyeon Ahn

Contents

1	Introduction	448
2	Carbon Nanotubes (CNTs)	451
3	Application of CNTs in LIBs	452
3.1	Application of CNTs as Cathode for LIBs	453
3.2	Anode Materials and Their Properties	461
3.3	Applications of CNTs in Lithium-air Batteries	472
4	Conclusions	473
	References	474

Abstract

Increasing demand for higher energy density and higher-power energy-storage devices from the portable power market and the automobile and

R. Prasanth (✉)

Department of Materials Science and Nanoengineering, Rice University, Houston, TX, USA

School of Materials Science and Engineering, and Energy Research Institute @ NTU,
Nanyang Technological University, Singapore, Singapore

Department of Chemical and Biological Engineering and Research Institute for Green Energy
Convergence Technology, Gyeongsang National University, Jinju, Republic of Korea
e-mail: prasanth.praghavan@rice.edu

R. Shankar

Nanoscience and Engineering Program, South Dakota School of Mines and Technology,
Rapid City, SD, USA

N. Gupta

School of Materials Science and Engineering, and Energy Research Institute @ NTU,
Nanyang Technological University, Singapore

J.-H. Ahn

Department of Chemical and Biological Engineering and Research Institute for Green Energy
Convergence Technology, Gyeongsang National University, Jinju, Republic of Korea

telecommunication industries have led to the search for novel materials for electrodes or electrolytes that offer higher capacities and energy densities and better performance than the electrochemical energy-storage devices available today. It is recognized that these requirements cannot be met solely by the capabilities of conventional systems and energy materials. Nanomaterials, a cutting-edge technology, can serve as an alternative to traditional materials. Among these, carbon nanotubes (CNTs) and their hybrid nanostructures have been extensively studied in electrochemical energy storage devices such as lithium-ion batteries (LIBs), supercapacitors, solar cells, and fuel cells as ideal electrode materials. This is because of their unique, one-dimensional (1D) tubular structure and high surface area, aspect ratio, chemical stability, electrical, and thermal conductivities, along with their extremely high mechanical strength. Studies show that CNTs are capable of greatly improving the electrochemical characteristics of energy-storage systems, with enhanced energy conversion and storage capacities. This chapter discusses recent advances in lithium-ion/air batteries based on CNTs and their functionalized derivatives for electrochemical energy storage.

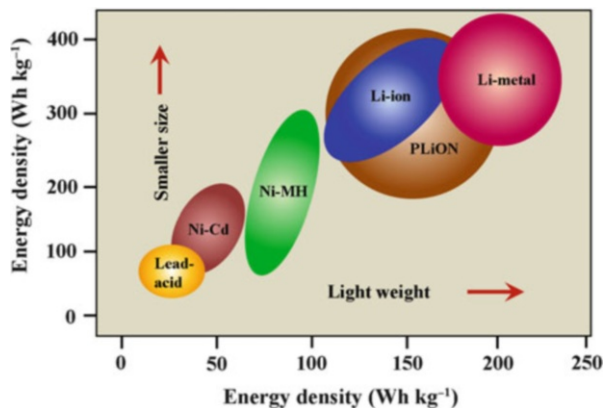
Key words

Lithium-ion batteries • Lithium-air batteries • Carbon nanotubes • Energy storage • Electrochemical properties

1 Introduction

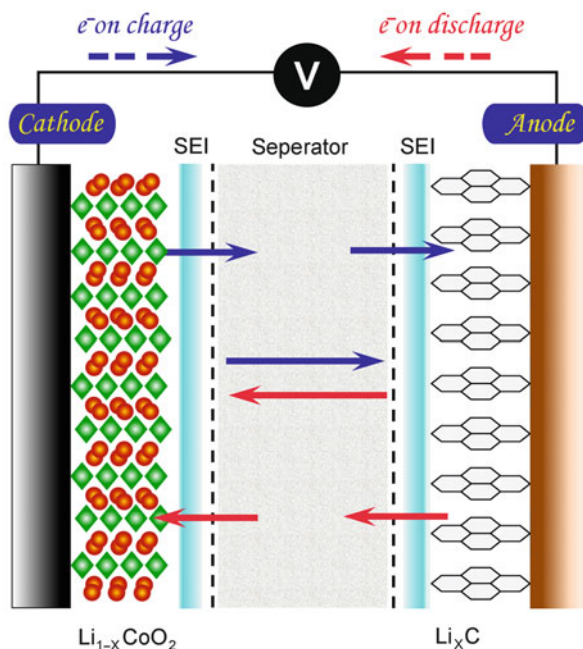
Today, as global attention focuses on energy conservation and harnessing renewable energy sources, significant efforts have been made to store energy efficiently and deliver it on demand. Energy can be stored in different ways: chemically, electrochemically, and electrically (biological, mechanical, thermal, and fuel conversion storage) [1–3]. In this chapter, the main focus is on electrochemical energy conversion and storage in lithium-ion/air batteries based on carbon nanotubes (CNTs). The basic principles of electrochemical energy conversion were discovered by Alessandro Volta in the late 1700s [4]. Typically, energy can be stored electrochemically in batteries (including fuel cells) and supercapacitors via conversion of chemical energy into electrical energy, and vice versa, taking place between two electrodes (anode and cathode) and the electrolyte by means of an electrochemical redox reaction [2]. Batteries are good at providing high power levels, but the amount of energy they can store per unit weight ($50\text{--}1,000\text{ W kg}^{-1}$) is lower than fuel cells because they can use up, at best, all the material on their electrodes and convert all the available chemical fuel into energy. Batteries are basically classified as primary and secondary [4]. A variety of primary and secondary batteries, including lead-acid, alkaline, nickel-iron (Ni-Fe), nickel-cadmium (Ni-Cd), nickel-metal hydride (Ni-MH), zinc-air, liquid redox, lithium-ion (Li-ion), and lithium-ion polymer, are commercially available in different sizes and shapes with different power and energy density (Fig. 18.1). Some of these batteries are discussed briefly below.

Fig. 18.1 Ragone plot of different battery technologies in terms of volumetric and gravimetric energy density

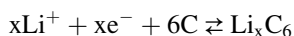


The lead-acid battery, a well-understood technology originally developed by Gaston Planté in 1859, is a combination of lead dioxide (cathode) and lead (anode) in dilute sulfuric acid (H_2SO_4) (electrolyte). The advantages of lead-acid batteries include long life, easy recyclability, and economy for a broad range of applications; however, they are heavy and their lifetime is reduced in high temperatures. Ni-Cd batteries were conceptualized in the late 1800s and consist of nickel hydroxide (cathode) and cadmium (anode) in an electrolyte solution (mostly potassium hydroxide (KOH)). These batteries have a long shelf life and offer high power delivery for a short duration in low-temperature applications. The disadvantages include high self-discharge rate, a memory effect, complexity in charging, and a lack of economically viable recycling options. Ni-MH batteries are similar to Ni-Cd, however, a metal alloy is employed as an anode that can store large amounts of hydrogen during the discharge process. They are free of cadmium, which makes them more environmentally friendly. Disadvantages include their expense, a memory effect, poor charge retention and energy density, and diverting focus from lithium-ion based technologies. The rechargeable lithium-ion battery (LIB) was first proposed by M. S. Whittingham in the 1970s using titanium (II) sulfide (cathode) and lithium metal (anode). LIBs have been widely used in portable electronic devices, telecommunications, automobile, aerospace, and defense applications. In LIBs, layered oxide (such as lithium cobalt oxide), a polyanion (such as lithium iron phosphate), or a spinel (such as lithium manganese oxide) material is used as cathode and intercalated lithium compound (Li in porous carbon or graphite) is used as the anodic material. Typically, lithium salts such as lithium hexafluorophosphate (LiPF_6), lithium hexafluoroarsenate monohydrate (LiAsF_6), lithium perchlorate (LiClO_4), lithium tetrafluoroborate (LiBF_4), or lithium triflate (LiCF_3SO_3) in a mixture of nonaqueous organic carbonates such as ethylene carbonate (EC) or diethyl carbonate (DEC) are used as the electrolyte. Figure 18.2 shows a schematic representation of the working principle of LIBs. During the charging of the cell, Li^+ ions are extracted from the cathode, which move through

Fig. 18.2 Schematic representation and operating principles of Li-ion batteries including the movement of ions between electrodes during charge (*blue*) and discharge (*red*) states



the electrolyte toward the anode. The opposite sequence takes place during the discharge. The cell reaction can be given as [5]:

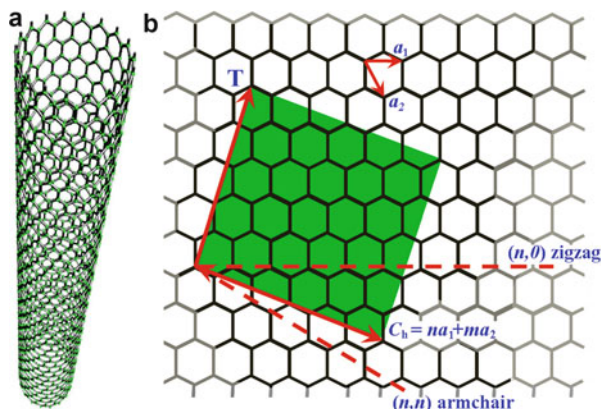


LIBs have high energy and power density, a long cycle life, no memory effect, and minimal self-discharge. Among the various energy-storage devices, LIBs currently outperform others, accounting for about 63 % of global sales values in portable batteries [6, 7]. Thus, continuous research efforts are inclined to improve the performance of LIBs and other energy-storage devices for high-power applications.

The lithium-air batteries (LABs), also known as Li-oxygen batteries, have received significant interest in recent years by researchers because of their significantly higher theoretical specific energy than LIBs, which makes them attractive for long-range electric vehicles. LABs couple a lithium anode to atmospheric oxygen through a carbon-based air cathode. However, with several daunting challenges, these batteries still have long way to go to see commercial reality [8].

Recently, many reports have been published using CNTs either as an additive for electrode materials or as replacement materials for anodes in energy storage and conversion devices such as rechargeable batteries and supercapacitors. In addition to being lightweight, CNTs have a large surface area, up to $1,315 \text{ m}^2 \text{ g}^{-1}$ for

Fig. 18.3 Schematic illustration of (a) CNT and (b) its unit vectors. The (n, m) nanotube naming scheme can be thought of as a vector (C_h) in an infinite graphene sheet that describes how to “roll up” the graphene sheet to make the nanotube. T denotes the tube axis, and a_1 and a_2 are the unit vectors of graphene in real space



single-walled CNTs, which is ~ 90 times more than graphite [5]. The various properties of CNTs for advancement in electrochemical technology are briefly discussed in the following sections.

2 Carbon Nanotubes (CNTs)

The first report on CNTs, by Radushkevich and Lukyanovich, came in 1952, and described them as hollow graphitic fibers. CNTs came into the limelight in the last couple of decades because of their interesting electronic and mechanical properties [9]. A CNT is considered to be an allotrope of carbon that has a cylindrical and tubular structure, however, it is different from other allotropes of carbon such as graphite, diamond, and fullerene. These are one-dimensional structures having a very high aspect ratio (length-to-diameter ratio), which opened up a new area of study in nanotechnology [10, 11]. CNTs are classified in two categories: (i) single-walled carbon nanotubes (SWNTs), which can be envisioned as a cylinder composed of a rolled-up graphene sheet around a central hollow core; and (ii) multi-walled carbon nanotubes (MWNTs), which consists of two or more graphene layers held together with van der Waals forces between adjacent layers and folded as hollow cylinders [12]. The chemical bonding of CNTs is sp^2 bonding similar to graphite. Based on the rolling angle of the graphite sheet against the tube axis, CNTs can have three kinds of structures: a) armchair, b) zigzag, and c) chiral.

The electronic properties of CNTs are determined by the chirality (Fig. 18.3). Based on the chirality, the nanotubes are classified as metallic, nonmetallic, or semiconducting in nature. The wrapping of the graphene sheet is represented by a pair of indices (n, m) , where n and m denote the number of unit vectors along the two directions of a hexagonal lattice. The chirality is defined by the chiral vector, $C_h = na_1 + ma_2$. CNTs have a zigzag structure for $m = 0$, an armchair structure for $n = m$, and, if both conditions are not satisfied, it is classified as chiral [13]. The chirality greatly affects the electronic properties of CNTs. For a given (n, m) ,

Table 18.1 Physical properties of CNTs, and other carbon allotropes (Adapted from Refs. [1, 2])

Property	Graphite	Diamond	SWNT	MWNT
Gravity (g cm^{-3})	2.09–2.23	3.5	0.8	1.8
Electrical conductivity (S cm^{-1})	2.5×10^{4p} 3.3 ^c	10^{-2}	10^2 – 10^6	10^3 – 10^5
Thermal conductivity ($\text{W m}^{-1} \text{K}^{-1}$)	3,000 ^p 6 ^c	900–2,320	~6,000	~2,000
Coefficient of thermal expansion (K^{-1})	-1×10^{-6p} 29×10^{-6c}	$1 \sim 3 \times 10^{-6}$	Negligible	Negligible
Thermal stability in air ($^{\circ}\text{C}$)	450–650	777	>600	>600
Surface area ($\text{m}^2 \text{g}^{-1}$)	Variable	10–50	>100	>100
Modulus (GPa)	1,000 ^p 36.5 ^c	500–1,000	1,200	1,000

p: in-plane and *c*: *c*-axis

if $(2n + m)$ is a multiple of 3 it is considered as metallic; otherwise, it is a semiconductor. CNTs in bulk can be produced by arc discharge, laser ablation, gas-phase catalytic growth of carbon monoxide, and chemical vapor deposition (CVD) techniques [13–17].

In terms of mechanical strength, CNTs are considered to have high tensile strength and elastic modulus to make them strong and stiff materials. The physical properties of CNTs are compared to other allotropes of carbon are described in Table 18.1. Considerable research efforts are underway to modify CNTs' properties such as chirality, purity, length, and surface for binding with various materials [13–17]. Based on their characteristic properties, CNTs are identified as an ideal material for energy storage, conductive adhesives, inks and grease, reinforcing fillers, catalyst supports, and many other advanced applications.

3 Application of CNTs in LIBs

The first report on an interaction study between lithium vapor and MWNTs, by Nalimova et al. in 1997, provided the direction for the use of CNTs in LIBs [18]. Computational results show a curvature-induced Li condensation inside the core of the CNTs that lead to a linear dependence with diameter. The theoretical reversible capacity $>1,116 \text{ mAh g}^{-1}$ is attainable for SWNTs, which exceeds limits of graphite for Li^+ -ion storage [19, 20]. An effective diffusion of Li^+ -ions into the intercalation sites located on the surface of CNTs and/or inside the individual nanotubes leads to high Li^+ -ion storage capacity in CNTs. Also, the Li^+ -ion intercalation can happen between the MWNTs layers due to diffusion through lattice defects. In LIBs, CNTs are employed as additives in electrode (anode and cathode) materials or as the replacement material for anodes, which enhances (i) electron transport properties, (ii) reversible Li^+ intercalation/deintercalation without destruction of the electrode material structure, (iii) Li^+ -ion

Table 18.2 Resistivity of different carbon additives and their discharge capacities

Conductive additives	Resistivity of electrode ($10^{-2} \Omega \text{ cm}$)	Initial discharge capacity (mAh g^{-1})	Capacity retention ratio after 20 cycles (%)
Carbon black (CB)	5,500	~85	70
Carbon fibers (CFs)	1,000	~104	90
MWNTs	375	~122	100

insertion/extraction rates due to the short transport path, and (iv) contact area with the electrolyte, reducing the volume changes associated with intercalation [21–30]. Recent developments on CNT-based electrode materials for LIBs are examined in the following sections.

3.1 Application of CNTs as Cathode for LIBs

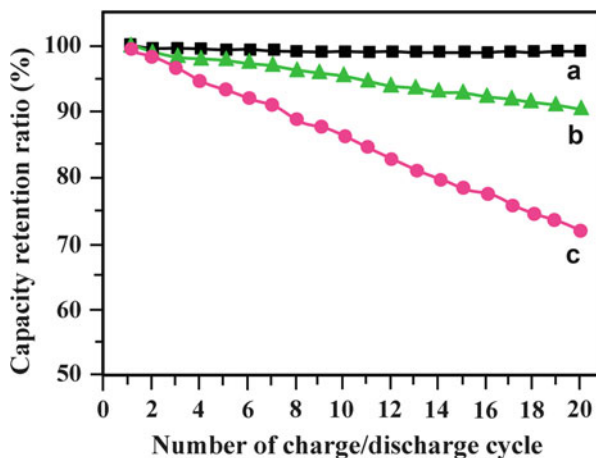
Different cathode materials, such as layer-structured LiMnO_2 , LiNiO_2 , LiCoO_2 , spinel $\text{Li}(\text{Ni}_{1/2}\text{Mn}_{1/2})\text{O}_2$, $\text{Li}(\text{Ni}_{1/3}\text{Co}_{1/3}\text{Mn}_{1/3})\text{O}_2$, $\text{Li}(\text{Ni}_{1/2}\text{Mn}_{3/2})\text{O}_4$, LiMn_2O_4 , ordered olivine lithium transition metal phosphates (LiMPO_4 ; $\text{M} = \text{Fe, Mn, Ni, or Co}$), and elemental sulfur, have been reported [31–42]. The characteristic properties, i.e., electrical and thermal conductivities and stability, are more important to ensure the high energy storage capacity, long lifetime, and high safety of LIBs. Among the aforementioned cathode materials, LiCoO_2 , LiMn_2O_4 , and LiFePO_4 have been studied extensively. The improvements in properties of cathode materials by the incorporation of CNTs are discussed in following sections.

3.1.1 Cathodes Based on Metal Oxides/CNTs

LiCoO_2 generally offers higher capacity compared with other metal oxides (LiMn_2O_4 and LiFePO_4) but has, in general, high electrical resistance, which causes serious polarization and poor utilization of active material. Compared with carbon black, carbon fibers and CNTs have been reported as effective conductive additives to improve the electronic conductivity of active material, i.e., LiCoO_2 , and thus the electrochemical performance of the composite cathode [43]. This can be attributed to three factors: (i) the high aspect ratio of CNTs favors the formation of continuous conductive networks at a very low percolation threshold, (ii) the nanoscale structure and high crystallinity of CNTs facilitate efficient electronic transport throughout the material, and (iii) the extremely high surface area of CNTs allows close contact with the active material. The resistivity of different carbon additives and their discharge capacities are listed in Table 18.2 [43].

Among the aforementioned conductive additives, MWNTs are outperformed. The cycle performance of composite cathode based on LiCoO_2 with various conductive additives is shown in Fig. 18.4. After 20 cycles, the capacity retention ratios for cathode material containing carbon fibers and carbon black were reduced by 10 % and 30 %, respectively. However, the composite cathode containing MWNTs shows negligible capacity fades.

Fig. 18.4 Effect of conductive additives on the capacity retention ratio at a rate of 2C: (a) MWNTs, (b) carbon fibers, and (c) carbon black (Adapted from Ref. [43])



A comparison is made between LiCoO_2 mixed with SWNTs and MWNTs. MWNTs with smaller diameter favor improving the electrochemical behavior of composite cathode at higher charge/discharge rate owing to their advantage in primary particle number in unit mass. It has been observed that at least 5 wt% of MWNTs (dia. 10–30 nm) is prerequisite to make full use of LiCoO_2 . Compared with MWNTs, SWNTs are not effective when added into LiCoO_2 composite cathode due to their tendency for bundle formation [44]. The electrochemical performance of composite cathode dispersed with mixture of MWNTs and acetylene black (AB) was investigated and observed to be better than the cathode loaded with individual additives. In the composite, MWNTs form a valid conducting network and AB has a large contact surface area with LiCoO_2 particles [45]. Thin MWNTs (t-MWNTs) and hollow MWNTs (h-MWNTs) were coated in 0.5 wt% on the surface of LiCoO_2 using electrostatic heterocoagulation. The volumetric specific discharge capacity of the cathode, initially and after 40 cycles, with t-MWNTs at 0.2C-rate was observed to be 624 and 403 mAh cm^{-1} , respectively [46]. The volumetric specific discharge capacity of the cathode, initially (0.2C-rate) and after 40 cycles (1C-rate), with 3 wt% MWNTs prepared by simple mixing was observed to be 546 and 310 mAh cm^{-1} , respectively [47]. The studies on composite LiCoO_2 cathodes with well-dispersed low- and high-density MWNTs showed the low-density MWNTs exhibit excellent high rate capabilities and cycle performance. The highest discharge capacity of 136 mAh g^{-1} was observed at 5C-rate and capacity fade of 3 % was observed for composite LiCoO_2 cathodes with 8 wt% MWNTs (low-density) after 50 cycles at 1C-rate [48]. Binder-free LiCoO_2 -superaligned CNT (SACNT) composite cathodes were prepared by an ultrasonication and co-deposition technique, which constructs a continuous, three-dimensional SACNT framework, embedding LiCoO_2 particles inside. The composite cathodes exhibited superior properties such as high conductivity, great flexibility, and outstanding cycling stability (151.4 mAh g^{-1} at 0.1C with cycle retention of 98.4 % over 50 cycles) and rate capability (137.4 mA h g^{-1} at 2C) than classical composite

cathodes (active material, Super P and binder) [49]. In consideration of the safety issues related to LiCoO_2 , partial substitution of Co was done by Al, Ga, Mg, or Ti to overcome the safety issues. Among these metal oxides, $\text{Li}(\text{Ni}_{1/3}\text{Co}_{1/3}\text{Mn}_{1/3})\text{O}_2$ and $\text{LiNi}_{0.7}\text{Co}_{0.3}\text{O}_2$ have been investigated with and without the presence of MWNTs [47, 50–53]. In both cases, addition of CNTs effectively improved the electron conduction as it acted as conductive networks between the metal oxide particles. P. M. Ajayan et al. reported on a paintable flexible battery with LiCoO_2 painted on a SWNT current collector prepared by painting SWNT in NMP ink using an air brush. LiCoO_2 paint was made by adding a mixture of LiCoO_2 , Super P conductive carbon, and ultrafine graphite to PVDF binder solution in NMP [54].

A cathode with 95 wt% $\text{LiNi}_{0.4}\text{Mn}_{0.4}\text{Co}_{0.2}\text{O}_2$ (NMC) and 5 wt% SWNTs, prepared by simple mixing, delivered a capacity of $\sim 130 \text{ mAh g}^{-1}$ at 5C and nearly 120 mAh g^{-1} at 10C, both for over 500 cycles, and showed significantly higher capacity as compared with the pristine NMC at rates of 5–10C. Addition of SWNTs to NMC improved both conductivity and surface stability at an exceptionally high rate of 10C (charge/discharge in 6 min) [55]. Other metal oxides like LiMn_2O_4 have also been reported to show improvement in electrochemical performance by adding MWNTs. Liu et al. prepared the $\text{LiMn}_2\text{O}_4/\text{MWNT}$ and LiMn_2O_4 using the facile sol-gel method and prepared a composite cathode composed of active material, conducting carbon (acetylene black), and binder (PVdF) (70:20:10). Both the initial discharge capacity and the cyclic performance of the LiMn_2O_4 -MWNT composite cathode with 1 M LiPF_6 in EC:DEC:EMC (1:1:1 vol%) were observed to be superior to the LiMn_2O_4 cathode. The initial discharge capacity of the LiMn_2O_4 and LiMn_2O_4 -MWNT cathodes was observed to be 54.7 and 66.5 mAh g^{-1} , respectively. The LiMn_2O_4 -MWNT cathode showed over 99 % of this capacity retention after 20 cycles and 4 % capacity fade after 100 cycles; LiMn_2O_4 showed 9 % loss of the initial capacity after 20 cycles [56].

Jia et al. reported on a direct-growth method to make a high-performance flexible and binder-free $\text{LiMn}_2\text{O}_4/\text{CNT}$ composite cathode via an in situ two-step hydrothermal process for flexible lithium battery applications. The electrochemical performance of flexible $\text{LiMn}_2\text{O}_4/\text{CNT}$ nanocomposite films was compared with that of a nanoparticle LiMn_2O_4 composite cathode (active material: CB:PVDF binder (80:10:10) using 1 M LiClO_4 in PC). The initial charge and discharge capacities of the hybrid cathode were 126 and 109 mAh g^{-1} , respectively, corresponding to a coulombic efficiency of 86.5 %, at a current density of 22 mA g^{-1} and a discharge capacity of 50 mAh g^{-1} was delivered at a relatively high current density of 550 mA g^{-1} . The flexible $\text{LiMn}_2\text{O}_4/\text{CNT}$ materials show superior capacity and stable cycling performance [57].

3.1.2 Li-transition Metal Phosphates/MWNTs as Cathode

Li-transition metal phosphates (M-PO_4) have an olivine-type structure where the transition metal can be Fe, Mn, Ni, or Co. These materials have been used as cathode due to their high theoretical specific capacity ($\sim 170 \text{ mAh g}^{-1}$) [58, 59]. LiFePO_4 is widely popular due to its high stability, compatibility, and environmental friendliness, together with low cost. However, for LiFePO_4 , claiming the full

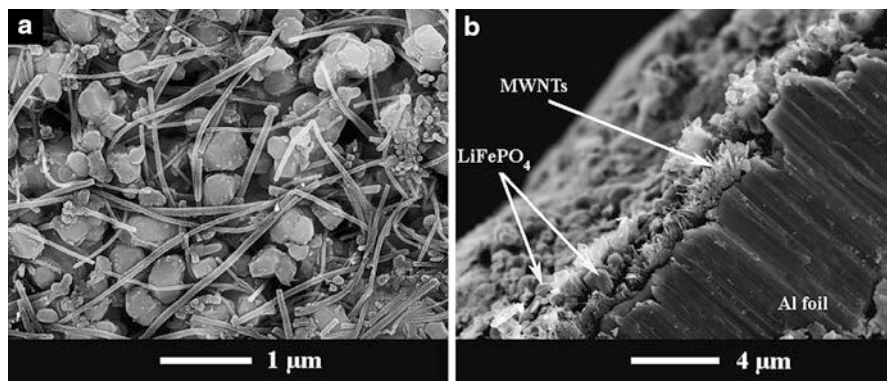


Fig. 18.5 SEM images of LiFePO₄/MWNTs composite cathode (a) plane section and (b) cross section (Adapted from Ref. [63])

theoretical capacity is difficult as it has a poor electrical conductivity ($\sim 10^{-9}$ S cm⁻¹). This leads to poor discharge capacity, cycle performance, and rate capability and slow Li⁺-ion diffusion. Traditionally, carbon black has been used as a filler to improve the conductivity of transition metal phosphate. However, cycle performance and rate capability of such composites is not significantly improved. Research on the influence of amount and type of CNTs on the performance of LiFePO₄ was carried out for optimizing electrical resistivity, specific capacity, specific surface area, and particle size distribution. Jin et al. reported that use of MWNTs (~ 5 wt%) with LiFePO₄ as a filler material showed superior electrochemical properties compared with classic composite cathode [60–62]. A close look at 3D networks (Fig. 18.5) consisting of LiFePO₄ and MWNTs shows that the metal phosphate particles are interconnected with the MWNTs, which effectively improves the electron transfer [63].

Different approaches have been explored to prepare the LiFePO₄/MWNTs cathode material. Wang et al. prepared the cathode material by microwave heating of MWNTs with LiFePO₄ in the presence of citric acid, where the electrode performance decreased slightly (from 90 to 70 mAh g⁻¹) after 50 charge–discharge cycles [64]. In another approach, a hierarchical FePO₄ nanostructure was grown on a CNT core to form FePO₄/CNT hybrid nanowires [65]. In this core-shell structure, Li⁺-ions and electrons can easily diffuse out due to very high surface area provided by the nanostructure. Mohamed et al. prepared composite cathode by growing CNTs, using a spray pyrolysis-modified CVD technique on LiFePO₄ synthesized via a mechanical activation and thermal treatment process. The composite cathode exhibited excellent electrochemical performances, with 163 mAh g⁻¹ discharge capacity and 94 % cycle efficiency at a 0.1C discharge rate in the first cycle, and a capacity fade of approximately 10 % after 30 cycles [66]. Kim et al. reported on LiFePO₄ (prepared by a hydrothermal process) composite cathodes mixed with MWNTs (5 wt%), and its performance was evaluated in a LiFePO₄-MWNT/Li cell at a current density of 0.1 mA cm⁻¹. The cell showed an initial discharge capacity

Fig. 18.6 Comparison of the rate performance of pristine porous LiFePO_4 and LiFePO_4 -CNT composites with charge/discharge rates of 10 – $1,000 \text{ mA g}^{-1}$ (Adapted from Ref. [68])

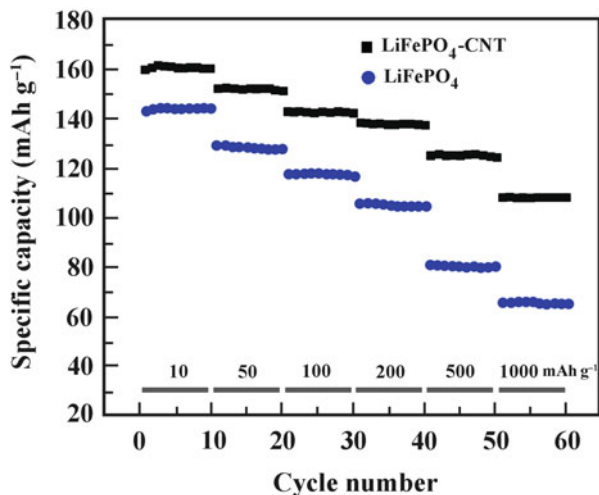
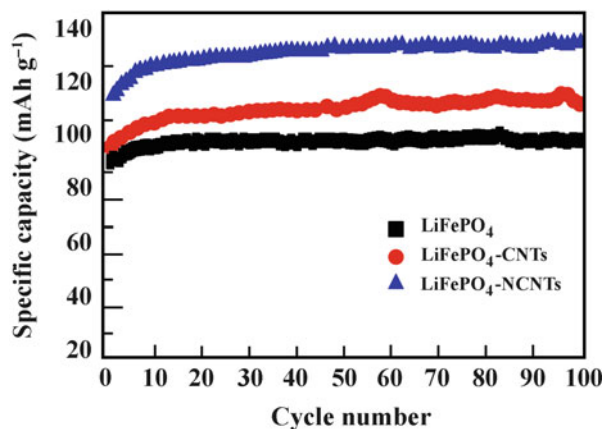


Fig. 18.7 Cycle performance of porous LiFePO_4 and its composites CNTs cycled at a current rate of 17 mA h g^{-1} (Adapted from Ref. [69])



of 124 mAh g^{-1} [67]. The porous, intimately interlaced, 3D composite network LiFePO_4 -MWNT composite (active material) was synthesized via a facile in situ sol-gel method, and the cell performance of the composite was compared with pristine porous LiFePO_4 cathode. The composite cathode was prepared by mixing active material with conducting carbon (Super P) and binder (PVdF). At low (10 mA g^{-1}) current density, the composite material and pristine LiFePO_4 showed a discharge capacity of 159 and 110 mAh g^{-1} , respectively. The study showed (Fig. 18.6) that there is a significant drop in pristine discharge capacity at higher rates. At a rate of $1,000 \text{ mA g}^{-1}$, the LiFePO_4 -MWNT composite delivered capacity $\sim 110 \text{ mAh g}^{-1}$, in contrast to $\sim 66 \text{ mAh g}^{-1}$ for the pristine material [68].

A porous composite of LiFePO_4 /nitrogen-doped CNTs (N-CNTs) with hierarchical structure was prepared by a sol-gel method without templates or surfactants. The cell studies showed (Fig. 18.7) good initial discharge capacity with stable cycle

performance. After 50 cycles, $\text{LiFePO}_4/\text{N-CNTs}$ composite cathode delivered a reversible discharge capacity of 138 mAh g^{-1} , while the $\text{LiFePO}_4/\text{CNTs}$ and LiFePO_4 cathode delivered 113 and 104 mAh g^{-1} , respectively, at a current density of 17 mA g^{-1} [69]. $\text{LiFePO}_4/\text{CNT}/\text{C}$ composite nanofibers were synthesized by a combination of electrospinning and the sol-gel method using $\text{LiFePO}_4/\text{CNT}/\text{PAN}$ precursors. The initial reversible capacities are 150, 162, and 169 mAh g^{-1} , respectively, for pristine LiFePO_4 powder, LiFePO_4/C composite nanofibers, and $\text{LiFePO}_4/\text{CNT}/\text{C}$ composite nanofibers. $\text{LiFePO}_4/\text{CNT}/\text{C}$ exhibited average reversible capacities of 134 and 121 mAh g^{-1} at 1 and 2C-rates, respectively [70]. Gnanavel et al. compared electrochemical properties of $\text{LiFePO}_4/\text{C}/\text{MWNTs}$ vs. LiFePO_4/C synthesized by the sol-gel method. The results showed that $\text{LiFePO}_4/\text{C}/\text{MWNTs}$ exhibited remarkable reversible cyclability and rate capability. In the current range ($30\text{--}1,500 \text{ mA g}^{-1}$), specific capacity of $\text{LiFePO}_4/\text{C}/\text{MWNTs}$ ($\approx 150\text{--}50 \text{ mAh g}^{-1}$) is observed to always be higher compared with LiFePO_4/C ($\approx 120\text{--}0 \text{ mAh g}^{-1}$). The exemplary performance of the $\text{LiFePO}_4/\text{C}/\text{MWNTs}$ is attributed to the combination of both enhanced LiFePO_4 structural stability and formation of an efficient percolative network of CNTs, which, during the course of galvanostatic cycling, is gradually transformed to graphitic carbon [71]. Murugan et al. reported that $\text{LiFePO}_4/\text{MWNT}$ nanocomposite exhibits discharge capacity 15 mAh g^{-1} higher than the bare LiFePO_4 ($\sim 145 \text{ mAh g}^{-1}$) at 0.1C-rate and retains $\sim 80\%$ of its capacity going from 0.1C-rate to 10C-rate. It also exhibits excellent cyclability with no noticeable capacity fade [72].

Zhou et al. reported on three-dimensional structured composite porous LiFePO_4 -CNT electrodes with improved electrochemical performance due to better accessibility and a decrease in inert “dead” zones provided by the interpenetrating conductive CNT network [68]. Li et al. demonstrated improvement in electronic conductivity as a result of formation of a three-dimensional network of MWNTs [63]. Jing Xu et al. reported an improvement in electrochemical performance via dispersion of MWNT in hydrothermally synthesized LiFePO_4 nanoplates [73]. Some reports employ bare MWNT [64, 72] or functionalized MWNT [74] to improve electrochemical performance of nanoparticles of LiFePO_4 -CNT synthesized using various methods. Encouraged by the success of LiFePO_4 , much research is now focused on the olivine LiMPO_4 ($M = \text{Mn, Co, and Ni}$) structures. Among them, LiMnPO_4 is of particular interest as it offers a higher potential of 4.1 V versus Li^+/Li compared with 3.4 V versus Li^+/Li of LiFePO_4 , in addition to expected safety features and abundance of resources. Unfortunately, LiMnPO_4 shows lower electronic conductivity ($< 10^{-10} \text{ Scm}^{-1}$) than that of LiFePO_4 (i.e., $1.8 \times 10^{-9} \text{ Scm}^{-1}$ at 25°C), rendering it difficult to obtain decent electrochemical activity. Similar to the LiFePO_4 electrode, a leading approach to improve the performance of LiMnPO_4 and LiCoPO_4 cathode materials is to use nano-sized particles, carbon coating, and CNTs. A series of nano-thumblike shapes, LiMPO_4 ($M = \text{Mn, Fe, Co, and Ni}$) prepared by a microwave-irradiated solvothermal method and networked with MWNTs by a simple, ambient-temperature procedure to overcome the poor electronic conductivity and electrochemical properties of LiMPO_4 without requiring any post annealing at elevated temperatures. This nanoscale networking with MWNTs enhances the

mobility of electrons between the adjacent LiMPO_4 particles during the lithiation/delithiation process without blocking the lithium-ion transport. The composite cathodes with active materials, conductive carbon, and teflonized acetylene black binder (50:25:25) for LiMnPO_4 and (75:12.5:12.5) for LiCoPO_4 and compared electrochemically with bare active materials at different C-rates. The LiMnPO_4 composite cathode with MWNTs shows discharge capacity of 45 mAh g^{-1} , while bare LiMnPO_4 shows the capacity of 30 mAh g^{-1} . There is no significant capacity increment observed for LiCoPO_4 at lower C-rates (0.1 C , $118 \pm 2 \text{ mAh g}^{-1}$), however, at higher C-rates ($>0.2\text{C}$), $\text{LiCoPO}_4/\text{MWNTs}$ outperforms bare LiCoPO_4 [72].

Hybrid materials composed of LiMPO_4 ($M = \text{Fe}$ or Co) with MWNTs were synthesized by tethering lithium phospho-olivines on isolated stochastically disordered MWNTs as well as on ordered 3D MWNT arrays via solution-based impregnation routes. Ordered 3D arrays of MWNT monoliths comprising MWNTs with nominal tube diameters of 60 and 200 nm were synthesized by a catalyst-free, template-based method, with porous aluminum oxide (PAOX) acting as a template. Li-ion extraction within the ordered 3D CNT/ LiCoPO_4 composites seems to be a two-step process and the Li intercalation a one-step process, highlighting the enhanced kinetics of the Li insertion process in the 3D CNT/ LiCoPO_4 composite in comparison with the isolated LiCoPO_4 phosphoolivine phase. The electrochemical measurements demonstrated the good electrochemical stability of the ordered 3D CNT/ LiCoPO_4 composites during cycling [75]. A composite cathode consisting of MnO_2/CNT (75:5) synthesized by a soft template approach has been employed for LIBs. The Li- MnO_2 and Li- MnO_2/CNT cells show discharge capacities 223.4 and 275.3 mAh g^{-1} , respectively [76]. Nano-sized lithium manganese oxide dispersed on CNT has been synthesized successfully via a microwave-assisted hydrothermal reaction at 200°C for 30 min using MnO_2 -coated CNT and an aqueous LiOH solution. The initial specific capacity is 99.4 mAh g^{-1} at a 1.6 C-rate, and is maintained at 99.1 mAh g^{-1} even at a 16 C-rate. The initial specific capacity is also maintained up to the 50th cycle to give 97 % capacity retention [77].

3.1.3 Conducting Polymer/MWNTs as Cathode

Intrinsically conducting polymers like polyaniline (PANI), polyacetylene, polypyrrole (PPy), polythiophene, and polymethylthiophene exhibit a wide range of electrochemical properties and have been used as cathode materials in energy storage devices, including supercapacitors and batteries, and they have many advantages over the metal oxide cathodes [78–80]. Among the conducting polymers, PANI has been studied extensively for use as a battery material. This organic conductor has good redox reversibility and high environmental stability. PANI has usually been employed as a cathode material in batteries with zinc or lithium as anode [81]. These batteries show a lower self-discharge rate, have a longer cyclic life, and have lower manufacturing cost and, due to their flexible shapes, they can be easily made into thin films. However, this class of electrodes has its own disadvantages, which are related to stability, adherence, and conductivity, which can affect the reversibility of the electrode. Studies have shown improvement in electrical properties of these conductive polymer electrodes by introducing MWNTs [81–86].

C. Y. Wang et al. compared solid PANI fiber with the same fiber containing CNTs (PANI/CNTs) using ionic liquid ethylmethyl imidazolium bis(trifluoromethanesulfonyl) amide (EMITFSA) as electrolyte. A discharge capacity of 11.2 mAh g^{-1} was obtained for a polyaniline fiber with 0.25 wt% CNT. These values are much higher than those obtained for pure polyaniline fiber (4.1 mAh g^{-1}) [85]. PANI/MWNT composite was synthesized by in situ chemical polymerization and used as an active cathode material in lithium metal-polymer cells assembled with IL electrolyte composed of 1-ethyl-3-methylimidazolium tetrafluoroborate (EMIBF₄) and vinylene carbonate (VC) as an additive, together with LiBF₄ and compared with commercial battery electrolyte (1 M LiBF₄ in EC/DMC, 1:1 v/v) and 1 M LiClO₄ in EC/DMC (1:1 v/v) and compared with cathode prepared by mechanically mixing the pristine PANI with CNT (PANI + CNT) or Super P carbon (PANI + SP) separately [84, 87]. Porous poly (vinylidene-*co*-hexafluoropropylene) (PVdF-*co*-HFP) film was used as a polymer membrane for assembling the cell. The cells assembled with IL electrolyte and liquid electrolyte (LiBF₄ in EC/DMC) initially delivered 101 and 149 mAh g⁻¹ at 0.2C-rate based on active cathode material, respectively, with good cycle properties up to 100 cycles. The specific capacity obtained is more than 10 times higher than that reported by C. Y. Wang et al. [85]. At the 0.02C-rate, the cells comprised of PANI/CNT, PANI + CNT, and PANI + SP cathodes with LiClO₄ in EC/DMC initially delivered 49.1, 19.4, and 16.6 mAh g, respectively. However, the cell with LiClO₄ in EC/DMC delivered a maximum discharge capacity of 86 mAh g^{-1} at the 80th cycle with an average coulombic efficiency of 98 %. The cell with PANI + CNT cathode showed a rise in discharge capacity value for up to only 40 cycles, where it delivers a maximum of 54 mAh g^{-1} . But the cell with PANI/CNT composite cathode showed an increase in discharge capacity for up to 80 cycles, where it delivered a maximum of 86 mAh g^{-1} . Therefore, in a composite cathode, the cell showed better performance in terms of cyclability and discharge capacity values. This result suggests that the cycling performances of the PANI electrode can be improved by employing a composite with CNT rather than physically mixing with CNT. MWNTs have an obvious improvement effect, which makes the composites have more active sites for faradic reaction and larger specific capacitance than pure PANI; it also results in enhanced electric conductivity, lowers the resistance, and facilitates the charge transfer of the composites. He et al. prepared PANI/MWNTs composites by an in situ chemical oxidative polymerization method and studied the electrochemical properties as cathode materials for rechargeable lithium batteries. The discharge capacity of PANI/MWNTs composites is as high as 122.8 mAh g^{-1} , and it is only 98.9 mAh g^{-1} for PANI at the current densities of 20 mA g^{-1} . The PANI/MWNT composite showed good cycle performance and coulombic efficiency (99 %) for 50 cycles [86].

3.1.4 Other Cathode Materials with MWNTs

Among other materials that have been used as cathode in LIBs are Co₃O₄, PVC (polyvinyl carbazole), and elemental sulfur. MWNTs coated with Co₃O₄ nanocomposites show improvement in electrochemical properties compared with

pristine Co_3O_4 [88]. Cathode using nanocomposites of PVC and CNTs were synthesized via an electrochemical polymerization method. A study was conducted with PVC with MWNTs and with SWNTs, and it was found that, in both cases, hybrid PVC/CNT nanocomposites performed better than neat PVC as cathode material. However, when comparing PVC/MWNT and PVC/SWNT nanocomposites, the PVC/MWNT presents a higher discharge capacity [89]. Elemental sulfur has also been used as a cathode material as it has a theoretical specific capacity of $1,672 \text{ mAh g}^{-1}$ and a theoretical specific energy of $2,600 \text{ Wh kg}^{-1}$. Considering Li and S (sulfur) as a redox couple, the reaction between Li and S forms Li_2S . The advantage of using sulfur is that it is inexpensive and environmentally benign; however, its low conductivity and easy dissolution in the electrolyte solution are major drawbacks. Cathode materials have been prepared by incorporating MWNTs into sulfur, resulting in improvement in the cyclic life and rate capability of sulfur. The structural modification of the CNTs' matrix and the adsorption of polysulfides formed as a result of dissolution of sulfur in electrolyte resulted in the improved performance of these electrodes [90].

Wei et al. reported sulfur-based ternary composite cathode materials containing MWNTs with excellent electrochemical performance. The composite materials exhibited sulfur utilization approaching 95.3 %, capacity retention close to 96.5 % (coulombic efficiencies of the cathode are close to 100 %) for 100 cycles, and high power rate capability up to 7C, which is attributed to the homogeneous dispersion of MWNTs in the composites. This not only accommodates the volume change during charge/discharge processes but also provides stable electrical and ionic transfer channels. Both sulfur utilization and cycling stability of cathode have been significantly improved by MWNTs [91].

Electrochemical properties of polyterthiophene (PTTh) cathode were improved by preparing composite with MWNTs. The composite was prepared by in situ chemical polymerization. The charge-discharge and cycle properties of PTTh/MWNTs cathode with an ionic liquid (IL) 1-ethyl-3-methylimidazolium tetrafluoroborate (EMIBF_4) containing LiBF_4 and a small amount of vinylene carbonate (VC) is compared with conventional battery electrolyte of 1M LiBF_4 in EC:DMC:DEC (1:1:1, vol. ratio). The specific capacity of cells with IL and conventional liquid electrolytes after the first cycle was 50 and 47 mAh g^{-1} , respectively, at the C/5 rate. The capacity retention after the 100th cycle was 78 % and 53 %, respectively. The lithium cell assembled with a PTTh/CNT composite cathode and a non-flammable IL electrolyte exhibited a mean discharge voltage of 3.8 V versus Li^+/Li and is a promising candidate for high-voltage power sources with enhanced safety [92].

3.2 Anode Materials and Their Properties

In LIBs, materials that can store lithium are generally used as anodes. Graphitic carbon is traditionally used as anodes in commercial lithium-ion batteries. Graphite is a stack of hexagonally bonded sheets of carbon held together by

van der Waals forces. In graphite, Li ions intercalate between graphite layers, which results in the configuration of one Li atom to every six C atoms, leading to formation of LiC_6 [93, 94], and possess storage capacity of 372 mAh g^{-1} . Lithium metal anodes demonstrate a very high capacity of $3,860 \text{ mAh g}^{-1}$ but are commercially unattractive because of the challenges related to reactivity with electrolyte, dendrite formation during recharging, and safety-related issues [95]. Recently, other high-capacity alternatives such as Al, Sn, Si, Bi, and Sb that can alloy with Li have shown potential in developing high-capacity anode materials [96–100]. However, these materials also suffer some drawbacks due to their poor cyclability and mechanical instability. The mechanical instability is generally caused by the mechanical cracking due to the volume expansion/contraction during the alloying and de-alloying reactions with Li ions [100]. Many approaches have been proposed to address these problems, including (1) application of pressure on cells, (2) using elastomeric binders, or (3) forming a composite with conductive materials such as CNTs [101–104]. Small particle size, high conductivity, and large electrochemically accessible surface area of CNT composites make them an ideal anode material.

3.2.1 CNTs as Anode Material

Full battery development using CNT freestanding anodes is something that was most recently reported by our group using LiCoO_2 and LiNiCoO_2 cathodes [105]. The most important factor in fabricating full batteries using free-standing CNT electrodes is the first cycle charge loss, which complicates capacity matching with cathodes.

CNT-based anodes have promise for future Li-ion battery applications. The improved electrochemical performance of LIBs in terms of energy and power densities, rate capacity, cyclic life, and safety are highlighted for both the anode and cathode electrodes made from composites containing CNTs. As an allotrope of graphite, CNTs are a good anode material for LIBs due to their unique structure (one-dimensional cylindrical tubule of graphite sheet), high conductivity (10^6 S m^{-1} at 300 K for SWNTs and $>10^5 \text{ S m}^{-1}$ for MWNTs) [106], low density, high rigidity (Young's modulus of the order of 1 TPa) [107, 108], and high tensile strength (up to 60 GPa) [109]. Reversible capacities of SWNTs fall anywhere from 300 to 600 mAh g^{-1} [20, 110–116], which is significantly higher than graphite. Furthermore, mechanical and chemical treatments to the SWNTs can further increase the reversible capacities up to 1,000 mAh g^{-1} [117–120]. To enhance the charge capacity of the LIBs and to reduce the irreversible capacity, a practical route could be to synthesize hybrid composites with CNTs [121–124].

The unique shape of CNTs causes effective diffusion of Li ions into electrochemically active sites located on the nanotube surface and/or inside the tubules through endcap or sidewall openings. In the case of MWNTs, Li-ion intercalation can occur between the layers and, similarly, in SWNTs this can happen in the interstitial sites formed during the close-packed bundles [19, 20, 110, 114, 125–131]. There are reports of curvature-induced lithium condensation inside the core of CNTs [132, 133]. This effect shows a linear dependence with diameter of

Table 18.3 Effect of processing and material parameters on electrochemical performance of CNT anode materials

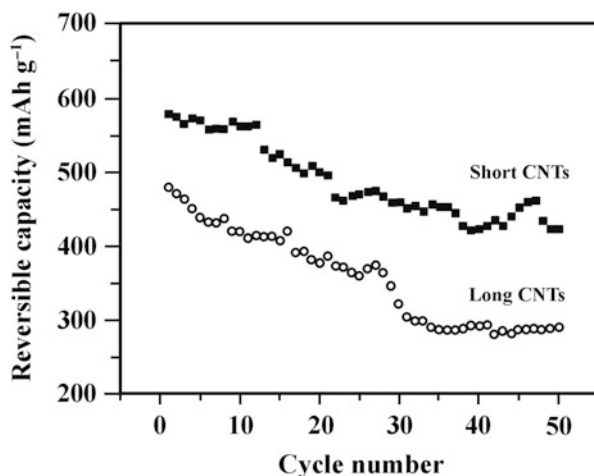
MWNT	The initial capacity (mAh g ⁻¹)		Cycle performance (cycles)	Residual capacity (mAh g ⁻¹)		References
	Charge	Discharge		Charge	Discharge	
Pristine	312					[112]
Chemically Etched	422	2,087	100			[112]
Purified	351	641	50	311		[134]
Ball-milling			50	616		[134]
Short CNTs	502	1,295	50		230	[135]
Long CNTs	188	615	50		142	[135]

CNTs, which means that the capacity can be improved with large-diameter CNTs. However, there can be other factors that affect the electrochemical performance of CNTs as an anode, which include the CNT surface condition and their length. Surface modification in MWNTs can be achieved through chemical etching, ball-milling, and shortening, and their influence is detailed in Table 18.3 [112, 117, 134–137].

As a result of chemical etching using nitric acid, a large number of defects and pores were introduced to MWNTs, which can enhance the capacity [112]. This is related to the preferential doping of Li ions onto the reactive defect sites rather than the perfect carbon structure [136]. Similarly, ball-milling treatment can increase both reversible and coulombic efficiency, however, a large voltage hysteresis occurred due to the formation of a large number of surface functional groups [134]. This hysteresis was found to be related to the kinetics of Li-ion diffusion into the inner tubules of MWNTs. Cutting MWNTs into shorter segments can help to reduce this hysteresis [117]. Another approach was developed where MWNTs were cut into about 200 nm segments from their conventional micrometer lengths, and it was found that the short MWNTs had a higher Li-extraction capacity compared with the long MWNTs, and the specific capacities became stable after 30 cycles for both electrodes. Again, the retention of specific capacities after 50 cycles was higher for short MWNTs compared with the long ones, as shown in Fig. 18.8 [137].

In MWNTs, Li-ion insertion occurs only in the low-potential region, and this is different from the case of graphite. For graphite, the discharge curve shows a staging phenomenon characterized by several potential plateaus; however, such behavior is not observed in MWNTs. The morphological complexity of CNTs and the identification of Li-storage sites in these structures pose a challenge in understanding the mechanism of Li-ion insertion. Compared with graphite, Li storage in CNTs is greatly affected by the presence of “3D defects” such as cavities and pores of different shape dimensions. Sometimes unexpected results are obtained when CNTs with unique structures are used as the anode material [138]. Among the CNT family, bamboo-shaped carbon nanotubes (BCNTs) and quadrangular carbon

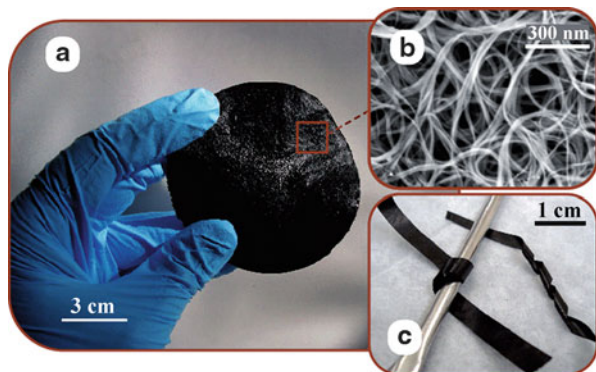
Fig. 18.8 Variation of discharge capacity of MWNTs with number of cycles at a current density of 25 mAh g^{-1} (Adapted from Ref. [137])



nanotubes (q-CNTs) have been considered more suitable for anode material due to the better cyclic stabilities and higher electrical conductivity than other class in CNTs [139, 140]. BCNTs usually have a high percentage of edge-plane sites on the surface that exhibit better electrochemical characteristics with a faster electron transport rate compared with the straight CNTs. In this case, the reduced resistance is observed due to the better wettability, more edge sites and more oxygen functional groups that form 3D electrical conduction networks within BCNTs. On the other hand, q-CNTs possess a novel nanostructure quadrangular cross-section, one open end, and “herringbone” like walls. This unique structure reduces the diffusion time by increasing diffusion coefficient and by decreasing the diffusion pathway, which results in excellent rate capability [140].

Doped CNTs using a heteroatom have also been explored for their efficiency in electrochemical improvement when used as an anode in LIBs. Among these, boron- and nitrogen-doped MWNTs exhibited higher discharge capacities compared with undoped counterparts. This kind of improvement by doping by B or N is considered to be to the result of a breakdown in in-plane hexagonal symmetry of CNTs walls, which results in increased electrical conductivity [141–143]. Nitrogen-doped CNTs developed by a floating catalyst chemical vapor deposition (FCCVD) method show approximately double reversible capacity of CNTs (494 mAh g^{-1}) and deliver the discharge capacity of 397 mAh g^{-1} in the 100th cycle versus 260 mAh g^{-1} for CNTs. They present a much better rate capability than CNTs. The significantly superior electrochemical performance could be related to the high electrical conductivity and the larger number of defect sites in highly nitrogen doped CNTs (HN-CNTs) for anodes of LIBs [144]. Other benefits of using CNTs include high electrical and thermal conductivities, which can promote effective heat dissipation in battery and thus potentially enhance the safety. CNTs also exhibit mechanical strength and flexibility, which further prevent cracking during the charging and discharging processes or in vibration environments.

Fig. 18.9 (a) Photograph of a free-standing SWNT paper prepared using vacuum filtration, (b) SEM image of the high purity SWNTs, (c) image of SWNT paper strips which are bent around a curved surface and twisted without any unintended or irreversible deformation to illustrate the flexible mechanical properties (Adapted from Ref. [7])



3.2.2 Free-Standing CNT Anode

The ability to maintain the bifunctionality where CNTs can act as both the active material as well as the current collector lead to the concept of using a free-standing CNT paper as an anode in LIBs; it is lightweight, flexible, binder free, and suitable for high-temperature applications. Fabrication of SWNT papers can be done by a pressure filtration technique where stable SWNT dispersions are eluted through an inert and porous support material, typically like Teflon, or by painting of CNT inks with air brush on a substrate and peeling off after drying [54, 145]. The tensile strength of such papers is 80–100 MPa and the Young's modulus is in the range of 5–10 GPa. This means that a large force can be applied to these CNT papers prior to plastic deformation, which is attractive as these can be shaped into any required form factor and can be cut easily with conventional cutters or shears. Figure 18.9 shows the photograph and SEM image of a free-standing flexible SWNT paper prepared using vacuum filtration. Typically, these SWNT papers show conductivity of about $5 \times 10^5 \text{ S m}^{-1}$, however, it can be improved with appropriate doping [146]. When used as an anode, the electronic transport can be similar to metallic conduction interrupted by tunneling barriers due to tube–tube interactions as well as due to the contributions from phonon backscattering and variable-range hopping [147]. These electrodes also exhibit high usable capacity, which is the actual electrode capacity defined as Ah/mass of electrode. This varies with the thickness of the electrode. Initial reported capacities using free-standing SWNTs have been found between 400 and 460 mAh g^{-1} . However, improvements have been made by shortening the SWNTs and by introducing sidewall defects to reach capacity close to 1,000 mAh g^{-1} [23, 120, 148–153].

On the other hand, MWNT free-standing papers fabricated using the CVD process exhibit irreversible capacity losses, which make them slightly less effective than SWNT electrodes. MWNTs synthesized on Cu current collectors act as binder-free anodes for LIBs and offered 140 % increment in capacity, as compared with conventional graphite anodes. Further, it has shown very good rate capability and an exceptional “zero capacity degradation” during long cycle operation [154]. CNTs were coated with ultrathin alumina by an atomic layer deposition technique. These alumina-coated CNT anodes further advance its capacity and safety features [155].

3.2.3 CNTs as Conductive Additive to Anode Materials

Use of CNTs as a conductive additive is advantageous when compared with other carbon additives like carbon black, acetylene black, or carbon nanofibers. High conductivity and high aspect ratio of CNTs allows for low wt% doping to other anode materials to achieve a comparable percolation threshold that sustains long-range connectivity in the composite structure to allow contiguous pathways for electrons to move. For comparison, conductivity compared with spherical particles can be achieved at very low wt%, i.e., 0.2 % w/w using SWNTs because of the formation of a percolation network. Considering other advantages of CNTs, due to the nature of π -orbital overlap in metallic CNT chiralities, electron conduction can occur via a ballistic transport phenomenon where electrons can transfer with mean free paths on the order of microns along the length of the nanotube unless scattered by a defect [156]. This property can improve the cyclic rate performance when CNTs are used as an additive. A variety of anode materials where CNTs have been used as an additive to improve Li storage have been reported; these include Sn/MWNT [111, 157], Bi/MWNT [100], SnSb/MWNT [158, 159], CoSb₃/MWNT [160], CoSn₃/MWNT [161], Ag/Fe/Sn/MWNT [162], TiO₂/MWNT [116, 163], SnO₂/MWNT [164–166], Li₄Ti₅O₁₂/MWNT [167], and Si/MWNT [168]. Table 18.4 summarizes the electrochemical parameters with and without CNTs additives in each case. The role of the CNTs in modifying the electrochemical properties is described in detail for each case in Table 18.4. Next, we will take a closer look at a few of the cases.

Li₄Ti₅O₁₂/MWNT

Li₄Ti₅O₁₂ with a spinel structure has been found promising because of zero strain insertion properties and high Li-ion mobility, however, it has a poor conductivity. Using CNTs as an additive with this material improves the conductivity and thus improves on rate capability and capacity retention [167]. It was reported that even after 500 cycles, ~98 % of the discharge capacity was retained. Li₄Ti₅O₁₂/CNT composites prepared by Li₄Ti₅O₁₂ nanoparticles with a size of about 50 nm homogeneously anchored on functionalized MWNTs. Li₄Ti₅O₁₂/CNT composite electrodes exhibited excellent cyclability with no noticeable decrease in performance over 100 cycles at 5C. In addition, the high-rate capacity of 112 mAh g⁻¹ at 20C is observed to be higher than that obtained at the 5C (106.5 mAh g⁻¹) for the bulk Li₄Ti₅O₁₂/CNTs [170].

Transition Metal Oxide/MWNT

Transition metal oxides such as CoO, CuO, NiO, Co₃O₄, and MnO [171–173] have been reported to have high capacity as anode materials in LIBs. The electrochemical reduction of these oxides versus Li involve two or more electrons from the 3-d orbital of transition metal transferred over to nanocomposite materials dispersed in an amorphous Li₂O matrix [171]. However, they suffer large hysteresis in their charge discharge curves and usually have relatively low conductivity. When MWNTs are mixed with these transition metal oxides based on various techniques, the resulting composites can have a compositional variation across the radial

Table 18.4 Electrochemical parameters of anode materials consisting of various types of MWNT-based nanocomposite

Electrode type	Current rate	Initial charge capacity (mA Hg ⁻¹)	Initial discharge capacity (mA Hg ⁻¹)	Cycle number	Residual reversible capacity (mA Hg ⁻¹)	Charge transfer resistance	References
Sn/MWNT	0.1 C	643	1,590	40	627	16.4	[111]
Sn/MWNT	50 mA g ⁻¹		570	30	442	17.3	[157]
SnI-MWNT	50 mA g ⁻¹		512	30	431		[157]
Bi/MWNT	25 mA g ⁻¹	308	570	50	315		[100]
Sb	50 mA g ⁻¹	648	1,023	30	115		[158]
SnSb _{0.5}	50 mA g ⁻¹	726	951	30	171		[158]
Sb/MWNT	50 mA g ⁻¹	462	1,266	30	287		[158]
SnSb _{0.5} /MWNT	50 mA g ⁻¹	518	1,092	30	348		[158]
CoSb ₃ /MWNT		312	915	30	265	7.2	[160]
Ag/Fe/Sn/MWNT	0.2 mA cm ⁻²	530		300	420		[162]
TiO ₂	50 mA g ⁻¹	52	287	75	21	123	[163]
TiO ₂ /MWNT	50 mA g ⁻¹	168	830	75	165	75	[163]
SnSb/MWNT	50 mA g ⁻¹	680	1,408	50	480		[159]
Ag-	0.2 mA cm ⁻²	500	250	30	172	15.8	[123]
TiO ₂ /MWNT	0.2 mA cm ⁻²			30	>400		[116]
SnO ₂ /MWNT	37.2 mA cm ⁻²		728	40	126.4		[169]
SnO ₂	37.2 mA cm ⁻²		665	40	505.9		[169]
SnO ₂ /MWNT	850 mA g ⁻¹	100	100			60	[167]
Li ₄ Ti ₅ O ₁₂	850 mA g ⁻¹	145	145	500	142	38	[166]
Li ₄ Ti ₅ O ₁₂ /MWNT	50 mA g ⁻¹		819	50	279		[166]
Si/MWNT (7:3)	50 mA g ⁻¹		1,770	50	1,250		[168]
Si/MWNT (5:5)	50 mA g ⁻¹		1,182	50	889		[168]
Si/MWNT (3:7)	0.25 mA cm ⁻²	960	1,882	30	1,066		[168]

C is the theoretical capacity of Sn

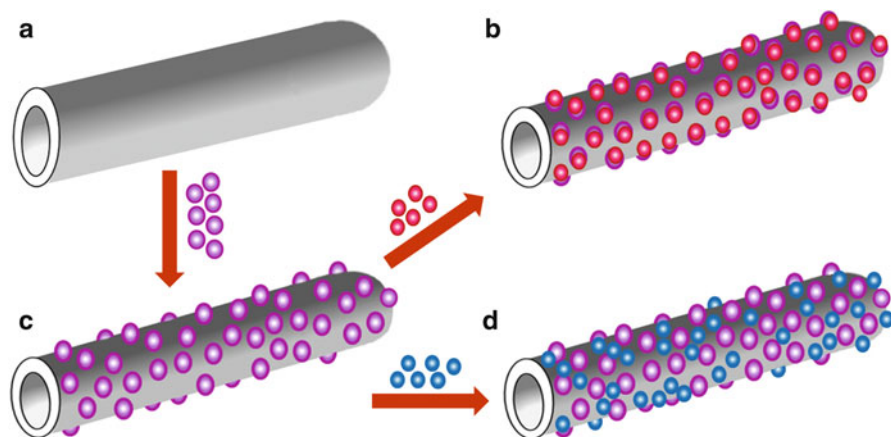


Fig. 18.10 Schematic illustrations of self-assembly for preparation of nanocomposites: (a) MWNT as primary support, (b) a second phase of nanoparticles (in pink) are anchored on to MWNT, (c) a third phase of nanoparticles (in purple) are attached to the surface of the second phase nanoparticles and (d) a third phase of nanoparticles (in blue) are also landed on to the MWNT (Adapted from Ref. [174])

direction and along the axial direction. However, recently, a self-assembly approach has become popular to allow a more homogeneous distribution of these oxide particles over the CNTs [174]. The schematic shown in the Fig. 18.10 allows the preparation of binary composites as well as even more complex systems. Here, the metal or metal oxide nanoparticles comprise the active phase and serve as the primary building block. Composite electrodes prepared using this self-assembly method were robust and usually show much better electrochemical performance. Almost all of the above-reported transition metal oxide composites with CNTs show better Li-storage capacity and excellent cyclability. Also, it has been previously mentioned that these composites need very small wt% of CNTs to achieve the improved electrochemical performance when compared with other forms of carbonaceous materials.

An advanced carbon-coated CNT@Fe₂O₃ hierarchical nanostructure has been constructed by bottom-up assembly of β -FeOOH nanospindles on CNT backbones and thermal transformation to hollow α -Fe₂O₃ nanohorns followed by carbon nanocoating. With the virtue of greatly enhanced electrode stability and kinetics for lithium storage, this unique hybrid structure exhibits very stable capacity retention of 800 mAh g⁻¹ over 100 cycles at a current density of 500 mA g⁻¹ and exceptional high-rate capability at high current densities of 1,000–3,000 mA g⁻¹ [175].

For TiO₂/MWNT composites, nanocomposites consisting of brookite TiO₂ nanoparticles attached to MWNTs were studied [176]. Brookite TiO₂ crystallizes in the orthorhombic system, which is different from the popular rutile and anatase form. The MWNTs, when decorated with uniformly dispersed TiO₂, exhibited a rough surface, which helped in increasing the ionic and electronic diffusion,

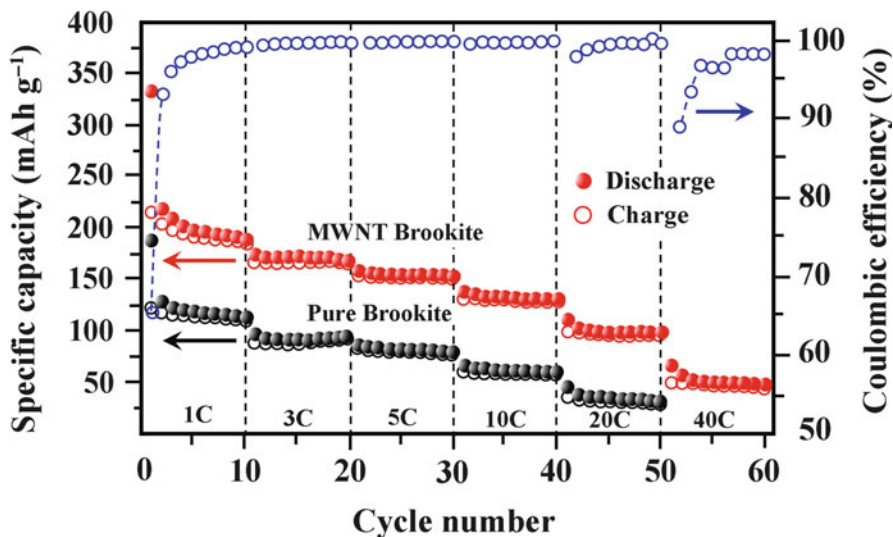
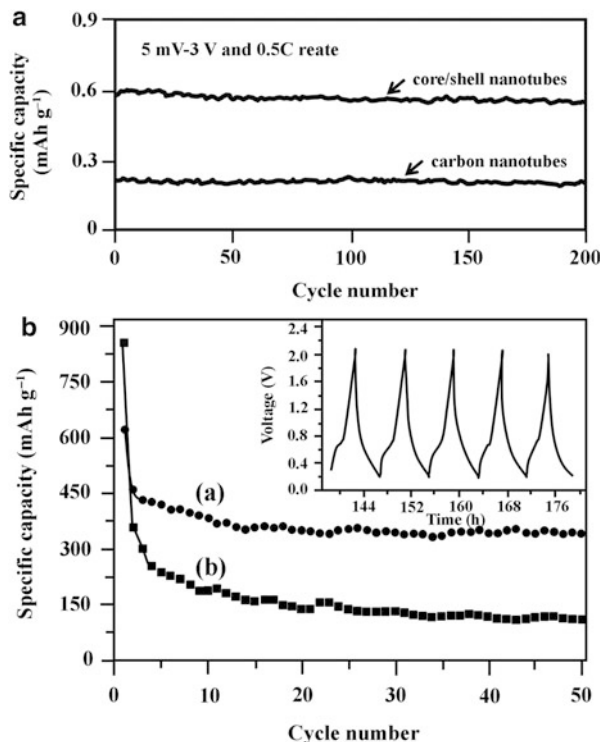


Fig. 18.11 Rate capability and Coulombic efficiency for neat brookite and brookite/MWNT nanocomposite at different C rates (Adapted from Ref. [176])

which results in achieving a high rate capability. When compared with neat brookite, TiO_2/MWNT composite electrodes (Fig. 18.11) exhibited high discharge capacity as well as showed a large difference in charge–discharge profiles. In addition, it was found that the reversible capacity was higher and the cell polarization was lower in the brookite/MWNT compared with neat brookite.

Compared to pure CNTs or neat TiO_2 only, the composite mix of these two showed a much improved rate capability and cycle performance. Pure SnO_2 has high specific capacity, i.e., 782 mAh g^{-1} , but it experiences a volume expansion of up to 260 % during the charge–discharge cycles [177]. Forming a composite of SnO_2 with MWNTs helps to reduce this volume expansion as well as improve the electronic conductivity. Compared with the random mixing of SnO_2 and MWNTs to form the composite, a new approach of synthesizing a coaxial SnO_2/CNT structure has been found to be more effective in delivering a reversible capacity (Fig. 18.12a). In this process, a porous SnO_2 nanotubes was first formed and then, on top of its external surface, a CNT overlayer was grown [164]. This unique nanostructure allows stress absorption by the CNT matrix and the hollow interior allows freedom in volumetric expansion. This organization also provides better electrical contact and improved Li-ion transport. A novel mesoporous-nanotube hybrid composite, namely mesoporous SnO_2 overlaying on the surface of MWNTs, was prepared by a hydrothermal method and its electrochemical properties were studied. Results showed that the mesoporous-tube hybrid composites displayed higher capacity and better cycle performance (Fig. 18.12b) in comparison with the mesoporous tin dioxide. A large improvement in electrochemical performance

Fig. 18.12 Cycle performance of (a) SnO₂-core/carbon-shell nanotubes and CNTs at a current rate of 0.5C and 5 mV to 3 V (vs. Li⁺/Li) voltage window (Adapted from Ref. [164]) and (b) mesoporous SnO₂ or SnO₂/MWNT at a current density of 33.3 mA h g⁻¹. Inset: the voltage capacity profiles of the 16th–20th cycles of SnO₂/MWNT (Adapted from Ref. [166])



within the hybrid composites may, in general, be related to the mesoporous-tube structure, which possesses such properties as a one-dimensional hollow structure, high strength with flexibility, excellent electric conductivity, and large surface area [166].

SnO₂/CNT nanocomposite electrodes, where SnO₂ nanoparticles were deposited on the functionalized SWNTs, have been shown to exhibit desirable electrochemical performances as the negative electrodes for the LIBs. CNTs not only suppressed the mechanical degradation of SnO₂ and therefore provided the composite electrode with excellent capacity retention (>650 mA h g⁻¹ with less than 10 % capacity loss after 100 cycles), but also enhanced the electronic conductivity of the electrodes leading to excellent rate capability [178]. CNT-encapsulated SnO₂ (SnO₂@CNT) core-shell composite anode materials prepared by chemical activation of CNTs and wet chemical filling exhibited reversible specific capacity of 829.5 mA h g⁻¹ and maintains 627.8 mA h g⁻¹ after 50 cycles at 0.1C. The excellent lithium-storage and rate-capacity performance of SnO₂@CNT core-shell composites makes them a promising anode material for lithium-ion batteries [179]. Flower-like SnO₂/CNTs composites synthesized by a one-step hydrothermal method showed the first discharge and charge capacities are 1,230 and 842 mA h g⁻¹, respectively. After 40 cycles, the reversible discharge capacity is still maintained at 577 mA h g⁻¹, much higher than that of bare SnO₂ (112 mA h g⁻¹) [180].

3.2.4 Silicon/MWNT as Anode

Silicon, which is a semiconductor material, reacts with lithium to form alloys by electrochemical processes that are partially reversible and of low voltage, which provides a specific capacity higher than the conventional graphite. Lithium-silicon alloy $\text{Li}_{4.4}\text{Si}$ has a theoretical specific capacity of $4,200 \text{ mAh g}^{-1}$ compared with $3,600 \text{ mAh g}^{-1}$ with metallic lithium and 372 mAh g^{-1} of graphite [98, 181]. However, such electrochemical performance cannot be achieved by an Si-only anode due to the mechanical strain generated during the alloying/de-alloying process. This results in enormous volume changes and thus causes cracking and crumbling of the electrode and gives poor electrochemical performance. Si/MWNT nanocomposites were fabricated using a core/shell structure to improve the cyclability of the Si-based anodes, where MWNTs act as a buffer to accommodate a large volume change during the electrochemical process [182]. Silicon monoxide/graphite/MWNT (SiO/G/CNTs) material was prepared by ball-milling followed by a CVD method and exhibited an initial specific discharge capacity of 790 mAh g^{-1} with a coulombic efficiency of 65 %. After 100 cycles, a high reversible capacity of 495 mAh g^{-1} was obtained [183]. Novel free-standing and flexible CNT-Si films composite films up to $4 \mu\text{m}$ in thickness were synthesized by CVD deposition of a-Si on CNT films or by a CNT-Si nanoparticle compositing technique. Such free-standing film has a low sheet resistance of $\sim 30 \Omega/\text{sq}$ and was demonstrated as a high-capacity anode material for LIB. CNT-Si film shows a high specific charge storage capacity ($\sim 2,000 \text{ mAh g}^{-1}$) and a good cycling life, superior to pure sputtered-on silicon films with similar thicknesses. The film can also “ripple up” to release the strain of a large volume change during lithium intercalation. The conductive composite film functioned as both anode active material and current collector and offers ~ 10 times improvement in specific capacity compared with widely used graphite/copper anode sheets [184]. The electrochemical characterization of silicon $\sim 10 \text{ nm}$ nanoparticles decorated vertically aligned CNTs (VACNTs) 5 nm in diameter directly grown onto metal foil via a two-step CVD process showed high reversible Li-storage capacity of $3,000 \text{ mAh g}^{-1}$ at 1.3C. Such a VACNT electrode exhibits an impressive rate capability: a capacity of $1,900 \text{ mAh g}^{-1}$ is achieved at 5C and 760 mAh g^{-1} at 15C. The VACNTs/Si sustained at very high C-rates without any significant polarization and without structural damaging. Cycling at 10C leads to a recovered capacity of 800 mAh g^{-1} , i.e., still two times the capacity of graphite [185]. Si/CNT nanocomposites have been prepared by a cost-effective wet-milling process exhibiting initial capacity $\sim 2,000 \text{ mAh g}^{-1}$, initial coulombic efficiency $\sim 80 \%$, and improved lifetime originated from the suppression of serious oxidation of silicon nanograins by selecting a proper liquid medium such as 1-octanol, the stronger linkage between silicon and CNT by a post-thermal treatment, and effective electrical conductivity through network structure by 1D CNTs [186]. A composite anode material of silicon/disordered carbon/CNTs (Si/DC/CNTs) was prepared by pyrolyzing the mixture of silicon (Si), CNTs, and polyvinyl chloride (PVC) as carbon source. The Si/DC/CNTs composite showed a discharge capacity of $1,254 \text{ mAh g}^{-1}$ in the first cycle, and a discharge capacity of 821 mAh g^{-1} after 20 cycles, which is much higher than that of

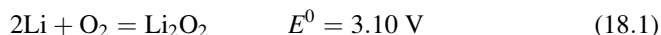
Si/DC composite (658 mAh g⁻¹). It was found that the excellent resiliency of the CNTs can assist the carbonaceous matrix derived from PVC to restore the volumetric changes of the Si [187].

3.2.5 Graphene/CNT Nanocomposites

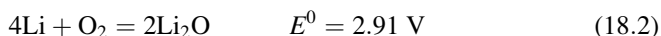
Chen et al. proposed the CNTs grown in situ on graphene nanosheets as superior anodes for LIBs. Multilayered graphene (GNS)–CNT hybrid nanostructure prevents grapheme restacking and facilitation of lithium diffusion into CNTs with large aspect ratio enhanced capacity, cyclability, and rate capability. The GNS-CNT composite with the shortest CNT decoration displayed highly reversible capacities of 573 mAh g⁻¹ at a small current of 0.2C and 520 mAh g⁻¹ at a large current of 2C [188].

3.3 Applications of CNTs in Lithium-air Batteries

The lithium-air battery (LAB) is a promising candidate for a portable power source for various commercial or military applications because it possesses the highest specific capacity of 11,972 Wh kg⁻¹ among all the known electrochemical couples [189]. In LABs, because the oxygen does not have to be stored internally, it is acquired from ambient air. As a result, the total mass of the battery can be significantly reduced. During the discharge process, O₂ molecules diffuse into the battery and are reduced at the air electrode of the LAB to deliver energy



and



However, several challenging problems such as ingress of moisture from the atmosphere into the battery via the air electrode, insufficient amount of O₂ for electrode reaction at high discharge rates due to the limited O₂ solubility in the electrolyte, and the deposition of Li₂O₂ or Li₂O at the surface of the air electrode still hinder the practical application of lithium–air batteries in ambient environment. For ambient air operation of a LAB, the most urgent problem to be solved is to prevent the side reaction of the Li anode with moisture from environmental air. Several approaches have been employed to improve air electrode porosity and maximize air electrode material utilization. Therefore, an optimized air electrode structure (e.g., with oxygen micro-channels and engineered porosity distribution) can significantly reduce oxygen starvation and improve air electrode utilization. CNTs are promising as cathode materials as their unique morphology could allow more efficient storage of Li₂O₂ discharge product. Free-standing CNT-based air-breathing electrodes are less corrosive and more thermally stable because of fewer molecular defects compared with carbon black, which is highly desirable

from an application point of view. Furthermore, it is easy to conduct surface coating and implanting to reduce catalyst usage and control catalyst particle size to optimize rechargeable LAB performance. Zhang et al. reported that a LAB made with an air electrode made up of CNTs/nanofiber mixed buckypapers delivered a high discharge capacity $2,500 \text{ mAh g}^{-1}$ at a thickness of $20 \text{ }\mu\text{m}$ with a discharge current density of 0.1 mA cm^{-2} ; however, it was reduced to 400 mAh g^{-1} when the thickness of the air electrode was increased to $220 \text{ }\mu\text{m}$. The CNT-based air cathode offers tailorable porosity, large surface area, and high conductivity $100\text{--}500 \text{ S cm}^{-1}$ [190]. Nitrogen-doped carbon nanotubes (N-CNTs), synthesized by a FCCVD method, were investigated as cathode material for LABs and exhibited a specific discharge capacity of 866 mAh g^{-1} , which was about 1.5 times that of CNTs [191]. The N-CNT electrode showed high electrocatalytic activities for the cathode reaction, thus improving the LAB performance.

4 Conclusions

The constant demand for electrical storage for daily communication and sustainable transportation is the motivation for thinner, lighter, space-effective, and shape-flexible batteries with higher energy density and cycling performance. This chapter discusses the technological developments and benefits, in terms of weight, size, and design flexibility, provided by today's state-of-the-art Li-ion battery technology and the development of new electrode materials and cell configurations. Recently, electrode research has provided new opportunities in the pursuit of novel hybrid nanostructures like CNTs to improve upon the performance of conventional materials. Compared with conventional carbon materials, the incorporation of CNTs as a conductive additive presents a more effective strategy to establish an electrical percolation network for improving the rate capability and cyclability due to their unique electrochemical and mechanical properties. In addition, CNTs allows fabrication of freestanding electrodes (without binder or current collector) as an active lithium-ion storage material or physical support for ultra-high-capacity materials. CNTs have been shown both theoretically and experimentally to possess extraordinary electronic conductivity and specific capacity at the individual nanotube level and thus are logically considered as ideal electrode materials for high-energy LIBs. However, the predicted dramatically enhanced conductivity in various novel anode and cathode materials upon the incorporation of CNTs has also been verified in several energy-storage systems, such as supercapacitors. Active material matrix with the dispersion of CNTs (single-walled or multi-walled CNTs) vs. carbon fillers were evaluated for a more direct comparison on the electrochemical performance in the resulting nanocomposites. Implications of the comparison between the nanotubes and activated carbon with respect to their potentials in conductive nanocomposites were discussed. The physical, transport, and electrochemical behaviors of the electrodes made from hybrid composite nanostructures containing CNTs were reported. The chapter highlights the electrochemical performance of LIBs affected

by the presence of CNTs in terms of energy and power densities, rate capacity, cyclic life, and safety in comparison with those without or containing other types of carbonaceous materials.

References

1. Nalwa HS (2000) Handbook of nanostructured materials and nanotechnology, vol 5. Academic, New York
2. Ajayan PM, Schadler LS, Braun PV (2003) Nanocomposite science and technology. Wiley-VCH, Weinheim
3. Aricò AS, Bruce P, Scrosati B, Tarascon J-M, van Schalkwijk W (2005) *Nat Mater* 4:366
4. Haas O, Cairns EJ (1999) *Annu Rep Prog Chem Sect C Phys Chem* 95:163
5. Liu X-M, Huang Z-DD, Oh S-WW, Zhang B, Ma P-C, Yuen MMF, Kim J-K (2011) *Compos Sci Technol* 72:121
6. Tarascon JM, Armand M (2001) *Nature* 414:359
7. Landi BJ, Ganter MJ, Cress CD, DiLeo RA, Raffaele RP (2009) *Energy Environ Sci* 2:638
8. Kraytsberg A, Ein-Eli Y (2011) *J Power Sources* 196:886
9. Iijima S (1991) *Nature* 354:56
10. Lin Y, Taylor S, Li H, Shiral Fernando KA, Qu L, Wang W (2004) *J Mater Chem* 14:527
11. Moniruzzaman M, Winey KI (2006) *Macromolecules* 39:5194
12. Bethune DS, Johnson RD, Salem RJ, de Vries MS, Yannoni CS (1993) *Nature* 366:123
13. Thostenson ET, Ren ZF, Chou TW (2001) *Compos Sci Technol* 61:1899
14. Journet C, Maser WK, Bernier P, Loiseau A, de la Chapelle ML, Lefrant S (1997) *Nature* 388:756
15. Ren ZF, Huang ZP, Xu JW, Wang JH, Bush P, Siegal MP (1998) *Science* 282:1105
16. Rinzler AG, Liu J, Dai H, Nikolaev P, Huffman CB, Rodriguez-Macias FJ (1998) *Appl Phys A* 67:29
17. Nikolaev P, Bronikowski MJ, Bradley RK, Fohmund F, Colbert DT, Smith KA (1999) *Chem Phys Lett* 313:91
18. Nalimova VA, Sklovsky DE, Bondarenko GN, Alvergnat-Gaucher H, Bonnamy S, Béguin F (1997) *Synth Met* 88:89
19. Zhao J, Buldum A, Han J, Lu JP (2000) *Phys Rev Lett* 85:1706
20. Nishidate K, Hasegawa M (2005) *Phys Rev B* 71:245418
21. Frackowiak E, Gautier S, Gaucher H, Bonnamy S, Béguin F (1999) *Carbon* 37:61
22. Liu P, Hornyak GL, Dillon AC, Gennett T, Heben MJ, Turner JA (1999) *J Electrochem Soc Proc Int Symp* 31
23. Claye AS, Fischer JE, Huffman CB, Rinzler AG, Smalley RE (2000) *J Electrochem Soc* 147:2845
24. Hsoeh HM, Tai NH, Lee CY, Chen JM, Wang FT (2003) *Rev Adv Mater Sci* 5:67
25. Whittingham MS (2004) *Chem Rev* 104:4271
26. Jiang C, Hosono E, Zhou H (2006) *Nano Today* 1:28
27. Chen J, Minett AI, Liu Y, Lynam C, Sherrell P, Wang C, Wallace GG (2008) *Adv Mater* 20:566
28. Whittingham MS (2008) *MRS Bull* 33:411
29. Li H, Wang Z, Chen L, Huang X (2009) *Adv Mater* 21:4593
30. Wallace GG, Chen J, Mozer AJ, Forsyth M, MacFarlane DR, Wang C (2009) *Mater Today* 12:20
31. Dahn JR, von Sacken U, Jozkowiak MW, Al-Janaby H (1991) *J Electrochem Soc* 138:2207
32. Li W, Resimiers JN, Dahn JR (1993) *Solid State Ion* 67:123
33. Resimiers JN, Dahn JR, von Sacken U (1993) *J Electrochem Soc* 140:2752

34. Koetschau I, Richard MN, Dahn JR, Soupart JB, Rousche JC (1995) *J Electrochem Soc* 142:2906
35. Pistoia G, Zane D, Zhang Y (1995) *J Electrochem Soc* 142:2551
36. Jeong IS, Kim JU, Gu HB (2001) *J Power Sources* 102:55
37. Rodrigues S, Munichandraiah N, Shukla AK (2001) *J Power Sources* 102:322
38. Suresh P, Rodrigues S, Shukla AK, Sivashankar SA, Munichandraiah N (2002) *J Power Sources* 112:665
39. Jin B, Kim JU, Gu HB (2003) *J Power Sources* 117:148
40. Kim JU, Jo YJ, Park GC, Gu HB (2003) *J Power Sources* 119–121:686
41. Suresh P, Shukla AK, Munichandraiah N (2005) *J Electrochem Soc* 152:A2273
42. Suresh P, Shukla AK, Munichandraiah N (2006) *J Power Sources* 161:1307
43. Wang G, Zhang Q, Yu Z, Qu M (2008) *Solid State Ion* 179:263
44. Wang G, Li H, Zhang Q, Yu Z, Qu M (2011) *J Solid State Electrochem* 15:759
45. Zhang Q-T, Qu M-Z, Niu H, Yu Z-L (2007) *New Carbon Mater* 22:361
46. Sheem KY, Sung M, Lee YH (2010) *Electrochim Acta* 55:5808
47. Sheem KY, Lee YH, Lim HS (2006) *J Power Sources* 158:1425
48. Park JH, Lee SY, Kim JH, Ahn S, Park J-S, Jeong YU (2010) *J Solid State Electrochem* 14:593
49. Luo S, Wang K, Wang J, Jiang K, Li Q, Fan S (2012) *Adv Mater* 24:2294
50. Li X, Kang F, Shen W (2006) *Electrochem Solid State Lett* 9:A126
51. Li X, Kang F, Shen W (2006) *Carbon* 44:1334
52. Huang ZD, Liu XM, Zhang B, Oh SW, Wong SK, Kim JK (2011) *Scripta Mater* 64:122
53. Huang ZD, Liu XM, Oh SW, Zhang B, Ma PC, Kim JK (2011) *J Mater Chem* 21:10777
54. Singh N, Galande C, Miranda A, Mathkar A, Gao W, Mohanareddy AL, Vlad A, Ajayan PM (2012) *Sci Rep* 2:481
55. Ban C, Li Z, Wu Z, Kirkham MJ, Chen L, Jung YS, Payzant A, Yan Y, Whittingham S, Dillon AC (2011) *Adv Energy Mater* 1:58
56. Liu X-M, Huang Z-D, Oh S, Ma P-C, Chan PCH, Vedam GK, Kang K, Kim J-K (2010) *J Power Sources* 195:4290
57. Jia X, Yan Z-C, Chen Z-Z, Wang R, Zhang Q, Guo L, Wei F, Lu Y (2011) *Chem Commun* 47:9669
58. Padhi AK, Nanjundaswamy KS, Goodenough JB (1997) *J Electrochem Soc* 144:1188
59. Bramnik NN, Bramnik KG, Buhrmester T, Baehtz C, Ehrenberg H, Fuess H (2004) *J Solid State Electrochem* 8:558
60. Jin B, Gu HB, Kim KW (2008) *J Solid State Electrochem* 12:105
61. Jin B, Gu HB, Zhang W, Park KH, Sun G (2008) *J Solid State Electrochem* 12:1549
62. Varzi A, Täubert C, Wohlfahrt-Mehrens M, Kreis M, Schütz W (2011) *J Power Sources* 196:3303
63. Li X, Kang F, Bai X, Shen W (2007) *Electrochem Commun* 9:663
64. Wang L, Huang Y, Jiang R, Jia D (2007) *J Electrochem Soc* 154:A1015
65. Kim SW, Ryu J, Park CB, Kang K (2010) *Chem Commun* 46:7409
66. Mohamed R, Ji S, Linkov V (2011) *Int J Electrochem* 283491:1
67. Kim EM, Park K-H, Gu H-B (2008) *J Adv Eng Technol* 1:107
68. Zhou Y, Wang J, Hu Y, O'Hayre R, Shao Z (2010) *Chem Commun* 46:7151
69. Yang J, Wang J, Li X, Wang D, Liu J, Liang G, Gauthier M, Li Y, Geng D, Li R, Sun X (2012) *J Mater Chem* 22:7537
70. Toprakci O, Toprakci HAK, Ji L, Xu G, Lin Z, Zhang X (2012) *ACS Appl Mater Interfaces* 4:1273
71. Gananavel M, Patel MUM, Sood AK, Bhattacharyya AJ (2012) *J Electrochem Soc* 159:A336
72. Murugan AV, Muraliganth T, Ferreira PJ, Manthiram A (2009) *Inorg Chem* 48:946
73. Xu J, Chen G, Li X (2009) *Mater Chem Phys* 118:9
74. Kavan L, Bacsa R, Tunckol M, Serp P, Zakeeruddin SM, LeFormal F, Zukulovs M, Graetzel M (2010) *J Power Sources* 195:5360

75. Schneider JJ, Khanderi J, Popp A, Engstler J, Tempel H, Sarapulova A, Bramnik NN, Mikhailova D, Ehrenberg H, Schmitt LA, Dimesso L, Förster C, Jaegermann W (2011) *Eur J Inorg Chem* 28:4349
76. Zou M-M, Ai D-J, Liu K-Y (2011) *Trans Nonferrous Met Soc China* 21:2010
77. Ma S-B, Nam K-W, Yoon W-S, Bak S-M, Yang X-Q, Cho B-W, Kim K-B (2009) *Electrochem Commun* 11:1575
78. Mohammadi A, Inganas O, Lundstrom I (1986) *J Electrochem Soc* 133:947
79. Osaka T, Naoi K, Ogano S (1988) *J Electrochem Soc* 185:1071
80. Novak P, Muller K, Santhanam KSV, Haas O (1997) *Chem Rev* 97:207
81. Goto F, Abe K, Okabayashi K, Yoshida T, Morimoto H (1987) *J Power Sources* 20:243
82. Cochet M, Maser WK, Benito AM, Callejas MA, Martinez MT, Benoit JM, Schreiber J, Chauvet O (2001) *Chem Commun* 16:1450
83. Cheng F, Tang W, Li C, Chen J, Liu H, Shen P, Dou S (2006) *Chem Eur J* 12:3082
84. Sivakkumar SR, MacFarlane DR, Forsyth M, Kim DW (2007) *J Electrochem Soc* 154:A834
85. Wang CY, Mottaghitalab V, Too CO, Spinks GM, Wallace GG (2007) *J Power Sources* 163:1105
86. He BL, Dong B, Wang W, Li HL (2009) *Mater Chem Phys* 114:371
87. Sivakkumar SR, Kimm DW (2007) *J Electrochem Soc* 154:A134
88. Shan Y, Gao L (2004) *Chem Lett* 33:1560
89. Baibarac M, Lira-Cantú M, Oro Sol J, Baltog I, Casañ-Pastor N, Gomez-Romero P (2007) *Compos Sci Technol* 67:2556
90. Han SC, Song MS, Lee H, Kim HS, Ahn HJ, Lee JY (2003) *J Electrochem Soc* 150:A889
91. Wei W, Wang J, Zhou L, Yang J, Schumann B, NuLi Y (2011) *Electrochem Commun* 13:399
92. Sivakkumar SR, Howlett PC, Winther-Jensen B, Forsyth M, MacFarlane DR (2009) *Electrochim Acta* 54:6844
93. Dahn JR (1991) *Phys Rev B* 44:9170
94. Satoh A, Takami N, Ohsaki T (1995) *Solid State Ion* 80:291
95. Reddy TB, Hossain S (2002) *Rechargeable Lithium Batteries (Ambient Temperature)*. In: Linden D, Reddy TB (eds) *Handbook of batteries*, 3rd edn., pp 34.1–34.62
96. Besenhard JO, Yang J, Winter M (1997) *J Power Sources* 68:87
97. Winter M, Besenhard JO (1998) *Adv Mater* 10:725
98. Winter M, Besenhard JO (1999) *Electrochim Acta* 45:31
99. Obrovac MN, Christensen L (2004) *Electrochem Solid State Lett* 7:A93
100. NuLi Y, Yang J, Jiang M (2008) *Mater Lett* 62:2092
101. Wu YP, Rahm E, Holze R (2003) *J Power Sources* 114:228
102. Guo ZP, Milin E, Wang JZ, Chen J, Liu HK (2005) *J Electrochem Soc* 152:A2211
103. Liu WR, Yang MH, Wu HC, Chiao SM, Wu NL (2005) *Electrochem Solid State Lett* 8:A100
104. Liu Y, Matsumura T, Imanishi N, Hirano A, Ichikawa T, Takeda Y (2005) *Electrochem Solid State Lett* 8:A599
105. Amaratunga G, Nathan A, Nookala M, Smart MC (eds) (2009) *Mater Res Soc Symp Proc* 1:1127-T03-06
106. Ando Y, Zhao X, Shimoyama H, Sakai G, Kaneto K (1999) *Int J Inorg Mater* 1:77
107. Treacy MM, Ebbesen TW, Gibson JM (1996) *Nature* 381:678
108. Lier GV, Alsenoy CV, Doren VV, Geerlings G (2000) *Chem Phys Lett* 326:181
109. Yu MF, Lourie O, Dyer MJ, Moloni K, Kelly TF, Ruoff RS (2000) *Science* 287:637
110. Meunier V, Kephart J, Roland C, Bernholc J (2002) *Phys Rev Lett* 88:075506(1)
111. Kumar TP, Ramesh R, Lin YY, Fey GTK (2004) *Electrochem Commun* 6:520
112. Mi CH, Cao GS, Zhao XB (2004) *J Electroanal Chem* 562:217
113. Morris RS, Dixon BG, Gennett T, Raffaele R, Heben MJ (2004) *J Power Sources* 138:277
114. Nishidate K, Sasaki K, Oikawa Y, Baba M, Hasegawa M (2005) *J Surf Sci Nanotechnol* 3:358
115. Kawasaki S, Hara T, Iwai Y, Suzuki Y (2008) *Mater Lett* 62:2917

116. Yan J, Song H, Yang S, Yan J, Chen X (2008) *Electrochim Acta* 53:6351
117. Gao B, Bower C, Lorentzen JD, Fleming L, Kleinhammes A, Tang XP, McNeil LE, Wu Y, Zhou O (2000) *Chem Phys Lett* 327:69
118. Maurin G, Bousquet C, Henn F, Bernier P, Almairac R, Simon B (2000) *Solid State Ion* 136–137:1295
119. Yang Z-H, Wu H-Q (2001) *Mater Lett* 50:108
120. Shimoda H, Gao B, Tang XP, Kleinhammes A, Fleming L, Wu Y, Zhou O (2002) *Phys Rev Lett* 88:015502
121. Eom JY, Park JW, Kwon HS, Rajendrana S (2006) *J Electrochem Soc* 153:A1678
122. Zhang Y, Zhao ZG, Zhang XG, Zhang HL, Li F, Liu C, Cheng HM (2008) *Int J Nanomanuf* 2(1/2):4
123. Reddy ALM, Shaijumon MM, Gowda SR, Ajayan PM (2009) *Nano Lett* 9(3):1002
124. Zhang HX, Feng C, Zhai YC, Jiang KL, Li QQ, Fan SS (2009) *Adv Mater* 21:2299
125. Dubot P, Cenedese P (2001) *Phys Rev B* 63:241402
126. Kar T, Pattanayak J, Scheiner S (2001) *J Phys Chem A* 105:10397
127. Yang J, Liu HJ, Chan CT (2001) *Phys Rev B* 64:085420
128. Garau C, Frontera A, Quinonero D, Costa A, Ballester P, Deya PM (2003) *Chem Phys Lett* 374:548
129. Garau C, Frontera A, Quinonero D, Costa A, Ballester P, Deya PM (2004) *Chem Phys* 297:85
130. Liu Y, Yukawa H, Morinaga M (2004) *Commun Mater Sci* 30:50
131. Udomvech A, Kerdcharoen T, Osotchan T (2005) *Chem Phys Lett* 406:161
132. Zhao M, Xia Y, Mei L (2005) *Phys Rev B* 71:165413
133. Zhao M, Xia Y, Liu X, Tan Z, Huang B, Li F, Ji Y, Song C (2005) *Phys Lett A* 340:434
134. Eom JY, Kim DY, Kwon HS (2006) *J Power Sources* 157:507
135. Wang XX, Wang JN, Su LF (2009) *J Power Sources* 186:194
136. Shimoda H, Gao B, Tang XP, Kleinhammes A, Fleming L, Wu Y, Zhou O (2002) *Physica B* 323:133
137. Wang XX, Wang JN, Chang H, Zhang YF (2007) *Adv Funct Mater* 17:3613
138. Kaskhedikar NA, Maier J (2009) *Adv Mater* 21:2664
139. Lv R, Zou L, Gui X, Kang F, Zhu Y, Zhu H, Wei J, Gu J, Wang K, Wu D (2008) *Chem Commun* 7:2046
140. Zhou J, Song H, Fu B, Wu B, Chen X (2010) *J Mater Chem* 20:2794
141. Carrol DL, Redlich P, Blase X, Charlier JC, Curran S, Ajayan PM et al (1998) *Phys Rev Lett* 81:2332
142. Wei B, Spolenak R, Redlich PK, Rühle M, Artz E (1999) *Appl Phys Lett* 74:3149
143. Landi BJ, DiLeo RA, Schauerman CM, Cress CD, Ganter MJ, Raffaele RP (2009) *J Nanosci Nanotechnol* 9:3406
144. Li X, Liu J, Zhang Y, Li Y, Liu H, Meng X, Yang J, Geng D, Wang D, Li R, Sun X (2012) *J Power Sources* 197:238
145. Gupta N, Toh T, Fatt MW, Mhaisalkar S, Srinivasan M (2012) *J Solid State Electrochem* 16:1585
146. Kaiser AB, Skakalova V, Roth S (2008) *Physica E* 40:2311
147. Jin B, Jin EM, Park KH, Gu HB (2008) *Electrochem Commun* 10:1537
148. Gao B, Kleinhammes A, Tang XP, Bower C, Fleming L, Wu Y, Zhou O (1999) *Chem Phys Lett* 307:153
149. Gao B, Shimoda H, Tang XP, Kleinhammes A, Fleming L, Wu Y, Zhou O (2001) *AIP Conf Proc* 590:95
150. Jeong SK, Inaba M, Mogi R, Iriyama Y, Abe T, Ogumi Z (2001) *Langmuir* 17:8281
151. Mukhopadhyay I, Kawasaki S, Okino F, Govindaraj A, Rao CNR, Touhara H (2002) *Physica B* 323:130
152. Ng SH, Wang J, Guo ZP, Chen J, Wang GX, Liu HK (2005) *Electrochim Acta* 51:23
153. Eom JY, Kwon HS (2008) *J Mater Res* 23:2458

154. Lahiri I, Oh SW, Hwang JY, Cho S, Sun YK, Banerjee R, Choi W (2010) *ACS Nano* 4:3440
155. Lahiri I, Oh SM, Hwang JY, Kang C, Jeon H, Banerjee R, Sun YK, Choi W (2011) *J Mater Chem* 21:13621
156. Dai H (2002) *Surf Sci* 500:218
157. Guo ZP, Zhao ZW, Liu HK, Dou SX (2005) *Carbon* 43:1392
158. Chen WX, Lee JY, Liu ZL (2003) *Carbon* 41:959
159. Park MS, Needham SA, Wang GX, Kang YM, Park JS, Dou SX, Liu HK (2007) *Chem Mater* 19:2406
160. Xie J, Zhao XB, Cao GS, Zhao MJ (2004) *Electrochim Acta* 50:2725
161. Zhai C, Du N, Zhang H, Yu J, Wu P, Xiao C et al (2011) *Nanoscale* 3:1798
162. Yin JT, Wada M, Kitano Y, Tanase S, Kajita O, Sakai T (2005) *J Electrochem Soc* 152: A1341
163. Huang H, Zhang WK, Gan XP, Wang C, Zhang L (2007) *Mater Lett* 61:296
164. Wang Y, Zeng HC, Lee JY (2006) *Adv Mater* 18:645
165. An G, Na N, Zhang X, Miao Z, Miao S, Ding K, Liu Z (2007) *Nanotechnology* 18:435707
166. Wen Z, Wang Q, Zhang Q, Li J (2007) *Adv Funct Mater* 17:2772
167. Huang J, Jiang Z (2008) *Electrochim Acta* 53:7756
168. Kim T, Mo YH, Nahm KS, Oh SM (2006) *J Power Sources* 162:1275
169. Fu Y, Ma R, Shu Y, Cao Z, Ma X (2009) *Mater Lett* 63:1946
170. Ni H, Fan LZ (2012) *J Power Sources* 214:195
171. Poizot P, Laruelle S, Grugeon S, Dupont L, Tarascon JM (2000) *Nature* 407:496
172. Tarascon JM, Grugeon S, Morcrette M, Laruelle S, Rozier P, Poizot P (2005) *CR Chem* 8:9
173. Taberna PL, Mitra S, Poizot P, Simon P, Tarascon JM (2006) *Nat Mater* 5:567
174. Li J, Tang S, Lu L, Zeng HC (2007) *J Am Chem Soc* 129:9401
175. Wang Z, Luan D, Madhavi Z, Hu Y, Lou XWD (2012) *Energy Environ Sci* 5:5252
176. Lee DH, Kim DW, Park JG (2008) *Cryst Growth Des* 8:4506
177. Zhang WJ (2010) *J Power Sources* 196:13
178. Ahn D, Xiao X, Li Y, Sachdev AK, Park HW, Yu A, Chen Z (2012) *Power Sources* 212:66
179. Zhang H, Song H, Chen X, Zhou J, Zhang H (2012) *Electrochim Acta* 59:160
180. Liu H, Huang J, Li X, Liu J, Zhang YJ (2012) *J Sol-Gel Sci Technol* 63:569
181. Huggins RA (1999) Lithium Alloy Anodes. In: Besenhard JO (ed) *Handbook of battery materials*. Wiley-VCH, Weinheim, Part III, Chapter 4, pp 359
182. Li H, Huang XJ, Chen LQ, Wu ZG, Liang Y (1999) *Electrochem Solid State Lett* 2:547
183. Ren Y, Ding J, Yuan N, Jia S, Qu M, Yu Z (2012) *J Solid State Electrochem* 16:1453
184. Cui LF, Hu L, Choi JW, Cui Y (2010) *ACS Nano* 4:3671
185. Gohier A, Laik B, Kim KH, Maurice JL, Ramos JPP, Cojocar CS, Vakm PT (2012) *Adv Mater* 24:2592
186. Lee J, Bae J, Heo J, Han IT, Cha SN, Kim DK, Yang M, Han HS, Jeon WS, Chung J (2009) *J Electrochem Soc* 156:A905
187. Zhou Z, Xu Y, Hojamberdiev M, Liu W, Wang J (2010) *J Alloys Compd* 507:309
188. Chen S, Chen P, Wang Y (2011) *Nanoscale* 3:4323
189. Zhang J, Xu W, Li X, Liu W (2010) *J Electrochem Soc* 157:A940
190. Zhang GQ, Zheng JP, Liang R, Zhang C, Wang B, Hendrickson M, Plichta EJ (2010) *J Electrochem Soc* 157:A953
191. Li Y, Wang J, Li X, Liu J, Geng D, Yang J, Li R, Sun X (2011) *Electrochem Commun* 13:668

Nanotechnology Advancements on Carbon Nanotube/Polypyrrole Composite Electrodes for Supercapacitors

19

Jayesh Cherusseri, Raghunandan Sharma, and Kamal K. Kar

Contents

1	Introduction	480
1.1	Relevance of Supercapacitor Technology	480
1.2	Nanotechnology for Supercapacitors	482
1.3	Supercapacitor Taxonomy	483
1.4	Nanocomposite Electrodes	485
1.5	Performance Parameters	485
1.6	Supercapacitor Architecture	486
2	Carbon Nanotube Electrodes	489
3	Polypyrrole Synthesis	491
3.1	Chemical	492
3.2	Electrochemical	492
4	Carbon Nanotube/Polypyrrole Nanocomposites	493
4.1	Synthesis of CNT/PPY Composite Electrodes	494
4.2	Supercapacitive Performances of CNT/PPY Composite Electrodes	498
5	Conclusions and Future Perspectives	503
	References	504

Abstract

Supercapacitors are energy boosters for various advanced applications. Carbon nanomaterials based electrochemical double layer capacitors are out-dated due

J. Cherusseri • R. Sharma

Advanced Nanoengineering Materials Laboratory, Materials Science Programme, Indian Institute of Technology Kanpur, Kanpur, India

e-mail: jayesh@iitk.ac.in; raghumsp@iitk.ac.in

K.K. Kar (✉)

Advanced Nanoengineering Materials Laboratory, Materials Science Programme, Indian Institute of Technology Kanpur, Kanpur, India

Advanced Nanoengineering Materials Laboratory, Department of Mechanical Engineering, Indian Institute of Technology Kanpur, Kanpur, India

e-mail: kamalkk@iitk.ac.in

to fewer performances. Redox-type nanocomposite electrodes are promising candidates for high performance supercapacitors. Carbon nanotube/electronically conducting polymer (CNT/ECP) nanocomposite electrodes have achieved much popularity due to their superior electrochemical properties. The nanoscale features of these electrodes have helped to enhance the supercapacitive performance. Among the various CNT/ECP nanocomposites, CNT/polypyrrole nanocomposite electrodes have achieved much importance since they possess high specific capacitance along with high energy density. These electrodes have shown good charge/discharge characteristics along with good environmental and chemical stabilities. Light-weight and flexibility are their added features. These electrodes are very promising candidates for the next generation flexible and wearable electronic devices.

Keywords

Supercapacitor • Energy storage • Carbon nanotubes (CNT) • CNT-electronically conducting polymer composites • Electropolymerization • Cyclic voltammetry • Impedance spectroscopy

1 Introduction

The noteworthy advancements in the field of nanoscience and nanotechnology have paved the way to utilize nanostructured materials for energy applications. This includes energy conversion devices as well as energy storage devices. Among the various energy storage devices, supercapacitors (SCs) have achieved much attention due to their unique capability to deliver high power. Redox type SCs are prepared either from electronically conducting polymers (ECPs) or from metal oxides. Various ECPs such as polypyrrole (PPY), polyaniline (PANI), polythiophenes (PThs), etc have been commonly used. Among the ECPs, PPY has achieved much attention due to its high specific capacitance and power capability. The performance of ECP electrodes-based SCs is restricted by their reduced charge storage ability, low cycling life and poor environmental stability. Hence in order to enhance the performance of ECP electrodes-based SCs, composite electrodes have been fabricated with nanostructured carbon materials. Among the various carbon nanomaterials, carbon nanotubes (CNTs) are prominent in their unique properties, hence they are the common materials used for making composite electrodes for high performance SCs. This chapter briefly reviews the recent developments on nanostructured electrodes based on CNT/PPY nanocomposites for application in high performance SCs.

1.1 Relevance of Supercapacitor Technology

The global energy consumption is increasing day by day and at the same time depletion of fossil fuels is increasing, hence it is very relevant to think about an

alternative solution to resolve the problem rapidly. This high energy consumption is one of the major challenges that our society faces today. Since our resources are limited, it is very difficult to resolve the problem in a single step. As a result, the main focus of present research is towards the use of sustainable, renewable and clean energy resources. One of the several advantages of using renewable resources for energy production is their eco-friendliness, whereas the fossil fuels are extremely harmful to the nature. Due to these reasons, ideas have been put forward towards the development of various renewable energy conversion and energy storage technologies. As we know, since wind energy and solar energy are of intermittent energy resources, it becomes necessary to have powerful energy storage devices coupled with such energy conversion technologies, in order to deliver the power on demand. Batteries and SCs have given much hope to the energy storage industries. These uninterrupted power devices are almost capable to resolve the major problems the electronics and other industries face today. Lithium ion batteries have become much popular for their energy density, but their inability to deliver the stored energy within a fraction of second makes them away from heavy-duty power applications like automobiles. On the other hand, the SCs are high power density devices (of the order of kW/kg) but they can't store the energy as much as the lithium ion batteries can. SCs based energy storage is a very promising technology among the other electrochemical energy storage technologies.

The principle behind the working of SCs has been well studied by the scientists almost 50 years back. One of the first studies in the field of SCs has been carried out by Becker in 1957 [1]. He has filed a patent on the assembly and working of an SC, but no attention has been received by the novel device, due to its lower performance. In early 1960s, researchers have been trying to fabricate SCs but failed to commercializing it due to their technical failure. One of the main reasons of the SCs rejection was the unpopularity when compared with the conventional capacitors and batteries. Of course, dielectric capacitors and batteries were there in the market for more than 100 years at that time. Hence, the industries have denied investing money on SCs by thinking that developing SCs are not good idea. But later on the situation has been changed in such a way that the companies put a long term goal on the research and development of the SCs. The reason of this novel thinking can be related to the fact that the dominant technologies like dielectric capacitors and batteries have not shown any tremendous achievements on those days. The efforts and imagination came true in 1980, when Sohio introduced a double layer capacitor named 'Maxcap' into the market [2].

SCs utilize large surface area electrodes when compared with the conventional capacitors [3]. Hence, SCs exhibit higher capacitance and energy density than that of conventional capacitors. Even though the conventional capacitors possess high power density, they fail when operated for a long duration since the energy density is very poor to meet the requirement. Recent researches on SCs have achieved energy densities comparable to that of lithium ion batteries. Other advantage of SC electrode is that it doesn't undergo any chemical changes during cycling, hence high cycle life and reversibility can be achieved. Again, SCs can operate in a wide temperature window compared to that of batteries. Although the high capital cost

restricts SCs in the market, as the global energy crisis is increasing, still there is a higher demand for SCs with high energy and power densities [4]. SCs are durable for almost 10 years with an efficiency of 95 %. But they have high energy dissipation rate up to 40 % per day [5–7]. In order to cope with the market requirements, SCs have to be improved at its best in terms of energy density and cost.

The applications of SCs can be categorized into three types, such as energy backup, main, and alternating power sources [8]. Power sources such as batteries face some critical problems while in operation such as power turn off, shock, voltage drop, etc. Hence, in energy back up applications, SCs are connected parallel with a main power source to provide energy to the system when the main power supply stops due to some reasons. A large percentage of SCs act as backup devices for the electronics industry. One of the other application lies on the automobile industries as a main power source. For example, SCs are having an energy storage capacity of 75–150 Wh when used in mild hybrid electric vehicles (MHEVs) [9, 10]. SCs have potential to be used in automobiles as they have advantages of comparable energy efficiency, high power density and absorb excess energy from regenerative braking [11]. Commercial SCs manufactured by Maxwell, Saft, CCR, Panasonic, Ness, EPCOS, etc. are widely used for power-assist applications in HEVs [12].

1.2 Nanotechnology for Supercapacitors

SCs are become an attractive research interest in the advanced power systems and other allied sectors due to the recent developments in the field of nanotechnology. Researchers are using various nanotechnology tools for the energy related research and development. The performance of SCs mainly depends on various selection procedures for each individual component. This includes the type of electrode materials and their synthesis procedure, type of electrolyte used, type of separator membrane, etc. SCs especially have benefitted from nanostructured electrodes and membrane electrolytes and therefore utilizing enlarged surface area. The impact of nanoscience and nanotechnology relies on the various research and development (R&D) considerations for the better performance of SCs. Rise in the development of novel nanomaterials has enabled the electrodes to have large surface area to volume ratios. This in turn changes the chemistry of the electrode surface and enables them to provide more effective surface area for the surface reactions. One such kind of electrode is based on the porous carbon nanomaterials that contains not only microporous but also mesoporous structure, which is a pre-requisite for the electrolyte ions to perform fast and reversible reactions as in the case of nanocomposite electrodes. Electrode nanomaterials can have a variety of morphologies such as nanoparticles, nanofibers, nanotubes, etc. The knowledge about nanomaterials synthesis and methods to prepare various types of electrode structures by varying the textures and morphologies enables the SC industry to reach a higher position among the energy storage devices. Tuning of the electrode morphology has not been possible without the knowledge of nanoscience and

technology. A further approach to nanostructured materials involves the development of polymer electrolyte membranes as well as solid polymer electrolytes. The recent research on the synthesis of novel ion permeable membranes and solid polymer electrolytes with nanostructured morphology features has helped the SCs to reduce the internal resistance thereby increasing the conductivity of the ions through the membrane. Hence the membranes with defined features in the nanometer range are intensively under development. Reduction in the electrochemical resistance is one of the major achievements in order to increase the overall performance of the SCs.

1.3 Supercapacitor Taxonomy

SCs (also known as electrochemical capacitors (ECs) or ultracapacitors) are different from the conventional dielectric capacitors in their mechanism of energy storage. The charge/discharge behaviour and other electrochemical performances are determined by how the system stores energy. In the conventional capacitors, energy is stored electrostatically between the two electrodes, whereas in batteries the storage comes as a result of net chemical reaction between electrode and electrolyte [13]. The charge-storage mechanisms in SCs are of two kinds – electrochemical double layer charge storage and pseudocapacitive charge storage. According to this, the SCs are named as (i) electrochemical double layer capacitors (EDLCs), (ii) pseudocapacitors, and (iii) hybrid capacitors.

1.3.1 Electrochemical Double Layer Capacitors

In EDLCs, the electrostatic force of attraction makes the ions to get attracted on the charged electrode surface [14, 15]. While charging, electric charges are accumulated on the either side of electrode/electrolyte interface, which lead to form an electrochemical double layer [16]. The capacitance of an EDL can be calculated by the equation:

$$C = \epsilon_r \epsilon_0 A/d \quad (19.1)$$

Where, ϵ_r is the relative dielectric constant in a double layer, ϵ_0 is the permittivity of free space, A is the electrode surface area and d is the double layer thickness. In the case of EDLCs, the charge stores purely by non-*faradaic* mechanism with no charge transfer across the electrode/electrolyte interface. Hence there is no chemical or compositional change during rapid charge/discharge cycles. Therefore, a very high degree of reversibility and long cycle life can be achieved in EDLCs [17]. EDLCs are commonly making use of porous carbon nanomaterials for their electrode construction. Recent application of EDLCs in Airbus A380 indicates that they are more safe and reliable and also capable for large-scale implementation [4]. Among the various carbon nanomaterials, CNTs are widely accepted as electrode material for EDLCs [18]. The schematic of an EDLC during the charge–discharge process is shown in Fig. 19.1.

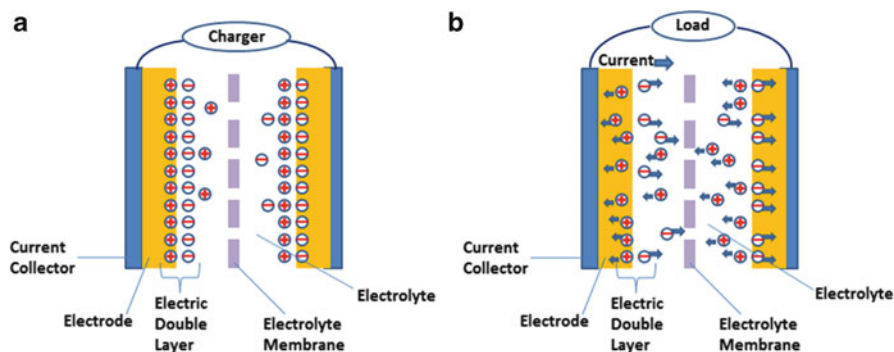


Fig. 19.1 Schematic of EDLCs while (a) charging and (b) discharging

1.3.2 Pseudocapacitors

Pseudocapacitors (otherwise known as redox capacitors) store energy very fast by reversible reactions on the electrode surface [2]. Pseudocapacitors are of *faradaic* type, where the active materials undergo continuous oxidation/reduction reactions during charge–discharge cycles. In the charging step, the electrolyte ions are adsorbed on surface of the electrodes, whereas in the discharging step, the adsorbed ions are desorbed to go back to the solution and the electrons are collected by the external circuit. The maximum number of ions adsorbed on the surface during charging depends mainly on the effective surface area of the electrode material. The electrodes fabricated with pseudocapacitive materials have maximum utilization of surface area and hence the capacitance of pseudocapacitors is higher than that of double layer capacitors [19, 20]. The commonly used active materials for pseudocapacitors are ECPs and transition metal oxides. These materials invariably perform the oxidation/reduction cycles for a long period of time and they can store more energy and are capable to deliver the high power too. Nanostructured ECPs based pseudocapacitors have shown superior performance due to their enhanced pseudocapacitive behaviours and the pseudocapacitive effects are much more prominent at nanoscale dimensions [21, 22].

1.3.3 Hybrid Capacitors

A new type known as ‘hybrid capacitor’ has also developed recently in the field of SCs. This new generation of SCs has received much attention since they are more advantageous than EDLCs and pseudocapacitors. Hybrid capacitor assembly constitutes an EDLC electrode and a battery-type electrode. Hence, they make use of *faradaic* and non-*faradaic* processes for their energy storage. Hence the combined effects have led to a higher performance index. Hybrid capacitors act as coupled energy and power sources and they have waived off the drawbacks of low energy and power densities simultaneously in a single device. Hybrid capacitors can produce larger working voltage and capacitances and they have a longer cycle life too [23, 24]. The energy densities of hybrid capacitors are of several orders

magnitude higher than the conventional SCs. A very important fact to remember in the construction of hybrid capacitors is that the ion exchange rates of both the electrodes (one *faradaic* type and the other battery-type) should have balance for the proper functioning [25]. One example of this kind is the SCs comprising of activated carbon cathode and a conducting polymer anode with many other combinations [26, 27]. This variant in SCs technology targets the next generation electronic and other industries where they require high energy and power densities simultaneously. Hybrid capacitors have washed out the drawbacks of both batteries and SCs and filled the gap between them.

1.4 Nanocomposite Electrodes

Now-a-days composite electrodes are receiving much popularity due to their superior electrochemical performances. Composite electrodes are fabricated by compositing two different kinds of active materials within a single electrode, as the name implies, integrate EDLC electrodes with pseudocapacitive materials. The composite electrodes thus prepared are known as ‘hybrid electrodes’. The very important point to be noted here is that the meaning of ‘hybrid electrodes for SCs’ is entirely different from ‘hybrid SCs utilizing electrodes’. Hybrid electrodes for SCs are prepared by compositing two or three different active materials in to a single electrode (correspondingly they are known as binary hybrids and ternary hybrids, respectively) [28–30]. One example for a binary hybrid electrode is the one fabricated with CNT/PPY composite. The composite electrodes store energy by both the physical as well as chemical means. This ‘two in one’ technology enables the composite electrodes to store more energy than the electrodes with a single active material in it. The composite electrodes have all the advantages of the individual materials and the demerits are abandoned [31, 119].

1.5 Performance Parameters

Two important performance parameters of SCs are (i) energy density and (ii) power density. Energy and power densities are either measured gravimetrically or volumetrically. Energy density refers to the energy stored per mass of the active material in the electrodes (gravimetric energy density) or the energy stored per unit volume of the cell (volumetric energy density). Power density refers to the time rate of energy transfer. The energy density of SCs can be expressed as

$$E = CV^2/2 \quad (19.2)$$

Where, C is the specific capacitance and V is the voltage. Energy density strongly depends on the square of the operable voltage of the SCs; this maximum

operable voltage depends on the type of electrolyte used. The operable limit is low for aqueous electrolytes whereas comparatively high for organic ones. While calculating the specific capacitance, it should be specified whether the capacitance is of the individual electrode or it is of the cell to avoid a possible confusion. The specific capacitances of SCs are generally lower than their individual electrode capacitance, if calculated. The power density can be expressed as

$$P = V^2/4R_s \quad (19.3)$$

Where, R_s is the equivalent series resistance (ESR), V is the initial voltage. The ESR strongly depends on the type of electrolyte used. Aqueous electrolytes offer less specific resistance, which results an increase in power density. On the other hand, the organic electrolytes offer high specific resistance and thus the SCs based on organic electrolytes have lower power density. Thus, the use of different type of electrolytes gives contradictory results for attaining both high energy and power density simultaneously. Thus the selection of proper electrolyte is one of the major challenges that need to be taken care for the better performance of SCs. The energy density of SCs is several orders of magnitude higher than that of a conventional capacitor but lower than that of batteries. But at the same time, the power density of SCs is superior to that of batteries; the low energy density is still a major problem. For short time applications, SCs are the best among others. The developments on the high performance SCs in terms of high energy and power densities and long cycle life are the pre-requisites for using them in the next generation electronic devices.

1.6 Supercapacitor Architecture

The main parts of SCs are the electrodes, current collectors, electrolyte, and separator membrane. Electrodes are having the main features like conductivity, higher surface area, mesoporosity, etc. EDLC electrodes do not undergo any chemical changes while storing the charges. But in pseudocapacitors, since the electrodes being 'electro-active' by nature, take part in the *faradaic*- surface reactions. The electrodes for EDLCs are usually very compact in nature whereas the conducting polymer based pseudocapacitive electrodes are much flexible. The function of current collector is to collect electrons from the electrode. Normally metal plates are employed for this purpose. The two major functions of separator membrane are to permeate the electrolyte ions through it and to avoid the electrodes to be short-circuited. Each component of SCs has a definite role in maintaining their better performance. The role of each component is discussed briefly in the following Section.

1.6.1 Electrode Materials

The proper selection of electrode materials is very important to achieve the best performance of SCs and hence their acceptance in the market. The performance of

both EDLCs and pseudocapacitors is dependent mainly on the electrode material. Nanoscience and nanotechnology has enabled us to synthesize various nanomaterials with tunable features for application in SCs. Nanostructured materials can provide higher specific surface area to the electrode since they have high surface area to volume ratio. Nanomaterials exhibit various attractive properties such as high conductivity, large surface area, good temperature stability, high corrosion resistance, etc. The porosity of the electrode also can be modified by using nanostructured materials. By using high surface area materials like carbon nanomaterials, the electrode specific capacitance can be enhanced. Carbon nanomaterials include CNTs and graphene, which are the rising nanomaterials today for electronic and energy storage devices [32]. The ease of processability of nanomaterials is an important benefit for making the composite architectures. The high compatibility of the nanomaterials with many systems has changed them very attractive candidates for the R&D on advanced composites. One of the other important issues rooted on the electrode materials is the safety. The electrodes of SCs are safer to use for a longer time, whereas major safety issues are arising with batteries [12, 33]. Depending on the utility of the materials in different types of SCs, the materials can be classified as (i) materials utilizing double layer capacitance (ii) materials utilizing pseudocapacitance and (iii) composite materials combining both double layer and pseudocapacitance. A brief outlook can be obtained from the Fig. 19.2.

1.6.2 Electrolyte

The properties of electrolyte have a major role in determining the performance of SCs as the ESR decides the power density. This ESR is a combination of all the resistances in the system. The higher electrolyte resistance lowers power density (from Eq. 19.3). Also the breakdown potential of electrolyte is critical in determining energy density. Various types of electrolytes used are aqueous, organic and ionic liquids. Choice of an electrolyte depends on various parameters like capacitance, resistance and the electrochemically stable potential window [34]. Aqueous electrolytes like acid and alkaline electrolytes offering low specific resistances are widely used in SCs. Aqueous electrolytes are less expensive when compared with organic ones. Organic electrolytes reduce the power density of SCs by offering high specific resistance. Disadvantages of using aqueous electrolytes include their instability at higher voltages and electrode corrosive as well as environment hazardous nature. In case of organic electrolytes, they are stable at higher voltages but still they are also highly toxic and flammable by nature. In aqueous electrolytes, protons with high mobility and small size reduce the resistances whereas large sizes of organic molecules increase the resistances [35]. While using organic electrolytes, it is a pre-requisite to know the pore sizes of the electrode. Energy density of SCs decreases due to 'electrolyte depletion'; this in turn increases resistances of the cell, which leads to a decrease in power density [36]. Hence, aqueous and organic electrolytes have been less preferred for commercial SCs. The preference has been given to a new class of ionic liquids. Ionic liquids have unique properties which are very promising for usage in next generation SCs. High conductivity and

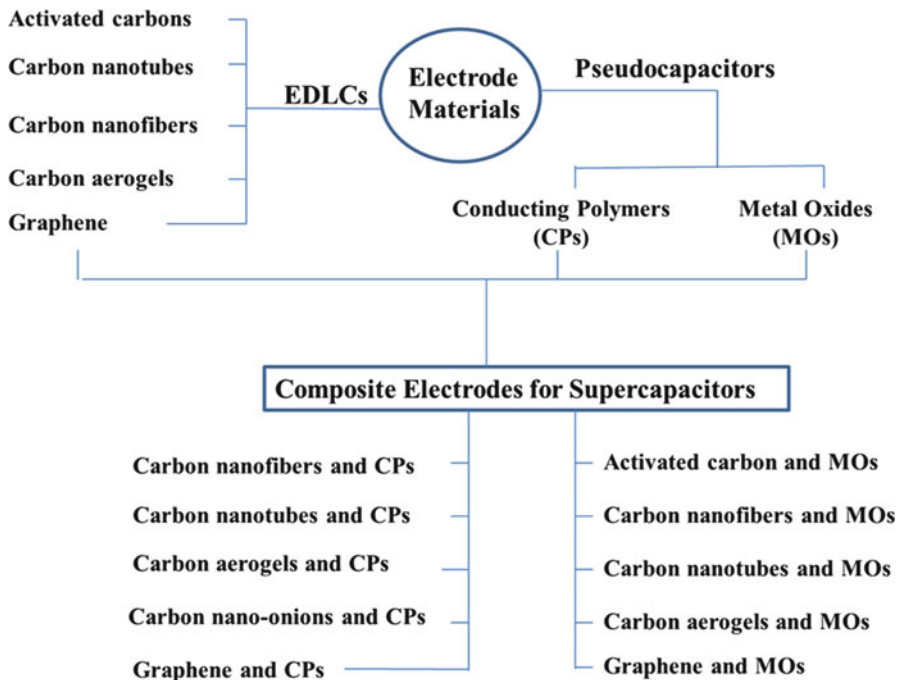


Fig. 19.2 Schematic of various electrode materials for SCs

wide electrochemical window are major advantages of ionic liquids [37]. They are also very safe to handle due to their non-flammable behaviour. The electrolyte depletion crisis can easily be defeated by keeping concentration of ionic liquids very high. A better chemical and environmental stability makes it safe to use the ionic liquids in SCs. Another group of electrolytes named ‘gel polymer electrolytes (GPEs)’ have been arrived and have achieved much popularity due to their specific electrochemical properties [38, 39]. Recent developments on flexible electronics technologies have created plenty of rooms for solid-state flexible SCs. For this purpose, the researchers have developed new kind of electrolytes known as ‘ionic liquid based gel polymer electrolytes (ILGPEs)’. ILGPEs have combined the major advantages of both the ionic liquids and GPEs.

1.6.3 Separator Membranes

The functions of separator membranes in SCs are (i) safe separation of anode and cathode without short-circuiting them, and (ii) allowing easy passage of electrolyte ions through it. Ionic conductivity is the most important property that determines whether the separator membrane is useful in SCs application or not. One commonly used separator membrane is Whatman™ filter paper. Recently, nanostructured polymer electrolyte membranes have been developed successfully. One of such a membrane with high market value is Nafion™. The high ionic conductivity of

Nafion™ membranes due to their invading nano-scale features has lifted them as a promising candidate in SCs. One main drawback of Nafion™ membrane is its high cost. Hence the researchers are trying to develop alternative nanostructured membranes with low cost polymers [40, 41].

1.6.4 Current Collectors

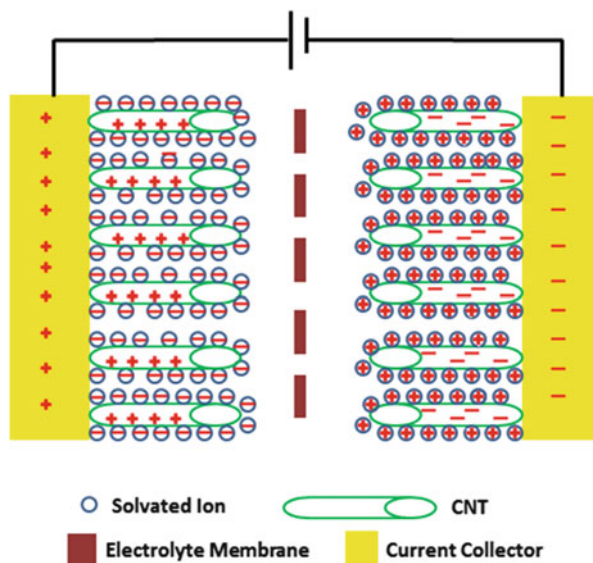
As name implies, the specific function of a current collector is the transportation of electrons from material system to the external load. The commonly used current collectors are metal plates due to their high conductance. Steel plates are also employed for the same purpose. Current collector/electrode interface engineering is very critical since a loss in contact results the system failure.

2 Carbon Nanotube Electrodes

Carbon nanomaterials have been effectively utilized in both EDLCs and in pseudocapacitors. The charge storage mechanism of carbon nanomaterials based electrodes is of non-*faradaic* type i.e. the energy storage mechanism is only by forming electrochemical double layers. For storing huge amount of energy, it is a pre-requisite to have the electrode surface highly porous since the enhancement on the reversible ion adsorption increases the performance of SCs. Not only the porous nature, pore- size distribution is also much important to yield high specific capacitance. The contribution to the ESR by electrode materials varies with their pore size and pore structure. Hence, selection of electrode materials with desired pore-size and pore-size distribution helps to reduce electrode resistance, which in turn increases the supercapacitance [42–44]. Mesoporous electrode materials have been preferred for high capacitance SCs due to their enhanced accessibility of pores with the electrolyte ions. Among the various carbon nanomaterials, CNTs (both single walled carbon nanotubes (SWNTs) and multi walled carbon nanotubes (MWNTs)) have been found to form entangled networks with mesoporous structure and hence become promising candidates as electrode materials in SCs. Schematic of CNT electrodes based EDLC in a fully charged condition is shown in Fig. 19.3.

CNTs based EDLCs have promised higher power density and longer cycle life [45]. Entangled conductive networks of CNTs are promising electrode candidates for storing enormous energy in SCs. The electrode specific capacitance depends mainly on the percentage of maximum accessible pores in the electrode structure and this necessitates higher surface area materials for this purpose. Not only higher surface area materials, high surface area materials with uniform pore structure are preferred. The pore sizes should reside in mesopores (in between micropores (<20 Å) and macropores (>500 Å) for enhanced electrolyte accessibility. This helps in effective and fast ion migrations and successful formation of electrochemical double layers. In case of activated carbons, although they have high surface area, but a large percentage of surface area lies on micropores instead of mesopores and hence, remains unable to support double layers [46]. Very large pore-size leads to increased electrolyte resistance, which in turn decreases the capacitance.

Fig. 19.3 Schematic of a CNTs based EDLC when fully charged



CNTs based SC electrodes outperform other carbon nanomaterials based electrodes due to many specific reasons. CNTs have unique properties like large surface area ($>2,000 \text{ m}^2/\text{g}$), high conductivity, and mesoporous structure [47–49]. The BET surface areas of CNTs have been reported to lie between $1,000$ and $2,500 \text{ m}^2/\text{g}$. CNTs also possess high chemical and thermal stability, percolated pore structure, etc [50, 51]. The interconnected network structure of CNTs is fabulous for their application as electrodes in SCs [52]. The unique mesoporous structure of CNTs combined with high usage efficiency of specific surface areas have changed them inevitable electrode candidates in SCs [46, 53–56]. The porous channels of CNTs are ideal paths for ion transportation with a reduced interfacial resistance [57, 58]. Vertically aligned MWNTs have also been employed in SCs for obtaining higher power density [59]. The presence of impurities on the CNTs reduces the double layer capacitance significantly as in EDLCs [60]. Impurities present on the walls of nanotubes hinder the movement of ions and hence reduce the utilization of available surface adsorption sites. This problem has been resolved by purifying the nanotube bundles. Purified CNTs perform well with orders of magnitude higher than non-purified ones. The reason is that the amount of adsorption sites on CNTs increases with increasing purity and this in turn increases the capacitance.

There are different methods available to attach CNTs on current collector surfaces. This is a very critical step in the preparation of electrodes since internal resistance can either increase or decrease with respect to the type of method opted. One of such method is the ‘transfer method’ in which the nanotubes are attached to the current collector surfaces mechanically [61, 62]. Another method is by opting chemical vapour deposition (CVD) for synthesis of CNTs on catalyst coated metal plates and use them as electrode cum current collector without undergoing any

further treatments (chemical or physical). This is a simple and economically viable method, which promises reduction in their internal resistance with very sharp conductive interfaces. One example for such a CVD technique is CNTs grown on nickel form framework [63]. Many other substrates have also been used as electrode cum current collectors for SCs [50, 64, 65].

One most important advantage of CNT is the possibility of surface functionalization, which has enabled us in tuning the surface chemistry according to our needs. For example, acid treatment on CNTs has been found to have improvement in electron transfer kinetics and enhances the effective adsorption sites [66, 67]. The physical properties of CNTs have been tuned reversibly by various electrochemical charge injection processes [68]. This, along with charge retention in CNT sheets has found to extend the charge-storage intervals even after removal of electrolytes while used in SCs [69]. Oxidative treatment on CNT electrodes have also led to increase in the specific capacitance [28]. Flexible SWNTs films have been widely used for making compact-designed SCs with higher power density [70]. The heat treatment on SWNTs at high temperatures has been found to reduce electrode resistances and hence enhances the capacitance [54]. One another advantage of heat treatment is that it helps to make the pore distribution in between 30 and 50 Å [71]. CNTs implanted-mesoporous carbon spheres have been found to decrease ESR [72].

3 Polypyrrole Synthesis

ECPs are speciality polymers in which their electrical conductivity can be tuned in a wide range from insulators to conductors. The conductivities of ECPs are controlled during the polymerization itself. Incorporation of dopant counter ions in specific concentrations leads to the preparation of highly conductive ECPs. But their low chemical and environmental stabilities and low mechanical strength make them difficult to use in many applications. ECPs with good mechanical and electrical properties have been achieved by making composites with carbon nanomaterials.

Among the various ECPs, PPY has achieved much attention due to their peculiar properties. Hence has found applications in various fields such as energy storage devices, biosensors, electrocatalysts, etc. PPY is a polyconjugated conducting polymer, which has a good electronic conductivity as that of metals. Mechanical and thermal properties of PPY have been found similar to other conventional polymers. A high electronic conductivity has been achieved by doping in the initial polyconjugated polymer. Doping can be done in two ways- (i) p- doping and (ii) n- doping. The type of doping determines the type of charge carriers in the polymer chains, whereas the level of doping determines the electronic conductivity. The easy processability of PPY by various methods such as oxidative chemical polymerization and electrochemical polymerization techniques has increased its importance among the ECPs.

3.1 Chemical

Chemical polymerization is a very simple and flexible method for making PPY as well as PPY composites. PPY prepared by oxidation of pyrrole monomer by various chemical oxidants results in the formation of black powder. Various oxidants such as ferric chloride, ammonium per sulphate, etc. have been widely employed. Various factors, which affect the electronic conductivity and yield are molar ratio of pyrrole/oxidant, type of solvent, temperature, reaction time, etc. Chemical polymerization is a versatile method to make PPY nanostructures [73]. PPY can be deposited on to a wide range of substrates. PPY has been deposited on textile fibers in order to make them electrically conductive textiles [74]. PPY has been coated onto electrospun polyacrylonitrile nanofibers using vapour phase polymerization [75]. The electrospun mats are initially dipped in the oxidant solution and then sent to a chamber containing monomer vapours in an inert atmosphere. PPY/clinoptilolite nanocomposite has been prepared by in-situ surface polymerization using Fe^{3+} as oxidant [76]. Preparation of various polymeric composite membranes based on PPY by oxidative polymerization of pyrrole monomer is a highly accomplished method in the recent research [77–79].

3.2 Electrochemical

Electrochemical synthesis includes electropolymerization of pyrrole monomer in a particular solvent on electrically conductive substrates. There are many advantages of electropolymerization technique over other conventional methods. First of all, a PPY thin film product is attached with the conducting substrate with high conductivity. Secondly, it is possible to control the yield in terms of polymer thickness by varying charge and electropolymerization time. Electrochemical polymerization methods are entirely different from other polymerization methods since here the polymerization is initiated electrochemically [80, 81]. Recent advancements in novel processing methods has enabled facile synthesis of nanostructured PPY such as nanoparticles [82, 83], thin films [84–87], nanotubes [88–90], core/shell nanostructures [91–94], etc. Electrosynthesis of PPY by high frequency ultrasound irradiation has been reported [87]. SEM images of PPY synthesized with and without ultrasonic irradiation are depicted in Fig. 19.4. In both cases, a nodular structure has been observed. A ‘hairy like’ tubular growth has been observed for PPY under silent (5 C/cm^2 deposition) whereas compact PPY film has been observed for PPY sample grown by ultrasound irradiation. Homogeneity in surface structure has been found for both the samples.

Zhang et al. have reported that PPY nanomaterials with tunable morphologies can be achieved by controlling electropolymerization time [95]. The morphology has been controlled in initial stages of electropolymerization itself, since the nucleation process determines the type of PPY nanostructure formed. For a short electropolymerization time, nanodots have been formed. Further extension of

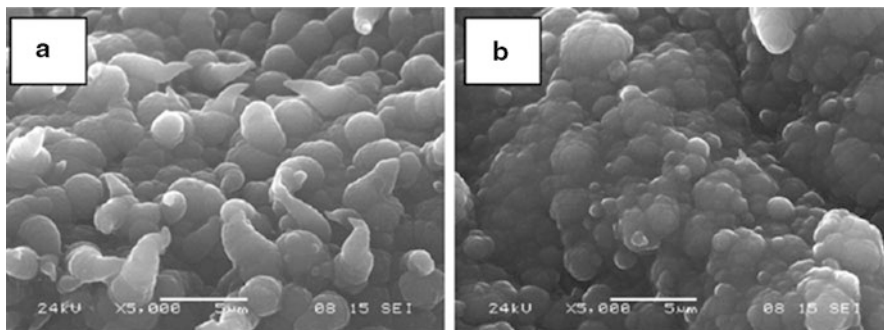


Fig. 19.4 SEM images of PPY/CIO₄⁻ synthesized electrochemically on FTO substrate without (a) and with (b) ultrasound irradiation (Reprinted with permission from [87])

polymerization time has led to a sudden change in the initial nanodot morphology to one-dimensional structures. SEM images of different morphologies of PPY such as nanodots, nanorod arrays, and nanowires are obtained by varying the electropolymerization time, as shown in Fig. 19.5.

4 Carbon Nanotube/Polypyrrole Nanocomposites

In order to increase the performance of SCs based on nanostructured PPY materials, composite electrodes have been fabricated with various carbon nanomaterials. This has led to the preparation of mesoporous carbon/PPY composites [96–99], carbon nanofiber/PPY composites [86, 100–104], graphene/PPY composites [105–109] and CNT/PPY composites. The composite electrodes should have high electrical conductivity, high charge transport capability and possess low ESR. Incorporation of nanostructured PPY materials into three dimensional CNT networks enhances the charge storage ability of SCs. The entangled structure of CNTs in nanocomposite electrodes increases effective surface area, thereby high accessibility to electrolyte ions with active materials. Recent research outcomes have shown that efficient use of nanocomposite electrodes in SCs increases their specific capacitance, energy density and cycle life [110]. Various parameters that determine the performance of electrodes in SCs should be extensively studied before preparing such composites. Superior electrochemical performances of CNT/PPY nanocomposite electrodes have shaped them promising candidates for SCs application. CNT/PPY nanocomposite electrodes comprise both types of charge storage mechanisms- double layer storage from CNTs and pseudo-*faradaic* storage from PPY. CNT/PPY nanocomposite electrode undergoes continuous surface redox reactions thereby improving the energy density of the system. The high reversibility in redox cycles promises PPY to use in CNTs based composite electrodes. Hence CNT/PPY nanocomposite electrodes have improved their capacitance properties than their individual ones.

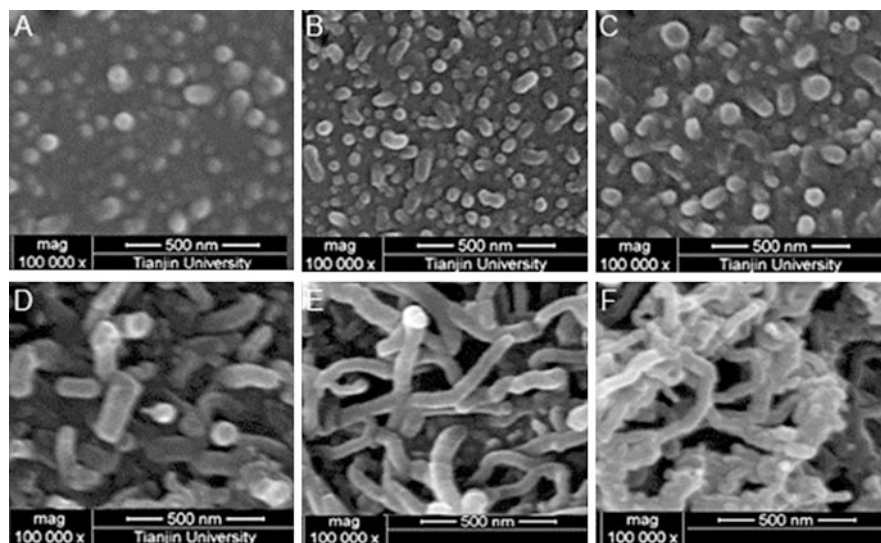


Fig. 19.5 SEM images of PPY nanomaterials formed on graphite rods by varying the electropolymerization time (Reprinted with permissions from [90])

4.1 Synthesis of CNT/PPY Composite Electrodes

Presently, researchers make use of various methods for preparing CNT/PPY composites. This includes in-situ chemical polymerization, electrochemical polymerization, and electrochemical co-deposition, etc. The preparation of nanocomposite electrodes sometimes requires some binders. The selection of binder is very important in the preparation of composite electrodes for SCs, since how binder and the active material surfaces behave in such a combination, will determine the overall performance of SCs. The need of binder is not a pre-requisite for making CNT/PPY electrodes. The ultimate aim of preparing a CNT/PPY composite is to attain high conductivity as well as porous structure in order to achieve superior supercapacitive properties. Various methods for making CNT/PPY nanocomposites are discussed briefly in this Section.

4.1.1 In-Situ Chemical Polymerization

Chemical oxidative polymerization is a very simple and versatile method to make CNT/PPY composites. This method pre-requisites pyrrole monomer to be dispersed in a suspension containing CNTs. SWNTs as well as MWNTs has been used for making composites with PPY with this method. Khomenko and co-workers have prepared composite electrodes prepared with MWNTs and PPY [111]. MWNTs have been synthesized by acetylene decomposition on MgO supports. Cobalt particles have acted as catalyst at a temperature of 600 °C for the growth of CNTs. MWNTs/PPY composite is prepared by chemically polymerizing pyrrole monomer on MWNTs surfaces. The composite electrode prepared by 20 wt%

MWNTs and 80 wt% chemically formed PPY loadings. Mesoporous MWNTs help in the increased charge propagation in the composites. PPY has been uniformly deposited onto MWNTs by in-situ chemical polymerization in a FeCl_3 /methanol/acetonitrile system [112]. It is observed that using FeCl_3 as an oxidant, an easy and quick preparation of MWNTs/PPY nanocomposite is possible in a feasible way. MWNTs/PPY nanocomposite electrodes are prepared by dry mixing MWNTs (80 %), activated carbon (10 %) and PVDF (10 %). A small amount of NMP is added in order to make a homogenous paste. This paste then spreads onto nickel collectors and subsequent pressing and drying leads to final form of the composite. Size-controllable MWNTs/PPY composites have been prepared by using a cationic surfactant, cetyltrimethylammonium bromide (CTAB) [113] where oxidative polymerization is directed by CTAB. MWNTs are synthesized by ethylene CVD with an average diameter of 40 nm and have achieved a purity of 90 % before making the composite. Core/shell tubular structure has been observed for composites with MWNTs core and PPY shell. The thickness of PPY shell varies from 20 to 40 nm and decreases with increasing CTAB concentration. MWCNTs can act as self-assembly hard templates for PPY deposition. MWNTs/PPY hybrid electrodes have been prepared with MWNTs synthesized by spray-pyrolysis method [114]. Aqueous solution containing pyrrole monomer and MWNTs are used for the composite preparation. A very thin layer of PPY is formed after the polymerization. Addition of Fe_3O_4 nanofluid leads to the formation of a new kind of nanostructured hybrid electrode which contains magnetic nanoparticles. A globular form of PPY has been found which makes the PPY coating on MWNTs very rough. High conductivity MWNTs/PPY composites have been prepared with ammoniumperoxodisulfate (APS) as the oxidant and cationic polyelectrolyte poly (styrenesulfonate) (PSS) as the dopant [115]. The fabricated composites have core-shell nanostructured morphology. The addition of PSS decreases the composite thickness from 250 nm to 100–150 nm. In order to improve the cycle life of the PPY based composite electrode, conductive carbons have been added along with MWNTs [116]. The role of adding conductive carbon is mainly to increase the conductivity of the composite electrodes. In an in-situ polymerization using pyrrole precursor and SWNTs as additive components, it is found that the surfaces of SWNTs act as nucleation sites for the growth of PPY [117]. PPY nanostructures can grow on SWNTs and can take different forms such as cylindrical, spherical, etc. Pyrrole treated functionalized-SWNT (*f*-SWNTs) composites have been prepared by Zhou and co-workers [118]. The SWNTs are functionalized with arylsulfonic acid before treating with pyrrole. In a CNT/PPY composite, CNTs play an important role in protecting the composite structure from any mechanical disturbances and also in the distribution of PPY in the composite structure [119]. A very important thing to be noted is that there should be an optimal concentration of CNTs in the composite in order to perform the composite electrodes better. An increase or decrease in the optimal concentration leads to a drastic change in the composite properties. It has been reported that approx. 20 wt% of CNTs is needed in a composite for the best results. Organometallic-*f*-CNTs are also been employed for making PPY based nanocomposites [120]. Initially CNTs are functionalized with organometallic

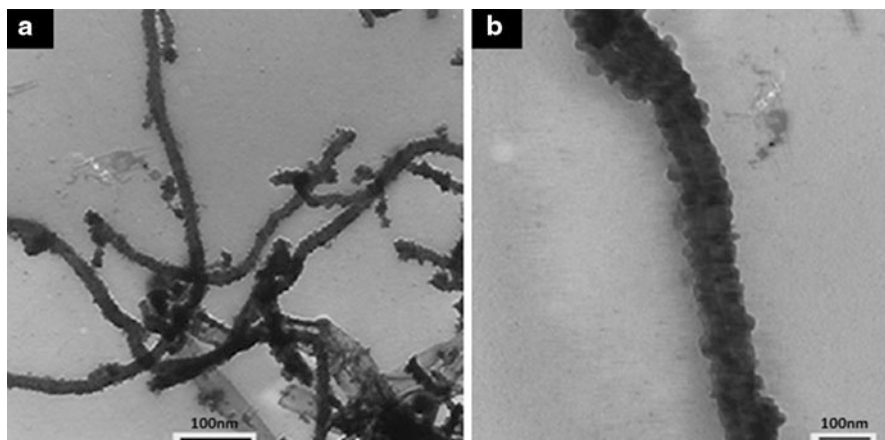


Fig. 19.6 TEM images of organometallic-*f*-CNTs/PPY composite at magnification of $\times 50,000$ (a) and $\times 100,000$ (b) (Reprinted with permissions from [120])

precursors by microwave hydrothermal route. One of such precursor is methyl orange-iron (III) chloride (MO-FeCl₃) complex. The morphology of MO-FeCl₃ complex is found as thorn-like structure. This structure determines what should be the structure after functionalization with CNTs. Obviously, the organometallic-*f*-CNTs also bears the same structure. In this structure, PPY nanoparticles are attached after the polymerization. Granular-like growth of PPY was seen due to the thorn-like shape of oxidative compound present on the surface of the CNTs. TEM images of organometallic-*f*-CNTs/PPY composite are shown in Fig. 19.6. The PPY nanoparticles on CNTs confirmed that Fe³⁺ in the CNTs/MO-FeCl₃ complex has initialized the polymerization reaction. CNT/PPY composites with tunable morphology can be prepared by the same method by altering the organometallic precursor.

Polytetrafluoroethylene (PTFE) is a common binder used for making thin sheets of SWNTs/PPY nanocomposites [80]. Mixing the binder (5 wt%) with SWNT-PPY powder in isopropyl alcohol followed by subsequent kneading and rolling by a bar-coater, leads to the formation of sheet electrodes. SWNTs function as a nanosize backbone for PPY polymerization thereby increase the effective surface area of the composite. Vacuum filtration technique also can be used for the preparation of SWNT sheets and for SWNTs/PPY composite sheet electrodes [121]. This is very versatile technique in which one can prepare surfactant-free composite sheet electrodes. Ceramic fabric has been utilized as a suitable substrate for making CNT/PPY composite [122]. Ceramic fabric can act as a substrate for CNT growth by CVD. PPY can be incorporated to the CNTs grown ceramic fabric by chemical polymerization. CNT/ceramic fabric electrodes have large surface area and high conductivity, which enhances the energy density of the SCs. Also, the chemical and thermal stability of ceramic fabric also helps to have the same features for the composite. The PPY incorporation helps to increase the energy

density by several orders of magnitude. PPY serves as a conductive binder to the CNT/ceramic fabric and also helps in increasing the interfacial adhesion between CNTs and ceramic substrate. PPY provides a low resistive conductive pathway by contacting each individual CNT on the fabric. The CNT arrays have found to deform after PPY addition. PPY coats on CNT arrays uniformly and this helps in the fast diffusion of ions.

4.1.2 Electropolymerization

Electropolymerization of pyrrole monomer on conductive substrates leads to the formation of PPY thin films. Various electrochemical techniques widely used for this purpose are cyclic voltammetry (CV), chronopotentiometry, pulsed amperometry, etc. PPY film thickness can effectively be controlled by increasing the electropolymerization time. The thickness can be increased from nanometers to micrometers. PPY can make composite with CNTs easily with this method. Uniformity in PPY coating on CNTs can be achieved by this method. Hu and co-workers have prepared defective CNTs (*d*-CNTs)/PPY composites [123]. Super-long CNT arrays have been prepared by CVD method. CNTs are converted to *d*-CNTs by CV scanning. By making the CNTs defective, the number of active sites can be increased by several orders of magnitude. These *d*-CNTs act as substrate for PPY deposition. PPY is deposited electrochemically onto the *d*-CNTs surface by using the same CV technique. Fang et al. have used pulsed electrodeposition method for coating PPY on to self-supported MWNTs membranes [124]. Homogeneous coating of PPY has been observed over the surfaces of MWNTs membranes. This method allows electrolyte ions to interact with external as well as internal spaces between the MWNTs. Again, it allows the preparation of self-supported composite electrodes without using any binders. Sharp metal microelectrodes have been used as substrate for CNTs growth [125]. PPY electrodeposited on to the CVD grown CNTs surface make them away from further transfer methods for application.

4.1.3 Co-Electropolymerization

Co-deposition of CNTs and ECPs is a viable method of making CNTs based ECPs composites. By taking CNTs and the monomers of ECPs in a polymerization bath and with the aid of electrochemical techniques, they can be co-deposited on various conductive substrates [126–129]. In a co-electropolymerization bath, CNTs have many functions such as (a) act as charge carriers during deposition; (b) act as a nanostructured scaffold for the ECPs deposition and (c) provide mechanical integrity and three-dimensional nano- porous structure to the composite. Since CNTs have large surface area and porosity, the CNT/ECP composites have improved surface area. This increment in surface area of the composites helps in enhanced redox reactions with the electrolyte ions thereby an improvement in the electrochemical properties of the composite electrodes. Peng and co-workers have used acid treated-CNTs and pyrrole suspension for making CNT/PPY composite electrodes [130]. It has been found that the CNTs in the suspension help in effective charge-balancing. Hughes and co-workers have taken oxidised MWNTs in order to

prepare MWNTs/PPY composite films by an electrochemical route [131]. The surface of MWNTs is functionalized with various groups such as carboxylic, hydroxyl, etc. by oxidizing the MWNTs. This helps in enabling their suspension in various polar solvents. The processability in making interconnected networks through the entire surface is an added advantage while preparing composite with MWNTs. Wang and co-workers have prepared two types of composite electrodes consisting of PPY with SWNTs and with *f*-SWNTs [132]. The composites have been prepared by electropolymerizing pyrrole with raw SWNTs and *f*-SWNTs in a bath containing their homogeneous suspension. The SWNTs are suspended in a concentrated acid solution and subsequent sonication leads to the preparation of *f*-SWNTs. It has been found that the SWNTs are cut during the functionalization process, hence shorter SWNTs coated with PPY is achieved. Mesoporous network of SWNTs have helped to enhance the surface area of the composite electrode and fast charging/discharging behaviours are also observed for the SCs [133]. H₂SO₄/HNO₃ based surface functionalization on SWNTs helps them to improve the capacitance features while making composite with PPY. Pore size of the three dimensional structure of CNTs can be controlled by using sacrificial fillers such as nanosize silica [134]. The size of fillers used in the CNT matrix determines the pore size of the composite structure. Initially nanosize silica is incorporated into the CNTs by electrostatic spray deposition method, then PPY electrochemically deposits on CNT/silica film electrode, and at last the removal of nanosize silica leads to the preparation of a three dimensional porous structured composite electrode. A higher loading of 80 wt% of PPY is achieved with this method. The role of dopants in a composite structure constitutes *f*-SWNTs and PPY has been investigated by Wang and co-workers [135]. Various dopant anions such as Cl⁻, toluenesulfonate (TOS⁻), and dodecylbenzenesulfonate (DBS⁻) are doped with the nanocomposite electrodes. These dopants are incorporated to the nanocomposite structure via electrochemical co-deposition method.

4.2 Supercapacitive Performances of CNT/PPY Composite Electrodes

A very important fact in calculating the specific capacitance of composite electrodes is that a three-electrode cell overestimates the specific capacitance. The actual capacitance of SCs can only be obtained from a two-electrode cell, which gives far lower value compared to that of three electrode cell. Galvanostatic charge/discharge (GCD) provides the actual capacitance of SCs. A synchronicity in specific capacitance calculation comes only when there are comparable values of specific capacitance calculated by both the ways (CV and GCD). Even though the specific capacitance can also be calculated from electrochemical impedance spectroscopy (EIS), this way of determining the capacitance is less preferred due to its complex nature. The pellet electrodes fabricated by MWNTs/PPY composite have been tested by putting in an asymmetric SC cell configuration [111]. Generally, the composite electrodes are mechanically pressed for the preparation of pellet

electrodes for SCs. The GCD study has shown that the MWNTs/PPY electrodes have achieved a specific capacitance of 320 F/g. It has also been found that the specific capacitance varies with the configuration of the cells. In the two electrode cell, the MWNTs/PPY electrode achieves a capacitance of 190 F/g, whereas a maximum of 1,100 F/g has been obtained in a three electrode cell. The MWNTs/PPY composite electrode prepared by using FeCl_3 as the oxidant, where each MWNT plays a role of minute electrode, exhibits increased volumetric energy storage due to their doping-de-doping processes [112]. Asymmetric supercapacitor composed of CNTs/CNTs-PPY electrodes has displayed a capacitance of 72 F/g, whereas at the same time the double layer CNT/CNT SCs exhibit only 21 F/g. The reason of this reduced capacitance of the CNTs/CNTs SC is attributed to the fact that the *faradaic* capacitance always dominates the double layer capacitance. CNT/CNT SCs have shown voltage decay with an increase in time. The specific energies of 1.33 Wh/kg and 0.58 Wh/kg are observed for CNT/CNTs-PPY SCs and for CNT/CNT SCs, respectively. The MWNTs/PPY nanocomposite electrodes prepared with CTAB exhibit two orders of magnitude higher electrical conductivities as compared to the PPY electrode without MWNTs [113]. The room temperature electrical conductivities of MWNTs and PPY have been found to be 200 and 0.1 S/cm, respectively. A small addition of CTAB during the preparation of composite enhances the conductivity from 0.1 to 2.28 S/cm. The effective percolation increases due to the MWNTs and hence the conductivity improves. The addition of dopants has been found to increase the conductivity of the composite electrodes. For instance, addition of dopant such as PSS has been found to increase the conductivity of MWNTs/PPY composite electrode up to a maximum value of 91 S/cm [115]. The main reason of this conductivity increment is that the poly-electrolyte acts as a dopant by incorporating with the PPY structure. Increasing the content of PSS in the composite reduces the thickness of the PPY and hence increases the conductivity. The MWNTs/PPY/conductive carbon electrodes have shown to perform well in terms of both rate capability and cycle life [116]. Addition of conductive carbon increases the specific capacitance. The specific capacitance also gets improved with increasing PPY content in the composite electrode. The CV studies have revealed that the composites are very stable during cycling, which shows good cycleability of the pseudo-*faradaic* reactions. The MWNTs/PPY/conductive carbon composite electrode shows low internal resistance, leading to a relatively high specific capacitance ranging from 200.7 to 238 F/g. Pyrrole treated *f*-SWNTs composite electrodes are very promising for SCs with higher energy and power densities [118]. The composite electrode in 6 M KOH electrolyte has achieved a high value of 350 F/g. This value is shown to be seven times higher than the pristine bucky paper electrode. The double layer capacitance of the electrode is $154 \mu\text{F}/\text{cm}^2$, as calculated according to the BET model. Electrochemical studies of this composite reveals that even macropore surface area of electrode also plays an important role in determining the specific capacitance. The power density and energy density of the composite electrodes have been found to be 4.8 kW/kg, and 3.3 kJ/kg, respectively. In order to increase the operating voltage of SCs, CNT/PPY composite electrode has been used in an asymmetric SC cell

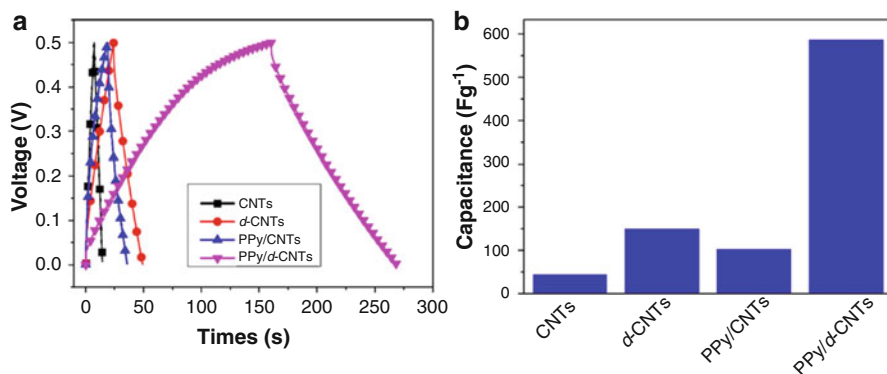


Fig. 19.7 GCD curves of different samples (a) and the specific capacitances calculated from GCD curves (b) (Reprinted with permission from [123])

configuration with CNT/PANI as anode [119]. The SC thus assembled has shown a specific capacitance of 320 F/g. The GCD study has revealed that the SC has cycleability up to 0.6 V. Organometallic-*f*-CNTs/PPY composite electrode prepared by in-situ chemical polymerization has shown very good electrochemical properties with a specific capacitance of 304 F/g in 1 M KCl solution [120]. GCD study performed with a current density of 1 mA/cm² has revealed that the composite electrodes have sharp pseudocapacitive behaviours. SWNTs/PPY composite electrode prepared with PTFE binder with 15 wt% of conductive agent has shown a specific capacitance of 265 F/g [136]. This value is large when compared with the bare SWNT electrodes and pure PPY electrodes. Conducting agents like acetylene black can be added to the composite electrode during their preparation itself. This decreases internal resistances of the composite and enhances the performance of SCs. Organic sulphuric acid-doped PPY has been used for the construction of SWNTs/PPY composite sheet electrodes, which possess a comparatively medium specific capacitance of 131 F/g at a 50 wt% PPY loading [121]. The GCD study reveals that SWNTs/PPY nanocomposite electrodes loaded with 50 wt% PPY possess a largest charge/discharge time duration. An enhancement in electrochemical properties of *d*-CNTs/PPY composite electrodes is observed due to the electrochemical pre-treatment carried out to make the CNTs defective [123]. The *d*-CNTs/PPY electrodes have achieved a maximum capacitance of 587 F/g. The GCD curves and the corresponding specific capacitance calculated for the various electrodes are shown in Fig. 19.7. Except a major enhancement in the capacitance, the defects on CNTs have not shown any undesirable influence on the stabilities of the electrodes.

PPY coated MWNT composite membrane electrodes prepared by pulsed electrodeposition method have shown excellent electrochemical performances [124]. The composite membrane electrode has achieved a specific capacitance of 427 F/g in 1 M Na₂SO₄ at a 5-s electrodeposition pulse. Acid-treated CNT/PPY composite electrode possesses higher conductivity [130]. It has been found that the

Fig. 19.8 Cyclic voltammograms of pristine CNTs (*dotted lines*) and acid-treated CNTs (*solid lines*) in 0.5 mol/L KCl (Reprinted with permission from [130])

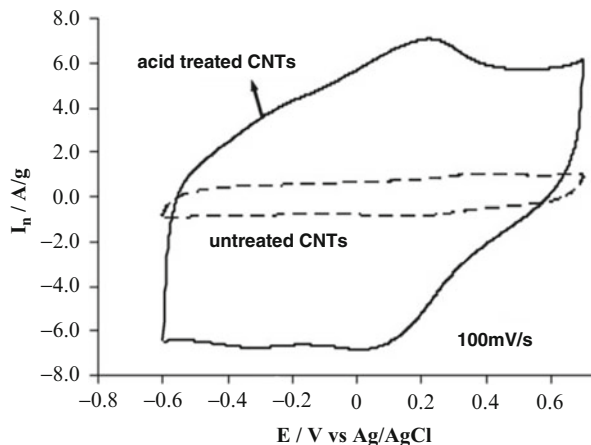
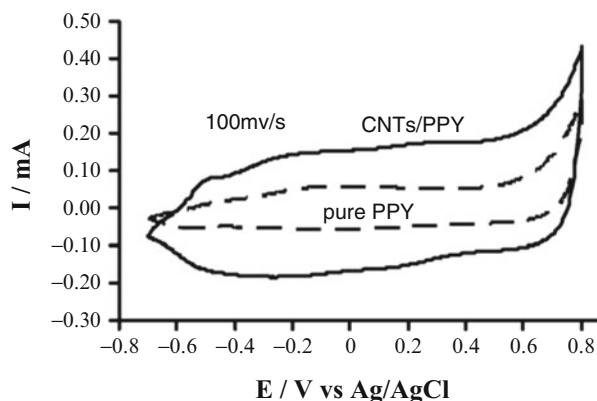


Fig. 19.9 Cyclic voltammograms of pure PPY (*dotted lines*) and CNTs/PPY composite (*solid lines*) in 0.5 mol/L KCl (Reprinted with permission from [130])



specific capacitance of CNT/PPY composite electrode is double than that of the pure PPY electrode. The CV studies of the electrodes showed that pure PPY film electrode exhibit a broad oxidation peak around -0.25 V. The CV studies of pristine CNTs and acid-treated CNT electrodes have revealed coupled oxidation/reduction peaks within a voltage window 0 to 0.2 V as shown in Fig. 19.8. The specific capacitance has been found to be 50 F/g and 10 F/g for the pristine CNTs, and for the acid-treated CNT electrodes, respectively. The CV curves of pristine PPY and CNTs/PPY composite electrodes scanned at a rate of 100 mV/s are shown in Fig. 19.9. It is very clear from the CV curves that PPY has changed from its conductive state to inactive and resistive state, as the currents decreased towards the negative end. While the composite electrode tested in the same potential window, two oxidation peaks (-0.50 V and -0.20 V) have been appeared. In the reduced state of pure PPY film as well as in the CNT/PPY composite film, the chains are not charged. Moreover, the oxidation leads the polymer chains to become positively charged in the case of pure PPY films. Electrical neutrality is maintained in the pure PPY films by the introduction of anions

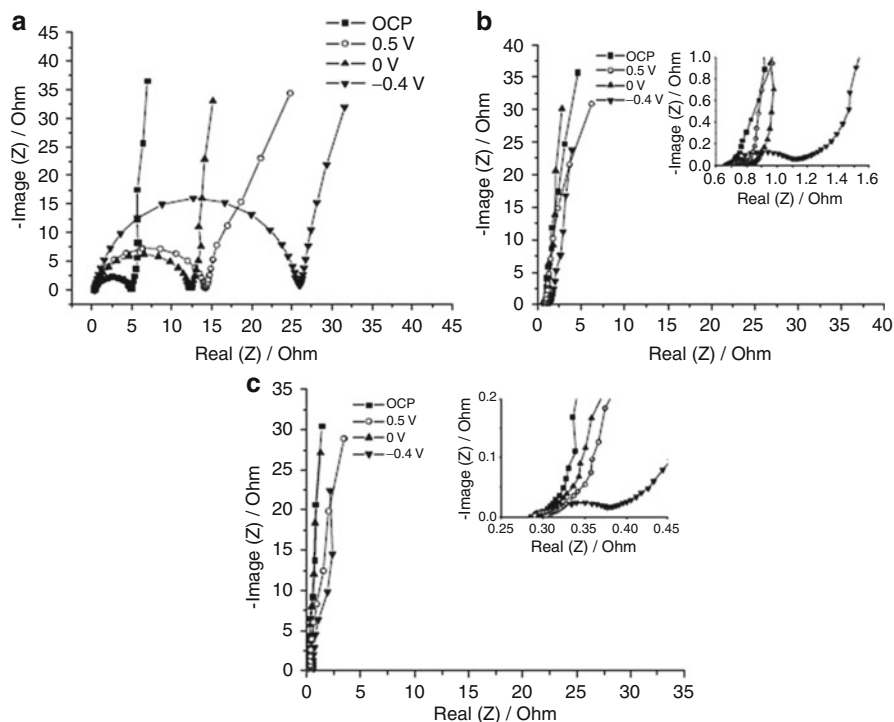


Fig. 19.10 EIS curves of (a) pure PPY, (b) SWNTs/PPY composite, and (c) *f*-SWNTs/PPY composites (Reprinted with permission from [132])

from electrolyte onto the PPY film. On the other hand, this is served by the cations from electrolyte in the case of composite electrode.

Nanoporous MWNTs/PPY composite structures have been found to enhance the electron and ion transfer thereby increasing the conductivities of composite electrodes [131]. The low-frequency capacitance of nanoporous MWNTs/PPY composite electrode is calculated to be 192 F/g and 1 F/cm² (mass specific and area specific capacitance, respectively). The composite SC has shown enhanced rates of charge/discharge when compared with the pure PPY film electrodes. The composite electrodes prepared by PPY with SWNTs and *f*-SWNTs have been found to offer lower resistance, which leads to the specific capacitances of 144 F/g and 200 F/g for SWNTs/PPY and *f*-SWNTs/PPY electrodes at a scan rate of 200 mV/s in 1 M KCl solution [132]. The pure PPY film electrodes experience larger resistance, which affects the specific capacitance in a negative way. The lower specific capacitance of the electrode is attributed to the volume change occurred during the charge/discharge process. In case of *f*-SWNTs/PPY composites, the immobile *f*-SWNTs-doped PPY are able to balance the cations, which causes weakening of ion-transfer polarization process, followed by enhancement of the capacitance. The EIS curves of pure PPY, SWNTs/PPY composite, and *f*-SWNTs/PPY composite films in 1 M KCl solution are shown in Fig. 19.10.

While comparing two SC electrodes consisting of SWNTs/PPY and *f*-SWNTs/PPY, it has been found that *f*-SWNTs/PPY electrodes have higher specific capacitance (243 F/g) than non-functionalized ones, which is almost true in most of the cases [133]. The reason is that the functionalized electrodes have low charge transfer resistance, which facilitates the kinetics of the ions in the electrolyte. The composite electrode fabricated by CNT/PPY using nanosized silica possesses a specific capacitance of 250 F/g at a scan rate of 10 mV/s [134]. It has been found that heavy loading of PPY in the composite leads to an increase in the rate capability of the SCs. Around 80 wt% of PPY is loaded with CNTs which has changed the electrode morphology and hence an enhancement in specific capacitance is observed. It has been observed that dopant anions of PPY affect both morphology and capacitance characteristics of the *f*-SWNTs/PPY nanocomposites [135]. The highest mass specific capacitance has been obtained for the one which doped with Cl⁻; lowest capacitance for the one doped with DBS⁻. The reason for this change in capacitance is the large size of dopant anion incorporated with the PPY matrix. This lowers the anion exchange during charging and discharging. It is evident that low level doping in PPY composites results in lowering the specific capacitance. The size of the dopant ions as well as the density of defects determines the specific capacitance in a doped nanocomposite electrode comprising SWNTs and PPY. The nanocomposite electrodes doped with TOS⁻ has shown faster charge/discharge behaviour than the one doped with Cl⁻.

5 Conclusions and Future Perspectives

Renewable energy technologies like solar energy technology and wind energy technology are suffering from their intermittent nature of the power conversion and hence not helpful to fulfil the energy need that we face today. Solar technology fails not only in the nights as well as when light intensity becomes very low. Fuel cell technology has been developed in order to avoid the demerits of solar and wind technologies. Fuel cells are capable to deliver power all the time if the inputs are consistent. But the major drawback of fuel cells is their high initial cost. Hence there exists an importance of energy storage technologies like batteries and supercapacitors. These energy storage technologies fill the gap between energy conversion technologies and consumption. Energy storage devices can store the energy from any of the sources and are capable to deliver the power on demand. Battery technology becomes very popular, but still there are lot many drawbacks that have to be rectified. SCs have a distinguishable role in the power industry. SCs are superior to conventional capacitors in terms of higher energy density, whereas higher power density has lifted them superior among the batteries. Energy conversion technologies individually can't resolve the energy crisis. Hence coupling the two technologies— conversion and storage, only gives a better solution for the future energy challenges. For example, SCs couple with energy conversion devices such as fuel cells/solar cells/thermo electric devices, etc.

ECPs based flexible SCs are very promising candidates for future energy storage devices. The availability and low cost of these materials results in the development of low cost, high efficiency SCs. CNTs are inevitable part of making ECPs based composite electrodes for energy application due to their high electrical conductivity, entangled three dimensional structure, mesoporosity, etc. Among the CNT/ECPs based composite electrodes, CNT/PPY has received much attention due to their superior performance. CNT/PPY composite electrodes can be prepared by several methods such as in-situ chemical polymerization method, co-electrochemical deposition method, etc. CNT/PPY nanocomposite electrodes possess excellent electrochemical properties. The mesoporous structure of composite electrodes gives rise to an enhancement in the specific capacitance as well as in the energy and power densities. CNT/PPY composite electrodes based SCs are very promising for future flexible and reliable electronics technologies. Composite SCs are capable to deliver high power and hence are promising candidates for HEVs. SC technology has to travel more miles in order to overcome the technical difficulties and challenges for the practical applicability of technology and hence their social acceptance world-wide.

Acknowledgment The authors acknowledge the financial support provided by Indian Space Research Organization, India for carrying out this work.

References

1. Becker HI (1957) Low voltage electrolytic capacitor US2800616, USA
2. Boos DL (1970) Electrolytic capacitor having carbon paste electrodes US3536963, USA
3. Arico AS, Bruce P, Scrosati B, Tarascon J-M, van Schalkwijk W (2005) Nanostructured materials for advanced energy conversion and storage devices. *Nat Mater* 4:366
4. Simon P, Gogotsi Y (2008) Materials for electrochemical capacitors. *Nat Mater* 7:845
5. Schainker RB (2004) Executive overview: energy storage options for a sustainable energy future. IEEE PES General Meeting, Palo Alto, USA, Vol. 2, pp.2309–2314
6. Ibrahim H, Ilinca A, Perron J (2008) Energy storage systems characteristics and comparisons. *Renew Sust Energ Rev* 12:1221
7. Hadjipaschalis I, Poullikkas A, Efthimiou V (2009) Overview of current and future energy storage technologies for electric power applications. *Renew Sust Energ Rev* 13:1513
8. Murphy TC, Wright RB (1997) Electrochemical capacitors II. In: *Proceedings of the electrochemical society proceedings series*, vol 96–25, Pennington, p 258
9. Lam LT, Louey R (2006) Development of ultra-battery for hybrid-electric vehicle applications. *J Power Sources* 158:1140
10. Burke AF (2007) Batteries and ultracapacitors for electric, hybrid, and fuel cell vehicles. *Proc IEEE* 95:806
11. Thounthong P, Rael S, Davat B (2009) Energy management of fuel cell/battery/supercapacitor hybrid power source for vehicle applications. *J Power Sources* 193:376
12. Chu A, Braatz P (2002) Comparison of commercial supercapacitors and high-power lithium-ion batteries for power-assist applications in hybrid electric vehicles I. Initial characterization. *J Power Sources* 112:236
13. Pandolfo AG, Hollenkamp AF (2006) Carbon properties and their role in supercapacitors. *J Power Sources* 157:11

14. Conway BE (1991) Transition from supercapacitor to battery behaviour in electrochemical energy storage. *J Electrochem Soc* 138:1539
15. Conway B (1999) *Electrochemical supercapacitors: scientific fundamentals and technological applications (POD)*. Kluwer Academic/Plenum, New York
16. Burke A (2000) Ultracapacitors: why, how, and where is the technology. *J Power Sources* 91:37
17. Du C, Pan N (2006) High power density supercapacitor electrodes of carbon nanotube films by electrophoretic deposition. *Nanotechnology* 17:5314
18. Wang G, Ling Y, Qian F, Yang X, Liu X-X, Li Y (2011) Enhanced capacitance in partially exfoliated multi-walled carbon nanotubes. *J Power Sources* 196:5209
19. Shukla AK, Sampath S, Vijayamohan K (2000) Electrochemical supercapacitors: energy storage beyond batteries. *Curr Sci* 79:1656
20. Zhang Y, Feng H, Wu X, Wang L, Zhang A, Xia T, Dong H, Li X, Zhang L (2009) Progress of electrochemical capacitor electrode material. *Int J Hydrogen Energ* 34:4889
21. Jamnik J, Maier J (2003) Nanocrystallinity effects in lithium battery materials aspects of nano-ionics part IV. *Phys Chem Chem Phys* 5:5215
22. Balaya P, Bhattacharyya AJ, Jamnik J, Zhukovskii YF, Kotomin EA, Maier J (2006) Nanoionics in the context of lithium batteries. *J Power Sources* 159:171
23. Cottineau T, Toupin M, Delahaye T, Brousse T, Belanger D (2006) Nanostructured transition metal oxides for aqueous hybrid electrochemical supercapacitors. *Appl Phys A* 82:599
24. Naoi K, Simon P (2008) New materials and new configurations for advanced electrochemical capacitors. *J Electrochem Soc* 17:34
25. Naoi K, Naoi W, Aoyagi S, Miyamoto J-I, Kamino T (2013) New generation nanohybrid supercapacitor. *Acc Chem Res* 46:1075
26. Du PA, Plitz I, Menocal S, Amatucci G (2003) A comparative study of Li-ion battery, supercapacitor and non-aqueous asymmetric hybrid devices for automotive applications. *J Power Sources* 115:171
27. Li H, Cheng L, Xia Y (2005) A hybrid electrochemical supercapacitor based on a 5V Li-ion battery cathode and active carbon. *Electrochem Solid State Lett* 8:A433
28. Frackowiak E, Jurewicz K, Delpeux S, Béguin F (2001) Nanotubular materials for supercapacitors. *J Power Sources* 97–98:822
29. Mastragostino M, Arbizzani C, Soavi F (2002) Conducting polymers as electrode materials in supercapacitors. *Solid State Ion* 148:493
30. Laforgue A, Simon P, Fauvarque JF, Mastragostino M, Soavi F, Sarrau JF, Lailler P, Conte M, Rossi E, Saguatti S (2003) Activated carbon/conducting polymer hybrid supercapacitors. *J Electrochem Soc* 150:A645
31. Jurewicz K, Delpeux S, Bertagna V, Béguin F, Frackowiak E (2001) Supercapacitors from nanotubes/polypyrrole composites. *Chem Phys Lett* 347:36
32. Li J, Cheng X, Shashurin A, Keidar M (2012) Review of Electrochemical capacitors based on carbon nanotubes and graphene. *Graphene* 1:1
33. Miller JR, Burke AF (2008) Electrochemical capacitors: challenges and opportunities for real-world applications. *Electrochem Soc Interface* 17:53
34. Tanahashi I, Yoshida A, Nishino A (1990) Comparison of the electrochemical properties of electric double-layer capacitors with an aqueous electrolyte and with a non-aqueous electrolyte. *Bull Chem Soc Jpn* 63:3611
35. Fic K, Lota G, Frackowiak E (2010) Electrochemical properties of supercapacitors operating in aqueous electrolyte with surfactants. *Electrochim Acta* 55:7484
36. Zheng JP, Huang J, Jow TR (1997) The limitations of energy density for electrochemical capacitors. *J Electrochem Soc* 144:2026
37. Buzzeo MC, Evans RG, Compton RG (2004) Non-haloaluminate room-temperature ionic liquids in electrochemistry – A review. *Chem Phys Chem* 5:1106
38. Song JY, Wang YY, Wan CC (1999) Review of gel-type polymer electrolytes for lithium-ion batteries. *J Power Sources* 77:183

39. Ciuffa F, Croce F, DEpifanio A, Panero S, Scrosati B (2004) Lithium and proton conducting gel-type membranes. *J Power Sources* 127:53
40. Cornet FN, Geble G, Mercier R, Pineri M, Sillion B (1997) In: Savogado O, Roberge PR (eds) *New materials for fuel cell and modern battery systems II*. Ecole Polytechnique de Montreal, Montreal, p 818
41. Steck AE, Stone C (1997) In: Savogado O, (Ed.) *New materials for fuel cell and modern battery systems II*. Ecole Polytechnique de Montreal, Montreal
42. Endo M, Kim YJ, Takeda T, Maeda T, Hayashi T, Koshiba K, Hara H, Dresselhaus MS (2001) Poly(vinylidene chloride)-based carbon as an electrode material for high power capacitors with an aqueous electrolyte. *J Electrochem Soc* 148:A1135
43. Shiraishi S, Kurihara H, Tsubota H, Oya A, Soneda Y, Yamada Y (2001) Electric double layer capacitance of highly porous carbon derived from lithium metal and polytetrafluoroethylene. *Electrochem Solid State Lett* 4:A5
44. Weng TC, Teng H (2001) Characterization of high porosity carbon electrodes derived from mesophase pitch for electric double-layer capacitors. *J Electrochem Soc* 148:A368
45. Kotz R, Carlen M (2000) Principles and applications of electrochemical capacitors. *Electrochim Acta* 45:2483
46. Niu C, Sichel EK, Hoch R, Moy D, Tennent H (1997) High power electrochemical capacitors based on carbon nanotube electrodes. *Appl Phys Lett* 70:1480
47. Dresselhaus MS, Dresselhaus G, Eklund PC (1996) *Science of fullerenes and carbon nanotubes: their properties and applications*. Academic Press, San Diego
48. Baughman RH, Zakhidov AA, de Heer WA (2002) Carbon nanotubes - the route towards applications. *Science* 297:787
49. Frackowiak E, Jurewicz K, Szostak K, Delpeux S, Beguin F (2002) Nanotubular materials as electrodes for supercapacitors. *Fuel Process Technol* 77–78:213
50. Emmenegger C, Mauron P, Züttel A, Nützenadel C, Schneuwly A, Gally R, Schlapbach L (2000) Carbon nanotube synthesized on metallic substrates. *Appl Surf Sci* 162–163:452
51. Chatterjee AK, Sharon M, Banerjee R, Neumann-Spallart M (2003) CVD synthesis of carbon nanotubes using a finely dispersed cobalt catalyst and their use in double layer electrochemical capacitors. *Electrochim Acta* 48:3439
52. Frackowiak E, Metenier K, Bertagna V, Beguin F (2000) Supercapacitor electrodes from multiwalled carbon nanotubes. *Appl Phys Lett* 77:2421
53. Diederich L, Barborini E, Piseri P, Podesta A, Milani P, Schneuwly A, Gally R (1999) Supercapacitors based on nanostructured carbon electrodes grown by cluster-beam deposition. *Appl Phys Lett* 75:2662
54. An KH, Kim WS, Park YS, Choi YC, Lee SM, Chung DC, Bae DJ, Lim SC, Lee YH (2001) Supercapacitors using single-walled carbon nanotube electrodes. *Adv Mater* 13:497
55. Hasobe T, Fukuzumi S, Kamat PV (2006) Stacked-cup carbon nanotubes for photo-electrochemical solar Cells. *Angew Chem Int Ed* 45:755
56. Miller AJ, Hatton RA, Silva SRP (2006) Interpenetrating multiwall carbon nanotubes electrodes for organic solar cells. *Appl Phys Lett* 89:133117
57. Hinds BJ, Chopra N, Rantell T, Andrews R, Gavalas V, Bachas LG (2004) Aligned multiwalled carbon nanotube membranes. *Science* 303:62
58. Majumder M, Chopra N, Andrews R, Hinds BJ (2005) Nanoscale hydrodynamics: Enhanced flow in carbon nanotubes. *Nature* 438:44
59. Pushparaj VL, Shaijumon MM, Kumar A, Murugesan S, Ci L, Vajtai R, Linhardt RJ, Nalamsu O, Ajayan PM (2007) Flexible energy storage devices based on nanocomposite paper. *Proc Natl Acad Sci* 104:13574
60. Frackowiak E, Bcguin F (2002) Electrochemical storage of energy in carbon nanotubes and nanostructured carbons. *Carbon* 40:1775
61. Zhang H, Cao GP, Yang YS (2007) Using a cut-paste method to prepare a carbon nanotube fur electrode. *Nanotechnology* 18:195607

62. Liu CG, Liu M, Li F, Cheng HM (2008) Frequency response characteristic of single-walled carbon nanotubes as supercapacitor electrode material. *Appl Phys Lett* 92:143108
63. Shi R, Jiang L, Pan C (2011) A single-step process for preparing supercapacitor electrodes from carbon nanotubes. *Soft Nanosci Lett* 1:11
64. Park D, Kim YH, Lee JK (2003) Synthesis of carbon nanotubes on metallic substrates by a sequential combination of PECVD and thermal CVD. *Carbon* 41:1025
65. Zhang H, Cao GP, Wang ZY, Yang YS, Gu ZN (2008) Electrochemical capacitive properties of carbon nanotube arrays directly grown on glassy carbon and tantalum foils. *Carbon* 46:822
66. Papakonstantinou P, Kern R, Robinson L, Murphy H, Irvine J, McAdams E, McLaughlin J, McNally T (2005) Fundamental electrochemical properties of carbon nanotube electrodes. Fullerenes, nanotubes. *Carbon Nanostruct* 13:91
67. Boyea JM, Camacho RE, Turano SP, Ready WJ (2007) Carbon nanotube-based supercapacitors: Technologies and markets. *Nanotech L and Bus* 4:19
68. Baughman RH, Cui C, Zakhidov AA, Iqbal Z, Barisci JN, Spinks GM, Wallace GG, Mazzoldi A, De Rossi D, Rinzler AG, Jaschinski O, Roth S, Kertesz M (1999) Carbon nanotube actuators. *Science* 284:1340
69. Zakhidov AA, Suh D-S, Kuznetsov AA, Barisci JN, Muñoz E, Dalton AB, Collins S, Ebron VH, Zhang M, Ferraris JP, Zakhidov AA, Baughman RH (2009) Electrochemically tuned properties for electrolyte-free carbon nanotube sheets. *Adv Funct Mater* 19:2266
70. Niu Z, Zhou W, Chen J, Feng G, Li H, Ma W, Li J, Dong H, Ren Y, Zhao D, Xie S (2011) Compact-designed supercapacitors using free-standing single-walled carbon nanotube films. *Energy Environ Sci* 4:1440
71. An KH, Kim WS, Park YS, Moon JM, Bae DJ, Lim SC, Lee YS, Lee YH (2001) Electrochemical properties of high-Power supercapacitors using single-walled carbon nanotube electrodes. *Adv Funct Mater* 11:387
72. Yi B, Chen X, Guo K, Xu L, Chen C, Yan H, Chen J (2011) High-performance carbon nanotube-implanted mesoporous carbon spheres for supercapacitors with low series resistance. *Mater Res Bull* 46:2168
73. Yang C, Liu P (2010) Water-dispersed polypyrrole nanospheres via chemical oxidative polymerization in the presence of castor oil sulfate. *Synth Met* 160:345
74. Kaynak A, Wang L, Hurren C, Wang X (2002) Characterization of conductive polypyrrole coated wool yarns. *Fiber Polym* 3:24
75. Laforgue A, Robitaille L (2010) Deposition of ultrathin coatings of polypyrrole and poly(3,4-ethylenedioxythiophene) onto electrospun nanofibers using a vapor-phase polymerization method. *Chem Mater* 22:2474
76. Rashidzadeh A, Olad A, Ahmadi S (2013) Preparation and characterization of polypyrrole/clinoptilolite nanocomposite with enhanced electrical conductivity by surface polymerization method. *Polym Eng Sci* 53:970
77. Jiang L, Jun H-K, Hoh Y-S, Lim JO, Lee D-D, Huh J-S (2005) Sensing characteristics of polypyrrole-poly(vinyl alcohol) methanol sensors prepared by in situ vapor state polymerization. *Sens Actuator B* 105:132
78. Yin Z, Zheng Q (2012) Controlled synthesis and energy applications of one-dimensional conducting polymer nanostructures: An overview. *Adv Energy Mater* 2:179
79. Shi Z, Phillips GO, Yang G (2013) Nanocellulose electroconductive composites. *Nanoscale* 5:3194
80. Diaz AF, Kanazawa KK, Gardini GP (1979) Electrochemical polymerization of pyrrole. *J Chem Soc Chem Commun* 635, doi:10.1039/c39790000635
81. Kanazawa KK, Diaz AF, Geiss RH, Gill WD, Kwak JF, Logan JA, Rabolt JF, Street GB (1979) 'Organic metals': polypyrrole, a stable synthetic 'metallic' polymer. *J Chem Soc Chem Commun* 854, doi:10.1039/c39790000854
82. Goel S, Gupta A, Singh KP, Mehrotra R, Kandpal HC, Srikanth K (2006) Structural and optical studies of polypyrrole nanostructures. *Int J Appl Chem* 2:157-158

83. Liu Y, Chu Y, Yang L (2006) Adjusting the inner-structure of polypyrrole nanoparticles through microemulsion polymerization. *Mater Chem Phys* 98:304
84. Ehrenbeck C, Jüttner K (1996) Ion conductivity and permselectivity measurements of polypyrrole membranes at variable states of oxidation. *Electrochim Acta* 41:1815
85. Arrieta Almarino AA, Vieira RL (2006) Study of polypyrrole films modified with copper and silver microparticles by electrochemical cementation process. *J Chil Chem Soc* 51:971
86. Sharma AK, Kim JH, Lee YS (2009) An efficient synthesis of polypyrrole/carbon fiber composite nano-thin films. *Int J Electrochem Sci* 4:1560
87. Et Taouil A, Lallemand F, Hihn J-Y, Hallez L, Moutarlier V, Blondeau-Patissier V (2011) Relation between structure and ions mobility in polypyrrole electrothesized under high frequency ultrasound irradiation. *Electrochim Acta* 58:67
88. Jang J, Oh JH (2004) A facile synthesis of polypyrrole nanotubes using a template-mediated vapor deposition polymerization and the conversion to carbon nanotubes. *Chem Commun* 882, doi:10.1039/b316083a
89. Yang X, Dai T, Zhu Z, Lu Y (2007) Electrochemical synthesis of functional polypyrrole nanotubes via a self-assembly process. *Polymer* 48:4021
90. Zhang H, Wang J, Shan Q, Wang Z, Wang S (2013) Tunable electrode morphology used for high performance supercapacitor: polypyrrole nanomaterials as model materials. *Electrochim Acta* 90:535
91. Selvan ST, Spatz JP, Klok H-A, Möller M (1998) Gold-polypyrrole core-shell particles in diblock copolymer micelles. *Adv Mater* 10:132
92. Hao L, Zhu C, Chen C, Kang P, Hu Y, Fan W, Chen Z (2003) Fabrication of silica core-conductive polymer polypyrrole shell composite particles and polypyrrole capsule on monodispersed silica templates. *Synth Met* 139:391
93. Mi H, Zhang X, Ye X, Yang S (2008) Preparation and enhanced capacitance of core-shell polypyrrole/polyaniline composite electrode for supercapacitors. *J Power Sources* 176:403
94. Xing S, Tan LH, Chen T, Yang Y, Chen H (2009) Facile fabrication of triple-layer (Au@Ag)@polypyrrole core-shell and (Au@H₂O)@polypyrrole yolk-shell nanostructures. *Chem Commun* 1653, doi:10.1039/b821125f
95. Zhang J, Liu X, Zhang L, Cao B, Wu S (2013) Reactive template synthesis of polypyrrole nanotubes for fabricating metal/conducting polymer nanocomposites. *Macromol Rapid Commun* 34:528
96. Choi M, Lim B, Jang J (2008) Synthesis of mesostructured conducting polymer-carbon nanocomposites and their electrochemical performance. *Macromol Res* 16:200, doi:10.1039/b821125f
97. Faye A, Dione G, Dieng MM, Aaron JJ, Cachet H, Cachet C (2010) Usefulness of a composite electrode with a carbon surface modified by electrothesized polypyrrole for supercapacitor applications. *J Appl Electrochem* 40:1925
98. Zhang J, Kong L-B, Cai J-J, Luo Y-C, Kang L (2010) Nano-composite of polypyrrole/modified mesoporous carbon for electrochemical capacitor application. *Electrochim Acta* 55:8067
99. Pacheco-Catalan CDE, Smit MA, Morales E (2011) Characterization of composite mesoporous carbon/conducting polymer electrodes prepared by chemical oxidation of gas-phase absorbed monomer for electrochemical capacitors. *Int J Electrochem Sci* 6:78
100. Wood GA, Iroh JO (1996) Efficiency of electropolymerization of pyrrole onto carbon fibers. *Synth Met* 80:73
101. Lin B, Sureshkumar R, Kardos JL (2001) Electropolymerization of pyrrole on PAN-based carbon fibers: experimental observations and a multiscale modeling approach. *Chem Eng Sci* 56:6563
102. Fletcher BL, McKnight TE, Fowlkes JD, Allison DP, Simpson ML, Doktycz MJ (2007) Controlling the dimensions of carbon nanofiber structures through the electropolymerization of pyrrole. *Synth Met* 157:282

103. Dumanlı A, Erden A, Yürüm Y (2012) Development of supercapacitor active composites by electrochemical deposition of polypyrrole on carbon nanofibres. *Polym Bull* 68:1395
104. Davoglio RA, Biaggio SR, Bocchi N, Rocha-Filho RC (2013) Flexible and high surface area composites of carbon fiber, polypyrrole, and poly(DMcT) for supercapacitor electrodes. *Electrochim Acta* 93:93
105. Biswas S, Drzal LT (2010) Multilayered nanoarchitecture of graphene nanosheets and polypyrrole nanowires for high performance supercapacitor electrodes. *Chem Mater* 22:5667
106. Zhang LL, Zhao S, Tian XN, Zhao XS (2010) Layered graphene oxide nanostructures with sandwiched conducting polymers as supercapacitor electrodes. *Langmuir* 26:17624
107. Bose S, Kim NH, Kuila T, Lau KT, Lee JH (2011) Electrochemical performance of a graphene-polypyrrole nanocomposite as a supercapacitor electrode. *Nanotechnology* 22:295202
108. Davies A, Audette P, Farrow B, Hassan F, Chen Z, Choi J-Y, Yu A (2011) Graphene-based flexible supercapacitors: pulse-electropolymerization of polypyrrole on free-standing graphene films. *J Phys Chem C* 115:17612
109. Li L, Xia K, Li L, Shang S, Guo Q, Yan G (2012) Fabrication and characterization of free-standing polypyrrole/graphene oxide nanocomposite paper. *J Nanopart Res* 14:1
110. Sahoo S, Karthikeyan G, Nayak GC, Das CK (2011) Electrochemical characterization of in situ polypyrrole coated graphene nanocomposites. *Synth Met* 161:1713
111. Khomenko V, Frackowiak E, Béguin F (2005) Determination of the specific capacitance of conducting polymer/nanotubes composite electrodes using different cell configurations. *Electrochim Acta* 50:2499
112. Xiao Q, Zhou X (2003) The study of multiwalled carbon nanotube deposited with conducting polymer for supercapacitor. *Electrochim Acta* 48:575
113. Wu TM, Lin SH (2006) Synthesis, characterization, and electrical properties of polypyrrole/multiwalled carbon nanotube composites. *J Polym Sci Pol Chem* 44:6449
114. Turcu R, Darabont A, Nan A, Aldea N, Macovei D, Bica D, Vekas L, Pana O, Soran M, Koos A (2006) New polypyrrole-multiwall carbon nanotubes hybrid materials. *J Optoelectron Adv Mater* 8:643
115. Wu T-M, Chang H-L, Lin Y-W (2009) Synthesis and characterization of conductive polypyrrole/multi-walled carbon nanotubes composites with improved solubility and conductivity. *Compos Sci Technol* 69:639
116. Paul S, Kim JH, Kim DW (2011) Cycling performance of supercapacitors assembled with polypyrrole/multi-walled carbon nanotube/conductive carbon composite electrodes. *J Electrochem Sci Technol* 2:91
117. Huyen DN, Tung NT, Vinh TD, Thien ND (2012) Synergistic effects in the gas sensitivity of polypyrrole/single wall carbon nanotube composites. *Sensors* 12:7965
118. Zhou C, Kumar S, Doyle CD, Tour JM (2005) Functionalized single wall carbon nanotubes treated with pyrrole for electrochemical supercapacitor membranes. *Chem Mater* 17:1997
119. Frackowiak E, Khomenko V, Jurewicz K, Lota K, Béguin F (2006) Supercapacitors based on conducting polymers/nanotubes composites. *J Power Sources* 153:413
120. Mi H, Zhang X, Xu Y, Xiao F (2010) Synthesis, characterization and electrochemical behaviour of polypyrrole/carbon nanotube composites using organometallic-functionalized carbon nanotubes. *Appl Surf Sci* 256:2284
121. Oh J, Kozlov ME, Kim BG, Kim H-K, Baughman RH, Hwang YH (2008) Preparation and electrochemical characterization of porous swnt-ppy nanocomposite sheets for supercapacitor applications. *Synth Met* 158:638
122. Lee H, Kim H, Cho MS, Choi J, Lee Y (2011) Fabrication of polypyrrole/carbon nanotube composite electrode on ceramic fabric for supercapacitor applications. *Electrochim Acta* 56:7460
123. Hu Y, Zhao Y, Li Y, Li H, Shao H, Qu L (2012) Defective super-long carbon nanotubes and polypyrrole composite for high-performance supercapacitor electrodes. *Electrochim Acta* 66:279

124. Fang Y, Liu J, Yu DJ, Wicksted JP, Kalkan K, Topal CO, Flanders BN, Wu J, Li J (2010) Self-supported supercapacitor membranes: polypyrrole-coated carbon nanotube networks enabled by pulsed electrodeposition. *J Power Sources* 195:674
125. Ansaldo A, Castagnola E, Maggolini E, Fadiga L, Ricci D (2011) Superior electrochemical performance of carbon nanotubes directly grown on sharp microelectrodes. *ACS Nano* 5:2206
126. Kmecko T, Hughes G, Cauller L, Lee JB, Romero-Ortega M (2006) Nanocomposites for neural interfaces. *MRS Proc* 926 null. 926:0926-CC04-06, doi:10.1557/PROC-0926-CC04-06
127. Green RA, Williams CM, Lovell NH, Poole-Warren LA (2008) Novel neural interface for implant electrodes: improving electroactivity of polypyrrole through mwnt incorporation. *J Mater Sci Mater Med* 19:1625
128. Keefer EW, Botterman BR, Romero MI, Rossi AF, Gross GW (2008) Carbon nanotube coating improves neuronal recordings. *Nat Nano* 3:434
129. Lu Y, Li T, Zhao X, Li M, Cao Y, Yang H, Duan YY (2010) Electrodeposited polypyrrole/carbon nanotubes composite films electrodes for neural interfaces. *Biomaterials* 31:5169
130. Peng C, Jin J, Chen GZ (2007) A comparative study on electrochemical co-deposition and capacitance of composite films of conducting polymers and carbon nanotubes. *Electrochim Acta* 53:525
131. Hughes M, Chen GZ, Shaffer MSP, Fray DJ, Windle AH (2002) Electrochemical capacitance of a nanoporous composite of carbon nanotubes and polypyrrole. *Chem Mater* 14:1610
132. Wang J, Xu Y, Chen X, Sun X (2007) Capacitance properties of single wall carbon nanotube/polypyrrole composite films. *Compos Sci Technol* 67:2981
133. Sun X, Xu Y, Wang J, Mao S (2012) The composite film of polypyrrole and functionalized multi-walled carbon nanotubes as an electrode material for supercapacitors. *Int J Electrochem Sci* 7:3205
134. Kim J-Y, Kim KH, Kim KB (2008) Fabrication and electro-chemical properties of carbon nanotube/polypyrrole composite film electrodes with controlled pore size. *J Power Sources* 176:396
135. Wang J, Xu Y, Yan F, Zhu J, Wang J, Xiao F (2010) Capacitive characteristics of nanocomposites of conducting polypyrrole and functionalized carbon nanotubes: effects of in situ dopant and film thickness. *J Solid State Electrochem* 14:1565
136. An KH, Jeon KK, Heo JK, Lim SC, Bae DJ, Lee YH (2002) High-capacitance supercapacitor using a nanocomposite electrode of single-walled carbon nanotube and polypyrrole. *J Electrochem Soc* 149:A1058

Jayachandran Venkatesan and Se Kwon Kim

Contents

1	Introduction	512
2	Bone Tissue Engineering	512
3	Carbon Nanotube	513
4	Carbon Nanotube Composites Biomaterials for Bone Tissue Engineering	516
4.1	Carbon Nanotube–Polymer Nanocomposite	516
4.2	Carbon Nanotube–Collagen Nanocomposite	516
4.3	Carbon Nanotube–Polylactic Acid Nanocomposite	518
4.4	Carbon Nanotube–Chitosan Nanocomposite	518
4.5	Carbon Nanotube–Polycaprolactone Nanocomposites	519
4.6	Carbon Nanotube–Hydroxyapatite Nanocomposite	520
4.7	Carbon Nanotube–Bioglass Nanocomposite	521
4.8	Carbon Nanotube Coating on the Polymeric Surface	522
5	Challenges and Future Directions	523
6	Conclusions	523
	References	523

Abstract

In the recent years, significant development has been achieved in tissue engineering for the artificial bone preparation. Metals, polymers, and ceramics are widely used biomaterials for bone implant. Apart from this, the infant material carbon nanotube (CNT) is an emerging biomaterial in the recent days, which are being checked for bone tissue engineering. CNT has unique properties such as electrical, mechanical, and thermal properties. Thus, addition of CNT in the polymer, ceramic, and metal matrix will be enhancing the function of the CNT.

J. Venkatesan • S.K. Kim (✉)

Department of Chemistry, Marine Bioprocess Research Center, Pukyong National University,
Busan, Republic of Korea

e-mail: venkatjchem@gmail.com; venkatjchem@pknu.ac.kr; sknkim@pknu.ac.kr

In this chapter, CNT–polymers, CNT–hydroxyapatite, and CNT/Bioglass composite biomaterials have been discussed and explored for bone tissue engineering application.

Keywords

Polymers • Bioglass • Chitosan • Toxicity • Hydroxyapatite

1 Introduction

In the recent years, significant development has been achieved in artificial biomaterials to treat the loss, defects, or failure of the bone. Autograft and allograft are promising materials to treat the bone defect or replacements; however, both methods are having disadvantages in donor sites and dangerous diseases transmissible. Thus, researchers have been paid an attention in the preparation of artificial bone materials using polymers, ceramics, and metals. Presently, metals are widely used for the treatments of bone defects and replacement due to its mechanical properties. Several synthetic and natural biopolymers, bioceramics, are being currently used to make the artificial bone; those biomaterials are in the laboratory stage to clinical level today. But still the problem exists in mechanical strength; to address this issue, carbon nanotube (CNT) might be a promising biomaterial to solve the problem. The common tissue engineering culture, replacement, and implant procedure have been shown in Fig. 20.1.

2 Bone Tissue Engineering

The bone is a hierarchical structure and it is made up of bioceramics (hydroxyapatite) and complicated biopolymer (collagen) as a major portion. The bone is not only giving the structural arrangement of the body; it keeps the internal organs such as the heart, brain, and lungs safe. Collagen and non-collagenous proteins are playing major role in the bone metabolisms. The loss, fracture, and diseases of the bone are the painful ones and also affect the human normal life. Several biomaterials are being used for the purpose of bone tissue engineering to solve the issues. Poly(methyl methacrylate), polyglycolic acid, polyvinylpyrrolidone, poly(propylene fumarate), polydopamine, polyvinyl alcohol, polycaprolactone, collagen, chitin, chitosan, and alginate [1, 2] are some of them. Synthetic and natural polymers have advantages and disadvantages. Synthetic polymers are in the problem of degradation and unwanted byproducts produced while degradation. Natural polymers degraded quickly and are also inexpensive. Apart from the polymers, ceramics are widely used biomaterials in the bone tissue engineered materials. Hydroxyapatite (HAp) materials are widely used in the bone tissue engineered materials due to its excellent biocompatibility with bone tissue. The schematic procedure of bone graft substitute has been shown in the Fig. 20.2.

Fig. 20.1 Basic tissue engineering

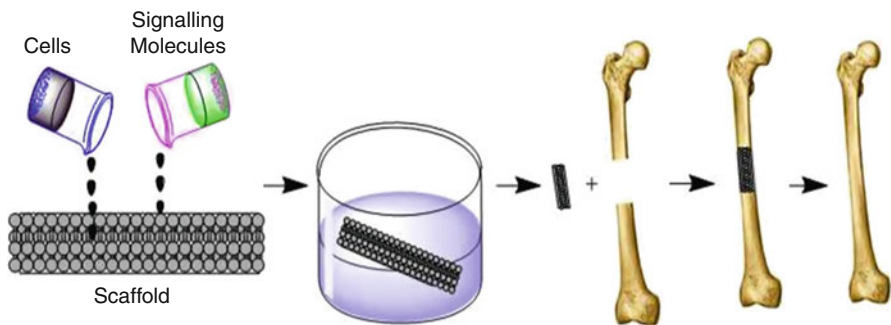
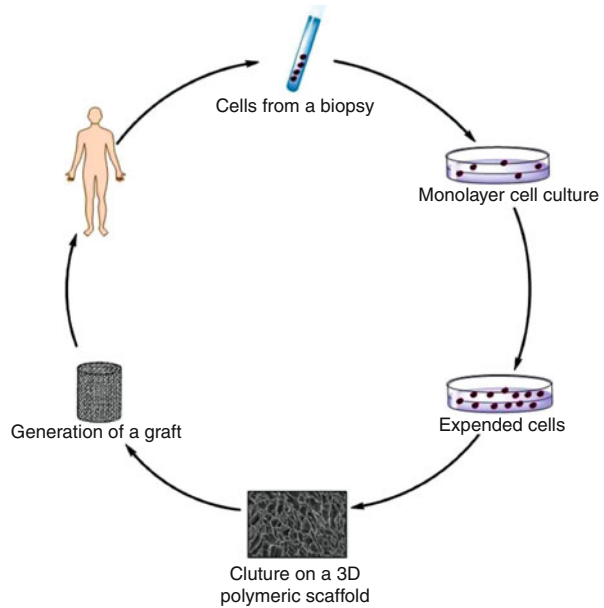


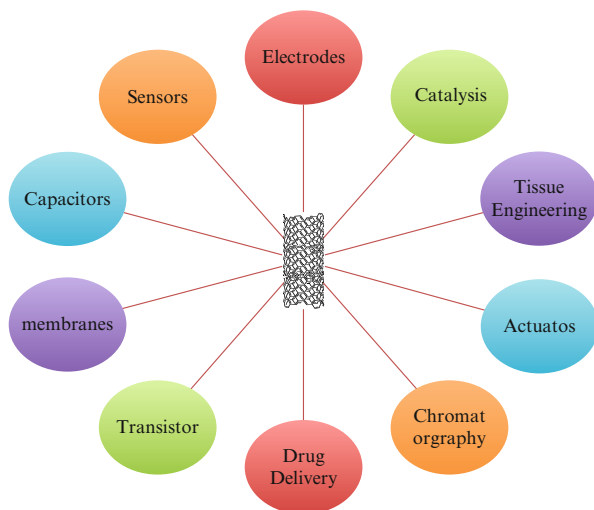
Fig. 20.2 Schematic procedure for tissue engineering scaffold transplantation

3 Carbon Nanotube

Carbon has different kinds of allotropes and it can be available in different forms such as diamond, fullerene, graphite, carbon nanotubes, and more recently graphene. Among the carbon nanotubes, single-walled carbon nanotube (SWNT) and multiwalled carbon nanotube (MWNT) are the most extensively studied bio-materials for various applications, as shown in Fig. 20.3.

CNT has unique properties such as electrical, mechanical, and thermal properties; thus, researchers are trying to use CNTs in the preparation of artificial bone

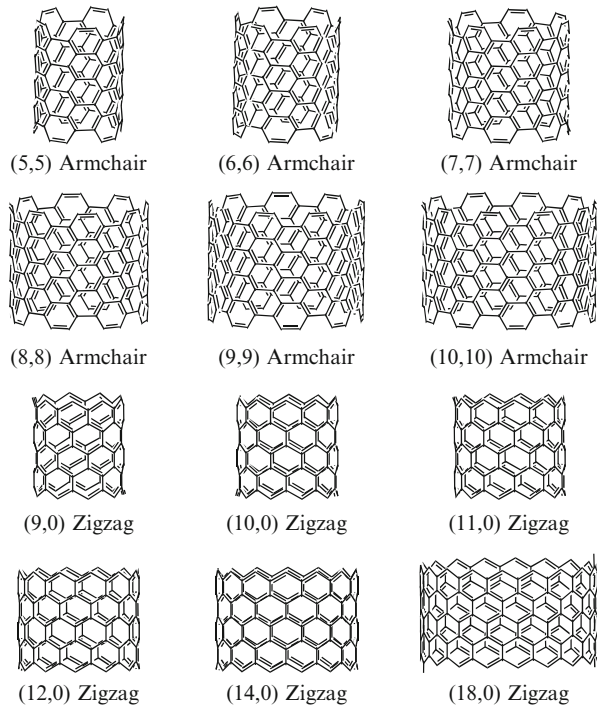
Fig. 20.3 Application of carbon nanotube



materials. But, the toxicity of CNTs is an important concern, whether it can be used for biometrics or not. It is a burning question in the recent research. In addition, the toxicity of CNTs is still obscure. Several controversy reports have been published in online for decades.

Horrison et al. suggest that CNTs can be used for improved tracking of cells, sensing the microenvironments, distribution of transfection agents, and scaffold incorporation with the host's body [3]. In another study, the comparison of MWNT and SWNT toxicities was performed at in vivo condition; CNTs' toxicity is dependent on size, shape, length, chemical surface, and aspect ratio [4] (Fig. 20.4). CNT alone was implanted in animal femur model without any binder, as a result of no severe inflammatory response and no toxicity, and it may be useful for bone regeneration [5]. The orientation of CNT is also important regarding toxicity concern; Namgung et al. suggested that aligned CNT networks exhibited enhanced proliferation and osteogenic differentiation compared to those on randomly oriented CNT networks [6].

Fullerene, graphene, and diamond are allotropes of carbon. To find out the toxicity of carbon allotropes, fullerenes C60 were deposited on microscopic glass coverslips with different heights of 128 ± 8 nm, 238 ± 3 nm, 326 ± 5 nm, and 1043 ± 57 nm. Until 326 ± 5 nm of fullerene layer, the adhesion and proliferation of human osteoblast-like MG 63 cells was similar as in control cells on polystyrene dishes. By increasing the layer content, 1043 ± 57 nm in height, the cells grew preferentially in grooves among the prominences. In another case, nanodiamond was deposited on silicon substrates and provided an excellent substrate for the adhesion, growth, and osteogenic differentiation of MG 63 cells [7, 8]. The gene transfection efficiency of cells grown on the CNT and graphene-coated substrates was improved up to 250 % that of cells grown on a cover glass [9].

Fig. 20.4 Different type of CNTs

In the case of MWNT, adjoining bones induce little local inflammatory reaction, show high bone tissue compatibility, permit bone repair, become integrated into new bone, and accelerate bone formation stimulated by rhBMP-2 [10]. In addition, few reports suggest that functionalization of CNT as carboxylated SWNTs and carboxylated MWNT inhibited the proliferation, osteogenic differentiation, adipogenic differentiation, and mineralization of MSCs [11].

The addition of CNTs in the composite materials is expected to be promising for high load-bearing orthopedic implants and does not only decrease the toxicity of the CNT but is also expected to mimic the natural function of the bone. The extensive review has been written for CNT, which can act as biomaterials for tissue regeneration [12–16].

The *in vivo* (mice nasal, oral, intratracheal, and intraperitoneal) study has been performed with pure MWNTs and N-doped MWNT. Extremely high concentrations of N-doped MWNT nanotubes administrated directly into the mice's trachea only induced granulomatous inflammatory responses. Importantly, all other routes of administration did not induce signs of distress or tissue changes on any treated mouse. The functionalizations of N-doped MWNT nanotubes are less harmful than MWNTs or SWNTs and might be more advantageous for bioapplication [17].

Functionalization of CNT significantly reduced its toxicity and is also used for several biomedical applications such as bone regeneration, neural regeneration,

drug delivery, and gene delivery [18]. The toxicity of SWNT has been reduced with the functionalization of poly-L-Lysine and used for cell adhesion [19, 20]. The metabolic activity of 3T3 cells was also dependent on SWNT preparation and concentration [21].

4 Carbon Nanotube Composites Biomaterials for Bone Tissue Engineering

4.1 Carbon Nanotube–Polymer Nanocomposite

The electrical and mechanical properties of CNTs are important key properties, which can be used for bone tissue engineering. Electricity properties of CNT might be used to stimulate the cell towards osteogenic differentiation, and mechanical properties can be used to mimic the mechanical strength of the bone. Several polymers have been widely used in tissue engineering due to their multifunctional nature, such as biocompatibility, biodegradability, favorable mechanical properties, being good for cell adhesion, direct contact with body fluids *in vivo*, and also being useful for cell adhesion, proliferation, and differentiation [22]. Poly(lactic acid), poly(glycolic acid), poly(ϵ -caprolactone), chitosan, and collagen have emerged as a class of biomaterials of growing interest for application in surgery, drug delivery, and bone tissue engineering.

4.2 Carbon Nanotube–Collagen Nanocomposite

Collagen is the promising biomaterial in bone tissue engineering in the recent years; the addition of collagen in MWNT could improve the surface properties for the cell growth and other osteogenic differentiation and increases the DNA content on the MWNT-coated sponge after 1 week, which is higher than on an uncoated collagen sponge. There was no significant difference between the estimated ALP activity normalized by DNA quantity on the MWNT-coated sponge and that on the uncoated collagen [24]. The fibril structure of collagen and nanotube structure of carbon has been shown in the Fig. 20.5.

In another study, it was proven that MWNT could be used for bone tissue engineering. Significant bone formation, earlier differentiation, alkaline phosphatase, and osteopontin contents have been observed in MWNT-coated collagen sponge scaffolds with rat primary osteoblast cell line, compared to uncoated sponges. Significantly more bone formation *in vivo* was observed around the MWNT-coated sponges than around the uncoated sponges [23, 24]. In another research, collagen–CNT composite materials were checked for bone tissue engineering [25]. The scanning electron microscopy (SEM) images of cells on collagen sponge and MWNT-coated sponge have been shown in Fig. 20.6.

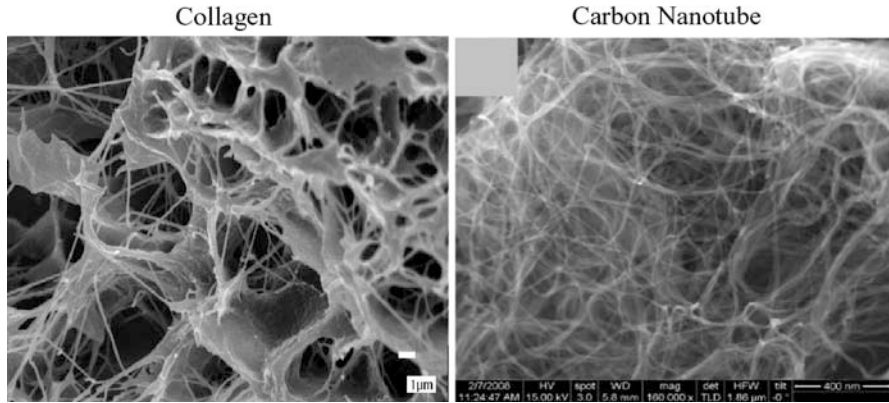


Fig. 20.5 Scanning electron microscope images of Collagen vs. CNT

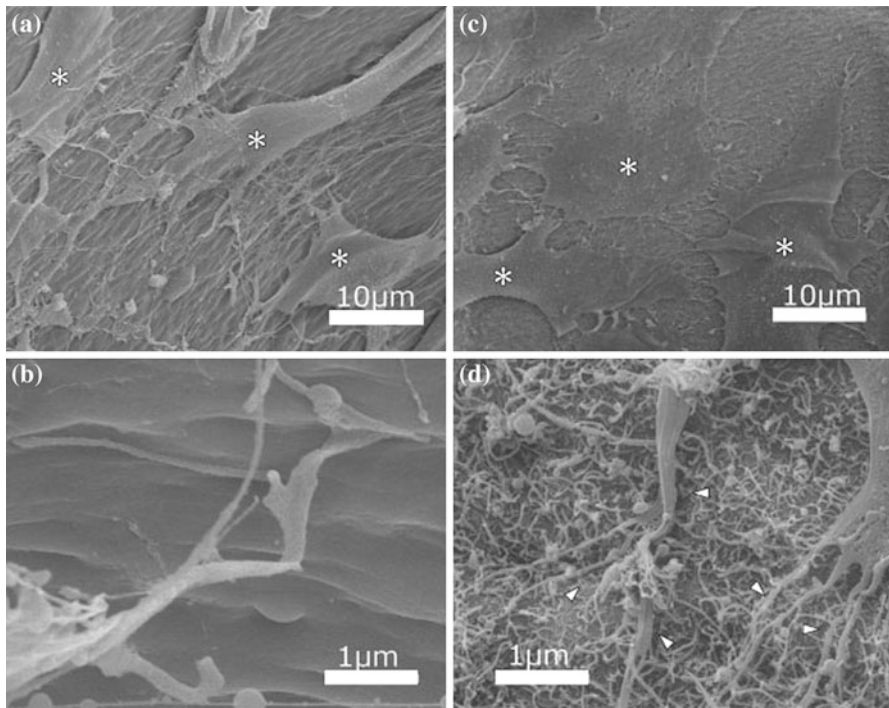


Fig. 20.6 SEM observation after 1-week incubation: cells (*asterisk*) grown on the (a) collagen sponge and (c) MWNT-coated sponge. SEM images at higher magnification: (b) collagen sponge, and (d) cytoplasmic elongations (*arrowhead*) intertwined with MWCNTs on the surface of the MWCNT-coated sponge [24]

4.3 Carbon Nanotube–Polylactic Acid Nanocomposite

Polyhydroxy acids are widely used biomaterials in therapeutic devices. Poly(lactic-co-glycolic acid) MWNT composite materials have been prepared using electrospinning and colloidal approach. As proven, incorporation of MWNTs in PLGA scaffolds was prepared to significantly promote fibroblast attachment, spreading, and proliferation when compared with PLGA fibrous mats and macroporous PLGA films without MWNTs [26]. In another study, different kinds of method (solvent casting technique) have been used to prepare the biodegradable PLGA/MWNT. The presence of MWNTs increased the mechanical properties of the nanocomposite. A seven-week period in vitro degradation test showed the addition of c-MWNTs accelerated the hydrolytic degradation of PLGA. Compared with control groups, MSCs cultured onto PLGA/c-MWNT nanocomposite exhibited better adhesion and viability and also displayed significantly higher production levels of ALP over 21 days of culture [27]. Electrically conductive nanofibers of polylactic acid with MWNT have been prepared using electrospinning methods. They found that cellular elongation and proliferation were mainly dependent on the electrical stimulation whereas the topographical features played a minor role [28].

The mechanical strength has been increased by the introduction of the CNT in the poly(propylene fumarate) matrix [29]. In addition, good cell viability, osteoconductivity, and marrow stromal cells demonstrated equally good cell attachment and proliferation on all scaffolds made up of different materials at each porosity [30, 31].

4.4 Carbon Nanotube–Chitosan Nanocomposite

Chitosan is a biopolymer and has considerably been employed as a scaffold in orthopedic and other biomedical applications due to its biocompatibility, biodegradability, pore formation behavior, suitability for cell ingrowth, and intrinsic antibacterial nature [1, 32, 33]. However, chitosan-based composite biomaterials have optimum mechanical strength and low interconnected porosity for cell attachment, which needs to be improved further. The addition of CNT in the chitosan matrix can solve the mechanical issues. For this, several reports have been published in the recent years; pristine SWNT, acid-functionalized SWNT, and glucosamine-functionalized SWNT (0.001–1.0 % wt/vol) were checked in vitro for bone tissue engineering, increasing concentrations of SWNT and resulting in a decrease of cell viability, which was dependent on SWNT preparation.

Venkatesan et al. [1] explained about chitosan–carbon nanotube composite scaffold preparation, mechanical strength, in vitro biological activity, and chemical interaction between chitosan and carbon nanotube [1] (Fig. 20.7).

Abarrategi et al. performed experiment with MWNT–chitosan composites for bone tissue engineering and interestingly found that implantation of MWNT–chitosan scaffolds adsorbed with rhBMP-2 in muscle tissue and ectopic formation of bone tissue and in vivo [34].

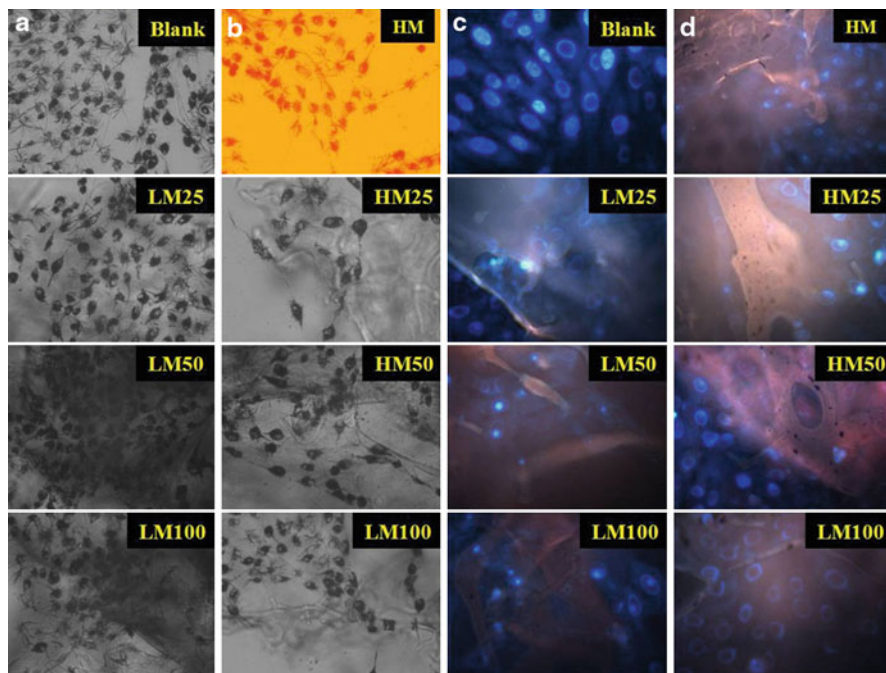


Fig. 20.7 Optical microscopy images of chitosan and their composite scaffolds (magnification = 20 \times) after the addition of MTT solution. (a and b) Blank, Low and high molecular weight chitosan scaffolds and their composite scaffolds, (c and d) Fluorescence microscopy images of chitosan and chitosan/f-MWCNT composite scaffolds (magnification = 40 \times) after Hoechst stain

4.5 Carbon Nanotube–Polycaprolactone Nanocomposites

Polycaprolactone (PCL) is a degradable polymer; it can degrade by hydrolysis of ester linkage in the physiological conditions. Thus, it has gained great importance in the preparation of artificial implantable biomaterials. Coaxial electrospun PCL, MWNT, and a hydrogel consisting of polyvinyl alcohol and polyacrylic acid have been prepared for skeletal muscle tissue replacement. Incorporation of MWCNT in the polymer matrix increased the conductivity and biocompatible was observed. MWCNT-containing scaffolds had higher strength than the rat and pig skeletal muscle. Although the mechanical properties were higher than the muscle, the PCL-containing MWCNT scaffold shows promise as a potential bioartificial nanoactuator for the skeletal muscle [35].

Micro fabricated CNT–polycaprolactone composites, by changing the ratio of CNT to polydopamine, the elastic modules of the nanocomposite, can vary between 10 and 75 MPa. In addition, PCL–CNT nanocomposite was able to sustain osteoblast proliferation and modulate cell morphology [36]. Pan et al. prepared the MWNTs/PCL composite scaffolds via solution evaporation technique.

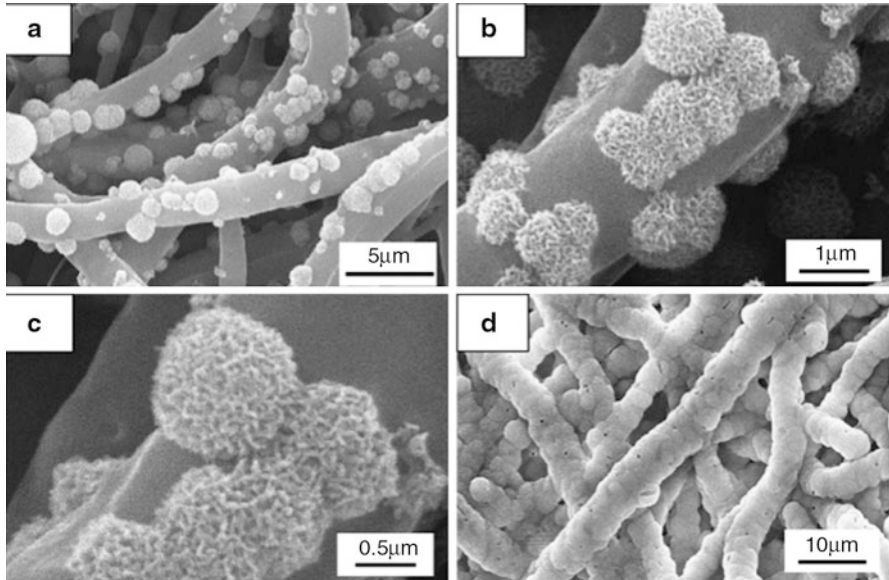


Fig. 20.8 SEM images of the PLGA/MWNTs scaffolds after immersion in $1.5 \times$ SBF for (a), (b), (c) 7 d and (d) 14 d

The scaffolds with low concentration (0.5 wt%) of MWNTs can enhance the proliferation and differentiation of the BMSCs more than that with higher concentration of MWNTs. It is concluded that MWNTs/PCL composite scaffolds have the potential for bone tissue engineering, and the relatively low concentration of MWNTs (0.5 wt%) is preferred [37].

4.6 Carbon Nanotube–Hydroxyapatite Nanocomposite

Hydroxyapatite (HAp) is one of the widely checked biomaterials for bone tissue engineering in the last two decades [38]. HAp is a bioceramics material used as bone implants because of its chemical composition that is similar to the inorganic portion of the bone and teeth [39, 40]. HAp has been used in clinical bone graft procedures for more than 25 years. But its poor tensile strength and fracture toughness compared with the bone make it unsuitable for major load-bearing devices. CNTs with their high aspect ratio and excellent mechanical properties have the potential to strengthen and toughen HAp without offsetting its bioactivity [41].

Composite scaffolds composed of PLGA with MWNTs were prepared by electrospinning, and scaffolds were immersed in a simulated body fluid ($1.5 \times$ SBF) at 37°C for 7, 14, and 21 days for biomimetic mineralization. After mineralization, apatite crystals were deposited on the PLGA/MWNTs composite scaffolds [42] (Fig. 20.8).

SDS has been used to carry out the biomimetic mineralization on MWNT with Ca/P solution [43]. BMP-2 has been used with the PLLA, CNT, and HAp scaffolds. Three-dimensional porous PLLA scaffolds have been mixed with SWNT, HAp, and BMP2; the role of the different biomimetic components added to the PLLA matrix was deciphered, with BMP2-added scaffolds showing the highest biomimetic activity on cells differentiating to mature osteoblasts [44].

Electrospinning a suspension consisting of PLLA, MWNT, and HAp membrane has been reported, enhanced the adhesion and proliferation of periodontal ligament cells (PDLCS) by 30 %, and inhibited the adhesion and proliferation of gingival epithelial cells by 30 %, compared with the control group [45]. Self-assembled nHAp/MWNT and collagen/MWNT composite were prepared. Spindle-shaped units that are detached from the MWNT template are able to maintain the ordered parallel structure of the nHAp polycrystalline fibril [46]. The HAp/MWNT composites were prepared by solution blending. The fracture toughness and flexural strength were improved by 50 % and 28 % separately when the volume percentage of MWNTs reached 7 % [47]. Some of the researchers said that CNTs with micro HAp containing composite materials are not recommended as a bone restorative material [48].

4.7 Carbon Nanotube–Bioglass Nanocomposite

Bioglass is composed of SiO_2 , Na_2O , CaO , and P_2O_5 in specific proportions; it is well proven that high amount of calcium and phosphorous can be used for apatite formation. Important advanced material can be produced by the addition of CNT in Bioglass for bone tissue engineering. Highly porous 45S5 Bioglass-based foam scaffolds were coated with MWNT by electrophoretic deposition technique. Increased electrical conductivity was reported by the addition of MWNT coating [49] (Fig. 20.9).

Poly(3-hydroxybutyrate) composites with bioactive glass particles and MWNTs have been reported. The presence of MWNTs (2–7 wt%) increased the surface roughness, and small amount of MWNT in the composite materials enhanced MG-63 osteoblast-like cell attachment and proliferation compared to composites with higher concentration of MWNTs [50]. 45S5 Bioglass-ceramic scaffolds were fabricated by the foam replication method and coated with CNT using EPD. In vitro cell culture using MSCs was carried out on both scaffold systems (with and without CNT coating) over a 4-week period. No cytotoxic effects of the CNT were observed under the conditions of the present experiments. Although a lower initial cell viability on the CNT-coated scaffolds were observed, no significant differences were found after 4 weeks of culture compared with the uncoated scaffolds. This work therefore shows that there is in principle no significant improvement of cellular responses by creating a CNT coating on this type of highly bioactive scaffolds. However, the electrical conductivity introduced by the coating might have the potential to increase cell viability and differentiation when cell culture is carried out under the effect of electrical stimulation [51].

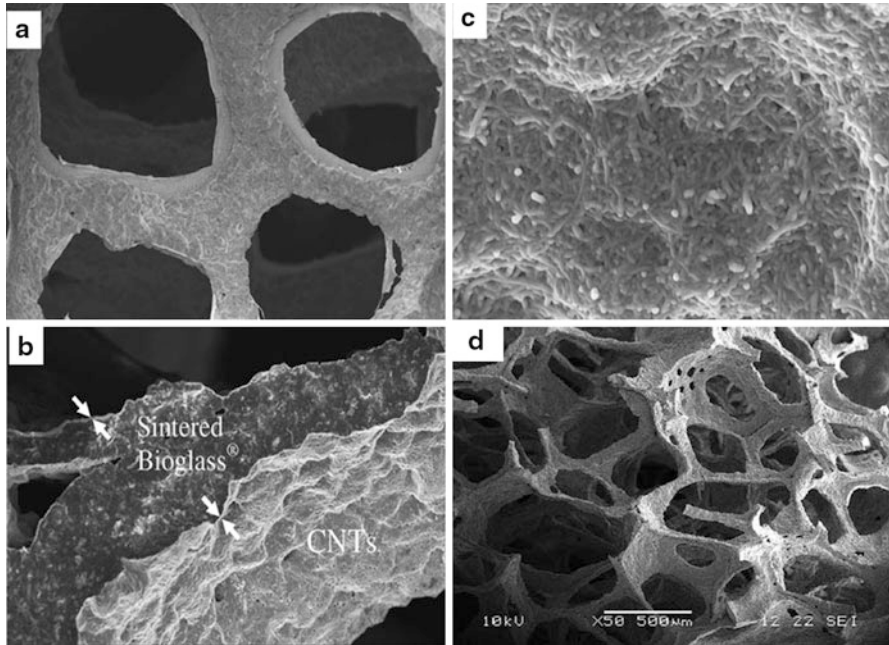


Fig. 20.9 SEM images showing the typical microstructure of a CNT coated scaffold, obtained by EPD (2.8 V, 10 min) at (a) low, (b) medium and (c) high magnifications. The CNT coating is indicated by the *arrows* in (b), (d) SEM micrograph showing the 3D microstructure of the highly porous glass-ceramic scaffold developed from Bioglass O powder by the foam replica technique [49]

4.8 Carbon Nanotube Coating on the Polymeric Surface

Surface chemistries TiO_2 nanotubes with carbon-coated TiO_2 nanotubes were compared for cell behaviour. The roles played by the material surface chemistry of the nanotubes did not have effects on the adhesion, growth, or morphology, but had a major influence on the ALP activity of osteoblast cells, with the original TiO_2 chemistry having higher ALP levels. Different chemistries caused different levels of osteogenic differentiation in MSCs; however, it was the carbon-coated TiO_2 nanotubes that had the greater advantage, with higher levels of osteo differentiation [52].

Conductive and nontoxic composites of CNF with agarose have been reported and demonstrated that these CNFs can be used for cell attachment and response both *in vitro* and *in vivo* [53]. Bhattacharya et al. reported the effects of layer by layered CNT composite on osteoblasts were compared against the effects by commercially available pure titanium. Cell proliferation on the CNT composite and Titanium were similar. When implanted in critical-sized rat calvarial defect, the CNT composite permitted bone formation and bone repair without signs of rejection or inflammation [54].

5 Challenges and Future Directions

Until now, CNT is a promising biomaterial and is used for different fields such as tissue engineering, drug delivery, and biosensors:

1. The toxicity and biocompatibility are important parameters for biomedical application. To find out the exact toxicity of CNT is a challenge for the current researchers; several kinds of research tools and experiments are available, but the toxicity of CNT is varied with production process, availability of toxic metals, size, functionalization, etc.
2. Surrounding tissues will come into surface contact with CNT composites, and compatibility between CNT and host cells must be addressed.
3. Amount of carbon nanotube in the polymeric matrix can also play a major role in osteogenic differentiation.

6 Conclusions

As a conclusion, with the initial stage of CNT in biomedical application, we are not concluding anything in this point. It will take several years, whether CNT can be used as implant material or not. However, it is difficult to use CNT alone in bone-related implant, due to formation of abacas sheet and aggregation. This will be avoided by using functionalization of CNT. Functionalization of CNT is an open way to use CNT as a potential material for further research. Thus, CNT-polymer with ceramics composites will be promising materials for the repair of bone defects.

Acknowledgements This work was supported by a grant from Marine Bioprocess Research Centre of the Marine Bio 21 Center funded by the Ministry of Land, Transport and Maritime, Republic of Korea.

References

1. Venkatesan J, Kim SK (2010) Chitosan composites for bone tissue engineering – An overview. *Mar Drugs* 8:2252–2266
2. Wang L, Shelton R, Cooper P, Lawson M, Triffitt J, Barralet J (2003) Evaluation of sodium alginate for bone marrow cell tissue engineering. *Biomaterials* 24:3475–3481
3. Harrison BS, Atala A (2007) Carbon nanotube applications for tissue engineering. *Biomaterials* 28:344–353
4. Fraczek A, Menaszek E, Paluszkiwicz C, Blazewicz M (2008) Comparative in vivo biocompatibility study of single- and multi-wall carbon nanotubes. *Acta Biomater* 4:1593–1602
5. Wang W, Yokoyama A, Liao S, Omori M, Zhu Y, Uo M, Akasaka T, Watari F (2008) Preparation and characteristics of a binderless carbon nanotube monolith and its biocompatibility. *Mater Sci Eng C* 28:1082–1086
6. Namgung S, Baik KY, Park J, Hong S (2011) Controlling the growth and differentiation of human mesenchymal stem cells by the arrangement of individual carbon nanotubes. *ACS Nano* 5:7383

7. Bacakova L, Grausova L, Vacik J, Lavrentiev V, Blazewicz S, Fraczek A, Kromka A, Haenen K (2011) Adhesion and growth of human osteoblast-like cell in cultures on nanocomposite carbon-based materials. *Nanosci Nanotechnol Lett* 3:99–109
8. Vandrovcová M, Bačáková L (2011) Adhesion, growth and differentiation of osteoblasts on surface-modified materials developed for bone implants. *Physiol Res* 60:403
9. Ryoo SR, Kim YK, Kim MH, Min DH (2010) Behaviors of NIH-3T3 fibroblasts on graphene/carbon nanotubes: Proliferation, focal adhesion, and gene transfection studies. *ACS Nano* 4:6587
10. Usui Y, Aoki K, Narita N, Murakami N, Nakamura I, Nakamura K, Ishigaki N, Yamazaki H, Horiuchi H, Kato H (2008) Carbon nanotubes with high bone-tissue compatibility and bone-formation acceleration effects. *Small* 4:240–246
11. Liu D, Yi C, Zhang D, Zhang J, Yang M (2010) Inhibition of proliferation and differentiation of mesenchymal stem cells by carboxylated carbon nanotubes. *ACS Nano* 4:2185–2195
12. Saito N, Usui Y, Aoki K, Narita N, Shimizu M, Hara K, Ogiwara N, Nakamura K, Ishigaki N, Kato H (2009) Carbon nanotubes: biomaterial applications. *Chem Soc Rev* 38:1897–1903
13. Zhang Y, Bai Y, Yan B (2010) Functionalized carbon nanotubes for potential medicinal applications. *Drug Discov Today* 15:428–435
14. Sahithi K, Swetha M, Ramasamy K, Srinivasan N, Selvamurugan N (2010) Polymeric composites containing carbon nanotubes for bone tissue engineering. *Int J Biol Macromol* 46:281–283
15. Li X, Fan Y, Watari F (2010) Current investigations into carbon nanotubes for biomedical application. *Biomed Mater* 5:022001
16. Li X, Liu X, Huang J, Fan Y, Cui F (2011) Biomedical investigation of CNT based coatings. *Surf Coat Technol* 206:759
17. Carrero-Sanchez J, Elias A, Mancilla R, Arrellin G, Terrones H, Laclette J, Terrones M (2006) Biocompatibility and toxicological studies of carbon nanotubes doped with nitrogen. *Nano Lett* 6:1609–1616
18. Tran PA, Zhang L, Webster TJ (2009) Carbon nanofibers and carbon nanotubes in regenerative medicine. *Adv Drug Del Rev* 61:1097–1114
19. Lin DW, Bettinger CJ, Ferreira JP, Wang CL, Bao Z (2011) A cell-compatible conductive film from a carbon nanotube network adsorbed on poly-L-lysine. *ACS Nano* 5:10026
20. Balasubramanian K, Burghard M (2005) Chemically functionalized carbon nanotubes. *Small* 1:180–192
21. Nimmagadda A, Thurston K, Nollert MU, McFetridge PS (2006) Chemical modification of SWNT alters in vitro cell-SWNT interactions. *J Biomed Mater Res* 76:614–625
22. Ravichandran R, Sundarrajan S, Venugopal JR, Mukherjee S, Ramakrishna S (2012) Advances in polymeric systems for tissue engineering and biomedical applications. *Macromol Biosci* 12:286
23. Hirata E, Uo M, Takita H, Akasaka T, Watari F, Yokoyama A (2011) Multiwalled carbon nanotube-coating of 3D collagen scaffolds for bone tissue engineering. *Carbon* 49:3284
24. Hirata E, Uo M, Takita H, Akasaka T, Watari F, Yokoyama A (2009) Development of a 3D collagen scaffold coated with multiwalled carbon nanotubes. *J Biomed Mater Res* 90:629–634
25. MacDonald RA, Laurenzi BF, Viswanathan G, Ajayan PM, Stegemann JP (2005) Collagen-carbon nanotube composite materials as scaffolds in tissue engineering. *J Biomed Mater Res* 74:489–496
26. Liu F, Guo R, Shen M, Cao X, Mo X, Wang S, Shi X (2010) Effect of the porous microstructures of poly (lactic-co-glycolic acid)/carbon nanotube composites on the growth of fibroblast cells. *Soft Mater* 8:239–253
27. Lin C, Wang Y, Lai Y, Yang W, Jiao F, Zhang H, Ye S, Zhang Q (2011) Incorporation of carboxylation multiwalled carbon nanotubes into biodegradable poly (lactic-co-glycolic acid) for bone tissue engineering. *Colloid Surf B* 83:367–375

28. Shao S, Zhou S, Li L, Li J, Luo C, Wang J, Li X, Weng J (2011) Osteoblast function on electrically conductive electrospun PLA/MWCNTs nanofibers. *Biomaterials* 32:2821
29. Shi X, Hudson JL, Spicer PP, Tour JM, Krishnamoorti R, Mikos AG (2005) Rheological behaviour and mechanical characterization of injectable poly (propylene fumarate)/single-walled carbon nanotube composites for bone tissue engineering. *Nanotechnology* 16:S531
30. Shi X, Sitharaman B, Pham QP, Liang F, Wu K, Edward Billups W, Wilson LJ, Mikos AG (2007) Fabrication of porous ultra-short single-walled carbon nanotube nanocomposite scaffolds for bone tissue engineering. *Biomaterials* 28:4078–4090
31. Shi X, Hudson JL, Spicer PP, James M, Krishnamoorti R, Mikos AG (2006) Injectable nanocomposites of single-walled carbon nanotubes and biodegradable polymers for bone tissue engineering. *Biomacromolecules* 7:2237–2242
32. Martino A, Sittinger M, Risbud M (2005) Chitosan: a versatile biopolymer for orthopaedic tissue-engineering. *Biomaterials* 26:5983–5990
33. Peter M, Binulal N, Nair S, Selvamurugan N, Tamura H, Jayakumar R (2010) Novel biodegradable chitosan-gelatin/nano-bioactive glass ceramic composite scaffolds for alveolar bone tissue engineering. *Chem Eng J* 158:353–361
34. Abarrategi A, Gutiérrez MC, Moreno-Vicente C, Hortigüela MJ, Ramos V, López-Lacomba JL, Ferrer ML, Del Monte F (2008) Multiwall carbon nanotube scaffolds for tissue engineering purposes. *Biomaterials* 29:94–102
35. McKeon-Fischer K, Flagg D, Freeman J (2011) Coaxial electrospun poly (ϵ -caprolactone), multiwalled carbon nanotubes, and polyacrylic acid/polyvinyl alcohol scaffold for skeletal muscle tissue engineering. *J Biomed Mater Res* 99:493
36. Mattioli-Belmonte M, Vozzi G, Whulanza Y, Seggiani M, Fantauzzi V, Orsini G, Ahluwalia A (2011) Tuning polycaprolactone-carbon nanotube composites for bone tissue engineering scaffolds. *Mater Sci Eng* 32:152
37. Pan L, Pei X, He R, Wan Q, Wang J (2012) Multiwall carbon nanotubes/polycaprolactone composites for bone tissue engineering application. *Colloid Surf B* 93:226
38. Wei G, Ma PX (2004) Structure and properties of nano-hydroxyapatite/polymer composite scaffolds for bone tissue engineering. *Biomaterials* 25:4749–4757
39. Sopyan I, Mel M, Ramesh S, Khalid K (2007) Porous hydroxyapatite for artificial bone applications. *Sci Technol Adv Mater* 8:116–123
40. Pallela R, Venkatesan J, Kim SK (2011) Polymer assisted isolation of hydroxyapatite from *Thunnus obesus* bone. *Ceram Int* 37:3489–3497
41. White AA, Best SM, Kinloch IA (2007) Hydroxyapatite–carbon nanotube composites for biomedical applications: a review. *Int J App Cer Tech* 4:1–13
42. Zhang H, Liu J, Yao Z, Yang J, Pan L, Chen Z (2009) Biomimetic mineralization of electrospun poly (lactic-co-glycolic acid)/multi-walled carbon nanotubes composite scaffolds in vitro. *Mater Lett* 63:2313–2316
43. Tan Q, Zhang K, Gu S, Ren J (2009) Mineralization of surfactant functionalized multi-walled carbon nanotubes (MWNTs) to prepare hydroxyapatite/MWNTs nanohybrid. *Appl Surf Sci* 255:7036–7039
44. Ciapetti G, Granchi D, Devescovi V, Baglio SR, Leonardi E, Martini D, Jurado MJ, Olalde B, Armentano I, Kenny JM (2012) Enhancing osteoconduction of PLLA-based nanocomposite scaffolds for bone regeneration using different biomimetic signals to MSCs. *Int J Mol Sci* 13:2439–2458
45. Mei F, Zhong J, Yang X, Ouyang X, Zhang S, Hu X, Ma Q, Lu J, Ryu S, Deng X (2007) Improved biological characteristics of poly (L-lactic acid) electrospun membrane by incorporation of multiwalled carbon nanotubes/hydroxyapatite nanoparticles. *Biomacromolecules* 8:3729–3735
46. Liao S, Xu G, Wang W, Watari F, Cui F, Ramakrishna S, Chan CK (2007) Self-assembly of nano-hydroxyapatite on multi-walled carbon nanotubes. *Acta Biomater* 3:669–675

47. Meng Y, Tang CY, Tsui CP, Chen DZJ (2008) Fabrication and characterization of needle-like nano-HA and HA/MWNT composites. *Mater Sci Mater Med* 19:75–81
48. Van der Zande M, Walboomers XF, Brännvall M, Olalde B, Jurado MJ, Álava JI, Jansen JA (2010) Genetic profiling of osteoblast-like cells cultured on a novel bone reconstructive material, consisting of poly-L-lactide, carbon nanotubes and microhydroxyapatite, in the presence of bone morphogenetic protein-2. *Acta Biomater* 6:4352–4360
49. Meng D, Ioannou J, Boccaccini ARJ (2009) Bioglass[®]-based scaffolds with carbon nanotube coating for bone tissue engineering. *Mater Sci Mater Med* 20:2139–2144
50. Misra SK, Ohashi F, Valappil SP, Knowles JC, Roy I, Silva SRP, Salih V, Boccaccini AR (2010) Characterization of carbon nanotube (MWCNT) containing P (3HB)/bioactive glass composites for tissue engineering applications. *Acta Biomater* 6:735–742
51. Meng D, Rath SN, Mordan N, Salih V, Kneser U, Boccaccini ARJ (2011) In vitro evaluation of 45S5 Bioglass[®]-derived glass-ceramic scaffolds coated with carbon nanotubes. *Biomed Mater Res* 99:435
52. Brammer KS, Choi C, Frandsen CJ, Oh S, Johnston G, Jin S (2011) Comparative cell behavior on carbon coated TiO₂ nanotube surfaces for Osteoblasts vs. Osteo-progenitor cells. *Acta Biomater* 7:2697
53. Lewitus DY, Landers J, Branch JR, Smith KL, Callegari G, Kohn J, Neimark AV (2011) Biohybrid carbon nanotube/agarose fibers for neural tissue engineering. *Adv Funct Mater* 21:2624
54. Bhattacharya M, Wutticharoenmongkol-Thitiwongsawet P, Hamamoto DT, Lee D, Cui T, Prasad HS, Ahmad M (2011) Bone formation on carbon nanotube composite. *J Biomed Mater Res* 96:75–82

Samantha Wijewardane

Contents

1	Direct Energy Conversions	528
1.1	Photovoltaic Cells	528
1.2	Antenna Solar Energy Conversion (Rectenna Solar Cells)	529
2	Hydrogen	535
2.1	Hydrogen Production	535
2.2	Hydrogen Storage	536
3	Future Directions	537
	References	538

Abstract

Applicability of CNT/CNT composites in clean energy applications has been demonstrated in a wide range from solar thermal conversion to more advanced antenna solar energy conversion (ASEC). So far the solar photovoltaic cells are the most promising and reliable way of converting solar power directly to electric power. Repeated demonstrations of single-wall carbon nanotubes' (SWNT) suitability to form ideal p-n junction diodes enhanced the possibility of photovoltaic cells made out of CNT and CNT/composites. Hydrogen is considered to be a clean energy carrier. But high production cost and lack of a feasible storage system hindered the potential use of hydrogen. Photocatalytic water splitting is one of the cheapest ways of producing hydrogen gas. TiO₂ has been the most widely used photocatalyst, but it has a low efficiency and a narrow light-response range. Combining TiO₂ with CNT is being investigated as a means of increasing the photocatalytic activity and has proven the ability to fabricate an efficient heterogenous catalyst. Also the convenient adsorption of hydrogen in CNT

S. Wijewardane
Clean Energy Research Center, College of Engineering, University of South Florida,
Tampa, FL, USA
e-mail: swijewar@mail.usf.edu

makes it a good candidate for developing a feasible hydrogen storage system. Lack of an easy and effective CNT purification procedure is a major drawback to have such a storage system. Antenna solar energy conversion is an upcoming technology to convert the power of solar radiation directly to electric power utilizing the wave nature (electromagnetic) of light. It has demonstrated the applicability of CNT/CNT composites for this concept too. A good processability of materials is what requires for fabrication of potential complex geometries in ASEC as well as in photovoltaic cells. Polymer/CNT composites are expected to have good processing characteristics of the polymer and excellent functional properties of the CNTs.

Keywords

Hydrogen storage • Hydrogen production • Direct energy conversion • Photocatalytic activity

1 Direct Energy Conversions

1.1 Photovoltaic Cells

CNTs have attracted great interest as a potential material for solar photovoltaic applications since the start of the last decade due to their unique geometry and excellent electronic, thermal, and mechanical properties [1]. Also SWNTS have direct bandgaps which are inversely proportional to the tube diameter. So by combining CNTs of different diameters and chiralities, it is possible to achieve continuous range of bandgaps which correspond to a broad spectral range [2]. It is reported that at room temperature, it is possible to achieve bandgap from 0.3 to 2.0 eV using CNTs. But the main obstacle is the cost associated with CNTs. At the moment, SWNTs are approximately 250 times expensive than the single-crystal silicon on weight basis [3]. Recently CNTs are used to form rectifying heterojunctions with semiconductor materials such as silicon and n-GaAs [4]. But the reported efficiencies are low; therefore, much intense research is required.

Today there is a huge effort to develop polymer-based solar cells as an alternative to crystalline technology. The attractive point is that they can be manufactured on plastic substrates by a range of printing techniques. It is estimated that the production costs of a polymer-based solar cell is just one third of the cost of silicon-based cell. Also the polymer-based cell has improved scalability, and it is lightweight, flexible, and disposable [5]. But the power conversion efficiency is about 6 % [6]; thus, significant improvements are needed to achieve the commercial level.

There are number of in-depth reviews regarding the material selection for polymer solar cells [7, 8]. The polymers which are most promising for this application are poly (3-hexylthiophene)-(P3HT) and poly (3-octylthiophene)-(P3OT) [9]. Conducting polymers like these have the ability to generate bound electron-hole pairs (excitons). Additives with high electron affinity are integrated with these polymeric

materials to dissociate the excitons into free carriers before recombination. CNTs are ideal additives as their work function is in the range of 4.5–5.1 eV which is close to the valance band of P3OT/P3HT. By integrating SWNT into P3OT, a comparatively high open-circuit voltage close to 1.0 V can be obtained, but power conversion efficiency is significantly low [10]. Also these SWNT additives too can absorb photons and create excitons which could contribute to the photoconductivity of polymer cells [11].

A thin film of ITO (indium tin oxide) is the vastly utilized anode in these structures to collect the generated holes. But with the high cost of indium and lack of flexibility of ITO layers, there is a trend to test newer materials as anode. SWNTs are a popular candidate for this purpose. Recently a random mesh network of SWNTs was successfully tested as the transparent electrode for organic electronic devices [12]. Also SWNTs meshes mixed with metallic grids were used to get the combine effect of optical absorption and high conductivity.

As there are many ways that CNTs can help to improve the performances of polymer-based solar cells, they will have a definite role to play when transferring polymeric solar cells into commercial level.

1.2 Antenna Solar Energy Conversion (Rectenna Solar Cells)

Widespread usage of the solar energy has stalled by many drawbacks, mainly the poor efficiencies of existing solar–electric conversions. Within this scope, it is expected that the successful implementation of the emerging technology, antenna solar energy conversion (ASEC) to the commercial level with optimistic high conversion efficiencies, would revolutionize the solar energy utilization. A rectenna (rectifying + antenna) uses the wave nature of radiation to convert electromagnetic radiation to electricity [13]. The antenna receives the radiation and acts as a waveguide, while the rectifier converts it to DC current. Brown [14] showed that radiation at 2.45 GHz (microwave) could be converted to electricity at an efficiency of more than 90 %. The potential high conversion efficiency has attracted many research groups to focus on rectenna development at ever-increasing frequencies.

However, the concept of antenna solar energy conversion is extremely challenging. Although the ASEC concept is emerging with proclaims of high efficiencies, for a successful utilization, it should eventually possess a level of techno-economic feasibility and reliability at least comparable to contemporary solar–electric conversions. Also finding a proper combination of material and technology for the fabrication of the rectenna, even to test the concept, is a challenge [13]. To evaluate materials for certain application, it is necessary to assume the properties of the materials should poses the ability to tackle the major requirements and potential obstacles by integrating available technologies, and more importantly the economic aspects of the material and relevant technologies. Goswami et al. have done a primary analysis of ASEC concept and pointed out the potential characteristics of material such as high aspect ratio, low dielectric losses, ability to work at nano-range, etc., and have reported probable challenging events such as impedance

matching, interconnections, etc. With the many remarkable electrical, chemical, and mechanical properties that CNT poses and the wide attention it gains recently in the research area, CNT is considered as a potential material to implement Asec.

1.2.1 Thermomechanical and Chemical Compatibility

CNTs are thermally stable up to 700 °C in air and up to 2,800 °C in a vacuum, and theoretically the thermal expansion is negligible [15]. It is impossible to meet such a high temperatures in ASEC concept and thus poses thermal properties well over requisite level. Nanotubes electronic structure has been found to be insensitive to air [16] and constituent gases of air [17]. However, SWCNTs strongly interact with NO₂, SO₂, and NH₃ molecules [17]. Good strain reversibility at room temperature [18] and with smooth surface topology, perfect surface specificity [19], and mechanical robustness [20] make them highly compatible regarding thermomechanical and chemical properties.

1.2.2 Interaction with Light

Einstein's exploitations led to a theory of unity between subatomic particles and electromagnetic waves called "wave-particle duality" in which particles and waves are neither one nor the other, but had certain properties of both. The ASEC concept relies on the wave "property" of this duality as photovoltaic technology accounts for the other property, the particle behavior. So as the name (ASEC) implies, the receiving part of the device should interact with light similar to a receiving antenna, and other light interacting phenomena should be suppressed.

MWCNTs show a large nonlinear absorption of light [21]. Mixtures of MWCNTs contain semiconducting nanotubes apart from the metallic ones with different bandgaps covering the whole optical spectrum. Periodic MWCNT arrays exhibit Bragg diffraction [22] and photonic bandgap properties [23]. Nevertheless the polarization effect (dipolar antenna behavior) was observed in the Raman response of isolated single-wall carbon nanotube [24]. Also [25] demonstrated the polarization effect of random array of MWCNTs. Also they observed the interference colors of the reflected light from an array and showed that they were resulted from the "length matching" antenna effect. They selected random arrays to suppress the inter-tube diffraction, which obscures the intra-tube effects. Recently [26] illustrated that by controlling the geometry and spacing of the arrays, it is possible to create structures that respond very strongly to specific wavelengths or bands of wavelengths. The outcome of the latter experiments strongly enhanced the possibility of using random nanotube arrays to implement the ASEC concept. But to obtain the optimistic higher efficiencies, intensified innovative researches should be needed.

1.2.3 Networks and Interconnections

SWCNTs can be joined to form the "X-," "Y-," or "T"-shaped junctions, by introducing pentagon/heptagon defects at joining regions [27]. These nanotube junctions can be constructed to form two- and three-dimensional (2D, 3D) CNT networks [28].

The match between the pentagonal or hexagonal rings of the fullerenes and the open ends of CNT is a key factor in construction. These networks can be used to form thin-film transistors [29] and many other nanodevices and would facilitate to form and integrate potential complex networks in rectenna. But the technology is still at its rudimentary stage.

Current-induced electromigration causes conventional metal wire interconnects to fail when the diameter becomes too small. The covalently bonded structure of carbon nanotubes opposes similar breakdown of nanotube wires [1], and the ballistic transport, high thermal conductivity, and mechanical strength of CNTs make them ideal candidates for electrical interconnects when downsizing the circuit dimensions. Srivastava et al. [30] have reported the integration of CNTs into electrical interconnecting applications. Experimental results have shown that metallic single-wall nanotubes can carry up to 109 A/cm^2 compared to current densities for normal metals being only 105 A/cm^2 [31]. However, a critical issue is the nanotube density. The total current density is given by the current per CNT times the density of nanotubes. The nanotube density is often small, typically 0.12–1 % of the total area [32]. Some efforts have to be taken to increase the nucleation density of CNT to improve the applicability of CNT as interconnects. Zhu et al. [33] have demonstrated a way of forming densely aligned arrays with controllable array size and height. Also Chen et al. [34] have reported a novel approach of growing structured, highly oriented, vertically aligned carbon nanotubes that can be connected to two device terminals. Development of these techniques to commercial level apparently eases the prospective interconnecting problems in rectenna.

1.2.4 Rectification

According to Goswami et al. [13], the biggest stumbling block in achieving the ASEC concept is the ability to rectify electromagnetic waves at the high-frequency range of visible and IR radiation. So far the frequency limit, which could be successfully rectified, lays several magnitudes below the visible frequency range. One of the latest trends in high-frequency (terahertz) technology is to use CNT as building blocks of novel terahertz devices [35]. Using the advantage of intrinsically low capacitance of CNT, Lu et al. [36] have demonstrated a fabrication process of Schottky diodes for radio-frequency applications. Dragoman et al. [35] have presented the simulation and physical implementation of a resonant-tunneling diode using CNT, which is applicable for the frequency limit of 16 THz. Also in this paper, the CNT properties which are exceeding the characteristics of semiconductor heterostructures were identified. But those indicated frequency levels are well below the optical range. Metal–insulator–metal (MIM) point contact diodes have been used for infrared applications over a long time [37]. These kinds of devices with CNT are already realty. Huang et al. [38] have found less symmetric I–V characteristic for the metal/MWCNT/metal sandwich structure. The equivalent circuit for this structure could be represented as two Schottky barrier diodes in a back-to-back configuration. Using the metallic CNT films as the electrodes and GaAs as the semiconductor, Behnam et al. [39] demonstrated the metal–semiconductor–metal (MSM) device which

exhibits higher properties over the conventional metal-based MSMs. Analyzing relevant publications for the last few years, we could assume a reasonable possibility to develop MIM point contact diodes with metallic SWCNT as electrodes to handle the optical frequencies. Difference in work functions of the metallic materials plays a key role in determining the upper frequency limit of these devices. Work function of 4.6–4.8 eV for individual MWCNT using transmission electron microscopy and values of 4.95 and 5.05 eV for MWCNTs and SWCNTs using photoelectron emission method was reported by [40]. A drastic decrease of the work function to about 2.4 eV was observed in the Cs-intercalated single-wall carbon nanotube bundles [41]. Shan and Cho [42] reported substantial changes of work function with diameter, length, and arrangement for nanotubes less than 1 nm in diameter. This increases the possibility of having a tunable work function.

To improve the high-frequency performances, the parasitic capacitance between electrodes should be a minimum. Dragoman and Dragoman [35] reported that for over a decade, there was no progress toward increasing the oscillation frequency of resonance-tunneling diodes (RTD) because of the inability to decrease further the values of inherent parasitic element either resistive or reactive due to physical and technological limitations. But with CNT they have overcome the performance limitations of RTD devices based on semiconductor heterostructures. Guo et al. [43] showed that by using an array of parallel nanotubes as the transistor channel in field-effect transistors (FET), a reduction of the parasitic capacitance per tube, hence, gained an improvement in high-frequency performances.

For the successful operations of the MIM diode in the optical range, the contact area should be very small. This makes the fabrication extremely challenging. But carbon nanotubes, which are born to work in the nanoscale, will make the fabrication easier. Nanodiodes based on CNT, which are very stable in ambient environment, were successfully fabricated [44]. Molecular RTDs with CNT, which are compatible with bioassembly techniques, are also proposed [45].

These findings simulate the possibility of optical frequency rectification diodes with CNT as the main material. Needless to say, such and laborious task will take some time to realize.

1.2.5 CNT Composites

Impedance matching can be identified as a major difficulty in nanodevices such as rectennas. Also CNTs may have high dielectric losses at optical frequencies due to its high conductance according to Maxwell theory. In this scope, CNT/polymer composites would be ideal as dielectric substrates or use as dielectric waveguides in resonant-type antennas. One of the main advantages of polymer/CNT composites relevant to ASEC is the ability to alter the electrical properties to facilitate the adjusting of the dielectric constant and the loss tangents and to enhance the overall impedance matching and thereby lowering the insertion loss of the device. Also polymer/carbon nanotube composites are expected to have good processability characteristics of the polymer and excellent functional properties of the CNTs [46]. The good processability enhances the fabrication of potential complex geometries in ASEC. First commercially recognized use for multi-wall nanotubes

was in fact electrically conducting components in polymer composites [1]. With reported mechanical and electrical properties of CNT, a whole new class of CNT composites with plenty of diversities could be possibly formed with wide range of materials such as ceramics, metals, and polymers. Ultrastrong and/or multifunctional composites can be derived depending upon the properties of the added material [47]. Bulk of the published papers on CNT composites are dealing with the polymer-based matrices.

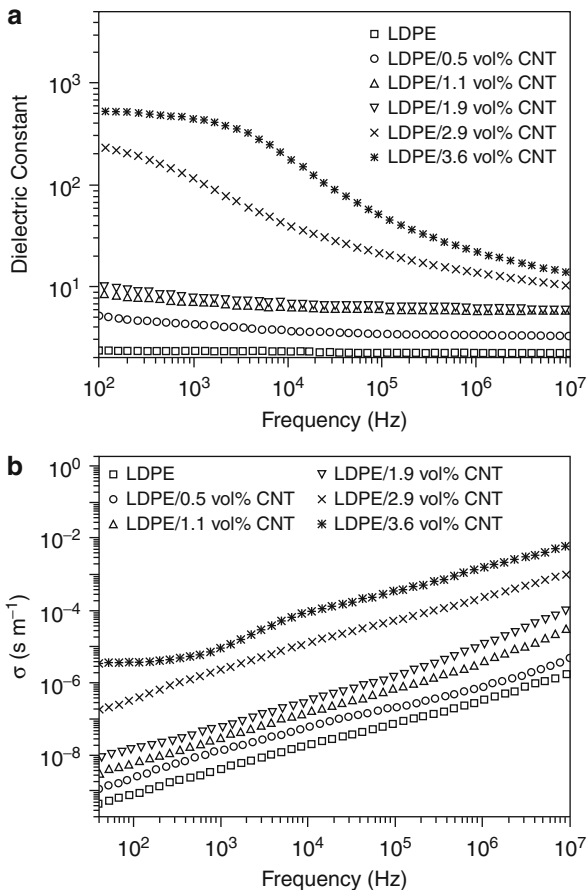
These composite structures have been targeted for optical and dielectric applications such as waveguides, antireflection coatings, EMI shielding, and films with high dielectric strengths and moderately high dielectric constants [48]. The dielectric properties of polymeric substances have long attracted the attention of many workers in science, technology, and engineering [49]. The dielectric properties of polymers are largely predictable from the chemical structure of the polymer. The chemical structure determines the polar or nonpolar nature of the final polymer and determines the behavior of the polymer under a variety of electrical situations. The low electrical conductivity and low dielectric losses, which many polymers exhibit, make them very useful for electrical insulation and encapsulation.

There is a great deal of available information on the dielectric behavior of many polymers. Most applications of thin polymer films make use of their dielectric properties. In addition, there are a great variety of polymer substances regarding chemical and thermal stability, mechanical strength, etc., which could be chosen for appropriate applications. These advantages open many options and conveniences for selecting suitable materials for the composites.

Carbon nanotubes have a substantially larger aspect ratio (1,000) in comparison with layered silicates (200) [50]. Carbon nanotubes provide the largest modulus enhancement in the polymer resins at fixed filler loading compared to silicate clays and nanoceramic particulates, because of the large aspect ratio, high mechanical strength, and stiffness of the nanotubes. Many applications only need a small amount of nanotubes to be added into the polymer-based materials [51]. To have the required properties, carbon nanotubes can be integrated into composites to improve the electrical properties, which can act as a polymer or metal [52]. The properties of nanocomposites depend greatly on the chemistry of polymer matrices, nature of nanofillers, and the way in which they are prepared [53]. Electrical properties of the composites may vary from those of an insulating material to those of conducting filler network, depending on the concentration, property of the conducting fillers, and dispersion of conducting fillers in polymeric matrix. Electrical properties of the conducting fillers/insulating polymer composites are often analyzed in terms of the statistical percolation theory.

At low concentration, conducting fillers are dispersed within polymeric matrix as insulated clusters. Beyond a critical concentration of conducting filler, known as percolation threshold, filler clusters begin to connect each other to form a filler network throughout the entire composite, which increase the conductivity and alter dielectric properties of the composite [54]. By analyzing electrical characteristics, Chauvet et al. [55] showed that the 3D network formed by

Fig. 21.1 (a) Dielectric constant and (b) resistivity versus frequency for low-density polyethylene (LDPE)/CNT nanocomposites [54]



SWNTs determines the conductivity at room temperature of polymeric matrix. The SWNT network inside the composite is of same electrical nature as in pellets.

The frequency (f) dependence of the dielectric constant (ϵ) of materials having percolation threshold (can be also used for just under the percolation threshold with reasonable accuracy) can be expressed as

$$\epsilon(f) \propto \omega^{-\mu}$$

and the dependence of conductivity (σ), on the frequency of dielectric materials, can be described as

$$\sigma(f) \propto \omega^{\nu}$$

where $\omega = 2\pi f$ and μ and ν are the critical exponent depending on the concentration of the composite [54] (Fig. 21.1).

These findings prove the possibility of predicting the electrical properties of CNT/polymer composites at higher optical frequencies. By extrapolating the x-axis (frequency) up to optical frequency (10^{15} Hz), the corresponding values of conductivity and dielectric constants can be predicted easily. This methodology facilitates the material selection criteria for devices, which deal with optical frequencies such as solar rectenna. Depending on the type and properties of CNT and the degree of their dispersion in the polymer matrix, percolation threshold for the formation of conductive CNT networks can be found as low as 1 wt% even for highly viscous polymer matrixes [56].

Many papers have published regarding the CNT/ceramic nanocomposites as well [57, 58]. These works demonstrated that CNTs are an effective reinforcement for brittle ceramics as well. Sivakumar et al. [47] report an improvement of thermal conductivity of the CNT/silica nanocomposites compared with pure SiO_2 matrix. SiO_2 (silica) is an ideal material to use as an antenna window material and has remarkable thermal and dielectric properties. The percolation of carbon nanotubes (CNT) in an electrical insulating ceramic (MgAl_2O_4) was studied by Rul et al. [59] and proved that the DC electrical conductivity is well fitted by the scaling law of the percolation.

CNT poses exceptional thermomechanical properties that suit for ASEC. The outcomes from the researches done on the interaction of visible light with SWCNT and CNT arrays favor the manufacturing of optical antennas with CNT. High-frequency diodes with CNT are becoming a reality. Nevertheless intense researches have to be focused to obtain the optimistic high efficiencies. CNT-related technologies have the potential to enhance the progress of the ASEC concept, but most of technologies are at their initial stages and would take some time to improve to the commercial level.

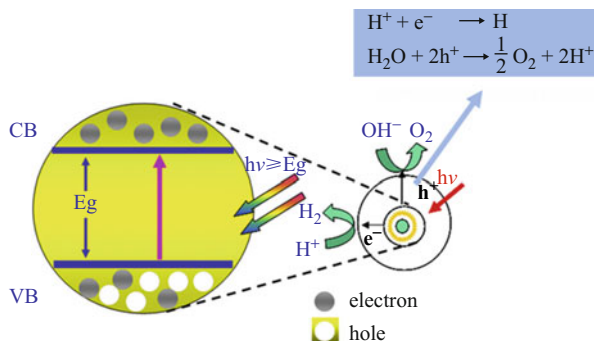
2 Hydrogen

2.1 Hydrogen Production

Hydrogen has gained much attention as the most promising energy resource to overcome the future energy crisis. With the shift toward a hydrogen economy which has been already forecasted, there will be a huge demand for hydrogen. Water is the ideal source for hydrogen. Therefore, water splitting using a renewable energy sources such as solar energy is one of the most sustainable ways of producing hydrogen gas without evolution of the greenhouse gases. Although water splitting is not economically competitive with current energy costs, when developed with economic viability in the future, this could be the eventual technology that could solve the energy problem and save the environment.

Photocatalytic water splitting using sunlight has been studied for a long time [60], and a good progress has been recorded in the recent past [61, 62]. Figure 21.2 illustrates the basic principle of water splitting [62]. Water splitting into H_2 and O_2 is highly endothermic. Therefore, the light-responsive photocatalyst should have a suitable thermodynamic potential for water splitting. Hundreds of materials and derivatives including semiconductor photocatalytics, such as TiO_2 , SiC, CdS, etc.,

Fig. 21.2 Basic principle of water splitting [62]



have been developed so far. Basic requirements for a potential photocatalytic material other than the thermodynamic potential are the following: (1) it should absorb efficiently the photons with required energy, (2) it should facilitate the separation of photo-generated electron–hole charges, and (3) it should transport these generated charges quickly to avoid electron–hole recombination. Although the theoretical efficiency of photocatalytic H_2 generation is about 30 % [63] in practice, the achieved efficiencies are well below this theoretical limit. The reason is lack of a semiconductor material that fulfills all the electronic, optical, and microstructural requirements.

Due to their special structures and unique electronic and physical properties, carbon nanotubes have gained much attention as a potential material to form binary nanocomposites with photocatalytic materials. These nanocomposites demonstrate enhanced photoactivity and photostability. MWCNTs have been successfully used to enhance the photocatalytic activity of semiconductors such as TiO_2 [64, 65] and CdS [66, 67] and even in metal-free organic semiconductors such as polymer graphite carbon nitride ($g\text{-C}_3\text{N}_4$) [68]. Also there are few reports about the usage of SWCNTs to enhance the photocatalytic activity of metal oxide semiconductors such as TiO_2 [69]. It is suggested that CNT enhanced the photocatalytic activity of composites in few different ways [70]. As CNT is an electron acceptor and a good electric conductor, it could facilitate an efficient charge transfer, thus reducing the charge recombination. And also CNT could act as a photosensitizer and enhance the photon absorption. In addition the morphological changes induced to the composites by adding CNT could increase the effective surface area for photon absorption.

2.2 Hydrogen Storage

Developing cost-effective, compact, and reliable hydrogen storage technologies is of prime importance for achieving a hydrogen economy. Hydrogen has very low energy content by volume compared to other energy sources such as gasoline. This makes it hard to achieve a cost-effective and compact storage system. Carbon is one of the better adsorbent of gases. Therefore, CNTs which have a large surface area, good chemical stability, and hollowness are an intuitive candidate for hydrogen storage.

First attempt to investigate the hydrogen storage capacity of CNT was reported in 1997 [71]. In this initial period of investigation, storage capacities well above the DOE limit of 6.5 wt% were reported. These results stimulated the more in-depth investigations of hydrogen storage capacities of CNT. But later it was found out that factors such as moisture in the hydrogen gas and metal particles in the nanotubes are largely responsible for those favorable results [72, 73]. The inconsistencies of the reported results further urged scientists to look into wider range of factors such as measurement methodology, synthesis techniques, structural perfection, etc., which influence the hydrogen storage capacities. But the recently reported values are still quite dispersed, ranging from 0.02 wt% to 17 wt% [74]. The exact reasons for this diverse results and the mechanism of hydrogen adsorption in carbon nanotubes are yet not clear. The existing agreeable view point is that CNTs have no significant capability of storing hydrogen at room temperature and considerable storage capacities can be only observed at high pressures and at cryogenic temperatures [75]. Although the current stance is not in favor of having a cost-effective hydrogen storage method using CNTs, researchers are continuing their efforts to get a deeper understanding of the mechanism of hydrogen adsorption and create more favorable nanocomposites based on CNTs for hydrogen storage. Therefore, CNTs remain as a potential material for hydrogen storage.

3 Future Directions

The research field of CNT and CNT/composites is very active, and significant improvements are emerging on a regular basis. So apart from conducting well-directed researches to improve the properties and functionality of CNT and CNT/composites as required by the energy applications, it is also important to scrutinize possible ways of effectively integrating the new breakthroughs to the energy applications. Recently a group of scientists have created nanotubes that can be expanded and contracted by changing the environmental temperature, without being broken down in the process [76]. These types of nanotubes may well be used as “nano-valves” that could fine-tune the hydrogen flow from the hydrogen storage systems. Also a recent simulation [77] shows that ultrathin CNTs with an outer diameter of 3.2 Å can be practically existed exclusively without being confined inside the thicker CNTs and they are stable even at very high temperatures. As the direct bandgaps are inversely proportional to the tube diameter, this finding expands the upper limit of frequency responsive range of a potential photovoltaic cell created using CNTs.

Also any energy harvesting method should produce energy economically, as to be competitive in the energy market. So other than improving the functionality of CNT and CNT/composites to suit the energy applications more effectively, researches should be focused on producing the CNT and CNT composites cheaply at an industrial scale. In this prospective, recently, one research group has come up with a low-cost solution to separate semiconducting nanotubes and nonconducting nanotubes from the bulk [78]. The preceding methods of separation are very expensive, and it is believed that careful optimism could take this new method to the industrial level.

To produce CNT itself, a significant amount of energy is required. Therefore, it is worthwhile to look into the possibilities to get this manufacturing energy from an ultimate clean energy source such as solar power. Already there are some suggestions to utilize the solar radiation to activate different catalysts which are used in the CNT manufacturing processes [79].

References

1. Baughman RH, Zakhidov AA, de Heer WA (2002) Carbon nanotubes the route toward applications. *Science* 297(5582):787–792
2. Elliott JA, Sandler JKW, Windle AH, Young RJ, Shaffer MS (2004) Collapse of single-wall carbon nanotubes is diameter dependent. *Phys Rev Lett* 92(9):1–4
3. Zhu H, Wei J (2009) Applications of carbon materials in photovoltaic solar cells. *Sol Energy Mater Sol Cells* 93:1461–1470
4. Liang CW, Roth S (2008) Electrical and optical transport of GaAs/carbon nanotube heterojunctions. *Nano Lett* 8:1809–1812
5. Brabec CJ (2004) Organic photovoltaics: technology and market. *Sol Energy Mater Sol Cells* 83:273–292
6. Park SH, Roy A, Beaupre S, Cho S, Coates N, Moon JS, Moses D, Leclerc M, Lee K, Heeger AJ (2009) Bulk heterojunctions solar cells with internal quantum efficiency approaching 100 %. *Nat Photonics* 3:297–303
7. Brabec CJ, Durrant JR (2008) Solution-processed organic solar cells. *MRS Bull* 33:670–675
8. Thompson BC, Frechet JM (2008) Polymer-fullerene composite solar cells. *Angew Chem Int Ed* 47:58–77
9. Chandross M, Mazumdar S, Jeglinski S, Wei X, Vardeny ZV, Kwock EW, Miller TM (1994) Excitons in PPV. *Phys Rev B* 50:14702–14705
10. Kymakis E, Amaratunga GAJ (2002) Single-wall carbon nanotube/conjugated polymer photovoltaic devices. *Appl Phys Lett* 80:112–114
11. Freitag M, Martin Y, Misewich JA, Martel R, Avouris P (2003) Photoconductivity of single carbon nanotubes. *Nano Lett* 3:1067
12. Wu Z, Chen Z, Du X, Lgan JM, Sippel J, Nikolou M, Kamaras K, Reynolds JR, Tanner DB, Hebard AF, Rinzler AG (2004) Transparent conductive carbon nanotube films. *Science* 305:1273–1276
13. Goswami DY, Vijayaraghavan S, Lu S, Tamm G (2004) New and emerging developments in solar energy. *Sol Energy* 76:33–43
14. Brown WC (1984) The history of power transmission by radio waves. *IEEE Trans Microw Theor Tech* MT32(9):1230e42
15. Nalwa HS (2000) Handbook of nanostructured materials and nanotechnology, vol 5. Academic, New York
16. Suzuki S, Watanabe Y, Kiyokura T, Nath KG, Ogino T, Heun S et al (2002) Effects of air exposure and Cs deposition on the electronic structure of multiwalled carbon nanotubes. *Surf Rev Lett* 9:431
17. Goldoni A, Larciprete R, Petaccia L, Lizzit S (2003) Single-wall carbon nanotube interaction with gases: sample contaminants and environmental monitoring. *J Am Chem Soc* 125:11329
18. Pham GT, Park Y, Liang Z, Zhang C, Wang B (2007) Processing and modeling of conductive thermoplastic/carbon nanotube films for strain sensing. *Composites Part B: Engineering* 39:209–216
19. Ajayan P, Zhou O (2001) Applications of carbon nanotubes. In: Mildred S. Dresselhaus, Gene Dresselhaus, Phaedon Avouris Carbon Nanotubes. UNC, Topics in Applied Physics; Volume 80, 2001, Springer Berlin Heidelberg 391–425

20. Wang WK, Cao LM (2001) Transformation of carbon nanotubes to diamond at high pressure and high temperature. *Russ Phys J* 44(2):178–182
21. Chen YC et al (2002) Ultrafast optical switching properties of single wall carbon nanotube polymer composites at 155 nm. *Appl Phys Lett* 81:975
22. Wu P, Kimball B, Carlson J (2004) Light scattering of periodic β aligned carbon nanotubes. *Phys Rev Lett* 93:013902
23. Kempa K et al (2003) Photonic crystals based on periodic arrays of aligned carbon nanotubes. *Nano Lett* 3:13–18
24. Jorio A, Souza Filho AG, Brar VW, Swan AK, Unlu MS, Dresselhaus MS (2002) Polarized resonant Raman study of isolated single-wall carbon nanotubes: symmetry selection rules, dipolar and multipolar antenna effects. *Phys Rev B* 65:121402R
25. Wang Y et al (2004) Receiving and transmitting light-like radio waves: antenna effect in arrays of aligned carbon nanotubes. *Appl Phys Lett* 85:2607–2609
26. Gregorczyk K, Kimball B, Carlson JB (2006) The complex optical response of arrays of aligned multiwalled carbon nanotubes. *Nanophotonic Mater III* 6321:63210G
27. Menon M, Andriotis AN, Srivastava D, Ponomareva I, Chernozatonskii LA (2003) Carbon nanotube “T Junctions”: formation pathways and conductivity. *Phys Rev Lett* 91:145501
28. Dag S, Senger RT, Ciraci S (2004) Theoretical study of crossed and parallel carbon nanotube junctions and three-dimensional grid structures. *Phys Rev B* 70:205407
29. Snow ES, Campbell PM, Ancona MG, Novak JP (2005) High mobility carbon-nanotube thin-film transistors on a polymeric substrate. *Appl Phys Lett* 86:033105
30. Srivastava N, Banerjee K (2004) Interconnect challenges for nanoscale electronic circuits. *J Mater* 56(10):30–31
31. Wei BQ, Vajtai R, Ajayan PM (2001) Reliability and current carrying capacity of carbon nanotubes. *Appl Phys Lett* 79(8):1172–1174
32. Robertson J (2007) Growth of nanotubes for electronics. *Mater Today* 10:36–43
33. Zhu L, Xu J, Xiu Y, Sun Y, Hess DW, Wong CP (2006) Growth and electrical characterization of high-aspect-ratio carbon nanotube arrays. *Carbon* 44:253–258
34. Chen Z, Merikhi J, Koehler I, Bachmann PK (2006) Sandwich growth of carbon nanotubes. *Diamond Relat Mater* 15:104–108
35. Dragoman D, Dragoman M (2004) Terahertz oscillations in semiconducting carbon nanotube resonant-tunneling diodes. *Phys E Low-Dimens Syst Nanostruct* 24(3–4):282–289
36. Lu C et al (2006) Schottky diodes from asymmetric metal-nanotube contacts. *Appl Phys Lett* 88:133501
37. Masalmeh SK, Stadermann HKE, Korving J (1996) Mixing and rectification properties of MIM diodes. *Physica B* 218:56–59
38. Huang S, Woodson M, Smalley R, Liu J (2004) Growth mechanism of oriented long single walled carbon nanotubes using “Fast-Heating” chemical vapor deposition process. *Nano Lett* 4:1025–1028
39. Behnam A et al (2008) Metal–semiconductor–metal photodetectors based on single-walled carbon nanotube film–GaAs Schottky contacts. *J Appl Phys* 103:114315
40. Su WS, Leunga TC et al (2007) Work function of small radius carbon nanotubes and their bundles. *Appl Phys Lett* 90:163103
41. Suzuki S et al (2000) Work functions and valence band states of pristine and Cs-intercalated single-walled carbon nanotube bundles. *Appl Phys Lett* 76:4007–4009
42. Shan B, Cho K (2005) First principles study of work functions of single wall carbon nanotubes. *Phys Rev Lett* 94:236602
43. Guo J, Hasan S, Javey A, Bosman G (2005) Assessment of high frequency performance potential of carbon nanotube transistors. *IEEE Trans Nanotechnol* 4:715–721
44. Chai Y, Zhou XL et al (2005) Nanodiode based on a multiwall CNx/carbon nanotube intramolecular junction. *Nanotechnology* 16:2134–2137
45. Pandey RR, Bruque N, Alam K, Lake RK (2006) Carbon nanotube – molecular resonant tunneling diode. *Phys Stat Sol A* 203:R5–R7

46. Xie XL, Mai YW, Zhou XP (2005) Dispersion and alignment of carbon nanotubes in polymer matrix: a review. *Mater Sci Eng R* 49:89–112
47. Sivakumar R, Guo S, Nishimura S, Kagawa Y (2007) Thermal conductivity in multi-wall carbon nanotube/silica-based nanocomposites. *Scr Mater* 56:265–268
48. Jiang B, Lianggou Hong B, John T et al (2007) Relationship between chemical structure and dielectric properties plasma-enhanced chemical vapor deposited polymer thin films. *Thin Solid Films* 515:3513–3520
49. Gregor LV (1968) Polymer dielectric films. *IBM Journal of Research and Development* 12:140–162
50. Potschke P, Bhattacharyya AR, Janke A (2003) Morphology and electrical resistivity of melt mixed blends of polyethylene and carbon nanotube filled polycarbonate. *Polymer* 44:8061
51. Kim YJ, Shin TS, Choi HD, Kwon JH, Chung YC, Yoon HG (2005) Electrical conductivity of chemically modified multiwalled carbon nanotube/epoxy composites. *Carbon* 43:23–30
52. Liu P (2005) Modifications of carbon nanotubes with polymers. *Eur Polym J* 41:2693–2703
53. Tjong SC (2006) Structural and mechanical properties of polymer nanocomposites. *Mater Sci Eng R* 53:73–197
54. Liang GD, Tjong SC (2006) Electrical properties of low-density polyethylene/multiwalled carbon nanotube nanocomposites. *Mater Chem Phys* 100:132–137
55. Chauvet O, Benoit JM, Corraze B (2004) Electrical, magnetotransport and localization of charge carriers in nanocomposites based on carbon nanotubes. *Carbon* 42:949–952
56. Grossiord N, Loos J, Koning CEJ (2005) Strategies for dispersing carbon nanotubes in highly viscous polymers. *Mater Chem* 15:2349
57. Wang X, Padture NP, Tanaka H (2004) Contact-damage-resistant ceramic/single-wall carbon nanotubes and ceramic/graphite composites. *Nat Mater* 3:539
58. Zhan D, Kuntz JD, Wan J, Mukherjee AK (2003) Single-wall carbon nanotubes as attractive toughening agents in alumina-based nanocomposites. *Nat Mater* 2:38
59. Rul S, Lef F et al (2004) Percolation of single-walled carbon nanotubes in ceramic matrix nanocomposites. *Acta Mater* 52:1061–1067
60. Fujishima A, Honda K (1972) Electrochemical photolysis of water at a semiconductor electrode. *Nature* 238:37–38
61. Maeda K, Domen K (2010) Photocatalytic water splitting: recent progress and future challenges. *J Phys Chem Lett* 1:2655–2661
62. Jing D, Guo* L (2010) Liang Zhao Efficient solar hydrogen production by photocatalytic water splitting: from fundamental study to pilot demonstration. *Int J Hydrogen Energy* 35:7087–7097
63. Walter MG, Warren EL, McKone JR, Boettcher SW, Mi Q, Santori EA et al (2010) Solar water splitting cells. *Chem Rev* 110:6446e73
64. Dai K, Peng TY, Ke DN, Wei BQ (2009) Photocatalytic hydrogen generation using a nanocomposite of multi-walled carbon nanotubes and TiO₂ nanoparticles under visible light irradiation. *Nanotechnology* 20:125603–1–6
65. Yao Y, Li GH, Ciston S, Lueptow RM, Gray KA (2008) Photoreactive TiO₂/carbon nanotube composites: synthesis and reactivity. *Environ Sci Technol* 42:4952–4957
66. Ma LL, Sun HZ, Zhang YG, Lin YL, Li JL, Wang EK, et al. (2008) Preparation, characterization and photocatalytic properties of CdS nanoparticles dotted on the surface of carbon nanotubes. *Nanotechnology* 19:115709–1–8
67. Cao J, Sun JZ, Hong J, Li HY, Chen HZ, Wang M (2004) Carbon nanotube/CdS core-shell nanowires prepared by a simple room-temperature chemical reduction method. *Adv Mater* 16:84–87
68. Suryawanshi A, Dhanasekaran P, Mhamane D (2012) Doubling of photocatalytic H₂ evolution from g-C₃N₄ via its nanocomposite formation with multiwall carbon nanotubes: electronic and morphological effects. *Int J Hydrogen Energy* 37:9584–9589
69. Ahmmad B, Kusumoto Y (2008) Carbon nanotubes synergistically enhance photocatalytic activity of TiO₂. *Catal Commun* 9:1410–1413

70. Xiaojing Liu, Peng Zeng, Tianyou Peng (2012) Preparation of multiwalled carbon nanotubes/Cd_{0.8}Zn_{0.2}S nanocomposite and its photocatalytic hydrogen production under visible-light. *Int J Hydrogen Energy* 37:1375–1384
71. Dillon AC, Jones KM, Bekkedahl TA, Kiang CH, Bethune DS, Heben MJ (1997) Storage of hydrogen in single-walled carbon nanotubes. *Nature* 386:377
72. Yang RT (2000) Hydrogen storage by alkali-doped carbon nanotubes-revisited. *Carbon* 38:623
73. Hirscher M, Becher M, Haluska M, von Zeppelin F, Chen XH, Dettlaff-Weglikowska U, Roth S (2003) Are carbon nanostructures an efficient hydrogen storage medium? *J Alloys Compd* 356–357:433
74. Liu C, Cheng H-M (2005) Carbon nanotubes for clean energy applications. *J Phys D Appl Phys* 38:R231–R252
75. Oriňáková R, Oriňák A (2011) Recent applications of carbon nanotubes in hydrogen production and storage. *Fuel* 90(11):3123–3140
76. Huang Z, Kang S, Banno M, Yamaguchi T (2012) Pulsating tubules from noncovalent macrocycles. *Science* 337(6101):1521–1526
77. Menéndez-Proupin E et al (2012) Ultrathin carbon nanotube with single, double, and triple bonds. *Phys Rev Lett* 109:105501
78. <http://spectrum.ieee.org/nanoclast/semiconductors/materials/carbon-nanotubes-get-a-new-and-simple-bulk-sorting-process>
79. Ozalp N, Epstein M, Kogan A (2010) Cleaner pathways of hydrogen, carbon nano-materials and metals production via solar thermal processing. *J Clean Prod* 18:900–907

CNT-Based Inherent Sensing and Interfacial Properties of Glass Fiber-Reinforced Polymer Composites

22

Zuo-Jia Wang, Dong-Jun Kwon, Ga-Young Gu, and Joung-Man Park

Contents

1	Introduction	544
2	Mechanical Properties of Glass Fiber	547
2.1	Surface Treatments on Glass Fiber	547
2.2	Analysis of Single Fiber Tensile Strength	549
3	Interfacial Evaluation of Glass Fiber/CNT–Polymer Composites	553
3.1	Measurement of Interfacial Shear Strength (IFSS)	553
3.2	Microdroplet Pullout Test	554
4	Measurements of Contact Angle, Wettability, and Surface Energies	556
4.1	Relationship Between Wettability and Interface	556
4.2	Static Contact Angle Test	556
4.3	Dynamic Contact Angle Test	558
4.4	Calculation of Work of Adhesion	560
5	Carbon Nanotubes Grafting on Glass Fiber	563
5.1	Interphase Sensors Based on Carbon Nanotubes	563
5.2	Preparation and Morphology of CNT-Coated GF Fibers	564
5.3	Mechanical Properties of CNT-Coated Glass Fiber	564
5.4	Interfacial Shear Strength of CNT-Coated GF Fibers	565
5.5	Evaluation on the Interphase Damage by the Interphase Sensor	566
6	Conclusions	570
	References	572

Z.-J. Wang • D.-J. Kwon • G.-Y. Gu

School of Materials Science and Engineering, Engineering Research Institute Gyeongsang National University, Jinju, South Korea

e-mail: wangzj@empas.com

J.-M. Park (✉)

School of Materials Science and Engineering, Engineering Research Institute Gyeongsang National University, Jinju, South Korea

Department of Mechanical Engineering, The University of Utah, Salt Lake City, UT, USA

e-mail: jmpark@gnu.ac.kr

Abstract

Carbon nanotubes (CNTs) are ideal candidates for reinforcement in composite materials due to their nanoscale structure, outstanding mechanical, thermal and electrical properties. Consideration has been given to introducing CNTs into conventional fiber reinforced composites, forming a hierarchical structure, where nanoscale reinforcement is made to work alongside more traditional microscale architecture. CNTs grafting onto fiber surface have been used to create electrically conductive interphases for introducing sensing capabilities in bulk nanocomposites. The intrinsic mechanical properties of CNTs have resulted in considerable interest in their use as reinforcement for composites. Nanocomposites filled with CNT have high stiffness, strength and good electrical conductivity at relatively low concentrations of these reinforcing materials. Gradient specimen which contains electrical contacts with gradually-increasing spacing is an effective test to observe the contact resistance at interface of CNT-polymer nanocomposites. Due to the presence of hydrophobic domains on the heterogeneous surface, CNT-polymer nanocomposites exhibit a hydrophobic property. Strong and durable interfacial adhesion is expected to transfer the stress efficiently from the matrix to the fiber, which may result in greatly improved mechanical properties in composites. Inherent sensing and interfacial properties of fiber reinforced CNT-polymer nanocomposites could be evaluated by electro-micromechanical and wettability measurements.

Keywords

Fragmentation test • Glass fiber reinforced plastics (GFRPs) • Interface • Interfacial shear strength (IFSS) • Interphase sensors • Micro-mechanics • Recycling • Surface treatment • Wettability

1 Introduction

Fiber-reinforced plastics (FRPs) have become one of the most important materials in the field of lightweight construction, especially in the aircraft and wind energy industries. Due to their high specific stiffness and strength as well as their outstanding fatigue performance, FRPs have become irreplaceable materials in structural component design. Among composite materials, glass fiber-reinforced plastics (GFRPs) are inexpensive and consequently have the most potential uses due to their cost-effectiveness [1–3]. Glass fibers are the type of high-strength fibers that are most commonly used to strengthen composites due to comparatively low cost as well as their considerable tensile strength and relatively high modulus.

Although glass fiber-reinforced composites are commonly used as lightweight materials for a wide variety of structural uses such as various marine applications, they are now also used extensively in the aerospace field together with carbon and other more advanced fiber-reinforced composites. Impetus for the rapid increase in usage of these materials includes their excellent mechanical properties, heat

Fig. 22.1 GFRP is used in latest high-speed train



Fig. 22.2 GFRP is used in wind turbine generator



stability, and low flammability. Public transportation is growing and is becoming faster and more advanced, and this is not without a risk. These improvements require more composites and electronics being used. It is important to make public transportation as safe as possible. Glass fiber comes in here since it plays an important role in increasing fire safety. Trains, busses, metros, and trams all increasingly use GFRP, and the latest train is shown in Fig. 22.1. Its lightness, rigidity, and flexibility make it the perfect material for public transportation. To ensure fire safety, Parabeam 3D Glass Fabrics, a woven fabric out of glass fiber, can be combined with phenolic resin. The combination of the glass fiber with the resin provides an enormous improvement in fire safety. Public transportation all around the world is already equipped with fiberglass and phenolic resin, to contribute to the safety of transportation. In Fig. 22.2, GFRPs used for the large-scale wind turbine blade required the high material strength and formability. The strength is improved by the addition of short fibers which distributes randomly in GFRP.

Glass fiber-reinforced laminates containing clay/polyamide 6 nanocomposites have been shown to exhibit significantly improved flexural and compressive strength [4]. Furthermore, significant improvements in electrical and thermal properties have been achieved in CNT–epoxy nanocomposites accompanying these reinforcing effects. Glass fiber-reinforced CNT–epoxy laminates have been shown to exhibit an increase of 20 % in the CNT–epoxy matrix-dominated interlaminar shear strength, whereas the tensile properties of the laminate were not significantly affected since these are microfiber-dominated properties [5].

Recently, carbon nanomaterials (CNMs) have attracted considerable attention in both research and industrial fields due to their unique mechanical and electrical properties for multifunctional purposes. The conductivity and high aspect ratios of CNT are attractive properties for producing conductive composites with minimum added constituents. CNT is an intriguing material that has attracted much attention from both scientists and engineers, since the early 1990s. Nanocomposites filled with CNT have high stiffness, strength, and good electrical conductivity at relatively low concentrations of these reinforcing materials [6, 7]. In particular CNTs could potentially be used as low-resistance ballistic interconnects for electron devices [8, 9]. The outstanding intrinsic mechanical properties of CNTs have resulted in considerable interest in their use as reinforcement for composites. The addition of a CNT network to a polymer matrix significantly improves the mechanical properties of the resulting composites.

Electrical resistance can be measured using either a two-point or a four-point method. For the two-point method, the specimen is kept at a certain potential, and the conductivity is measured by applying a small AC or DC voltage between two probes [10–12]. The electrical resistance measured by this technique includes both the volume resistance of the composite and the contact resistance between the contacting materials and the composite. As a consequence, the results obtained by this method may contain large errors due to the contribution of the contact resistance [13, 14]. On the other hand, in the four-point method, a constant current is introduced between two outer probes, and the potential difference between the inner probes is measured by a voltmeter. Since the current through a typical voltmeter is very nearly zero, the contact resistance between the two inner probes and the composites has almost no influence on the composite's electrical resistance measurement [15].

It is generally accepted that super-hydrophobicity exhibits an important interface characteristic, possibly exhibiting a water droplet advancing contact angle of 150° or higher. Such wetting phenomenon allows rain droplets to simply roll off of surfaces, thus rinsing away dirt and debris [16, 17]. Measurements are widely used for investigating surface characteristics on various materials. The surface free energy of a material controls its adhesion, adsorption, lubrication, joint strength, wettability, etc. [18]. The adhesive strength of an interface depends on the thermodynamic work of adhesion which, in a fiber-reinforced composite, is closely related to the surface energy between fibers and matrix [19]. The macroscopic Young–Dupre equation correlates the contact angle to the surface and interfacial tensions, which may be further decomposed into Lifshitz-van der Waals (LW) and the polar components of

the surface energies [20]. Different routes of surface energy analyze have been outlined by Zisman. The harmonic mean and Lifshitz-van der Waals/acid–base methods produce different outcomes and meanings.

Strong and durable interfacial adhesion is expected to transfer the stress efficiently from the polymer matrix to the fiber, which may result in greatly improved mechanical properties in composites. Several researchers have attributed interfacial adhesion to the formation of interfacial chemical bonds by interactions between polar groups such as hydroxyl or carboxyl at the surface of the reinforcing fiber and active groups present in the matrix resin [21–23]. An electro-micromechanical technique has been proposed and studied as an economical new nondestructive evaluation (NDE) method to monitor curing characteristics, interfacial properties, and nondestructive behavior. This is a particularly useful method because a conductive fiber can act as a sensor “itself” as well as a reinforcing fiber [24, 25].

2 Mechanical Properties of Glass Fiber

2.1 Surface Treatments on Glass Fiber

Glass fiber is the reinforcement component in a wide variety of composite applications ranging from aircraft and automobiles to printed wire circuit board substrates and sporting goods. While an ultimate stress of 3.5 GPa has been measured in small diameter glass fibers [26]. The performance of glass fiber-reinforced composites is strongly influenced by the functionality of composite interphases [27]. Interfacial modification is therefore tailored to improve the transfer of stress from the matrix to the fiber reinforcement by enhancing fiber wettability, adhesion, compatibility, etc. The key technology affecting the performance of composite material is the surface treatment, the interaction at interfaces between the fiber and the matrix, and the reinforcement and matrix materials [28]. The current research in coating and grafting technologies is aimed at high-performance composites, which mainly use carbon, aramid, or polyethylene fibers. However, the world market is dominated by glass reinforcement in unsaturated polyester, which comprises almost 90 % of the total market. Approximately 1.8×10^6 t of E-glass fiber is manufactured annually for use in composites and 50 % goes into continuous and long-fiber-reinforced thermosets [29]. The surface of the fiber and the nature of the interfacial bonding are related to the surface properties of the glass fibers. When using surface modification techniques such as acid treatment, silane treatment, or plasma treatment, it is well-known that compatibility between inorganic fillers and polymer matrices improves. Thus, it is possible to improve the adhesion between fiber and matrix.

The plasma technique was used as a gentle but powerful tool for the surface treatment and modification of fibers, which retain their mechanical properties. Using plasmas touching the fiber surface (plasma treatment), the plasma-activated species initiate chemical and physical reactions at the surface causing alteration of surface properties and surface morphology. Thin polymer films may be deposited on the fiber surface (plasma modification) when plasma interacts with organic molecules in

vapor. This process is known as plasma polymerization [30, 31]. Most researches employ the plasma-treatment technique to increase the wettability and the roughness of fiber surface [32] and consequently the fiber/matrix adhesion, which supports composite strength enhancement, but at the expense of composite toughness [33]. An effective solution on how to simultaneously improve composite strength and toughness is the coating technique (plasma polymerization). Thin polymer films prepared by the plasma-polymerization technique may be formed as homogeneous with respect to thickness, uniformity, composition, and structure. The adhesion of films deposited on glass substrates using organosilicon monomers is excellent, and the polymer material is highly cross-linked [34]. Plasma surface treatment and plasma polymerization as alternative coating techniques have been mainly used for surface modification of fibers [35].

In industry, silane coupling agents by wet-chemical process are applied for surface modification of glass reinforcements (fibers, particles) in order to form a functional interlayer. The silane molecule is a multifunctional one, which reacts at one end with the glass surface and at the other with the polymer matrix [36–39]. Organosilanes have the general structure, X_3Si-R . R is a group which can react with the resin, and X is a group which can hydrolyze to form a silanol group in aqueous solution and, thus, react with a hydroxyl group of the glass surface. The trihydroxy silanols, $Si(OH)_3$, are able to compete with water at the glass surface by hydrogen bonding with the hydroxyl groups at the surface. When the treated fibers are dried, a reversible condensation takes place between the silanol and OH groups on the glass fiber surface, forming a polysiloxane layer which is bonded to the glass surface. Therefore, once the silane-coated glass fibers are in contact with uncured resins, the R-groups on the fiber surface react with the functional groups present in the polymer resin, such as methacrylate, amine, epoxy, and styrene groups, forming a stable covalent bond with the polymer [40]. This bond improves not only the mechanical strength but also the resistance to extreme environmental conditions, such as prolonged moisture exposure and thermal cycling [41]. With regard to silane-treated glass fiber-reinforced polymer composites, many studies have been performed to understand the relationships between the interfacial structure and the properties of the fiber/matrix composites [42, 43]. Park and Jin [44] examined the surface treatment of glass fibers with different concentrations to improve the interfacial adhesion at interfaces between fibers and matrix. They used the methacryloxypropyltrimethoxysilane (90 %) containing aminopropyltriethoxysilane (10 %) for the surface treatment of glass fibers. From the experimental results, the presence of coupling agent does lead to an increase of ILSS (interlaminar shear strength) of the composites, which can be related to the effect of increasing the degree of adhesion at interfaces among the three elements, i.e., fiber, matrix, and silane coupling agent. On the basis of experimental results, it was also reported that the mechanical interfacial properties of the composites decrease due to excess silane layer physisorbed onto the glass fiber at a given higher silane coupling agent concentration. Park and Jang [45] investigated the effect of the surface treatment of the glass fiber on the mechanical properties of glass fiber/vinyl ester composites. It is important to point out that the values of the flexural strength and the ILSS of methacryloxypropyltriethoxysilane (MPS)-treated glass fiber/vinyl ester composites increase up to 0.3 %

silane concentration and then decrease smoothly after the maximum point. Their results indicate that physisorbed MPS layers are formed on the chemisorbed layer by an excess amount above 0.3 % concentration. This layer acts as a lubricant or deformable layer. Briefly, the interfacial adhesion and, therefore, the mechanical properties of the composites are mainly controlled by silane coupling agents.

However, acid treatment has been mainly used for surface modification of glass fibers. However, the influence of pretreatment with dilute HCl acid solution of the glass fibers to regenerate the hydroxyl groups on the glass fiber surface prior to the silanization on the mechanical properties of the composites was not evaluated. According to Gonza'lez-Benito et al. [46], the acid activation of glass fibers greatly changes the surface composition and the hydration state of the glass fiber. Under acidic conditions, a great number of silanol groups are generated: although a substantial number of these silanols are of internal character, greater coating degrees can be achieved. There are only very few articles dealing with pretreatment of glass fiber prior to silanization. Olmos et al. [47] studied the effect of the nature of glass fiber surface in the water absorption of glass fibers/epoxy composites. Hydrochloric acid (HCl, 37 wt%) was used for the glass fiber surface activation before different silane coatings. The results obtained show that the presence of silanized fibers seems to induce changes in the process of water absorption of the epoxy resin, decreasing the relative gain of mass at equilibrium. Gonza'lez-Benito [48] investigated the curing process of an epoxy system at the interface formed with a silane-coated glass fiber by using FTIR imaging. In the study, glass fibers were activated (hydroxyl regeneration) in a 10 % (w/w) HCl aqueous solution for 1 h and silanized with a 1 % (v/v) aqueous solution of 3-aminopropyltriethoxysilane (APTES). In the other work performed by Gonza'lez-Benito et al. [46], glass fiber has been treated by two different activation methods, reflux with neutral water and reflux with 10 % HCl aqueous solution. The influence of different activation pretreatments of glass fibers on the structure of an aminosilane coupling agent layer was investigated. They concluded that acid treatments hydrolyze Si–O bonds, greatly changing the composition of the glass and regenerating silanol groups, some of them being of intraglobular nature.

2.2 Analysis of Single Fiber Tensile Strength

The strength of a glass fiber is often analyzed by the Weibull statistical model which is based on the weakest link theory. According to this theory, the most severe defect among all defects existing on the fiber dominates the fiber failure process [49]. Generally, the unimodal Weibull distribution does not fit well the experimental data because of the presence of various kinds of imperfections such as surface defects and internal defects including misoriented crystallites and undetectable defects [50–53]. But, the Weibull distribution curve predicted from the bimodal distribution is known to be a better fit with the experimental data than the unimodal distribution [54, 55]. For this reason, the unimodal distribution model used in simulation theories needs to be modified to a multimodal distribution model if the fiber strength data reveal more than one type of defect. The cumulative bimodal

Weibull distribution function based on the presence of two kinds of defect is described. The probability density function of the Weibull distribution can be obtained by differentiating the cumulative distribution function. Generally, the low-strength portion is generated by defects caused by surface damage during handling, and the high-strength portion is due to the internal defects [56]. The tensile strength distribution of the glass fibers was obtained using approximately 50 specimens, analyzed by both unimodal and bimodal Weibull distributions, so as to obtain statistically meaningful values [57]. The fiber failure process, of the unimodal cumulative Weibull distribution function, based on one type of defect is

$$F(t) = 1 - \exp\left[-\left(\frac{t}{\alpha}\right)^\beta\right] \quad (22.1)$$

in which α and β are scale and shape parameters, respectively. The cumulative bimodal Weibull distribution function, based on the presence of two kinds of defect, is given by

$$F(t) = 1 - \left\{ p \exp\left[-\left(\frac{t}{\alpha_1}\right)^{\beta_1}\right] + q \exp\left[-\left(\frac{t}{\alpha_2}\right)^{\beta_2}\right] \right\} \quad (22.2)$$

in which p and q are the portions of the low- and high-strength population, respectively, and α_1 , β_1 , α_2 , and β_2 are scale and shape parameters of the low- and high-strength portions, respectively.

The values of F are determined from experimental tensile strength measurements by the value of fracture cumulative probability. The mean value of the probability is taken as

$$F = \frac{i}{N + 1} \quad (22.3)$$

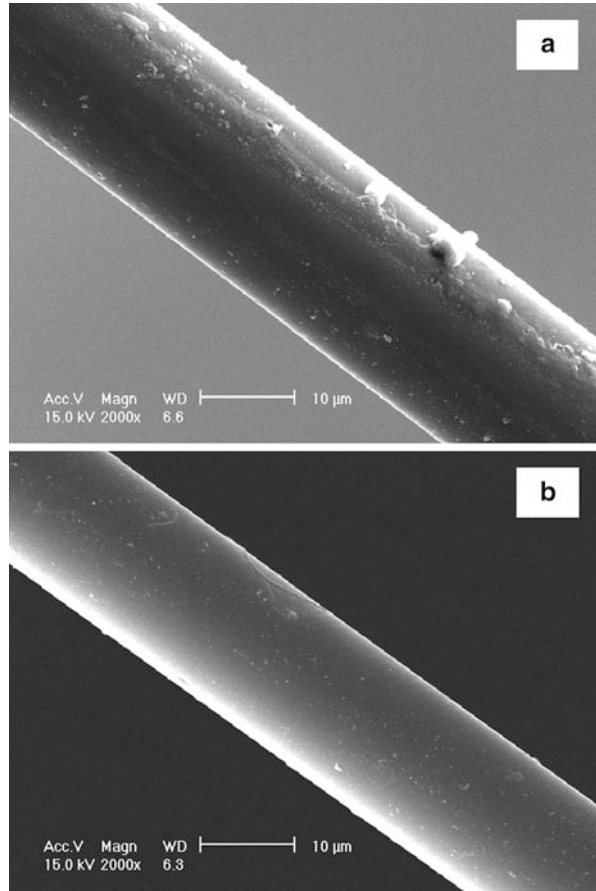
where N is the total number of tested fibers and i is the number of the ascendingly ordered strength data. Equation 22.1 can be rewritten as

$$\ln[-\ln(1 - F)] = \beta \ln(t) - \beta \ln \alpha \quad (22.4)$$

Thus a plot of $\ln[-\ln(1 - F)]$ versus $\ln(\text{aspect ratio})$ yields a straight line whose slope and intercept yield α and β , respectively.

Figure 22.3 shows the surface morphology of glass fibers for (a) a neat glass fiber and (b) a glass fiber after acid cleaning. Figure 22.3a shows some of the sizing materials along with some dust adhering to the surface of neat glass fiber, whereas after the acid-cleaning process, almost all the sizing material and other adherents were removed. However, some etched flaws might exist on such fiber surfaces, as shown in Fig. 22.3b. Figure 22.4 shows the stress-strain curves for glass fibers for the two different surface conditions. After acid cleaning, both the tensile strength

Fig. 22.3 Surface morphology of glass fiber: (a) sized glass fiber and (b) acid-cleaned glass fiber



and the failure strain of the glass fibers were significantly decreased. This can probably be attributed to flaws introduced of the etched fiber surface during the removal of the sizing material. There was, however, no distinct change in the tensile modulus of the glass fibers which is apparently an inherent property of the glass in the fibers.

Figure 22.5 shows the single fiber cumulative strength distribution for a 20 mm gauge length of glass fibers, for the two different surface conditions. Clearly the tensile strength for glass fibers after acid cleaning was significantly lower than that for uncleaned neat glass fibers, which is, again, attributed to stress concentrations due to surface flaws, induced by etching of the glass fibers' surface. Table 22.1 shows the mechanical properties of glass fiber for the two different surface conditions. Bimodal Weibull distributions approximate the experimental data better than unimodal Weibull distributions, for both cases, which implied the existence of two different flaw types.

Fig. 22.4 Stress–strain curves of glass fibers with different surface conditions

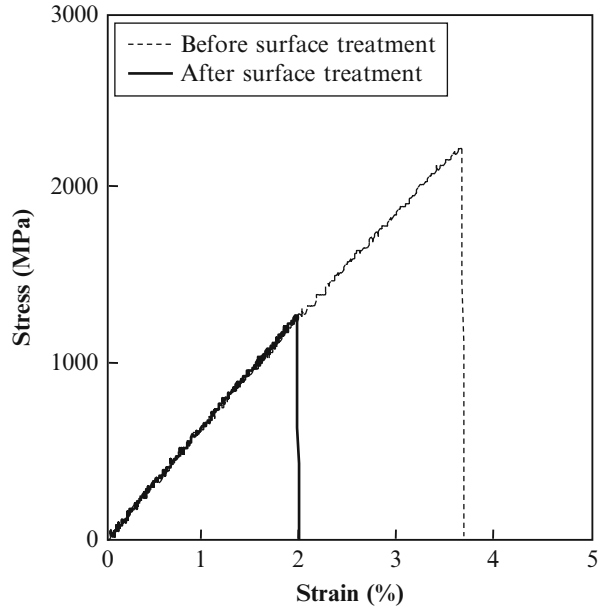


Fig. 22.5 Cumulative strength distribution for glass fibers with different surface conditions

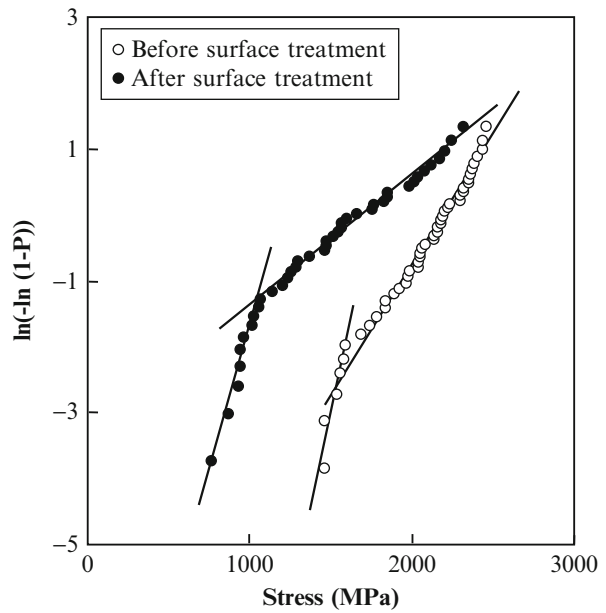


Table 22.1 Mechanical properties of sized glass fiber and acid-cleaned glass fiber

Fiber conditions	Diameter (μm)	Strength (MPa)	Modulus (GPa)	Strain (%)	α^a	β^b	α_1	β_1	α_2	β_2
					Neat glass fiber	16.33 (0.75) ^c	2056 (320)	76.4 (4.7)	2.58 (0.68)	2185
Cleaned glass fiber	15.47 (0.83)	1512 (445)	69.2 (13.3)	2.08 (0.70)	1675	3.7	1265	7.5	1722	3.2

^aScale parameter for fiber strength^bShape parameter for fiber strength^cStandard deviation (SD)

3 Interfacial Evaluation of Glass Fiber/CNT–Polymer Composites

3.1 Measurement of Interfacial Shear Strength (IFSS)

In the fiber-reinforced composite system, one of the most important controlling factors is the interfacial property which relates to the capacity of stress transfer from the matrix to the reinforcing fiber. Although the high strength of a composite is due to strong bonding between the fiber and the matrix, a low interfacial bonding strength due to a relatively weak bonding improves the fracture toughness of the composite. For this important reason, many investigations are devoted to research characterizing the interfacial behavior in the composite system.

Micromechanical tests employing the single fiber composite specimen [58, 59] can simply evaluate the interface strength. One of these tests, the cruciform specimen test, is a promising method for evaluating interface strength because the interface failure initiates from a uniform stress region, not from a part where a stress singularity exists, making it different from conventional tests. The cruciform specimen test was first implemented by Gundel et al. [60] and then studied further by Tandon and Kim [61] and the authors [62]. These articles present the interfacial failure envelope under combined stresses, obtained using a cruciform specimen test in which the off-load axis is varied to create various normal/shear stress ratios. An earlier study [63] solved the important problem of the unclear microscopic location of interfacial failure initiation using a novel method. However, the failure envelope remains partially indeterminable considering the following points. The analysis that was performed assumes an elastic body. The assumption of an elastic body might engender misunderstanding with respect to interface stress when the stress level at the interface failure exceeds the range of elastic deformation of matrix resins. Another point is that the interface strength obtained using the cruciform specimen test has not been compared with that obtained from other tests on combined stress failure envelopes [64].

Conventional works are classifiable into three groups: articles mainly presenting interfacial tensile strength [65], articles involving a combined stress state of normal and shear [66], and articles dealing fundamentally with interfacial shear strength [67]. Zhandarov and Mader [68] and Piggott [69] reviewed very well the numerous other studies that have been conducted mainly to assess interfacial shear strength. Several methods for evaluating interfacial shear strength have been compared [70, 71], including the fragmentation test, push-out test, pullout test, and microdroplet method. Moreover, the test-type dependence of the obtained interface strength has been examined. Such comparisons can be effective proof in demonstrating that the evaluation methods are reasonable. Some reports, however, have indicated that the results obtained using different tests differ, although the material systems are identical among studies [72]. A typical discussion specifically examines shear stress, not a combined stress state, which might be a factor causing the test-dependent differences. Implementing only one test is useful for qualitative comparison. Some examples are that interface strength has been evaluated using a microdroplet pullout test [73, 74].

3.2 Microdroplet Pullout Test

The interfacial shear strength of the glass fiber/CNT–epoxy nanocomposites could be measured by a microdroplet pullout test. Figure 22.6 shows the scheme of the microdroplet pullout test system and specimen for measuring IFSS. One of the major advantages of microdroplet techniques is that the value of forces at the moment of debonding can be measured. The microdroplet specimen was fixed by a microvice using a specially designed micrometer. The IFSS was calculated from the measured pullout force, F , using the following equation:

$$\tau = \frac{F}{\pi D_f L} \quad (22.5)$$

where D_f and L are the fiber diameter and the fiber embedded length in the matrix, respectively.

Figure 22.7 shows plots of pullout force versus the embedded area between the glass fibers and the matrix. Figure 22.7a shows results for pullout tests for microdroplets of neat epoxy with sized glass fibers before and after acid cleaning. Figure 22.7b shows results for pullout tests for microdroplets of CNT–epoxy nanocomposites before and after acid cleaning of the sized glass fibers. The interfacial adhesion was greater for the acid-cleaned surfaces due to their higher surface energy. It is also thought that the sizing and other material on the surface of the untreated fibers may, as well, act as a weak boundary. The acid treatment of the surface may also tend to roughen the surface on a microscale, further enhancing adhesion. Based on these observations the behavior illustrated in Fig. 22.7 might now be explained. The first region of these curves exhibits a relatively strong dependence of the pullout load on the embedded area. This may be attributed to the fact that in this region the pullout force is largely adhesion controlled. Since the

Fig. 22.6 Scheme of the microdroplet pullout test system and specimen for measuring IFSS

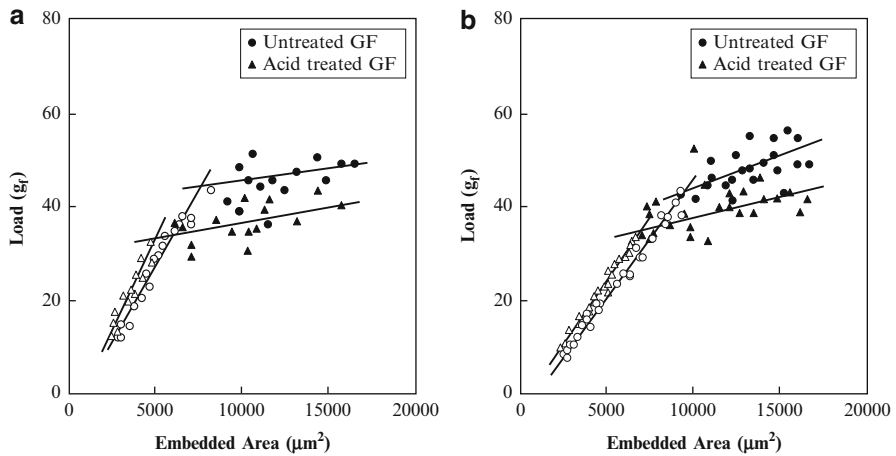
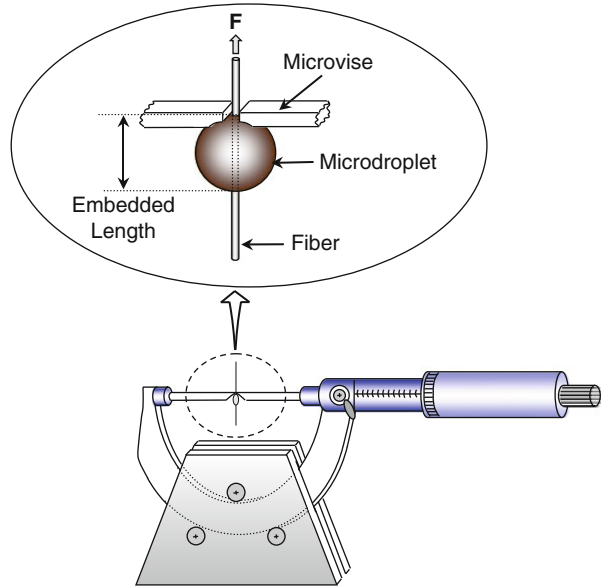


Fig. 22.7 Plots of the pullout force versus embedded area between glass fiber and (a) neat epoxy and (b) CNT-epoxy nanocomposites

interfacial adhesion is greater for the acid-treated fibers, in this region, they exhibit greater pullout strength than do the untreated fiber. For all the curves shown in Fig. 22.14, there are sudden breaks in the curves beyond which the failure load is much less sensitive to the embedded area. Beyond this critical point, failure involved more fracture of the fibers than simple fiber pullout, and as noted

previously acid cleaning reduced the tensile strength of the fibers. Hence, in this region the failure load was greater for the sized fibers than for the treated ones.

Figure 22.8 shows photographs of microdroplets for pullout tests for acid-cleaned glass fibers with (a) neat epoxy and (b) CNT–epoxy nanocomposite matrix material. The microdroplet tests, again, exhibited two distinct pullout patterns, depending on differences in the embedded area and interfacial adhesion. Microdroplet slippage was observed when the applied force exceeded the interfacial adhesion, whereas glass fiber fracture was observed when the interfacial force exceeded the glass fiber's tensile strength.

4 Measurements of Contact Angle, Wettability, and Surface Energies

4.1 Relationship Between Wettability and Interface

For good bonding and stress transfer, fibers are generally sized or coated with thin polymer film after surface treatment that removes weak boundary layers [75–77]. Sizing has an adhesion and wetting promotion function but is particularly important for facilitating fiber handling during composite manufacture acting as a lubricant to prevent fiber damage. The effectiveness is confirmed by the off-axis strength which is usually close to the strength of the polymer [78, 79]. It has been also reported that the presence of sizing may improve the wetting of the fiber by the matrix resin and protect its reactivity [80, 81]. Wetting is a prerequisite to good adhesion [82]. However, good adhesion also requires functional groups, vis-a-vis Lewis acidic and basic sites in the interfacial region between the fiber and the matrix resin. The concepts proposed by Fowkes [83, 84], regarding the short-range hydrogen bonding interactions which are important in adhesion, make it possible to assess the acid–base character of the surfaces using contact angle measurements. The acid–base nature of the fiber surface is a significant factor in determining the degree of adhesion of these fibers in a given resin matrix. If the acid–base properties of the matrix resin are also determined, it should be possible to choose a fiber to matrix pair to maximize adhesion. The adhesion strength of the interface depends on the thermodynamic work of adhesion that is closely related to the surface energy of the fiber and matrix [85]. Surface energy of fibers has been determined quantitatively by measurement of the contact angles by using Wilhelmy plate technique [86–90]. An excellent comprehensive summary of both the theoretical and experimental aspects of contact angles has been published recently [91].

4.2 Static Contact Angle Test

The static contact angles of water droplets on the CNT–epoxy nanocomposites and neat epoxy plate surface were measured by an optical microscope. The spherical surface area for the water droplets on these two specimen types is minimized due to the surface tension resulting from intermolecular forces.

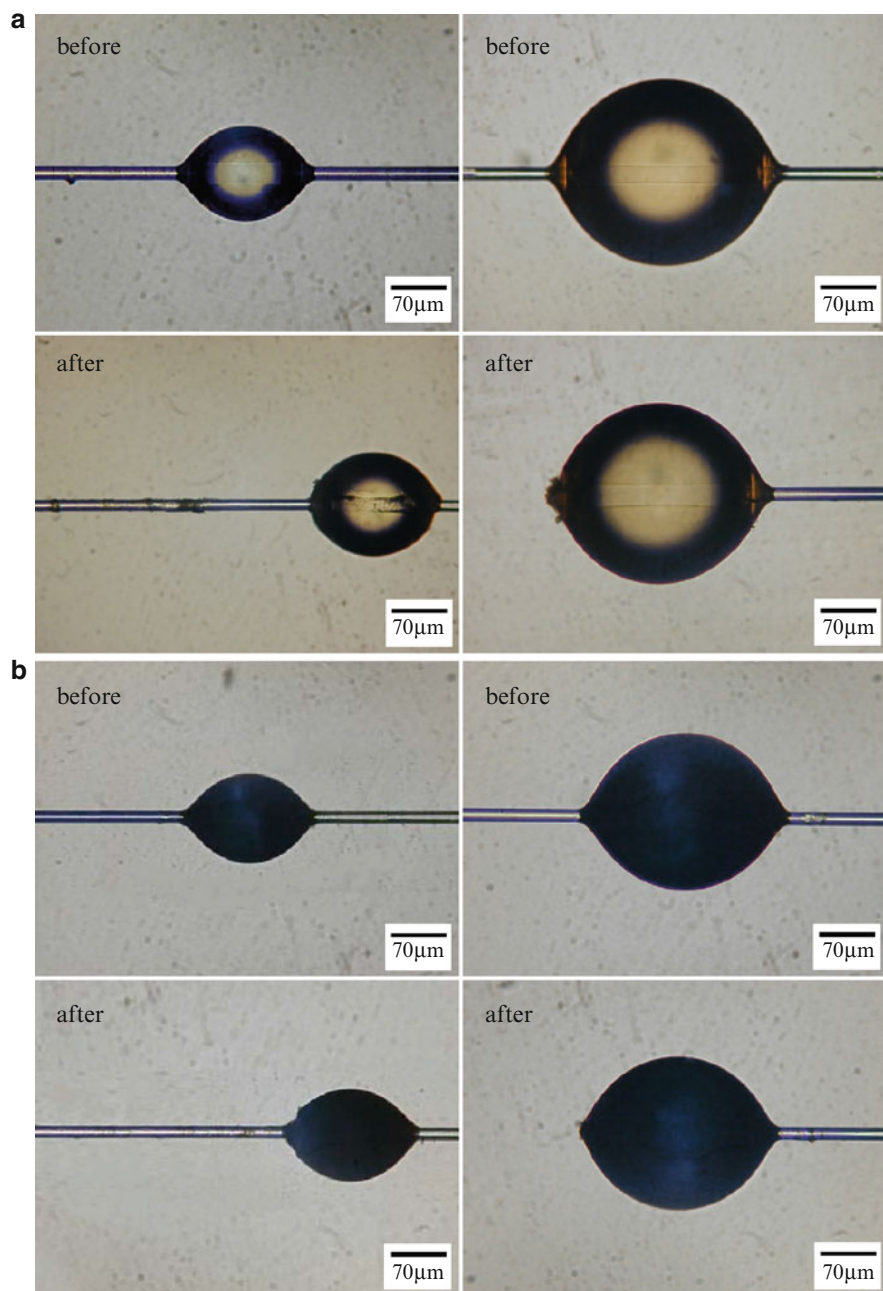


Fig. 22.8 Optical photographs of pullout specimen patterns for small and large microdroplets before and after pullout (a) neat glass fiber/epoxy and (b) neat glass fiber/CNT–epoxy nanocomposite

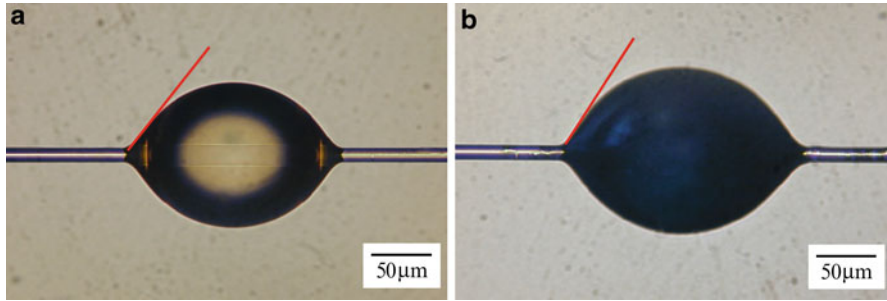


Fig. 22.9 Optical photographs of different meniscus microdroplets on glass fiber surfaces for (a) glass fiber/epoxy and (b) glass fiber/CNT–epoxy nanocomposites

Figure 22.9 shows typical photographs for two different microdroplets on glass fiber surfaces: (a) neat epoxy and (b) CNT–epoxy microdroplets. The contact angle of the CNT–epoxy nanocomposite was higher than that of the neat epoxy, implying a higher hydrophobicity for CNT–epoxy nanocomposite than for the hydrophilic neat epoxy.

Figure 22.10 shows optical photographs of water droplets in static contact angle measurements on (a) a neat epoxy plate, (b) CNT–epoxy nanocomposites, and (c) a leaf for comparison. The CNT–epoxy nanocomposites exhibit a more hydrophobic nature, with a static contact angle of about 120° , whereas the static contact angle for the neat epoxy is much lower. Compared to (a) and (b), the leaf in Fig. 22.9c exhibited very high hydrophobicity and a static contact angle of more than 150° (i.e., super-hydrophobicity). This surface behavior might be related to how the CNT nanostructure is arranged in the epoxy matrix in which this increment in contact angle may be attributed to heterogeneity effects [92].

4.3 Dynamic Contact Angle Test

Dynamic contact angles of glass fiber and CNT–epoxy composites were measured using the Wilhelmy plate technique (Sigma 70, KSV Co., Finland) [93, 94]. Figure 22.11 shows the scheme of dynamic contact angle measurement by Wilhelmy plate method. The four dipping liquids used were double-purified water, formamide, ethylene glycol, and diiodomethane. In this way the dynamic contact angle, surface energies, donor and acceptor components, polar and dispersive free energy terms of glass fiber with different conditions, and CNT–epoxy composites were determined. The basic equation for the Wilhelmy plate method is

$$F = mg + P\gamma_{LV} \cos \theta - F_b \quad (22.6)$$

where F is the total force, m is the mass of plate, g is the acceleration of gravity, F_b is the buoyancy force, P is a fiber perimeter, γ_{LV} is the surface tension of the liquid, and $F - mg$ is equal to the measured force. Since the buoyancy force is zero at the immersing interface, Eq. 22.8 can be arranged as

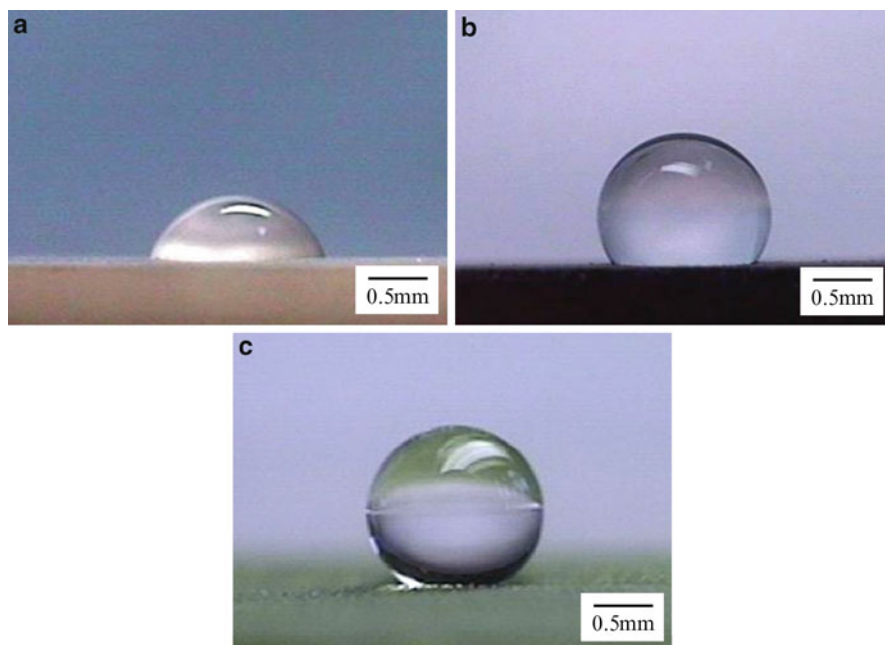


Fig. 22.10 Static contact angles of water droplets on the (a) neat epoxy, (b) CNT-epoxy nanocomposites, and (c) neat leaf plate

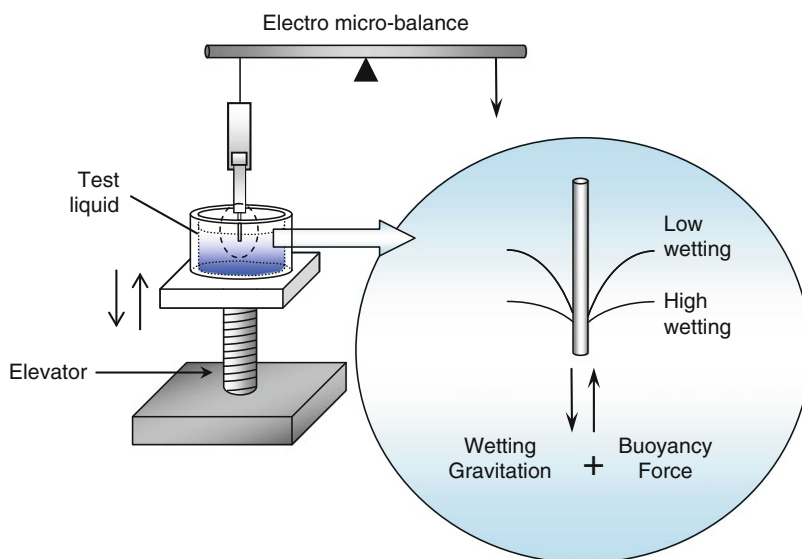


Fig. 22.11 Scheme of dynamic contact angle measurement by Wilhelmy plate method

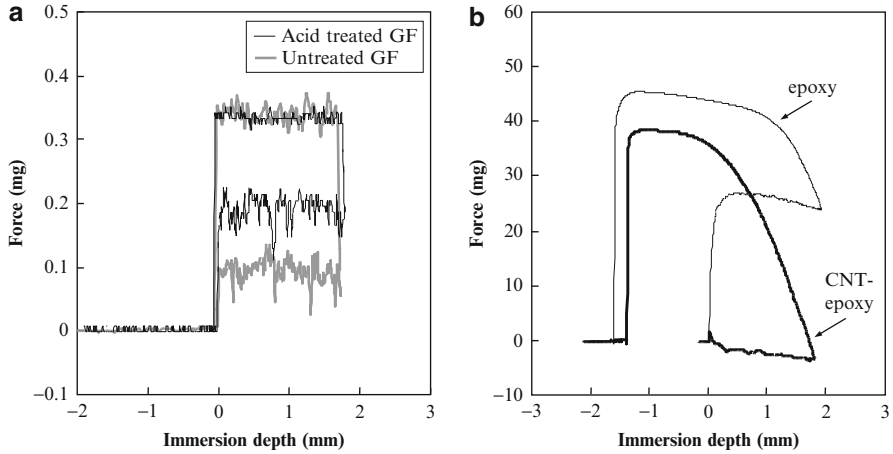


Fig. 22.12 Dynamic contact angles for (a) sized glass fibers and after acid-cleaned glass fibers and (b) neat epoxy and CNT–epoxy nanocomposite

$$\cos \theta = \frac{Mg}{\pi D \gamma_{LV}} \tag{22.7}$$

where M is the measured force.

Figure 22.12a shows plots of advancing and receding dynamic contact angles for the untreated and acid-treated glass fibers. Wettability increased with acid cleaning which resulted in a higher surface energy. Figure 22.12b illustrates effects consistent with the different trends in dynamic contact angles of neat epoxy plate and CNT–epoxy nanocomposite plate, respectively.

4.4 Calculation of Work of Adhesion

The total surface energy, γ^T , is the sum of the Lifshitz-van der Waals component, γ^{LW} , and acid–base component, γ^{AB} . For the solid and the liquid, these are related by

$$\gamma_S^T = \gamma_S^{LW} + \gamma_S^{AB}, \gamma_L^T = \gamma_L^{LW} + \gamma_L^{AB} \tag{22.8}$$

The acid–base component (or hydrogen bonding) includes the electron acceptor, γ^+ , and electron donor, γ^- , components, which are not additive and can be expressed for a solid and liquid as

$$\gamma_S^{AB} = 2(\gamma_S^+ \gamma_S^-)^{\frac{1}{2}}, \gamma_L^{AB} = 2(\gamma_L^+ \gamma_L^-)^{\frac{1}{2}} \tag{22.9}$$

The calculation of the above components, following the modified Young–Dupre equation of the work of adhesion, W_a , can be expressed as

$$W_a = \gamma_L(1 + \cos \theta) = 2(\gamma_L^{LW}\gamma_S^{LW})^{\frac{1}{2}} + 2\left[(\gamma_S^-\gamma_L^+)^{\frac{1}{2}} + (\gamma_S^+\gamma_L^-)^{\frac{1}{2}}\right] \quad (22.10)$$

The value of γ_S^{LW} for the solid is evaluated from the contact angle of an apolar liquid, which is a nonpolar liquid without donor and acceptor components (such as diiodomethane), on the solid, in which case the above equation reduces to

$$\gamma_L(1 + \cos \theta) = 2(\gamma_L^{LW}\gamma_S^{LW})^{\frac{1}{2}} \quad (22.11)$$

If it is assumed that the liquid has negligible acid–base interaction with the solid, γ_L , γ_L^{LW} , γ_L^+ , and γ_L^- are known for the testing liquids and $\cos\theta$ can be determined using Eq. 22.9. With known γ_S^{LW} and the contact angles obtained using different liquids on the solid, the two equations in Eq. 22.11 can be solved to obtain γ_S^+ and γ_S^- using two test solvent sets.

A commonly used approach for consideration of solid surface energies is to express them as a sum of dispersive and polar components, which can influence the work of adhesion, W_a , between the reinforcement material's surface and the matrix material. To determine the polar and dispersive surface free energies, the Owens–Wendt equation [95] is expressed as

$$W_a = \gamma_L(1 + \cos \theta) = 2(\gamma_S^d\gamma_L^d)^{\frac{1}{2}} + 2(\gamma_S^p\gamma_L^p)^{\frac{1}{2}} \quad (22.12)$$

where γ_L , γ_L^d , and γ_L^p are known for the testing liquids and γ_S^p and γ_S^d can be calculated from the measured contact angles. In this way the dispersive and acid–base components of both the reinforcement material and the matrix can eventually be determined. It is possible to calculate the work of adhesion, W_a , between glass fiber (F) and neat epoxy, CNT–epoxy matrix (M) at the interface using the following equation:

$$W_a = 2\left[(\gamma_F^{LW}\gamma_M^{LW})^{\frac{1}{2}} + (\gamma_F^-\gamma_M^+)^{\frac{1}{2}} + (\gamma_F^+\gamma_M^-)^{\frac{1}{2}}\right] \quad (22.13)$$

Figure 22.13 shows the calculated donor and acceptor components and polar and dispersive free energy terms using four different solvents, based on the equations developed earlier (see Eqs. 22.6 through 22.12), and Table 22.2 shows the acid–base and polar–dispersion surface energy components of glass fiber, neat epoxy, and CNT–epoxy nanocomposites. CNT–epoxy nanocomposite exhibited a higher surface energy due to the CNT microstructures on the surface of CNT–epoxy nanocomposites.

Table 22.3 shows a comparison of work of adhesion, IFSS, and apparent modulus between glass fiber and CNT–epoxy nanocomposites. The apparent modulus increased as the IFSS increased, implying that the interfacial adhesion between glass fibers and the CNT–epoxy nanocomposites was higher than that between glass fibers and neat epoxy. For the glass fiber case, the interfacial adhesion was also

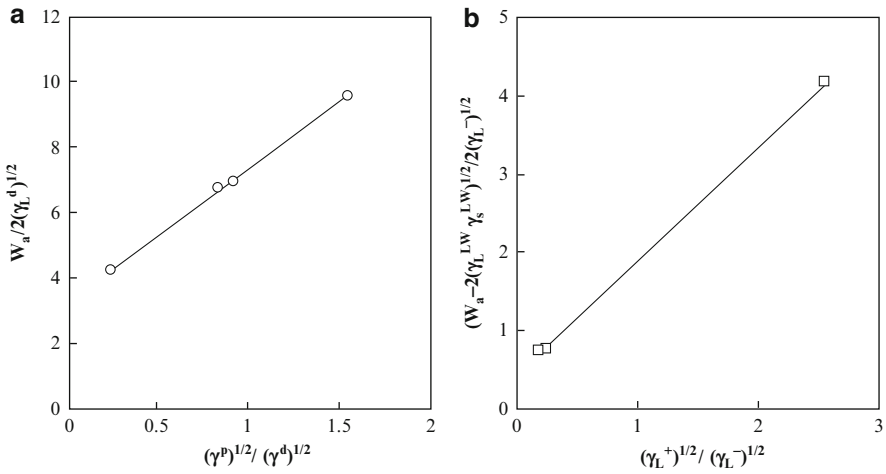


Fig. 22.13 Plots of (a) polar and dispersive free energy terms and (b) donor and acceptor components

Table 22.2 Acid–base interaction and polar–dispersion surface energy components (mJ/m²)

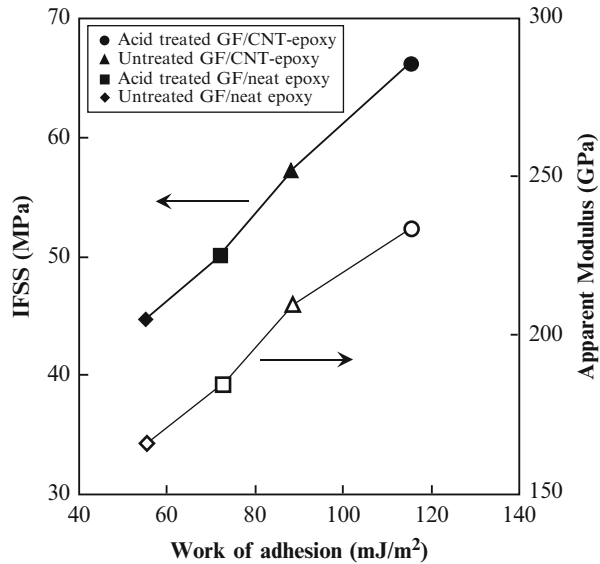
Type	γ_s^{LW}	γ^-	γ^+	γ^d	γ^p	γ_s^T
Neat glass fiber	30.6	4.3	0.2	18.0	10.5	32.5
Cleaned glass fiber	53.2	5.1	0.5	19.0	18.1	56.4
CNT–epoxy	57.1	1.1	0.6	33.6	1.6	58.7
Neat epoxy	21.0	2.4	0.4	29.4	21.1	23.0

Table 22.3 Relationship of work of adhesion, IFSS, and apparent modulus

Composites	Fiber conditions	IFSS (Mpa)	Apparent modulus (Gpa)	W_a (mJ/m ²)
Neat epoxy	Neat glass fiber	44.9	164.4	54.7
	Cleaned glass fiber	50.3	184.6	71.9
CNT–epoxy	Neat glass fiber	56.9	207.7	87.7
	Cleaned glass fiber	66.2	233.7	115.1

increased after acid cleaning. The results of interfacial adhesion were generally consistent with the thermodynamic work of adhesion, W_a . The work of adhesion of the acid-cleaned glass fiber/CNT–epoxy nanocomposites was higher than that of the untreated glass fiber, indicating more stable mechanical adhesion at this interface. Figure 22.14 shows the correlation between the IFSS, the apparent modulus, and the work of adhesion. Both the IFSS and the apparent modulus increased as work of adhesion increased, indicating that the effective stress transferring mechanism works at the interface.

Fig. 22.14 Plots of IFSS and apparent modulus versus work of adhesion showing correlation



5 Carbon Nanotubes Grafting on Glass Fiber

5.1 Interphase Sensors Based on Carbon Nanotubes

CNTs have been incorporated into the interphase of fiber-reinforced composites in order to achieve multifunctional effects. Although only a comparably little volume is affected when CNTs are concentrated in the composite interphase, its modification results in improved mechanical properties [96–98]. Besides the attempts aiming at enhanced mechanical properties, CNTs have been used as well for functionalizing the interphase region. It is being increasingly considered for the production of nanostructured coatings and layers on a variety of substrates, i.e., coatings for wear and oxidation resistance, bioactive coatings for biomedical implants, and functional coatings for photocatalytic, electronic, magnetic, and related applications [99, 100].

As a useful and additional application, investigations of functional interphases have been concerned for detecting stress/strain and damage of composites in generally electrical conductive carbon fiber composites [101]. Since a conventional glass fiber is an electrically insulating material, traditionally, the monitor for GFRPs damage is completed by external sensor, which degrades the mechanical properties of the structure and increases the cost [102]. There is a growing interest in techniques without requirement of additional sensors in composites; therefore the development of new GFRPs with an in situ self-detecting function is desirable. Functionalization of traditional glass fiber surfaces by nano-reinforcements is leading to the tremendous potential for multifunctional GFRPs [103].

Performing Raman spectroscopy on CNT-modified GFs, certain band shifts of the CNTs can be related to the externally applied strain allowing for interface strain

mapping [104–106]. Moreover, CNTs have been used to create electrically conductive interphases for realizing sensing capabilities comparably to the sensing approach in bulk nanocomposites. It was shown that single GFs, coated by CNTs via electrophoretic deposition and dip coating, can act as sensor elements [107].

5.2 Preparation and Morphology of CNT-Coated GF Fibers

Glass fibers were spun and dip coated as described in [108, 109]. For preparation of the CNT-coated GF, E-glass fibers with an average diameter of 15 μm were continuously spun and sized with an aqueous 1 wt% 1-aminopropyltriethoxysilane (APS) solution at the Leibniz Institute of Polymer Research Dresden. The yarn count of the GF filament yarn was 111 tex, containing 204 filaments. In a subsequent step, the GF yarns were coated with a CNT/film former system containing 0.5 wt% CNTs relative to the solid content of the film former on a horizontal vertical padder type HVF in combination with a continuous coating system type KTF (both Werner Mathis AG, Switzerland). The solid content of the CNT coating on the GF yarns was determined by thermogravimetric analysis (TGA; Q500, TA Instruments).

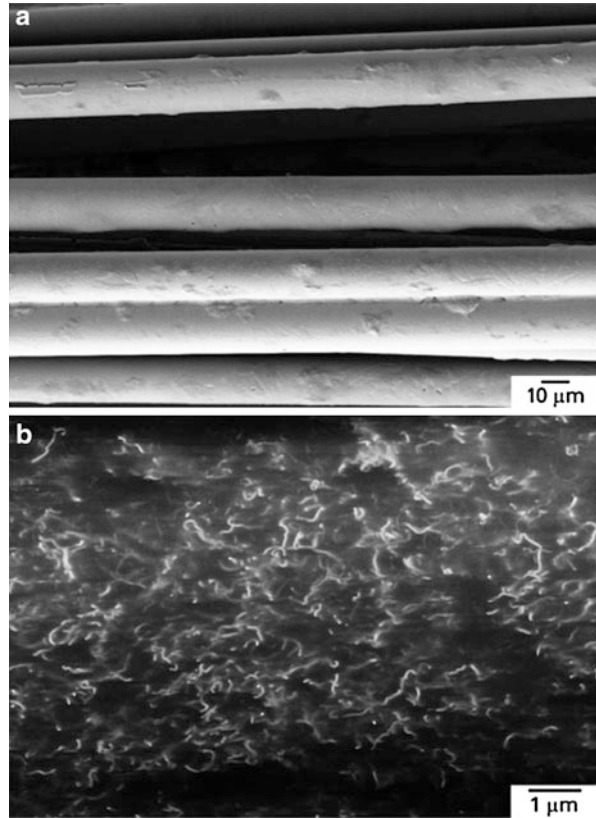
For dip coating on the glass fibers, 0.5 wt% MWCNT dispersion was prepared in the presence of 0.75 wt% Igepal CO 970. Then, the glass fibers were dipped into dispersion for 15 min, withdrawn with their axes perpendicular to the solution surface, and dried in a vacuum oven at 40 $^{\circ}\text{C}$ for 8 h. To check how many MWCNTs were successfully deposited onto glass fiber, the fiber mass was measured before and after depositing MWCNTs.

The morphologies of MWCNT coatings on the glass fiber surface were investigated using a scanning electron microscopy. Figure 22.15 shows SEM micrographs of the coated GF and visualizes the CNT network on an annealed GF employing the charge contrast imaging technique. It can be observed that the CNTs are well dispersed and distributed on the glass fiber surface. A similar distribution and state of dispersion of CNTs can be expected for all areas on the GF covered by the film former. Hence, in the case of interphase sensors based on CNT networks on the GF surface, any change in electrical resistance as a function of applied stress involves information of all continuously connected areas on the GF covered with the CNT coating as well as conductive paths between adjacent fibers. Whenever a single GF fails or the interfacial shear stress exceeds a critical limit and locally causes the interphase to fail, this will be reflected in a permanent increase of resistance, as certain conductive paths cease to exist.

5.3 Mechanical Properties of CNT-Coated Glass Fiber

Tensile tests of single filaments were conducted on a FAVIGRAPH Semiautomatic Equipment (Textechno Company, Germany) at a strain rate of 0.5 per minute. Approximately 50 single fibers for each surface treatment were used to determine the fiber strength at gauge lengths of 30, 20, and 10 mm, respectively. Based on

Fig. 22.15 SEM micrographs of GF with CNT coating. (a) Surfaces of GF after annealing at 200 °C for 15 min and (b) higher magnification of CNT coating on a GF after annealing at 200 °C for 15 min [108]



a vibration method [110] in accordance with ASTM-D-1577-96 and DIN EN ISO 53812, the diameter of each selected fiber was determined. The coating on the surface of the fibers by dip coating was decreased in single fiber tensile strength as revealed in Table 22.4. The same findings of reduced strengths of glass fibers due to agglomerated carbon nanotube-epoxy coatings have also been reported [111]. This can be understood by noting that the bigger the flaw arising from irregular coating present in the surface layer, the lower is the expected value of the ultimate tensile strength of the fiber [112]. Consequently, the inhomogeneous and agglomerated MWCNT coating caused an irregular stress distribution along interphase region.

5.4 Interfacial Shear Strength of CNT-Coated GF Fibers

The fragmentation test has been used for assessing interfacial shear strength, where the tensile load in the specimen is transferred to the fiber by shear stresses in the matrix through the interphase. The fiber keeps breaking until the fragments become too short to build up sufficiently high tensile load to cause further fragmentation

Table 22.4 Average single fiber tensile strength for different gauge length (L_0) [109]

Fiber conditions	$L_0 = 10$ mm	$L_0 = 20$ mm	$L_0 = 30$ mm
Neat glass fiber	2102 (321) ^a	1999 (260)	1890 (243)
Dip-coated glass fiber	1473 (321)	1333 (219)	1301 (247)

^aStandard deviation (SD)

with increasing specimen strain. Based on a force balance in a micromechanical model of Kelly and Tyson [113, 114], the interfacial shear strength is given by

$$\tau = \frac{\sigma_f d}{2L_c} \quad (22.14)$$

where σ_f is the tensile strength determined at the critical fragment length, d is the fiber diameter, and L_c is the critical fragment length of the fiber. This critical fragment length is defined as the shortest fragment length that breaks due to a stress application.

Three different interphase structures were proposed: (1) homogeneous interphase, (2) mid-homogeneous interphase, and (3) inhomogeneous interphase. Figure 22.16 shows the birefringence patterns under polarized light of single fiber model composites together with the schemes for these proposed interphases and the stress profiles along the fiber when the fragment number reached saturation. Clearly, the stress birefringence of neat fibers and CNT-coated fibers suggests that the interphases suffered from extensive shear stresses and the crack tended to expand along the interphase. Through focusing on the fiber break point, the apparent matrix crack failure mode could be observed in the coated fiber samples, which indicated improved interfacial strength due to the presence of the MWCNT coating. The neat fiber with homogeneous surface possessed the highest value of the Weibull shape parameter, suggesting uniform interfacial adhesion. Due to the differences in thickness of the MWCNT layers or the heterogeneous adhesion modes from MWCNTs, the reinforcement effect was unequal along the whole fiber. Both strong bonding and relatively weak bonding coexist, leading to wider distribution of fragment lengths.

5.5 Evaluation on the Interphase Damage by the Interphase Sensor

To provide a unique opportunity for the in situ load and damage detection, the self-diagnosing effects were exploited, as pilot approach, of semiconductive MWCNT–glass fiber in composites during tensile test. Figure 22.17 shows the electrical resistance and stress as a function of applied strain. Three stages of resistance variation were identified basically in (i) linear, (ii) nonlinear, and (iii) abrupt changes. At the first stage, the linear behavior of the electrical resistance increased proportionally with strain up to approximately 1.5 %, which is possibly linked to the elastic deformation of the interphase. For strains higher than 1.5 %, the

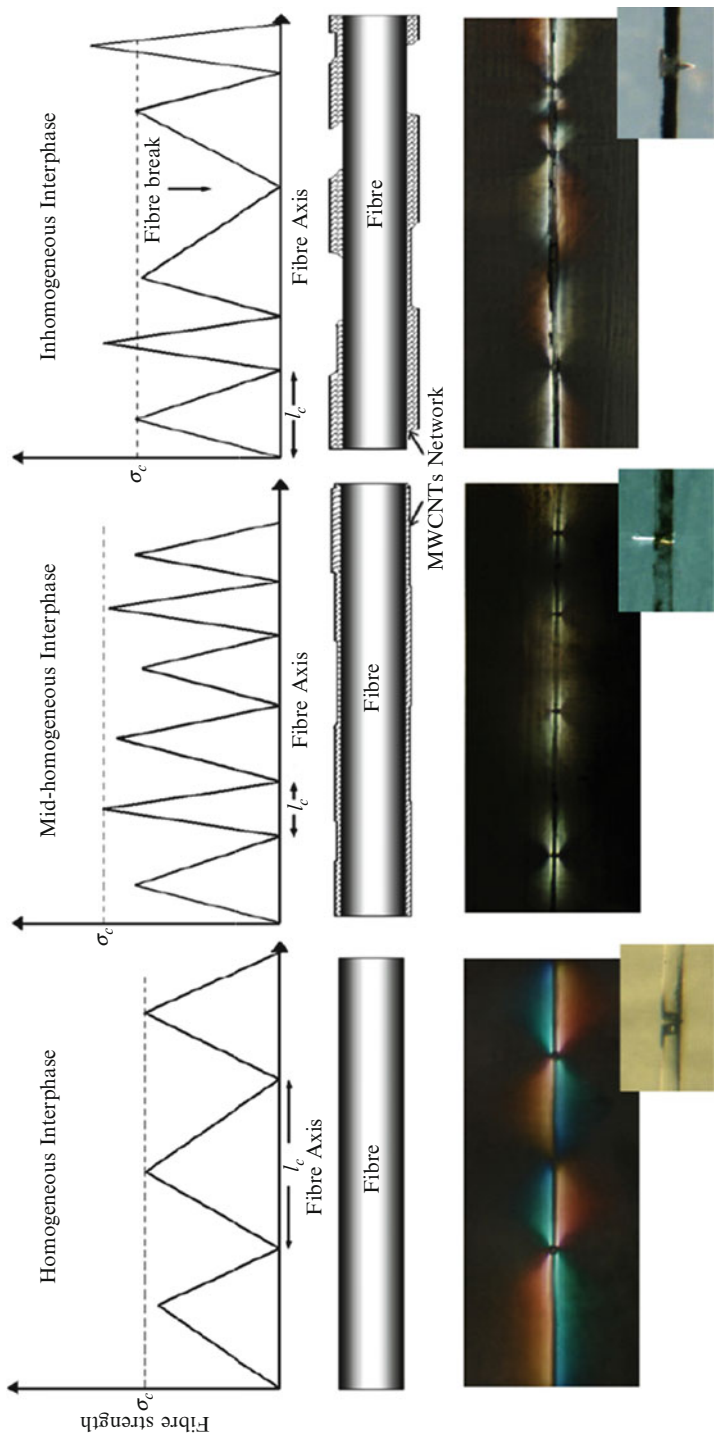


Fig. 22.16 Three kinds of stress profiles along the fiber axis as a function of position when fracture number reaches its saturation; the birefringence patterns are shown by cross-polarized light for saturation at a magnification of ten. Inset images are the enlarged views of broken points [109]

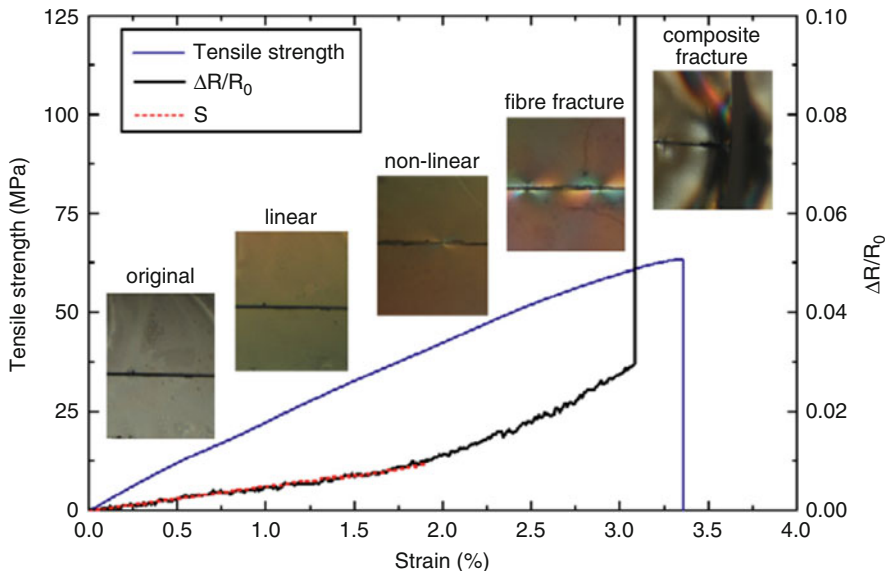


Fig. 22.17 Simultaneous change of electrical resistance and stress as a function of strain for single CNT-coated fiber/epoxy composite [109]

slope of the resistance–strain curve increased exponentially with strain. This exponential behavior of resistance change is related to the interphase plastic deformation of CNT networks, associated with stress concentration before fiber breakage, increase of nanotube–nanotube interspace, and loss of junction points arising from permanent change in network shape during loading. This interphase deformation possibly caused irreversible resistance changes. At the third stage, the interphase failed completely and the resistance jumps “infinite” (the resistance exceeds measurable range). Finally, after interphase fracture, the coated fiber/epoxy composites failed at a strain of about 3.4%. An important feature occurring in the measurements is that the three stages of the resistance variation are highly consistent and reproducible, thus making such single-coated glass fiber as a small and sensitive rapid response mechanical sensor.

Based on the data of the quasi-static tensile loading, GF failure can be excluded for the applied stress limits. Hence, all resistance change occurring during testing is related to interphase damage, rather than to failure of the reinforcement fibers. Combining mechanical testing with simultaneous resistance measurements, a set of data is originated consisting of force and displacement as well as information on resistance change. For CNT-filled nanocomposites, it has been shown that resistance change data follows the displacement of the system and allows monitoring the system deformation as well as the occurrence of micro cracks [115, 116].

Figure 22.18 shows the behavior of the resistance change during the cyclic loading between 0 and 22 MPa. After the first load cycle, the viscoelastic and/or

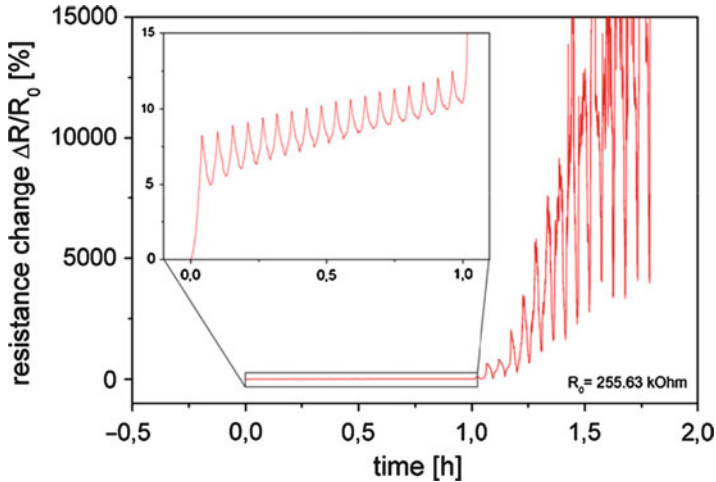


Fig. 22.18 Resistance change of interphase sensor during stress-controlled cyclic loading between 0 and 22 MPa. The inset figure shows the amplitude of the resistance change before the occurrence of severe interphase damage, which causes a distinct change of the amplitude pattern [118]

viscoplastic deformation results in an increase of resistance change of 5 %. Any further load cycle causes as well an increase in resistance change due to sample deformation, however, only to a minor extent. Thus, a steady increase of resistance change up to approximately 1 h is observed, when the amplitude of the resistance change increases drastically together with the value of resistance change in the unloaded state. This is indicative of a severe interphase failure, cutting off the majority of the conductive paths. However, first signs of micro cracks can already be observed at the very beginning of the cyclic loading by the unsymmetrical shape of the load cycles. As mentioned by Thostenson and Chou [117], the “shoulders” in the resistance change curve at the beginning and end of the load cycles can be related to crack reopening and subsequent closing upon unloading of the system. Although the resistance change curve indicates clearly when the failure of the interphase takes place, it remains unclear whether the preexisting micro cracks have reached a critical size causing unstable crack growth or the sudden initiation of a bigger single crack in the interphase is the reason for the observed resistance change [118].

Similarly to the results shown in Fig. 22.18, the resistance change during cyclic loading between 0 and 20 MPa is displayed in Fig. 22.19. Lowering the upper stress limit by only 2 MPa but adjusting it below the critical interphase stress identified in Fig. 22.3, the structural integrity of the interphase region is preserved for much longer time than for the system stressed up to 22 MPa. For up to 22 h, the amplitude of the resistance change remains stable at low levels, indicating that no severe damage of the interphase has occurred. However, at higher times the resistance

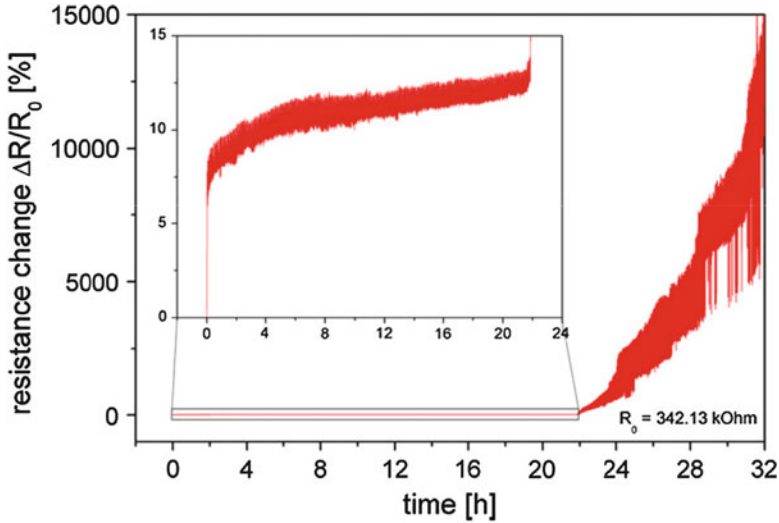


Fig. 22.19 Resistance change of interphase sensor during stress-controlled cyclic loading between 0 and 20 MPa. The inset figure shows the amplitude of the resistance change before the occurrence of severe interphase damage, which causes a distinct change of the amplitude pattern [118]

change increases stepwise, related to the initiation of first larger defects which continue to grow with additional load cycles. In general, the behavior of the resistance change up to 22 h resembles the displacement or strain during fatigue loading. At the first 4 h, the resistance changes faster as it is the case between 4 and 21 h, where a fairly linear increase is observed. This corresponds to the higher extent of plastic deformation at the beginning of the loading. In the linear part between 4 and 21 h, the additional plastic deformation of every load cycle is comparably small. As the resistance change corresponds to the integrity of the conductive paths, one can assume that its increase is due to a deformation of the whole CNT-network structure as well as stable and slow growth of all existing micro cracks. As can be inferred from the inset in Fig. 22.19, at approximately 21 h, right before the resistance change shoots up for the first time, the resistance change follows not any more the linear relationship as before. It rather shows a distinct increase in resistance change with every load cycle, indicating the onset of a faster crack growth in the interphase region resulting in significantly increased amplitudes of resistance change.

6 Conclusions

Interfacial properties of glass fiber-reinforced CNT–epoxy nanocomposites could be investigated using electro-micromechanical tests and wettability tests.

The tensile strength of glass fiber decreased significantly after acid cleaning which is attributed to removal of the sizing material and thereby partially etching the surface. There was, however, no distinct change in the tensile modulus of the glass fibers since this is an inherent property of materials itself. Through spun or dip coating, a conductive pathway can be created by the randomly oriented carbon nanotube networks on the curved fiber surface, and the electrical resistance value of coated fibers reached the semiconductive range. The CNT-coated fibers also gained higher interfacial shear strength without degradation of the fiber strength compared with the neat fiber. The electrical resistance measurement of single fiber/epoxy composites under tensile loading indicated this semiconductive glass fiber composite is capable of early warning before composite fracture, and the inherent damage can be monitored simultaneously. This effect can be used for in situ sensor development for composite damage process instead of external sensors.

Single glass fiber/CNT-epoxy nanocomposites exhibited a higher bonding than neat epoxy due to stress transferring effects of the CNT reinforcement. Interfacial adhesion between the acid-cleaned glass fibers and CNT-epoxy nanocomposites was higher than that between the sized glass fiber and CNT-epoxy composites due to increased surface energy and perhaps due to the weak boundary layer on the sized materials. CNT-epoxy nanocomposites exhibited a higher surface energy than did neat epoxy, and the work of adhesion of acid-cleaned glass fiber with CNT-epoxy nanocomposites is higher than that of sized glass fiber nanocomposites. It is thought that CNT nanostructures, arranged heterogeneously in the epoxy matrix, may also contribute to the hydrophobic nature of the CNT-epoxy nanocomposites. Both the interfacial adhesion and the apparent modulus of CNT-epoxy nanocomposites and glass fibers were consistent with an increased thermodynamic work of adhesion.

Industries such as wind energy, industrial, and automotive are pushing suppliers and manufacturers to improve upon glass fibers and bring down costs. Wind energy seeks longer, lighter, stiffer blades. Industrial markets require corrosion-resistant products, and automotive companies want lightweight solutions. In the next several years, the following trends will shape the glass fiber industry: increased competition among suppliers, product and process innovations, the emergence of nanomaterials and biocomposites, and the development of new specialty fibers.

The recovered glass fibers with strength degradation can be used in making thermal resistance insulation materials. Without proper solutions to the recycling issue for the glass fiber-reinforced polymer composite materials, more use of strong and lightweight composites will be strongly limited. All the industrial development trends will give more incentives and raise higher demand for better and true recycling of composite materials. The first-generation wind turbines are reaching their end of life. The turbine blades made of glass fiber-reinforced plastics need immediate recycling. With further new technological advancement in glass fiber and polymer resins, their composites always have been able to satisfy the need of any engineering field.

References

1. Böger L, Wichmann MHG, Meyer LO, Schulte K (2008) Load and health monitoring in lass fibre reinforced composites with an electrically conductive nanocomposite epoxy matrix. *Compos. Sci. Technol* 68:1886
2. Varelidis PC, Kominos NP, Papaspyrides CD (1998) Polyamide coated glass fabric in polyester resin: interlaminar shear strength versus moisture absorption studies. *Compos Part A* 29(12):1489
3. Lee SB, Rockett TJ, Hoffman RD (1992) Interactions of water with unsaturated polyester, vinyl ester and acrylic resins. *Polymer* 33(17):3691
4. Shen ZQ, Bateman S, Wu DY, McMahon P, DellOlio M, Gotama J (2009) The effects of carbon nanotubes on mechanical and thermal properties of woven glass fibre reinforced polyamide-6 nanocomposites. *Compos Sci Technol* 69:239
5. Wichmann MHG, Sumfleth J, Gojny FH, Quaresimin M, Fiedler B, Schulte K (2006) Glass-fibre-reinforced composites with enhanced mechanical and electrical properties – benefits and limitations of a nanoparticle modified matrix. *Eng Fract Mech* 73:2346
6. Thostenson ET, Ren Z, Chou TW (2002) Advances in the science and technology of carbon nanotubes and their composites: a review. *Compos Sci Technol* 61:1899
7. Fujiwara A, Iijima R, Suematsu H, Kataura H, Maniwa Y, Suzuki S, Achiba Y (2002) Local electronic transport through a through a junction of SWNT bundles. *Physica B* 323:227
8. Tans SJ, Devoret M, Dai H, Thess A, Smalley RE, Geerligs LJ, Dekker C (1997) Individual single-wall carbon nanotubes as quantum wires. *Nature* 386:474
9. White CT, Todorov TN (1998) Armchair carbon nanotubes as long ballistic conductors. *Nature* 393:240
10. Wei D, Espindola P, Lindfors T, Kvarnstrom C, Heinze J, Ivaska A (2007) In situ conductance and in situ ATR-FTIR study of poly(N-methylaniline) in aqueous solution. *J Electroanal Chem* 602:203
11. Pagels M, Heinze J, Geschke B, Rang V (2001) A new approach to the mechanism of polymerisation of oligovinylthiophene. *Electrochim Acta* 46:3943
12. Csahok E, Vieil E, Inzelt G (2000) In situ dc conductivity study of the redox transformations and relaxation of polyaniline films. *J Electroanal Chem* 482:168
13. Klauk H, Schmid G, Radlik W, Weber W, Zhou L, Sheraw CD, Nichols JA, Jackson TN (2003) Contact resistance in organic thin film transistors. *Solid State Electron* 47:297
14. Rep DBA, Morpurgo AF, Klapwijk TM (2003) Doping-dependent charge injection into regioregular poly(3-hexylthiophene). *Org Electron* 4:201
15. Oussalah S, Djezzar B, Jerisian R (2005) A comparative study of different contact resistance test structures dedicated to the power process technology. *Solid State Electron* 49:1617
16. Hsieh CT, Chen JM, Huang YH, Kou RR, Lee CT, Shih HC (2006) Influence of fluorine/carbon atomic ratio on superhydrophobic behavior of carbon nanofiber arrays. *J Vac Sci Technol B* 24(1):113
17. Jeong HJ, Kim DK, Lee SB, Kwon SH, Kadono K (2001) Preparation of water-repellent glass by sol-gel process using perfluoroalkylsilane and tetraethoxysilane. *J Colloid Interface Sci* 235:130
18. Karim A, Slawecki TM, Kumar SK, Douglas JF, Satija SK, Han CC, Russell TP, Liu Y, Overney R, Sokolov J, Rafailovich MH (1998) Phase-separation-induced surface patterns in thin polymer blend films. *Macromolecules* 31:857
19. Dilsiz N, Wightman JP (2000) Effect of acid-base properties of unsized and sized carbon fibers on fiber/epoxy matrix adhesion. *Coll Surf A* 164:325
20. Balkenende AR, Boogaard AP, Scholten M, Willard NP (1998) Evaluation of different approaches to assess the surface tension of low-energy solids by means of contact angle measurements. *Langmuir* 14:5909
21. Park SJ, Jang YS (2001) Interfacial characteristics and fracture toughness of electrolytically Ni-plated carbon fiber-reinforced phenolic resin matrix composites. *J Coll Interf Sci* 237:91

22. Park SJ, Kim MH, Lee JR, Choi SW (2000) Effect of fiber-polymer interactions on fracture toughness behavior of carbon fiber-reinforced epoxy matrix composites. *J Coll Interf Sci* 228:287
23. Jin L, Qun F, Chen WH, Huang KB, Ling CY (2006) Effect of electro-polymer sizing of carbon fiber on mechanical properties of phenolic resin composites. *Trans Nonferrous Met Soc* 16:457
24. Wang X, Chung DDL (1996) Improving the bond strength between carbon fiber and cement by fiber surface treatment and polymer addition to cement mix. *Cem Conc Res* 26:1007
25. Park JM, Lee SI, Kim KW, Yoon DJ (2001) Interfacial properties of electrodeposited carbon fibers/epoxy composites using electro-micromechanical technique and nondestructive evaluation. *J Colloid Interf Sci* 237:80
26. Griffith AA (1920) Phenomena of rupture and flow in solids. *Philos Trans R Soc Lond A* 221:163
27. Kim JK, Mai YW (1998) Engineered interfaces in fibre reinforced composites. vol 6. Elsevier, Amsterdam
28. Labronici M, Ishida H (1994) Toughening Composites by Fiber Coating: a Review. *Compos Interfaces* 2:199
29. Bader MG (2000) The composite market. vol 6, Elsevier, Amsterdam
30. Biederman B, Osada Y (1992) Plasma Polymerization Processes. Elsevier, New York
31. Inagaki N (1996) Plasma surface modification and plasma polymerization. Technomic, Lancaster
32. Li R, Ye L, Mai YW (1997) Application of plasma technologies in fibre-reinforced polymer composites: a review of recent developments. *Compos Part A* 28(1):73
33. Cech V (2000) New progress in composite interphases: a use of plasma technologies. *Proceedings of FRC 2000, Newcastle*, p 246
34. Segui Y (1997) Plasma deposition from organosilicon monomers. Kluwer, Dordrecht, p 305
35. Cech V, Prikryl R, Balkova R, Vanek J, Grycova A (2003) The influence of surface modifications of glass on glass fiber/polyester interphase properties. *J Adhes Sci Technol* 17(10):1299
36. Park SJ, Jin JS (2003) Effect of silane coupling agent on mechanical interfacial properties of glass fiber-reinforced unsaturated polyester composites. *J Polym Sci Pol Phys* 41(1):55
37. Zhao FM, Takeda N (2000) Effect of interfacial adhesion and statistical fiber strength on tensile strength of unidirectional glass fiber/epoxy composites. Part I: experiment results. *Compos Part A* 31(11):1203
38. Prikryl R, Cech V, Kripal L, Vanek J (2005) Adhesion of pp-VTES films to glass substrates and their durability in aqueous environments. *Int J Adhes Adhes* 25(2):121
39. Cech V, Inagaki N, Vanek J, Prikryl R, Grycova A, Zemek J (2006) Plasma-polymerized versus polycondensed thin films of vinyltriethoxysilane. *Thin Solid Films* 502(1–2):181
40. Kim JK, Mai YW (1998) Engineered Interfaces in Fibre Reinforced Composites. Elsevier, UK
41. Brill RP, Palmese GR (2006) Cure behavior of DGEBA vinyl ester–styrene resins near silane-treated interfaces. *J Appl Polym Sci* 101(5):2784
42. Wang TWH, Blum FD, Dharani LR (1999) Effect of interfacial mobility on flexural strength and fracture toughness of glass/epoxy laminates. *J Mater Sci* 34(19):4873
43. Saidpour SH, Richardson MOW (1997) Glass fibre coating for optimum mechanical properties of vinyl ester composites. *Compos Part A* 28(11):971
44. Park SJ, Jin JS (2001) Effect of silane coupling agent on interphase and performance of glass fibers/unsaturated polyester composites. *J Colloid Interface Sci* 242(1):174
45. Park R, Jang J (2004) Effect of surface treatment on the mechanical properties of glass fiber/vinylester composites. *J Appl Polym Sci* 91(6):3730
46. Gonzalez-Benito J, Baselga J, Aznar AJ (1999) Microstructural and wettability study of surface pretreated glass fibres. *J Mater Process Technol* 93:129

47. Olmos D, Lopez-Moron R, Gonzalez-Benito J (2006) The nature of the glass fibre surface and its effect in the water absorption of glass fibre/epoxy composites. The use of fluorescence to obtain information at the interface. *J. Compos Sci Technol* 66(15):2758
48. Gonzalez-Benito J (2003) The nature of the structural gradient in epoxy curing at a glass fiber/epoxy matrix interface using FTIR imaging. *J Colloid Interface Sci* 267(2):326
49. Weibull W (1951) A statistical distribution function of wide applicability. *J Appl Mech* 18:293
50. Johnson DJ (1987) Variable resistors based on composites. *J Phys D Appl Phys* 20:386
51. Hiltchon JW, Phillips DC (1979) The dependence of the strength of carbon fibres on length. *Fibre Sci Technol* 12:217
52. Bennett SC, Johnson DJ, Johnson W (1983) Strength structure relationships in PAN based C-fibres. *J Mater Sci* 18:3337
53. Own SH, Subramanian RV, Saunders SC (1986) A bimodal lognormal model of the distribution of strength of carbon fibres: effects of electrodeposition of titanium di (dioctyl pyrophosphate) oxyacetate. *J Mater Sci* 21:3912
54. Goda K, Fukunada H (1986) The evaluation of the strength distribution of silicon carbide and alumina fibres by a multi-modal Weibull distribution. *J Mater Sci* 21:4475
55. Beetz CP (1982) The analysis of carbon-fiber strength distributions exhibiting multiple-modes of failure. *Fibre Sci Technol* 16:45
56. Donnet JB, Bansal RC (1990) *Carbon Fibers*. Marcel Dekker, New York, p 289
57. Jung TH, Subramanian RV, Manoranjan VS (1993) Prediction of fibre strength at the critical length: a simulation theory and experimental verification for bimodally distributed carbon fibre strengths. *J Mater Sci* 28:4489
58. Chua PS, Piggott MR (1985) The glass fibre-polymer interface: I-theoretical consideration for single fibre pull-out tests. *Compos Sci Technol* 22:33
59. Beckert W, Lauke B (1997) Critical discussion of the single-fibre pull-out test: does it measure adhesion? *Compos Sci Technol* 57:1689
60. Gundel DB, Majumdar BS, Miracle DB (1995) Evaluation of the intrinsic transverse response of fiber-reinforced composites using a crossshaped sample geometry. *Scripta Metall Mater* 33:2057
61. Tandon GP, Kim RY (2002) Fiber-Matrix Interfacial Failure Characterization Using a Cruciform-Shaped Specimen. *J Compos Mater* 36:2667
62. Koyanagi J, Ogihara S (2011) Temperature dependence of glass fiber/epoxy interface normal strength examined by a cruciform specimen method. *Compos Part B* 42:1492
63. Ogihara S, Koyanagi J (2010) Investigation of combined stress state failure criterion for glass fiber/epoxy interface by the cruciform specimen method. *Compos Sci Technol* 70:143
64. Koyanagi J, Nakatani H, Ogihara S (2012) Comparison of glass-epoxy interface strengths examined by cruciform specimen and single-fiber pull-out tests under combined stress state. *Compos Part A* 43:1819
65. Koyanagi J, Yoneyama S, Nemoto A, Melo J (2010) Time and temperature dependence of carbon/epoxy interface strength. *Compos Sci Technol* 70:1395
66. Koyanagi J, Shah PD, Kimura S, Ha SK, Kawada H (2009) Mixed-mode interfacial debonding simulation in single-fiber composite under a transverse load. *J Solid Mech Mater Eng* 3:796
67. Zhandarov SF, Pisanova EV (1997) The local bond strength and its determination by fragmentation and pull-out tests. *Compos Sci Technol* 57:957
68. Zhandarov S, Mader E (2005) Characterization of fiber/matrix interface strength: applicability of different tests, approaches and parameters. *Compos Sci Technol* 65:149
69. Piggott MR (1997) *Compos Sci Technol* 57:965
70. Zhou XF, Wagner HD, Nutt SR (2001) Interfacial properties of polymer composites measured by push-out and fragmentation tests. *Compos Part A* 32:1543
71. Yang L, Thomason JL (2010) Interface strength in glass fibre-polypropylene measured using the fibre pull-out and microbond methods. *Compos Part A* 41:1077

72. Park JM, Kim JW, Yoon DJ (2002) Comparison of Interfacial Properties of Electrodeposited Single Carbon Fiber/Epoxy Composites Using Tensile and Compressive Fragmentation Tests and Acoustic Emission. *J Colloid Interf Sci* 247:231
73. Liu Z, Yuan X, Beck AJ, Jones FR (2011) Analysis of a modified microbond test for the measurement of interfacial shear strength of an aqueous-based adhesive and a polyamide fibre. *Compos Sci Technol* 71:1529
74. Yang L, Thomason JL, Zhu W (2011) The influence of thermo-oxidative degradation on the measured interface strength of glass fibre-polypropylene. *Compos Part A* 42:1293
75. Drzal LT, Micheal RJ, Koenig MF, Lloyd PF (1983) Adhesion of graphite fibers to epoxy matrices. II. The effect of fiber finish. *J Adhes* 16:133
76. Iroh JO, Yuan W (1996) Surface-Properties of Carbon-Fibers Modified by Electrodeposition of Polyamic Acid Polymer. *Polymer* 37:4197
77. Drzal LT (1983) Composite Interphase Characterization. *SAMPE J* 19:7
78. Piggott MR (1989) The interface in carbon fibre composites. *Carbon* 27:657
79. Blacketter DM, Vpadyaya D, King TR, King JA (1993) *Polym Compos* 14:430
80. Huttlinger KJ, Krekel G (1991) Polydimethylsiloxane coated carbon fibres for the production of carbon-fibre reinforced carbon. *Carbon* 29:1065
81. Chang TH, Zhang J, Yumitori S, Jones FR, Anderson CW (1994) Sizing resin structure and interphase formation in carbon fibre composites. *Composites* 25:661
82. Bradley RH, Ling X, Shutherland I (1993) An investigation of carbon fibre surface chemistry and reactivity based on XPS and surface free energy. *Carbon* 31:1115
83. Fowkes FM, Adhes J (1987) Role of acid-base interfacial bonding in adhesion. *Sci Tech* 1:7
84. Fowkes FM, Tischler DO, Wolfe JA, Lannigan LA, Ademu-John CM, Halliwell MJ (1984) Acid- base complexes of polymers. *J Polym Sci Chem Ed* 22:547
85. Tsutsumi K, Ban K, Shibata KS, Okazaki S, Kogoma M (1996) Wettability and Adhesion Characteristics of Plasma-Treated Carbon Fibers. *J Adhes* 57:45
86. Drzal LT, Madhukar M, Waterbury MC (1994) Adhesion to carbon fiber surfaces: surface chemical and energetic effects. *Compos Struct* 27:65
87. Chan D, Hozbor MA, Bayramli E, Powell RL (1991) Surface characterization of intermediate modulus graphite fibers via surface free energy measurement and ESCA. *Carbon* 29:1091
88. Le CV, Ly NG, Stevens MG (1996) Measuring the Contact Angles of Liquid Droplets on Wool Fibers and Determining Surface Energy Components. *Text Res J* 66:389
89. Hoecker F, Karger-Kocsis J (1996) Surface energetics of carbon fibers and its effects on the mechanical performance of CF/EP composites. *J Appl Polym Sci* 59:139
90. Huang Y, Gardner DJ, Chen M, Biermann CJ (1995) Surface energetics and acid-base character of sized and unsized paper handsheets. *J Adhes Sci Technol* 9:1403
91. Neumann AW, Spelt JK (1996) Thermodynamic status of contact angles. *Applied surface thermodynamics*. Marcel Dekker, New York
92. Kim SH (2008) Fabrication of Superhydrophobic Surfaces. *J Adhes Sci Technol* 22:235
93. Park JM, Kim DS, Kim SR (2003) Interfacial properties and microfailure degradation mechanisms of bioabsorbable fibers/poly-L-lactide composites using micromechanical test and nondestructive acoustic emission. *Compos Sci Technol* 63:403
94. Park JM, Kim DS, Kim SR (2004) Nondestructive evaluation of interfacial damage properties for plasma-treated biodegradable poly(p-dioxanone) fiber/poly(L-lactide) composites by micromechanical test and surface wettability. *Compos Sci Technol* 64:847
95. Owen DK, Wendth RC (1969) Estimation of the surface free energy of polymer. *J Appl Polym Sci* 13:1741
96. Rausch J, Zhuang RC, Mäder E (2009) Application of nanomaterials in sizings for glass fibre/polypropylene hybrid yarn spinning. *Mater Technol* 1(24):29
97. Warriar A, Godara A, Rochez O, Mezzo L, Luizi F, Gorbatiikh L (2010) The effect of adding carbon nanotubes to glass/epoxy composites in the fibre sizing and/or the matrix. *Compos A* 41(4):532

98. Godara A, Gorbatikh L, Kalinka G, Warriar A, Rochez O, Mezzo L (2010) Interfacial shear strength of a glass fiber/epoxy bonding in composites modified with carbon nanotubes. *Compos Sci Technol* 70(9):1346
99. Boccaccini AR, Chicatun F, Cho J, Bretcanu O, Roether JA, Novak S (2007) Carbon nanotube coatings on bioglass-based tissue engineering scaffolds. *Adv Funct Mater* 17(15):2815
100. Bekyarova E, Thostenson ET, Yu A, Kim H, Gao J, Tang J (2007) Multiscale carbon nanotube-carbon fiber reinforcement for advanced epoxy composites. *Langmuir* 23(7):3970
101. Muto N, Arai Y, Shin SG, Matsubara H, Yanagida H, Sugita M (2001) Hybrid composites with self-diagnosing function for preventing fatal fracture. *Compos Sci Technol* 61(6):875
102. Wang S, Chung DDL (1997) Self-monitoring of strain and damage by a carbon-carbon composite. *Carbon* 35(5):621
103. Gao SL, Mäder E, Plonka R (2007) Nanostructured coatings of glass fibers: improvement of alkali resistance and mechanical properties. *Acta Mater* 55(3):1043
104. Zhao Q, Wood JR, Wagner HD (2001) Stress fields around defects and fibers in a polymer using carbon nanotubes as sensors. *Appl Phys Lett* 78(12):1748
105. Sureeyatanapas P, Young RJ (2009) SWNT composite coatings as a strain sensor on glass fibres in model epoxy composites. *Compos Sci Technol* 69(10):1547
106. Sureeyatanapas P, Hejda M, Eichhorn SJ, Young RJ (2010) Comparing single-walled carbon nanotubes and samarium oxide as strain sensors for model glass-fibre/epoxy composites. *Compos Sci Technol* 70(1):88
107. Gao SL, Zhuang RC, Zhang J, Liu JW, Mäder E (2010) Glass fibers with carbon nanotube networks as multifunctional sensors. *Adv Funct Mater* 20(12):1885
108. Rausch J, Mäder E (2010) Health monitoring in continuous glass fibre reinforced thermoplastics: manufacturing and application of interphase sensors based on carbon nanotubes. *Compos Sci Technol* 70(11):1589
109. Zhang J, Zhuang RC, Liu JW, Mäder E, Heinrich G, Gao SL (2010) Functional interphases with multi-walled carbon nanotubes in glass fibre/epoxy composites. *Carbon* 48(8):2273
110. Dart SL, Peterson LE (1952) An improved vibroscope. *Textile Res J* 22(12):819
111. Siddiqui NA, Sham ML, Tang BZ, Munir A, Kim JK (2009) Tensile strength of glass fibres with carbon nanotube-epoxy nanocomposite coating. *Compos Part A* 40(10):1606
112. Gao SL, Mäder E, Abdkader A, Offermann P (2003) Sizings on alkaliresistant glass fibers: environmental effects on mechanical properties. *Langmuir* 19(6):2496
113. Netravali AN, Henstenburg RB, Phoenix SL, Schwartz P (1989) Interfacial shear strength studies using the single-filament composite test. Part I: experiments on graphite fibers in epoxy. *Polym Compos* 10(4):226
114. Kelly A, Tyson WR (1965) Tensile properties of fibre-reinforced metals: copper/tungsten and copper/molybdenum. *J Mech Phys Solids* 13:329
115. Park JM, Kim DS, Kim SJ, Kim PG, Yoon DJ, DeVries KL (2007) Inherent sensing and interfacial evaluation of carbon nanofiber and nanotube/epoxy composites using electrical resistance measurement and micromechanical technique. *Compos Part B* 38(7):847
116. Böger L, Wichmann MHG, Meyer LO, Schulte K (2008) *Compos Sci Technol* 68(7-8):1886
117. Thostenson ET, Chou TW (2008) Real-time in situ sensing of damage evolution in advanced fiber composites using carbon nanotube networks. *Nanotechnology* 19:215713
118. Rausch J, Mäder E (2010) Health monitoring in continuous glass fibre reinforced thermoplastics: Tailored sensitivity and cyclic loading of CNT-based interphase sensors. *Compos Sci Technol* 70(11):2023

Peter Lobotka and Pavol Kunzo

Contents

1	Introduction	577
2	Composite Carbon Nanoparticles/Nonconducting Polymers	578
3	Preparation of CNT/Polymer Nanocomposites	582
3.1	Carbon Nanotubes for Sensors	582
3.2	Functionalization of CNTs by Polymers	582
3.3	CNT/Polymer Nanocomposites for Sensors	584
4	Electrical Transport Mechanisms in CNT/Conducting Polymer Composites	586
5	Sensors Based on CNT/PANI Nanocomposites	588
5.1	Gas Sensors	588
5.2	Biosensors	594
5.3	Other Sensors	595
6	Conclusion	596
	References	597

1 Introduction

It is indisputable that sensors are indispensable in our daily life. In parallel to the research in the field of organic electronics, there is a serious effort to develop technologically compatible sensors based on polymers. Due to the widespread usage of microelectronics, it is quite natural that the main effort is focused on the development of sensors providing electrical output. But until the discovery of conducting polymers, it was necessary to find a way how to increase the basic electrical conductivity of the polymers, which had been considered to be perfect insulators. The easiest way to do it is to add and disperse in a polymer a small amount of conducting or semiconducting material with particles on the micro- or

P. Lobotka (✉) • P. Kunzo

Institute of Electrical Engineering, Slovak Academy of Sciences, Bratislava, Slovak Republic
e-mail: Peter.Lobotka@savba.sk

sub-micrometer scale, for example, carbon fibers or carbon black. A proper concentration of the “filler” is around the percolation threshold, at which the sensor’s sensitivity reaches the maximum. The details are described in Sect. 2.

With the advent of carbon nanotubes in 1991, the fibers and carbon black were replaced by the single- and multi-walled carbon nanotubes (SWNT and MWNT), by fullerenes, and recently by graphene flakes.

Regarding the abovementioned conducting polymers (CPs), it was found already by the end of the 1980s that they alone are a suitable material for sensors, mainly for sensors of organic vapors and various gases [1–6]. In 2000, Kong et al. reported on excellent gas-sensing properties of a single SWNT [7]. So, before we start to discuss the sensors based on carbon nanoobjects/conducting polymer composites, it is worth pointing out that both constituents possess interesting and commercially exploitable sensing properties.

But first we shall discuss the archetypal sensor – insulating polymer (e.g., polystyrene or polymethyl methacrylate) mixed with a carbon filler (e.g., carbon black or carbon fibers).

2 Composite Carbon Nanoparticles/Nonconducting Polymers

This kind of sensor is based on composites consisting of carbon particles embedded in an insulating polymeric matrix. Before carbon nanotubes (CNTs) had come on the scene, it was the carbon black material (CB) – a form of amorphous carbon – that played the role of the electrically conducting constituent. CB is a well-known material commonly used for toners in laser printers or tires. Many polymers were used as the matrix material. According to reference [8], around 20 polymers were tested – polyvinylchloride, polystyrene (PS), polymethyl methacrylate (PMMA), polycaprolactone, and polyethylene oxide, to name just a few. The concentration of the constituent responsible for the electrical conductivity has to be near the percolation threshold, which is, in the literature dealing with composites, usually taken as the volume fraction at which measurements on specimens or results of numerical simulations begin to show percolation behavior [9, 10]. From the engineering viewpoint the percolation threshold is the point on the steep slope of the dependence shown in Fig. 23.1.

The typical mechanism of electronic transport is the tunnelling of electrons between the adjacent CB (or other carbon) particles through a barrier represented by the insulating polymer in between the particles (depicted as gray areas between the CB particles in Fig. 23.2). The distance between the particles must be around 2–3 nm in order to obtain a reasonable tunnelling current. The bulk composite can be considered a serial–parallel network of such tunnelling junctions. It is well known from the quantum theory of tunnelling that the tunnelling current is exponentially dependent on the barrier thickness. This relationship predestines the sensing mechanism – modulation of the barrier thickness – which makes of such a composite either a very sensitive strain sensor [13] or an organic vapor sensor

Fig. 23.1 Logarithmic conductivity versus carbon black concentration in a polystyrene matrix [11]

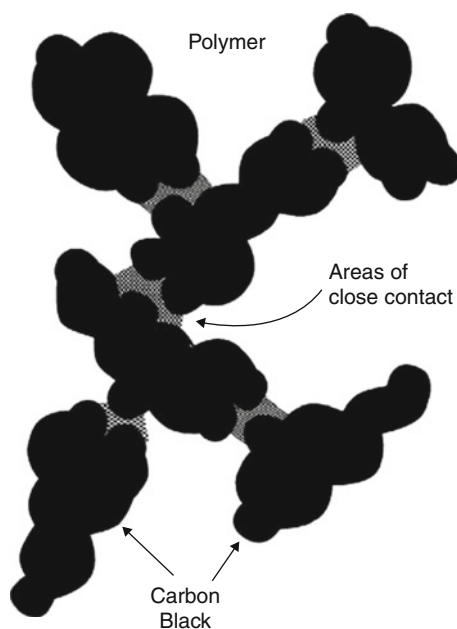
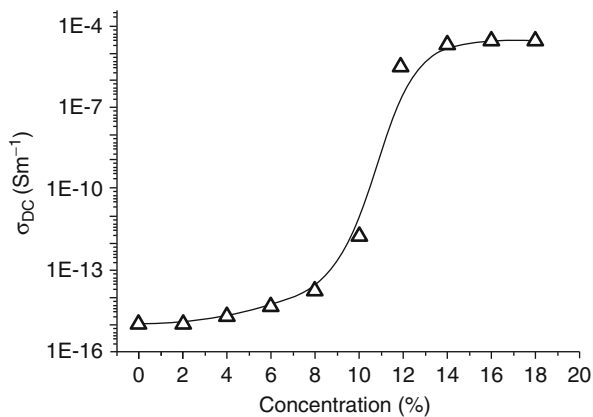


Fig. 23.2 Illustration of the model of a carbon black/polymer composite [12]

based on swelling of a matrix [14]. On the other side, this exponential dependence can be also the source of undesirable interference in the sensor output signal, since it is difficult to distinguish whether the change in tunnelling current is due to variation in the vapor concentration, strain, humidity, or ambient temperature. Anyway, these CB/polymer composites served as a model material in gathering deep insight in the sensing mechanisms, so nowadays, when the CB in the composites is replaced almost entirely by CNTs, the research community can make a profitable use of this knowledge. The reader, who is interested in knowing more details about the mechanism of the electric transport in CB/polymer composites, is referred to the review article [11].

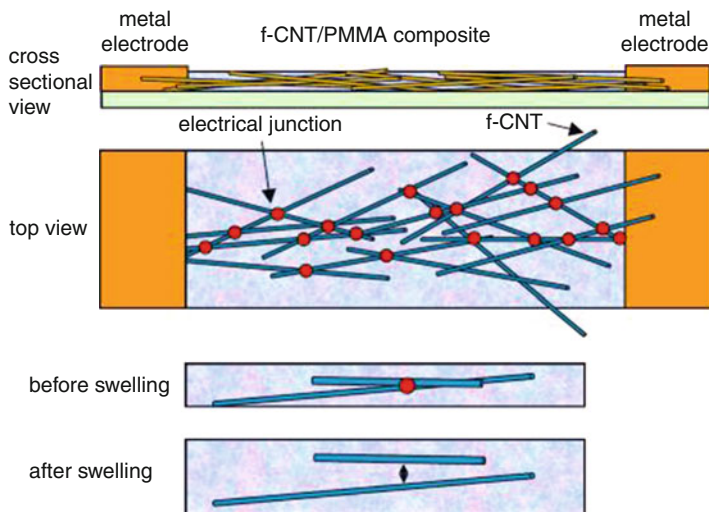


Fig. 23.3 Illustration of the sensing mechanism of a CNT/PMMA composite vapor sensor [19]

In Fig. 23.3, the principle of the CNT/nonconducting polymer sensor based on the swelling of the polymer matrix is depicted. The swelling is caused by the absorption of organic vapors (mostly ethanol, methanol, acetone, chloroform, benzene, or toluene) by the polymeric matrix. The overall volume of the composite increases and so does the distance between the adjacent CNTs. The result is a remarkable decrease in electrical conductivity (or in other words – an increase in resistance). When the input of an analyte is stopped, the absorbed analyte starts to desorb and after some time the current (the sensor resistance) reaches its basic value. Obviously, the rate of the analyte diffusion is polymer dependent, which opens a possibility to obtain sensors that are selective. Unfortunately, it is impossible to prepare CB/polymer composite that would be sensitive only to a single analyte. The composites are sensitive to several analytes but with a different sensitivity to each of them. (There is a sort of “sensing spectrum” that is unique for each CB/polymer composite.) This fact opens a possibility to design the so-called electronic nose, consisting of many different composite sensors, each of them being sensitive to a unique group of the analytes, e.g., alcohols, halides, esters, etc. Then, the output signals from every single sensor are analyzed by pattern recognition algorithms [15]. In this way it is possible not only to classify but in some cases also to quantify the analyte of interest [16, 17]. In some cases, the speed of the sensor response (the response and recovery times) can be also used as the discriminant factor [17].

CB/polymer sensors are cheap and they can operate at room temperature (which is a certain advantage in comparison with the metal oxide sensors that must be heated up to 200–400 °C). The typical sensitivity is above 1,000 ppm that is sufficient in some applications, and the calibration curves, at such relatively high concentrations, are quite linear for most vapors [14].

Fig. 23.4 Electrical resistance change versus tensile strain in a composite sensor MWNT/polyethylene oxide polymer [20]

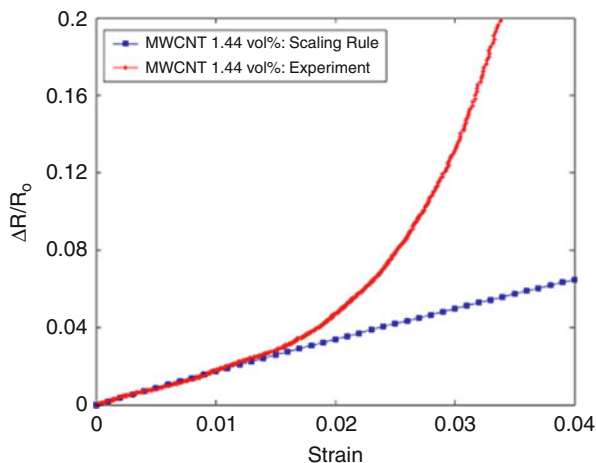
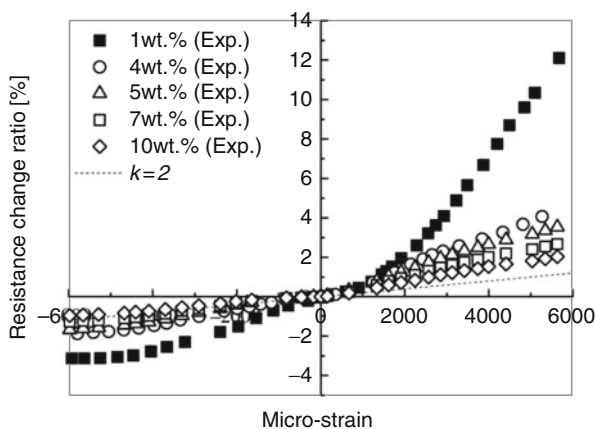


Fig. 23.5 Resistance change due to compressive strain (negative values) and tensile strain (positive values) in a composite MWNT/epoxy resin [18]



Up to now, we were discussing the chemiresistors. But the carbon/nonconducting polymer composites were tested also as piezoresistors. The strain sensors used to have the same design as the vapor sensors – a composite film on a substrate with two electrodes enabling to monitor the sensor resistance. Figure 23.4 shows the transfer function of a strain sensor made of a composite MWNT/polyethylene oxide polymer. It is seen that up to some strain value, the dependence is linear, but above this value, it becomes nonlinear. The linearity range is dependent on the filler concentration – the higher the volume fraction of the nanotubes, the wider the linear range. The nonlinearity is related to the exponential dependence of the tunnelling current on the inter-nanotube distance. The plot in Fig. 23.4 is related to the tensile stress. In case of a compressive stress (left side of the plot in Fig. 23.5), the situation is even less favorable, because the sensitivity is lower and saturates. The reason is that starting from a certain level of the compression, all relevant MWNTs are already in a good contact and the resistance does not change anymore [18].

3 Preparation of CNT/Polymer Nanocomposites

Preparation of CNT/polymer composites was first reported by Ajayan et al. in 1994 [21]. In the study, the composites were prepared by the mechanical mixing of multi-walled CNTs and epoxy resin. Since then, a considerable effort has been done to improve the design and technology to meet the requirements put on the nanocomposite materials in various applications.

3.1 Carbon Nanotubes for Sensors

Regarding the preparation of CNT-based materials, one of the difficulties is the scalable and high-yield production of CNTs with uniform properties. In general, the fabrication process yields a mixture of SWNTs and MWNTs with varying diameter, length, chirality, and number of walls. The defects and impurities contribute to this nonuniformity. Therefore, a great effort is devoted to the development of new preparation methods and new techniques for cleaning, separation, and chemical treatment of CNTs [22]. Especially, in the case of the SWNTs, the effective separation of CNTs with metallic and semiconducting character of conductivity remains a challenge. This is essential for sensing applications (e.g., in gas sensors) where useful effects provided by semiconducting CNTs – e.g., varying the hole density by the amount of adsorbed NH_3 molecules [23] – can be cancelled by short-circuiting nanotubes with metallic conductivity. An AC dielectrophoresis was reported to be capable of separating metallic SWCNTs from the semiconducting ones in a sodium dodecyl sulfate suspension [24]. The method is based on the difference in the relative dielectric constants of metallic and semiconducting SWNTs with respect to the solvent, resulting in an opposite movement of the two species along the electric field gradient. Another study by K. Hyeok et al. [25] takes advantage of the preferential binding of nitronium ion (NO_2^+) on metallic tubes due to a higher electron density at the Fermi level. The nitronium ion adsorption and subsequent charge transfer lead to the disintegration of the metallic SWNTs. According to another solution [26], in an aligned array of nanotubes deposited over microelectrodes, the metallic SWNTs were destroyed by a short current pulse. The semiconducting nanotubes were not destroyed due to their high resistance. A similar removal of metallic SWNTs can be achieved by laser irradiation [27].

3.2 Functionalization of CNTs by Polymers

The sensoric properties of the composite are determined by the physicochemical properties of the CNTs, their volume fraction within the composite, their resistance to agglomerate, their capability to “survive” the mixing procedure, etc. Therefore, the preparation methods are continuously improving in order to preserve the superb properties of the CNTs also in the composite. Two main issues must be taken into account: the dispersion of CNTs and their chemical affinity to the

Fig. 23.6 Schematic drawing of the non-covalent wrapping of the polymer chain to SWNT [34]



polymer matrix [28]. Regarding the latter, there are two categories: the composites with covalent and non-covalent bonding of the CNTs to the polymer.

3.2.1 Non-covalent CNT to Polymer Bonding

In non-covalent functionalization, the polymer is bound to CNT sidewalls by physical adsorption or wrapping (Fig. 23.6). Such composites can be prepared simply by adding carbon nanotubes to a polymer-containing solution. The desired material, for example, in the form of a casted or spin-casted film, can be obtained after the evaporation of the solvent [29]. Conjugated polymers or polymers with heteroatoms containing free electron pairs can interact with CNTs through π -stacking [30–33]. In such an interaction, π -electrons of conducting polymers bond to the conjugated electrons within the CNT sidewall.

3.2.2 Covalent CNT to Polymer Bonding

Regarding the composites with covalent filler-to-matrix bonding, firstly, the monomer or low-molecular weight species (oligomers) are adsorbed onto the CNT sidewalls. Secondly, they are polymerized directly on the surface of CNTs. Such a procedure is usually referred as the “grafting from” approach. The alternative is a “grafting to” approach, where a polymer-containing solution can be prepared prior to the composite synthesis. As the CNTs are added to the solution, the chains of the organic molecules are immobilized on the CNT surfaces through a chemical reaction. Therefore, the polymer molecules typically contain some functional reactive group with affinity to the CNT sidewall. Disadvantageously, the content of grafted polymer is limited by relatively low reactivity of the polymer chains and the steric hindrance of macromolecules. Chemical reactivity of the CNT surface also plays an important role in the CNTs to polymer bonding. Therefore, the CNTs are usually functionalized with various functional groups (e.g., carboxyl or hydroxyl ones) to mediate the covalent binding of the polymer. The functionalization of CNTs can be achieved by chemical treatment [35, 36], but also other methods such as plasma treatment were reported [37]. Several studies showed that the oxygen plasma pretreatment of CNTs can enhance the sensing properties of CNT/conducting polymer composites used for gas sensors [38, 39]. An advantage of the plasma treatment is that together with the introduction of the functional groups, it removes the amorphous carbon residues from the surface of the CNTs.

Although covalent CNT/polymer bonding leads to enhanced interaction between the CNT filler and the matrix material, chemical functionalization can destroy the conjugated system of the CNT sidewalls, which can deteriorate the electronic transport properties of CNTs [28].

3.3 CNT/Polymer Nanocomposites for Sensors

On the one hand, research into the CNT/polymer nanocomposites has been conducted with an objective to enhance the mechanical and electrical properties. On the other hand, in a branch of the sensors, the aim is to improve the sensing properties of the composites. As already mentioned, the composites are used in the form of nano-devices (e.g., nanowires) or even more sophisticated structures – MEMS or NEMS. To utilize the properties of CNT/polymer nanocomposites, their design and preparation have to be adapted to certain sensor architectures. Together with the cost-effective dispersion methods, the structuring or manipulation with individual CNTs can also play an important role in the sensor fabrication [40].

3.3.1 Composites CNTs/Nonconducting Polymers

Most of the researchers have incorporated nanotubes into different thermoplastic nonconducting polymers due to easy processing. As already mentioned, the sensors based on these composites utilize the matrix deformation due to the gas or vapor absorption or mechanical loading, which results in the resistance changes [41]. Polymethyl methacrylate is one of the most used thermoplastic polymers. A strain sensor based on CNT-filled PMMA film can be prepared by melt processing or solution casting [42]. The same composite in the form of a thin film prepared by dip coating can be used as a sensor of organic vapors [43]. In another study [44], an immunosensor based on MWCNTs embedded in a PS matrix was prepared by the solution casting. In the sensor structure PS played only the role of a mechanical stabilizer; thus, the sensor performance was enhanced after the partial removal of PS from the MWNTs surfaces by plasma etching, so the MWNTs were partially uncovered at the composite surface. Other polymers, like epoxy resin [45], can be used in similar electroanalytical sensors. The enhanced performance of the composite sensors originates from the high surface area, conductivity, electrochemical activity, or specific chemical functionalization of CNTs.

3.3.2 Composite CNTs/Conducting Polymers

Conducting polymers (CPs) are a specific branch of polymeric materials, which are interesting for many sensoric applications. Since the first study on metal-to-insulator transition and doping of polyacetylene in 1977 [46], a great effort has been dedicated to the development of the conjugated CPs. Figure 23.7 shows some of the frequently used conducting polymers.

CP-based nanocomposites have high application potential in sensors, actuators, batteries, supercapacitors, and other devices. Regarding the gas sensors, a large

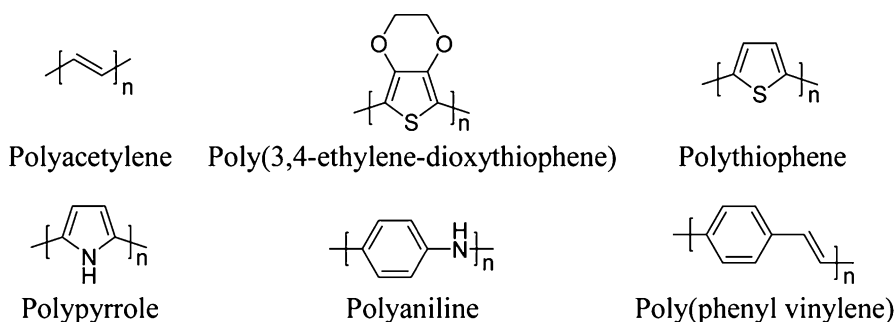


Fig. 23.7 Schematic structure of several conducting polymers [47]

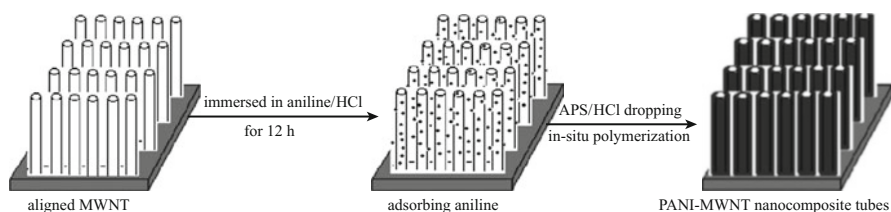


Fig. 23.8 Sketch of the preparation procedure of an MWNT/PANI nanocomposite film. The vertically aligned MWNT film is deposited on quartz substrate [50]

number of sensor structures based on CPs were designed, and they showed very good performance [47–49]. Compared to nonconducting polymers, many conducting polymers (e.g., polyaniline) show a lack of processibility, as they are thermosets not soluble in common solvents. Therefore, the conventional methods of the composite preparation cannot be used. Instead, the in situ polymerization is applied. Chemical polymerization of the monomer adsorbed on the surface of pre-deposited CNTs is the most common way to obtain a CNT/CP composite [50]. Figure 23.8 illustrates the synthesis of an MWNT/polyaniline nanocomposite film. An array of vertically aligned MWNT grown on a quartz substrate was dipped into a solution of HCl and aniline monomer. After the adsorption of the monomer on the surface of carbon nanotubes, it was polymerized in the presence of ammonium persulfate.

In addition to chemical polymerization, the polymerizations enabled by the UV light, plasma, or microwave radiation were reported [51–53]. A technologically important advantage of the conducting polymers is that they can be prepared by electrochemical polymerization. Conductive and transparent films were obtained by electrochemical synthesis of CNT/CP nanocomposites [54]. Randomly oriented network of CNTs (CNT mat) served as the working electrode in the process of electrochemical polymerization. Conducting polymer (polyaniline or polypyrrole) was deposited to reduce the contact resistance between individual CNTs.

4 Electrical Transport Mechanisms in CNT/Conducting Polymer Composites

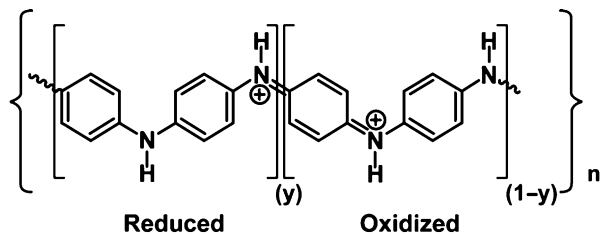
In sensoric applications of CNT/CP composites, they usually serve as both the sensing material and the transducer. This is enabled by the electrical properties of the composites which are related to the quantity to be detected. Thus, understanding of the electrical properties of CNT/CP composites is essential for sensor design. Here we focus on the properties of CPs, mainly polyaniline (PANI), as the properties of CNTs are discussed in other chapters.

CPs – usually referred as intrinsically conducting polymers – are extensively conjugated organic molecules (Fig. 23.7). The conductivity of the CPs depends on the doping process as the CPs in their natural state are either insulators or wide-gap semiconductors [55]. Depending on doping, the conductivity can vary in a wide range from values typical for insulators up to 10^4 S/cm [56]. Typical CPs with an electron-conjugated structure are polyacetylene (PA), polyaniline (PANI), polypyrrole (PPy), polythiophene (PTH), polyfuran (PFU), poly(para phenylene vinylene), and polycarbazole [48]. Mainly due to their physical properties, they are attractive for various applications, such as antistatic protection and electromagnetic shielding, capacitors, electrodes in polymer batteries, sensors and actuators, protective coating materials, electronic displays, and many others. Electronic properties of CPs originate from their conjugated structure, the alternation of single and double bonds along the polymer chain, leading to delocalized molecular orbitals (i.e., p_z orbitals in C atoms) [57]. Properties, such as conductivity, closely relate to the excitations within the π -band of delocalized orbitals and depend on the degree of its filling. The degree of filling of the π -band structure is affected by the doping process, shifting the CP from its ground state. The most common doping mechanism is the chemical doping provided by the redox process. In the redox doping the electrons are either removed from the π -valence band (oxidation) or added to the π^* conduction band (reduction). The excited states can be provided also by other doping mechanisms, such as electrochemical doping [58], direct charge injection, or photoexcitation [59]. Regarding nanocomposite materials, functional groups on the surface of the nanoparticle fillers can affect the doping state of the matrix polymer by injecting or accepting the free electrons. The study by Gao et al. [60] shows that graphene oxide can be used as an effective dopant for p-doped conjugated polymer. The doping is driven by oxygen-containing groups located on the graphene sheets.

Except polyacetylene, CPs typically show aromatic structure where the preferred sense of bond alternation is typically connected with benzenoidal configuration. This is referred as a ground state of the polymer structure. On the contrary, the excited states are described as polarons, showing the molecule geometry shifted toward the quinoidal structure.

In our research, we focus on the materials based on PANI, which is specific among the other conducting polymers due to versatility of its chemical structure, high electrical conductivity, stability, and many potential applications, mainly in

Fig. 23.9 Chemical structure of PANI



sensors. The specificity of PANI originates from its molecular structure containing nitrogen atoms directly in the path of conjugated bonds. Bonding of hydrogen to these imine nitrogen ($-\text{N}=\text{C}$) atoms affects the oxidation state of the polymer and configuration of the adjacent phenylene rings. The ratio ($-\text{N}=\text{C}$)/($-\text{NH}-$), marked as y in Fig. 23.9, determines the different forms of PANI. The fully reduced form ($y = 1$) is called leucoemeraldine base (LB) which is an insulator. The half-oxidized ($y = 0.5$) emeraldine base (EB) form of PANI is also an insulator with a large gap ($E_g \sim 3.6$ eV). The fully oxidized form is called pernigraniline base (PNB) ($y = 0$). It was calculated that PNB form of PANI has an energy gap of $E_g \sim 1.4$ eV [61]. The next specificity of PANI is that besides the redox doping, it has an additional type of doping – protonation. It relies on the conversion of EB or PNB from the base to the salt forms. Unlike the redox doping, this specific kind of doping preserves the number of conjugated electrons within the polymer chain. The protonation is achieved upon the exposure of PANI base to protonic acids. Figure 23.10 depicts the structure of emeraldine salt after the bonding of protons (H^+) to the nitrogen imine sites of PANI. Through the geometric relaxation and charge redistribution of protonated sites, the spinless bipolarons are converted to the so-called polaron lattice consisting of delocalized polarons distributed along the chains.

The conductivity mechanism in PANI is very complex. It involves the interchain movement of charge carriers along the polymer molecules, intra-chain transport between the molecules, and interparticle hopping at the macroscopic level. Various models were proposed to explain the charge transport in the CPs [63]. Regarding PANI, the Mott's variable-range hopping model is usually considered [64]. It describes the hopping of weakly localized charge carriers to the next energetically favorable states. Thus, the character of the temperature dependence of conductivity $\sigma(T)$ depends on a dimensionality (d) of the transport process ($d = 1, 2, \text{ or } 3$):

$$\sigma(T) = \sigma_0 \exp \left[-\left(\frac{T_0}{T} \right)^{\frac{1}{1+d}} \right] \quad (23.1)$$

where σ_0 and T_0 are temperature-independent quantities explained in detail in [64].

Structure and conductivity of PANI enable the unique sensing mechanisms, exploitable especially in gas sensors. Adsorbed gas molecules can change the doping level altering the conductivity of PANI. Besides the various oxidative and reducing gases, also the gases causing the deprotonation of PANI can be detected. PANI-based gas sensors are most frequently used for detection of

Fig. 23.10 Emeraldine salt form of PANI with different redistribution of protonated sites along the chain. A^- states for the counterpart anion of the protonic acid [62]

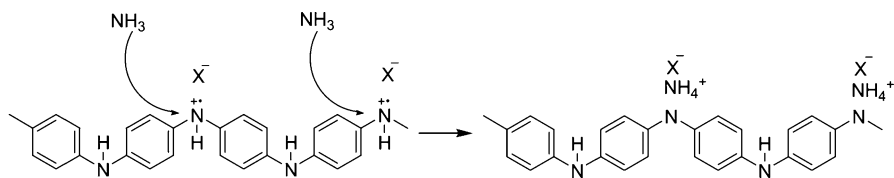
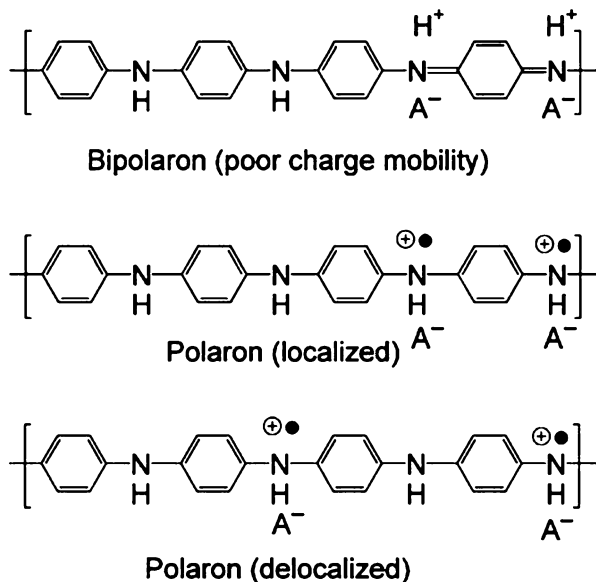


Fig. 23.11 Ammonia detection mechanism in PANI [47]

ammonia, as it is considered a very strong deprotonating agent. The sensitive detectors for low ammonia concentrations are needed to monitor the environment. It can be even argued that ammonia became a kind of reference gas used to compare the properties of different PANI-based sensors. Molecules of NH₃ interact with the protonated sites and the doping state is compensated through the transfer of protons from the -NH- groups to the NH₄⁺ cation radical (Fig. 23.11). The process is accompanied with a sharp fall in conductivity by few orders of magnitude.

5 Sensors Based on CNT/PANI Nanocomposites

5.1 Gas Sensors

Interaction of gases with CPs or CNTs occurs through adsorption processes which can be divided into two classes: gases that undergo the chemical reactions with the surface and gases that are physically adsorbed at the surface. Chemical

reactions can either oxidize or reduce the surface, depending on the ratio of electron affinities of the gas molecules and the surface material. Common oxidation gases, such as O_2 , O_3 , and NO_2 , accept the electrons from the surface. Oppositely, reduction gases, e.g., H_2S , NH_3 , and N_2H_4 , donate electrons to the surface. The adsorption of gas analytes with electron acceptor or electron donor properties leads to a change in the electrical or optical properties of the sensing element. For chemiresistive gas sensors, the change in the electrical conductivity is the most important factor.

5.1.1 Gas Sensor Based on Pristine Carbon Nanotubes

The oxidation/reduction of CNTs is related with the change in the number of charge carriers within the nanotube sidewalls. The chemisorption of gas molecules is conducted through the active sites, which are generally the defects in the graphitic sidewalls. Thanks to the very high surface-to-volume ratio, pristine single-walled and multi-walled carbon nanotubes as well as aligned CNTs (ACNTs) showed very good sensitivity to various analytes [65] (Table 23.1). Thus, many different gas sensors based on pristine CNTs were investigated [47].

Figure 23.12 shows a change in the conductance of an individual SWNT when exposed to oxidizing or reducing gases [7]. One can see that the conductivity increases upon the oxidation of the SWNT and decreases by its reduction. Although such a sensor has an extraordinary sensitivity, its technology is rather complicated and requires the individual nanotube to be electrically contacted, which hinders the mass production of such sensors.

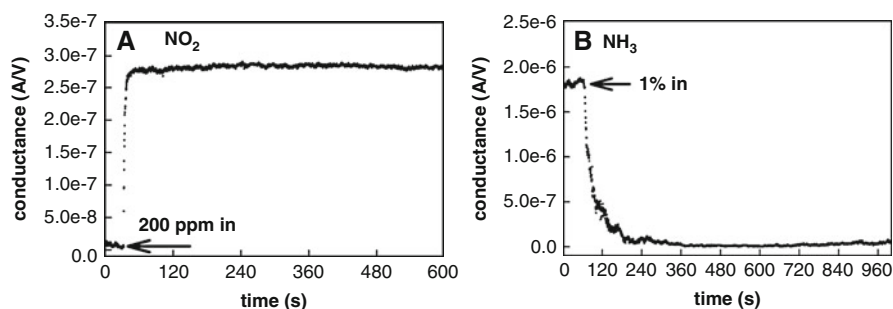
5.1.2 Gas Sensor Based on CNT/PANI Nanocomposites

Although CNT-based gas sensors offer high sensitivity, fast response, small size, and low power consumption, the chemical sensing is provided through the active sites, such as defects and functional groups. Finally, researchers started to functionalize them with conducting polymers to gain better sensitivity and selectivity. Modification of CNTs by conducting polymers like PANI can change their electronic properties and boost the gas-sensing performance. First, such composite gas sensors become very sensitive and selective and can operate at room temperature due to the favorable properties of the conducting polymer. Second, carbon nanotubes bring a large surface-to-volume ratio and enhance the electrical conductivity of the composite [66].

The unique properties of CPs applicable to gas sensors are mainly related to their conductivity mechanism based on the oxidation/reduction or acid/base doping. In a study by Mangu et al. [38], the gas sensors comprising of the arrays of vertically aligned MWCNTs functionalized with different conducting polymers showed corresponding selectivity to oxidizing or reducing gases. This implies that the electrical transport properties of the CPs are crucial for the performance of CP-based sensoric structures. Because of the superior position of PANI among CPs, we shall focus on the sensors based on CNT/PANI composites in the following text. Among them the chemiresistive gas sensors have gained the largest interest. Different PANI nanostructures, including thin films [67–69], nanoparticles [70],

Table 23.1 Gas-sensing performance of different CNT-based gas sensors [65]

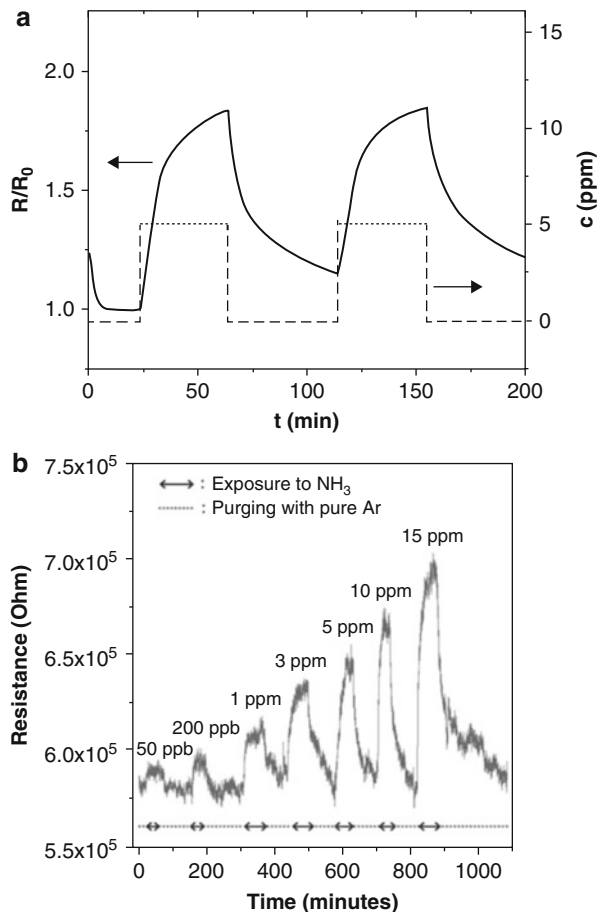
CNT type	Sensor configuration	Targeted analytes	Detection limit	Response time	Recovery time
S-SWCNT	FET	NO ₂ , NH ₃	2 ppm NO ₂ , 0.1 % NH ₃	<10 min	~1 h(200 °C)
SWCNTs	Resistor	NO ₂ , nitrotoluene	44 ppb NO ₂ , 262 ppb nitrotoluene	10 min	10 min (UV)
SWCNTs	Resistor	NH ₃	5 ppm	~10 min	~20 min (80 °C)
SWCNTs	Resistor	NH ₃	5 ppm	~10 min	~10 min (70 °C) several days
MWCNTs	Capacitor and resistor	NH ₃	10 ppm	2–3 min	(100 °C in vacuum)
MWCNTs	Resistor	NH ₃	2,500 ppm	N/S	N/S
MWCNTs	FET	NO ₂	50 ppm	~500 s	~10 min (10 V bias potential)
MWCNTs	Resistor	SO ₂ , HF	10 ppm SO ₂ , 4 ppm HF	N/S	N/S
MWCNTs	Electrochemical gas sensor	Cl ₂	100 ppm	~150 s	~150 s
ACNTs	Resistor	NO ₂	10 ppb	~60 min	~60 min (165 °C)
ACNTs	Resistor	NO ₂	10 ppm	N/S	N/S
ACNTs	Resistor	NO, NO ₂	2 ppm NO ₂ , 2 ppm NO	N/S	~20 min (150 °C and UV)
ACNTs	Resistor	NH ₃	~0.1 %	N/S	N/S
ACNTs	FET	N ₂	50 mTorr	N/S	N/S

**Fig. 23.12** Opposite responses of a single carbon nanotube to NO₂ (oxidizing) and NH₃ (reducing) gases [7]

nanobowls [71], nanotubes [64], or nanofibers [72, 73], showed very good room-temperature sensitivity to NH₃, NO, NO₂, CO₂, H₂, or organic vapors.

Probably the simplest way to prepare PANI/CNT nanocomposite sensor is the in situ chemical polymerization of aniline in a CNT-containing solution. The product of

Fig. 23.13 Dynamic response of different PANI-based gas sensors to ammonia: (a) a thin film of PANI. (b) CNT/PANI nanocomposite [75]



the polymerization can be washed and filtered afterward. A thin film gas sensor can be prepared, for example, by spin-coating of a solution containing the nanocomposite [74]. Such sensors show high sensitivity to ammonia (even in the ppb range).

Figure 23.13 presents dynamic responses of a thin PANI film and CNT/PANI nanocomposite film. Nanocomposite sensor was prepared by the electrochemical deposition of PANI over the network of CNTs dispersed across the interdigitated microelectrodes. An excessive noise level in the output signal is evident in the response of the nanocomposite sample. The noise in the CNT composite materials is caused probably by the large number of CNT/polymer interfaces in the conducting path [76]. So from the point of view of electrical engineering, the non-composite sensing materials seem to be superior, since they offer higher signal-to-noise ratio.

Despite that, CNT/CP composites can show the properties which are superior over each of the constituent materials [77]. Filler-to-matrix interface can play an important role in the sensing mechanism. It can be explained on a structure where

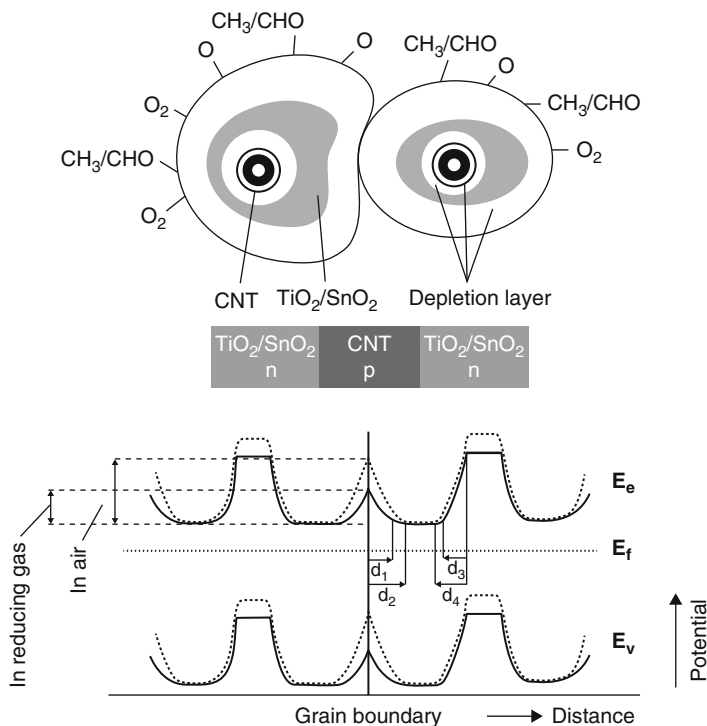


Fig. 23.14 Schematic of the band diagram of the CNT/metal oxide composite with potential barriers at grain boundaries and p-n heterojunctions. Widths of the depletion layers in ethanol (d_1, d_3) and in air (d_2, d_4) are different [78]

the metal oxide matrix was used instead of conducting polymer. In the study by Duy et al. [78], SWNTs were embedded in a mixture of SnO_2 and TiO_2 prepared by sol-gel method. Figure 23.14 shows that in addition to the potential barriers at grain boundaries of the adjacent metal oxide grains, p-n heterojunctions appear at the interfaces between p-type SWNTs and n-type metal oxide grains. The p-n junctions imply the existence of depletion layers which is the most sensitive part of the sensor, because small change in the concentration of free charge carriers substantially changes the overall conductivity. This concentration is modified by the oxidation or reduction reactions caused by the adsorbed gas molecules. Obviously, the largest improvement of the sensor performance is possible when the filler-to-matrix interface is easily accessible by ambient gas.

The abovementioned principle can be used also in the case of SWNT/polymer composites. But, the p-type conductivity of SWNTs has to be switched to n-type by functionalization. The reason is that PANI has sufficiently high conductivity only in a form of p-type semiconductor.

To obtain very sensitive sensor with short response times and low noise level, one can prepare the ordered structure of SWNTs prior the deposition of the

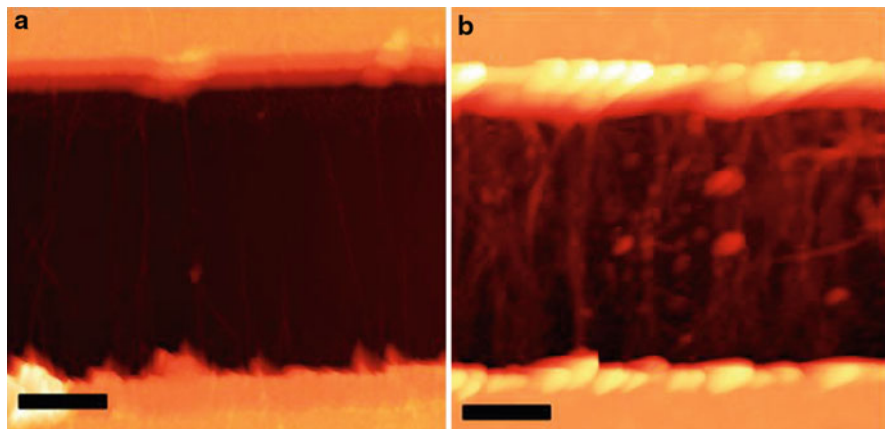


Fig. 23.15 AFM images of a network of aligned SWNTs before (a) and after (b) the functionalization with PANI [79]. The scale bar corresponds to 1 μm

polymer. In the work by Lim et al. [79], carboxylated SWNTs were dielectrophoretically aligned in between microfabricated electrodes (Fig. 23.15). Afterward, the nanotube network was functionalized with PANI by controlled electrochemical polymerization of aniline on the surface of the nanotubes. PANI-functionalized SWNTs showed approximately five times higher sensitivity to ammonia than the pristine SWNTs. Moreover, the sensitivity of horizontally aligned SWNT/PANI network was more than twice as high as the sensitivity of randomly oriented nanotubes functionalized with PANI. The detection limit of this ammonia sensor was better than 10 ppb.

Interaction between the carbon nanotubes and PANI plays a very important role in the performance of the nanocomposite. It was shown that functionalization of CNTs by the carboxyl groups prior the deposition of PANI leads to the enhanced sensitivity, stability, and faster response of the gas sensors. Hydrophilic carboxyl groups were created by the oxygen plasma treatment [39] or by the oxyfluorination treatment in a mixture of oxygen and fluorine gases [80].

As already mentioned above, the majority of published works on PANI-based sensors report on the NH_3 -sensing properties. Nevertheless, such nanocomposites show also the response to other gases. CNT/PANI gas sensors are typically sensitive also to oxidation gases, such as NO_2 [79]. Hydrogen sensors based on thin composite films of PANI and MWNT or SWNT were reported [81]. Carbon nanotubes were added to the solution of PANI and spin-coated over the interdigitated electrodes on a glass substrate. Sensitivity of the nanocomposite films was two times higher than that of PANI film without CNTs. We recently published a study on the hydrogen-sensing properties of a thin PANI film treated shortly by oxygen plasma [82]. We showed that the hydrogen sensitivity of the PANI film can be remarkably enhanced by such a treatment. We achieved as large as 30 % a change in the sensor resistance upon exposure to 10 ppm of H_2 . The detection limit of the sensor was below 1 ppm.

As already mentioned in Sect. 2, the most reliable way to solve the selectivity issue is to use an array of gas sensors with different sensitivities to individual gases (i.e., electronic nose). In this way, each sensor has to be slightly modified, for example, CNT-based gas sensors can be functionalized with different conducting polymers [38]. Another possibility is the decoration of CNTs with nanoparticles of noble metals [83]. This way the selectivity of individual sensors can be tailored for the recognition of a certain analyte.

5.2 Biosensors

This is a very important research field, since according to Frost and Sullivan [84], the medical applications are the major driving force for the development of sensor technologies. The biosensor market is expected to grow from \$6.72 billion in 2009 to \$14.42 billion in 2016. In this paragraph we shall focus on electrochemical biosensors that are closely related to the kernel of this book – CNT/polymer composites.

As can be inferred from the name “biosensor,” the carbon/polymer composite alone is incapable to fulfill this role, so a third biologically active constituent must be added, e.g., an enzyme or antibody. It must be pointed out that in these composites, only the polymers that are conducting are used, mainly PANI. Typically, the sensor consists of three electrodes: an active electrode, a counter electrode, and a reference electrode. Since the biosensor must reliably work in liquid environments, it brings along a new problem – how to efficiently fix the enzyme to the composite film. There are many methods to immobilize the enzymes, such as adsorption, physical entrapment in gels or membranes, cross-linking, covalent binding, doping, etc., [85]. Usually, the biosensor is fabricated by the electrochemical deposition of a conducting polymer from a solution containing its monomer, dispersed carbon nanotubes, and an enzyme (or other biologically active constituent). The microstructure of the resulting composite is shown in Figs. 23.16, 23.17, and 23.18. As can be seen, CNTs play an important role in the immobilization of the biologically active constituent as they form lots of cavities. The active electrode is a combination of any electrochemical probe (amperometric, potentiometric, or conductometric) with a thin layer (10–200 nm) of an immobilized enzyme. PANI is used not only for the physical entrapment of the enzymes during electrodeposition but also as a matrix for covalent enzyme immobilization. A comprehensive review of biosensors based on conducting polymers is given in [85]. CNT/polymer biosensors can be fabricated on flexible substrates, their sensitivity in some cases approaches that of HPLC (high-performance liquid chromatography), but the price is incomparable.

The composite sensors were successfully used for the detection of, for example, glucose [87], hydrogen peroxide [88], lactate [89], oxalate [90], creatinine [91], cholesterol [92], and carbamate pesticides [86]. Additional information on composite biosensors can be found in the books [93–95].

Fig. 23.16 SEM micrograph of an MWNT mat – a starting material for the fabrication of a biosensor for electrochemical detection of carbamate pesticides in fruit and vegetables [86]

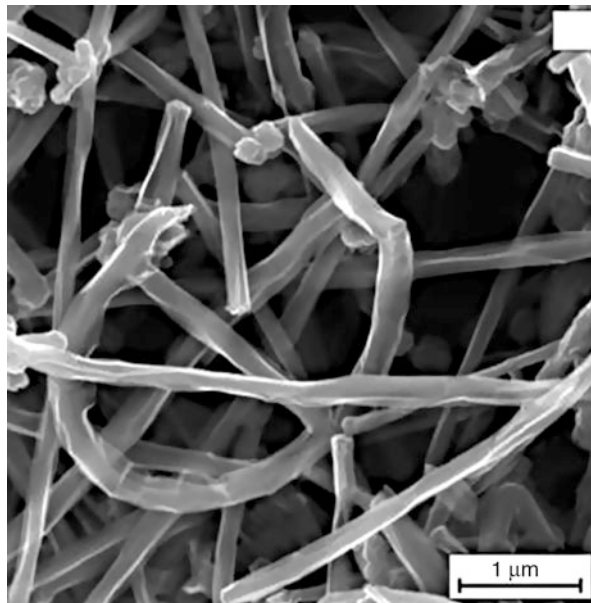
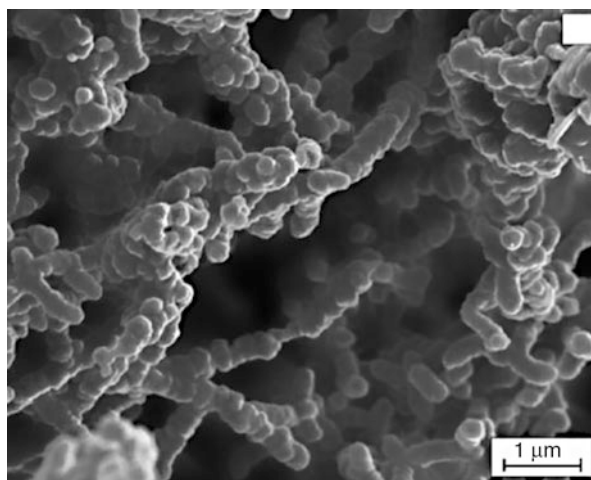


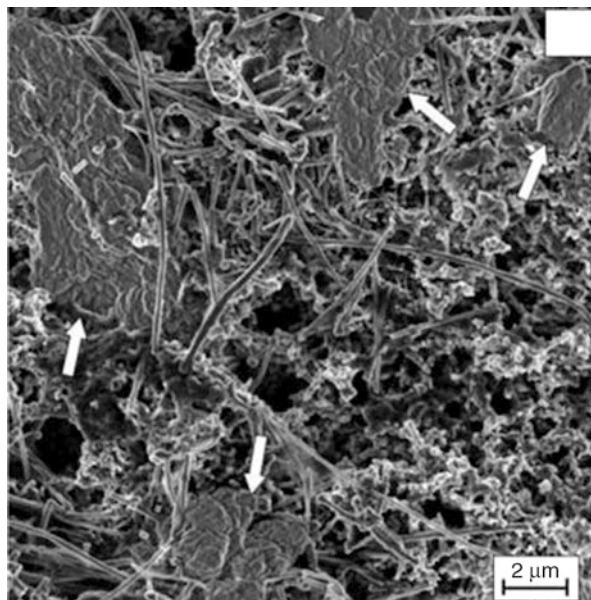
Fig. 23.17 Step two – MWNTs coated by electrochemically polymerized aniline



5.3 Other Sensors

It is well known that an SWNT mat is a suitable material for bolometers [96]. (Bolometers are sensitive detectors of electromagnetic radiation based on a unique property of some materials – a steep dependence of their resistance on temperature. The absorbed radiation increases the temperature of a sensing element and the corresponding change in its resistance is the measure of a radiation.) If the radiation dose is too high, the SWNT mat can even burn out – Ajayan et al. discovered

Fig. 23.18 Step three – the biologically active material – acetylcholinesterase enzyme (indicated by the *white arrows*) immobilized within the composite cavities



accidentally that SWNTs ignited when exposed to a conventional photographic flashlight [97]. In 2006, Singamaneni reported the same effect but in a SWNT/polyurethane composite film [98]. Maybe from these two accidental experiments, Pradhan et al. deduced that SWNT/nonconducting polymer could be a proper material for infrared detector. In [99] they compared the response of an SWNT-mat bolometer and that of an SWNT-mat/polycarbonate composite bolometer. Surprisingly, they found that the composite showed not only the bolometric response but also a photoresponse, which increased the overall sensor sensitivity about four times. The origin of the photocarriers was not unambiguously explained (the authors presented two possible explanations). A similar enhancement of the composite response to IR radiation is reported in [100]. Here, the block copolymer consists of two polymers – poly(3-hexylthiophene)-block-polystyrene. They explain the photoresponse due to exciton dissociations and charge carrier separation caused by a Schottky barrier at the metallic electrode–SWCNT interface.

Finally, in [101], it is shown that CNT/PPy and CNT/PANI composites can be used as solid-state pH sensors: the electrical response is linear, fast, and reproducible. Compared with pure CNT networks, the linearity and stability are improved.

6 Conclusion

This chapter presents a concise but very limited review about the use of CNT/polymer composites in sensors. This area is so wide that it is impossible to present all interesting results achieved in the field of gas or vapor sensors,

biosensors, and even infrared sensors in a short chapter. The field of biosensors based on composites is booming since the sensors are cheap and easy to operate.

In many composite sensors, the conducting polymers have proven to be superior over the nonconducting ones. Although both composite constituents – carbon nanotubes and conducting polymer – have good sensing properties, their combination brings a synergic effect. This is evident particularly in gas sensors and biosensors, where the good performance exhibited by carbon nanotubes can be improved by their functionalization with conducting polymers. In this way the p-n heterojunctions with depletion layers can be formed at the interfaces between semiconducting SWNTs and conducting polymer with complementary type of conductivity.

In this area, PANI plays the most significant role due to its specific physico-chemical properties. In our opinion, after some improvements (e.g., shortening of the response and recovery times, elimination of the baseline shift) achievable by consistent application of nanotechnologies, these composite sensors working at room temperature could progressively replace the common metal oxide sensors that require heating up to 200–400 °C.

References

1. Bartlett PN, Ling-Chung SK (1989) Conducting polymer gas sensors part III: results for four different polymers and five different vapours. *Sensors Actuators* 20:287–292
2. Boyle A, Geniès EM, Lapkowski M (1989) Application of the electronic conducting polymers as sensors: polyaniline in the solid state for detection of solvent vapours and polypyrrole for detection of biological ions in solutions. *Synth Met* 28:769–774
3. Bartlett PN, Ling-Chung SK (1989) Conducting polymer gas sensors part II: response of polypyrrole to methanol vapour. *Sensors Actuators* 19:141–150
4. Bartlett PN, Archer PBM, Ling-Chung SK (1989) Conducting polymer gas sensors part I: fabrication and characterization. *Sensors Actuators* 19:125–140
5. Krinichnyi VI, Yeremenko ON, Rukhman GG, Letuchii YA, Geskin VM (1989) Sensors based on conducting organic polymers. *Polyaniline Polym Sci USSR* 31:1819–1825
6. Polak A, Petty-weeks S, Beuhler AJ (1986) Applications of novel proton-conducting polymers to hydrogen sensing. *Sensors Actuators* 9:1–7
7. Kong J, Franklin N, Zhou C, Chapline M, Peng S, Cho K et al (2000) Nanotube molecular wires as chemical sensors. *Science* 287:622–5
8. Severin EJ, Doleman BJ, Lewis NS (2000) An investigation of the concentration dependence and response to analyte mixtures of carbon black/insulating organic polymer composite vapor detectors. *Anal Chem* 72:658–668
9. Mamunya Y (2011) Carbon nanotubes as conductive filler in segregated polymer composites – electrical properties. In: Yellampalli S (ed) *Carbon nanotubes -polymer nanocomposites*. InTech, Rijeka, pp 173–196
10. Li C, Thostenson ET, Chou T-W (2010) Carbon-nanotube-based composites and damage sensing. In: Leng J, Lau AK-T (eds) *Multifunctional polymer nanocomposites*. CRC Press, Boca Raton, pp 159–281
11. Costa LC, Henry F (2011) DC electrical conductivity of carbon black polymer composites at low temperatures. *J Non Cryst Solids* 357:1741–1744
12. Balberg I (2002) A comprehensive picture of the electrical phenomena in carbon black–polymer composites. *Carbon* 40:139–143

13. Wang X, Chung DDL (1995) Short-carbon-fiber-reinforced epoxy as a piezoresistive strain sensor. *Smart Mater Struct* 4:363–367
14. Doleman BJ, Lonergan MC, Severin EJ, Vaid TP, Lewis NS (1998) Quantitative study of the resolving power of arrays of carbon black-polymer composites in various vapor-sensing tasks. *Anal Chem* 70:4177–4190
15. Sisk BC, Lewis NS (2003) Estimation of chemical and physical characteristics of analyte vapors through analysis of the response data of arrays of polymer-carbon black composite vapor detectors. *Sensors Actuators B* 96:268–282
16. Jurs PC, Bakken GA, McClelland HE (2000) Computational methods for the analysis of chemical sensor array data from volatile analytes. *Chem Rev* 100:2649–2678
17. Bicego M, Tessari G, Tecchiolli G, Bettinelli M (2002) A comparative analysis of basic pattern recognition techniques for the development of small size electronic nose. *Sensors Actuators B* 85:137–144
18. Yin G, Hu N, Karube Y, Liu Y, Li Y, Fukunaga H (2011) A carbon nanotube/polymer strain sensor with linear and anti-symmetric piezoresistivity. *J Compos Mater* 45:1315–1323
19. Yoon H, Xie J, Abraham JK, Varadan VK, Ruffin PB (2006) Passive wireless sensors using electrical transition of carbon nanotube junctions in polymer matrix. *Smart Mater Struct* 15: S14–S20
20. Park M, Kim H, Youngblood JP (2008) Strain-dependent electrical resistance of multi-walled carbon nanotube/polymer composite films. *Nanotechnology* 19:55705–55711
21. Ajayan PM, Stephan O, Colliex C, Trauth D (1994) Aligned carbon nanotube arrays formed by cutting a polymer resin-nanotube composite. *Science* 265:1212–1214
22. Journet C, Picher M, Jourdain V (2012) Carbon nanotube synthesis: from large-scale production to atom-by-atom growth. *Nanotechnology* 23:142001
23. Quang N, Vantrinh M, Lee B, Huh J (2006) Effect of NH₃ gas on the electrical properties of single-walled carbon nanotube bundles. *Sensors Actuators B* 113:341–346
24. Krupke R, Hennrich F, Löhneysen HV, Kappes MM (2003) Separation of metallic from semiconducting single-walled carbon nanotubes. *Science (NY)* 301:344–347
25. An KH, Yang C-M, Seo K, Park KA, Lee YH (2006) A diameter-dependent separation of semiconducting from metallic single-wall carbon nanotubes by using nitronium ions. *Curr Appl Phys* 6:e99–e109
26. Ho X, Ye L, Rotkin SV, Xie X, Du F, Dunham S et al (2010) Theoretical and experimental studies of Schottky diodes that use aligned arrays of single-walled carbon nanotubes. *Nano Res* 3:444–451
27. Mahjouri-Samani M, Zhou YS, Xiong W, Gao Y, Mitchell M, Lu YF (2009) Laser induced selective removal of metallic carbon nanotubes. *Nanotechnology* 20:495202, 5 pp
28. Spitalisky Z, Tasis D, Papagelis K, Galiotis C (2010) Carbon nanotube–polymer composites: chemistry, processing, mechanical and electrical properties. *Prog Polym Sci* 35:357–401
29. Safadi B, Andrews R, Grulke EA (2002) Multiwalled carbon nanotube polymer composites: synthesis and characterization of thin films. *J Appl Polym Sci* 84:2660–2669
30. Haddad R, Cosnier S, Maaref A, Holzinger M (2009) Non-covalent biofunctionalization of single-walled carbon nanotubes via biotin attachment by pi-stacking interactions and pyrrole polymerization. *Analyst* 134:2412–8
31. Chang Y-C, Chen Y-D, Chen C-H, Wen Y-S, Lin JT, Chen H-Y et al (2008) Crystal engineering for pi-pi stacking via interaction between electron-rich and electron-deficient heteroaromatics. *J Org Chem* 73:4608–14
32. Roquelet C, Lauret J-S, Alain-Rizzo V, Voisin C, Fleurier R, Delarue M et al (2010) Pistacking functionalization of carbon nanotubes through micelle swelling. *Chemphyschem* 11:1667–72
33. Tournus F, Latil S, Heggie M, Charlier J-C (2005) π -stacking interaction between carbon nanotubes and organic molecules. *Phys Rev B* 72:1–5
34. Hirsch A (2002) Functionalization of single-walled carbon nanotubes. *Angew Chem Int Ed* 41:1853–59

35. Xiao Y, Ye X, He L, Che J (2012) New carbon nanotube-conducting polymer composite electrodes for drug delivery applications. *Polym Int* 61:190–196
36. Park SH, Bandaru PR (2010) Improved mechanical properties of carbon nanotube/polymer composites through the use of carboxyl-epoxide functional group linkages. *Polymer* 51:5071–5077
37. Ionescu R, Espinosa EH, Softer E, Llobet E, Vilanova X, Correig X et al (2006) Oxygen functionalisation of MWNT and their use as gas sensitive thick-film layers. *Sensors Actuators B* 113:36–46
38. Mangu R, Rajaputra S, Singh VP (2011) MWCNT-polymer composites as highly sensitive and selective room temperature gas sensors. *Nanotechnology* 22:215502
39. Yoo K-P, Kwon K-H, Min N-K, Lee MJ, Lee CJ (2009) Effects of O₂ plasma treatment on NH₃ sensing characteristics of multiwall carbon nanotube/polyaniline composite films. *Sensors Actuators B* 143:333–340
40. Pradhan B, Kohlmeyer RR, Chen J (2010) Fabrication of in-plane aligned carbon nanotube–polymer composite thin films. *Carbon* 48:217–222
41. Li C, Thostenson ET, Chou T-W (2008) Sensors and actuators based on carbon nanotubes and their composites: a review. *Compos Sci Technol* 68:1227–1249
42. Pham GT, Park Y-B, Liang Z, Zhang C, Wang B (2008) Processing and modeling of conductive thermoplastic/carbon nanotube films for strain sensing. *Compos B Eng* 39:209–216
43. Abraham JK, Philip B, Witchurch A, Varadan VK, Reddy CC (2004) A compact wireless gas sensor using a carbon nanotube/PMMA thin film chemiresistor. *Smart Mater Struct* 13:1045–1049
44. Mendoza E, Orozco J, Jiménez-Jorquera C, González-Guerrero AB, Calle A, Lechuga LM et al (2008) Scalable fabrication of immunosensors based on carbon nanotube polymer composites. *Nanotechnology* 19:075102
45. Olivé-Monllau R, Esplandiú MJ, Bartrolí J, Baeza M, Céspedes F (2010) Strategies for the optimization of carbon nanotube/polymer ratio in composite materials: applications as voltammetric sensors. *Sensors Actuators B* 146:353–360
46. Chiang C, Fincher C, Park Y, Heeger A, Shirakawa H, Louis E et al (1977) Electrical conductivity in doped polyacetylene. *Phys Rev Lett* 39:1098–1101
47. Bai H, Shi G (2007) Gas sensors based on conducting polymers. *Sensors* 7:267–307
48. Lange U, Roznyatovskaya NV, Mirsky VM (2008) Conducting polymers in chemical sensors and arrays. *Anal Chim Acta* 614:1–26
49. Gerard M, Chaubey A, Malhotra BD (2002) Application of conducting polymers to biosensors. *Biosens Bioelectron* 17:345–359
50. Feng W, Bai X, Lian Y, Liang J, Wang X, Yoshino K (2003) Well-aligned polyaniline/carbon-nanotube composite films grown by in-situ aniline polymerization. *Carbon* 41:1551–1557
51. Li X, Guan W, Yan H, Huang L (2004) Fabrication and atomic force microscopy/friction force microscopy (AFM/FFM) studies of polyacrylamide–carbon nanotubes (PAM–CNTs) copolymer thin films. *Mater Chem Phys* 88:53–58
52. Mi H, Zhang X, An S, Ye X, Yang S (2007) Microwave-assisted synthesis and electrochemical capacitance of polyaniline/multi-wall carbon nanotubes composite. *Electrochem Commun* 9:2859–2862
53. Murguruma H (2010) Amperimetric biosensor based on carbon nanotube and plasma polymer. In: Serra PA (ed) *Biosensors*. InTech, Vukovar, pp 47–70
54. Ferrer-Anglada N, Kaempgen M, Skákalová V, Dettlaf-Weglikowska U, Roth S (2004) Synthesis and characterization of carbon nanotube-conducting polymer thin films. *Diamond Relat Mater* 13:256–260
55. Lakshmi K, John H, Joseph R, George KE, Mathew KT (2008) Comparison of microwave and electrical properties of selected conducting polymers. *Microw Opt Technol Lett* 50:504–508
56. Epstein AJ (2000) Electrical conductivity in conjugated polymers. In: Rupprecht L (ed) *Conductive polymers and plastics in industrial applications*. William Andrew, New York, pp 1–9
57. Foot PJS, Kaiser AB (2000) Conducting polymers. In: Kirk-Othmer (ed) *Encyclopedia of chemical technology*. Wiley, Hoboken

58. Tang S, Irgum K, Edman L (2010) Chemical stabilization of doping in conjugated polymers. *Org Electr* 11:1079–1087
59. Fung S, Moratti SC, Graham SC, Friend RH (1999) Photoinduced doping in conjugated polymers. *Synth Met* 102:1167–1168
60. Gao Y, Yip H-L, Chen K-S, O'Malley KM, Acton O, Sun Y et al (2011) Surface doping of conjugated polymers by graphene oxide and its application for organic electronic devices. *Adv Mater* (Deerfield Beach, Fla) 23:1903–8
61. dos Santos M, Brédas J (1989) Nonlinear excitations in pernigraniline, the oxidized form of polyaniline. *Phys Rev Lett* 62:2499–2502
62. Hino T, Seida Y, Takahashi T, Kuramoto N (2006) Synthesis and characterization of polyanilines doped with several carboxylic acids and with a carboxylic acid equivalent. *Polym Int* 55:243–247
63. Bohli N, Gmati F, Mohamed AB, Vigneras V, Miane J-L (2009) Conductivity mechanism of polyaniline organic films: the effects of solvent type and casting temperature. *J Phys D Appl Phys* 42:205404
64. Bhadra S, Khastgir D, Singha NK, Lee JH (2009) Progress in preparation, processing and applications of polyaniline. *Prog Polym Sci* 34:783–810
65. Zhang W-D, Zhang W-H (2009) Carbon nanotubes as active components for gas sensors. *J Sens* 2009:1–16
66. Ma Y, Cheung W, Wei D, Bogozi A, Chiu PL, Wang L et al (2008) Improved conductivity of carbon nanotube networks by in situ polymerization of a thin skin of conducting polymer. *ACS Nano* 2:1197–1204
67. Lobotka P, Kunzo P, Kovacova E, Vavra I, Krizanova Z, Smatko V et al (2011) Thin polyaniline and polyaniline/carbon nanocomposite films for gas sensing. *Thin Solid Films* 519:4123–4127
68. Nicolas-Debarnot D, Poncin-Epaillard F (2003) Polyaniline as a new sensitive layer for gas sensors. *Anal Chim Acta* 475:1–15
69. Takeda S (1999) A new type of CO₂ sensor built up with plasma polymerized polyaniline thin film. *Thin Solid Films* 343–344:313–316
70. Crowley K, Morrin A, Hernandez A, Omalley E, Whitten P, Wallace G et al (2008) Fabrication of an ammonia gas sensor using inkjet-printed polyaniline nanoparticles. *Talanta* 77:710–717
71. Jiang S, Chen J, Tang J, Jin E, Kong L, Zhang W et al (2009) Au nanoparticles-functionalized two-dimensional patterned conducting PANI nanobowl monolayer for gas sensor. *Sensors Actuators B* 140:520–524
72. Yan XB, Han ZJ, Yang Y, Tay BK (2007) NO₂ gas sensing with polyaniline nanofibers synthesized by a facile aqueous/organic interfacial polymerization. *Sensors Actuators B* 123:107–113
73. Sadek AZ, Wlodarski W, Kalantar-Zadeh K, Baker C, Kaner RB (2007) Doped and dedoped polyaniline nanofiber based conductometric hydrogen gas sensors. *Sensors Actuators A Phys* 139:53–57
74. He L, Jia Y, Meng F, Li M, Liu J (2009) Gas sensors for ammonia detection based on polyaniline-coated multi-wall carbon nanotubes. *Mater Sci Eng B* 163:76–81
75. Zhang T, Nix MB, Yoo B-Y, Deshusses MA, Myung NV (2006) Electrochemically functionalized single-walled carbon nanotube gas sensor. *Electroanalysis* 18:1153–1158
76. Collins PG, Fuhrer MS, Zettl A (2000) 1/f noise in carbon nanotubes. *Appl Phys Lett* 76:894
77. Lu J, Park BJ, Kumar B, Castro M, Choi HJ, Feller J-F (2010) Polyaniline nanoparticle-carbon nanotube hybrid network vapour sensors with switchable chemo-electrical polarity. *Nanotechnology* 21:255501
78. Van Duy N, Van Hieu N, Huy PT, Thamilselvan M, Yi J (2008) Mixed SnO₂/TiO₂ included with carbon nanotubes for gas-sensing application. *Physica E* 41:258–263
79. Lim J-H, Phiboolsirichit N, Mubeen S, Deshusses MA, Mulchandani A, Myung NV (2010) Electrical and gas sensing properties of polyaniline functionalized single-walled carbon nanotubes. *Nanotechnology* 21:75502, 7 pp

80. Yun J, Im JS, Kim H-I, Lee Y-S (2012) Effect of oxyfluorination on gas sensing behavior of polyaniline-coated multi-walled carbon nanotubes. *Appl Surf Sci* 258:3462–3468
81. Srivastava S, Sharma SS, Agrawal S, Kumar S, Singh M, Vijay YK (2010) Study of chemiresistor type CNT doped polyaniline gas sensor. *Synth Met* 160:529–534
82. Kunzo P, Lobotka P, Micusik M, Kovacova E (2012) Palladium-free hydrogen sensor based on oxygen-plasma-treated polyaniline thin film. *Sensors Actuators B* 171–172: 838–845
83. Leghrib R, Felten A, Demoisson F, Reniers F, Pireaux J-J, Llobet E (2010) Room-temperature, selective detection of benzene at trace levels using plasma-treated metal-decorated multiwalled carbon nanotubes. *Carbon* 48:3477–3484
84. Analytical Review of World Biosensors Market (2010) <http://www.frost.com/prod/servlet/report-toc.pag?repid=N810-01-00-00-00>
85. Wei D, Ivaska A (2006) Electrochemical biosensors based on polyaniline. *Chem Anal (Warsaw)* 51:839–852
86. Cesarino I, Moraes FC, Lanza MRV, Machado SAS (2012) Electrochemical detection of carbamate pesticides in fruit and vegetables with a biosensor based on acetylcholinesterase immobilized on a composite of polyaniline-carbon nanotubes. *Food Chem* 135:873–879
87. Alwarappan S, Liu C, Kumar A, Li C-Z (2010) Enzyme-doped graphene nanosheets for enhanced glucose biosensing. *J Phys Chem C* 114:12920–12924
88. Sheng Q, Wang M, Zheng J (2011) A novel hydrogen peroxide biosensor based on enzymatically induced deposition of polyaniline on the functionalized graphene-carbon nanotube hybrid materials. *Sensors Actuators B* 160:1070–1077
89. Rahman MM, AShiddiky MJ, Rahman MA, Shim Y-B (2009) A lactate biosensor based on lactate dehydrogenase/nicotinamide adenine dinucleotide (oxidized form) immobilized on a conducting polymer/multiwall carbon nanotube composite film. *Anal Biochem* 384:159–165
90. Yadav S, Devi R, Kumari S, Yadav S, Pundir CS (2011) An amperometric oxalate biosensor based on sorghum oxalate oxidase bound carboxylated multiwalled carbon nanotubes-polyaniline composite film. *J Biotechnol* 151:212–217
91. Yadav S, Kumar A, Pundir CS (2011) Amperometric creatinine biosensor based on covalently coimmobilized enzymes onto carboxylated multiwalled carbon nanotubes/polyaniline composite film. *Anal Biochem* 419:277–283
92. Dhand C, Arya SK, Datta M, Malhotra BD (2008) Polyaniline-carbon nanotube composite film for cholesterol biosensor. *Anal Biochem* 383:194–199
93. Lu L, Hu Y, Chang C, Chen W (2011) Carbon nanotubes engineering assisted by natural biopolymers. In: Yellampalli S (ed) *Carbon nanotubes – polymer nanocomposites*. InTech, Rijeka, pp 15–35
94. Serra PA (ed) (2010) *Biosensors*. InTech, Vukovar
95. Kumar CSSR (ed) (2007) *Nanomaterials for biosensors (nanotechnologies for the life sciences)*. Wiley-VCH, Weinheim
96. Itkis ME, Borondics F, Yu A, Haddon RC (2006) Bolometric infrared photoresponse of suspended single-walled carbon nanotube films. *Science (NY)* 312:413–416
97. Ajayan PM, Terrones M, de la Guardia A, Hue V, Grobert N, Wei BQ et al (2002) Nanotubes in a flash—ignition and reconstruction. *Science (N Y)* 296:705
98. Singamaneni S, Shevchenko V, Bliznyuk V (2006) Unusual ignition behavior of polyurethane/carbon nanotube composites with a He–Ne laser excitation (632.8 nm) during micro-Raman spectroscopy. *Carbon* 44:2191–2195
99. Pradhan B, Setyowati K, Liu H, Waldeck DH, Chen J (2008) Carbon nanotube-polymer nanocomposite infrared sensor. *Nano Lett* 8:1142–1146
100. Sarker BK, Arif M, Khondaker SI (2010) Near-infrared photoresponse in single-walled carbon nanotube/polymer composite films. *Carbon* 48:1539–1544
101. Ferrer-Anglada N, Kaempgen M, Roth S (2006) Transparent and flexible carbon nanotube/polypyrrole and carbon nanotube/polyaniline pH sensors. *Physica Status Solidi (b)* 243:3519–3523